2018 International Conference on Machining, Materials and Mechanical Technologies

IC3MT 2018

Proceedings

19th – 22nd September, 2018, Rex Hotel, Ho Chi Minh City, Vietnam

WELCOME MESSAGE

Prof. Dr. Nguyen Thanh Nam

> - *Chair of the 3rd International Conference of Machining, Materials, and Mechanical Technologies, IC3MT2018.*
> - *Director of the DCSELAB, HCMUT, VNU-HCMC, Vietnam.*

Distinguished Guests and Participants:

Today, we have a great honor to welcome all of you to the 3rd International Conference of Machining, Materials, and Mechanic al Technologies (2018 IC3MT) that is co-organized by our three initial members: the National Key Laboratory of Digital Control and System Engineering (DCSELAB), Ho Chi Minh University of Technology, VNU - HCM, Vietnam, the Japan Society of Precision Engineering (JSPE), Japan and the National Central University (NCU), Taiwan. The 2018 IC3MT conference in Rex Hotel (http://www.rexhotelvietnam.com/) Ho Chi Minh City, Vietnam is the 3rd conference that is a continuous succession of the 1st and the 2nd conference of IC3MT in 2014 and 2016 held in Taipei capital, Taiwan, and Matsue City, Japan.

Researches and studies on the 3M (Machining, Material and Mechanical Technology) that have advanced considerably on the last decades through many dedicated individuals and teams efforts of our community, are impacted directly nowadays by the industrial revolutions 4.0 and might be extending into various fields in both science and engineering. With the extending purpose, DCSELAB is honored together with Japan Society of Precision Engineering (JSPE) and the National Central University, Taiwan to organize this conference as well as to devote all of our effort to the common success of our community. We have a strong belief that this conference will be an occasion for our experts and colleagues to come closer together to discuss on 3M researches and applications. The conference is also intended to provide a forum for researchers and experts of all around the world to exchange all the state-of-the-art Machining, Material, and Mechanical Engineering researches and development. In addition, this conference is also a good chance for us to enhance the network of our collaboration and solidarity forever.

We do hope that the successful results of the conference will significantly contribute the improvement, the application and the real effect of our researches on Machining, Material, and Mechanical Engineering Technology to develop our community.

Finally, I wish all of you, colleagues, guests and participants of the IC3MT 2018 conference, have a good time and wonderful experiences at Ho Chi Minh City, the most dynamic large city of Vietnam.

Best wish to all of you and your family!
Thank you.

Prof. Dr. NGUYEN Thanh Nam
Chair of the Third International Conference of Machining, Materials, and Mechanical Technologies, IC3MT 2018

COMMITTEES

Advisory Committees

BANH, Tien Long	Hanoi University of Science and Technology, Vietnam
LIU, De-Shin	National Chung Cheng University, Taiwan
LIN, Ta-Hui	National Cheng-Kung University, Taiwan
NGUYEN, Hay	Nong Lam University Ho Chi Minh City, Vietnam
USUKI, Hiroshi	University of Tokyo, Japan
CHEN, Ching-Yao	National Chiao Tung University, Taiwan

Technical Committees

AYANO, Takashi	Kurume National College of Technology, Japan
CHEN, Kuan-Yu	Chung Yuan Christian University, Taiwan
CHIOU, Shean-Juinn	National Chung Hsing University, Taiwan
CHIOU, Yuang-Cherng	National Sun Yat-Sen University, Taiwan
CHUNG, Chih-Ang	National Central University, Taiwan
FUH, Yiin-Kuen	National Central University, Taiwan
HSIAU, Shu-San	National Central University, Taiwan
HUNG, Jung-Chou	Feng Chia University, Taiwan
HWANG, Yean-Ren	National Central University, Taiwan
INOUE, Takashi	Daido Institute of Technology, Japan
JANG, Shian-Ching	National Central University, Taiwan
KANEEDA, Toshiaki	Okayama University of Science, Japan
LEE, Shuo-Jen	Yuan Ze University, Taiwan
LIN, Chih_Kuang	National Central University, Taiwan
LAI, Jiing-Yih	National Central University, Taiwan
MATSUMURA, Takashi	Tokyo Denki University, Japan
LIN, Yan-Cherng	Nan Kai University of Technology, Taiwan
LIN, Jing-Chie	National Central University, Taiwan
OKADA, Akira	Okayama University, Japan
LIN, Shih-Chieh	National Tsing Hua University, Taiwan
OKADA, Masato	University of Fukui, Japan
LIN, Shih-Chie	National Central University, Taiwan
OKAMOTO, Yasuhiro	Okayama University, Japan
OKUDA, Koichi	University of Hyogo, Kobe, Japan
SASAHARA, Hiroyuki	Tokyo University of Agriculture and Technology, Japan
SATO, Masahiko	Tottori University, Japan
SAWA, Takekazu	Shibaura Institute of Technology, Japan
SEKIYA, Katsuhiko	Hiroshima University, Japan
SHEU, Dong-Yea	National Taipei University of Technology, Taiwan
SUGINO, Tadanori	Oshima National College of Maritime Technology, Japan

TSAI, Hai-Ping	National Central University, Taiwan
WANG, A-Cheng	Chien Hsin University of Science and Technology, Taiwan
WAKABAYASHI, Toshiaki	Kagawa University, Japan
YAMAMURA, Kazuya	Osaka University, Japan
YAN, Biing-Hwa	National Central University, Taiwan
VO, Tuyen	Ho Chi Minh City University of Food Industry, Vietnam
YAMAGUCHI, Kenji	National Institute of Technology, Yonago College, Japan
NGUYEN, Huu Loc	Ho Chi Minh University of Technology, Vietnam
LE, Hieu-Giang	Ho Chi Minh University of Technology and Education, Vietnam
HO, Pham-Huy-Anh	Ho Chi Minh University of Technology, Vietnam
LE, Thanh Long	Ho Chi Minh University of Technology, Vietnam
NGUYEN, Duy Anh	Ho Chi Minh University of Technology, Vietnam
LE, Khanh Dien	DCSELAB-Ho Chi Minh University of Technology, VNU-HCM, Vietnam
TRAN, Ngoc Huy	Ho Chi Minh University of Technology, Vietnam

Secretariat

NGUYEN, Huy Bich	Nong Lam University-HCMC, Vietnam
HO, Jeng - Rong	National Central University, Jhongli, Taiwan
KATSUHIKO, Sekiya	Hiroshima University, Japan
LE, Thanh Long	Ho Chi Minh University of Technology, Vietnam

Local Organizing Committees

VO, Thi Thanh Huong	DCSELAB-Ho Chi Minh University of Technology, VNU-HCM, Vietnam
NGUYEN, Thi Bao Tran	DCSELAB-Ho Chi Minh University of Technology, VNU-HCM, Vietnam
DO, Thi Thu Hien	DCSELAB-Ho Chi Minh University of Technology, VNU-HCM, Vietnam
HUYNH, Thi Thanh Truc	DCSELAB-Ho Chi Minh University of Technology, VNU-HCM, Vietnam
LAI, Thi Xuan Dao	DCSELAB-Ho Chi Minh University of Technology, VNU-HCM, Vietnam
NGUYEN, Thi Yen Ngoc	DCSELAB-Ho Chi Minh University of Technology, VNU-HCM, Vietnam
THIEU, Thi Tuyen	DCSELAB-Ho Chi Minh University of Technology, VNU-HCM, Vietnam
LE, Thanh Long	Ho Chi Minh University of Technology, Vietnam

CONFERENCE SCHEDULE

Tuesday, September 18, 2018

Registration desk open 15:00 – 18:00

Wednesday, September 19, 2018

Registration desk open 07:30 – 09:00 **Opening ceremony 09:00 – 09:40** Welcome remarks from Prof. Nguyen Thanh Nam, DCSELAB-HCMUT, VNU-HCM, Vietnam Welcome remarks from Prof. Jyh-Chen Chen, National Central University, Taiwan Welcome remarks from Prof. Keiji Yamada, Hiroshima University, Japan Welcome speech by invited guest Photo session: 9.40-9.50
Coffee break
Keynote Lecture 1 10:10 – 10:50 Prof. Chih-Kuang Lin (National Central University, Taiwan) "Effects of Flexural Deformation on the Functional Properties of Conductive and Encapsulation Thin Films in Flexible Electronics"
Keynote Lecture 2 10:50 – 11:30 Dr. Naruhiro Irino (Dmg Mori Co. LTD., Japan) "On-machine Measurment Technology for Machine Tools"
Keynote Lecture 3 11:30 – 12:10 Prof. Nguyen Thanh Nam (DCSELAB-Ho Chi Minh University of Technology, VNU-HCM, Vietnam) "An Overview of Study and Application of Incremental Sheet Forming (ISF) Technology Over the Current Decade in Vietnam"
Lunch (Rex Hotel)

PART I (13:30-15:10)			
Section I	**Section II**	**Section III**	**Section IV**
Chair: Takashi Inoue Co-Chair: Yasuhiro Okamoto In detail for each session	Chair: Hidetake Tanaka Co-Chair: Hai-Ping Tsui In detail for each session	Chair: Jeng-Rong Ho Co-Chair: Huy-Bich Nguyen In detail for each session	Chair: Hiromichi Toyota Co-Chair: Duy Anh Nguyen In detail for each session

Coffee Break

PART II (15:30-17:10)			
Section I	**Section II**	**Section III**	**Section IV**
Chair: Hiroyuki Sasahara Co-Chair: Kazuhito Ohazhi In detail for each session	Chair: Jing-Chie Lin Co-Chair: Takekazu Sawa In detail for each session	Chair: Chih-Kuang Lin Co-Chair:Togo Shinonaga In detail for each session	Chair: Yasuo Yamane Co-Chair: Truong Quoc Thanh In detail for each session

Thursday, September 20, 2018

Part III (08:30-10.10)			
Section I	**Section II**	**Section III**	**Section IV**
Chair: Keiji Yamada Co-Chair: Masahiro Anzai In detail for each session	Chair: Sheng-Long Lee Co-Chair: Le The Truyen In detail for each session	Chair: Chih-Ang Chung Co-Chair: Thanh-Long Le In detail for each session	Chair: Chung-Jen Tseng Co-Chair: Ly Hung Anh In detail for each session

Coffee Break			
Part IV (10h30-12h10)			
Section I	**Section II**	**Section III**	**Section IV**
Chair: Ryutaro Tanaka Co-Chair: Vu Anh Duy Nguyen In detail for each session	Chair: Masato Okada Co-Chair: Shinfuku Nomura In detail for each session	Chair: A-Cheng Wang Co-Chair: Koichi Okuda In detail for each session	Chair: Cho Jong-Rae Co-Chair: Phu Thuong Luu Nguyen In detail for each session
Lunch (Rex Hotel)			
Part V (13:00-14:20)			
Section I	**Section II**	**Section III**	**Section IV**
Chair: Tadanori Sugino In detail for each session	Chair: Jiing-Yih Lai Co-Chair: Ju-Yi Lee In detail for each session	Chair: Shu-San Hsiau Co-Chair: Chatchapol Chungchoo In detail for each session	Chair: Bernard Haochih Liu Co-Chair: Nguyen Huu Tho In detail for each session
Part VI (14:20-16:00)			
Section I	**Section II**	**Section III**	**Section IV**
Chair: Ching-Shiow Tseng Co-Chair: Huy-Hoang Pham In detail for each session	Chair: Chia-Wen Tsao Co-Chair: Kenji Yamaguchi In detail for each session	Chair: Lih-Wu Hourng Co-Chair: Chung-Neng Huang In detail for each session	Chair: Jai Hyuk Hwang Co-Chair: Jyh-Chyang Renn In detail for each session
Coffee Break			
Part VII (16:15-17:55)			
Section I	**Section II**	**Section III**	**Section IV**
Chair: Yu-Ren Wu Co-Chair: Kyoungjin Kim In detail for each session	Chair: Akira Okada Co-Chair: Tatsuaki Furumoto In detail for each session	Chair: Chao-Yaug Liao Co-Chair: Bui Trong Hieu In detail for each session	Chair: Choi Hyeung-Sik Co-Chair: Tran Ngoc Huy In detail for each session
Gala dinner 18:45-21:30			

Friday, September 21, 2018

Field Trip 08:00 – 17:00

KEYNOTE LECTURE

10:10 - 10:50, Wednesday, September 19, 2018
Conference hall – 2nd floor – East wing

Prof. Chih-Kuang Lin

Effects of Flexural Deformation on the Functional Properties of Conductive and Encapsulation Thin Films in Flexible Electronics

Chih-Kuang Lin
Department of Mechanical Engineering, National Central University, Taiwan

Abstract

Flexible electronic devices have had a great potential for widely novel applications as they can conform to a desired shape, or flex during their use. As organic semiconducting materials have the ability to flex such that they are the key materials in flexible electronic devices such as organic light-emitting diode (OLED), organic photovoltaic (OPV), and organic thin-film transistor (OTFT). In a typical flexible electronic assembly (e.g. in OLED and OPV), transparent conductive thin-film electrode and encapsulation thin-film barrier are two of the major components. A highly transparent, conductive electrode is needed for light transmitting and an effective encapsulation barrier is needed to protect the device from exposure to the environment. In practical applications of such flexible electronic devices, they might be subjected to long-term static and/or cyclic flexural deformation which may cause damages in their components and degrade their performance. In particular, flexural-deformation induced damages (e.g. microcracking and/or delamination) would reduce the electronic conductance of transparent conductive thin-film electrode and increase exposure to water vapor and oxygen leading to adverse oxidation of functional layers. In this regard, structural reliability is one of the greatest challenges which must be addressed prior to wide spread commercial application of flexible organic devices. For this reason, it is necessary to investigate the mechanical behavior of transparent conductive thin film and encapsulation thin film for use in flexible electronic devices and how their functional properties are affected, when subjected to long-term static and/or cyclic flexural deformation. In this paper, we will mention about the recent research results of the effects of flexural deformation on the electrical conductance of a transparent indium tin oxide (ITO) thin film and on the encapsulation properties of a barrier thin film for flexible organic optoelectronics are presented. In particular, change of electrical resistance of the given ITO thin film is characterized for various flexural loadings and correlated with the failure mechanism. Water vapor transmission rate (WVTR) of the given barrier film is measured after various cyclic bending conditions to characterize the degradation in encapsulation performance. Finite element models are also developed to simulate the flexural behavior and provide an insight into understanding the failure mechanisms that cause the change in electrical conductance of ITO thin film and in water transportation resistance of barrier thin film.

About the Speaker

Chih-Kuang Lin is a Distinguished Professor at the Department of Mechanical Engineering, National Central University, Taiwan. He recieved his Ph.D in Physics from University of Illinois at Urbana-Champaign (USA). He is a recipient of numerous awards and honorary appointment. His expertise include: fatigue, fracture, and creep analysis, mechanical properties of materials, stress analysis, flexural behavior of functional thin films in flexible electronics, thermal and residual stresses in laser additive manufacturing process, thermal and residual stresses in welding process.

KEYNOTE LECTURE

10:50 - 11:30, Wednesday, September 19, 2018
Conference hall – 2nd floor – East wing

Dr. Eng, Naruhiro Irino

On-machine Measurement Technology for Machine Tools

Naruhiro Irino
DMG Mori Co., Ltd. Experimental Development

Abstract

Measurement with precision is always the most important procedure of any process. This keynote paper introduces two measurement technologies for machine tool. First, on-machine three dimensional shape measurement method is adopted for large-sized bevel gears. This method is also possible to apply to various kinds of 3D surfaces manufactured on the 5 axis-CNC machine tool as well. Next, the paper also mentions about the two dimensional motion trajectory thermal deformation measurement technology using a tracking interferometer is applied for machining center. This method is possible to visualize the thermal deformation, in two-dimensional plane on a machine tool.

About the Speaker

Naruhiro Irino is the Doctor graduated from Chuo University Graduate School of Science and Engineering. Since 2016, he has been the General Manager, Development HQ, Experiment Department of DMG MORI CO., LTD. His research interests include: Milling operations use an automated test and evaluation system; Finish-milling operations consider the sensor's transmissibility, Simulation of machine process interaction with flexible mulit-body simulation.

KEYNOTE LECTURE

11:30 - 12:10, Wednesday, September 19, 2018
Conference hall – 2nd floor – East wing

Prof. Nguyen Thanh Nam

An Overview of Study and Application of Incremental Sheet Forming (ISF) Technology Over The Current Decade In Vietnam

Nguyen Thanh Nam
DCSELAB- Ho Chi Minh City University of Technology, VNU-HCM, Vietnam

Abstract

Although the Incremental Forming Sheet technology was invented by Leszak in 1967 via the US patent "Apparatus and Process for Incremental Dieless Forming", the state of the art forming sheet technology was systematically studied by researchers in the world from 2000. Especially in our country, National Key Laboratory of Digital Control and System Engineering (DCSElab) only studied the ISF technology continuously from 2008 up to now with some modest results. This paper aims to provide an overview of study and application of ISF of our own laboratory through the last decade. In recognition of the application of ISF in Vietnam, we studied on the influences of forming parameters to the formability, springback phenomena, productivity and the quality of the surfaces of sheet products of 3 typical materials that are very popular in industry: A1050 H14, SS330 and SUS304. For the hard material such as Titanium, to improve the formability of the sheet workpiece, the application of Hot Single Point Incremental Forming (Hot SPIF) was carried out with satisfactory results. Finally, the application of Two Point Incremental Forming (TPIF) in forming 3D hollow bust of typical products were also performed. We consider that DCSElab has a certain pace in study and application of ISF technology in over the last ten years.

About the Speaker

Nguyen Thanh Nam is a Professor at Ho Chi Minh City University of Technology, Vietnam National University. He received his Ph.D. in mechanical engineering from Technical University, Sofia, Bulgaria. He is currently a director of the National Key Lab of Digital control and Systems Engineering. Up to now, he co-authored 7 books and published over 100 papers on national and international journals and conference proceedings. His current research interests include designed and manufactured with the aid of computers, Automation, Modeling and Simulation of industrial equipment systems.

SECTION SCHEDULE

Wednesday, September 19, 2018

Part	Section I	Section II	Section III	Section IV
	Chair: Takashi Inoue Co-Chair: Yasuhiro Okamoto	Chair: Hidetake Tanaka Co-Chair: Hai-Ping Tsui	Chair: Jeng-Rong Ho Co-Chair: Huy-Bich Nguyen	Chair: Hiromichi Toyota Co-Chair: Duy Anh Nguyen
Part I **(13:30-15:10)**	2305, Effects of Peheating Temperature at Primary Shear Zone in Laser Assisted Milling Process, Jamkamon Kamonpong*, Keiji Yamada, Katsuhiko Sekiya, Ryutaro Tanaka	2352, Smoothing of Hole Bottom Surface by Guiding Large-area Electron Beam with Magnet, Mitsuhiro Kimura*, Togo Shinonaga, Akira Okada, Motohiro Inoue	2391, Numerical Investigation of the Flow Inside and Around a Spherical Fish Cage, Cuong Mai Bui*, Thinh Xuan Ho, Loc Huu Khieu	2334, Combined Cyclic-Static Bending Effect on the Encapsulation Properties of a Barrier Thin Film for Flexible Organic Optoelectronic Devices, Dinh-Phuc Tran*, Chih-Kuang Lin, Bao-Dong To
	2325, A Study on Micro Groove Cutting of TiAl Alloy, Yuma Iwatani*, Koichi Okuda, Masayuki Nunobiki	2436, Effect of Cathodes Modified by Ag-Deposition on the Charging-discharging of Zinc Air Batteries, Choung-Yheo Chiang, Jing-Chie Lin*, Yee-Cheng Lee, Mao-Chia Huang, Ching-Chen Wu	2300, Numerical Investigation of the Thermocapillary Migration of a Water Droplet in a Microchannel by Applying Heat Source, Thanh-Long Le*, Jyh-Chen Chen, Huy-Bich Nguyen	2519, Study on the Design of Bamboo Grinding Machine, Vo Tuyen*, Le Khanh Dien, Tran Trong Hy, Nguyen Tan Hung
	2329, Surface Characteristic on Curved Grinding of Titanium Alloy with Coolant Supplying from Inner Side of Grinding Wheel, Sumito Toyokawa*, Nagatoshi Nakatsuka, Atsushi Kusakabe, Hiroyuki Sasahara	2360, The Effects of Cu, Zn on the Solution Temperature and Quenching Sensitivity of Al-Zn-Mg-Cu Alloys, Albert Chiu*, Sheng-Long Lee	2397, Recovery at an Oblique Interface in Recovery-based Discontinuous Galerkin for Diffusion, Phuc T. Huynh*, Loc H. Khieu	2442, Research on Application of 3D Parametric Software for Design and Shaping of Bus Frame Structure, Nguyen Thanh Cong*
	2333, Effect of Pick Feed on Machining Characteristic of Up Cutting in the High-efficient Machining by Small Diameter Radius End Mill, Hisaaki Nakai*, Takekazu Sawa, Masahiro Anzai	2359, Laser-shock Peening on Tool Steel and its Shock-pressure Measurement, Yu-Chi Shih, Jeng-Rong Ho*	2410, Experimental Study of Circular Inlets Effect on the Performances of Gas-liquid Cylindrical Cyclone Separators (GLCC), Ho Minh Kha*, Nguyen Thanh Nam, Vo Tuyen, Nguyen Tan Ken	2505, Study on a Neural Network for Position Determination Using Optical Sensor, Thieu Quang Minh Nhat*, Hyeung-Sik Choi, Joono Sur, Jinil Kang, Hyun-Joong Son
	2341, Evaluation Method for Machining Fluids Using Cutting Force in Micro Feed End Milling, Tomohiko Kitamura*, Ryutaro Tanaka, Yasuo Yamane, Katsuhiko Sekiya, Keiji Yamada	2355, Effect of Tib2 on the Microstructure, Mechanical and Casting Properties of A201 Alloys, Denny Chen*, Albert Chiu, Sheng-Long Lee	2517, A Research on the Design a Bamboo Powder Drying Machine, Tran Van Hung*, Le Khanh Dien, Vo Tuyen	2340 (Poster), The Role of Kaempferol Treatments in Alternating Murine Tibia Strength, Hanjong Kim, Changwan Han, Seonghun Park*

Part	Section I	Section II	Section III	Section IV
	Chair: Hiroyuki Sasahara Co-Chair: Kazuhito Ohazhi	Chair: Jing-Chie Lin Co-Chair: Takekazu Sawa	Chair: Chih-Kuang Lin Co-Chair: Togo Shinonaga	Chair: Yasuo Yamane Co-Chair: Truong Quoc Thanh
Part II (15:30-17:10)	2317, Effect of Face-Milling Process Parameters on Deformation of AISI304, Masahiro Hagino*, Kouji Ikeuchi, Hiroshi Usuki, Takashi Inoue	2343, Decorative Film Forming by Inkjet Printing with Gold Nanoparticles for Crafts, Mitsugu Yamaguchi*, Shun Kambayashi, Satoshi Sakamoto, Yasuo Kondo, Kenji Yamaguchi	2304, Time-frequency Analysis of Vibration in Curved Surface Milling Based on Hilbert-Huang Transform, Muizuddin Azka*, Keiji Yamada, Mahfudz Al-Huda, Yean-Ren Hwang, Ryutaro Tanaka, Katsuhiko Sekiya	2318, Effect of Crucible and Crystal Rotations on the Solute Distribution in Large Size Sapphire Crystals During Czochralski Growth, Tran-Phu Nguyen*, Jyh-Chen Chen
	2331, Machinability of Unwoven Fabric Material by End-mill, Hidetake Tanaka*, Kyosuke Takabayashi	2346, Deformation of the Material During Bending in Cold-stamping Method, Hoang Quoc Hung*, Luu Thanh Tung	2319, Identification of Vibration Parameters of Mechanical System Utilizing Low-cost MEMS Accelerometers, Khanh Duong Quang*, Huong Vuong Thi, Van Anh Luu	2311, Hole Recognition and Removal on Mold Base for the Application in Mold Flow Analysis, Pei-Pu Song, Jiing-Yih Lai*, Chia-Hsiang Hsu, Yao-Chen Tsai
	2381, Influence of Grinding Atmosphere on Grinding Characteristics of CFRP, Shingo Okazaki*, Yifan Jiang, Hiroyuki Kodama, Hiroyuki Yoden, Kazuhito Ohashi	2347, Surface Roughening of Silicon Wafer Solar Cell by Using ECDM Method, Hai-Ping Tsui*, Kuang-Hua Chang, Biing-Hwa Yan	2353, Simulate and Evaluate the Application Range of Energy Recovery Circuits Generated by Mechanical Vibration through Bond-Graph, Duong Quang Thien, Nguyen Thi Hai Van*	2315, Modeling and Simulation of Brine Droplets Using the Volume of Fluid Method: Ambient Temperature Effect, Bo-Hsuang Wu, Chih-Ang Chung*
	2384, Cutting Force Changes During One Cut in End Milling with a Throw-away Insert - difference between Up-cut and Down-cut, Kota Matsuda*, Ryutaro Tanaka, Katsuhiko Sekiya, Keiji Yamada	2523, Experimental and Numerical Studies on Rotary Friction Welding of Ti-6Al-4V, Ho Thi My Nu*, Luu Phuong Minh, Nguyen Huu Loc	2366, DEM Simulation of Particle Segregation on a Vertical Vibrating Screen, Shih-Hao Chou*, Shu-San Hsiau	2301, Contact Force Analysis for a Variable-Pitch Rotor Pair in Twin-Screw Vacuum Pump Generating by CNC Turning Process, The Van Tran, Thanh-Long Le, Trung-Tin Pham*
	2400, Effect of Cutting Liquid on Tool Wear in Turning of Sintered Steel, Hideo Takino*, Masashi Ota, Shutaro Yamamoto		2524, Analysis and Experiment Design of Damper and Cutting Parameters on Spindle Vibration of CNC Router, Huu Loc Nguyen, Van Thuy Tran, Hoang Hiep Nguyen	2383, Designing and Simulating a Flexible Mechanical System, Phu Thuong Luu Nguyen*

Thursday, September 20, 2018

Part	Section I	Section II	Section III	Section IV
Part III (08:30-10:10)	Chair: Keiji Yamada Co-Chair: Masahiro Anzai	Chair: Sheng-Long Lee Co-Chair: Le The Truyen	Chair: Chih-Ang Chung Co-Chair: Thanh-Long Le	Chair: Chung-Jen Tseng Co-Chair: Ly Hung Anh
	2322, Investigation on Osteoconductivity of EDMed Titanium Alloy Surface in Deionized Water,	2510, A Big Data Analysis Technology for Catching Usual/Unusual State of Cutting Tool, Yasuo Kondo*, Mitsugu	2313, Influence of Forming of Warm Oxide Layer on Hydrophilicity, Akihiro Takemura*, Kazuhisa Yuki	2338, A Semi – Active Controller for an Aircraft Landing Gear Equipped Magnetorheological

Part	Section I	Section II	Section III	Section IV
	Yuta Iida*, Keita Fujii, Togo Shinonaga, Akira Okada	Yamaguchi, Satoshi Sakamoto		Damper, Luong Quoc Viet*, Jai-Hyuk Hwang
	2335, High-speed Wire EDM by Newly Developed Copper-Zirconium Wire Electrode, Ayaka Kuwada*, Naokuni Muramatsu, Kazuhiro Nomura, Yasuhiro Okamoto, Akira Okada	2369, Synthesizing Cubic Diamond Crystal Using DC Plasma Jet CVD, Hiromichi Toyota, Xia Zhu, Ryoya Shiraishi, Kazuto Nakajima*, Yukiharu Iwamoto, Shinfuku Nomura	2321, Impact of Ar/He Purge Gas Flow, Heater and Post-chamber Length, and Draw Speed on Rapid Drawing and Cooling of Silica Glass Fiber in Optical Fiber Draw Furnace, Gia Ginelle Carandang*, Kyoungjin Kim	2342, Thermo-mechanical Analysis of Laser Additive Manufacturing for Metals, Hsuan-Hao Shih, Chih-Kuang Lin*
	2388, Study on Improvement of Wear Resistance for Zirconia by Large-area EB Irradiation, Togo Shinonaga*, Mitsuhiro Kimura, Motohiro Inoue, Akira Okada	2377, Simultaneous Synthesis of Diamond and Hydrogen, Ryoya Shiraishi*, Hiromichi Toyota, Shinfuku Nomura, Kazuto Nakajima, Xia Zhu, Yukiharu Iwamoto	2375, CFD Study on the Cold Flow Model of Dual Fluidized Bed System Applied for Biomass Gasification, Cong-Binh Dinh*, Shu-san Hsiau, Meng-Yuan Tsai, Chien-Yuan Su	2382, Design and Analysis of a Flexible Cantilever by Using Different Sections, Phu Thuong Luu Nguyen*
	2323, Influence of Molten Area on Joining Strength in Micro-welding of Glass by Picosecond Pulsed Laser, Yuta Ogino*, Zhiyong Ouyang, Yasuhiro Okamoto, Togo Shinonaga, Akira Okada	2370, 3D Printed AFM Fluid Cell and Its Applications on Live Biological Samples, Nguyen Thi Phuong Linh*, Bernard Haochih Liu	2376, Numerical Simulation of the Heat and Mass Transfer During Czochralski Silicon Crystal Growth under the Application of Crystal-crucible Iso-rotation, Thi Hoai Thu Nguyen*, Jyh-Chen Chen, Chieh Hu, Chun Hung Chen	2405, Study on Analysis and Design of An VIAM-AUV200 Autonomous Underwater Vehicle (AUV), Ngoc-Huy Tran, Thanh-Hai Chau*, Quang-Vinh Dinh
	2349, Effects of the Helical Passageways in Complex-hole Finishing by Abrasive Flow Machining, A-Cheng Wang*, Ken-Chuan Cheng, Kuan-Yu Chen, Yan-Cherng Lin		2411, Experimental Study of Square Inlets Effect on the Performances of Gas–Liquid Cylindrical Cyclone Separators (GLCC), Ho Minh Kha*, Nguyen Thanh Nam, Vo Tuyen, Nguyen Tan Ken	2457, Adaptive Multilayer T-S Fuzzy Controller for Nonlinear SISO System Optimized by Differential Evolution Algorithm, Cao Van Kien, Ho Pham Huy Anh, Nguyen Ngoc Son
Part IV (10:30-12:10)	Chair: Ryutaro Tanaka Co-Chair: Vu Anh Duy Nguyen	Chair: Masato Okada Co-Chair: Shinfuku Nomura	Chair: A-Cheng Wang Co-Chair: Koichi Okuda	Chair: Cho Jong-Rae Co-Chair: Phu Thuong Luu Nguyen
	2316, Characteristics of Cutting Resistance in Microendmilling of Titanium Alloy, Shinya Fujimoto*, Koichi Okuda, Masayuki Nunobiki	2504, Effect of the Type of Grinding Wheel on the Surface Characteristic of Titanium Alloy with Internal Coolant Supply, Nagatoshi Nakatsuka*, Sumito Toyokawa, Atsushi Kusakabe, Shinya Nakatsukasa, Hiroyuki Sasahara	2386, Structural Dynamics Analysis of 3-U CubeSat, Minh Vu Chau, Bich Hien Vo*	2435, Effect of Steam to Fuel Ratio on a Proton Conducting Solid Oxide Fuel Cell Hybrid System Fueled by Methanol, Ethanol, Isooctane and Methane, Sasmoko*, Chung-Jen Tseng, Cheng-Hao Yang, Wen-Sheng Chang, I.N.G. Wardana
	2506, Diamond Fly Cutting Applied to Improve Form Accuracy by In-process Measurement and Control on an Ordinary Milling Machine, Jinhui Wang*,	2350, Manufacturing of Cycloid Tooth Profile with Threaded Wheel Hobbing and Grinding for RV and Cyclo Drives, Ling-Chiao	2433, Study of Design and Manufacture for One-line Rice Color Sorting Machine, Nguyen Tan Y*, Le Thanh Son, Tran Quang Tuyen,	2508, Performance Characteristics of Small Diesel Engine Using Different Geometry Intake Parts, Le Viet Hung*, Do

Part	Section I	Section II	Section III	Section IV
	Takanori Yazawa, Guochen Gu, Tomonori Kato, Tatsuki Otsubo	Chang*, Shyi-Jeng Tsai, Jason Wei, Pin-Ching Chen	Nguyen Huy Bich, Nguyen Truong Thinh	Van Dung, Nguyen Anh Thi
	2420, Possibility of Repeated Recycle of Water-soluble Cutting Fluids, Kenji Yamaguchi*, Mitsugu Yamaguchi, Yasuo Kondo, Satoshi Sakamoto	2356, High-quality Machining of CFRP with DLC-coated and Diamond-coated End Mills, Shota Tanaka*, Akira Hosokawa, Goshi Hoshino, Tomohiro Koyano, Tatsuaki Furumoto, Yohei Hashimoto	2461, Optimal Dynamic Routing for 2 Forklifts in Narrow-aisle Racking Warehouse, Ngoc Cuong Truong*, Truong Giang Dang, Duy Anh Nguyen	2447, Simulation and Experiment of Tig Welding Assisted by Hybrid Friction Stir Welding Between Steel and Aluminum, Truong Minh Nhat*, Luu Phuong Minh, Truong Quoc Thanh, Mai Dang Tuan
	2426, Optimum Cutting Conditions of Materials Using Coated Radius End Mill, Nobunao Kato*, Masahiro Anzai, Takekazu Sawa	2396, Development of a Decision Support System for Selection of Optimal Machining Parameters and Tool Inserts in Turning Process, Tho Nguyen*, Tho Trinh, Hung Ly, Nhiem Tran, Nghi Huynh, Thanh-Long Le	2412, A Research on a New Structure of Forming Tool for Single Point Incremental Forming (SPIF), Le Khanh Dien*, Le Khanh Tan, Vo Tuyen, Nguyen Thanh Nam	2409, Motion Analysis and Fabrication of a Low-Cost Underwater Thruster Using Magnetic Coupling, Ngoc-Huy Tran, Thanh-Hai Chau, Quoc-Tien-Dung Tran
	2362, Fundamental Study on Curved Hole by EDM Drilling Using a Suspended Ball Electrode into Practical Materials, Kohei Ota*, Shuoxun Li, Akira Okada, Yasuhiro Okamoto, Atsushi Yamaguchi	2515, Research on the Design of the Laser Beam in SLS Rapid Prototyping Machine, Vo Tuyen*, Tran Trong Hy, Le Khanh Dien	2520 (Poster), The Waste Remover in Aquaculture Ponds, Le The Truyen*, Thanh-Long Le	2458, Advanced Speed Control of IPMSM Motor Using Adaptive Neural FOC Approach, Ho Pham Huy Anh, Cao Van Kien, Pham Quoc Khanh
Part V **(13:00-14:20)**	Chair: Tadanori Sugino	Chair: Jiing-Yih Lai Co-Chair: Ju-Yi Lee	Chair: Shu-San Hsiau Co-Chair: Chatchapol Chungchoo	Chair: Bernard Haochih Liu Co-Chair: Nguyen Huu Tho
	2302, Design Modification of Additive Manufacturing Parts Using Texture Information of 3D Model, Tsung-Chien Wu*, Jiing-Yih Lai, Yu-Wen Tseng, Chao-Yaug Liao, Ju-Yi Lee	2413, A Recommendation of Analytical Computing of Stresses and Strains in Single Point Incremental Forming (SPIF), Le Khanh Tan*, Le Khanh Dien, Nguyen Huy Bich, Tran Van Hung	2314, Study of Water Electrolysis by Dual Electrolytes and Cells, Lih-Wu Hourng*, Yun-Tin Chen, Ming-Yuan Lin	2312, Optimal Design of Cam Mechanism for Smallest Size, Pham Huy Hoang*, Le Khanh Dien
	2354, Development of 3D Printable Bone Model with Fracture Lines for Additive Manufacturing Applications, Yu-Wen Tseng, Chao-Yaug Liao*, Idram Irwansyah, Jiing-Yih Lai	2440, The Influence of Magnetic Fiber Orientation on the Electric Properties of Conductive Polymer Composite Material by Using Magnetic-assisted Injection Molding, Chen-Yuan Chung*, Shia-Chung Chen, Kuan-Ju Lin	2348, Optimal Design for a Waste-heat Recyclable Gasifier, Chung-Neng Huang*, Yu-Chang Yen, Shiuh-Ming Chang	2330, Basic Research on Development of Automatic Dental Treatment Equipment, Yusuke Nozaki*, Takanori Yazawa, Tatsuki Otsubo
	2371, A Design of the Recycling System on the Metal Additive Manufacturing, Shu-San Hsiau*, Yi-Lun Xiao, Li-Tsung Sheng	2423, Stability Analysis of a Proximate Time Optimal Controlled Electrostatic Suspension System Using Piezo Actuator, Le The Truyen*, Nguyen Minh Huy, Thanh-Long Le	2374, The Effect of Current Crowding on the Efficiency Droop of Vertical Single-quantum-well Light-emitting Diodes, Quoc-Hung Pham*, Jyh-Chen Chen	2395, A Novel Rotor Profile Generation Method for Claw-type Vacuum Pumps Based on Sealing Line, Trong-Linh Nguyen*, Yu-Ren Wu

Part	Section I	Section II	Section III	Section IV
	2452, A Study on Technology of Latex Rubber Freezing in Manufacturing Standard Vietnamese Rubber 10, Nguyen Huu Hung, Nguyen Ngoc An, Bui Huu Phu	2513, Research on the Powder Lifting Carriage of the SLS Rapid Prototyping Machine, Tran Van Hung*, Le Khanh Dien, Vo Tuyen	2394, Generation of Waves and Their Interaction with a Floating Object for Wave Energy Harvesting, Thinh Xuan Ho*, Phuong Ha, Thanh Quoc Truong, Son Doan Tran	2431, A Study the Gasoline Injection Tester Device for Automobile, Nguyen Huy Bich, Tran Dinh Hy
	2351(Poster), Conical Roll-twisting Process for Fabrication of Archimedes Blades, Sanghu Park, Sungmoon Yang*			
	Chair: Ching-Shiow Tseng Co-Chair: Huy-Hoang Pham	Chair: Chia-Wen Tsao Co-Chair: Kenji Yamaguchi	Chair: Lih-Wu Hourng Co-Chair: Chung-Neng Huang	Chair: Jai Hyuk Hwang Co-Chair: Jyh-Chyang Renn
	2430, Study and Trial Production the Machine That Can Be Continuous Manufacturing Buckypapers, Bui Quang Vinh, Hua Nguyen Dang Thy, Vu Ngoc Long, Do Huu Quyet	2367, Study on High Quality Thermal Stress Cleavage of Thick Sapphire Wafer, Tomoya Kawabe*, Tatsuaki Furumoto, Yohei Hashimoto, Tomohiro Koyano, Yuzo Ochi, Kentaro Oguchi, Yuji Chino, Akira Hosokawa	2444, Apply Twisted Savonius Rotor with Two Deflector Plates in Power Take Off Systems, Cao Dang Long*, Cao Hung Phi, Nguyen Minh Huy, Dao Thanh Liem, Truong Quoc Thanh	2357, An Ultrasound-guided Robotic HIFU Ablation System with Respiration Induced Displacement and Time Delay Compensation, Ching Shiow Tseng*, Chih Yu An, Yung Lun Hsu
Part VI (14:20-16:00)	2432, Experimental Study on Red Dragon Fruits Powder Dried by Spray Drying Technology, Nguyen Huy Bich, Nguyen Tuan Linh	2379, Development and Analysis for a New Compliant XY Micropositioning Stage Applied for Nanoindentation Tester System, Minh Phung Dang, Thanh-Phong Dao, Hieu Giang Le	2441, Behavior of Multi-corner Thin-walled Structure Subjected to Low Velocity Axial Impact Load, Ly Hung Anh*, Ngo Anh Vu	2372, Adaptive Robust Heading Control Design for a New Ray-type Hybrid Underwater Glider, Duc Nguyen Ngoc*, Hyeung-Sik Choi, Jong-Seok Han, Nhat Thieu Quang Minh, Ji-Youn Oh
	2437, Optimal Job Scheduling of Multiple Rail Cranes in Rail Stations with Simulated Annealing Algorithm, Vu Anh Duy Nguyen*, Thanh Hung Ly	2368, Investigation of the Bio-nanomechanical Effects of Citric Acid on Staphylococcus Aureus by 3D Printed AFM Fluid Cells, Nguyen Thi Phuong Linh, Bernard Haochih Liu*	2445, Design and Fabrication of Wave Generator Using an Oscillating Wedge, Phuong Ha*, Liem Thanh Dao, Son Doan Tran, Thanh Quoc Truong	2428, A Measure of Control of Submerging and Surfacing of an Autonomous Underwater Vehicle for Exploring Underwater of Rivers, Le Khanh Dien*, Le Khanh Tan, Tran Ngoc Huy, Pham Huy Hoang, Vo Tuyen
	2455, Develop a Novel Microbiological Product to Process Household Waste in Vietnam, Huynh Quyen, Bui Huu Phu, Nguyen Huu Phep, Truong Quang Vinh	2380, Development of Visual Inspection Using Patterned Area Illumination Method: Simulation for Classifier Based on Deep Learning, Tadanori Sugino*, Kakeru Nakamura, Yasuo Yamane	2454, Design and Implement of a Smart Watering System Used an Unmanned Aerial Vehicle Applicable to Agriculture in Vietnam, Nguyen Van Hoc, Do Phu Loc, Tran Minh Khoi, Pham Manh Cuong, Bui Huu Phu	2373, Design Controller for Time-domain Simulation of Automatic Berthing Operation of an USV, Mai The Vu*, Hyeung-Sik Choi, Ji-Youn Oh, Han Jong Seok
	2522, Study on Rice Husk Husking Machine Improvement, Tran Quoc Nhiem	2439, The Inductance of the Very Short Conductors of Rectangular Cross Section in Program, T. Truong Cong*, L. Fakri Bouchet	2514, Research on the Establishing on the Program of Control of the SLS Rapid Prototyping Machine, Nguyen Thanh Nam, Le Khanh Dien*, Svetlin Anatonov	2404, GPS/INS Integrated Navigation System for Autonomous Robot, Ngoc-Huy Tran, Quoc-Tien-Dung Tran*

Part	Section I	Section II	Section III	Section IV
	2521(Poster), Experimental Operation and Performance Evaluation of Waste Remover in Aquaculture Ponds, Le The Truyen*, Thanh-Long Le			
	Chair: Yu-Ren Wu Co-Chair: Kyoungjin Kim	Chair: Akira Okada Co-Chair: Tatsuaki Furumoto	Chair: Chao-Yaug Liao Co-Chair: Bui Trong Hieu	Chair: Choi Hyeung-Sik Co-Chair: Tran Ngoc Huy
	2364, Microstructure of Built Part Obtained by Powder Bed Fusion Process With Metal, Tatsuaki Furumoto*, Kyota Egashira, Souta Matsuura, Makoto Nikawa	2320, Influence of Tool Feed Conditions on Surface Integrity in Roller Burnishing with Rolling and Sliding Effects, Masato Okada*, Makoto Shinke, Takuya Kitagawa, Tomoaki Inoue, Satoshi Yasutani, Takuya Miura, Masaaki Otsu	2328, A Best Practice Guidelines for Inspecting Precision Machined Parts by Using Several CMMs, Phaireepinas Phimpisan, Chatchapol Chungchoo*	2363, Active Closed-loop Gap Control for Hydrostatic Bearing, Jyh-Chyang Renn*, Guan-Yi Wu
	2378, Precision Polymer Microfabrication of Microfluidic Model for Biological and Environmental Investigations, Chia-Wen Tsao*	2512, Structural Integrity Analysis of the Plate Pack in Plate and Shell Heat Exchanger in High Temperature and Pressure Applications, Hyun-Seok Noh*, Jong-Rae Cho, Seung-Hun Song	2336, A Study on Dynamics Behavior of the Spindle System for Machine Tools, Nguyen Ngoc Nam, Sam-Sang You, Boc Minh Hung, Hwan-Seong Kim	2406, Modeling, Design and Control of Low-cost Remotely Operated Vehicle for Shallow Water Survey, Tran Ngoc Huy, Huynh Tan Dat*, Chau Thanh Hai
Part VII (16:15-17:55)	2453, Research and Develop a Multiple Parameter Monitoring and Control System Applicable for Greenhouse in Vietnam, Nguyen Van Ton, Van Thanh Vinh, Tran Dinh Duong, Le Tuan Anh, Dinh Ngoc Phu, Nguyen Dang Nghia, Bui Huu Phu	2418, Effect of Amorphous Silicon Carbide Interlayer on Diamond-like Carbon Film Quality, Yutaro Kimura*, Xia Zhu, Hiromichi Toyota, Yukiharu Iwamoto, Shinfuku Nomura	2451, Optimization of Milling Process for Improving Technological Performances, Trung-Thanh Nguyen*, Tat-Khoa Doan	2407, Image Processing Method to Classify Objects on Dynamic Conveyor, Ngoc-Huy Tran, Van-Thinh Pham, Nguyen-Hoang-Phuc Le*
	2456, Design and Implement of a Smart Door Lock System Based on RFID Technology, Hoang Ngoc Tuyen, Nguyen Viet Tien, Trinh Ngoc Thanh Bao, Phan Van Phung, Truong Dai Hiep, Bui Huu Phu	2446, Study the Effects of Process Parameters on Surface Quality in Electrochemical Machining, Nhung Nguyen*, Liem Thanh Dao, Thanh Quoc Truong	2339, Incremental Bulging Process for Discontinuous-fiber Thermoplastic CFRP, Tatsuki Ikari*, Keisuke Sato, Hidetake Tanaka	2425, Study on Pest Visualization/Identification by Ultrasound, Masaki Okugumo*
	2518, A Design of Bamboo Plywood Pressing Machine, Nguyen Thanh Nam, Le Khanh Dien*, Hoang Duc Lien, Svetlin Antonov	2448, Research on the Effects Temperature Using Minimum Quantity Lubrication to Tool Wear and Surface Roughness in Turning C45 Steel, Tran Trong Quyet*, Tran Anh Son, Dao Thanh Liem, Truong Quoc Thanh	2516, Research on the Design of the Powder Roller Module in Selective Laser Sintering (SLS) Rapid Prototyping Machine, Tran Trong Hy*, Le Khanh Dien, Vo Tuyen	2459, Identification and Control of Pneumatic Artificial Muscle PAM Manipulator Using Adaptive Fuzzy Sliding Mode Control, Ho Pham Huy Anh, Cao Van Kien, Nguyen Ngoc Son, Nguyen Thanh Nam

TABLE OF CONTENTS

PART II, SECTION IV
Other Topics

PART III, SECTION I
Machining Technology

PART III, SECTION II
Materials Technology

PART III, SECTION III
Mechanical Technology

PART VI, SECTION I

Machining Technology

PART VI, SECTION II

Materials Technology

PART VI, SECTION III

Mechanical Technology

PART VI, SECTION IV

Other Topics

PART I, SECTION I

Machining Technology
(Difficult-to-cut and Free Machining; Non-conventional Machining;
Green Process/Manufacturing; Cutting Mechanisms…)

Effects of Preheating Temperature at Primary Shear Zone in Laser Assisted Milling Process

Jamkamon Kamonpong, Keiji Yamada, Katsuhiko Sekiya, Ryutaro Tanaka
Hiroshima University, 1-4-1 Kagamiyama, Higashi-Hiroshima, Hiroshima, 739-8527, Japan

ABSTRACT

In this paper, temperature was investigated for the laser assisted machining (LAM) of Inconel 718 under different conditions. Besides, cutting forces were also measured to evaluate the effect of laser heating in LAM process, and it was found that the resultant cutting force in LAM was lower than that in the conventional machining. In addition, the influence of cutting temperature to the tool wear and quality of machined surface were also evaluated to compare with the conventional machining process.

Keywords; Laser assisted machining (LAM), Preheating temperature, Milling, Inconel 718

1. Introduction

It is well known that the hot machining technique can improve the machinability of difficult-to-cut materials. This technique needs the external heat source such as induction, plasma, gas torch or laser in order to reduce the refractory of work materials prior to the material removal by cutting tool [1]. Laser assisted machining (LAM) has been widely applied in various machining process, because the laser is a rapid heat source, which has high energy concentration to heat the material locally in the machined zone [2].

The preheating temperature within the machining zone requires the sufficient laser power to significantly reduce the mechanical strength and hardness. In addition, the cutting conditions affect the requiring laser power. It is well known that the hardness of Inconel 718 reduces rapidly when the temperature is higher than 650oC [3] and exhibits significantly reduced tensile strength when the temperature is above 750oC [4]. Whereas, the peak temperature higher than 950oC (recrystallization) would damage the machined surface, because the mechanical properties and microstructure of material are changed [1]. Thus, in order to soften the work materials and avoid the damage from laser heating, the peak heating temperature and preheating temperature at the primary shear zone must be evaluated and controlled.

The goals of this study are to evaluate and control the laser power from the viewpoint on peak and preheating temperature at the primary shear zone of work material in the milling experiment. Furthermore, the influential effects of cutting conditions on resultant force, temperature at the region of tool-chip interface, tool wear and hardness of machined surface are examined to compare the obtained results with conventional machining.

2. Experimental procedure

Two stages of experiment were performed in this study. The first stage, a K-type thermocouple was embedded to measure temperature in the Inconel 718 with the varied laser power irradiated on the surface of workpiece in order to calibrate the laser power for the preheating temperature at primary shear zone of 700oC. In addition, the peak heating temperature was limited below 950oC.

In the second stage, uncoated carbide insert was used in the process of LAM for face milling Inconel 718 in order to compare the cutting performance with conventional machining.

2.1 Calibrating laser power

A diode laser (Laserline LDF 6000-40) with the maximum power of 6.6 kW was used as a heat source. The focusing head was mounted on the spindle head of a vertical milling machine, and the laser beam axis was set at 50o to x-y plane and 45o to y-z plane as show in the Fig. 1 (a). The beam spot of 3.5-4 mm was positioned 2 mm on the surface of workpiece ahead of the cutting point.
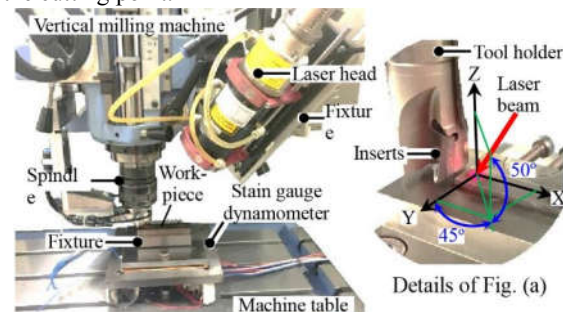
(a) Position of laser head was fixed on milling machine.
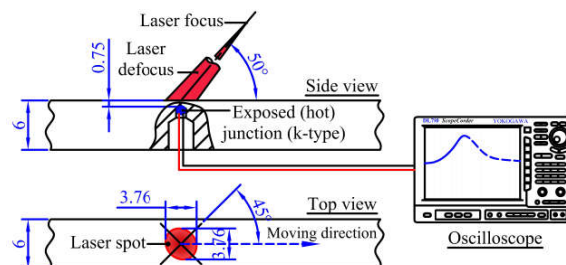
(b) Details of laser assisted machining setup

Fig 1 Schematic illustration of experimental setup

A K-type thermocouple with the diameter of 1.0 mm was inserted into the drilled hole (Ø ≈ 1.2 mm). The hot junction contacted with the hole bottom at the depth 0.75 mm and the thermal electromotive force (EMF) was detected and recorded by oscilloscope as shown details in Fig. 1 (b). In order to evaluate the relationship between the laser power and temperature, the experiments were conducted under the conditions shown in Table 1 and Table 2.

Table 1 Cutting conditions in experiment

Condit-ions	Vc m/ min	Feed (mm/ tooth)	Tool Ø (mm)	Axial depth of cut (mm)	Spindle speed (rpm)
1	30				600
2	50	0.05	16	0.75	1000
3	75				1500

Table 2 Laser power used for calibrating temperature

Table speed (mm/min)	Laser power (W)			
	Level 1	Level 2	Level 3	Level 4
30	119	165	223	313
50	150	190	253	332
75	190	232	310	388

2.2 Laser assisted machining (LAM) experiments

Symmetric face milling tests were performed to evaluate the cutting performance with constant preheating temperature appropriated 700±25oC for all cutting tests. The cutting tool was an uncoated cemented carbide inserts (APKR1003PDR-H IC28, ISCAR). A single insert was mounted onto the tool holder (HM90A-D160-2-C16, ISCAR) in order to avoid the influence of difference in height of cutting edges between teeth and maintain the constant depth of cut (DoC). Inconel 718 was a work materials, which was mounted onto the dynamometer (refer Fig. 1 (a)). The maximum resultant cutting force (FR) was used to observe the performance of preheating temperature, it can be obtained by following equation.

$$F_R = \sqrt{F_x^2 + F_y^2 + F_z^2} \qquad (1)$$

The cutting temperature at the region of tool-chip interface was measured by tool-work thermocouple [5]. The cutting temperature can be derived by test results of calibrated curves as follows,

$$T = 0.0358x^3 - 1.3681x^2 + 66.876x + T_R \quad (2)$$

where, T (oC) is the temperature measured, x (mV) is the EMF from tool-work thermocouple and TR (oC) is the room temperature (≈ 20oC).

The maximum flank wear was measured with a toolmaker's microscope (Mitutoyo). In addition, the hardness on the machined surface was evaluated by Vickers hardness tester (MATSUZAWA). The load in tests was 200g (1.96 N) and the average hardness value was calculated from the fifteen points testing.

It should be noted that prior to the machining experiments, a skin cut of 0.2 mm thickness is done in order to remove any deformities on the surface, and it was sandblasted to keep same surface absorption as in the process of calibrating laser power.

3. Results and Discussion

3.1 Laser power to preheating temperature

Figure 2 shows the temperature profiles measured for the table speed of 30 mm/min. It was found that the peak heating temperature (Tp) was 268, 424, 694 and 943oC when the laser power varied at 119, 165, 223 and 313W, respectively. The obtained results showed that the temperature proportionally increased with the laser power as shown in Fig. 3. However, the region of primary shear zone is 2 mm behind the laser spot. Therefore, the preheating temperature at shear zone (Ts) is slightly lower than the peak temperature (Tp) for each laser power, because of the cooling time of 8 s. For example, it can be observed that the laser power of 313 W yielded the preheating temperature of 708oC, and the peak temperature of 943oC.

Figure 4 shows the profiles of temperature measured for the table speed of 50 mm/min. The peaks heating temperature (Tp) of 324, 405, 681 and 904 were obtained when the laser power varied at 150, 190, 253 and 332W, respectively. These results show that the temperature was proportionally increased as a function of laser power as shown in Fig. 5. The offset in feed direction caused 4.8s cooling time for the cutting speed of 50 m/min. Thus, the preheating temperature at primary shear zone (Ts) can be approximated 691oC and the peak heating temperature can be approximated 904oC for the laser power 332W.
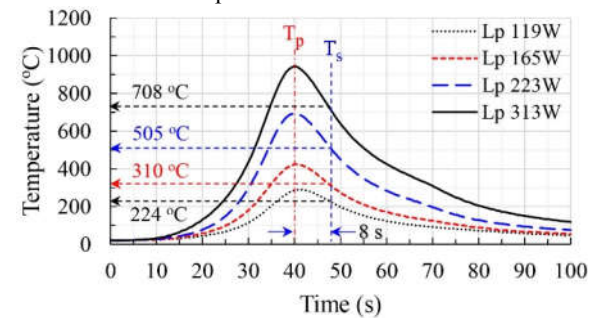
Fig 2 Profile of temperature for the table speed 30 mm/min
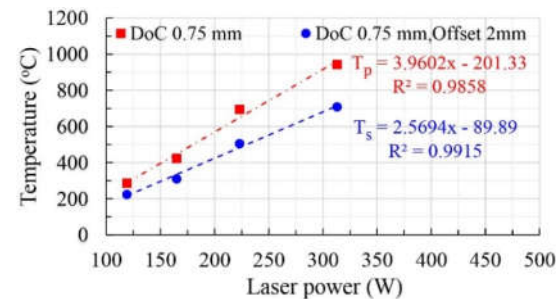
Fig 3 Relationship between laser power and heating temperature (table speed 30 mm/min)

Figure 6 shows the temperature profiles measured for the table speed of 75 mm/min, and Fig. 7 shows the relationship between the laser power and temperature. These results show that the peak heating temperature (Tp) of 336, 409, 705 and 917oC were obtained when the laser power varied 190, 232, 310 and 388W. Here, the preheating temperature in the primary shear zone (Ts) can be estimated with the cooling time of 3.2 s. So, the preheating temperature (Ts) of 708oC and peak heating temperature (Tp) of 917oC were obtained when the laser power was 388W in experiment.
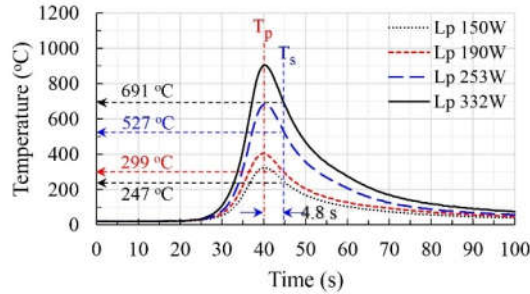
Fig 4 Profile of heating temperature for the table speed 50 mm/min
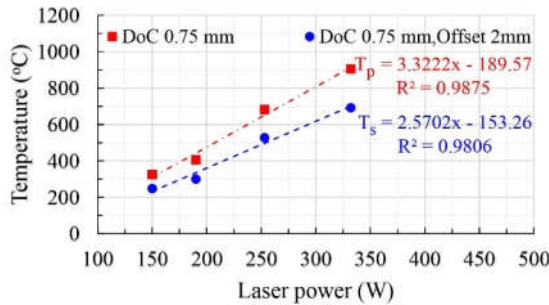
Fig 5 Relationship between laser power and heating temperature (table speed 50 mm/min)
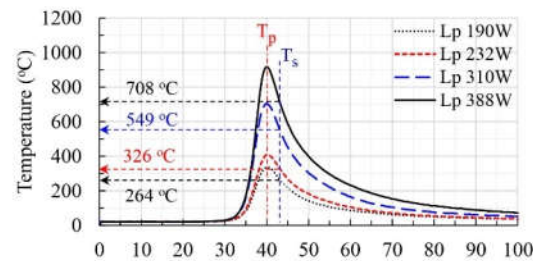
Fig 6 Profile of heating temperature for the table speed 75 mm/min
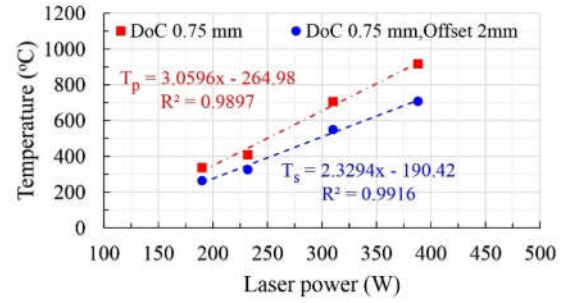
Fig 7 Relationship between laser power and heating temperature (table speed 50 mm/min)

Comparing results in Figs. 2, 4 and 6, it can be confirmed that the profiles of heating temperature changed as the table speed increased. This is because the period time for thermal diffusion decreased. Thus, under the conditions used here the uncertain of estimated preheating temperature and the experimental setup in the range ± 0.5 mm were responded to the error of temperature ±25oC (±3.57% of the estimated preheating temperature).

From the obtained results in Figs. 3, 5 and 7, it can be assumed that the requirement of laser power for the constant preheating temperature of 700oC was increased as a linear function of the table speed. This is because the heating time was reduced when the table speed was increased. These relationships can be used to estimate the laser power for each preheating temperature and peak heating temperature in this study.

3.2 Effects of preheating temperature in milling process

In this study the resultant cutting force was used to describe and compare the machinability of Inconel 718 under the conventional machining and LAM process as shown in Fig. 8. In the cases of conventional machining, the highest resultant cutting force occurred at cutting speed of 30 m/min, while it was almost constant for the cutting speed of 50 and 75 m/min. It is believed that the heat generated in the primary shear zone and frictional heat generation at the tool-chip interface zone affected to increase the strain hardening [6], therefore the cutting force was increased for efficient shearing of the workpiece. Whereas, in the case of the LAM, the resultant cutting force was reduced when the cutting speed increased, and was lower than conventional machining approximated with 11, 21 and 28% for the cutting speed of 30, 50 and 75 m/min, respectively. This is possible that the thermal softening dominates over the strain rate hardening [7].

Figure 9 shows the cutting temperatures in the region of tool-chip interface, which were measured by tool-work thermocouple. It can be seen that the cutting temperature increased as a function of cutting speed due to more heat generation at the high strain rate of materials and high sliding velocity at the tool-chip interface. However, according to the results by Liao et

al. [6], the insufficient cutting temperature to soften Inconel 718 under the conventional machining leads to increase work hardness. This could be affected to increase the resultant cutting force (Fig. 8) and tool wear (Fig. 10) when the cutting speed was increased. In LAM, the preheating temperature was sufficient to soften Inconel 718, whereas the cutting temperature was higher than conventional machining approximated with 65% due to the high temperature of workpiece. However, the cutting temperature in these experiments was lower than 1100oC, which is the softening temperature of the uncoated carbide tool [8,9].

Figure 10 shows the width of flank wear land (VB-max) for the cutting distance of 4.5 m. It can be observed that the tool wear increased as a function of cutting speed under the conventional machining. In LAM, the tool wear was higher than conventional cutting for the cutting speed of 30 and 50 m/min. However, the tool wear under the LAM at cutting speed 75 m/min decreased and lower than conventional machining. These could be due to the reducing of resultant cutting forces in LAM process (Fig. 8), which was caused by softening of work materials (Fig. 9).

Figure 11 shows the hardness on the machined surface. It can be seen that the hardness had not changed for the conventional machining. Whereas, the hardness of machined surface increased in LAM from 436 Hv to 452 Hv when the cutting speed was increased from 30 to 75 m/min. This result shows that higher heat input caused the thermal influence on the work materials.
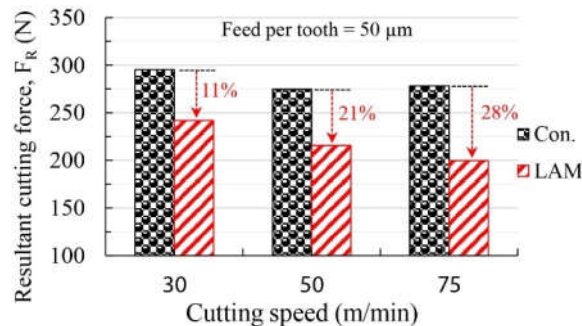
Fig 8 Comparison of resultant cutting force under the conventional machining and LAM
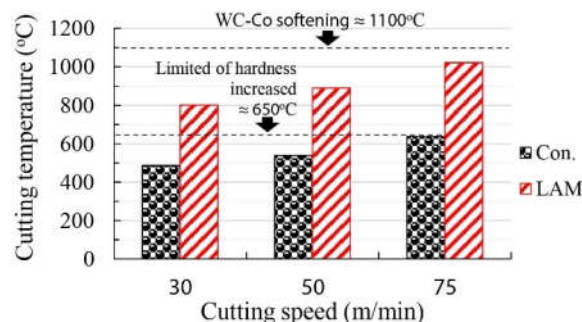
Fig 9 Comparison of cutting temperature under the conventional machining and LAM
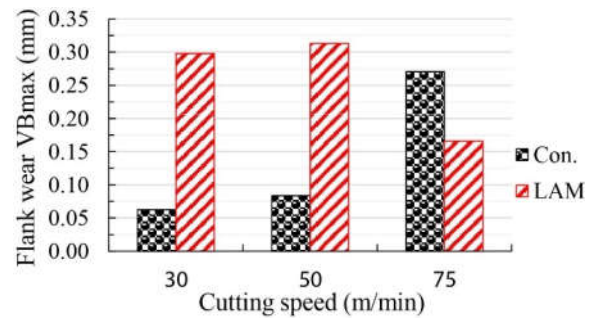
Fig 10 Comparison of tool wear under the conventional machining and LAM
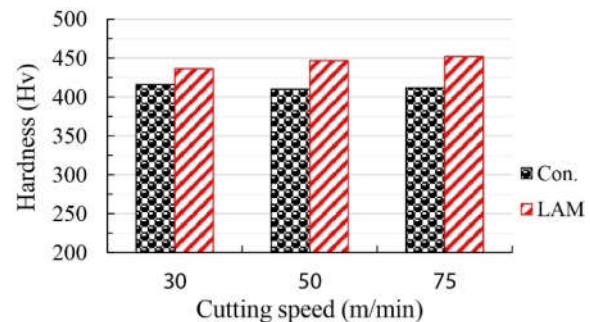
Fig 11 Comparison of hardness on machined surface under the conventional machining and LAM

4. Conclusion

The results of this study can be concluded as follows:

1)   The preheating temperature at primary shear zone can be controlled approximately 708, 691 and 708oC and the peak temperature 943, 904 and 917oC, when the laser power of 313, 332 and 388W were used for the table speed of 30, 50 and 75 m/min, respectively.

2)   Increased cutting speed at 50 and 75 m/min for conventional cutting had negligible effects on the resultant cutting force. When the LAM was used for preheating work materials, the resultant cutting force was decreased lower than conventional machining approximated 11, 21 and 28% for the cutting speed of 30, 50 and 75 m/min, respectively.

3)   The cutting temperature under LAM was higher than conventional machining approximately 65%. However, the chip-tool temperature in experiment could be lower than softening temperature of carbide tool.

4)   The tool wear in LAM was higher than conventional machining, but the wear could be improved at relatively high cutting speed of 75 m/min.

5)   The hardness of machined surface with LAM had a trend to increase as a function of cutting speed, and it was slightly higher than conventional machining.

References

[1]   W.-S. Woo, C.-M. Lee, A Study of the Machining Characteristics of AISI 1045 Steel and Inconel 718 with a Cylindrical Shape in Laser-assisted Milling, Applied Thermal Engineering, 91 (2015) 33-42.

[2]   C. -M. Lee, D.-H. Kim, J.-T. Baek, E. Kim, Laser Assisted Milling Device: A Review, Int. J. of Precision Engineering and Manufacturing Green Technology, 3 No. 2, (2016) 199-208.

[3]   A. Shokrani, V. Dhokia, S.T. Newman, Environmentally Conscious Machining of Difficult-to-machine Materials with Regard to Cutting Fluids, In. J. of Machine Tools and Manufacture, 57 (2012) 83-101.

[4]   H. Krain, A. Sharman, K. Ridgway, Optimisation of Tool Life and Productivity when End Milling Inconel 718 TM, J. of Materials Processing Technology, 189 (2007) 153-161.

[5]   I. Martinez, R. Tanaka, Y. Yamane, K. Sekiya, K. Yamada, T. Ishihara, S. Furuya, Wear mechanism of coated tools in the turning of ductile cast iron having wide range of tensile strength, Precision Engineering, 47 (2017) 46-53.

[6]   Y. Liao, H. Lin, J. Wang, Behaviors of end Milling Inconel 718 Superalloy by Cemented Carbide Tools, J. of Materials Processing Technology, 201 (2008) 460-465.

[7]   S. Sun, M. Brandt, M. Dargusch, The Effect of a Laser Beam on Chip Formation during Machining of Ti6Al4V Alloy, Metallurgical and Materials Transactions A, 41 (2010) 1573-1581.

[8]   E.O. Ezugwu, J. Bonney, Y. Yamane. An Overview of the machinability of aeroengine alloys, J. of Materials Processing Technology, 134 (2003) 233-253.

[9]   W. Akhtar, J. Sun, P. Sun, W. Chen, Z. Saleem, Tool wear mechanisms in the machining of Nickel based super-alloys: A review," Frontiers of Mechanical Engineering, 9 (2014) 106-119.

A Study on Micro Groove Cutting of TiAl Alloy

Yuma IWATANI[1], Koichi OKUDA[1], Masayuki NUNOBIKI[1]
[1]Graduate School of Engineering, University of Hyogo
2167 Shosha, Himeji, Hyogo 671-2280, Japan

ABSTRACT

In this study, the micro end milling of experiments of TiAl alloy were carried out in order to investigate the effect of the cutting conditions on the cutting force, the tool wear and the surface roughness. As a result, the cutting force components were almost same level in the range of cutting speed 30 to 60 m-1. In contrast, the tool wear increased with an increase in the cutting speed. The chipped edge were observed at the workpiece after cutting instead of the rollover burr.

1. Introduction

Recently, TiAl alloy with high heat force and the high strength has been developed and then has been substituted for Inconel in a part of the turbine blades of the jet-plane engine. This material is expected to spread into a lot of industrial fields because of the superior property. We focused on the micro and precise groove cutting in the field of micro processing.

Ti alloy such as a Ti-6Al-4V is well-known as the difficult-to-cut material. The tool wear remarkably progresses with an increase in the cutting speed. However, the machinability, especially micro end milling of TiAl alloy is hardly reported because of new material. In this study, the micro end milling of experiments of TiAl alloy were carried out in order to investigate the effect of the cutting conditions on the cutting force, the tool wear and the surface roughness.

2. Experimental Method

An ultra-precision vertical milling machine (Toshiba Machine Ltd.; model UVM-450C) with a spindle rotation of 6000- 60000 min-1 was employed for the micro milling experiments. Cutting tests were carried out using a two-blade end mill (Mitsubishi Materials Co.; model VC2SSD0050) having a diameter of 0.5mm. Fig.1 shows the schematic diagram of the experimental apparatus. The workpiece of TiAl alloy with size of 10 x 30 x 25 mm was mechanically fixed to the jig plate. The force transducer for measuring the cutting force was fixed between the workpiece and the jig plate.

Table 1 shows the main cutting conditions. Mainly the effect of the cutting speed was investigated. Micro groove cutting was performed at a cutting speed of 30, 45, 60 m/min. For measurement of the cutting force during cutting, the signal generated from the three-component force converter (KISTLER 9251A) was amplified with a charge amplifier (KISTLER 5070) and data was collected. Three force components Fx, Fy and Fz are in the force perpendicular to feed direction, the feed direction of the tool and the tool axial direction, respectively. An optical microscope was used for observation of the tool and the workpiece after the cutting. For measuring the surface texture of the finished surface, an optical surface texture measuring machine (ZYGO new view 7300) was used.

3. Results and Discussion

3.1 Effect of Cutting Speed on Cutting force

Fig.2 shows the measurement results of cutting force Fx and Fy when the cutting speed was varied. The maximum values of the middle part excluding the beginning and the ending of slot milling were plotted. Both Fx and Fy tend to increase with an increase in the cutting speed. However, Fx and Fy obtained under 45 m/min were very large. As shown in later, there was not larger chipping and wear at the cutting edge comparing with that obtained under other cutting speed. Then, the effect of vibration can be considered.

Fig.3 shows the cutting force waveform measured during milling in 45 m/min. It is thought that the waveform of the cutting force is generated at a cycle of 1.05 msec calculating from the spindle rotational speed. However, the measured waveform of Fy fluctuates in a cycle of shorter than the calculated one.

In small diameter end mill processing, it is reported that the tool bends during cutting [1]. Furthermore, the cutting force waveform greatly fluctuates to positive and negative as shown in Fig.3. From these facts, it is considered that the tool deflection in the feed direction also affected the slot milling of micro groove. The same tendency was observed under other cutting speed conditions, but it was particularly large under the condition of 45 m/min. Under this experimental condition, notable chatter was not observed, but there is a possibility that the main spindle rotation speed and the vibration characteristics of the workpiece support system are related to the cutting force.
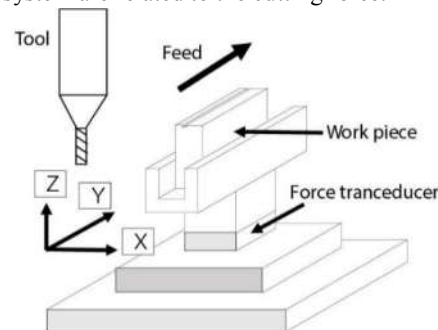
Fig 1 Schematic diagram of the experimental apparatus

Table 1 Cutting conditions

Work material	TiAl
Cutting speed	30,45,60 m/min
Cutting depth	50 μm
Feed per tooth	10 μm/tooth
Cutting length	30 mm
Coolant	dry
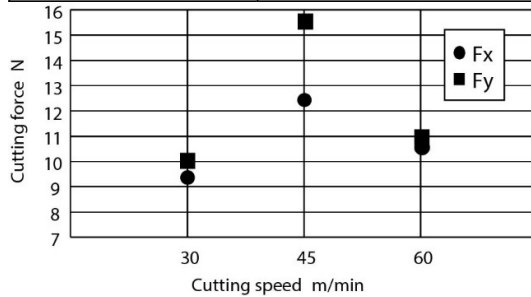
Fig 2 Effect of cutting speed on cutting force
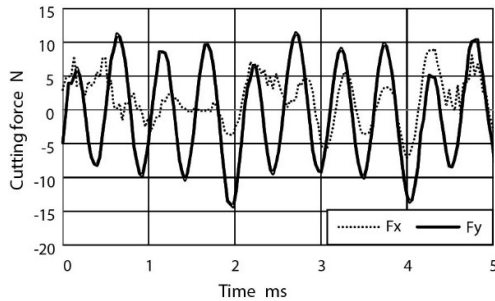
Fig 3 Example of cutting force waveform measured during milling in 45m/min

3.2 Effect of cutting speed on tool wear

Tool wear on the radial relief face and the land of end cutting edge was observed. Fig.4 shows the flank face of unused tools and the worn tool at each cutting speed after cutting a groove distance of 30 mm. From the observation of the radial relief face, it can see that the wear with the width of 5 to 10 μm was generated at the cutting-edge tip under all conditions. Within the range from the edge tip to 50 μm corresponding to the axial depth of cut, there is almost no wear under the condition of 45 m/min, while the wear with the width of 10 μm was generated under the condition of 30 and 60 m/min. On the other hand, the wear on the land of end cutting edge increases with an increase in the cutting speed. The width of wear reached to the maximum of approximately 30 μm under the maximum cutting speed of 60 m/min.

The wear of cutting edge tip makes the sharpness of edge dull and disturbs smooth engagement to the workpiece. The cutting-edge burnishes on workpiece surface firstly and then begins to cut. The geometrical cut thickness at that time is defined as the minimum cut thickness [2].

In the slot milling of micro groove, the cutting process is considered to be unstable if a feed per tooth is equal to or less than the minimum cut thickness [2]. Under the conditions of this experiment, the wear was an order of 10μm which is close to 10 μm/tooth of tool feed.
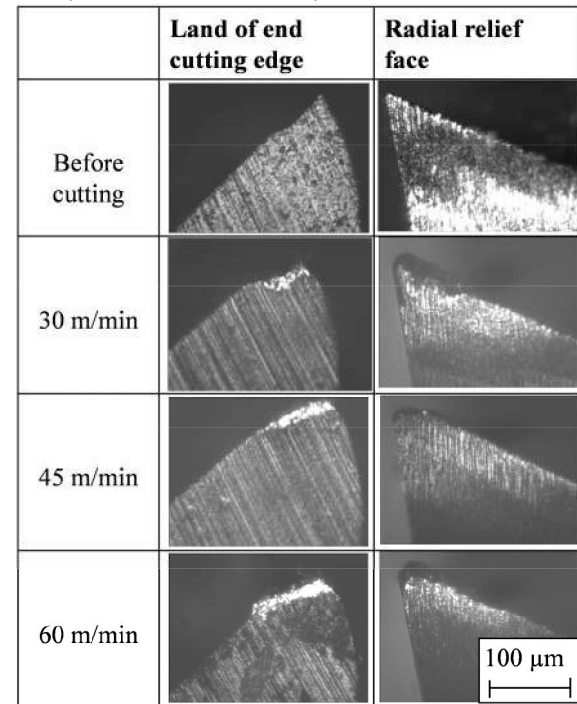
Fig 4 Observation of tool wear after cutting one grove (30mm) in each cutting speed

3.3 Edge quality of micro groove

Fig. 5 shows an observation example of the edge portion of groove under the condition of cutting speed of 60 m/min. The rollover burrs generated in a conventional metal cutting were not observed. Chipping or racking occurred at the edge. This is a similar phenomenon when the metal materials with low ductility such as cast iron are machined. There are all sorts of burr or chipping size along the groove edge. Then, the average size measured at four places of the edge is representative of the chipping size under each condition. The average chipping size under the conditions of 30, 45 and 60 m/min was 19.5, 18.2 and 13.3 μm, respectively. The chipping size decreases with an increase in the cutting speed.

From above fact, it is considered that the cutting mechanism of TiAl alloy is close to the mechanism with crack propagation in the cutting deformation region despite the same level hardness with Ti alloy (Ti-6Al-4V).

Finished surface of groove bottom Edge Uncut surface

Feed

50μm
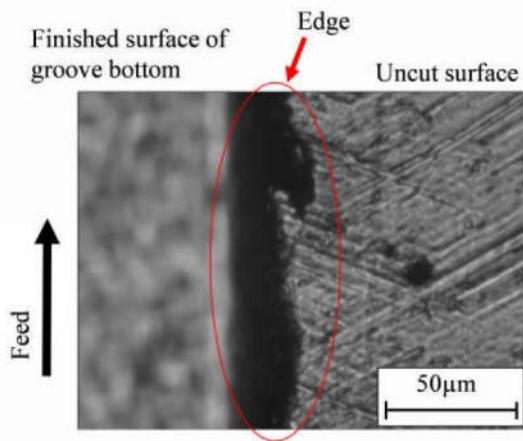
Fig 5 Example of photograph of groove edge after cutting in 60 m/min

3.4 Measurement results of finished surface

Fig.6 shows the graphical asperity of finished bottom surface measured by ZYGO. Geometrical pattern decided by the rotation and feed of the tool is seen in every condition. However, many small holes or voids are observed on the finished surface. The maximum height Rz was measured from the cross section in the surface image. Rz is different depending on the measurement place and ranges from 0.4 to 1.0 μm. In micro grooving processing, it is reported that the center area of the groove can be deeply ploughed by the bending of the tool [3]. From the data processing of measured images in Fig.6, the center area is lower under the condition of 60 m/min than other area, while it is higher under 30 and 45 m/min.

Fig.7 shows the photographs of the finished surface observed by optical microscope under the condition of cutting speeds of 30, 45 and 60 m/min. The finished surface obtained by milling under the condition of 60 m/min is more deteriorated than that under 30 and 45 m/min. The interval of cutter marks is smaller than feed per tooth (10μm). As the tool wear under the condition of the cutting speed of 60 m/min was largest among the cutting conditions, it is considered that the wear of land of end cutting edge affected to the surface integrity.

3.5 Relation between tool rotation angle and surface roughness

As mentioned in previous section, the minimum cut thickness is important in the slot milling of micro groove. Fig.8 shows the measurement position of the roughness and the relationship between the tool rotation angle and the geometrical cut thickness. Fig.9 shows the surface roughness Ra under each cutting speed corresponding to the rotation angle of cutting tool. Ra tends to become small with the tool rotation. Ra in the down-cut area (90 ° to 180 °) is smaller than that in the up-cut area (0 ° to 90 °).

In slot milling with the conventional end mills, the difference in roughness is explained as the reason that

the cutting phenomenon varies depending on the cutting area as described above [4]. In up-cut area, the cutting-edge burnishes for a moment from the engagement and then begins to cut. The burnish area broadens when the tool wear progresses and the end mill with small diameter is used.

+0.95019

Height μm

-0.91247

Cutting speed 30 m/min 100 μm

+0.83426

Height μm

-1.26456

Cutting speed 45 m/min 100 μm

+1.14264

Height μm

-0.90785

Cutting speed 60m/min
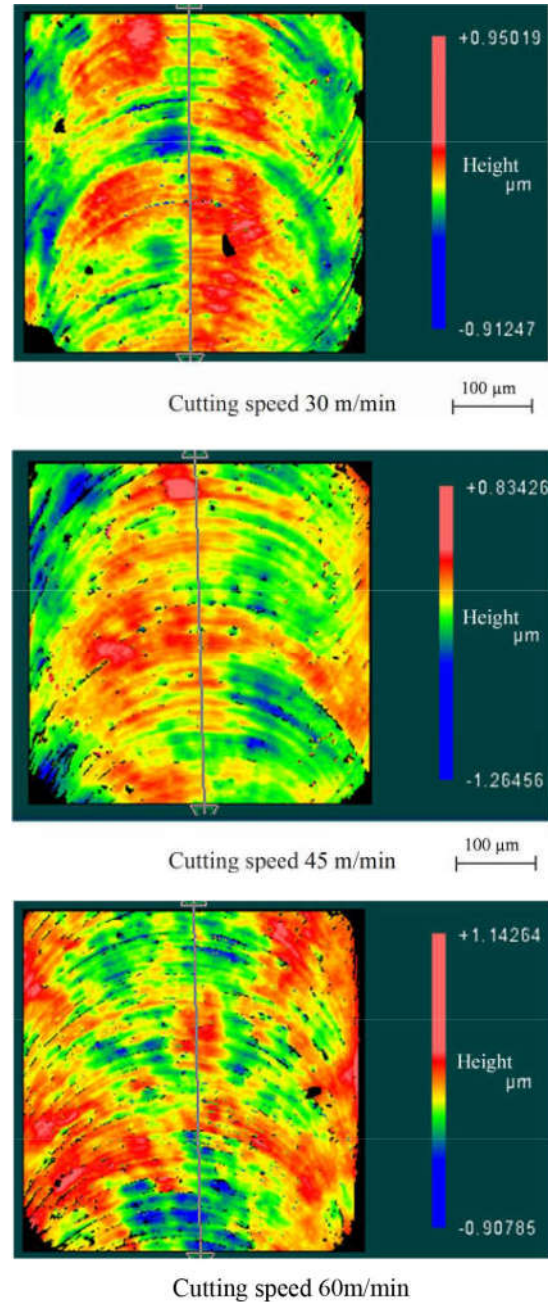
Fig 6 Observation of finished surface of groove bottom, Effect of cutting speed

9

Cutting speed 30 m/min   Cutting speed 45 m/min

50μm

Cutting speed 60 m/min
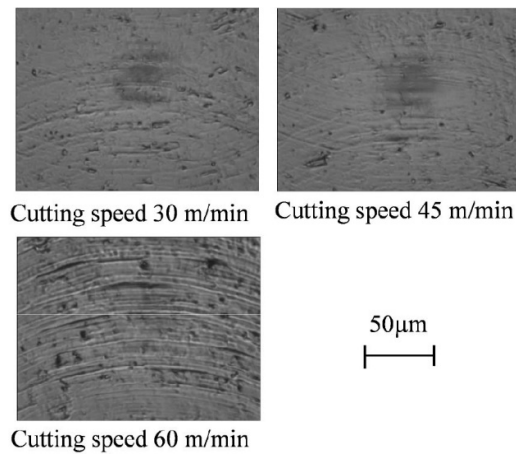
Fig 7 Surface observation results by microscope
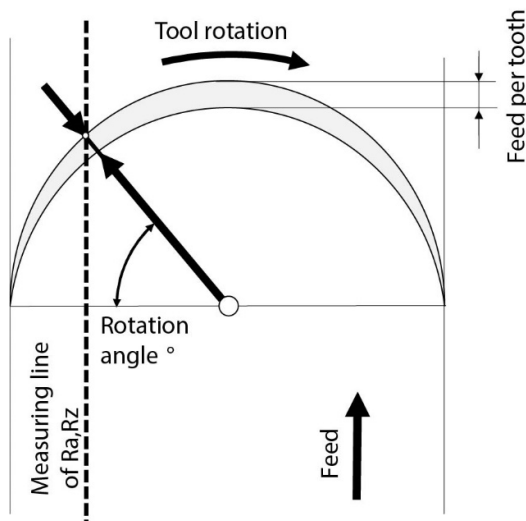
Fig 8 Relationship between rotation angle of tool and the measurement position of the roughness
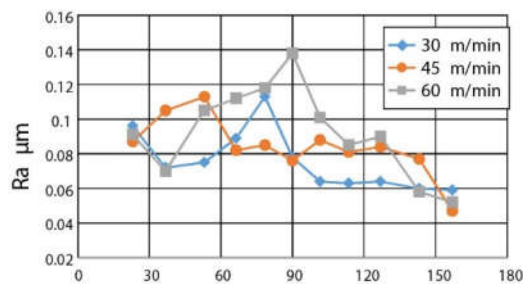
Fig 9 Influence of tool rotation angle on Ra at each cutting speed

4. Conclusion

In this experiment, in order to clarify the characteristics in slot milling of TiAl alloy with micro end mill, the experiment was conducted by changing the cutting speed and the following results were obtained.

1.   Cutting force tends to increase as cutting speed increases. Especially at 45 m/min, it became extremely large.

2.   The flank wear width of the land of end cutting edge increased with an increase in the cutting speed. The wear of about 5 to 10 μm was observed in the tip part of cutting edge regardless of the cutting speed.

3.   The rollover burrs generated in a conventional metal cutting were not observed. Chipping or racking occurred at the edge, as if the metal materials with low ductility such as cast iron are machined.

4.   No significant effect on the finished surface roughness due to the increase in the cutting speed was observed, but there was a tendency that Ra became better on the down-cut side.

References

[1]   Toyama University Yuta KAMIDAI, Chiba University Noboru MORITA, Toyama University Shigeru YAMADA, Noboru TAKANO, Fujikoshi Corporation Toru SEKIGUCHI, Research on the vector of milling force and cutting phenomena in micro end milling, The proceeding of conference of Hokuriku-Shinetsu Branch (2012)

[2]   Mitsuyoshi NOMURA, Takahiro KAWASHIMA, Takayuki SHIBATA, Yoshihiko MURAKAMI, Masami MASUDA, Osamu HORIUCHI, Unique cutting phenomena in micro-end-milling –Mechanism and possibility of occurrence-, journal of the japan Society for Abrasive Technology vol.54 No.10 (2010) OCT. 598-602

[3]   Masami MASUDA, Wataru TAKAHASHI, Osamu HORIUCHI, Takayuki SHIBATA, Yoshihiko MURAKAMI, Investigation on Profile Errors of Groove Cross-section in Micro end Milling, Journal of the Japan Society of Precision Engineering Vol.79, No.4, (2013)

[4]   Cutting Characteristics on Slotting of End-mill, Journal of the Japan Society of Precision Engineering Volume 53 Issue 10 Pages 1555-1561 (1987)

Surface Characteristic on Curved Grinding of Titanium Alloy with Coolant Supplying from Inner Side of Grinding Wheel

Sumito Toyokawa[1], Nagatoshi Nakatsuka[1], Atsushi Kusakabe[2], Hiroyuki Sasahara[1]

[1]Department of Mechanical Systems Engineering, Tokyo University of Agriculture and Technology, 2-24-16 Nakacho, Koganei-shi, Tokyo 184-8588, JAPAN

[2]Heiwa sangyo corporation,

1-1544-10 Kaijin-chominami Funabashi-shi Chiba-ken 108-0073, JAPAN

ABSTRACT

We applied the supplying cutting fluid from inner side of the tool, which supplies the grinding point with coolant through grinding wheel, for machining on the curved surface of titanium alloy. In the conventional external coolant supply, the number of nozzles was changed and compared. As a result, surface roughness decreased by about 10% for the concave surface in the supplying cutting fluid from inner side of the tool, about 20% for the single nozzle for the convex surface, and about 9% for the 7 nozzles.

Keywords : Grinding, Titanium alloy, Curved surface, Grinding surface characteristic

1. Introduction

Titanium alloys are widely used in aerospace industry due to its high specific strength and heat resistance [1,2]. Among them, many turbine blades made of titanium alloy are used for aircraft engines. The nozzle for supplying the grinding fluid interferes with the workpiece and the air layer generated on the surface of the grinding wheel prevents the supply of the grinding fluid and it is difficult to supply the grinding fluid efficiently. As a method of efficiently supplying the grinding fluid to the grinding point, there are a shoe nozzle [3], a jet nozzle [4], but these methods are not effective because there is a possibility of interference of the apparatus with curved workpiece.

We are advancing research and development of a grinding fluid supply mechanism that supplies grinding fluid from inner side of grinding wheel and performs grinding with simultaneous multi-axis control machine tools [5]. This system has advantages that the nozzle for coolant supply is not required, coolant is supplied directly to the grinding point, and less effect from a layer of air generated on the grinding wheel. In previous studies, some advantages such that grinding temperature and grinding wheel wear are suppressed were shown comparing with the coolant supply from the external nozzle [6].

Then, the objective of this paper is to clear the effect of coolant suppling methods, namely a coolant supply from inner side of grinding wheel and an external nozzle supply, on the surface characteristics on concave and convex curved surface of grinding of the titanium alloy. Then the finish grinding of turbine blade shape was conducted to demonstrate the excellent performance of the proposed methods.

2. Exprimental method

Figure 1 shows the schematic of the coolant supplying system. The grinding wheel is built into tool holder with flanges. It is attached to the machining center spindle. A coolant is supplied by using the spindle through mechanism of the machining center. And a coolant could be supplied through the interior of the grinding wheel pores to the outside of it. One of the benefits of this method is that a coolant can be supplied directly to the grinding point.

Figure 2 shows the grinding wheel used in this experiment. A silicon carbide vitrified bonded grinding wheel (GC80K14V) was used. The wheel diameter and thickness is 75 mm and 13 mm respectively. The grinding wheel included many porosities, with the spaces accounting for about 50 % of its volume.
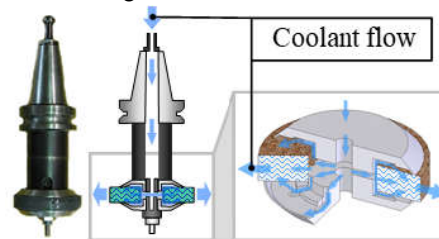
Fig 1 Schematic of the coolant supplying system
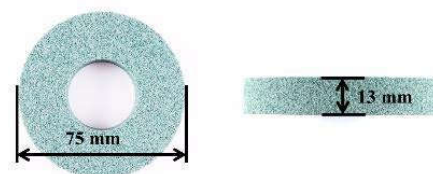
Fig 2 Grinding wheel

In order to clarify the influence on the finished surface roughness for the curved surface machining of titanium alloy, concave and convex shaped workpiece were

prepared. The workpiece of each shape was machined with internal coolant supply and external coolant supply, and the workpiece surface roughness was compared.

Figure 3 shows the workpiece shape and fixing method of the workpiece. The workpiece thickness is 3 mm and concave/convex radius is 100 mm. The material is Ti-6Al-4V. For the convex type workpiece, not only one external nozzle but also 7 external nozzles as shown in Fig 4 were used.

Figure 5 shows the experimental setup. Thin workpiece was attached to a jig with a slit-like window frame, then the surface temperature of the back side of the grinding point was measured. Table 1 shows the machining conditions. In this experiment, depth of cut was set to 0.06 mm, and feed rate was set to 500 mm/min. This was very severe condition for grinding.

(a) Concave surface   (b) Convex surface
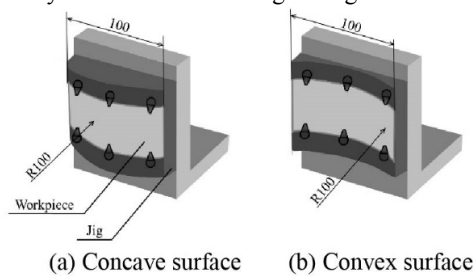
Fig 3 Workpiece and fixture
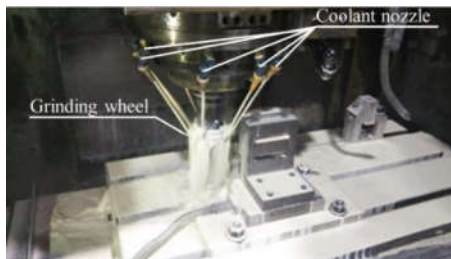
Fig 4 Outer nozzles setting
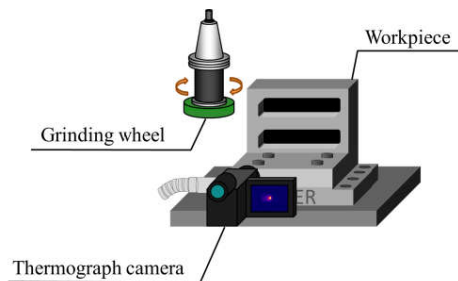
Fig 5 Experimental set up for temperature measurement

Table 1 Grinding conditions

Type of coolant supply		External , Internal
Type of grinding wheel		GC Vitrified Bonded
Grinding velocity V	m/s	20
Feed rate F	mm/min	500
Depth of cut d	mm	0.06
Grinding fluid		Emulsion type
Amount of coolant supply Q_{total}	L/min	10
Grinding method		Down
Material of work piece		Ti-6Al-4V

3. Results and discussion

Fig. 6 shows the surface roughness. In any of the workpiece shapes, the surface roughness on the internal coolant supply was smaller. On the case of concave surface, surface roughness with internal coolant supply was improved by 10% compared with that with external supply from one nozzle. On the case of convex surface, surface roughness with internal coolant supply was improved by 20% compared with that with external supply from one nozzle and 9% compared with that from seven nozzles. In the case of using the external nozzle, the variation in the surface roughness depending on the machining position was large. Since the nozzle position is fixed, depending on the situation, the supply amount varies depending on the position to be machined.

Figure 7 shows the maximum temperature on the back side of the grinding point. In the convex type workpiece, when the only one nozzle is used, the position of the nozzle is directed toward the grinding point at the machining start point and efficient cooling is performed, and the temperature is not so different from internal coolant supply as well. However, the position of the nozzle was not directed toward the grinding point at the machining end point and efficient cooling became impossible, and the temperature increased.

(a) Concave surface

(b) Convex surface
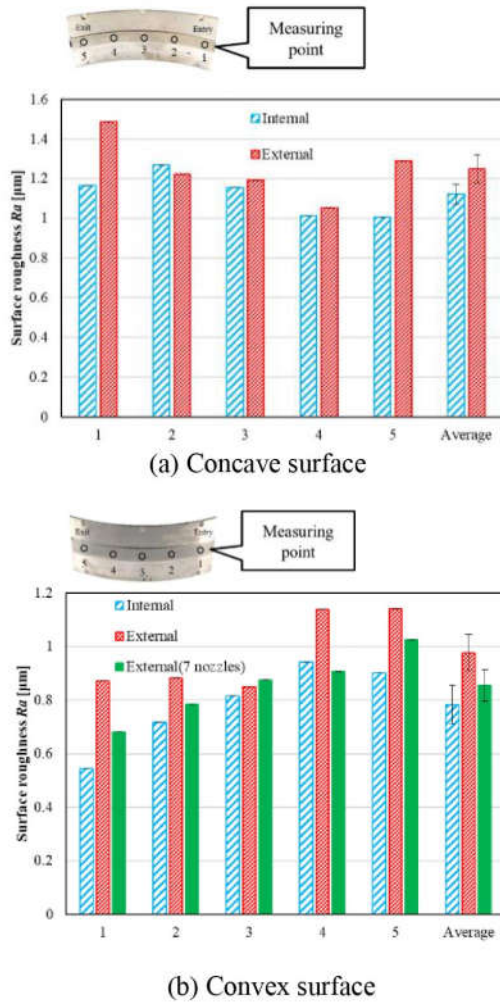
Fig 6 Effect of machining surface curvature and coolant supply on surface roughness
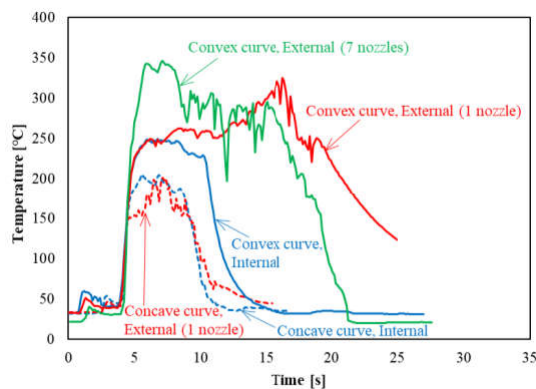
Fig 7 Effect of machining surface curvature and coolant supply on maximum temperature on the back surface of specimen

As shown in Figure 6(b), when the one nozzle was used, the surface roughness increased as it approached the machining end point due to the influence of the temperature rise. When seven nozzles were used, since a lot of nozzles were directed to places other than the machining point, the amount of coolant which could be supplied directly to the machining point was reduced as compared with the case of using one nozzle, the temperature was higher than internal coolant supply. In the case of internal coolant supply, the measured temperature decreased during grinding because the atomized coolant was reflected between the thermograph camera and the workpiece.

Figure 8 shows the machined surface of the convex workpiece. In case of using external nozzles, grinding burning occurred regardless of the number of nozzles, but internal coolant supply in which temperature reduction in Fig. 7 is indicated, no grinding burn had occurred. On the other hand, on concave workpiece, temperature was lower than that of convex workpiece and grinding burn was not observed under any conditions.

(a) Internal   (b) External,   (c) External,
          1 nozzle   7 nozzles
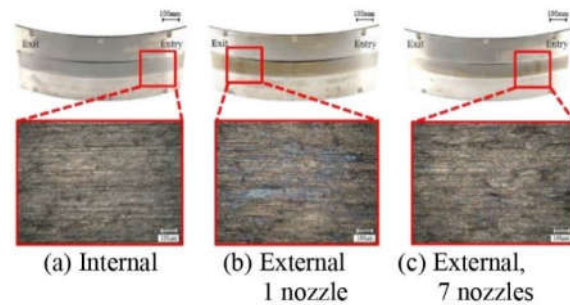
Fig 8 Machined surface of convex workpiece

One of the reasons for the difference in temperature between the convex shape and the concave shape was that there was a difference in the feed rate of the actual machining point. The feed rate F was the moving speed of the grinding wheel center, but the feed rate of the actual machining point was lower in the convex shape which was closer to the center of the arc of the tool path, and it was higher in the concave shape. When the feed rate at the center of the grinding wheel was 500 mm/min, the feed rate of the actual machining point of the convex type was 364 mm/min 800 mm/min respectively.

Then the feed rate at the grinding wheel center was set to 697 mm/min so that the feed rate of the actual machining point was 500 mm/min, and the surface roughness and temperature at the time of grinding the convex shape workpiece were measured. Fig. 9 shows the surface roughness of the workpiece. The surface roughness with internal coolant supply decreased. It could be seen that the surface roughness decreased at a feed rate of 500 mm/min. This was because the smaller the feed rate was the smaller the removal volume per unit time.

Fig. 10 shows maximum temperature on the back side of the grinding point at that time. Regardless of the coolant fluid supply method, it was found that the temperature was lower than the case shown in Fig. 7 where the actual machining point feeding speed was

low. Since the titanium alloy has a low thermal conductivity, it can be seen that when the moving speed of the machining point serving as the heat source is low, heat accumulates near the machining point and the temperature increases. Therefore, the reason for the difference in temperature between the concave type and the convex type in Fig. 7 is considered to be that the feed rate of the actual machining point of convex type is lower than that of the concave type.
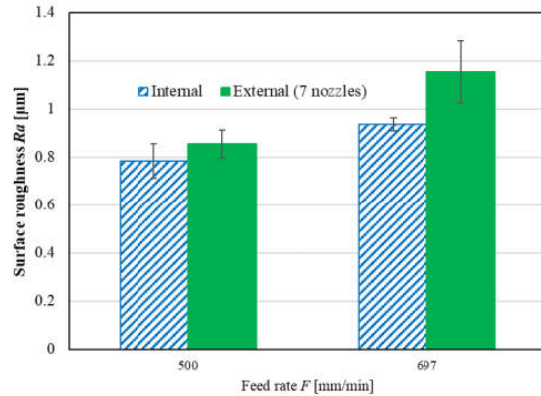
Fig 9 Effect of feed rate and coolant supply method on surface roughness
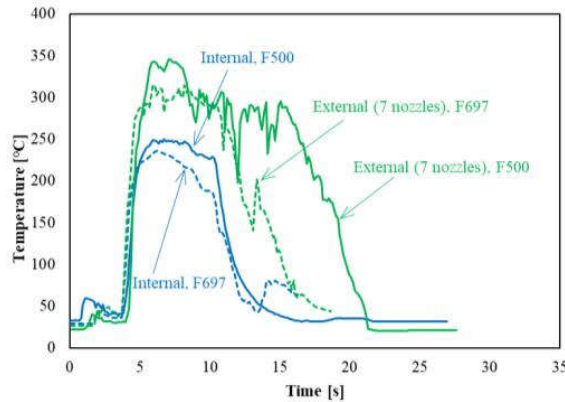
Fig 10 Effect of feed rate on maximum temperature on the back surface of specimen

4. Finish grinding of turbine blade shape

As a case study, the turbine blade shape with a combination of various curvature of convex and concave surfaces was grinded with internal coolant supply, and the finished surface roughness and accuracy were investigated. Fig. 11 shows the blade shaped workpiece to be machined and its cross-sectional shape. The end milled object was finished by grinding. The upper part was finished by grinding with external supply from seven nozzles, and the lower part was finished by grinding with the internal coolant supply.

After pre-machining, the main grinding with a depth of cut of 0.06 mm was performed, and thereafter, one pass

of sparkout was performed. Grinding wheel engaged at point 3 and contouring was conducted clock wise and disengaged at point 3.
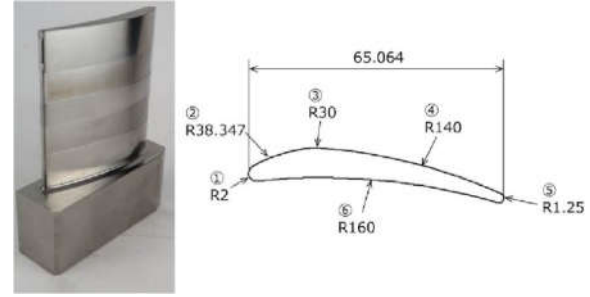
Fig 11 Machined turbine blade shape and its cross section

Fig.12 shows the surface roughness. The surface roughness of internal coolant supply decreased by 56% compared with the case of using seven nozzles. In the case of using seven nozzles, the variation of the measured roughness is large, and the roughness largely fluctuates depending on the curvature of each point. The machining accuracy was measured using a noncontact three-dimensional shape measuring machine. It was found that the removal amount normal to the contour on internal coolant supply was about 0.02 mm larger than that on the external supply from seven nozzles. It was shown that even for the turbine blade shape having a various curvature convex and concave surface, it is possible to supply the grinding fluid more efficiently by internal coolant supply, and it is possible to realize the superior grinding performance with excellent surface roughness and shape accuracy.
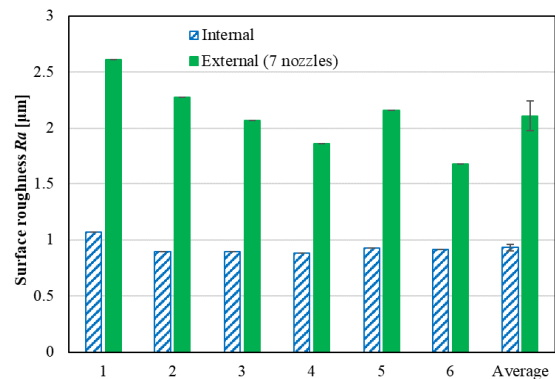
Fig 12 Surface roughness on blade shape workpiece

5. Conclusions

In this paper, the influence of the coolant supply method on the surface roughness on the concave and convex titanium alloy with concave and convex shapes with the curvature radius of R100 mm was investigated. The main findings are as follows:

(1)   For both concave and convex surfaces, surface roughness on the internal coolant supply was smaller

than external coolant supply even if the seven nozzles were used.

(2)   With the external nozzle, the actual amount of the coolant supply to the machining point varies during the curved surface grinding. On the other hand, the actual amount of the coolant supply is stable on the case of internal supply. So, the maximum temperature on the back side of grinding point of the convex shape specimen with internal coolant supply was lower than that with the external supply.

(3)   The difference between the convex and the concave shaped workpiece on the maximum temperature on the back side of grinding point depends on the difference in the feed rate at the actual machining point.

(4)   For convex shaped specimens with a low feed rate of actual machining point, grinding burn occurred in external coolant supply regardless of the number of nozzles.

(5)   A turbine blades shape specimen was finished with the grinding employing the internal coolant supply and demonstrated that it showed excellent roughness and shape accuracy.

References

[1]   S. Jiao, C. Gao, L. Cheng, X. Li, Y. Feng. A very high-cycle fatigue test and fatigue properties of TC17 titanium alloy, J Mater Eng Perform, 25(3) (2016) 1085－93.

[2]   P. Xu, L. Li, C. Zhang, Microstructure characterization of laser welded Ti-6Al-4V fusion zones, Mater Charact, 87 (2014) 179－185.

[3]   F. Klocke, A. Baus, T. Beck , Coolant induced forces in CBN high speed grinding with shoe nozzles, Annals of the CIRP, 49 (1) (2000) 241－244.

[4]   J. Webster, E. Brinksmeier, C. Heinzel, M. Wittmann,
K.   Thoens, Assessment of grinding fluid effectiveness in continuous-dress creep feed grinding, Annals of the CIRP, 51 (1) (2002), 235－240.

[5]   Y. Yao, Y. Fuwa, H. Sasahara, Development of a device for coolant supply from inside of grinding wheel and its application for profile machining of difficult to grinding materials, Proc. 4th CIRP Int. Conf. on High Performance Cutting, 1(2010) 417－420.

[6]   Y. Yao, S. Ri, K. Nakae, H. Sasahara, Minimization of grinding fluid by employing the supplying system from inner side of grinding wheel and its effect, Journal of Japan Society of Precision Engineering, 78 (8) (2012) 710－715.

Effect of Pick Feed on Machining Characteristic of Up cutting in the High-Efficient Machining by Small Diameter Radius End Mill

Hisaaki Nakai[1], Takekazu Sawa[2], Masahiro Anzai[2]
[1]Aomori Prefectural Industrial Technology Research Center
1-4-43 Kita-inter-kogyodanchi, Hachinohe City, Aomori, 039-2245, Japan
[2]SHIBAURA INSTITUTE OF TECHNOLOGY
3-9-14 Shibaura, Minato-ku, Tokyo, 108-8548, Japan

ABSTRACT
In order to improve efficiency of high speed milling, effects of pick feeds of up cutting and down cutting on tool wear and processing characteristics were investigated after cutting pre-hardened steel NAK 55 by TiAlN-coated carbide radius end mill. Flank wear of the tools after up cutting was less than down cutting when the pick feed was smaller than 0.1 mm, which tendency changed when the pick feed was larger than 0.3 mm.

1. Introduction

Recently, an efficient cutting method has been required in the mold industry as the need for small lot production of many products has increased. High speed milling technology is attracting attention as an effective method for quickly, accurately, and inexpensively manufacturing industrial products (molds, machine parts, etc.). High speed milling is an intermittent cutting method as premises that shallow of cut and high feed. Therefore, the load on the tool can be reduced as much as possible, and a cutting surface can be finished fine [1]. In addition, high speed milling is that the tool wear is small even in the dry cutting, because the contact time per revolution of the tool and the workpiece is short, and the heat generation of the tool is suppressed. Therefore, high speed milling is that it can contribute to reduce loads on the environment. High speed milling by using a small diameter tool makes possible machining with a few tools. Therefore the burden of CAM operation can be reduced [2]. However, when a small diameter tool is used, there is a problem that the cutting time is prolonged because the removal volume per unit time is small. In addition, since the small diameter tool has low rigidity, there is concern about the influence of deflection of the tool.

In this research, in order to further improve the efficiency of die processing by high speed milling, basic cutting characteristics in ultra-high speed rough machining were investigated. A machining center with a maximum rotation speed of about 160,000 min - 1 and a maximum feed speed of 15,000 mm / min was used as a means of ultra-high speed rough milling. Also, a radius end mill which is advantageous in terms of cutting efficiency as compared to the ball end mill was used [3].

In the present report, a small diameter radius end mill which can be machined from rough cutting to micro machining was used for reduction of labor in the CAM operation. In previous studies, we investigated the effect of axial depth of cut and pick feed on tool wear and machining characteristics in face cutting and side cutting. As a result of cutting at a cutting speed of 500 m / min, the flank wear of the end cutting edge in side cutting was large than that of the face cutting, and it was found that face cutting was more effective. On the other hand, in the previous research, there was a report that the tool life increased by 1.3 times in up cutting than down cutting in the side cutting using the extremely small diameter end mill of φ 0.5 mm [4]. In addition, in machining small diameter tapered holes by helical feed using a small diameter ball end mill, there was a report that it is possible to improve the tool life by about 2 times by up cutting as compared with down cutting [5]. Generally, it is said that down cutting tends to make the progress of mechanical abrasion on the flank face gentle and its tool life becomes longer than the up cutting [6]. However, there are still many unclear points in the machining mechanism by the small diameter tool, and it is considered that there is a possibility of high efficiency machining with up cutting. Therefore, in this report, for the purpose of further improving the efficiency, we investigated the effect of the pick feed in the up cutting and down cutting of the face cutting on flank wear of the end cutting edge and processing characteristics.

2. Method

2.1 Processing characteristics by up cutting and down cutting

Fig. 1 shows a schematic diagram of up cutting. The up cutting is a cutting method in which the incision of the cutting edge to the workpiece gradually becomes thicker from the thinner side, and its reverse is the down cutting. In this report, as face cutting is presupposition, the axial depth of cut Ad was fixed at 0.1 mm and pick feed was changed. The face cutting referred to here is a machining method in which cutting is mainly performed using an end cutting edge in shoulder face milling using an end cutting edge and a peripheral flute.
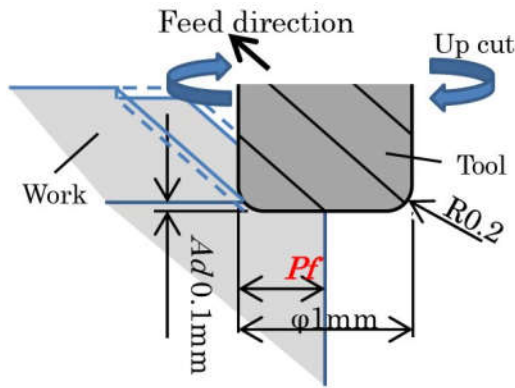
Fig 1 Schematic diagram of up cutting

2.2 Experimental equipment and experimental conditions

The linear motor-driven machining center L-CART was used in this experiment. L-CART was developed by RIKEN and Sodick Co., with a high-speed air turbine spindle ABT-1600(manufactured by Nakanishi Co., Ltd.). Cutting experiments of high speed rotation and high-speed feed were carried out using a high speed milling machine at a maximum rotation speed of about 160,000 min -1 and a maximum feed rate of 15,000 mm/min.

Table 1 shows experimental conditions. In order to grasp processing phenomena in high speed milling, Pre-hardened steel NAK 55 (38 HRC) [7] which is widely used as a die material was used as the workpiece. A 2-flutes TiAlN coated carbide radius end mill (MSRS 230 made by Nisshin Tool Co., Ltd.) with a diameter of 1 mm and a corner radius of 0.2 mm was used a cutting tool. The handlebar stem extension length was set to 14 mm which is maximum length specified in the specification of the air turbine spindle. Since the corner radius is 0.2 mm in the radius end mill, face cutting is theoretically possible with 0.6 mm. But it was made up to 0.5 mm at intervals of 0.1 mm with a margin so that it can't be scraped off due to deflection and run out of the tool. The cutting speed was 500 m / min, and the feed rate was 0.047 mm / tooth, which was dry cutting. In the cutting method, processed surface of 20 mm × 20 mm was cutting in one direction by up cutting or down cutting, and an approach distance of 30 mm was provided before and after cutting so that the feed rate during cutting was constant. Tool wear was observed with a scanning electron microscope FlexSEM 1000 (manufactured by Hitachi, Ltd.), and the surface roughness was measured with a confocal microscope OPTELICS® HYBRID (manufactured by Laser Tech Corp.).

3. Results and Discussion

3.1 Influence of pick feed on machining characteristics of up cutting

Fig. 2 shows an SEM image of the flank of the tool end cutting edge after machining with a pick feed at intervals of 0.1 mm from 0.1 mm to 0.5 mm with a machining distance of 60 m with up cutting. (a) pf 0.1 is the least worn, and the maximum flank wear width is about 5.0 μm. The maximum flank wear was almost equivalent, and the larger the pick feed, the greater the wear. (e) pf 0.5 was significantly worn out on one side of the cutting edge. Fig. 3 shows an enlarged view of the worn part of (e) pf 0.5 at 40 m and 60 m cutting length. Chipping was seen in the cutting edge at the cutting length of 40 m. It is considered that the cutting edge was remarkably worn out from the chipping seen at the cutting length of 40 m.

Fig. 4 shows the change in the flank wear of the end cutting edge in the up cutting process. According to the report of Imada et al., when the average flank wear VB becomes about 10 μm, the biting of the cutting edge worsens so that the machined surface and the dimensional accuracy deteriorate [8]. Therefore, in this report the tool life is defined maximum wear width VBmax as 10 μm. (e) pf 0.5 was discontinued at a cutting length of 60 m due to severe wear of the tool cutting edge. The flank wear of the end cutting edge with (a) pick feed of 0.1 mm increased in proportion to the cutting length, and the flank wear of the end cutting edge reached about 10.5 μm at the cutting length of 200 m. The flank wear of the end cutting edge of (b) pf 0.2 and (c) pf 0.3 and (d) pf 0.4 changed in the same way. The flank wear of Pf 0.2 - 0.4 mm was almost the same, reaching about 10 μm at the cutting length of 80 m. Fig. 5 shows the flank wear of the end cutting edge of up cutting and down cutting for each pick feed. (a) pf 0.1 has less flank wear of the end cutting edge in up cutting,(b) pf 0.2 is almost equal for up cutting and down cutting, (c) pf 0.3 and (d) pf 0.4. The flank wear of the end cutting edge of the down cut was small. As reported by Imada et al., it was confirmed that the up cutting has less wear than the down cutting in the high speed milling of the small diameter tool. This phenomenon was seen on the side where the pick feed became smaller. Also, when the pick feed became 0.3mm or more, since the down cutting has contrarily less wear than the up cutting, it seems to suggest that the pick feed has a boundary between 0.1 mm and 0.3 mm.

Fig. 6 shows the rate of change of the spindle speed during cutting. Since the rotational speed of the high speed air turbine spindle changes due to the cutting resistance, it is considered that it is possible to find the cause of tool wear from the load on the tool. In (e) pf 0.5mm, both the up cutting and the down cutting had the same rate of change of the spindle speed, but the rate of change of the spindle rotational speed was slightly smaller in the up cutting than the other. Therefore, it is inferred that the cutting resistance received by the tool is smaller when the pick feed is

smaller with up cutting. In Fig. 5, as for the point where the tool wear width reverses between pick feed of 0.1 mm and 0.3 mm, factors such as the direction of the cutting resistance and the shock at the time of cutting can be considered, but it is to be set as the next task.

Table 1 Cutting conditions

Work piece	NAK55(38HRC)
Tool	TiAlN coated cemented carbide Radius end mill, φ1.0mm, CR0.2mm , 2-flute
Cutting direction	Up cutting, Down cutting
Pick feed : Pf mm	0.1,0.2,0.3,0.4,0.5
Axial depth of cut : Ad mm	0.1
Cutting speed : V m/min	500
Feed rate : Sz mm/tooth	0.047
Coolant	Dry

(a)Pick feed 0.1mm　(pf0.1)

(b)Pick feed 0.2mm　(pf0.2)

(c)Pick feed 0.3mm　(pf0.3)

(d)Pick feed 0.4mm　(pf0.4)

(e)Pick feed 0.5mm　(pf0.5)
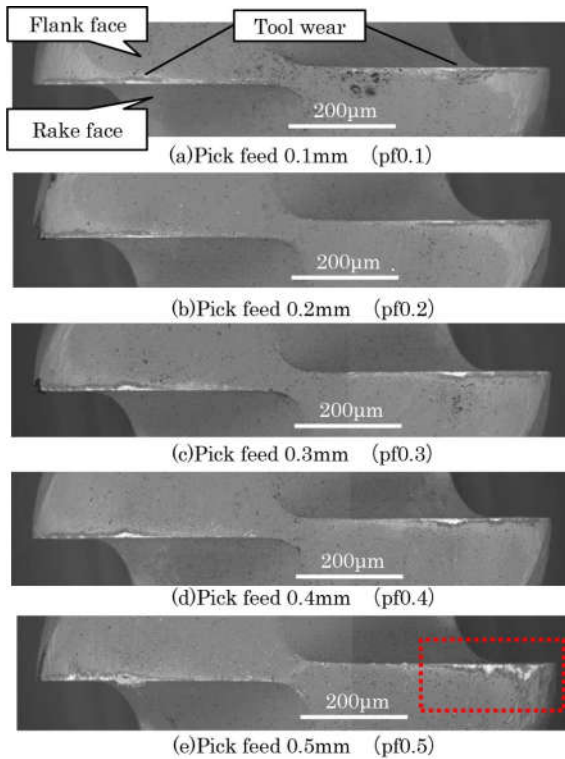
Fig 2 SEM image of tool wear on flank face by up cutting
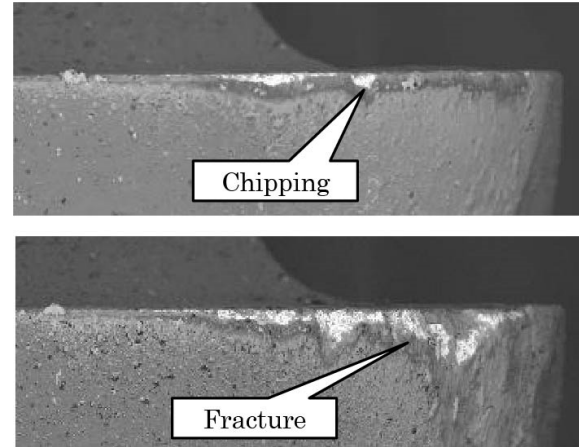
Fig 3 Enlarged view of SEM image of tool wear on flank face by up cutting with (e)pf0.5
(Upside: Cutting length 40m, Downside: Cutting length 60m)
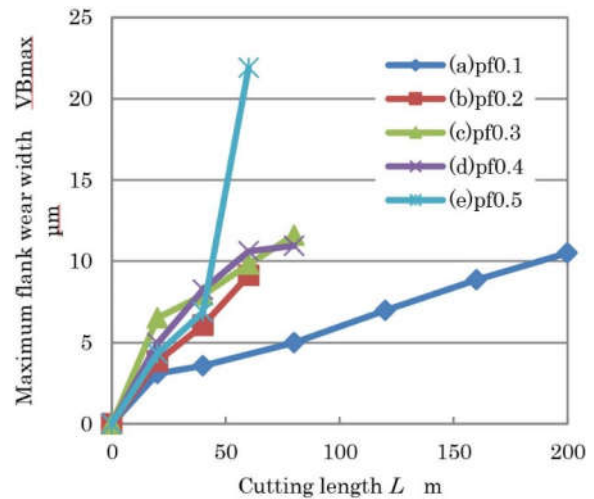
Fig 4 Effect of pick feed on flank wear of up cutting in the high-efficient machining by small diameter radius end mill

3.2 Irregular pick feed reciprocating cutting

As mentioned in the previous section, when the pick feed is large, the flank wear of the end cutting edge is small due to down cutting, and when the pick feed is small, the flank wear of the end cutting edge is small due to up cutting, and it seems to suggest that the pick feed has a boundary between 0.1 mm and 0.3 mm. From the above, it is considered that there is an appropriate value for the pick feed setting in the cutting direction. As shown in Fig. 7, it is considered that tool wear can be reduced compared to ordinary reciprocating cutting by setting pick feed at an appropriate amount in the direction of reciprocating cutting, and this was investigated. (Hereinafter, in the reciprocating cutting, a processing method for separately setting pick feed for each cutting direction is called irregular pick feed reciprocating cutting.)

From the results in Fig. 5, it was paid attention to the pick feed rate of 0.2 mm which is presumed to be a boundary. And the pick feed of ordinary reciprocating cutting was set to 0.2 mm and the processing width of reciprocating 0.4 mm was set in the verification experiment. Regarding the irregular pick feed reciprocating cutting, the pick feed on the up cutting side was set small, and the pick feed on the down cutting side was set large. And the combination of up cutting and down cutting was set to 0.1 mm and 0.3 mm so that the reciprocating cutting width would be the same. Here, as a result of investigating the rate of change of the spindle speed in the preliminary experiment, the rate of change in reciprocating cutting showed about 2.5 times as compared with unidirectional cutting. This is considered as follows. The rotation speed is restored while returning to the initial position after cutting in unidirectional cutting. But, other cutting starts immediately after one cutting is finished in reciprocating cutting. Therefore, it is considered that next cutting starts without restoring the spindle speed in reciprocating cutting. To prevent the load on the spindle from becoming too large, the feed speed of the tool was set at 0.016 mm / tooth which is one third of the reciprocating cutting with a margin. Fig. 8 shows the effect of irregular pick feed reciprocating cutting at cutting length of 20 m on flank wear of the end cutting edge. The flank wear of the end cutting edge is slightly less (b)the irregular pick feed reciprocating cutting (Up0.1-Down0.3) than (a)the normal reciprocating (Up0.2-Down0.2). Therefore, it is thought that the effect of reducing tool wear by an irregular pick feed appeared.

4. Conclusion Remarks

Effects of pick feeds of up cutting and down cutting on tool wear and processing characteristics were investigated in order to improve processing efficiency.

(1)   Flank wear of the tools after up cutting was found to be less than down cutting when the pick feed was smaller than 0.1 mm. On the contrary, flank wear of tools after down cutting was found to be less than up cutting when the pick feed was larger than 0.3 mm. There seemed to be the threshold value of pick feed between 0.1 mm and 0.3 mm.

(2)   Flank wear of tools after irregular pick feed reciprocating cutting, where the pick feed were 0.1 mm and 0.3 mm in up cutting and down cutting respectively, was slightly less than regular reciprocating processing.

References

[1]   T. Matsuoka, M. Anzai, Deep-Sea Research Part 1, 58 (2006) 567-574.

[2]   T. Sakamoto, Y. Takeuchi, I. Takahashi, K. Kase, M. Anzai, The Japan Society for Precision Engineering, Vol.67, No.2(2001) 284-288.

[3]   T. Matsuoka, Kata Gijutsu, 31,6(2016)

[4]   T. Imada, H. Nakagawa, K. Ogawa, H. Kojima, H. Kino, 2013 JSPE Autumn Conference, (2013)441-442.

[5]   H. Onozuka, I. Kono, T. Yoshikawa, T. Obikawa, Journal of JSPE, Vol.78, No.9(2012)

[6]   Furaisu Kakou Handbook, (1988) 13-18.

[7]   T. Watanabe, K. Isokawa, Bulletin of the Japan Institute of Metals, Vol.17, No.4(1978)360-361.

[8]   T. Imada, H. Nakagawa, K. Ogawa, H. Kojima, H. Kino, 2012 JSPE Autumn Conference, (2012) 153-154.

Evaluation Method for Machining Fluids using Cutting Force in Micro Feed End Milling

Tomohiko Kitamura[1], Ryutaro Tanaka[2], Yasuo Yamane[2], Katsuhiko Sekiya[2], Keiji Yamada[2]

[1]Lubricants Research Laboratory, Idemitsu Kosan Co., Ltd., Japan

[2]Graduate School of Engineering, Hiroshima University, Japan

ABSTRACT

In conventional friction tests, it is difficult to realize high pressure and high temperature conditions such as the tool-work contact area in cutting. In this study, friction properties of machining fluids were evaluated using friction coefficient calculated from the cutting force in micro feed end milling. The finished surface roughness in conventional end milling decreased with friction coefficient of machining fluids obtained by this method. Also, cutting speed dependence of friction coefficient and the influence on biting property of cutting edge could be evaluated by this method.

Keywords: machining fluids, friction test, micro feed end milling, cutting force, finished surfaces

1. Introduction

Machining fluids are contributing to increase the productivity in the manufacturing industry by improving machining accuracy and reducing tool failure [1,2] in various machining process. The use of machining fluids will aid development in machining technology, but easy evaluation method to predict cutting performance accurately for machining fluids isn't established. The reason is that conventional friction tests never realize high pressure, high temperature and newly-formed surface friction conditions such as the tool-work contact area in cutting. As for conventional friction tests, result of four-ball test, falex test and so on don't show strong relation with cutting performance [3,4]. Moreover, newly-formed surface friction test [5,6] have been proposed to realize high pressure and high temperature conditions, newly formed surface contact. However, this method was subject to special equipment and skilled technique.

In this study, friction properties of machining fluids were evaluated using cutting force in micro feed end milling. The feed rate was less than the roundness of cutting edge to decrease the influence of plastic deformation force and emphasize friction factor in cutting force. Using this method, the in-situ evaluation for machining fluids could be carried. In addition, because throw-away insert was used as a specimen, it didn't require a special specimen. The effectiveness of this evaluation method was discussed compering to conventional friction tests.

2. Experimental procedure

2.1 End milling test

Table 1 shows the experiment conditions. The work material was S45C. TiAlN coated cemented carbide insert tool was used.

Cutting force was measured at the feed rate of 1-10μm/rev and cutting speed of 50, 150m/min. Finished surface roughness by end cutting edge was measured at the feed rate of 25μm/rev and cutting speed of 50, 150m/min.

2.2 Machining fluids

Table 2 shows the composition and the characteristic values of tested machining fluids for end milling test. Soda four-ball test was selected as conventional friction test because this is evaluation method of JIS K 2241(cutting oil).

Table 1 End milling test conditions

Work material	S45C (annealed), w57× b60× h25mm
Tool holder	MTES335(KYOCERA)
Number of insert	One
Insert	TEEN1603PETR1 TiAlN coated cemented carbide Cutting edge: Chamfer honing
Projecting length	43mm
Machine tool	NV5000α1/A4(DMG MORI)
Cutting direction	Up cut
Cutting speed	50m/min, 150m/min
Feed rate	1-25μm/rev
Axial rake	+15°
Radial rake	0°
Axial depth of cut	1.0mm
Radial depth of cut	17.5mm

Table 2 Composition and characteristic values of used machining fluids for end milling test

Sample name	Mineral VG8	Mineral VG20	Synthetic VG8
Composition	Mineral oil	Mineral oil	Synthetic oil
Kinematic viscosity at 40°C, mm²/s	7.827	20.44	8.030
Sizure load of soda four-ball test, MPa[※1]	0.20	0.25	0.40
Finished surface roughness Ra, μm (Cutting speed: 50m/min)[※2]	1.261	0.823	0.326
Finished surface roughness Ra, μm (Cutting speed: 150m/min)[※2]	0.494	0.361	0.230

[※1] JIK K 2519, [※2] Refer to section 2.1

The each tested machining fluid showed different friction property in kinematic viscosity and composition and cutting performance. As stated above, the difference of friction coefficient in the machining fluids were investigated in micro feed end milling.

3. Results and Discussion

3.1 Caluclation method of friction coefficient using cutting force

Figure 1 shows force interacting on workpiece and tool in end milling. Workpiece was fixed on dynamometer. Cutting force was recorded in x-y coordinate system as figure 2. Cutting force Fx and Fy were converted into radial component force Fn and tangential line direction component force Ft in tool rotary circle as follows.

$$F_t = F_x \times \sin\theta + F_y \times \cos\theta \qquad (1)$$
$$F_n = -F_x \times \cos\theta + F_y \qquad (2)$$

By way of example, figure 3 shows the time change of cutting force Fn and Ft in end milling. Then, friction coefficient was defined as follows.

$$\mu = \frac{F_t}{F_n} \qquad (3)$$

By way of example, figure 3 shows the time change of friction coefficient.

3.2 Measure conditions of friction coefficient in micro end milling

At first, measure conditions of friction coefficient in end milling were searched for suitable evaluation of machining fluids. Feed rates were set to less than the cutting edge roundness of 3μm because of burnishing area without chip generation [7]. This reason was to decrease the influence of plastic deformation force and emphasize friction factor in cutting force. Figure 4 shows the influence of feed rates for cutting force Ft in end milling. The cutting force Ft were easy to variable and instability at the feed rate of less than 3μm/rev. Therefore, the feed rate of 5μm was selected for evaluation condition of machining fluids because cutting force was stable and uncut chip thickness was thin relatively in this condition.

However, in the average friction coefficient until cutting time of 30ms, as figure 5, the difference of friction coefficient in machining fluids were almost none. In these cases, discussions of cutting mechanism were as follows.
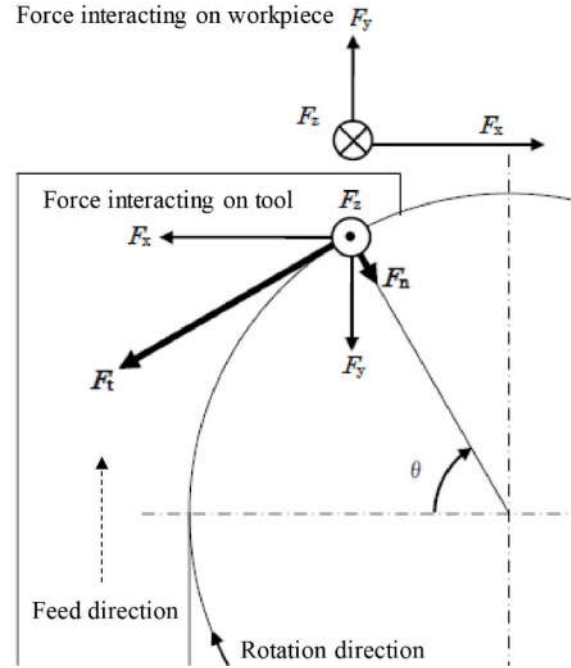
Fig 1 Force interacting on workpiece and tool in cutting
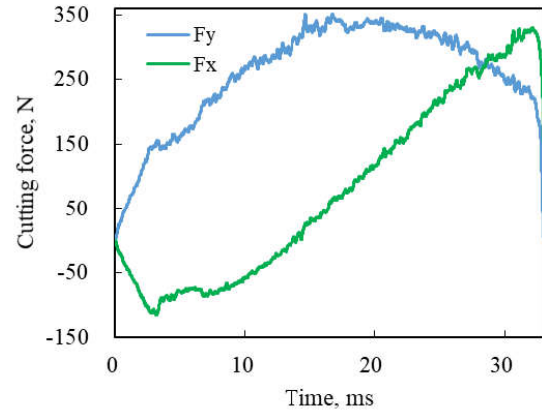
Fig 2 The time change of cutting force Fx, Fy in end milling in dry condition
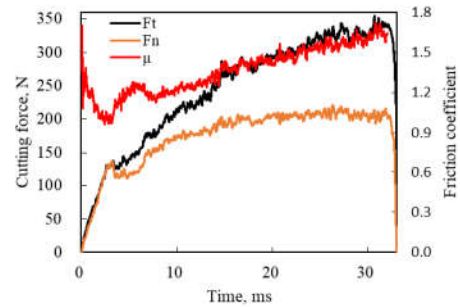
Fig 3 The time change of cutting force F_t, F_n, and friction coefficient in end milling.
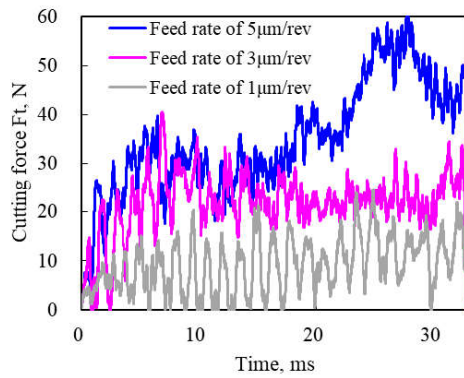
Fig 4 Effect of feed rate on cutting force Ft at the cutting speed of 50m/min, with mineral oil VG8

Therefore, cutting force was difficult to be influenced by machining fluids in plastic contact area. While, friction coefficient were very low immediately after beginning cut in figure 6. This tool-work contact condition was possible to be elastic contact because of friction coefficient in dry conditions was almost 0.35 as the past reports[9]. If machining fluids were mainly working on boundary parts, the friction coefficient evaluations of elastic contact area were found to be appropriate for machining fluids. Therefore, the cutting time 0.1-0.3ms were selected to friction coefficient measure conditions, because friction coefficient was almost 0.35 at dry conditions. The uncut chip thickness was 0.02-0.07μm for cutting time 0.1-0.3ms, and these values were very smaller than the cutting edge roundness of 3μm. These showed that the cutting edge-work contact area could be elastic contact.

3.3 Relationship between finished surface roughness and friction coefficient

Figure 7 shows the relationship between surface roughness Ra at the feed rate of 25μm and friction coefficient at the feed rate of 5μm in end milling. The finished surface roughness in conventional end milling decreased with friction coefficient of machining fluids. Also, the friction coefficient of all used machining fluids increased with cutting speed, but the finished surface roughness at the cutting speed of 150m/min trended to depend on friction coefficient too.

Figure 8 shows finished surface profile at the cutting speed of 50m/min, at the feed rate of 5μm in end milling. The used machining fluids with low friction coefficient effectively reduced the region where assumed to be generated by tears compared with dry condition. From the results, the finished surface roughness in end milling were supposed to depend on lubricity of tool-work in elastic contact area.

3.4 Comparison with conventional friction test

Figure 9 shows relationship between friction coefficient of micro end milling and seizure load of soda four-ball test as conventional friction test. In the cutting speed of 50m/min, the correlation coefficient was very high. While, the correlation coefficient in the

cutting speed of 150m/min was considerably lower than the case at the cutting speed of 50m/min. This main reason was found that frictional speed of soda four-ball test was lower than end milling.
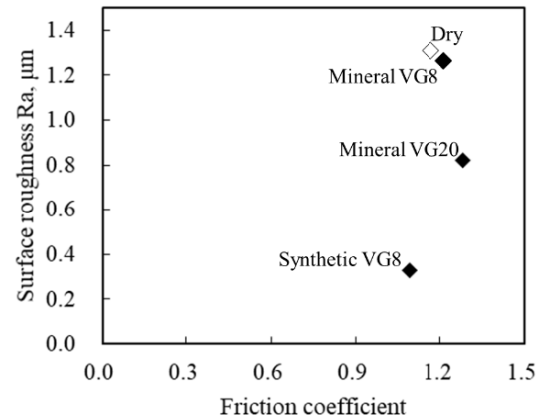
Fig 5 Relationship between surface roughness Ra at the feed rate of 25μm and friction coefficient at the feed rate of 5μm in end milling
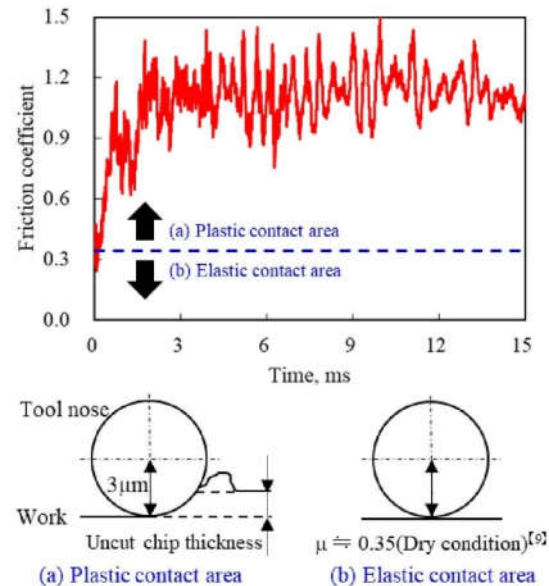
Fig 6 Relationship between friction coefficient and cutting times and contact situation of cutting edge-work in end milling at the cutting speed of 50m/min, at the feed rate of 5μm in dry condition
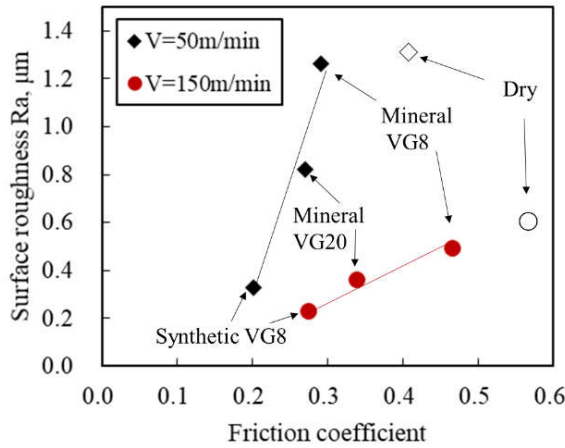
Fig 7 Relationship between surface roughness Ra at the feed rate of 25μm and friction coefficient at the feed rate of 5μm in end milling
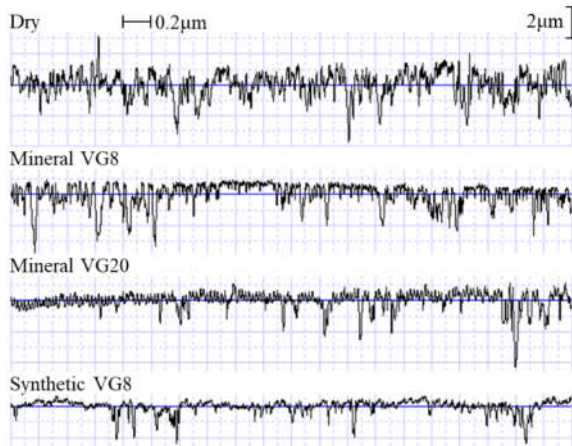
Fig 8 Finished surface profile at the cutting speed of 150m/min, at the feed rate of 25μm in end milling

3.5 Biting property of cutting edge in machining fluids

Figure 10 shows that Comparison of dry condition and synthetic VG8 in drifting cutting force Ft at the cutting speed of 50m/min, at the feed rate of 5μm in end milling. The cutting force Ft of synthetic VG8 with low friction property were drifting highly compared with dry condition. The cutting edge was supposed to be difficult to bite workpieces in case of synthetic VG8 because of low friction oil film.

The red line in figure 10 shows max accumulation value of cutting force Ft. In this time, specific values that the average of the difference between max accumulation value of cutting force Ft and cutting force Ft divided by the average of cutting force Ft were defined as cutting force instability rate.

Figure 11 shows the relationship between cutting force instability rate and feed rate at the cutting speed of 50m/min with synthetic VG8. The cutting force instability rate decreased with the feed rate. In case of

using the low friction machining fluids, especially feed rate should increase to stabilize cutting force.
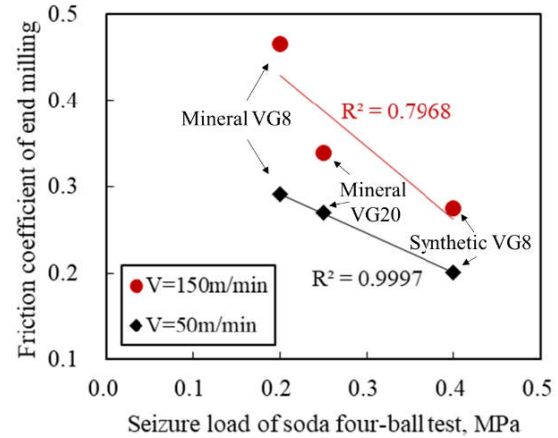
Fig 9 Relationship between friction coefficient of micro end milling and seizure load of soda four-ball test
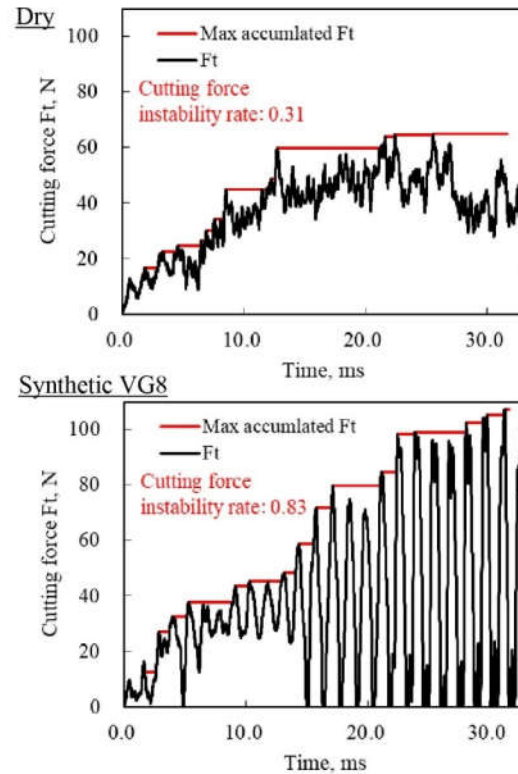
Fig 10 Drifting cutting force Ft and cutting force instability rate.

4. Conclusions

In this study, friction properties of machining fluids were evaluated using friction coefficient calculated from the cutting force in micro feed end milling.

23

1) The finished surface roughness in conventional end milling decreased with friction coefficient of machining fluids obtained by this method.

2) The cutting speed dependence of friction coefficient and the influence on biting property of cutting edge could be evaluated by this method.

References

[1] K. Ono, S. Kawamura, M. Kitano, T. Shimamune, Theory cutting engineering, gendaikougakusha, (1979).

[2] T. Kitamura, Technical Trend of Environmentally Friendly Cutting Fluid, J. Jpn. Soc. of Tribologists, 7(2014)413.

[3] T. Nakayama, Evaluation of Machinability of Cutting Fluids, Lubrication, 6(1977)352.

[4] S. Hara, Cutting Fluids, J. Jpn. Soc. of Tribologists, 10(1994)897.

[5] T. Hatta, F. Itoigawa, A. Sugino, T. Kimura, Elucidation of Friction Behavior on Rake Surface of Cutting Tool using Newly-Formed Surface Friction Test, Electric furnace steel, 2(2011)109.

[6] M. Yamamoto, F. Itoigawa, T. Nakamura, S. Suda, Study on Lubrication Mechanism with Minute Amount of Lubricant on Tool Face Friction in MQL Cutting, Precision Engineering Society Spring Meeting academic lecture Proceedings, (2006).

[7] Precision machine tools Handbook, (1992)15.

[8] A. Yamamoto, S Nakamura, Study on Rubbing-Cutting Transition Phenomena at the Depth of Cut Increase Gradually, Precision Machinery, 5(1967) 314.

PART I, SECTION II

Materials Technology
(Functional Materials; Technologies of Materials; Materials Characterization and Evaluation;
High Speed Machining and Abrasive Machining; Micro- and Nano-Systems Engineering and
Emerging Technologies; Surface Integrity and Machining Quality…)

Smoothing of Hole Bottom Surface by Guiding Large-area Electron Beam with Magnet

Mitsuhiro Kimura[1], Togo Shinonaga[1], Akira Okada[1], Motohiro Inoue[2]
[1]Graduate School of Natural Science & Technology, Okayama University, Japan
[2]Sodick Co., Ltd, Japan

ABSTRACT

In a large-area electron beam (EB) irradiation method developed recently, high energy density of the EB can be obtained without focusing the beam by using an Explosive Electron Emission phenomenon. Previous studies showed that surface smoothing could be performed in a short time for metal mold steels having surface roughness with several micro meters by the large-area EB irradiation. However, it is difficult to smooth a hole bottom surface, since the EB tends   to concentrate on the entrance edge or upper side wall of the hole. In this study, guiding the EB to the hole bottom surface and smoothing of the surface are experimentally investigated in a large-are EB irradiation.

Keywords: Large-area EB irradiation, Smoothing, Hole bottom surface, Magnetic force line, Magnet

1. Introduction

In a large-area electron beam (EB) irradiation method developed recently, high energy density of the EB can be obtained without focusing the beam by using an Explosive Electron Emission phenomenon. Therefore, the large-area EB with diameter of approximately 60 mm can be used for instant melting and evaporating of the wide area on the material surface, and highly efficient surface finishing of the metal surface is possible. Previous studies showed that surface smoothing could be performed in a short time for metal mold steels having surface roughness with several micro meters by the large-area EB irradiation [1-4].

However, when the workpiece has a hole shape, the EB tends to concentrate on the entrance edge or upper side wall of the hole, and the energy density of the EB may decrease on the hole bottom surface. Therefore, it is difficult to smooth the hole bottom surface by the large-area EB irradiation. Then, a method for guiding the EB to the hole bottom surface is required.

During the large-area EB irradiation, lines of magnetic force are generated by solenoid coils set on the outside of a chamber. If the non-magnetic material is placed in the chamber, the lines of magnetic force are diffused from cathode to the workpiece. Then, the energy density of EB reduces on the non-magnetic material surface, since the electrons tend to move spirally along the lines of magnetic force. On the other hand, the lines of magnetic force concentrate and direct towards the magnetic material. In the pre-experiments, it has been clarified that the surface smoothing effect of the magnetic materials improves compared with the non-magnetic materials under the same EB irradiating conditions[5]. This result suggests that the EB more concentrates and higher energy density of the EB may be obtained on the magnetic materials compared with non-magnetic ones. Therefore, it is highly expected that the EB can be guided to the hole bottom surface by

setting a magnet under the workpiece in the large-area EB irradiation.

In this study, guiding the EB to the hole bottom surface is proposed by setting the magnet under the workpiece in a large-area EB irradiation. Then, smoothing of the hole bottom surface is experimentally investigated. Moreover, the expansion of smoothed area is also examined by changing the setting position of the magnet

2. Experimental Procedure

Stainless steel SUS304 in JIS specification is used as workpiece material. Table 1 shows material properties of SUS304. Surface roughness of the workpiece was fixed about 4.5μmRz by wire electric discharge machining. At first, the large-area EB was irradiated to the SUS304 plate to investigate influence of the EB irradiating conditions on the surface smoothing effect for the SUS304. In the experiments, energy density was changed from Ed=1.0 to 15 J/cm2, and the number of irradiation was fixed at N=30 shots.

Table 1 Material properties of SUS304

Melting point	1,673 [K]
Thermal conductivity	16.7 [W(m・K)]
Density	7,930 [kg/m³]
Specific heat	0.59 [kJ/(kg・K)]
Relative permeability	1.004

Next, smoothing of the hole bottom surface was examined based on the EB irradiation conditions obtained in the experiment for the SUS304 plate. Figure 1 shows schematic illustration of the workpiece which has the hole bottom surface used in this experiment. The workpiece with the hole was prepared by combining side workpiece having a hole with diameter of 20 mm and bottom workpiece of 25x25x5 mm to

make it easy to evaluate smoothed area on the hole bottom surface.

(a) Without magnet　　(b) With magnet
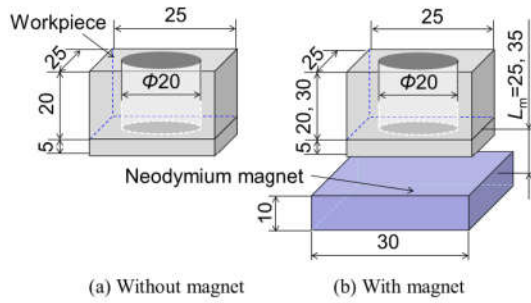
Fig. 1 Schematic diagram of workpiece with and without magnet

Then, hole depth of the workpiece was set at H_h=20 mm, 30 mm. In this experiment, neodymium magnet of 30x30x10 mm was placed under the workpiece at distance from the hole bottom surface of L_m=25, 35 mm. The large-area EB was irradiated to the upper side of the hole. Surface roughness of the hole bottom surface was measured by contact type surface profilometer in range of distance from the center to the edge of D_c=0 to 10 mm. Moreover, surface roughness was measured at intervals of 20 μm by using a micrometer in the range of more than 9 mm to the judge smoothed area in detail. Figure 2 shows predicted electron tracks with or without magnet. It is considered that the EB concentrates on the entrance edge and upper side wall of the hole surface in the case without magnet. However, it is expected that the smoothed area is expanded by guiding EB to whole area of the hole bottom surface with magnetic field of the magnet.

(a) Without magnet　　(b) With magnet
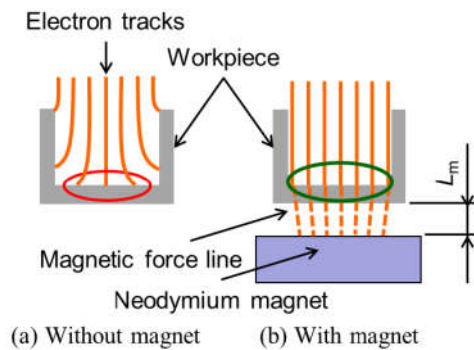
Fig. 2 Expected electron tracks with and without magnet

3. Result and Discussion

3.1 Smoothing effect on SUS304 plate

At first, the large-are EB is irradiated to the SUS304 plate and smoothing effect on the workpiece are investigated by changing the energy density of EB. Figure 3 shows optical images of the workpiece and optical microscope images of center part of the workpiece with and without the large-area EB

irradiation. At energy density of Ed=1.0 J/cm2, glossy and smooth surface is obtained, although small craters are generated on the surface at Ed=3.0 J/cm2. When the energy density increases to the Ed=5.0 J/cm2, the crater disappears, and smooth and glossy surface is obtained again. However, at Ed=7.5 J/cm2, craters are re-generated on the surface. It is made clear that the smoothing surface without craters can be obtained by large-area EB irradiation at appropriate energy density conditions.
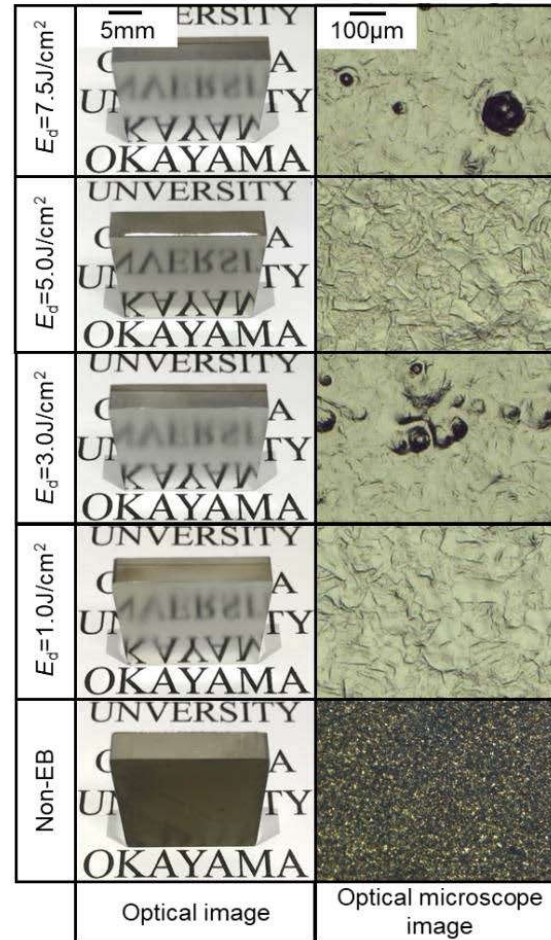
Fig. 3 Optical images and optical microscope images of SUS304 plate

Figure 4 shows the surface roughness and the glossiness on the workpiece with energy densities. Energy density at Ed=0 J/cm2 shows surface roughness and glossiness of the non-EB irradiation surface. As shown in the figure, surface roughness decreases from the initial roughness of 4.5 μmRz after large-area EB irradiation. Moreover, the surface roughness becomes lower than 1.0 μmRz at Ed=5.0 J/cm2. When the energy density becomes more than Ed=7.5 J/cm^2, the surface roughness gradually increases. On the other hand, the glossiness increases as the surface roughness

becomes small. The glossiness becomes highest at Ed=5.0 J/cm^2.
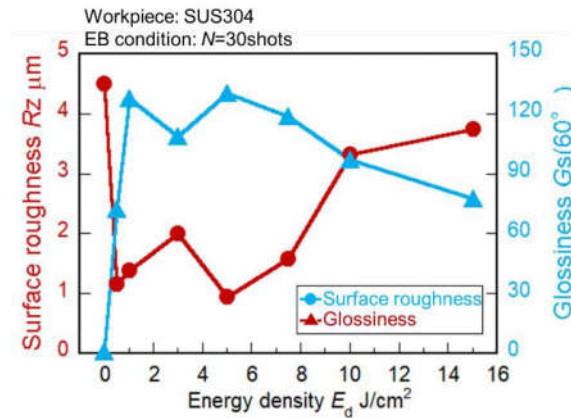
Fig. 4 Variations of surface roughness and glossiness on plate surface with energy density

Therefore, surface roughness of approximately 1.0 µmRz and high glossy surface can be obtained on the SUS304 plate by large-area EB irradiation with appropriate energy density.

3.2 Smoothing of hole bottom surface

After the EB irradiation under appropriate EB condition, sufficiently smooth surface can be obtained on the SUS304 plate, and surface roughness is reduced from 4.5 µmRz to lower than 1.0 µmRz. These results suggest that the limit value for reducing surface roughness on the SUS304 plates is about 1.0 µmRz. Therefore, if the roughness on the hole bottom surface decreases to less than 1.5 µmRz, the smoothing effect is judged to be sufficient in this study. When the large-area EB is irradiated to the hole bottom surface, the center area of the hole bottom surface may be preferentially smoothed, as shown in Fig. 5. Then, the smoothed area of the hole bottom surface is defined as the area whose surface roughness is less than 1.5 µmRz.
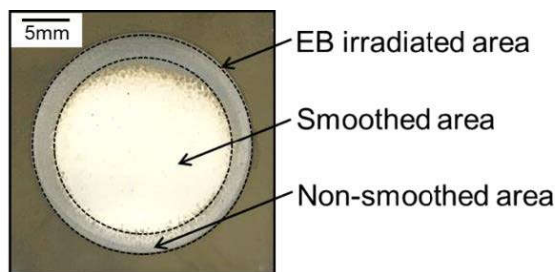
Fig. 5 Definition of smoothed area and non-smoothed area
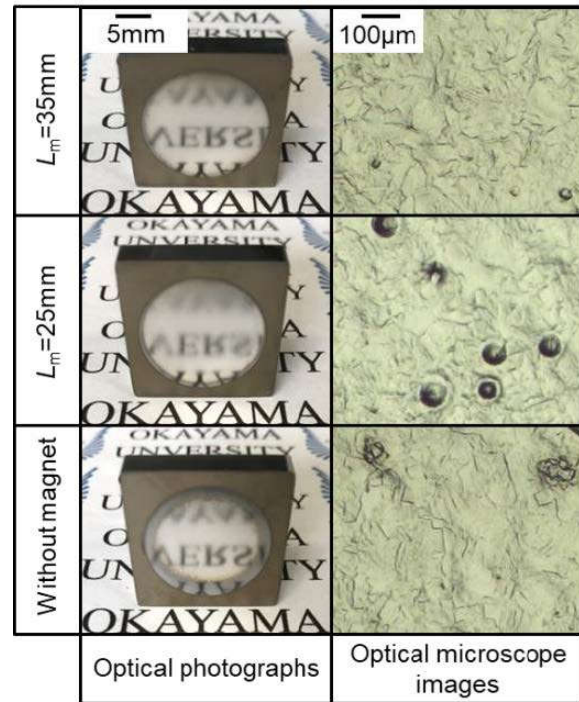
Fig. 6 Optical photographs and optical microscope images of bottom hole surface

In the pre-experiments, the workpiece with a hole depth of Hh=20 mm was irradiated at the energy density of Ed=3.0 and 5.0 J/cm^2. Large craters were generated on the hole bottom surface with and without magnet. This result suggests that excessive energy density is irradiated to the center part of the hole bottom surface. Therefore, energy density of the EB reduces to Ed=1.0 J/cm^2. Then, the magnet is set at Lm=25 and 35mm. Figure 6 shows optical photographs of the hole bottom surface and optical microscope images at the center part of workpiece after the EB irradiation. Generation of the craters can hardly be confirmed by setting magnet at Lm=35 mm, and smooth surface can be obtained. Moreover, changing in hue is confirmed at the edge of the hole bottom surface in this case without magnet from the optical photograph, although changing in hue is not confirmed by setting magnet at Lm=25 mm and 35 mm. In the case of Lm=35 mm, the hole bottom surface having high glossiness can be obtained compared with Lm=25 mm.

Figure 7 shows variations of surface roughness on the hole bottom surface at Dc=0 mm to 10 mm. In the case with magnet at Lm=25 mm, surface roughness increases in the area excluding the center of the hole bottom surface compared to the case without magnet. Then, smoothed area radius of the hole bottom surface is Ds=7.0 mm. This is because the EB is guided to the hole bottom surface with magnet at Lm=25 mm, and

excessive energy density of the EB is irradiated to the hole bottom surface at center area to generate small craters. On the other hand, uniform smoothed the area having roughness of 1.5 µmRz or less can be obtained in area of Dc=0 mm to 9 mm without and with magnet at Lm=35 mm. Moreover, it is possible to confirm reduction of the surface roughness with magnet at Lm=35 mm as compared with the case without magnet.
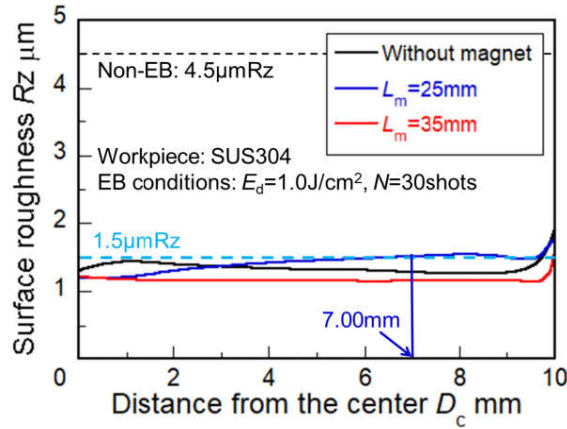
Fig. 7 Variations of surface roughness on hole bottom surface with and without magnet

Figure 8 shows variations of surface roughness on the hole bottom surface at Dc=9 mm to 10 mm. In the case without magnet, smoothed area radius is Ds=9.76 mm. In contrast, the smoothed area radius becomes Ds=9.98 mm, and the area almost equal to the hole bottom radius is obtained in the case with magnet at Lm=35 mm. These results suggest that the EB can be guided along line of magnetic field to the edge of hole bottom surface by setting appropriate position of the magnet under the workpiece.

Finally, the possibility of the smoothing on the hole bottom surface with high hole depth is examined by changing the hole depth from Hh=20 mm to 30 mm. Figure 9 shows surface roughness distribution of the hole bottom surface with high hole depth at Dc=9 mm to 10 mm after large-area EB irradiation. As shown in the figure, in this case of Hh=30 mm, the smoothed area radius is Ds=9.74 mm, and the area slightly decreases as compared with the case of Hh=20 mm. It is considered that this is because the energy density on the hole bottom surface decreases as the depth of hole increases.

In the future, we will investigate whether the smoothed area equivalent to the hole diameter can be obtained even in the workpiece with high hole depth by changing the EB irradiation conditions, setting position and the shape of the magnet.
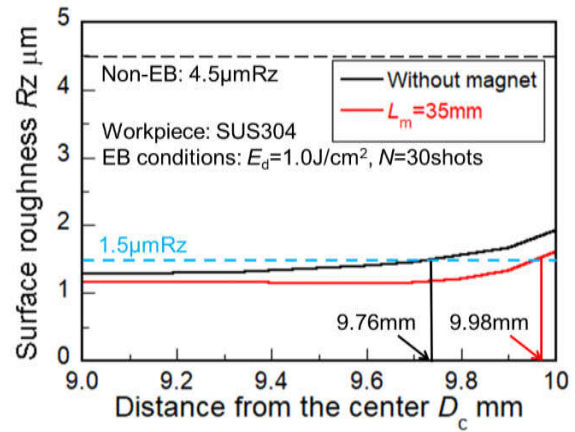
Fig. 8 Variations of surface roughness on hole bottom surface with distance from the center Dc=9mm to 10mm
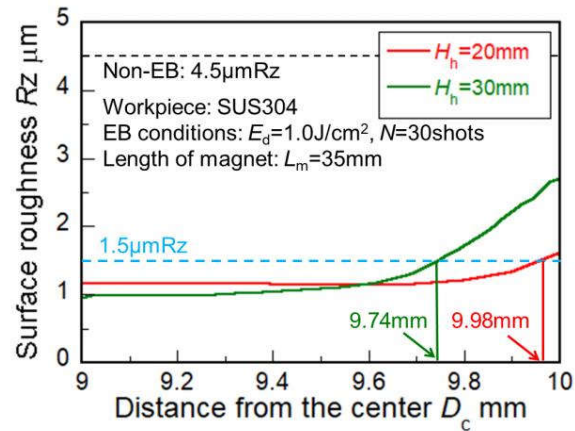
Fig. 9 Variations of surface roughness on hole bottom surface with and without magnet as a function of distance from the center Dc = 9mm to 10mm at difference hole depth Hh = 20mm and 30mm

4. Conclusion

In this study, smoothing of hole bottom surface is experimentally investigated by guiding EB to the hole bottom surface with magnet. Main conclusions obtained in this study are as follows:

(1) Surface roughness of 1.5 µmRz or less can be obtained in the center area of hole bottom surface by large-area EB irradiation at appropriate energy density setting under the workpiece with or without magnet.

(2) EB can be guided along line of magnetic field to edge of hole bottom surface by setting appropriate position of magnet under the workpiece. Then, smoothed area almost equivalent hole diameter can be obtained on the hole bottom surface with hole depth and diameter of 20 mm by guiding EB to hole bottom surface with magnet.

References

[1]   A. Okada, Y. Uno, N. Yabushita, K. Uemura, P. Raharjo: High Efficiency Surface Finishing of Metal Mold by Large-area Electron Beam Irradiation (1st Report), Journal of the Japan Society for Precision Engineering, Vol.69, No.10 (2003), 1464-1468.

[2]   A. Okada, Y. Okamoto, Y. Uno, K. Uemura: Improvement of surface characteristics for long life of metal molds by large-area EB irradiation, Journal Materials Processing Technology, Vol.214 (2014), 1740-1748.

[3]   Y. Uno, A. Okada, K. Uemura, P. Raharjo, T. Furukawa, K. Karato: High Efficiency Surface Finishing Process for Metal Mold by Large-area Electron Beam Irradiation, Precision Engineering, Vol.29 (2005), 449-455.

[4]   Y. Daichi, S. Sano, Y. Uno, A. Okada: Surface Finishing of SKD11 Tool Steel via Plasma-based Electron Beam Irradiation, Key Engineering Materials, Vol.364-366 (2007), 302-307.

[5]   T. Shinonaga, T. Sakai, Y. Kimura, A. Okada: Study on Variation of Burr Height in Micro-deburring with Large-area Electron Beam, International Journal of Electrical Machining, No.23 (2018), 45-50.

Effect of Cathodes Modified by Ag-Deposition on the Charging-discharging of Zinc Air Batteries

Choung-Yheo Chiang[1], Jing-Chie Lin[1, 2], Yee-Cheng Lee[3], Mao-Chia Huang[3], Ching-Chen Wu[3]

[1]Department of mechanical Engineering, National Central University, Jhong-li Dist., Taoyuan City, Taiwan 320

[2]Institute of Materials Science and Engineering, National Central University, Jhong-li Dist., Taoyuan City, Taiwan 320

[3]Institute of Green Energy and Environment, Industrial Technology Research Institute, Hsinchu County, Taiwan 300

ABSTRACT

A novel rechargeable cathode was developed for Zn-air batteries. This cathode was prepared by Ag-electrochemical deposition on a stainless-steel mesh (SS-mesh) in the nitrate bath, which was addition-free (AF), addition with A or with B additive. Through SEM, XRD, CV, EIS studies, we found that the cathodes reveal a superior order depending on the bath A > B > AF. The OER and ORR on the cathodes are discussed to comprehend their distinction on mechanism.

Keywords: cathode, zinc-air batteries, cyclic voltammetry, OER, ORR.

1. Introduction

Zinc air batteries are categorized as ones of metallic air batteries [1-4] to reveal the advantages such as low cost, low pollution, light weight, relatively high specific capacity/energy density, and good safety. Therefore, they become very competitive in comparison with the traditional lead-acid batteries as well as the modern Li-ion batteries. Highly theoretical charge capacity (at 820 mAh g-1) and density (at 1312 Wh kg-1) [4] engage them as promising candidates in electrochemical energy storage devices and power sources.

Typical zinc-air battery cells consist of a couple of electrodes and a separator soaked with electrolyte. The electrodes (i.e., anode and cathode) act as the current collector, whereas the electrolyte provides the way for ionic transportation. The anode can be simply made of metallic zinc; however, the cathode needs a little complicate design, which consisting of a gas diffusion layer (GDL) and a catalyst layer, not only to provide channels for feasible transport of oxygen gas and water but also to offer catalytic sites for oxygen reduction reaction (ORR) and oxygen evolution reaction (OER). In zinc-air battery, it is popular that gas-diffused electrodes composed of carbonaceous powder pressed on both sides of a metallic nickel mesh current-collector.

Silver was reported to display an excellent electrocatalyst on the O2-reduction superior to platinum in the alkaline solution [5, 6]. In the present work, we attempted to deposit a silver coat on the metallic nickel mesh, and so treated this Ag-coated mesh directly as a high efficient cathode for the zinc-air batteries. The silver coating was electrochemically carried out in the baths varying in additives and the effect of additives was investigated.

2. Method

A sheet of stainless steel T316L mesh was cut into rectangular pieces in dimension of 40 mm x 70 mm. The mesh, shown its size of 35 μm, was woven by the wires in a diameter of 42 μm. The composition (wt. %) of this mesh consists of 66.2 Fe, 17.9 Cr, 13.7 Ni and 2.2 Mo. Each rectangular mesh was used as the working electrode, in company with a platinized Ti-mesh (as the counter electrode denoted as Pt) and a saturated calomel electrode (as the reference electrode denoted as SCE) to undergo electrochemical deposition in a standard 200 mL threeneck cell. There are three baths to be used. The bath containing pure 0.2 M silver nitrate, was named addition-free (AF). The other two involving additives A and B in the pure bath were named as A and bath B. The electrochemical process conducted in all the baths was controlled at a constant current (50 mA) for 2h. Finishing Ag-deposition, the deposited specimens were removed to dry, ready for examination, testing and further assembling into a full cell of zinc batteries for evaluation. The surface morphology of the samples was observed by a scanning electron microscope (SEM, JSM-7401F), their crystal structure was examined by X-ray diffractometer (XRD).

The Ag-deposited specimens resulted from different baths were subjected to cyclic voltammetry (CV) in a solution of 6 M KOH combined with 0.2 M zinc acetate to evaluate their cathode behavior. In the performance of CV, Ag-deposited specimens were acted as working electrode, a tin plate was the counter and the SCE as the reference. Cyclic scan was set in the range from 0.40 V to -0.45 V Vs. SCE in a scan rate at 1, 2 and 3 mV/s.

3. Result and Discussion

3.1 Surface morphology and crystal structure

Figure 1 depicts the surface morphology of the silver deposited specimens from different baths. It is evident, from Fig. 1 (a), that the specimen AF revealing a separated distribution of silver particles on the frame of SS mesh. A large portion of the SS mesh is exposed due to an incomplete coverage by the silver particles whose size appears greater than the mesh of the SS frame. In

comparison, Figs. 1 (b) and (c) demonstrate that silver particles deposited in a relative smaller size from the baths in the presence of additives A and B.
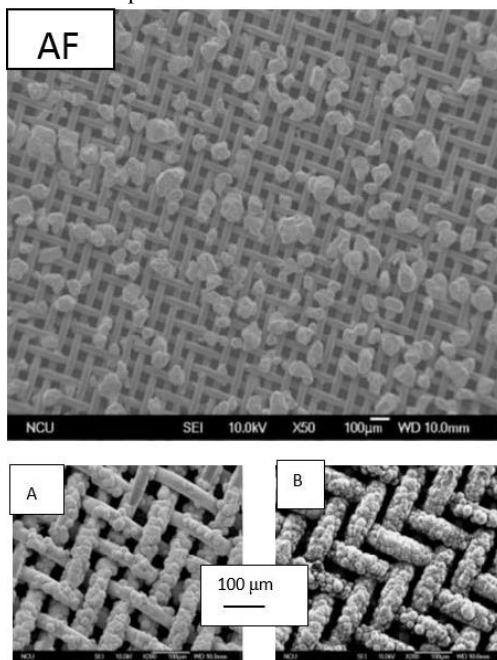
Fig. 1 The stainless-steel mesh decorated by Ag-electrochemical deposition in the baths that is (a) addition-free, (b)with additive A, and (c) additive with B.

These small silver particles are inclined to coating on each wire of the mesh frame. As a result, the coverage of Ag-deposition on the mesh frame is greatly enhanced in the bath containing additives A and B. Examining the morphology of the specimens A and B in high magnification, as shown in Fig. 2, we found that the coatings on the wire of the mesh are established by different elements in distinctive shapes. In the specimen A, the silver coating seems to be constructed by micro nodules which are in turn developed by silver nanorods. In contrast, in the specimen B, the silver coating may arise from a packing of micro balls of yarn, which is basically developed by silver nanowires.
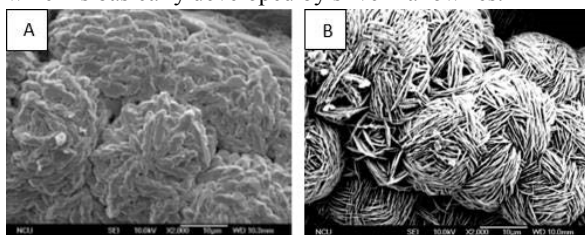
Fig. 2 Magnified surface morphology of silver decorated on the SS via electrochemical deposition in the bath with (a) A additive and (b) B additive

Figure 3 displays the XRD pattern for the specimen AF. Characteristic peaks of silver (111), (200) and (220) are found and perhaps there is an overlap between Ag(200), coming from the Ag-deposit, and the austenite (111), arisen from the substrate of SS mesh, Specimens A and B also display a similar pattern in XRD but their intensity of the silver character peaks is lower and broader as compared to that of specimen AF. This fact reflects that the deposited silver particles are finer in specimens A and B than in specimen AF.
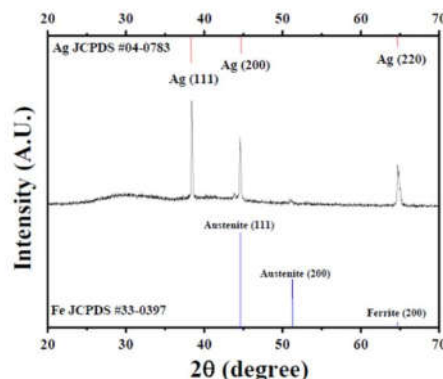
Fig. 3 XRD pattern for the specimen AF
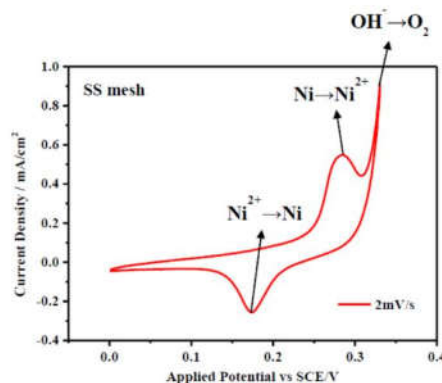
Fig. 4 CV of the SS mesh in a solution of 6 M KOH combined with 0.2 M zinc acetate

3.2 Cyclic voltammetry study

Figure 4 indicates the CV of the bare SS mesh in a solution of 6 M KOH combined with 0.2 M zinc acetate. In comparison with Fig. 4 and Fig. 5, we can realize the effect of Ag-deposition on the electrochemical redox reaction of the SS mesh, which is considered the pristine cathode, in the electrolyte of the zinc-air batteries. Fig. 4 shows that CV diagram is scanned from 0.4Vto -0.45V with a scan rate of 2 mV/s. In this diagram, there is a symmetric redox couple that is oxidation peak located at 0.28V (vs. SCE) in company with a reduction one at 0.28V (vs. SCE). They are corresponding the nickel oxidation to form nickel oxide and its reversible reduction. The peak to the extremely right, at 0.37 V (vs. SCE), is ascribed to OER on the surface of bare SS mesh.

32
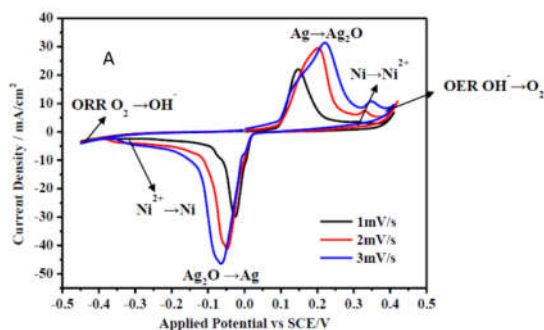
Fig. 5 CV of the specimen A in a solution of 6 M KOH combined with 0.2 M zinc acetate

Figure 5 shows the CV of the specimen A in a solution of 6 M KOH combined with 0.2 M zinc acetate. There are three pairs of peaks in the CV voltammogram: the first oxidation peak, positioned at 0.1~0.28 V (vs. SCE) with its peak current at 30 mA/cm2, indicates the oxidation of silver particles to form silver oxide. The second oxidation peak at 0.3~0.36 V (vs. SCE) may be ascribed to nickel oxidation. This contribution by nickel oxidation is not significant because the intensity of this peak is tiny. The third oxidation peak, positioned at 0.37 V (vs. SCE), is arisen from OER on the surface of SS mesh. To the opposite, the first reduction peak at -0.013~-0.1 V (vs. SCE) is attributed to silver reduction from silver oxide. The current peak is 40 mA/cm2 which is higher than others. In this diagram, no obvious peaks with response to nickel reduction. This fact implies that almost all the surface of SS mesh having been completely coated by silver powders, therefore, redox reaction of silver is much superior to the nickel redox reaction. The peak to the most left at -0.37 V(vs. SCE) is considered as the ORR.

3.3 Evaluation of ORR and OER of a full cell

Figure 6 reveals the picture of a full cell zinc-air battery. The cell was assembled with the same components except the cathode chosen from the Ag-deposited specimen resultant from various baths in the work. The ORR character of the cathode in the full cell could be estimated by charging the cell; whereas the OER would be evaluated by discharging the cell.
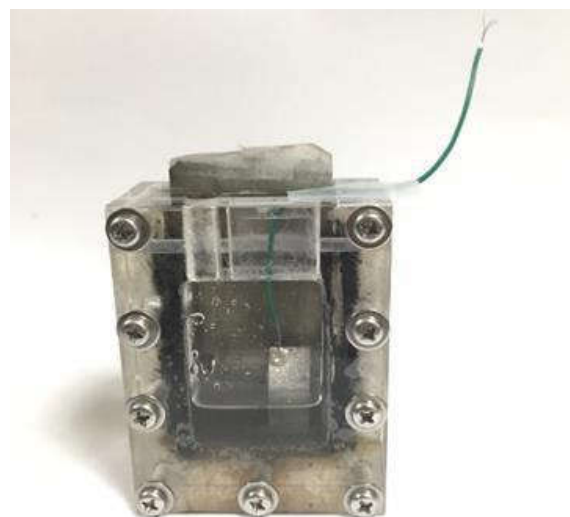
Fig. 6 The picture of a full cell zinc-air battery assembled from the same components except the cathode of Ag-deposited specimen resultant from the bath AF, A or B.

Figures. 7, 8 and 9 indicate the results of repeated charging-discharging test of the full cell as shown in Fig. 6; however, the cell composed of different cathode discriminated by Ag-deposition bath AF, A and B, respectively. The diagrams are plotted with a ordinate of voltage (dimension in V) against a horizontal of cell capacity (dimension in mA h). According to an existence of two- stage in either charging or discharging, this cell is categorized as a composite cell. In Fig. 7, we found that at first stage, the cell charges (in response to silver oxidation) at 1.7 V and it discharges (corresponding reduction of the silver oxide) at 1.5 V. The capacity of the cell is equal to 0.10 mA h. As for the second stage, it charges at 2.0 V and discharges at 0.9 V, corresponding to oxygen oxidation catalyzed by few Ag particles coated on the SS mesh from the specimen AF. The overall capacity of the cell is equal to 0.25 mA h. The phenomenon of the charging-discharging in two stages is more prominent in Fig. 8. As in Fig. 7, the charging and discharging processes in the first-stage take place at 1.7 and 1.5 V, respectively. With respect to the second stage, those corresponding processes happen at 2.0 and 0.9 V, as shown in Figs. 8 and 9. The overall capacity is equal to 0.47 mA h for the cell assembled with a cathode of Ag-deposited from bath A. According the Fig. 9, the capacity is much higher (at 0.85 mA h) for the cell assembled with a cathode of Ag-deposited from bath B.
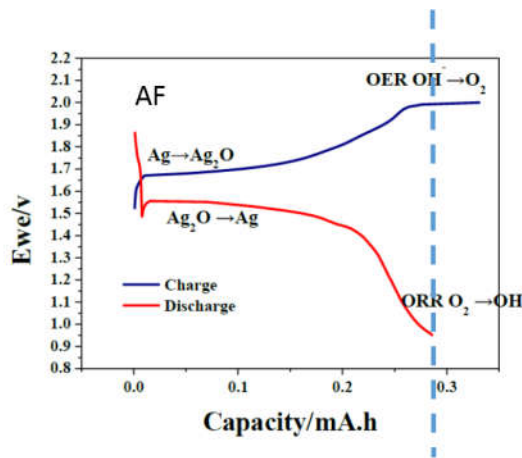
Fig. 7 Charging and discharging for the full cell assembled with the cathode prepared specimen AF
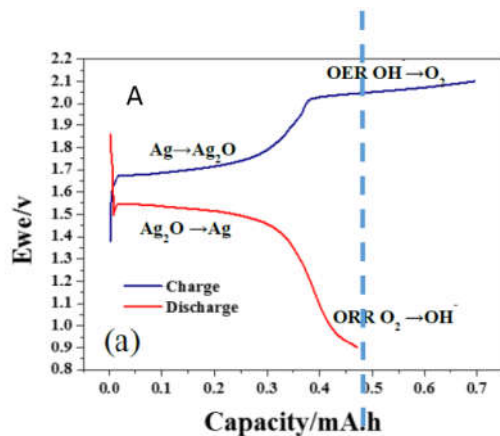
Fig. 8 Charging and discharging for the full cell assembled with the cathode prepared specimen A

A full cell assembled by the cathode prepared by Ag-deposited specimen from bath B was evaluated in comparison with that assembled by the cathode prepared by commercial catalyst Pt/C. The data of the coulomb efficiency, voltage efficiency and energy efficiency for both different full cells were listed in Table 1. According to the results shown in Table 1, we concluded that the cathode prepared from the Ag-specimen derived from bath B is superior to that from the commercial Pt/C.

4. Concluding Remarks

Cathodes made of SS mesh decorated with silver by electrochemical deposition significantly enhance the
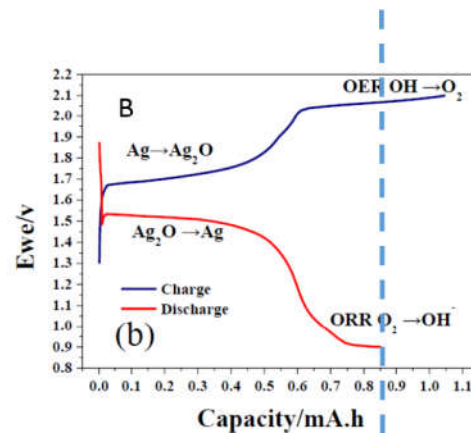
Fig. 9 Charging and discharging for the full cell assembled with the cathode prepared specimen B

Table 1 Efficiency of zinc-air cells based on the cathode made of commercial Pt/C compared to that made of specimen B in this work

Type of efficiency	From Pt/C	From B specimen
Coulombic efficiency	95%	98%
Voltage efficiency	64%	75%
Energy efficiency	61%	74%

catalytic reactivity of ORR and OER so that improve the specific capacity and specific energy of zinc–air battery.

References

[1]   C. Chakkaravarthy, A.K. Abdul Waheed, H.V.K. Udupa, J. Power Sources 6 (1981) 203
[2]   F. Beck, P. Rüetschi, Electrochim. Acta 45 (2000) 2467.
[3]   W.H. Zhu, B.A. Poole, D.R. Cahela, B.J. Tatarchuk, J. Appl. Electrochem. 33 (2003) 29.
[4]   C.Y. Wu, P.W.Wu, P. Lin, Y.Y. Li, Y.M. Lin, J. Electrochem. Soc. 154 (2007) B1059.
[5]   B.B. Blizanac, P.N. Ross, N.M. Markovic, Electrochim. Acta 52 (2007) 2264.
[6]   M.A. Kostowskyj, R.J. Gilliam, D.W. Kirk, S.J. Thorpe, Int. J. Hydrogen Energy 33 (2008) 5773.

The Effects of Cu, Zn on the Solution Temperature and Quenching Sensitivity of Al-Zn-Mg-Cu Alloys

Albert Chiu[1], S.S. Lee[1.2]

[1]National Central University, Institute of Materials Science and Engineering, Jhongli 32001, Taiwan
[2]National Central University, Department of Mechanical Engineering, Jhongli 32001, Taiwan

ABSTRACT

By experiment, when the high copper alloy went through heat treatment over 530□, melting phenomena of the grain boundary could be obviously observed. After a certain amount of copper was reduced, homogenizing heat treatment made the eutectic T phase (Mg3Zn3Al2) and η phase (MgZn2) of the Al-Zn-Mg-Cu alloy dissolved fully in the aluminum base. It did not precipitate the low melting point's (~495□) S phase (Al2CuMg). Thus, the alloy solution temperature was enhanced, and the solution heat treatment efficiency was improved. Besides, by adding a certain amount of zinc to the alloy, the precipitation amount of strengthening phase η'(MgZn2) was increased. It compensated for the reduced mechanical strength of the alloy which contained less copper. The results showed that zinc atoms not only elevated the strength of the alloy, but also had no damage to the ductility of the alloy. Furthermore, it improved the quenching sensitivity of the alloy with the addition of zirconium atoms.

Keywords: Al-Zn-Mg-Cu, solution temperature, mechanical properties, quenching sensitivity

1. Introduction

In order to solve the low solution temperature and high quenching sensitivity, an attempt is made to design and develop a new type of alloy which can replace AA7075 aluminum alloy[1.2.3]. It is expected to upgrade the solution temperature of the alloy and lower its quenching sensitivity without degrading its mechanical properties (strength and ductility). According to the documents gathered[5.6], so far no related study of the theme has been reported[7.8].

2. Method

After the purity 99.7% aluminum ingot had melted at 750□ in the crucible of the electric resistance furnace, respectively a scheduled amount of Al-50Cu master alloy, Al-10Zr master alloy, purity 99.9% Mg, purity Zn etc. were added. When all of these melted, they were fully and evenly stirred. Then after purity argon (Ar) gas had been used for degassing for 20 minutes, the solution was left to stand for 10 minutes. After the slag removal, the solution was cast in a preheated (300□) Ø125mm×200mm columned metal mold.

After being homogenized 460□x24hrs and put in a preheated 430□ x 3hrs Ø100mm ingot container, the cast alloy went through 70-85% deformation by heat extrusion (from Ø100mm to Ø31mm and then to Ø16mm). After heat extrusion, the test piece went through solution treatment 470□x2 hrs and then water cooling or air cooling individually until room temperature to explore the quenching sensitivity of the alloy. After the alloy solution cooled, the alloy went through 120□x24hrs aging treatment.

After the extruded alloy went through solution treatment 470□ x 2hrs, it was cooled by water or air individually until room temperature. Then after 120□x24hr aging treatment, the 10 Ton Universal Material Testing Machine (UTM, CHUNYEN, CY-6040A4) was used to make a tensile test at a strain rate

$(1.3×10^{-3}s^{-1})$ at room temperature. The test piece was shown in Figure 1[1.9]. After 470□x2hrs solution treatment, water was injected to the end quenching device to cool the alloy until room temperature in order to evaluate the quenching sensitivity of the alloy. The test piece was shown in Figure 2[9]. The Rockwell Hardness Tester-Rockwell B scale ） was used to measure the alloy hardness.

3. Results and Discussion

Through the alloy design, the purpose of this study was to upgrade the solid solution temperature of the commercial AA7075 aluminum alloy and lower its quenching sensitivity. The design steps for this experiment were described as follows (Table 1: Alloy component analysis (wt%) in the above)：

1. The commercial AA7075 aluminum alloy which was provided by Ye Fong Aluminum Company served as a baseline for the comparison with the modified Al-Zn-Mg-Cu alloy.

2. In order to improve the quenching sensitivity of AA7075 aluminum alloy, Zr7075 alloy was created by replacing the Cr in AA7705 alloy with Zr.

3. In order to explore the influence of the Cu content on the solution temperature and mechanical properties of AA7075 aluminum alloy, the modified MZr7075 alloy was created by reducing the Cu content (1.6wt%→1.0wt %) in Zr7075 alloy.

4. In order to explore the influence of Zn on enhancing the mechanical strengthening properties of the Al-Zn-Mg-Cu lloy, HZn alloy was created by increasing the strengthening Zn content (5.6wt%→7wt%) in MZr7075 alloy.

Certainly, the above designed and experimental alloys could not fully or satisfactorily replace the functions of AA7075 alloy. For one thing, the tensile test could not cover the complete mechanical properties. For another, the chemical and physical properties of the alloys were

to be continuously explored. However, this study might offer a valuable reference for future researchers.

4. Conclusion remark

1. By decreasing the Cu content, the eutectic low melting point (~495℃) S phase (Al$_2$CuMg) in the Al-Zn-Mg-Cu alloy could be eliminated. This method could enhance the solid solution temperature to the temperature which was slightly lower than its melting temperature (~575℃). It also could effectively enhance the efficiency of the solid solution heat treatment of the alloy.

2. By adding Zn content, it compensated for the reduced mechanical strength of the alloy which contained less Cu. It also caused no damage to the ductility of the alloy.

To sum up, by reducing Cu, and adding more Zn, we can upgrade the solution temperature of the Al-Zn-Mg-Cu alloy and lower its quenching sensitivity without degrading its mechanical properties: strength and ductility.

Reference

[1] ASTM A255-10, "Standard Test Methods for Determining Hardenability of Steel", (2014).

[2] ASTM B557M-15, "Annual Book of ASTM Standards", (2015).

[3] Tolga Dursun, Costas Soutis, Materials & Design, vol.56 (2014) pp.862–871.

[4] T.H. Sanders, Jr. and E. A. Starke, Jr., Metall. Trans., vol.7A (1976) pp. 1407-1418.

[5] X.-M. Li, M. J. Starink, Mater. Sci. Techn, vol.17 (2001), pp.1324-28.

[6] Shengdan Liu, Qimin Zhong, Yong Zhang, , Materials & Design, vol.31 Issue 6 (2010) pp.3116-3120.

[7] LIU Shengdan, LI Chengbo, The Chinese Journal of Nonferrous Metals, vol.23 No.4 (2013) pp.927-938.

[8] Qingjiang Meng and G. S. Frankel, , Journal of The Electrochemical Society, vol.151 (2004) pp.271-283.

[9] Xi-gang FAN, Da-ming JIANG, Qing-chang MENG, , Transactions of Nonferrous Metals Society of China, vol.16 Issue 3 (2006) pp577-581.

Laser-shock Peening on Tool Steel and Its Shock-pressure Measurement

Yu-Chi Shih[1] and Jeng-Rong Ho[2]

[1]Graduate Institute of Optomectronic Engineering, National Central University Chungli, Taoyuan, 32054, Taiwan

[2]Department of Mechanical Engineering, National Central University Chungli, Taoyuan, 32054, Taiwan

ABSTRACT

Laser shock peening (LSP) is the use the high pressure, resulting from a momentum impulse generated by material vaporization at the target surface when rapidly heated by an ultrashort laser pulse, to impart long term, beneficial residual stresses in materials. To generate an instantaneously high-pressure shock wave, the laser peak power should be very high, which is usually achieved by an ultrashort pulsed laser with pulse durations less than several nanoseconds. After the LSP processing, the surface is finer, and roughness becomes smaller. The residual stress generated by LSP can reach 1 ~ 2 mm in depth that can effectively restrain the propagation of surface crack. In this study, the target is SKD 61 tool steel immersed in deionized water and the light source is from a pulsed Nd:YAG laser, with pulse duration of 5 ns and repetition rate of 10 HZ. We discuss the improvements in the surface hardness and roughness of the target by LSP at various laser operation parameters. Surface hardness of the as-received SKD 61 was measured to be 200 HV. It can be apparently enhanced to 300 HV. LSP treatment can also significantly reduce the surface roughness, the average roughness (Ra) showed an average decrease of 25% and the maximum roughness (Rmax) decreased by an average of 47%. The hardening mechanism of LSP is the impulse pressure from shock waves, generated by laser induced plasma. Thus, the magnitude of shock wave pressure is the key to the result of the surface modification. Therefore, we also obtain the plasma pressure in the LSP process. This is accomplished by directly measuring the shock speeds based on the photo-acoustic effect, then convert them to the corresponding plasma pressures. Results show that, in this study, the speed of the shock wave is 3.99 km/s at a laser power of 450 mW, and the corresponding plasma pressure is 0.484 GPa.

1. Introduction

Laser shock peening (LSP) has been proposed as a means of introducing compressive stresses in the surface of the material in order to increase their fretting fatigue resistance. LSP is capable of introducing significant compressive surface stress in flat plates to a much greater depth which is typically at 1 to 2 mm than with the traditional techniques such as shot peening process. The atoms in the surface of a piece of manufactured metal will be under tensile stresses from grinding, welds, heat treatments and other stressful production processes. Cracks generated easily in areas of tensile stress because the tensile stresses will pull the atoms of the metal apart. As the LSP is performed, the atoms on the surface of the metal become crowded and try to restore the metal's original shape by pushing outward. The atoms which is deeper into the metal will be pulled toward the surface by their bonds with the atoms become to the compressive layer. These deeper atoms resist the outward pull creating internal tensile stress that keeps the part in equilibrium with the compressive stress on the surface.

When laser irradiating a target with a high-energy focused and pulsed laser beam, the laser energy will be absorbed in a thin layer and generated a high-pressure plasma. If the target has been covered by a water layer, the plasma is generated and its expansion is delayed. This water confined regime configuration, and mainly the shock wave system transmitted to the targets, has already shown its efficiency for material surface processing

2. Experimental method

2.1 Materials

ASIS H13 tool steel also known as SKD61 was used in this study in precision molds of manufacturing tools for processing since it has advantages of high resistance, thermal fatigue, high abrasion resistance and heat resistance. However, it has the characteristics of large amount of changes of measurement and twisting of materials during heat treatment. So, it is usual to have roughing processing due to the large amount of changes of measurement and to have electric discharge machining after heat treatment. Laser surface hardening technology was applied to overcoming the disadvantages above.

2.2 Laser shock process (LSP)

The experiments were performed with a Q-switched Nd:YAG (neodymium-doped yttrium aluminum garnet) laser with a wavelength of 532 nm and a frequency of 10 Hz. The laser emitted a 3–5 ns Gaussian distributed pulse. The laser beam was focused to a diameter of 200 μm using a 70 mm focal length lens. The power density from 0.1 to 2 GW/cm2.T The left and right margins in a page must be 2 cm, the top and the bottom margins must be 2.5 cm.

2.3 Photoacoustic wave Pressure

Two He-Ne laser beams separated by 1 mm were used to measure the shock velocity. The signal was recorded by an oscilloscope (Rohde&Schwarz RTE1052 500

MHzbandwidth) and transferred to a computer for processing.

3. Results and Discussion

3.1 Micro hardness

This study discuss the effect of the micro hardness with the different laser powers and X,Y table scan speeds. Assume that the laser spot size is constant, the lower the scan speed is the higher the laser overlapping is. In the Figure 1, when the scan speed is lower the micro hardness increased more than that is higher. However, when the scan speed is 1 mm/s, we can separate the result into two parts. The first part is average laser power ranging from 200 mw to 450 mw and the second part of that is ranging from 450 mw to 700 mw. In the first part, the result shows that the original micro hardness of the material is around 200 HV and the micro hardness is increased with the enhancement of the laser power. The micro hardness reaching 290 HV at laser power 450 mW. However, when the laser power higher than the 450 mW the micro hardness doesn't increase with the higher laser power. Instead of the higher micro hardness, the result shows that trend become a horizon line or even decreased. The same phenomena is also observable in the scan speed at 0.8 mm/s. When the laser power is higher than the 400 mW, the micro hardness is reaching around 300 HV rather than increased apparently. Therefore, using the photoacoustic to measure the shock wave pressure generated by laser, ensuring that the shock wave pressure is increased with the laser power. Showing that the material micro hardness limit is around 300 HV rather than the error of the experiment process.
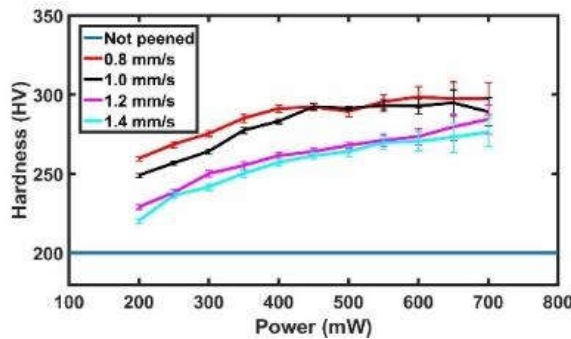
Fig. 1 Hardness as a function of laser power

3.2 Surface roughness

Figure 2 shows the differences between the peened area and un-peened area. Before the LSP process, the surface roughness Ra and $Rmax$ of SKD 61 are 5.4 μm and 13.7 μm, respectively. However, after the LSP, with the laser power ranging from 200 mW to 650 mW, surface roughness reduce to average 4.04 μm in Ra and 7.3 μm in R_{max} . Although there isn't an apparent trend shows that the surface roughness is more great with the higher laser power but this experiment assures that LSP can reduce the surface roughness
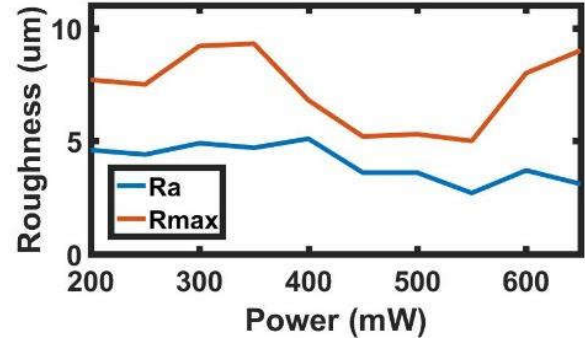
Fig. 2 Surface roughness as a function of laser power

3.3 Pressure measurements

The shock wave pressure is related to the shock velocity through Newton's second law across the shock wave [1]

$$P - P_0 = U_s u_p \varrho_0 \qquad (1)$$

where P and P_0 are the shock pressure and the hydrostatic pressure, respectively, Us is the shock velocity, u_p is the particle velocity and ϱ_0 is the density of the water. P_0 is much smaller than the shock pressure and can be neglected. The shock and particle velocities are related through the equation of state. It can be written as

$$U_s = A + Bu_p \qquad (2)$$

For water, the values of A and B are 1.48 km/s and 2.07 km/s, respectively. For a shock wave that has separated from the expanding bubble, the total momentum of the shock front is conserved. For a spherically symmetric shock wave, the conversation of the total momentum at a distance r from the center of the plasma can be written as:

$$4\pi r^2 U_s \Delta t \varrho_0 u_p = const \qquad (3)$$

where Δt is the rise time. Substituting u_p from the equation of state of water (2) into (3), we derive

$$U_s (U_s - A) = \frac{C}{r^2} \qquad (4)$$

where C includes the constants B, ϱ_0 and Δt. Equation (4) can be solved for U_s to derive the expression of the shock velocity vs. distance from the center of the plasma.

$$U_s(r) = \frac{A}{2} + \sqrt{\frac{A^2}{4} + \frac{C}{r^2}} \qquad (5)$$

Substituting (5) into (2), we derive an expression for the particle velocity:

$$u_p(r) = \frac{1}{B}\left(\sqrt{\frac{A^2}{4} + \frac{C}{r^2}} - \frac{A}{2} \right) \qquad (6)$$

The shock wave pressure can be calculated from the shock and particle velocities and the jump condition. If (5) and (7) are substituted into (1), we derive an expression for the pressure as a function of the distance from the center of the plasma.

$$P = C\frac{\varrho_0}{B}\frac{1}{r^2} \qquad (7)$$

Two He-Ne laser beams separated by 1 mm were used to measure the shock velocity, as shown in Figure 3.
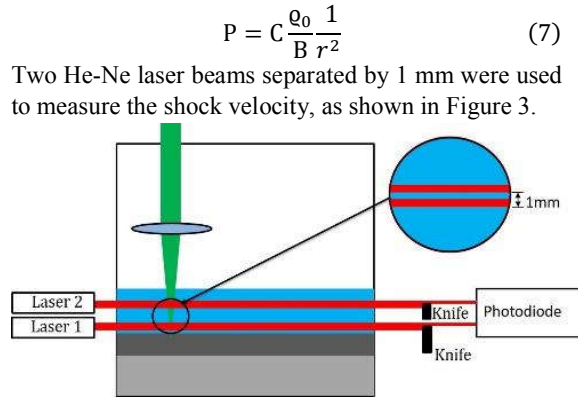
Fig. 3 Schematic showing shock speed measurement

Due to the two probe beams, the oscilloscope will capture two shock wave signals. Using the time different between the two shock wave signals, we can get the time Δt that shock wave movement. Knowing the Δt, we can get the shock wave velocity U_s. This experiment uses signal process to measure the shock pressure. The steps are as follows: (a) Turn on Laser 1 and Laser 2, the oscilloscope will capture two troughs of wave which are the all signal that photodiode captured from the He-Ne laser; (b) Turn off the Laser 2, the signal represents the time of shock wave reach the first probe beam; (c) Turn off Laser 1, the signal represents the time of shock wave reach the second probe beam; (d) Translation step 3 signal and superimpose with the step. Record the translate time Δt and compared with the step 1; (e)
Get the shock wave velocity

$$U_s\left(\frac{km}{s}\right) = 10^{-6}/\Delta t \qquad (8)$$

We have reported in Figure 4, the peak pressure levels obtained experimentally with the follow equations. The pressure increases with the power density up to 2.708 GPa.

Figure 5 show the calculated shock wave pressures in the radial and axial directions. It should be noted that the pressure calculated from our velocity measurements only relates to the shock waves. The shock pressure decreases rapidly so that at distances over 1 mm it is close to zero. The far field pressure computed from the shock velocity is not accurate because the velocity of the pressure wave is very close to the velocity of sound and the error of the experiment is not sufficient to allow for an accurate measurement of the velocity in this range. Consequently, the pressure in the far field is underestimated. The following equation is valid only in the near field where the pressure waves generated by the laser shock peen are manifested as shock waves.
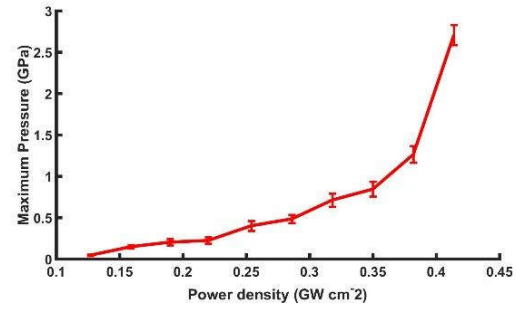
Fig. 4 Maximum pressure as a function of power intensity
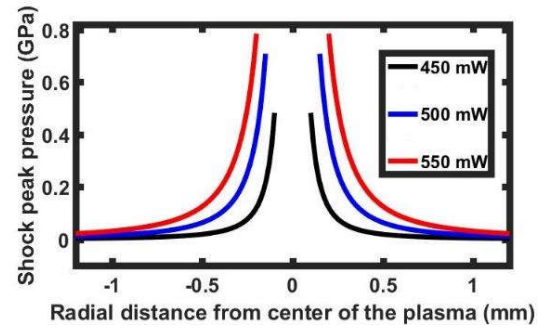
Fig. 5 Shock pressure from the center of the plasma.

4. Concluding Remarks

Based on the technique of laser shock peening (LSP), we use a pulsed Nd:YAG laser, operating at 532 nm, to enhance surface hardness and reduce surface roughness of AISI-H13 tool steel. Major conclusions are as follows. Hardness is first increased monotonically with the enhancement of laser power: from 240 HV at 200 mW to 290 HV at 450 mW. However, the hardness can't be increased furthermore and remains almost unchanged if the laser power is larger than 450 mW. For the present LSP configuration, the upper limit is around 300 HV. And with appropriate laser power, the surface roughness can be also apparently reduced.

With an additional continuous probe laser beam, the shock wave due to the laser induced plasma is well captured by the technique of photoacoustic wave detection. With the laser power 450mW, we can measure the shock pressure around 3.99 km/s and shock pressure 0.484 GPa. The shock wave pressure increases with the rise of the laser power.

References

[1.] Doukas, A. G., Zweig, A. D., Frisoli, J. K., Birngruber, R., & Deutsch, T. F. (1991). Non-invasive determination of shock wave pressure generated by optical breakdown. *Applied Physics B, 53*(4), 237-245.
[2.] Rubio-González, C., Felix-Martinez, C., Gomez-Rosas, G., Ocana, J. L., Morales, M., & Porro, J. A. (2011). Effect of laser shock processing on fatigue crack growth of duplex stainless steel. *Materials Science and Engineering: A, 528(3), 914-919.*

[3.] Lim, H., Kim, P., Jeong, H., & Jeong, S. (2012). Enhancement of abrasion and corrosion resistance of duplex stainless steel by laser shock peening. *Journal of Materials Processing Technology*, *212*(6), 1347-1354.

[4.] Kruusing, A. (2004). Underwater and water-assisted laser processing: part 1—general features, steam cleaning and shock processing. *Optics and Lasers in Engineering, 41*(2), 307-327.

[5.] Fabbro, R., Fournier, J., Ballard, P., Devaux, D., & Virmont, J. (1990). Physical study of laser☐ produced plasma inconfined geometry. *Journal of applied physics, 68*(2), 775-784.

[6.] Berthe, L., Fabbro, R., Peyre, P., Tollier, L., & Bartnicki, E. (1997). Shock waves from a water-confined laser-generated plasma. *Journal of Applied Physics, 82*(6), 2826-2832.

[7.] Guo, Y. B., & Caslaru, R. (2011). Fabrication and characterization of micro dent arrays produced by laser shock peening on titanium Ti–6Al–4V surfaces. *Journal of Materials Processing Technology*, *211*(4), 729-736.

[8.] Braisted, W., & Brockman, R. (1999). Finite element simulation of laser shock peening. *International Journal of Fatigue, 21(7), 719-724.*

Effect of TiB₂ on the Microstructure, Mechanical and Casting Properties of A201 Alloys

Denny Chen[1], Albert Chiu[1], S.S. Lee[1,2]

[1] National Central University, Institute of Materials Science and Engineering, Jhongli 32001, Taiwan

[2] National Central University, Department of Mechanical Engineering, Jhongli 32001, Taiwan

ABSTRACT

A201(Al-Cu-Mg-Ag) alloy is classified as a heat treatable high strength aluminum alloy, the precipitation strengthening effect is achieved with the precipitations of Ω phase and θ'phase. It has been found in composites that the addition of Al-Ti and Al-B master alloys to aluminum alloys can form in-situ TiB2 particles during casting. TiB2 particles act as the heterogeneous sites during solidification, lead to the reduction in the grain size, and thus improve the mechanical properties of the alloy.

The effects of TiB2 additions on the microstructure, mechanical and casting properties of A201 alloys were investigated. Experimental results indicated that addition of TiB2 to A201 alloys could produce grain refinement because TiB2 particles could act as the heterogeneous sites during solidification. After T7 treatment, the hardness and strength of these alloys increased with the precipitations of Ω and θ'phase. With the increasing amount of TiB2, the hardness and strength enhanced by TiB2 particles which dispersed in the Al matrix; furthermore, the ductility was also improved.

Keywords : Al-Cu alloys, in-situ, TiB2

1. Introduction

A201 alloy has excellent mechanical properties [1] and latent deformation resistance [2]. However, hot cracking is likely to occur during casting, due to its wide solidification range, resulting in a decrease in the casting yield of A201 alloy [3.4]. It is known from the literature that grain refinement can slow down the hot cracking of alloys, and that TiB2 addition to aluminum alloys can refine grains and serve as a strengthening phase in composites to enhance the mechanical properties of aluminum alloys [5.6]. By adding TiB2 ceramic particles to the A201 alloy, this experiment is to verify that this method can improve the mechanical properties of the A201, slow the hot cracking of the alloy during solidification, and improve its castability [7].

2. Method

The A201 ingot was placed in a resistance furnace crucible at 800°C to be melted. Al-8B, Al-75Ti, Al-75Mn, Al-50Cu master alloys and pure magnesium were added according to the materials required for the alloy. Then it was degassed with argon for 15 minutes and left to stand for 20 minutes. Finally, it was cast to a metal mold with dimensions of 125mm× 100mm× 25mm and a thermal cracking analysis mold.

In order to explore the effect of TiB2 addition to the A201 aluminum alloy, three alloys were experimentally prepared. They were named Alloy A (A201), Alloy B (A201+1 wt% TiB2), Alloy C (A201+2wt% TiB2) respectively. The composition of the alloy was analyzed by the Optical Emission Spectroscopy (OES). The composition was shown in Table 1.

3. Results and Discussion

3.1 Microstructure

After the process and heat treatment of the alloy, the SEM, and conductivity were used to explore and observe the alloy microstructures. The results are discussed as follows:

In order to clearly observe the distribution of TiB2 particles, the distribution of EPMA elements was confirmed by their mappings, and the more powerful electron microscope was used to observe their shapes. At the end of the investigation, EPMA was used to quantitatively analyze each eutectic phase, precipitates, and TiB2 particles to determine whether their composition was consistent with the literature.

Table 1 Alloy component analysis (wt%)

element / Alloy	Si	Fe	Mn	Cu	Mg	Ag	Ti	B	Al
A (A201)	0.06	0.08	0.31	4.58	0.28	0.7	0.25	N.D.	Rem.
B (A201+1wt% TiB_2)	0.08	0.12	0.28	4.61	0.27	0.68	0.94	N.D.	Rem.
C TiB_2	0.11	0.11	0.29	4.62	0.28	0.67	1.69	N.D.	Rem.

Note : Rem.-Remainder, N.D.-Not Detectable

(a) BEI image

(b) B element mapping

(c) Ti element mapping
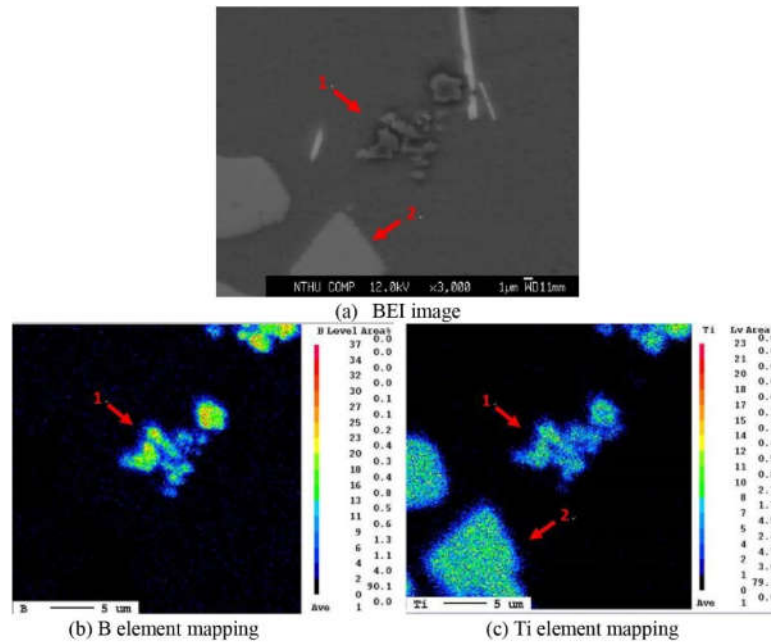
Fig 1 Alloy C image mappings of TiB_2 particles and Al_3Ti analyzed through the Electron Microprobe, （a）BEI image mappings （b）B element mapping （c）Ti element mapping (Arrow 1 indicates TiB_2 particles ; Arrow 2 indicates Al_3Ti)

Table 2 Analysis results of various elements' content in as-cast Alloy A and Alloy C by EPMA

Alloy		Element (at.%)					
		Al	Cu	Ti	Ag	Mg	B
A (A201)	1	68.91	31.05	0.03	N.D.	N.D.	N.D.
	2	75.19	0.61	23.98	N.D.	N.D.	N.D.
C (A201+2wt%TiB_2)	1	68.24	30.59	0.03	N.D.	N.D.	N.D.
	2	74.25	0.52	23.81	N.D.	N.D.	N.D.

Note：at%(Atomic Percent), N.D.(Not Detectable)

BEI and Mapping analyses were performed by using an electron microprobe (EPMA) for the as-cast alloy C. Figure.1 shows the X-ray mapping results of the BEI images taken with EPMA and the individual elements of Ti and B. By cross-checking the Mapping and BEI images, the gray-colored phase (as indicated by Arrow 1) in the BEI image could be identified as containing TiB_2 particles of Ti and B. The whiter color of the lower left corner (as indicated by Arrow 2) contained Ti and Al and was regarded as a Al_3Ti phase. The result was consistent with the results of point analysis described later (Table.2).

3.2 Mechanical Properties

By comparing the mechanical property analysis with the microstructure analysis, the effects of the whole properties of Alloy A, Alloy B, and Alloy C could be understood. In addition, the difference in the solid solution content of Cu, Mg, and Ag elements and the TiB_2 addition amount also changed the effects of solid solution strengthening, precipitation strengthening after artificial aging, and TiB_2 particle dispersion strengthening during the solution treatment of the alloys. Furthermore, the strength of the alloys were affected.

A201 (Al-Cu-Mg-Ag) Alloy can precipitate the θ' phase and the Ω phase by heat treatment to enhance the material. Therefore, its strength will change due to the total amount of precipitation of the θ' phase and the Ω phase. The more the total amount of precipitation is, the stronger the intensity of the alloy becomes. The results of the tensile properties of the three alloys after artificial aging (190°C × 5 hrs) in Table.3 showed that

although the precipitation amounts of the strengthening phases of Alloy B and Alloy C were not higher than that of Alloy A. the tensile strengths of Alloy B and Alloy C were higher than that of Alloy A.

The reason was that the $TiB2$ particles had dispersive and strengthening functions in the aluminum alloy. The tiny particles could effectively prevent the dislocation slip in the aluminum base, so the tensile strength was higher. The results of the tensile test were consistent with the results of the hardness test. It is worth noting that Alloy B and Alloy C not only increased in strength but also improved the elongation.

3.3 Hot Cracking Analysis

After the alloy was cast into the mold and solidified, the tensile stress was generated due to the limitation of the mold in which it cannot be freely contracted. From Figure. 2(a), it could be observed that all the six alloy bars had cracks, while in Figure .2(b) and Figure. 2(c) only three test bars did not break. This indicates that the alloy's resistance to hot cracking increase after the $TiB2$ particles were added. From the grain state diagram, it could be seen that the alloy grains were significantly refined. The grain refinement could improve the liquid film replenishment at the initial stage of cracking, reduce the thickness of the liquid film between grains (formula 1.1: P = 2αF / 1000 gb), increase the force P needed to separate the liquid films, and therefore enhance the thermal cracking resistance of the alloy. In Figure .2(b) and Figure .2(c), respectively three test bars were not broken, indicating that there was no significant difference in the thermal cracking resistance between Alloy B and Alloy C. It indicated that the grain refinement could improve the hot cracking resistance, but the grain refinement to a certain size would have no obvious effect.

4. Concluding Remarks

1. From the metallographic diagrams and the results of the component analysis, it was confirmed that. TiB2 formed in the aluminum alloy. It was proved that the A201+1wt%TiB2 and A201+2wt %. TiB2 alloys were successfully produced by the melting method of the master alloys (Al-8B and Al-75Ti).

2. Because TiB2 particles in the aluminum base had dispersing strengthening effects and could refine the grains, the alloys which contain TiB2 (A201+1wt%TiB2, A201+2wt% TiB2) had higher hardness than that of the alloy which did not contain TiB2.

3. After the three alloys, A201, A201+1wt%. TiB2, and A201+2wt%. TiB2 went through T7 treatment, the tensile strength of the alloys were all enhanced due to the strengthening θ'phase and the precipitation of Ω. The more. TiB2 the alloy contained, the more their tensile strength and the ductility increased.

4. The results of the hot cracking analysis showed that the alloys which contained. TiB2 had better hot cracking resistance than the alloy which did not contain. TiB2, but it could not be clearly judged whether the addition of more. TiB2 (2wt%) had even better hot cracking resistance.
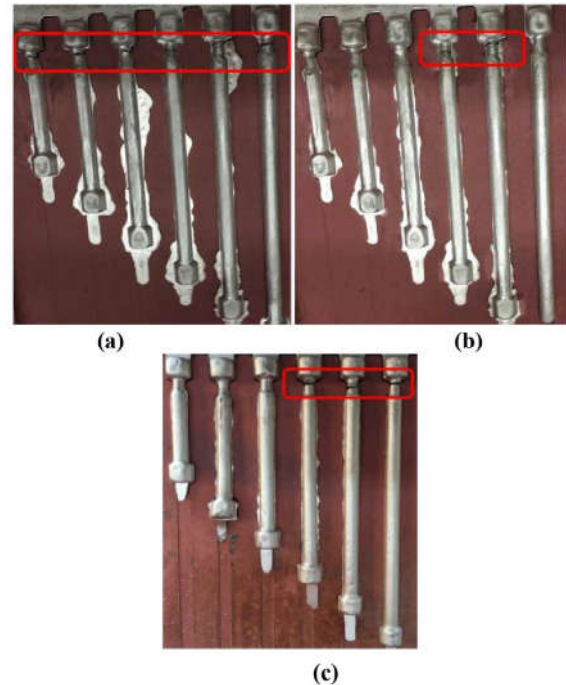
Fig 2 Hot cracking analysis of the alloys (a) Alloy A (A201); (b) Alloy B (A201+1 wt%$TiB2$); (c) Alloy C (A201+2 wt%$TiB2$)

References

[1] Anandkumar, R., Almeida, A. and Vilar, R., Surface and Coatings Technology, Vol.205(13), pp.3824-3832 (2011)

[2] Basu, B., Raju, G. and Suri, A., International materials reviews, Vol.51(6), pp.352-374(2006)

[3] L. Bichler, A. Elsayed, K. Lee, International Journal of Metalcasting, vol.2(1), pp. 43-54. (2008)

[4] J. R. Davis and Associates, ASM International Materials Park, Ohio, pp.25(1994)

[5] J. R. Davis and Associates, ASM International Materials Park, Ohio, pp.706-707(1994)

[6] Dragut, D. V., Moldovan, P. and Butu, M., Revista de Chimie, Vol.63(9), pp.925-928(2012)

[7] M. Emamy, M. Mahta and J. Rasizadeh, Composites Science and Technology, Vol.66, pp.1063–1066. (2006)

PART I, SECTION III

Mechanical Technology
(Heat transfer, Thermal, and Fluid Engineering; Structures and Fluids; Vibration;
Energy Engineering; CAD/CAM/CAE/RP…)

Numerical Investigation of the Flow Inside and around a Spherical Fish Cage

Cuong Mai Bui, Thinh Xuan Ho, Loc Huu Khieu

Faculty of Engineering, Vietnamese-German University

Le Lai Street, Hoa Phu Ward, Thu Dau Mot City, Binh Duong Province, Vietnam

ABSTRACT

A numerical approach is employed to study the water flow inside and around a spherical fish cage totally submerged in the water. The cage is modeled as a hollow sphere, whose cover comprising the net and the mechanical frame is modeled as a thin porous layer. The computational package of Fluent is employed. Various characteristics of the flow inside and outside of the cage are investigated and presented in this report. Moreover, simulations of a flow over a solid sphere, equivalent to e.g. zero porosity, are also performed for the purpose of verification.

1. Introduction

Offshore fish farming has recently been received great attention from farmers, policymakers and scientists as it can solve problems that traditional inshore farming faces; these include being away from contaminant sources, healthy environment for fish and less harm to the aquatic ecosystem. However, as it is in the open sea and prone to violent currents, high waves and even storms, it requires a good mooring system, a strong and durable mechanical frame and probably an appropriate operating program according to various weather conditions. It is, therefore, important to investigate the interaction between the currents and the cages.

There have been a number of studies about this topic conducted, both experimentally and numerically, in recent years. Huang et al. [1] studied experimentally effects of reducing current velocity by a square net cage structure and found that the velocity behind the cage reduces between 20 and 45%. Subsequently, experiments were carried out by [2] using PIV to investigate the flow around and inside cylinder-shaped fish cages and impacts of the inclination and porosity on the flow field. With the use of a CFD approach, Shim et al. [3] studied the flow through and around a cage, which was considered as a circular cylinder with a porous jump boundary condition; effects of bio-fouling on net structures and flushing of the cage were also investigated. It was stated that the drag coefficient increases when porosity decreases. Patursson et al. [4] developed a porous media model, in which the net was described as a thin volume. Good agreement with measurement data was declared. Recently, Zhao et al. [5] carried out a numerical study on the flow through a net panel, considered as a porous layer, at different attack angles and inclinations, and then the flow through a net cage made of multiple net panels [6]. It was argued that the flow velocity reduces approximately 10-17% inside the cage. Bi et al. [7] studied the hydrodynamic characteristics of a net cages using both numerical and experimental approaches. The net cages were of cylindrical shape and composed of a flexible net. For different incoming velocities, a velocity reduction of ~8.3% was found inside the cages with a little deviation.

In this work, we investigate a spherical cage, which has a mechanical frame and a net wrapping around it. The cage is modeled as a hollow sphere with its outer layer being considered as a porous shell. The shell is thin with respect to the sphere. Various characteristics of the flow around and inside the cage at different Reynolds numbers are analyzed.

The rest of paper is organized in 5 sections. In Section 2, the methodology is introduced. In Section 3, a study of the flow over a solid sphere is carried out in order to verify the numerical method employed. Simulation results of the flow over and through a spherical cage is shown in Section 4. Summary is given in Section 5.

2. Method

2.1 Governing equations

Continuity equation:

$$\frac{\partial \rho}{\partial t} + \frac{\partial (\rho u_i)}{\partial x_i} = 0 \qquad (1)$$

RANS momentum equation:

$$\frac{\partial (\rho u_i)}{\partial t} + \frac{\partial (\rho u_i u_j)}{\partial t} = \rho f_i + \frac{\partial}{\partial x_j}\left[-p\delta_{ij} + \mu\left(\frac{\partial u_i}{\partial x_j} + \frac{\partial u_j}{\partial x_i}\right) + \tau_{ij} \right]$$

$$(2)$$

Here ρ and μ are the density and dynamic viscosity; t is time; p is pressure, u_i and u_j are the velocity components; $\tau_{ij} = \mu_t(\partial u_i/\partial x_j + \partial u_j/\partial x_i) - (2/3)\rho k\delta_{ij}$, where k is the turbulent kinetic energy and μ_t is the eddy viscosity; f_i is the body force component.

The standard k-ε model uses the following transport equations for k and ε:

$$\frac{\partial (\rho k)}{\partial t} + \frac{\partial (\rho k u_i)}{\partial x_i} = \frac{\partial}{\partial x_j}\left[\frac{\mu_t}{\sigma_k}\frac{\partial k}{\partial x_j} \right] + 2\mu_t S_{ij}.S_{ij} - \rho\varepsilon \qquad (3)$$

$$\frac{\partial (\rho \varepsilon)}{\partial t} + \frac{\partial (\rho \varepsilon u_i)}{\partial x_i} = \frac{\partial}{\partial x_j}\left[\frac{\mu_t}{\sigma_k}\frac{\partial \varepsilon}{\partial x_j} \right] + C_{1\varepsilon}\frac{\varepsilon}{k}2\mu_t S_{ij}.S_{ij} - C_{2\varepsilon}\rho\frac{\varepsilon^2}{k}$$

$$(4)$$

S_{ij} is the mean rate of strain tensor:

$$S_{ij} = \frac{1}{2}\left(\frac{\partial u_i}{\partial x_j} + \frac{\partial u_j}{\partial x_i}\right) \tag{5}$$

LES momentum equation:

$$\frac{\partial(\rho \bar{u}_i)}{\partial t} + \frac{\partial(\rho \bar{u}_i \bar{u}_j)}{\partial t} = \frac{\partial}{\partial x_j}(\sigma_{ij}) - \frac{\partial p}{\partial x_i} - \frac{\partial \tau_{ij}}{\partial x_j} \tag{6}$$

where τ_{ij} is the subgrid scale stress and σ_{ij} is the stress tensor due to molecular viscosity.

2.2 Coefficients and resistances of porous media model

The porous medium in this study is modeled as a packed bed of spherical particles. The pressure drop through it is determined as:

$$\Delta p = \frac{150\mu L}{D_p^2}\frac{(1-\varepsilon)^2}{\varepsilon^3}u + \frac{1.75L\rho}{D_p}\frac{(1-\varepsilon)}{\varepsilon^3}u|u| \tag{7}$$

The viscous resistance:

$$\frac{1}{\alpha} = \frac{150}{D_p^2}\frac{(1-\varepsilon)^2}{\varepsilon^3} \tag{8}$$

The inertial resistance:

$$C_2 = \frac{3.5}{D_p}\frac{(1-\varepsilon)}{\varepsilon^3} \tag{9}$$

Here, L is the thickness of the porous medium, D_p is the diameter of packing particles, ε is the porosity, α is the face permeability and C_2 is the inertial resistance.

2.3 Drag force and drag coefficient

The drag force on a solid sphere:

$$F_{d,solid} = \frac{1}{2}\rho C_d A u^2 \tag{10}$$

For the spherical cage, the drag force can be determined based on the momentum balance:

$$F_{d,porous} = -\iint_S (\rho u_i dS_i)\, u_{j=x} \tag{11}$$

where S is the closed surface defined as in Figure 1, dS_i is the i component of the elemental area vector $d\mathbf{S}$. Here $j = x$, i.e. the drag force. The drag coefficient C_d is determined as:

$$C_{d,solid} = \frac{2F_d}{\rho u^2 A} \tag{12}$$
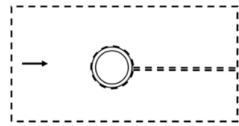
Figure 1. Closed surface (dashed line) surrounding a control volume excluding the sphere.

2.4 Computational implementation

Simulations of a flow over a solid sphere at several Reynolds numbers, e.g. 100, 300, 10^4 and 10^6, are first carried out in order to verify the numerical method; subsequently, those of a flow over and inside the cage are performed. Different values of the porosity are realized to evaluate the influence of the bio-fouling on the flow. The diameter of the packing particles characterizing the porous medium is chosen so that the resulting flow field agrees with experimental data and/or that of previous studies available in the literature. The three-dimensional simulation geometry for the solid sphere and the spherical fish case is shown in Figure 2. The thickness of the porous layer is chosen to be 0.025D.
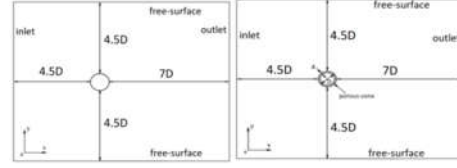
Figure 2. Geometry for the case of the solid sphere (L) and the fish cage (R).

Unstructured mesh is employed for all the simulations. A grid convergence study has been carried out in [8] and the results indicated that an unstructured mesh with 650000 elements provides good results within a reasonable computational time. An example of the mesh is shown in Figure 3. For the solid sphere, three layers of computational elements with height ratio of 1.2 are built around the sphere. For the fish cage, it is three layers inside, three layers outside the surface, and at least two layers inside the porous shell.

We choose the velocity boundary condition for the inlet, pressure for the outlet, no slip boundary for the sphere and free-surface for all other faces of the domain. First-order upwind scheme is utilized to discretize the governing equations. All simulations reported in this work are transient with the SIMPLE algorithm being used for the pressure-velocity coupling.
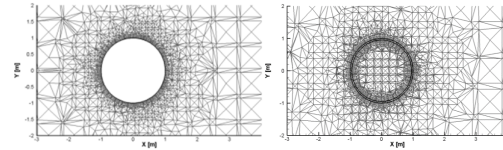
Figure 3. Computational mesh for the solid sphere (L) for the cage (R) viewed in the xy plane.

3. Flow over a solid sphere

For the verification purpose, we first simulate a standard problem of a water flow over a smooth solid sphere. This corresponds to an extreme case in which total bio-fouling occurs, i.e. $\varepsilon = 0$, blocking the flow through the cage. Results for the drag coefficient obtained in laminar flow (Re = 100, 300) and turbulent flow (Re = 10^4, 10^6) regimes are compared with data available in the literature. The comparison is presented in Figure 4. As can be seen, our simulated results agree well with previous studies, with a maximum deviation of about 5%. In addition, for the turbulent regimes, both Large Eddy Simulation (LES) model and k-ε model are utilized; and the former is found to produce better

estimation than the latter. This is in line with Jones and Clarke [9].
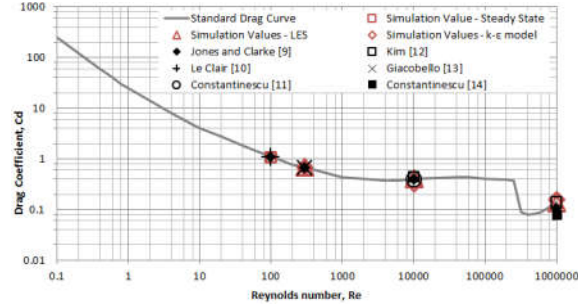
Figure 4. Comparison of drag coefficient with previous studies; the curve is from Clift et al [15].

Distributions of the velocity and pressure around the solid sphere at Re = 10^6 are shown in Figure 5.
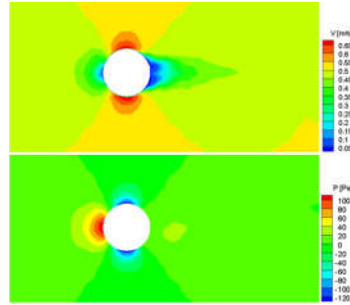
Figure 5. Velocity (T) and pressure (B) distributions around the sphere at Re = 10^6 in xy plane.

4. Flow over a spherical cage

In this section, influences of the bio-fouling phenomena and the incoming velocity or Reynolds number on the flow field are studied and discussed.

4.1 Resistances of the porous medium

The porous shell consisting of the net and the mechanical frame is estimated to have a porosity of 75%; it can be a typical value for this type of cage structure. The diameter of the packing particles, D_p, is chosen to fit experimental data available in the literature. To this end, a number of test runs with different D_p are carried out. It is found that with D_p = 0.25 m the results for the velocity reduction inside the cage to be approximately 16%, which is in line with Zhao [6] who found it to be 10-17% and Freriksson [16] to be ~10%.

The resistances of the porous medium can be calculated from Equations (8) and (9). It is good to note that, with the chosen data, our inertial resistance is found to be of the same magnitude with that of Zhao et al. [5], who determined it experimentally for a plane net (see Table 1). However, our viscous resistance is much smaller than that of Zhao et al. [5], i.e. ~20 folds. Nevertheless, simulations with a wide range of the viscous resistance

show its negligible effect on the flow field. It is actually evident from the RHS of Equation (7), in which the first term associated with the viscous resistance contains a factor of $\mu \sim 10^{-3}$, while the second term associated with the inertial resistance contains $\rho \sim 10^3$, making the inertial resistance a dominant role over the viscous one.

Table 1. Porous resistances used in this work and in Zhao et al.[5]

D_p	ε	Viscous Resistance ($1/m^2$)	Inertial Resistance ($1/m$)
0.25	0.75	355.56	8.3
Zhao et al. [5]		75990	8.087

Results for the velocity and pressure contours at Re = 10^6 are shown in Figure 6.
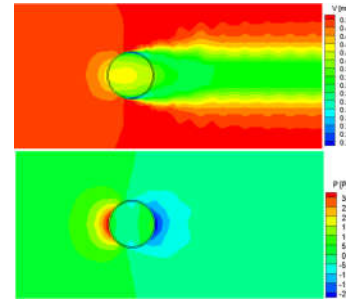
Figure 6. Velocity (T) and pressure (B) distributions around and inside the cage at Re = 10^6 in xy plane.

4.2 Influence of the bio-fouling

Bio-fouling on the net and frame structure can reduce the water flowability and/or the circulation of well-oxygenated water and nutrients inside the cage. We model the bio-fouling by associating it with the porosity; when bio-fouling occurs, the porosity decreases. In this part, simulations with different values of the porosity (see Table 2) are presented.

Table 2. Information about test cases with different values of porosity.

ε	Viscous Resistance ($1/m^2$)	Inertial Resistance ($1/m$)
0.90	32.921	1.92
0.825	130.89	4.36
0.75	355.56	8.3
0.5	4800	56
0.25	86400	672

Results for the velocity magnitude and pressure along the x-axis crossing the cage's center for various values

of ε are shown in Figure 7. As can be seen, the velocity reduces significantly when the porosity decreases; at, for example, $\varepsilon = 0.25$ the velocity reduction inside the cage reaches ~80%, drastically reducing the water exchange between the inside and outside of the cage. However, it is noted that at very low porosities, i.e. $\varepsilon = 0.25$ and 0.5, the velocity magnitude behind the cage is larger than that right inside the cage. The reason for this is probably because of the flow outside the cage, which seems to be faster than the flow through it, specifically through the rear wall. Moreover, at $\varepsilon = 0.25$, the pressure behind the cage is found to be even larger than that inside the cage.
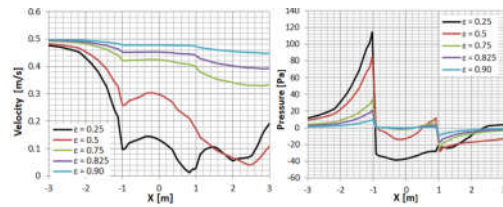
Figure 7. Velocity magnitude and pressure along the *x*-axis crossing the center at different ε.

Figures 8 and 9, respectively, present the velocity and pressure distributions inside and around the cage at some different values of ε.
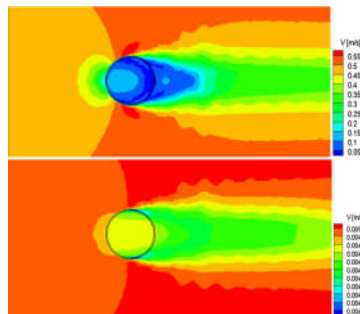
Figure 8. Velocity distribution around and inside the cage at $\varepsilon = 0.25$ (T) and $\varepsilon = 0.9$ (B) in *xy* plane.
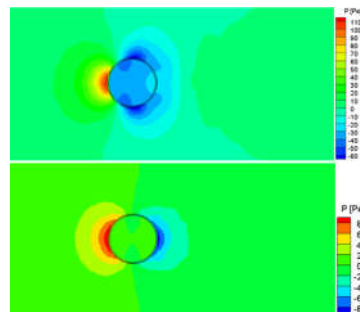
Figure 9. Pressure distribution around and inside the cage at $\varepsilon = 0.25$ (T) and $\varepsilon = 0.9$ (B) in *xy* plane.

4.3. Influence of the incoming velocity

Simulations are performed at different Reynolds numbers, i.e. Re = 10^4, 10^5 and 10^6, corresponding to an incoming velocity of, respectively, 0.005, 0.05 and 0.5 m/s. It is noted that in these simulations, D_p is kept constant, i.e. 0.25 m, while ε varies from 25% to 90%. Results for the velocity reduction at these cases are shown in Figure 10. As can be observed, the velocity reduction decreases with the increasing porosity and its trend is almost identical for all three Reynolds numbers.
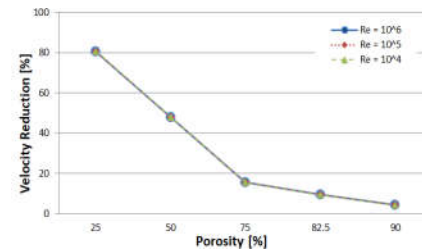
Figure 10. The velocity reduction at different Reynolds number.

5. Summary

A 3D numerical model has been built to study the flow around and inside a spherical fish cage. The cage was modeled as a hollow sphere with the outer layer being considered as a porous layer. The characteristic parameters of the porous layer were determined by fitting the resulting flow field with that of previous studies available in the literature. It was found that with $D_p = 0.25$ m and $\varepsilon = 0.75$, the simulated results for the velocity reduction agrees well with previous studies.

The influence of the porosity mimicking the biofouling phenomena on the flow was investigated. It was shown that small porosities result in low flowability or circulation of water in the cage. Indeed, at $\varepsilon = 0.25$, the velocity in the cage reduced substantially, i.e. up to 80%. Furthermore, the incoming velocity or Re was found to have a negligible impact on the flow reduction.

This is an on-going study with the next step being to evaluate the hydrodynamic forces acting on the cage. This would eventually contribute to the improvement of the design and operation of an offshore fish cage. Additionally, the interaction between the flow and multiple cages would be analyzed in the future.

References

[1]   L.Y. Huang, Z.L. Liang, W.H. Song, F. F. Zhao, L.X. Zhu, Journal of Fishery Sciences of China, 14 (2007) 860-863.

[2]   A. Harendza, J. Visscher, L. Gansel, B. Pettersen, ASME 2008 Int. Conf. on OMAE, (2008), 555-563.

[3]   K. Shim, P. Klebert, A. Fredheim, ASME 28th Int. Conf. on Ocean, Offshore and Arctic Engineering, (2009), 581-587.

[4]   O. Patursson, M.R. Swift, I. Tsukrow, K. Simonsen, K. Baldwin, D.W. Fredriksson, B. Celikkol, Ocean Engineering, 37 (2010), 314-324.

[5]   Y.P. Zhao, C.W. Bi, G.H. Dong, F.K. Gui, Y. Cui, C.T. Guan, T.J. Xu, Ocean Engineering, 62 (2013), 25-37.

[6]   Y. P. Zhao, C.W. Bi, G.H. Dong, F.K. Gui, Y. Cui, T.J. Xu, Aquacultural Engineering, 52(2013), 1-13.

[7]   C.W. Bi, Y.P. Zhao, G.H. Dong, Y.N. Zheng, F.K. Gui, Aquacultural Engineering, 59(2014), 1-12.

[8]   C.M. Bui, T.X. Ho, L.H. Khieu, 21st Vietnam National Conference on Fluid Mechanics, (2018).

[9]   D.A. Jones, and D.B. Clarke. "Simulation of Flow Past a Sphere using the Fluent Code", (2008).

[10]   B.P. Le Clair, A.E. Hamielec and H.R. Pruppacher, J. Atmos. Sci., 27 (1970), 308-315.

[11]   G.S. Constantinescu, M.C. Chapelet and K.D. Squires, AIAA Journal, 41(2003), 1733-1742.

[12]   S.E. Kim, 34th AIAA Fluid Dynamics Conference and Exhibit, (2004), AIAA paper number 2004-2548.

[13]   M. Giacobello, PhD thesis, The Uni. Of Melbourne, (2005).

[14]   G.S. Constantinescu, M.C. Chapelet and K.D. Squires, Phys. Fluids, 16 (2004), 1449-1466.

[15]   R. Clift, J.R. Grace, M.E. Weber, M.F. Weber Bubbles, Drops, and Particles, (1978). Academic Press, New York, USA.

[16]   D.W. Fredriksson, PhD Dissertation, University of New Hampshire, (2001).

Numerical Investigation of the Thermocapillary Migration of a Water Droplet in a Microchannel by Applying Heat Source

Thanh-Long Le[1,4], Jyh-Chen Chen[2], Huy-Bich Nguyen[3]

[1]Faculty of Mechanical Engineering, Ho Chi Minh University of Technology (HCMUT), VNU-HCM, Vietnam
[2]Department of Mechanical Engineering, National Central University, Jhongli 320, Taiwan
[3]Faculty of Engineering and Technology, Nong Lam University, Ho Chi Minh City, Vietnam
[4]Key Laboratory of Digital Control and System Engineering, HCMUT (DCSELAB), Vietnam

ABSTRACT

In this study, the numerical computation is used to investigate the transient thermocapillary migration of a water droplet in a microchannel. For tracking the evolution of the free interface between two immiscible fluids, we employed the finite element method with the two-phase level set technique to solve the Navier-Stokes equations coupled with the energy equation. Both the upper wall and the bottom wall of the microchannel are set to be an ambient temperature. 40mW heat source is placed at the distance of 1 mm from the initial position of a water droplet. When the heat source is turned on, a pair of asymmetric thermocapillary convection vortices is formed inside the droplet and the thermocapillary on the receding side is smaller than that on the advancing side. The temperature gradient inside the droplet increases quickly at the initial times and then decreases versus time. Therefore, the actuation velocity of the water droplet first increases significantly, and then decreases continuously. The dynamic contact angle is strongly affected by the oil flow motion and the net thermocapillary momentum inside the droplet. The advancing contact angle is always larger than the receding contact angle during actuation process.

Keywords: Numerical simulation; thermocapillary migration; microchannel, surface tension, heat source.

1. Introduction

Recently, microfluidics technique has significantly attracted owing to its diverse applications in Lab-on-a Chip devices (LOC), Micro-Electro-Mechanical System (MEMS) or protein crystallization [1-3]. The thermocapillary migration is a great important to manipulate the droplet behavior and optimize the performance of the behavior of the droplet-based microfluidics [4, 5]. The droplet transport behavior in a microchannel actuated by a transient temperature gradient has already been investigated in numerous studies [6-14]. Brochard [6] indicated that the contact angle of a liquid droplet at rest, static contact angle (SCA), is altered to the dynamic contact angle (DCA) when the droplet moves on a solid surface. The difference in the DCA between the advancing and receding sides, so-called contact angle hysteresis (CAH), is strongly affected by the temperature gradient.

The experimental results of Chen et al. [7], developed from Ford and Nadim's work [8], indicated that a fixed CAH influences the droplet velocity and threshold values much more significantly than the slip length. Le et al. [9] showed the effect of upper wall condition on the liquid droplet migration behavior in a microchannel. The movement of a liquid droplet in a microchannel is strengthened due to the net thermocapillary momentum generated by the unequal size of the two vortices inside the droplet. The results showed the actuation velocity and the DCA of the droplet are strongly affected by the thermal condition of upper wall. In addition, the numerical results from Le et al. [10] demonstrated that the silicone plug motion

inside capillary tube is influenced by the net thermocapillary momentum generated by the temperature gradient along the gas-liquid interface and the capillary force caused by the temperature difference between the ends of the liquid plug. The numerical results are in good agreement with the previous experimental results [11]. Liu et al. [12] developed a lattice Boltzmann phase-field model to numerically simulate the thermocapillary flows in a microchannel. Their results indicated that the contact angle strongly influences the droplet dynamic behavior and the droplet motion driven by shear flow at the inlet of a confined microchannel is completely blocked by using a laser source to heat the fluids at the advancing side of a droplet. Recently, Le et al. [13] studied the droplet migration behavior in a microchannel under a blocking effect from the heated upper wall. Their results showed that thermocapillary momentum assists the droplet movement when the smallest temperature on the free interface of a liquid droplet shifts from the mid-plane to the advancing side. The thermocapillary momentum then resist the movement of droplet as the highest temperature appears on the free interface. Moreover, the capillary force also strongly affects the droplet migration.

For lab-on-a-chip (LOC) applications, a drop could be flexibly manipulated the motion directions. The experimental work of Vincent et al. [14] investigated the localized thermocapillary stresses on the interface of flowing droplets subjected to the laser source. Their results indicated that high velocity droplet switching and sorting in a microchannel depends on laser-induced thermocapillary stresses. It is very interesting to use

numerical methods to investigate the thermocapillary migration of a liquid droplet in a microchannel under heat source and then verify the experimental results. It has not been well studied.

In this study, the numerical computation scheme developed by Le at el. [9, 10, 13] and Nguyen and Chen [15-17] is used to explore the thermocapillary migration of a water droplet in a microchannel by applying heat source. The conservative level set method and the arbitrary Lagrangian Eulerian (ALE) technique are applied to trace the evolution of the free interface. We used the finite element method to solve the Navier-Stokes equations coupled with the energy equation. A water droplet is place at the bottom wall. Both the upper wall and the bottom wall of the microchannel are subjected to an ambient temperature.

2. Methodology

A small water droplet is placed at the bottom solid wall in a microchannel with a cross-sectional area H x W in which H is the height and W is the length of the microchannel. The shape of the liquid droplet is initially assumed to be that of a cylindrical cap with a static contact angle θ, maximum height h_m, and footprint radius L (Fig. 1). Both the upper wall and the bottom wall of the microchannel are subjected to an ambient temperature. Since the droplet is considered to be very small in size, the influence from the body force can be neglected. The properties of the fluids are listed in Table 1.
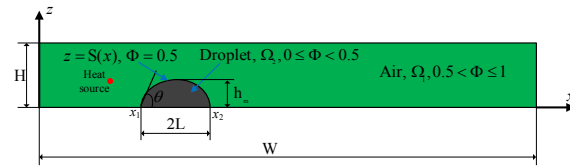
Fig. 1. Schematic representation used for computation. The value of the level set function Φ is equal to 0.5 at the hexadecane/droplet interface. The hexadecane (subdomain Ω_1) and the water (subdomain Ω_2) are represented by $0.5 < \Phi \leq 1$ and $0 \leq \Phi < 0.5$, respectively.

Table 1. Physical properties of the fluids (at 298K).

Parameter	Water	Hexadecan Oil (C16H34)
ρ (kg/m3)	998.23	775
σ (N/m)	71.8x10-3	28.12x10-3
γ_T (mN/m.K)	0.1514	0.06
μ (Pa.s)	9x10-4	0.003
α (m2/s)	1.458x10-7	3.976x10-7
k (W/m.K)	0.6084	0.154
CP (J/kg.K)	4181.3	499.72

Numerical simulations are used to investigate the thermocapillary actuation behavior of a water droplet in a microchannel under a heat source. The numerical methods for predicting the liquid migration must be able to track the movement and deformation of the interface. The conservative level set method [18, 19] is commonly used to deal with the deformation of the free interface during the droplet motion. In this method, the hexadecane subdomain Ω_1 and the water droplet subdomain Ω_2 are separated by the interface $S(x)$ with the level set function $\Phi = 0.5$. The value of Φ goes smoothly from 0 to 1 with $0 \leq \Phi < 0.5$ in the water droplet subdomain Ω_2 and $0.5 < \Phi \leq 1$ in the hexadecane subdomain Ω_1 (Fig. 1). The equation describing the interface reinitialized convection is written as:

$$\frac{\partial \Phi}{\partial t} + V_i \cdot \nabla \Phi = \lambda \nabla \cdot \left[\varepsilon \nabla \Phi - \Phi(1-\Phi) \frac{\nabla \Phi}{|\nabla \Phi|} \right] \tag{1}$$

where λ denotes the amount of reinitialization parameter, ε determines the thickness of the layer around the interface and V_i is the velocity vector. The dense mesh must be located near the free interface during migration to ensure the accuracy of the numerical simulations. The ALE technique is used to ensure that the fine mesh moves simultaneously with the interface. The finite element method developed by Comsol Multiphysics is used to solve the governing equations with the correlative boundary and initial conditions, employing second-order Lagrange triangular elements. The dependency of the element number on the simulation results has been determined to ensure the accuracy of the solution.

The two-dimensional equations for the conservation of mass, momentum, and energy for Newtonian incompressible fluids are written as:

$$\left[\frac{\partial u}{\partial x} + \frac{\partial v}{\partial z} \right]_i = 0, \tag{2}$$

$$\rho_i \left[\frac{\partial u}{\partial t} + u\frac{\partial u}{\partial x} + v\frac{\partial u}{\partial z} \right]_i = -\frac{\partial p}{\partial x} + \mu_i \left[\frac{\partial^2 u}{\partial x^2} + \frac{\partial^2 u}{\partial z^2} \right]_i + F_x, \tag{3}$$

$$\rho_i \left[\frac{\partial v}{\partial t} + u\frac{\partial v}{\partial x} + v\frac{\partial v}{\partial z} \right]_i = -\frac{\partial p}{\partial z} + \mu_i \left[\frac{\partial^2 v}{\partial x^2} + \frac{\partial^2 v}{\partial z^2} \right]_i + F_z, \tag{4}$$

$$\rho_i C_{Pi} \left[\frac{\partial T}{\partial t} + u\frac{\partial T}{\partial x} + v\frac{\partial T}{\partial z} \right]_i = k_i \left[\frac{\partial^2 T}{\partial x^2} + \frac{\partial^2 T}{\partial z^2} \right]_i + Q_s, \tag{5}$$

where u_i and v_i are the velocity components in the x- and z- directions, respectively; p is the pressure and ρ_i is the fluid density; μ_i is the dynamic viscosity; C_{Pi} is the specific heat; k_i is the thermal conductivity; and T is the temperature. The subscripts i = "w" and i = "o" represent water and hexadecane oil, respectively. F_x and F_z are the surface tension force in the x- and z- directions, respectively. Q_s is the heat source.

The dependence of fluids density on temperature can be expressed as

$$\rho_i = \rho_{ref\_i}(1 - \beta_i(T_i - T_{ref})), \tag{6}$$

where ρ_{ref} is the fluid density at the reference temperature, and β_i is the thermal expansion coefficient of the fluid.

The continuum surface force method developed by Brackbill et al. [20] is used to deal with the existence of the surface tension along the free interface. The surface tension force at the free interface can be modeled by

$$F = \sigma \kappa \delta n , \qquad (7)$$

where σ is the surface tension; δ is the Dirac delta function that is a nonzero value at the droplet/air interface only; n is the unit normal vector to the interface; and κ is the local interfacial curvature. The surface tension σ can be assumed to vary linearly with temperature [21], i.e.,

$$\sigma = \sigma_{\text{ref}} - \gamma_T (T - T_{\text{ref}}) , \qquad (8)$$

where σ_{ref} is the surface tension at the reference temperature T_{ref} and $\gamma_T = -\partial\sigma / \partial T$ is the coefficient of the surface-tension.

The boundary conditions for the flow and temperature fields are given by

$$p = p_o ; \ \frac{\partial u_o}{\partial x} = 0 ; \ \frac{\partial T_o}{\partial x} = 0 \ \text{ at } x = 0 \text{ and } x = \text{W}, \qquad (9)$$

$$u_o = v_o = 0 ; \ T_o = T_{\text{ref}} \ \text{ at } 0 < x < \text{W}, \ z = \text{H}, \qquad (10)$$

$$u_o = v_o = 0 \text{ at } 0 < x < x_1 \text{ and } x_2 < x < \text{W}, \ z = 0, \qquad (11)$$

$$T_i = T_{\text{ref}} \ \text{ at } 0 \leq x \leq \text{W}, \ z = 0, \qquad (12)$$

where x_1 and x_2 are locations of the droplet's two contact points. The Navier slip condition is applied at the water-solid and oil-solid boundary

$$u_\tau = b_{\text{is}} \frac{\partial u}{\partial z} , \qquad (13)$$

where b_{is} is the slip length. The order of slip length b_{is} depends on the roughness of solid surface and the type of fluid flow and it can be determined by the experiments or molecular dynamics simulations. Its order is a few nanometers [22, 23]. The water/oil interface S(x) is set to ensure the continuum of flow and temperature

$$V_{\text{w}} \cdot \nabla \text{S} = V_o \cdot \nabla \text{S} , \ T_o = T_{\text{w}} \qquad (14)$$

where $V = ui + vj$.

Before a thermal gradient is imposed on the bottom wall, the droplet is placed on the wall at $x = 2.5\text{H}$ in the ambient temperature. Thus, the initial conditions are set as the following equations:

$$V_{\text{w}}(X,0) = V_o(X,0) = 0 , \qquad (15)$$

$$T_{\text{sub}}(x,0,0) = T_{\text{ref}} , \qquad (16)$$

$$T_{\text{w}}(X,0) = T_o(X,0) = T_{\text{ref}} , \qquad (17)$$

where $X = xi + zj$.

3. Results and Discussion

The water droplet actuated in a microchannel is selected to be $\theta = 90^0$, $T_{\text{w,o}} = 298$ K, L = 0.55 mm, and $h_m = 0.55$ mm. Figure 2 shows the evolution of streamlines and isotherms with time with $b_s = 1$ nm, W = 10 mm, and H = 1 mm. Both the upper wall and the bottom wall of the microchannel are set to be an ambient temperature. 40mW heat source is placed at the distance of 1 mm from the initial position of a water droplet. The imbalance in the surface tension along the free surface causes two thermocapillary vortices inside and outside the liquid droplet. The total strength of these vortices on the hot (left) side is larger than on the cold (right) side due to higher temperature gradient. The thermocapillary migration results in the net thermocapillary momentum which drives the liquid droplet moves from the hot side of the open channel to the cold side. In addition, the flow motion in oil solution strongly affects the droplet migration. At the initial stage, the size and strength of thermocapillary vortice on the receding side of the droplet are small. The heat energy transfers from the heat source to the droplet. As the time passes, the size and strength of thermocapillary vortices on the receding side get larger while they get smaller on the advancing side. The isotherms inside the droplet are extremely distorted by the thermocapillary convection. The temperature distribution in the oil region is the concentric circles diffused to the droplet and distorted when it bumps against the droplet. The highest temperature of the droplet is located at the free interface during actuation process. The location of the highest temperature on the free interface moves from the rear contact line towards the apex of the interface.

Fig. 3 illustrates the temperature gradients inside the droplet on the receding (ΔT_R) and advancing (ΔT_A) sides. The temperature gradient on the receding and advancing side are defined by $\Delta T_R = T_{\text{max}} - T_R$ and $\Delta T_A = T_{\text{max}} - T_A$, respectively. Where T_{max} is the highest temperature of the droplet; T_R and T_A is the temperature of the liquid droplet which is located at the rear and front contact line, respectively. The temperature gradients increase rapidly first and then decreases continuously. This means thermocapillary convection increases at the initial stage and decreases when the time increases to a certain value. The temperature gradient inside the droplet on the receding side is always smaller than that on the advancing side during actuation process. It leads to the thermocapillary force assists the movement of the droplet in a microchannel.
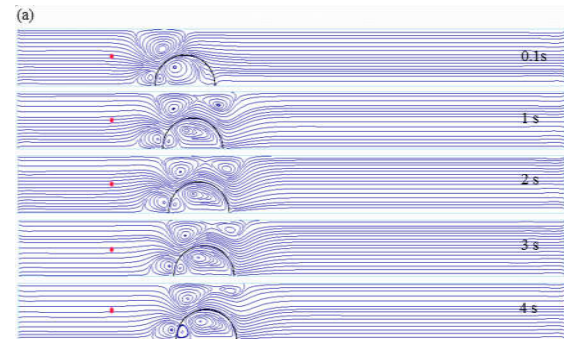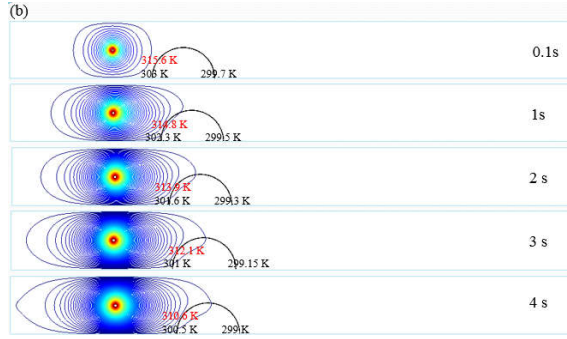
Fig. 2. (a) Streamlines and (b) isotherms inside the channel at different times with $b_s = 1$ nm, $\theta = 90^0$, $W = 10$ mm, and $H = 1$ mm.
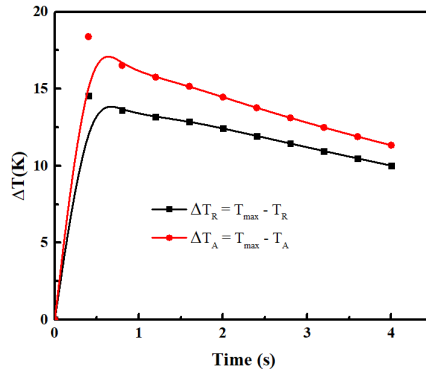
Fig. 3. Temperature gradient inside the droplet on the receding (ΔT_R) and advancing (ΔT_A) sides versus time with $b_s = 1$ nm, $\theta = 90^0$, $W = 10$ mm, and $H = 1$ mm.

Fig. 4(a) shows the evolution of the silicone droplet position in a microchannel versus time with $b_s = 1$ nm, $\theta = 90^0$, $W = 10$ mm, and $H = 1$ mm. The tendency of silicone droplet velocity versus time is also plotted in Fig. 4(b). The actuation velocity of the liquid droplet first increases significantly, and then decreases dramatically. According to Nguyen and Chen [15-17], the actuation of the behavior of the droplet depends on the net momentum of thermocapillary convection created inside the droplet. The Marangoni number (Ma) represents the strength of thermocapillary convection, which is proportional to the temperature difference inside the droplet. As a consequence, the Ma increases rapidly first and then decreases continuously when time reaches to a certain value.
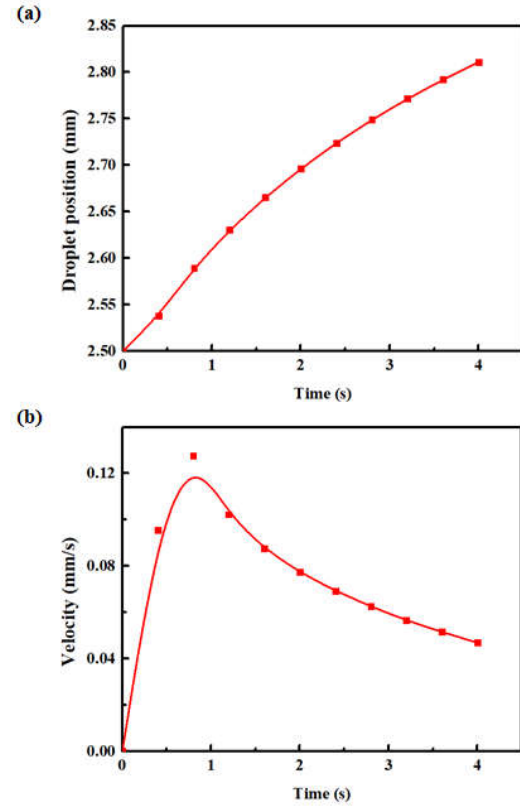
Fig. 4. (a) Displacement and (b) droplet actuation velocity versus time with $b_s = 1$ nm, $\theta = 90^0$, $W = 10$ mm, and $H = 1$ mm.

Fig. 5 shows the pressure differences ($\Delta P = p_w - p_o$) on both side of the droplet and the variation of DCA during the migration process with $b_s = 1$ nm, $\theta = 90^0$, $W = 10$ mm, and $H = 1$ mm. The pressure difference at the receding (ΔP_R) and the advancing side (ΔP_A) of the droplet is negative and positive, respectively (Fig. 5a). The present results show that the DCA alternates during the actuation process (Fig. 5b). The DCA behavior strongly depends on the pressure difference acting on the droplet. The receding contact angle (RCA, θ_R) decreases strongly first and then increases significantly while the advancing contact angle (ACA, θ_A) increases rapidly first and then decrease continuously. The ACA is always larger than the RCA due to the magnitude of ΔP_A is smaller than that of ΔP_R. Since $\theta_A > 90 > \theta_R$ and $\sigma_A > \sigma_R$, $\sigma_A cos\theta_A - \sigma_A cos\theta_A < 0$. Therefore, the thermocapillary force acts against the movement of the water droplet in a microchannel.
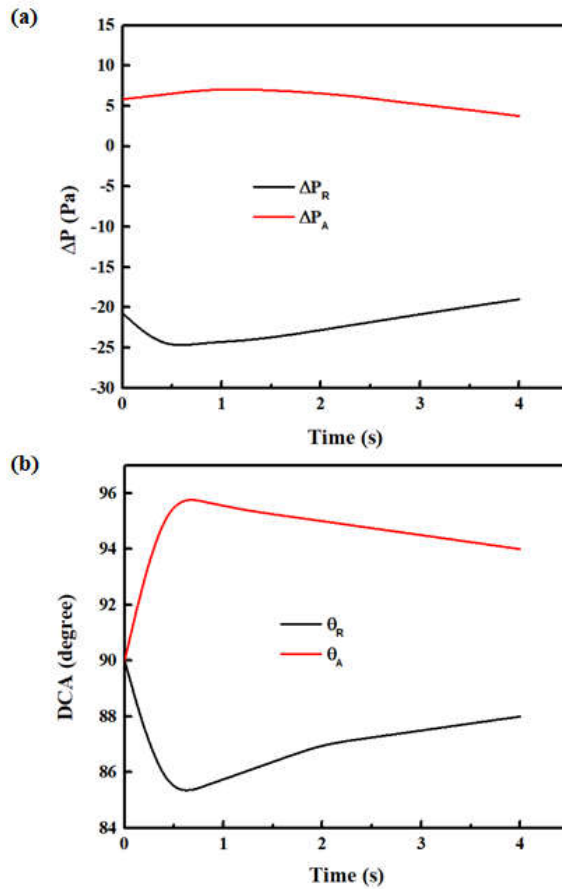
Fig. 5. (a) The pressure differences on both sides of a water droplet and (b) dynamic contact angle during the actuation process with $b_s = 1$ nm, $\theta = 90^0$, $W = 10$ mm, and $H = 1$ mm.

4. Concluding Remarks

The transient thermocapillary migration of a water droplet in a microchannel subjected to a heat source has been investigating numerically. Both the upper wall and the bottom wall of microchannel are set to be an ambient temperature. The results indicate that the actuation behavior of the droplet is strongly influenced by a heat source. The actuation velocity of the liquid droplet initially accelerates, and then goes down rapidly. During the actuation process, the thermocapillary vortices inside the droplet on the receding side is always smaller than that on the advancing side. The isotherms inside the droplet are notably distorted by the thermocapillary convection. The DCA of the droplet alternates versus time due to the pressure difference acting on the droplet. The ACA first increases rapidly and then decreases continuously while the RCA first decreases strongly and then increases significantly. The ACA is always larger than the RCA during the actuation process.

Acknowledgement

References

[1] S. Haeberle and R. Zengerle, Microfluidic platforms for lab-on-a-chip applications, Lab Chip **7** (2007) 1094-1110.

[2] F. Yu, L. Ai, W. Dai, N. Rozengurt, H. Yu, T. K. Hsiai, MEMS thermal sensors to detect changes in heat transfer in the pre-atherosclerotic regions of fat-fed New Zealand white rabbits, Ann Biomed Eng. **39** (2012) 1736-1744.

[3] L. Wang, K. Sun, X. Hu, G. Li, Q. Jin, J. Zhao, A centrifugal microfluidic device for screening protein crystallization conditions by vapor diffusion, Sensors and Actuators B: Chemical **219** (2015) 105-111.

[4] N. T. Nguyen and S.T. Wereley, Fundamentals and applications of microfluidics, Artech House, Boston, 2006.

[5] N. T. Nguyen, S. Lassemono, F. A. Chollet, Optical detection for droplet size control in microfluidic droplet-based analysis systems, Sensors and Actuators B **117** (2006) 431-436.

[6] F. Brochard, Motions of droplets on solid surfaces induced by chemical or thermal gradients, Langmuir **5** (1989) 432-438.

[7] J. Z. Chen, S. M. Troian, A. A. Darhuber, S. Wagner, Effect of contact angle hysteresis on thermocapillary droplet actuation, J. Appl. Phys. **97** (2005) 014906.

[8] M. L. Ford, A. Nadim, Thermocapillary migration of an attached drop on a solid surface, Phys. Fluids **6** (1994) 3183-3185.

[9] T.-L. Le, J.-C. Chen, B.-C. Shen, F.-S. Hwu and H.-B. Nguyen, Numerical investigation of the thermocapillary actuation behavior of a droplet in a microchannel, Int. J. Heat Mass Transfer **83** (2015) 721-730.

[10] T.-L. Le, J.-C. Chen, F.-S. Hwu and H.-B. Nguyen, Numerical study of the migration of a silicone plug inside a capillary tube subjected to an unsteady wall temperature gradient, Int. J. Heat Mass Transfer **97** (2016) 439-449.

[11] N. T. Nguyen, X. Y. Huang, Thermocapillary effect of a liquid plug in transient temperature fields, J. Appl. Phys. **44** (2005) 1139-1142.

[12] H. Liu, A. J. Valocchi, Y. Zhang, Q. Kang, Lattice Boltzmann phase-field modeling of thermocapillary flows in a confined microchannel, J. Comput. Phys. **256** (2014) 334-356.

[13] T.-L. Le, J.-C. Chen, and H.-B. Nguyen, Numerical study of the thermocapillary droplet migration in a microchannel under a blocking effect from the heated wall, Appl. Thermal Eng. **122** (2017) 820-830.

[14] M. R. S. Vincent, R. Wunenburger, J. P. Delville, Laser switching and sorting for high speed digital microfluidics, Applied Physics Letters **92** (2008) 154105.

[15] H.-B.Nguyen and J.-C.Chen, A numerical study of thermocapillary migration of a small liquid droplet on a horizontal solid surface, Phys. Fluid **22** (2010) 062102.

[16] H.-B.Nguyen and J.-C.Chen, Numerical study of a droplet migration induced by combined thermocapillary-bouyancy convection, Phys. Fluid **22** (2010) 122101.

[17] H.-B.Nguyen and J.-C.Chen, Effect of slippage on the thermocapillary migration of a small droplet, Biomicrofluidics **6** (2012) 012809.

[18] E. Olsson, G. Kreiss, A conservative level set method for two phase flow, J. Comput. Phys. **210** (2005) 225-246.

[19] E. Olsson, G. Kreiss, and S. Zahedi, A conservative level set method for two phase flow II, J. Comput. Phys. **225** (2007) 785-807.

[20] J. U. Brackbill, D. B. Kothe, C. Zemach, A continuum method for modeling surface tension, J. Comp. Phys. **100** (1991) 335-354.

[21] J.-C. Chen, C.-W. Kuo, G. P. Neitzel, Numerical simulation of thermocapillary nonwetting, Int. J. Heat Mass Transfer **49** (2006) 4567-4576.

[22] P. Tabeling, Investigating slippage, droplet breakup, and synthesizing microcapsules in microfluidic system, Phys. Fluids **22** (2010) 021302.

[23] J. Koplik, J. R. Banavar, and J. F. Willemsen, Molecular dynamics of fluid flow at solid surfaces, Phys. Fluids A **1** (1989) 781-794.

Recovery at An Oblique Interface in Recovery-based Discontinuous Galerkin for Diffusion

Phuc T. Huynh[1], Loc H. Khieu[1]
[1]Computational Engineering, Vietnamese-German University
Le Lai Street, Hoa Phu Ward, Thu Dau Mot City, Binh Duong, Vietnam

ABSTRACT

In this paper, we study the reconstruction of the recovery function at an oblique interface for the Recovery-based Discontinuous Galerkin method. This method has been working very well on Cartesian grids, ergo we have sought to extend it to triangular grids, which is the grid of choice for complex geometries. On the former grid, the common interface between two arbitrary elements is parallel to one of the coordinate axes, which is no longer applicable on the latter grid. This has necessitated us studying recovery at an oblique interface with respect to the coordinate system. This oblique interface is generated by rotating the common vertical interface between two side-by-side squares an angle α in counterclockwise direction.

1. Introduction

The Recovery-based Discontinuous Galerkin (RDG) discretization was first introduced in 2005 by Prof. Bram van Leer at the University of Michigan (Ann Arbor, MI, US) [1] and developed fully by his doctoral student [2]. It has been proved to be one of the best DG discretizations for diffusion problems on Cartesian grid [3]. On Cartesian grids, the natural type of basis is the tensor-product basis, and RDG has demonstrated an order of accuracy $3p+1$ for odd p and $3p+2$ for even p, where p is the order of the polynomial basis.

However, Cartesian grid is not suitable for handling complicated and irregular geometry. Since unstructured triangular grid is the popular choice, working well on triangles is a definite advantage. However, the natural type of polynomial basis for triangles—the so-called minimal basis—yields a lower order of accuracy, proportional to just $2p$ [4]. One possible explanation is that the minimal basis contains less information than a tensor-product of the same order. Naturally, we want to switch to tensor-product basis to restore the accuracy.

On Cartesian grids, all common interfaces are parallel to one of the coordinate axes, and reconstructing the recovery function is now a routine business. To simulate the non-parallel interfaces that inevitably appear on triangular grid, the common interface of two side-by-side squares is rotated counterclockwise an angle of α, as shown in Fig. 1. We then study the change of the recovery procedure with the rotation.
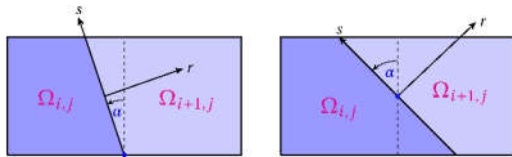
Fig. 1 The common interface is rotated an angle α around the bottom endpoint (on the left) or the middle point (on the right).

The rest of the paper is organized as follows. A short description of RDG for the scalar linear diffusion is presented in Section 0. We then discuss the reconstruction of the crucial recovery function in two dimensions in Section 0. Our provisional conclusions are then present in the last section, Section 0.

2. DG formulation in 2D

2.1 DG formulation for 1D linear diffusion

Considering a scalar linear diffusion equation in one dimension

$$\partial_t u = \mathcal{D} \partial_{xx} u, \tag{1}$$

where $\mathcal{D}$ is the diffusivity coefficient, and $u = u(t,x)$ is the unknown. A weak form is obtainable after multiplication with a test function $v(x)$ and integration by parts twice over the interior of an one-dimensional element, or cell, $\Omega_j \in \left[x_{j-1/2}, x_{j+1/2} \right]$ as shown in Fig. 2:

$$\frac{\partial}{\partial t} \int_{\Omega_j} v u \, dx = \mathcal{D} \underbrace{\left[v \frac{\partial u}{\partial x} - u \frac{dv}{dx} \right]_{x_{j-1/2}}^{x_{j+1/2}}}_{\text{boundary integral}} + \mathcal{D} \underbrace{\int_{\Omega_j} u \frac{d^2 v}{dx^2} \, dx}_{\text{Volume integral}}. \tag{2}$$

With DG discretization, the exact solution $u(t,x)$ is approximated by a polynomial of degree p,

$$u_j^{(p)}(t,x) = \sum_{\alpha=0}^{p} a_j^{(\alpha)}(t) \phi_j^{(\alpha)}(x). \tag{3}$$

These $p+1$ functions $\phi_j^{(\alpha)}(x)$ are called basis functions and defined with in Ω_j only, i.e., they are zero outside that cell. There are various options for us to choose from, e.g., Legendre, Lagrange, or *monomial* bases—we use Legendre to formulate RDG due to the latter's modal nature. This formulation also use those basis functions for the test functions in (2). The numerical solutions are generally discontinuous at two endpoints of Ω_j because there is no constraint on

continuity, ergo the name *Discontinuous* Galerkin (see Fig. 4 for typical numerical representation).
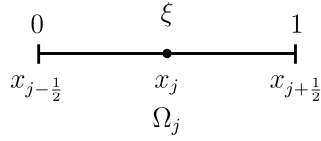
Fig. 2 Geometry of an arbitrary cell in one dimension. The global coordinate x spans $\left[x_{j-1/2}, x_{j+1/2}\right]$ while the local coordinate ξ spans $[0, 1]$.

The expressions of the basis functions in the x–coordinate, called *global* coordinate, will vary between cells. When we switch to a local coordinate ξ as defined in Fig. 2, however, expressions of $\phi_j^{(\alpha)}(\xi)$ for a particular α stay unchanged among all cells. Table 1 lists the Legendre polynomial basis functions up to degree four $(p = 4)$ in one dimension.

Table 1 The Legendre polynomial basis expressed in the local coordinate

$\phi(x)$	
$\phi^{(0)}(\xi)$	1
$\phi^{(1)}(\xi)$	$-1 + 2\xi$
$\phi^{(2)}(\xi)$	$1 - 6\xi + 6\xi^2$
$\phi^{(3)}(\xi)$	$-1 + 12\xi - 30\xi^2 + 20\xi^3$
$\phi^{(4)}(\xi)$	$1 - 20\xi + 90\xi^2 - 140\xi^3 + 70\xi^4$

In DG, the numerical solutions are the values of the polynomial coefficients $a_j^{(\alpha)}$ in (3). They are called *DG coefficients* or *moments*, and their update equations are derived from the weak form (2):

$$\frac{\partial}{\partial t}\int_{\Omega_j}\phi_j^{(\alpha)}\,u\,dx = \underbrace{\mathcal{D}\left[\phi_j^{(\alpha)}\frac{\partial u}{\partial x} - u\frac{d\phi_j^{(\alpha)}}{dx}\right]_{x_{j-1/2}}^{x_{j+1/2}}}_{\text{boundary integral}}$$
$$+ \underbrace{\mathcal{D}\int_{\Omega_j}u\frac{d^2\phi_j^{(\alpha)}}{dx^2}\,dx}_{\text{Volume integral}} \quad \forall\,\alpha \in [0, p]. \tag{4}$$

This is a system of $p+1$ *ordinary differential equations,* in which $a_j^{(\alpha)}$ are the unknowns. We will then use a time-marching discretization for the temporal terms on the left hand side, e.g., the venerable Runge–Kutta (RK) scheme. The resultant fully discretized scheme is usually abbreviated to RKDG or RK-DG.

The calculation of the volume integral is straightforward; expressions of $\phi_j(x)$ are known and the exact solution $u(x)$ is substituted by its numerical

approximation $u_j^{(\alpha)}(x)$ in (3). The subtleties lie within the evaluation of the boundary integral. In one dimension, it reduces to a calculation using only function values and derivatives at the two boundary points $x_{j-1/2}$ and $x_{j+1/2}$. Values of $\phi_j^{\alpha}(x_{j\pm1/2})$ are readily available, but those of $u(x_{j\pm1/2})$ and $\partial_x u(x_{j\pm1/2})$ are nontrivial owing to the discontinuous nature of DG. There are two generally different values of u and two of $\partial_x u$ at each cell boundary. *Which value should we use?*

2.2 Recovery function at the interface

We let two elements Ω_j and Ω_{j+1} sharing the common interface $x_{j+1/2}$ and the numerical solutions are expressed as follows:

$$u_j^{(p)}(t, x) = \sum_{\alpha=0}^{p}a_j^{(\alpha)}(t)\phi_j^{(\alpha)}(x), \text{ and} \tag{5}$$

$$u_{j+1}^{(p)}(t, x) = \sum_{\alpha=0}^{p}a_{j+1}^{(\alpha)}(t)\phi_{j+1}^{(\alpha)}(x). \tag{6}$$

We then construct a new polynomial of degree $2p+1$ using all information from both Ω_j and Ω_{j+1}. This reconstructed polynomial function is called *recovery function,* denoted by $f_{j+1/2}$, associating with the interface $x_{j+1/2}$ and defined over the union of Ω_j and Ω_{j+1}—we also say that f is centered at $x_{j+1/2}$.

$$f_{j+1/2}(x) = \sum_{\alpha=0}^{2p+1}b_{j+1/2}^{(\alpha)}\psi_{j+1/2}^{(\alpha)}(x), \tag{7}$$

where $b_{j+1/2}^{(\alpha)}$ are the *recovery* coefficients that are unknown and $\psi_{j+1/2}^{(\alpha)}$ are the recovery basis functions spanning the union of both elements Ω_j and Ω_{j+1}. For illustrative purposes, it suffices to use monomial basis to for the recovery basis, $\psi_{j+1/2}^{(\alpha)}(x) = x^{\alpha}$.

The formulation of the recovery basis is described graphically in Fig. 3 for piecewise constant and linear cases. The blocks on the left and right of the dashed line are basis functions for cells Ω_j and Ω_{j+1}, respectively. The blocks after the arrow are the resultant recovery basis. On the first row, the DG approximation in each cell has only one *moment* because it is piecewise-constant case. Stacking the blocks together, we then have two blocks, or two pieces of information, enough to construct a linear function. Thus, the recovery basis comprises 1 and x, representing a polynomial basis of degree 1. It is similar for the case of piecewise linear: two moments in each cell, stacking to form four blocks or pieces of information, enough to construct a cubic polynomial.
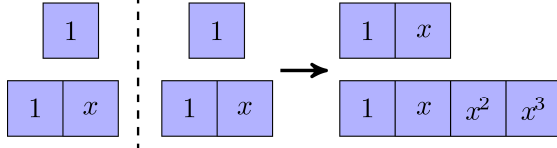
Fig. 3 Recovery bases for $p=0$ (top row) and $p=1$ (bottom row). We will discuss in more details in Section 0.

Fig. 4 A representative cartoon of piecewise-linear numerical solutions.

In RDG, the constraints on f are as follows:

$$\begin{cases} \int_{\Omega_j} \phi_j^{(\alpha)} u_j dx = \int_{\Omega_j} \phi_j^{(\alpha)} f_{j+1/2} dx \\ \int_{\Omega_{j+1}} \phi_{j+1}^{(\alpha)} u_{j+1} dx = \int_{\Omega_{j+1}} \phi_{j+1}^{(\alpha)} f_{j+1/2} dx \end{cases} \forall \alpha \in [0, p]; \quad (8)$$

these equations are called *recovery* equations. This will assure that f is weakly equivalent to u_j on Ω_j and u_{j+1} on Ω_{j+1}. Subscript $j+1/2$ is subsequently dropped as it is obvious which interface we are discussing. Inserting (5), (6), and (7) into (8) yields the linear system:

$$\mathbf{M} \vec{a}_{j,j+1} = \mathbf{R} \vec{b} \quad (9)$$

where $\mathbf{M}$ is a block diagonal matrix, $\vec{a}_{j,j+1}$ is a vector of size $2p+2$ that contains all DG coefficients of both cells, $\mathbf{R}$ is a generally dense matrix, and vector $\vec{b}$ contains the unknown recovery coefficients $b_{j+1/2}^{(\alpha)}$ that are solution of the linear system (9). We then use the obtained f for both the function value and the function derivative at the cell interfaces in the boundary integral.

$$\begin{cases} u(x_{j\pm1/2}) = f_{j\pm1/2}(x_{j\pm1/2}) \\ \partial_x u(x_{j\pm1/2}) = \dfrac{df_{j\pm1/2}}{dx}(x_{j\pm1/2}) \end{cases}. \quad (10)$$

The RHS of (4) is now *fully defined*.

2.3 Piecewise-linear RDG semi discrete equation

As a typical example, we present the results for a piecewise approximation. A representative cartoon of the numerical solutions is shown in Fig. 4:

$$u_j^{(1)}(t,x) = \sum_{\alpha=0}^{1} a_j^{(\alpha)}(t)\phi_j^{(\alpha)}(x)$$
$$= a_j^{(0)}(t)\phi_j^{(0)}(x) + a_j^{(1)}(t)\phi_j^{(1)}(x), \quad (11)$$

where

$$\phi_j^{(0)}(x) = 1,$$
$$\phi_j^{(1)}(x) = -1 + 2\left(\frac{1}{2} + \frac{x - x_j}{\Delta x}\right). \quad (12)$$

The recovery function at an arbitrary interface is now a polynomial of degree $2p+1 = 2\times1+1 = 3$. Solving the recovery equations (9), we obtain the following expressions for the recovery coefficients.

$$\begin{pmatrix} b^{(0)} \\ b^{(1)} \\ b^{(2)} \\ b^{(3)} \end{pmatrix}_{j,j+1} = \begin{pmatrix} \frac{1}{2}\left(a_j^{(0)} + a_{j+1}^{(0)}\right) + \frac{1}{3}\left(a_j^{(1)} - a_{j+1}^{(1)}\right) \\ \frac{9}{4}\left(a_{j+1}^{(0)} - a_j^{(0)}\right) - \frac{5}{4}\left(a_j^{(1)} + a_{j+1}^{(1)}\right) \\ a_{j+1}^{(1)} - a_j^{(1)} \\ \frac{5}{2}\left(a_j^{(0)} - a_{j+1}^{(0)}\right) + \frac{5}{2}\left(a_j^{(1)} + a_{j+1}^{(1)}\right) \end{pmatrix}. \quad (13)$$

Subsequently, the semi-discrete system to update the DG coefficients is

$$\frac{d}{dt}\begin{pmatrix} a_j^{(0)} \\ a_j^{(1)} \end{pmatrix} = \frac{\mathcal{D}}{(\Delta x)^2}\left(\begin{bmatrix} \frac{9}{4} & \frac{5}{4} \\ -\frac{5}{4} & -\frac{7}{12} \end{bmatrix}\begin{pmatrix} a_{j-1}^{(0)} \\ a_{j-1}^{(1)} \end{pmatrix}\right.$$
$$+ \begin{bmatrix} -\frac{9}{2} & 0 \\ 0 & -\frac{23}{6} \end{bmatrix}\begin{pmatrix} a_j^{(0)} \\ a_j^{(1)} \end{pmatrix} + \left.\begin{bmatrix} \frac{9}{4} & -\frac{5}{4} \\ \frac{5}{4} & -\frac{7}{12} \end{bmatrix}\begin{pmatrix} a_{j+1}^{(0)} \\ a_{j+1}^{(1)} \end{pmatrix}\right). \quad (14)$$

3. RDG function in 2D

In this section, we will present the recovery reconstruction in two dimensions. Unlike one-dimensional recovery, one has to be careful with how one formulates the recovery basis. Interested readers can read the doctoral dissertation by Marcus Lo [2] for the detailed picture.

3.1 Types of polynomial basis and recovery basis

In two dimensions (as well as three dimensions), we introduce the recovery coordinates, denoted by r and s for the face-normal and face-tangential directions, respectively. (See .Fig. 1.) Another fundamental difference in two-or-three dimensions is that there are two different kinds of polynomial basis, namely *minimal* and *tensor-product* bases. The former is used on triangular elements (*simplex* element in general) and the latter on quadrilateral ones. Fig. 5 shows the samples of minimal-basis type for $p=1$ and $p=2$ approximations and the corresponding recovery bases. Fig. 6 shows the same for tensor-product bases. In both cases, the recovery function has the following general expression.

$$f = \sum_{\alpha=1}^{N} b^{(\alpha)}\psi^{(\alpha)}(r,s), \quad (15)$$

where $N = (p+1)(p+2)$ for minimal basis and $2(p+1)^2$ for tensor-product basis.
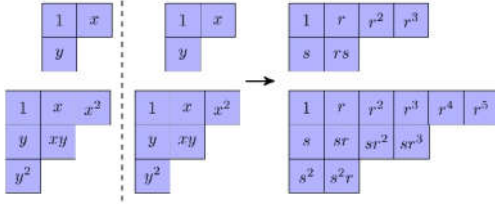
Fig. 5 The recovery basis in 2D for minimal DG basis
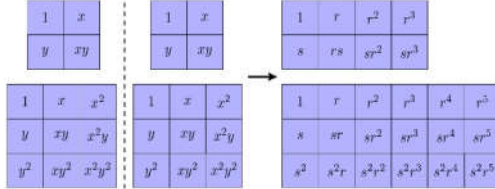
Fig. 6 The recovery basis in 2D for tensor-product DG basis

We can see that in the two-dimensional recovery basis derived from tensor-product basis contains more information than one from minimal basis. It partially explains the drop in order of accuracy we previously experienced with RDG on unit right-triangular elements [4]. (It is proportional to $2p$ for the former, versus $3p$ of the latter.)

3.2 Configuration 1: The pivot at the center of the interface

Inspired by the better performance of the tensor-product basis, we attempt to use it for triangles. For RDG, the crucial component is the reconstruction of the recovery function, so naturally our first task is to reconstruct the recovery function f at a non-parallel-to-axis interface, which is not presented on Cartesian grids but will inevitably appear on triangular grids.

Our initial geometry is two squares side by side, on which we have confirmed the success of reconstructing the recovery function. The common interface is then rotated at the middle point counterclockwise an angle α as shown in Fig. 1 to form an oblique interface. The geometry will change from two side-by-side squares, to two right trapezoids, and finally to two right triangles as shown in Fig. 7. The reconstruction of the recovery function will be study as the angle α changes from 0 to $\tan^{-1}(2)$.
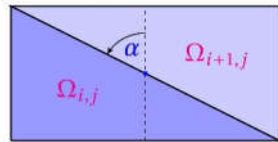
Fig. 7 Geometry of the extreme case with the middle-point pivot and $\alpha = \tan^{-1}(2)$.

We have the following coordinate transformation between the global and recovery coordinates:

$$\begin{cases} r = \dfrac{2}{h}[\cos(\alpha)(x - x_M) - \sin(\alpha)(y - y_M)] \\ s = \dfrac{2}{h}[\sin(\alpha)(x - x_M) + \cos(\alpha)(y - y_M)] \end{cases}, \quad (16)$$

where (x_M, y_M) are the coordinates of the pivot, and h is the length of the that interface. The recovery equations in two dimensions retain the same form as (9), and the expressions for matrices $\mathbf{M}$ and $\mathbf{R}$ for the case $p = 0$ are shown below. (Despite being the simplest, this lowest-order approximation is representative for the rest.)

$$\mathbf{M} = h^2 \begin{pmatrix} 1 - \dfrac{1}{2}\tan(\alpha) & 0 \\ 0 & 1 + \dfrac{1}{2}\tan(\alpha) \end{pmatrix}, \text{ and}$$

$$\mathbf{R} = h^2 \begin{pmatrix} 1 & -\dfrac{1}{8}[5\cos(2\alpha) + 3]\sec[\alpha] \\ 1 & \dfrac{1}{8}[5\cos(2\alpha) + 3]\sec[\alpha] \end{pmatrix}.$$

The recovery mass matrix R is invertible exactly at $\alpha = \tan^{-1}(2)$, i.e., the reconstruction *fails* at the common interface between two right triangles. *Choppy sea is waiting ahead!*

3.3 Configuration 2: The pivot is at the endpoint of the interface

We have learned that the recovery fails at least at the common hypotenuse between to abutting right triangles as shown in Fig. 7. What if only one cell is triangle? We can easily construct this arrangement by rotating the common interface of two squares at the endpoint instead, as in Fig. 8.
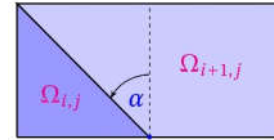
Fig. 8 Geometry of the extreme case with the endpoint pivot and $\alpha = \pi/4$.

In this case, two squares will morph into one right trapezoid and one right triangle when $\alpha = \pi/4$. We have

$$\mathbf{M} = h^2 \begin{pmatrix} 1 - \dfrac{1}{2}\tan(\alpha) & 0 \\ 0 & 1 + \dfrac{1}{2}\tan(\alpha) \end{pmatrix}, \text{ and}$$

$$\mathbf{R} = h^2 \begin{pmatrix} -\dfrac{1}{2}[\tan(\alpha) - 2] & [\sin(\alpha) - \cos[\alpha]] \\ \dfrac{1}{2}[\tan(\alpha) + 2] & [\sin(\alpha) + \cos[\alpha]] \end{pmatrix}.$$

The determinant of the recovery mass matrix $\mathbf{R}$ remains non-zero for all $\alpha \in [0, \pi/4]$, i.e., the reconstruction of

the recovery function is *always successful* on the second configuration.

4. (Provisional) Conclusions

We have presented a brief description of the Recovery-based Discontinuous Galerkin (RDG), which is capable of achieving an order of accuracy proportional to $3p$, which has been shown to be the best DG schemes for diffusion on a Cartesian grid with compact stencil. However, the adaptation to triangular grids proves not at all trivial. The crucial enabling factor is the ability to reconstruct the so-called recovery function that is weakly identical to the numerical solutions. Our preliminary results show that the reconstruction at the common hypotenuse of two right triangles will fail. One possible remedy is to change one of two cells to a quad, transforming the configuration from triangle-triangle to triangle-quadrilateral.

References

[1] B. Van Leer and S. Nomura, AIAA 2005-5108, (2005), DOI: 10.2514/6.2005-5108.

[2] K. H. M. Lo, Doctoral Dissertation, The University of Michigan, Ann Arbor, (2011) [link].

[3] H. T. Huynh, AIAA 2009-0403, (2009), DOI: 10.2514/6.2009-403.

[4] L. Khieu, and B. Van Leer, AIAA 2013-2691, (2013), DOI: 10.2514/6.2013-2691.

Experimental Study of Circular Inlets Effect on the Performances of Gas-Liquid Cylindrical Cyclone Separators (GLCC)

Ho Minh Kha[1,2]; Nguyen Thanh Nam[2]; Vo Tuyen[3]; Nguyen Tan Ken[3]
[1] Ho Chi Minh City University of Technology and Education (HCMUTE), Vietnam
(e-mail: 1424003@student.hcmute.edu.vn)
[2] DCSELAB - **Ho Chi Minh City University of Technology,** VNU – HCM, Vietnam
[3] Ho Chi Minh City University of Food Industry (HUFI), Vietnam

ABSTRACT

The gas-liquid cylindrical cyclone (GLCC) separators is a fairly new technology for oil and gas industry. The current GLCC separator, a potential alternative for the conventional one, was studied, developed and patented by Chevron company and Tulsa University (USA). It is used for replacing the traditional separators that have been used over the last 100 years. In addition, it is significantly attracted to petroleum companies in recent years because of the effect of the oil world price. However, the behavior of phases in the instrument is very rapid, complex and unsteady which may cause the difficulty of enhancing the performance of the separation phases. The multiple recently research show that the inlet geometry is probably the most critical element that influences directly to the performance of separation of phases. Though, so far, most of the studies of GLCC separator were limited with the one inlet model. The main target of the current study is to deeply understand the effect of different geometrical configurations of the circular inlet on performances of GLCC by the experimental method for two phases flow (gas-liquid). Two different inlet configurations are constructed, namely: One circular inlet and two symmetric circular inlets. As a result, we propose the use of two symmetric circular inlets to enhance the separator efficiency because of their effects.

Keywords: Gas-liquid cylindrical cyclone separator; GLCC; cyclone separator; multiphase flow.
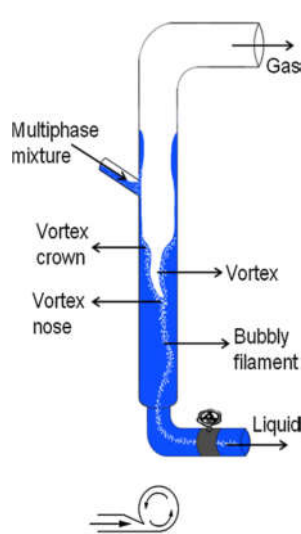
1. Introduction

Figure 1. *The Gas-Liquid Cylindrical Cyclone separator*

In the petroleum industry, separating the single phases of gas and liquid from a multiphase product is an important stage of the production process. The tradition type separators, that have been popularly used for this work, are big, heavy, bulky, and costly in purchasing and operating. The gas-liquid cylindrical cyclone (GLCC) separator, a potential substitute for the conventional one, was patented by Chevron Petroleum Technology Company and Tulsa University [1].

The GLCC is a simple, compact, low-weight, low inhabitancy time and the low-cost separator that is rapidly gaining popularity as an alternative to conventional gravity-based separators. Shown in Figure 1 is a GLCC consisting of a vertical pipe with a tangential inlet and outlets for gas and liquid. The tangential flow from the inlet to the body of the GLCC causes the flow to swirl with sufficient tangential velocity to produce centripetal forces on the entrained which are an order of magnitude higher than the force of gravity. The combination of gravitational and centrifugal forces pushes the liquid radially outward and downward toward the liquid exit, while the gas is driven inward and upward toward the gas exit [1, 2, 3].

The operational envelope of a GLCC is described by two phenomena: Liquid carry-over (LCO) in the gas stream and gas carry-under (GCU) in the liquid stream. The start of liquid carry-over is identified by the first trace of liquid in the gas stream. Similarly, the first visible bubbles in the liquid underflow mark the onset of gas carry-under. The difficulty in developing accurate performance predictions arises largely from the variety of complex flow patterns that can occur in the GLCC. The flow patterns above the inlet can include bubble, slug/churn, annular-dispersed, and liquid ribbon flow. Below the inlet, the flow generally consists of a liquid vortex with a gas-core filament. Although they have potential applications, the complex phenomenon affecting the separating efficiency have not been studied completely in the past [1, 4, 5, 6].

This difficulty in predicting the hydrodynamic performance of the GLCC has been the single largest obstruction to broader use of the GLCC. Even without tried and tested performance predictions, several successful applications of GLCC's have been reported [3]. The development of reliable performance-prediction tools will improve GLCC's through hardware modifications and, ultimately, will govern the speed and extent to which GLCC technology is deployed in existing and new field applications. Recent laboratory

observations and computer simulations indicate that hardware modifications to the GLCC can have a profound effect on GLCC performance [2]. The GLCC performance is dependent upon the tangential velocities of the swirling fluids, especially that of the liquid. The inlet is the single most redesigned component of the GLCC because of the inlet's influence on tangential velocity [1, 2]. Kouba and Shoham (1996) [1] observed experimentally that the optimal inclined inlet angle is 27° which allowed to retard significantly the onset of liquid carry-over (LCO) in comparison with the horizontal inlet. Most of the previous studies of GLCC separator were limited with the one inlet model [7, 8, 9, 10]. Movafaghian et al [11] researched the effects of geometry, fluid properties and pressure on the hydrodynamics of GLCC with one and two inlets. But the two inlets is the same of the side.

Recent studies, they propose the use of multiple tangential inlets to improve separation efficiency in GLCC. Such inlet configuration leads to lower swirl intensity decay than the unique inlet configuration. It also engenders a more axisymmetric flow, which would improve the GLCC performance with respect to LCO [12, 13, 14, 15]. Thus far, over the past 22 years, more than 6500 GLCCs have been installed around the world by the petroleum and related industries [16]. However, the research has not been conducted on two symmetric inlet types to compare the effect of one type of inlet with the same angle of inclination and the area of the nozzle when it uses to separator multiphase.

II. Experimental program
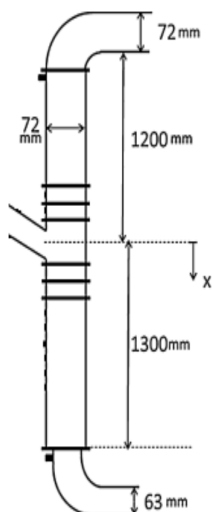
***Figure 2**. Main dimensions of the GLCC*

The GLCC' geometry is modeled size parameters along with experimental models of Hreiz. R et al [13, 14] (Figure 2). According to the diameter size of the pipe available on the market, in this investigation, two different inlet configurations (Figure 3) are constructed with the same inclined inlet is 27° and the cross-sectional area of the inlet was approximately (27-28%) compared to the cross-sectional area of GLCC. The two-phase mixture is introduced into the GLCC through a Y junction and the static mixer (Figure 4). The schematics of the GLCC test section shows in Figure 5. The experimental facility meets the following requirements:

- ➤ Two-phases (air-liquid), full separator.
- ➤ Easy and quick change of different inlet configurations.

- ➤ The GLCC body is transparent to allow visualizations and is manufactured in Acrylic
- ➤ The inlets are manufactured by stainless steel
- ➤ One phase, 1 HP centrifugal pump, capable of producing 5-266 L/min (at max. head of 22 m).
- ➤ One phase, 3HP ring blower, capable of producing 325 m³/h (at max. head of 36 KPa).
- ➤ Two rotameters (1.6-16 m³/h) and flow rate measurement tree to measure flow rates for different inlet configurations.
- ➤ One measures air flow
- ➤ A 120 liter storage tank
- ➤ Two static mixers

One circular inlet (I.D 38mm)   Two circular inlets (I.D 27mm)

***Figure 3**. The different inlet configurations*
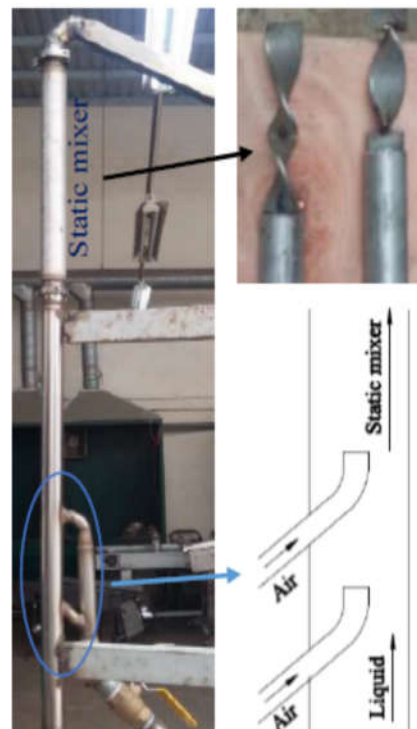
***Figure 4**. The Y junction and static mixer*
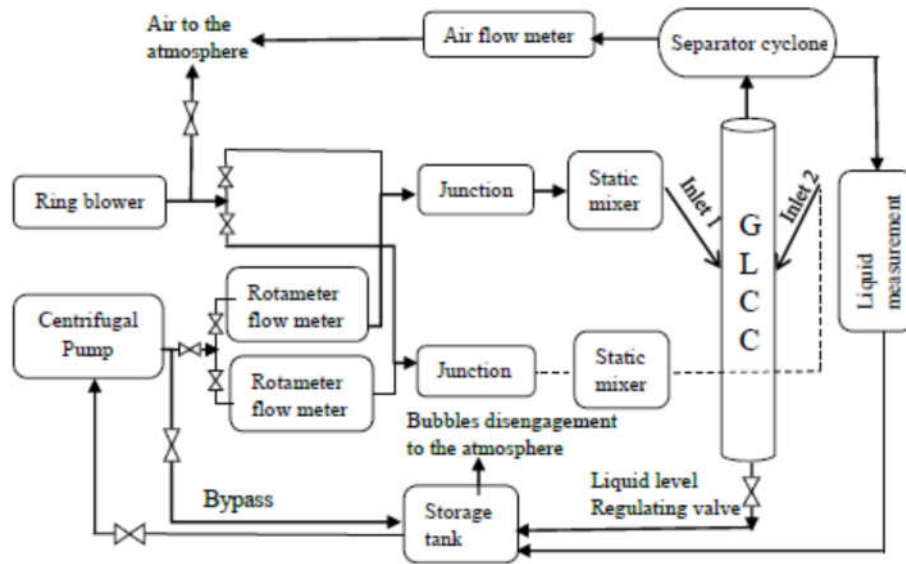
Figure 5. *Schematics of the GLCC test section*

III. Results

1. The flow hydrodynamics in the GLCC

In the GLCC upper part, liquid droplets are pushed toward the walls by centrifugal force and combine into a liquid layer. As this liquid layer is compact compared to discrete droplets, the gas flow will have more difficulties to take it up to the top outlet. The liquid from the wall layer falls down by gravity into the liquid vortex thereafter. However, if the gas flow rate is increased beyond a certain threshold, the liquid is carried over with the gas stream in the GLCC upper outlet. This limiting phenomenon is called Liquid Carry-Over (LCO) [14].

The LCO in the gas stream is largely dependent on the flow pattern in the upper part of the GLCC. Flooding may occur in the GLCC at high liquid levels and low gas rates, producing bubbly flow. The unsteady liquid fluctuations, characteristic of churn flow at moderate gas rates, may jump liquid into the gas outlet. The liquid can also be carried out in droplets at the onset of annular mist flow at high gas rates. At very high gas rates, the centrifugal force of the swirling gas pushes the liquid to the wall of the pipe, where it may form an upward-spiraling continuous ribbon of liquid [1, 2, 17].

In our study, the GLCC is operated under conditions of LCO. When the superficial gas velocity in the cylindrical (Vsg) decreases from about 9 m/s to about 1 m/s and simultaneously, the superficial liquid velocity (Vsl) in the cylindrical increases from 0.1 m/s to 0.5 m/s. The upper flow component of the GLCC also transitions from the annular flow to the flow churn (Figure 6) as the one inlet is used. However, when using the two-inlet type, the velocity value of Vsg and Vsl inside the cylindrical will be higher than the one inlet of the operational envelope of LCO. Effect of inlet geometry on the operational envelope for liquid carry-over (LCO) threshold are presented below.

Annular flow [18] is a flow regime of two-phase gas-liquid flow. It is characterized by the presence of a liquid film flowing on the channel wall (in a round channel this film is annulus-shaped which gives the name to this type of flow) and with the gas flowing in the gas core. The flow core can contain entrained liquid droplets. In this case, the region is often referred to as annular-dispersed flow, where the entrained fraction may vary from zero (a pure annular flow) to a value close to unity (a dispersed flow). Often both types of flow, pure annular and annular-dispersed, are known under the general term of annular flow (Figure 6 a).
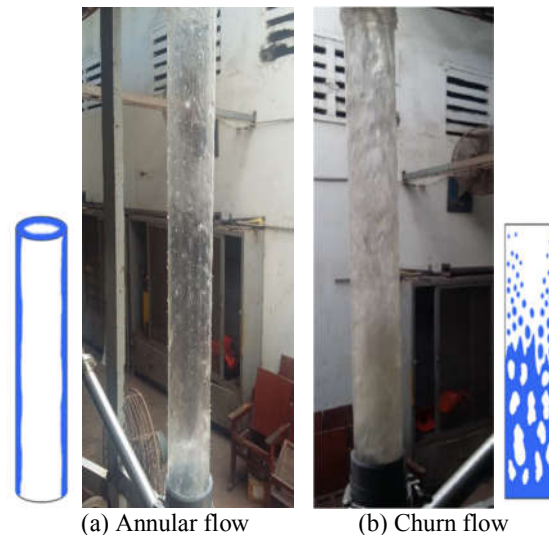
(a) Annular flow   (b) Churn flow
Figure 6. *Schematics of different LCO flow regimes*

The churn flow LCO regime the churning flow (Figure 6 b) is a very chaotic and turbulent regime characterized by unstable vertical oscillations of the flow that can occur for moderate to high liquid flow rates. According to our visual observations, beyond a certain air flow rate, the USLF (Upper Liquid Swirling Film) is destabilized, mainly because of the air flow that tries to lift it up. Thus,

the USLF loses its integrity, which results in a churn flow regime with violent oscillations just above the inlet level. Liquid droplets are ejected from the churn flow region and may splash up to the gas outlet, thereby initiating the LCO. If the gas flow rate is increased further, more liquid is lifted by the gas, and the churn flow regime invades all the upper part of the GLCC [14, 19].

With two symmetric inlets and when the GLCC is operated in a state of churn flow (Vsg < 4 m/s and Vsl > 0.25 m/s). The flow in the upper of the GLCC fluctuates very strongly and continuously changes. It is characterized by the presence of a very thick and unstable liquid film, with the liquid often oscillating up and down in cycles (Figure 7). But, there is a really interesting which is the oscillation around the tube is relatively uniform when using the two inlet type compared to the other inlet. This will affect the performance of the separator.

(a)   (b)   (c)
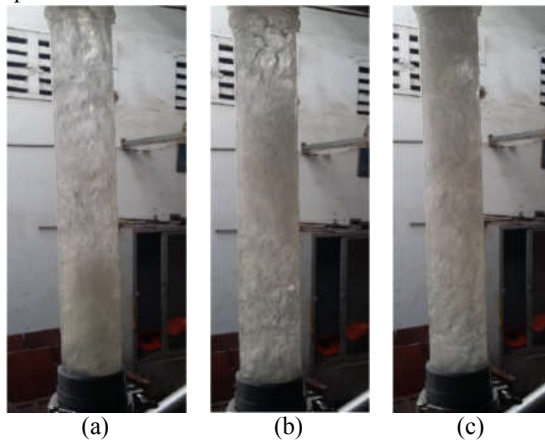
Figure 7. Fluctuations up and down in cycles of the churn flow LCO regime

In the GLCC lower part, if the swirl intensity is high enough, the free gas-liquid interface gets carved out and the vortex can be observed. The liquid flows from the inlet nozzle to the vortex in a thin swirling film (Figure 1), to which we will refer to as Lower Swirling Liquid Film, LSLF. Large bubbles quickly move toward the free interface due to buoyancy. Smaller bubbles, while being dragged downward by the liquid, are pushed radially toward the vortex center. They form a bubbly filament which allows a nice visualization of the vortex core. These bubbles are supposed to rise up to the free interface and to disengage [1, 14].

A variety of experiments has been conducted with the both of the inlets to investigate the different flow patterns in the lower part of the GLCC. The study was restricted to gas-liquid flow rates upper the LCO limit. The top part of the vortex, the crown, was maintained about 100 mm below the inlet nozzle through a valve installed on the GLCC lower outlet (Figure 5). The vortex level was not set closer to the entrance level for two reasons. The first reason is that in field conditions, gas and liquid flow rates fluctuate in time. Thus, the vortex level in the GLCC

must be maintained at a certain distance from the inlet, so that the control system has enough time to react in the case of a sudden increase of the liquid flow rate, and prevents the vortex to exceed the inlet level and to lead to a precocious LCO. The second reason is that when the vortex level is too close to the entrance, we observed that the flow gets disrupted. As noticed by Shoham and Kouba (1998), some distance from the entrance is necessary to achieve an optimal swirl intensity [14].

Based on visual observations, the bubbly filament presents a very complex hydrodynamics. The flow pattern depends mainly on the liquid flow rate and the number of the inlet. An increase in the gas flow rate has little effect on the flow pattern but increases the number of bubbles in the flow. As Vsl increases and Vsg decreases, the flow pattern is characterized by important centrifugal forces and so, the vortex becomes deeply excavated and shows tortuosities. Bubbles tend to be smaller and, as the swirl intensity becomes higher, most of the bubbles concentrate in the filament, and bubble dispersion decreases (Figure 8). The warping of the vortex comes from the use of a unique inlet nozzle, which induces a pronounced asymmetry in the flow. Extremely few bubbles are found outside the region around the bubbly filament and the zone near the vortex interface.

(a) Excavated vortex flow (Vsl=0.27m/s, Vsg= 10.5 m/s

(b) Deeply excavated vortex flow (Vsl = 0.41m/s, Vsg = 6.4m/s

Figure 8. Different vortex regimes in the GLCC lower part (case two inlets is used)

Figure 9 displays the filament core of a one and two circular inlets. The upward and downward flow region near the cylindrical center line for one inlet has a helical (spiral) shape. But, the upward and downward flow region near the cylindrical center line of two nozzle inlets is a quite axisymmetric flow field. In GLCC's design, this means that there is more space to capture bubbles at the center and uplift them to the gas-liquid interface for the separation.

One circular inlet   Two circular inlets

***Figure 9**. The filament core in the GLCC lower part*

2. Liquid carry-over (LCO)

In order to determine the start of liquid carry-over LCO for a given liquid flow rate, a series of experiments is done at a fixed liquid flow rate. A gas flow rate is chosen, the mixture is introduced into the GLCC, and it is observed whether or not the liquid reaches the upper outlet

Figure 10 shows the variations of the operational envelope for liquid carry-over (LCO) threshold with the GLCC inlet configurations, at atmospheric pressure for an air-water system. Two different inlet configurations were used: a 38 mm I.D single-inlet and 27 mm I.D for two symmetric inlets.
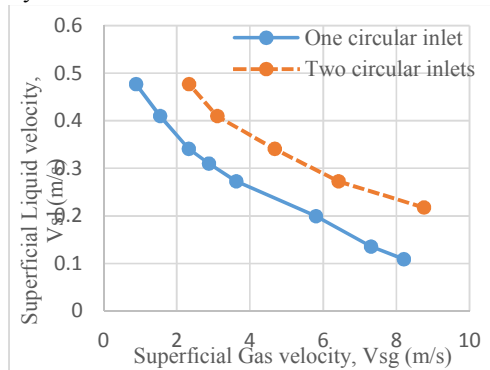
***Figure 10**. Effect of inlet geometry on the operational envelope for liquid carry-over (LCO) threshold*

Comparison between the liquid carry-over (LCO) operational envelopes for them reveals that the operational envelope of LCO expands significantly for the two symmetric inlets than the operational envelope of LCO for single-inlet. It demonstrates that, the performance of the two symmetric inlets better than the performance of single-inlet for conditions approaching the operational envelope for LCO.
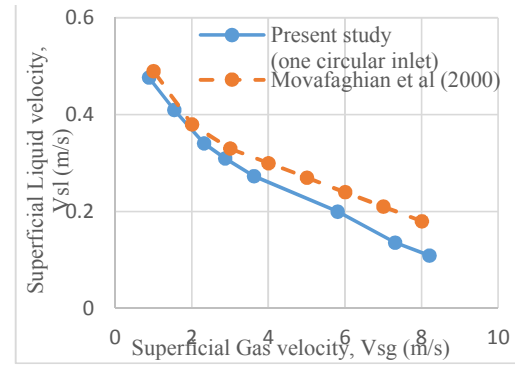
***Figure 11**. Comparison of the operational envelope for liquid carry-over (LCO) threshold*

In addition, to increase the reliability of research data, the comparison between the present data and the data reported by Movafaghian *et al* (2000) is presented in Figure 6. Note that the present data are for a 72 mm ID GLCC while the data of Movafaghian *et al* (2000) were obtained for a 76.2 mm ID GLCC. Then, this pipe area is gradually reduced by placing a plate within the inlet pipe to reduce the inlet area to about 25% of the area of the cylinder (crescent nozzle). The results show that the operational envelope of Movafaghian *et al* (2000) data expands lightly compared to the other. This is consistent with the research results of Shoham and Kouba (1998) that the concentric-circular nozzle configuration had the poorest performance, while the crescent nozzle performed closest to the rectangular slot with the same cross-sectional area.
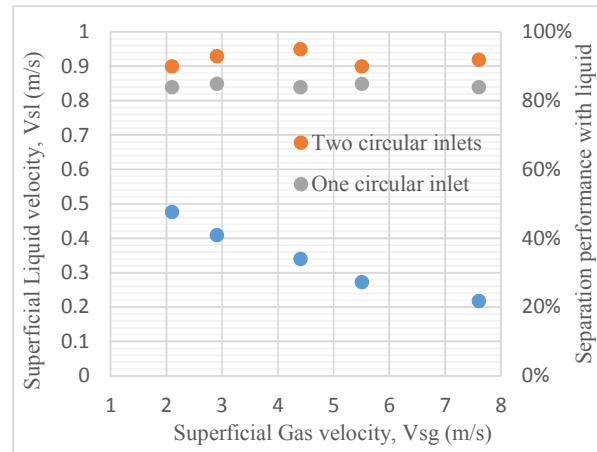
***Figure 12**. Separation performance with liquid*

A series of experiments were conducted to compare the performance of GLCC, the top part of the vortex, the crown, was maintained about 100 mm below the inlet nozzle. Test results show that the effect of structure and number of inlets has a clear impact on the performance of the separator. When using the two symmetric inlets type, the separation efficiency of liquid is higher than the separation efficiency of liquid for the one-inlet type (Figure 12).

4. CONCLUSIONS AND RECOMMENDATIONS

For the GLCC design, besides cylindrical cyclone diameter, the inlet nozzle geometry is probably the most important parameter because it controls directly the swirl intensity in the flow [14, 16]. In this research, the effect of two different nozzles design of inlet on the hydrodynamics and the performances of a gas-liquid cylindrical cyclone (GLCC) working in a full gas-water separator configuration was investigated by experiments. The measure has been used as a potential tool to ameliorate the influence of the different geometrical configurations of the inlet on complex flow patterns of the GLCC separators. The following conclusions can be extracted from this study:

Comparison of the operational envelopes for liquid carry-over (LCO) reveals that the two symmetric inlet configuration is superior to the single-inlet.

The separation efficiency of the device will be higher when using two symmetric inlets. However, the manufacturing is more difficult and takes up more space than the other. In addition, the two-phase flow balance for the two inlets should also be considered.

Finally, we suggest the application of two symmetric inlets type that is the same angle of inclination and the area of the nozzle with the unique inlet configuration to improve separation efficiency in GLCC. Such inlet structure leads to lower swirl intensity decay than one inlet configuration. Besides, it also creates a more axis symmetric flow at the center line, which would improve the uplift of air bubbles in the performance of GLCC.

Acknowledgements

References

[1] Kouba, G. E. A., and O. Shoham. 1996, "Review of gas-liquid cylindrical cyclone technology," International Conference of Production Separation Systems, Aberdeen, UK.

[2] Shoham, O., Kouba, G.E, "State of the art of gas/liquid cylindrical-cyclonecompact-separator technology," *SPE*, Vol 2-5, pp. 462-471, 1998.

[3] Arpandi, I. *et al,* "Hydrodynamics of Two-Phase Flow in Gas/Liquid Cylindrical-Cyclone Separators," *SPE Journal* (December 1996) 427.

[4] Gomez, L. E., R. S. Mohan, O. Shoham, J. D. Marrelli, and G. E. Kouba. 1999, "State-of-the-art simulator for field applications of gas-liquid cylindrical cyclone separators," *SPE Annual Technical Conference and Exhibition,* Houston, Texas

[5] Erdal, F., and S. Shirazi. 2001, "Local velocity measurements and computational fluid dynamics (CFD) simulations of swirling flow in a gas–liquid cylindrical cyclone separator," *Engineering Technology Conference on Energy*, Texas, 15:23–30.

[6] Mohan, R. 2013. Internal report. TUSTP.

[7] Hreiz, R., Gentric, C., Midoux, N., 2011, "Numerical investigation of swirling flow in cylindrical cyclones. Chem. Eng. Res. Des. 89, 2521–2539.

[8] Lê Văn Sỹ. 2015, "Nghiên cứu động lực học dòng chảy trong bộ tách lọc dầu/khí glcc," Tuyển tập công trình hội nghị khoa học cơ học thủy khí toàn quốc năm 2015.

[9] Le Van Sy, 2016, "Influence of inlet angle on flow pattern and performance of gas-liquid cylindrical cyclone separator," *Particulate Science And Technology* http://dx.doi.org/10.1080/02726351.2016.1180336.

[10] S. Kolla, S. Mohan and O. Shoham "Experimental investigation of liquid carry-over in GLCC separators for 3-phase flow" Paper No. IMECE2016-67457, pp. V007T09A006; 10 pages doi:10.1115/IMECE2016-67457.

[11] S. Movafaghian *et al* "The effects of geometry, fluid properties and pressure on the hydrodynamics of gas-liquid cylindrical cyclone separators" *International Journal of Multiphase Flow* 26 (2000) 999-1018.

[12] Erdal, F., Shirazi, S., 2002, "Effect of inlet configuration on flow behavior in a cylindrical cyclone separator," In: *ASME Eng. Technol. Conf. on Energy.*

[13] Hreiz, R. *et al*., 2014, "Hydrodynamics and velocity measurements in gas–liquid swirling flows in cylindrical cyclones," *Chemical engineering research and design*. http://dx.doi.org/10.1016/j.cherd.2014.02.029

[14] Hreiz, R. *et al*., 2014, "On the effect of the nozzle design on theperformances of gas–liquid cylindrical cyclone separators," *Int.J. Multiphase Flow* 58, pp15–26.

[15] Ho Minh Kha, Nguyen Ngoc Phuong and Nguyen Thanh Nam. "The effect of different geometrical configurations of the performances of Gas-Liquid Cylindrical Cyclone separators (GLCC)." System Science and Engineering (ICSSE), 2017 International Conference on DOI: 10.1109/ICSSE.2017.8030955, pp. 646-651.

[16] S. Kolla et al "Structural integrity analysis of gas-liquid cylindrical cyclone (GLCC) separator inlet". Journal of Energy Resources Technology - MAY 2018, Vol. 140. DOI: 10.1115/1.4038622.

[17] http://www.thermopedia.com/content/8/. Kataoka, Isao , Serizawa, Akimi DOI: 10.1615/AtoZ.b.bubble_flow.

[18] http://www.thermopedia.com/content/11/. Zeigarnik, Yuri Albertovich. Doi: 10.1615/AtoZ.a.annular_flow.

[19] http://www.thermopedia.com/content/264/. Jayanti, Sreenivas. Doi: 10.1615/AtoZ.c.churn_flow.

A Research on the Design a Bamboo Powder Drying Machine

Tran Van Hung[1], Le Khanh Dien[2], Vo Tuyen[3]
[1] Ho Chi Minh City University of Technology, VNU-HCM, Vietnam
[2] DCSELAB **-** Ho Chi Minh City University of Technology, VNU-HCM, Vietnam
[3] Ho Chi Minh City University of Food Industry (HUFI), Vietnam

ABSTRACT

Bamboo powder drying machine plays a very important role in the production process of bamboo plywood. The function of the machine is drying bamboo powder to get the technical required appropriate moisture before pressing it into the standard bamboo boards. This article presents a design of bamboo powder drying machine with simple structure, long life, medium productivity and price suitable for medium and small scale production of Vietnam market. The The first bamboo powder drying machine that was manufactured in DCSElab and its products are considered to respond the technical requirements of customers.

Keywords: Bamboo powder drying machine, moisture, medium productivity, technical requirements.

1. Introduction

Bamboo is a sustainable and environmental friendly material that has the potential to improve the global decline of natural resources. Bamboo is very popular in countryside of almost all Southeast countries, particularly in Vietnam. Its ability can replace some kinds of wood in decoration and household goods. Bamboo grow up rapidly and can be harvested within 3 to 5 years of planting, in the meanwhile the harvesting time of other hardwood trees must be from 8 to 10 years or longer. The inherent characteristics of bamboo is lighter than other wood materials and has a value in social and environmental benefits. Its advances in manufacturing technology have created high value products such as bamboo flooring and bamboo furniture that can substitute for wood flooring and wood furniture. According to the biology studies, the bamboo has the characteristics that can replace the natural wood, but the direction of development from the stage of cultivation to the stage of finished products has not been exploited thoroughly. The closure and restrictive exploitation of forests in many countries around the world are an opportunity, but also a big challenge for businesses in developing wood alternative products of bamboo, especially in Vietnam [1].

With abundant bamboo resources, the production of bamboo plywood will become a great potential for the bamboo plywood industry in Vietnam. However, the bamboo plywood industry in Vietnam is only developing and stopping in the production of pressed bamboo. Therefore, instead of using the technology of squeezing bamboo together, we can chop and grind the bamboo tree to powder that is dried and pressed into bamboo plywood by specialized machine similar to the production artificial wood particleboard (PB). Bamboo waste such as bamboo shoots thrown away after harvesters can be used to recycle and produce bamboo boards, both for environmental protection and for economic benefit [2].

In the production process of bamboo plywood powder, bamboo pulp dryer plays a very important role. The function of the studied machine is drying bamboo powder to get the technical appropriate dryness before the pressing prosess to the bamboo board. Therefore, the research design of the bamboo powder drying machine is necessary in the whole chain of production of bamboo plyboard [3]

2. Design structure for bamboo dryer machines

Functional analysis of bamboo powder dryer as shown in Figure 1 [4].
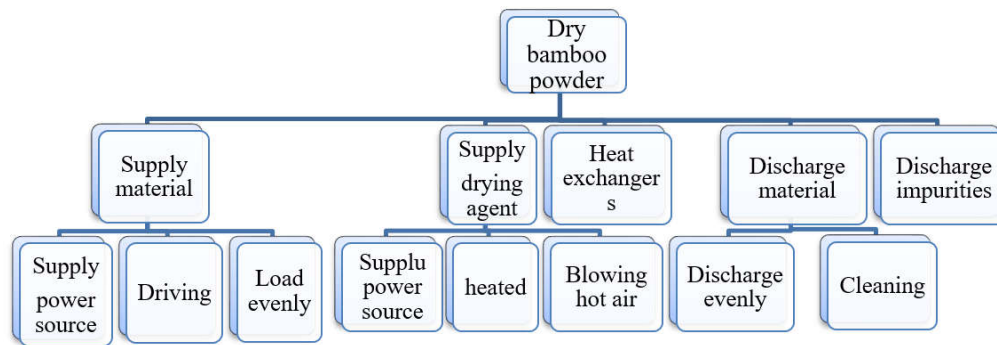
***Figure 1.** Diagram of functional analysis of bamboo powder drying machine [4]*

Arranging the functions of the bamboo powder drying machine, we have the following diagram (Figure 2). [4]:
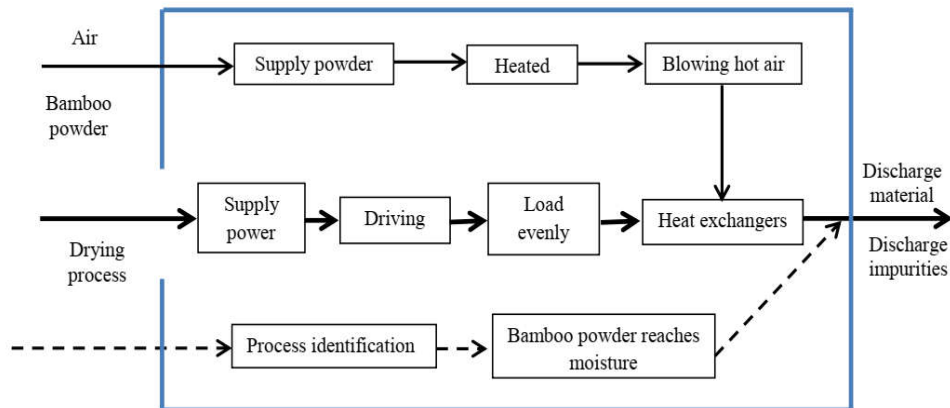
Figure 2. *Diagram of arranging sub function of bamboo powder drying machine*

Finally, the modular structure of the bamboo powder dryer is illustrated in Figure 3 [4]:
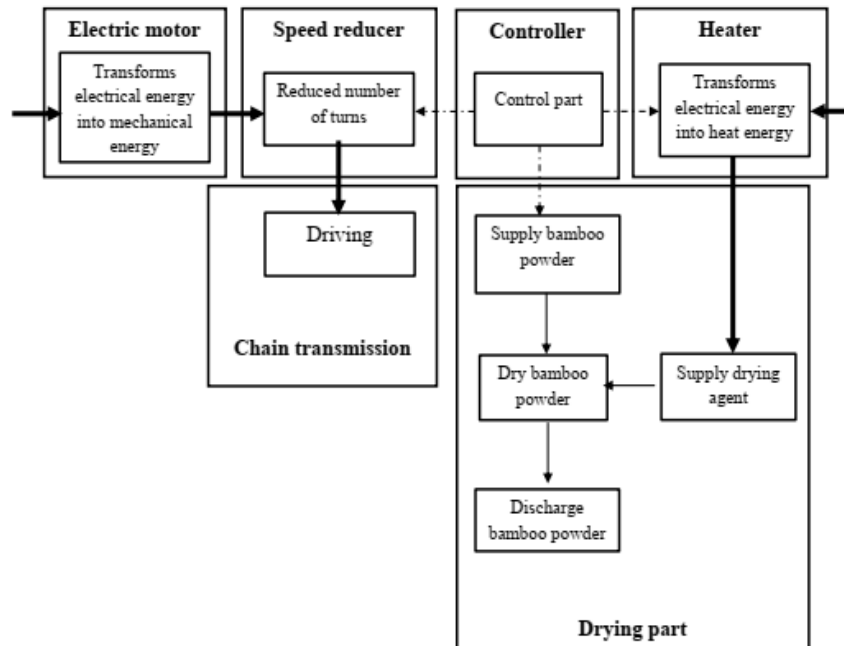
Figure 3. *Structure diagram of bamboo powder dryer machine*

Therefore, the bamboo pulp dryer consists of the following main components: 1) Electric motors; 2) Gearbox; 3) controller; 4) heating element; 5) Transmission chain; 6) Drying drum.

3. Calculating design for bamboo powder drying machine

a. Initial data and technical requirements

- Moisture of the initial pulp $\omega_1 = 26\% = 0.26$;
- Moisture of the finished pulp $\omega_2 = 4\% = 0.04$;
- Average remained moisture of pulp $\omega_{tb} = 0.5x$ ($\omega_1 + \omega_2$) = 0.15 = 15 %;
- Initial temperature of pulp $t_{v1} = 30^0C$;
- Output temperature of pulp $t_{v2} = 40^0C$;
- Medium size of bamboo powder d = 1mm;
- Specific weight of material $\rho_v = 300$ kg/m^3;
- Temperature of drying agent: input $t_1 = 150\ ^0C$; output $t_2 = 40\ ^0C$.
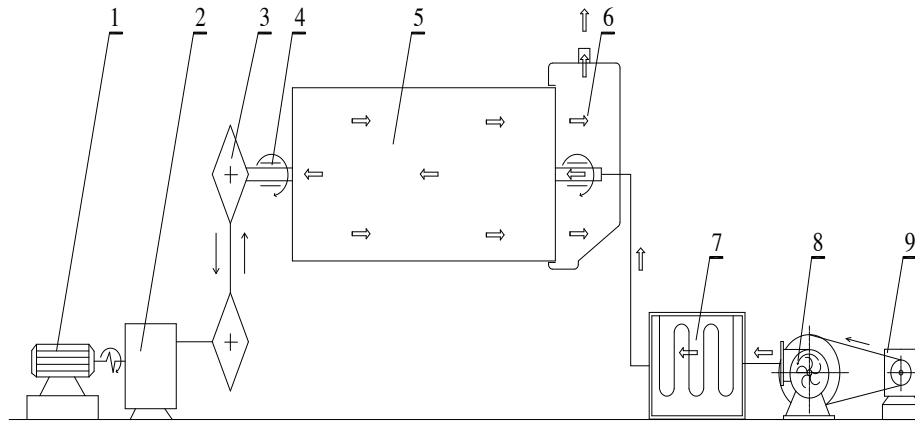
Figure 4. *Kinematic diagram of bamboo powder drying machine*

b. Determining the size of the drying drum

Drying time
$$\tau = \frac{120\beta\rho(\omega_1 - \omega_2)}{A(200 - (\omega_1 + \omega_2))} \text{ (min)} \quad [5]:$$

Herein: β : Filling coefficient; ρ: Average foam density of material (kg/m³); ω_1, ω_2 : Input and output moisture of material (%); A: Evaporation intensity (kg/m³.h).
A: The productivity of dryer: 200 kg/h. We divided into 2 batches, each batch of 100 kg dried in 30 minutes. From the above formula, the filling coefficient of the bamboo powder in the drum with drying time of 30 minutes:

$$\beta = \frac{\tau A(200 - (\omega_1 + \omega_2))}{120\rho(\omega_1 - \omega_2)} = \frac{30.40.(200 - (26 + 4))}{120.250.(26 - 4)} = 0,31$$

Volume of the drying bamboo powder:

$$V_{vls} = \frac{G}{d} = \frac{100}{300} = 0,333 m^3$$

Herein: G: weight of bamboo powder; d: Specific weight of bamboo powder;
Volume of drying drum: $V_{ts} = \frac{V_{vls}}{\beta} = \frac{0,333}{0,31} = 1.07 \text{ m}^3$
With filling coefficient β= 0.31, select L/D=2.5÷7, therefore with the diameter of drum is: D = 0.8m, the length of drum is: L= 2 (m)
Determine the thickness of the drum body: selected drum material is SS330 steel with bending stress $[\sigma]$ = 140 N/mm²; calculated pressure in the lower part of the body drum [5]:
p = p_m + gρH
p=1+9.8x300x0.25x10⁻⁶= 1.003 MN/m²=1 .003 N/mm²
Herein: p_m is the atmospheric pressure 1Mn/m²; g: Gravity acceleration; H: the height of the material in the drum ≈ 0.25m; the low thickness of the drum body is calculated according to the formula [5] (φ: reliability of welded structures 0.95):
S= $\frac{D.p}{2[\sigma]\varphi}$ = $\frac{0,8.10^3.1,001}{2.140.0,95}$ ≈ 3 mm; Choose a body thickness of 3 mm

c. Determine the temperature in and out of the dryer

Select the rotating speed of drying drum 10 RPM so the stay time is: $\tau = \frac{60}{10} = 1,5 \ s$
The required temperature for heating the pulp to attain the technical required dryness [3]:
$$t_h = 2,218 - 3,343 \ln(\tau) + \frac{23,5}{0,37 + 0,63\omega_{tb}}$$
With $\tau = 1,5(s)$, $\omega_{tb} = 0,015 => t_h = 62.79^0C$
Maximum temperature of the drying agent: t_2= t_h + (5÷10) = 62.79 + 5= 67.79^{0}C
Mean temperature difference is taken from the empirical diagram [6] the mean difference in temperature is determined $\Delta_t \approx 60^0$C. The temperature on the drying agent is determined by the formula:

$$\Delta t = \frac{(t_1 - t_{v1}) - (t_2 - t_{v2})}{\ln \frac{(t_1 - t_{v1})}{(t_2 - t_{v2})}} \quad \rightarrow t_1 = 173,74^0C$$

d. Calculating the heat of the drying process

The specific heat of vaporization of the drying agent in state d_1 [6]:
$C_{dx}(d_1)$ = 1.004+1.842d_1 = 1.04 kJ/kg.k
Moisture regain of drying agent:
$$d_2 = 0,0193 + \frac{1,04(150 - 45)}{2574 - (-50)} = 0,061 \ kg / kga$$

$$d_2 = d_1 + \frac{C_{dx}(d_1)(t_1 - t_2)}{i_2 - \Delta}$$

Enthalpy of drying agent after drying process:
Moisture of the drying agent out of the drying drum:

$$I_2 = 1,004 t_2 + d_2(2500 + 1,842 t_2)$$

$$I_2 = 156,560 \ kJ / kg$$

$$\varphi_2 = \frac{d_2}{p_{bh2}(0,621 + d_2)}$$

$$\varphi_2 = \frac{0,0610}{0,0949(0,621 + 0,0610)} = 86 \ \%$$

Actual flow of drying agent L:

$$L = \frac{1}{d_2 - d_1}$$

$$L = \frac{1}{0,0610 - 0,0193} = 23,98 \; kg / kgam$$

$$L = l.W$$

$$L = 1100 \; kg / h$$

Volume flow V_1 (m³/h):

$$V = L.v = L.\frac{1}{\rho_{tb}} \; (m^3 / h)$$

Herein: ρ_{tb} is average specific weight of dry air:

$$\rho_{tb} = 0,5.(\rho_1 + \rho_2)$$
$$\rightarrow \rho_{tb} = 1,05 \; kg / m^3$$

$$V = 1047 \; m^3 / h$$

$$v = 0,919 \; m / s$$

The average speed of the drying agent in the dryer: $\quad Q_c = L(I_1 - I_0)$

Heat consumption for drying process: $\quad Q_c = 1100.(204,18 - 77,35)$

$$Q_c = 139513 (kJ/ h) \approx 38,75 \; kW$$

The amount of heat required per kg of moisture air: $\quad q_c = \frac{Q_c}{W}$

The demanded heat for evaporating 1 kg of moisture: $\quad q_c = \frac{98820}{22,92.2} = 3000 \; kJ / kgam$

$$Q_i = q_i.W = 115866 \; (kJ/h) \approx 32,18 \; kW$$

$$q_i = r + C_a.(t_2 - t_{v1})$$

$$q_i = 2500 + 1,842(45 - 30) = 2527,63 \; kJ / kgam$$

C_a is specific heat of moisture is equivalent to steam C_a= 1.842 kJ.kg.k

Heat due to moisture content:

$$WC_a.t_{v1} = 22,92.4,18.30 = 2874 \; (kJ/h) \approx 0,8 \; kW$$

Heat losses caused by the drying agent Q_{tn}:

$$Q_{tn} = q_{tn}.W = 37852 \; (kJ/h) \approx 10,5 \; kW$$

$$q_{tn} = l.C_{dx}(d_1).(t_2 - t_0)$$

$$q_{tn} = 52,63.1,046(45 - 30) = 825,76 \; kJ / kgam$$

The amount of heat provided for the actual drying process:

$$Q_t = Q_i + Q_{mt} + Q_v + W.C_a.t_{v1} + Q_{tn}$$

$$Q_t = 32,18 + 0,28 + 0,33 + 0,8 + 10,5$$

$$Q_t = 44,09 \; kW$$

Drying performance: $\quad \eta_1 = \frac{q_i}{q_t} = 72,98 \; \%$

e. Select the drive system

Required power for rotating the drying drum:

$$N = 0,13.10^{-2}.D.L.\alpha.n.\rho \; (kW)$$

Herein: D: Rotating drum diameter (m); L: Rotating drum length (m); α: wing shape coefficient; With filling coefficient $\beta = 0.31$, selected $\alpha = 0.071$; n: rotation of drum, n = 10RPM; ρ: specific weight of material (kg/m³).

$$\rightarrow N = 0,13.10^{-2}.0,8.2.0,071.10.300 = 0,44 \; kW$$

Hence the power of motor: $N_{dc} = \frac{N}{\eta} = \frac{0,44}{0,83} = 0,53$ kW

Herein: N: the needed capacity to rotate the drum; η- the overall performance of the system.

$\eta = \eta_{hgt}\eta_{ol}\eta_x\eta_{kn} = 0,92.0,99.0,93.0,99 = 0.83$

Specification for Roller Chain Design: power of transmission: $P_1 = 0,44$ kW; Transmission ratio: $u_x = 2$; revolution of drive sprocket: $n_1 = 10$ RPM; torque: $T_x = 9,55.10^6 .\frac{P_x}{n_x} = 9,55.10^6 .\frac{0,44}{10} = 420200$ Nmm. Choose the type of roller chain with the parameters as follows:

Parameter	u_x	P1 (kW)	z_1	z_2	X	a (mm)	d_1 (mm)	d_{a1} (mm)	d_2 (mm)	d_{a2} (mm)
Value	2	0.33	25	50	98	760	202	220	404	422

f. Selection of fans and wings of drying drum

* Fan selection:

Pressure through the layer of drying material:

$$\Delta p_{ts} = \frac{a.L.v^2.\rho_k.C}{2g.d}$$

a: hydraulic coefficient.

$$\Delta p_{ts} = \frac{14,41.1,5.1,5^2.0,996.0,06}{2.9,81.3.10^{-3}} = 49,38 \; mmH_2O$$

Herein: L– length of the drum (m); drying agent velocity v = 1.5 m/s;

ρ_k - Specific gravity of the drying agent based on average temperature (kg/m³);

g: Gravity acceleration (m/s²);

d: the diameter of the drying material;

Resistance of radiator $\Delta p_{cl} = 14,67 \; mmH_2O$, local and additional losses are about 5%. So the total static pressure:

$$\Delta p_d = \frac{20^2.0,996}{2.9,81} = 20,3 \; mmH_2O$$

$$\Delta p_T = 1,05.(\Delta p_{ts} + \Delta p_{cl}) = 67,25 \; mmH_2O$$

Pressure loss at the inlet of the fan ($v = 20$ (m/s)) [6]:

$$H = \Delta p_T + \Delta p_d = 87,55 \; mmH_2O$$

Necessary pressure to overcome the fan:
Fan power:

$$N = k.\frac{V.\rho_o.\Delta p}{3600.102.\rho.\eta_q}$$

Herein: k– reserve factor, k = (1.1 ÷ 1.2); η_q = (0.4÷ 0.6) – performance of the fan; ρ_0 – specific gravity of air at standard conditions ρ_0 = 1.293 kg/m³;

$$N = 1,2.\frac{3731,17.1,293.87,55}{3600.102.0,996^2.0,6} = 2,3 \; kW$$

Motor power running fans: $N_{dc} = \frac{N}{\eta}\,\varphi = \frac{2,3}{0,95}.1,3 = 3,15$ kW

⇨ Select fan number U3-57 N⁰4 with parameters: A = 5500, n = 1400 RPM
* Select the size of the wing in the drum:
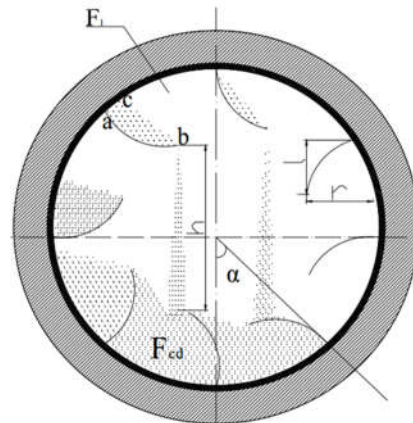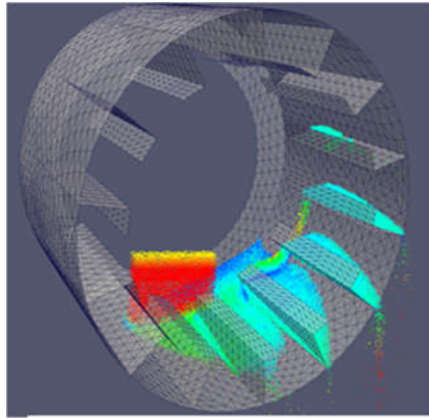
Figure 5. *Wing of rotary barrel of bamboo powder dryer*

Selected parameters of wing: Filling coefficient: 0.31; wing fold coefficient: 140. Hence: $\frac{h_{tb}}{D_T} = 0,576$ and $\frac{F_c}{D_T 2} = 0,122$.

Herein : h_{tb}- average height of the material; D_T- diameter of drying drum; F_c- surface of wing material:
$F_c = 0.122 \times 0.8^2 = 0.032$ m²
$h_{tb} = 0.576. 0.8 = 0.46$ m
 The selected geometrical parameters of the wings: a = 100mm; b = 50mm;
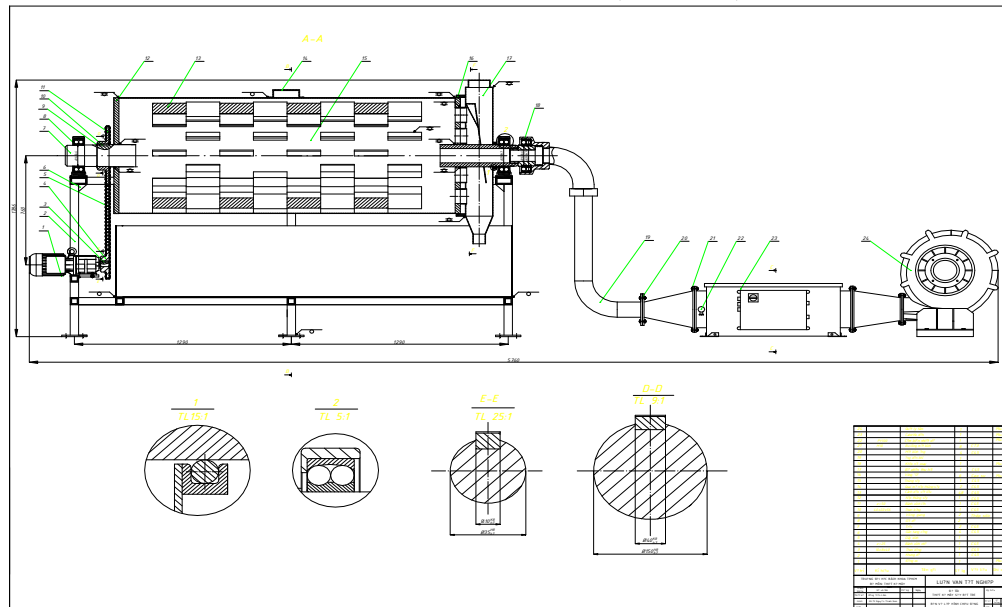
Figure 6. *Overall drawing of bamboo powder dryer*

➔ $c = \frac{F_c}{a+b} = \frac{0,032}{0,1+0,05} = 0,2$ m; d = 5 mm; $\alpha = 45^0$

The height of the material in the bin: h= R (1-cosα) = 0.4x(1-cos45⁰)= 0.117m; Number of wings on one side:

8 wings. The designed bamboo powder-drying machine shown in Figure 6.

4. Conclusion

Performing an effective design of a technical required bamboo powder dryer is essential in saving effort and finance for manufacturing processes that provide more cheap domestic materials for decoration and construction in Vietnam.

Acknowledgement

References

[1] D. M. Nazmul Alam, Khandkar- Siddikur Rahman, Sourav Bagchi Ratu1, Arifa Sharmin, Tania Islam, Md. Abu Wabaeid Hasan and Md. Nazrul Islam, Properties of Particleboard Manufactured from Commonly Used Bamboo (Bambusa vulgaris) Wastes in Bangladesh. SCIENCEDOMAIN international, 75:203-211, 2015.

[2] Viện khoa học lâm nghiệp Việt Nam, Nghiên cứu một số yếu tố công nghệ sản xuất ván dăm chất lượng cao làm nguyên liệu cho sản xuất đồ mộc trong điều kiện miền bắc Việt Nam.

[3] Trần Văn Hưng, Nguyễn Tấn Hùng, *Nghiên cứu, thiết kế và chế tạo thiết bị phục vụ sản xuất ván ép bột tre*, Báo cáo đề tài nghiên cứu khoa học GEN 2016.48.02 02.06, 2016.

[4] Nguyễn Thanh Nam, *Phương pháp thiết kế phát triển sản phẩm*, NXB ĐHQGTP Hồ Chí Minh, 2014.

[5] Ts. Trần Xoa, PGS,Ts. Trần Trọng Khuông, *"Sổ tay quá trình và công nghệ hóa chất tập 2"*, Nhà xuất bản Khoa học và Kỹ thuật, 2006.

[6] PGS.TSKH Trần Văn Phú, *"Tính toán và thiết kế hệ thống sấy"*, Nhà xuất bản Giáo dục, 2002.

PART I, SECTION IV

Other Topics Related to Machining, Materials and Mechanical Technology
(Mechanics of Solid; Analysis and Simulation; New Machine Tools and Tooling Technology;
Dynamics and Control…)

Combined Cyclic-Static Bending Effect on the Encapsulation Properties of a Barrier Thin Film for Flexible Organic Optoelectronic Devices

Dinh-Phuc Tran[1], Chih-Kuang Lin[1,*], and Bao-Dong To[2]
[1] Department of Mechanical Engineering, National Central University
Jhong-Li District, Tao-Yuan City 32001, Taiwan
[2] Department of Physics, National Chung Cheng University,
Min-Hsiung, Chia-Yi 62102, Taiwan

ABSTRACT

Water vapor transmission rate (WVTR) of a barrier film is evaluated after combined cyclic-static bending. Results show that cyclic bending combined with a static bending deteriorates the barrier performance to a greater extent, compared with pure cyclic bending. For a severe bending radius of 2.5 mm, WVTR is increased at the beginning of combined cyclic-static bending. There is a little effect of static bending on WVTR for a short hold time. However, for a longer period of static hold-time, the contribution of static bending to deterioration in the performance of barrier thin film is visible.

1. Introduction

Flexible optoelectronic devices such as organic light emitting diode (OLED), organic photovoltaic (OPV), organic field effect transistor (OFET), organic photo detector (OPD), flexible liquid crystal display (LCD), and touch panel are currently interesting candidates for the next generation of optoelectronics due to its low-cost, printable, massive roll-to-roll, and flexible abilities [1-3]. These optoelectronic devices require barrier films to protect their vulnerably contained layers from surrounding moisture during long-term storage and/or routine service. However, one concern of barrier films is that it may be damaged and does not maintain its encapsulation properties when subjected to mechanical bending. Under bending stress, cracks may be initiated and propagate from initial defects in barrier thin film. Surrounding moisture could go through these cracks and enhance chemical reactions with semiconductor stacks. It causes an increase in moisture diffusion rate and consequently leads to faster failure of the encapsulated optoelectronic layers.

Currently, various testing methods are performed to characterize the damage accumulation and its effects on encapsulation performance of barrier thin film under various types of loading [4-14]. However, there is still lack of studies focused on effect of combined cyclic-static loading on encapsulation properties of barrier thin film. This work is a continuation of previous investigations [10,11] in which pure cyclic and static deformation effects on encapsulation performance of a given barrier thin film were separately studied.

2. Experimental

In order to investigate the effect of combined cyclic-static bending on the barrier's performance, a fixture was fabricated and integrated with a driving module to generate a combined cyclic-static bending, as shown in Fig. 9. The driving module consists of a microcontroller (Arduino Mega 2560, Arduino LLC, Peidmont)

integrated with a stepping motor. In each combined cyclic-static test, after a cycle of pure cyclic bending is applied, the barrier sample is subjected to a static bending for a certain period of time (1, 10, and 100 h) to make a loading block of combined cyclic-static bending, as shown in Fig. 10. This loading bock is repeated for 10 times for each bending radius. Two bending radii of 5 and 2.5 mm are selected for such test.
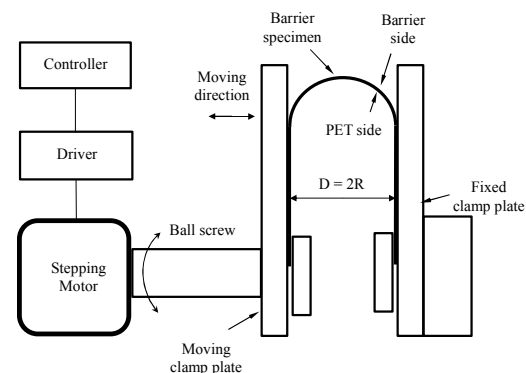
Fig. 9 Schematic of combined cyclic-static bending test for barrier thin film.
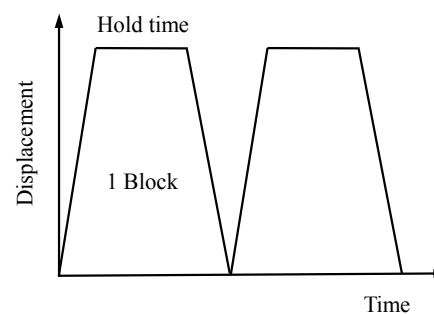
Fig. 10 Schematic of combined static-cyclic bending block.

The water vapor transmission rate (WVTR) of bent barrier specimens is then determined using a calcium (Ca) corrosion test. Ca corrosion sensors are fabricated in a glove box system by depositing an aluminum (Al) film as electrodes and a Ca layer onto a glass substrate, as shown in Fig. 11. Conductance change of Ca sensor in a controlled humidify environment (40 ℃, 90% RH) is then recorded and steady-state slope of conductance change is used to determine WVTR. Details of Ca corrosion test and calculation of WVTR can be found in our previous studies [10,11]. In this study, three tests are repeated for each bending condition to assure reproducibility.
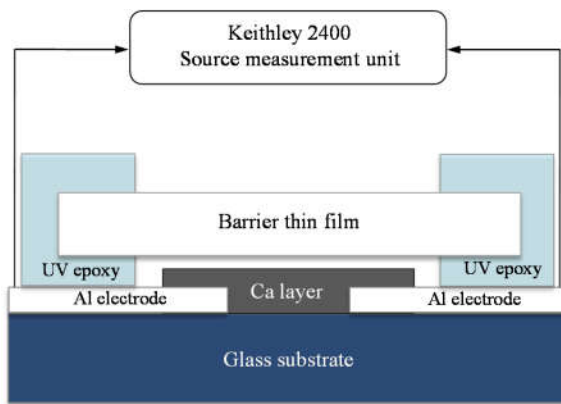
Fig. 11 Schematic of electrical resistance measurement of Ca sensor.

3. Results and Discussion

In the combined cyclic-static bending test, after a pure cyclic bending cycle, the barrier specimen was statically bent for a certain period of hold time to generate a block of combined cyclic-static bending. This loading bock is repeated for 10 times for each bending radius. The effect of combined cyclic-static bending on WVTR of barrier thin film is shown in Fig. 12 and Table 1. Given a 5-mm bending radius, the highest WVTR values measured are of 2.57×10^{-3} and 3.72×10^{-3} g m^{-2} day^{-1} for 10 and 10^2 h of static holding, respectively (Fig. 12(a)). The lowest counterpart WVTR values are of 4.63×10^{-4} and 3.83×10^{-4} g m^{-2} day^{-1}, respectively. As shown in Fig. 12(a), at a bending radius of 5 mm, no obviously detrimental effect of static holding on the encapsulation performance is found. The cyclic bending takes a primary role in damaging the barrier performance (Fig. 12(a)). As shown in Fig. 12(b), for a 2.5-mm bending radius, the highest WVTR is of 6.65×10^{-3}, 7.74×10^{-3}, and 4.39×10^{-2} g m^{-2} day^{-1} for 1, 10, and 10^2 h of static holding, respectively. The lowest counterpart WVTR values are of 1.55×10^{-4}, 1.43×10^{-3}, and 8.22×10^{-3} g m^{-2} day^{-1}, respectively. Given a bending radius of 2.5 mm, the influence of static bending on WVTR is unclear for a short holding time in a combined cyclic-static bending block, as cyclic bending takes a dominant role (Fig. 12(b)). However, for a longer holding period of 100 h under static bending, WVTR of the barrier film under

combined cyclic-static bending is clearly increased, compared to that of pure cyclic bending. The contribution of a longer hold time of static bending to deterioration in the encapsulation performance of barrier thin film is obvious in this case. In addition, a cyclic bending combined with a static bending under a smaller bending radius apparently generates a larger amount of damage than that of a larger bending radius. It leads to an increase of WVTR of the given barrier thin film (Fig. 12). Static holding plays a more important role in the combined cyclic-static bending damage for a smaller bending radius of curvature.

(a)

(b)
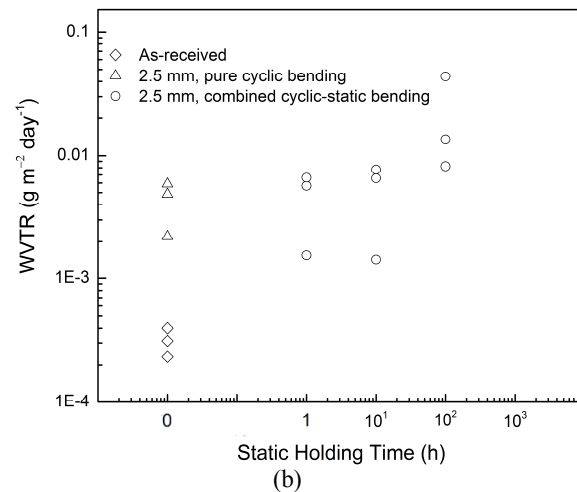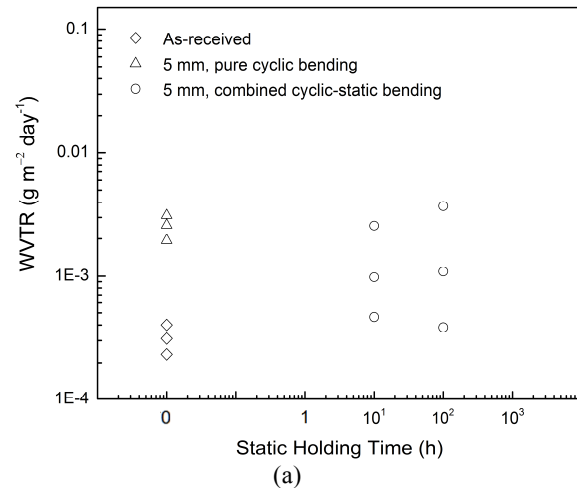
Fig. 12 Change of WVTR of barrier thin film under 10 repetitions of pure cyclic and combined cyclic-static bending.

Optical micrographs of barrier thin films before and after combined static-cyclic bending are shown in Fig. 13. As shown in Fig. 13, several cracks are found in the barrier thin film of bent samples. These straight cracks are perpendicular to the direction of loading and roughly parallel to each other. Cracks are formed and lead to an increase in WVTR of such barrier thin film. As shown in Fig. 13(b) and Fig. 13(c), crack density in

the barrier thin film is about 23 and 24 cracks mm^{-1}, respectively. As shown in Fig. 13(b) and Fig. 13(c), the amount of damage generated is comparable between the

barrier samples after 10 repetitions of pure cyclic bending and combined static-cyclic bending. It indicates that effect of static

Table 2 WVTR of barrier thin film under combined cyclic-static bending of various radii.

Bending radius	Hold time	WVTR (g m^{-2} day^{-1})		
		Minimum	Middle	Maximum
As-received	-	2.33×10^{-4}	3.12×10^{-4}	4.01×10^{-4}
2.5 mm	No-hold time	2.21×10^{-3}	4.86×10^{-3}	5.89×10^{-3}
	1	1.55×10^{-4}	5.68×10^{-3}	6.65×10^{-3}
	10	1.43×10^{-3}	6.56×10^{-3}	7.74×10^{-3}
	10^2	8.22×10^{-3}	1.35×10^{-2}	4.39×10^{-2}
5 mm	Non-hold time	1.94×10^{-3}	2.60×10^{-3}	3.12×10^{-3}
	10	4.63×10^{-4}	9.80×10^{-4}	2.57×10^{-3}
	10^2	3.83×10^{-4}	1.09×10^{-3}	3.72×10^{-3}

bending on the encapsulation performance under combined cyclic-static bending for a short period of holding time is not obvious. As shown in Fig. 13(c) and Fig. 13(d), crack density in the barrier thin film is about 24 and 34 cracks mm^{-1}, respectively. Given a bending radius of 2.5 mm, a longer holding period of 100 h generates a larger amount of damage resulting in an apparent increase in WVTR. These observations provide more evidence of contribution of static bending when the barrier thin film is subjected to a smaller bending radius for a longer holding period.

(b)

(a)
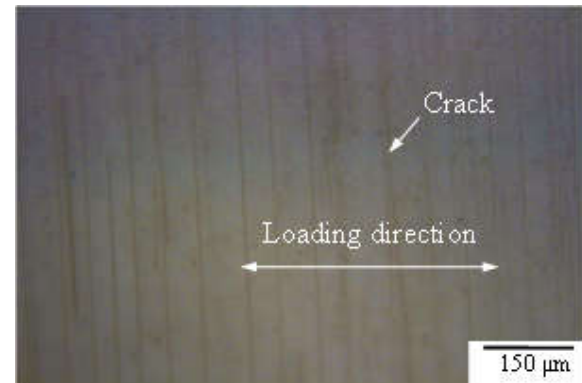
(c)
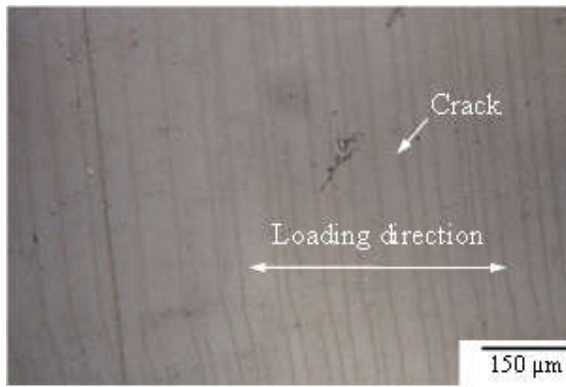
(d)

Fig. 13 Optical micrographs of barrier thin films: (a) as-received specimen; (b) after 10 cycles of bending at a 2.5-mm radius of curvature; (c) after 10 cycles of bending at a 2.5-mm radius combined with 10 h of static holding; (d) after 10 cycles of bending at a 2.5-mm radius combined with 100 h of static holding.

4. Concluding Remarks

Cyclic bending combined with a static bending deteriorates the encapsulation performance to a greater extent, compared with pure cyclic bending. It causes an increase in WVTR of the given barrier thin film. For a severe bending radius of 2.5 mm, WVTR of the barrier film is significantly increased at the very beginning of combined cyclic-static bending. Given a short holding period of static bending, there is very little effect of static bending on the encapsulation performance under combined cyclic-static bending. Cyclic bending plays a primary role in damaging the barrier film. However, for a longer period of 100 h of static holding, the contribution of static bending to deterioration in the encapsulation performance of barrier thin film is apparent for a smaller bending radius. Moreover, a cyclic bending combined with static holding under a smaller bending radius generates a larger amount of damage than that of a larger bending radius.

References

[1] S. Tekoglu, G. Hernandez-Sosa, E. Kluge, U. Lemmer, N. Mechau, *Org. Electron.,* 14 (2013) 3493-3499.
[2] J. Shi, M.B. Chan-Park, C.-M. Li, *Org. Electron.,* 10 (2009) 396-401.
[3] C. Koidis, S. Logothetidis, A. Ioakeimidis, A. Laskarakis, C. Kapnopoulos, *Org. Electron.,* 14 (2013) 1744-1748.
[4] J. Lewis, *Mater. Today*, 9 (2006) 38-45.
[5] Y.C. Han, E. Kim, W. Kim, H.-G. Im, B.-S. Bae, K.C. Choi, *Org. Electron.*, 14 (2013) 1435-1440.
[6] S. Majee, M.F. Cerqueira, D. Tondelier, J. Vanel, B. Geffroy, Y. Bonnassieux, P. Alpuim, J.E. Bourée, *Thin Solid Films*, 575 (2015) 72-75.
[7] N. Kim, W.J. Potscavage Jr, A. Sundaramoothi, C. Henderson, B. Kippelen, S. Graham, *Sol. Energ. Mat. Sol. Cells*, 101 (2012) 140-146.
[8] S.-W. Seo, E. Jung, H. Chae, S.J. Seo, H.K. Chung, S.M. Cho, *Thin Solid Films*, 550 (2014) 742-746.
[9] S. Majee, B. Geffroy, Y. Bonnassieux, J.-E. Bourée, *Surf. Coat. Technol.*, 254 (2014) 429-432.
[10] H.-I. Lu, D.-P. Tran, C.-K. Lin, B.-D. To, *Coatings*, 8 (2018) 127-1-14.
[11] D.-P. Tran, C.-K. Lin, B.-D. To, *Thin Solid Films*, 650 (2018) 20-31.
[12] N. Kim, S. Graham, *Thin Solid Films*, 547 (2013) 57-62.
[13] A.R. Cho, E.H. Kim, S.Y. Park, L.S. Park, *Synth. Met.*, 193 (2014) 77-80.
[14] S.-W. Seo, E. Jung, S. Joon Seo, H. Chae, H. Kyoon Chung, S. Min Cho, *J. Appl. Phys.*, 114 (2013) 143505-1-8.

Study on the Design of Bamboo Grinding Machine

Vo Tuyen[1], Le Khanh Dien[2], Tran Trong Hy[2], Nguyen Tan Hung[2],
[1] Ho Chi Minh City University of Food Industry (HUFI), Vietnam
[2] DCSELAB - **Ho Chi Minh City University of Technology**, VNU-HCM, Vietnam

ABSTRACT

Bamboo is one of the popular flora in Southeast of Asia, it is also a traditional plant that grow abundantly in Vietnamese villages from north to south. In the developing of domestic materials for construction and decoration, bamboo plywood plays an important role in the replacing time by time the imported plywood. The first step in the plywood production chain is the grinding bamboo to powder ready for the next following processes to finished bamboo plywood. The aim of this article is a representation of a design of bamboo grinding machine that is sustainable, responds to technical requirements and protect of environment. The manufactured bamboo machine by CAD-CAM workshop of DCSElab that was evaluated with satisfaction by Phu An bamboo village corporation is a realistic proof of the design.

Keywords: Bamboo polywood, Bamboo powder, Grinding machine

1. Introduction

Bamboo is a sustainable and environmentally friendly material that has the potential to improve the global decline of natural resources, particularly its ability of replacing the natural wood. From planting to harvesting there are only 3 to 5 years in comparison of the hard tree, it must be from 10 to 20 years to mature for harvesting. The inherent characteristics of bamboo in daily life, decoration and construction confirm its valuable position in consumer market such as: leaves for covering some kinds of traditional cakes, stem for column of thatched cottage, bamboo mat, baboo plywood... Abundance and cheap price are the bamboo specificity that it can substitute for wood in flooring furniture with social and environmental benefits. Currently, according to the biology studies, the bamboo has the characteristics that can replace the natural wood, but the direction of development from the stage of cultivation to the stage of finished products has not been exploited and applied logically in our country. The closure and restrictive exploitation of forests in many countries around the world are an opportunity for the great demand of bamboo, but it is also a big challenge for businesses in developing of quality bamboo in Vietnam[1].

With abundant bamboo resources, the production of bamboo plywood becomes a great potential for the domestic bamboo plywood industry. The first process after bamboo harvesting is grinding bamboo to pulp or powder. All kind of bamboo waste such as bamboo shoots, bad stems, roots can be raw material for the process [2].

In the production process of bamboo plywood powder, the bamboo grinding machine plays a very important role in the production of bamboo powder, the basic material for plywood. The schema of grinding process is illustrated tin figure 1 [3].
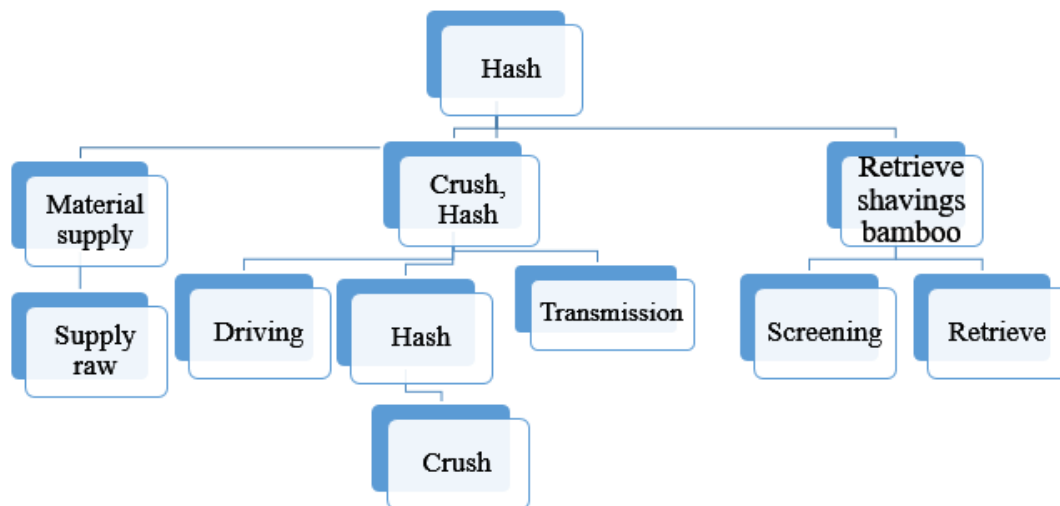
Figure 1. *Schema of production of bamboo powder in functional modules*

2. Structural Design for Bamboo grinding machine [4]

Functional analysis of bamboo grinding machines is illustrated in diagram in figure 2:
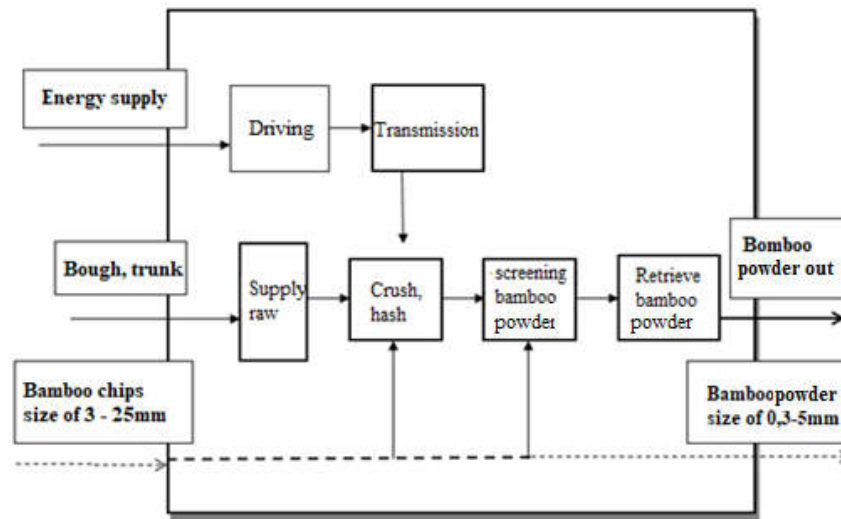
Figure 2. *Functional map of the bamboo crusher*

Figure 3 represents the structure of the designed bamboo-grinding machine:
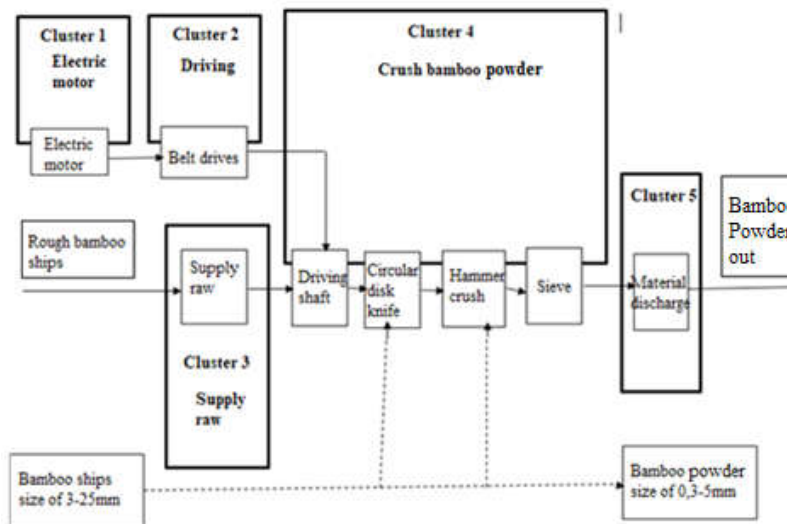
Figure 3. *Structural diagram of bamboo crush machine*

Generally, a bamboo grinding machines consists of the following main components:
- Electric motors
- Mechanical transmission
- Feeder (feed hopper)
- Grinding spindle of the machine (disk of cutters, hammers…)
- Discharge unit

3. Computing strength material of grinding bamboo machine

a. Initial data
- Productivity 200 Kg/h;
- Main raw materials: bamboo shoots, stem, roots;
- Size of raw materials: 20 - 100mm.
- Size of bamboo powder after grinding process: 0.5 - 3mm;
- Specific density of bamboo: 800 Kg/m^3;
- Average powder moisture 12-14%.

The general structure of the machine is as shown in Figure 4.
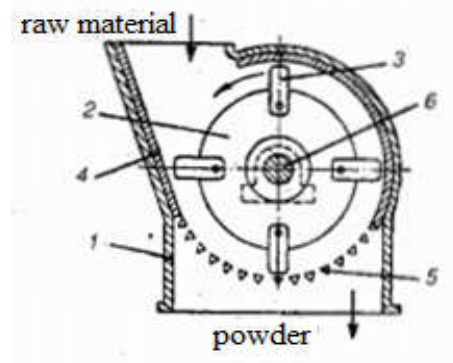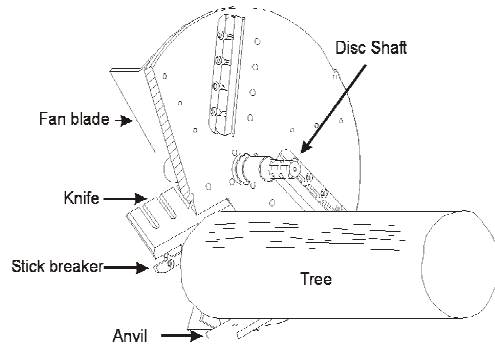
Figure 4. *Structure of the designed bamboo-grinding machine*
1- Machine cover;2 Cutter plate;3-Cutters;4-Protection plate;5-filter;6-Cutter plate spindle

b. Calculation of the bamboo grinding machine

Cutting parts:

According to the principle of slice pieces [5], the 4 cutters are freely mounted on the disk via a hinge that allows the cutter a free rotation of an angle $\pm 60^o$ around its radial position that formed in advance by the centrifuge force in operation.

Cutting angle α of the cutter blade is selected about 12 – 15° because of cutting of tough and medium wood materials.

Cutting speed is selected in a range of 30-60 m/s)

The power of cutting is determined by the formula [5]:
$N_1 = k.b.h.v /10^2$.

Herein: b: Cutting thickness is about 0,5mm;

h: thickness of the raw bamboo material is 25÷50mm;

k: specific deflection coefficient is 1;

v- velocity of the hash, v = 30m/s.

We have : $N_1 = k.b.h.v/10^2 = 1.0,5.50.30/10^2 = 7,5$ kW

The revolution on the spindle is calculated according to

the formula: $\omega = \dfrac{v_b}{R}$;

Herein: v_b = 30m/s

Radius of cutter point on plate R = 100mm = 0,1m

The revolution of the tool shaft is:

$n = 30. \omega / \pi = 30.v_b / (\pi.R) = 30.30 / (\pi.0,1) = 2864$ RPM.

Selected transmission ratio for the drive system is 1, we have the number of motor rotation n = 2864 vg / ph.

Grinding parts:

Because of the product size of 0.5-3mm with the impact velocity of the machine is about 25-60m/s, combined with the condition of cutting speed, the cutting speed...The selected weight of each cutter is about 30-50N.

Selective shape of cutter is triangle with 3-4 rows of cutters.

The power of the grinding machine is determined by the formula:

$N_2 = 0,15.D^2.L.n.i = 0,15.0,2^2.0,1.2864.3 = 5,2kW$

Herein: D- rotor diameter, D = 60.v / $(\pi.n)$ = 60.30 / $(\pi.2864)$ = 0,2m; L rotor length,

L = 0,1m, rotor rotation number = 2864 RPM, i: number of cutters rows, i = 3.

Motor and transmission selection:

The belt feeder is used to transfer power from the engine to the grinder. With the transmission rate is 1, total performance coefficient is $\eta = \eta_1.\eta_2 = 0,99.0,96 = 0,95$; $\eta_1.\eta_2$ - efficiency of the drive and belt transmission → $P_{ct} = P_1 + P_2 = 7,5 + 5,2 = 12,7kW$;

The **3K200M8** electric motor is selected with motor power of 15kW and revolutions of 2800 rpm.

Figure 5. *Experimental bamboo grinding machine*

4. Conclusion

The research performed an efficient design process to produce bamboo-grinding machine that meet the technical requirements. Experimental results show that complete grinding bamboo machine responds all the technical requirements of the production system of bamboo plywood powder.

5. Acknowledgement

References

[1] D. M. Nazmul Alam, Khandkar- Siddikur Rahman, Sourav Bagchi Ratu1,Arifa Sharmin, Tania Islam, Md. Abu Wabaeid Hasan and Md. Nazrul Islam, Properties of Particleboard Manufactured from Commonly Used Bamboo (Bambusa vulgaris) Wastes in Bangladesh. SCIENCEDOMAIN international, 75:203-211, 2015.

[2] Viện khoa học lâm nghiệp Việt Nam, Nghiên cứu một số yếu tố công nghệ sản xuất ván dăm chất lượng cao làm nguyên liệu cho sản xuất đồ mộc trong điều kiện miền bắc Việt Nam.

[3] Trần Văn Hưng, Nguyễn Tấn Hùng, *Nghiên cứu, thiết kế và chế tạo thiết bị phục vụ sản xuất ván ép bột tre*, Báo cáo đề tài nghiên cứu khoa học GEN 2016.48.02 02.06, 2016.

[4] Nguyễn Thanh Nam, *Phương pháp thiết kế phát triển sản phẩm*, NXB ĐHQGTP Hồ Chí Minh, 2014.

[5] TS. Nguyễn Như Nam – TS. Trần Thị Thanh (2000), *Máy gia công cơ học nông sản – thực phẩm*, Nhà xuất bản giáo duc.

Research on Application of 3D Parametric Software for Design and Shaping of Bus Frame Structure

Thanh Cong Nguyen

Faculty of Mechanical Engineering, University of Transport and Communications

Cau Giay Street, Dong Da District, Hanoi City, Vietnam

ABSTRACT

The bus frame structure is mainly subject to the complex loads that affect the vehicle during operation, so the design of frame structure is always a key issue in the design, consuming a lot of time and effort. To enhance the flexibility of the design and calculation process, minimize the changes in design of the same type of bus, enhance the level of standardization and mass production of the product, the using of 3D parametric software to carry out designing the bus frame structure has become an indispensable trend in the development of automotive manufacturing technology. This article presents the results of research on the features of the geometric model establishment of Solidworks software as well as the interactive ability, data access between Solidworks and Excel software. Based on the features of the software and on the basis of the analysis of the design process, the structural features of the bus frame, the method of rapid shaping is set up. The application of rapid shaping by using Solidworks and Excel software to increase productivity, reduce time, effort and budget for frame structure design process of bus.

Keywords: Bus frame, 3D Parametric Software, Design and Rapid Shaping, Solidworks, Excel software

1. Background

Together with the rapid development of science and technology, automotive manufacturing and assembling technology is constantly improving. Automotive manufacturing industry in general and passenger car sector in particular are increasingly focusing on new solutions in the design and manufacture of products in order to further enhance the quality, performance and comfort of automobiles. New product development phase is always the key to success.

Bus frame structure is mainly subject to complex loads that affect the vehicle during operation, so the design of frame structure is always a key issue in the design, consuming a lot of time and effort. The main purpose and tasks in the design phase of the vehicle frame structure are to choose an appropriate structural layout and profile for the most optimal pats. This is an important pre-condition in the design of the vehicle frame structure to save materials and ensure the durability[1].

Today, in the design and manufacture/shaping phases, major automotive manufacturers in the world are using CAD/CAE simulation tools to design, analyze, and simulate the process in order to predict and restrict changes in design. In the process of vehicle frame structure design, geometric or dynamic models are developed in the virtual space based on CAD and CAE techniques to enhance the flexibility of the design and calculation process, minimize the changes in design of the same type of bus, enhance the level of standardization and mass production of the product, and thereby improving the speed of new vehicle frame structure designs, reducing the number of prototypes, as well as reducing time and costs of product development[2].

Solidworks software is one of 3D parametric design software specifically published by Dassault System for small- and medium-sized enterprises to meet the most demanding engineering needs in today's market. SolidWorks software provides users with a number of design features, including such common features as designing 3D blocks, assembling 3D blocks to form parts of machines, creating 2D drawings of those details. Integrating a lot of features, modules and add-ins in SolidWorks software makes it easier for users to specialize on this software without using softwares to perform various tasks.

2. Bus frame structure design basis

2.1. Characteristic design techniques for detailed structural elements in Solidworks

Product design is completed by one or more functional structures referred to as product design structures [3]. A product design structure can be a product (PRO), a constituent object (CO), a detail (PA), a characteristic structural detail element (F), or a structural geometric element of detail (G). Product design hierarchy is shown in Figure 1.

SolidWorks software utilizes visualization techniques based on detailed structural elements to create complete models of details. The introduction of this visualization technique provides designers with a human-machine interface that helps designers focus their resources on more advanced design issues to shorten time and enhance design quality. In structuring technique that is based on structural characteristics, the main characteristic is the structural constituent element. Thus, a characteristic can be defined as a shape formed by a combination of geometric elements (surface or block) having a certain associated connection.

There are two methods of defining a detailed structural element: pre-definition of structural element characteristic and post-definition of structural element characteristic[4][5]. Method of pre-defining a structural element characteristic means defining shape characteristic before defining geometric element. The user directly defines the shape characteristic, from which CAD system will be based upon characteristic

parameters entered to create the geometric element combination (surface or block). This type of method can be used in the structural design phase. The designer relies upon detail shape data as the basis for constructing the entity and uses that entity to identify the detailed structural element characteristics, and geometric element that constitutes these characteristics will also be formed. Changes in characteristic parameters will cause geometric element to change. Method of post-defining a structural element

characteristic means defining shape characteristic after defining geometric element. The designer relies on geometric shape of the details to construct geometric elements. From those geometric elements, they continue building element characteristics. Thus, based on characteristic structural element design technique, a change in the characteristic parameter of structural element or a change in the parameter of geometry element during design phase will help rebuild the total product model.
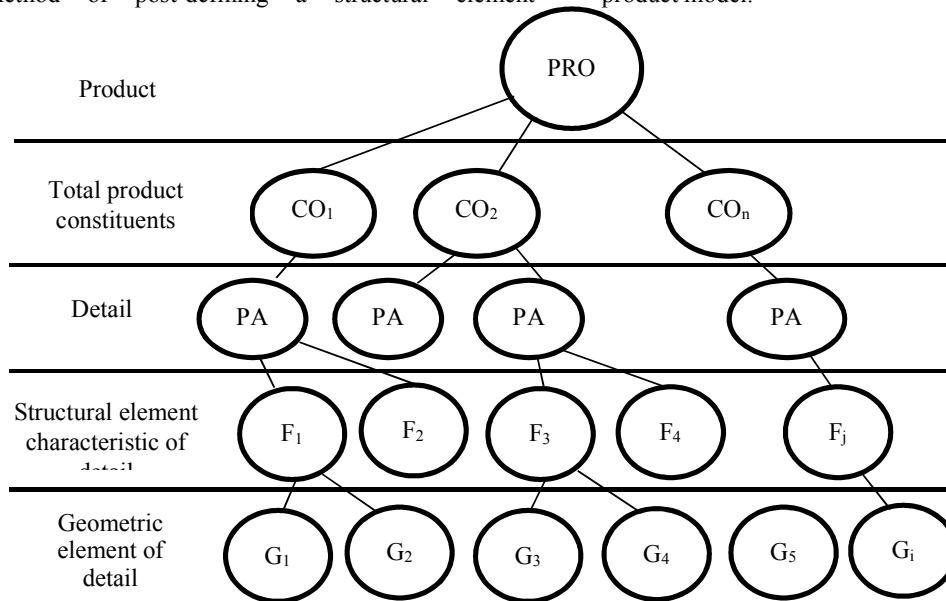
Figure. 1 Product design hierarchy

2.2. Interaction between Excel and Solidworks software.

Solidworks software allows to use point and line macros by reading point coordinate data from Excel files. From SolidWorks toolbar, use Macros tool to create Microsoft Visual Basic editor environment as shown in Figure 2. In this environment, it is possible to write code that performs the function of reading point coordinates and creating straight lines between them. Using Macros makes it easy to build point and line segments without the need to perform point-to-point and line-by-line operations like manual step in the past.
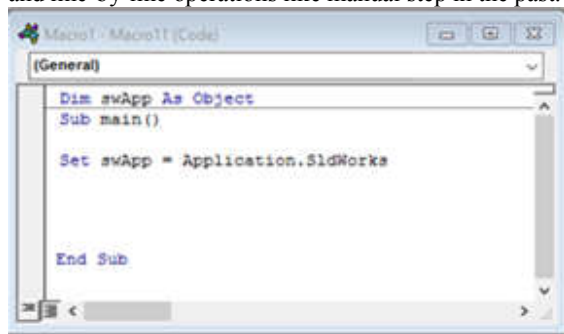
Figure. 2 Microsoft Visual Basic editor environment created by Macros in Solidworks

2.3. Structural Member function in Solidworks

SolidWorks software provides Structural Member function in Weldments tool that enables the assignment of cross sections to wireframe model lines.

You can either use existing sections in Weldments library or create different sections to add to the Structural Member library as shown in Figure 3.
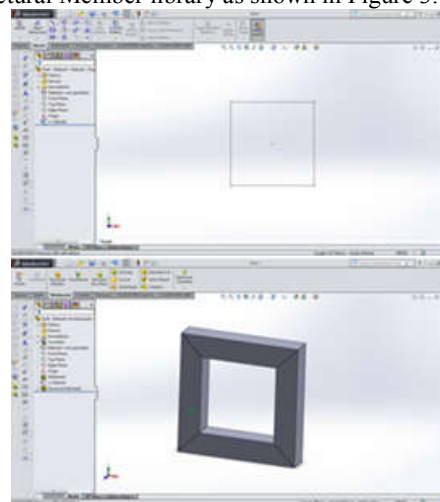
Figure. 3 Creating cross section library for wireframe model

3. 2. Quick design of bus frame structure

This paper presents the way to use above-

mentioned approaches to design frame structure for a 39-seat bus. A bus is structured with 2 entrance/exit doors to facilitate passengers to get on/off: entrance door is single-type and exit door is double-type. Bus route is shown in Figure 4.
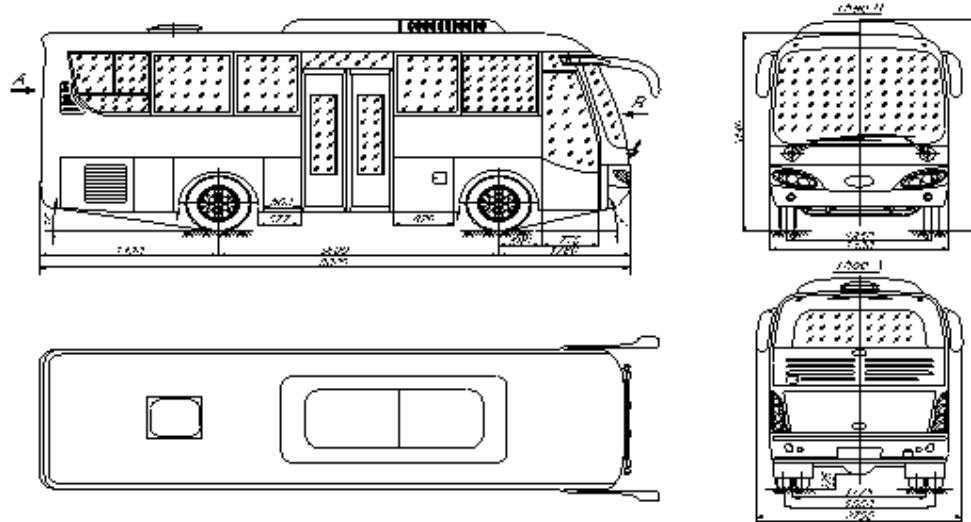
Figure. 4 Reference bus route

Bus frame structure is usually divided into 6 arrays including: front, rear, roof, left, right and floor. Based on current design experience and standards, we have established initial shape of each array of bus frame structure in form of points and lines, which are numbered as illustrated in Figure 5 and Figure 6. After designing the whole 6 arrays, we assemble the arrays together into the complete bus frame.
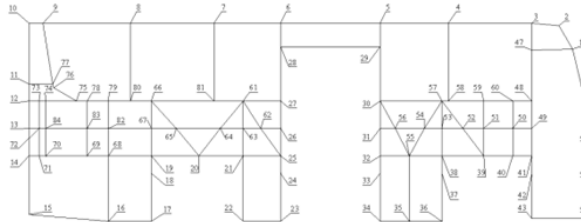
Figure. 5 Initial shape of bus frame structure in form

Of numbered points
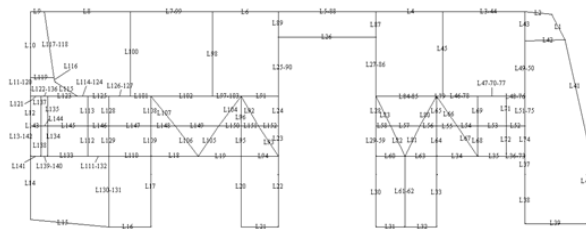
Figure. 6 Initial shape of bus frame structure in form

of numbered line frames

We then summarize to determine the coordinates of intersections of structural beams in the bus frame, which are listed in Excel table as shown in Figure 7.

Time	X	Y	Z
1	0	0	2370
2	0	1020	2370
3	287	2195	2370
4	465	2500	2370
5	820	2530	2370
6	820	2182	2370
7	820	1522	2370
8	820	1168	2370
9	820	808	2370
10	820	0	2370
11	0	0	2370

Figure. 7 Coordinates of cross-sections between the beams in right array of the bus frame in Excel format

The management of these coordinates in Excel will help designer change point positions in order to change the frame shape conveniently and quickly. With an Excel table containing an array of point coordinates, Macros are used to create a Microsoft Visual Basic editor environment and write a code sequence to read coordinate data points from Excel into Solidworks as follows:

```
Dim swApp As Object
Dim XData As Double
Dim YData As Double
Dim ZData As Double
SetswApp= CreateObject("SldWorks.Application")
Set Part = swApp.ActiveDoc
Part.ClearSelection
Part.SetAddToDB (True)
Part.Insert3Dsketch
Do While Cells(Counter, 2) <> ""
    XData = Cells(Counter, 2) / 1000#
    YData = Cells(Counter, 3) / 1000#
```

```
    ZData = Cells(Counter, 4) / 1000#
    Part.CreatePoint2 XData, YData, ZData
    Counter = Counter + 1
Loop
Part.ViewZoomToFit
        End
Sub
```

After reading point coordinates from Excel, in the environment of Solidworks, points of the bus frame will be generated as shown in Figure 8.
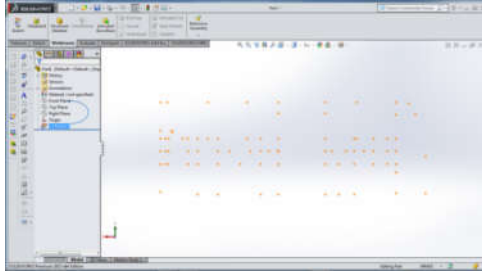
Figure. 8 Points of the bus frame in SW software

To join these points together and form the framework model of bus frame structure, we use Macros to create a Microsoft Visual Basic editor environment and write a code sequence to merge the points we just created. The wireframe model is as follows:

```
 Dim swApp As Object
Dim OldXData As Double
Dim OldYData As Double
Dim OldZData As Double
Dim Length As Double
Dim i As Integer
Sub xyzPoints()
Counter = 2
SetswApp= CreateObject("SldWorks.Application")
Set Part = swApp.ActiveDoc
Counter = 2
Part.ClearSelection
Part.SetAddToDB (True)
Part.Insert3Dsketch
OldXData = Cells(Counter, 2) / 1000#
OldYData = Cells(Counter, 3) / 1000#
OldZData = Cells(Counter, 4) / 1000#
Counter = Counter + 1
Do While Cells(Counter, 1) <> ""
   XData = Cells(Counter, 2) / 1000#
   YData = Cells(Counter, 3) / 1000#
   ZData = Cells(Counter, 4) / 1000#
   Length = ((OldXData - XData) ^ 2 + (OldYData -
YData) ^ 2 + (OldZData - ZData) ^ 2) ^ 0.5
      If (Length > 0.01 / 1000#) Then
         Part.CreateLine2   OldXData,   OldYData,
OldZData, XData, YData, ZData
         OldXData = XData
         OldYData = YData
         OldZData = ZData
      End If
```

```
   Counter = Counter + 1
Loop
Part.ViewZoomToFit
 End Sub
```

After automatically joining the points in environment of Solidworks by using Macros, we obtain the wireframe structure model shown in Figure 9.
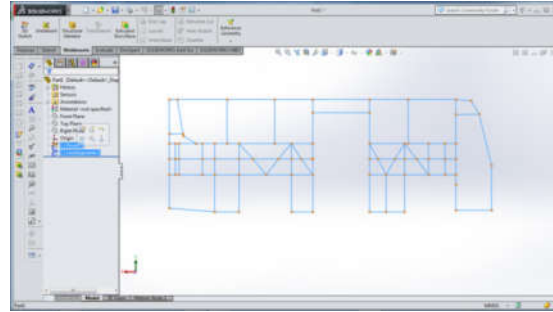
Figure. 9 Wireframe structure model of right array

After obtaining the wireframe model for the bus frame, we proceed to assign cross sections of the material to the model. It is possible to use existing cross-section library of SolidWorks software or you may build your own cross-section library for each array of the bus frame. For each line, we have different cross sections. Assigning cross-sections to each of the lines, we obtain the structural 3D model of the bus frame as shown in Figure 10.
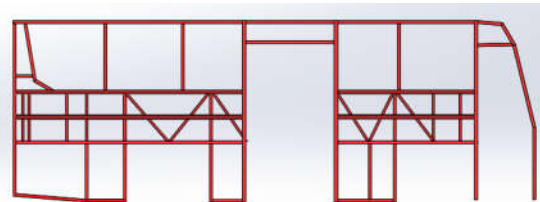
Figure. 10 Right rear array after assigning the cross-sections

After assigning cross-sections, the link between beams should be processed. Depending on the structure or position between the beams, we choose an appropriate type of link. In Weldments module in Solidworks, select Trim/Extend function to perform the linking operation between the beams, as shown in Figure 11.

85
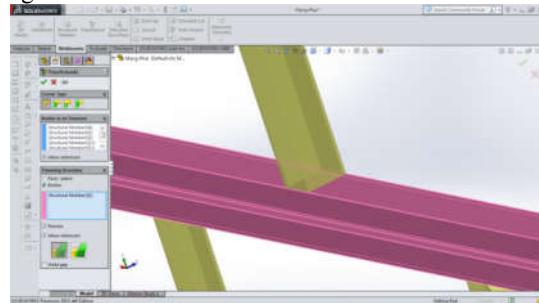
Figure. 11 Processing links between the beams in Solidworks

In designing, because size parameter of the main structure of side array is the highest, yet not the most complicated, we choose to model the side array as the focus point. Then, based on the rear array, roof array, and the most complex one, floor array, proceed with modeling work. In assembling, based on actual bus frame, consider floor array as a fixed coordinate system, and depend on the order of right, rear, roof arrays, and other components to proceed with the assembling work as illustrated in Figure 12 as follows:

Floor array → Right array → Left array → Rear array → Front array → Roof array
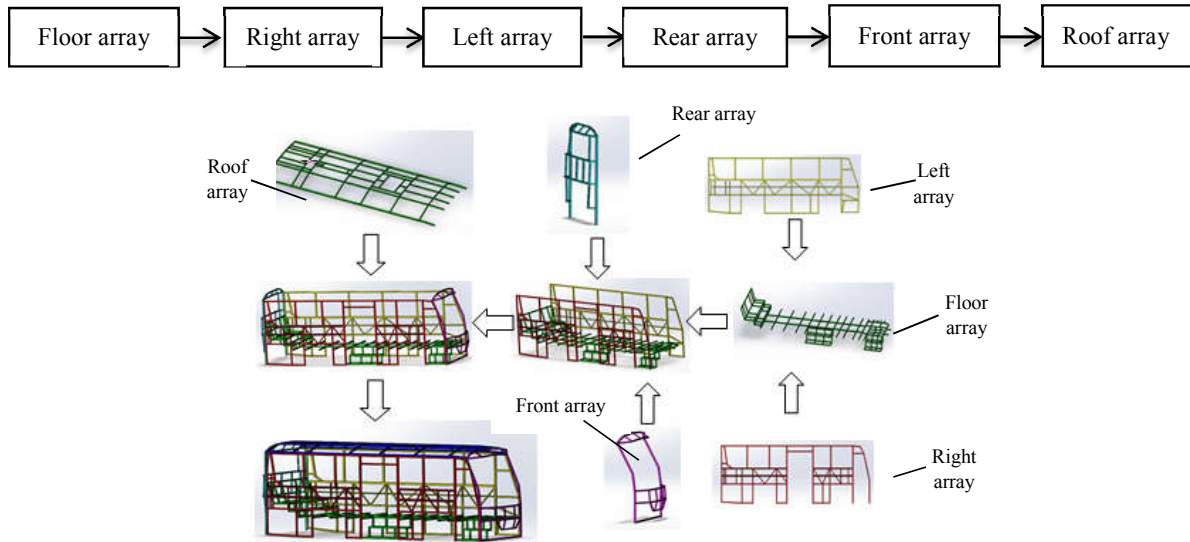
Figure. 12 Overall assemble diagram of the bus frame structure.

After completing the entire assembly of the bus frame model using Solidwork, export all of parameters defined by the dimension in table format as shown in Figure 13. This allows to control and edit design parameters quickly. Based on calibrated parameters, Solidworks will rebuild 3D model with new dimension parameters as shown in Figure 14.
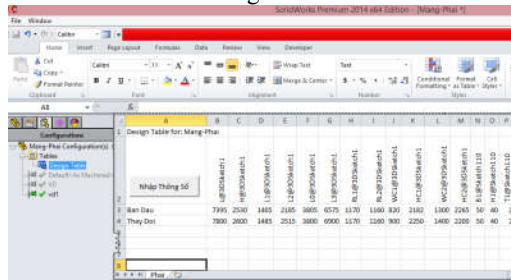
Figure. 13 Dimension parameters of the design model
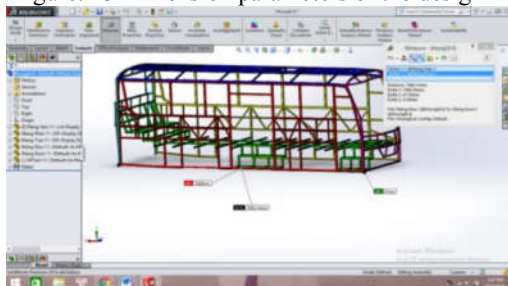
Figure. 14 Bus frame after changes of dimension

4. Conclusion

Bus frame design process is a complex process that consumes a lot of time and effort of the manufacturers. Based on visual modeling capabilities of SolidWorks software as well as interactivity and data access between Solidworks and Exel, as well as based upon the analysis of design process and structural characteristics of bus frame, the shap of bus frame structure is then developed. Research results show that using SolidWorks software will allow to create bus frame in a fast and convenient manner, easily change to enhance the flexibility of the design process, minimizing changes for the same type of vehicle, enhancing the level of standardization and mass production, increasing productivity, and reducing time, effort and costs during the design of bus frame.

Reference

[1] Prasannapriya. Chinta, Dr.L.V. Venugopal Rao. A New Design and Analysis of BUS Body Structure. IOSR Journal of Mechanical and Civil Engineering 2320-334X, Volume 11, Issue 5 Ver.1 ,PP 39-47

[2] C. C. Liang & G. N. Le. Lightweight optimization of bus frame structure considering rollover safety. WIT Transactions on Ecology and The Environment, Vol 155

[3] Craig B. Chapman, Martyn Pinfold. The application of a knowledge based engineering approach to the rapid design and analysis of an automotive structure. Advances in Engineering Software 32 (2001) 903-912

[4] H.M.A Hussein and Alexander Harrich. Computer Aided Bus Skeleton Design. International Journal of Engineering and Technology IJET-IJENS Vol: 12 No:04

[5] Lingxia Kong, Chunning Jin, Qinghong Xu, Guofu Yang and Dongbin Kan. Development of Knowledge-Based System for Bus Body Concept Design. Advances in Mechanical and Electronic Engineering pp 555-561

Study on a Neural Network for Position Determination Using Optical Sensor

Thieu Quang Minh Nhat[1], Hyeungsik Choi[1], Joono Sur[2], Jinil Kang[1], Hyunjoong Son[1],

[1] Division of Mechanical Engineering, College of Engineering Korea Maritime and Ocean University

[2] Chief of Marine Unmanned System Center, College of Engineering Korea Maritime and Ocean University

ABSTRACT

The navigation is a very important issue in AUVs (Autonomous Unmanned Vehicles) docking system. In this paper, to apply the system using optical sensors for detecting the docking system position using a light source and optical sensor to homing of the AUV under the water, we study the system in air beforehand. We study two algorithms for detecting the docking station position: a pinhole camera model and neural network (NN) that determine the position of AUV and docking station using beacons and optical sensors. To evaluate the performance of this we performed an experiment. The result shows that the neural network algorithm is compatible with AUV docking system using optical sensors.

Keywords: pinhole camera, neural network, navigation

1. Introduction

AUV is suitable to perform a variety of underwater missions autonomously. However, the battery duration of AUVs is limited. Because of this restriction, we need a docking station where the AUV can recharge the battery, transfer data, and do safe parking.

For the AUV docking, a number of studies about the detection position of AUV in short distance have been performed so far. Normally, they use cameras and other sensors (USBL, DVL USBL) with pinhole camera method to determine the position of AUV and station [2]-[6]. Moreover, a CNN is presented in [9] to find the position of AUV. However, these methods have a disadvantage that systems use camera is only suitable for the distance below 10m.

In this study, we propose a method that uses optical sensors and the neural network algorithm for detecting the docking system position. In order to validate the effect of the proposed method, we make the experiment in air beforehand. We then compare the result of the neural network with the pinhole camera algorithm. This experiment is a pre-test before applying it to an underwater system.

2. Pinhole camera model
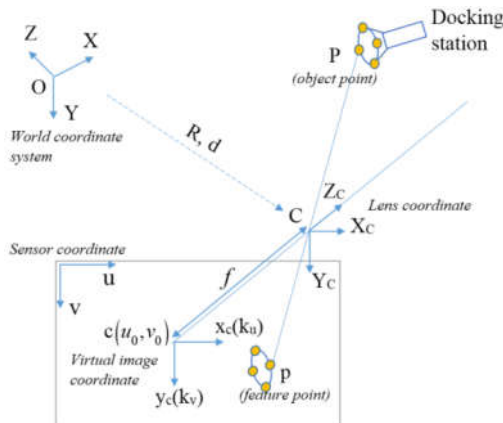
Figure 1: Definition of coordinate

In this part, we briefly introduce a pinhole camera model to detect the position of AUV for docking. Firstly, we define the lens coordinate system (C, X_C, Y_C, Z_C) which is centered at the optical center C, two axes of coordinates parallel to the image plane while the third one is the optical axis as shown in Fig. 1. In two coordinate systems, the relationship between the word coordinate and camera coordinate is simply expressed:

$$\begin{bmatrix} X_C \\ Y_C \\ Z_C \\ 1 \end{bmatrix} = \begin{bmatrix} R & d \\ 0_3^T & 1 \end{bmatrix} \begin{bmatrix} X \\ Y \\ Z \\ 1 \end{bmatrix} \quad (1)$$

Secondly, we define the virtual image coordinate system (c, x_c, y_c) which is centered at principal point (u_0, v_0), where x_c, and y_c axes parallel to X_C-axes, and Y_C-axes of lens coordinate. The virtual image coordinate system (c, x_c, y_c) is a projection of the lens coordinate (C, X_C, Y_C, Z_C) as Eq. (2). The projection can be defined in Fig.2:

$$\begin{bmatrix} x_c \\ y_c \\ 1 \end{bmatrix} = \begin{bmatrix} -f & 0 & 0 \\ 0 & -f & 0 \\ 0 & 0 & 1 \end{bmatrix} \begin{bmatrix} \dfrac{X_C}{Z_C} \\ \dfrac{Y_C}{Z_C} \\ 1 \end{bmatrix} \quad (2)$$

where, f is focal length of the lens.

Finally, the relationship between the object point and the image point can be denoted as:
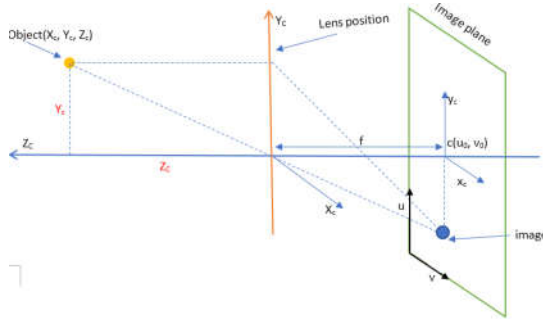
Figure 2: The projection from Object to image plane

$$\begin{bmatrix} X & Y & 0 & 0 & -\dfrac{uk_u}{f}X & -\dfrac{uk_u}{f}Y & 1 & 0 & -\dfrac{uk_u}{f} \\[2mm] 0 & 0 & X & Y & -\dfrac{vk_v}{f}X & -\dfrac{vk_v}{f}Y & 0 & 1 & -\dfrac{vk_v}{f} \end{bmatrix} r$$
$$= 0 \qquad (6)$$

where k_u and k_v are the actual size of a pixel (an optical sensor) in u and v direction, respectively. X, Y are object position point in world coordinate.

$$r = \begin{bmatrix} R_{11} & R_{12} & R_{21} & R_{22} & R_{31} & R_{32} & d_x & d_y \end{bmatrix}^T$$

Furthermore, the closed-form solution of (6) can be found in [8].

3. NN algorithm for detection of AUV position

In this section, we briefly present the NN algorithm. Fig. 3 shows the framework for training and implementing the NN algorithm of AUV docking system. First, the network gets sensors data that are called sample data. Next, the external positioning system then measures the real position of AUV which is called the target. Lastly, the back-propagation algorithm can find the weights of NN to match the sample with the target.

The basic idea of the NN algorithm is from [7], but the complexity of the network is reduced to avoid over-fitting. Its parameters are shown in Table 1.

Table 3: The parameters of convolution neural network

Convolution Layer	Kernel size	Stride	Filters
Conv 1	2x2	2	3
Conv 2	2x2	2	3
Fully connected layer	Size		
FCL 1	8		
FCL 2	8		
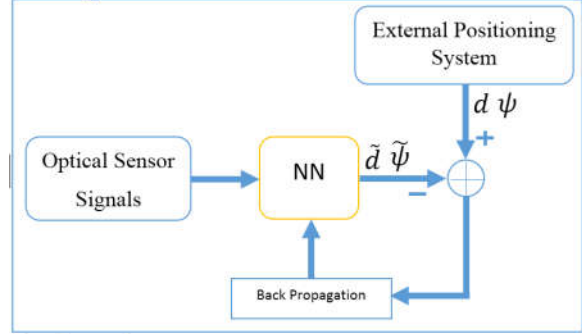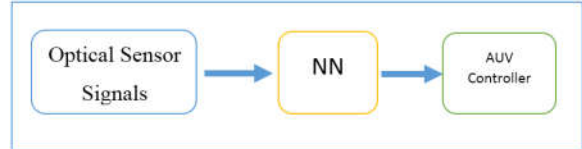
Figure 3: Framework for training and implementing for AUV docking

4. Experiment

This section contains the results of experiment in air. In this experiment, we use two LEDs and one actuator to carry the optical sensor plane as show in Fig. 4 and 5. The purpose is to determine the distance from the LEDs to the sensor plane. The steering angle in this experiment always is zero.

First, The LEDs are put 14m far from sensor plane as show in Fig.4. The actuator bringing the sensor plane then move toward two LEDs.

Figure 4: The setting up experiment

Figure 5: The actuator bring the sensor plane
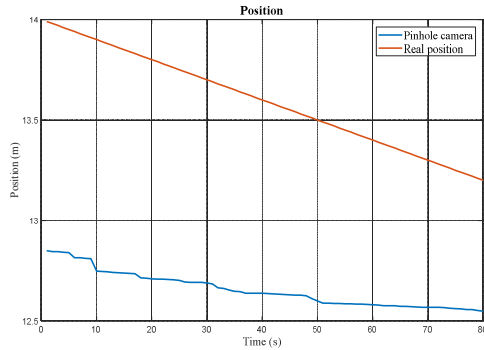
Figure 6: The result of first experiment with pinhole camera model

In first experiment, the actuator moves from 14m to 13.2m. The Fig. 6 shows the result of this experiment.

The second experiment, the actuator from 13m to 14m. The result is showed in Fig. 7.
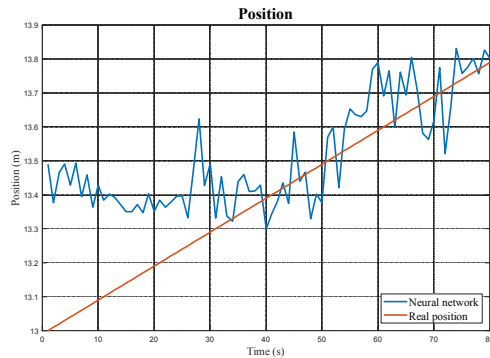
Figure 7: The result of second experiment with the neural network algorithm

Fig. 8 shows the square error of the pinhole camera and the neural network. The figure has proven that the neural network algorithm is better than the pinhole camera algorithm.
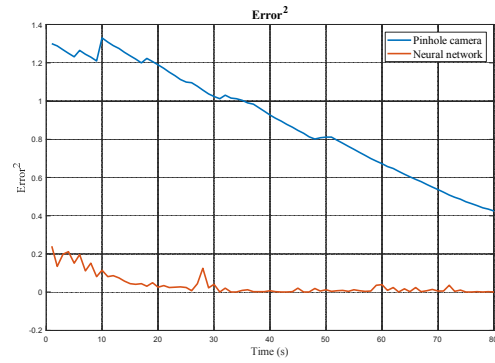
Figure 8: The square error

5. Conclusion

In this paper, we presented a method which locates an object position using beacons, lens, and optical sensors. Based on the experiment results, we can see that the neural network is more accurate than the pinhole camera. Moreover, the neural network will "learn" the properties of our system by using sample data. Hence, even if the lens is distorted the system will be trained again in order to get the good performance. However, the neural network algorithm still has the following disadvantages as: First, it is sensitive to environmental changes. Secondly, the neural network algorithm needs a big sample data to receive a good performance. In other words, the bigger the sample data we have, the more accurate result we get. Because the docking station is normally static and in a deep sea, thus, the first restriction is not a big problem. Moreover, if we have a huge data sample at the docking station position, the result will be more accurate than other methods. For the further work, we will apply this method to an AUV docking system.

Reference

[1] Firat Eren, Shachak Pe'eri, "Position, Orientation and Velocity Detection of Unmanned Underwater Vehicles (UUVs) Using an Optical Detector Array", *Journal of Sensors 2017*

[2] Tomeu Palmer, David Ribas, Pere Ridaoy, "Vision Based Localization System for AUV Docking on Subsea Intervention Panels", *IEEE OCANS '09 – EUROPE, May 2009*

[3] Andre B. Figueiredo, Bruno M. Ferreira, Aníbal C. Matos, "Vision-based localization and positioning of an AUV", *IEEE OCEANS '16 – Shanghai, April 2016*

[4] Jin-YeongPark, Bong-huanJun, Pan-mookLee, "Experiments on vision guided docking of an autonomous underwater vehicle using one camera", *Journal of Ocean Engineering, January 2009*

[5] Hayato Kondo, Kenji Okayama, Jin-Kyu Choi, "Passive Acoustic and Optical Guidance for Underwater Vehicles", *IEEE OCEANS '12 – Yeosu, May 2012*

[6] Szymon Krupinski, Francesco Maurelliy, Angelos Malliosz, "Towards AUV docking on sub-sea structures", *IEEE OCEANS '09 – EUROPE, May 2009*

[7] M. Bojarski, D. Del Testa, D. Dworakowski, B. Firner, B. Flepp, P. Goyal, L. D. Jackel, M. Monfort, U. Muller, J. Zhang et al., "End to end learning for self-driving cars," *arXiv preprint arXiv:1604.07316, 2016.*

[8] Zhengyou Zhang, "A Flexible New Technique for Camera Calibration", *IEEE Transactions on Pattern Analysis and Machine Intelligence, December 2000*

[9] Albert Sans-Muntadas, Kristin Y. Pettersen, Edmund Brekke, "Learning an AUV docking maneuver with a convolutional neural network", *OCEANS 2017*

The Role of Kaempferol Treatments in Alternating Murine Tibia Strength

Hanjong Kim[1], Changwan Han[1], and Seonghun Park[1]
[1]School of Mechanical Engineering, Pusan National University
Busandaehak-ro 63beon-gil, Geumjeong-gu, Busan, 46241, Republic of Korea

ABSTRACT

Kaempferol is a typical flavonol-type flavonoid and has a protective effect on postmenopausal bone loss, and previous studies have reported that Kaempferol treated groups show an increase in biomechanical properties when compared with untreated control groups in the bone healing process. The current study is designed to investigate the role of Kaempferol treatments in alternating mechanical properties of non-fractured murine tibia near fracture sites, by measuring Kaempferol dose-dependent mechanical properties in the bone healing process.

A stabilized fracture was generated at tibia by minor modification of the Hiltunen method for 8 weeks old ICR mice with weights of 29.0 ~ 30.5 g. Experimental mice were divided into 4 groups. Kaempferol of 0.2, 1.0, 5.0 mg/kg (body weight) with 20 % ethanol was administered to 3 groups and the remaining one group was only treated with 20 % ethanol as a control group. Three-point bending fracture tests were conducted to measure the mechanical properties (fracture load, fracture energy, stiffness) of murine tibiae at non-fractured regions near fracture sites 21 days after Kaempferol treatments, via a custom-made biomechanical testing system (BTS, KST Co., Korea).

The 1.0 mg/kg Kaempferol treated group shows higher fracture load (38.07 ± 10.57 N) than the control group (23.13 ± 3.04 N) with a statistically (student's t-test) significant difference ($p = 0.003$). Fracture energy, total energy applied to tibia up to bone fracture, exhibited no significant differences between the control group and any of the Kaempferol treated groups, although both the 1.0 mg/kg Kaempferol treated and control groups showed a little higher fracture energy than the 0.2 and 5.0 mg/kg Kaempferol treated groups. Bone stiffness also did not show statistically significant differences between the control group and any of the Kaempferol treated groups, with the highest stiffness value observed in the 1.0 mg/kg Kaempferol treated group.

Keywords: Mechanical Response, Ultimate Force, Fracture Energy, Kaempferol, Three-Point Bending

1. Introduction

Kaempferol is a typical flavonol-type flavonoid that is present in a variety of vegetables and fruits and has a protective effect on postmenopausal bone loss. Recently it has been suggested that Kaempferol may be a promising agent for the prevention or treatment of bone loss. Initially Kaempferol was known to have anti-osteoclastogenic effect. Kaempferol acts directly on the precursors of osteoclastogenic cells as well as on the mature osteoclasts to inhibit their differentiation and induce apoptosis, respectively (Wattel, Kamel et al. 2003). It has been shown that Kaempferol inhibits TNF-α-induced secretion of key osteoclastogenic cytokines, MCP-1 and IL-6, and inhibits NF-kB signaling in osteoblasts (Pang, Ricupero et al. 2006). Quercetin and Kaempferol, two of the most widespread flavonols, decrease osteoclastic bone resorption in vitro by targeting directly the mature osteoclast by a mechanism involving, at least in part, the ER(estrogen receptor) (Wattel, Kamel et al. 2003).

The promoting effect of Kaempferol on the differentiation and mineralization of murine pre-osteoblatic cell line also has been introduced (Miyake, Arai et al. 2003). Kaempferol treatment of OVx (ovariectomy) rats resulted in the increase in osteoprogenitor cells as well as inhibition of adipocyte differentiation from BMCs compared with the OVx group (Trivedi, Kumar et al. 2008). Taken together, Kaempferol seems to be non-estrogenic *in vivo* and exerts bone anabolic activity with attendant inhibition of bone marrow adipogenesis (Trivedi, Kumar et al. 2008).

Twelve daily injections of 5 microM Kaempferol directly into the periosteum of parietal bones of newborn rats increased new bone formation, suggesting that Kaempferol could induce osteoblast activities in the early stage of bone formation (Yang, Takai et al.; Trivedi, Kumar et al. 2009). Miyake et al. reported the promoting effect of Kaempferol on the differentiation and mineralization of murine pre-osteoblatic cell line (Miyake, Arai et al. 2003). Kaempferol has been shown to promote differentiation of osteoblast-like MG-63 cells (Prouillet, Maziere et al. 2004) and also to promote differentiation and mineralization of a mouse osteoblast cell line, MC3T3-E1 (Kim, Kim et al. 2003; Prouillet, Maziere et al. 2004).

However, no data are available on the effects of Kaempferol on fracture healing process. Therefore in the present study, the author would like to elucidate the roles of Kaempferol on the fracture healing using standardized murine tibial fracture model produced by standardized fracture machine designed by this institute.

2. Method

Generation of Standardized Fracture of Mouse Tibia Shaft

Eight weeks old ICR mice weighing 29.0 ~ 30.5 g were used. A stabilized fracture was generated as previously reported with minor modifications (Hiltunen, Vuorio et al. 1993). Briefly, a closed

diaphyseal fracture of the tibia was produced bilaterally in each animal, which was anesthetized with intraperitoneal injection of pentobarbital (50 mg/kg). The animals were prepared for surgery by shaving and
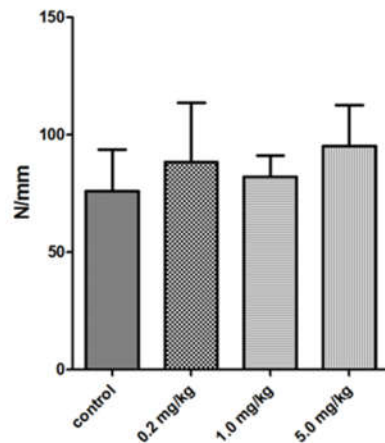
Fig. 4 Stiffness in the hard callus of fractured tibia at 21 day after oral administration of Kaempferol

scrubbing of both thighs. A short incision was made on the dorsolateral side of the thigh and was extended over the knee region. A longitudinal incision was made in the patellar tendon, and a 0.5 mm hole was drilled above the tibia1 tuberosity. Intramedullary fixation was made by placing an Anticorro insect pin (Fine Science Tools, http://www.finescience.com/) in into the intramedullary canal of the tibia. The wound was closed, and the procedure was repeated on the contra lateral side. Under anesthesia, the animal was placed supine under the apparatus, and the anteromedial diaphysis of the tibia in the region of the lower midshaft was exposed to the blunt blade. A weight of 220 g was dropped from a height of 195 mm, producing a closed fracture (Fig.1).

3. Results and Discussion

Mice were divided into groups: control group (fracture only), 1st group (Kaempferol at 0.2 mg/kg dose), 2nd group (Kaempferol at 1.0 mg/kg dose), and 3rd group (Kaempferol at 5.0 mg/kg dose) as described in Materials and Methods. At 21st day, mice were sacrificed and dissected. The tibia which has callus formation was collected from both legs.

In the tibia of all Kaempferol treated groups, the volume of callus formation was increased compared with control group. The representative picture of tibia from each group was taken. The callus formation around fracture site was obviously shown. The most important outcome in fracture repair is restoration of biomechanical integrity. Therefore at 3 weeks after fracture, bony strength of hard callus was evaluated postmortem using a custom biomaterial testing device (Biomechanical Testing Machine, KST Co. Korea).

The metal wire was removed and entire tibia was obtained. Bony strength was measured using a three-point bending method. As expected, better biomechanical strength was observed at the level of ultimate force (N), energy to failure (mJ) and stiffness (N/mm) in the Kaempferol treated tibia fracture groups which also show lager callus diameter.

Kaempferol treatment (5 mg/kg) significantly increased mechanical properties of fractured tibia as evidenced by 8.78% gain of ultimate force (Fig. 2).

Kaempferol treatment (1 mg/kg) also significantly
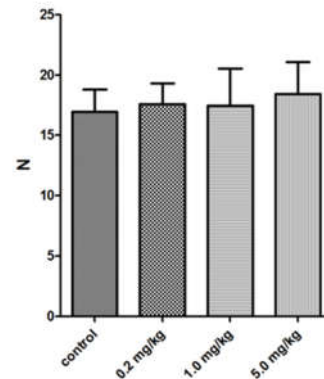
Fig. 2 Ultimate force of healing callus from tibia fracture at 21 day after oral administration of Kaempferol

increased the energy to failure (mJ) of healing callus of fractured tibia as evidenced by 13.4% gain (Fig. 3).

Kaempferol treatment (5 mg/kg) also significantly increased the stiffness (N/mm) of healing callus of
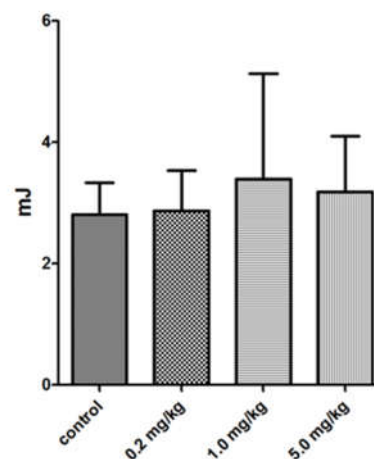
Fig. 3 Energy to failure (mJ) in the hard callus of fractured tibia at 21 day after oral administration of Kaempferol

fractured tibia as evidenced by 25% gain (Fig. 4).

These experiments sought to test the complementary

hypotheses that Kaempferol affects fracture repair. Overall, the results obtained support these hypotheses, as healing callus of fractured tibiae of mice treated with Kaempferol were larger, more mineralized, and biomechanically superior to those from untreated group. However, as the biomechanical analyses were conducted solely on day 21, further studies will be required to ascertain if fracture repair with the treatment of Kaempferol to mice is promoted or impaired. In addition, underlying molecular signaling mechanism of action from Kaempferol in fracture repair remains to be elucidated.

Next to this result, the present study also demonstrated that the mouse can be used as an experimental animal in fracture healing studies. To study the biology of fracture repair, controlled fracture machine was modified for the production of a standard closed experimental fracture in the mouse tibia. A 0.2 mm stainless-steel rod was introduced into the medullar cavity and the tibial shaft was fractured by an impact device, which resulted in a reproducible fracture pattern. The biomechanical, histological, and biochemical characteristics of murine tibial fracture healing do not seem to deviate markedly from those described for other species. The current fracture model apparently is a useful tool for fracture repair studies of cell and molecular biology.

Kaempferol is a typical flavonol-type flavonoid that is present in a variety of vegetables and fruits and has a protective effect on postmenopausal bone loss. Recently it has been suggested that Kaempferol may be a promising agent for the prevention or treatment of bone loss. Initially Kaempferol was introduced focused on its anti-osteoclastogenic effect. Recent studies have begun to show that Kaempferol promotes its apoptosis (Wattel, Kamel et al. 2003), promotes differentiation of an osteoblast-like MG-63 cell line (Prouillet, Maziere et al. 2004), and attenuates TNF-α signaling in the MC3T3-E1 mouse osteoblast cell line(Pang, Ricupero et al. 2006). The promoting effect of Kaempferol on the differentiation and mineralization of murine pre-osteoblatic cell line also has been introduced (Miyake, Arai et al. 2003; Trivedi, Kumar et al. 2008), suggesting that Kaempferol could induce osteoblast activities in the early stage of bone formation (Yang, Takai et al.). However, despite of the reports concerning enhanced ostegenic activity of Kaempferol, no data has been available on the effects of Kaempferol on fracture healing process.

Therefore the present study first demonstrated that administration of Kaempferol, from 0.2 to 5.0 mg/kg, increased callus formation in standardized mouse fracture model. Specially, an oral dose of 1 mg/kg body weight of Kaempferol in mouse resulted in a peak volume of callus size, suggesting its potent fracture healing activity. However, the most important outcome in fracture repair is restoration of biomechanical integrity. Therefore, in the present study, three point bending tests were conducted on the isolated tibia. As expected, biomechanical properties showed enhanced ultimate force (N) in the Kaempferol treated tibial fracture group. Kaempferol treatment significantly increased the mechanical properties of fractured tibia as evidenced by 8.78 % gain of ultimate force with 5.0 mg/kg of Kaempferol treatment (Fig. 2). Kaempferol treatment also increased the energy to failure (mJ) and stiffness (N/mm) of healing callus of fractured tibia (Fig. 3 and 4).

4. Concluding Remarks

Based on these in vivo studies, we hypothesized that Kaempferol might have a positive role in bone remodeling such as fracture healing. First of all, in vitro effect of Kaempferol was determined in promoting fracture repair by inducing callus formation. Rapid increasing callus formation in fracture site can be the ultimate aim of any bone anabolic therapy. Therefore, it seems to be concluded that Kaempferol has therapeutic promise for rapid and effective fracture healing, as it affects bone remodeling by potentiating callus formation in fracture site.

References

[1] G. O. Young, "Synthetic structure of industrial plastics (Book style with paper title and editor)," in Plastics, 2nd ed. vol. 3, J. Peters, Ed. New York: McGraw-Hill, 1964, pp. 15–64.

[2] W.-K. Chen, Linear Networks and Systems (Book style).Belmont, CA: Wadsworth, 1993, pp. 123–135.

[3] H. Poor, An Introduction to Signal Detection and Estimation. New York: Springer-Verlag, 1985, ch. 4.

[4] B. Smith, "An approach to graphs of linear forms (Unpublished work style)," unpublished.

[5] E. H. Miller, "A note on reflector arrays (Periodical style—Accepted for publication)," IEEE Trans. Antennas Propagat., to be published.

[6] J. Wang, "Fundamentals of erbium-doped fiber amplifiers arrays (Periodical style—Submitted for publication)," IEEE J. Quantum Electron., submitted for publication.

[7] C. J. Kaufman, Rocky Mountain Research Lab., Boulder, CO, private communication, May 1995.

[9] Y. Yorozu, M. Hirano, K. Oka, and Y. Tagawa, "Electron spectroscopy studies on magneto-optical media and plastic substrate interfaces(Translation Journals style)," IEEE Transl. J. Magn.Jpn., vol. 2, Aug. 1987, pp. 740–741 [Dig. 9th Annu. Conf. Magnetics Japan, 1982, p. 301].

[10] M. Young, The Techincal Writers Handbook. Mill Valley, CA: University Science, 1989.

[11] J. U. Duncombe, "Infrared navigation—Part I: An assessment of feasibility (Periodical style)," IEEE Trans. Electron Devices, vol. ED-11, pp. 34–39, Jan. 1959.

[12] S. Chen, B. Mulgrew, and P. M. Grant, "A clustering technique for digital communications channel equalization using radial basis function networks," IEEE Trans. Neural Networks, vol. 4, pp. 570–578, July 1993.

[13] R. W. Lucky, "Automatic equalization for digital communication," Bell Syst. Tech. J., vol. 44, no. 4, pp. 547–588, Apr. 1965.

[14] S. P. Bingulac, "On the compatibility of adaptive controllers (Published Conference Proceedings style)," in Proc. 4th Annu. Allerton Conf. Circuits and Systems Theory, New York, 1994, pp. 8–16.

[15] G. R. Faulhaber, "Design of service systems with priority reservation," in Conf. Rec. 1995 IEEE Int. Conf. Communications, pp. 3–8.

[16] W. D. Doyle, "Magnetization reversal in films with biaxial anisotropy," in 1987 Proc. INTERMAG Conf., pp. 2.2-1–2.2-6.

PART II, SECTION I

Machining Technology
(Difficult-to-cut and Free Machining; Non-conventional Machining;
Green Process/Manufacturing; Cutting Mechanisms…)

Effect of Face-milling Process Parameters on Deformation of AISI304

Masahio Hagino[1], Kouji Ikeuchi[2], Hiroshi Usuki[1] and Takashi Inoue[3]

[1]The University of Tokyo Institute of Industrial Science

5-1-5, Kashiwanoha, Kashiwa-shi, Chiba 277-8574 JAPAN

[2]Motoyama Goukin Seisakusyo Co., Ltd.

1645-20, Aza-Midoriyama, Ayabe, Tsuyama-shi, Okayama 708-1104 JAPAN

[3] Daido University, Department of mechanical engineering

10-3, Takiharu-cho, Minami-ku, Nagoya 457-8530 JAPAN

ABSTRACT

In this study performed to a machining on stainless steel AISI304 by face-milling. Design of experiment (DOE) was implemented to develop the experiment lay-out. The aim of this work is to relate the response to the process parameters. Optimization routine was applied to find out the optimal conditions that would enhance minimize the deformation of it. As a result, mathematical models were developed to determine the relationship between the process parameters and the deformation after machining. Process parameters effects on the deformation amount have been defined.

1. Introduction

Recently, high precision and high efficiency of machining has been advanced. They are produced by cutting out from block materials by machining process when high-precision and high strength are also required for large-sized structure. However, residual stress is generated in the material due to the influence of the processing heat and the cutting force generated by the cutting process, in addition to the residual stress possessed by the material. Due to the influence of this residual stress, problems such as reduction in dimensional accuracy by deformation after processing and deterioration due to a change in mechanical properties occur [1]. Therefore, there is a need for a cutting method that does not cause residual stress or can control residual stress. Many researches are being conducted on residual stress. Murakami and Ibuchi [2] and E. Capello [3,4] were being experimentally conducted on regarding the relationship between machining conditions and residual stress. In addition, Shirakashi et al. [5-7] and M. Mohammadpour et al. [8] reports a method to predict the occurrence of residual stress by simulation analysis. However, actual processing without applying residual stress is difficult.

In particular, deformation such as warping or twisting tends to occur when the workpiece is an elongated thin plate. At the actual manufacturing floor, the worker fix this with hand finishing and completed to the final product. Regularity is not recognized in this deformation, making it difficult to determine the fixed part, which greatly increases working time and becomes one of causes of increase in processing cost. Therefore, in this research an examination optimizing cutting conditions and controlling material deformation after cutting.

2. Experiment design

The experiment was designed based on a central composite design.

The cutting input parameters taken into consideration are cutting speed (A) and feed rate (B).

Cutting speed (130-180m/min) and feed rate (0.06-0.2 mm/tooth) are the process input parameters.

Table 1. Cutting parameters

Parameter	Code	Unit	-1	0	+1
Cutting speed	A	m/min	120	150	180
Feed rate	B	mm/rev	0.06	0.13	0.2

$$Y = b_0 + \sum b_i x_i + \sum b_{ii} \ x_{ii}^2 + \sum b_{ij} x_i x_j \quad (1)$$

Trial runs of face milling were performed by varying one of the process factors at a time to determine the range of each factor.

Table 1 shows face-mill cutting parameters and experimental design levels used. Response surface methodology (RSM) was applied to the experimental data using statistical software, Design-Expert V9. Second order polynomials were fitted to the experimental data to obtain the regression equations. The sequential F-test, lack-of-fit test and other adequacy measures were used to select the best fit. A step-wise regression method was used to fit the second order polynomial Eq. (1) to the experimental data and to find the significant model terms [9]. The same statistical software was used to generate the statistical and response plots as well as the optimization.

3. Experimental work

Austenitic stainless steel in flat bar form of standard grade of AISI304 made by hot rolling method was used as workpiece material. The flat bar dimensions were

Length (L) = 1840 mm, Width (W) = 58 mm with thickness of 16 mm.

Cutting test was used MILLAC 852V by OKUMA Co.. Face mill was used Φ100 mm of WSX445 and cutting insert was SNGU140812 coated on MP7130 by Mitsubishi material Co.. In the experiment, thickness is cut from 16 mm to 12 mm. The first surface is machined with a depth of cut of 0.2 mm, the second surface on the back side is machined with a depth of cut of 3.5 mm.

Response of a warp value, spindle road, process time

Table 2. Design matrix of process conditions

Factors			
Std	Run	Cutting speed (m/min)	Feed rate (mm/tooth)
1	12	120	0.06
2	2	180	0.06
3	11	120	0.2
4	4	180	0.2
5	9	120	0.13
6	13	180	0.13
7	7	150	0.06
8	1	150	0.2
9	6	150	0.13
10	10	150	0.13
11	8	150	0.13
12	5	150	0.13
13	3	150	0.13

and tool wear to a minimum are the criteria of selecting the cutting parameters ranges. The main experiment was performed according to the design matrix in a random order to avoid any systematic error.

The response measurements are as follows. A warp value is measured three points (P1, P2, P3) of in length direction set to the level block. It measured clearance between specimen and level block by the clearance-gage. The results are indicated by the average of three points. Cutting time is measured by cycle time displayed on machining center. Spindle load is measured by displayed on machining center during processing. Spindle load was measured as one index of cutting resistance. That is recorded by operator. Tool wear of flank face is measured by microscope. Measurement of it was indicated by the average value measured at seven points because face mill has seven points of cutting insert.

Table 2 and Table 3 shows the design matrix of process conditions and the average measured responses.

4. Result and discussion

4.1 Analysis of variance

An analyze the measured responses was used to the design expert software V9. The fit summary output indicates that for all responses, the quadratic models are statically recommended for further analysis as they have the maximum predicted and adjusted R^2. The test for significance of the regression models, the test for significance on individual model coefficients and the lack of fit test were performed using the same statistical process for all responses. The insignificant model terms can be automatically eliminated by selecting the step-wise regression method.

Table 4 shows the resulting ANOVA (Analysis of variance) table for the reduced quadratic models outline the analysis of variance for each response and illustrate the significant model terms. The lack of fit F-value of 0.19 implies the lack of fit is not significant relative to

Table 3. Average of experimentally measured responses

Std	Warp P1 (mm)	Warp P2 (mm)	Warp P3 (mm)	Ave. warp (mm)	Cutting time (min)	Spindle load (%)	Tool wear (µm)
1	0.5	1	0.5	0.67	26	19	70
2	2.2	2.5	2.5	2.40	17.53	18	80
3	0.5	0.3	0.2	0.33	8.267	42.5	50
4	0.1	0.1	0.5	0.23	5.683	39.5	70
5	4	5	3.5	4.17	12.67	31.5	60
6	1.5	0.5	1	1.00	8.7	29.5	80
7	0.5	0	0.5	0.33	21	19	90
8	0.5	0.3	0.5	0.43	6.683	41	70
9	2	2.5	2	2.17	10	31	110
10	0.5	0	0.3	0.27	10	31	140
11	0.5	0	1	0.50	10	31	140
12	2.5	3	2.5	2.67	10	31	140
13	2	2	1.5	1.83	10	31	140

the pure error. To more information, in this table 4 case adequacy measures R^2=0.89432, adjusted R^2=0.81885 and predicted R^2=0.72858. The entire adequacy measures are close to 1, which are in reasonable agreement and indicates adequate models [10,11]. The adequate precision compares the range of the predicted value at the design points to the average prediction error. In this case the values of adequate precision ratios are dramatically greater than 4. An adequate precision ratio above 4 indicates that the model is adequate. In this model an adequate precision ratio was 10.7899. An adequate model means that the reduced model has successfully passed all the required statistical tests and can be used to predict the responses or to optimize the process, etc. For other responses, ANOVA results based on this rule are obtained.

The final mathematical model terms of actual factors as determined by design expert software are shown in Eqs. (2)-(5).

4.2 Effect of process conditions on the responses

4.2.1 Average warp

Figure 1 shows the perturbation plot for the result of average warp value. The perturbation plot helps to compare the effect of all factors at a particular point in

the design space. This type of display does not show the effect of interactions. The lines represent the behaviors of each factor, while holding the others constant (i.e. center point by default). In the case of more than one factor this type of display could be used to find those factors that most affect the response [9].

From Fig. 1 that the average warp value increase as the feed rate decrease. In this case it considered that the higher cutting speed and higher feed rate conditions can be decrease warp value.

Figure 2 shows the 3D plot showing of the relation of cutting speed, feed rate and average warp value. It is understood that the slope at the feed speed side is tight

Table 4. ANOVA table for average warp value reduced quadratic model

Source	Sum of Squares	df	Mean Square	F Value	Prob > F
Model	38.8547	5	7.7709	11.84870	0.002617
A	2.3646	1	2.3646	3.605456	0.099380
B	24.5362	1	24.5362	37.41158	0.000483
AB	3.0044	1	3.0044	4.581010	0.069600
A^2	0.7604	1	0.7604	1.159441	0.317285
B^2	8.8687	1	8.8687	13.52258	0.007887
Residual	4.5909	7	0.6558		
Lack of Fit	0.5851	3	0.1950	0.19477	0.894938
Pure Error	4.0057	4	1.00144		

$$\text{Ave. warp} =$$
$$-13.13272 + 0.2494809 \times Cutting\ speed$$
$$-62.0674 \times Feed\ rate$$
$$-0.412698 \times Cutting\ speed \times Feed\ rate$$
$$-0.000583 \times Cutting\ Speed^2$$
$$+365.7049 \times Feed\ rate^2 \qquad (2)$$

$$\text{Cutting time} =$$
$$74.691757 - 0.327109 \times Cutting\ speed$$
$$-417.9869 \times Feed\ rate$$
$$+0.718254 \times Cutting\ speed \times Feed\ rate$$
$$+0.0005032 \times Cutting\ Speed^2$$
$$+791.40277 \times Feed\ rate^2 \qquad (3)$$

$$\text{Spindle load} =$$
$$5.4231468 + 0.0431787 \times Cutting\ speed$$
$$+217.12116 \times Feed\ rate$$
$$-0.059524 \times Cutting\ speed \times Feed\ rate$$
$$-0.000211 \times Cutting\ Speed^2$$
$$-191.7664 \times Feed\ rate^2 \qquad (4)$$

$$\text{Tool wear} =$$
$$-823.7233 + 11.535988 \times Cutting\ speed$$
$$+1203.202 \times Feed\ rate$$
$$-1.190476 \times Cutting\ speed \times Feed\ rate$$
$$-0.038123 \times Cutting\ Speed^2$$
$$-3940.887 \times Feed\ rate^2 \qquad (5)$$

and the amount of warpage increases when the feed rate is low even by looking at the combination with each cutting speed. Herewith, obvious that the condition where the greatest warpage occurs is the case of high cutting speed and low feed rate.

4.2.2 The other responses

For other responses, there is no graph display, but the relation with the cutting conditions was as follows. Cutting time is strongly affected by feed speed. Spindle load was measured as one index of cutting resistance. It is strongly affected by feed speed. When the feed is fast, the spindle load is large. With regard to tool wear, the measured wear amount was small, and no clear difference was observed.
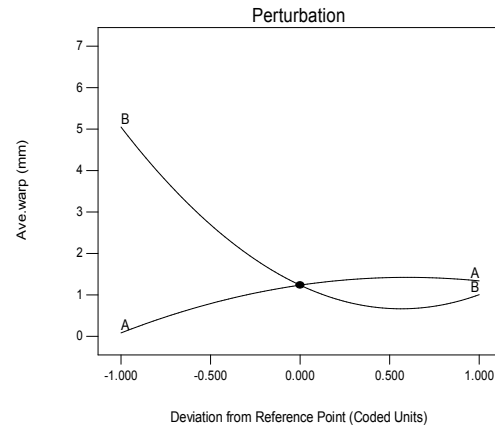
Fig. 1 Perturbation plot showing the value of average warp.
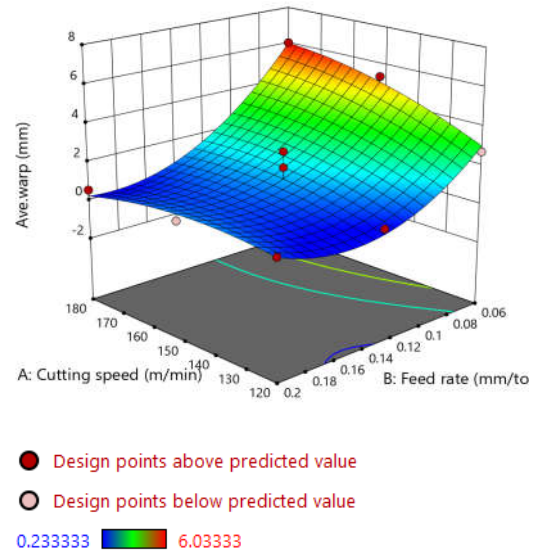
Fig. 2 3D plot showing of the relation of cutting speed, feed rate and average warp value.

5. Optimization

In this research needs to be assessed carefully to achieve the most desirable results. As shown in Table 5, a threshold value for importance was set for warpage

and cutting time reduction. The higher the importance is, the higher the priority is given to the result.

Figure 3 shows the optimum machining condition range obtained. The range indicated by colored is the range that satisfies the condition shown in Table 5

Table 5. Criteria for numerical optimization

Name	Goal	Lower Limit	Upper Limit	Importance
Cutting speed	in range	120	180	3
Feed rate	in range	0.06	0.2	3
Ave. warp	minimize	0.2333	6.0333	5
Cutting time	minimize	5.6833	26	3
Spindle load	in range	18	42	3
Tool wear	in range	60	130	3
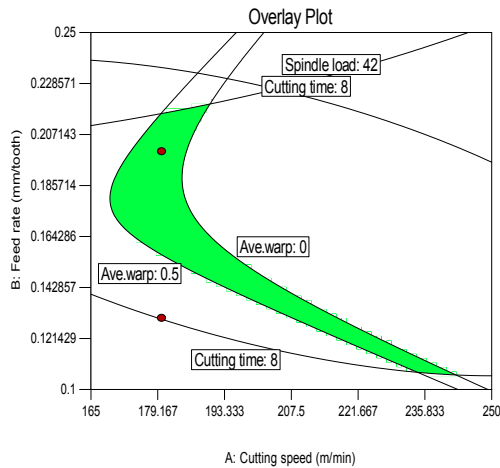
Fig. 3 Overlay plot shows the region of optimal cutting condition based on the first criterion for flat bar AISI 304 by face milling

Table 6 shows cutting conditions predicted that the warp amount is the smallest in the range shown in Fig. 5. Three conditions out of several calculations are shown. From these results, it was shown that the desirability of the result exceeds 0.99 and the warpage amount can be suppressed to 0.2 mm or less. The closer the reliability is to 1, the more effective the result is.

6. Conclusions

In this research, our group have clarified the contribution of process condition on warpage caused by machining and proposed a calculation model. It been also clarified cutting conditions leading to suppression of deformation of long flat bar of stainless steel after processing. These were realized with the experimental model designed by the design expert 9. And it was revealed that the influence of the feed rate is great for deformation after machining. By using the optimum conditions clarified in this experiment showed be that the amount of warp of the material can be suppressed

up to about 90%. Furthermore, since the cutting conditions were able to be increased compared to the conventional machining conditions, the machining time was shortened by 1 min, resulting in cost reduction.

Table 6. Criteria for numerical optimization

No.		1	2	3
Cutting speed	m/min	179.9994	179.9861	180.0000
Feed rate	mm/tooth	0.1823	0.1843	0.1804
Ave. warp	Mm	0.1805	0.1766	0.1878
Cutting time	min	5.7863	5.7893	5.7896
Spindle load	%	37.6285	37.8914	37.3575
Tool wear	μm	66.8753	66.0287	67.7459
Desirability	−	0.9981	0.9980	0.9980

References

[1] E. Brinksmeier, J.T. Cammett, W. König, P. Leskovar, J. Peters and H.K. Tönshoff, *CIRP Annals*, Vol.31, Issue 2, (1982), pp.491-510

[2] Y. Murakami and H. Ibuchi, *Journal of Material*, Vol.16, No.171, (1967) pp.966-971 (Japanese)

[3] E. Capello, *Journal of Materials Processing Technology* Vol.160, (2005), pp.221-228

[4] E. Capello, *Journal of Materials Processing Technology* Vol.172, (2006), pp.319-326

[5] T. Shirakashi, T. Obikawa, H. Sasahara and T. Wada, *Journal of the Japan Society for Precision Engineering,* Vol.59, No.10, (1993), pp.1695-1700

[6] T. Shirakashi, T. Obikawa, H. Sasahara and T. Wada, *Journal of the Japan Society for Precision Engineering,* Vol.59, No.12, (1993), pp.2003-2008

[7] H. Sasahara, T. Obikawa and T. Shirakashi, *Journal of the Japan Society for Precision Engineering,* Vol.60, No.12, (1994), pp.1801-1805

[8] M. Mohammadpour, M.R. Razfar and R.J. Saffar, *Journal of Simulation Modelling Practice and Theory* Vol.18, (2010), pp.378-389

[9] H.A. Eltawahni, M. Hagino, K.Y. Benyounis, T. Inoue and A.G. Olabi, *Journal of Optics & Laser Technology,* Vol. 44, (2012) 1068-1082

[10] Eltawahni, H.A., Olabi, A.G., Benyounis, K.Y., *Journal of Materials & Design* Vol. 31. No8, (2010) 4029–4038.

[11] Eltawahni, H.A., Olabi, A.G., Benyounis, K.Y., *Journal of Optics and Laser Technology* Vol. 43, No. 3, (2011) 648–659

Machinability of Unwoven Fabric Material by End-mill

Hidetake Tanaka[1], Kyosuke Takabayashi[1]
[1]Sophia University

ABSTRACT

Recently, plastic materials e.g. composite, CFRP and fabric are widely used for structural materials for automotive and aviation industries. Especially, unwoven fabric materials are used for inner part materials of automobiles. Basically, the materials are fabricated as fabric material and formed by mold techniques. However nowadays, the unwoven fabrics are adopted in combination with composite materials in order to satisfy the demand of reduction of weight for energy saving. In such cased, making fastening holes and trimming cutting are required to combine the other parts. In addition, burrs are generated by molding process frequently due to their difficulties of workability. In order to improve the machinability, the authors tried to investigate the characteristics of machinability of the materials by use of flat end-mill. It deals with the possibility of automated deburring, trimming and boring process by end-mills. Thermo-plastic CFRP (3K-700 twill, 2mm in thickness) plates and 2 types of unwoven fabric materials (PA) were tested as helical milling and side cutting experiment. A high-speed steel end-mills with no helix angle were used. An air turbine spindle unit was used. In both cases, ultra-high speed cutting speed could improve the machinability. However, in the case of larger cutting depth, the cutting speed was decreasing due to the cutting force and insufficiency torque of the turbine, then burrs were generated with lower cutting speed. From the experimental result, burrs generation were suppressed from cutting speed 1,500m/min and more. It has been demonstrated that the ultra-high speed cutting with flat end-mill improves the machinability of composite materials.
Keywords: Unwoven fabric, Composite material, end-mill, CFRTP

1. Introduction

Recently, non-metallic synthesized plastic materials e.g. composite, CFRP and woven or unwoven fabric materials are widely used for structural materials for automotive and aviation industries. [1,2] Especially, unwoven fabric materials are used for inner part materials of automobiles and other transportations. The materials have typical specifications, which are light weight, high strength, easy to fabricate and functionalities. Basically, those materials are fabricated as synthesized plastic materials and formed by mold techniques. However nowadays, the unwoven fabrics are adopted in combination with composite materials in order to satisfy the demand of reduction of weight for energy saving and/or other functionalities. The entire shape of such materials are formed by molding, however additional machining processes are required. In such cases, making fastening holes and trimming cutting are required to combine the other parts. Conventional machining process are adopted for the post-processing of the materials. In addition, burrs are generated by molding process frequently due to their difficulties of workability and deburring process is also required to separate from the guiding runner part of molding. After the post processing by machining, the edge of machined workpieces could be fluffed and many uncut fibers are remained with inadequate cutting conditions. In order to improve the machinability, the authors tried to investigate the characteristics of machinability of the materials by use of end-mills. Especially, flat shaped end-mills made of high speed steel materials which enables to create more sharp cutting edge rather than the carbide materials are focused. And it is demonstrated that ultra-high speed machining process can improve the machinability of the materials to suppress generation of fluffing and burrs.

2. Unwoven fabric materials

Unwoven fabric materials are categorized as fabric materials however the structure of the material is quite different from the woven fabrics. Orientation and length of the fibre in the unwoven fabric materials are random. Basically, mechanical properties and functionality of an unwoven fabric material can be modified to satisfy the purpose of use nevertheless it fabricated with simple fiber material. The fibers in unwoven materials are entwined and fixed each other. The form of the materials is known as thin sheet and thick plate.

Base materials of unwoven fabric is not only synthetic plastics fibre but also natural fibres. Basic configuration of unwoven fabric consists of 3-dimensionally entwined fibres and voids. In other words, unwoven fabric is one of a porous material and the typical characteristics are known as follows;

- Moisturizing
- Soundproofing
- Dusting
- Lightweight
- Water absorption, liquid absorption
- Thermal insulation
- Liquid retention
- Impregnation
- Moisture permeation
- Bacteria prevention
- Impermeability
- Wiping and evaporation
- Safety and recyclability.

In the automotive industry field, the amount of use of unwoven fabric materials are rapidly increasing in order

to achieve soundproofing, thermal insulation, lightweight, high productivity and high cost-effective production of automobiles.

Primary fibres of unwoven fabric materials is synthetic thermo-plastic fibres as follows;
· Polyethylene terephthalate
· Polyethylene
· Polybutylene terephthalate
· Polypropylene
· Polyamide
· Polyurethane.

And part of the unwoven fabric applications in the automobiles are as follows;
· Engine hood cover
· Transmission tunnel
· Battery cover
· Oil filter
· Floor mat
· Floor lining
· Air bag cover
· Seat cushion
· Doors and side panels
· ABC pillars
· Ceiling
· Shelf
· Trunk cover
· Underbody
· Exhaust pipe cover

Recently, many composite materials such as CFRP are also used. Especially, CFRTP (Carbone Fibre Reinforced Therm-Plasic) is often used combining with unwoven fabric materials. [3]

3. Objectives

The applications of unwoven fabric for automobiles as well as other industrial products, drilling, trimming and finishing process by machining shall be required. In order to improve the machinability of such kind of materials, investigation of machinability by rotational cutting tools are required. In the study, Basic machining test was carried out and improvement of machinability in terms of ultra-high speed cutting was examined. The target materials are unwoven fabric as well as CFRTP.

4. Fundamental experiment 1

Once the authors had tried to cut an unwoven fabric and CFRTP with a conventional square end-mill under general cutting conditions as shown in table 1 with the experimental apparatus as shown in figure 1. The cutting experiment was carried out by use of a linear-motor high speed machining centre (Sodick Corp.; MC430L). A high-speed steel end-mill (Sanko Mfg. Co.) was used for unwoven fabric because the cutting edge of the high-speed steel tool is shaper than the cemented carbide. The rake angle of the high-speed steel tool is also large. On the other hand, a diamond sintered edge end-mill (Dijet Ind. Co.) is adopted for

CFRTP, because, machining of carbon fibre must cause severe cutting edge wear.

(a) Conventional cutting direction

(b) Climbing cutting direction
Figure 3CFRTP (Twill woven PAN fibre, Matrix: PA6)

Table 2. Cutting conditions for helical milling of unwoven fabric

No.	Cutting speed	Feed rate/rev	Eccentricity
1	377 m/min	0.25 mm	0.5 mm
2	377 m/min	0.5 mm	0.5 mm
3	377 m/min	1.0 mm	0.5 mm
4	754 m/min	0.25 mm	0.5 mm
5	754 m/min	0.5 mm	0.5 mm
6	754 m/min	1.0 mm	0.5 mm

Table 3. Experimental results of unwoven fabric

Table 4. Measurement results of diameter

(1)	(2)	(3)	(4)	(5)	(6)
4.038	3.809	3.553	4.019	3.853	3.649

Table 1. Cutting conditions for trimming experiment

No.	Cutting speed	Feed rate	Depth of cut
1	75.4 m/min	0.2 mm	1.5 mm
2	377 m/min	1.0 mm	1.5 mm

As shown in figure 2, which taken by a microscopy, tremendous fluffs, un-cut fibres and burrs are generated on both cases of unwoven fabric material. From the point of view of cutting direction, conventional cutting direction is suitable with lower cutting speed, however climbing cutting direction seems to be suitable in the case of higher cutting speed based on the visual inspection. Anyway huge fluff and burrs remained with lower cutting speed conditions.

(a) High-speed steel end-mill (b) Diamond sintered

(c) Experimental linear motor machining centre
Figure 1. Experimental apparatus

Vc: 377m/min   Vc: 75.4m/min
(a)   Conventional cutting direction

Vc: 75.4m/min   Vc: 377m/min
(b) Climbing cutting direction
Figure 2. Unwoven fabric (Fibre material classified)

CFRTP trimming experimental result is shown in figure 3. From the point of view of cutting direction, climbing cutting direction is suitable based on the visual inspection. Difference of cutting speed is not clear in the case of CFRTP.

5. Fundamental experiment 2

Drilling experiment was carried out for only unwoven fabric materials. Notice that the CFRTP drilling test results are reported by the author's past studies. [4]

The experimental apparatus was same as the fundamental experiment 1. In this case, helical milling technique was adopted to drill. A high-speed steed end-mill with 3mm in diameter was used. The cutting conditions are shown in table 2. The target diameter of drilled hole is set as 4mm.

Utilizing the helical milling, the drilling of unwoven fabric has been succeeded. Table 3 shows the drilled hole appearance visually inspected from entrance side. Fluffs, un-cut fibres and burrs are generated on the all cases. From the visual inspection, burrs and fluffs are generated in the case of lower cutting speed. Drilled hole diameter was measured by microscopic measurement instrument (NIKON Co. MM-800, Objective lens magnification: 10x) as shown in table 4. The deviation of measured diameter is quite large due to the adhesive fluff and uncut fibres. It is seemed that the tendency of drilled diameter is gradually small along to the feed rate.

The machinability of CFRTP trimming seems similar as the CFRTP drilling with the inclined planetary milling, which conducted by the authors past studies. [4] Therefore in the study, the authors decided to focus on the machinability of unwoven fabric materials only.

6. Ultra-high speed milling experiment

From the fundamental experimental result of unwoven fabric materials, machinability i.e. smooth finishing and fibre cutting ability is strongly depended on the cutting speed. And smooth cutting fibres without fluffs and burrs require sharp cutting edge with large

rake angle.

The authors tried to carry out an ultra-high speed milling experiment for the unwoven fabric material trimming process. An additional ultra-high speed spindle unit (Nakanishi Machinery Co. HTS1500S-M2040) was adopted to the experiment due to the maximum rotation speed of the machining centre is limited up to 40,000 min^{-1}. The ultra-high speed spindle unit as shown in figure 4 was pneumatic driven motor. The maximum output is 25W and max rotation speed is 150,000min^{-1}.
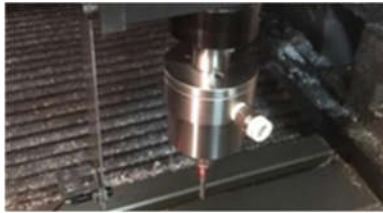
Figure 4. A pneumatic ultra-high speed spindle unit

A slotting end-mill without twist angle (2-flutes, high-speed steel, 4mm in diameter) is adopted as the cutting tool to achieve higher rake angle and sharpness of cutting edge as shown in figure 5. The cutting conditions are shown in table 5. Spindle speeds are set form 80,000min^{-1} to 150,000min^{-1} in order to achieve the cutting speed could be excess 1,000m/min at least. The cutting direction is climbing on the basis of the fundamental experimental result. The depth of cut is fixed in 1mm to prevent from the cutting speed reduction due to the friction and radial machining force. Even though the depth of cut is only 1mm, spindle speed could be approximately 10% decreased during machining.

Figure 6 shows the experimental result. The tendency of burrs and fluffs suppression is improved along to the increasing of cutting speed as shown in figure 6 visually. Especially, large size burrs of 1mm in length was not observed with the ultra-high speed machining. And from the point of view of feed rate per tooth, 0.1mm/min could obtain the smoothest trimming result throughout the 3 different feed rate conditions.

The cutting speed conditions having more than 1,000m/min can improve the machinability of unwoven fabric materials in the case of ultra-high speed machining process. It seems that too slow feed rate does not improve the machinability. The authors believe that lower feed rate with ultra-high speed cutting can generate higher machining heat and it might cause secondly burrs and fluffs. For the future work, high speed camera observation is required to clarify the burrs and fluffs suppression mechanism.

7. Concluding Remarks

Fundamental machining experiment with unwoven fabric materials and ultra-high speed machining experiment were carried out. From the experimental results, following concluding remarks are obtained.

(1) Ultra-high speed cutting process is suitable for the machining process of unwoven fabric materials

Figure 5. A slotting end-mill without twist angle

Table 5. Cutting conditions for ultra-high speed machining

Spindle speed (min^{-1})	Feed rate / tooth (mm)	Feed rate (m/min)	Cutting speed (m/min)	Depth of cut (mm)
80,000	0.025	4	1,005.3	1
	0.05	8		
	0.1	16		
100,000	0.025	5	1,256.6	1
	0.05	10		
	0.1	20		
120,000	0.025	6	1,508.0	1
	0.05	12		
	0.1	24		
150,000	0.025	7.5	1,885.0	1
	0.05	15		
	0.1	30		

Figure 6. Experimental result of ultra-high speed machining of unwoven fabric

(2) 1,000m/min or more cutting speed can improve the machinability and suppress the burrs and fluffs.

(3) Too slow feed rate does not improve the smoothness of trimming process.

References

[1] Kentaro Shima, *Development of functional unwoven fabric materials*, (2004) 4 – 14, CMC publishing. (in Japanese)

[2] Toray Industries Research Institute, *Recent trends in the nonwoven fabric market and technical product development*, (Referred date: 4th Feb. 2018) http://www.tbr.co.jp/pdf/trend/tre_a123.pdf

[3] Fukuzo Yagishita, *Machining of CFRP*, (2014), 14 – 33, The Nikkan Kogyo Shimbun, Ltd. (in Japanese)

[4] H. TANAKA, M. KITAMURA and T. SAI, *An Evaluation of Cutting Edge and Machinability of Inclined Planetary Motion Milling for Difficult-to-cut Materials*, Proc. CIRP, Vol. 35 (2015), pp. 96-100

Influence of Grinding Atmosphere on Grinding Characteristics of CFRP

Shingo Okazaki[1], Yifan Jiang[1], Hiroyuki Kodama[1], Hiroyuki Yoden[2] and Kazuhito Ohashi[1]

[1] Graduate School of Okayama University

3-1-1 Tsushima-naka, Kita-ku, Okayama, 700-8530, Japan

[2] Industrial Technology Center of Okayama Prefecture

5301 Haga, Kita-ku, Okayama, 701-1296, Japan

ABSTRACT

In this study, we investigated the influence of grinding atmosphere on grinding characteristics of CFRP by SEM observation of ground surfaces, analysis of grinding temperature and so on. The grinding temperature at wheel surface contact increases up to about 500°C in dry grinding however it increased up to about 200°C in wet grinding which has enough cooling ability by coolant. In addition, good grinding wheel surfaces could be generated at any wheel depth of cut in wet grinding. The transformations of carbon fiber and matrix resin on ground surface of CFRP under dry grinding are confirmed by SEM observation.

Keywords: CFRP, grinding, grinding temperature, grinding atmosphere

1. Introduction

CFRP (Carbon Fiber Reinforced Plastic) has not only very high specific strength and elastic modulus compared with any practical metal materials but also high corrosion resistance. Therefore, CFRP is used in the industries of aerospace and automobile and so on. However, CFRP is one of the difficult-to-cut materials because of the composite material consist of two opposite materials which are carbon fibers and thermoset resin. The material characteristics prevent the easy application of CFRP to many industrial fields. This study deals with the characteristics in grinding of CFRP which is expected to decrease the machining cost and to improve surface finish compared with cutting from a viewpoint of a tool wheel life. However, the heat generation during grinding process is a problem to high quality of CFRP parts because of poor heat resistance of matrix resin of CFRP.

The carbon fiber peeling at interfaces between matrix resin and carbon fibers due to the machining heat causes a deterioration of the surface quality in the grinding of CFRP. Therefore, the investigation of thermal influence at the grinding point of CFRP is very important for application of CFRP.

In the previous study, the measuring technique in the grinding temperature of grain at grinding point and that at wheel contact area of CFRP is developed based on the Seebeck effect, and influence of grinding atmosphere, in which dry grinding, wet grinding supplying water-soluble coolant on grinding temperature of CFRP is experimentally investigated. In addition, the ground surface characteristics, surface finish and grinding force ware analyzed in grinding of CFRP with each grinding atmosphere [1].

In this study, we investigated the effect of grinding atmosphere on grinding characteristics of CFRP by SEM observation of ground surfaces, grinding wheel surface, analysis of grinding temperature and so on.

2. Experimental procedure

Figure 1 shows a schematic of experimental setup for grinding tests. A vitrified bonded diamond wheel is selected for grinding tests of CFRP. CFRP in which carbon fibers are perpendicular to the ground surface (θ
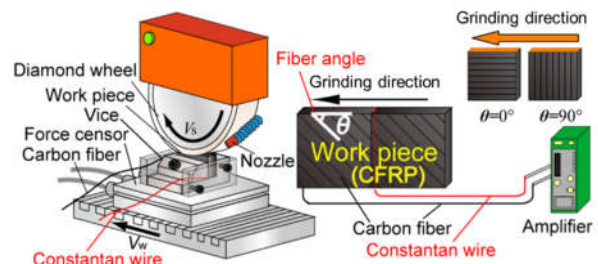
Fig. 1 Experimental setup and measuring system of grinding temperature

Table 1. Grinding conditions

Grinding wheel	SD23F75V(ϕ 250 × 10)
Workpiece	CFRP(UD)(θ = 0°, 90°) (20 × 20 × 5mm)
Grinding direction	Down-cut grinding
Periphheral wheel speed	V_S=23.6m/s
Workpiece speed	V_W=0.08m/s
Setting depth of cut	Δ = 40,100,200,400
Grinding atmosphere	Dry,Wet
Dressung/Truing	Rotary dresser (WA320/GC80)
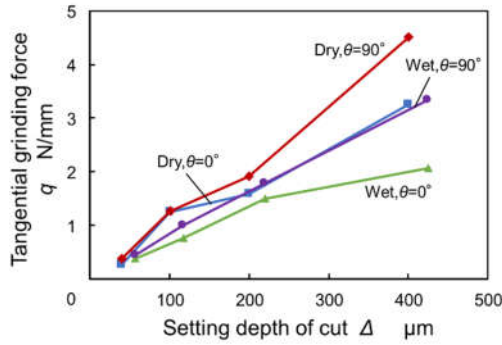
Fig. 2 Relationships between setting depth of cut and tangential grinding force

＝90°) or parallel to the ground surface (θ＝0°) is set to the vice. The grinding temperature is measured by the thermocouple consisting of a constantan wire (ϕ 0.13mm) coated with polyester film and carbon fibers. In addition, the electromotive force is calibrated based on K-type thermocouple [1,2]. Grinding force was measured with Kistler's quartz type force sensor, and ground surface roughnesses are measured with a stylus type surface roughness tester. Table 1 shows the main grinding conditions.

3. Results and discussions

3.1 Grinding force

Figures 2 and 3 show relationships between setting depth of cut and tangential grinding force or normal grinding force respectively. In each processing atmosphere, both of the tangential and the normal grinding force increase as the setting depth of cut increased. In addition, CFRP with the fiber angle of $\theta = 90°$ shows higher tangential grinding force than CFRP with fiber angle of $\theta = 0°$. It is considered that in the case of fiber angle of $\theta = 90°$, the tangential grinding force increases by fracturing force of carbon fibers perpendicularly to the grinding direction. The tangential force in wet grinding is smaller than that in dry grinding, by the lubrication effect of coolant.

3.2 Grinding temperature

Figure 4 shows an example of variation of grinding temperature at a point on CFRP surface by the developed CF-constantan thermocouple with DC amplifier (sampling rate 100Hz). Grinding temperature rapidly increases as soon as the grinding wheel contacts with the developed thermocouple on the surface of CFRP. After the point of maximum temperature, the temperature gradually decreases as the wheel passes through. The maximum value in the variation of temperature is defined as the grinding temperature at wheel contact area of CFRP (T_m) [1,2]. As a result, grinding temperature at wheel contact area of CFRP increases up to about 140ºC in dry grinding. Therefore, the result suggests that the surface of CFRP is exposed

to severe-time thermal environment for a moment in grinding process.

Figure 5 shows relationships between the setting depth of cut and the grinding temperature at wheel contact area of CFRP in the dry or wet grinding. In both grinding atmospheres, the grinding temperature at wheel contact area of CFRP increases with increasing setting depth of cut. The grinding temperature under wet grinding increases gradually rather than under dry grinding. It is considered that the CFRP surface is cooled effectively by the coolant. From these results, it is considered that the influence of grinding heat on the matrix resin of CFRP in wet grinding is smaller than dry grinding. The higher grinding temperature is caused by the larger tangential grinding force at the fiber angle of $\theta = 90°$ as shown in Fig. 2.

3.3 Wheel surface

Figures 6 and 7 show the photos of wheel surface after
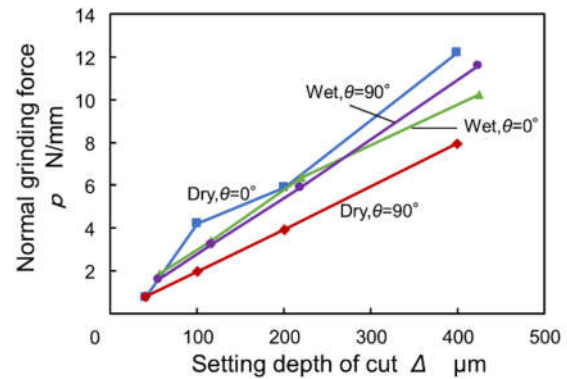
Fig.3 Relationships between setting depth of cut and

normal grinding force
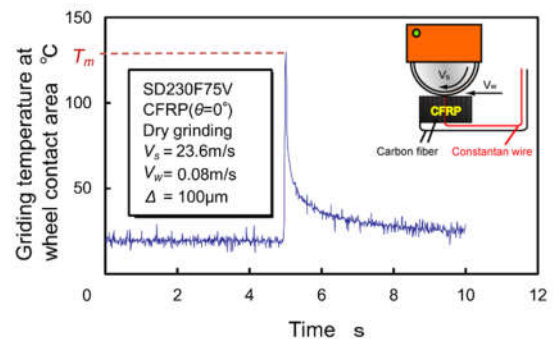
Fig. 4 The example measured grinding temperature at wheel contact area of CFRP
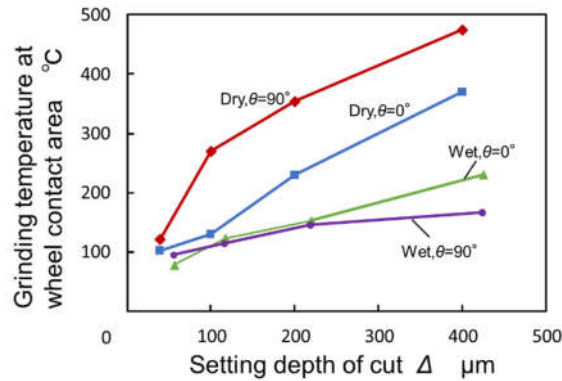
Fig. 5 Grinding temperature at wheel contact area

grinding with each setting depth of cut. In dry grinding, chips of CFRP can be confirmed even in the case of 40μm in setting depth of cut. Also, most wheel surface is covered with chips of CFRP in the case of 400μm in setting depth of cut. However, there exist little chips of CFRP on the wheel surface at both 40μm and 400μm in setting depth of cut in wet grinding. Most abrasive grains appear on the wheel surface, and such result suggests that the grinding ability of diamond wheel is kept in wet grinding of CFRP. Furthermore, some carbon fiber chips can be confirmed on the wheel surface at the fiber angle of $\theta = 0°$, however they cannot be confirmed at the fiber
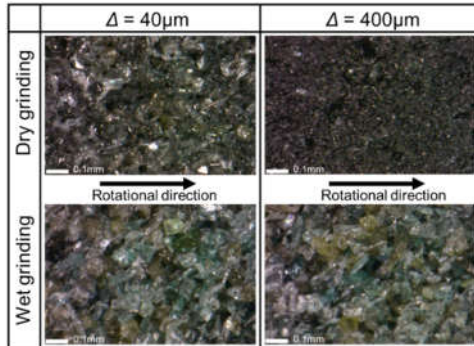
Fig. 6 Wheel surfaces after grinding (fiber angle of θ=0°)
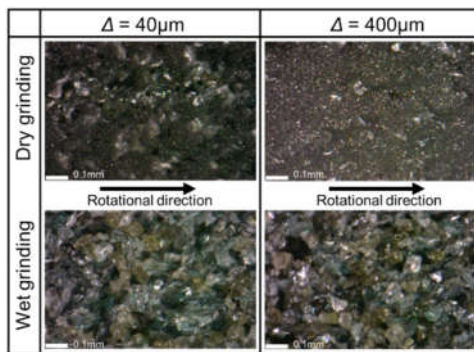
Fig. 7 Wheel surfaces after grinding (fiber angle of θ=90°)

angle of $\theta = 90°$. At the fiber angle of $\theta = 90°$, from the observations as shown in the photos of wheel surface, it is considered that the carbon chips of CFRP fracturs to small pieces by interference of abrasive grains because the carbon fibers exist perpendicularly to the grinding surface.

3.4 Ground surface quality

Figures 8 and 9 show SEM photos of ground surface after grinding with 40μm and 400μm in the setting depth of cut respectively. In the case of 40μm in the set grinding depth cut in dry grinding, there is a matrix resin between the carbon fibers, and the carbon fibers seem to be hold by matrix resin on ground surface. However, in the case of 400μm in the setting depth of cut, the matrix resin between the carbon fibers are thermally decomposed, and the bonding of fibers seems to be weakened. It can be considered that the matrix resin is thermally decomposed because the grinding temperature at wheel contact area is higher on setting depth of 400μm than 40μm as shown in Fig. 5. Thermal decomposition of the matrix resin in wet grinding could not occur at any setting depth of cut, and the resin between fibers is also confirmed. It is considered that the evaporation of the matrix resin could be reduced because the grinding temperature at wheel contact area of wet grinding is lower than dry grinding. However, much damage to carbon fibers in wet grinding occurred than that of dry grinding. This is considered that CFRP is quenched and its heat shrinkage is caused due to the cooling effect of coolant. The grinding temperature of grain at grinding point is not significantly different between dry grinding and wet grinding in previous studies [3,4], so the carbon fiber becomes very high temperature instantaneously. In addition, it is thought that it is rapidly cooled down by the coolant just after interference of grains in wet grinding. Although the amount of shrinkage varies depending on the content of carbon fiber and the type of matrix resin, since there are cases of shrinkage due to temperature, it is considered that the damage of carbon fibers on wet grinding surface is the effect of heat shrinkage [5, 6].
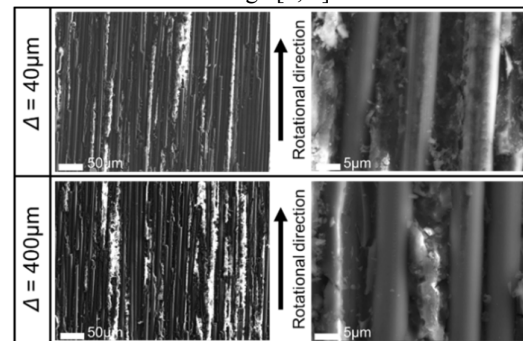
Fig. 8 Ground surfaces by dry grinding
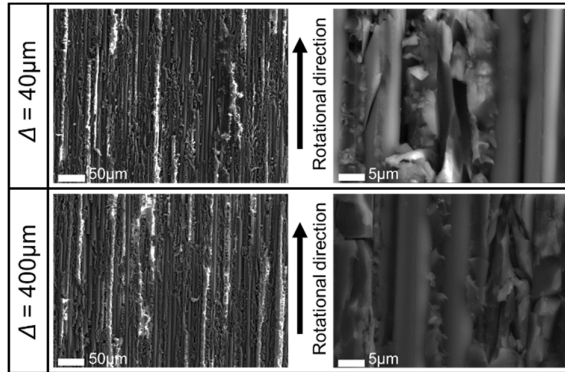
Fig. 9 Ground surfaces by wet grinding

3.5 Ground surface roughness

Figures 10 and 11 show the relationships between the setting depth of cut and the ground surface roughness Ra and Rz. The variations of surface roughness Ra and Rz with the setting depth of cut show similar tendencies. In dry grinding of fiber angle of θ=0°, both grinding surface roughness Ra and Rz tend to increase with an increase in the setting depth of cut. In wet grinding of fiber angle of θ=0°, both surface roughnesses don't vary at any setting depth of cut. Grinding temperature at wheel contact area in dry grinding is higher than that of wet grinding, therefore the matrix resin on ground surface evaporates. The ground surfaces of CFRP with carbon fibers parallel
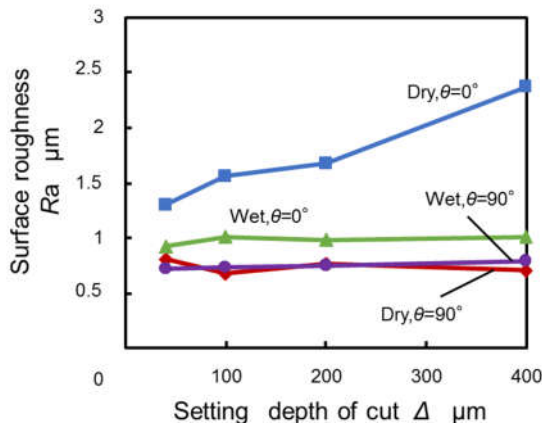
Fig. 10 Relationships between setting depth of cut and the ground surface roughness of Ra
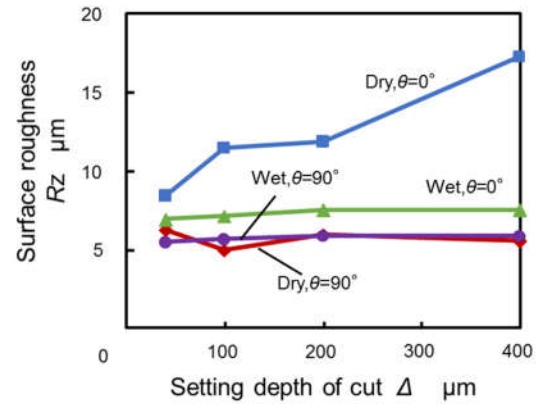
Fig. 11 Relationships between setting depth of cut and the ground surface roughness of Rz

to ground surface, θ=0°, almost consist of carbon fibers in dry grinding because of evaporation of matrix resin. Most fibers are removed after the fracture by interference of abrasive grain. As the results, the surface roughnesses Rz are larger than 7μm as the fiber diameter, and Rz increases up to the several times of fiber diameter in dry grinding. As mentioned above in 3.3, although damage in carbon fiber is concerned in the wet grinding, the damage of carbon fibers doesn't affect on the ground surface roughness. As the results, the wet grinding can reduce the evaporation of the matrix resin due to the cooling effect of the coolant and a good ground surfaces can be generated. The surface roughness Rz are smaller than the fiber diameter 7μm at any setting depth of cut.

4. Conclusion

In this study, we investigated of the influence in grinding atmosphere of CFRP. The main results obtained are as follows:

(1) The influence of grinding heat on the matrix resin is reduced in the wet grinding.

(2) The grinding temperature at the fiber angle of θ = 90° is higher than that of fiber angle of θ = 0°.

(3) CFRP chips adhere on wheel surface at more than 40μm in the setting depth cut in dry grinding. However, the wet grinding prevents the adhesion even with the setting depth of 400μm to perform higher grinding ability than dry grinding.

(4) At the fiber angle of θ=0°, the thermal decomposition of the matrix resin, which makes the fiber bonding weak to lead the increase of surface roughness, occurs on the ground surface with the setting depth of 400μm in the dry grinding. However, the thermal decomposition of the matrix resin does not occur at the setting depth of 400μm in wet grinding.

(5) There exists much damage on carbon fibers at ground surface in wet grinding rather than dry grinding.

(6) Ground surface roughness increases with increasing the setting depth of cut in dry grinding, however the surface roughness in wet grinding doesn't depend on the setting depth of cut and is smaller than that of dry grinding. The wet grinding is suitable for fine surface quality.

Acknowledge

References

[1] K. Ohashi, H. Maeno, R. Fujihara, S. Kubota, M. Yoshikawa, S. Tsukamoto, Influence of Grinding Atmosphere on Grinding Characteristics of CFRP (Effect of Soluble Coolant or Liquid Nitrogen Supply), Transactions of the Japan Society of Mechanical Engineers, Series C, Vol.79, No. 808 (2013) 543-553 (in Japanese).

[2] S. Tsukamoto, K. Ohashi, T. Fujiwara, Measurement Technology of Grinding - the Latest Measurement Technology and its Know-How, Yokendo, (2005) 49-66 (in Japanese).

[3] R. Fujiwara, K. Ohashi, M. Yoshikawa, S. Kubota, T. Onishi S. Tsukamoto, Investigation of Grinding Temperature of Carbon Fiber Reinforced Plastics, Proceedings of the 7th International Conference on Leading Edge Manufacturing in 21st Century, (2013) 103-106

[4] R. Tani, K. Ohashi, M. Yoshikawa, S. Kubota, S. Tsukamoto, Investigation of thermal environment at grinding point of CFRP, Proceedings of the 8th International Conference on Leading Edge Manufacturing in 21st Century (LEM21), E38(2015)

[5] M. Takeno, S. Nishijima, T. Okada, K. Fujioka, Y. Kuraoka Thermal and Mechanical Properties of Advanced Composite Materials at Low Temperatures, Cryogenics and Superconductivity Society of Japan Vol. 21 No. 3 (1986) 182-187 (in Japanese)

[6] E. Yasuda, Y. Tanabe, H. Machino, S. Kimura, Thermal Expansion Behaviour of Carbon Fiber Reinforced Thermosetting Plastics during Carbonization, The Carbon Society of Japan TANSO Volume 1988 Issue 135 (1988) 275-277 (in Japanese)

Cutting Force Changes During One Cut in end Milling with a Throw-away Insert - Difference between Up-cut and Down-cut

Kota Matsuda[1], Ryutaro Tanaka[1], Katsuhiko Sekiya[1], Keiji Yamada[1]
[1] Graduate School of Engineering, Hiroshima University
1-4-1 Kagamiyama, Higashi-Hiroshima City, Hiroshima, 739-8527, Japan

ABSTRACT

In this study, the transition of cutting force in the tangential and radial direction during one cut was investigated in milling of AISI-1045, AISI-304, and Ti-6Al-4V with a TiN coated carbide throw-away insert. In the case of 1045 and Ti-6Al-4V, there was not obvious difference in tangential forces between up-cut and down-cut. However, up-cut showed larger radial force than down-cut in any material. In down-cut, tangential force showed almost the same regardless of radial depth of cut. 304 and Ti-6Al-4V caused larger radial force with the increase of radial depth of cut at the same cut chip thickness.

1. Introduction

In order to reduce both of size and weight of industrial products, the shape of these parts becomes complicated to consolidate multiple parts, as a result, high precision machining for high strength material has been required. To keep accuracy of product, the machining such as end milling supported CAM and CAD is performed. In the NC program creating process, cutting resistance is calculated by cutting simulation software. Then, tool deflection and work material deformation are calculated and program correction is carried out. Because the cutting thickness changes during one cut in intermittent cutting, the cutting state constantly changes. However, when measuring the cutting force and the cutting temperature, it is common to use only the maximum value during one cut as an evaluation value. R. Tanaka [1] have reported that the transition in cutting temperature during one cut in end milling. there is a difference in cutting temperature at the moment of the same cutting position in up-cut and down-cut. Therefore, it is thought that not only the maximum value of the cutting characteristic but also its transition during one cut is important. In this study, the transition of cutting force in tangential and radial direction during one cut was investigated in end milling of carbon steel AISI-1045, austenitic stainless AISI-304, and titanium alloy Ti-6Al-4V with a TiN coated carbide throw-away insert under dry conditions.

2. Experimental method

In this study, the work material was fixed on a table of machining center via a piezoelectric element type tool dynamometer, and side cutting was performed using the throw away insert. The output voltage from a tool dynamometer was output to the digital oscilloscope through a charge amplifier and recorded. The measured cutting force F_x, F_y converted into tangential force F_c and radial force F_n.

Figure 1 shows the relation between cutting position and uncut chip thickness. As for cutting position, rotation angle was 0 at the position where uncut chip thickness is 0. Up-cut starts at the position where uncut chip thickness is 0 and ends at the position where uncut

chip thickness shows maximum. In the opposite, down-cut starts at the position where uncut chip thickness shows maximum and ends at the position where uncut chip thickness is 0. In this study, feed rate f is enough small compared to the tool diameter D. Therefore, the uncut chip thickness t can be approximated by the equation (1).

$$t = f \sin\theta \qquad ((1)$$

In up-cut, F_c and F_n are expressed by following equations.

$$F_c = F_x \sin\theta + F_y \cos\theta \qquad ((2)$$

$$F_n = - F_x \cos\theta + F_y \sin\theta \qquad ((3)$$

(a) up-cut   (b) down-cut
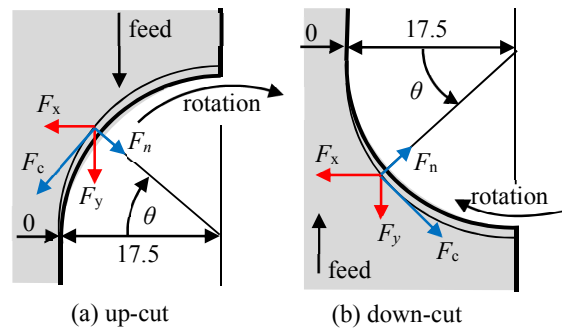
Fig. 1 Rotation angle of cutting position and uncut thickness in up-cut and down-cut

Table 1 Cutting conditions

Work material	AISI-1045, AISI-304, Ti-6Al-4V
Tool holder	KYOCERA MTES335
Insert	TiN coated carbide TEEN1603PETR1
Tool diameter, D	35 mm
Cutting speed, v	150 m/min
Feed rate, f	0.1 mm/rev
Radial rake	0 °
Axial rake	+15 °
Radial depth of cut, R_d	1.5, 7.0, 17.5 mm
Axial depth of cut, A_d	1.0 mm
Cutting direction	up-cut, down-cut
Cutting atmosphere	dry cutting

In down-cut, F_c and F_n are expressed by following equations.

$$F_c = - F_x \sin\theta + F_y \cos\theta \qquad ((4)$$

$$F_n = - F_x \cos\theta - F_y \sin\theta \qquad ((5)$$

Table 1 shows the cutting conditions. The used tool holder and insert was KYOCERA MTES335 and TiN coated carbide TEEN1603PETR1, respectively. Only one insert was attached on the holder. Cutting speed was 150 m/min. Feed rate was 0.1 mm/rev. Radial depth of cut was 1.5 mm, 7.0 mm and 17.5 mm. Axial depth of cut was 1 mm. AISI-1045, AISI-304 and Ti-6Al-4V were used as a work material. Milling was conducted on up-cut and down-cut under dry condition. In this experiment, the axial rake is 15° and the radial rake is 0°, therefore it can be seen as an oblique cutting with the oblique angle is 15° and rake angle is 0° expect for the corner part. In this study, for the simplification of the analysis, it is treated as orthogonal cutting.

3. Experimental results

3.1 Difference in repeatability of cutting force

v=150 m/min, f=0.1 mm/rev,
A_d=1.0mm, R_d=17.5mm
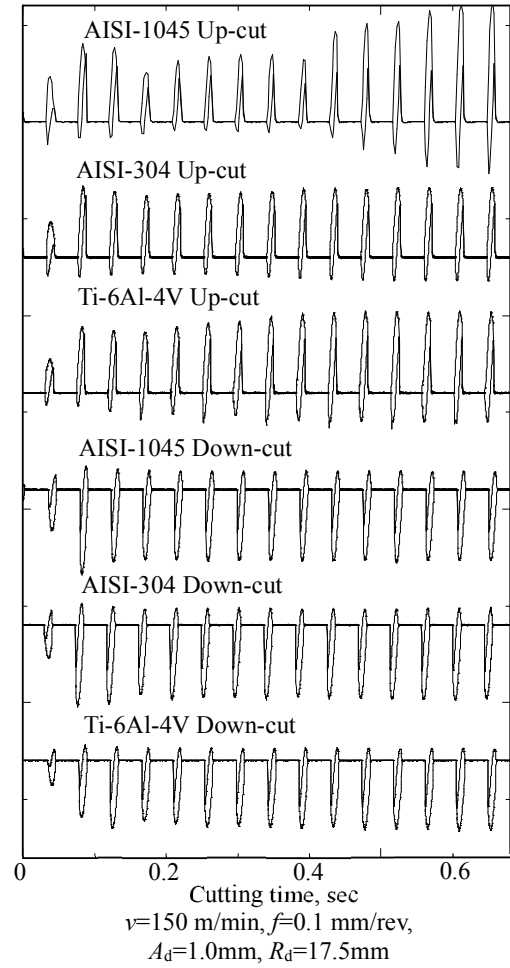
Fig. 2 Cutting force during one process for each material
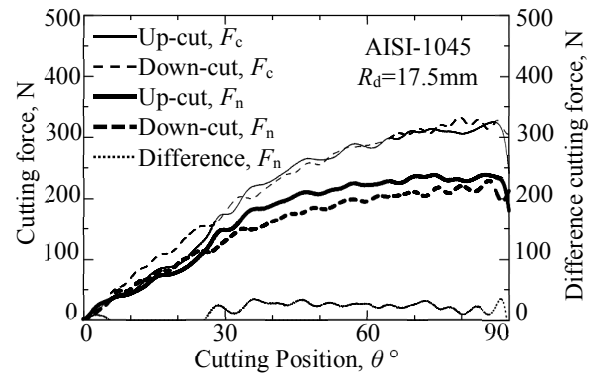
Fig. 3 Transition of cutting force during one cut in up-cut and down-cut, and difference F_n between up-cut and down-cut for AISI-1045
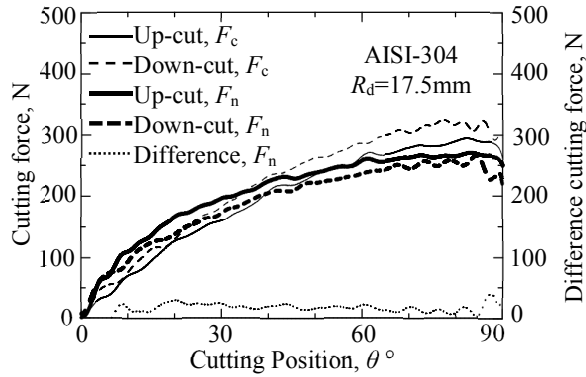
Fig. 4 Transition of cutting force during one cut in up-cut and down-cut, and difference F_n between up-cut and down-cut for AISI-304
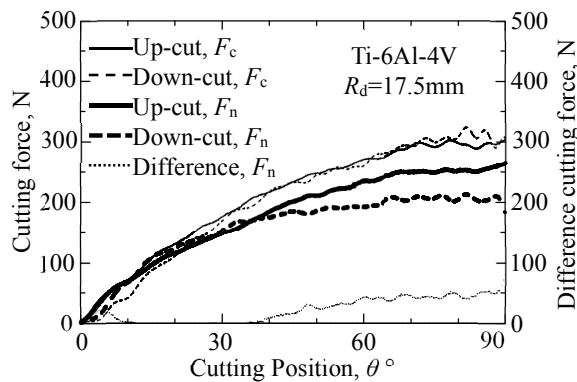
Fig. 5 Transition of cutting force during one cut in up-cut and down-cut, and difference F_n between up-cut and down-cut for Ti-6Al-4V

Figure 2 shows the cutting force during one process for each material. The two lines in each condition show cutting force F_x and F_y. In this experiment, one process consists of 15 times intermittent cutting. On the calculation, the cutting force output pattern should be repeated. However, in up-cut of all material, the amplitude of measured pattern gradually increased from the beginning of cut. Therefore, cutting force output in beginning of cut was used in discussing about the difference between up-cut and down-cut.

3.2 Difference of cutting force transition between up-cut and down-cut

Figure 3 shows the transition of cutting force during one cut in up-cut and down-cut for AISI-1045. Comparing the cutting force of the same cutting position, there was not obvious difference in tangential force F_c between up-cut and down-cut. However, up-cut caused larger radial force F_n than down-cut over the rotation position 30°.

Figure 4 shows the transition of cutting force during one cut in up-cut and down-cut for AISI-304. F_c in up-cut was slightly smaller than that in down-cut. On the other hand, F_n in up-cut was slightly larger than that in down-cut at any cutting position.

Figure 5 shows the transition of cutting force during

one cut in up-cut and down-cut for Ti-6Al-4V. there was not obvious difference in tangential force F_c between up-cut and down-cut. However, up-cut caused larger radial force F_n than down-cut over the cutting position 30°. The difference in F_n was larger at the larger cutting position θ.
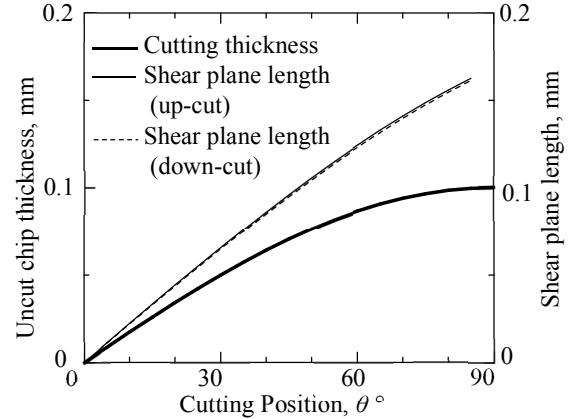
Fig. 6 Uncut chip thickness and calculated shear plane length at any cutting position

Figure 6 shows the uncut chip thickness and calculated shear plane length at any cutting position. The cutting direction of up-cut and down-cut are opposite, so the chip uncut work material thickness distribution in front of cutting edge is different even at the same cutting position. If both the shear angle and shear stress is same in up-cut and down-cut, the shear place length becomes different, as a result cutting force should be different. Therefore, the calculate shear place length in up-cut and down-cut were obtained assuming the shear angle was 30°. This shear angle was investigated experimentally by Nakayama [2]. The calculated shear plane length in up-cut was slightly larger than that in down-cut. However, the difference was less than 1.5%. therefore, it is thought that there are some factors other than geometric factor.
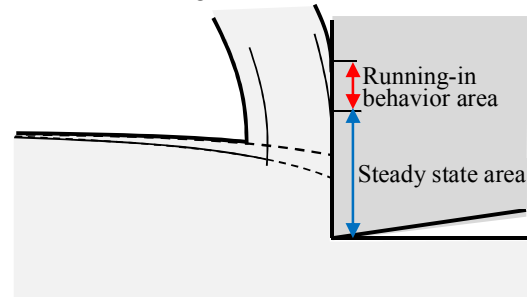
Fig. 7 Image of tool-work material contact in up-cut

Figure 7 shows the image of tool-work material contact in up-cut. In down-cut, the uncut chip thickness gradually decreases from the beginning of cut. So, contact length never increases during one cut. On the other hand, in up-cut, the uncut chip thickness gradually increases constantly from the beginning of cut. Accordingly, new contact surface always occurs constantly. In the friction test such as ball on disk test,

the steady state appeases after running-in behavior where the friction coefficient becomes high [4]. In down-cut, the running-in behavior occurs only at the beginning of cut and the steady state area gradually decreases. In up-cut, the steady state area gradually increases and the running-in behavior area always exists. The change rate of uncut chip thickness shows f $\cos\theta$, this rate is larger in smaller θ. Therefore, in the case of AISI-304, the cause of difference in F_n is thought the running-in behavior. As for AISI-1045 and Ti-6Al-4V, the difference increased with cutting time. Therefore, it thought that the tool-work affinity increased with contact time.

3.3 Influence of radial depth of cut on radial force in down-cut
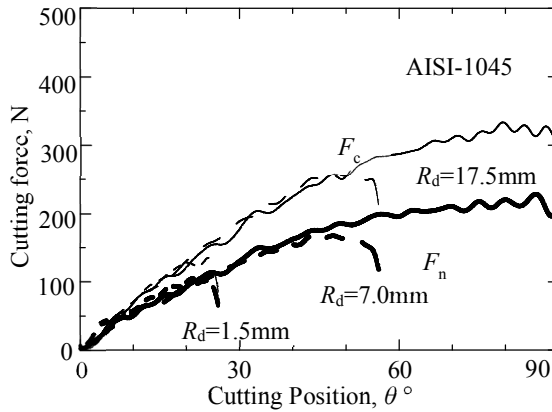
Fig. 8 Transition of cutting force during one cut in down-cut for AISI-1045 at different radial depth of cut

Figure 8 shows the transition of cutting force during one cut in down-cut for AISI-1045 in different radial depth of cut. Both tangential force F_c and radial force F_n showed almost the same regardless of radial depth of cut.

Figure 9 shows the transition of cutting force during one cut in down-cut for AISI-304 in different radial depth of cut. F_c showed almost the same regardless of radial depth of cut. The larger R_d caused larger F_n at the same cutting position.
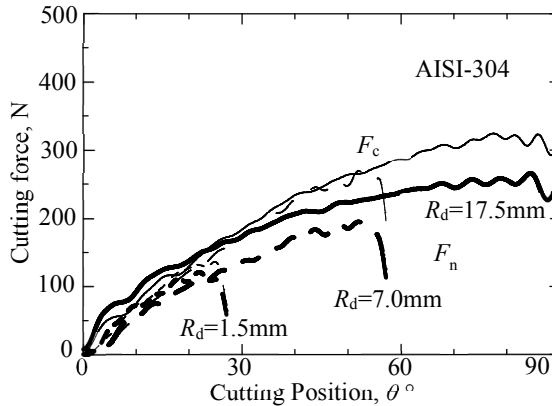
Fig. 9 Transition of cutting force during one cut in down-cut for AISI-304 at different radial depth of cut

Figure 10 shows the transition of cutting force during one cut in down-cut for Ti-6Al-4V in different radial depth of cut. F_c showed almost the same regardless of radial depth of cut. The larger R_d caused larger F_n at the same cutting position. This tendency was clearer than AISI-304.
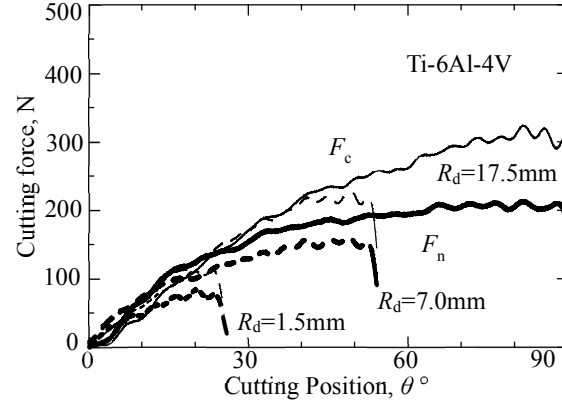
Fig. 10 Transition of cutting force during one cut in down-cut for Ti-6Al-4V at different radial depth of cut

With the obtained results, the difference in radial force F_n at the same tangential force F_c was discussed.

Figure 11 shows the geometric relationship of forces acting on tool rake face and shear plane. In this experiment, since the rake angle is 0°, F_c is equal to the rake face vertical force and F_n is equal to the frictional force on rake face. It is assumed that the shear stress at the shear plane is the same value at the same cutting conditions. If the frictional force on rake face is F_n, the shear force at the shear plane is expressed by the equation (6).

$$F_s = F_c \cos\phi - F_n \sin\phi \qquad ((6)$$

Considering the case where the shear angle and F_c do not change and only F_n increases by dF_n in a very short time, the shear force at the shear plane after dF_n increased Fs' is expressed by the equation (7).

$$F_{s'} = F_c \cos\phi - (F_n + dF_n) \sin\phi \qquad ((7)$$

However, because the shear plane area does not change and $F_{s'}$ becomes smaller than F_s, the shear stress after d F_n increase becomes smaller than that before after d F_n increase. The assumption that the shear stress at the shear plane is the same value at the same cutting conditions is not true. In order to make this assumption, it is necessary to decrease the shear angle. For the shear stress at the shear plane to be equal, the shear angle decreases by $d\phi$ and the following equation (4) must complete.

$$\sin(\phi - d\phi)\{F_c \cos(\phi - d\phi) - (F_n + dF_n)\sin(\phi - d\phi)\}$$
$$= \sin\phi \, (F_c\cos\phi - F_n \sin\phi) \qquad ((8)$$
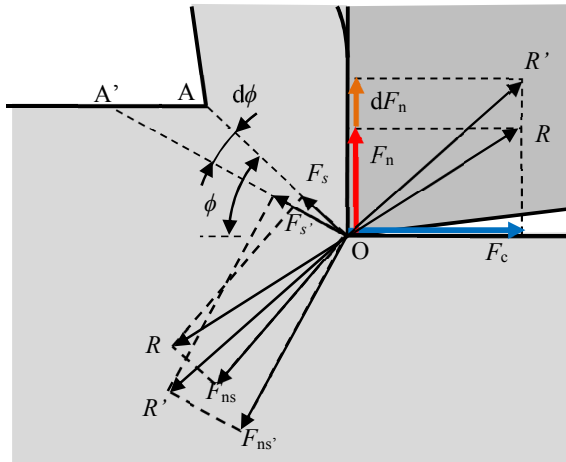
Fig. 11 Geometric relationship of forces acting on tool rake face and shear plane

Therefore, when only friction on the rake face increases, only F_n increases on the calculation. The influence of friction on the rake face is thought the cause of the difference in radial force F_n at the same tangential force F_c.

4. Conclusions

In this study, the transition of cutting resistance during one cut was investigated in end milling of carbon steel AISI-1045, stainless steel AISI-304, and titanium alloy Ti-6Al-4V with a TiN coated carbide throw away insert under dry condition. The results of this study can be summarized as follows:

1) The amplitude of measured pattern gradually increased from the beginning of cut in 15 times continuous cutting in up-cut.

2) There was not obvious difference in tangential force between up-cut and down-cut. However, up-cut caused larger radial force than down-cut.

3) In down-cut of AISI-304 and Ti-6Al-4V, tangential force showed almost the same at the same uncut chip thickness regardless of radial depth of cut. The larger radial depth of cut caused larger radial force at the same uncut chip thickness.

References

[1] R. Tanaka, A. Hosokawa, T. Furumoto, M. Okada and T. Ueda: Influence of cutting fluid on tool edge temperature in end milling titanium alloy, Journal of Advanced Mechanical Design, Systems, and Manufacturing Vol.9, No.5, (2015) p.JAMDSM0074.

[2] K.Nakayama, M.Arai, On the Storage of Data on Metal Cutting Forces, Annals of the CIRP Vol.25, (1976), p.13.

[3] Jiaren Jiang, R.D.Arnell, On the running-in behavior of diamond-like carbon coatings under the ball-on-disk contact geometry, Wear Vol.217, (1998), p190.

Effect of Cutting Liquids on Tool Wear in Turning of Sintered Steel

Hideo Takino[1], Masashi Ota[1], Shutaro Yamamoto[2]

[1]Chiba Institute of Technology

2-17-1 Tsudanuma, Narashino, Chiba 275-0016, Japan

[2]NEOS Company Limited

1-1 Oikemachi, Konan, Shiga 520-3213, Japan

ABSTRACT

The effectiveness of various cutting liquids on the reduction of tool wear in the turning of sintered steel was investigated. The workpieces were impregnated with the cutting liquids under a reduced-pressure environment before turning. It was found that the cutting liquids containing water caused a large amount of tool wear. Such tool wear may have resulted from the oxidation of the workpiece surface and the tool at the cutting point. Using a mineral oil as the cutting liquid had a small effect on reducing tool wear. This reduction probably resulted from the lubrication effect of the mineral oil.

1. Introduction

Sintered steel parts are manufactured by the following steps. Metal powders with a specific ratio are mixed, pressed with a mold, and then heated in a furnace [1, 2]. Thus, the productivity of sintered steel parts is higher than that of mechanically machined parts. For this reason, sintered steel parts are widely used as the mechanical parts of mass-produced machines such as automobiles.

To produce sintered steel parts with high accuracy, secondary processing is generally conducted, in which cutting processes, such as milling and turning, are effectively performed. However, the cutting tool used in the secondary processing is prone to wear; one reason for this is considered to be that the cutting tool is affected by the micro-pores existing in sintered steel parts. Thus, many experimental studies dealing with the tool wear in the machining of sintered steel have been conducted [3-6]. However, few reports are available on the effect of cutting liquids on the tool wear in the machining of sintered steel [7, 8].

In this study, we investigate the effectiveness of various cutting liquids on the machining of sintered steel parts. In particular, we focus on the tool wear in the turning process. In our experiment, sintered steel workpieces are impregnated with a cutting liquid before turning. This ensures the supply of the cutting liquid to the cutting point more easily than by its external supply. The workpieces impregnated with various cutting liquids are turned with a cermet tool. We discuss the effectiveness of each cutting liquid for reducing the tool wear in this study.

2. Experimental

The side surface of a cylindrical workpiece made from sintered steel was turned as shown in Fig. 1. After the turning, the flank wear of the tip of the cutting tool was examined with an optical microscope. We investigated the change in the tool wear with increasing cutting distance. The workpieces were impregnated with various cutting liquids before turning to investigate the effectiveness of each cutting liquid. The experimental method and conditions are described in detail as follows.
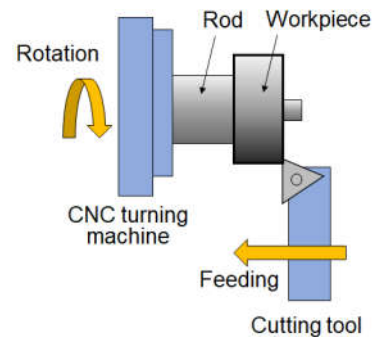
Fig. 1. Method of turning workpiece. The side surface of the cylindrical workpiece made from sintered steel was turned.

2.1 Workpieces

The workpieces were sintered steel cylinders with a height of 20 mm and a diameter of 40 mm. Each workpiece had a hole at its center so that it could be fixed to a computer numerical control (CNC) turning machine using a rod as shown in Fig. 1.

The chemical components of the sintered steel are shown in Table 1. The Rockwell hardness of the workpieces was 72 and their density was 6.8 g/cm^3.

Table 1. Chemical components of sintered steel. The remainder of the steel is Fe.

Cu	C	Mn
1.5%	0.85%	0.13%
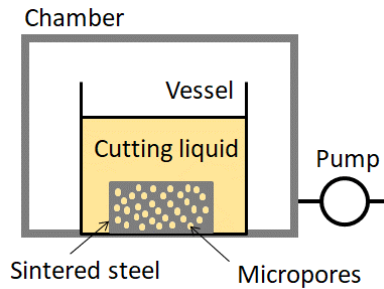
Fig. 2. Method of impregnating sintered steel with cutting liquid. The impregnation was conducted under a reduced-pressure environment to fill the micropores with the cutting liquid by drawing air from the micropores.

Before the cutting experiment, the workpieces were impregnated with various cutting liquids under a reduced-pressure environment as follows. As shown in Fig. 2, the workpiece was placed in a cutting liquid in a vessel, which was installed in a chamber. The pressure of the chamber was reduced to 80 kPa using a pump. As a result, the air in the micropores in the workpiece was released to the cutting liquid, which led to the injection of the cutting liquid into the micropores to replace the air. The filling of the micropores with the cutting liquid was confirmed by measuring the weight of the workpiece before and after the impregnation process.

2.2 Cutting Conditions

The material of the cutting tool was cermet (Sumitomo Electric Hardmetal Corporation, T1000A), the main chemical component of which is TiCN, in which Co and Ni are used as binders for TiCN grains. The cutting tool was triangular without a chip breaker, and the radius of its nose part was 0.4 mm. The cutting tool was not coated.

The turning machine used in this experiment was a CNC turning machine (Okuma Corporation, Space Turn LB3000EX). The depth of cut and feed rate were 0.3 mm and 0.08 mm/rev, respectively. The cutting speed was maintained at 200 m/min during the cutting process by controlling the rotation speed of the workpiece through a computer numerical controller. The side surface of the workpiece was turned repeatedly to achieve a specific cutting distance; the maximum cutting distance was 1.6 km.

3. Experiment using Water-Based Cutting Liquid

3.1 Water-Soluble Cutting Liquid

The workpieces impregnated with a water-soluble cutting liquid were turned. The water-soluble cutting liquid used in this experiment was prepared by diluting a commercially available stock liquid (NEOS Company Limited, Finecut R-5000HPA) with tap water to a concentration of 5%.

The experimental results for the change in tool wear are

shown in Fig. 3, in which the tool wear for turning
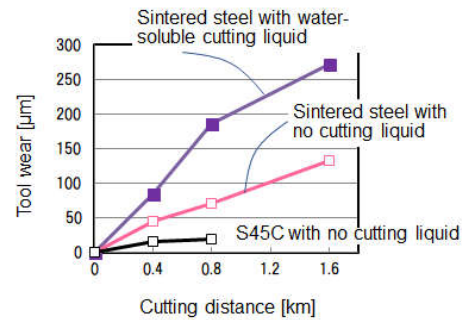
Fig. 3. Change in tool wear with increasing cutting distance for sintered steel using water-soluble cutting liquid, no cutting liquid, and S45C without cutting liquid.

without the impregnation of the cutting liquid is also shown. Moreover, the tool wear for the turning an S45C carbon steel ingot, as defined by Japan Industrial Standards, without the cutting liquid is also shown for comparison. As shown in Fig. 3, the tool wear when using the water-soluble cutting liquid is larger than that without the cutting liquid. We expected less tool wear when using the water-soluble cutting liquid owing to its cooling and lubricating effects, but the experimental results showed the opposite behavior.

3.2 Effect of Tap Water

Since the water-soluble cutting liquid used in our study was the liquid diluted with tap water to obtain a concentration of 5%, its main component was tap water. Thus, we assumed that one cause of the tool wear was the supply of tap water to the cutting point. Thus, to investigate the effect of the tap water, the workpiece was impregnated with only tap water and then turned. Figure 4 shows the experimental results for the tool wear. As shown in this figure, the tool wear for the use of tap water was relatively similar to that for the use of the water-soluble cutting liquid. Thus, when the water-soluble cutting liquid is used, the water at the cutting point may cause a chemical reaction, such as oxidation, to wear the tip of the cutting tool.

3.3 Addition of pH Control Agent to Tap Water

With the aim of preventing the chemical reaction at the cutting point, we examined the effect of adding a pH control agent to the tap water used as a cutting liquid. Generally, in an alkali aqueous solution, passive films can be formed on Fe, Co, and Ni. Therefore, if passive films are successfully formed on the workpiece and tool surfaces, it
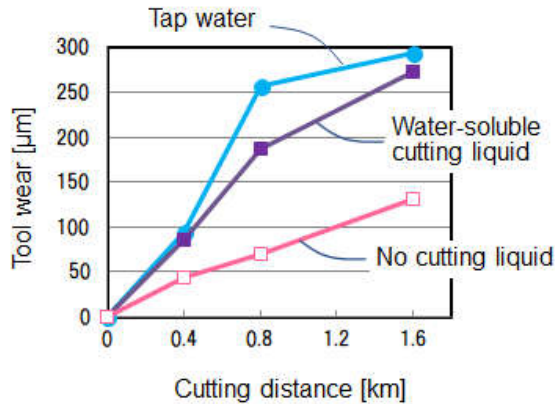
Fig. 4. Change in tool wear with increasing cutting distance for sintered steel using tap water, water-soluble cutting liquid, and no cutting liquid.

will be possible to prevent the oxidation of the workpiece and tool, which will reduce tool wear. Thus, the concentration of the pH control agent was set to 5% in this study, which increased the pH of the tap water to an alkali value of more than pH12.

The experimental results when using the water with the pH control agent as a cutting liquid are shown in Fig. 5. As shown in this figure, the addition of the pH control agent reduces the tool wear, as we expected. Thus, for the water-soluble cutting liquid, the tool wear may result from the oxidation of the workpiece surface and the tool at the cutting point.

4. Experiment using Mineral Oil Cutting Liquid
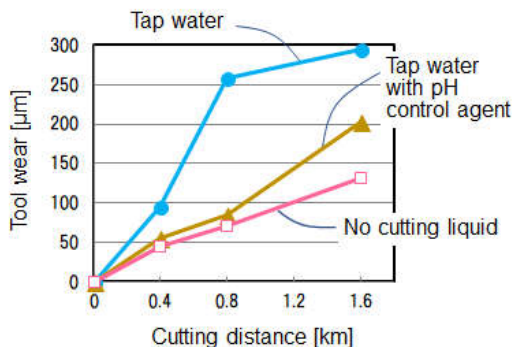
Fig. 5. Change in tool wear with increasing cutting distance for sintered steel using tap water, tap water with pH control agent, and no cutting liquid.

The tool wear was affected by water supplied to the cutting point, as described in section 3. Thus, we investigated the effectiveness of a mineral oil as the cutting liquid. In the same way as described in the previous section, workpieces were impregnated with mineral oil and then turned.

Figure 6 shows the experimental results. As shown in this figure, the mineral oil was found to reduce tool wear compared with the case of using no cutting liquid

although the reduction was small. This reduction
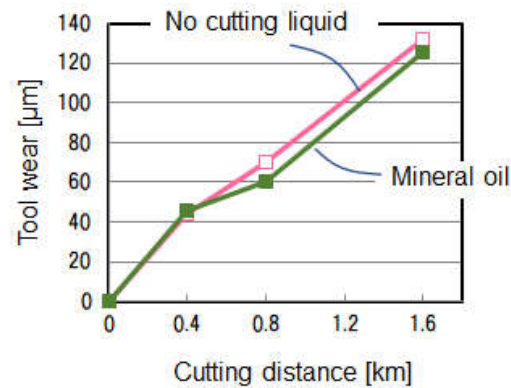
Fig. 6. Change in tool wear with increasing cutting distance for sintered steel using mineral oil and using no cutting liquid.

probably resulted from the lubrication effect of the mineral oil.

5. Conclusions

We investigated the effectiveness of cutting liquids on the machining of sintered steel parts. The tool wear in the turning process was examined for various cutting liquids. In our experiment, sintered steel workpieces were impregnated with a cutting liquid before turning. The impregnation was conducted under a reduced-pressure environment to fill the micropores in the workpiece with the cutting liquid by drawing air from the micropores.

It was found that the cutting liquids containing water caused a large amount of tool wear. Moreover, adding a pH control agent reduced the tool wear. This indicates that the tool wear is affected by water supplied to the cutting point, which induces oxidation of the workpiece surface and the tool at the cutting point. Using a mineral oil as the cutting liquid had a small on reducing tool wear. This reduction probably resulted from the lubrication effect of the mineral oil.

References

[1] T. Tsutsui, Technology trend and future outlook of structural materials, *Hitachi Powdered Metals Technical Report*, 7 (2008) 2-6. (in Japanese)

[2] T. Tsutsui, Recent Technology of Powder metallurgy and applications, *Hitachi Chemical Technical Report*, 54 (2011) 13-21. (in Japanese)

[3] N. Narutaki, A. Murakoshi, Machinability of Sintered Steels, *Journal of the Japan Society of Precision Engineering*, 47, 12 (1981) 1516-1522. (in Japanese)

[4] T. Wada, T. Toihara, Cutting Performance of CBN Tools in Cutting of Sintered Steel, *Journal of the Japan Society of Powder and Powder Metallurgy*,

49, 9 (2002) 773-779. (in Japanese)

[5] S . Furuta, S. Masuda, Effect of Complex Calcium Oxide Admix Ratio on Machinability for Sintered Steel, *Journal of the Japan Society of Powder and Powder Metallurgy*, 53, 10 (2006) 827-829. (in Japanese)

[6] T. Wada, K. Iwamoto, H. Hanyu, K. Kawase, Tool Wear of (Al, Cr) N Coated Cemented Carbide in Cutting Sintered Steel, *Journal of the Japan Society of Powder and Powder Metallurgy*, 58, 8 (2011)

459- 462. (in Japanese)

[7] T. Obikawa, T. Ohno, M. Yamaguchi, T. Maetani, S. Unami, Y. Ozaki, Machinability of Sintered Steel for Different Tools and Cooling/Lubrication Conditions, *Proc. JSPE Autumn Meeting* (2011) G16, 223-224. (in Japanese)

[8] T. Obikawa, T. Ohno, Machinability of Sintered Steel Fe-2%Cu-0.8%C, *SEISAN KENKYU*, 65, 6 (2013) 827-830. (in Japanese)

PART II, SECTION II

Materials Technology
(Functional Materials; Technologies of Materials; Materials Characterization and Evaluation;
High Speed Machining and Abrasive Machining; Micro- and Nano-Systems Engineering and
Emerging Technologies; Surface Integrity and Machining Quality…)

Decorative Film Forming by Inkjet Printing with Gold Nanoparticles for Crafts

Mitsugu Yamaguchi[1], Shun Kambayashi[1], Satoshi Sakamoto[2], Yasuo Kondo[3], Kenji Yamaguchi[4]

[1]Department of Mechanical and Electronic Engineering, Salesian Polytechnic
[2]Faculty of Education, Yokohama National University
[3]Faculty of Engineering, Yamagata University
[4]Department of Mechanical Engineering, Yonago National College of Technology

ABSTRACT

This paper presents the formation of a decorative film by inkjet printing with gold nanoparticles for crafts such as lacquerware. The proposed method consists of on-demand process, which makes design changeable without masking. The aims are threefold: 1) to establish a sintering process of gold nanoparticles for acrylonitrile butadiene styrene (ABS) and phenol resin substrates used for synthetic resin products; 2) to characterize the sintered gold film; 3) to examine applicability to industry.

Keywords: gold nanoparticle, inkjet printing, craft, lacquerware, decorative method

1. Introduction

The crafts such as lacquerware have made unique strides through decorating techniques using gold such as "Makie", the technique to draw picture by scattering powdered gold, and "Chinkin", the technique to rub gold into the design engraved by carving knives [1]. In conventional techniques, practical knowledge and ability are essential to make craft products. Therefore, screen printing which consists of simple processes has been developed [2]. However, screen printing requires a masking plate made of silk or nylon to create patterns for transcribing ink into objects.

Unlike the above-mentioned processes, inkjet printing of metal nanoparticle paste followed by sintering have been researched for fine wiring and extremely small functional-film formation [3]. It is well known that the use of metal nanoparticles with a high specific surface area depresses melting point, which enables low-temperature sintering around 500 K [4]. The metal nanoparticles start bonding together with the vaporization of solvent and dispersant in the paste, yielding a metal film [5]. Inkjet printing enables direct drawing of a decorative film due to on-demand process without masking. Researches on sintering with gold nanoparticles have been reported extensively [6, 7]. In the area of application to crafts such as lacquerware, however, there are few researches on the mechanism of film formation.

This paper presents the formation of a decorative film by inkjet printing with gold nanoparticles for crafts including lacquerware. Lacquerware products made of synthetic resin are popular because of their superior properties such as formability, durability and treatability. The proposed method consists of on-demand process, which makes design changeable without masking. The aims are threefold: 1) to establish a sintering process of gold nanoparticles for acrylonitrile butadiene styrene (ABS) and phenol resin

substrates used for synthetic resin products; 2) to characterize the sintered gold film; 3) to examine applicability to industry. This paper first describes optical properties of a gold nanoparticle film with reference to spectroscopic analysis. Second, the sintering experiment to form a decorative film on synthetic resin substrates made of ABS and phenol resin. Finally, Adhesion between the sintered film and substrates is tested with a view to its practical applications.

2. Method

Table 1 lists the materials and sintering parameters used. The substrates are boards of ABS and phenol resin (25 mm×20 mm×5 mm, respectively), which are widely used for lacquerware products. The dispersed gold

Table 1. Substrate, paste and sintering conditions

Substrate	
Material	Acrylonitrile butadiene styrene resin Phenol resin
Dimension	25 × 25 × 5 mm
Paste	
Nanoparticle	Gold
Mean particle size	7 nm
Concentration	57 mass%
Solvent	Naphthene-based solvent
Spin coating	
Number of revolution	2000 rpm
Time	60 s
Sintering conditions	
Temperature	323 - 473 K
Time	1 h

Table 2. Properties of substrates

Properties	ABS	Phenol
Specific gravity (g/cm^3)	1.05	1.4
Tensile strength (MPa)	39	—
Bending strength (MPa)	64	120-180
Compressive strength (MPa)	—	250-320
Thermal expansion coefficient (℃$^{-1}$)	9.5×10^{-5}	1.6×10^{-4}

nanoparticles, provided by Harima Chemicals Group,

Inc., have a mean diameter of 7 nm, a metal content of 57 mass%, and a viscosity of 7.5 mPa·s. The viscosity has been adjusted with naphthenic-base solvent.

The dispersed nanoparticle paste of 4 µL is atmospherically dispensed onto substrates to make a specimen. The specimen is setting on a spin coater at 2000 r/min for 60 s, yielding a gold nanoparticle film about 0.3-µm in thickness. The specimen is heated at 323-473 K for 1 h by an electric furnace.

Cross-cut test was carried out to assess the resistance of the sintered film to separation from substrates. The sintered film was cutting into a right angle lattice pattern by a sharp knife, and then peeling by an adhesive tape (adhesive peel strength: 3.93 N/ 10 mm) at a low speed of 10 mm/s.

Visible and near-infrared spectroscopic analysis (Hitachi Ltd., Spectrophotometer, U-4100) was conducted as follows: a nanoparticle paste of 20 µL was dispensed onto a borosilicate glass substrate (22 mm^2, 0.12-0.17 mm in thickness), followed by forming a thin uniform film 0.3-µm thick using a spin coater at 2000 r/min × 60 s, and then the specimen was dried by a hotplate at 373-573 K for 60 s before spectroscopic analysis.

3. Results and Discussion

3.1 Optical properties of gold nanoparticle film

The color of an object depends on optical properties including reflectance in the visible wavelength region, at 380-780 nm [8]. The optical properties of the gold nanoparticle film vary with the vaporization of dispersant and solvent in the paste. Therefore, an appearance and reflectance spectra of the gold nanoparticle film in the course of sintering process were evaluated.

Figure 1 shows an appearance of the gold nanoparticle paste. The paste had the particular color of dark red.

Figure 2 shows optical micrographs of the gold nanoparticle film at different heat temperatures of 373-473 K for 60 s. The gold nanoparticle film had a color of yellow tinged with green at a heat temperature of 373 K. In contrast, the gold nanoparticle film showed golden yellow at a heat temperature of 473 K. It can be observed that a good surface integrity without any voids is obtained. This short heating time is sufficient to decorate lacquerware products at the high-heat temperature.

Figure 3 shows the reflectance spectra of the gold nanoparticle paste at different heat temperatures. One of spectrum is an even level in the visible wavelength region at a heat temperature of 373 K. The other spectra sharply increase from 500-nm wavelength, and become almost constant above 600 nm. Since the boiling point of the naphthenic base solvent in the gold nanoparticle paste is 555 K, it is considered that almost all the

solvents were removed by heating over 523 K, yielding a similar level of reflectance.
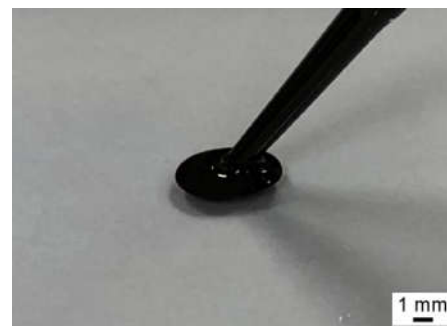
Fig. 1 Appearance of gold nanoparticle paste
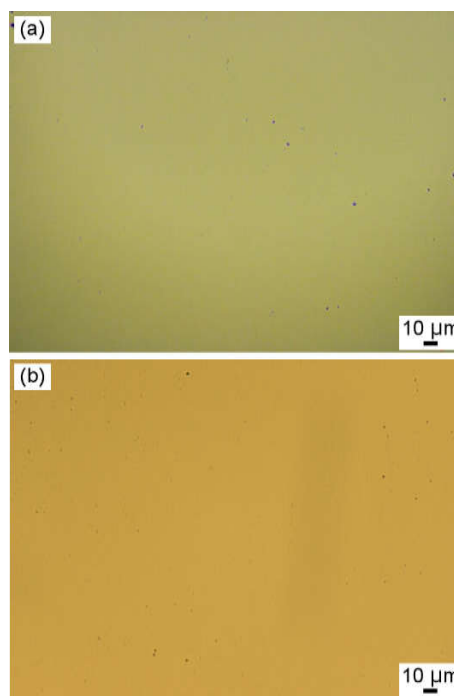
Fig. 2 Optical micrographs of gold nanoparticle film at heat temperature of (a) 373 K and (b) 473 K
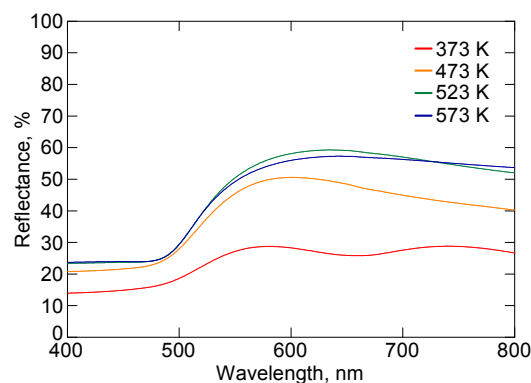
Fig. 3 Reflectance spectra of gold nanoparticle film

3.2 Heat resistance of substrates and adhesion of gold nanoparticle film

In the present study, heat resistance of the substrate and adhesion of the sintered film were tested with a view to its practical applications.

Figure 4 shows optical micrographs of the ABS resin substrate at the heat temperature of 323-423 K. As for the ABS resin substrate, there was no thermal damage to the substrate at the heat temperature of 323 K and 373 K. In the case of 423 K, the substrate suffered from thermal damage, yielding the deformation of the substrate sufficiently.

Figure 5 shows optical micrographs of the phenol resin substrate at the heat temperature of 323-473 K. As for the phenol resin substrate, it can be observed that an
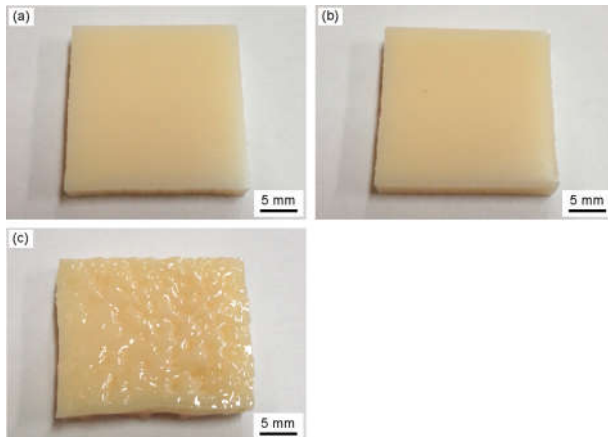
Fig. 4 Optical micrographs of phenol resin substrate at heat temperature of (a) 323 K, (b) 373 K and (c) 423 K for 1 h.
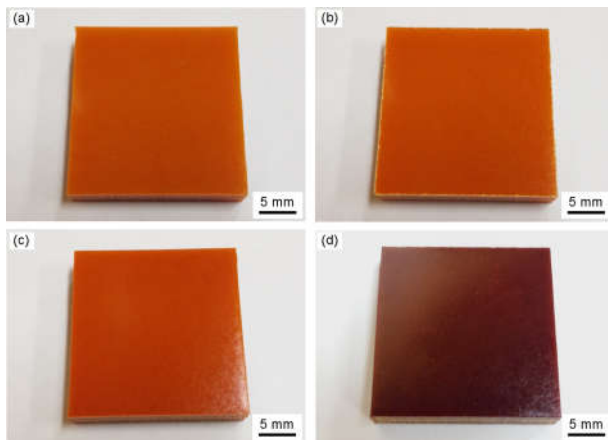
Fig. 5 Optical micrographs of phenol resin substrate at heat temperature of (a) 323 K, (b) 373 K , (c) 423 K and (d) 473 for 1 h

appearance of the substrate without thermal damage is obtained. In contrast, the substrate gradually discolored when the heat temperature increases over 423 K. Especially, the significant heat affect was observed at the heat temperature of 473 K.

Consequently, the proper conditions of sintering for its practical applications are follows; the ABS resin is

below 373 K, and the phenol resin is below 423 K, respectively.

Figure 6 shows optical micrographs of the sintered gold film on the ABS resin substrate after cross-cut test, under the sintering conditions of 323-373 K for 1 h. A lattice pattern indicates the place where the cutting was carried out. The film had golden yellow at the heat temperature over 323 K for 1 h. It seems that the sintering time prolonged accelerates vaporization of solvent and dispersant. The film had flaked along the edges at the intersections of the cuts. A cross-cut area significantly was affected at the heat temperature of 323 K. The edged of the cuts were completely smooth at the heat temperature of 373 K.Figure 7 shows optical
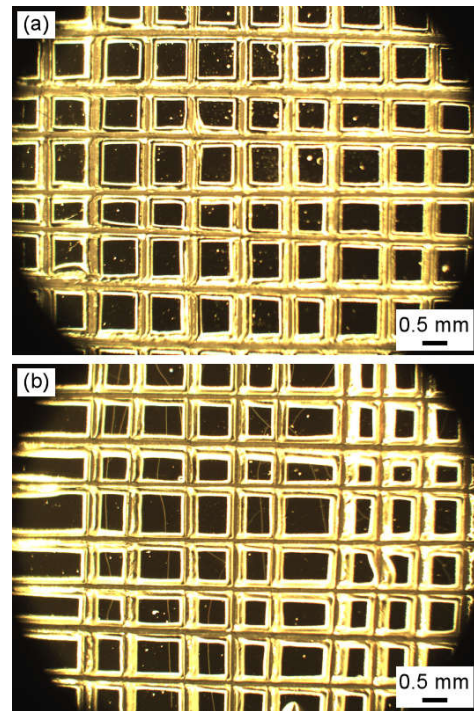
Fig. 6 Optical micrographs of sintered gold film on ABS resin substrate at heat temperature of (a) 323 K and (b) 373 K after cross cut test

micrographs of the sintered gold film on the phenol resin substrate after cross-cut test, under the following sintering conditions of 323-473 K for 1 h. The film had flaked along the edges at the intersections of the cuts. Moreover, the partial separation of the film, shown by circle mark in the Fig., can be seen. It seems that the heat temperature is sufficient to sinter the gold nanoparticles. The edged of the cuts are completely smooth at the heat temperature of 373 K and 423 K. In the case of the heat temperature of 473 K, the film had also good adhesion to the substrate, however the substrate suffered from thermal damage.

Figure 8 shows an example of product application. The proposed method applied a lacquerware product made of ABS resin, yielding the decorative film of

"ALESIO".
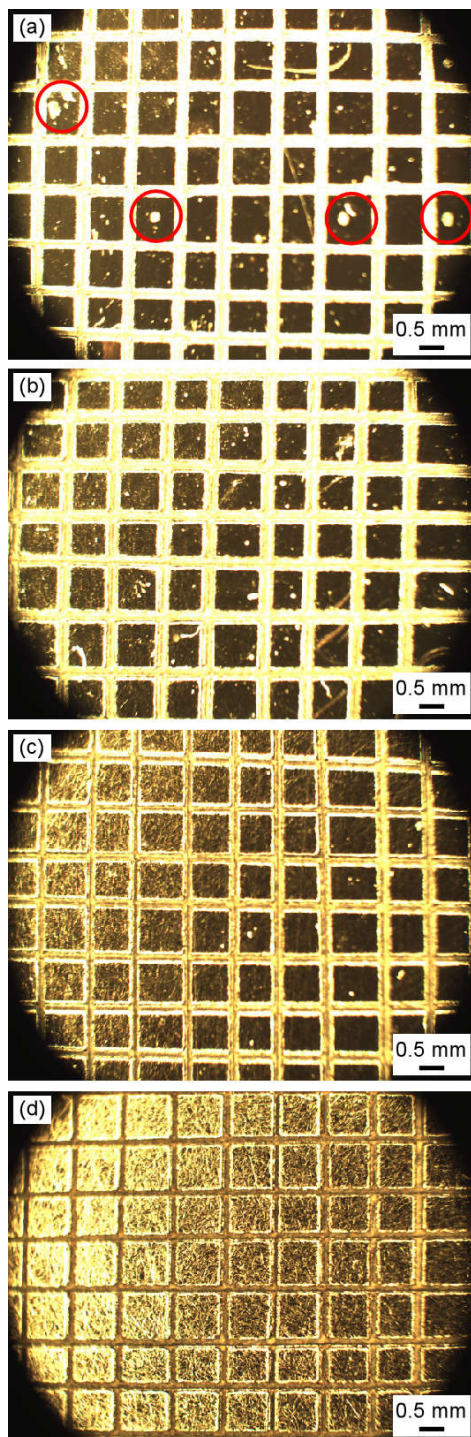
Fig. 7 Optical micrographs of sintered film on phenol resin substrate at heat temperature of (a) 323 K, (b) 373 K , (c) 423 K and (d) 473 after cross cut test .

It can be seen that a good appearance is obtained. Moreover, the film had good adhesion to the substrate. The decorative film forming by inkjet printing with gold nanoparticles has advantage, no need for masking processes to create design patterns.

4. Conclusions

This paper presents the formation of a decorative film by inkjet printing with gold nanoparticles for crafts such as lacquerware. The major results obtained are as follows.

1) The gold nanoparticle film showed golden yellow at a heat temperature of 473 K for 60 s. It can be observed that a good surface integrity without any voids is obtained. This short heating time is sufficient to decorate lacquerware products.

Fig. 8 An example of product application

2) The reflectance spectra of the gold nanoparticle paste were an even level in the visible wavelength region at a heat temperature of 373 K. In contrast, spectra sharply increased from 500-nm wavelength, and became almost constant above 600 nm at heat temperature over 473 K.

3) The proper sintering conditions which prevent thermal damage to substrates are follows; the ABS resin is below 373 K, and the phenol resin is below 423 K, respectively.

4) The gold film possessed a good appearance when the sintering temperature over 323 K for 1 h. The film had such a high adhesion to the substrate that no separation occurred on both substrates after cross-cut test.

5) The proposed method applied a lacquerware product made of ABS resin, yielding the decorative film of "SALESIO" . It can be seen that a good appearance is obtained. Moreover, the film had good adhesion to the substrate.

References

[1] Hiroshi OYABU, "Urushi Work and Its Science", *SHIKIZAI*, 75, 10 (2002) 486-492.

[2] Yoichi ITO, "Present Status and Future of Functional Screen Printing Technology", *J. Ptg., Sci. and Technol.*, 40, 1(2003) 2-9.

[3] Tomohiro YAMAZAKI, "Application of the Printing Technology to Electronics and the Technical Subject to Expansion", *J. Jpn. Soc. Precis. Eng.*, 80, 3 (2014) 265-269.

[4] Ph. Buffat and J-P. Borel, "Size effect on the melting temperature of gold particles", *Phys. Rev. A*, 13, 6 (1976) 2287-2298.

[5] Nobuto. TERADA, "Fine Pattern Formation by Ink-Jet Printing Using Conductive Nano Paste and Its Application", *J. Jpn. Inst. Electron. Packag*., 11, 4 (2008) 300-306.

[6] Satoshi INOUE and Tatsuya SHIMODA, "Electronic Devices Using Micro-Liquid Process", *J. Jpn. Soc. Precis. Eng.*, 69, 7 (2003) 935-938.

[7] Hideo ISHIBASHI, "Preparation of Metal Nano-Particles and Their Application to Circuit Pattern Formation by Ink Jet Printing", *J. Jpn. Inst. Electron. Packag*., 11, 2 (2008) 157-163.

[8] P. Peng, A. Hu and Y. Zhou, "Laser sintering of silver nanoparticle thin films: microstructure and optical properties", *Appl. Phys A*, 108, 3 (2012) 685–691.

Deformation of The Material During Bending in Cold-Stamping Method

Hoàng Quốc Hùng[1], Lưu Thanh Tùng[1]
[1]Affiliation
268 Lý Thường Kiệt Street, District 10, Hồ Chí Minh City, 740500, Việt Nam

ABSTRACT

Today sheet-metal forming technology is widely used in the mechanical industry, which requires a very high precision of the product. Especially the bending process, the bend-allowance calculations are important to achieving the finished products. The bend allowance refers to the elongation of the sheet during bending. Therefore, it is necessary to have an algorithm to accurately predict this factor. Any inaccurate calculation can lead to an incorrect development of the length of the sheet. In this paper, the method to determine the bend allowance within acceptable accuracy during bending process with different kind of materials.

1. INTRODUCTION

Bending methods are widely used in the cold stamping industry, where bending is the most used method. The important challenge of bending is to maintain the exact shape of the final product. This problem is due to elongation / compression caused when the metal sheet undergoes deformation.

The bend allowances must be accurately predicted for proper changes in the tooling so that accuracy can be achieved in the final part.

There are a lot of analyzes and calculations to predict distortion during bending. A number of important studies will be provided below.

A model is given by Hill [1] to calculate the Bend Allowance. He proposed a theory that at R / t <5, transverse stress could be ignored, which would lead to an increase in inaccuracy in predicted bend allowance. Boljanovic [2] has grown experimental rules for calculating the position of the neutral axis based on the geometry of the deformed shape of the plate. In that model, he assumed that the neutral fiber and the unstretched fiber are same. Pure plastic bending of the sheet, assuming the material as perfectly plastic under plane-strain conditions has been analyzed by Lubahn and Sachs [3]. Wang, Kinzel and Altan [4] used Swift's model to represent strain-hardening behavior. They give a model to predict the springback of the sheet and develop practical design aids and adaptive control of press brakes. This model indicates that the bent sheet can be divided into four different distortion regions, namely, plastic, elastoplastic, elastic, and rigid zones. Prasad and Somasundaram [5] give a calculation model bend allowance base on Ludwik's material model. This method overcomes the weaknesses of other methods because it indicates that neutral fibers and unstretched fibers are different. In addition, this method also calculates the reduction in sheet thickness during bending. Combining the Wang and Prasad method will obtain an equation for the bend allowance and predict the spring back and final shape of the product after being unloaded.

2. DEFORMATION ZONE

The position of the important fibers along the sheet thickness is shown in Figure 1.
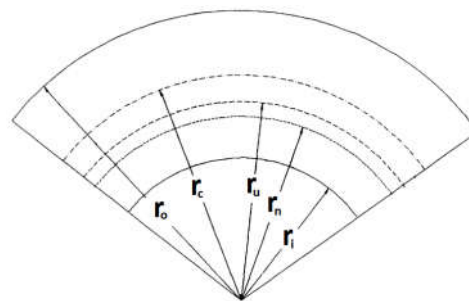
Fig1: Location of important fibers in bending
r_o = Radius of outer fiber
r_c = Radius of central fiber
r_u = Radius of unstretched fiber
r_n = Radius of neutral fiber
r_i = Radius of inner fiber

Neutral fiber is fiber at which the stress moves from tension to compression. On the other hand, unstretched fiber undergoes the same amount of compression as the tension.. All fibers from r_o to r_c are only stretched during bending: those between r_c and r_u are first compressed and then stretched more than they were compressed originally. At r_u the stretch equals the compression. Fibers between r_u and r_n. are first compressed and subsequently stretched less than they were compressed originally. Fibers between r_n, and r_i are compressed only.

The stress-distribution region may be divided into two zones:
Zone 1: $r_n \leq r \leq r_o$
Zone 2: $r_i \leq r \leq r_n$

3. LOCATION OF THE NEUTRAL FIBER

In this model Ludwik's equation is chosen to represent the strain-hardenable property of material.

The property of a rigid work-hardenable material is shown as: $\bar{\sigma} = \sigma_y + k\bar{\varepsilon}^n$ (1)

The equivalent or effective stress is given by:

$$\bar{\sigma} = (\frac{1}{2}((\sigma_1 - \sigma_2)^2 + (\sigma_2 - \sigma_3)^2 + (\sigma_3 - \sigma_1)^2))^{\frac{1}{2}} \quad (2)$$

Which σ_1, σ_2, σ_3 as the element is subjected to three-dimensional stresses.

For plane-strain conditions: $\sigma_3 = \frac{\sigma_1 + \sigma_2}{2}$ (3)

From (2) and (3): $\bar{\sigma} = \frac{\sqrt{3}}{2}(\sigma_1 - \sigma_3)$(4)

At the convex surface, the tensile stress σ_θ is largest and σ_r is the smallest principal stress. Then equation (4) becomes: $\bar{\sigma} = \frac{\sqrt{3}}{2}(\sigma_\theta - \sigma_r)$(5)

Similarly, the effective or equivalent strain is

$$\bar{\varepsilon} = (\sqrt{2}/3).((\varepsilon_1 - \varepsilon_2)^2 + (\varepsilon_2 - \varepsilon_3)^2 + (\varepsilon_3 - \varepsilon_1)^2)^{\frac{1}{2}} \quad (6)$$

Under plane-strain conditions. Equation (6) becomes:
$\bar{\varepsilon} = \left(\frac{\sqrt{2}}{3}\right)\varepsilon_\theta$(7)

Stress in the bend region

Figure 3(b) shows a section of the wide plate of constant curvature. By resolving the forces across the radial direction.

Force on side 1= $(\sigma_r + d\sigma_r)(r + dr)d\theta$

Force on side 2= $(\sigma_r)rd\theta$

Force on side 3= force on side 4= $\sigma_\theta dr$

(a)

(b)
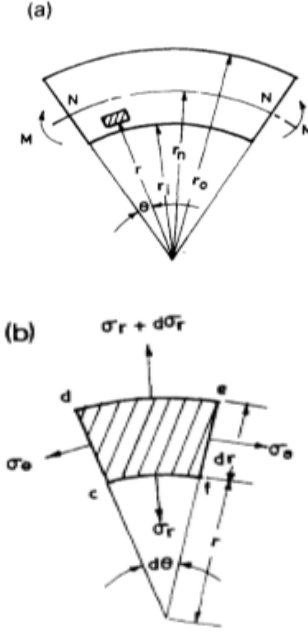
Fig 3: Typical stresses in an element of the bent sheet.

$$\Sigma upward\ forces = (\sigma_r + d\sigma_r)(r + dr)d\theta$$
$$= (r\sigma_r + rd\sigma_r + \sigma_r dr)d\theta$$

$$\Sigma downward\ forces = (\sigma_r rd\theta) + 2(\sigma_\theta dr)\sin\left(\frac{d\theta}{2}\right) \approx (\sigma_r rd\theta) + (\sigma_\theta drd\theta)$$

Under the equilibrium condition, upward forces and downward forces are equal. The differential equation for equilibrium in plane-strain bending is: $r\frac{d\sigma_r}{dr} = \sigma_\theta - \sigma_r$(8)

- *Stress-strain relationship in the deformed zones*

From (1) and (7) obtained the stress-strain relationship in zone I:$\sigma_y + k\bar{\varepsilon}^n = \left(\frac{\sqrt{3}}{2}\right)(\sigma_\theta - \sigma_r)$(9)

With $k_0 = \frac{\sigma_y}{\sqrt{3}}$ and $k_1 = k(2/\sqrt{3})^{n+1}$

Equation (9) becomes: $(\sigma_\theta - \sigma_r)_I = 2k_0 + k_1\left(\ln\left(\frac{r}{r_u}\right)\right)^n$ (10)

Similarly, the stress-strain relationship in zone II can be written as: $(\sigma_\theta - \sigma_r)_{II} = 2k_0 - k_1\left(\ln\left(\frac{r}{r_u}\right)\right)^n$

- *Radial stresses in the deformed zones*

Differential equation (8) is to be integrated by applying boundary conditions in the two deformation regions.

$$(\sigma_r)_I = \int_r^{r_0}\frac{2k_0}{r}dr + \int_r^{r_0}\frac{k_1\left(\ln\left(\frac{r}{r_u}\right)\right)^n}{r}dr$$

Rewriting the second part of the integral

$$k_1 \int_{\ln\left(\frac{r}{r_u}\right)}^{\ln\left(\frac{r_o}{r_u}\right)} x^n dx = \frac{k_1}{n+1}\left((\ln\left(\frac{r_o}{r_u}\right))^{n+1} - \left(\ln\left(\frac{r}{r_u}\right)\right)^{n+1}\right)$$

The radial stress in deformed zone I is

$$(\sigma_r)_I = 2k_o\left(\ln\left(\frac{r_o}{r}\right)\right) + k_2\left(\left(\ln\left(\frac{r_o}{r_u}\right)\right)^{n+1} - \left(\ln\left(\frac{r}{r_u}\right)\right)^{n+1}\right) \quad (11)$$

Which: $k_2 = k_1/n + 1$

Similarly, the radial stress in deformed zone II is

$$(\sigma_r)_{II} = 2k_o\left(\ln\left(\frac{r}{r_i}\right)\right) + k_2\left(\left(\ln\left(\frac{r}{r_u}\right)\right)^{n+1} - \left(\ln\left(\frac{r_u}{r_i}\right)\right)^{n+1}\right) \quad (12)$$

At $r = r_n$, radial stress from zone I equal with radial stress from zone II

$$2k_o\left(\ln\left(\frac{r_o}{r}\right)\right) + k_2\left(\left(\ln\left(\frac{r_o}{r_u}\right)\right)^{n+1} - \left(\ln\left(\frac{r}{r_u}\right)\right)^{n+1}\right) =$$
$$2k_o\left(\ln\left(\frac{r}{r_i}\right)\right) + k_2\left(\left(\ln\left(\frac{r}{r_u}\right)\right)^{n+1} - \left(\ln\left(\frac{r_u}{r_i}\right)\right)^{n+1}\right) \quad (13)$$

As $\frac{k_2}{2k_0} = \frac{\left(\frac{2}{\sqrt{3}}\right)^n}{n+1} \cdot \frac{k}{\sigma_y}$

Then equation (13) becomes

$$\frac{\left(\frac{2}{\sqrt{3}}\right)^n.k}{(n+1).\sigma_y}\left(\left(\ln\left(\frac{r_u}{r_i}\right)\right)^{n+1} - \left(\ln\left(\frac{r_o}{r_u}\right)\right)^{n+1}\right) + \ln\left(\frac{r_n^2}{r_i.r_o}\right) = 0 \quad (14)$$

Solve equation (14) to find the value of r_n.

4. THICKNESS OF SHEET

To determine the reduction of plate thickness. Use the integral to calculate the total strain in the plate. The thickness remains constant and the neutral fiber remains at a fixed distance (r_n-r_i) from the concave surface and the length L_0 remains fixed as shown in Fig. 4. If the radius r_i rotates around one end of the neutral axis at an angle $d\theta$, then the radius of the curvature will change to a small interval dr_i. For the outer end of the neutral axis, the $_{Lri}$ length of the concave surface and the $_{Lro}$ of the convex surface will vary by a small amount of dL_{ri} and dL_{ro}.
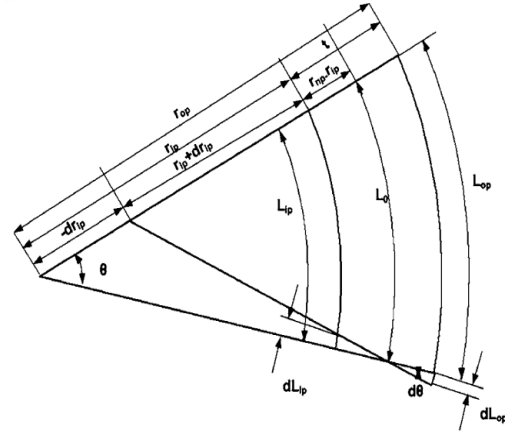
Fig 4: Geometrical changes during an infinitesimal interval of bending

The length of the innermost fiber (L_{ri}) and the length of the outermost fiber (L_{ro}) of the surface fibers can be calculated as follows: $L_{ri} = \theta r_i (15)$
$L_{ro} = \theta r_o = \theta(r_i + t)(16)$

and $dL_{ri} = (r_i - r_n)d\theta(17)$

$$dL_{ro} = (r_o - r_n)d\theta = ((r_i + t) - r_n)d\theta \quad (18)$$

From the constancy-of-volume condition

$$t\left(\frac{L_{ri} + L_{ro}}{2}\right) = t_0 L_0 (19)$$

By definition of strain $e_{ri} = \frac{\delta L}{L_o} = \frac{L_{ri}}{L_o} - 1(20)$

From equation (19), (21) and (22) obtained

$$\frac{t_0}{t} = \frac{1}{2}\left(\frac{L_{ri}}{L_o} + \frac{L_{ro}}{L_o}\right) = 1 + \frac{1}{2}(e_{ri} + e_{ro})(23)$$

Use equation (23) to predict the reduction in thickness.

On the other hand, based on volume constancy, it is possible to calculate the radius of the unstretched fiber: $r_{up} = \frac{t}{t_0}\left(r_i + \frac{t}{2}\right)(24)$

Suppose the material is not compressed. The volume of the plate before and after bending is equal, the following equation is obtained: $V_0 = L_0 W_0 t_0 (25)$

$$V_1 = \frac{(r_o^2 - r_i^2)}{2}W_0\theta(26)$$

Equation (25) with equation (26) is obtained

$$r_{up} = \left(\frac{(r_o^2 - r_i^2)}{2t_0}\right)(27)$$

This radius of the unstretched fiber is then used to calculate the bend allowance.

4. COMPARISON OF THE PRESENT MODEL WITH EXISTING MODELS

Table 1: Parameters of r_n, r_u, t through the calculation function

Material	Boljanovic	Lubah and Sachs	Present model		
	r_n	r_n	r_n	r_u	t
A-K HS	2,5	2,449	2,339	2,417	0,972
2036-T4	2,5	2,449	2,33	2,42	0,973
Al 70:30	2,5	2,449	2,29	2,397	0,965
Brass Al	2,5	2,449	2,352	2,417	0,972

(Initial radius r_i = 2mm, initial thickness t_o = 1mm)

Table 2 : Prediction of sheet thickness

Mtrl	Simulation results (BA)	Present model		Boljanovic's model	
		BA	Error (%)	BA	Error (%)
2036-T4	3,792	3,796	-0,009	3,927	-2,7
Brass Al	3,763	3,765	-0,014	3,927	-2,8

Table 3 :Verification model through simulation
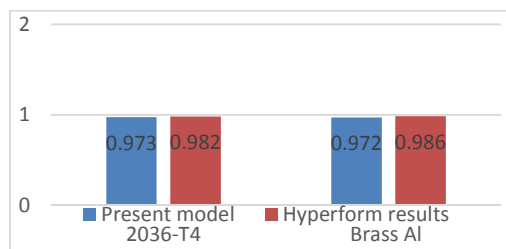
To compare the results obtained from the present model with other models, computations made for different materials are presented in Tables 1, 2 and 3. These results show the variation of the bend allowance as a function of the bend radius and the sheet thickness for different materials.

Various materials have been selected to study the effect of materials on the bend allowance. From Table 1, the values of the bend allowance can be obtained through Boljanovic method, Sachs Method, and the present model. From Table 2, it can be concluded that for highly durable materials, unstretched fiber varies considerably, leading to predictive deviations using the Boljanovic method. Table 3 shows the predicted change in plate thickness with very small errors compared to the simulation results.

5. CONCLUSIONS

This article has provided a method for accurately calculating the bend allowance parameter. In addition, restrictions on other methods are also given. The results from the present model show that it yields greater accuracy than other methods. Based on that, accurate predictions can be made in mold making.

REFERENCES

[1] R. Hill, "The Mathematical Theory of Plasticity", Oxford, London, 1950.

[2] Vukota Boljanovic, Ph.D, "Sheet metal forming processes and Die design" Industrial Press Inc, 2004.

[3] J.D. Lubahn and G. Sachs, "Bending of an ideal plastic metal", Trans. ASME, 72 (1950)

[4] Chuantao Wang, Gary Kinzel and Taylan Altan, "Mathematical modeling of plane-strain bending of sheet and plate", Journal of Materials Processing Technology, 1992.

[5] Y.K.D.V.Prasad and S.Somasundaram, "A mathematical Model for bend-allowance calculation in automated sheet-metal bending", Journal of Materials Processing Technology, 1993.

Surface roughening of silicon wafer solar cell by using ECDM Method

Hai-Ping Tsui[1], Kuang-Hua Chang[1], Biing-Hwa Yan[1]

[1]Department of Mechanical Engineering, National Central University, Chung-Li, Taiwan

ABSTRACT

This research proposes surface roughening of silicon wafer solar cell by electrochemical discharge machining (ECDM). The stainless steel was used as negative electrode. The graphite was used as the positive electrode acting as the auxiliary electrode. The potassium hydroxide was used as the electrolyte. The processing parameters include the machining voltage, the processing time, the machining gap, the electrolyte concentration, the additive agent concentration, pulse frequency and duty factor, etc. The result of experiments reveals that appropriate concentrations of ethanol can expand the size of the pores and enhance surface roughening effect. The appropriate processing parameters are a machining gap of 200μm, voltage of 48V, concentration of potassium hydroxide of 3M, concentration of ethanol of 4%. The electrochemical discharge machined surface roughness was increased from 0.417μm to 0.915μm using one-minute processing time. The average reflectance rate of the textured surface was decreased from 29.6% to 12.7%. This study reveals that ECDM method has the advantage of short processing time and can generate a higher surface roughness and the porous structure.

1.Introduction

The petroleum becomes an indispensable resource in the economy for more than one century to provide the transportation power for billions of vehicles, vessels and airplanes. Facing global economic growth in a drastic way, the petroleum will be gradually run out. As a result, the alternative energy becomes a future development focus substitute for human being.

Current renewable energy includes solar, wind, hydro, tidal, biomass, geothermal and so on. The solar life may last 5 billions of year, the solar energy is regarded as inexhaustible one before its life expires. Additionally solar energy is equipped with clean, safe and zero pollution that poses a potential development among renewable energies.

For the last few years, solar energy has experienced a rapid growth globally. Among which silicon solar cell become the main stream of energy industry. There are three principles to develop solar energy technology, including high efficiency, low cost and excellent reliability. To increase the conversion efficiency, the surface texture of solar cells is a very important factor in the process as surface texture enables the light through many times of reflection in the structure to increase the opportunities for light entering the solar cells. Additionally surface texture increases the absorption path [1] of light in the solar cells, indicating that solar cells absorbing efficiency can be effectively increased.

Using surface texture increases the absorbing efficiency of silicon solar cell is considered as a common method. Acid texture and alkaline texture are popularly adopted for surface texture.

Most of acid texture uses the mixed liquid of hydrofluoric acid (HF) and HNO3. The etching will produce bubbles to form the difference etching and further produces surface texture; however hydrofluoric acid (HF) is strong acid that poses an extreme risk to operators.

Alkaline texture usually uses the mixed liquid of NaOH or KOH and isopropyl alcohol (IPA), heats the liquid up to 85℃ and cyclically soaks for 60 minutes. Since silicon direction bonding ability is different, (100) direction will be etched to expose (111) crystal face, further produces pyramid texturing structure.

However etching takes a long time and isopropyl alcohol (IPA) will generate the problem of waste water treatment to be dealt with. Compared with acid texture and alkaline texture, electrochemical discharge machining (ECDM) uses discharging phenomenon to produce high temperature melting material, while high temperature can assist chemical etching mechanism. ECDM is equipped with excellent machining speed and degree of freedom toward machining of semi-conductor material and non-conducting material. ECDM applies voltage to positive and negative electrodes to facilitate electrolysis on the electrode surface and further produces large quantity of bubbles. The bubbles are combined into gas film that sufficiently blocks the conduction between electrode and electrolyte. The ECDM generates the discharging phenomenon like EDM in this insulation state. The discharging phenomenon can be interpreted as discharging model in the gas [2]. High temperature generated by the discharging sparkles accelerates chemical etching speed of electrolyte. The materials surrounded around electrode was removed by the ECDM discharging. Discharge machining mechanism of ECDM mainly covers electrochemical reaction, sparkles discharging and chemical etching [3,4]. ECDM process can generate a higher surface roughness and porous structure. ECDM process acts as the surface texturing process of solar cells.

This study uses ECDM as a Eco-friendly method to to achieve low cost, low pollution, high surface roughness and rapid production.

2. Experimental setup and procedures

This research uses ECDM features on non-conducting materials surface texturing. The surface of p type mono-crystalline silicon is textured with aim of changing surface structure and increasing the frequency of light reflection to push up photoelectric conversion efficiency of solar cells.

The auxiliary electrode must be installed to achieve the required complete loop of ECDM. The auxiliary electrode plays the role of anode to form a complete discharging loop. To avoid anode dissolution and affect ECDM reaction process due to auxiliary electrode material connects the positive electrode, graphite of low chemical activity is adopted. The area of the graphite is larger than cathode by tens or hundreds of times in the experiment. The tool electrode connected to negative pole is used to produce sparkle discharging reaction. The stainless steel is adopt possess high mechanic strength and high temperature resistance to sustain high temperature at discharging. To increase electrochemical reaction efficiency, the potassium hydroxide which has strong dissociation is adopted.

ECDM basic layout is shown as Fig. 1. DC voltage is applied between two electrodes and the current loop is formed through electrolyte. Electrochemical reaction is immediately occurred when cathode is merged into the electrolyte. As soon as applied voltage is larger than critical voltage, the negative electrode occurs ECDM discharging phenomenon due to break through insulating gas film. If the distance bewteen work piece and electrode is close enough, the energy of discharging sparkles generated by electrode will melt the work piece and accelerate chemical etching, further removes the materials.
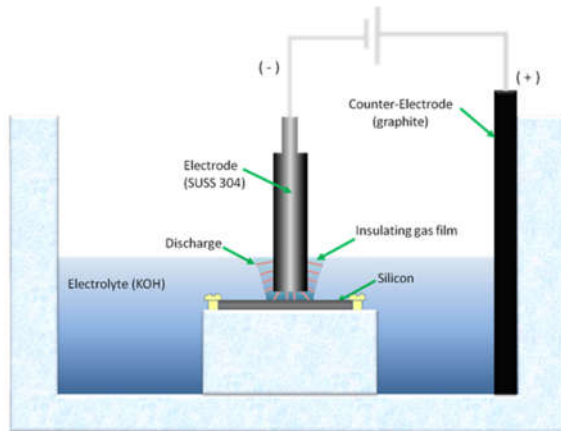
diameter of 2mm was used as cathode clamped on the spindle of the micro EDM system, equipped with Z axis of 0.1um precision. The graphite used as auxiliary anode was clamped at the side of machining tank. A 200μm-thick block gauge was installed between the P type mono-crystalline silicon and stainless steel electrode. The block gauge was used to measure the machining gap of 200μm and was take away before the experiments performing. The stainless steel electrode was not moved throughout the experiments. The KOH was poured into the machining tank. Pulse machining voltage is connected to stainless steel electrode (cathode) and graphite auxiliary electrode (anode). A peristatic pump is used to cycle electrolyte, The experiment parameters includes machining voltage, processing time, machining gap, electrolyte concentration, ethanol concentration, pulse frequency, duty factor, etc. Table 1 presents the experiment parameters of the ECDM.The electricity can push the electrochemical reaction in facilitating surface texturing of the mono-crystalline silicon.After completing ECDM, 2D surface roughness measurement instrument is used to measure surface roughness. Then scanning electron microscope (SEM) is adopted to observe their morphologies. The experimental results was also discussed.

Table.1 The experiment parameters of the ECDM

machining gap	200 μm
machining time	60 sec
ethanol concentration (wt %)	0、4%、8%、12%、16%
machining voltage	24V、36V、42V、48V、54V
electrolyte concentration(M)	0.5、1、2、3
pulse frequency(Hz)	1、10、100、1k、10k、100k
duty factor	25%、50%、75%、100%

Fig.1 ECDM Basic Layout

The experimental equipment used in this research is illustrated as Fig. 2. A rectangular P type mono-crystalline silicon of dimensions 18mm× 18mm× 0.18mm was mounted in the micro ECDM tank in the experiment. The stainless steel electrode with a
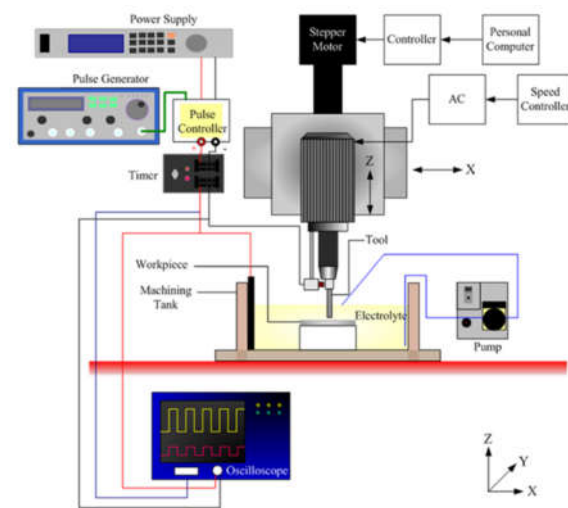
Fig. 2 Illustration of Experimental Equipment

3. Results and Discussion

3-1 Influence of ethanol concentration on surface roughness

The purpose of additive of ethanol in the chemical etching process of mono-crystalline silicon intends to accelerate hydrogen and oxygen escape from silicon surface and increases reaction rate and etching uniformity [5]. Different weight percentage concentration of ethanol are added into 1M KOH and 2M KOH respectively. The influence of ethanol concentration on surface roughness are studied in the ECDM. Experimental results are revealed in Fig. 3. The surface roughness without adding ethanol into 1M KOH is 0.544µm. When ethanol weight percentage concentration is 4wt%, the surface roughness 0.751µm is the best result. Following the increase of ethanol concentration, surface roughness is gradually decreasing.

Taking current waveform during machining explains discharging situation.

Fig. 3 Relation between Ethanol and Surface Roughness

Fig.4 shows the current waveform response of different ethanol concentration. The current is steady and discharging phenomenon is less when ethanol is not added. Adding of 4 wt% ethanol assists the occurrence of discharging phenomenon. However concentration is up to 12wt%, the current is extremely not steady. Nevertheless more discharging phenomena generates higher electrochemical etching rate.
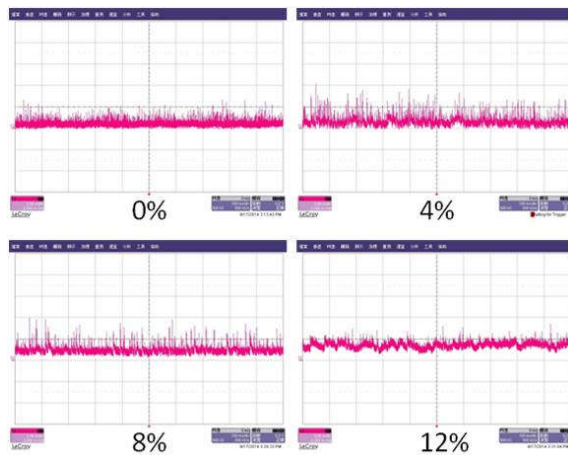
Fig. 4 Current Waveform Response of Different Ethanol Concentration

The experiment uses SEM by inclining 30 degree via vertical view to reveal the surface morphology, shown as Fig. 5. Without adding ethanol, the surface morphology indicates that the original surface is etched by ECDM. Though the pores are found but rather

smaller. After adding ethanol, the size of the pores are expanded and the connecting pores produce grooves alike. The ethanol concentration is increased, the pores size is increased and the surface roughness is decreased
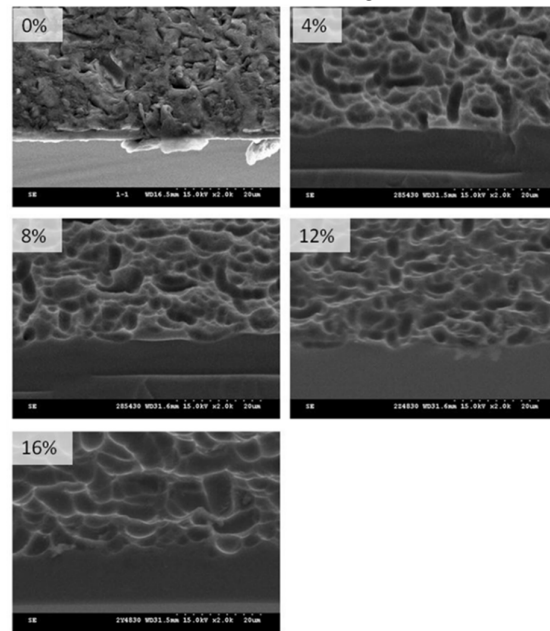
Fig. 5 SEM Comparison of Different Ethanol Concentration

3-2 Influence of machining voltage on surface roughness

Machining voltage is considered as an important parameter in the ECDM. When input voltage does not sufficiently produce large quantity of bubbles, it cannot construct a complete gas film to generate the electrochemical discharge and the electrochemical etching efficiency can not be increased. The applied voltage must exceed the critical voltage to generate the discharging situation. Fig. 6 reveals the relationship between machining voltage and surface roughness. When the machining voltage are from 24V to 36V, the surface roughness doesn't show significant change and electrochemical etching efficiency is poor. While the machining voltage is up to 42V, the surface roughness is increased. When the machining voltage is at 48V, the best surface roughness comes out no matter electrolyte concentration is 1M or 2M or 3M. When voltage is 54V, surface roughness is decreased. SEM photos are taken on specimen at different voltage, shown as Fig. 7. After comparison, no pores and grooves are occurred at the surface between 24V and 36V so that surface roughness is low. Starting from 42V, discharging the pores and grooves are seen on the surface. The electrochemical etching phenomenon is not significant and grooves are widely distributed, since the energy power is not sufficient,. When the machining voltage is set at 48V, better surface texture can be generated due to good

131

performance of discharging power and electrochemical etching. Though discharging and electrochemical etching phenomenon are seen at 54V voltage, the large melting energy causes the recast layer on the surface. The recast layer result in the surface roughness decreasing.
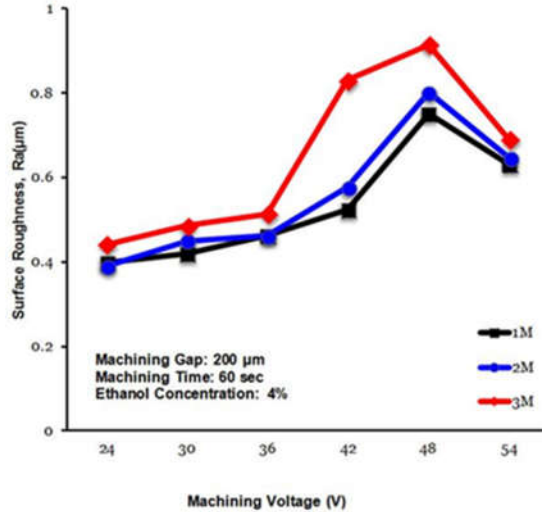
Fig. 6 Relationship between Machining voltage and Surface Roughness
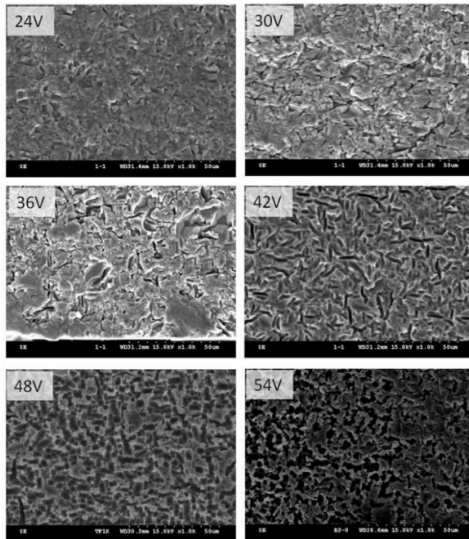
Fig. 7 SEM Comparison of Different Voltage

3-3 Influence of electrolyte concentration on surface roughness

In the ECDM, electrolyte concentration affects electrochemical etching rate and electrolyte conductivity. Fig.8 illustrates the relationship between electrolyte concentration and surface roughness. The surface roughness at 48V increased with the increasing of KOH concentration. The results indicate that better surface texture can be obtained under higher KOH concentration. When the KOH concentration is 3M, a better surface roughness 0.915μm can be acquired. Fig.

9 shows SEM photos with different concentration of electrolyte at machining voltage 48V. When KOH concentration is 3M, the surface morphology pores are evenly distributed.
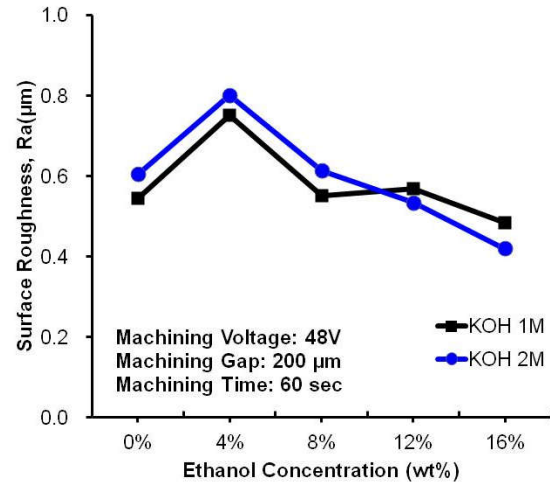
Fig. 8 Relation between Electrolyte Concentration and Surface Roughness
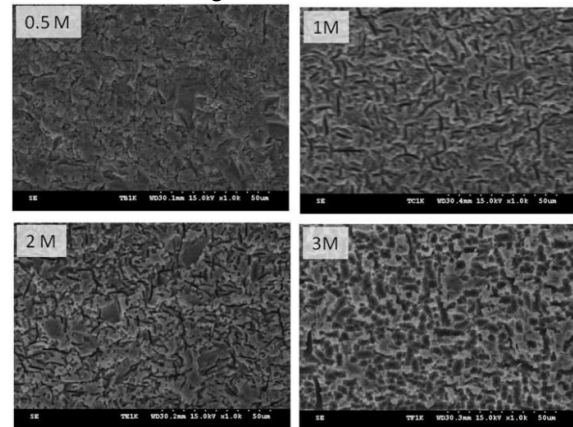
Fig. 9 SEM Comparison of Different Electrolyte Concentration

3-4 Influence of pulse frequency on surface roughness

In terms of ECDM, pulse frequency decides the duration and times of discharging. Single discharging time also affects the formation of gas film and times of sparkles. Fig. 10 shows the relationship between pulse frequency and surface roughness. When pulse frequency is set at 10 Hz, high surface roughness is gernerated. Since total discharging time is only half of continuous current, the obtained surface roughness is lower than that of continuous current. Because single discharging time is short at higher pulse frequency, gas film is reformed at each discharging so that machining effect is poor owing to total discharging time is less.
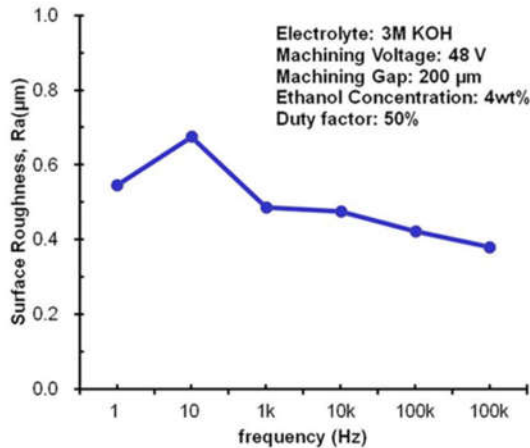
Fig. 10 Relationship between Pulse Frequency and Surface Roughness
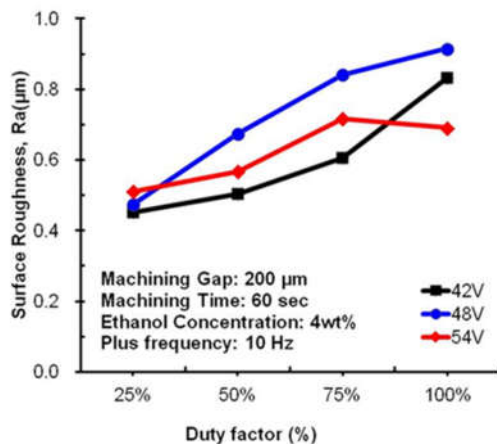
Fig.11 Relationship between Duty Factor and Surface Roughness

3-5 Influence of duty factor on surface roughness

Definition of duty factor indicates the ratio between discharging time and single pulse cycle time. Under same energy input frequency, larger duty factor means longer discharging time in single pulse cycle. The longer discharging time is, the more the material removal is. The pulse frequency was fixed at 10Hz and different duty factor is used in the experiment. Fig.11 shows the relationship between duty factor and surface roughness. Surface roughness presents a positive proportion to duty factor. When duty factor is 100%, surface roughness comes out the highest. When the machining voltage is at 42V and 48V, ECDM can achieve higher surface roughness without using pulse frequency. Surface roughness declines due to melting phenomenon when machining parameter is at 54V and duty factor is 100%.

3-6 Comparison of before and after ECDM

Since mono-crystalline solar cell wafer uses wire cutting to 180μm thickness. Before ECDM, the surface looks flat and the average surface roughness is 0.417μm. The appropriate processing parameters are a machining gap of 200μm, voltage of 48V, concentration of potassium hydroxide of 3M, concentration of ethanol of 4%. The surface roughness after ECDM increased from 0.417μm to 0.915μm using one minute.

To investigate whether surface texture after ECDM can decrease light reflectance, the integration spectroscopic reflectometer is used to perform measurement. First of all, verification is made before ECDM, the mono-crystalline silicon is measured at five points on the surface. The average reflection rate is 29.695%. The average reflection rate is 12.727% between wave length 350μm and 1050μm after ECDM.

4.Conclusions

In this study, the surface of P type mono-crystalline silicon is textured by ECDM. This study uses stainless steel and graphite as negative electrode and positive electrode respectively, meanwhile graphite also acts as the auxiliary electrode. The electrolyte adopts potassium hydroxide. The ECDM acts as a Eco-friendly method to achieve low cost, low pollution, high surface roughness and rapid production.The principal conclusions were as follows.

Experiment proves ECDM has machining ability toward surface texturing of mono-crystalline silicon.

Proper concentration of ethanol will enlarge the the size of the pores and increase surface texturing effect in the ECDM.

Using the combination of the machining parameters such as KOH concentration 3M, weight percentage concentration of ethanol 4%, machining voltage of 48V, machining gap of 200μm and machining time of 60 seconds, ECDM can increase the surface roughness of mono-crystalline silicon from 0.417μm to 0.915μm without using pulse frequency and duty factor.

After ECDM, the average reflection rate is decreased from 29.695% to 12.727% between wave length 350μm and 1050μm.

References

[1] Parretta, A. Sarno, P. Tortora, H. Yakubu, P. Maddalena, J. Zhao,A. Wang, "Angle-dependent reflectance measurements on photovoltaic materials and solar cells", optics communications, Vol.172, pp.139-151,1999.

[2] V. K. Jain, P. M. Dixit, and P.M. Pandey, "On the Analysis of Electro Chemical Spark Machining Process, " International Journal of Machine Tools & Manufacture, pp.165-186.,1999

[3] Kurafuji and K. Suda, "Electrical discharge drilling of glass, "Annals of the CIRP , Vol.16 ,pp.415–419, 1968

[4] C.K Yang, C.P. Cheng, C.C. Mai, A.C. Wang, J.C. Hung, B.H. Yan, "Effect of surface roughness of toolelectrode material in ECDM performance, " Internal Journal of Machine Tools & Manufacture, Vol.50,pp.1088-1096,2010

[5] V.Reghuram, "Expermental observations of the ECD phenomena,"Dissertation Thesis, Indian Institute of Technology, Kanpur, India, 1983

Experimental and Numerical Studies on Rotary Driction Welding of Ti-6Al-4V

Ho Thi My Nu[1,2], Luu Phuong Minh[2], Nguyen Huu Loc[2], Le The Truyen[1]

[1]Ho Chi Minh City University of Food Industry

140 Le Trong Tan Street, Ho Chi Minh City, 760310, Viet Nam

[2]Ho Chi Minh City University of Technology

1 - 268 Ly Thuong Kiet Street, Ho Chi Minh City, 740400, Viet Nam

ABSTRACT

Increased performance is goals for aerospace structures result in the increasing selection of high strength titanium alloys. In order to reduce cost, fabricated structures are of great of interest, however, conventional fusion welding of high strength titanium alloys often leads to poor mechanical properties. Friction welding is a potential route to obtain enhanced mechanical properties in suitable geometry components. The present work investigates the feasibility of producing similar metal joints of this titanium alloys by rotary friction welding method (RFW). A thermomechanical model was developed to predict the upset and temperature and stress distributions, as well as to identify the suitable and safe range of parameters. The upset and temperature predicted by the finite element simulations were compared to the upset and temperature obtained by the experimental results. Good comparisons between numerical and experimental results were observed. Particularly, high upset rates due to specific heat power and forging pressure overload occurred during the welding process were investigated.

1. Introduction

Titanium alloy (Ti-6Al-4V) is a lightweight, durable material that is widely used in aeroplane and space industries. It gets also important for other fields production such as car-components, medical instruments or in leisure industries [1]. Titanium alloys also used in highly stressed gas turbine components such as the disc and spacer assembly. Such components are machined from one-piece closed die forgings, a technique which entails considerable machining and raw material waste. The use of three separate sections such as a flat pancake forging and two rolled rings inertia welded together was conceived as a potential cost reduction. Furthermore, the use of weldments for this type of component opens design options for other structures which cannot be feasibly made from one piece. However, the successful application of the alloy in some important areas depends on suitable joining techniques. Friction welding has many advantageous features to be chosen for joining titanium alloys because of its low energy consumption and high productivity. Compared to other welding methods, friction welding has many advantages such as no smoke and welding dust, no need for fill material, without using external heat source [2, 3].

Two cylindrical titanium alloy components can be welded together by the frictional heat generated. In rotary friction welding process, the work pieces are brought together under load, one part being revolved against the other so that frictional heat is developed at the inner face. When the joint area is sufficiently plastic as a result of the increase in temperature the rotation is halted and the end force is increased to forge and consolidate the joint. The process is considered to be solid state welding because the temperature in the welding process is lower than the melting point of the material. During friction welding the temperature, stress, and deformation vary depending on the parameters of the process, understanding the relationship will help determine the optimal parameters of the process and the way to improve the design quality, and manufacture of friction welding products. The effect of forging pressure is to promote the mixing of the two materials, which consolidates the weld. The basic parameters of the friction welding process are therefore the friction pressure, friction time, rotational speed and forging pressure.

Many works on rotary friction welding for various materials such as stainless steel ANSI 304, aluminum alloys, carbon steels, copper alloys have been published for many years [4]. But quite a few studies have reported the rotary friction welding of titanium alloys. Previous research has shown that titanium alloys can be welded by linear methods with excellent crystal structure of joint weld. Linear friction welding (LFW) is an established technology for the manufacture of titanium alloy integrated bladed disks for aero-engines [5-8]. Unfortunately, there have been few reports of friction welding for titanium alloys in recent years. M. Avinash et co. [9] investigated the feasibility of producing similar metal joints of this titanium alloy by rotary friction welding method. The joints are produced at three different speeds and the performances of the welded joints are evaluated by conducting microstructure studies, Vickers Hardness and tensile tests at the joints. It is found that the weld joints produced are sound and the ductile fractures in the tensile weld specimens occur at locations away from the welded joints. In studying friction welding, the problem that one usually faces is how to experimentally measure the temperature variation from the center to the periphery, as well as the stress developed during the

process. However, this is difficult to investigate with experiment because of the complexity of thermal mechanics, such as the change in thermal properties of the material as the temperature changes as well as the mechanical properties of the material change as deformation increases. All of this makes it difficult to install a direct temperature gauge on the solder parts. On the other hand, costly materials such as titanium should be limited to testing to reduce costs. Thus, numerical simulation with modern computational tools will solve the challenges of friction welding with titanium alloys. Hence, modeling techniques are employed to understand the physical phenomena. The thermodynamic model is used on the basis of the Johnson-Cook material model. A fully coupled thermomechanical finite-element analysis of the rotary friction welding process is combined with the basic physical metallurgy of Ti-6Al-4V to predict microstructure and mechanical properties within the RFW joints. Simulation results were validated using experimental measurements of the thermal field near the weld interface during friction welding, using infrared imaging.

2. Numerical modeling

Abaqus / Standard software is used to simulate the heat transfer and deformation of solder elements during rotary friction welding. Due to axial symmetry, 2-D model is used to reduce computational time. The 2-D model runtime is a few hours versus a few days when using 3D modeling. Temperature-dependent physical properties and mechanical properties as well as a viscoplastic constitutive equation were used in the model. The thermal and mechanical responses to the material during the friction welding process were investigated by finite element simulations. In this paper, a coupled thermomechanical model was developed for analysis.

Suitable grid technique ALE is supported by Abaqus / Standard is used in large thermal deformation problems. This technique is used to maintain the state of the grid that it is not destroyed due to large distortion in the calculation process. After calculation steps, the elements are redistributed to adapt to the new model parameters so as not to be destroyed. This process is repeated while calculation process until the simulation is finished.

One challenge in modeling friction welding is the analysis and determination of the friction coefficient μ. Some authors argue that the coefficient of friction is a constant or the function of radius of the components [2, 3]. The authors in [5] suggested that the coefficient of friction is proportional to the pressure acting on the welding surface and the angular velocity. Although the coefficient of friction changes continuously during the welding cycle, as the value $\mu > 1$ at the beginning then proceed to 0 when the temperature reaches the melting point at the surface, but for simplicity and it is perfectly appropriate to assume that the coefficient of friction in the welding process is constant [10].

Modeling the thermal flow during friction welding is a precise description of the heat supplied at the contact surfaces of the welding parts. Overview, the torque required to create rotational motion for the welded parts under the pressure of axial thrust on the components is determined as follows [10]:

$$M = \int_0^{M_p} dM = \int_0^R \mu P 2\pi r^2 dr$$
$$= \frac{2}{3}\mu\pi P R^2 \tag{1}$$

M is torque (Nm), μ is the coefficient of friction, R (mm) is the radius of the contact surface, and P (N/mm^2) is the pressure distributed on the contact surface. If the whole work at the frictional contact surface, thermal energy per unit area is [3]:

$$\frac{q_0}{A} = \frac{1}{A}\int_0^{M_r} \mu P v dA$$
$$= \frac{1}{A}\int_0^R \mu P v_{max} \frac{r}{R} 2\pi r dr \tag{2}$$
$$= \frac{2}{3}\mu P v_{max}$$

q_0 is heat power (W), P is the pressure, A is the cross-sectional area (mm^2), v_{max} is the maximum long velocity at the outermost point (m/s) and μ is the coefficient of friction.

So, the heat created at the contact surface of two welding parts is a function of angular velocity and pressure. In this paper, the coefficient of friction is chosen as constant throughout the modeling and the value of the friction coefficient is chosen as 0.577.

There is a part of the heat transferred from the welding parts to the surrounding air environment through the radiation and convection phenomenon. These two parameters are the convection coefficient and the radiation coefficient that can be found in the technical manuals. The initial temperature of the components is determined by the room temperature of 25 °C. The convective heat transfer coefficient between the welded face part and the surrounding environment was chosen as 100 W / (m^2. K) [11].

The difficulty in simulating friction welding is the high nonlinearity of the material model. Choosing the right material model is important to obtain the accuracy of the simulation results. In this study, the Johnson-Cook material model is used to simulate the rotational friction welding process of titanium alloy. In this model, von Mises's plastic stress varies with temperature and deformation ratio as shown in the following formula [12, 13]:

$$\sigma = \left(A + B\varepsilon_p^n\right)\left(1 + C ln \dot{\varepsilon}^*\right)\left(1 + (T^*)^m\right) \tag{3}$$

Where A, B, C, m, n are material constants, ε_p is the degree of plastic deformation, $\dot{\varepsilon}^*$ is the plastic deformation ratio and T* is the temperature parameter is determined as follows:

$$T = \begin{cases} 0 & T_r < T_m \\ \dfrac{(T - T_r)}{(T_m - T_r)} & T_r \leq T \leq T_m \\ 1 & T > T_m \end{cases} \quad (4)$$

With T_m being the melting temperature of the material, T_r is the temperature of the environment. In this simulation, the melting temperature of TC4 titanium alloy material was chosen to simulate 1680 °C [12]. Parameters of the model are presented in Table 1.

The thermal properties of the material such as the thermal conductivity, the specific heat are changed with variation of the temperature. For titanium alloys, these relationships are shown in Fig. 1.

Table 1
Parameters of Jonhson -Cook model for Ti-6Al-4V

A (MPa)	880
B (MPa)	685
n	0.47
C	0.035
m	1
T_r (ºC)	25
T_m (ºC)	1680
$\dot{\varepsilon}$	1
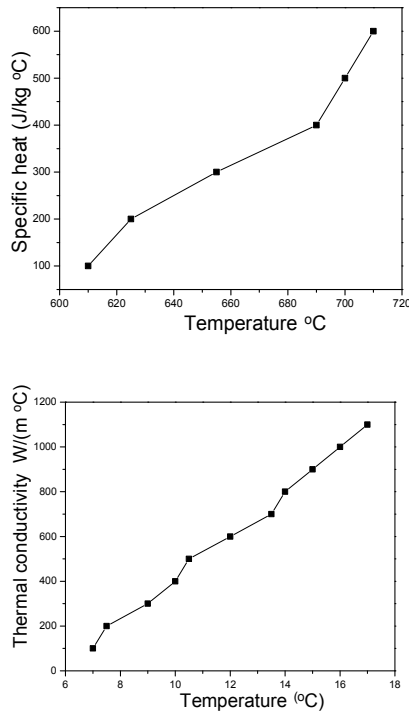
Fig. 1 The variation of specific heat and thermal conductivity with temperature

3. Simulation and experimental results

3.1 Thermal results and discussion

Above 800 °C, Ti-6Al-4V has a reduced strength due to the high temperature experienced and becomes a single phase material when reaching the beta-transus temperature at approximately 1000 °C where its strength significantly reduces. For successful friction welding, the temperature should be in range of 800 °C and 1000 °C [11].

Fig. 2 illustrates the temperature profile in the workpiece during the heating stage, assuming a heat flux of 4 W/mm². The pressure applied in the first stage is 200 MPa and the second stage is 350 MPa. The times in heating stage is 5 s and in forging stage 2.5 s. For this flux, one can see that a temperature of 917 ºC is reached in about 5 seconds.
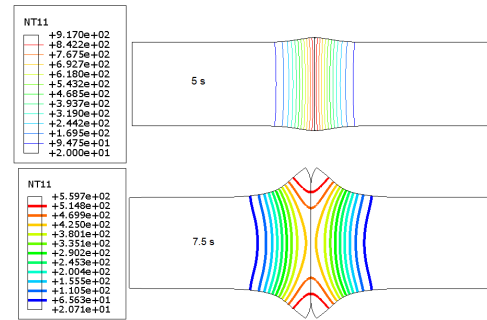
Fig. 2. Distribution of temperature at 5 s and 7.5 s

The thermal histories of regions close to the weld-line are of interest, since these will control the microstructure and properties exhibited. In Fig. 3a, the specific power is again taken to be 4.3 W/mm² for the heating stage; after 5 s the welding interface is kept at 917 ºC, and cooling follows. One can see that the region near the welding interface, for example, at the point z = 0.8 mm, reaches the highest temperature at the end of the heating stage, while for the region further from the weld line, for example at the points z = 3.2 mm, z= 4.8 mm and z = 6.4 mm, the highest temperature appears during the cooling stage. This is because of the heat transferred from the zone near the weld line with the higher temperature.

During the burn-off stage, hot material at the weld interface is forced radially outward to form the flash, while fresh material is constantly brought to the weld interface by the relative axial displacement of the two workpieces. Hence, in order to measure the temperature at the interface, infrared thermography, which is a noncontact temperature measuring method, was used. Fig. 3b shows the contour plot of surface temperature distribution at the interface, as recorded by an infrared camera during friction welding of titanium alloys. As the results shown in Fig. 3b, the temperature at the interface is about 930 ºC with the specific power is 4.3 W/mm² for the time of heating stage is 5 s The comparisons between experiment and numerical results are found to be good.
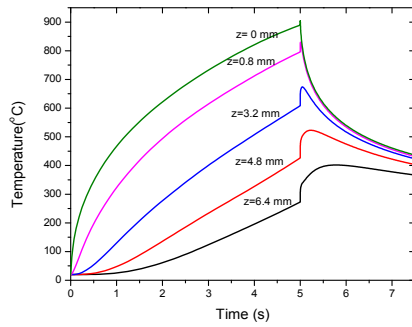
a) Predicted thermal history at different points away from the weld interface

b) Surface temperature distribution along the interface obtained by infrared thermography

Fig. 3 Predicted and measured temperatures during welding process

3.2 Upset results and discussion

The results of the upset estimated with different forging pressure are presented in Fig.4. The simulation results shown that the values of the upset drops greatly from 9.35 mm to 4 mm when the forging pressure decreases from 370 MPa to 280 MPa. Simulation results also show that the duration of the forging period has little effect on the upset. The upset is almost unchanged throughout this period.
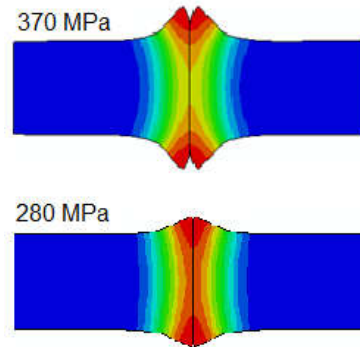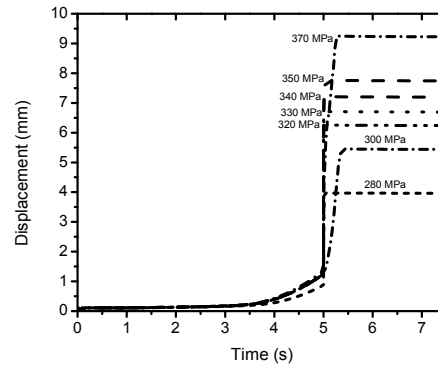
Fig. 4 Simulation results of influence of the forging pressure on the upset of Ø18 mm titanium alloys lap with specific heat 4.3 W/mm^2
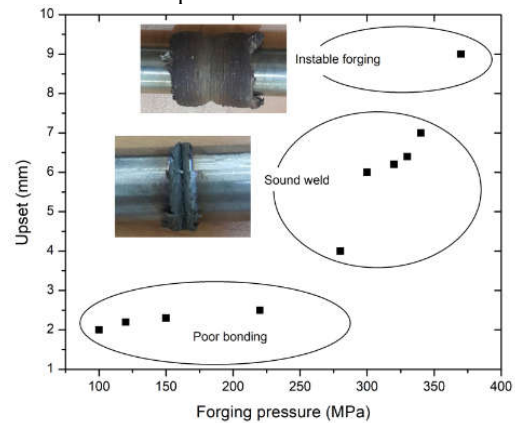
Fig. 5 Influence of the forging pressure on the upset

Figure 5 presents experimental results of titanium friction welding with specific heat power of 4.3 W. When the forging pressure is greater than 350 MPa, the upset is too large. A sound weld zone of forging pressure is observed in the range of 270 MPa to 350 MPa.

137
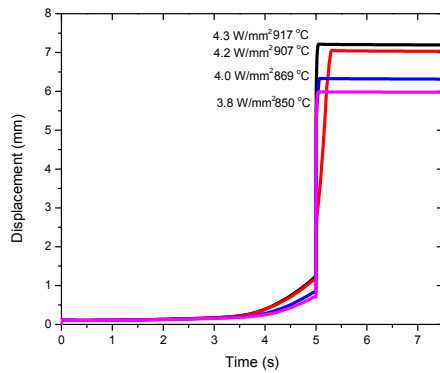
Fig. 6. Simulation results of influence of the specific weld energy on the upset of Ø18 mm titanium alloys lap with forging pressure of 340 MPa

The temperature at the well interface varies with the specific well energy. Simulation results given in Fig. 5 are shown that with the friction time 5 s the temperatures at the well interface are 917 ºC, 907 ºC, 869 ºC and 850 ºC when the specific heat are 4.3 W/mm², 4.2 W/mm², 4.0 W/mm² and 3.8 W/mm² respectively. In these simulations, the forging pressure is kept constant at 340 MPa. The upset tends to increase as the specific heat power rises.

Figure 7 presents the experimental results with different specific heat power. The low specific well energy resulted in small upsets while very high specific weld energies caused large upsets. In cases the specific heat power is bigger than 4.6 W the process became instable due to excessive plastic deformation. A sound weld zone of the specific heat power is observed in the range of 3.8 W to 4.3 W.
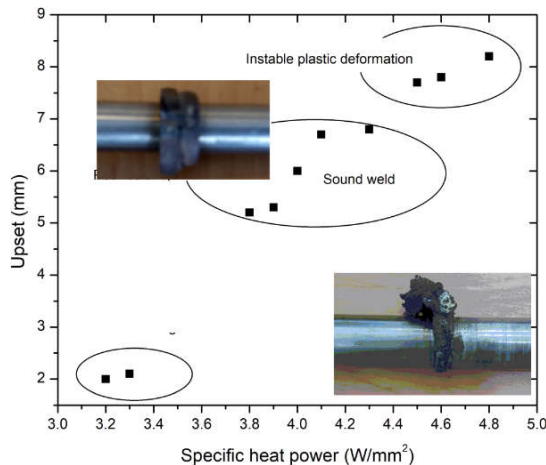
Fig. 7 Influence of the specific heat power on the upset
The two parameters that affect the upset during rotary friction welding are the specific heat power and pressure. However, the equation (2) shown that the specific heat power depends on rotational speed and friction pressure. Therefore, the process of friction welding allows a larger variation of welding parameters

to produce good bonding welds. It was possible to vary the friction pressure, forging pressure, friction time and spindle deceleration. The forging time almost does not effect on upset.

4. Conclusions

Rotary friction welding for Ti-6Al-4V titanium alloy has been studied by numerical and experiments. Ti-6Al-4V similar metal joints were welded successfully by rotary friction welding process. An increase of the forging pressure results in an increased upset. Therefore, a small forging pressure is preferred in friction welding process. Upset thresholds were determined between 5 mm and 7 mm for small-size specimens of Ti-6Al-4V. Below 5 mm insufficient bonding was observed, above 7 mm the weld process became unstable.

During initial friction stage, the temperature in friction interface raises rapidly, while during steady friction stage the temperature becomes uniform and almost constant.

Over all, the study proves the viability of rotary friction welding as a possible means of joining Ti-6Al-4V.

References

[1] Flipo B, Beamish K, Humphreys B, Wood M. Linear friction welding of Ti 6Al 4V for aerostructure applications. Trends Weld. Res. Proc. 10th Int. Conf., Tokyo, Japan; 11–14 October 2016.

[2] Uday MB, Ahmad Fauzi MN, Zuhailawati H, Ismail aB. Advances in friction welding process: a review. Sci Technol Weld Join 2010; 15:534–58.

[3] Chamanfar A, Jahazi M, Cormier J. A review on inertia and linear friction welding of Ni-based superalloys. Metall Mater Trans A 2015;46: 1639–69.

[4] Bhamji I, Preuss M, Threadgill PL, Moat RJ, Addison AC, Peel MJ. Linear friction welding of AISI 316L stainless steel. Mater Sci Eng A 2010; 528:680–90.

[5] Mc Andrew AR, Colegrove PA, Addison AC, Flipo BCD, Russell MJ, Lee LA. Modelling of the workpiece geometry effects on Ti-6Al-4V linear friction welds. Mater Des 2015;87: 1087–99.

[6] Li W, Vairis A, Preuss M, Ma T. Linear and rotary friction welding review. Int Mater Rev 2016;61: 71–100.

[7] Ma TJ, Zhong B, Li W-Y, Zhang Y, Yang S, Yang C. On microstructure and mechanical properties of linear friction welded dissimilar Ti-6Al-4V and Ti-6 5Al-3 5Mo-1 5Zr-0 3Si joint. Sci Technol Weld Join 2012;17: 9–12.

[8] Daymond MR, Bonner NW. Measurement of strain in a titanium linear friction weld by neutron diffraction. Physica B 2003;325: 130–7.

PART II, SECTION III

Mechanical Technology
(Heat transfer, Thermal, and Fluid Engineering; Structures and Fluids; Vibration;
Energy Engineering; CAD/CAM/CAE/RP…)

Time-Frequency Analysis of Vibration in Curved Surface Milling Based on Hilbert-Huang Transform

Muizuddin Azka[1,2], Keiji Yamada[1], Mahfudz Al-Huda[2], Yean-Ren Hwang[3], Ryutaro Tanaka[1], Katsuhiko Sekiya[1]

[1]Graduate School of Engineering, Hiroshima University
1-4-1 Kagamiyama, Higashi-Hiroshima, Hiroshima, 739-8527, Japan
[2]Agency for the Assessment and Application of Technology (BPPT)
PUSPIPTEK Area, Serpong, Tangerang Selatan, 15314, Indonesia
[3]Department of Mechanical Engineering, National Central University
Zhongda Rd., Zhongli District, Taoyuan City, 32001, Taiwan

ABSTRACT

This paper focuses on vibration detection technique in curved surface milling. Commonly, the stability lobe diagram (SLD) provides the machining stability and the cutting conditions to avoid the vibration. However, the stability limit is not constant but changes as the cutting forces vary during the curved surface milling. Therefore, in this paper, Hilbert-Huang transform (HHT) was used for time-frequency analysis of vibration. The HHT revealed the transition of vibration: the vibration has suddenly occured and become highest for a particular tool inclination angle.
Keywords: chatter vibration, curved surface milling, time-frequency analysis, Hilbert-Huang Transform

1. Introduction

The high degree of freedom (DoF) of multi axis machining center enables the ball-end milling operations for complex shaped product, such as: propeller, impeller, turbine blade, dies and molds. But in the operation with 3-axis machining center, it is difficult to keep the tool at an arbitrary inclination angle against the work surface. The angle continually changes during the tool travels along the cutting path on the curved surface, and then geometry of active cutting edge varies, too. This leads the changes in cutting stiffness and machinery stiffness, which affect the stability both. So that, authors investigated the influence of tool inclination on chatter vibration in ball-end milling [1].

Considering the stability transition of cutting system in the curved surface milling, some sort of time-frequency analysis (TFA) is needed to monitor the vibration. Fast-Fourier transform (FFT), in which time domain signals are transformed into frequency domain [2], is well known as an effective means for analysis of stationary signals [3]. Conversely, the short-time Fourier transform (SFT) and the wavelet transform are commonly used to analyze nonstationary signals. However, in those analyses based on FFT, both of the time resolution and the frequency resolution cannot be sufficiently increased at the same time.

Hilbert-Huang transform (HHT) is one of the TFA methods for nonstationary signals [4]. This method is a powerful signal processing because of an empirical mode decomposition of the signals, which provides high time and frequency resolutions [5]. The HHT has been successfully applied for many solutions of signal data in many fields [5-9].

This paper focuses on detection for the transition of vibration signals in curved surface milling by means of the HHT. The vibrating acceleration signals were measured by a 3-axis accelerometer in the slot milling on cylindrical surface in which the machining stability varies continuously. The obtained signals were investigated by HHT to extract the features and analyze the stability of the process.

2. Hilbert-Huang transform (HHT)

Hilbert-Huang transform (HHT) is a combination of empirical mode decomposition (EMD) and Hilbert transform (HT). This method can analyze the nonlinear and nonstationary signals, especially for time-frequency analysis [9].

Firstly, EMD decomposes the original signals into intrinsic mode functions (IMFs). A decomposition of the original time series signal $v(t)$ into n IMFs can be expressed as:

$$v(t) = \sum_{j=1}^{n} C_j(t) + r_n(t)$$

where $v(t)$ is the original signal measured, C_j is the j-th IMF, and r_n is the residue of the EMD process [9].

Next, HT is carried out to build a two-dimensional time-frequency plot providing the instantaneous frequency and amplitude, which is called Hilbert-Huang spectrum. With this plot, we can see the transition of power spectrum of signals.

3. Experimental Procedures

Table 1 shows tool specifications and cutting conditions in the experiments, which were conducted with the cylindrical workpieces (73.5 mm in diameter, 127.5 mm in length) of stainless steel (JIS SUS304) on a CNC turning center (NT 4300 DCG, DMG Mori Co. LTD). As illustrated in Fig. 1, vibration was measured using a 3-axis accelerometer mounted on the end section of workpiece, and then was stored by a data acquisition system (Yokogawa DL-750) with a sampling rate of 20 kHz during the slot milling under dry cutting. Ball-end mills with two flutes (HGOB2060-PN, Mitsubishi Hitachi Tool Eng. Ltd.) were used to make slots with the constant depth of a.

In order to examine the influence on stability by the

posture of tool, the stability lobe diagrams (SLDs) were built for several conditions. Altintas presented the 3-dimensional model providing stability limits for the vibration in milling [10], which was calculated from the modal parameters of cutting system and the cutting force coefficients of work material under certain cutting conditions.

Hammering test was conducted to get the modal parameters, such as: natural frequency f_n, damping ratio ζ, and stiffness k of cutting system. The obtained results are as follow:

$G_{xx} = [f_n = 900$ Hz; $\zeta = 0.022$; $k = 11.25$ MN/m];
$G_{yy} = [f_n = 830$ Hz; $\zeta = 0.024$; $k = 20.75$ MN/m];

and $G_{zz} = [f_n = 830$ Hz; $\zeta = 0.024$; $k = 103.75$ MN/m]. Here, G_{xx}, G_{yy}, and G_{zz} are direct transfer function, which describe the dynamic response of cutting tool and spindle for the force inputs.

Then, cutting force coefficients, that is to say, the specific cutting forces were obtained from the cutting force measurement in milling tests previously conducted under different feed rates. Obtained parameters were as: $K_{tc} = 3700$ N/mm^2 in tangential direction, $K_r = 0.54$ in radial, $K_a = 0.42$ in axial, respectively.

Figure 2 is a SLD obtained for the slot milling operation with parameters shown above. In this figure, the cutting system is unstable in the region above lobes drawn, while it becomes stable below the lobes. In this study, the spindle rotation was constant; $n = 3750$ min^{-1}, but the depth of slot were $a = 0.25$, 0.33 and 0.40 mm shown as (a), (b) and (c) in Fig. 2. It indicates that experimental conditions were chosen in the stable, the slightly unstable, and the completely unstable in slot milling of the flat work surface ($\theta = 0°$).

Here, it should be noted that this SLD shows the
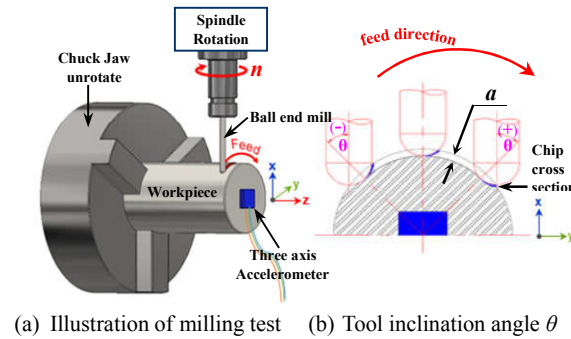
(a) Illustration of milling test   (b) Tool inclination angle θ
Fig. 1. Experimental setup in curved surface milling.

Table 1. Tool and cutting parameters

Tool parameters of ball-end mill			
Tool diameter (mm)	6	Material	Carbide
Number of flutes	2	Coating	PN
Helix angle (°)	30	Tool length (mm)	90
Flute length (mm)	12	Overhang (mm)	60
Cutting parameters for milling tests			
Spindle rotation n (min^{-1})	3750	Depth of slot a (mm)	Fig. 2
Feed per tooth f_z (mm/th)	0.02	Milling process	Slotting
Feed speed V_f (mm/min)	150	Tool inclination θ (°)	-40 to 40

stability limit without the effect of the tool inclination angle against the work surface θ. As shown in Fig. 1(b), the cutting path in this operation was along the cylindrical surface. Therefore, the tool inclination angle θ changes during the operation, and the stiffness against cutting forces also continuously varies.

4. Results and Discussion

4.1. Experimental Results

The acceleration signal was captured during the whole slotting operation corresponding to the inclination angle of $\theta = -40°$ to $+40°$. Figure 3 shows examples of transition of the vibrating signal on X and Y axes, because the signal on Z axis showed no distinctive transition, was not significant in the tests conducted.

It can be seen from Fig. 3 that the vibration was excited with $\theta > 22.5°$ for $a = 0.25$ mm, $\theta > 26°$ for $a = 0.33$ mm, and $\theta > 28.5°$ for $a = 0.40$ mm. However, the
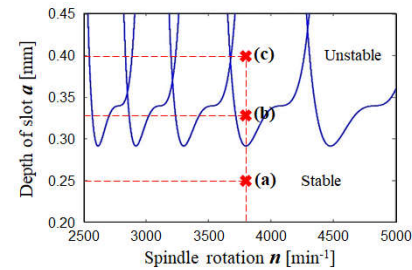
Fig. 2. Stability lobe diagram (SLD)

machining status was stationary for the lower inclination angle. This would be due to the damping effect by the tool-tip center, which contacts with the workpiece but has a slight cutting effect [1].

4.2. Vibration Analysis by FFT

FFT analysis was conducted to identify the frequencies of regenerative chatter (f_c), tooth-passing (f_T) and its harmonics, and other distinctive features. The tooth-passing frequency can be calculated using :

$$f_T = \frac{n}{60} N_t$$

where n and N_t are the spindle rotation and the number of flutes, respectively.

To compare the frequency spectrum during the transition of vibration, and the spectrum before and after the transition, 3 durations were chosen for FFT analysis. These are indicated as "A", "B" and "C" in Figs. 3(b) and (c), which correspond to the inclination angle $\theta = 24°-25°$; $27°-28°$; $30°-31°$, respectively.

Figure 4 shows frequency spectra for above durations, which reveal some frequencies; tooth-passing harmonics (625, 750, 875 Hz) and the regenerative chatter (810 Hz). For the slot depth of $a = 0.33$ mm, only tooth-passing harmonics were observed in $\theta = 24°-25°$, while the regenerative chatter was detected in $\theta = 27°-28°$ and $\theta = 30°-31°$ both. For $a = 0.40$ mm, only tooth-passing harmonics were observed in $\theta = 24°-25°$ and $\theta = 27°-28°$, while the regenerative chatter was detected in $\theta = 30°-31°$.

As results shown in those figures, FFT is an effective method to unveil the frequency components included in signals. However, it is difficult to observe instantaneous changes in spectra, because we cannot simultaneously increase the time and the frequency resolutions both in FFT. In the next section, HHT applies to analyze the transition of vibration and compare the results with FFT.

4.3. Time-Frequency Analysis by HHT

In this study, EMD process sifted out 12 IMFs from the experimentally measured signals. As an example of IMFs, Fig. 5 provides 4 IMFs containing distinctive features and a monotonic residue for an example of $a = 0.33$ mm on Y-axis. The figure also gives the frequency spectra obtained by FFT for each IMF. It should be noted that those spectra show the frequency components included for the long cutting time, so we cannot identify when the cutting status changed.

In these figures, it can be confirmed that the EMD extracted unique sub-signals from the original signal. The regenerative chatter ($f_c = 810$ Hz) and tooth-passing harmonics were contained in IMF1 which has the highest frequency component among all IMFs. Besides, IMFs 2-4 show tooth-passing harmonics only. Other IMFs (IMF 5-12) contained no significant frequency component, in this study.
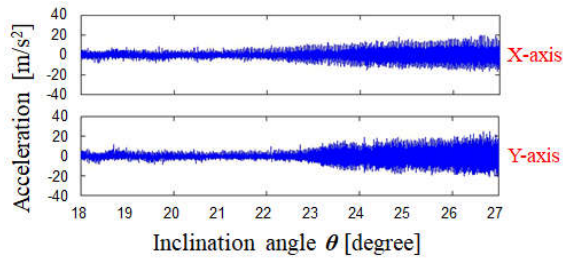
(a) Acceleration signals for $a = 0.25$ mm
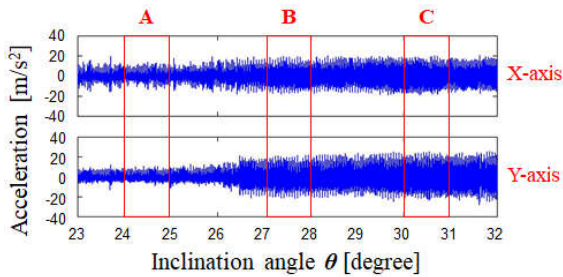
(b) Acceleration signals for $a = 0.33$ mm
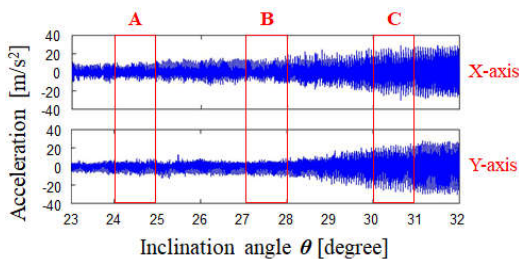
(c) Acceleration signals for $a = 0.40$ mm

Fig. 3. Effect of slotting depth on machining stability

Figure 6 shows Hilbert-Huang spectra obtained for vibration signals on X and Y axes. In any spectrum, the regenerative chatter suddenly appeared and the power became highest at a particular tool inclination angle θ. Obviously, the status for $a = 0.25$ mm with the angle $\theta < 22.5°$ was stable, because no vibration is observed. Other stable regions were found for $a = 0.33$ with $\theta < 26°$, and for $a = 0.40$ mm with $\theta < 28.5°$, too. For any slot depths, the power of particular frequency became high with the angle larger than the stability limit. And it should be noted that the maximum power increased as the depth of slot a. It can be seen that the time-frequency analysis by HHT is appropriate to detect the transition of vibration.

The experimental results show that the SLD in slot
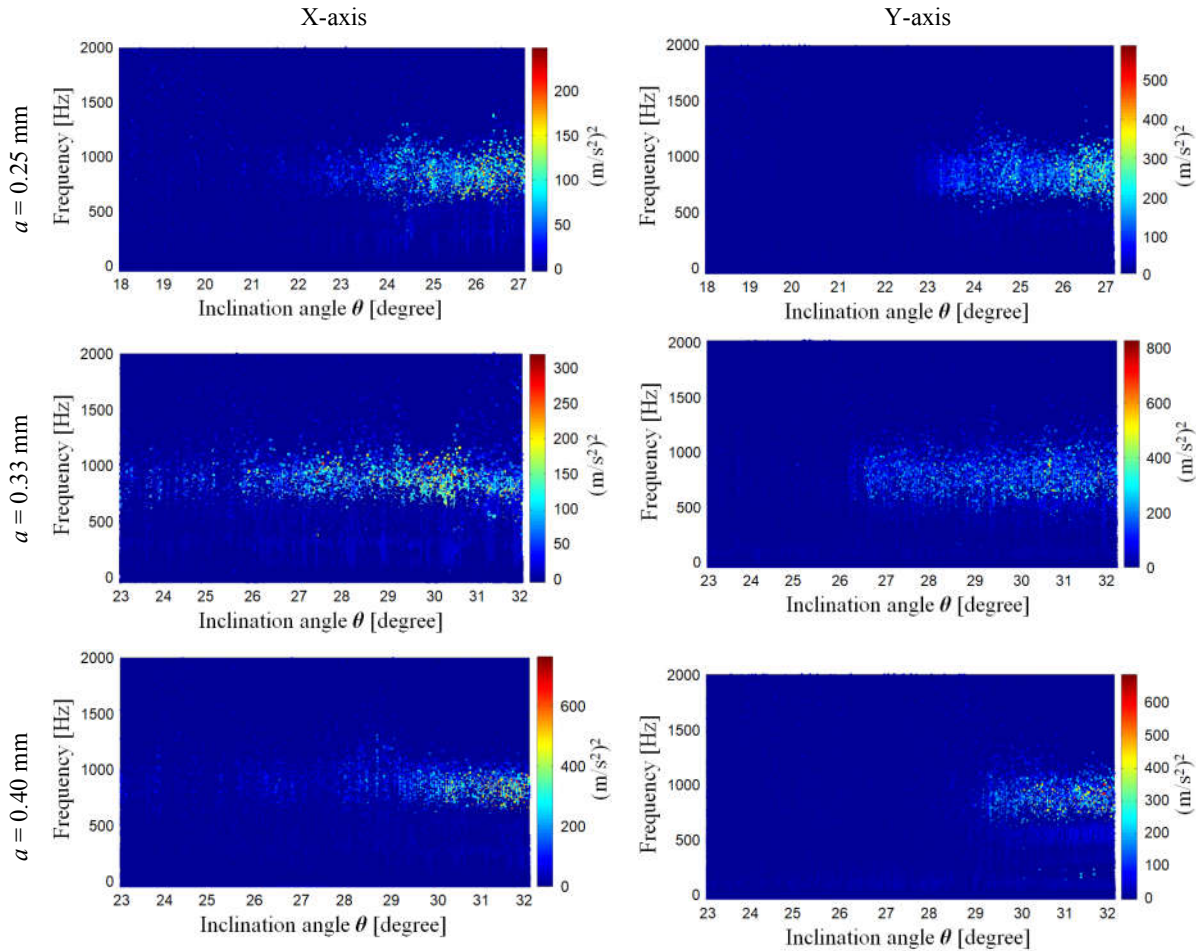
Fig. 6. Hilbert-Huang spectra for *a* = 0.25; 0.33; 0.40 mm

milling of the flat work surface ($\theta = 0°$) cannot be appropriately used for predicting the machining stability in curved surface milling. This is because the various directional forces are exerted on the ball end-mills during the machining operation of curved surface, so that the cutting stiffness is not constant but fluctuates and stability limit varies, too. In our opinion, the direction of cutting force might affect to the machining stability during milling of curved surface, which will change the stability status in SLD. Therefore, it is interesting for the next future research.

5. Conclusions

In this paper, the time-frequency analysis of vibration in curved surface milling was conducted. Hilbert-Huang transform (HHT) can detect the transition of vibration; from stable to unstable.

And, the Hilbert-Huang spectrum described the power distribution on the time-frequency plots.

6. Acknowledgements

References

[1] Azka, M., Mani, K., Yamada, K., et al., 2017. *Influence of Tool Inclination on Chatter Vibration in Ball-End Milling*. JSME Conference.

[2] Altintas, Y., Stepan, G., Merdol, D., 2008. *Chatter Stability of Milling in Frequency and Discrete Time Domain*. Annals of the CIRP, Vol.1, pp.35–44.

[3] Kalvoda, T., Hwang, Y-R., 2010. *A Cutter Tool Monitoring in Machining Process Using Hilbert-Huang Transform*. Int. J. of Machine Tools & Manufacture, Vol.50, pp.495–501.

[4] Lu a, C., Ding, P., Chen, Z., 2011. *Time-Frequency Analysis of Acoustic Emission Signals Generated by Tension Damage in CFRP*. Int. Conf. on Power Electronics and Engineering Application, Vol.23, pp.210–215.

[5] Susanto, A., Liu, C., Yamada, K., Hwang, Y-R., et al., 2018. *Application of Hilbert-Huang Transform for Vibration Signal Analysis in End-Milling*. Precision Engineering.

[6] Liu, M., Tran, Q., Qui, Y., Chung, C., 2017. *Chatter Detection in Milling Process Based on Time-Frequency Analysis*. Proceeding of ASME.

[7] Susanto, A., Yamada, K., Mani, K., et al., 2017. *Vibration Analysis in Milling of Thin-Walled*

Workpieces using Hilbert-Huang Transform. The 9th Int. Conf. on Leading Edge Manufacturing in 21st Century (LEM21).

[8] Fu, Y., Zhang, Y., Zhou, H., et al., 2016. *Timely Online Chatter Detection in End Milling Process.* Mechanical Systems and Signal Processing, Vol.75, pp.668-688.

[9] Huang, N.E., and Shen, S., 2005. *Hilbert-Huang Transform and Its Applications.* World Scientific Publishing, Singapore.

[10] Altintas, Y., 2001. *Analytical Prediction of Three Dimensional Chatter Stability in Milling.* JSME Int. Journal, Vol.44, No.3, pp.717-723

Identification of Vibration Parameters of Mechanical System Utilizing Low-Cost MEMS Accelerometers

Khanh Duong Quang[1], Huong Vuong Thi[1], Van Anh Luu[2]

[1]Faculty of Information Technology, University of Transport Technology, Address: Trieu Khuc No. 54, Thanh Xuan, Hanoi, Vietnam, Email: khanhdq@utt.edu.vn, huongvt@utt.edu.vn

[2]Faculty of Mechanical Engineering, University of Transport Technology, Address: Trieu Khuc No. 54, Thanh Xuan, Hanoi, Vietnam, Email: luuvananh@utt.edu.vn

ABSTRACT

Multi-axial mechanical systems commonly encounter the problem of vibration while attempting to drive machining systems at high speed. Many effective methods based on feed-forward and feedback control have been proposed and applied for vibration reduction. In order to design controllers all methods require the exact knowledge of system parameters: vibration frequency and damping ratio. In recent years, low-cost Micro Electro Mechanical Systems (MEMS) accelerometers have been used for many applications in industry. This paper utilized the measured acceleration obtained from MEMS accelerometer to identify vibration parameters of mechanical systems.

Keywords: MEMS accelerometer, vibration, flexible systems, low pass filters

1. Introduction

Multi-axial mechanical systems commonly encounter the problem of vibration, especially with the systems travel along the toolpath at high speed. Vibration occurs due to the physical deformation of the structure in the links or joints and results in reducing the positioning accuracy of the machines. Many methods including feedforward control and feedback control have been proposed and proved the effectiveness for vibration reduction. In that, all methods require the exact knowledge of system parameters: damped natural frequency and damping ratio. In terms of feedforward control technique low pass filters are widely applied for filtering input signals. With respect to vibration reduction, input shaping can be considered as Finite Impulse Response (FIR) filter and demonstrates more effectively than other conventional filters [1, 2]. The method is based on the convolution of the desired input and a sequence of Dirac impulses to produce a shaped reference input.

In order to identify the dynamic vibration parameters, the position tracking of the endpoint of the mechanical systems is required to be recorded [3, 4]. Based on some derived equations they can be calculated directly. The position of the marker of the load can be also measured using a three-dimensional camera installed on the trolley as non-contact sensor [5]. However, visual system is convenient only for systems machining at low speed. The identification achieves high accuracy at the expense of expensive measuring tool. Needs for alternatives to expensive conventional devices in vibration measurements have been arisen. Micro-Electro Mechanical Systems (MEMS) is one of the available options. Thanks to their reduced size, weight, cost and improved performance, MEMS inertial accelerometers are rapidly utilized in many industrial applications. The basic principle of operation behind the MEMS accelerometer is that of a simple spring mass system. MEMS accelerometers are divided into two main types: Piezoresistive and capacitive based accelerometers [7]. Once the acceleration is measured from the MEMS accelerometers with low noise, the vibration parameter can be analyzed in both time and frequency domain response.

This paper will present the preliminary equations for parameter identification. Both high precision of 182 grid encoder and LSM303DLHC MEMS accelerometer are used and compared.

2. Identification of the vibration parameters

2.1. Mathematical derivation of the vibration parameters

An under-damped second-order system has an undamped natural frequency of ω_n and a damping ratio of ζ can be generally described by:

$$F(s) = \frac{\omega_n^2}{s^2 + 2\zeta\omega_n + \omega_n^2} \qquad (1)$$

The machining process is driven by input command impulses. The residual vibration response to the sequence of impulses is given as [1, 8]:

$$y(t) = \frac{\omega_n}{\sqrt{1-\zeta^2}} e^{-\zeta\omega_n t} A \sin(\omega_d t - \psi) \qquad (2)$$

$$C(\omega_n, \zeta) = \sum_{i=1}^{m} A_i e^{\zeta\omega_n t_i} \cos(\theta_i) \qquad (3)$$

$$S(\omega_n, \zeta) = \sum_{i=1}^{n} A_i e^{\zeta\omega_n t_i} \sin(\theta_i) \qquad (4)$$

$$\omega_d = \omega_n\sqrt{1-\zeta^2} \; , \; \theta_i = \omega_d t_i \qquad (5)$$

$$A = \sqrt{C^2 + S^2} \ , \ \psi = \tan^{-1} \frac{S}{C} \qquad (6)$$

where A_i is the amplitude of the i-th impulse, t_i is the time shift (time location) of the i-th impulse, ω_d is the damped natural frequency.

The damped period time, T_d and the damped natural frequency of the structural vibration, ω_d can be identified by deriving the relationship between two successive peaks of the decaying oscillation. Let Λ be the logarithmic decrement of the amplitude ratio at the time t_o and at the one periodic time later $(t_o + T_d)$:

$$\Lambda = \ln\left(\frac{y(t_o)}{y(t_o + T_d)} \right) \qquad (7)$$

The damping ratio is then calculated as:

$$\zeta = \frac{\Lambda}{\sqrt{1 + 4\pi^2}} \qquad (8)$$

The damped angular natural frequency ω_d is obtained by a simple formula:

$$\omega_d = \frac{2\pi}{T_d} \qquad (9)$$

The reliability of the parameters identification can be improved by repeatedly reading amplitude maximums located at multiples of the damped period. For the n-th peak of the damped amplitude the formula for damping ratio is given by:

$$\zeta = \frac{\Lambda}{\sqrt{1 + 4\pi^2 n^2}} \qquad (10)$$

The analytically preliminary equations 7, 8, 9, 10 are used later to identify the damping ratio and the damped period with the data obtained from the measurements.

2.2. KGM 182 grid encoder

In order to prove the advantages of MEMS sensors the high precision of the measuring tool KGM 182 grid encoder was used [10]. During the machining process, position tracking of the endpoint is recorded to identify exactly the system parameters. However, the main function of the KGM grid encoder is to evaluate machining quality of CNC controlled machine tools.
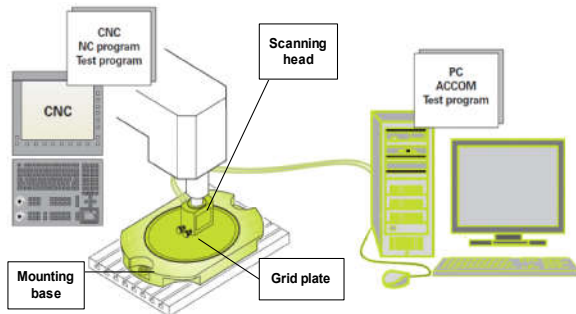
Fig. 1 Configuration setup for inspecting a machine tool [10]

The KGM grid encoders consist of a grid plate with a waffle-type graduation, which is embedded in a mounting base, and a scanning head (Figure 1). The mounting base is fixed on the machining table. During measurement, the scanning head moves over the grid plate without making mechanical contact. The KGM encoders capture any motions in a plane, and output the values measured for the two axes separately. There is no communication between the CNC and the PC. The measured data are processed by the ACCOM evaluation software with the accuracy of $2[\mu m]$. They are saved automatically in ASCII format that can be loaded by other program (e.g. Matlab, Excel, etc.).

Since the KGM 182 grid encoder records the position tracking of the tool tip, we can utilize the high precision of the measuring tool to identify the parameters of the system vibration. The data were measured at the sampling period of $0.21[ms]$. For the specified movement of $40[mm]$ along the axis in the direction x and y, the deviations of the position response are plotted out in Figure 2 and 3. The residual vibration response at the x axis expresses fairly different from the characteristics of damped vibration. This may be caused by the other structural modes of vibration. Power spectral density depicted in Figure 4 states that the system at the x axis has more than one mode of vibration. The system is vibrated at the frequencies $f_{nx} = 4, \ 30, \ 54[Hz]$. By reading the first, second, third and fifth maximum amplitude of oscillation and the corresponding time locations and using related equations, we see that the system oscillation is dominantly affected by the structural mode of the frequency $f_{nx} = 33[Hz]$ and damping ratio $\zeta_x = 0.75$. For the y axis drive, the system vibrates dominantly at the frequency $f_{ny} = 31[Hz]$, $\zeta_y = 0.65$.
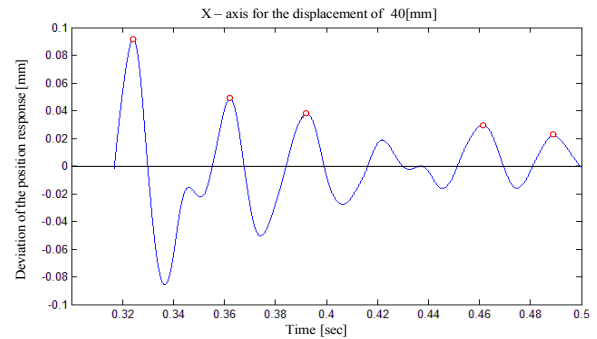
Fig. 2 Deviation of the position response along the x axis
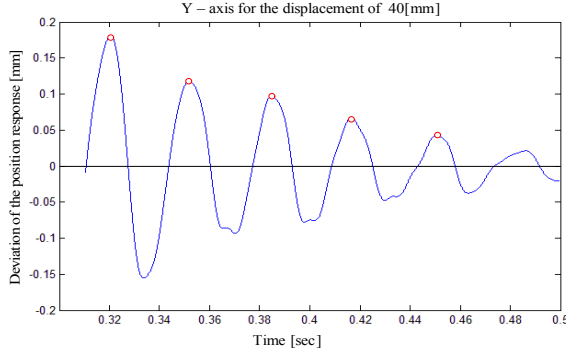
Fig. 3 Deviation of the position response along the y axis

2.3. MEMS accelerometer

In comparison with the expensive KGM 182 grid encoder, the low-cost MEMS accelerometer was used to prove the feasibility. The acceleration was measured by the 3D digital linear acceleration sensor and 3D digital magnetic sensor LSM303DLHC. The sensor is integrated into the STM32F3DISCOVERY board that is mounted to the endpoint of the machine tool (Figure 4). The 32-bit ARM® Cortex™-M4 mixed-signal MCU controls the motion sensor through the I2C interface. The output data was saved by selecting the sampling rate of 400Hz and the linear acceleration full scale of $\pm 2g$.
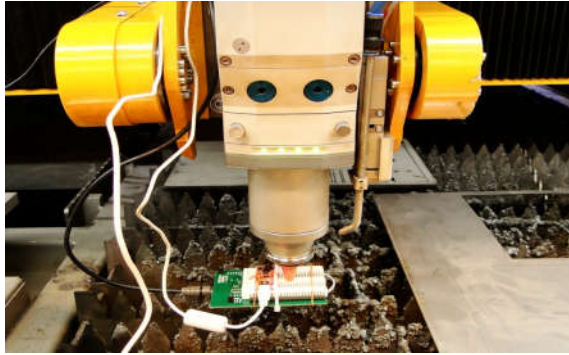
Fig. 4 The STM32F3DISCOVERY board mounting for acceleration measurements

In a steady-state on the surface, the sensor measures $0g$ on the x and y axis whereas $1g$ on the z axis. The normalized measurements a_x, a_y, a_z can be obtained from the raw measurements by assuming the length of the measured vector equal to the Earth's gravity of $1g$.

$$\sqrt{a_x^2 + a_y^2 + a_z^2} = 1 \qquad (11)$$

The board is mounted perpendicular to the z axis of the machine tool. When a movement is made in the xy space, the value of acceleration in the z direction does not change and equal or close to $1g$. In addition, for applications that require improved tilt sensitivity and

accuracy, we can use the z axis to combine with the x and y axes.
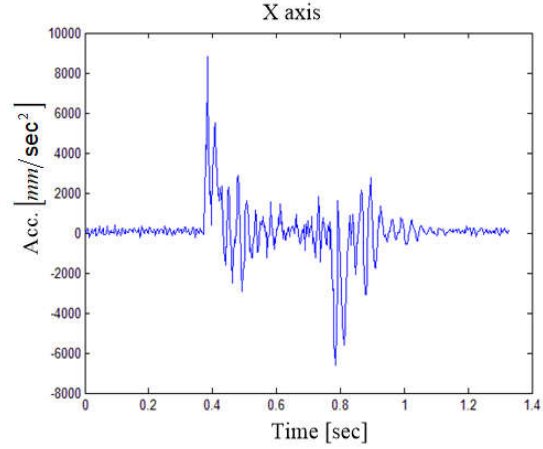
Fig. 5 Measured accelerations for the x axis drive
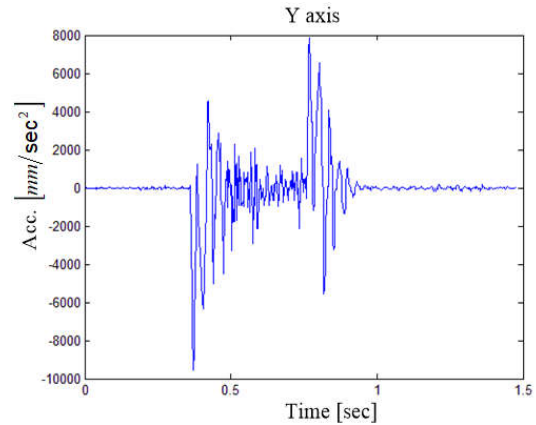
Fig. 6 Measured accelerations for the y axis drive

The raw data are transferred from the device to the host through the Virtual COM port. Figure 5 and Figure 6 depict the measured accelerations when the machine tool moves along the x and y axes, respectively. The frequency content shows the same natural frequency of vibration obtained by using the high precision of the KGM 182 grid encoder. At the last time interval, the measured acceleration expresses explicitly as the typical damped oscillation. Again, by reading out the maximum values of acceleration and applying equations 8, 9 the natural frequency of vibration and damping ratio are approximated to $f_{nx} = 32\,[Hz]$, $\zeta_x = 0.078$ for the x axis and $f_{ny} = 31\,[Hz]$, $\zeta_y = 0.071$
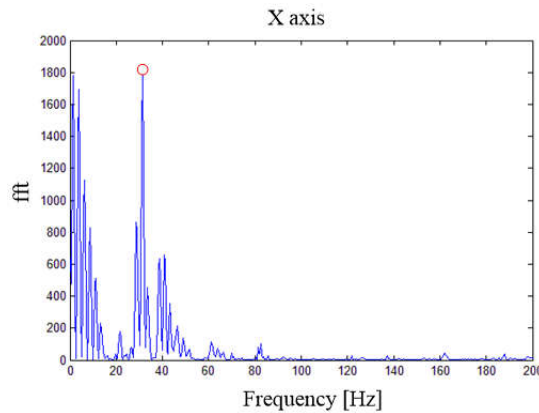
Fig. 7 Power spectral density for the x axis drive
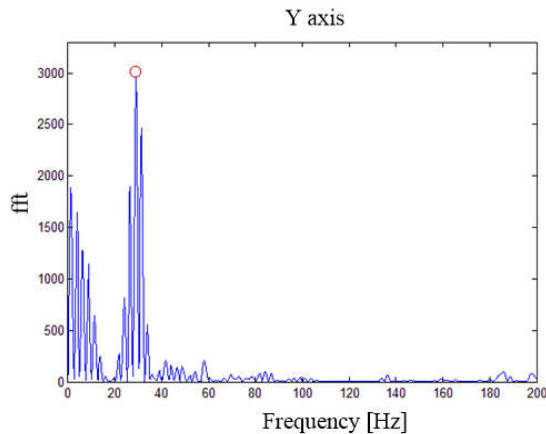
Fig. 8 Power spectral density for the y axis drive

3. Results and Discussion

In comparison with the results obtained from the KGM 182 grid encoder, we can conclude that the low-cost accelerometer allows identifying the same properties of vibration for the given system. For some specific cases, the use of accelerometer is very convenient. For instance, when the machine is affected by an unexpected disturbance, the frequency of the structural mode can differ slightly from the original. Instead of using the high cost machining tool, the accelerometer also provides the same results.

References

[1]. N.C. Singer, W.P. Seering, "Preshaping Command Inputs to Reduce System Vibration," *ASME Journal of Dynamic System, Measurement and Control*, (1990), 112(1).

[2]. W. E. Singhose, N. Singer, W. Seering, "Comparison of Command Shaping Methods for Reducing *Residual* Vibration," *In Proc. 3rd European Control Conference*, (1995).

[3]. S. Brock, "Identification of the parameters in inverted pendulum model [DC motor control], " *Proc. 7th International Workshop on Advanced Motion Control,* Slovenia, (2002).

[4]. I. Ivanov, P. Hubinsky, L. Jurisica, "Elimination of Pendulum Residual Oscillation in Electromechanical System Containing Pendulum," *Proc. 14th International Conference on Electrical Drives and Power,* (2001).

[5]. Y. Yoshida, H. Tabata, "Visual feedback control of an overhead crane and its combination with time-optimal control," *Proc. 2008 IEEE/ASME International Conference on Advanced Intelligent Mechatronics,* (2008).

[6]. A. Albarbar, S. Mekid, A. Starr and R. Pietruszkiewicz, "Suitability of MEMS Accelerometers for Condition Monitoring: An experimental study," *Sensors*, (2008), 8(2).

[7]. R. Gao, L. Zhang, "Micromachined Microsensors for Manufacturing," *IEEE Instrumentation & Measurement Magazine*, (2004), 7(2)

[8]. Q. K. Duong, Motion Control of Multi-axial Vibrational Mechatronic Systems (Doctoral Dissertation), (2016), Slovak University of Technology.

[9]. Q. K. Duong, P. Hubinsky, "Shaping NURBS Curve Based on Genetic Algorithms for Vibration Reduction," *International Journal of Mechanics and Control*, (2017), 18(2).

[10].
http://www.heidenhain.com/fileadmin/pdb/media/img/20887128_Measuring_Devices_For_Machine_Tool_Inspection_and_Acceptance_Testing.pdf

[11].
https://www.st.com/resource/en/datasheet/DM00027543.pdf

Simulate and Evaluate the Application Range of Energy Recovery Circuits Generated by Mechanical Vibration through Bond-Graph

Dương Quang Thiện[1], Nguyễn Thi Hải Vân[1]
[1]University of Technology and Education, The University of Danang
48 Cao Thang, Hai Chau district, Danang city, Vietnam

ABSTRACT

Mechanical vibrations occur mostly in production systems, and it also causes some damage. To detect the cause of this situation, the collection of parameters during operation is essential. This article uses an intermediate control circuit to convert the energy generated by mechanical vibration into electrical energy (current and voltage), in which the piezoelectric sensors or piezoelectric beam are placed on the structures to be measured, we will receive oscillations at different frequencies, so that we can analyze the damage caused by vibration and evaluate the application range of piezoelectric sensors and piezoelectric beam on a case-by-case basis. The purpose of this paper is to use Bond-Graph to optimally simulate this energy recovery process. This is also a very good solution for generating energy for the SHM system from other mechanical energy sources.

Keywords: Energy recovery, monitoring system, mechanical vibrations, piezoelectric, sensors, SHM system.

1. Introduction

Energy recovery is an area that provides the opportunity to develop science and technology applications that are currently struggling to obtain a reliable source of energy. This technology is suitable for Structural Health Monitoring (SHM) systems because it takes advantage of the different mechanical energy generated by the means of transport in moving process; The SHM system monitors the operation, detects and locates the damage occurring in vehicle structure (aircraft, space ship, etc.), thereby evaluating the nature and severity of the damage. "Structural Health Monitoring (SHM) systems have become a part of new avionic systems which will formfuture aircraft. Their objectives are to detect and locate damages occurring within the aircraft structure." [1] , "SHM has become a part of new avionic systems which will form future aircrafts. To allow their deployment throughout the aircraft, they have to be autonomous. Vibration Energy Harvesting is a promising solution to provide energy to such systems" [5]

2. Research and survey results

For this study, the author made a simple energy recovery circuit, based on the working principle of LTC 3588-1 IC; using this circuit to obtain the measured parameters, source of the experiment is the mechanical vibration source generated from a vibrator with a constant frequency. Based on the above parameters, we simulate on 20-sims software and comment on results.

2.1. Energy recovery circuit and experimental diagram
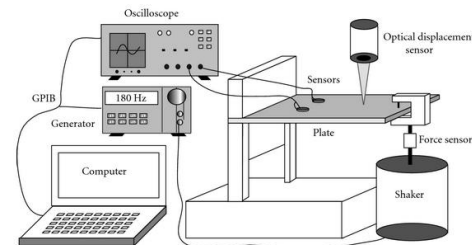
Fig. 1. Energy recovery experiment [3]
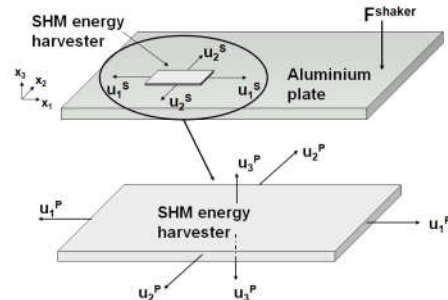
Fig. 2. Energy recovery principal

On the diagram, the piezoelectric sensors or piezoelectric beams will be placed on a thin tin sheet (2 - 3 mm), the oscillating source will impact the tin plate with a variable frequency vibration, and the sensors will transfer mechanical energy into electrical energy, then introducing into the recovery circuit and the resulting electrical signals to the subsequent processing.

The parameters taken from the experiments for piezoelectric sensors or beams are different, which clearly shows the difference in methodology and scope of use in this article.

2.2. Simulation

To simulate the above experiment, we use the Bond-Graph [2] model. In the principle diagram, it is easy to see that energy exists in two forms: the input is mechanical energy (F, V) and the output is the electrical energy (U, I). When performing simulation with other

tools (block diagram, signal diagram,...), we have to convert to a unit. Bond-Graph, however, is in the "multi-energy" field, meaning it can incorporate many fields seamlessly. This is a powerful tool because of the ability to represent physical quantities in the form of bi-directional exchange [3]. The diagram below shows the transformation from the principle diagram to the Bond-Graph of the energy recovery circuit.

Fig.3. Experimental diagram and Bond-Graph. [4]

Fig.4. Bond-Graph diagram for whole circuit

We create Bond-Graph and put the data that are measured and calculated into the software 20-Sims, the graph will show the change of quantities when the transition occurs. When testing the system with oscillations at different frequencies, we obtain a graph representing the dependence of the voltage as well as the power on the oscillation frequency.

2.3 Research results

After the experiment, based on the data sheet of the thin tin plate and the oscillation values generated on it, we have constructed the graphs that distinguish the function of the piezoelectric sensor and piezoelectric beam as follows:

Fig.5. Graphical representation of the quantities when the sensor is working

Fig.6. Voltage graph and power of the sensor in terms of frequency

Throughout the table, we find that there are some very large parameters compared with the rest. This is understandable because during the simulation, these parameters are directly related to the operating range of the piezoelectric sensor when working in high frequency conditions.

SHM is a widely used system in developed countries around the world. The purpose is to measure, retrieve information and to provide a reasonable analysis of the structural damage of large and modern buildings (bridges, tall buildings, works of politic and military,...). In recent years, combined with a number of energy recovery devices, SHM has been used in many scientific and daily life applications, contributing to significant benefits. The transportation industry is not out of the law and it is particularly significant for the aerospace industry. The characteristics of the SHM system are well suited to this sector because of the fluctuations that occur when vehicles travel, and it further exerts its advantage for large and modern means of transport.

Currently in Vietnam, SHM system has not been widely applied. This system is only used to test the stability and safety of large, highly feasible bridges. However, it has not been widely used in other industries as well as in life. Due to limited reasons, this paper presents only very small aspects of the topic. Therefore, we can only apply this energy recovery circuit in the small power circuits, the output voltage is only provided to the amplifier as well as the source for the power circuits or the experimental set in the school.

4. Conclusion

Bond-Graph is a tool used in the field of mechatronics, especially in the field of integrated energy. In Vietnam, Bond-Graph has not been applied widely in simulation such as Matlab. Using Bond-Graph will open up a new direction for similar studies.

Through the voltage and frequency-power graph, it can be seen that the piezoelectric sensors only work (resonate) at high vibration frequencies and large oscillaton resistance, in contrast, piezoelectric beam works only where the frequency is low and the resistor is small or medium. We recognize the value of use of these devices when they are used in different working conditions; especially in harsh climates like in Vietnam. In the future, wireless technology will be studied to increase the usability and economy for large and high-space architectures, contributing to aesthetics. In the future, we will study about liquid media in highly complex scientific areas of social and industrial life.
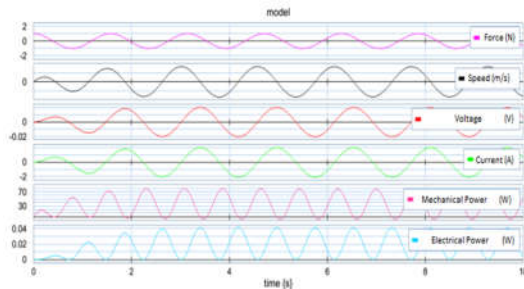
Fig.7. Graphical representation of the quantities when the piezoelectric beam is working
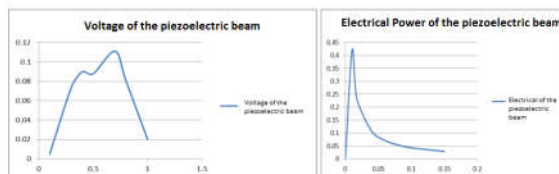
Fig.8. Voltage and power graph of piezoelectric piezoelectric

In contrast to the piezoelectric beam, the parameters are very small, the change in the parameters through simulation is often difficult to see and it only really changes when working at low frequencies.

3. Discussion

Throughout the experiment, we noticed the fundamental differences in the use of piezoelectric sensors and piezoelectric beams. It is found that piezoelectric sensors only have resonance at high oscillation frequencies, so they are suitable for use in vehicles operating under harsh conditions (aircraft, spaceship…). In contrast, piezoelectric beams only have resonance at low frequencies, so they are suitable for use in light industries with high reliability.

References

[1] T. Sainthuile, S. Grondel, C. Delebarre, S. Godts, C. Paget, "Energy harvesting process modeling of an Aeronautical Structural health Monitoring system using a Bond-Graph approche", *International Journal of Aerospace Sciences* 2012, 1(5), p107-115.

[2] T. Sainthuile, C. Delebarre, S. Grondel, C. Paget, "Bond graph model of a thin SHM piezoelectric energy harvester," *Proceedings of the 8th International Workshop on Structural Health Monitoring (F. Chang, ed.), (Stanford, CA, USA),* pp. 618–625, DesTech Publications, 2011.

[3] C. Delebarre, T. Sainthuile, S. Grondel, C. Paget, "Power harvesting capabilities of SHM ultrasonic sensors", *Hindawi Publising Corporation, Smart Materials Research*, Article ID 387638, 2012, 7 pages.

[4] T. Sainthuile, "Récupération d'Énergie Vibratoire pour Système de Contrôle Santé Intégré de Structure Aéronautique", *PhD Thesis, Université de Valenciennes et du Hainaut Cambrésis. IEMN-DOAE,* 2012.

[5] S. R. Anton and H. A. Sodano, "A review of power harvesting using piezoelectric materials", *Smart Materials and Structures, vol. 16, no. 3, 2007.*

DEM Simulation of Particle Segregation on a Vertical Vibrating Screen

Shih-Hao Chou, Shu-San Hsiau

Department of Mechanical Engineering, National Central University

Jhongli Dist., Taoyuan City, Taiwan 32001, R.O.C.

ABSTRACT

In this study, the Discrete Element Method (DEM) is employed to simulate the motion of granular materials in a vibrating sieve system. Two sizes of spherical glass beads with diameters of 5mm and 1mm were used for all cases. A vertical-horizontal coupling vibration sieving mode were used to make three-dimensional motion of particles. The results show that the variation of sieving efficiency with time is an exponential decay. We also found that the influence of horizontal vibration frequency and amplitude are inconsistent for the sieving efficiency.

Keywords: DEM, Granular, Sieving, Vibration acceleration amplitude

Analysis and Experiment Design of Damper and Cutting Parameters on Spindle Vibration of CNC Router

Huu Loc Nguyen[1], Van Thuy Tran[1], Hoang Hiep Nguyen[1]

[1]Faculty of Mechanical Engineering, Ho Chi Minh University of Technology (HCMUT), VNU-HCM, Vietnam

ABSTRACT

An understanding of the dynamic characteristics of a CNC machine is a vital element in the control of the machine which has a direct effect on the machining precision. The ways in which energy is dissipated, such as friction and damping, have a significant effect on the dynamic behavior and spindle vibration of a CNC machine. The paper presents the effect of the damper and the cutting parameters such as feed rate, cutting speed, and cutting depth on the dynamic behavior and spindle vibration of a CNC machine. Experimental results have established a second-order regression equation that demonstrates the effect of three parameters such as feed rate, cutting speed, and cutting depth on the vibration amplitude of the spindle. In addition, the comparison results show that the spindle head vibration amplitude of the machine using the damper is smaller than the spindle head vibration amplitude of the machine not using the damper
.

1. Introduction

Vibrations are a common problem during machining and reduces productivity and performance of the machine tools which also contributes to reduce the tool life [1, 2]. The vibrations are induced due to machine faults, cutting parameters, cutting tool, work piece deformation, etc. Cutting parameters especially feed rate, depth of cut and spindle speed if not properly controlled can increase the vibration in the machining process. Too high vibration is very dangerous and may lead to serious injury. Therefore, vibration must be minimized to stabilize the cutting process, improve surface roughness and prevent tool from breaking. The effect of cutting tool vibration on surface roughness of work piece in dry turning operation and a correlation between surface roughness and cutting tool vibration in turning [3]. Forced and self-excited vibration limits the stability of cutting and lead to tool and machine damage. It also limits the productivity of machining operation. Controlling spindle vibration of machine tool is one of the approaches for enhancing the quality of the product. Reducing these vibrations by damping is a common way to address the problem. Passive damping methods have been used for a long time, the first tuned mass damper was patented in1909 [4]. The most common passive dampers for damping the amplitude of the resonance vibrations are tuned mass dampers and vibration absorbers.

Although different kinds of mechanical dampers, used at the interface of the sliding elements, that is, table, saddle, and bed, are designed to improve the damping characteristics of the linear guide ways, the heavy damper serves its purpose of damping the system as well as increasing its modal frequency; however, it still retains much of the low damping characteristics of the linear guide system in machine tools [5]. Investigated the influence of the lubricant film on the damping characteristics of a deep groove ball bearing. Through experiments, they have found that the damping of bearing is reduced when the viscosity or the thickness of the lubricant film decreases [6]. In recent years, magneto rheological damper has become the most promising semi-active energy absorber; its advantages are mainly manifested in low power consumption, wide dynamic range, fast response, simple structure, continuous controllable damping force, environmental robustness easily be controlled with microcomputer etc. [7]. Analysis and simulation of machine tool vibration based on Magneto-rheological Dampers, designed specifically on the local application of magneto-rheological dampers for varying magnetic flux damper mounted machine made dynamic performance test responses. Based on this, magneto rheological dampers combine structural and performance characteristics, simulating the motion by using ADMS [8].

In addition, several researchers have studied the effect of cutting parameters such as spindle speed, feed rate, axial and radial depth of cut, appropriate selection of tool material and tool geometry in machining of aluminum based alloys [9, 10] Prediction of surface roughness in end face milling based on Gaussian process regression and cause analysis considering vibration of cutting tool [11]. Experimental investigation on the effect of cutting parameters on the spindle vibration and surface roughness in the precision end-milling process using the singular spectrum analysis [12-14]. An experimental investigation on the effect of machining and geometrical parameters such as spindle speed, feed rate, axial and radial depth of cut and radial rake angle on responses during end milling operation on the surface roughness and its defects of AL 6061-T6 [15].

Surface roughness is mainly affected by machine tool vibration. To improve the surface roughness, it is very essential to know the influences of damper and cutting parameters on machine tool vibration. The purpose of this research is to investigate on the influences of damper and cutting parameters on spindle vibration amplitude of CNC machine.

2. Kinetic analysis of the CNC machine damper system

The gantry CNC machine of 800x800x320 mm was designed. Machining operation speed of 15000 rpm and accuracy of 0.03mm were predicted as the machine's capability. The 3D design model of the CNC machine and damper are illustrated in Fig. 1.

a)   b)
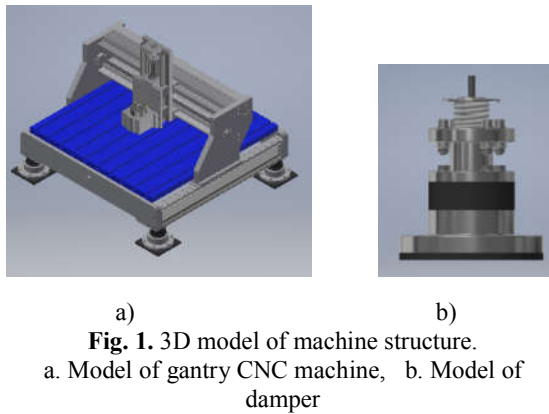
Fig. 1. 3D model of machine structure.
a. Model of gantry CNC machine,   b. Model of damper

Fig. 1b shows a mass-spring-damper system. We have constructed the physical model of the mass-spring-damper system as shown in Fig. 2
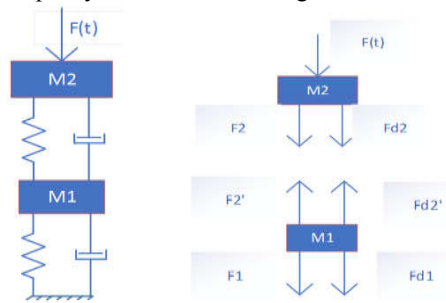
Fig. 2. Force analysis model of the damping system.

With force analysis model of the mass-spring-damper system are illustrated in Fig. 2, equation of motion is calculated by Eq. (1)

$$M\ddot{x}(t) + C\dot{x}(t) + Kx(t) = F(t) \qquad (1)$$

Set up the simulation problem of the CNC machine damping system on the Matlab program as shown in Fig. 3. The simulation result is shown in Fig. 4.
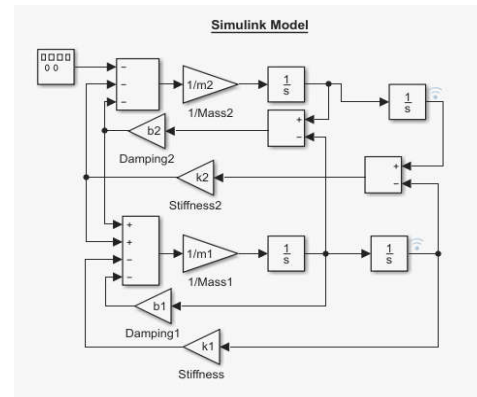
Fig. 3. Simulink model in Matlab.
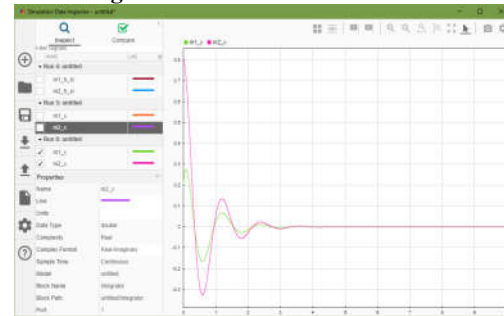
Fig. 4. Simulation results in Matlab.

3. Experimental methodology

3.1 Experimental setup

The experiments have been performed on welded structure of CNC wood milling machine. The device used for the spindle vibration test of CNC milling machine consists of instrument accelerometer sensor PCB 603C01, PCB Group, the accelerometer sensitivity 10.2 mV/g.
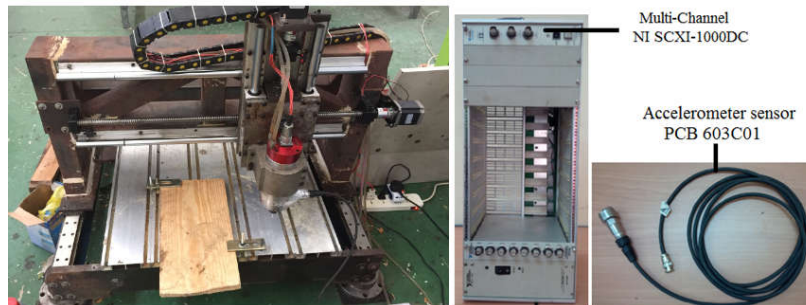
Fig. 5. Experimental setup.

The Multi-Channel NI SCXI-1000DC System was used to analyze the vibration detected by the accelerometer. For a good operating of the NI SCXI-1000DC system, the NI Signal Express software displayed the result of vibration data and a personal computer. The work piece material used in this study is fir wood. The experimental setup for operation is shown in Fig.5. In particular, the acceleration sensor is attached to the spindle head of the machine, the NI SCXI-1000DC measurement device is connected to the acceleration sensor and the computer.

Measurement data is collected and displayed through the NI Signal Express software

3.2 Design of Experiment (DOE)

The machining parameters were selected are spindle speed, feed rate and depth of cut. Cutting parameters were considered as input factors, spindle vibration was considered as output parameters during this analysis. The number of levels for each factors considered in this DOE is as shown in Table 1.

Experimental matrix based on the symmetrically mixed quadratic planning model with 3 coded factors as shown in Table 2.

Table 1. Design schema of cutting parameters and their levels.

Variables or parameter	Factor symbol		interval of variation	Variable range of cutting parameters				
	Actual factor	Code factor		level $-\alpha$	level (-1)	level (0)	level (+1)	level $+\alpha$
Spindle Speed [rev/min]	n	x_1	5000	2590	6000	11000	16000	19410
Depth of Cut [mm]	t	x_2	0.6	0.29	0.7	1.3	1.9	2.31
Feed Rate [mm/ min]	s	x_3	500	159	500	1000	1500	1841

Table 2. Experimental matrix of 3 factors.

	N⁰	X₀	X₁	X₂	X₃	X₁X₂	X₁X₃	X₂X₃	X₁₁	X₂₂	X₃₃
Number of experiments in nucleus 2^k	1	+1	+1	+1	+1	+1	+1	+1	+1	+1	+1
	2	+1	-1	+1	+1	-1	-1	+1	+1	+1	+1
	3	+1	+1	-1	+1	-1	+1	-1	+1	+1	+1
	4	+1	-1	-1	+1	+1	-1	-1	+1	+1	+1
	5	+1	+1	+1	-1	+1	-1	-1	+1	+1	+1
	6	+1	-1	+1	-1	-1	+1	-1	+1	+1	+1
	7	+1	+1	-1	-1	-1	-1	+1	+1	+1	+1
	8	+1	-1	-1	-1	+1	+1	+1	+1	+1	+1
Number of experiments in point start (*)	9	+1	+1.682	0	0	0	0	0	$2\sqrt{2}$	0	0
	10	+1	-1.682	0	0	0	0	0	$2\sqrt{2}$	0	0
	11	+1	0	+1.682	0	0	0	0	0	$2\sqrt{2}$	0
	12	+1	0	-1.682	0	0	0	0	0	$2\sqrt{2}$	0
	13	+1	0	0	+1.682	0	0	0	0	0	$2\sqrt{2}$
	14	+1	0	0	-1.682	0	0	0	0	0	$2\sqrt{2}$
Number of experiments in the planning center	15	+1	0	0	0	0	0	0	0	0	0
	16	+1	0	0	0	0	0	0	0	0	0
	17	+1	0	0	0	0	0	0	0	0	0
	18	+1	0	0	0	0	0	0	0	0	0
	19	+1	0	0	0	0	0	0	0	0	0
	20	+1	0	0	0	0	0	0	0	0	0

The mean results of measuring the spindle vibration amplitude of 20 experiments and each experiment were repeated 7 times as shown in Table 3.

Table 3. The results the spindle vibration amplitude.

N⁰	$\bar{y}$	s_i^2	N⁰	$\bar{y}$	s_i^2
1	0.0189	0.0035	11	0.0383	0.0011
2	0.0781	0.0057	12	0.0086	0.0009
3	0.0054	0.0005	13	0.0235	0.0013
4	0.0366	0.0024	14	0.0153	0.0005
5	0.0115	0.0025	15	0.0174	0.0003
6	0.0627	0.0022	16	0.0175	0.0012
7	0.0048	0.0004	17	0.0173	0.0002
8	0.0446	0.0019	18	0.0172	0.0002
9	0.0081	0.0006	19	0.0177	0.0002
10	0.0996	0.0142	20	0.0173	0.0002

4. Results and discussion

4.1 The coefficients of regression equation

With this Box-Hunter experimental model, the coefficients of regression equation were obtained by the results of experimental data and expressed by the following Eq. 2.

$$y = 0.0731 - 0.1597 x_1 + 0.0498 x_2 + 0.0208 x_3$$
$$+ 0.0489 x_1 x_2 - 0.0086 x_{13} + 0.0104 x_{23} +$$
$$+ 0.1689 x_1^2 + 0.0943 x_2^2 + 0.0413 x_3^2 \qquad (2)$$

4.2 The testing of the individual regression coefficients

After calculating the value of the coefficients of the regression equation, it is necessary to test their significance and eliminate the insignificant individual

regression coefficients [16, 17]. The computational results are shown in Table 4.

Table 4. Significance test of individual regression coefficients

Tern	Value of Coefficient	SE coefficient	T	P-Value	
b_0	0.0174	0.00134	12.996	0.000	
b_1	-0.0413	0.00149	-27.621	0.000	
b_2	0.0159	0.00149	10.688	0.000	
b_3	0.0036	0.00149	2.416	0.036	
b_{12}	-0.0139	0.00328	-4.229	0.002	
b_{13}	0.0002	0.00328	0.060	0.953	Insignificant
b_{23}	0.0106	0.00328	3.219	0.009	
b_{11}	0.0363	0.00245	14.82	0.000	
b_{22}	0.0059	0.00245	2.393	0.038	
b_{33}	0.0018	0.00245	0.739	0.477	Insignificant

In the Significance test table, P value of less than 0.05 indicates that the model terms can be considered significant. Table 4 presented of Significance test table for regression equation coefficients. There are 2 coefficient b_{13} and b_{33} are not significant because its P value is more than 0.05. We remove these coefficients, and then we rewrite the matrix and recalculate the coefficients. Through the backward elimination process, the final quadratic models of response equation in terms of coded factors are presented as follows Eq. 2.

$$y = 0.0174 - 0.0413\,x_1 + 0.0159\,x_2 + 0.0036\,x_3$$
$$- 0.0139\,x_1 x_2 + 0.0106\,x_{23} + 0.0363\,x_1^2 + 0.0059\,x_2^2$$
(2)

4.3 Testing lack of fit in regression

For testing lack of fit in regression, to perform the analysis of variance for Significance of regression is shown in Table 5

Table 5. Analysis of variance for Significance of regression

Source	Sum of Squares	DF	Mean Square	F	P-Value
Model	0.0122	7	0.001358	125.82	0.00
Residual Error	0.0001	12	0.000011		
Lack-of-Fit	0.0001	8	0.000022	652.37	0.00
Pure Error	0.0000	4	0.000000		
Total	0.01236	19			

The model was developed with 95% confidence interval. Because $F_{model} = 125.82 > F_{0.05,7,12} = 2.91$ and $F_{LOF} = 652.37 > F_{0.05,8,4} = 6.04$. Also, note that the P-value for F_{model} and F_{LOF} (shown in Table 5) is considerably smaller than $\alpha = 0.05$. The regression model is fitting well.

4.4 Evaluation of experimental results

In the milling process, the machining parameters adopting the spindle speed, the feed rate, and the depth of cut were chosen as the three factors so as to investigate the influences on the vibration amplitude. The influences of machining parameters on the performance of the vibration amplitude have been analyzed, which is based on the above proposed mathematical model.
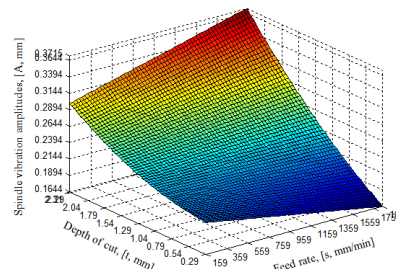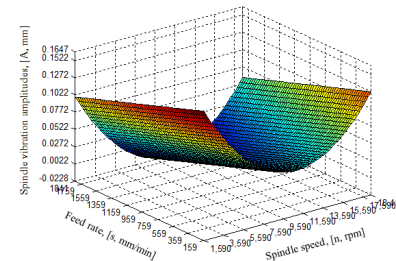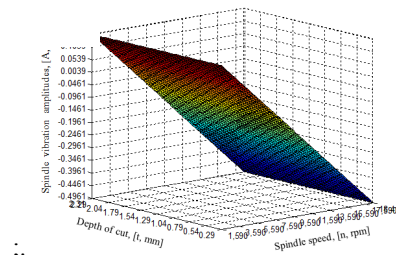
Fig. 6. (a) Effect of n and t on the spindle vibration amplitude; (b) Effect of n and s on the spindle vibration amplitude and (c) Effect of t and s on the spindle vibration amplitude

In graphs Fig. 6 shows the relationship between the feed rate, cutting speed, cutting depth and the spindle vibration amplitude of the CNC milling machine. In Fig. 3, the local reasonable cutting parameters valued (within the scope of the survey) so that the spindle vibration amplitudes is minimal as follows: $n = 13420$ rpm, $s = 1057$ mm/min and $t = 1.009$ mm => spindle vibration amplitude: $A_{min} = 0.0042$ mm.

The comparison results of spindle vibration amplitude for two different machine structure types are the structures using damper and the structures no using damper. The comparison results show that the spindle head vibration amplitude of the machine using the damper is smaller than the spindle head vibration amplitude of the machine not using the damper.

5. Conclusions

The paper presents the effect of damper and the cutting parameters such as feed rate, cutting speed, and cutting depth on the vibration amplitude of the spindle when machined on CNC milling machine by experimental design method (DOE). Using the Box-Hunter method of experimentation to construct a second-order regression equation representing the relationship between the cutting parameters and the vibration amplitude of the spindle to survey the effect of the cutting parameters on the spindle vibration in machining process. The result show that when using damper, the spindle's vibration amplitude is greatly decreased. The results also show that as the spindle speed increases, the rotational stability of the spindle head is promoted, which reduces the vibrations amplitude and the spindle vibration amplitudes increase with increasing the value of cutting depth and feed rate to cause the instability of cutting process and exhibit the result of the worst machined surface. In addition, this study also identified the most appropriate cutting parameters for machining on CNC wood milling machine.

The comparison results show that the spindle head vibration amplitude of the machine using the damper is smaller than the spindle head vibration amplitude of the machine not using the damper.

References

[1] A. Harms, B. Denkena, N. Lhermet, interface 506 (2004) 3425.

[2] A. Ganguli, A. Deraemaeker, M. Horodinca, A. Preumont, Proceedings of the Institution of Mechanical Engineers, Part I: Journal of Systems and Control Engineering 219 (2005) 359-369.

[3] S.Y. Kassab, Y.K. Khoshnaw, Engineering and technology 25 (2007) 879-889.

[4] H. Frahm, Device for damping vibrations of bodies, Google Patents, 1911.

[5] M. Rahman, M. Mansur, L. Lee, J. Lum, International Journal of Machine Tools and Manufacture 41 (2001) 431-441.

[6] W. Jacobs, R. Boonen, P. Sas, D. Moens, Mechanical Systems and Signal Processing 42 (2014) 335-350.

[7] Y. Kim, R. Langari, S. Hurlebaus, Mechanical Systems and Signal Processing 23 (2009) 300-315.

[8] S. Liu, X.L. Zhang, Analysis and Simulation of Machine Tool Vibration Based on Magneto-Rheological Dampers, Advanced Materials Research, vol 971, Trans Tech Publ, 2014, pp. 368-371.

[9] M. Sayuti, A.A. Sarhan, M. Hamdi, The International Journal of Advanced Manufacturing Technology 67 (2013) 833-849.

[10] G. Mahesh, S. Muthu, S. Devadasan, The International Journal of Advanced Manufacturing Technology 77 (2015) 369-381.

[11] G. Zhang, J. Li, Y. Chen, Y. Huang, X. Shao, M. Li, The International Journal of Advanced Manufacturing Technology 75 (2014) 1357-1370.

[12] C.-C. Chen, N.-M. Liu, K.-T. Chiang, H.-L. Chen, The International Journal of Advanced Manufacturing Technology 63 (2012) 797-815.

[13] B. Kilundu, P. Dehombreux, X. Chiementin, Mechanical Systems and Signal Processing 25 (2011) 400-415.

[14] N. Kusuma, M. Agrawal, P. Shashikumar, (2014).

[15] N. Zeelanbasha, V. Senthil, B. Sharon Sylvester, Metalurgija 57 (2018) 121-124.

[16] D.C. Montgomery, Design and analysis of experiments, John wiley & sons, 2017.

[17] H.L. Nguyen, Experimental Design, National University publisher HCMC, Viet Nam, 2014.

PART II, SECTION IV

Other Topics Related to Machining, Materials and Mechanical Technology
(Mechanics of Solid; Analysis and Simulation; New Machine Tools and Tooling Technology;
Dynamics and Control…)

Effect of Crucible and Crystal Rotations on the Solute Distribution in Large Size Sapphire Crystals During Czochralski Growth

Tran Phu Nguyen[1], Jyh-Chen Chen[1]
[1]National Central University, Jhongli (Taiwan)

ABSTRACT

In this study, the flow, temperature and solute concentration fields in the melt during the CZ growth process are numerically investigated. The results show that the magnitude and distribution of the solute concentration in the melt is strongly affected by the convective flow and thermal distribution. The maximum solute concentration always occurs at the crucible sidewall where the maximum temperature in the melt is found and the solute concentration at the crystal-melt interface increases from the triple point to the centerline. Heat transport from the side crucible wall towards the crystal-melt interface is enhanced by the crucible rotation. The level of the solute concentration inside the melt is reduced due to the lowering of the maximum temperature at the crucible wall. As a consequence, the distribution of the solute concentration along the crystal-melt interface becomes smaller and more uniform as the crucible rotation rate increases. However, after the crucible rotation rate becomes large enough, the maximum solute concentration and the solute concentration along the crystal-melt interface start to increase. Heat transport inside the melt is also affected by the crystal rotation. The centrifugal force induced by the crystal rotation generates a vortex below the crystal-melt interface. This vortex gets larger and stronger as the crystal rotation rate increases. In the smaller crystal rotation rate regime, this vortex is very small, suppressing the solute concentration at the crystal-melt interface. Therefore, the solute concentration along the crystal-melt interface becomes less when the crystal rotation rate is higher, although there is an increase in the maximum solute concentration in the melt due to the higher maximum temperature. In the higher crystal rotation rate regime, there is a reduction in the convexity of the crystal-melt interface due to enhancement of heat transport from the bottom wall of the crucible by vortex motion under the crystal-melt interface. Therefore, there is a switch to an increase in the transport of solute impurities into the crystal-melt interface. Hence, the solute concentration along the crystal-melt interface increases as the crystal rotation rate increases. However, with a further increase in the crystal rotation rate, as the shape of the crystal-melt interface changes becoming concave towards the melt, the solute concentration along the crystal-melt interface decreases because the maximum temperature is significantly reduced. In this study, both counter- and iso-rotations are considered. The results of a comparison of the cases of iso- and counter- crystal rotation show that the lowest and most uniform solute distribution along the crystal-melt interface is achieved when there is no crystal rotation and the crucible rotation rate is fixed at 1 rpm. In other words, the lowest and most uniform solute concentration can be achieved with the only crucible rotation.

Keywords: Numerical simulation, Sapphire, Czochralski method, Solute concentration, Crucible and crystal rotations.

Hole Recognition and Removal on Mold Base for the Application in Mold Flow Analysis

Pei-Pu Song[1], Jiing-Yih Lai[1], Chia-Hsiang Hsu[2] and Yao-Chen Tsai[2]

[1]Department of Mechanical Engineering, National Central University, Taoyuan, Taiwan

[2] CoreTech System (Moldex3D) Co., Ltd., Taiwan

ABSTRACT

Holes are a common feature in CAD design and exist enormously on the CAD models of a mold base. When a mold base is meshed in mold flow analysis, the existing of enormous holes would result in substantial increase on meshes as the size of holes is smaller than theirs neighboring features or surfaces. The purpose of this study is to propose a hole recognition algorithm to recognize all holes on the CAD models of a mold base and remove them from the CAD models. The most challenge problem in this issue is that holes may connect with each other and form a complex hole structure. The relationship of holes and faces composition on the hole structure should be detected and recorded. An algorithm to recognize the holes that connect with each other is presented; the topological data of these holes is described and recorded. A real mold base with six components is used to demonstrate the feasibility of the proposed algorithm. The successful rate of the proposed hole recognition algorithm is satisfied, with only two out of 307 holes failed.

Keywords: Hole recognition, Feature recognition, Mold base, Mold flow analysis.

1. Introduction

Mold flow analysis is commonly used in injection molding processes because it can be used to evaluate the defects that might occur in product design, mold design and injection process. In mold flow analysis, it is necessary to generate solid meshes for the CAD models of products, runners, cooling channels, and mold base. Though a mold base is generally composed of many components, it is often represented as a simple rectangular box for simplifying the mold structure. However, the required accuracy of mold flow analysis has been increased in recent years. In some applications, it is necessary to import all real components of a mold base and convert all of them into solid meshes. As the total amount of meshes would be increased tremendously, the mesh reduction becomes an important issue to address.
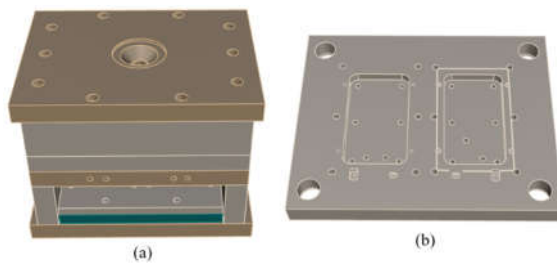
Fig. 1: A typical injection mold, (a) the mold base, and (b) part of the mold base.

Holes are a common feature in CAD design and exist enormously in injection molds, as depicted in Fig. 1. Some of them are such as holes for screws ejector pins, guide bushes, return pins, etc. Most of these holes may not be necessary in mold flow analysis as they are not empty during the injection molding process. If these holes are kept in meshing, the mesh size near a hole must be adjusted in order to maintain the circular shape faithfully, which not only increases the manual effort

required in editing, but also increases the total amount of meshes tremendously. Therefore, when a full mold is considered in mold flow analysis, it may be necessary to recognize and remove holes from the CAD models first.

In feature recognition, most investigations employ the topological relationship of adjacent entities for the recognition of features. Floriani et al. [1] introduced a method called face adjacency graph to establish a graph of the topological relationship of adjacent faces and developed a flowchart and associated rules to distinguish several types of features. This algorithm was valid for simple holes only. Joshi et al. [2] proposed a method called attributed adjacency graph (AAG), which basically adopted the concept of the face adjacency graph, but added rules in accordance with the angle between adjacent faces to distinguish the feature type. The edge type was included in the face adjacency graph. Once the graph of all adjacent faces was established, additional rules were employed to distinguish the feature type. Tian et al. [3] modified the definition of the edge type between adjacent faces from two to five types, which made the judgment of the holes more accurate. However, for the above-mentioned methods, all fillets are not considered.

When a hole is filleted at its boundary, it may be necessary to recognize the fillets first, and then perform hole recognition in terms of the fillet information. A fillet is also called a blend face in literature. Li et al. [4] indicated that a fillet with both edge blend face and vertex blend face may exist and named it hybrid-convex vertex blend face. Cui et al. [5] classified the blend face as three types: edge blend face, vertex blend face and mixed blend face. They claimed that cliff edge blend face was a special type of edge blend face and was generally discussed individually. They presented an algorithm in accordance with smooth edge, support face and span angle for the recognition of edge blend faces. Li et al. [6] introduced an algorithm in accordance with smooth

edges, normal vectors, span angles and the area of the target feature for automatic recognition and screening of blend faces. Li et al. [7] proposed a new method in terms of the topological relationship of the boundary representation (B-rep) model to solve the problem that the boundary of the holes cannot be filleted in the AAG method. It utilized the property that a hole was always accompanied with an inner loop in the B-rep model. All adjacent faces corresponding to an inner loop were found and the type of the loop was judged in accordance with the angle between adjacent faces. However, the types of hole that can be recognized are still limited.

Holes can be classified as many types. Some of them are blind holes, whereas the others are through holes. On the other hand, according to the relationship between holes, some of them are independent, whereas the others may be related to each other. Hence, trying to recognize and remove holes manually on all CAD models of an injection mold is not only troublesome, but also time consuming. The aim of this study is to develop algorithms for the recognition of holes and generating the data needed for removing holes from an injection mold.

2. The Proposed Method

2.1 Classification of Holes

As Fig. 2 depicts, a hole essentially includes base face, side face and bottom face. The base face denotes the face that a hole resides. It is typically on the top of a hole. The bottom face denotes the bottom of a hole. The side face is the face neighboring both base and bottom faces. Holes are classified in accordance with the shape, composition of faces, and boundary conditions. First, the shape of a hole can either be circular or non-circular. The property of a conic hole is similar to that of a circular one and can be considered as a circular hole. A hole with other kinds of shape is regarded as non-circular. Second, a hole can either be formed by a single surface or multiple surfaces. The number of surfaces forming a hole is proportional to the number of edges on the hole. A topological relationship of all faces sharing the same hole should be established in order to recognize the entire hole. Third, the boundary edge of a hole can either be filleted or not. When it is filleted, a blend face exists between the hole face and its base face. On the contrary, when it is not filleted, the hole face is directly adjacent to its base face. Finally, a hole can either be blind or through, depending on whether the other side of the hole is covered by another face or not. For a through hole, the base and bottom faces can be exchanged, whereas for a blind hole, the base and bottom faces are different.

The left and right plots in Fig. 2 depict a simple hole and a complex hole, respectively. The simple hole is with the conditions of single surface, circular shape, through hole, and without fillet at both boundary edges; whereas the complex hole is with the conditions of multiple surfaces, non-circular shape, blind hole, and with fillets at both boundary edges. In addition, some holes may connect with each other and form a complex structure. It is necessary to recognize this kind of situation and record the topological data of the holes in each hole structure.

Only the attribute "through or blind type" is related to the complexity of a hole structure and is recognized individually; while the other three attributed are considered as the property of a hole.
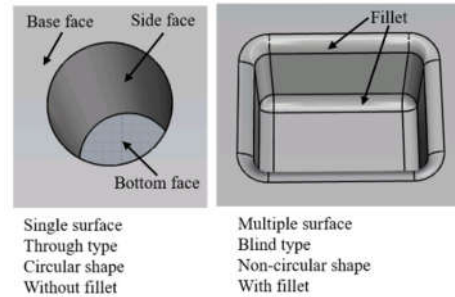
Fig. 2: Hole classification and face composition.

2.2 The Proposed Hole Recognition Algorithm

Fig. 3 depicts the procedure of the proposed hole recognition algorithm. The input loop data (Fig. 3(a)) is obtained from preliminary functions. The loop can lie either on a single surface or across faces that are G^0, G^1 or G^2 continuous [8]. The search of the holes is performed loop by loop in sequence. Assume that the loop L_i is considered, where i is the loop index. The base face F_{bi} and the number of edges on L_i are evaluated first. For each of the edges, say E_j, in L_i, check whether it is convex or concave. If all edges on L_i are convex, then a hole exists and the side face F_{si} adjacent to F_{bi} can be obtained. Otherwise, no hole exists on L_i. If E_j is a smooth edge, the blend face is recorded as the neighboring face of F_{bi}, and the other face adjacent to the blend face is used to check the concave and convex properties of E_j. Once the side face F_{si} is obtained, the bottom face F_{bmi} adjacent to F_{si} can be obtained. This process is performed for all loops to obtain all holes and the corresponding base, side and bottom faces for each of the holes. Fig. 3(b) shows that four holes corresponding to four loops for the case in Fig. 3(a) are recognized, and all side and bottom faces are colored.
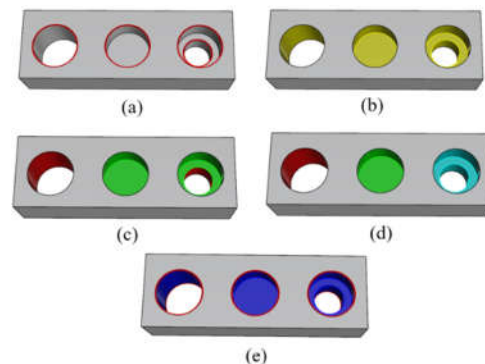
Fig. 3: Hole recognition procedures, (a) input loop data, (b) search faces composition on each hole, (c) compute type and associated properties of each loop, (d) detect related holes, and (e) output data for hole removal.

Once all holes are obtained, the blind or through type of each hole is checked one by one. If all edges between the side and bottom faces are concave, this hole is blind; whereas if all edges between the side and bottom faces are convex, this hole is through. It is noted that the two loops of a through hole are checked individually and it may result in two identical holes. To eliminate this problem, the side faces of different holes are compared and action is taken in accordance with the conditions in Fig. 4. Fig. 4(a) indicates that the two loops of a through hole share the same side faces. Hence these two loops should be considered as one loop. Fig. 4(b) indicates that the two loops of a through hole shares partial side faces. These two loops should also be considered as one loop. Fig. 4(c) indicates that a through hole could have one loop only, and hence no hole merging is necessary. Fig. 3(c) shows that two blind holes and two through holes are recognized for the case in Fig. 3(a), with different colors for the blind and through holes, respectively.
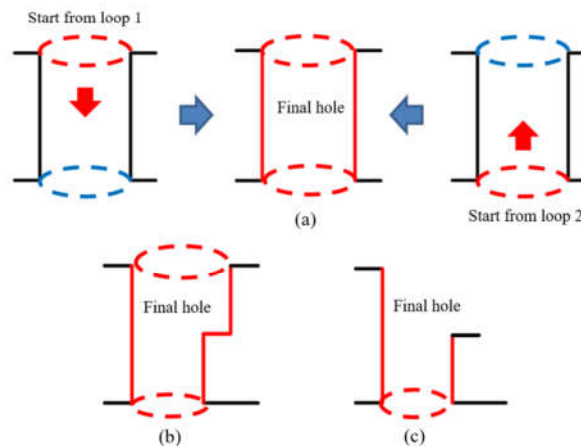
Fig. 4: Detection of three kinds of through hole, (a) two loops share the same side face, (b) two loops share partial side faces, and (c) only one loop exists.

When several holes connect with each other, the topological relationship of these holes are detected and recorded. If a hole connects with another hole, its base or bottom face should be recorded by the latter also. Therefore, by recording the index of the latter that shares the same base or bottom face of the former, the relationship of these two holes can be obtained. Consider Fig. 5(a) as an example, where hole 7 is related to both 5 and 8 through its base face and bottom face, respectively, and hole 5 is related to both 7 and 13 through its bottom face. Such data is recorded by arrays shown in Fig. 5(b). A special case of complex hole structure is called "ladder hole", in which all related holes are connected in sequence, as shown in Fig. 6. To search a ladder hole and its holes composition in a complex hole structure, the first step is to search the first layer of the ladder hole. There are two conditions for a hole to be the first layer: (1) the hole related to its bottom face should at least be 1, and (2) its base face is not counted by other holes, as shown in Fig. 6(a). Once the first layer of holes is obtained, the

next layer can be obtained in accordance with three conditions: (1) the neighboring faces of its bottom face do not belong to any hole, (2) the neighboring hole is a through hole, and (3) the difference of the perimeter of the two holes is sufficiently large. Such a search is continued until the final layer is a blind hole. Fig. 6(b) depicts the second and third layers of the holes obtained. Once all holes are obtained, they can be combined and form a ladder hole, as shown in Fig. 6(c), in which a series of hole indices is recorded in sequence to denote the data of a ladder hole.
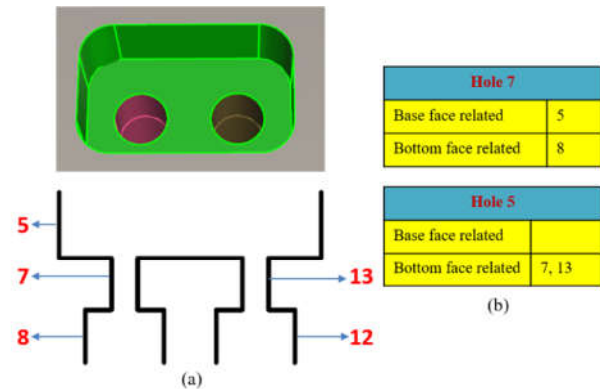
Fig. 5: An example for illustrating the data recording of complex hole structure, (a) hole composition, and (b) data recorded for holes 5 and 7.
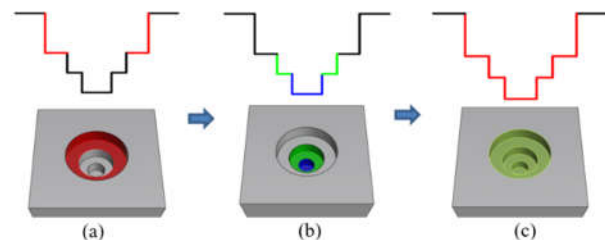
Fig. 6: Ladder hole detection, (a) search the first layer of the ladder hole, (b) search the other layers, and (c) record the data of a ladder hole.

3. Results and Discussion

The mold base with six main components, as shown in Fig. 1, is employed to test the feasibility of the proposed hole recognition algorithm. As the mold base is from a real industrial case, all types of hole may exist in different components of the mold base. The results of hole recognition for all six components are depicted in Fig. 7. Here blind holes and through holes are colored in green and red, respectively, while each set of hole structure (at least two hole connected with each other) is colored differently. The result indicates that 305 out of 307 holes are successfully recognized, with only 2 holes wrongly recognized. The successful rate is 99.9%, which is very high. When a hole is cut by other surfaces and forms a more complex situation, it will result in a complex loop between the base and side faces. This is why two holes are wrongly recognized. Nevertheless, the proposed algorithm works very well for typical holes that are fully

developed and have not been interfered by other features. Once holes are recognized, they can be removed from the original CAD model. For a blind face, its base face is kept, while the other two faces are removed. For a through face, both the base and bottom faces are kept, while the side face is removed. A ladder hole can be considered as a complex blind or through hole, and the faces can be manipulated in a similar way. Fig. 8 depicts an example of hole recognition and removal, where Fig. 8(a) indicates the recognition of holes, Fig. 8(b) indicates the data recorded in each hole to be removed, and Fig. 8(c) indicates the result after all holes are removed. It is noted that it might be necessary to leave some of the larger holes, instead of removing all of them. It can be achieved by adding a threshold to specify smaller holes that should be removed.

Fig. 7: Results of hole recognition for the mold base in Fig. 1.
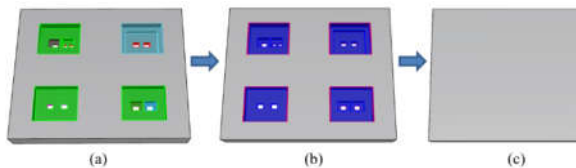
Fig. 8: An example illustrating the removal of holes, (a) recognition of the holes, (b) related data recorded on each hole or hole structure, and (c) after all holes removed.

4. Conclusion

The proposed hole recognition algorithm has been demonstrated to be able to recognize almost all holes on the CAD models of a mold base. Once all holes are recognized, they can easily be removed from the CAD model. The most significant contribution of the proposed algorithm is that it emphasizes the establishment of the topological data on a complex hole structure that involves a series of holes connecting with each other. A special case of such a complex structure is a ladder hole, in which all related holes are connected in series. In this study, we have demonstrated that such a complex hole structure can be recognized and dealt with easily. There are still some special situations, such as hole with chamfer and hole cut by other features, which cannot be manipulated. Nevertheless, the successful rate of the proposed hole recognition algorithm is very high, which demonstrates the feasibility of the proposed hole recognition algorithm.

References

[1] L.D. Floriani, S. Ansaldi, B. Falcidieno, Geometric Modeling of Solid Objects by Using a Face Adjacency Graph Representation, SIGGRAPH '85 Proceedings of the 12th Annual Conference on Computer Graphics and Interactive Techniques, (1985), 131-139.

[2] S. Joshi, T.C. Chang, Graph-Based Heuristics for Recognition of Machined Features from a 3D Solid Model, Comput. Aided Design, 20 (1988), 58-66.

[3] F. Tian, X. Tian, J. Geng, Z. Li, Z. Zhang, A Hybrid Interactive Feature Recognition Method Based on Lightweight Model, ICMTMA, 1 (2010), 113-117.

[4] B. Li, J. Liu, Detail Feature Recognition and Decomposition in Solid Model, Comput. Aided Design, 34 (2002), 405-414.

[5] X. Cui, S. Gao, G. Zhou, An Efficient Algorithm for Recognizing and Suppressing Blend Features, Computer-Aided Design and Applications, 1 (2004), 421-428.

[6] J. Li, G. Tong, D. Shi, M. Geng, H. Zhu, I. Hagiwara, Automatic Small Blend Recognition from B-rep Models for Analysis, EWC, 25 (2009), 279-285.

[7] J. Li, L. Sun, J. Peng, J. Du, L. Fan, Automatic Small Depression Feature Recognition from Solid B-rep Models for Meshing, ICECE, (2011), 4386-4389.

[8] J.Y. Lai, M.H. Wang, Z.W. You, Y.K. Chiu, C.H. Hsu, Y.C. Tsai, C.Y. Huang, Recognition of Virtual Loops on 3D CAD Models Based on the B-Rep Model, EWC, 32 (2016), 593-606.

Modeling and Simulation of Brine Droplets Using the Volume of Fluid Method: Ambient Temperature Effect

Bo-Hsuang Wu[1], Chih-Ang Chung[1,2]

[1] Department of Mechanical Engineering, National Central University, Taiwan, ROC

[2]Graduate Institute of Energy Engineering, National Central University, Taiwan, ROC

ABSTRACT

This paper proposes a mathematical model for simulating the evaporation of a solution droplet. The volume of fluid method (VOF) was adopted to capture the liquid-gas interface. The entire drying process was analyzed using a brine droplet as an example. Simulations were performed to investigate the influence of ambient temperature on the final structure of the precipitate particle. Two distinct particle structures have been discussed. The droplet solidifies into a solid particle when the ambient temperature is low, while a hollow sphere when the ambient temperature is high. The mechanisms underlying these two particle forms are discussed.

Keywords: Spray drying, evaporation, precipitation, volume of fluid method, powder structure

1. Introduction

Spray drying has the advantages for low cost, simple process, large-scale industrial production and easy control of powder-molded structures that it has become one of the most common methods of producing functional powders. Functional powders have complicated structures that the analysis of the corresponding drying process has become an important issue in the manufacturing.

The theoretical model of spray drying technology is based on a single solution droplet which undergoes the process of drying and precipitation [1]. Temperature profoundly influence the mass transfer rate across the droplet surface [2]. Traditionally the entire drying process was regarded to contain two drying stages: temperature adjustment, and isothermal drying [3]. Once the precipitates form, the distribution of solids affects the liquid evaporation too [3]. The solidified shell is treated as a porous medium through which solvent vapors are transported to the open air [5, 6]. In order to take into account the effect of the precipitate shell, the droplet drying process was considered to consist of four stages: temperature adjustment, isothermal drying, solidified shell formation, and the shell thickening [7].

To date, different mathematical models have been developed for each of the different drying stages. The environmental impacts such as the temperature and concentration distribution over the gas surrounding the droplets have been simplified theoretically. We aim to develop a fully comprehended model that can include all of the four different stages using the same set of equations. The simulation was then performed using ANSYS Fluent 17.2 via the user-defined functions (UDFs). The influence of the environmental gas temperature on the formation of the powder structure was investigated using droplets of sodium chloride solution as an example.

2. Mathematical Formulation

We model a brine droplet that is dried in the air, assuming all the fluids are incompressible, and neglecting the gravitational force. The materials involved in the drying process include brine, air and the precipitated sodium chloride. These three phases are denoted by their corresponding volume fraction, respectively. The method of volume of fluid (VOF) was used to capture their interfaces [8]. Considering the water evaporation and salt precipitation, the mass conservation equations for the brine solution, the salt precipitate and air in terms of their volume fraction α_l, α_s and α_g are

$$\frac{\partial}{\partial t}\left(\alpha_l \rho_l\right) + \nabla \cdot \left(\alpha_l \rho_l V\right) = -\dot{m}_{\text{lg}} - \dot{m}_{ls} \tag{1}$$

$$\frac{\partial}{\partial t}\left(\alpha_s \rho_s\right) + \nabla \cdot \left(\alpha_s \rho_s V\right) = \dot{m}_{ls} \tag{2}$$

$$\alpha_g = 1 - \left(\alpha_l + \alpha_s\right) \tag{3}$$

where $\dot{m}_{\text{lg}}$ is the water evaporation rate, $\dot{m}_{ls}$ the salt precipitation rate. In the momentum equation, the continuum surface force is included to account for the surface tension of the liquid as follows [9]

$$\frac{\partial}{\partial t}\left(\rho V\right) + \nabla \cdot \left(\rho V V\right)$$
$$= -\nabla P + \nabla \cdot \left(\mu \left(\nabla V + \left(\nabla V\right)^T\right)\right) + \boldsymbol{F}_{CSF} \tag{4}$$

where the continuum surface force is modeled as

$$\boldsymbol{F}_{CSF} = \sigma \kappa \nabla \alpha_l \tag{5}$$

with σ being the surface tension, κ the liquid surface curvature, which is calculated by

$$\kappa = -\nabla \cdot \left(\nabla \alpha_l / |\nabla \alpha_l|\right) \tag{6}$$

and the overall viscosity is evaluated in a volume-average way

$$\mu = \alpha_l \mu_l + \alpha_g \mu_g + \alpha_s \mu_s \tag{7}$$

where a large-valued pseudo viscosity μ_s is assumed for the solid phase that prevents the relative deformation of the solid phase. The overall mass conservation equation is

$$\frac{\partial \rho}{\partial t} + \nabla \cdot \left(\rho V\right) = 0 \tag{8}$$

with the overall mass density being evaluated in a volume-average way too

$$\rho = \alpha_l \rho_l + \alpha_g \rho_g + \alpha_s \rho_s \tag{9}$$

The temperature is predicted with the energy equation

$$\rho C_p \frac{DT}{Dt} = \nabla \cdot (k \nabla T) - \dot{m}_{lg} L_{lg} \tag{10}$$

where L_{lg} is the latent heat of evaporation, and the specific heat and thermal conductivity are in a mass-average and volume-average form, respectively as

$$k = \alpha_l k_l + \alpha_g k_g + \alpha_s k_s \tag{11}$$

$$\rho C_p = \alpha_l \rho_l C_{pl} + \alpha_g \rho_g C_{pg} + \alpha_s \rho_s C_{ps} \tag{12}$$

The amount of water vapor in the air increases as water evaporates from the liquid droplet to air, accordingly

$$
\begin{aligned}
&\frac{\partial}{\partial t}(\alpha_g \rho_g Y_{g,1}) + \nabla \cdot (\alpha_g \rho_g Y_{g,1} V) \\
&= \nabla \cdot (\alpha_g \rho_g D_{g,1} \nabla Y_{g,1}) + \dot{m}_{lg}
\end{aligned}
\tag{13}
$$

and

$$Y_{g,2} = 1 - Y_{g,1} \tag{14}$$

where $Y_{g,1}$ is the mass fraction of water vapor in the air, and $Y_{g,2}$ the mass fraction of the dry air. The water concentration in the liquid droplet is solved using the following mass conservation equation for water content in the solution

$$
\begin{aligned}
&\frac{\partial}{\partial t}(\alpha_l \rho_l Y_{l,1}) + \nabla \cdot (\alpha_l \rho_l Y_{l,1} V) \\
&= \nabla \cdot (\alpha_l \rho_l D_{l,1} \nabla Y_{l,1}) - \dot{m}_{lg}
\end{aligned}
\tag{15}
$$

$$Y_{l,2} = 1 - Y_{l,1} \tag{16}$$

where $Y_{l,1}$ is the mass fraction of water in the liquid solution, and $Y_{l,2}$ the soluble salt. The thermal physical properties inclusive of mass density, thermal conductivity and specific heat of the liquid phase ($\rho_l, k_l, C_{p,l}$) and gas phase ($\rho_g, k_g, C_{p,g}$) are functions of the corresponding water concentration, while the properties of solid phase ($\rho_s, k_s, C_{p,s}$) are assumed to be constant.

In order to close the formulation, two rate equations are needed to quantify the water evaporation and salt precipitation rates. In this paper, we adopt the Hertz-Knudsen equation for water evaporation as follows [11]

$$
\begin{aligned}
&\dot{m}_{lg} \\
&= \left(\frac{2\bar{\sigma}}{2-\bar{\sigma}}\right)\left(\frac{MW_{H_2O}}{2\pi\bar{R}}\right)^{0.5} \frac{(P_{sat,vap} - P_{vap})}{T_{vap}^{1/2}} |\nabla \alpha_l| \alpha_l^{\beta}
\end{aligned}
\tag{17}
$$

where the saturation vapor is a function of temperature, which is empirically correlated as

$$P_{sat,vap} = P_{sat,vap,0} \exp\left(\frac{17.27T}{T + 237.3}\right) \tag{18}$$

the empirical coefficient β=2, and the partial pressure of water vapor

$$P_{vap} = \frac{MW}{MW_{H_2O}} Y_{g,1} P \tag{19}$$

The salt precipitation rate is described by the empirical correlation as follows [12]

$$\dot{m}_{ls} = \frac{6C_G}{D_{sm}} \alpha_s \left(Y_{l,2} - Y_{sat}\right)^G \tag{20}$$

where the empirical coefficient $C_G = 2.98 \times 10^{-5}$, the power $G = 1.21$, the Sauter diameter $D_{sm}=5.64 \times 10^{-8}$ m, and the saturation concentration $Y_{sat} \approx 0.275$ for the temperature ranging from 20 to 60 °C.

Table 1. Initial conditions of droplet drying for comparison with literature [7].

variable	Description	value
V	velocity	0 m/s
T_{air}	Air temperature	24°C
$T_{droplet}$	Droplet temperature	18.35°C
$Y_{g,1}$	Water concentration in air (relative humidity 55%)	0.01045 kg/kg
$Y_{l,1}$	Water concentration in solution	0.95 kg/kg
P_{air}	Air pressure (gage)	0 Pa
$P_{droplet}$	Droplet pressure (gage)	242 Pa
R_0	Droplet radius	595 μm

The numerical simulations were performed using ANYSIS Fluent 17.2, which adopts a finite volume method to discretize the governing equations. The rate equations (17) and (18) were included in the computation using the user defined functions in Fluent. Equations (1)-(3) are solved for the volume fractions. Equations (4) and (8) are solved for the velocity and pressure variables. Energy equation (10) is for temperature, and Eqs. (13)~(16) are for mass fractions.

As for the initial and boundary conditions, we consider the saline-solution droplet initially at a temperature 20 °C is surrounded by initially stationary dry air of different temperatures. The initial conditions are summarized in Tables 1 and 2. The case of Table 1 is used to validate the model by comparing simulation results with experimental data in literature [7], and those in Table 2 are to investigate the influence of gas temperature. The computational domain is set as axial symmetry to save computational time. The computational domain is as shown in Fig. 1. It is assumed that at boundaries 1-3, the air pressure maintains at P_{air}, and the gradients of velocity, temperature and concentration are zero. Boundary 4 is the axis of symmetry.
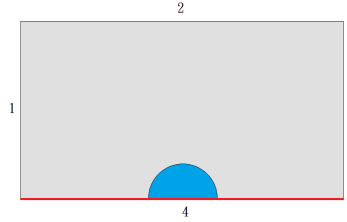
Fig. 1 Computational domain, in which a brine droplet (blue) of initially a spherical shape surrounded by dry air (gray). The numbers on the domain boundaries indicate the boundary number.

3. Results and Discussion

Figure 2 shows the results of mesh independence tests. Relative errors reduce to 5% as the total number of the uniform grid increases to 35556, which was then used for the following simulations.

Table 2. Initial conditions of droplet drying for investigating the impact of air temperature. The initial temperature of air is 40, 60 and 80 °C, respectively.

R_0	$T_{droplet}$	$Y_{l,1}$	$P_{droplet}$	$Y_{g,1}$	P_{air}	V
$10_{\mu m}$	20 °C	0.82	14.4kPa	0	0	0
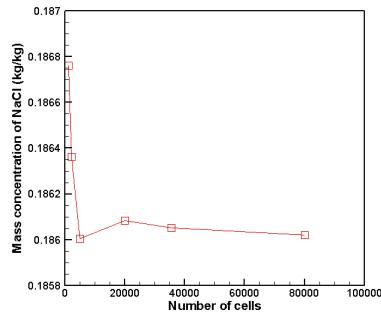
Fig. 2 Results of the mesh independence test. We decided on the mesh number = 35556 for relatively error small than 5%.
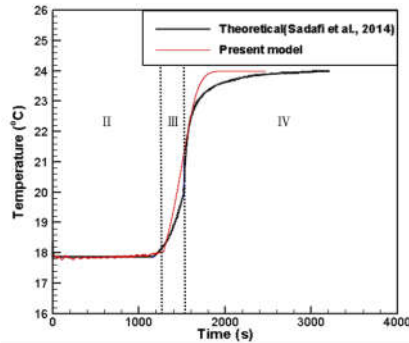
Fig. 3 Comparison with literature shows the droplet temperature increases with time as the drying proceeds.
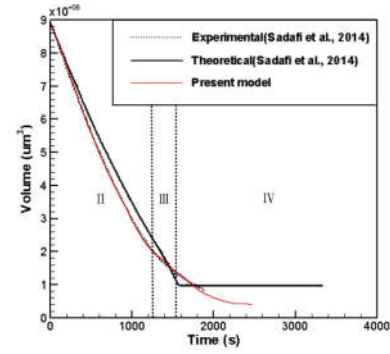
Fig. 4 comparison with literature shows droplet volume decreases with time as the drying proceeds sequentially.

The model was validated by comparison with previous experiment and theoretical model provided in literature [7], of which the drying conditions are summarized in Table 1. The drying process consists of four stages in a time sequence: (I) temperature adjustment, (II) isothermal drying, (III) solidified shell formation, and (IV) shell thickening (Figs. 3 and 4). Note that the first stage is too short to be seen in the figure, in which the droplet temperature drops from initially 18.35 °C to the well-bulb temperature about 17.8 °C, within 3 sec. Then the droplet temperature remains at the well-bulb temperature across stage 2 for about 1200 sec. In the second stage, the required latent heat of evaporation is balanced by the heat transfer from the air into the droplet. When the remaining salt concentration in the liquid increases and reaches the saturated value first at the droplet surface, salt precipitates appear at the surface and a solid shell gradually forms and grow inwards. The solid shell retards water evaporation and the need of heat to support latent heat requirement decreases. The heat gained from the air then exceeds the latent heat required that the droplet temperature begins to rise in stage III. In the end of the drying process, the droplet temperature approaches the environmental temperature accompanied by the thickening of the solidified shell in stage IV, and finally the solid particle

form as the water evaporation ends.

The model proposed was used to investigate the influences of environmental temperature. Three different air temperatures of 40, 60 and 80 °C were considered with other simulation conditions as listed in Table 2. Figure 5 shows the droplet temperature evolves over stages I and II. The droplet temperature declines from the initial temperature 20 °C across stage I to 15.8 °C, and then remains at 15.8 °C during stage II for the ambient temperature of 40 °C . While the droplet temperature rises at stage I for the other two higher ambient temperatures. Two distinct particle structures have been found accordingly. The droplet solidifies into a solid particle when the ambient temperature is 40 °C, and a hollow sphere forms when the ambient temperature is 60 and 80 °C (Fig. 6). This is because the shell forms beginning at the droplet surface where the water changes first from liquid to vapor. The salt concentration at the surface mostly quickly reaches the saturated concentration and solid salts begins to

(a)

(b)

(c)

Fig. 6 Effects of environmental temperature on the form of the solidified particle. (a) $T_{air} = 40\,°C$, (b) $T_{air} = 60\,°C$, and (c) $T_{air} = 80\,°C$.

precipitate at the surface too. Then the shell gradually grows inwards from the surface to the droplet center. If the air temperature is high, then the water evaporation rate is high enough that all the salts are solidified before the shell can grow to the center, which results in a hollow powder structure. The results of simulation show a more concentrated and a thinner shell could form with higher environmental temperatures. This is consistent with the drying particle formation mechanism as aforementioned.

4. Concluding Remarks

Droplet spray drying can form different solid particle structures. An entire drying process sequentially consists of four stages: temperature adjustment, isothermal drying, solidified shell formation, and shell thickening. Theoretical formulation nowadays models these four stages using different models to simplify the mathematical complication. This paper proposes a fully comprehended model that can account for and simulate all of the four different stages with no need for changing equations. The drying process is demonstrated using a brine droplet as an example. Results of simulation show the environmental temperature has a profound impact on the final structure of the solidified powders. Two kinds of powder structure was shown. The droplet solidifies into a solid particle when the ambient

(a)

(b)

(c)

Fig. 5 Effects of environmental temperature on the evolution of droplet temperature. (a) $T_{air} = 40\,°C$, (b) $T_{air} = 60\,°C$, and (c) $T_{air} = 80\,°C$.

168

temperature is low, and a hollow sphere when the ambient temperature is high. This is determined by the relative rates of heat transfer, solute diffusion and solid precipitation, which determines the final form of the solidified particle.

References

[1] D.H. Charlesworth, W.R. Marshall, Evaporation from drops containing dissolved solids, AIChE Journal, 6 (1960) 9-23.

[2] N. Abuaf, F. W. Staub, Drying of liquid-solid slurry droplets. General Electric, (1985) Corporate Research and Development.

[3] S. Nešić, J. Vodnik, Kinetics of droplet evaporation, Chem. Eng. Sci. 46 (1991) 527-537.

[4] T. Elperin, B. Krasovitov, Evaporation of liquid droplets containing small solid particles, Int. J. Heat Mass Transfer, 38 (1995) 2259-2267.

[5] M. Mezhericher, A. Levy, I. Borde, Theoretical drying model of single droplets containing insoluble or dissolved solids, Drying Technol., 25 (2007) 1025-1032.

[6] M. Mezhericher, A. Levy, I. Borde, Heat and mass transfer of single droplet/wet particle drying, Chem. Eng. Sci., 63 (2008) 12-23.

[7] M.H. Sadafi, I. Jahn, A.B. Stilgoe, K. Hooman, Theoretical and experimental studies on a solid containing water droplet, Int. J. Heat Mass Transfer. , 78 (2014) 25-33.

[8] C.W. Hirt, B.D. Nichols, (1981). Volume of fluid (VOF) method for the dynamics of free boundaries, J. Comput. Phys., 39 (1981) 201-225.

[9] J.U. Brackbill, D.B. Kothe, C. Zemach, A continuum method for modeling surface tension, Journal of computational physics, 100 (1992) 335-354.

[10] A.J. Chorin, Numerical solution of the Navier-Stokes equations. Math. Comput., 22 (1968) 745-762.

[11] L.J. Thibodeaux, D. Mackay, Eds. *Handbook of chemical mass transport in the environment*, (2010) CRC Press.

[12] S. Al-Jibbouri, J. Ulrich, The growth and dissolution of sodium chloride in a fluidized bed crystallizer. J. Cryst. Growth, 234 (2002) 237-246.

Contact Force Analysis for a Variable-Pitch Rotor Pair in Twin-Screw Vacuum Pump Generating by CNC Turning Process

Van-The Tran[1], Thanh-Long Le[2,3], Trung-Tin Pham[2,3]

[1]Department of Mechanical Engineering, Hung Yen University of Technology and Education, Vietnam
[2] Faculty of Mechanical Engineering, Ho Chi Minh University of Technology (HCMUT), VNU – HCM, Vietnam
[3]Key Laboratory of Digital Control and System Engineering, HCMUT (DCSELAB), Vietnam

ABSTRACT

The variable pitch twin-screw vacuum pump has more advantage than the uniform pitch twin-screw vacuum pump. Its energy efficiency and volumetric compression ratio are specifically high. Under the cyclic gas pressure and working temperature, the rotors of vacuum pump often deform and interfere that leads to noise, vibration and rotor abrasion. In this paper, a 3D model of the variable pitch rotor generating by CNC turning process is constructed to reasonably estimate the rotor load and deformation in operation. The contact force have analyzing to show the advantages of variable pitch rotors.

Keywords: variable pitch rotor, uniform pitch rotor, vacuum pump, contact force, turning process

1. Introduction

Screw rotors are core elements in the vacuum pump. They usually have uniform pitch or variable pitch. Both the screw threads can be turned by a CNC lathe by using an appropriate cutting tool. Thus the rotor with uniform pitch and variable pitch can be manufactured by turning process.

The most mathematical models of profile for rotors or gears with conjugated surface are derived by the enveloping theory [1]. A vacuum pump with a variable pitch will perform more efficiently than one with a uniform pitch. An asymmetric transverse profile of the rotor with three sections are proposed Becher [2]. And a screw rotor with the variable pitch and conical shape is presented that has a root diameter of the rotor increasing whereas the pitch of the rotor threads decreasing in a direction from inlet to outlet of the pump [3]. Yan et al. [4] developed a surface geometry and machine tool settings for a double-threaded variable pitch lead screw with four cylindrical meshing elements. Lee et al. [5] presented a method for generating the tooth profile of a helical rotor on five-axis machine.

This study proposes a novel method to manufacture the tooth profile of screw rotors with variable pitch. According to the simulation results, the tooth profile error of the proposed rotor with the variable pitch and uniform pitch is reached the required precision and the proposed CNC turning process is feasible and flexible.

2. Mathematical model for turning screw rotor by the lathe machine

The tooth profiles of rotors can be obtained by using the mathematical equation or discrete data points. If the tooth profile of rotor 1 is given, $\mathbf{r}_1(x_1(u_1), y_1(u_1))$, and mating rotors are conjugated (Fig. 1), the tooth profile of rotor 2 can be calculated by applying the envelope theory. The position vector of rotor 2 is the locus of rotor 1 in coordinate system $S_2(x_2, y_2)$:

$$\mathbf{r}_2(u_1, \phi_1) = \mathbf{M}_{21}(\phi_1) \cdot \mathbf{r}_1(u_1) \qquad (9)$$

The equation of meshing between two matting rotors can be presented as

$$f(u_1, \phi_1) = \left(\mathbf{k} \times \frac{\partial_{u_1}(\mathbf{r}_2)}{\sqrt{\partial_{u_1}\mathbf{r}_2 . \partial_{u_1}(\mathbf{r}_2)}} \right) \cdot \partial_{\phi_1}\mathbf{r}_2 = 0 \qquad (10)$$

where u_1 is the profile parameter of the rotor, ϕ_1 and ϕ_2 is the rotational angles of rotors, $\phi_1 = i\phi_2$, $\mathbf{M}_{21}$ is transformation matrix from coordinate system S_1 to S_2 and $\mathbf{k} = [0, \; 0, \; 1]$ is the unit vector of the z-axis.
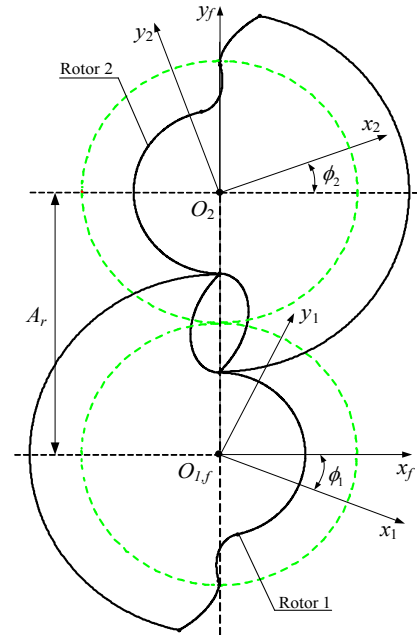
Fig. 1 Coordinate systems of two meshing rotors.

The turning process for generating tooth profile of the rotor needs two simultaneously motions: one is the

cutter moved horizontally along the rotational axis and other one is the rotor rotated about its rotational axis.

As shown in Fig. 2, Coordinate systems $S_1(x_1, y_1, z_1)$ and $S_3(x_3, y_3, z_3)$ are rigidly connected to the transversal and axial sections of the rotors, respectively. The axial tooth profile of the rotor 1 and rotor 2 can be derived as follows

$$\mathbf{r}_{3i} = \mathbf{M}_{31}(\theta_3).\mathbf{r}_i, \quad (i = 1, 2) \tag{11}$$

where $\mathbf{M}_{31}(\theta_3)$ is the coordinate transformation matrix. θ_3 is the rotational angle of rotor. It is defined as $\theta_3 = p / w$, p is the pitch of rotor and w is the parameter that depends on the positional curve. When w is changed along rotor axis, the pitch of the rotor is variable. The 3D models of the rotor pair with uniform pitch and variable pitch are shown Fig. 3.

Fig. 2 Coordinate system for generating screw rotor on turning machine.

Fig. 3 3D model of the rotor pair with: (a) uniform pitch and (b) variable pitch.

3. Contact force model

The coordinate system of two meshing screw rotors is presented in Fig 4. The determination of contact forces on the screw rotor pairs are difficult because the contact boundary is changed non-linear, very sensitive to boundary discretization and contact boundary varies node to node. Therefore, the contact forces on the screw rotor pairs are changed extremely abrupt. The contact function can be replaced the abrupt change in contact condition with a smooth but highly nonlinear function.

Theoretically, there is no need to distinguish rotor 1 from rotor 2. However, the distinction is often made for numerical convenience, as shown in Fig. 5. The contact condition is the rotor 2 no penetrate into the rotor 1. The contact condition is considered between a node on profile of rotor 2 and a segment on profile of rotor 1. The gap between profile of rotor 1 and profile of rotor 2:

$$g = (\mathbf{x} - \mathbf{x}_c^0) \cdot \mathbf{e}_n \geq 0 \tag{12}$$

where node $\mathbf{x}$ of rotor profile 2 is projected onto the piecewise linear segments of the rotor profile 1 with $\mathbf{x}_c$ ($\mathbf{x} = \mathbf{x}_c$) as the projected point. If the gap $g > 0$, two rotors have no contact and if the gap $g < 0$, two rotors have contact.

For those contacting rotor pairs, penetration needs to be corrected by applying a contact force and more penetration needs more contact force:

$$F_C = K_n \langle -g \rangle \tag{13}$$

where penalty parameter (K_n) is contact stiffness. It depends on material stiffness and allows a small penetration (g < 0). A bigger contact stiffness K_n => the less allowed penetration. The proper contact stiffness can be determined from allowed penetration by experience.

The Lagrange multiplier method can impose contact condition exactly. The contact force is a Lagrange multiplier to impose impenetrability condition and an independent variable. The contact force, $F_C(d)$, depends on displacement, d, and external force, F, as follows:

$$[K_n]\{d\} = \{F\} - \{F_C(d)\} \tag{14}$$

Fig. 4 Coordinate system of two meshing screw rotors.

171

Fig. 6 Friction force between two meshing screw rotors.

5. Numerical examples

5.1. Example 1

In order to determine the contact force between two rotors, the rotors are assembled at a practical center distance of A_r = 120 mm. The basic parameters are given in Table 1. And the contact settings and material properties are given in Table 2. The input power of rotor is P = 3 kW and the rotational speed of rotor is n = 3000 rpm. The contact forces are determined for two rotor pairs: one is the uniform pitch rotor pair and other one is the variable pitch rotor pair.

Table 1. Basic parameters of screw rotor.

Basic parameters of screw rotor	Value
Wrap angle (deg.)	1800
Lead of rotor with uniform pitch (mm)	78.5
Maximum lead of the rotor with variable pitch (mm)	104
Minimum lead of the rotor with variable pitch (mm)	36
Helix angle (deg.)	78.02
Thread number of rotor	1
Revolution number of thread	4
Length of rotor (mm)	314
Diameter of rotor (mm)	120

Fig. 5 Gap and contact force between two meshing screw rotors.

4. Friction force

The friction force is produced by a relative motion in the interface. It is applied to the parallel direction. The friction force is indeterminate when two bodies are stick no unique determination of friction force. There is a small elastic deformation before slip, as shown in Fig. 6.

The coulomb friction force in static friction

$$F_f = \mu_s F_C, \qquad\qquad ((15)$$

The coulomb friction force in kinetic friction

$$F_f = \mu_k F_C \qquad\qquad ((16)$$

Where μ_s is the coefficient of static friction and μ_k is the coefficient of kinetic friction.

Table 2. Contact settings and material properties.

Contact settings	
Item	**Value**
Contact stiffness of the rotors (K_n) (N.mm^{-1})	1.8×10^5
Force exponent (e)	2.2
Damping coefficient of the rotors (C_n)	0.27
Penetration depth (d_s) (mm)	0.01
Material properties	
Density (kg/mm^3)	7.8×10^{-6}
Elastic modulus (N.mm^{-2})	2.07×10^5
Poisson's ratio	0.29
Coefficient of static friction (μ_s)	0.23
Coefficient of kinetic friction (μ_k)	0.16

The contact force between two uniform pitch rotors and two variable pitch rotors are shown in Figs. 6-9. On time domain, the average contact force between two uniform pitch rotors, 30350 N, is much higher than

that of the contact force between two variable pitch rotors, 28013.9 N. Besides, maximum and minimum contact forces between two uniform pitch rotors are also higher than those of the contact force between two variable pitch rotors, as shown in Figs. 7-8. On frequency domain, the contact force between two uniform pitch rotors has much changed extremely abrupt than that of the contact force between two variable pitch rotors, as shown in Figs. 9-10. Therefore, the contact force of variable pitch rotors have more advantages than that of the uniform pitch rotors.
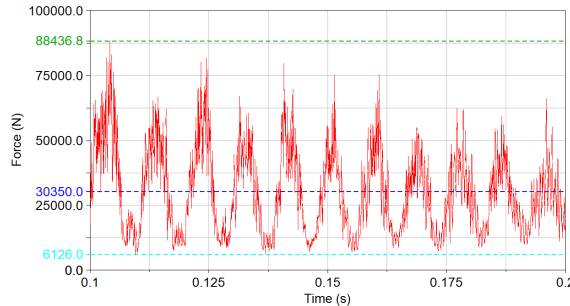
Fig. 7 The contact force between two uniform pitch rotors on time domain.
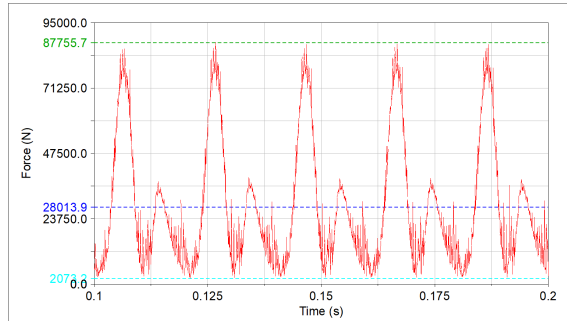
Fig. 8 The contact force between two variable pitch rotors on time domain.
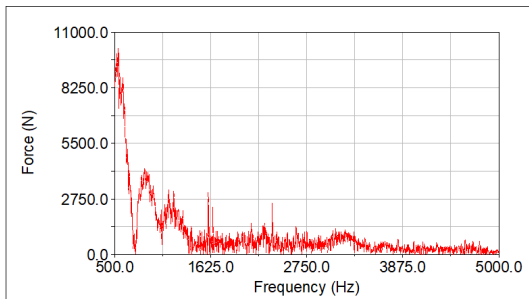
Fig. 9 The contact force between two uniform pitch rotors on frequency domain.
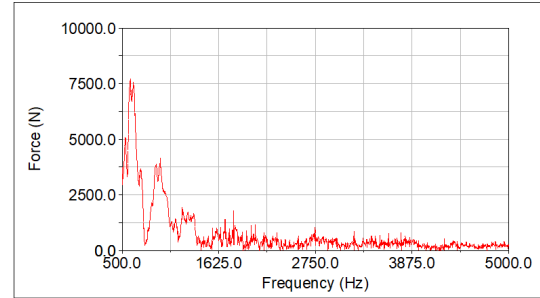
Fig. 10 The contact force between two variable pitch rotors on frequency domain.

5.2. Example 2

In this example, the effects of rotor's speed, damping coefficient (C_n) and contact stiffness (K_n) to the contact force between two variable pitch rotor pair are considered. The basic parameters, contact settings and material properties are also given in Table 1 and Table 2. The contact forces of variable pitch rotor pair are determined with variations of rotational speed from n = 3000 rpm to n = 2500 rpm and n = 3500 rpm, as shown in Figs. 11 and 12. It's presented that the contact forces are extremely increased with the increase of the rotational speed.
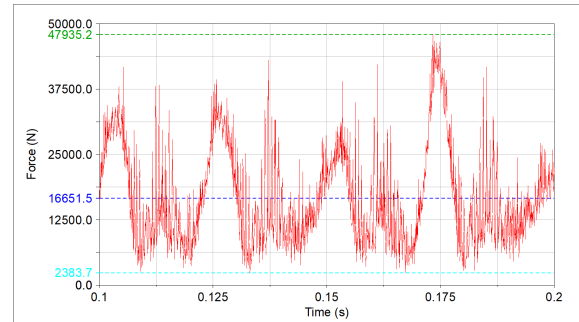
Fig. 11 The contact force between two variable pitch rotors with rotational speed n = 2500 rpm.
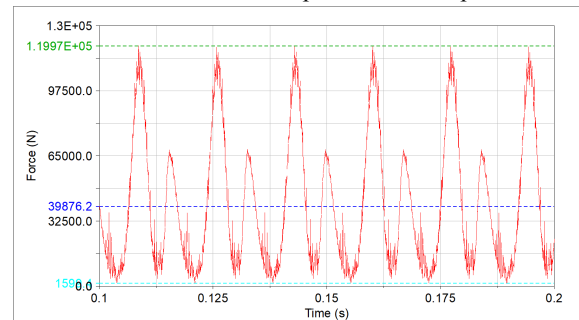
Fig. 12 The contact force between two variable pitch rotors with rotational speed n = 3500 rpm.

The variation of damping coefficient (C_n) and contact stiffness (K_n) have slight effected to contact force between two variable pitch rotor pair. The contact force are augmented with the increase of damping coefficients and reduced with the increase of contact stiffness, as shown in Figs. 13-16.

173
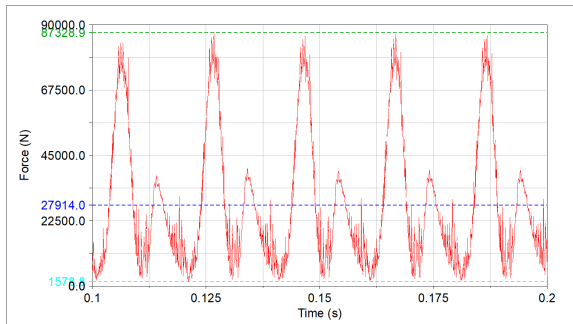
Fig. 13 The contact force between two variable pitch rotors with damping coefficient $C_n = 0.25$.

Fig. 14 The contact force between two variable pitch rotors with damping coefficient $C_n = 1.0$.
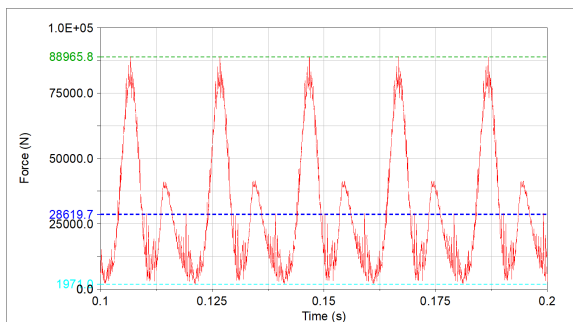
Fig. 15 The contact force between two variable pitch rotors with contact stiffness $K_n = 1.6 \times 10^5$.
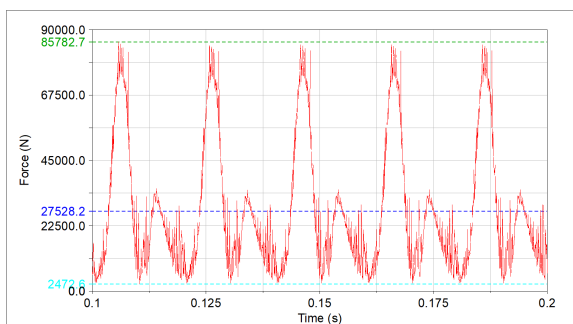
Fig. 16 The contact force between two variable pitch rotors with contact stiffness $K_n = 2.0 \times 10^5$.

6. Concluding Remarks

In this paper, a 3D screw-rotor models for both uniform pitch and variable pitch rotors are constructed by using CNC turning machine. The contact forces of a pair intermeshing rotors are analyzed under combining the torque on the rotor 1 and rotor 2 with the rotation angle of rotor 1. The simulated results show that the contact forces of variable pitch rotors have more advantages than that of the uniform pitch rotors. The effects of rotor's speed, damping coefficient and contact stiffness to the contact forces between two variable pitch rotor pair are also researched. The rotor's speed have much effected to the contact force between two variable pitch rotor pair.

References

[1] F.L. Litvin, A. Fuentes, Gear Geometry and Applied Theory (2nd ed.), *Cambridge University Press, Cambridge*, 2004.

[2] U.F. Becher, Twin Screw Rotors and Displacement Machines Containing the Same, *U. S. Patent No. 6702558B2* (2004).

[3] M.H. North, Vacuum Pump, *U. S. Patent No. 6672855B2* (2004).

[4] H.S. Yan and J.Y. Liu, Geometric Design and Machining of Variable Pitch Lead Screws with Cylindrical Meshing Elements, *ASME Transactions, Journal of Mechanical Design*, 115(3) (1993) 490-495.

[5] J.N. Lee, C.B. Huang, T.C. Chen, Tool path generation method for four-axis NC machining of helical rotor, *Journal of Achievements in Materials and Manufacturing Engineering*, 31(2) (2008) 510-517.

Designing and Simulating A Flexible Mechanical System

Nguyen Phu Thuong Luu

Automotive Engineering Department, HUTECH University, Ho Chi Minh, Vietnam

ABSTRACT

This paper presents the kinematic modeling and simulation of a flexible cantilever mechanical system. The aim of this article is to develop a functional model of the flexible mechanical system in ADAMS/View software, and its following complete kinematical analysis. In this research, ADAMS/Flex is used to import the flexible mechanical part to the cantilever model to achieve more realistic simulation results. This paper is intended to provide some experience and familiarity with MSC ADAMS/Flex.

Keywords: ADAMS/View, ADAMS/Flex, Cantilever, Design, Kinematic.

1. Introduction

Dynamics simulation and structural analysis are researched by many organizations such as robots is an important aspect for robots structural design, in former dynamics analysis, the parts of built model are all regarded as rigid bodies, and elastic deformation is neglected [1]. But in fact, under condition of heavy load or accelerate, decelerate, robots will have big deformation and changed displacement [2]. Not only the robot fields the automotive engineering fields also study on it such as using CATIA design vehicle system them import to ADAMS to simulation. A geometric model of a car's suspension arm was prepared and subsequently imported into the MSC.Adams environment dedicated to studying dynamics of multi-body systems and then broken down into finite elements [3]. The analysis of robots considering the elastic characteristics of its members has been receiving considerable attention in recent years [2]. Due to the high non-linear coupling between the global movement of the links and their deformations, not so many techniques are suitable for the control of a general flexible robot. ADAMS is a kind of software which is extensively applied in dynamics analysis of mechanical system, its research object is rigid multibody, but it supplies flexible module which can replace rigid body by flexible body for fulfilling dynamics simulation of flexible multibody [4]. In this paper the two kinds of software were united, the flexible bodies can be built in ANSYS, NASTRAN or ABAQUS and then were transmitted into ADAMS for establishing flexible multibody system of mechanicals, and dynamics simulation was carried out.

2. Building the model

2.1 Creating the flexible link into the database

In this section, We will import the modal neutral file (MNF) containing the flexible link into the mechanical model. The flexible link is defined in the file link.mnf in the working directory which can be made by ABAQUS, NASTRAN or ANSYS.

1. From the **Build** menu, point to **Flexible Bodies**, and then select **ADAMS/Flex**. The Create a Flexible Body dialog box appears as shown below.
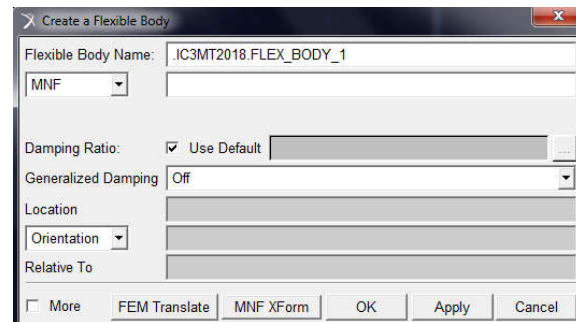
Fig 1: The Create a Flexible Body dialog box

2. Right-click the **Modal Neutral File Name** text box, and then select **Browse** from your data base where the MNF model was saved.
3. Select the **file name.mnf**, and then select **OK**.
4. Select **OK**. Then a 0.5 meter long flexible link appears in ADAMS/View. With the information below:
Mass   : 1.2 kg
CM Location: 250, 0.0, 0.0 mm, mm, mm.
Inertia Tensor: (relative to the Local Body Reference Frame)
IXX : 120.9239956271 kg-mm^2
IYY : 1.0044961891E+005 kg- mm^2
IZZ : 1.0051173775E+005 kg- mm^2
IXY : 1.4150312188E-009 kg- mm^2
IZX : 0.0 kg- mm^2
IYZ : 0.0 kg- mm^2
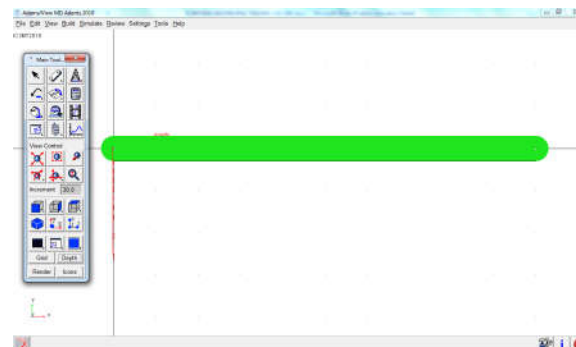
Fig 2: The flexible link in ADAMS/View

2.2 Creating the load

In this paper, the load is made by rigid body box 20 cm^3 as shown in Fig 3. The link was fixed to the ground, the load was attached to the right end of the link. The load was adjusted to its center goes through the center line of the link.

1. From the **Geometric Modeling** tool stack of the main toolbox, select the **square** tool .

2. Click the left mouse button anywhere in the screen and drag the cursor until you have a square approximately 0.2 meters in dimension as shown in Fig 3 below.

3. From the **Move** tool stack of the main toolbox, select the **Point-to-Point** tool .

4. Following the instructions in the status bar, select the load as the object to move. Click near the left edge of the square to indicate the point to move from, and then, click on node 1001 at the right end of the link to indicate the point to move to. Press the **Ctrl** key to use grid points or zoom in on the model to gain greater accuracy. The complete flexible mechanical models are shown in Fig 4.

Material   : .IC3MT2018.steel
Material Density: 7.801E-006 (7801.0(kg/meter^3))
Calculated Mass   : 62.408 kg
Calculated Volume : 8.0E+006 mm^3
Mass Inertia Tensor :
    IXX : 4.1605333333E+005 kg- mm^2
    IYY : 4.1605333333E+005 kg- mm^2
    IZZ : 4.1605333333E+005 kg- mm^2
    IXY : 0.0 kg-mm^2
    IZX : 0.0 kg-mm^2
    IYZ : 0.0 kg-mm^2
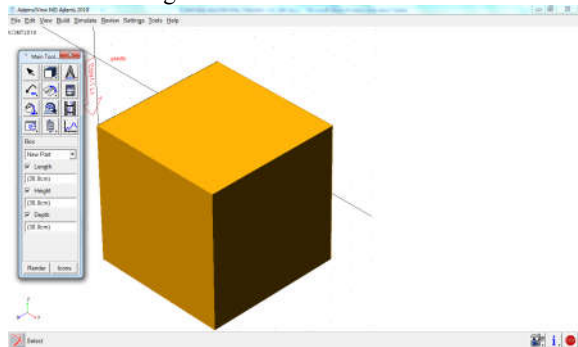
Fig 3: The rigid body box in ADAMS/View
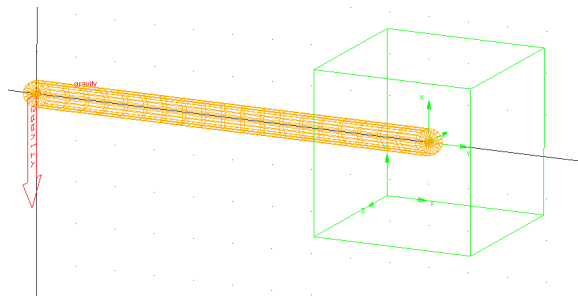
Fig 4: The Flexible mechanical system

2.3 Adding the fixed joints

To fix the flexible link to the ground using a fixed joint.

1. From the **Joint** tool stack of the Main toolbox, select the **Fixed Joint** tool.

2. In the construction container of the Main toolbox, select the construction method **1 Location**.

3. Place the cursor at the left end of the link. Node numbers flash on the screen as you move the cursor. Select node 1000 for the location of the fixed joint by clicking the left mouse button when the cursor is over node 1000. Figure 5 shows the location for the fixed joint. Node 1000 is at (0; 0; 0).

The final step in creating the cantilever link is to fix the load to the link using a fixed joint.

1. From the **Joint** tool stack of the Main toolbox, select the **Fixed Joint** tool.

2. In the construction container of the Main toolbox, select the construction method **2 Bod - 1 Loc**.

3. Select the link, the load, and the end of the link where it coincides with the square (FLEX_BODY_1.N1001). ADAMS/View attaches a fixed joint.
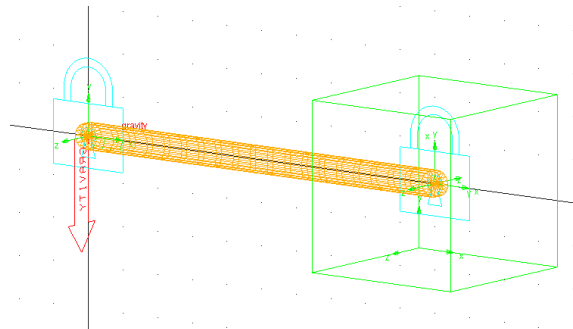
Fig 5: The position of fixed joints in the model

3. Simulating the flexible model

In this section, the simulation of the cantilever link was presented as shown in Fig 6.

1. From the Main toolbox, select the **Simulate** tool.

2. In the Simulation container in the Main toolbox, enter the following:

- In the **End Time** text box, enter **1** second.
- In the **Steps** text box, enter **100**.

3. Select the **Simulation Start** tool. You see the cantilever link oscillating because of the force of gravity.
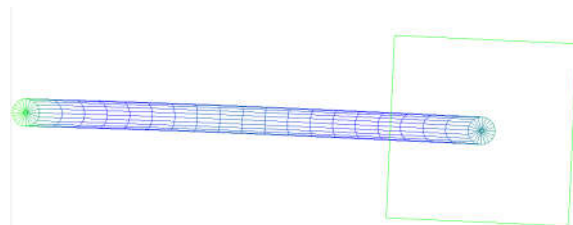
Fig 6: The simulation result of cantilever link

3.1 Displaying the flexible body modify dialog box

All the changes to a flexible body, which were made through the Flexible Body Modify dialog box as shown

in Fig 7. The display of the dialog box just as We would any modify dialog box in ADAMS/View.

1. In the Simulation container of the Main toolbox, select the Reset tool to return to modeling mode.

2. Double-click the flexible body to display the Flexible Body Modify dialog box shown in the next figure. The figure indicates the three controls that you use to change the deformation display of a flexible body.
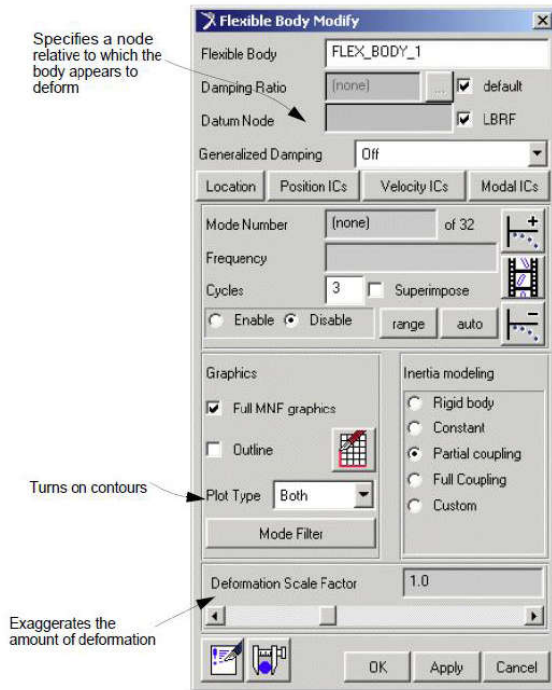
Fig 7: The Create a Flexible Body dialog box

3.2 Adding color contour

By default, ADAMS/Flex considers the deformation to be relative to the origin of the flexible body (its local body reference frame (LBRF) or coordinate system). The notice that at the start of the animation, the flexible link is completely blue. As the animation runs, it changes to red to indicate where and when the maximum deformation occurred as shown in Fig 8.

1. From the Flexible Body Modify dialog box, set **Plot Type** to **Contour**.

2. From the Main toolbox, select the **Animation** tool.

3. In the Animation container on the Main toolbox, be sure that **Contour Plots** is selected.

4. From the Animation container, select the **Play** tool.
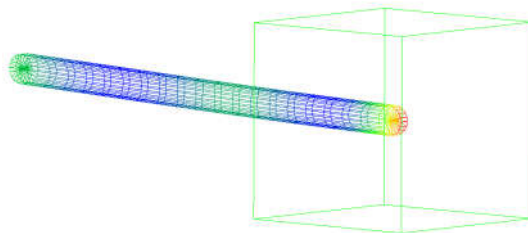
Fig 8: The result of simulation with contour plots

3.3 Viewing numeric results

By default, when the flexible body was added in the model, ADAMS/View measures specific attributes of the flexible body, as well attributes of markers and points on the flexible body.

In this section, the plot and the measures that ADAMS/View has tracked during the latest simulation presented in the plotting window. We set the plotting window to surf so that We can quickly view each measure plotted against time without having to add pages to the plotting window as shown in Fig 9 to Fig 15.

1. In the Main toolbox, select the **Post Processing** tool.

2. In the dashboard that appears along the bottom of the screen, set **Source** to **Objects**.

3. From the **Filter** list, select **body** and then, from the **Object** list, select **FLEX_BODY_1**.

4. Select a characteristic and component of the flexible body to measure. Start by selecting CM Position and Y to view the position of the center of mass of the flexible body over time.

5. Select **Surf** on the right of the dashboard.

6. Continue selecting characteristics and components of the flexible body to view. We can find interesting the translational deformation of markers on the flexible body, particularly in the y direction. Notice that the deformations are relative to the LBRF of the flexible body regardless of whether you set a different datum node.

7. When the process is finished, from the **File** menu, select **Close Plot Window** to return to the ADAMS/View main window.
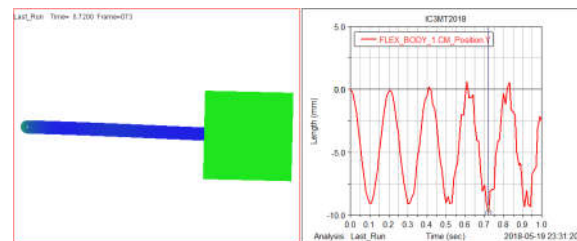
Fig 9: The result of flexible body Y direction position
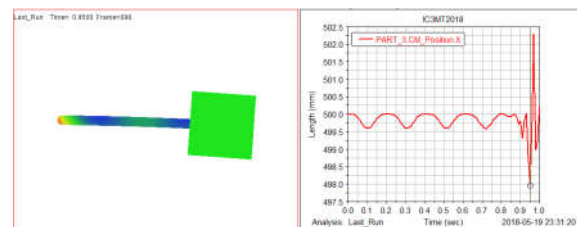
Fig 10: The result of flexible body X direction position

177
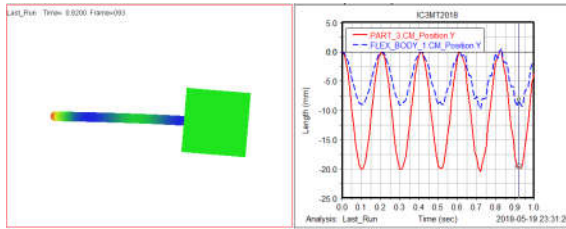
Fig 11: The comparison position of flexible body and load in Y direction
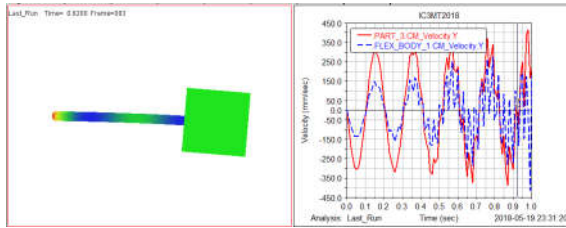
Fig 12: The comparison velocity of flexible body and load in Y direction
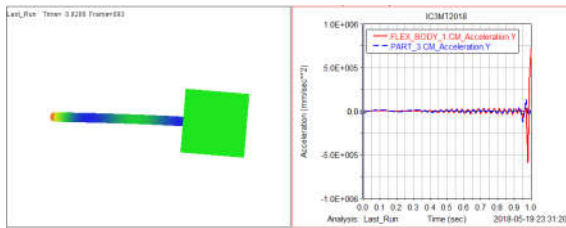
Fig 13: The comparison acceleration of flexible body and load in Y direction
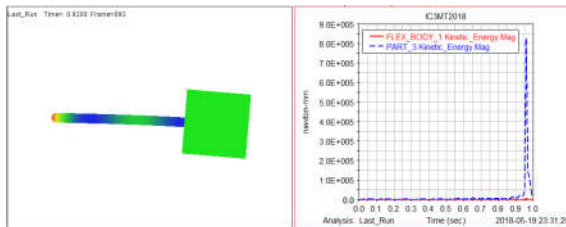
Fig 14: The comparison kinetic energy of flexible body and load
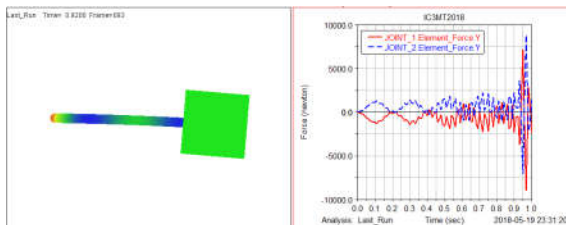
Fig 15: The comparison element force of flexible body and load in Y direction

4. Concluding Remarks

Generally, the dynamics modeling of multibody system is based on the assumption that the system's components are perfect. In actual systems, however, clearances, friction, material non-uniformities and manufacturing and assembly errors have significant effects on the system. In this paper, the dynamics model for the flexible body and a simulation method are developed. The simulation using ADAMS and ABAQUS can reflect practical motion characteristic; the parts deformation can be easily observed when simulating; system performance can be predicted exactly; all above can offer references for structural improvement and optimization. We don't need to analyze, derive and reason the equations of motion in mathematic by using virtual prototype technique; Kinematics and dynamics can be easily analyzed and reasoned by applying software, so the dynamics model with flexible and rigid bodies will be a good way for study on optimal design, it is helpful for saving time when designing structures.

References

[1] C.X. Zhua, Y.X. Liu, G.Q. Cai and L.D. Zhu. **Dynamics Simulation Analysis of Flexible Multibody of Parallel Robot**, *Applied Mechanics and Materials Vols. 10-12 (2008) pp 647-651.*

[2] A.A. Shabana, **Flexible Multibody Dynamics: Review of Past and Recent Developments**, Journal of Multibody System Dynamics, Vol. 2 (1997), pp.189-222. doi:10.1023/A:1009773505418

[3] Ł. Konieczny, R. Burdzik, B. Łazarz, **Analysis of properties of automotive vehicle suspension arm depending on different materials used in the MSC.Adams environment**, *Archives of Materials Science and Engineering* 58/2 (2012) 171-176.

[4] Luu Nguyen Phu Thuong, **Electric hybrid vehicles noise control at speed-up**, Inter-noise, New York, 2012.

PART III, SECTION I

Machining Technology
(Difficult-to-cut and Free Machining; Non-conventional Machining;
Green Process/Manufacturing; Cutting Mechanisms…)

Investigation on Osteoconductivity of EDMed Titanium Alloy Surface in Deionized Water

Yuta lIDA[1], Keita FUJII[1], Togo SHINONAGA[1], Akira OKADA[1]

[1]Graduate School of Natural Science and Technology, Okayama University

3-1-1, Tsushimanaka, Kita-ku, Okayama, 700-8530, Japan

ABSTRACT

In recent years, early fixation of artificial joints to bones is required in medical field. With the intent of efficiently machining the joint shape by electrical discharge machining (EDM) and simultaneously formation of a surface with osteoconductivity, this study discusses the possibility of adding osteoconductivity to an EDMed titanium alloy surface. Therefore, creating an EDMed surface that precipitate tricalcium phosphate (TCP) which shows high osteoconductivity was investigated by optimizing the EDM conditions. As a result, it is conformed that there is possibility of adding cytocompatibility and precipitation ability of TCP on EDMed surface.

Keywords: EDM, Titanium alloy, Osteoconductivity, Tricalcium phosphate, Cytocompatibility

1. Introduction

In late years, a replacement surgery with an artificial joint is commonly carried out for losses in joint function caused by osteoarthritis or rheumatoid arthritis. Currently, two main procedure types are in clinical use to fixate an artificial joint component to a bone. One uses bone cement, while the other (cementless) does not. In the cement fixation procedure, an artificial joint component and bone are adhered with bone cement, which contains poly methyl methacrylate as a main component. The procedure requires a short period of time before the fixation completes. However, the cement deterioration reduces the cementing strength over time. In addition, reports have been made of the necrosis of bone tissue caused by excessive compression and fever at the time the bone cement is filled [1], as well as of reductions in blood pressure and shock symptoms caused by the cement monomer components [2]. For this reason, cementless fixation procedures with high biocompatibility and safety are typically used in the current clinical practice. However, a long period of time is necessary before the fixation occurs, lasting several months before complete fixation of bone tissue to the artificial joint is achieved [1].

In order to reduce the period of time necessary to fixate the bone tissue and the artificial joint component, it is necessary to add osteoconductivity to the artificial joint component surfaces that make contact with bone. Osteoconductive hydroxyapatite (HAp) has been directly coated on the artificial joint component surface using a plasma spraying as a currently practiced method [3-6]. However, a clear interface exits between base material and the coating layer, so the delamination of the coating layer is seen as a problem. In addition, the HAp particles are exposed to active plasma with high temperature during the plasma spraying, hence its composition and crystalline properties would be changed.

On the other hand, as presented in Fig. 1, it is possible to impart osteoconductivity on a rutile titanium oxide (TiO_2) layer formed by oxidation treatment after groove machining on the surface of the titanium-series [7]. However, required groove shape size is as small as submillimeter order, and the excellent mechanical and chemical characteristics of titanium-series material cause high difficulties in machining of the grooves by milling with an end-mill in terms of the machining efficiency and tool cost. The thermal oxidation treatment for forming of TiO_2 layer also requires some hours. Therefore, efficient processes to add osteoconductivity to the artificial joint component is required.

In this study, the machining of fine grooves on a titanium-series surface by electrical discharge machining (EDM) in deionized water is proposed. The EDM is a thermal material removal process unaffected by the mechanical characteristics of a workpiece material and effective for fine shapes such as groove because of its extremely small machining force acting on the tool electrode and workpiece. In addition, EDM in deionized water has high possibility to oxidize the titanium surface with its chemical and thermal reactions, simultaneously with the groove machining. Our previous study confirmed the possibility to form tricalcium phosphate (TCP) on the EDMed surface with deionized water during the immersion experiment using a simulated body fluid (SBF). The TCP is superior to HAp in terms of osteoconductivity. However, EDMed surface using brass electrode may deteriorate cytocompatibility since it contains copper component. Then, the influences of EDM conditions on copper content, the TCP formability and cytocompatibility on the EDMed titanium alloy surface are experimentally investigated in this study.

2. Osteoconductivity evaluation method

For the purpose of the basic evaluation of the hydroxyapatite formation ability of an EDMed surface, this study selected a flat EDMed surface as the target, instead of a groove shape. An EDMed titanium-series material surface was immersed for 7 days in 30 mL of 36.5°C SBF with the surface facing downwards and with appropriate gap spaces provided between the surface and a polytetrafluoroethylene. The apatite formation ability of the EDMed surface was evaluated. This evaluation method using SBF is effective as a method for evaluating biocompatibility in vitro [8] and is registered by the International Standard Organization (ISO) [9]. Adopting an evaluation using SBF, this study examined the possibility of the addition of osteoconductivity to the titanium material by EDM based on the deposition of hydroxyapatite or its equivalent calcium phosphate series on the machined surface.

3. Precipitation of calcium phosphate compound

With the intent of precipitating hydroxyapatite on the TiO_2 layer, formation of a TiO_2 layer on the titanium alloy surface has been attempted by EDM. A white precipitate was obtained by repeating the experiment of immersing the EDMed surface in SBF. A detailed examination was performed because this white precipitate was expected to be a kind of osteoconductive calcium phosphate, similar to hydroxyapatite.

An optical image of the area of white precipitation is shown in Fig. 2. The original purpose was precipitation of hydroxyapatite. Therefore, the machined titanium was immersed such that the EDMed surface of the specimen faced downwards and an appropriate gap space was provided between the surface and the polytetrafluoroethylene. A great amount of white precipitation was formed in the upper area of the specimen, i.e., not on the gap space side but on the upper face side. This area is a rough machined surface by the first-cut, where wire EDM was performed with large energy EDM conditions in order to cut the specimen to an appropriate size.

This rough machined surface is not uniform, but shows a slightly yellow hue at upper side of wire running (top end of the specimen). For this reason, in order to obtain a uniform machined surface, die-sinking EDM was performed in deionized water using a brass electrode. Then, under the machining conditions presented in Table 1, a uniform machined surface was obtained on which white material was precipitated during immersion in SBF.

Table 1 EDMed conditions

Electrode	Brass
Workpiece	Ti-6Al-4V
Discharge current i_e	15A
Discharge duration t_e	25μs
Pulse interval t_0	100μs
Working fluid	Deionized water
Electrode polarity	(+)
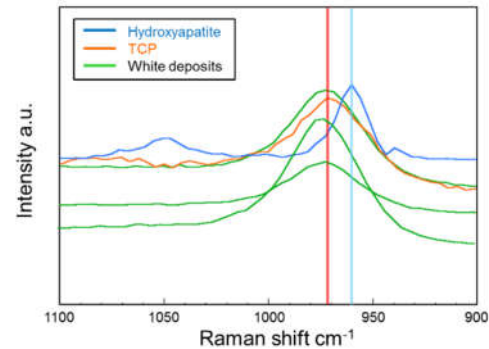
Fig. 3 Raman spectra from white deposit

3.1. Identification by Raman spectroscopic analysis

Next, the white precipitate was analyzed by Raman spectroscopy, in which a microscale region of the most superficial surface can be analyzed. Figure 3 presents the Raman spectra of white precipitate. The peaks obtained by analyzing the three different white materials on the machining surface are located at approximately 971 cm^{-1} each. This peak does not match the peak of hydroxyapatite, but matches the peak of tricalcium phosphate (TCP) indicated by the orange color line in the figure. This result indicates that the white precipitate is highly likely to be TCP. Similar to hydroxyapatite, TCP is a kind of osteoconductive materials. While hydroxyapatite is not well absorbed in a living body, TCP is gradually absorbed and replaced by natural bone [10].

3.2. Identification of white material by precipitation mechanism

It was made clear by Raman spectroscopic analysis that the white material obtained on the die-sinking EDMed surface was highly likely to be TCP. However, the peak could differ slightly in Raman spectroscopic analysis, so the material was also identified considering its

Fig. 1 Stem design for high osteoconductivity

(a) Precipitation area in SBF. (b) White precipitate on surface.
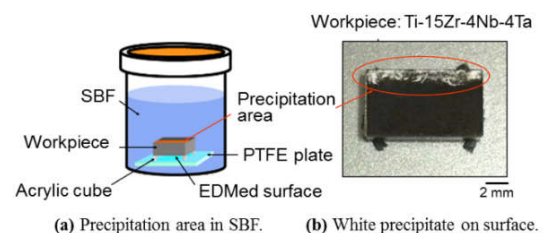
Fig. 2 Precipitation area and image of white precipitate on surface

formation mechanism. Figure 4 schematically presents the nucleation mechanism for a precipitated calcium phosphate-series material. The nucleation mechanisms of calcium phosphate-series materials are generally classified into two types; non-uniform and uniform nucleation. In non-uniform nucleation, a calcium ion and a phosphate ion in the SBF are attracted to an OH group and an oxygen ion on the specimen surface; the primary nucleus first forms on the specimen surface. Then, the calcium ion and the phosphate ion in the SBF are further bonded to the formed primary nucleus, and a crystal grows at the specimen surface. Repetition causes the particles to grow more. Meanwhile, in uniform nucleation, the primary nucleus is formed not on the specimen surface but in fluid near the surface by a specimen surface effect. After that, similar to the non-uniform nucleation, a calcium ion and a phosphate ion in the SBF are attracted and bonded to the formed primary nucleus, and a crystal grows in the fluid near the specimen. When it reaches a certain size, it makes contact with the specimen surface and is deposited. In general, hydroxyapatite precipitates via non-uniform nucleation, while TCP precipitates via uniform nucleation.

In order to confirm the precipitation mechanism of the white material, an immersion experiment was conducted with the specimen placed in the SBF so that the machined surfaces faced upward in the horizontal direction and sideways in the vertical direction. An outline of the immersion experiment and optical images of the specimen's machined surface after the immersion experiment are shown in Fig. 5. In the immersion method with the machining surface facing upwards in the horizontal direction, a sufficient amount of white material was expected to precipitate uniformly on the machining surface via either non-uniform nucleation or uniform nucleation. However, for the machined surface facing sideways in the vertical direction, a material precipitating via uniform nucleation, could not be deposited on the vertical machining surface, and hence amount of precipitate would decrease. By comparing the amount of deposited white precipitate on the machined surfaces by these immersion methods, we confirmed that the white material was precipitated by which mechanism whether non-uniform or uniform nucleation. As demonstrated from the optical images of the specimen machined surface after the immersion experiment, the white precipitation amount when the machined surface faces upwards in the horizontal direction is larger than that the machined surface faces sideways in the vertical direction. In addition, a white floating substance is present in the fluid when the machining surface faces sideways in the vertical direction. In other words, the white material precipitates via uniform nucleation, and this clearly indicates that this precipitation formed by uniform nucleation on the EDMed surface is TCP.

These results indicate that the TCP formation ability, in other words, osteoconductivity, can be added to the titanium alloy surface by EDM under the appropriate
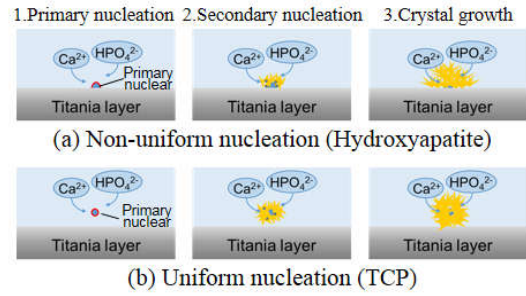
Fig. 4 Nucleation mechanism
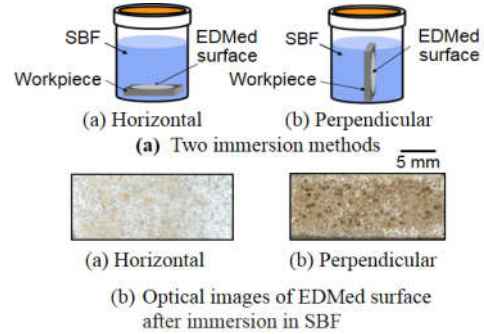
Fig. 5 Two immersion methods and optical images of EDMed surface

Table 2 Experimental conditions for cell test

Sample	a. Brass (t_e=5μs, t_0=40μs) b. Brass (t_e=25μs, t_0=100μs) c. Zn(t_e=25μs, t_0=100μs)	
Cell	Osteoblast (MG-63)	
Medium	α MEM (10 % FBS, 1% penicillin)	
Incubation	37℃, 5%CO$_2$	
Culture time	3 h	
Fix	8%Paraformaldehyde	
Immunostaining	Blue	Nuclear
	Red	Actin

Brass (t_e=5μs, t_0=100μs) Cu:11.7%, Zn:3.2%	Brass (t_e=25μs, t_0=100μs) Cu:19.3%, Zn:4.4%	Zn (t_e=25μs, t_0=100μs) Cu:0% Zn:8.5%
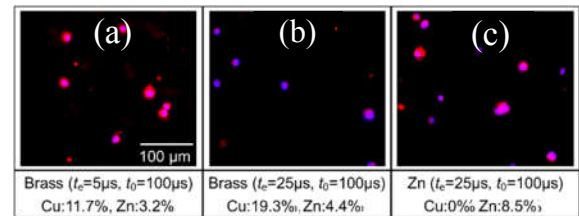
Fig. 6 Fluorescence microscopy image for various conditions

electrical conditions presented in Table 2.

3.3. Cytocompatibility of the EDMed surface

TCP is precipitated on the EDMed surface by using brass electrode, and the machined surface contains copper and zinc components. If a large amount of copper and zinc components is contained on EDMed surface, there is a possibility that cytocompatibility may be inferior. Therefore, the cytocompatibility on the EDMed surface was examined by conducting a cell test. Table 2 presents the cell test conditions. In the cell test, sample(a) and (b) are titanium alloys subjected to die-sinking EDM by brass electrode, and sample(c) is

sample by using zinc electrode. (a) and (b) is the EDMed surface which contains of copper components about 10% and 20%, respectively, and a small amount of zinc. (c) is a machined surface which contained zinc and no copper component. Osteoblast (MG-63) are cultured for 3 hours in an incubator on a sample containing copper and zinc components on the EDMed surface, then the cells were fixed by 8% paraformaldehyde and immunostained. Then, the state of cell spreading on EDMed surface was observed by the fluorescence microscope, blue and red color shows nuclear and actin of the cells. The presence or absence of cytocompatibility was discussed.

Figure 6 shows the florescence images on the EDMed surfaces with different copper and zinc components. This result indicates that, on the machined surface (b) with a high content of copper, only the nucleus of the cell can be observed, and cells spreading can not be observed. In contrast, a small amount of actin that appears red color observes on the machined surface with low copper content (a), and the machined surface with zinc contained (c). From this, it is considered that the copper and zinc components are contained in the machined surface, excessive the copper component, leads to deterio ration of cell spreading, and it is expected that these EDMed surfaces are low cytocompatibility. Therefore, if the contents of copper and zinc on the machined surface decreases, it is expected that the good cytocompatibility can be obtained on the EDMed surface.

4. Investigation of EDMed conditions

Table 3 EDMed conditions

Electrode	Zinc→Copper
Workpiece	Ti-6Al-4V
Discharge current i_e	15A(Zinc) 0.4-1.9A(Copper)
Discharge duration t_e	25μs
Pulse interval t_0	100μs
Working fluid	Deionized water
Electrode polarity	(+)
Processing time	20min(Zinc) 3min(Copper)
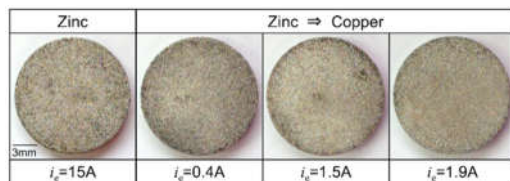
Fig. 7 EDMed surface images
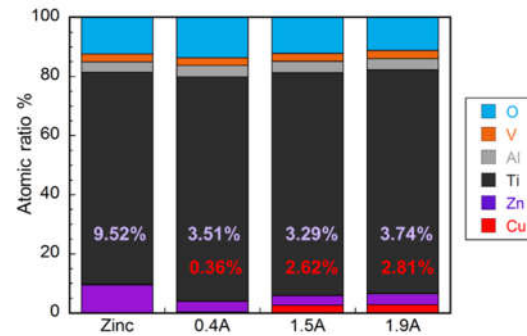
Fig. 8 Component analysis of EDMed surfaces

Next, influence of EDM conditions on zinc and copper components on the EDMed surface is investigated in order to form EDMed surfaces have both osteoconductivity and cytocompatibility. From previous experimental results it is considered that appropriate EDMed surface, to obtain osteoconductivity and cytocompatibility is as follows; (1) The content of copper and zinc on the processed surface is about 5% and 3%, respectively. (2) It is desirable that distribution is uniform to some extent. (3) The machined surface roughness is uniform.

Reduction of copper and zinc components on the machined surface under various EDM conditions is proposed by using brass electrodes, although low contains of copper and zinc can't be achieved. Therefore, electrode is changed from brass to the zinc and copper. The experimental conditions are shown in Table 3. A zinc electrode is used in deionized water to contain zinc component on the machined surface. After that, the electrode was changed to a copper electrode and processed in the same way to try to reduce the zinc component and to contain the copper component on the surface. At that time, in order to suppress the excessive inclusion of the copper component on the machined surface, the discharge current value was set low and processing was carried out for a short time. Then, the machined surface was observed by SEM and the component analysis by EDX was carried out.

Figure 7 shows the optical photographs of the respective machined surfaces processed at the discharge current values of 0.4 A, 1.5 A, and 1.9 A, and Fig. 8 shows the result of component analysis near the center of the machined surface by EDX. For the sake of reference, the machined surface and the component analysis result before machining with the copper electrode are also in shown in the figure. From the optical photographs, it can be seen that all the machined surfaces have substantially uniform hues. Component analysis results indicate that the content of zinc decreases on the surface machined by the copper electrode compared with before machining. A small amount of copper is contained over 1.5A by using copper electrode. Appropriate copper and zinc components can be obtained on the EDMed surface by using zinc and copper electrodes.

5. Conclusions

(1) White material is precipitated on the titanium wire-EDMed surface in SBF. The white precipitate is osteoconductive TCP by Raman spectroscopic analysis and by its precipitation mechanism. Therefore, osteoconductivity can be added to titanium surfaces by EDM in deionized water.

(2) When a brass electrode is used in wire EDM, the uniform formarion of TCP is possible by the uniform distribution of brass components on the EDMed surface.

(3) Cytocompatibility of the EDMed surface containing much copper and zinc becomes low.

(4) Appropriate copper and zinc components can be obtained on the EDMed surface by using zinc and copper electrode under appropriate conditions.

References

[1] J.A DiPisa, G.S. Sih, A.T. Berman, Clin. Orthop, Res., Vol.121, pp.95-98, 1976.

[2] W. Petty, J. Biomed. Mater. Res., Vol.14, pp.427-434, 1980.

[3] L. Sun C.C. Berndt K.A. Gross A. Kucuk, J. Biomed. Mater. Res., Vol.58, pp.570-592, 2001.

[4] T.D. Driskell, Philadelphia: ASTM Publication, p.3, 1994.

[5] W.R. Lacefield, L.L. Hench, J. Wilson (Eds.), Singapore: World Scientific, p.223, 1993.

[6] K. de Groot, R.G.T. Geesink, C.P.A.T. Klein, and P. Serekian, J. Biomed. Mater. Res. Vol.21, pp.1375-1381, 1987.

[7] J. Lu, M.P. Rao, N.C. MacDonald, D. Khang, and T.J. Webster, Acta Biomater. Vol.4, pp. 1518-1529, 2008.

[8] T. Kokubo, and T. Takadama.: How useful is SBF in predicting in vivo bone bioactivity? Biomaterials, Vol.27, pp.2907-2915, 2006.

[9] ISO 23317:2007.

[10] S.V. Dorozhkin, BIO, Vol.1, pp.1-51, 2011.

High-speed Wire EDM by Newly Developed Copper-Zirconium Wire Electrode

Ayaka Kuwada[1], Naokuni Muramatsu[2], Kazuhiro Nomura[2], Yasuhiro Okamoto[1], Akira Okada[1]

[1] Graduate School of Natural Science and Technology, Okayama University,
3-1-1, Tsushimanaka, Kita-ku, Okayama, 700-8530, Japan

[2] NGK INSULATORS, LTD., 1, Maegata-cho, Handa, Aichi, 475-0825, Japan

ABSTRACT

For higher wire EDM performance, a new type thin wire electrode was proposed in this study, and the wire EDM characteristics using a copper-zirconium (Cu-Zr) wire, and zinc or brass coated ones were experimentally evaluated. The results showed that the cutting speed using the Cu-Zr wire itself was lower than those using the conventional wires, but it could be significantly improved by plating brass or zinc layer around the Cu-Zr wire and became higher than conventional ones, since the coating increases the energy distribution given to the discharge gap into the workpiece.

Keywords: wire EDM, copper-zirconium, coated wire, cutting speed, electrode wear

1. Introduction

In recent years, along with the miniaturization and weight reduction of industrial products, high precision processing technology has been strongly required. For this purpose, fine discharge pulse circuit, accurate gap control system, and thin wire electrode have been developed in wire electrical discharge machining (EDM). In fine wire EDM using thin wires with a diameter of 100μm or smaller, electrical conditions with larger discharge energy and higher wire tension cannot be applied, since wire breakage easily occurs under such conditions. In addition, the electrical discharge concentration is likely to occur due to its small discharge area and narrow gap. Therefore, the improvement in the fine wire EDM performance using conventional wire electrodes is limited only by optimizing discharge pulse conditions and gap control. In order to achieve higher-performance fine wire EDM, a new type thin wire electrode with high- conductivity for higher removal rate and higher accuracy in wire EDM was proposed in this study. The wire EDM characteristics using copper-zirconium alloy (Cu-Zr alloy) wire, and zinc or brass coated ones were experimentally evaluated. Cu-Zr is an alloy in which a few percent of zirconium is added to copper, and its wire has high conductivity and sufficient tensile strength for wire EDM [1, 2].

2. Wire electrode

The wire electrode used for wire EDM is required to have high conductivity and high tensile strength. Copper has high conductivity after silver, but it has very low tensile strength. In general, the strength can be increased by adding various elements to copper and alloying. Cu-Zr is an alloy which is composed of copper and several percent of zirconium. It is characterized by being a copper alloy with high conductivity and high strength. Figure 1 shows SEM photographs of cross-sectional structure of the Cu-Zr wire. As shown in the figure, Cu-Zr wire has white conductive fiber structure and black reinforcing fiber one.

Cross-sections of six types of wire electrode with a diameter of 70 μm used in this experiment are schematically shown in Fig. 2. Table 1 shows the tensile strength and the electrical conductivity of these electrodes.

First three wires (a) - (c) have been conventionally

Table 1 Tensile strength and electrical conductivity of wire electrodes
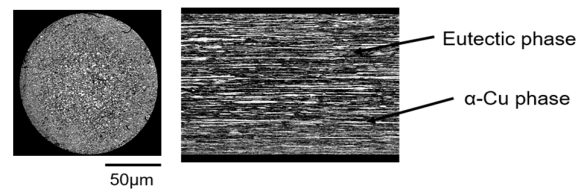
Fig. 1 SEM photographs of a cross-sectional structure of a Cu-Zr wire
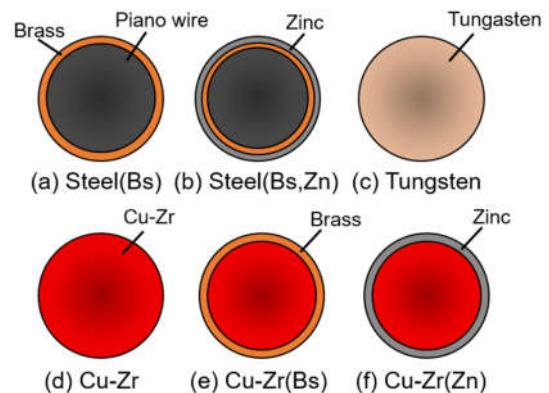
Fig. 2 Cross-sectional illustration of six types of wire electrodes with a diameter of 70 μm

Wire	Tensile strength T_s [MPa]	Electrical conductivity λ [%IACS]
Steel(Bs)	2,323	15.6
Steel(Bs,Zn)	2,353	19.2
Tungsten	2,738	37.1
Cu-Zr	1,734	28.3
Cu-Zr(Bs)	1,435	41.5
Cu-Zr(Zn)	1,521	39.5

applied. In the case of Steel(Bs), a piano wire is used as a core wire and brass layer is coated on the surface[3,4]. In the case of Steel(Bs,Zn), zinc layer is further coated on the Steel(Bs) wire. Tungsten wire has widely applied to finer wire EDM because of its highest tensile strength.

Others (d)-(f) are newly developed wires in this study. As shown in the table, Cu-Zr wire has high electrical conductivity and sufficient tensile strength to be used for wire EDM as wire electrode. This is because high cutting speed is expected by supplying a large discharge current to the machining gap by using a wire with high conductivity. In addition, brass layer was coated on the surface in the case of Cu-Zr(Br). On the other hand, zinc layer is coated in Cu-Zr(Zn), since increase in cutting speed is highly expected by its discharge stability effect. In these wire names, Bs and Zn in bracket after
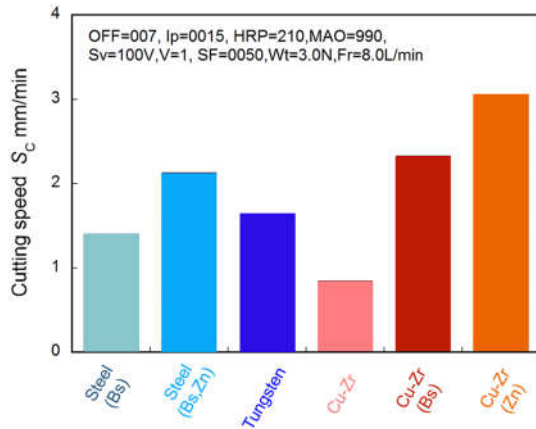
Fig. 3 Dfference in cutting speed S_c with type of wire electrode

the core wire name indicate brass coating and zinc one, respectively.

3. Wire EDM characteristics

3.1 Cutting speed

Figure 3 shows the comparison of cutting speed using each wire. The line cutting experiments were carried out in a kerosene type working fluid using a high-precision wire electrical discharge machine (Sodick AP 200 L). The workpiece material was

SKD11 in JIS specifications used widely as a metal mold. The electrical conditions were based on the 1st cutting condition recommended by the EDM machine maker for cutting steel plate using brass coating steel wire Steel(Bs) with a diameter of 70 μm.

As can be seen from the figure, it is clear that the cutting speed using the Cu-Zr wire is small, compared with three conventional wires. On the other hand, the cutting speeds using coating wires of Cu-Zr(Bs) and Cu-Zr(Zn) become higher than that of Cu-Zr wire, and it is also higher than those of the conventional wires. From these results, the cutting speed can be improved by coating
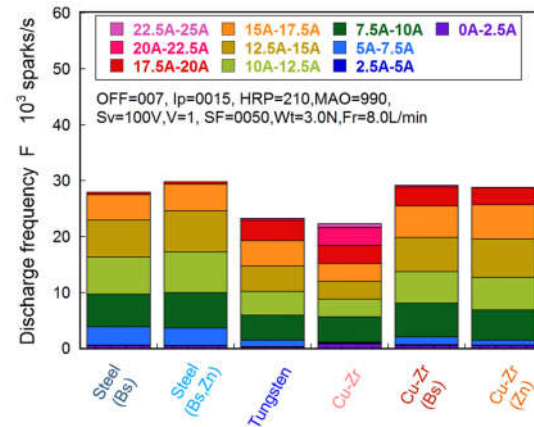
Fig. 4 Difference in actual discharge frequency F and distribution of discharge current peak values with electrode

brass or zinc layers around the core Cu-Zr wire with high electrical conductivity.

3.2 Discharge frequency

In order to discuss the cause of high cutting speed using coated Cu-Zr wires, the number of discharges per unit time during process, that is, actual discharge frequency, and the distribution of those peak current values were measured. Figure 4 shows the results. As shown in the figure, there are differences in discharge frequency and discharge current peak value distribution with the type of wire electrode, even under the same setting conditions. The discharge frequency using Cu-Zr wire or tungsten one was low, whereas those using of brass and/or zinc coated steel wire or Cu-Zr one were high.

Zinc has a much lower melting and boiling points than other major electrode materials, which makes its surroundings to be rapidly cooled down and promotes dielectric recovery of the gap[5]. Better dielectric recovery would results in stable discharge generation, uniform spark distribution, and prevent electrodes from braking.

The figure also shows that the current peak values using the Cu-Zr wires are higher than those using the coated steel wires. Cu-Zr wire can supply large discharge energy to the working gap for its high conductivity.
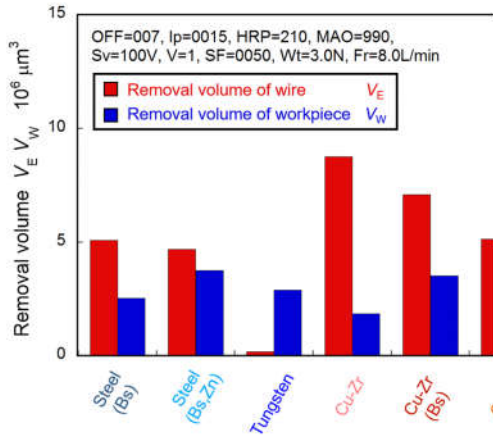
Fig. 5 Wire electrode removal volumes V_E and workpiece removal ones V_W

Furthermore, coated Cu-Zr wire increases discharge frequency, as shown in the figure. By these two factors, usage of coated Cu-Zr wires significantly improved the cutting speed.

3.3 Electrode wear

Electrode wear rate of each wire was compared in order to estimate how the discharge energy given to the discharge gap is distributed to the workpiece and the
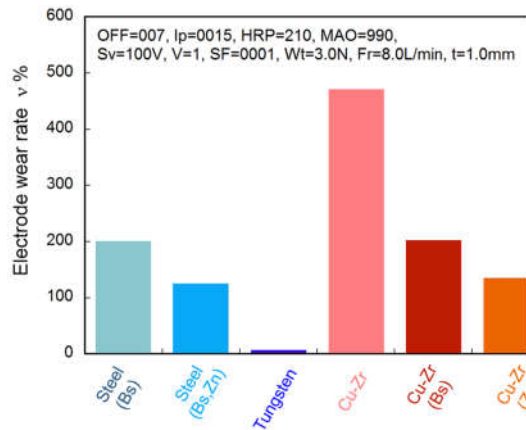
Fig. 6 Comparison of electrode wear rate v with type of wire electrode

electrode. The difference in mass between the wire electrode and the workpiece before and after cutting were measured by using a digital scale. The removal volume of the workpiece V_W and that of the wire electrode V_E were calculated using the density of each material. Figure 5 shows the removal volume of wire electrode and workpiece with red bar and blue one, respectively.

In the case of Cu-Zr wire electrode, the removal volume of electrode is very large and that of the workpiece is the smallest. However, the removal volume of wire

electrode decreases and that of the workpiece increase by applying the brass or zinc coating. Then, the electrode wear rate v was obtained by the Equation 1.

$$v = V_E/V_W \qquad (Eq.(17)$$

The calculated electrode wear rates v are shown in Fig. 6. The rate of the Cu-Zr wire was remarkably large, compared with other wires. From this result, it is understood that a lot of discharge with large current peak value occurs in the gap and large discharge energy is supplied to the gap in the case of Cu-Zr wire, but much of the energy are wasted to remove the wire electrode instead of the workpiece. Therefore, the Cu-Zr wire showed small cutting speed in spite of the large energy given to the gap. On the other hand, the the coated Cu-Zr wires showed smaller electrode wear rate than that of Cu-Zr wire. The discharge energy used for removal of wire electrode would be reduced, and more energy was used for cutting the workpiece by coating. Then, the cutting speed became significantly larger.

3.4 Kerf width

In fine wire EDM using a thin wire electrode, the vibration of wire electrode during cutting[6, 7] is promoted due to its small diameter. The wire vibration influences the cutting speed, since large vibration amplitude leads to wide kerf width. According to the mechanical properties of each wire shown in Table 1, Cu-Zr wires have lower tensile stress than the conventional wires. Therefore, the small tensile strength of the Cu-Zr wires would result in large vibration amplitude.

Figure 7 shows difference in width of wire EDMed kerf with type of wire electrode. It can be seen that the kerf widths using Cu-Zr wires are slightly larger than those using the conventional wires, and they are about 5% wider than those of the conventional wires. Therefore, it is considered that the material removal in the direction perpendicular to the cutting direction would be larger in wire EDM using Cu-Zr wires.

Table 2 High-speed observation conditions

Recording speed	8,000 fps
Shutter speed	1/40,000 sec
Recording time	5.0 sec
Observation size	0.4 mm×0.2 mm
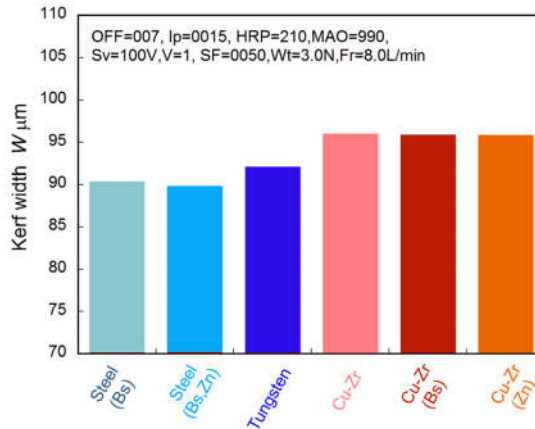
Fig. 7 Comparison of wire EDMed kerf width *W* with type of wire electrode

In order to observe the wire behavior during cutting, a high-speed camera system (KEYENCE VW-6000) was used, and the wire vibration amplitude was investigated from the recorded movie[8]. The observation direction is the same direction as the cutting direction, and the wire movements of the wire perpendicular to the cutting direction are observed with the high-speed video camera. The recording speed was set mainly to 8,000fps. The observation conditions are listed in Table 2.

Figure 8 shows observed position and size in the high-speed observation of wire electrode during cutting. The position is 1 mm above the upper end of the workpiece and the size is 0.4×0.2mm. The wire vibration amplitude during cutting is obtained by tracking the center position of the wire electrode in the observation range using an image analysis software.
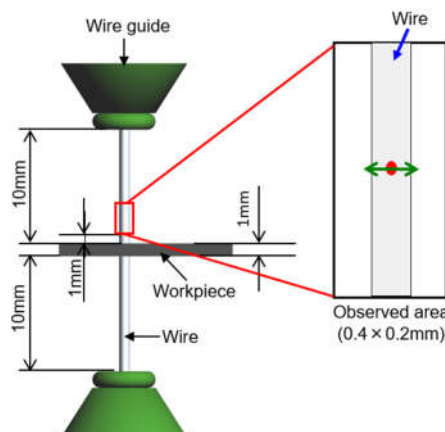
Fig. 8 Position and size for high-speed observation of wire vibration

Figure 9 shows the vibration amplitude of each wire during 1st cut. Although the tensile strength of the Cu-Zr wires are smaller than those of the conventional wires, the amplitude of the wire is slightly small. The

Cu-Zr wires have sufficient tensile strength to suppress the vibration during machining, as is the case of conventional wires. As mentioned above, the Cu-Zr wires can supply large discharge energy to the gap, because of their high electrical conductivity of the core. Therefore, it is considered that the slight increase in kerf width using Cu-Zr wires would result not from large wire vibration amplitude, but from large discharge energy supplied to the gap.
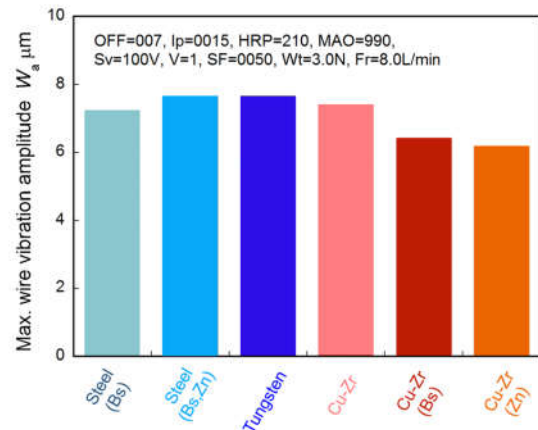
Fig. 9 Maximum wire vibration amplitudes W_a of six wires during 1st cutting

7. Conclusions

Main conclusions obtained in this study are as follows:

(1) The cutting speed using the Cu-Zr wire is considerably small, compared with those using conventional wires.

(2) The cutting speed using Cu-Zr wire can be increased by coating brass or zinc layer around the wire.

(3) The peak discharge current values in the case of Cu-Zr wires are higher than those in conventional wires, because of its high electrical conductivity.

(4) The wire vibration amplitudes using the Cu-Zr wires are almost same or slightly smaller, compared with those using conventional wires.

Acknowledgements

References

[1] N. Muramatsu, H. Kimura, and A. Inoue, *Development and Microstructure of Cu-Zr Alloy Wire with Ultimate Tensile Strength of 2.2 GPa*, Materials Transaction, Vol. 53, No. 6 (2012) 1062 – 1068.

[2]   N. Muramatsu, T. Nakajima, T. Fukuoka, R. Monzen, *Influence of Thermo-mechanikal Treatment on Electrical Conductivity and strength of A dilute Cu-Zr Alloy*, Journal of Japan Institute of Copper, Vol. 56, No. 1 (2017) 39 – 44.

[3]   T.Yamauchi, A. Okada, M. Morita, T.Shimizu, Y. Uno, *Development of Coat Wire Electrode for High Performance WEDM (1ˢᵗ report)*, Journal of JSEME, Vol. 39, No. 92 (2005) 28 – 35.

[4]   A. Okada, T. Yamauchi, K. Arizono, Y. Uno, *Effect of Surface Quality of Brass Coating Wire on Wire EDM Characteristics*, Journal of Advanced Mechanical Design System and Manufacturing, Vol. 2, No. 4 (2008) 735 – 741.

[5]   E. Bud Guitrau, *The EDM Handbook*, Hanser Gardner Publications (1997) 152 – 156.

[6]   N. Kinoshita, M. Fukui, K. Kimura, *Study on Wire-EDM Inprocess Measurment of Mechanical behavior of Electrode-Wire*, CIRP Annals, Vol. 33, No. 1(1984) 89 – 92.

[7]   H. Yamada, N. Mohri, N. Saito, T. Magara, *Model Analysis of Wire Electrode Vibration in Wire-EDM,* IJEM, No. 2 (1997) 19 – 24.

[8]   A. Okada, Y. Uno, M. Nakazawa, T. Yamauchi, *Evaluation of spark distribution and wire vibration in wire EDM by high-speed observation*, CIRP Annals, Vol. 59, No. 1 (2010) 231 – 234.

Study on Improvement of Wear Resistance for Zirconia by Large-area EB Irradiation

Togo Shinonaga[1], Mitsuhiro Kimura[1], Motohiro Inoue[2], Akira Okada[1]

[1] Graduate School of Natural Science and Technology, Okayama University
3-1-1, Tsushimanaka, Kita-ku, Okayama, 700-8530, Japan
[2] Sodick Co., Ltd
3-12-1, Nakamachidai, Tsuzuki-ku, Yokohama, 224-8522, Japan

ABSTRACT

Zirconia has been widely applied for cutting tools and biomaterials, since it has superior mechanical properties such as high fracture toughness and bending strength in ceramics. In order to maintain its surface functions for long-term, further improvement of the wear resistance for zirconia has been required. In this study, improvement of the wear resistance of the zirconia surface by large-area electron beam (EB) irradiation is experimentally investigated. It is made clear that the wear resistance of the zirconia surface significantly improved by the EB irradiation.

Keywords: Large-area EB irradiation, Zirconia, Surface topography, Coefficient of friction, Wear resistance

1. Introduction

Ceramics has high wear resistance, corrosion resistance and heat resistance, compared with metal materials. In particular, zirconia has been widely applied for cutting tools, manufacture parts operating in aggressive environments, and biomaterials in dental treatment, since it has superior mechanical properties such as high fracture toughness and bending strength in ceramics [1]. In order to maintain its surface functions for long-term, further improvement of the wear resistance for zirconia has been required.

Meanwhile, in a large-area electron beam (EB) irradiation method developed recently, high energy density of the EB can be obtained without focusing the beam. Then, the large-area EB with uniform energy density distribution of approximately 60mm in diameter can be used for melting and evaporating material surface instantly [2-7]. Our previous study showed that surface roughness of metal molds made of steel decreased from several μmRz to less than 1.0μmRz in a few minutes under appropriate EB conditions [3]. Thus, highly efficient surface finishing of the metal molds was possible by using the large-area EB. This technique was also applied for biomaterial [4,5] and cemented carbide [6]. Furthermore, surface functions such as wear resistance, water repellency and corrosion resistance of the EB irradiated metal molds were improved, since the material surface was melted and re-solidified layer was formed on the workpiece surface [7]. Therefore, it is highly expected that surface function such as wear resistance of the zirconia will be also improved by the large-area EB irradiation.

In this study, improvement of the wear resistance of the zirconia surface is proposed by large-area EB irradiation. The surface topography and crystal structure of the EB irradiated zirconia surface is evaluated in order to discuss the change of wear resistance for the zirconia surface.

2. Experimental procedure

In the experiments, 3mol% yttria partially stabilized zirconia was used as the workpiece. It has crystal structures of tetragonal and monoclinic phases as major and minor ones at room temperature. Workpiece size was 10×10×0.5mm, and material properties of the zirconia was shown in Table1. In this experiment, initial surface roughness of ground zirconia surface was fixed at about 5.8μmRz.

Schematic illustration of a large-area EB irradiation equipment is shown in Fig.1. The large-area EB irradiation is performed in an argon (Ar) gas ambience of about 10^{-2} Pa. At first, a magnetic field is generated by the solenoid coils set on the outer side of the chamber. When the magnetic field takes a maximum intensity, pulse voltage is loaded to the anode. Then, Ar plasma is generated in the operating chamber by rapid changes in magnetic and electric fields. Next, a pulse voltage is applied to the cathode, and the electrons are explosively emitted from the cathode by high electric field near the cathode. Therefore, large-area EB with uniformly high energy density sufficient to melt and evaporate the workpiece surface can be obtained.

Table 1 Properties of zirconia

Density	r	[g/cm³]	6.0
Specific heat	c	[J/(g · K)]	0.46
Thermal conductivity	k	[W/(m · K)]	3.0
Melting point	T_m	[K]	2,998
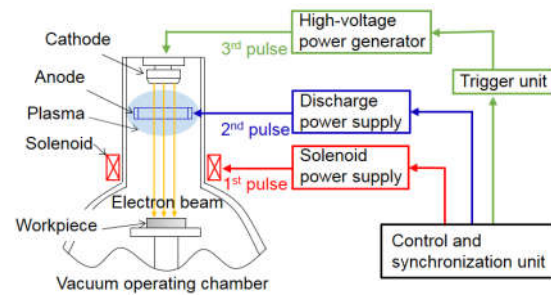
Fig.1   Schematic illustration of large-area EB irradiation apparatus

Table 2 EB irradiating conditions

Energy density	E_d	[J/cm²]	2.5-12.5
Shot number	N	[shots]	1
Pulse duration	t_p	[μs]	2

Table 3 Friction and wear test conditions

Ball material			SiC
Load	L_f	[N]	7.84
Stroke	L_s	[mm]	3.0
Time	t_s	[min]	100
Sliding speed	v_s	[mm/min]	720

The large-area EB was irradiated upper side of the zirconia surface. EB irradiating conditions were shown in Table 2. Energy density E_d was varied from 2.5 to 12.5J/cm². Shot number N and pulse duration t_p were fixed at 1shot and 2.0μs. The EB irradiated zirconia surface was observed by using a scanning electron microscope (SEM), and surface roughness of the zirconia surface was measured by using a surface profilometer in order to evaluate change of surface topography.

The coefficient of friction and wear resistance of the zirconia surface before and after the large-area EB irradiation were evaluated by using a friction and wear tester. Experimental conditions of friction and wear test was shown in Table 3. SiC was used as ball material, since hardness of SiC was higher than that of the zirconia. The SiC ball repeatedly slid on the zirconia surface for 100min. The load, sliding speed and stroke were fixed at 7.84N, 720mm/min and 3.0mm,

respectively. After friction and wear test, the SiC ball and zirconia surfaces were observed by using optical microscope, and worn amount of the zirconia was measured by the surface profile of the wear track. Finally, crystal structures of the EB irradiated zirconia surface were investigated by using thin film x-ray diffraction method in order to discuss the change of wear resistance in the large-area EB irradiation.

3. Results and Discussion

3.1 Change of surface topography

SEM images of the zirconia surface after the large-area EB irradiation at energy densities of E_d=5.0 and 12.5J/cm² are shown in Fig.2. The image of non-EB irradiated surface (ground surface) is also shown in the figure. As shown in the figure, grooves are clearly observed on the ground surface. After the large-area EB irradiation at E_d=5.0J/cm², the small grooves are removed and spacing of the grooves seems to increase. Moreover, the grooves dose not clearly observe on the EB irradiated surface at E_d=12.5J/cm². In order to evaluate surface topography of the zirconia in detail, roughness curve is measured by using a surface profilometer. The roughness curve on the each conditions is shown in Fig.2. The roughness curve on the zirconia surface shows that parts of the ground surface with small surface roughness are removed, and mean width seems to increase with increasing energy density in the large-area EB irradiation.

In order to compare the surface topography of the zirconia before and after the large-area EB irradiation quantitatively, variations of surface roughness and mean width with various energy densities are shown in Fig.3. As shown in the figure, surface roughness of the EB irradiated zirconia surface is almost same as the ground surface. On the other hand, the mean width of the zirconia surface significantly increases after the large-area EB irradiation, compared with that of ground surface. In addition, the mean width lineally increases with increasing energy density of the EB, and the mean width of the EB irradiated zirconia surface at E_d=12.5J/cm² is 5 times higher than that of the ground surface.

Therefore, it is made clear that mean width of the EB irradiated zirconia surface increases with increasing the energy density of EB, although surface roughness is almost same as the ground surface. This is probably because that the parts of ground surface with small surface roughness can be easily evaporated or melted instantly, while it is difficult to remove the parts with large surface roughness of several micro meter after the large-area EB irradiation.

3.2 Improvement of wear resistance

The coefficient of friction and worn amount of the zirconia surface before and after the large-area EB irradiation are investigated. Variations of coefficient of friction for zirconia with time at various energy densities are shown in Fig.4. In the cases of the non-EB and the energy density of E_d=2.5J/cm², the coefficient of friction increases with increasing time and it

becomes constant over 2000s, while it becomes constant over 3000s in the cases of the energy densities of E_d=5.0, 7.5 and 12.5J/cm². Then, variations of coefficient of friction with various energy densities are shown in Fig.5. As shown in the figure, the coefficient of friction decreases with increasing the energy density of the EB. Moreover, the coefficient of friction on the EB irradiated zirconia surface at more than E_d=5.0J/cm² becomes lower than that on the ground one. This results suggest that the SiC ball material smoothly slides on the zirconia surface after the large-area EB irradiation under the appropriate energy density, since the mean width of the zirconia surface increases with increasing energy density of the EB.

Optical images of the SiC ball material surface and surface profile of the wear track on the zirconia surface are shown in Fig.6. As shown in the optical images of the ball material surface, grooves along the sliding direction are clearly observed on the ball material surface in the cases of sliding on the ground surface and the EB irradiated zirconia surface at the energy density of E_d=7.5J/cm². On the other hand, there is no grooves on the ball material surface in the case of sliding on the

EB irradiated zirconia surface at E_d=12.5J/cm². These results show that the wear form on the zirconia surface is changed after the EB irradiation at high energy density, since the ball material smoothly slides on the EB irradiated surface at high energy density due to increment of the mean width on the surface. As shown in the surface profiles of the wear track on the zirconia surface, the width and depth of the wear track reduces on the EB irradiated surface at E_d=7.5J/cm², compared with that on the ground surface. In addition, the width and depth of the wear track increases as the energy density increases from E_d=7.5 to 12.5J/cm². Then, the worn amount S_w is measured by calculating the area of the wear track from baseline as shown in Fig. 7.

Figure 8 shows variations of the worn amount on the zirconia surface with various energy densities. The worn amount significantly reduces on the EB irradiated zirconia surface at E_d=2.5, 5.0 and 7.5J/cm², compared with the ground surface. Then, the worn amount of the EB irradiated zirconia surface at E_d=5.0J/cm² becomes smallest and almost half of the ground surface. On the other hand, the worn amount increases by the large-area EB irradiation at excessive energy density of E_d=12.5 J/cm².

These results indicate that the wear resistance of the zirconia surface significantly improves by the large-area EB irradiation under the appropriate energy density. One of the reasons for improvement of the wear resistance is increment of the mean width and reduction of the coefficient of friction for the zirconia surface by the large-area EB irradiation.

3.3 Transformation of crystal structure

The wear resistance of the zirconia surface improves at
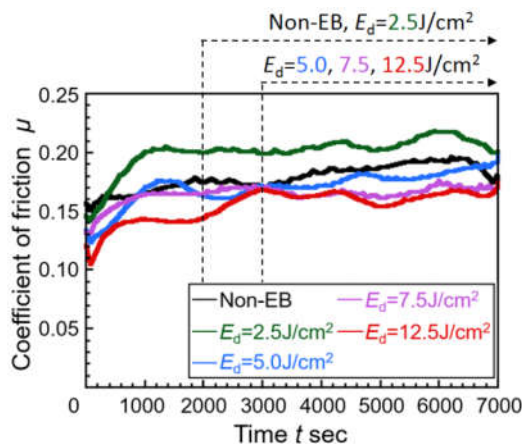
Fig.4 Variations of coefficient of friction on zirconia surface
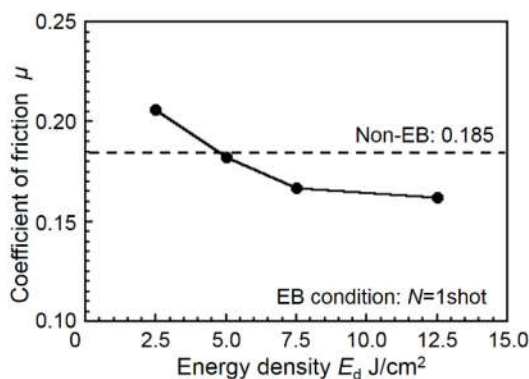
Fig.5 Variations of coefficient of friction with energy density
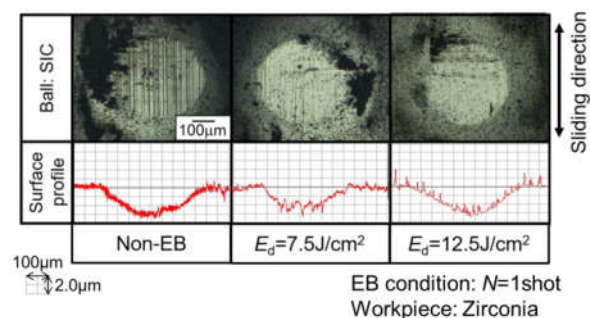
Fig.6 Optical images of SiC ball surface and surface profile of wear tracks on zirconia surface
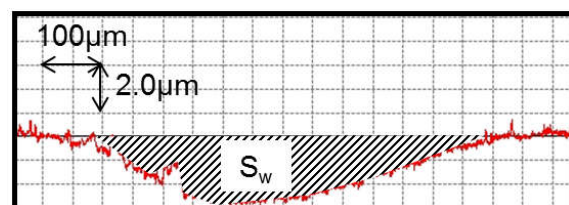
Fig.7 Measurement of worn amount from surface profile of wear track

the appropriate energy density, while it reduces at energy density of E_d=12.5 J/cm². It is expected that the excessive energy density of the EB leads to transformation of crystal structure due to thermal effect. Therefore, the crystal structure of the zirconia surface is measured by thin film x-ray diffraction method.

Figure 9 shows XRD spectra of zirconia surface before and after the large-area EB irradiation with various energy densities. As shown in the figure, the non-EB irradiated zirconia surface has tetragonal and monoclinic phases, and it does not change after the EB irradiation at the energy density less than E_d=5.0J/cm². On the other hand, only tetragonal phase can be detected at the energy density more than E_d=7.5J/cm². In general, 3mol% yittria partially stabilized zirconia has tetragonal and monoclinic phases. Existence of the monoclinic phase prevents generation of micro-cracks into the zirconia surface, and high wear resistance can be realized for the zirconia ceramics. Then, it is reported that transformation of crystal structure from monoclinic to tetragonal phase is caused at about 1443K [1].
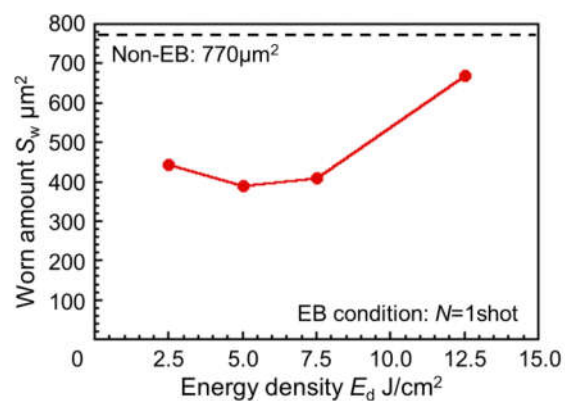
Fig.8 Variation of worn amount with energy density
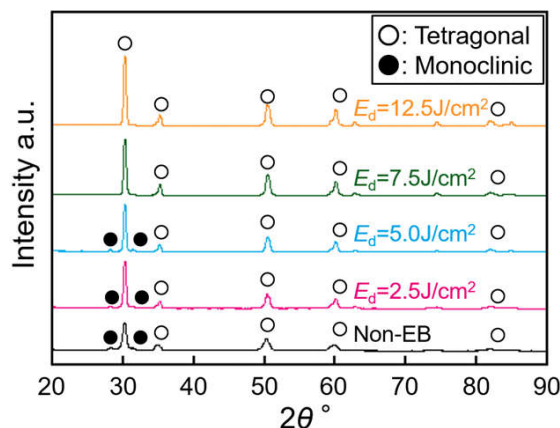
Fig.9 XRD spectra of zirconia surface before and after EB irradiation surface with energy density

Therefore, it is considered that the reduction of wear resistance on the EB irradiated zirconia surface at high energy density is caused by transformation of crystal structure from monoclinic to tetragonal phase due to thermal effect of excessive energy density in the large-area EB irradiation.

4. Conclusions

In this study, improvement of wear resistance for zirconia is proposed by the large-area EB irradiation. Main conclusions obtained in this study are as follows,

(1) Mean width of EB irradiated zirconia surface increases with increasing energy density, although surface roughness is almost same as the ground surface.

(2) Coefficient of friction for zirconia decreases and wear resistance significantly improves by large-area EB irradiation under appropriate energy density.

(3) Excessive energy density of EB leads to reduction of wear resistance for zirconia, since crystal structure is changed from monoclinic to tetragonal phase due to thermal effect of the EB irradiation.

References

[1] C. Piconi, G. Maccauro, *Biomaterials*, 20 (1999) 1-25.

[2] T. Shinonaga, A. Okada, T. Miyoshi, *International Journal of Machine Tools and Manufacture*, 110 (2016) 18-26.

[3] Y. Uno, A. Okada, K. Uemura, P. Raharjo, T. Furukawa, K. Karato, *Precision Engineering*, 29 (2005) 449-455.

[4] A. Okada, Y. Uno, N. Yabushita, K. Uemura, P. Raharjo, *Journal of Materials Processing Technology*, 149 (2004) 506-511

[5] J.C. Walker, J.W. Murray, M. Nie, R.B. Cook, A.T. Clare, *Applied Surface Science*, 311 (2014) 534-540.

[6] A. Okada, R. Kitada, Y. Okamoto, Y. Uno, *CIRP Annals*, 60/1 (2011) 575-578.

[7] A. Okada, Y. Okamoto, Y. Uno, K. Uemura, *J Journal of Materials Processing Technology*, 214 (2014) 1740-1748.

Influence of Molten Area on Joining Strength in Micro-welding of Glass by Picosecond Pulsed Laser

Yuta OGINO[1], Zhiyong OUYANG[1], Yasuhiro OKAMOTO[1], Togo SHINONAGA[1], Akira OKADA[1]

[1] Graduate School of Natural Science and Technology, Okayama University

3-1-1 Tsushimanaka, Kita-ku, Okayama 700-8530, Japan

ABSTRACT

Micro-welding of glass by using an ultra-short pulsed laser has been expected to apply to industrial applications, but further stable processing and high strength of weld joint are required. Thus, the influences of focusing characteristics such as numerical aperture on molten area formation of glass were experimentally investigated in micro-welding of glass by picosecond pulsed laser, and its processing characteristics were analyzed by high-speed observation of molten area formation. Moreover, the influences of molten area and processing phenomena on joining strength were discussed.

Keywords: Glass, Micro-welding, Ultrashort pulsed laser, Picosecond laser, High-speed video camera

1. Introduction

Glass material has been widely used in many products such as optical components and semiconductor devices because of its unique characteristics such as excellent optical transparency, chemical durability and heat resistance. In these products, precision joining methods of glasses are required owing to the demand of small and complicated components. Adhesive joining has been commonly used as a bonding method of glasses, but this method might deteriorate its characteristics in chemical durability, joining strength and heat resistance. Therefore, attention has been paid to direct fusion micro-welding technologies of glasses, without any intermediate layer, using an ultra-short pulsed laser [1]. The irradiation of ultra-short laser pulses with high intensity at a tightly focused point inside the glass makes it possible to generate a nonlinear absorption phenomena in the vicinity of focal point. Moreover, in this process, molten area is formed inside the glass by energy accumulation of multiple laser pulses with the periodical movement of absorption point in irradiation direction of laser beam [2, 3]. Therefore, it is considered that focusing characteristics such as numerical aperture of focusing lens have the great influence on the formation of molten area inside the glass. In general, laser beam can be focused into the tiny spot using a high numerical aperture lens, while Rayleigh length is shorter with high numerical aperture lens. Furthermore, when focusing the laser beam into glass, spherical aberration occurs due to the difference in refractive indexes between the atmosphere and the glass, and then its focusing characteristics change greatly. Further stable processing and higher strength of weld joint are required for the application of the joining technology.

Thus, a picosecond pulsed laser beam was irradiated inside the glass by varying numerical aperture of focusing lens with aberration correction. The influences of focusing characteristics such as numerical aperture and spherical aberration on molten area formation of borosilicate glass were experimentally investigated, and its processing characteristics were analyzed by high-speed observation of molten area formation. Moreover, the influences of molten area and processing phenomena on joining strength were discussed.

2. Experimental Method

2.1. High-speed observation of molten area formation

In order to investigate the influences of numerical aperture of focusing lens on molten area shape and molten area formation, the laser beam irradiated zone was observed by using the experimental setup shown in Fig. 1. Borosilicate glass (Schott, D263) of 1.1 mm thickness was used as a specimen. A picosecond pulsed laser with a wavelength of 1064 nm, a pulse duration of 12.5 ps and a pulse repetition rate of 1 MHz was used as a laser source. A laser beam with a spot diameter of 3.6 μm was focused inside the glass plate at the position of D_{df}=300 μm below the top surface by using focusing lenses of numerical apertures (N.A.) 0.45, 0.65 and 0.85 with aberration correction. Generation of plasma in the irradiated area of laser beam was observed by using a high-speed video camera (Shimazu HPV-2A) with a frame rate of 63 kfps and an exposure time of 4.0 μs. The movement of the absorption point was calculated by using the feed rate of the specimen.

2.2. Measurement method of absorption rate

The influences of focusing characteristics such as numerical aperture and spherical aberration on molten area formation were evaluated by the absorption rate of
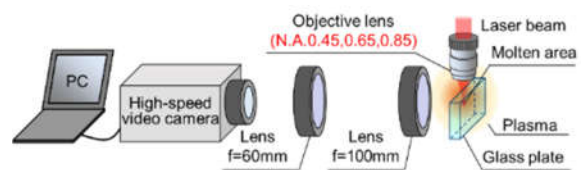
Fig. 1 Schematic illustration of setup for observation of absorption point using high-speed video camera.

laser energy A_{ab}, which is given by equation (1) [1, 2]:

$$A_{ab} = \frac{E_{ab}}{E_{in}} = \frac{E_{in}(1-R)^2 - E_{tr}}{E_{in}(1-R)} \qquad (1)$$

where E_{ab} is the laser energy absorbed into the specimen, and E_{in} is the laser energy irradiated on the specimen by focusing lens. Energy losses due to reflection on each surface of the glass were taken into consideration by using the Fresnel reflectance, R. Therefore, the absorption rate A_{ab} can be calculated by measuring the laser energy transmitting through the glass, E_{tr}.

2.3. Setup of breaking test

Breaking stress of fusion welded zone was measured to evaluate the joining strength of weld glass. Figure 2 shows the setup of specimen for breaking test and schematic illustration of the breaking test. In this experiment, fusion welding was conducted only at interface of glasses with optical contact. As shown in Fig. 2 (a), the optical contacted area, 1 mm wide, was performed by etching process in order to minimize the influence of the optical contact on joining strength as much as possible [4]. Non-overlapping multiple weld beads were created within an area of 1 mm × 10 mm, and the glasses were welded together. Figure 2 (b) shows the schematic illustration of breaking test method. A pull test perpendicular to the weld area makes it possible to suppress the influence of frictional force due to the optical contact [2]. The speed of the crosshead was set to 0.5 mm/min. Perpendicular tensile stress was calculated by dividing the breaking load by the welding area. The perpendicular tensile stress was recorded as a breaking stress, and joining strength in micro-welding of glass by picosecond pulsed laser was evaluated.

3. Results and Discussion

3.1. Influence of numerical aperture on formation of molten area

High-speed observation of laser beam irradiated zone without illumination light made it possible to record only the location of plasma for each time [2, 3]. As shown in Fig. 3, the movement of absorption point during steady state was measured by considering the location of plasma as an absorption point, and the bottom point of absorption point was set to $H_a = 0$ μm. The smaller the numerical aperture, the higher the maximum height of the absorption point and the longer the interval of absorption point movement. In the processing phenomena, the initial absorption point was generated in the vicinity of the focal point. As multiple laser pulses were irradiated, one teardrop shape was created by periodic movement of the absorption point in the irradiation direction. Since the power density of laser beam decreases with moving in the upper direction of laser beam axis from the focal point, the absorption rate of laser beam decreases. Therefore, the formation of another teardrop was started again from the bottom edge of absorption point movement, and this periodic phenomenon was repeated.

Figure 4 shows the state of molten area formation in the

(a) Laser irradiation area   (b) Perpendicular pulling load
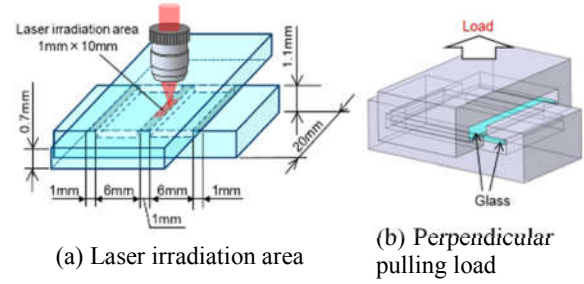
Fig. 2 Schematic illustration of laser irradiation area and breaking test with perpendicular pulling load.
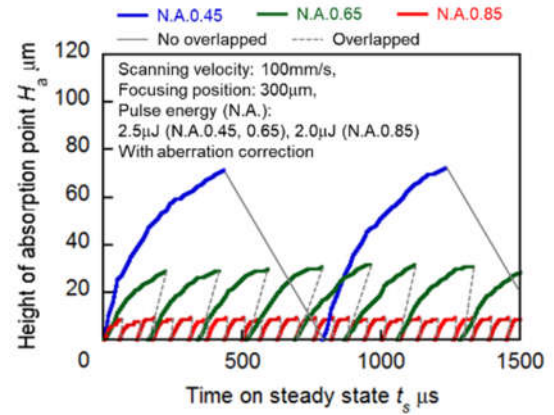
Fig. 3 Replationships between height of absorption point and time using different numerical aperture.
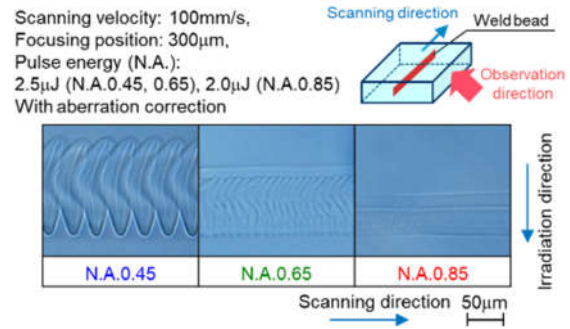
Fig. 4 Optical images of molten area in the scanning direction of laser beam.

scanning direction of laser beam, which was observed by an optical microscope. The numerical aperture had an influence on size of molten area, and a smaller numerical aperture could create a large molten volume. Furthermore, the numerical aperture also influenced the shape of molten area, and a remarkable spike shape in the lower tip of the molten region was observed in the case of N.A. 0.45. As observed in the cases of N.A. 0.65 and 0.85 shown in Fig. 3, the absorption point was simultaneously formed and overlapped in the upper and lower parts of the molten area, which resulted in continuous formation of molten area with a small interval in the scanning direction of laser beam. On the other hand, the formation of the absorption point by

195

using N.A. 0.45 did not overlap at the bottom edge of molten area, which resulted in the spike shape at the lower tip of molten region.

3.2. Influence of focusing characteristics on formation of molten area

Figure 5 shows the absorption rate of laser energy under different focusing characteristics. For each numerical aperture, applying spherical aberration correction led to efficient absorption of laser energy, and nonlinear absorption phenomena occurred even at a smaller pulse energy. It is considered that aberration correction made it possible to suppress the diffusion of the laser beam in the direction of the optical axis, and the power density of laser beam became larger than the case without aberration correction under the same pulse energy condition. Hence, aberration correction led to stable creation of molten area even at a smaller pulse energy [2].

A small numerical aperture has time intervals, in which the laser energy is not absorbed as shown in Fig. 3, and the absorption rate of laser beam decreases. In the case of a large numerical aperture, diffused rays in irradiation direction of laser beam increases, and the absorption rate of laser beam decreases. Therefore, it is considered that the absorption rate became the highest in the case of using medium numerical aperture of 0.65. Figure 6 shows the influences of numerical aperture on stability of molten area formation. The laser intensity absorbed at focal point I_{ab}, which is given by equation (2):

$$I_{ab} = \frac{2E_{in}A_{ab}}{\pi d_s^2 \tau_p} \qquad (2)$$

where d_s is diameter of laser beam at focal point. Laser intensity was varied by pulse energy based on the measurement of absorption rate of laser beam, as shown in Fig. 5. In the case of N.A. 0.45, cracks tended to appear at the lower part of the molten area with increasing the laser intensity I_{ab}, and there was instability of molten area formation. When an absorption point drops down from the top edge to the bottom one of molten area, the temperature of glass material rapidly increases from a temperature below the softening point of glass material to one above it, and an absorption point is generated at the bottom edge of molten area again. It is considered that cracks were likely to occur due to this rapid variation in temperature. On the other hand, in the cases of N.A. 0.65 and 0.85, simultaneous absorption of laser energy at the upper part and lower part of molten area led to slow variations in temperatures compared to those by using N.A. 0.45, which resulted in higher stability of molten area creation without cracks.

The influences of focusing characteristics such as difference of numerical aperture on the formation of the molten area were summarized as follows. It is expected that middle numerical aperture such as N.A. 0.65 had excellent focusing characteristics inside the glass, and it also had long and high power density region of laser
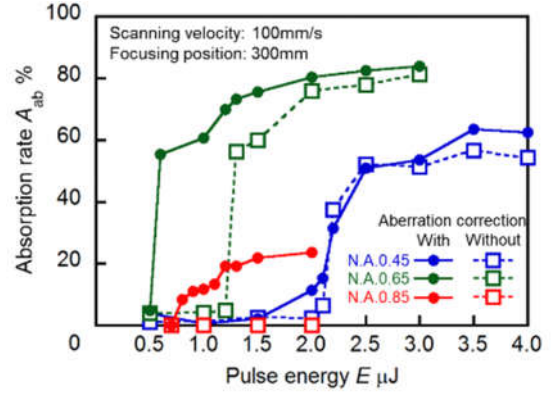
Fig. 5 Relationships between absorption rate and pulse energy for various numerical apeartures.
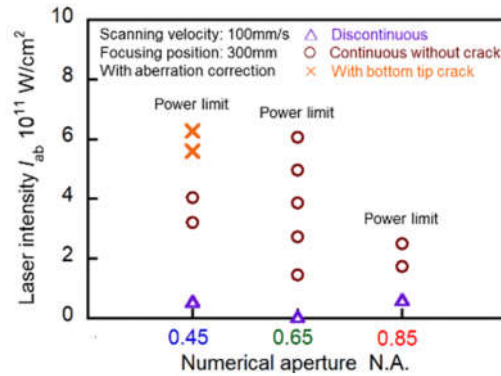
Fig. 6 Influence of numerical aperture on stability of molten area formation.
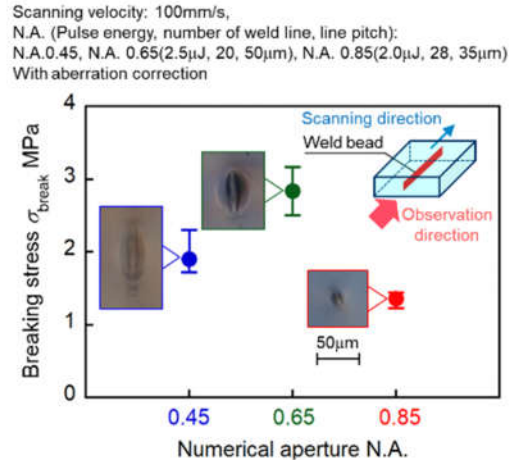
Fig. 7 Influence of numerical aperture on breaking stress.

beam in the optical axis direction. As a result, these focusing characteristics made it possible to create a large molten area without cracks stably.

3.3. Influence of numerical aperture on breaking stress

Numerical aperture influenced the shape of molten area as mentioned above. Therefore, the influences of

numerical aperture on joining strength of glass were experimentally investigated. In order to equalize the welded area, the number of weld lines and line pitches were adjusted. Figure 7 shows breaking stress of the specimen welded by using different numerical apertures. In the case of middle numerical aperture of 0.65, the breaking stress was the highest. From the observation of fracture surface, numerous cracks were generated in the case of N.A. 0.45. It is expected that the crack propagation was likely to be generated at the remarkable spike shape as shown in Fig. 4, which resulted in a low joining strength. In the case of N.A. 0.85, the fracture surface after breaking test was most stable, but the breaking stress was the smallest. The size of molten area created by using N.A. 0.85 was the smallest among the conditions, while a larger and more stable molten area created by using N.A. 0.65 indicated the highest breaking stress. Therefore, it is considered that three-dimensional size of molten area affected the joining strength.

3.4. Influence of molten area size on breaking stress

The influence of the size of molten area on joining strength was investigated by using N.A. 0.65, which gave the highest joining strength. Figure 8 shows the variation of breaking stress with pulse energy. In order to equalize the welded area, the number of weld lines and line pitches were adjusted. As the pulse energy increased, that is, as the size of the molten area increased, and then high breaking stress was obtained. During the formation of molten area by using the ultra-short pulsed laser, higher absorbed energy led to variation in density of glass [5], and the molten area was expected to increase in mechanical strength more than the other area. Therefore, when molten area could be created without cracks, the laser beam with larger pulse energy made it possible to have higher strength and three-dimensional larger molten area, so that improvement of joining strength was achieved.
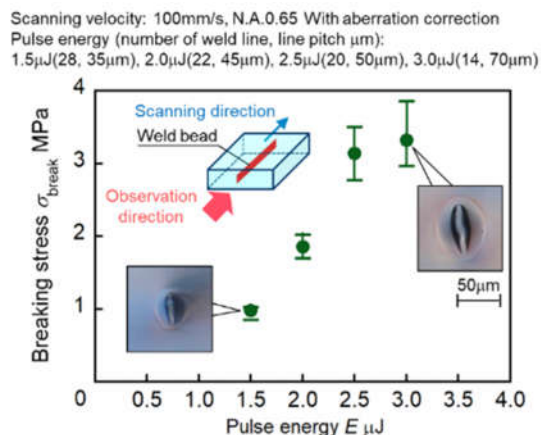
Fig. 8 Influence of molten area size on breaking stress using N.A. 0.65.

3.5. Relationship between breaking stress and scanning velocity

Figure 9 shows breaking stress of specimen welded at different scanning velocities by using N.A. 0.65. In this experiment, in order to equalize the size of molten area, pulse energy was changed for each scanning velocity. In the case of low scanning velocity by using N.A. 0.65, the formation interval of spike shape was smaller, and molten area was created continuously. Therefore, the breaking stress increased with decreasing the scanning velocity despite the small pulse energy when the size of molten area is equal. On the other hand, N.A. 0.65 could input larger pulse energy under higher scanning velocity. Higher pulse energy and scanning velocity could create larger molten size, and its breaking stress of 3.0 µJ and 100 mm/s, as shown in Fig. 8, was higher than that under low pulse energy and scanning velocity of 1.0 µJ and 20 mm/s, as shown in Fig. 9. Therefore, in the case of focusing characteristics such as N.A. 0.65, a large molten area without cracks can be stably formed even at higher pulse energy, which led to high joining strength and high processing speed.

4. Conclusions
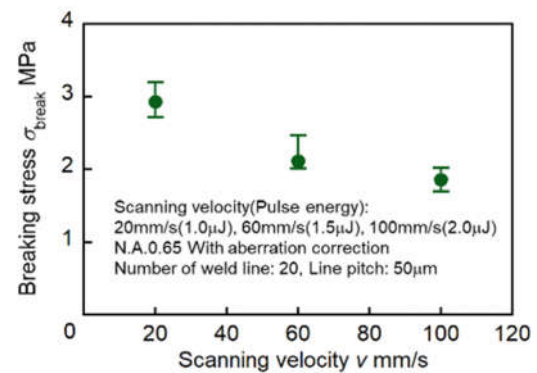
Fig. 9 Relationship between breaking stress and scanning velocity by using N.A. 0.65.

The main conclusions obtained in this study are as follows:

(1) With increasing the numerical aperture, the maximum height of the absorption point becomes smaller, and a continuous molten area with a small formation interval is created in the scanning direction of laser beam.

(2) Middle numerical aperture such as N.A. of 0.65 has excellent focusing characteristics inside the glass, and it also has long and high power density region of laser beam in the optical axis direction. Even when the pulse energy is increased, these focusing characteristics make it possible to create a large molten area stably without cracks.

(3) Depending on the numerical aperture, the formation states of molten area are different and the joining strength is affected. Stable creations of a large molten area without cracks can achieve high joining strength.

References

[1] I. Miyamoto, K. Cvecek, Y. Okamoto, M. Schmidt, *Appl. Phys. A*, (2014), 114: 187.

[2] I. H. W. Nordin, Y. Okamoto, A. Okada, T. Takekuni, T. Sakagawa, *Appl. Phys. A*, (2016), 122: 492.

[3] I. Miyamoto, Y. Okamoto, R. Tanabe, Y. Ito, K. Cvecek, M. Schmidt, *Optics Express*, (2016), Vol. 24, No. 22, p. 25718.

[4] Y. Okamoto, I. Miyamoto, K. Cvecek, A. Okada, K. Takahashi, M. Schmidt, *Jounal of Laser Micro / Nanoengineering*, (2013), Vol. 8, No. 1, p. 65.

[5] K. Hirao, Industrial Application of the Advanced Glass and New Processing, *CMC Publishing*, (2009), p. 67.

Effects of the Helical Passageways in Complex-hole Finishing by Abrasive Flow Machining

A-Cheng Wang[1], Ken-Chuan Cheng[1], Kuan-Yu Chen[2], and Yan-Cherng Lin[3]

[1] Department of Mechanical Engineering, Chien Hsin University of Science and Technology, Tao-yuan 32097, Taiwan

[2] Department of Mechanical Engineering, Chung Yuan Christian University, Tao-yuan32023, Taiwan

[3] Department of Mechanical Engineering, Nan Kai University of Technology, Nantou 54243, Taiwan

ABSTRACT

Since gel abrasives are flexible media therefore it can be easily extruded into the complex holes in abrasive flow machining (AFM). At the same time the smooth surfaces of these holes are able to get in the process. Therefore, the abrasive media are the key elements that dominate the polishing behavior in AFM. However, the abrading mechanism of these media are not easy to understand because of the complex motion of the gel abrasives in AFM, resulting in many finishing works need lots of time to design the machining process. Relationships between viscosities and shear rates are studied here to evaluate the non-Newtonian flow of the gel abrasives firstly. Then different gel abrasives are utilized to finish the complex holes to find out the abraded abilities of different viscosities. Moreover, in the polishing process of complex holes, it is easy to cause uneven abrading forces in the complex holes; hence, traditional AFM has difficulty to achieve the uniform roughness in the radial direction of the complex holes. So, a helical passageway is proposed to create a multiple motion of abrasive medium and to obtain the even surface of the complex holes in AFM process. The results show that silicone rubber with additives creates good abrasive ability in AFM, and roughness improvement ratio in AFM can reach to 77% when a 5 helical grooves cylinder is utilized as a mold core.

Keywords: abrasive flow machining, gel abrasive, helical passageway, surface roughness

1. Introduction

The benefits of AFM method consist of convenient operation, lower manufacturing cost, complex shape machining, and higher polishing efficiency. It is widely used to deburr, radius, polish, and remove recast layer of the complex geometries and hard materials. However, such as other non-conventional polishing processes, a smoother surface of workpiece is not easily obtained after AFM polishing, since this process had the constraint in the lower rates of material removal. To overcome different limitations of the traditional AFM process, there are many kinds of different skills and methods to be developed [1-5]. By using AFM as a base process, a lot of hybrid polishing process like magnetic abrasive finishing, magneto rheological finishing, magnetic float polishing, elastic emission machining, etc. have been developed having component and material specific finishing capabilities. A hybrid finishing process like rotational abrasive flow finishing (R-AFF) is one of modifications to raise the radial force and the polishing efficiency in AFM operation [6-8]. R-AFF had an approving performance in terms of better polishing and higher finishing rate, but this method may either rise apparatus cost of extra rotational mechanism or limit the machining complex shapes to process. Furthermore, Magneto-rheological abrasive flow finishing (MR-AFF) is also one of the improving actions as compared to the common AFM process [9-10]. In MR-AFF, the magnetic field applied to increase the abrasive forces, but this method was limited to the simple geometries of machining workpiece. In order to improve the limitations of MR-AFF method, the rotational magneto-rheological abrasive flow finishing

(R-MRAFF) had been developed [11-12]. The R-MRAFF method draws on the simultaneous rotational and reciprocal motions of the MR-AFF fluid induced by rotating permanent magnets and a hydraulic unit. An important advantage of R-MRAFF is the flexibility of the MRA fluid and its adaptability to those parts with complex geometries.

Recently, a novel conception with inserting a mold core into a machining passageway to enhance the polishing rates was developed. The results indicated that surface roughness of the cylindrical passageway notably decreased to 0.28 μm Ra from an initial value of 1.8 μm Ra after 5 working cycles [13]. Based on experimental study, it was observed that abrasive mesh size and percentage of abrasive concentration in media are the most significant parameters for material removal and improvement in surface roughness. Also viscosity of media was found as significant parameter for material removal for the considered size and shape of the workpiece. Moreover, a unique mechanism with a helical mold was created to build helical flowing paths. This design is an easier modification of mechanism with powerful rotation to raise the radial force in AFM process [14-16]. The experimental results indicated that the helical passageways performed better than the original passageways during AFM in terms of efficiency and creating polishing uniformity of the polygonal holes.

Abrasive media plays a major role in AFM because of its ability to precisely polish the selected surfaces along the media flow passageway. Thus, the investigation of different gels is an extremely importance in AFM field. Researchers have attempted to enhance the

performance capabilities of AFM and also in development of superior and alternative to commercially available media. Davis et al. [17] investigated rheological study on different medium by homogeneously mixing polyborosiloxane (PBS) with silicon carbide (SiC) grits in varying proportion. Jain et al. [18] demonstrated the same by conducting AFM experiments using medium of different viscosities. Media usually contains two major roles as the carrier and the solid phase. The physical, chemical, material, and rheological characteristics significantly influence the overall performance of the AFM. Besides, the mechanical properties of polymer depend on local chain motions and intermolecular interactions between chains had been published [2]. Sinhg et al. [19] reported the work to model forces responsible for shearing of the roughness peaks during AFM, and their correlation with rheological properties of the medium. It is the complex shear modulus of the medium which governs the magnitude of forces generated in AFM by applying a MATLAB program. Wan et al. [20] performed the CFD simulation of the two-way AFM process during finishing of straight tubes with ellipsoidal cross sections. Final surface roughness of the workpiece is simulated and validated with the experimental result.

In this research, lower-cost and polymer based environmental media are developed to form abrasive gels (PAGs) of various grades and upon trial on AFM setup. This study will evaluate the viscosity of polymer gel; then, a series of AFM experiments were utilized to verify the effects of these abrasive gels. Moreover, a helical passageway is proposed to create a multiple motion of abrasive medium in polishing method to improve the performance of the traditional AFM.

2. Methods

2.1 Gel Materials

The most important factor which can affect the finishing result in AFM is the abrasive medium. In this study, a pure silicone rubber (P-Silicone) and silicone rubber with additives (A-Silicone) are chosen as the media. In general, P-Silicone is used to make the plastic mold in metal casting with low melting temperature. This kind of macromolecule gel belongs to high density visco-elastic rubber compound, mainly plays the role of mixed adhesive abrasive in mixed polymer gel and provides flow property, so that it can be deformed by different processing shapes. The composition of the polymer formula is as shown in Fig. 1. Moreover, the actually manufacturing procedure of polymer silicon rubber is the first through the acidification process to destroy the molecular chain. Then, the gel medium is made through the high temperature synthesis of polymer compounds after several times repeatable processes. This material is a vinyl-based silicone rubber compounds with several hundred thousand molecules. Figure 2 shows that diagrams regarding (a) the transparent gel of P-Silicone and (b) the gel mixed with abrasive grains.
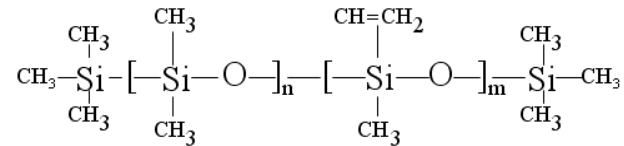
Fig. 1 Composition of the silicone polymer

(a) P-silicone gel without abrasive

(b) P-silicone gel with abrasive

Fig. 2 Diagrams regarding the gel of P-Silicone mixed with/without abrasive grains

A-Silicone is much like the material of the silly putty which is used for the toy clay. This material is also a vinyl-based silicone rubber compounds but being higher density with several million molecules. These silicone gels have lower flow property and do not stick on the workpiece surface after contact, so that they are the good abrasive media in AFM. The complicated shape can be polished uniformly using this kind of silicone gels. Because the gels have good deformability, the abrasive particles must have high hardness to execute the polishing process. Figure 3 displays that diagrams regarding (a) the orange color gel of A-Silicone and (b) the polymer gel mixed with abrasive particles. Consequently, the silicon carbide (SiC) is chosen as the main abrasive material and uniformly mixed with the silicone gel. Table 1 shows the viscosity of P- and A-silicone without abrasive.

Table 1 Viscosity of three clay gels

Clay	P-Silicone gel	A-Silicone gel
Viscosity (Pa*S)	120	500

(a)A-silicone gel without abrasive

(b)A-silicone gel with abrasive

Fig. 3 Diagrams regarding the gel of A-Silicone mixed with/without abrasive grains

2.2 AFM setup and workpiece material

In the traditional AFM, deformable abrasive tool better than cutting tool known as flexible media is extruded over the surfaces to be finished because of imparting external pressure P. A machining model of the velocity and force components during AFM process is presented in Figure 4. The medium motion reciprocates at velocity V_a and exerts axial force F_a on an abrasive particle along the axial direction of the workpiece. This demonstrates that the abrasive medium retains a unitary axial motion. It also exerts radial force F_r on an abrasive particle interacting with theworkpiece due to the visco-elastic character of the abrasive medium. The penetration depth of the abrasive grains in the workpiece surface depends on F_r and the corresponding compressive strength of the abrasive medium, extrusion pressure and grain size. Then, axial force F_a removes the material in the form of micro bits during the material removal process. In this present work, a novel mechanism with a helical passageway is developed to perform multiple flowing paths of abrasive medium by modifying AFM set-up. The diagram of the velocity and force components in AFM with a helical passageway is shown in Figure5. In such a case, the helical motion in the polishing area exerts an additional tangential force F_t along the tangential direction of workpiece; the following mathematical formula describing the total force F_c of an abrasive particle as Eq. (1) has been calculated. Resistance offered by the workpiece for removal of material in the form of microchips is expressed by F_s as Equation (2). From a physical point of view, the material is removed in the form of microchips if $F_c > F_s$, and in some cases it may take place if $F_c = F_s$; then, the material removal just starts:

$$F_c = \sqrt{F_r^2 + F_a^2 + F_t^2} \quad \text{.................................(1)}$$

$$F_s = \tau_s * A \quad \text{..(2)}$$
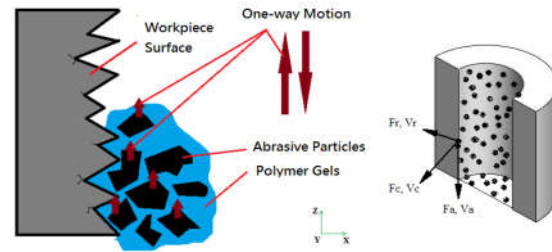
Fig. 4 Diagram of the velocity and force components in traditional AFM
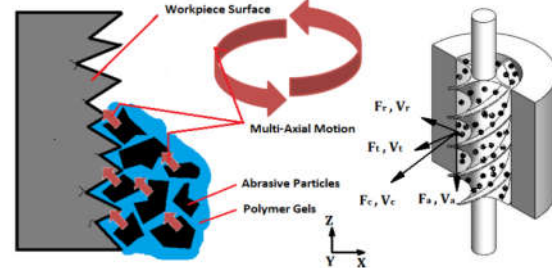
Fig. 5 Diagram of the velocity and force components in AFM with a helical passageway
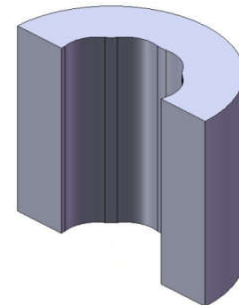
(a) SKD-11 workpiece of a complex-hole after WEDM
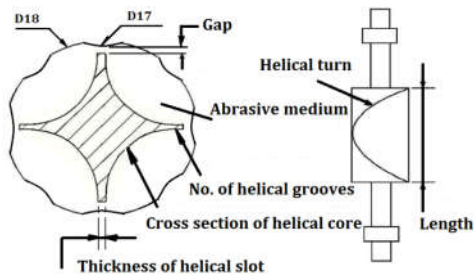
(b)cross-section diagram of a helical core

Fig. 6 Diagrams of a complex-hole specimen, and cross-section of a helical core

This investigation focuses on increasing roughness improvement rate (RIR) of a radial distribution when polishing workpieces with A-silicon material. The mold steel SKD-11 is selected as workpiece material. It is widely used in the sheet metal punching or injection molds. Batch complex-hole samples of SKD-11 steel are cut out using the WEDM process, in which the initially average SR of all these workpieces is approximately 0.65μm Ra after WEDM machining under the same conditions. The outer diameter of each complex-hole workpiece is 18.0 mm, the inner diameter is 17.0 mm, and the length is approximately 30.0 mm. Figure 6 shows the diagrams regarding (a) the cutting part of a complex-hole specimen and (b) design parameters of a helical core.

3. Results and Discussion

3.1 Material viscosities

The rheological properties of the medium play an important role to find the good surface quality in AFM. In this experiment, a rheological apparatus is utilized to measure the medium viscosities when the abrasive concentration of the medium is 50%. Figure 7 shows the effects of shear rates on medium viscosities. The result shows that the A-Silicone has higher viscosity than the P-Silicone in strain rate test. And the viscosities are decreased with increasing the strain rates both two silicon materials. It also shows that the high viscosity medium can make good elongation in the deformation test.
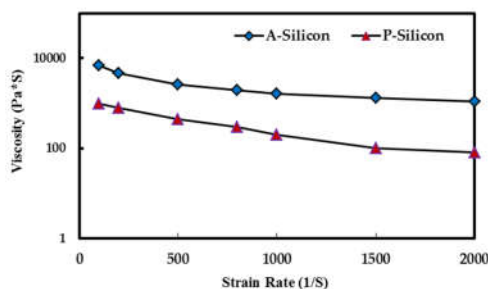
Fig. 7 Diagram of the effect of strain rates on the viscosities for the different gels

3.2 Durable properties of the abrasive media

The abrasive media must have stable chemical and physical properties, so that they are suitable for long duration of use in AFM. The goal is to verify the polishing effects for different passageways regarding material removal (MR) and roughness improvement ratio (RIR). To achieve the stated objective, material weight measurements and surface roughness measurements are taken to demonstrate the deviation for the items of MR and RIR in the radial direction after the AFM process. A series of experiments picked up eight positions in a radial surface to test the surface roughness during AFM. The RIR is defined as the following equation (3):

$$RIR = \frac{SR_{origin} - SR_{polishing}}{SR_{origin}} \quad \text{............................} \quad (3)$$

where SR_{origin} represents the original surface roughness before AFM, and $SR_{polishing}$ describes the surface roughness after AFM polishing. Figure 8 represents the durable property of the same abrasive grain and concentration with the different gels. The effects of the number of up and down cycles on the surface roughness are observed. It is illustrated that an increase in the cycles results in an associated decrease in the overall surface roughness. In general, the roughness is better with increasing number of up and down cycles. It is also shown that A-Silicone can polish a smoother surface than P-Silicone in AFM due to A-silicone has the higher viscosity and more materials to be removed. The medium temperature of both A-silicon and P-silicon is only risen 2 to 4 degrees Centigrade after 25 cycles in AFM. So the polishing effect is stable and a more precise surface can be obtained when A-Silicone is used as the medium. Figure 8 also displays the effects of the number of up and down cycles on RIR. It shows that the RIR is always maintained at 60% when the same A-Silicone is used to polish the workpieces after 25 cycling times. The RIR can also be maintained at a stable value of 38% if the same work is done by the P-Silicone. The reason is that A-Silicone and P-Silicone are flexible media; they can change their shape easily during the machining process. So the abrasive force is small and it reduces the particle abrasion in AFM. Furthermore, the new abrasives will always appear on the work surface when the abrasive medium changes its shape. Hence, no matter

the A-Silicone or the P-Silicone is used, the durable property of these media is good to depend on.
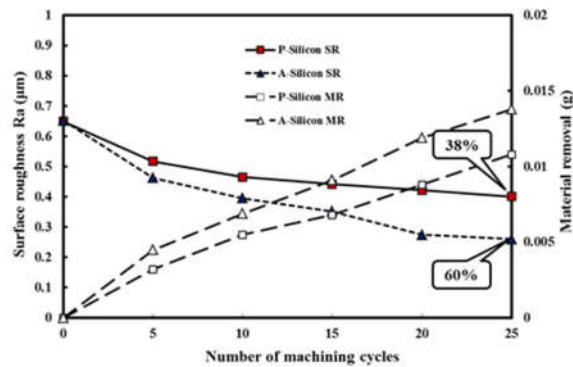
Fig. 8 The durable property of the same abrasive media in different silicon materials

3.3 Polishing effect of different parameters

In this present work, the task is to find the optimum conditions for different design parameters of a helical passageway in complex-hole flowing. Therefore, the control factors of the helical core include the number of helical grooves, the gap between workpiece surface and helical edge, the thickness of helical slot, and the number of helical spins.

3.3.1 Effect of different numbers of helical grooves

The measurement procedures of surface roughness are taken to demonstrate the experimental results in RIR per 5 cycles after the AFM process. Figure 9 presents the polishing effects of the different numbers of helical grooves on surface roughness for various alternating cycles. It illustrates that an increase in the working cycles results in an obvious decrease on the data sheet for surface roughness. This figure shows that the RIR of three-helix grooves reach 72%; the RIR come to 77% both in four-helix grooves and five-helix grooves after 25 machining cycles. According to the RIR results, it reveals that the flowing behavior of a four-helix and five-helix passageway can achieve more polishing effectiveness to reduce surface roughness than that of the three-helix passageway. In this approach, the four-helix passageway was adopted based on the symmetric motion in helical passageway and easier manufacture of core specimen.
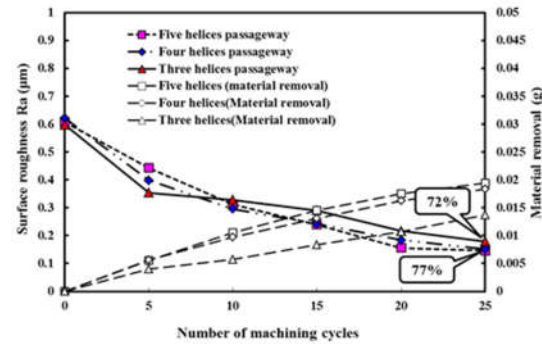
Fig. 9 Effects of working cycles with different helical grooves on surface roughness of complex holes

3.3.2 Effect of different gaps of helical passageway

The helical passageway will create motion in multiple directions to increase the shear force and abrasive area in the radial direction. However, the gap between workpiece surface and helical edge is the main factor, which can perform single flowing or multiple flowing on workpiece surface. Figure 10 presents the polishing effects of the different gaps of helical passageway on surface roughness for various alternating cycles. Experimental results illustrate that an increase in the working cycles results in an obvious decrease on the data sheet for surface roughness. It shows that the RIR of 0.5 mm gap reach 77% for a highest improvement rate; the RIR come to 58% in 1.0 mm gap case; and the worst case of RIR only improve 51% for 1.5 mm gap after 25 machining cycles. Based on the above RIR results, it reveals that the flowing characteristic of a 0.5 mm gap can obviously reduce surface roughness. On the other hand, the larger gaps of 1.0 mm and 1.5 mm result in the worse RIR (51%~58%) than the RIR (60%) of original passageway. In general, the larger gap will introduce straight motion near workpiece' surface, and multiple motions in internal helical area at same time. The side effect of larger gap will produce an interference flowing field to deteriorate polishing effectiveness.
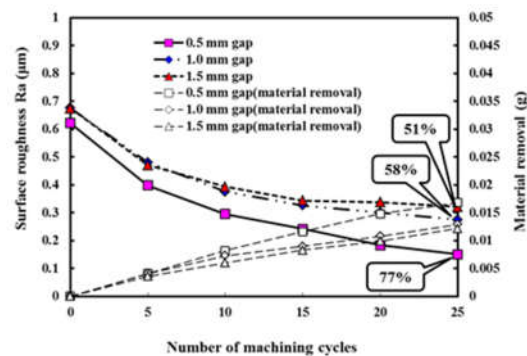
Fig. 10 Effects of working cycles with different gap between workpiece and helical core

3.3.3 Effect of different thicknesses of helical slot

The third factor is the thickness of helical slot, which include 0.5 mm, 1.0 mm and 1.5 mm thickness of helical slot. Figure 11 represents the polishing effects of the different thicknesses on surface roughness for various alternating cycles. Experimental results shows that the RIR of 0.5 mm thickness reach 77% for a highest improvement rate; the RIR come to 58% in 1.0 mm thickness case; and the worst case of RIR only improve 54% for 1.5 mm thickness after 25 machining cycles. The larger thicknesses of 1.0 mm and 1.5 mm result in the worse RIR (54%~58%) than the RIR (60%) of original passageway. It indicated that larger thickness also produce an interference flowing field to deteriorate polishing effectiveness according to the RIR results.
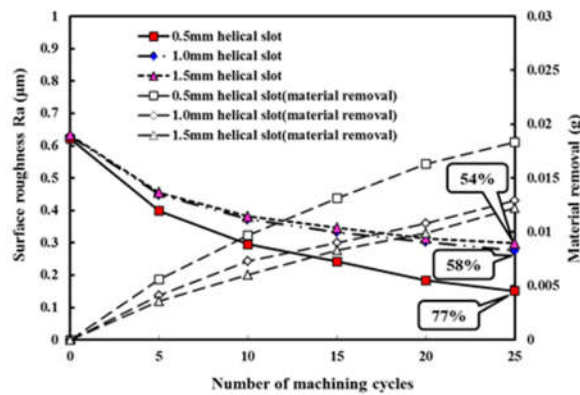
Fig. 11 Effects of working cycles with different thicknesses of helical slot

3.3.4 Effect of different helical spins

The last factor of a helical core is the number of helical spin. Similarly, the helical spin is extremely critical since it affects the angle of multi-axial motions. Figure 12 shows the polishing effects of the different spins of helical grooves on surface roughness for various alternating cycles. This figure shows that the RIR of a one helical spin can reach 77%; the RIR come to 67% for a 0.7 helical spin. The worst case of RIR is only 64% after 25 machining cycles for a 0.5 helical spin. Therefore, to analyze the difference of the RIR results, here find that the angles are distributed within 23~45 degree when the spin numbers from low to high. It reveals that the angle of a one helical spin is near 45 degree to obtain the highest tangent force.
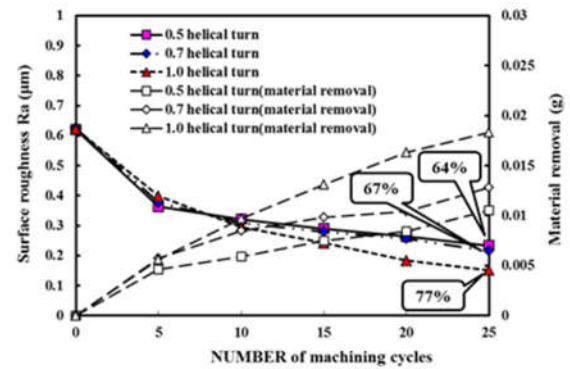
Fig. 12 Effects of working cycles with different helical spins

3.3.5 Effect of different concentration of mixed gels

Based on experimental results of above mentioned database, it was observed that the optimal parameters of a helical core included a four-helix groove, a 0.5 mm gap, a 0.5 mm thickness of the helical slot, and a one helical spin. Then, considering demonstrated the polishing effect of different concentration of mixed gels, which include three cases of concentration ratio: 1.0 : 0.5, 1.0 : 1.0, and 1.0 : 1.5. Figure 13 presents the polishing effects of the different concentration of mixed gels on surface roughness. It illustrates that an increase in the abrasive concentration results in an obvious variance for surface roughness. This figure shows that the RIR of 1.0 : 0.5 concentration only reach 35%; and the RIR come to 77% in 1.0 : 1.0 concentration; furthermore, RIR can increase to 84% of 1.0 : 1.5 concentration after 25 machining cycles. The results represent that the cutting force is proportional to the abrasive concentration, higher concentration performs higher RIR.
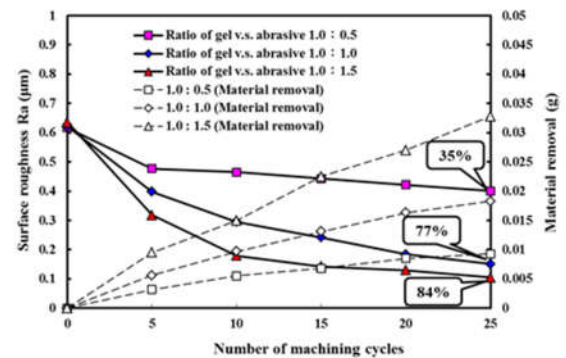
Fig. 13 Effects of working cycles with different concentration of mixed gels

3.4 Effects on surface roughness

This subsection states the polishing effectiveness of abrasive medium with/without a helical core in polishing the complex-hole. Figure 14 presents the polishing effects on SR and MR after 25 AFM cycles in

different passageways. This figure shows that a four-helix passageway performed better than a complex-hole passageway after AFM polishing in terms of efficiency; the RIR is only 60% in a complex-hole passageway, but the RIR can reach 84% in a four-helix passageway. This is largely owing to the abrasive medium in a complex-hole passageway only created unitary axial motion; that is why SR is slowly reduced in AFM. Relatively, the flowing paths in a four-helix passageway created dramatic variety when an abrasive medium is pushed through the passageway. Additionally, the MR of a four-helix passageway is also significantly better than a complex-hole passageway during AFM. Therefore, this study demonstrates that the effectiveness of a helical passageway obviously affected the average RIR and MR.
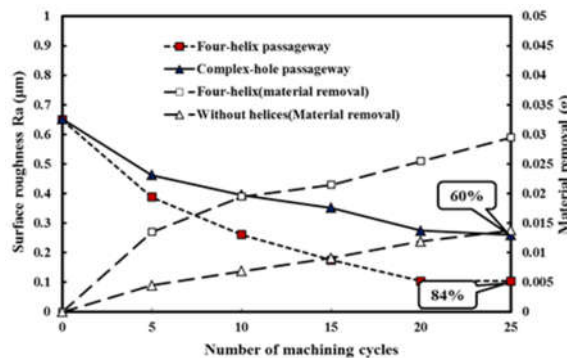
Fig. 14 The Effects of surface roughness and material removal.

3.5 Effects on uniformity of surface roughness

In this present study, surface roughness measurements of workpieces along the radial direction are led to verify the efficiency of the helical passageway during AFM polishing. Further, roughness uniformity (RU) is evaluated by measuring the changed deviation of the whole curve of surface roughness. The RU is defined by the deviation of surface roughness along the axial direction as shown in equation (4):

$$RU = SR_{max.} - SR_{min.} \qquad (4)$$

Where $SR_{max.}$ represented the maximum surface roughness, and $SR_{min.}$ described the minimum surface roughness. Ten positions are picked during a series of experiments in a section to evaluate the surface roughness after AFM. Figure 15 shows the effect of different passageways on RU. According to the test results, the distribution of RU is 0.144 μm Ra with a complex-hole passageway in AFM; but RU can reduce to 0.032 μm Ra when a four-helix passageway is utilized. These results indicate that surface of the complex holes are not uncommonly even in the radial direction. On the

other hand, surface roughness is smoother when a four-helix core utilized as finishing passageway.
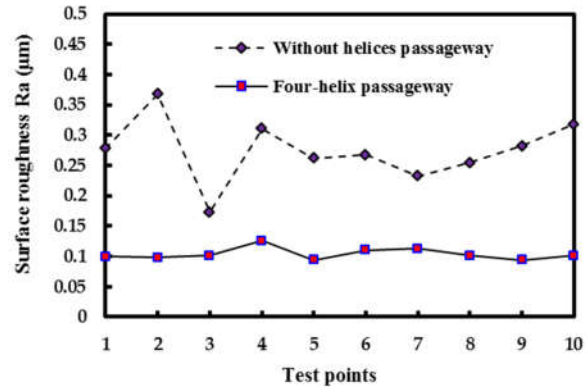
Fig. 15 The Effects of different passageways on roughness uniformity

4. Concluding Remarks

Based on the foregoing results in investigating the flowing behaviors of the abrasive media in complex holes AFM polishing, the main conclusions are summarized as follows.

1. The experimental results show that A-silicon performed better than P-silicon after AFM process in terms of polishing efficiency; the RIR was only 35% in P-silicon gels, but the RIR could reach 58% in A-silicon gels. This indicated that A-Silicone has higher viscosity and lower flowing velocity than the P-Silicone to result in a higher material removal rate and lower deviation of strain rate distribution.

2. The results reveal that the helical passageway can perform better than the original passageway after AFM polishing in terms of efficiency.

3. According to the experimental results represent that the optimal parameters of a helical passageway included a four-helix groove, a 0.5 mm gap, a 0.5 mm thickness of the helical slot, and a one helical spin.

4. **A** helical passageway with the optimum parameters show that SR significantly decreased from 0.65 μm Ra down to 0.104 μm Ra, and calculating the percentage of improvement rate approximately 84% presented an excellent solution to improve surface precision in AFM processes.

5. This study demonstrates the efficiency of a optimum four-helix passageway in surface roughness uniformity based on calculating the percentage of improvement ratio around 78%.

References

[1] M. R. Sankar, J. Ramkumar, and V. K. Jain, "Experimental investigation and mechanism of material removal in nano finishing of MMCs using abrasive flow finishing (AFF) process," Wear, Vol. 266(7–8), pp. 688–98, 2009.

[2] M. R. Sankar, V. K. Jain, and J. Ramkumar, "Experimental investigations into rotating workpiece abrasive flow finishing," Wear, Vol. 267, pp. 43–51, 2009.

[3] J. L. Rhoades, "Orbital polishing apparatus and method, Extrude Hone Corporation," United States Patent No.7,255,631, August 2007.

[4] R. S. Walia, H. S. Shan, and P. Kumar, "Determining dynamically active abrasive particles in the media used in centrifugal force assisted abrasive flow machining process," Int. J. Adv. Manuf. Technol., Vol. 38, pp. 1157–1164, 2008.

[5] M. R. Sankar, S. Mondal, J. Ramkumar, and V. K. Jain, "Experimental investigations and modeling of drill bit guided abrasive flow finishing (DBG-AFF) process," Int. J. Adv. Manuf. Technol., Vol. 42(7–8), pp. 678–88, 2009.

[6] G. Eason, M. R. Sankar, V. K. Jain, and J. Ramkumar, "Rotational abrasive flow finishing (R-AFF) process and its effects on finished surface topography," Int. J. Mach. Tools Manuf., Vol. 50, pp. 637-650, 2010.

[7] M. R. Sankar, V. K. Jain, and J. Ramkumar, "Nano-finishing of cylindrical hard steel tubes using rotational abrasive flow finishing (R-AFF) process," Int. J. Adv. Manuf. Technol., Vol. 85, pp. 2179-2187, 2016.

[8] A. Azami, A. Azizi, and A. Khoshanjam, "Nanofinishing of stainless-steel tubes using rotational abrasive flow finishing (R-AFF) process," Int. J. Manuf . Processes, Vol. 34, pp. 281-291, 2018.

[9] K. P. Hong, Y. K. Cho, B. C. Shin, M. W. Cho, S. B. Choi, W.S. Cho, and J. J. Jae, "Magneto-rheological (MR) Polishing of Alumina-Reinforced Zirconia Ceramics Using Diamond Abrasives for Dental Application," Mater Manuf. Process, Vol. 27(10), pp. 1135-1138, 2012.

[10] A. C. Wang, L. Tsai, C. H. Liu, K. Z. Liang, and S. J. Lee, "Elucidating the Optimal Parameters in Magnetic Finishing with Gel Abrasive," Mater. Manuf. Process, Vol. 26(5), pp. 786-791, 2011.

[11] M. Das, V. K. Jain, and P. S. Ghoshdastidar, "The Out-of-Roundness of the Internal Surfaces of Stainless Steel Tubes Finished by the Rotational–Magneto-rheological Abrasive Flow Finishing Process," Mater. Manuf. Process, Vol. 26(8), pp. 1073-1084, 2011.

[11] S. Kumar, V. K. Jain, and A. Sidpara, "Nanofinishing of freeform surfaces (knee joint implant) by rotational-magnetorheological abrasive flow finishing (R-MRAFF) process," Precis. Eng., 2015.

[12] A. C. Wang, L. Tsai, K. Z. Liang, C. H. Liu, and S. H. Weng, "Uniform surface polished method of complex holes in abrasive flow machining," T. Non-ferr. Metal Soc., Vol. 19, pp. 250-257, 2009.

[13] A. C. Wang, L. Tsai, K. Z. Liang, C. H. Liu, and S. H. Weng, "Uniform surface polished method of complex holes in abrasive flow machining," T. Non-ferr. Metal Soc., Vol. 19, pp. 250-257, 2009.

[14] C. T. Lin, L. D. Yang, and H. M. Chow, "Study of magnetic abrasive finishing in free-form surface operations using the Taguchi method," Int. J. Adv. Manuf. Technol., Vol. 34, pp.122-130, 2007.

[15] A. C. Wang, K. C. Cheng, K. Y. Chen, and C. C. Chien, "Elucidating the optimal parameters of a helical passageway in abrasive flow machining," Int. J. Surf. Sci. Eng., Vol. 9(2/3), pp. 145-158, 2015.[16] K. Y. Chen, and K. C. Cheng, "A study of helical passageways applied to polygon holes in abrasive flow machining," Int. J. Adv. Manuf. Technol., Vol. 74, pp.781-790, 2014.

[17] P. J. Davies, A. J. Fletcher, "The assessment of the rheological characteristics of various polyborosiloxane/grit mixtures as utilized in the abrasive flow machining process," Ins. of Mech. Eng., Vol. 209, pp. 409–418, 1995.

[18] V. K. Jain, C. Ranganatha, and K. Muralidhar, "Evaluation of rheological properties of medium for AFM process," Mach. Sci. Tech., Vol. 5(2), pp. 151-170, 2001.

[19] S. Singh, A. S. A. Raj, M. R. Sankar, and V. K. Jain, "Finishing force analysis and simulation of nanosurface roughness in abrasive flowfinishing process using medium rheological properties, " Int. J. Adv. Manuf. Technol., Vol. 85, pp. 2163-2178, 2016.

[20] S. Wan, Y. J. Ang, T. Sato, and G. C. Lim, "Process modeling and CFD simulation of two-way abrasive flow machining," Int. J. Adv. Manuf. Technol., Vol. 71, pp. 1077-1086, 2014.

PART III, SECTION II

Materials Technology
(Functional Materials; Technologies of Materials; Materials Characterization and Evaluation;
High Speed Machining and Abrasive Machining; Micro- and Nano-Systems Engineering and
Emerging Technologies; Surface Integrity and Machining Quality…)

A Big Data Analysis Technology for Catching Usual/unusual State of Cutting Tool

Yasuo Kondo[1], Mitsugu YAMAGUCHI[2], Satoshi Sakamoto[3]

[1]Yamagata University, 4-3-16, Jhonan, Yonezawa, 992-8510, Japan
[2] Salesian Polytechnic, 4-6-8 Koyamagaoka, Machida, Tokyo, 194-0215, Japan.
[3]Yokohama National University, 79-1, Tokiwadai, Hodogaya, Yokohama, 240-8501, Japan

ABSTRACT

We tried to design a big data analysis technology for catching the usual/unusual state of the cutting tool from the spindle power consumption changes. The absolute value of power consumption tended to increase with the number of cutting cycles and the excessive repetitions of grooving brought the trend changing of power consumption. To facilitate the statistical analysis, the correlation coefficient R was calculated from the single regression analysis between two different cycles of data. The correlation coefficient R is closer to 1.0 if the changing trends are similar between the sample and reference cycles and the R had a strong relation with the condition changes of tool wear. The overwritten drawing of time-series data can catch the condition changes of tool wear visually. These facts indicate that the correlation coefficient R and the overwritten drawing of time-series data become powerful tools to catch the usual/unusual state of the cutting tool.

1. Introduction

In order to achieve the further improving of precision and efficiency of cutting, it must be required to monitor the material removal state and tool wear condition in real time. The monitoring of cutting state is usually based on the big data obtained from sensors foe temperature, cutting force, vibration, AE, power, etc., and the sensors have traditionally been monitored according the thresholds (alarm values) set based on the design and achievements of past operations. This had led to the problem that the detection of unusual signs below the thresholds is hard to execute uniformly because it critically depends on human experience and knowledge [1-3]. To realize a higher productive and accurate machining, an innovative monitoring system should be required to catch the something different and special than usual, such as the lowering of cutting characteristics of cutting tool, in the machining operation.

The authors have been studying a technique to monitor the material removal state and tool wear from the spindle power consumption changes. The spindle power consumption change strongly reflects the cutting force changes because the spindle provides the mechanical force necessary to remove material from the part. In this study, we tried to design a big data analysis technology for catching the usual/unusual state of the cutting tool from the spindle power consumption changes [4, 5].

2. Experiments

Measurement of spindle power consumption. The experimental setup for measuring the power consumption for material cutting is shown in Fig.1. Only electric power consumed by the spindle motor Pmeasure was measured at 0.2 seconds interval by using a power tester (Hioki model 3333). Then the net power consumption in the cutting process Pcut was estimated by subtract the power consumption at idle running Pidle from the measured spindle power. The evolution of net power consumption is a picture of the evolution of cutting force and a fairly accurate measure of he deterioration of tool condition as shown in equation (1).

$$P_{cut} = F_c \cdot V / (60 \times 1000 \times \eta) \qquad (1)$$

where, P [kW] is net effective power, Fc [N] is principal cutting force, V [m/min] is cutting speed and η is mechanical efficiency.

A grooving of 0.1mm depth was conducted on a vertical bench type CNC with an AC spindle motor by using a Φ2mm of two-flute end mill. The grooving conditions are summarized in Fig.2. The workpiece material was a commercial brass plate (JIS C3604) and the shape of groove consisted on a straight section and two curved sections with curvature radius of 10mm and
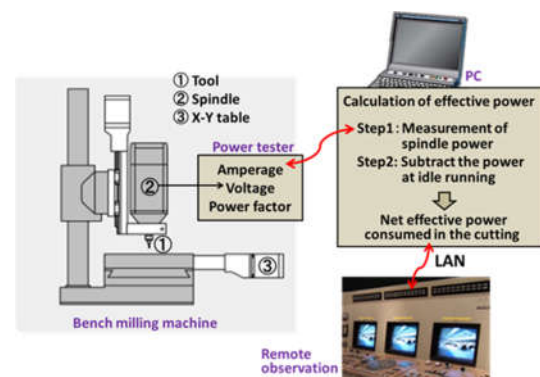
Fig.1 Experimental setup for material cutting

Machining tool	CNC milling machine
Groove shape	See Fig.1
Cutting tool	ϕ 2mm of two-flute end mill
	High speed tool steel
Workpiece	JIS C3604
Work feed speed	1200 mm/min
Revolution of tool	7000 rpm
Cutting depth	0.1 mm
Lubrication	Insoluble cutting oil
Measuring interval	Input power 0.2 s
	Acceleration 0.2 ms
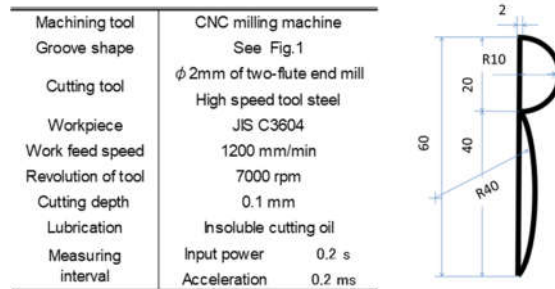
Fig.2 Summary of cutting conditions

40mm as shown in Fig.2. To acquire a large volume sensor data, input power consumption supplied to the spindle were measured at 0.2s interval by using a power meter. The grooving with 0.1mm of cutting depth had been repeated 1000 times and the tool wear was measured every 100 times grooving by using a digital microscope.

Statistical analysis. To analyze the time-series data, the concepts called cycle is set. The one "cycle" corresponds to one round of grooving from the straight section to the curved sections with curvature radius of 40mm via the curved sections with curvature radius of 10mm. To facilitate the statistical analysis, the time-series data obtained from the one cycle of grooving were divided at a second interval. Then the average power consumption, zone average power consumption, were calculated every one second as shown in Fig.3. Finally, the correlation coefficient R was calculated from the single regression analysis between two different cycles of time-series zone average power consumption. As the correlation coefficient R is closer to 1.0, the time-series sensing data in the two different cycles have a more similar power consumption changes over times with each other.
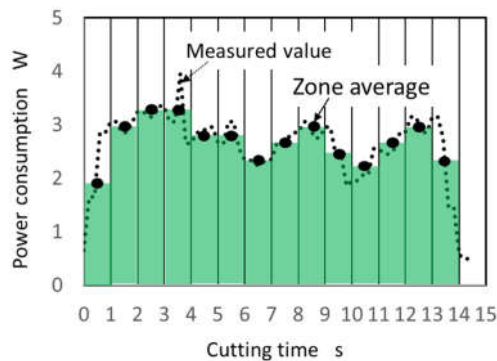
Fig.3 Calculation model of zone average value

Visualization of time-series data. To provide a technique for catching the time-series changes of sensor data by a visual sense, we tried to introduce the overwritten drawing of time series data. At first, the set number of overwriting N=100 is determined. Then, 100 times time-series data, the data form the 100(k-1)+1 ~ 100k cycles (k = 1, 2, 3 ··· ; number of stage), were overwritten on the same coordinate system. The 1st 100 sets of time series data (1st Stage), a group of sensor data collected from 1st to 100th machining operations,

was defined as the "reference data band". The reference data set basically forms a band shape feature. Since then, 2nd, 3rd and more number of Stage's data sets were collected and eachband shape feature was drawn in one by one. Catching the usual/unusual state of cutting tool condition had been made by comparing the band shape feature of the nth Stage with the reference data band.

3. Results and discussions

The nature of time-series data. Figure 4 shows the time-series data obtained from the 30, 91, 249, 498, 616, 752, 851, 985 and 1000th cycles of grooving. The absolute value of power consumption tended to increase with the number of cutting cycles, but the changing trends of power consumption with the cutting time are similar with each other. Figure 5 shows the detailed comparison of power consumption trends among the 91, 249 and 752th cycles of grooving. Although the changing trends of the 91 and 249th cycles are quite similar over the entire of grooving, the changing trend of the 752th cycle showed the opposite trend of 91 and 249th cycles at the first parts of curved section with curvature radius of 10mm and 40mm. This means that the excessive repetitions of grooving would bring the trend changing of power consumption as well as the increasing of its absolute value.

Fig.4 Time-series power consumption data
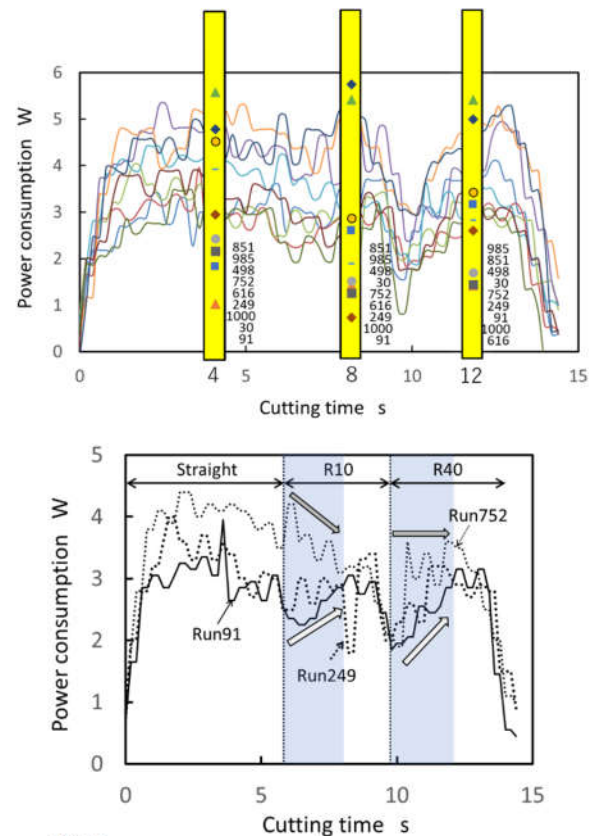
Fig.5
Detailed comparison of power consumption trends

Statistical analysis of time-series data. Figure 6 shows the correlation coefficient R calculated from the

single regression analysis between 91th and 249th cycles and 91th and 752th cycles of time-series zone average power consumption. Where the time-series zone average power consumption in the 91th cycle is considered as the reference data set which represents the typical power consumption changing trend in the usual cutting condition because there is no apparent tool wear after 91th cycle of grooving as shown in Fig.7. The correlation coefficient between 91th and 249th and 91th and 752th are 0.88 and 0.75 respectively. As mentioned above, the power consumption changing trends in the 91th and 249th cycles are quite similar over the entire of grooving while the changing trend at the 752th cycle showed the opposite trend of 91th cycles at the first parts of curved section. Namely, as the changing trends of power consumption in sample cycle (249th, 752th) are more similar to that of reference cycle (91th), the correlation coefficient R is closer to 1.0 as supposed.

Figure 8 shows the correlation coefficient R of 30, 249, 498, 616, 752, 851, 985 and 1000th cycles of grooving when the changing trend of 91th cycle is set as the reference data set. A sharp drop and increase of correlation coefficient R are seen near the 700~800th and 1000th cycles respectively. These changes in correlation coefficient had a relation with the condition changes of tool wear. The tool abrasion loss rapidly increased between 700th and 800th cycles and the cutting tool was worn out near the 1000th cycle as shown in Fig.7. These facts indicate that the correlation coefficient R would
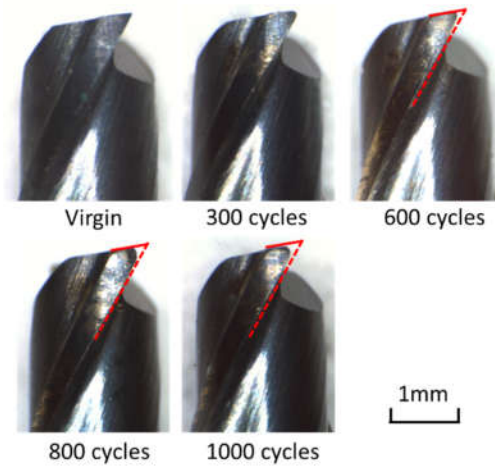
Fig.7 Progress of tool wear with grooving cycle
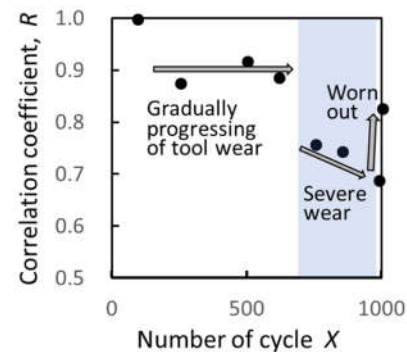
Fig.8 Relation between correlation coefficient R and number of grooving cycle

become an influential tool for catching the usual/unusual state of the cutting tool from the spindle power consumption changes.

Visualized analysis of time-series data. Figure 9 shows the data bands of time-series power consumption in the 2nd, 5th, 8th and 10th stages. The reference data band is also displayed with the black continuous lines. The position of data band gradually moved in the Y-axis direction as the cutting cycle was increased. Figure 10 shows relation between the number of stage and the Range of data band, the difference between the lower and upper values of power consumption in the nth stage's data

Fig.6 Correlation coefficient R calculated from the single regression analysis
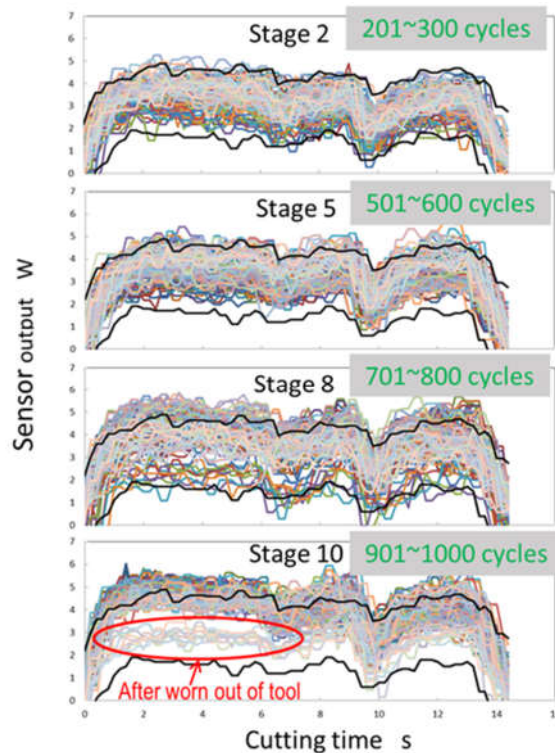
Fig.9 Data bands of time-series power consumption band, at 4s of cutting time. The Range of data band gradually decreased up to the 7th stage, but the monotone decreasing of Range was disappeared at 8th stage. The changing pattern of Range with the grooving cycles is in good agreement with that of correlation coefficient R. To explain differently, the overwritten drawing of time-series power consumption data could become a powerful tool to catch the usual/unusual state of the cutting tool visually.
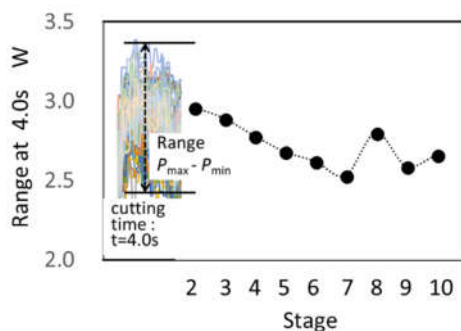
Fig.10 Relation between number of stage and Range of data band

4. Concluding Remarks

We tried to design a big data analysis technology for catching the usual/unusual state of the cutting tool from the spindle power consumption changes. The spindle power consumption change strongly reflects the cutting force changes because the spindle provides the mechanical force necessary to remove material from the part. A grooving of 0.1mm depth was conducted 1000times on a vertical bench type CNC with an AC spindle motor by using a Φ2mm of two-flute end mill. To acquire a large volume sensor data, input power consumption supplied to the spindle were measured at 0.2s interval by using a power meter. The absolute value of power consumption tended to increase with the number of cutting cycles and the excessive repetitions of grooving would bring the trend changing of power consumption as well as the increasing of its absolute value. To facilitate the statistical analysis, the time-series sensor data were divided at a second interval and the zone average power consumption was calculated every one second. Then the correlation coefficient R was calculated from the single regression analysis between two different cycles of time-series zone average power consumption. The correlation coefficient R is closer to 1.0 if the changing trends of power consumption is similar between the sample cycle and reference cycle and the R had a strong relation with the condition changes of tool wear. The overwritten drawing of time-series power consumption data can catch the condition changes of tool wear visually. These facts indicate that the correlation coefficient R and the overwritten drawing of time-series data could become a powerful tool to catch the usual/unusual state of the cutting tool.

References

[1] T.Hey, S.Tansley, K.Tolle, eds, The Fourth Paradigm: Data-Intensive Scientific Discovery, Microsoft Research, (2009), 289.

[2] G.Jiang, H.Chen, Y.Yoshihara, Discovering likely invariants od distributed transaction systems for autonomic system management, The 3rd International Confluence on Autonomic Computing, Dublin, Ireland, June (2006).

[3] N.Yoshinaga, I. Hino, S.Terasawa, K.Maeda, Y.Shigemoto, K.Inoue, Power Plant Fault Sign Monitoring Solution Based on System Invariant Analysis Technology, NEC Technical Journal, 10-2 (2016)58-61,

[4] Y.Kondo, Y.Higashimoto, S.Sakamoto, T.Fujita, K.Yamaguchi, Feature Extraction from Sensor Data Streams for Optimizing Grinding Condition, Materials Science and Engineering, 229(2017) 1-6.

[5] Y.Kondo, S.Mizunoya, S.Sakamoto, K.Yamaguchi, T.Fujita, M.Yamaguchi, A Utilization Method of Big Sensor Data to Detect Tool Anomaly in achining Process, Key Engineering Materials, 719(2016)122-126

Synthesizing Cubic Diamond Crystal Using DC Plasma Jet CVD

Hiromichi Toyota[1], Xia Zhu[1], Ryoya Shiraishi[1], <u>Kazuto Nakajima</u>[1], Yukiharu Iwamoto[1] , Shinfuku Nomura[1]

[1]Graduate School of Science and Engineering, Ehime University,

3 Bunkyo-cho, Matsuyama, Ehime 790-8577, Japan

ABSTRACT

Diamond crystals are successfully synthesized by irradiating DC arc plasma jet to the substrate set in a methanol solution. It is the important procedure to preheat the substrate by inert Ar plasma jet before introducing the methanol solution gas to the plasma jet gun. The effects of two experimental conditions, the incident power and the substrates, are investigated. In the case of the Si substrate, cubic crystalline diamond grains of same size are synthesized at the plasma power of 470W. High speed hetero epitaxy is expected by using this method. In the case of the tungsten carbide substrate, diamond crystals and carbon nanotubes are simultaneously synthesized at the plasma power of 260W. The catalytic effect of Co binder in the substrate may cause the chemical reaction of the nanotube synthesis.

1. Introduction

Diamond is an allotrope of C with three-dimensional bonds, has not only excellent mechanical properties such as high hardness, high Young's modulus, abrasion resistance but also very high heat conductivity, high acid resistance, and chemically inactive at room temperature.

A pure diamond is an insulator, it has semiconductor properties, if trivalent impurities such as boron and aluminum are doped in it. Because of these properties, diamond is very useful for industrial application. Nowadays, it is used in wide field, not only for tools such as dies, cutting tools, drills, but also abrasives, files, heat sinks. Diamond is expected to be used for semiconductor. Diamond artificial synthesis has been researched in the world, because generally natural diamond is very expensive, causing high costs. The most common method for diamond synthesis is gas phase plasma chemical vapor deposition (PCVD) [1-3]. In this method, compound gases are decomposed by plasma, and diamond crystals grow on a substrate surface.

As a plasma excitation source, various methods have been used such as hot filament [4], microwave [5], high frequency electrical source [6], DC glow discharge [7], DC arc discharge [8], and combustion method [9]. However, gas phase CVD has a disadvantage, that is manufacturing cost is high, because its diamond film synthesis rate is slow, not suitable for mass production. Also, a substrate or a deposition target may be broken because they are exposed very high temperature of plasma. So, it is difficult to make diamond film on a "heat sensitive materials". Diamond synthesis at low temperature has been also researched [10,11], has not been put into practical use yet. Therefore, this research aims to synthesize a diamond crystal with high speed on the substrate of Si and tungsten carbide. A high speed diamond synthesizer needs the high power plasma because the synthesis speed is proportional to the plasma power [12]. The in-liquid plasma CVD process is the best method for increasing the plasma power because of its high cooling ability of the instruments. However, there is a problem that is power adjustment is very difficult because of propagation matching between a microwave electrode and an ingredient liquid. This problem is caused by impedance variation caused by temperature increase of the electrode and surrounding equipment. On the other hands, DC arc jet plasma process is the easiest method for putting high power into the plasma because its electric propagation impedance is fixed. Therefore, both methods of the in-liquid plasma and the DC arc jet are combined and adopted to this research.

2. Experimental Method

The experimental equipment of In-liquid plasma jet CVD method is shown in Fig. 1. A cylindrical positive electrode and a bar type negative electrode are fixed on the same axis, this structure make it easier that changing a head of positive electrode. Cupper is used for the positive electrode, and tungsten is used for the negative electrode. A TIG welding machine (MIGHT INDUSTRY MT-200WA) is used for DC electrical source, and argon gas is used for a working gas. Flow rate of the working gas and current between electrodes are adjusted to generate the arc plasma, and the voltage is measured during the arc plasma generation. The experimental procedure is mentioned below. A substrate is polished with a sand paper (#2000) for 2 minutes, then ultrasonic cleaning is conducted for the substrate with a colloidal liquid whose composition rate is methanol : diamond powder = 5 : 1 in weight ratio. These processes are seeding process to fix diamond seeds on the substrate. Then this substrate is fixed at 1.0 to 1.5 mm form the top of the nozzle.
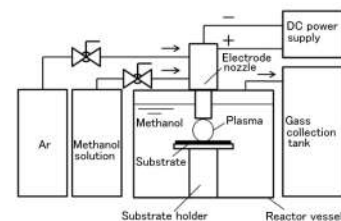
Fig. 1 Experimental equipment of the in-liquid plasma jet CVD method

The Ar gas (5 L/min) plasma jet is generated, and this heats the substrate for 60 s up to optimum temperature for the diamond film synthesis (700 ℃). Then, the ingredient gas is flowed (5 L/min), diamond film synthesis is conducted. Crystalline of the material made on the substrate surface is analyzed by scanning electron microscope (SEM) (JEOL JSM-6060) and Raman microspectroscopic system (RENISHAW inVia Reflex, 150mW, spot size 1.4 μ m , YAG532nm).

3. Results and Discussion

In this experiment, effects of two experimental condition, input power and kind of substrate are investigated. Si and cemented carbide (WC : Co = 5 : 1 weight ratio) is used for the substrates. The experimental conditions are the composition rate of solution is M : E = 97 : 3 in weight ratio, flow rate of Ar gas is 5 L/min, distance between electrodes is 1.5 mm, target substrate temperature is 650 to 750 □. The diamond film synthesis results shown in Fig. 2. Diamond looks crystalline structures are observed at 220 to 260 W of input power. In this power range, crystal precipitation in wide region is only observed at 260 W. The Raman scattering spectrum of the sample obtained with 260W input power condition is shown in Fig. 3. Also, as shown in Fig. 4, in this condition, some materials which has string structures is found, and this may be carbon nanotubes. In Fig. 3 a sharp peak is found at 1332.5 cm^{-1}, proving this is a diamond. Also, G peak and other peaks corresponding to non-diamond carbon is not found, this indicate that crystallinity of this diamond is good. This because the carbon

supersaturation of the cemented carbide is small, is 1.9 $\times$ 10^{-10} (2238K), so carbons do not spread inside the substrate, and shift to diamond crystalline growth in the early stage.

In Fig. 2, diamond like crystals are found but these are found in just local area, a large part of area is covered by amorphous carbon. This may be caused by defects shortage of the substrates surface. The tungsten carbide used in this experiment is very hard Hv1800. It is very difficult to scratch the surface. Therefore, it is considered that defects generation process with sand papers and ultrasonic is not sufficient. Usually, diamond particles enter into the defects by ultrasonic polishing treatment and become seeds of the diamond growth. The tungsten carbide used for this experiment is obtained by sintering crystals of tungsten carbides (WC) with Co binder, and its weight ratio is WC : Co = 5 : 1. Generally, Co is used as a catalyst promoting the generation of non-diamond carbon such as graphite and carbon nano-tube (CNT), and it is known that if the Co concentration is bigger than 10 %, crystallinity of this diamond gets worse. Also, in this experiment, catalytic effect of Co effect disturbs the growth of diamonds.

Actually, CNT like material synthesis is confirmed. In Fig. 4, D-band derived from defects is found at 1350 cm^{-1}, G-band derived from graphite is found at 1580 cm^{-1}, and two 2D-band are found at 2700 cm^{-1}. However, the carbon nano-tube peak whose specific position is 100 cm^{-1} to 300 cm^{-1} (Radial Breathing Mode (RBM)) is not found. From these, it is confirmed that they are fibrous carbon but its diameters are irregular.
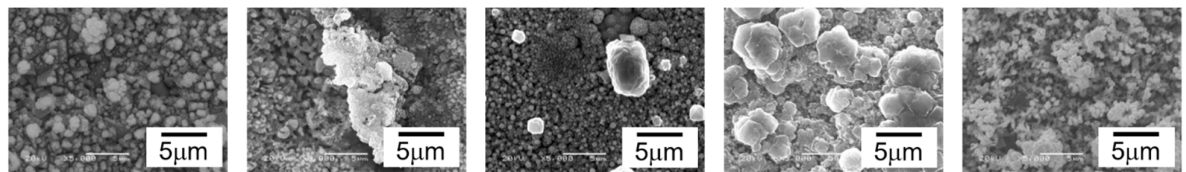
180W (610~730℃)   220W (730~820℃)   245W (750~1072℃)   260W (690~860℃)   360W (770~830℃)

Fig. 2 SEM images of compounds synthesized on cemented carbide substrate with various input power.
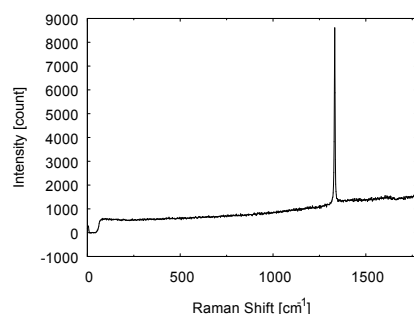
Fig. 3. Raman scattering spectrum of the sample synthesized with 260 W input power.
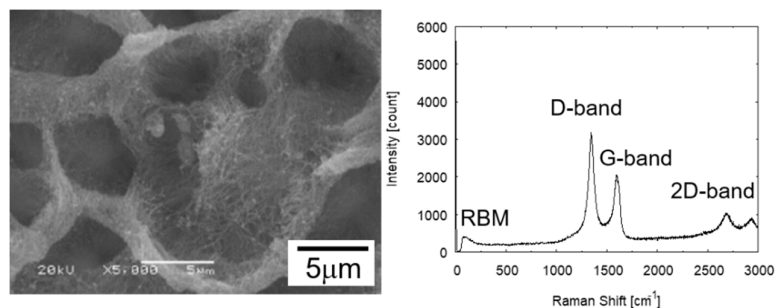
Fig.4. SEM image of CNT found in the sample with 260 W input power, and its Raman scattering spectrum.

To confirm that CNT synthesis is possible, synthesis experiment is conducted with 1mm of distance between electrode and substrate, 190 W of input power, 900 □ of substrate temperature, and no seeding treatment. To remove the oxidized part on the substrate surface, it is polished by sand paper (#220) for 1 minute and then treated by ultrasonic polishing in methanol for 10 minutes. Then the experiment is conducted with same method as explained above. SEM image and Raman scattering spectrum obtained from this sample are shown in Fig. 5. In Fig. 5, D-band derived from defects is found at 1350 cm^{-1}, G-band derived from graphite is found at 1580 cm^{-1}, 2D-band are found at 2700 cm^{-1}, and the carbon nano-tube peak whose specific position is 100 cm^{-1} to 300 cm^{-1} (Radial Breathing Mode (RBM)) is found. This means that CNT synthesis is confirmed.

Then, the experimental results with Si substrate are shown in Fig. 6. 230, 240, 320, 470 W, in all power condition, single crystals with cubic structure are found. Especially, at 320 W, it is synthesized on wide area. Also, when the input power is 230 W, polycrystalline crystals are found as well. At 470 W, wide area of the substrate surface is covered by films composed of cubical diamonds.

On the substrate surface, carbon saturate because the source gas decomposition increase with high input power, promoting the growth of diamond crystal. And usually, diamond coverage increases with core growth over time, and carbons used for that growth. As a result, the supersaturation decreases around the substrate surface, allowing the crystals diameter increase, but here obtained results against it. At 470 W, this because even after the progress of the diamond deposition with the hydrocarbon decomposition, the carbon supersaturation is maintained and this makes an atmosphere which improves continuous generation of second secondary cores. To evaluate the crystals, crystal identification is conducted by Raman spectroscopy. The peak derived from SP3 bond of diamond is found in that observation. From this result, the peaks derived from diamond are found at 1332.5 cm^{-1} in four substrates, this prove these are diamond. At 230, 320 470 W, the peak whose name is G peak is found at 1580 cm^{-1} derived from graphite. And this indicates that graphite exists around the crystals, and overall wide peak indicates existence of amorphous carbon.
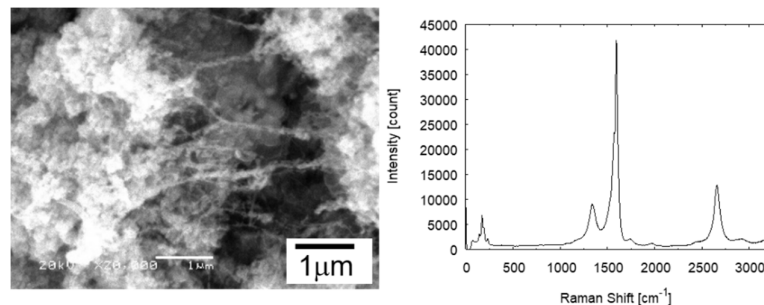
Fig.5 SEM image and Raman scattering spectrum of the sample synthesized at 190W input power.

230W (710~940℃)

240W (680~890℃)

320W (680~750℃)

470W (670~740℃)
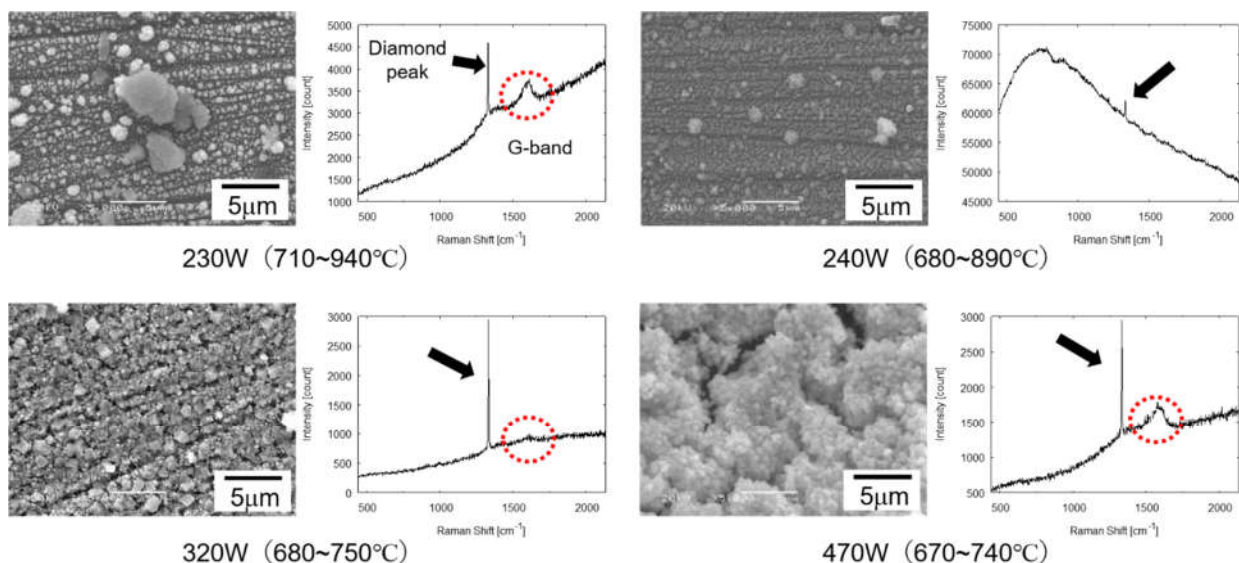
Fig. 6. SEM images and Raman scattering spectra of the samples synthesized on the Si substrate with various input power.

4. Conclusion

In this experiment, the purpose is diamond synthesis on the Si or cemented carbide substrate by in-liquid plasma CVD device utilizing DC arc discharge. The effect of input power has been investigated with various input power. And the effect of kind of substrate material is investigated with Si and cemented carbide. The results mentioned below is obtained.

1. Diamond core synthesis is confirmed at 5 L/min of the Ar gas flow rate, 5 L/min of the source mixture gas flow rate, 650 □ or over of the substrate temperature.

2. In the experiments with Si substrate, the core synthesis are observed, but its crystal growth speed is slow, and it grows in the shape of a cube.

3. Generally, the synthesis amount increases with increase of carbon supersaturation as input power increases, but in here crystals diameter is small, because second core generation is promoted.

4. In the experiment with the cemented carbide substrates, the good crystal is obtained, because the crystal grows at the beginning of the process due to its carbon diffusion coefficient is small. Non-diamond carbon synthesis also improved by catalytic effect of Co.

5. In the experiment with the cemented carbide, the carbon nano-tube (CNT) synthesis is observed, and it is caused by Co catalytic effect.

References

[1] W.G. Eversole, *US Patent*, 3030188, April 1962.

[2] J.M. Larson, M.T. Swihart 1, S.L. Girshick, *Diamond and Related Materials,* 8 (1999) 1863–1874.

[3] J.W. Lindsay, J.M. Larson, S.L. Girshick, *Diamond and Related Materials*, 61(1997)481 485.

[4] S. Matsumoto, Y. Sato, M. Tsutsumi and N. Setaka, *J. Mater. Sci.*, 17 (1982), p. 3106.

[5] M. Kamo, Y. Sato, S. Matsumoto, N. Setaka, *J.Cryst. Growth*, 62(1986)642.

[6] S. Matsumoto, M. Hino and T. Kobayashi, *J. Appl. Phys. Lett.*, 51, p. 737 (1987).

[7] N.V. Samokhvalov a, V.E. Strel'nitskij a, V.A. Below ', V.P. Zubar b, A.G. Timchuk b,.D. Obraztsova ', V.G. Ral'chenko, *Diamond and Related Materials,* 4 (1995) 964-967

[8] K. Kurihara, K. Sasaki, M. Kawarada, N. Koshino, *Appl. Phys. Lett.*, 52(1988)437.

[9] L.M. Hanssen a, W.A. Carrington b, J.E. Butler c, K.A., *Snail a Materials Letters*, 61 (2007) 2847–2850

[10] F. Piazza, J. A. Gonzáles, R. Velázquez, J. D. Jesus, S. A. Rosario, G. Morell, *Diamond Relat. Mater.*, 15, (2006) 109.

[11] F. Silva, A. Gicquel, J. Achard, *Diamond Relat. Mater.*, 9, (2000) 1965.

[12] H. Toyota, S. Nomura, S. Mukasa, Y. Takahashi, S. Okuda, *Diamond Relat. Mater.*, 19, (2010) 1965.

Simultaneous Synthesis of Diamond and Hydrogen

Ryoya Shiraishi[1], Hiromichi Toyota[1], Shinfuku Nomura,[1] Kazuto Nakajima[1], Xia Zhu[1], Yukiharu Iwamoto[1]

[1]Graduate school of Science and Engineering, Ehime University,

3 Bunkyo-cho Matsuyama Ehime 790-8577 Japan

ABSTRACT

A relationship between diamond synthesis and hydrogen production in in-liquid plasma method have been investigated. Approximately 60 % energy can be recovered by collecting hydrogen gas made by ingredient solution decomposition. The relationship is trade-off. When higher energy is used to maintain the substrate temperature, the hydrogen production rate gets faster, but the diamond synthesis rate gets slower. To increase diamond synthesis rate, a method should be established which maintains the substrate temperature by lower energy and generates less hydrogen gas.

Keywords: Diamond, Hydrogen, In-liquid plasma, Chemical vapor deposition

1. Introduction

Diamonds have attractive physical properties such as hardness, heat conductivity, dielectric breakdown voltage. Now, high-performance diamond tools and diamond heat sinks had been already commercialized by utilizing such physical properties. Also, diamond semiconductors are a subject of particular attention. If it is developed, thousands time faster and energy-saving devices will be realized in the future[1,2]. For diamond synthesis, "Chemical vapor deposition" (CVD) method has been put to practical use. In CVD method, an ingredient such as methane is decomposed on the substrate surface, and carbons made by the decomposition are deposit on the surface as diamonds. A particularly attractive method is in-liquid plasma chemical vapor deposition which discharges in ingredient "liquid" such as methanol. Because a liquid has higher molecular density than a gas, its synthesis rate is vastly greater than that of conventional gas phase plasma CVD (about 1000 times faster). Additionally, a cooling device is not needed because liquid has strong cooling effect[3–5]. In this method, liquid methanol is decomposed and gasified, hydrogen gas is generated as a by-product. Hydrogen is also an attractive material as a clean energy, because it does not emit any greenhouse gases such as CO_2. Also, it is a worthy material as an ingredient for various chemicals such as ammonia. Therefore, by collecting the hydrogen gas, it is expected that net energy cost for diamond synthesis can be reduced. Hence, in this research, the hydrogen production rate during a diamond synthesis by in-liquid plasma CVD has been investigated. Also, in this method, because a diamond and hydrogen are made from same ingredient at the same time, so by monitoring hydrogen production rate, diamond production rate may be monitored indirectly. Hence in this research, the relationship between the diamond synthesis rate and the hydrogen production rate is investigated in detail.

2. Method

The schematic image of experimental set up is shown in Fig. 1. A 4 mm diameter tungsten electrode is fixed on the bottom of the reactor vessel and a $28 \times 8 \times 0.5$ mm silicon (100) substrate is fixed at 1.5 mm from the top of the electrode. A 400 mL methanol solution is made based on Bachmann diagram (methanol : ethanol = 97 : 3 volume ratio)[6,7], and it is injected into reactor vessel, immersing the electrode and the substrate completely. The eductor pump is turned on, decompressing the reactor vessel at 40 to 50 kPa. This pressure is maintained during whole duration of diamond synthesis. A 2.45 GHz microwave is irradiated with 130 to 190 W via the waveguide and the cavity resonator, generating a plasma at the tip of the electrode. By this plasma, the solution is decomposed and a part of carbon deposit as a diamond on the substrate surface. The substrate temperature is a very important factor for diamond synthesis. So, upper surface temperature is monitored by an infrared thermometer, and it is maintained at 650 to 700 ℃ by adjusting the input power. The diamond synthesis duration is 30 minutes. The gas generated by the solution decomposition is collected by water replacement, and the time it takes to collect 250 mL of gas is measured. This measurement is conducted 3 times in total at 5, 10, 20 minutes and average gas production rate has been calculated. Also, the gas sample collected at 20 minutes is analyzed by gas chromatograph. After diamond synthesis, remaining solution in the reactor vessel is measured and solution consumption is calculated. The synthesized diamond is observed by scanning electron microscope (SEM), roughness tester, and Raman scattering spectroscopy.
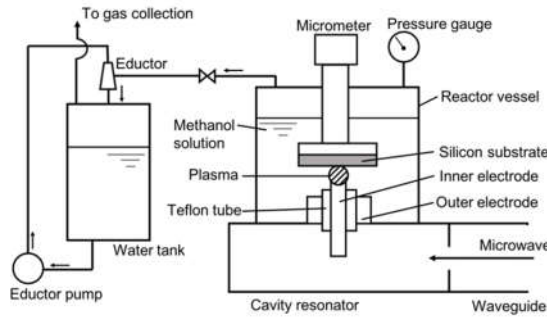
Fig. 1 The schematic image of experimental set up

3. Results and Discussion

Typical observation results of SEM and Raman scattering spectroscopy obtained in this experiment are shown in Fig. 2. A 2 mm diameter sediment with polycrystalline structure is observed in SEM images. In the Raman spectrum of this sediment, sharp peak is observed at 1333 cm^{-1} which is diamond specific peak position, proving this is a diamond. Showing all images of samples are omitted, but it has been confirmed that all samples obtained in this experiment are polycrystalline diamond.
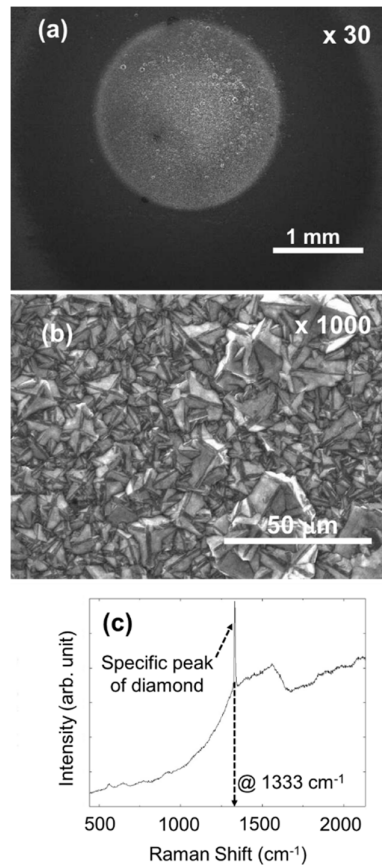
Fig. 2. Typical observation results of the diamond. (a), (b); SEM image, (c); Raman spectrum.

An example of the diamond height profiles obtained by the roughness tester measurement are shown in Fig. 3. The height profiles are measured two ways in each sample toward long side and short side of the substrate. As shown in Fig. 3, each diamond height prolife shows almost symmetrical mountain shape. Hence, a Gaussian function is fitted to the measured profile by nonlinear least square method. The equation of Gaussian function is shown in Eq. (1). In Eq. (1)., C, σ, μ are coefficients and the Gaussian function is fitted by selecting optimum values for each coefficient. As shown in Fig. 3. The Gaussian function fit the measured profile well. Then, to simulate the volume of the diamond, the volume of mountain made by rolling this Gaussian function around "μ" is calculated by piecewise quadrature method. The volume of diamond is determined by taking average of calculation result at long side and short side.
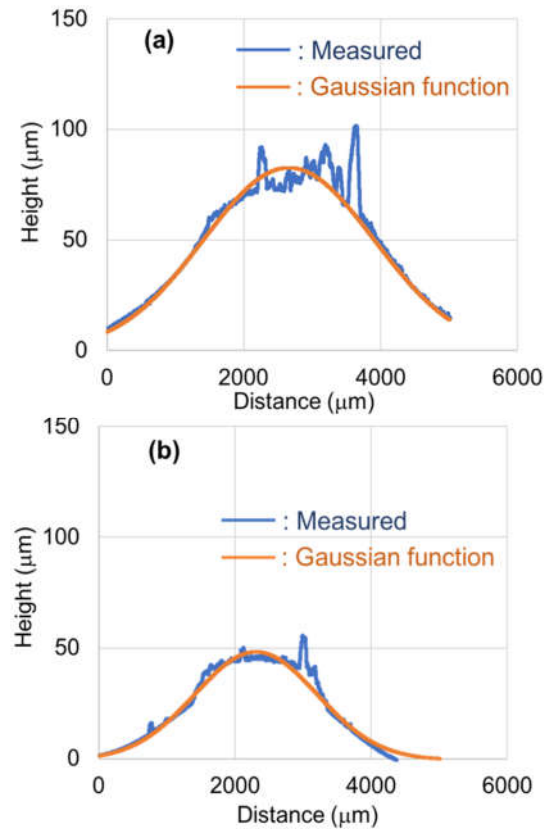
Fig. 3. Height profiles of the diamond. (a); at long side, (b); at short side.

$$f(x) = \frac{C}{\sqrt{2\pi}\sigma} exp\left\{-\frac{(x-\mu)^2}{2\sigma^2}\right\} \tag{1}$$

The gas composition rates analyzed by gas chromatograph are shown in Fig. 4. As shown in Fig. 4.,

the composition rate of each sample is almost same and it is 64 % H_2, 31 % CO, 5 % others such as CO_2, CH_4, C_2H_2.

This composition rates are expected completely by methanol decomposition reaction shown in Eq. (2). Therefore, it is found that no data about diamond synthesis is obtained from gas composition rate.

$$CH_3OH \rightarrow 2H_2 + CO \qquad (2)$$

Next, the relationship between diamond synthesis and hydrogen production is shown in Fig. 5. As shown in Fig. 5(a), the volume of diamonds is 0.15 to 0.30 mm^3 and the hydrogen production rates is 6.4 to 8.7 mL/s. Fig. 5(a) is converted to efficiency of diamond synthesis and hydrogen production as shown Fig. 5(b). The diamond synthesis efficiency is 2.0 to 4.1 mm^3/kWh, and the hydrogen production efficiency is 0.16 to 0.22 Nm^3/kWh. The combustion reaction of hydrogen is shown in Eq. (3) and its combustion heat is 286 kJ/mol.

$$H_2 + 1/2O_2 \rightarrow H_2O \ (\Delta h = -286 \ kJ/mol) \qquad (3)$$
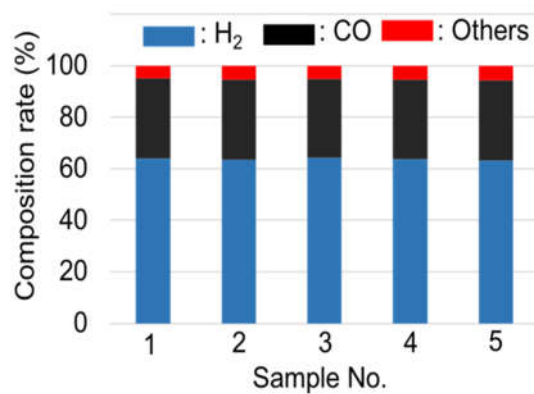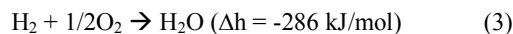
Fig. 4. Gas composition rate for each sample.
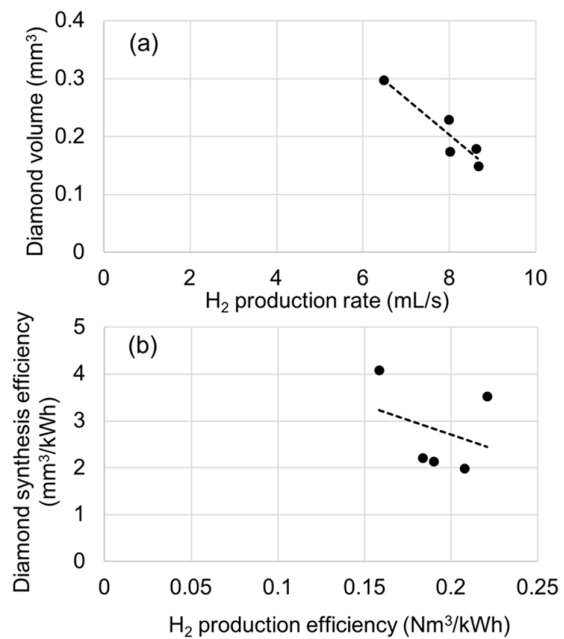
Fig. 5. Relationship between diamond synthesis and hydrogen production
(a); diamond volume versus hydrogen production rate,
(b); diamond synthesis efficiency versus hydrogen production efficiency.

The energy amount obtained by collecting hydrogen is calculated by the heat combustion energy of hydrogen and the hydrogen production rate reported above. The result is 80 to 111 W is recovered, and this value is approximately 60 % of input energy. Note that this input energy is the energy used for emitting microwave, the energy used for driving the eductor pump is not included.

In this experimental system, the relationship between diamond synthesis and hydrogen production is trade-off. As shown in Fig. 5(a), the diamond volume decrease in proportion to hydrogen production rate. As shown In Fig. 5(b), the trade-off relationship is found in efficiencies as well. As reference, in in-liquid plasma method which is optimized for hydrogen production by methanol decomposition, the hydrogen production efficiency is 0.37 Nm^3/kWh[8]. This value is approximately double the value obtained in this experimental condition optimized for diamond synthesis. The prime factor determining "diamond priority" or "hydrogen priority" is the distance between the electrode and the substrate. The distance is 3.5 mm in the Ref. 8, 1.5 mm in this experiment. This because heating the silicon substrates is needed to maintain optimize temperature for diamond synthesis by bringing the electrode closer to the substrate. Namely, because the energy is used for not only methanol decomposition and gasification but also substrate heating, so hydrogen production rate is deteriorated under the condition optimized for diamond synthesis. In this experiment, because the distance is unified to

1.5 mm accurately by using the micrometer, so the results also should be unified. However, the results have variability. Another factor which effects diamond synthesis rate and hydrogen production rate is input power. The input power effect for various elements is shown in Fig. 6. Here, input power is the average value for 30 minutes. As mentioned above, substrate temperature is a very important factor for diamond synthesis, and it is maintained at 650 to 700 ℃ by adjusting input power. So, Fig. 6(a) means that sometimes the temperature maintained by lower input energy, but sometimes it needs higher energy. As shown in Fig. 6(a), (b), the solution consumption and hydrogen production rete are increase in proportion to input power. This means lager amount of the solution is decomposed and gasified. However, in inverse proportion to that, diamond volume decreases. Therefore, when higher energy is needed for maintaining the substrate temperature, it can be expected that the condition is good for hydrogen production rather than diamond synthesis.

Also, methanol consumption in 30 minutes diamond synthesis duration is approximately 300 mL, and this corresponds to 7 mol. 1 mol of methanol has 1mol of carbon, and molecular weight of carbon is 12 g/mol. So, it is calculated that 84 g of carbon has been supplied for diamond synthesis reaction field. However, the volume of diamond obtained in this experiment is approximately 0.2 mm^3, the mass of this diamond is 0.7 mg if the specific gravity of diamond 3.5 g/cm^3. Hence, because ingredient supply is saturated, so no effect will be obtained if increasing methanol decomposition aiming to increase diamond synthesis rete. Preferably, when the diamond is synthesized with lower input power and less solution decomposition, it can be expected that the condition is optimized for diamond synthesis.

The time variation in input power for each sample is shown in Fig. 7. Note that the substrate temperature is maintained constant in this duration. As Shown in Fig. 7., sometimes increasing input power is needed at the latter half of the duration. Although, the cause has not been clarified, the expected cause is that composition of solution is getting different as the time goes on, because of the difference between the boiling point of methanol and ethanol. It is a future task to clarify the cause of the change in input power required to maintain the substrate temperature.
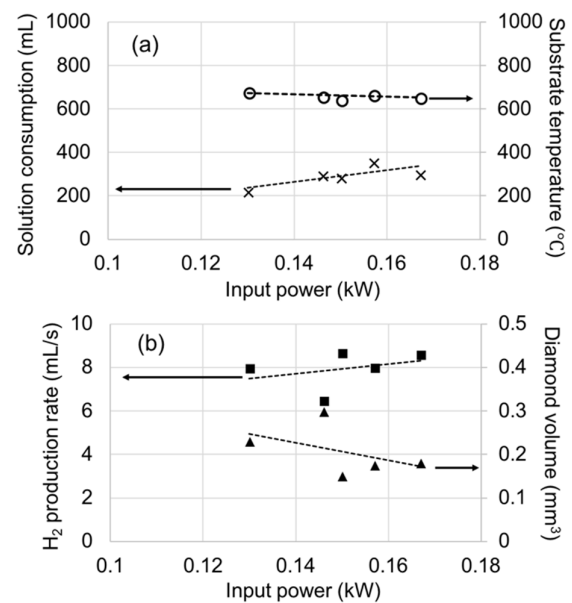
Fig. 6. Input power effect on various elements. (a); on solution consumption and substrate temperature, (b); on hydrogen production rate and diamond volume. The input power is the average value for 30 minutes.
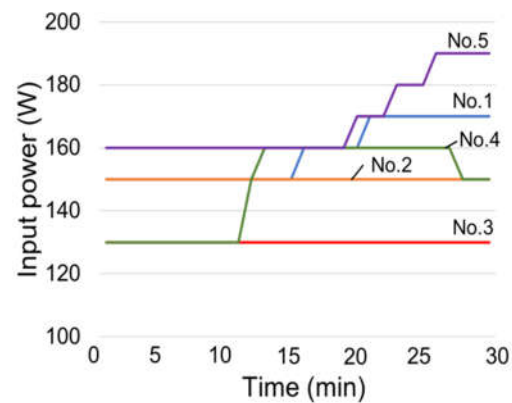
Fig.7 Time variation in input power for each sample

4. Concluding Remarks

To reduce the energy cost of diamond synthesis and establish the method which can monitor diamond synthesis rate, relationship between diamond synthesis rate and hydrogen production rate in in-liquid plasma CVD method have been investigated. Approximately 60 % energy can be recovered by collecting hydrogen gas made by ingredient solution decomposition. The relationship between diamond synthesis and hydrogen production is trade-off. When higher energy is used to maintain the substrate temperature, hydrogen production rate gets faster, but diamond synthesis rate gets slower. To increase diamond synthesis rate, a method should be established which maintain the

substrate temperature by lower energy and generates less hydrogen gas.

References

[1] S. Shikata, Diamond & Related Materials, 65 (2016) 168-175.

[2] C.J.H. Wort, R.S. Balmer, materialstoday 11 (2008) 22-28

[3] S. Nomura, H. Toyota, S. Mukasa, M. Kimura, H Kakimoto, Thermal Science and Engineering, 12 (2004) 49-50

[4] H. Toyota, S. Nomura, Y. Takahashi, S. Mukasa, Diamond & Related Materials, 17 (2008) 1902-4

[5] Y. Takahashi, H. Toyota, S. Nomura, S. Mukasa, T. Inoue, Journal of Applied Physics, 105 (2009) 13-16

[6] P. Bachmann, D. Leers, D. Wiechert, Journal de Physique IV Colloque, 2 (1991) C2-907 - 913

[7] H. Toyota, S. Nomura, S. Mukasa, H. Yamashita, T. Shimo, S. Okuda, Diamond & Related Materials, 20 (2011) 1255-8

[8] R. Shiraishi, S. Nomura, S. Mukasa, R. Nakano, R. Kamatoko, International Journal of Hydrogen Energy, 43 (2018) 4305-10

3D printed AFM fluid cell and its applications on live biological samples

Nguyen Thi Phuong Linh[1], Bernard Haochih Liu[1]

[1]Department of Materials Science and Engineering, National Cheng Kung University, Taiwan

ABSTRACT

Atomic Force Microscopy (AFM) is one member in the Scanning Probe Microscopy family which has powerful applications in various materials, especially in the biological field. For bio-samples, AFM scanning in liquid has been applied especially nowadays to develop the advanced nanoscale analysis. However, conventional liquid scan uses chemical coated glass substrates, which has drawbacks such as the evaporation of the liquid if the specimen needs to be effectively observed for a long period of time. Developments in the fluid cell are being done to overcome such drawback as well as others. The self-designed fluid cell can help researchers to change the solution used in experiments without restarting the calibration of the AFM mode again. In this work, a 3D printed fluid cell was designed, fabricated, and applied on an AFM system to study biological samples. Several designs of the 3D fluid cell were developed using Solidworks and ANSYS software; and it was produced using a commercial 3D printer. This fluid cell has been successfully tested on biological samples by liquid-phase continuous scanning for bacteria such as *Streptococcus mutans* and *Staphylococcus aureus*. According to the ANSYS simulation and AFM experimental results, the 3D printed fluid cell had proved valuable to bio-medical experiments.

Keywords: AFM, 3D printing, fluid cell, liquid-phase scan, *Streptococcus mutans, Staphylococcus aureus*, finite element simulation

PART III, SECTION III

Mechanical Technology
(Heat transfer, Thermal, and Fluid Engineering; Structures and Fluids; Vibration;
Energy Engineering; CAD/CAM/CAE/RP…)

Influence of Forming of Warm Oxide Layer on Hydrophilicity

*A. Takemura[1], K. Yuki[2]

[1]Department of Integrated Science and Technology, National Institute of Technology, Tsuyama College, 624-1, Numa, Tsuyama, Okayama, 708-8509 Japan

*takemura@tsuyama-ct.ac.jp

[2]Department of Mechanical Engineering, Faculty of Engineering, Tokyo University of Science, Yamaguchi, 1-1-1, Daigaku-Dori, Sanyo-Onoda, Yamaguchi, 756-0084 Japan

ABSTRACT

Modern electronic devices often generate excess heat. Heat exchangers with efficient heat-transfer are required for effective device cooling. While, electronic devices are required the downsizing and weight saving. The heat-transfer performance of a heat exchanger is highly dependent on the area of heat-transfer and the thermal conductivity of the metallic material. With the miniaturization of electronic devices, it is important to improve the heat-transfer performance per unit area.

Previous studies have reported the influence of a nanoparticles-assembled biporous layer on heat-transfer in the boiling process[1]. A nanoparticles-assembled biporous layer, which is repared by evaporation deposition, has nanoscale and microscale porous structures, which promote capillary action and improve heat-transfer performance. Nanoparticles-assembled biporous layer is produced by evaporation deposition. When the nanoparticles-assembled biporous layer is produced on the copper alloy of a heat exchanger, the copper alloy is oxidized by the heat of evaporation deposition.

In a previous study, the authors reported that the copper warm oxide layer improved the wettability and hydrophilicity of the surface[2]. The high hydrophilic copper warm oxide layer was found to improve heat-transfer performance[3]. SEM observation results revealed that the surface of copper warm oxidized layer had a nanoscale porous structure. The authors attributed the improvement of wettability and hydrophilicity to capillary action, caused by the nanoparticles-assembled biporous layer.

In this study, we focus on the influence of the heat-transfer properties of hydrophilic copper warm oxidized layers. The copper warm oxide layers were produced under warm conditions, from 200 to 350 °C, to promote oxidation for improved wettability. The results of XRD analysis showed that the copper warm oxidized layers were composed of Cu_2O. The peak of Cu_2O intensity increased with increasing warm oxidation time and temperature. The authors found that the increased Cu_2O intensity peak was related to improved hydrophilicity. The hydrophilic Cu_2O layer reduces the interfacial free energy between the solid and liquid. The authors also discuss the influence of nanoscale porous hydrophilic Cu_2O on hydrophilicity.

REFERENCE

[1] K. Yuki, K. Fukushima, A. Takemura and K. Suzuki; Feasibility study on Performance Enhancement of Copper-based heat Transport Devices by Short-term Oxidation, Transactions of The Japan Institute of Electronics Packing, Vol.8, 1(2015), p68-73.

[2] A. Takemura, K. Yuki and A. Sadayuki: "Influence of Warm Oxide Layer on Wettability and Contact Angle for Heat Transport Devices", Journal of Mechanics Engineering and Automation Volume 7, Number 7, 2017 of JMEA, p341-347.

[3] Pierre-Gilles de Gennes, Francoise Brochard-Wyart, David Quere. Capillarity and Wetting Phenomena: Drops, Bubbles, Pearls, Waves. Springer-Verlag New York, p17-27.

Impact of Ar/He Purge Gas Flow, Heater and Post-Chamber Length and Draw Speed on Rapid Drawing and Cooling of Silica Glass Fiber in Optical Fiber Draw Furnace

Gia Ginelle Carandang[1], Kyoungjin Kim[1]
[1]Kumoh National Institute of Technology
61 Daehak-ro, Gumi, Gyeongbuk, 39177, Korea

ABSTRACT

Glass fiber drawing process inside draw furnace for optical fiber mass manufacturing system is generally divided into two parts: preform heating and post-chamber cooling zones. A 1D axial momentum balance is employed for prediction of heated preform neck-down shape and 2D thermo-fluid analysis for radiative preform heating and post-chamber convective cooling of glass fiber. The effects of flow rates and helium contents in purge gas and drawing speeds as well as the heater and post-chamber lengths are numerically studied to achieve rapid drawing and cooling of silica glass fibers.

1. Introduction

A typical optical fiber used in telecommunication applications is created from a high-purity silica glass of varying preform sizes (5~15cm) [1] which is drawn into very thin glass fiber of 125 μm diameter. The drawing process begins from a high purity silica glass preform that is fed into the furnace with a very high temperature shown in Fig. 1. The softening and dramatic change of silica preform or neck-down shape occurs due to intensive heating of the furnace which creates the preform tip for thin glass fiber. Glass fiber drawing system enables to continuously pull the heated preform tip from the furnace to extend into a thin glass fiber by means of draw tension. The drawn thin glass out from the preform heating is cooled in the post-chamber zone with supplying of helium/argon gas mixture, adjusting draw speed and as it goes out to the post-chamber zone. It is ideal to have proper cooling of the drawn thin glass fiber inside the furnace to ensure removal of impurities and defects as well as a higher speed drawing for faster production.

Over the years, researchers are in continuous progress for the development of optical fibers mass manufacturing. Researchers such as Paek and Runk [2] investigated on the behavior of the neck-down profile during furnace region. Lee and Jaluria [3] and Wei et al. [4] used two-dimensional computation for thermal transport processes. Many more significant research works up to date regarding optimization and fluid models of drawing optical fibers [5-9].

In this computational study, both heating and cooling process inside draw furnace are considered. The main objective is to show how optical glass fiber furnace in terms of purge gas flow, heater and post-chamber length and draw speed can be used to achieve rapid drawing and cooling of silica glass fiber inside draw furnace.

2. Computational Model

The computational model starts from feeding purity silica glass from the furnace until the end of the furnace muffle tube. The feeding speed of the preform is set to be $v = V_p$ and radius of $R = R_p$ at the inlet. The heating zone comprises of the insulation and graphite heating while the post-chamber zone is represented after the insulation until the glass fiber out of the furnace. At the exit, $v = V_f$ as the glass fiber drawing speed and $R = R_f$ for glass fiber radius. The silica glass preform is drawn by a proper amount of draw tension and drawing speed as shown in Fig. 2.

Fig. 1 Glass fiber vertical drawing system setup.
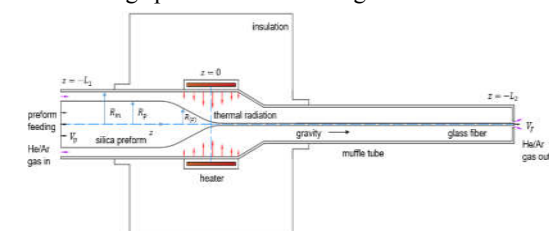
Fig. 2 Schematics of draw furnace for glass fiber drawing.

The heating zone under intensive radiative heating forms the silica glass preform neck-down shape. The neck-down shape is due to drastic change of silica viscosity which is exponential function of temperature. From experimental silica viscosity correlation [6]:

$$\mu = 0.1 \exp(-14.368 + 61939.54/T) \qquad ((18)$$

And using 1D approximation for force balances [2],

$$\frac{dv}{dz} = \frac{3}{\rho}\frac{d}{dz}\left(3\frac{\mu(T)}{v}\frac{dv}{dz}\right) + \frac{g}{v} \qquad ((19)$$

where ρ, μ, v and g are mass density and viscosity of silica, axial velocity of preform and gravitational constant in axial direction (z). Conservation of mass for steady-state process must be satisfied:

$$Q = \pi R^2 v = \pi R_p^2 V_p = \pi R_f^2 V_f \qquad ((20)$$

At neck-down melted tip, the thin glass fiber is pulled from the heated silica preform. The glass fiber while drawing is cooled through convection below the muffle tube until travels out of the furnace [10,11]. The radiative heating inside the furnace is modeled using S2S radiation assuming all surfaces are gray and diffuse between the furnace and participating glass. The surface emissivity of the preform and glass fiber is assumed to be constant at 0.885. The pressure, temperature and flow fields are solved using pressure-implicit with splitting of operators (PISO) algorithm suitable for staggered grid system.

A 2D axisymmetric thermo-fluid with predicted neck-down shape and glass fiber is used along with 1D computation using iterative computational scheme. The temperature calculated from 2D computation is supplied from the 1D computation for updated neck-down. The substitution is repeated until reaching a certain criteria.

The draw tension acting on glass fiber can be calculated [5].

$$F_T(z) = 3\pi\mu R^2 \frac{dv}{dz} - \pi\rho g \int_{-L_1}^{L_2}\left(R^2 v\frac{dv}{dz} - gR^2\right)dz \qquad ((21)$$

The inert gases of He and Ar are modelled using ideal gas law. The thermal conductivity and viscosity are calculated based on gas mixture using semi-empirical formula of Wilke [12].

$$k_{mix} = \sum_{i=1}^{n}\frac{x_i k_i}{\sum_{j=1}^{n} x_j \Phi_{ij}} \qquad ((22)$$

$$\mu_{mix} = \sum_{i=1}^{n}\frac{x_i \mu_i}{\sum_{j=1}^{n} x_j \Phi_{ij}} \qquad ((23)$$

$$\Phi_{ij} = \frac{1}{\sqrt{8}}\left(1 + \frac{M_i}{M_j}\right)^{-\frac{1}{2}}\left[1 + \left(\frac{\mu_i}{\mu_j}\right)^{\frac{1}{2}}\left(\frac{M_j}{M_i}\right)^{\frac{1}{4}}\right]^2 \qquad ((24)$$

where k_{mix} and μ_{mix} are the thermal conductivity and viscosity of the mixture respectively, n is the number of chemical species in the mixture, i and j are the two different species, μ is the viscosity, M is the molar weights, and Φ is the dimensionless correlation.

3. Results and Discussion

The proposed furnace geometry model is simulated using axisymmetric condition in cylindrical coordinate. The graphite heater is fixed at 2450K and length of 0.2m covered with insulation and an extended muffle tube 3m in length for cooling. The assumption of laminar flow is applied due to the high viscosity of glass because of intensive heating inside the furnace. The center of heating region is set to be at z=0 and fiber is cooled while travelling to muffle tube exit. The gases used to aid cooling are helium and argon with same volume ratio neglecting diffusion due to very small temperature difference of the purge gases. Meanwhile, the silica glass preform neck-down shape is found from the iteration between the 1D and 2D computations validated by experimental results shown in Fig. 3b [9]. Fig. 3a shows the contours of static temperature between case of industry drawing speed of 30 m/s and a higher speed of 50 m/s.

(a)

(b)
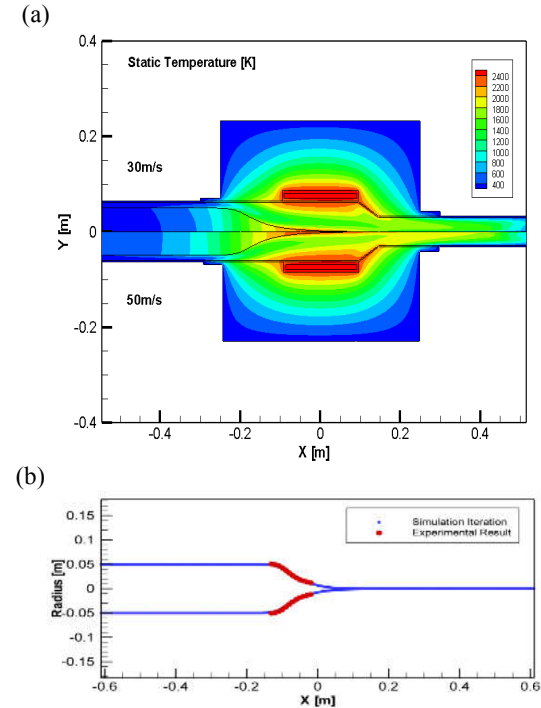
Fig. 3 a) Contour of Static Temperature b) Simulation vs Experimental.

Furthermore, different cases of controlling gas flow rates (LPM), heater and post-chamber length and draw speed are analyzed. Industry-used draw tension of 100g is maintained as a reference considering high draw tension will cause breakage and very low will cause defects. The effects of gas flow rates on both draw

tension (Ft) and cooling exit (Tend) are shown on Fig. 4a and 4b.

(a)
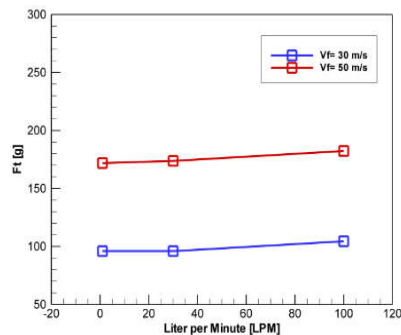
(b)
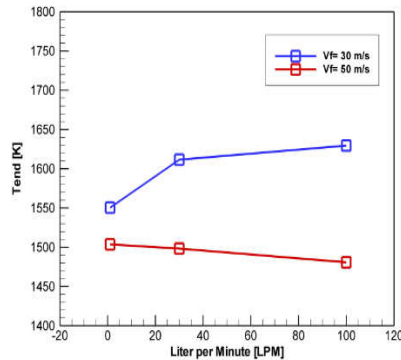
Fig. 4 a) Draw tension b) Temperature at exit for 30 m/s and 50 m/s drawing speed and varying gas flow rates.
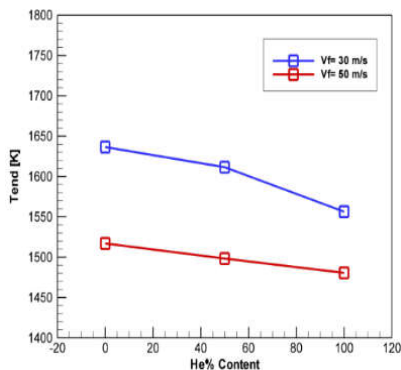
Fig. 5 Fiber temperature at cooling exit with the use of different He contents in gas mixture.

The effects of gas flow rates show little significance on draw tension on both cases of 30 m/s and 50 m/s. A lower value of gas flow rate is much desired for conservation of gases during production. It is also important to monitor the fiber exit temperature and the use of He and Ar gas to achieve a much faster drawing

and efficiency. Fig. 5 shows how the He and Ar gases volume ratios affect cooling exit temperature. The cooling exit temperature decreases as He is added but the main use of the inert gases are just to prevent oxidation and defects of optical fiber glass [10].

The results show that an increase in gas flow rate and varying He/Ar volume ratio percentage contributes less on both draw tension and fiber exit cooling but very significant for fine tuning of draw tension and cooling exit temperature. It can be seen that the draw tension and fiber exit cooling are greatly affected by draw speed. It is found that a higher drawing speed can give a lower cooling end value for the given geometry. However, higher drawing speed results to higher draw tension. Increasing heater temperature can be used to maintain a lower value of draw tension as shown in Fig 6a. The draw tension decreases with increase of furnace temperature due to the exponential function of glass viscosity on temperature. A higher drawing speed can be valid for a higher temperature of the heater and/or increasing the furnace length. It is to consider that very high heater temperature can decrease the life span of the heater. The advantage of using a longer heating zone instead of increasing heater temperature is that the glass viscosity for longer heating zone changes more gradually than increasing heater temperature [5].

(a)
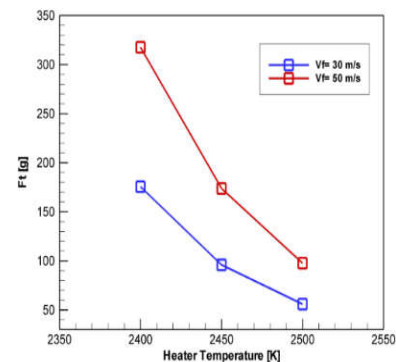
(b)
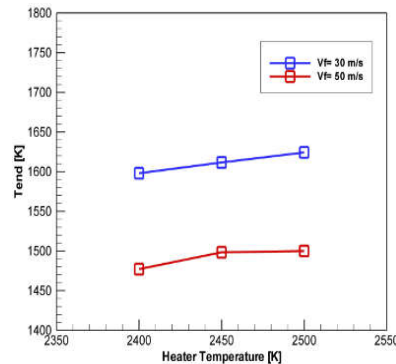
Fig. 6 a) Draw tension b) Temperature at exit for 30 m/s and 50 m/s drawing speed and varying heater temperature.

Fig. 6b shows the desired lower value of fiber exit temperature for high-speed drawing. In this case, post-chamber length for cooling is taken into investigation for better cooling which is shown on Fig. 7. As Reynolds number and post-chamber length increases the advection becomes stronger than air convection giving a lower end value [6]. It shows that using high speed drawing produces a boundary layer of air near the end which requires a longer post-chamber.
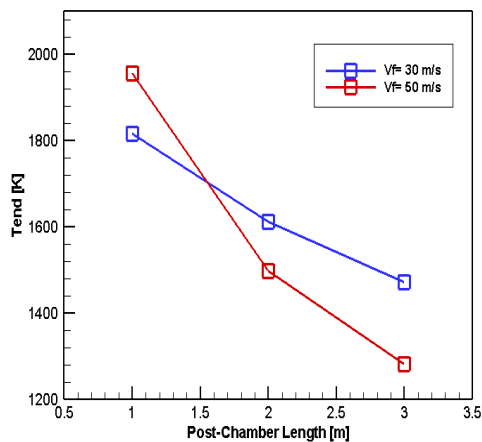
Fig. 7 Effect of post-chamber length on cooling exit temperature of glass fiber.

4. Concluding Remarks

The glass fiber drawing process inside draw furnace is numerically modeled using iterative computational scheme between 1D force balances and 2D thermo-fluid analysis. 1D steady-state force balance is used to model silica elongation while 2D thermo-fluid analysis is used for radiative heating and convective cooling of the silica preform. The silica preform neck-down profile, He/Ar purge gas flow, draw tension and drawing speed are numerically studied.

It is investigated that the effects of increase in gas flow rates and adding He content on gas mixture contribute less for cooling because of the inert properties of the gases. A high speed drawing for better cooling is expected with longer post-chamber length. Additionally, as the draw speed increases draw tension also increases. A higher heater temperature or longer heater length can significantly use to decrease the draw tension value. However, high draw tension causes breakage of the thin glass while very low causes defects and instabilities which requires appropriate tuning. It is recommended that for high speed drawing to use a higher heater

temperature and/or a longer heater length to compensate for low draw tension due to high speed drawing while rapid cooling can be achieved by using higher draw speed with a longer post-chamber length.

References

[1] Y. Kim, J. Choi, H.S. Kwak, K. Kim, Numerical modeling and analysis of glass fiber drawing process from large sized silica preform, *J. Therm. Sci. Tech.* (2017), pp.JTST0030-1-14.

[2] U.C. Paek, R.B. Runk, Physical behavior of the neck-down region during furnace drawing of silica fibers, *J. Appl. Phys.*, (1978), pp. 4417-4422.

[3] S.H.-K Lee, Y. Jaluria, Simulation of the transport processes in the neck-down region of a furnace drawn optical fiber, *Int. J. Heat Mass Transfer*, (1977), pp. 843-856.

[4] Z. Wei, K.-M. Lee, S.W. Tchikanda, Z. Zhou, S.-P., Free surface flow in high speed fiber drawing with large diameter glass preforms, *J. Heat Transfer*, (2004), pp. 713-722.

[5] X. Cheng, Y. Jaluria, Optimization of a thermal manufacturing process: drawing of optical fibers, *Int. J. Heat Mass Transfer*, (2005), pp. 3560-3573.

[6] K.-M. Lee, Z. Wei, Z. Zhou, S.-P. Hong, Computational thermal fluid models for design of a modern fiber draw process, *IEEE Trans. Autom. Sci. Eng.*, (2006), pp. 108-118.

[7] Z. Yin, Y. Jaluria, Thermal transport and flow in high-speed optical fiber drawing, *ASME J. Heat Transfer* (1998), pp. 916-930.

[8] Z. Wei, K.-M. Lee, Computational model for predicting the location of glass solidification in optic fiber drawing, *ASME J. Heat Transfer* (2004), pp. 921-927.

[9] H.S. Kwak, D. Kim, K. Kim, High-speed glass fiber drawing from heated and softened silica preform in an optical fiber draw furnace, *Adv. Sci. Lett.* (2012), pp. 439-444

[10] H. Reeve, A. Mescher, A. Emery, Investigation of convective heating in a polymer fiber drawing process, *Polym. Compos.* (2003), pp. 211-290.

[11] K. Kim, H.S. Kwak, D. Kim, The role of helium/argon gas flow in a glass fiber drawing furnace, *Comp. Therm. Sci.*, (2012), pp. 263-270.

[12] R.B. Bird, W.E. Stewart, E.N. Lightfoot, *Transport Phenomena*, 2nd ed., New York: Wiley, 2001.

CFD Study on the Cold Flow Model of Dual Fluidized Bed System Applied for Biomass Gasification

Cong-Binh Dinh[1], Shu-San Hsiau[1], Meng-Yuan Tsai[1], Chien-Yuan Su[2]

[1] Department of Mechanical Engineering, National Central University, Taiwan

[2] Biothermal Department, Industrial Technology Research Institute, Taiwan

ABSTRACT

The present work studies the hydrodynamics of the gas-solid flow occurring in a two-dimensional dual fluidized bed gasification system by using the computational fluid dynamics (CFD) software ANSYS FLUENT. A combination of the Eulerian multiphase flow model and the kinetic theory of granular flow was applied to perform the unsteady flow behaviors of the fluidizing gas (air) and bed material (silica sand) during the entire process. The air inlet velocity and initial sand bed heights were found to significantly affect the distributions of sand volume fraction, mixture static pressure, and sand circulation rate throughout the system.

Keywords: dual fluidized bed, computational fluid dynamics, multiphase flow model, kinetic theory of granular flow, unsteady flow behaviors

Numerical Simulation of the Heat and Mass Transfer During Czochralski Silicon Crystal Growth under the Application of Crystal-crucible Iso-rotation

Thi Hoai Thu Nguyen[1], Jyh Chen Chen[1,*], Chieh Hu[1], Chun Hung Chen[2]

[1] Department of Mechanical Engineering, National Central University, Taiwan;

[2] Research and Development Division, GlobalWafers Co., Ltd., Taiwan;

ABSTRACT

Quasi-steady numerical simulations have been done to investigate the effects of using crystal-crucible iso-rotation on heat and mass transfer during Czochralski growth of an 8-inch diameter silicon crystal. When the crystal is iso-rotated faster than crucible, the lower concentration and more uniform radial distribution of oxygen impurity can be obtained as compared to the crystal-crucible counter rotation. Moreover, the flatter defect transition and lower content of point defects affecting the quality of silicon wafer are also shown.

Keywords: Computer simulation; Convection; Diffusion; Czochralski method; Single crystal growth

Experimental Study of Square Inlets Effect on the Performances of Gas–Liquid Cylindrical Cyclone Separators (GLCC)

Ho Minh Kha[1,2]; Nguyen Thanh Nam[2]; Vo Tuyen[3]; Nguyen Tan Ken[3]

[1] Ho Chi Minh City University of Technology and Education (HCMUTE), Vietnam
(e-mail: 1424003@student.hcmute.edu.vn)
[2] DCSELAB- Ho Chi Minh City University of Technology, VNU-HCM, Vietnam
[3] Ho Chi Minh City University of Food Industry (HUFI), Vietnam

ABSTRACT

In the gas-oil field, the gas-liquid cylindrical cyclone (GLCC) separator has potential replaced the traditional separator that is used over the century. It is also interesting for petroleum companies in recent years because of the effect of the oil world price. However, the behavior of phases in the equipment is very rapid, complex and unsteady which may cause the difficulty of enhancing the performance of the separation phases. The much research demonstrates that the geometry and the number of the inlet is probably the most important factor that impacts directly to the performance of separation of phases of the device. The main goal of the research paper is to deeply understand the effect of different geometrical configurations of the square inlet on hydrodynamics and performances for two phases flow (air-water). Two different inlet configurations are constructed, namely: One square inlet with the gradually reduced nozzle and two symmetric square inlets with the gradually reduced nozzle. As a result, we propose the use of two symmetric square inlets to enhance the separator efficiency because of their benefits. Besides, this study can be viewed as a padding step to optimizing the operative parameters of GLCC in the further study.

Keywords: Gas-liquid cylindrical cyclone separator; GLCC; cyclone separator; multiphase flow.

1. Introduction
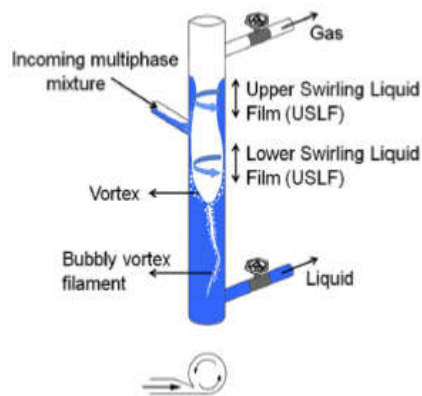
Figure 1. The Gas-Liquid Cylindrical Cyclone separator

The GLCC (Figure 1) consists of a vertical pipe with a tangential inclined inlet and outlets for gas and liquid. The tangential flow from the inlet to the body of the GLCC creates a swirl that produces centrifugal and buoyancy forces on the fluids that are an order of magnitude higher than the force of gravity. The combination of gravitational, centrifugal, and buoyancy forces separates the gas and liquid. The liquid is pushed radially outward and downward toward the liquid exit, while the gas is driven inward and upward toward the gas outlet. The low-cost, low-weight, compact GLCC separator offers an attractive alternative to the conventional separator which has been popularly used for

this task, are large in size, bulky, and costly in purchasing and operating [1, 2, 3].

The operational envelope of a GLCC is defined by two limiting phenomena: Liquid carry-over (LCO) in the gas stream and gas carry-under (GCU) in the liquid stream. The onset of liquid carry-over is identified by the first trace of liquid in the gas stream. Similarly, the first observable bubbles in the liquid underflow mark the onset of gas carry-under. The difficulty in developing accurate performance predictions arises largely from the variety of complex flow patterns that can occur in the GLCC. The flow patterns above the inlet can include bubble, slug, churn, mist, and liquid ribbon. Below the inlet, the flow generally consists of a liquid vortex with a gas-core filament. Although, they have potential applications, complex phenomenon affecting the separating efficiency have not been studied completely in the past [1, 2, 4, 5, 6]

This difficulty in predicting accurate the performance of the GLCC has been the single largest obstruction to the wide use of the GLCC. Even without tried and tested performance predictions, several successful applications of GLCC's have been reported [3]. The development of reliable performance-prediction tools will improve GLCC's through hardware modifications and, ultimately, will govern the speed and extent to which GLCC technology is deployed in existing and new field applications. Recent laboratory observations and computer simulations indicate that hardware modifications to the GLCC can have a profound effect on GLCC performance [2]. The GLCC performance is dependent upon the tangential velocities of the swirling

fluids, especially that of the liquid. The inlet is the single most redesigned component of the GLCC because of the inlet's influence on tangential velocity [1, 2]. Kouba and Shoham (1996) [1] observed experimentally that the optimal inclined inlet angle is 27° which allowed to retard significantly the onset of liquid carry-over (LCO) in comparison with the horizontal inlet.

Most of the previous studies of GLCC separator were limited with the one inlet model [7, 8, 9, 10]. Movafaghian et al [11] researched the effects of geometry, fluid properties and pressure on the hydrodynamics of GLCC with one and two inlets. But the two inlets is the same of the side. Erdal et al [12] studied two symmetric circular inlet models but the authors only analyzed with a liquid phase.

Recent studies propose the use of multiple tangential inlets to improve separation efficiency in GLCC. Such inlet configuration leads to lower swirl intensity decay than the unique inlet configuration. It also engenders a more axisymmetric flow, which would improve the GLCC performance with respect to LCO [12, 13, 14, 15]. Thus far, over the past 22 years, more than 6500 GLCCs have been installed around the world by the petroleum and related industries [16]. However, the research has not been conducted on two symmetric inlet types to compare the effect of one type of inlet with the same angle of inclination and the area of the nozzle when it uses to separator multiphase.

2. Experimental program
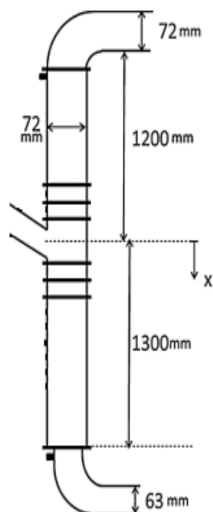
***Figure 2**. Main dimensions of the GLCC*

The GLCC' geometry is modeled size parameters along with experimental models of Hreiz. R et al [13, 14] (Figure 2). According to the diameter size of the pipe available on the market, in this investigation, two different inlet configurations (Figure 3) are constructed with the same inclined inlet is 27° and the cross-sectional area of the inlet was approximately 28% compared to the cross-sectional area of GLCC. The two-phase mixture is introduced into the GLCC through a Y junction and the static mixer (Figure 4). The schematics of the GLCC test section shows in Figure 5. The experimental facility meets the following requirements:

➢ Two-phases (air-liquid), full separator.
➢ Easy and quick change of different inlet configurations.
➢ The GLCC body is transparent to allow visualizations and is manufactured in Acrylic
➢ The inlets are manufactured by stainless steel
➢ One phase, 1 HP centrifugal pump, capable of producing 5-266 L/min (at the max head of 22 m).
➢ One phase, 3 HP Ring Blower, capable of producing 325 m^3/h (at the max head of 36 KPa).
➢ Two rotameters (1.6-16 m^3/h) and flow rate measurement tree to measure flow rates for different inlet configurations.
➢ One measures air flow
➢ A 120-liter storage tank
➢ Two static mixers

| Type 1: One square inlet (38 x 38 mm) with the gradually reduced nozzle (38 x 30 mm) | Type 2: Two symmetric square inlets (38 x 38 mm) with the gradually reduced nozzle (38 x 15 mm) of each |
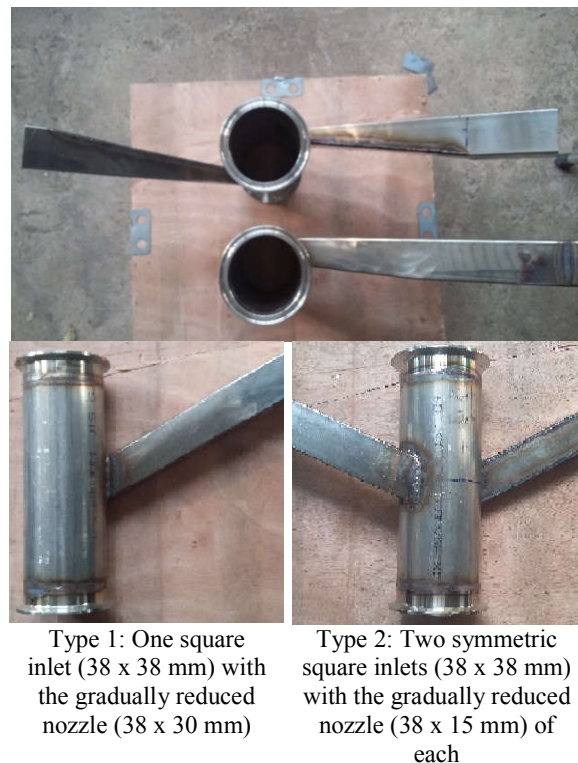
***Figure 3**. The different inlet configurations*
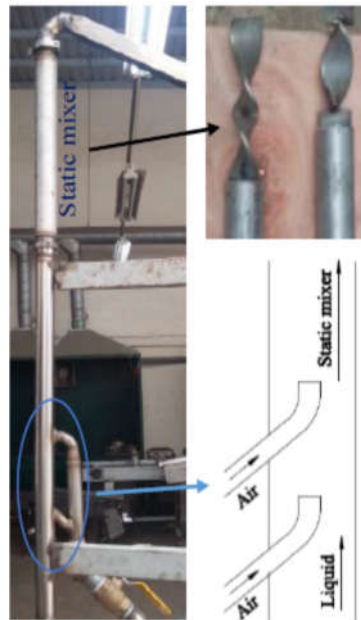
Figure 4. The Y junction and static mixer
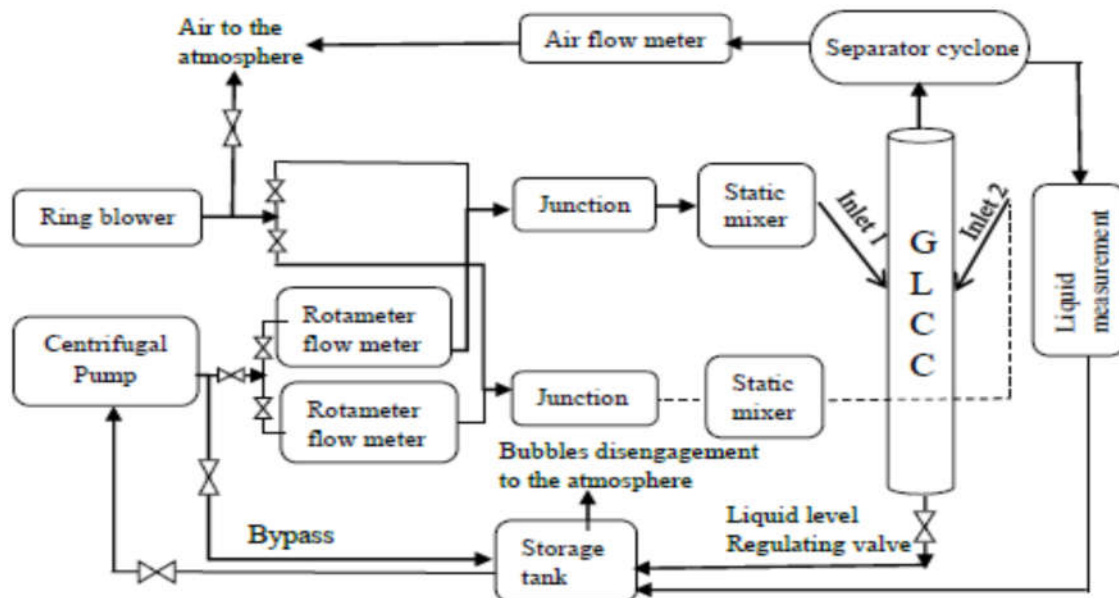
Figure 5. Schematics of the GLCC test section

3. Results

3.1 The flow hydrodynamics in the GLCC

In the GLCC upper part, liquid droplets are pushed toward the walls by centrifugal force and combine into a liquid layer. As this liquid layer is compact compared to discrete droplets, the gas flow will have more difficulties to take it up to the top outlet. The liquid from the wall layer falls down by gravity into the liquid vortex thereafter. However, if the gas flow rate is increased beyond a certain threshold, the liquid is carried over with the gas stream in the GLCC upper outlet. This limiting phenomenon is called Liquid Carry-Over (LCO) [14].

The LCO in the gas stream is largely dependent on the flow pattern in the upper part of the GLCC. Flooding may occur in the GLCC at high liquid levels and low gas rates, producing bubbly flow. The unsteady liquid fluctuations, characteristic of churn flow at moderate gas rates, may jump liquid into the gas outlet. The liquid can also be carried out in droplets at the onset of annular mist flow at high gas rates. At very high gas rates, the centrifugal force of the swirling gas pushes the liquid to the wall of

the pipe, where it may form an upward-spiraling continuous ribbon of liquid [1, 2, 17].

In our study, the GLCC is operated under conditions of LCO. When the superficial gas velocity in the cylindrical (Vsg) decreases from about 12.5 m/s to about 1 m/s and simultaneously, the superficial liquid velocity (Vsl) in the cylindrical increases from 0.1 m/s to 0.62 m/s. The upper flow component of the GLCC also transitions from the annular flow to the flow churn (Figure 6) as the one inlet is used. However, when using the two-inlet type, the velocity value of Vsg and Vsl inside the cylindrical will be higher than the one inlet of the operational envelope of LCO. Effect of inlet geometry on the operational envelope for liquid carry-over (LCO) threshold are presented below.

Annular flow [18] is a flow regime of two-phase gas-liquid flow. It is characterized by the presence of a liquid film flowing on the channel wall and with the gas flowing in the gas core. The flow core can contain entrained liquid droplets. In this case, the region is often referred to as annular-dispersed flow, where the entrained fraction may vary from zero (a pure annular flow) to a value close to unity (a dispersed flow). Often both types of flow, pure annular and annular-dispersed, are known under the general term of annular flow (Figure 6 a).

(a) Annular flow   (b) Churn flow
Figure 6. *Schematics of different LCO flow regimes (Vsl = 0.341 m/s; Vsg = 7.583 m/s)*

The churn flow LCO regime the churning flow (Figure 6 b) is a very chaotic and turbulent regime characterized by unstable vertical oscillations of the flow that can occur for moderate to high liquid flow rates. According to our visual

observations, beyond a certain air flow rate, the USLF (Upper Liquid Swirling Film) is destabilized, mainly because of the air flow that tries to lift it up. Thus, the USLF loses its integrity, which results in a churn flow regime with violent oscillations just above the inlet level. Liquid droplets are ejected from the churn flow region and may splash up to the gas outlet, thereby initiating the

LCO. If the gas flow rate is increased further, more liquid is lifted by the gas, and the churn flow regime invades all the upper part of the GLCC [14, 19].

With two symmetric inlets and when the GLCC is operated in a state of churn flow (Vsg < 4.5 m/s and Vsl > 0.28 m/s). The flow in the upper of the GLCC fluctuates very strongly and continuously changes. It is characterized by the presence of a very thick and unstable liquid film, with the liquid often oscillating up and down in cycles (Figure 7). But, there is a really interesting which is the oscillation around the tube is relatively uniform when using the two inlet type compared to the other inlet. This will affect the performance of the separator.
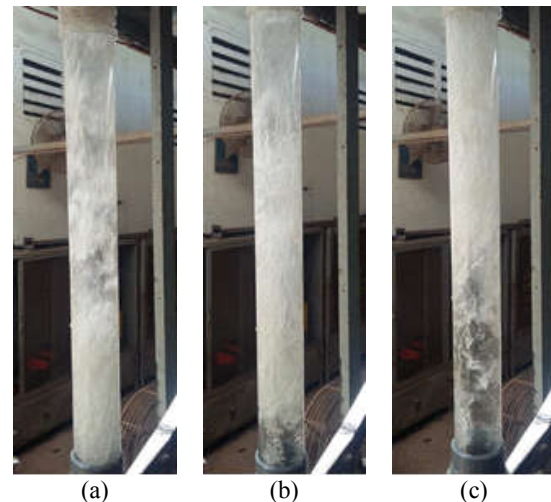
(a)   (b)   (c)
Figure 7. *Fluctuations up and down in cycles of the churn flow LCO regime (Vsl = 0.41 m/s; Vsg = 6.4 m/s)*

In the GLCC lower part, if the swirl intensity is high enough, the free gas-liquid interface gets carved out and the vortex can be observed. The liquid flows from the inlet nozzle to the vortex in a thin swirling film (Figure 1), to which we will refer to as Lower Swirling Liquid Film, LSLF. Large bubbles quickly move toward the free interface due to buoyancy. Smaller bubbles, while being dragged downward by the liquid, are pushed radially toward the vortex center. They form a bubbly filament which allows a nice visualization of the vortex core. These bubbles are supposed to rise up to the free interface and to disengage [1, 14].

A variety of experiments has been conducted with the both of the inlets to investigate the different flow patterns in the lower part of the GLCC. The study was restricted to gas-liquid flow rates upper the LCO limit. The top part of the vortex, the crown, was maintained about 100 mm below the inlet nozzle through a valve installed on the GLCC lower outlet (Figure 5). The vortex level was not set closer to the entrance level for two reasons. The first reason is that in field conditions, gas and liquid flow rates fluctuate in time. Thus, the vortex level in the GLCC must be maintained at a certain distance from the inlet, so that the control system has enough time to react in the case of a sudden increase of the liquid flow rate, and

prevents the vortex to exceed the inlet level and to lead to a precocious LCO. The second reason is that when the vortex level is too close to the entrance, we observed that the flow gets disrupted. As noticed by Shoham and Kouba (1998), some distance from the entrance is necessary to achieve an optimal swirl intensity [14].

Based on visual observations, the bubbly filament presents a very complex hydrodynamics. The flow pattern depends mainly on the liquid flow rate and the number of the inlet. An increase in the gas flow rate has little effect on the flow pattern but increases the number of bubbles in the flow. As Vsl increases and Vsg decreases, the flow pattern is characterized by important centrifugal forces and so, the vortex becomes deeply excavated and shows tortuosities. Bubbles tend to be smaller and, as the swirl intensity becomes higher, most of the bubbles concentrate in the filament, and bubble dispersion decreases (Figure 8). The warping of the vortex comes from the use of a unique inlet nozzle, which induces a pronounced asymmetry in the flow. Extremely few bubbles are found outside the region around the bubbly filament and the zone near the vortex interface.

(a) Excavated vortex flow (Vsl=0.273 m/s, Vsg= 10.5 m/s

(b) Excavated vortex flow (Vsl = 0.41 m/s, Vsg = 6.4 m/s

(c) Deeply excavated vortex flow (Vsl = 0.546 m/s, Vsg = 3,1 m/s

Figure 8. *Different vortex regimes in the GLCC lower part (case type 2 is used)*

Figure 9 displays the filament core of a one and two circular inlets. The upward and downward flow region near the cylindrical center line for one inlet has a helical (spiral) shape. But, the upward and downward flow region near the cylindrical center line of two nozzle inlets is a quite axisymmetric flow field. In GLCC's design, this means that there is more space to capture bubbles at the center and uplift them to the gas-liquid interface for the separation.

Type 1   Type 2

Figure 9. *The filament core in the GLCC lower part*

3.2 Liquid carry-over (LCO)

A series of experiments is done at a fixed liquid flow rate. A gas flow rate is chosen, the mixture is introduced into the GLCC, and it is observed whether or not the liquid reaches the upper outlet to determine the start of liquid carry-over (LCO). Figure 10 shows the variations of the operational envelope for liquid carry-over (LCO) threshold with the GLCC inlet configurations, at atmospheric pressure for an air-water system.

Figure 10. *Effect of inlet geometry on the operational envelope for liquid carry-over (LCO) threshold*

Comparison between the liquid carry-over (LCO) operational envelopes for them reveals that the operational envelope of LCO expands significantly for the two symmetric inlets than the operational envelope of LCO for single-inlet. It demonstrates that the performance of the two symmetric inlets better than the performance of single-inlet for conditions approaching

the operational envelope for LCO. In addition, when using this double inlet type is the working range is also significantly increased.
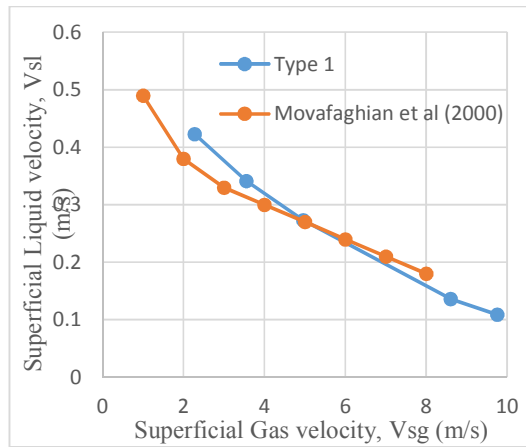
***Figure 11**. Comparison of the operational envelope for liquid carry-over (LCO) threshold*

The present data and the data reported by Movafaghian *et al* (2000) is presented in Figure 11. Note that the present data are for a 72 mm ID GLCC while the data of Movafaghian *et al* (2000) were obtained for a 76.2 mm ID GLCC. Then, this pipe area is gradually reduced by Many experiments were conducted to compare the performance of GLCC, the top part of the vortex, the crown, was maintained about 100 mm below the inlet nozzle. The results show that the effect of structure and number of inlets has a clear impact on the performance of the separator. When using the two symmetric inlets type, the separation efficiency of liquid is higher than the one for the single inlet (Figure 12).

4. CONCLUSIONS

For the GLCC'geometry, the inlet structure is probably the most important parameter because it controls directly the swirl intensity in the flow [14, 16]. In this research, the effect of two different inlets design on the hydrodynamics and the performances of GLCC working in a full gas-water separator configuration was investigated. The following conclusions can be extracted from this study:

The operational envelopes for the liquid carry-over (LCO) of single inlet occur earlier than the one of the two symmetric inlet configuration. Besides, when using this double inlet type is the working range is also significantly increased.

The separation efficiency of the device will be higher when using two symmetric inlets. However, the manufacturing is more difficult and takes up more space than the other. In addition, the two-phase flow balance for the two inlets should also be considered.

Finally, we suggest the application of two symmetric inlets type that is the same angle of inclination and the area of the nozzle with the unique inlet configuration to improve separation efficiency in GLCC. Such inlet structure leads to lower swirl intensity decay than one

placing a plate within the inlet pipe to reduce the inlet area to about 25% of the area of the cylinder (crescent nozzle). The results show that the operational envelope of type 1 is quite similar to Movafaghian *et al* (2000) study. This is consistent with the research results of Shoham and Kouba (1998) that the crescent nozzle performed closest to the rectangular slot with the same cross-sectional area.
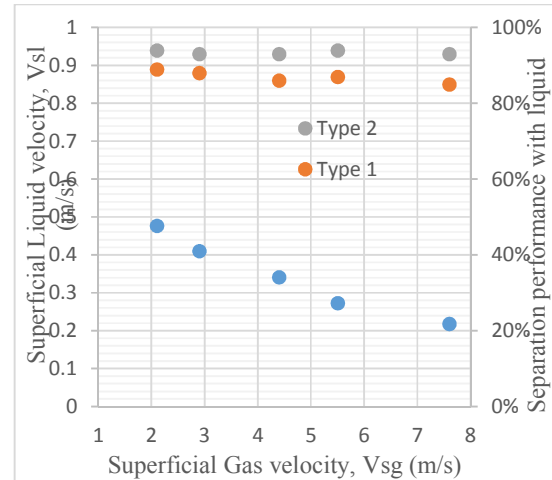
***Figure 12**. Separation performance with liquid*

inlet configuration. Besides, it also creates a more axis symmetric flow at the center line, which would improve the uplift of air bubbles in the performance of GLCC.

Acknowledgements

References

[1] Kouba, G. E. A., and O. Shoham. 1996, "Review of gas-liquid cylindrical cyclone technology," International Conference of Production Separation Systems, Aberdeen, UK.

[2] Shoham, O., Kouba, G.E, "State of the art of gas/liquid cylindrical-cyclonecompact-separator technology," *SPE*, Vol 2-5, pp. 462-471, 1998.

[3] Arpandi, I. *et al,* "Hydrodynamics of Two-Phase Flow in Gas/Liquid Cylindrical-Cyclone Separators," *SPE Journal* (December 1996) 427.

[4] Gomez, L. E., R. S. Mohan, O. Shoham, J. D. Marrelli, and G. E. Kouba. 1999, "State-of-the-art simulator for field applications of gas-liquid cylindrical cyclone separators," *SPE Annual Technical Conference and Exhibition,* Houston, Texas

[5] Erdal, F., and S. Shirazi. 2001, "Local velocity measurements and computational fluid dynamics (CFD) simulations of swirling flow in a gas–liquid cylindrical cyclone separator," *Engineering*

Technology Conference on Energy, Texas, 15:23–30.

[6] Mohan, R. 2013. Internal report. TUSTP.

[7] Hreiz, R., Gentric, C., Midoux, N., 2011, "Numerical investigation of swirling flow in cylindrical cyclones. Chem. Eng. Res. Des. 89, 2521–2539.

[8] Lê Văn Sỹ. 2015, "Nghiên cứu động lực học dòng chảy trong bộ tách lọc dầu/khí glcc," Tuyển tập công trình hội nghị khoa học cơ học thủy khí toàn quốc năm 2015.

[9] Le Van Sy, 2016, "Influence of inlet angle on flow pattern and performance of gas-liquid cylindrical cyclone separator," *Particulate Science And Technology*
http://dx.doi.org/10.1080/02726351.2016.1180336.

[10] S. Kolla, S. Mohan and O. Shoham "Experimental investigation of liquid carry-over in GLCC separators for 3-phase flow" Paper No. IMECE2016-67457, pp. V007T09A006; 10 pages doi:10.1115/IMECE2016-67457.

[11] S. Movafaghian *et al* "The effects of geometry, fluid properties and pressure on the hydrodynamics of gas-liquid cylindrical cyclone separators" *International Journal of Multiphase Flow* 26 (2000) 999-1018.

[12] Erdal, F., Shirazi, S., 2002, "Effect of inlet configuration on flow behavior in a cylindrical cyclone separator," In: *ASME Eng. Technol. Conf. on Energy.*

[13] Hreiz, R. *et al*., 2014, "Hydrodynamics and velocity measurements in gas–liquid swirling flows in cylindrical cyclones," *Chemical engineering research and design*.
http://dx.doi.org/10.1016/j.cherd.2014.02.029

[14] Hreiz, R. *et al*., 2014, "On the effect of the nozzle design on theperformances of gas–liquid cylindrical cyclone separators," *Int.J. Multiphase Flow* 58, pp15–26.

[15] Ho Minh Kha, Nguyen Ngoc Phuong and Nguyen Thanh Nam. "The effect of different geometrical configurations of the performances of Gas-Liquid Cylindrical Cyclone separators (GLCC)." System Science and Engineering (ICSSE), 2017 International Conference on DOI: 10.1109/ICSSE.2017.8030955, pp. 646-651. ISSN: 2325-0925

[16] S. Kolla et al "Structural integrity analysis of gas-liquid cylindrical cyclone (GLCC) separator inlet". Journal of Energy Resources Technology - MAY 2018, Vol. 140. DOI: 10.1115/1.4038622.

[17] http://www.thermopedia.com/content/8/. Kataoka, Isao , Serizawa, Akimi DOI: 10.1615/AtoZ.b.bubble-flow.

[18] http://www.thermopedia.com/content/11/. Zeigarnik, Yuri Albertovich. Doi: 10.1615/AtoZ.a.annular_flow.

[19] http://www.thermopedia.com/content/264/. Jayanti, Sreenivas. Doi: 10.1615/AtoZ.c.churn_flow.

PART III, SECTION IV

Other Topics Related to Machining, Materials and Mechanical Technology
(Mechanics of Solid; Analysis and Simulation; New Machine Tools and Tooling Technology;
Dynamics and Control…)

A Semi – Active Controller for an Aircraft Landing Gear Equipped Magnetorheological Damper

Luong Quoc Viet[1], Jai – Hyuk Hwang [2]

[1] Mechanical Aerospace Engineering, Korean Aerospace University
76, Hanggongdaehang-ro, Deogyang-gu, Goyang-si, Gyeonggi-do, 412-791, South Korea.
[2] Mechanical Aerospace Engineering, Korean Aerospace University
76, Hanggongdaehang-ro, Deogyang-gu, Goyang-si, Gyeonggi-do, 412-791, South Korea.

ABSTRACT

The magnetorheological (MR) damper is a newest approach to replace the traditional passive damper which cannot change their dynamics in response to different operating conditions of the aircraft landing gear. This paper presents the simulation study of a semi-active controller for a landing gear equipped MR damper. Furthermore, a new method combined skyhook control with force control, called hybrid control, is developed to improve the performance of the MR damper landing gear. Finally, the numerical simulation result of the landing gear using SIMSCAPE-Simulink is discussed.

Keywords: Magneto-rheological (MR) damper, Landing gear, Skyhook method, Force control method, SIMSCAPE– Simulink (MATLAB).

1. Introduction

The shock absorber is the heart of the landing gear in the aircraft [1]. It absorbs the energy of the landing impact and reduces vibration when the aircraft lands. Due to the short duration of impulsive impact of an aircraft during touchdown, a traditional landing gear can only achieve limited performance [2-3]. To attenuate the landing impact transmitted to aircraft, many active or semi active types of landing gear systems have been developed [2-3]. Semi active control using magnetorheological damper is the most appropriate candidates to invest because of its fast response characteristic to magnetic field, compact size, and, hence, wide control bandwidth [4-13].

In this paper, a technique combined skyhook control and force control, called hybrid control, has been investigated not only to reduce vibration but also to improve the shock absorber efficiency. The paper follows the contents. Chapter 2 shows the hybrid control technique. In chapter 3 the simulation results are discussed. In chapter 4 the conclusions are presented.

2. Control Method
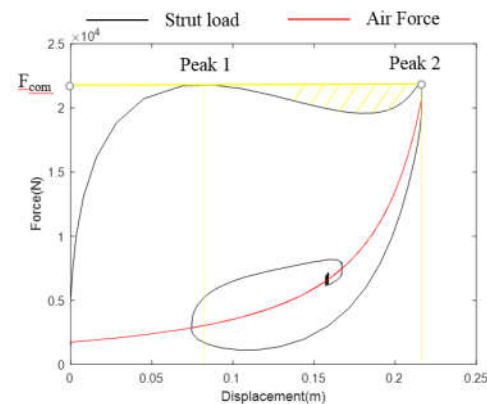
Fig.1. Strut load of an aircraft landing gear using skyhook control with a special gain.

The skyhook control is the most common technique in control suspension [14]. It reduces the displacement of aircraft by the adding a virtual damper in the sky. The maximum of shock absorber efficiency is reached when the first peak and second peak have the same force value (F_{com}). To improve the performance, the force is added in the period between first peak and second peak with the same force value (F_{com}) (Fig.1). This control technique is called the hybrid control because it adopts the skyhook control and force control simultaneously.

3. Results and Discussion

a)   Displacement

b) Strut load
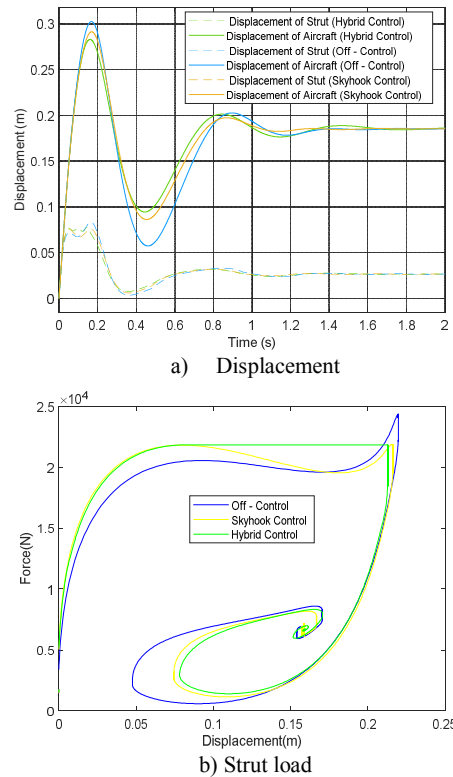
Fig. 2. The comparison of performance of aircraft using the different methods.

As can be seen on Fig. 2, the hybrid control has the lowest displacement compared to the passive and skyhook control methods. That means the hybrid control can reduce vibration. In addition, the shock absorber efficiency is the highest at 93% (Table 1).

TABLE 1
THE COMPARATION OF PERFORMANCE OF AIRCRAFT USING DIFFERENT ALGORITHM

	Maximum of stroke (m)	Maximum of damping force (N)	Shock absorber efficiency (%)
Off – Control	0.2198	24346	80.0
Skyhook Control	0.2162	21861	91.3
Hybrid Control	0.2135	21984	93.3

4. Concluding Remarks

This research investigated a telescopic type of landing gear system using magnetorheological shock. In the mathematical model, the hybrid control is applied to improve the shock absorber efficiency and decrease vibration. All calculations and simulates have been done by using SIMSCAPE – Simulink (MATLAB) which can easily apply for practice. In the future, an experimental research on aircraft landing gear will be performed to verify the simulation results of the mathematical model.

References

[1] Norman S. Currey, *Aircraft Landing Gear Design: Principle and Practices*. American Institute of Aeronautics and Astronautics, Washington, D.C. 1988, pp. 69 – 121.
[2] Benjamin Milwitzky and Francis E. Cook, "Analysis of landing – Gear Behavior", Langley Aeronautical Laboratory Langley Field, Rep. 1154, May. 1948.
[3] John R. McGehee and Huey D. Carden, "A mathematical model of an active control landing gear for load control during impact and roll – out", NASA Langley Research Center Hampton, Va. 23665, Rep. NASA TND -8080, February 1976.
[4] Gian Luca Ghiringhelli, "Testing of Semi – Active Landing Gear Control for a General Aviation Aircraft", Journal of Aircraft, Vol.37, No. 4, pp. 606 – 616, July – August 2000.
[5] D Y Lee, "Performance evaluation on vibration control of MR landing gear", Presented at 11th Conference on Electrorheological Fluids and Magnetorheological Suspensions.Doi:10.1088/1742-6596/149/1/012068.
[6] Li Hua – Lin, " Fuzzy PID Control for Landing Gear based on Magneto – Rheological (MR) damper", Apperceiving Computing and Intelligence Analysis, 2009. ICACIA 2009, pp. 22 – 25, October. 2009.
[7] Liu Hui, "Application of High – Speed Solenoid Valve to the Semi – Active Control of Landing Gear", Chinese Journal of Aeronautics 21 (2008) 232-240, pp. 232 – 240, January 2008.
[8] X.M. Dong and G.W. Xiong, "Vibration Attention of Magnetorheological Landing Gear System with Human Simulated Intelligent Control", Mathematical Problems in Engineering Volume 2013, Article ID 242476, October 2013.
[9] Ajinkya A. Gharapurkar, "Robust Semi – Active Control of Aircraft Landing Gear System Equipped with Magnetorheological Dampers", M.S. thesis, Department of Mechanical Engineering, Concordia University, Montreal, Quebec Canada, 2014.
[10] Young – Tai Choi and Norman M. Wereley, "Vibration Control of a Landing Gear System Featuring Electrorheological/Magnetorheological Fluids", Journal of Aircraft Vol. 40, No.3, pp. 432 – 439, May – June 2003.
[11] G. Mikulowski, "Adaptive aircraft shock absorbers", AMAS Workshop on Smart Materials and Structures, SMART'03, pp.63 – 72, September. 2003.
[12] Louise A. Powell, "Magnetorheological Fluids and Applications to Adaptive Landing Gear for a Lightweight Helicopter", Ph.D. dissertation, Department of Aerospace Engineering, University of Maryland, College Park, Maryland, 2014.
[13] Tak, Jun Mo, "A Hybrid Control Technique of the Intelligent Landing Gear with Variable Damping Force", M.S. thesis, Department of Mechanical Engineering, Korean Aerospace University, 2017.
[14] Seung – Bok Choi and Young – Min Han, *Fluid Technology Applications in vehicle systems*, CRC Press Taylor & Francis Group, pp. 2 – 11, 2013.

Thermo-mechanical Analysis of Laser Additive Manufacturing for Metals

Hsuan-Hao Shih, Chih-Kuang Lin

Department of Mechanical Engineering, National Central University, Jhong-Li District, Tao-Yuan 32001, Taiwan

ABSTRACT

The aim of this study is to develop a finite element analysis technique to characterize the distributions of temperature and stress in the process of multilayer deposition of metallic powders by laser additive manufacturing (LAM). Simulation results indicate the residual normal stress in the laser moving direction is greater than that in other directions due to a larger temperature gradient, and it increases with number of deposited layers. Highly residual stresses are present in the LAM build and at the base nearby the interface between the build and base.

Keywords: laser additive manufacturing, metal, finite element analysis, temperature gradient, residual stress

1. Introduction

Recently, more and more attention has been paid to the capacity of laser additive manufacturing (LAM) process. Thanks to its mechanism of depositing metallic material on a base, LAM can fabricate a new build with a high flexibility of structural geometry. However, thermal stresses are generated during laser scanning, and the remains become residual stress in the build [1]. The residual stress may exceed the yield strength of material and cause distortion, cracking, and delamination in the LAM products [2]. To avoid such failure and improve the quality of a LAM product, reduction of residual stress is needed.

Laser scanning strategy in an LAM process could affect the temperature and stress distributions. It can effectively reduce the residual stress in a new build with optimized LAM process parameters. Instead of a costly trail-and-error approach by experiment, finite element method (FEM) provides a beneficial and effective way to find a suitable laser scanning strategy to reduce the residual stress in a given build configuration [3]. Thermo-mechanical analyses are thus conducted in this study through FEM modeling to calculate the distributions of temperature and stress in LAM process of metallic multilayer powder deposition. Experiment of line segment irradiation by a moving laser is also conducted to validate the thermal FEM modeling.

2. Method

2.1 FEM modeling

3D models for simulating the laser processing are constructed using a commercial FEM code, ANSYS. The thermo-mechanical analysis is conducted to simulate formation of residual stress in a laser process. In the simulation, the base plate or powder material heated by a laser beam heat source is melted and then solidified after cooling. A transient thermal analysis of the entire process is conducted to acquire the global thermal history. The thermal history of the model is then applied into the mechanical analysis as thermal loadings. The thermal and residual stresses in the model are then calculated. An element birth-and-death technique is applied in both thermal and mechanical modeling. Additionally, the heat loss of convection and radiation is considered in this simulation, but the diffusion mechanism in the molten pool is not.

There are two materials used in this study. One is AISI 1015 steel which is applied as a base in experiment and simulation, and the other is Ti6Al4V titanium powder which is used in simulation of LAM multilayer deposition. Diameter of Ti6Al4V powder used in this study is less than or equal to 45 μm. In an LAM process, temperature change in a material is quiet large such that temperature-dependent thermal and mechanical properties are needed in simulation. The temperature-dependent density, thermal conductivity, enthalpy, thermal expansion coefficient, stress-strain relation, and mechanical properties of AISI 1015 and Ti6Al4V are given in Ref. [4-7] and applied in the simulation.

In the modeling for experimental validation of line movement of laser irradiation, a $30 \times 30 \times 2$ mm square steel plate is used as a base. The spot size of fiber laser used is 100 μm in diameter. A half-symmetric FEM model is constructed for this case (Fig. 1). A moving Gaussian heat flux [8] is applied on the top surface as a heat source. The absorptivity of steel plate is taken as 0.4 [9] for fiber laser with a wavelength of 1.07 μm.
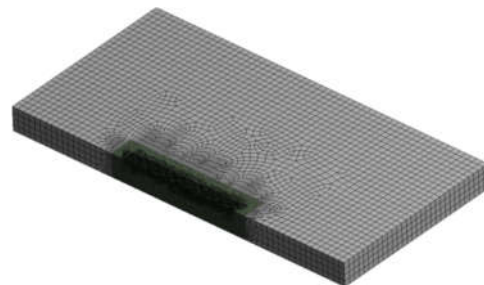
Fig. 1 Half-symmetric FEM model for moving laser

irradiation.

To simulate an LAM process of multilayer deposition of Ti6Al4V powder, a two-layer build in dimensions of 0.4 mm × 0.4 mm is deposited at the center of a square steel base of dimensions 1.2 × 1.2 × 0.8 mm. For simulating such an LAM process, elements of the build are constructed and meshed on the base at beginning (Fig. 2) and an element death-and-birth technique is applied in simulating the powder deposition process. The laser heat source only scans the square pattern elements of the powder layers at the central portion (Fig. 3). The thermal properties of Ti6Al4V in powder state are changed to those in molten pool when the temperature at heated elements reaches the melting point. The changes in absorptivity and volume from powder state to molten state are also considered at the same time. Absorptivity of the Ti6Al4V in powder state and molten state is 0.77 and 0.4, respectively [10,11]. The model is fixed at all surfaces of the base, except the top surface.
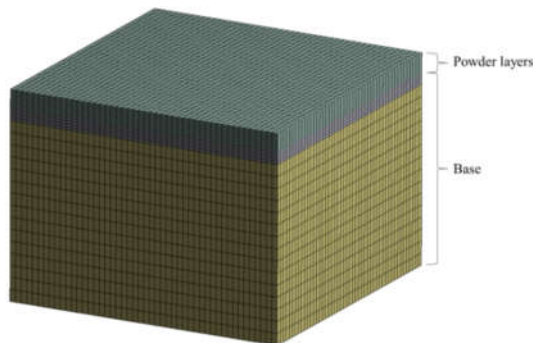
Fig. 2 FEM model for multilayer powder deposition.
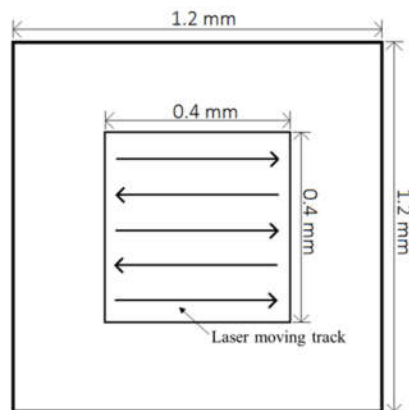
Fig. 3 Laser scanning path in the deposition area.
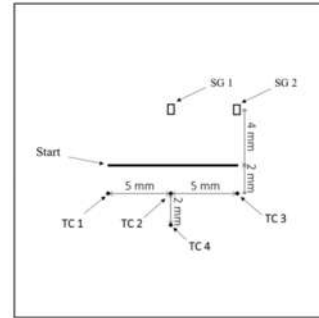
Fig. 4 Location of thermocouples in moving laser irradiation experiment.

2.2 Experiment

In order to validate the FEM modeling, experiment of line movement of laser irradiation on the aforementioned steel plate is conducted and temperature at selected points is measured by K-type thermocouple to compared with simulation results. Fig. 4 shows 4 positions (TC1-TC4) on the top surface of the steel plate are selected for temperature measurement.

(a)

(b)

(c)

(d)
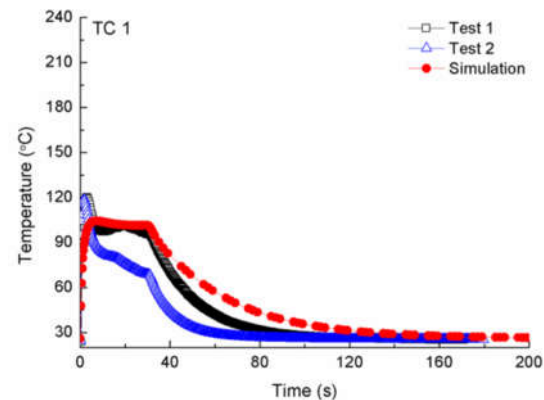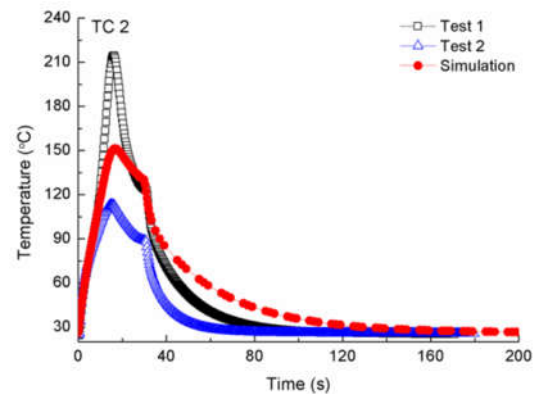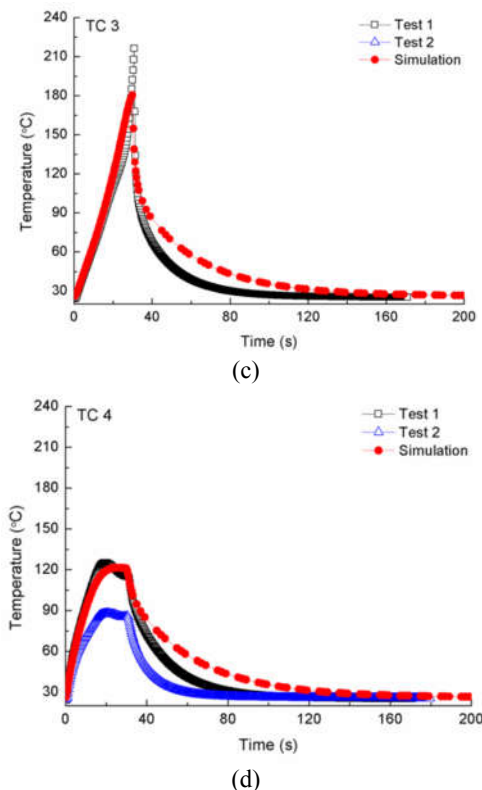
Fig. 5 Comparison of temperature variation at selected positions: (a) TC 1; (b) TC 2; (c) TC 3; (d) TC 4.

3. Results and Discussion

3.1 Line movement of laser irradiation

A line segment of 10 mm for laser irradiation with a laser power of 80 W and scanning speed of 0.33 mm/s is conducted in the experiment (Fig. 4). Comparison of temperature variation at selected points is shown in Fig. 5. Two tests are conducted to compare with the simulation results. Note that TC 3 in Test 2 is broken, so there is no data of TC 3 in Test 2. The trends of thermal history at the selected points in experiment concur with the simulation results. For the two tests conducted, the tendency of temperature variation at each measurement point is similar, but the magnitude of temperature shows a difference at the heating stage. However, the temperature values at the heating stage in simulation are located within the data range of the experiment for all of the selected points. Particularly, Test 1 has good agreement with the simulation results.

3.2 Temperature and stress distributions in multilayer powder deposition

A laser power of 100 W, with a scanning speed of 2000 mm/s and the given scanning path (Fig. 3), is applied for deposition of a two-layer Ti6Al4V powder on the base. Temperature distribution on the top surface of the second layer at the end of the final track is presented in Fig. 6. As shown in Fig. 6, a tail-shape temperature distribution is observed. The temperature at the center of the laser spot reaches 2700 °C and above; however,

that at the edge of the laser spot is around 1900 °C. The temperature at the region on which the laser does not directly irradiate is equal to the ambient temperature of 25 °C. It is also seen that the temperature at the region after scanning quickly decreases to a temperature below the melting point. For such a high temperature gradient, a large thermal stress is expected to be generated in the build.

Distributions of normal stress σ_{xx} on the top surface of the build at the end of the final track and after complete cooling are presented in Fig. 7(a) and 7(b), respectively. As shown in Fig. 7(a), compressive stress is initially generated when a region is heated by the laser beam, and it becomes tensile stress when the laser beam moves away and the region starts cooling. Such thermal stresses are induced by the constraint from the surrounding material during the thermal expansion and contraction. Hence, compressive stress is formed when the temperature increases, and then tensile stress is generated after cooling on the top surface of the second layer. The tensile stress is generated after deposition and gradually increases until the end of cooling process (Fig. 7(b)).
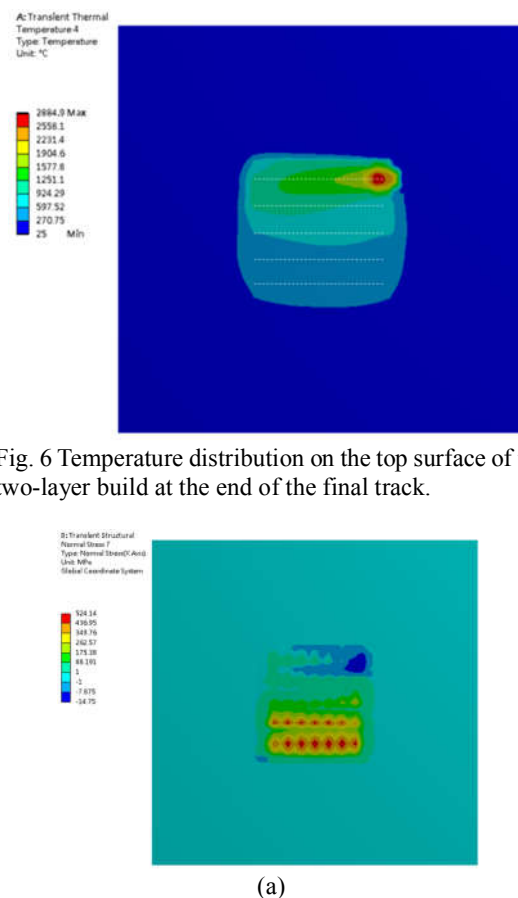
Fig. 6 Temperature distribution on the top surface of the two-layer build at the end of the final track.

(a)

(b)
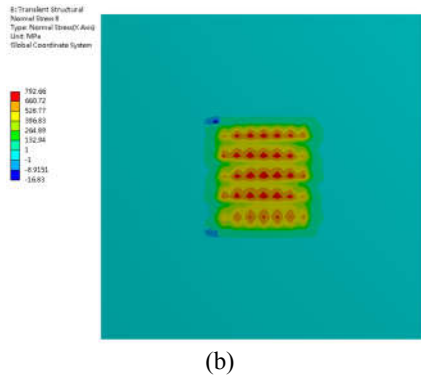
Fig. 7 Distribution of σ_{xx} on the top surface of the build: (a) at the end of final track; (b) after complete cooling.
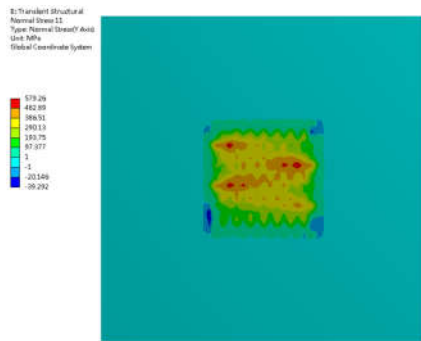
Fig. 8 Distribution of σ_{yy} on the top surface of the build after complete cooling.
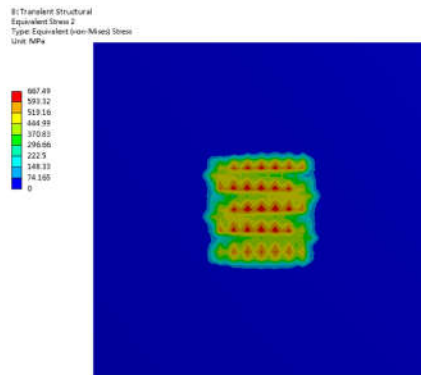
Fig. 9 Distribution of von-Mises stress on the top surface of the build after complete cooling.

Distribution of σ_{yy} on the top surface of the two-layer build after completely cooling down is shown in Fig. 8. Comparison of Figs. 7(b) and 8 indicates the residual stress in x-x direction (σ_{xx}) is much larger than that in y-y direction (σ_{yy}). As the temperature gradient along the direction of laser track (x-x direction) is greater than that in the transverse direction (y-y direction), the residual stress along the moving direction of the heat source is thus larger than that in other directions. Distribution of von-Mises equivalent stress on the top surface of the two-layer build after complete cooling is presented in

Fig. 9. After complete cooling, the von-Mises equivalent stress reaches a highest value and becomes the residual stress in the build.

(a)

(b)
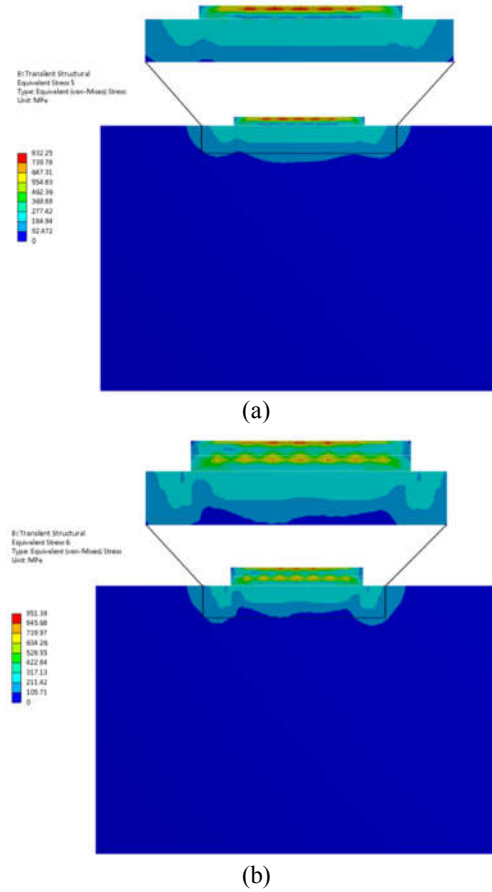
Fig. 10 von-Mises stress on the cross section along the first track at different stages: (a) completion of first-layer; (b) completion of second layer.

Distributions of von-Mises equivalent stress in the deposited build and base on the cross section along the first laser track at different stages are presented in Fig. 10. Note that in Fig. 10, boundaries between the build and base and between deposited layers are represented by the dash lines. The stress distribution in Fig. 10(a) can be seen as the residual stress in a one-layer build, as it is calculated in 10 s after completing the first-layer deposition. Comparison of Fig. 10(a) and 10(b) indicates the residual stress in the build increases when more layers are deposited on the base. As shown in Fig. 10(b), the residual stress in the second layer is higher than that in the first layer when the entire two-layer build is cooled down. Highly stressed regions are mainly located in the build as well as at the top region of the base near the interface. The von-Mises equivalent stress in some regions of the build (Fig. 10(b)) is close to the yield strength of Ti6Al4V. As a result, plastic deformation, cracking, and delamination may be

243

induced in the build and/or at the interface between build and base.

4. Concluding Remarks

A CAE technique using FEM is developed to predict the variation of temperature and thermal stress in moving laser irradiation process, in which the thermal simulations are validated by counterpart experiments. For multilayer powder deposition by LAM, compressive stress is observed at the melted region on the top surface of the build, and it becomes tensile stress whose magnitude generally increases when the deposited part cools down. Residual normal stress in the laser moving direction is significantly larger than that in other direction due to a steep temperature gradient along the laser moving direction. The residual stress in the build increases with increasing number of deposited layers and highly stressed regions are present in the build as well as at the top region of the base nearby the interface.

Acknowledgements

References

[1] W. J. Sames, F.A. List, S. Pannala, R.R. Dehoff, S.S. Babu, *Inter. Mater. Rev.,* 61 (2016) 315-360.

[2] Y. Li, D. Gu, *Additive Manufact.,* 1-4 (2014) 99-109.

[3] B. Schoinochoritis, D. Chantzis, K. Salonitis, *Proc. Inst. Mech. Eng., Part B: J. Eng. Manufac.,* 231 (2015) 96-117.

[4] Y.S. Touloukian, R.K. Kirby, R.E. Taylor, P.D. Desai, *Thermal Expansion: Metallic Elements and Alloys*, IFI/Plenum, Wilmington, USA, 1975.

[5] K.C. Mills, *Recommended Values of Thermophysical Properties for Selected Commercial Alloys*, Woodhead Publishing, Cambridge, UK, 2002.

[6] *Military Handbook-MIL-HDBK-5H: Metallic Materials and Elements for Aerospace Vehicle Structures*, U.S. Department of Defense, 1998.

[7] *An Overview of Fire Protection in Buildings*, FEMA, www.fema.gov/pdf/library/fema403_apa.pdf, accessed on May 26, 2017.

[8] M. Labudovic, D. Hu, R. Kovacevic, *J. Mater. Sci.,* 38 (2003) 35-49.

[9] K.C. Lee, W.K. Baek, H.J. Kwon, A.B. Gojani, J.J. Yoh, *Proc. 49th AIAA Aerospace Sci. Meeting*, 2011.

[10] N.K. Tolochko, T.Laoui, Y.V. Khlopkov, S.E. Mozzharov, V.I. Titov, M.B. Ignatiev, *Rapid Prototyping J.,* 6 (2000) 155-161 2000.

[11] H. Zamani, J.-P. Hermani, B. Sonderegger, C. Sommitsch, *Proc. CIRP,* 8 (2013) 75-80.

Design and Analysis of a Flexible Cantilever by Using Different Sections

Nguyen Phu Thuong Luu

Automotive Engineering Department, HUTECH University, Ho Chi Minh, Vietnam

ABSTRACT

This paper presents the design and analysis of a flexible cantilever mechanical system. The aim of this article is to develop a flexible cantilever model in CATIA software which is simulation and kinematical analysis mechanical structure. In this research, CATIA/Generative structural analysis is used to make the flexible mechanical part to the cantilever model to achieve more realistic simulation results. Different kinds of sections are introduced to analysis the cantilever structure. This paper is intended to provide some experience and familiarity with CATIA analysis and simulation.

Keywords: CATIA, Analysis, Cantilever, Design, Kinematic.

1. INTRODUCTION

Highly competitive nature of the automotive industry propels car manufacturers toward producing safer cars with lower price and better dynamic performance in a shorter time frame. This necessitates automotive engineers to consistently investigate safety and reliability characteristics of the vehicle to reach the optimum designs which can meet often conflicting design criteria. In recent years, use of computer-aided engineering (CAE) methods has been a good asset for engineers, particularly, at the early stages of body-in-white (BIW) structure design or frame structure design as presented [1]. However, parameterization of the design as a detailed FE model could be costly and time-consuming, also exact geometrical configuration of the vehicle may not be completely determined. Additionally, exact investigation of vehicle structure effects on the vehicle dynamic performance, after each series of design optimization, in conceptual steps could be challenging for small overlap frontal impact. By means of this optimal model, without any need for extensive prior knowledge of the vehicle dimensions and geometry, engineers will be able to assess different design characteristics and apply custom modifications more easily [2].

Luu et al. (2017) presented a reduced damage from crash for passengers inside the vehicle. They also analyzed concept modifications in the longitudinal structure design and focus on the thickness of the optimal components. They also developed special finite element software for structural modeling and analysis of crashworthiness. Small overlap impact is the serious accident occurred which cause the death for passengers inside [3]. In recent researches, the longitudinal has the structure the same as cantilever but in most case the longitudinal deformation following the horizontal direction. In this paper, the author study on vertical deformation of longitudinal as we call cantilever.

2. BUILDING THE MODEL

2.1 2D Sketch

The structure investigated in this study is a longitudinal structure. The total length of the cantilever model is $L = 500$ mm. The geometrical configuration of the rail is shown in Fig. 1.
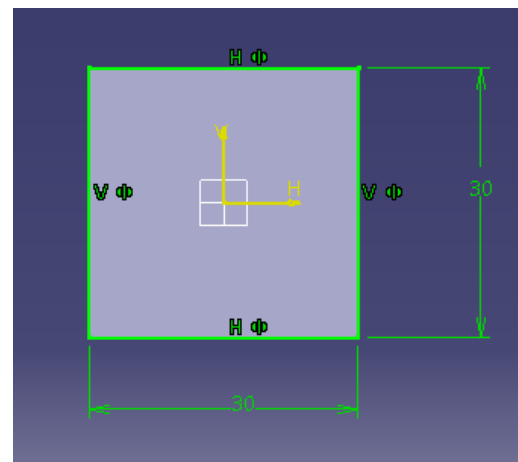
Fig 1: The sketch 2D of cantilever

2.2 3D model

All cantilevers taken into account are under the same longitudinal impact loading conditions, as depicted in Fig. 2. The cantilever is impacted onto a rigid wall with 1100 N in the y direction at the top of cantilever. A single surface contact algorithm and an automatic node to surface contact algorithm are used to account for the contact between lobes and the contact between column and rigid wall, respectively. For both static and dynamic frictions, the friction coefficient of 0.2 is adopted for all contact conditions.
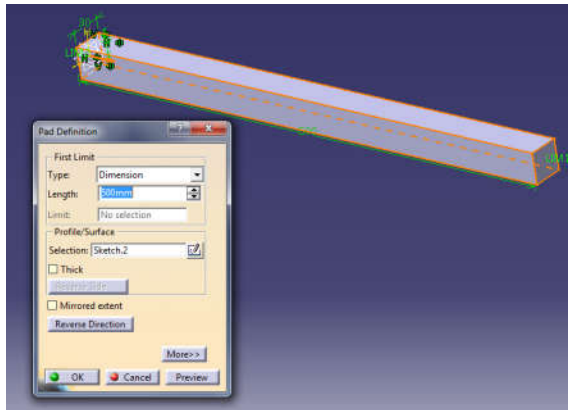
Fig 2: The 3D of cantilever model

2.3 Apply materials

We can apply the material in the CATIA library or build the material for the model by this step **start/infrastructure/material library** as shown in Figures below. We can input the characteristics of new material by double click on the material symbol.
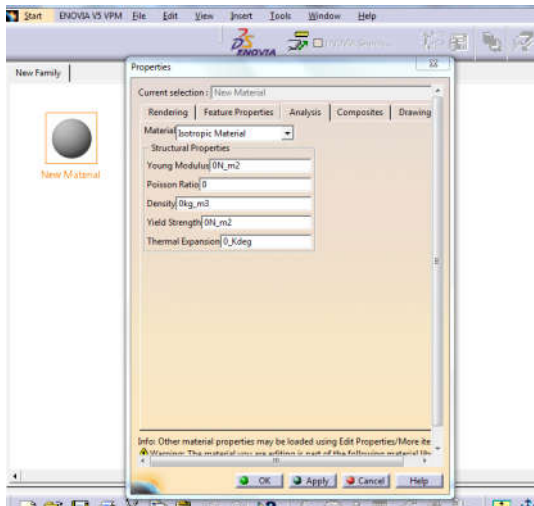
Fig 3: The applied properties of cantilever
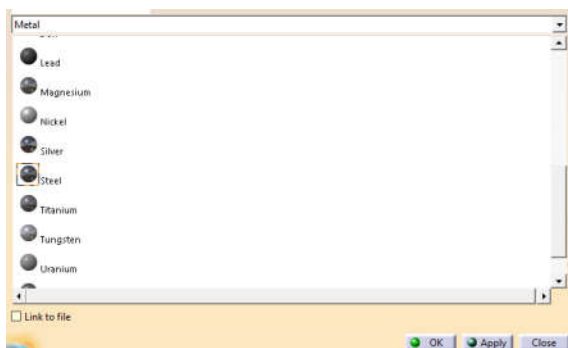
Fig 4: The chosen material of cantilever
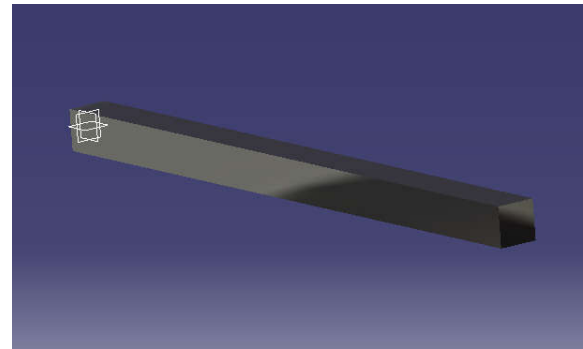
Fig 5: The shading model with steel material

2.4 Finite element model

The calculation time depend on the size of elements**.** In this paper, the meshing tool in CATIA/Analysis and Simulation was used to finite element the cantilever structure model. The results of the meshings are shown in Figure 6. The sizes of the elements were chosen as shown in Figure 7 and 8.
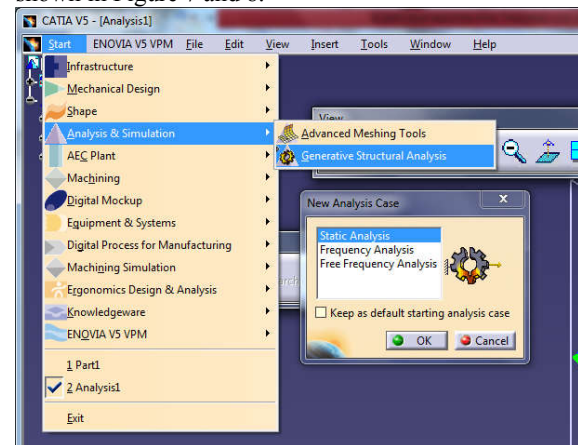
Fig 6: The finite element model building
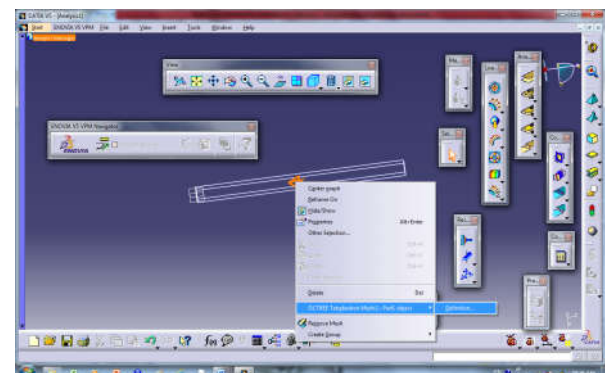
Fig 7: The meshing size elements of cantilever
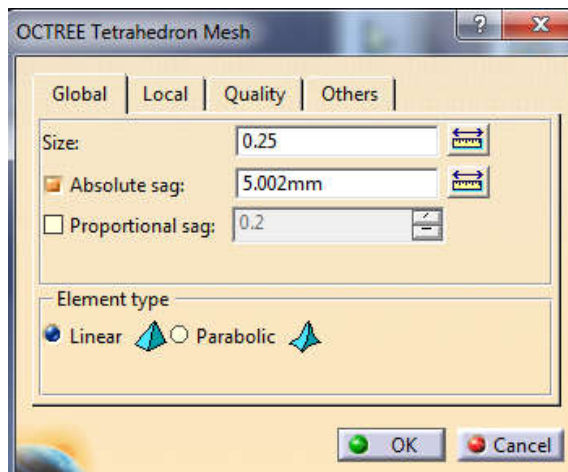
Fig 8: The octree tetrahedron mesh information

2.5 Set up constraints and forces

The boundary condition was set as shown in Figure 9. The clamp constraints were set at the surface of cantilever which was high lighted. The distributed forces were applied on the edge of cantilever as shown in Figure 10. With different experiments we can choose the others forces by click on the icons in Load menu.
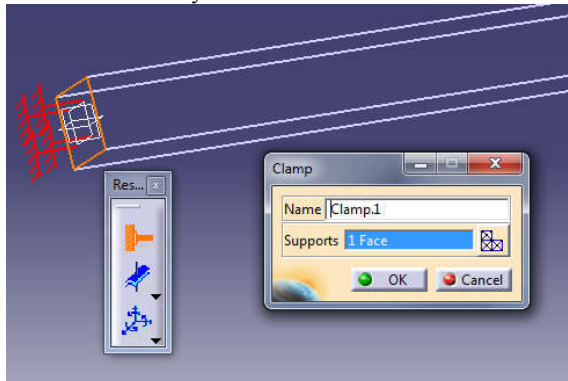
Fig 9: The clamp constraints at a surface of cantilever
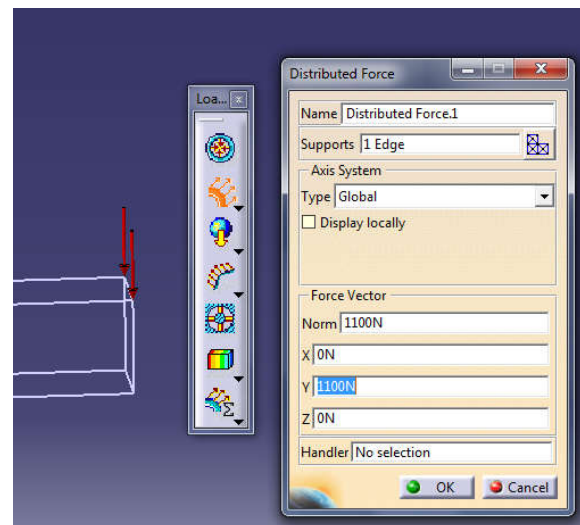
Fig 10: The distributed force setting at an edge of cantilever

3. Calculating and simulating the model

3.1 Square cantilever

The first experiment in this paper is study on the square cantilever shape. After the boundaries conditions were set as presented in 2.5 sections, the calculation was run as shown in Figure 11. The CPU time was shown in Figure 12. The running time was depended on the computer hardware in case with very small meshing size may cause the memory errors.

The results are shown in Figure 13 and Figure14. Diverse results can be seen such as the von misses stress results in Figure 13 and the translational displacements results in Figure 14. The minimum and maximum of the values of each are shown in the column on the top right of the screen.
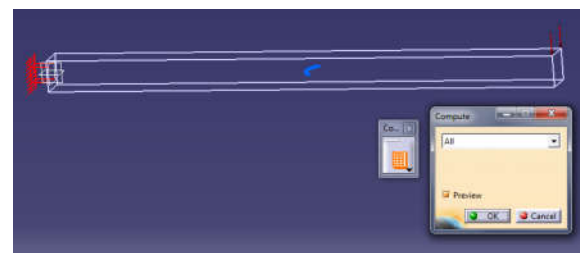
Fig 11: The calculation mechanical system
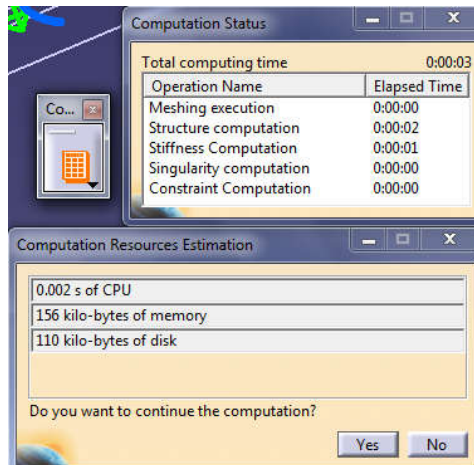
Fig 12: The computation status and resources estimation
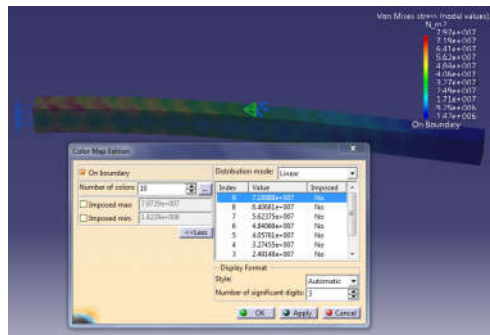
Fig 13: The von misses stress results
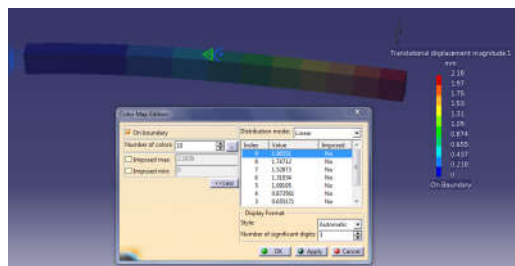
Fig 14: The translational displacement results

3.2 Different sections comparison

In this section, different shapes of cantilever were researched, the details information are shown in table 1 below. The mass of each case study are different but they are the same density.

Table 1 Numerical simulation results cantilever with different sectional shape

Sections	Max deform (mm)	Max stress (N-m²)	Areas (m²)	Mass (kg)	Density Kg-m3
	2.2	7.8e+7	9e-4	3.537	7860
	2.0	7.5e+7	5e-4	1.965	7860
	5.3	2.5e+8	7.1e-4	2.778	7860
	6.9	2.3e+8	3.9e-4	1.543	7860
	8.3	2.9e+8	5e-4	1.965	7860
	12.5	4.4e+8	2.8e-4	1.081	7860
	4.2	1.5e+8	7.8e-4	3.063	7860
	5.5	2.0e+8	4.3e-4	1.702	7860

4. Concluding Remarks

In the presented research, 8 different approaches for cantilever shapes simplified modeling were introduced and investigated. The models were formed based on different coupling of surface and beam elements as well as different extent of geometric simplification. Torsional and bending stiffness, regarding the same boundary conditions in experimental tests, were calculated successfully for each model. Obtained results were compared and evaluated in details. It was shown that small meshing size modeling gives acceptable results for bending stiffness, however, under torsional loading the error percentage increases considerably. The implemented approach in structure analysis in CATIA was proved to lead to a good trade-off model considering simplicity of the use, the ability to apply custom modification as well as level of accuracy in prediction of safety attributes.

References

[1] N.P.T. Luu, etc.., "Analysis of vehicle structural performance during small overlap frontal impact", IJAT, vol 16, pp 799-805, 2015.

[2] N.P.T. Luu, etc.., "A study on optimal design of vehicles structure for improving small overlap rating", IJAT, vol 16, pp 959-965, 2015.

[3] Luu Nguyen Phu Thuong, "An optimisation approach to choose thickness of three members to improve IIHS small-overlap structural rating", IJ CRASHWORTHINESS,DOI:10.1080/13588265.2017. 1281203.

Study on Analysis and Design of An VIAM-AUV200 Autonomous Underwater Vehicle (AUV)

Ngoc-Huy Tran[1], Thanh-Hai Chau[2], Quang-Vinh Dinh[2]
[1] Ho Chi Minh City University of Technology, VNU-HCM
Ly Thuong Kiet Street, Ho Chi Minh city, 700000, Viet Nam
[2] National Key Lab. of Digital Control and System Engineering, HCMUT, VNU-HCM
Ly Thuong Kiet Street, Ho Chi Minh city, 700000, Viet Nam

ABSTRACT

This paper presents the design of the VIAM-AUV2000 autonomous underwater vehicle (AUV) with a built-in cylinder for floatation and counterbalance. The modular structure including mechanical design, electronic system, and control algorithm ensures continuous operation for the vehicle at a depth of 50 meters underwater. The main content will consist of two parts: the mechanical implementation and the electrical system. The mechanical implementation part will focus on calculating ship hull profile and material selection; computing and simulating stress and distortion on ship hull and waterproof covering using finite element method with NX Nastran; analyzing and planning cylinder and counterbalance arrangements. The electrical system for the robot is also mentioned and clarified by the selection of sensors, actuators, hardware designs and the results that the team achieved in design, manufacture, control thruster and constructor tri-axis rotation angles estimator.

Keywords: AUV, diving/ floating mechanism, thruster, tri-axis rotation angles estimator.

1. Introduction

Nowadays, along with the rapid revolution of humankind, science and technology become more modern day by day, we gradually explore and conquer the mysteries of nature. However, the ocean is still a mystery far away from our reach and understanding. The research of ocean, decryption of the mystery in the deep of the sea required modern technology such as unmanned underwater vehicles, which can swim in the deep that no human can reach. In order to investigate the water environment, examine the ecosystem, probe the environmental fluctuation, or use for the military purpose, national defense, and observation… many prototypes of AUVs have been researched and developed. AUV Remus 100 of Woods Hole Oceanographic Institution [1] can dive to 100 meters in more than 10 hours at the velocity of 2,3 m/s. Lightweight AUV [2] developed by Porto University in cooperation with OceanScan work at 20 meters depth in 8 hours at 1,5-2m/s. Autosub6000 of Autonomous Underees Vehicle Applications Center can dive to 6000 meters in 30 hours at 5km/h. Slocum Glider without thruster can work in several months. [3]

Vietnam is a coastal country with more than 3.200 kilometers of coastline, and the sea area is about 1.000.000 square kilometers. Economic, scientific, tourism activities and national defense that take place on the sea are playing a very important role. Nowadays, many constructions are built on the sea such as ports, oil platforms, oil and gas pipelines, etc. At the same time, the arising of critical demand for surveying the topography and environment deep down the water surface as well as maintenance and equipment inspection. In the military, the demand for observation and mine removal also experience great increasing… That why the research and development of devices working underwater is one of the most important missions in order to take advantage of the sea and marine resources.

a) Lightweight AUV

b) AUV Remus   c) Slocum glider
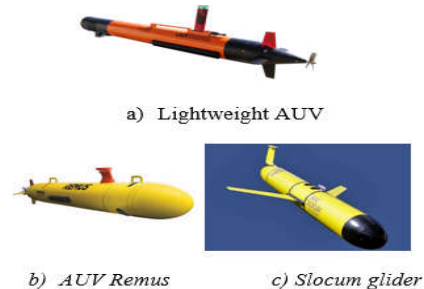
Figure 1. *AUV with torpedo shape*

This paper will focus on the design of AUV hull; using Finite element analysis to determine the suitable thickness of hull's part; design the diving and floating mechanism; and design the control system for AUV.

2. Design of AUV-VIAM2000

2.1. Design Ideas.

Design specifications:

- Torpedo shape
- Maximum depth: 50 meters
- Maximum velocity: 2 meters per second
- Time of continuous working: 2 hours
- Maximum weight: 70 kilograms

The design idea for diving/floating mechanism has been integrated into five design plans (1 – 5) which shown in figure 2 – 6. Where: [4]

1: VIAM-AUV2000's head

2: VIAM-AUV2000's body

3: VIAM-AUV2000's tail

4: Cylinder (Figure 4)

5: CounterWeight (Figure 2, 4)

6: Control board (Figure 3)

7: Battery (Figure 3)

8: Cylinder (Figure 3, Figure 6)

9: Stern wing (Figure 3, Figure 6)

10: Thruster (Figure 3)
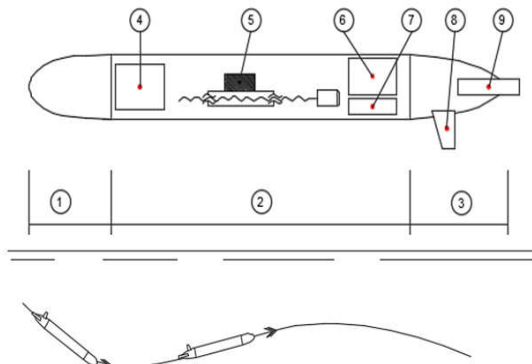
Figure 2. *Diving/floating mechanism using a counterweight.*
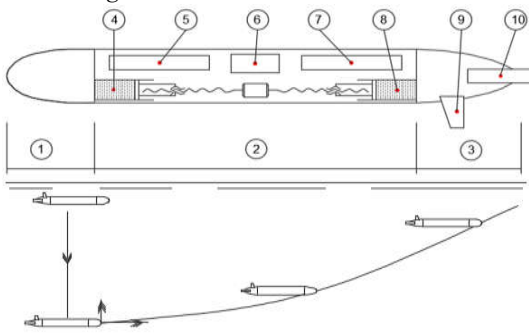
Figure 3. *Diving/floating mechanism using two cylinders controlled by one motor*
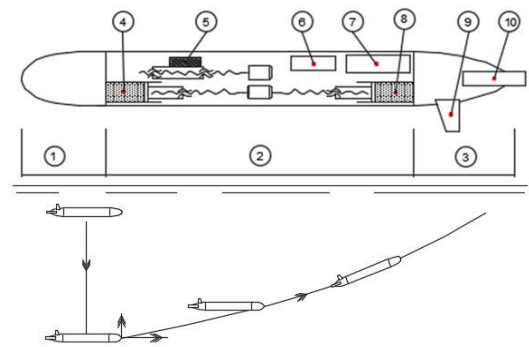
Figure 4. *Diving/floating mechanism using 2 cylinders controlled by one motor and counterweight*
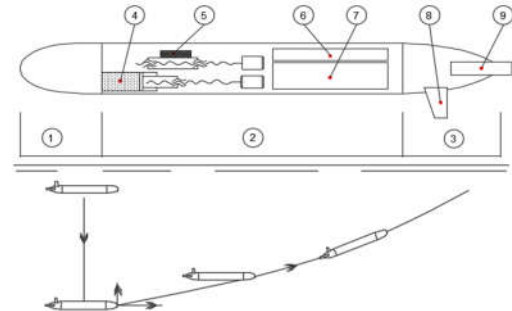
Figure 5. *Diving/floating mechanism using one cylinder and counterweight*
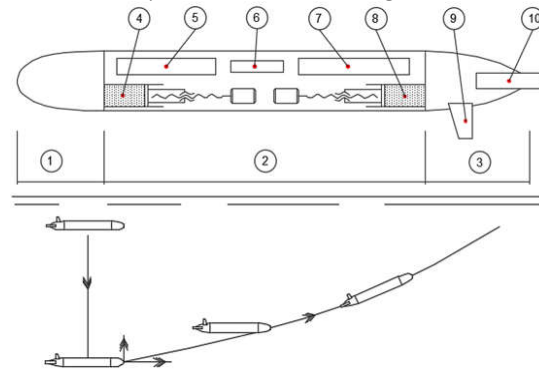
Figure 6. *Diving/floating mechanism using 2 independent cylinders*

Those design plans are considered by using the decision matrix [8], with plan 1 is chosen to be the standard for comparison.

Table 1. Decision matrix for design plans

Plan Standard	1	2	3	4	5
Easy for manufacturing	0	-	-	-	-
Easy for assembly and maintenance	0	-	-	-	-
Simple in control	0	0	-	+	-
Flexible	0	-	+	+	+
Good arrangement	0	0	-	+	-
Balance	0	-	+	+	+
Total Score	0	-4	-2	2	-2
Decision	No	No	No	**Yes**	No

From the result of table 1, our team decided to choose plan 4: diving/floating mechanism using one cylinder and counterweight (Figure 5).

2.2. Design of shape and AUV hull

Almost torpedo shaped AUV based on Myring shape (Figure 7) with the cylinder body, the head and stern will be designed according to formula (1) and (2). [9]
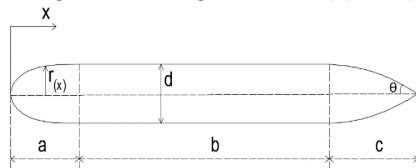
Figure 7. *Myring shape*

Head's shape:

$$r_{(x)} = \frac{1}{2}.d.\left[1-\left(\frac{x-a}{a}\right)^2\right]^{\frac{1}{n}}$$ (1)

Stern's shape:

$$r_{(x)} = \frac{1}{2}.d-\left[\frac{3d}{2c^2}-\frac{tan\theta}{c}\right].(x-a-b)^2$$
$$+\left[\frac{d}{c^3}-\frac{tan\theta}{c^2}\right].(x-a-b)^3$$ (2)

Where:

$r_{(x)}$: radius of section at position x.

d: the maximum of diameter at the cross-section.

a, b, c: length of head, body, and stern of AUV.

θ: angle at the end of the stern.

n: parameter of the head's shape.

Parameters for designed AUV shape included a, b, c, n, θ is shown in table 2. [6]

Table 2. Parameters of AUV's shape

Parameters	Value
a	300 mm
b	1400 mm
c	330
d	250 mm
n	2
θ	25º

Base on AUV prototypes that have been built in the world and the other underwater vehicles, especially vehicles work in the sea environment, we decided to use Aluminium Alloy T6 – 6061 with mechanical properties shown in table 3. [6]

Table 3. *Aluminium Alloy T6 – 6061 mechanical properties*

Ultimate tensile strength (MPa)	Tensile yield strength (MPa)	Drag race	Thermal conductivity (BTU hr.ft.°F)
≥ 310	≥ 270	10%	1160

Using finite element method (FEM) with NX Nastran apply for AUV hull, 4mm thickness, 800mm length, 250mm outside diameter, two end fixed by the flange, the pressure at 50m depth is 0,5MPa. The result show that the maximum stress on AUV hull is 14,94 MPa << [σ_c] = 275 Mpa and maximum displacement is 0,0287mm.
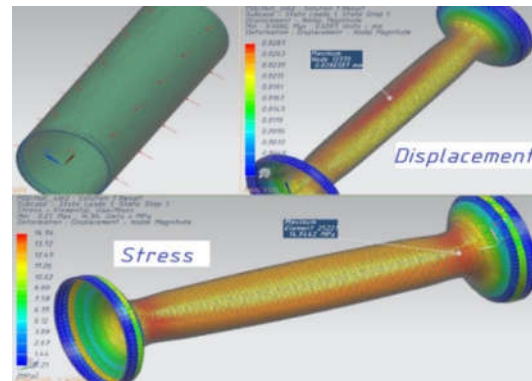
Figure 8. *Finite element analysis for AUV hull.*

Using FEM apply for AUV flange with 3, 4, 6 mm thickness, the result is shown in figure 9, and table 4.
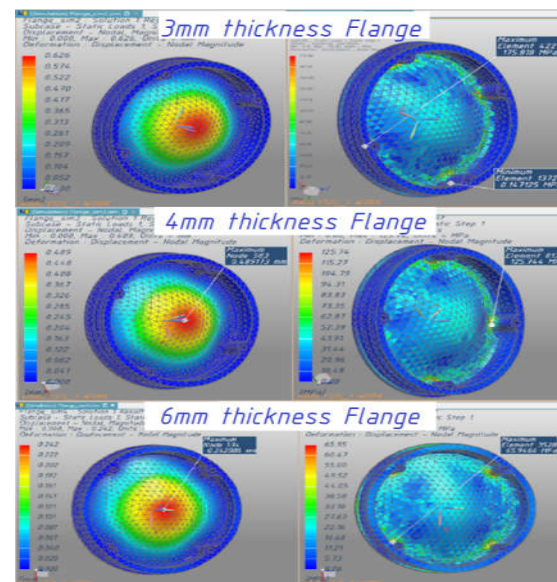
Figure 9. *Displacement (left) and stress (right) on different thickness AUV flange*

Table 4. *Value of maximum stress and displacement on AUV hull.*

Thickness (mm)	Maximum stress (MPa).	Maximum displacement(mm)
3	175,8	0,626
4	125,8	0,489
6	65,94	0,242

The flange with 6mm thickness is the most suitable for AUV body. However, with the demand for setting up other components, AUV flanges have to bear lots of loads, such as the mass of components inside AUV,… By optimizing the structure of the flange and using FEM, we got the structure of the particular flange shown in figure 10. The figure also indicates the maximum stress and displacement, which is 48,84Mpa and 0.0577mm respectively.
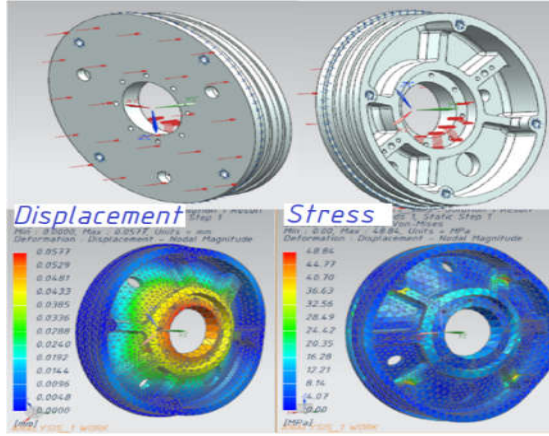
Figure 10. *FEA of designed AUV flange*

2.3. Design of diving/floating mechanism

2.3.1. Piston-cylinder pump
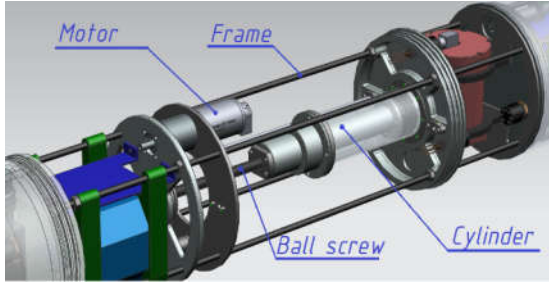
Figure 11. *Piston-cylinder 3D model*

Axial force acting on the cylinder is calculated with formula (3) include friction force between O-ring and cylinder wall (4), water pressure acting on the piston (5), pneumatic pressure while piston moving (6).

$$F_a = F_p - F_{ms} - F_n \qquad (3)$$

The friction force between the O-ring cylinder wall:

$$F_{ms} = F_c + F_h$$
(4)

Where:

- $F_c = f_c.L_p$ is the friction force created by the compression the O-ring:

f_c: friction force acting on 1cm length [N/cm]
L_p: Length of O-ring

- $F_h = f_h.A_p$ is the friction force created by contact surface of the O-ring and the cylinder wall:

f_h: friction force acting on 1cm^2 area of the contact surface.
A_p: area of the contact surface.

Axial load F_p created by water pressure (Figure 12):
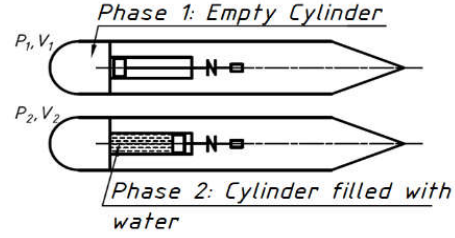
Figure 12. *Cylinder status.*

$$F_p = p.A_{piston} \qquad (5)$$

Where:
p: Water pressure.
- A_{piston}: area of the piston

Pneumatic pressure: $\quad F_n = P_2 / A_p \qquad (6)$

Let assume that the process is isothermal:

$$P_1V_1 = P_2V_2 \Leftrightarrow P_2 = P_1V_1 / V_2$$

The preliminary diameter of ballscrew is calculated with formula (7). [6]

$$d_1 \geq \sqrt{\frac{4.1,3.F_a}{\pi.[\sigma_k]}} \text{ (mm)} \qquad (7)$$

Where $[\sigma_k]$: tensile yield strength of the material.
Torque on ballscrew:

$$T = \frac{F_aP_h}{2\pi.\eta_1} \text{ (Nm)} \qquad (8)$$

Lead angle: $\gamma = arctg\left[\dfrac{p_h}{\pi.d}\right] (^o) \qquad (9)$

Where
P_h: pitch (mm)

- η_1: efficiency (%)

The overall parameters of the cylinder's ballscrew are shown in table 5.

Table 5. *Parameters of cylinder's ballscrew*

p (mm)	d_1 (mm)	N (rpm)	F_a (N)	T (Nm)	P (W)
10	10	60	2187	3,55	22,31

Overall efficiency:
$\eta_{ch} = \eta_{motor}.\eta_{gearbox}.\eta_{belt}.\eta_{bearing}^2.\eta_{tv}^2 =$
$0,8.0,7.0,95.0,99^2.0,95^2 \simeq 0,47 \qquad (10)$
The required motor capacity:
$P_{dc} = 22,31/0,47 \simeq 47,5$ W

For the cylinder system, use MAXON motor EC-I 52ϕ52mm, brushless, 180W (Part number 574741), maximum torque T_{max}=12,2Nm, N = 4720 rpm, and planetary gear box GP 52 C ϕ52, with transmission ratio 81:1

2.3.2. Counterweight
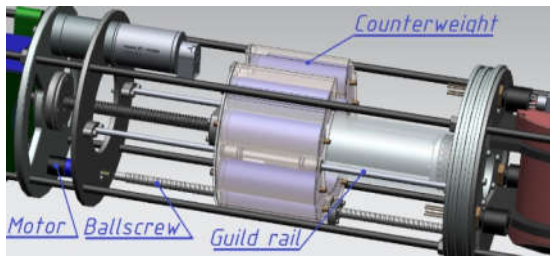
Figure 18. *Counterweight 3D model*

Counterweight includes 8 round battery with is 310g/battery, linear bearing, $P_{counterweight} \simeq 3kg$

After considering (7), (8), (9) and standard specification selection, the parameters of counterweight's ballscrew is shown in table 6. The axial load F_a is calculated while AUV swimming in the glider's journey (Figure 19). Let assume that $F_a \simeq P_{counterweight} = 30N$

Table 6. *Parameters of Counterweight's ballscrew*

p (mm)	d_1 (mm)	N (rpm)	F_a (N)	T (mNm)	P (W)
4	10	150	30	20	0,3
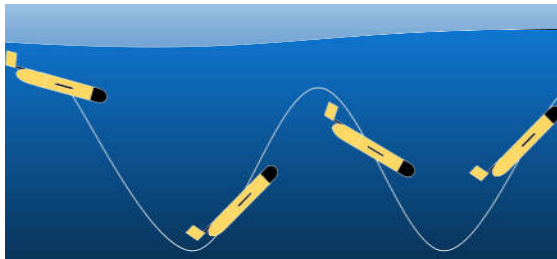
Figure 19. *Glider*

For the counterweight, Faulhaber 2444 motor 51W would be use for counterweitght with some specification such as aximum torque 18mNm, 45000rpm, and planetary gearbox 23/1 with transmission ratio 43:1, maximum torque 0,7Nm
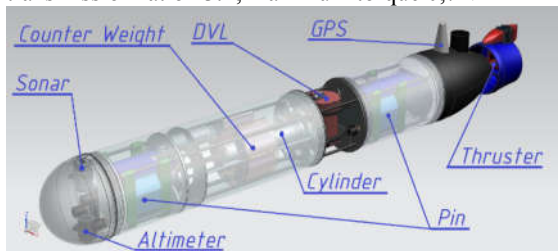
Figure 20. *Completed 3D model of AUV*

1.4. Design and manufacture thruster:
The thruster was designed using a magnetic coupling as shown in figure 21 with specifications [7]:
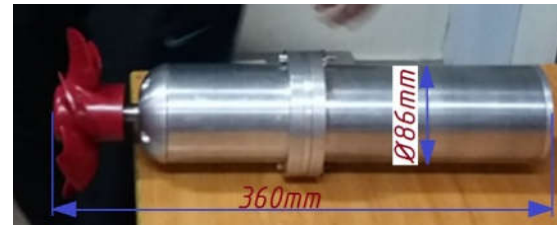
Figure 21. *Thruster of AUV-VIAM2000*
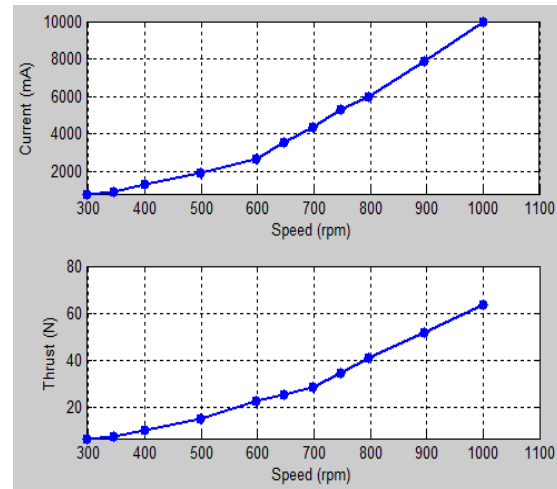
Figure 22. *BLDC Motor Current/Speed and Thrust/Speed Curves*

Table 7. *Specifications of thruster*

Type	Brushless DC
Size (mm)	L360mm x D86mm
Power (W)	600
Speed (rpm)	1850
Depth rate (m)	100
Max. thrust (kgf)	8
Number of wings of the propeller	6
Power supply (Vdc)	48
Communication	CANBUS

2. The electrical system of the AUV-VIAM2000
The robot is connected to the control center located on the surface (on the shore, on the mothership,…), data will be transmitted to the central station for management and command control via RF wireless system, GSM/GPRS, and Sonar.
The electrical system structure of the AUV is shown in figure 24. The high performance central processing unit allows the AUV to process received data at high speed, creating a premise for the AUV applies the advanced algorithms of guidance and control to serve each specific operating requirement. Data acquisition systems from sensors and actuator controllers are designed using high-speed ARM core microcontrollers (STM32Fx), which are interconnected via the CAN communication standard with a transfer rate of up to 1Mbit. The robot is equipped with a variety of sensors to collect information of the operating state of the robot

and the surrounding environment, thereby assisting the robot to make precise control decisions. The sensor system includes: GPS sensor (error < 1m horizontal), DVL velocity sensor (error 1% ± 1 mm/s), altimeter sensor and depth sensor (pressure sensor). In addition, tri-axis rotation angles estimator as shown in figure 23 with high accuracy (error < 2 degrees) integrated into the AUV.

Figure 23. Tri-axis rotation angles estimator (left) and its algorithm (right)

The algorithm in the tri-axis rotation angles estimator consists of two layers, each with an extended Kalman filter. Table 8 shows the error of the system in the static state, rotating around the x, y, z-axes, in the static state influenced by the external magnetic, and rotating around the z-axes influenced by the external magnetic.
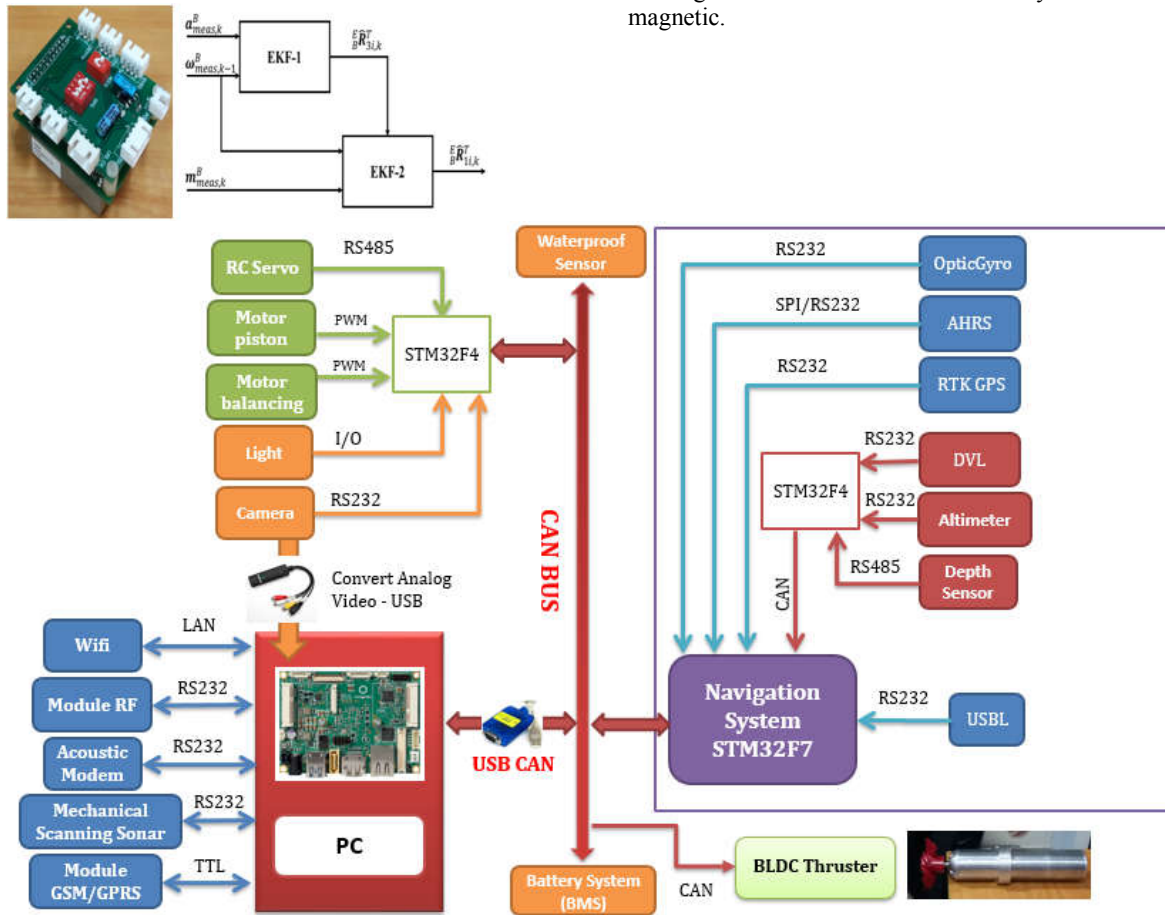
Figure 24. The electrical system of AUV-VIAM2000

Table 8. Results of the experimental error of the system

Experiment	RMS error (deg)		
	ϕ	θ	θ
STATIC	0.4055	0.0989	0.2977
TURN_X	0.2640	0.2892	0.3077
TURN_Y	0.4324	0.3495	0.3278
TURN_Z	0.6066	0.6297	0.5540
TURN_XYZ	0.5103	0.5013	0.7047
STATIC_MAG_EXT	0.3729	0.3529	0.7769
TURN_Z_MAG_EXT	0.4903	0.5509	2.7880

3. Conclusion:

This paper has analyzed and selected the complete design options for the AUV-VIAM2000, capable of diving/floating at a depth of 50m by a combination of cylinder and counterbalance. Through stress simulation, finite element analysis has been used to select materials and suitable shell thickness, ensuring that the robot can operate at a stable design depth. Last but not least, the research has achieved some goals in building electrical system comprising sensors and actuators selection, hardware design, thruster manufacture and control as well as tri-axis rotation angles estimator implementation.

REFERENCES

[1] Kukuly A., et al.,. "*Under-ice operations with a REMUS-100 AUV in the Arctic*", Proc. AUV 2010 IEEE Conference, Monterey, CA, USA (2010).

[2] Alexandre S., et al.,. "LAUV: The man-portable Autonomous Underwater Vehicle", IFAC Proceedings, 2012.

[3] Russell W., et al.,. "*Global Inventory of AUV and Glider Technology available for Routine Marine Surveying*," Marine Renewable Energy Knowledge Exchange Program, 2013.

[4] Vikrant P.Shah, "*Design Considerations for Engineering Autonomous Underwater Vehicles*," B.S Thesis, The University of Texas at Austin, 2005.

[5] Prestero T., et al., (2001). *Verification of a six-degree of freedom simulation model for the REMUS autonomous underwater vehicle*. M.S. Thesis, Massachusetts Institute of Technology, USA.

[6] Joseph Shigley, Charles Mischke, "*Standard handbook of machine design*", McGraw-Hill, 1996.

[7] Ngoc-Huy Tran, et al.,. "*Study on Design, Analysis and Control an Underwater Thruster for UUV*", Lecture Notes in Electrical Engineering 465, 2017

[8] David Ullman, "*The Mechanical Design Process, Fourth Edition*," Mcgraw-Hill Series in Mechanical Engineering, 2010, The McGraw-Hill Companies, Inc.

[9] D.F.Myring (1981), "*A Theoretical Study of the effects of body shape and mach number on the drag of bodies of revolution in subcritical axisymmetric flow*", Technical Report 81005.

Adaptive Multilayer T-S Fuzzy Controller for Nonlinear SISO System Optimized by Differential Evolution Algorithm

Cao Van Kien[1], Ho Pham Huy Anh[1], Nguyen Ngoc Son[2]

[1]FEEE, Ho Chi Minh City University of Technology, VNU-HCM, Viet Nam

[2]Faculty of Electronics Technology, Industrial University of Ho Chi Minh City, Viet Nam

ABSTRACT

This paper proposes a novel adaptive multilayer T-S fuzzy controller (AMTFC) for a class of uncertain nonlinear SISO systems. First, a new multilayer T-S fuzzy model optimized by the differential evolution DE algorithm is used to offline identify the inverse nonlinear system with uncertain parameters. Second, based on Lyapunov stability theory, a fuzzy adaptive based a sliding mode surface is designed to guarantee that the closed-loop system is asymptotically stable. Furthermore, simulation tests are given to illustrate the effectiveness of the proposed control scheme.

Keywords: Multilayer T-S Fuzzy, Inverse Controller, Adaptive Control, Differential Evolution, Lyapunov Theory.

1. Introduction

Fuzzy logic was first proposed in 1965 by Zadeh [1]. There are many studies developed based on this fuzzy-based domain, such as Fuzzy type-2, Fuzzy type-n, neural fuzzy, hierarchical fuzzy to model and control nonlinear system, [2-3]. Recently, Takagi–Sugeno (T–S) fuzzy model can provide a modeling frame for nonlinear systems. The advantage of T–S fuzzy systems is that they allow us to use a set of local linear systems with corresponding membership functions to represent nonlinear systems. The T-S fuzzy model is widely accepted as a powerful modeling tool and it's applications to various kinds of non-linear systems can be found in [4–9]. Based on the T-S fuzzy model of a plant, paper [10-13] introduced a fuzzy control design method for nonlinear systems with a guaranteed H2/∞ model reference tracking performance. However, if the membership functions of the T–S fuzzy system encounter parametric-uncertainty problem, the T–S fuzzy system cannot operate efficiently. Moreover, with a complex system, the more time it requires for training, the more complex membership functions that eventual fuzzy rule-table will become.

To achieve a higher precision from the Fuzzy model, its parameters are required to be optimized and the fuzzy structure is needed to be changed. Recently, Type-2 fuzzy sets [14-16] have been shown that they prove better than type-1 ones both on representing the nonlinear systems and handling the uncertainties. Paper [17] presented the problem of fuzzy control for nonlinear networked control systems with packet dropouts and parameter uncertainties based on the interval type-2 fuzzy-model-based approach. Paper [18] introduced an inverse controller based on a type-2 fuzzy model control. Moreover, many researchers used the optimization algorithms such as a cuckoo search algorithm (CSA) [19], Particle Swarm Optimization (PSO) [20], genetic algorithm (GA) [21], differential evolution (DE) [22-23] to optimize the parameters of the fuzzy Type-1 logic controller as to handle the nonlinear characteristics. Unlike a traditional Fuzzy set, multilayer Fuzzy model can't be built based on the experience of the designer. It is only available to be trained with soft computing optimization algorithm. Then it can be applied to identify and control of complex MIMO systems and be easy to scale for both of large or simple system [24]. Paper [25] successfully proposed the concept of Multilayer Fuzzy model for identifying uncertain nonlinear MISO system.

Furthermore, in order to compensate the uncertainties and guarantee the asymptotic stability, there are many different adaptive fuzzy control methods based on the classic advanced control algorithm such as sliding mode control (SMC) [26-32], H2/∞ technique [10-13], linearization feedback control [33-36], back-stepping technique [37-40]. However, these above-mentioned techniques require knowing in advance the characteristics of nonlinear uncertain SISO or MIMO system. Moreover, the adaptive fuzzy controller starts with the random coefficients which make the initial process difficult to control. It issues the system response will be overshoot with long settling time.

To overcome these drawbacks above-mentioned, this paper proposes the adaptive multilayer T-S fuzzy control approach for a class of uncertain nonlinear SISO systems. First, a new multilayer T-S fuzzy model optimized by the DE algorithm is used to offline identify the inverse nonlinear dynamic system with uncertain parameters. However, the fact is that the inverse controller is difficult to ensure system asymptotically stable. It needs an additional demonstration based on Lyapunov stability principle. Second, based on Lyapunov stability theory, an adaptive fuzzy control using a sliding mode surface is designed to guarantee that the closed-loop system operation is asymptotically stable. Furthermore, some

simulation benchmark tests are investigated to illustrate the effectiveness of the proposed control scheme.

The rest of this paper is organized as follows. Section II describes the formulation problem. Section III presents the proposed adaptive multilayer T-S Fuzzy controller design. Section IV presents the simulation results to show the effectiveness and robustness of the proposed controller and section V concludes the paper.

2. Problem formulation

General mathematical of SISO n-th order nonlinear systems is as follows

$$x(n) = f(x,t) + g(x,t)u$$
$$y = x \tag{1}$$

with f (x,t) and g(x,t) representing unknown nonlinear functions, $0 £ \le g(x,t) < +\infty$, $x = [x, \dot{x}, \dots x^{(n-1)}]^T$ as state vector of the system, u as the control input and y as the output of system.

The control problem is to design a stable control law for the state x tracking a desired reference signal xd. Inverse nonlinear controller represents open-loop control whose controller denotes an inverse model of the system. The inverse system is modelled through the use of a neural network NN or fuzzy logic FL with delay at its input and output and a feedback loop (see Figure 1).

The inverse control takes advantage of optimized algorithm. Inverse controller can efficiently control nonlinear system without knowing exactly the mathematical model of system. It only requires an inverse model identified in advance. In practice, designing the perfect inverse controller is very difficult. Practically, inverse control can ensure the nonlinear system is stable, but it is difficult to make the system asymptotically stable.
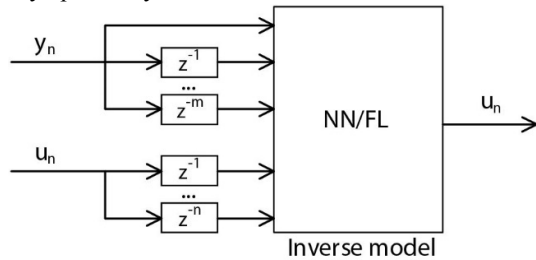
Figure 1. Generalized Inverse model

3. Proposed adaptive multilayer fuzzy control

3.1 Multilayer Fuzzy logic

In this paper, Multilayer Fuzzy logic is proposed for identifying inverse model. We propose Multilayer Fuzzy model to identify inverse model includes multiple fuzzy models.

It depends on the concrete complex system and if the structure of multilayer fuzzy model is scalable with

more or less single TS Fuzzy model in the system with a fixed number of inputs.

The proposed Multilayer Fuzzy structure used for identifying inverse model is shown in Figure 3. This is an example of the structure of multilayer fuzzy model. It composes of 2 Fuzzy models for the first layer. The output is sum of the two fuzzy model outputs.

Each TS Fuzzy system consists of two-input with 3 triangular membership functions. That means each fuzzy system includes 9 rules and 6 variables for membership structure. Consequently, the inverse model has 30 variables total.
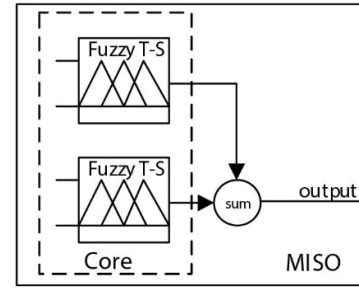
Figure 3. Proposed Multilayer Fuzzy system

From Figure 3, it is easy to see that there are 2 TS Fuzzy models in the inverse model. The first TS Fuzzy describes the effect of previous water level to output (voltage control), the other describes effect of previous voltage control to output and the output is sum of two TS Fuzzy model outputs.

3.2 Differential evolution algorithm

Nowadays, Differential evolution (DE) algorithm [10] is a popular optimization algorithm.

In this paper, it is used for learning Multilayer Fuzzy membership structures and rules by minimizing the cost function that denotes the error between actual output and multilayer Fuzzy predicted output.

The cost function follows the mean squared error (MSE) standard and is defined as:

$$J = \frac{1}{N}\sum e^2 \tag{2}$$

In which

$$e = y - \hat{y}$$

N represents number of samples, $\hat{y}$ denotes output of Fuzzy models and y represents output of real data collected from experiment.

The principal steps of DE algorithm are described as follows:

Initialization

The initial vector is randomly chosen with NP D-dimension and should cover the entire parameter

$$X_{i,g} = [x_{1,i,g}, x_{1,i,g}, \dots, x_{D,i,g}] \tag{3}$$

In which, G represents the number of generations:

G = 0, 1…Gmax , and i =1, 2,..., NP

Mutation

DE generates new parameter vectors by adding the weight difference between two population vectors to a third vector. This operation is called mutation. For each target vector $x_{i,g}$ a mutant vector is generated as

$$v_{i,G+1} = x_{r_1,G} + F(x_{r_2,G} - x_{r_3,G}) \qquad (4)$$

With r_1, r_2, r_3,...,$\in$ NP represent random indexes.

The randomly chosen values r_1, r_2, r_3 are selected from the running index i. F represents the real and constant coefficient F$\in$ [0, 2].

Crossover

After generating the resulting vector through mutation, the crossover step is carried out to enhance the diversity of the population pool. The donor vector exchanges its components with the target vector$\overrightarrow{X_{i,g}}$ to form the trial vector $\overrightarrow{U_{i,G}} = [u_{1,i,g}, u_{1,i,g}, ..., u_{D,i,g}]$. The DE algorithm often uses the binomial crossover method. The binomial crossover scheme may be outlined as

$$u_{j,i,G} = \begin{cases} v_{ij,G} \ if(\ rand_{i,j}[0, 1] < C) \\ x_{ij,G} \ otherwise \end{cases} \qquad (5)$$

Selection

This phase is used to decide whether it should become a member of generation (G+1). The target vector $\overrightarrow{X_{i,G}}$ is compared to the trial vector $\overrightarrow{U_{i,G}}$, and the one with a lower function value survives to the next generation. The selection operation is described as:

$$x_{i,G} = \begin{cases} u_{i,G} \ if \left(f(u_{i,G}) < f(x_{i,G}) \right) \\ x_{i,j,G} \ otherwise \end{cases} \qquad (6)$$

Termination

This is a condition to stop the loop process of DE algorithm. The algorithm stops when one of the followed conditions is satisfied:

- When maximum generation is reached
- When the best fitness is lower than desired fitness
- When the best fitness cannot increase for a long time

The flow chart of DE algorithm is shown in Figure 4. This is the process of DE algorithm. By the end of the process, the termination is satisfied with the predicted output will be nearly the same with actual output.
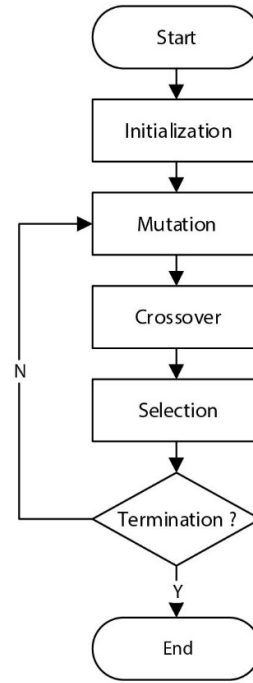
Figure 4. Flow chart of DE algorithm

3.3 Adaptive Inverse Multilayer Fuzzy controller

Adaptive Inverse Multilayer Fuzzy controller with structure presented in Figure 5 is combined between the Inverse Multilayer Fuzzy and the Adaptive Fuzzy model.

The parameters of Inverse Multilayer Fuzzy model will be optimally trained by DE algorithm. Since Inverse controller is difficult in practice to ensure system asymptotically stable, it needs an additional proof based on Lyapunov stability principle.
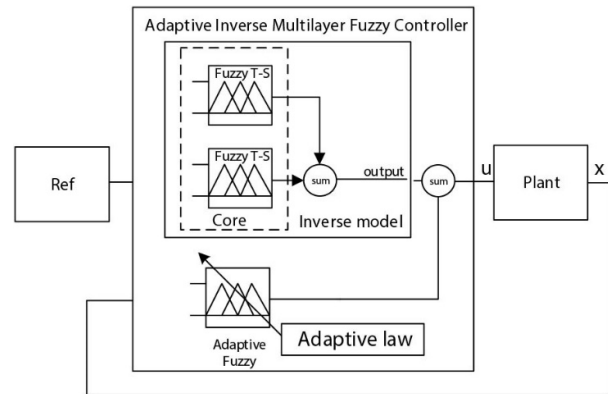
Figure 5. Block diagram of proposed fuzzy controller scheme

The system control law consists of 2 components, including Inverse control law and Adaptive control law.

$$u = u^*_{ifm} + \theta_u^T \xi(x) \qquad (7)$$

with u_{ifm}^* represents the output of optimized inverse fuzzy model of which parameters are optimized with DE algorithm. In detail u_{ifm}^* is described as

$$u_{ifm}^* = \arg_{u_{ifm} \in \Omega_u} \min\left(\sup|u_{ref} - u_{ifm}|\right) \quad (8)$$

where Ω_u represents constraint sets for u_{ifm}

$\theta_u^T \xi(x)$ is the output of Adaptive Fuzzy model.

The inverse control had to guarantee the stability of close-loop system. There may be some steady-state error with inverted controller. The Adaptive law is designed to guarantee that the closed-loop system is asymptotically stable.

Let define u^* which represents optimized control law.

$$u^* = u_{ifm}^* + \theta_u^{*T}\xi(x) \quad (9)$$

From (7) to (9),

$$\hat{u} - u^* = \tilde{\theta}_u^T \xi(x) \quad (10)$$

where

$$\tilde{\theta}_u - \theta_u = \theta_u^*$$

Furthermore, the control signal is determined as:

$$u = \hat{u} + u_{sw} \quad (11)$$
$$\dot{e} + \eta e = -g(x)\tilde{\theta}_u^T \xi(x) - g(x)u_{sw} \quad (12)$$

Lyapunov function is selected as,

$$V = \frac{1}{2g(x)}e^2 + \frac{1}{2}\tilde{\theta}_u^T \alpha \tilde{\theta} \quad (13)$$

$$V = \frac{\dot{e}.e}{g(x)}\tilde{\theta}_u^T \alpha \dot{\theta}$$

$$= e\left[-\tilde{\theta}_u^T \xi(x) - u_{sw} - \frac{\eta}{g(x)}e\right] + \tilde{\theta}_u^T \alpha \dot{\theta} \quad (*)$$

$$= -\frac{\eta}{g(x)}e^2 + \tilde{\theta}_u^T[\alpha\dot{\theta} - e\xi(x)] - eu_{sw} \quad (*)$$

The equation (*) proves that system satisfy asymptotically stable condition. Based on (*), adaptive law is then selected as,

$$\dot{\theta}_u = \alpha^{-1}e\xi(x) \quad (14)$$
$$u_{sw} = K sign(e) \quad (15)$$

with K represents positive constant.

4. Simulation & Results

4.1 Simulation Experimental setup

We perform the experiment controlling the fluid level of single tank system in simulation (see Figure 6).
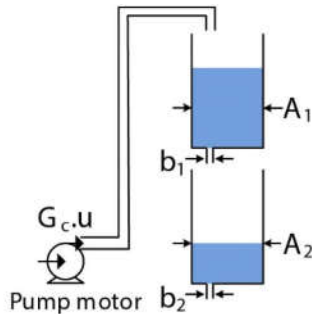
Figure 6. Coupled tank model

The coupled tank system possesses the state equation as,

$$\begin{cases} \dot{x}_1 = \dfrac{Ku}{A_1} - \dfrac{b_1 C}{A_1}\sqrt{2gx_1} \\ \dot{x}_2 = \dfrac{b_1 C}{A_2}\sqrt{2gx_1} - \dfrac{b_2 C}{A_2}\sqrt{2gx_2} \\ \quad\quad y = x_2 \end{cases} \quad (16)$$

with parameters of coupled tank system described in Table 1.

Table 1. Physical meaning and numerical value used in the Simulation

Notation	Physical Meaning	Value (unit)
A_1	Cross sectional area of Tank 1	16.619 (cm^2)
A_2	Cross sectional area of Tank 2	16.619 (cm^2)
b_1	Cross sectional area of outlet of Tank 1	0.4 (cm^2)
b_2	Cross sectional area of outlet of Tank 2	0.5 (cm^2)
C	The discharge coefficient of the outlet	0.8
g	Gravity	981 (cm/s^2)
G_c	Gain of the pump	6.94 (cm^3/(s.V))

4.2 Training Inverse Fuzzy model

Inverse model used in inverse Multilayer Fuzzy controller needs to be trained at first. In the simulation platform, training data was collected by step time of 1 second. Data for training are shown in Figure 7. Input data are random values from 3V to 13V, and experiment collected data is updated every 100 seconds.
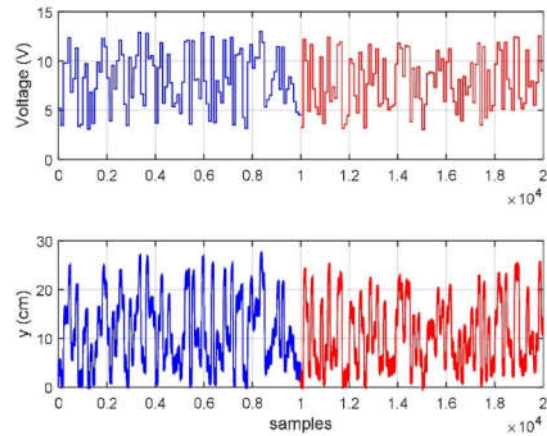
Figure 7. Training and evaluating dataset

Data for validating are shown in Figure 8. It is evident that validating data is different from training data with its random values from 3V to 13V and with 100 second interval for update too.

For training inverse fuzzy model, proposed Multilayer Fuzzy model is used with 2 inputs (y[n], y[n-1]) and one output (u[n]). All parameters of the proposed Multilayer Fuzzy model were trained by DE algorithm. Results

was validating of prediction method. In this paper, one step prediction is applied. Figure 8 shows the validating results based on another data set with the same resulting fuzzy structure from previous training phase. The results show that predicted output seems nearly equal to the actual system output
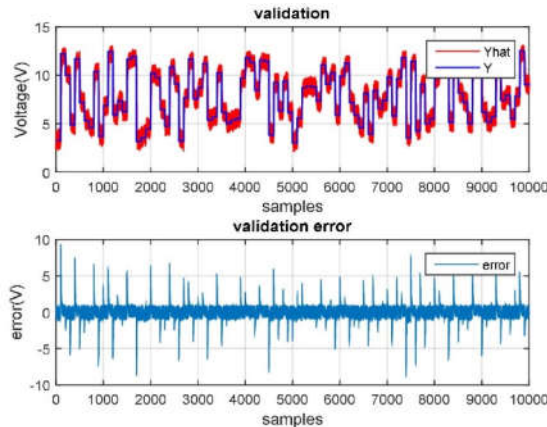
Figure 8. Validation result

4.3 Control results

In simulation platform, three tests are realized. The first test is for the proposed Adaptive Inverse Multilayer Fuzzy controller (AIMFC or IFC+AF), the second is for the inverse Multilayer Fuzzy controller without adaptive fuzzy (IFC), and the last test is for only Adaptive Fuzzy controller (AFC). All tests run with the same reference signal.

The unique input of Adaptive Fuzzy control composes of 5 Gaussian membership functions with s = 3 and its mean values of [0, 7.5, 15, 22.5, 30].

Adaptive Fuzzy parameter θ_u starts with random value. The random number in simulation gives [8.573, 0.1714, 4.537, 0.0326, 6.109].

Figure 9,10,11 and Table 2 show that the proposed Adaptive Inverse Multilayer Fuzzy controller (IFC+AF) obtains the best performance compared to the Inverse Fuzzy controller (IFC) and Adaptive Fuzzy controller (AFC).

At the end of process, AFC and IFC+AF show the same performance because both of them utilize the same adaptive law. The difference between AF and IFC+AF is related to the start-up feature. Meanwhile the IFC+AF starts up based on identified multilayer Fuzzy inverse model, and the AFC starts up with random parameter.

The IFC controller has poor performance but it shows that proposed controller can handle it. With poor performance IFC, the proposed controller has better performance than AF controller. With better IFC controller, the proposed controller can be even better.

Table 2 tabulates the comparative performance of three controllers through standard LMSE errors computed as follows,

$$LMSE = \frac{1}{T} \int e^2 \qquad (17)$$
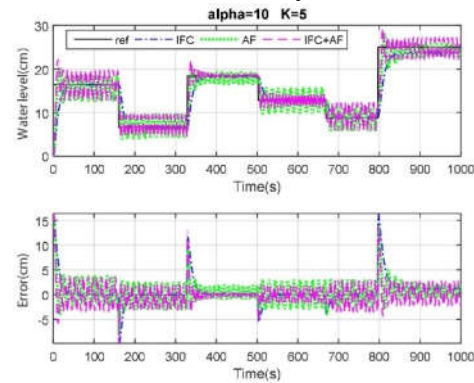
Figure 9. Comparison results of algorithms with alpha=10, K=5
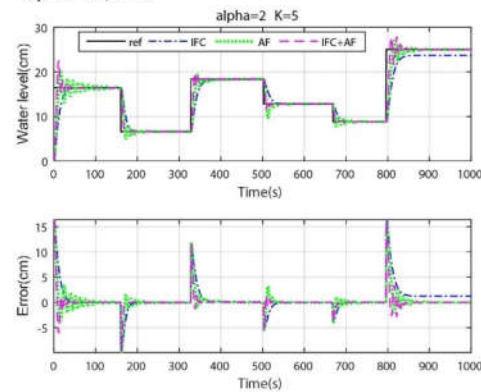
Figure 10. Comparison results of algorithms with alpha=2, K=5
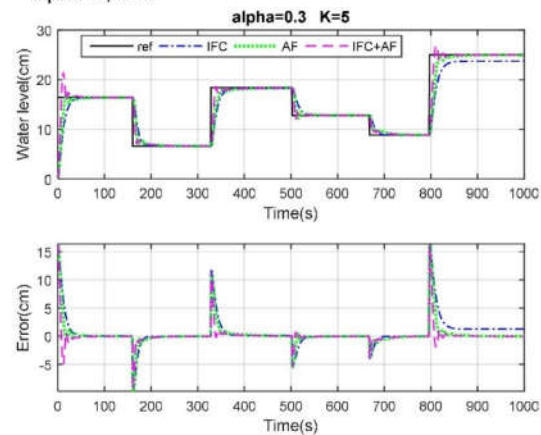
Figure 11. Comparative results of algorithms with alpha=0.3, K=5

261

Table 2. Comparative performance of three controllers

Method	LMSE	
	a = 2	a = 0.3
Inverse Fuzzy Control (IFC)	6.322	6.322
Adaptive Fuzzy Control (AFC)	4.229	4.675
Proposed Inverse Fuzzy Control with Adaptive Fuzzy (IFC+AFC)	2.648	2.8

5. Conclusions

In this paper, we propose an adaptive inverse multilayer fuzzy control for single tank system fluid level regulation. The adaptive inverse multilayer fuzzy logic controller is created from the multiple TS fuzzy models and adaptive fuzzy model. The simulation results show that proposed adaptive multilayer fuzzy logic controller can be efficiently applied for control nonlinear system. The proposed controller possesses better control quality and proves strongly robust due to satisfy Lyapunov stability principle. It is available for applying a scalable multilayer fuzzy model to a more complex nonlinear uncertain system. Thus, these results also ensure that proposed multilayer fuzzy controller can be used to successfully control of uncertain nonlinear complex system in near future study.

Acknowledgement

References

[1] L. A. Zadeh, "Fuzzy sets," Information and Control, vol. 8, no. 8, pp. 338–3365, 1965.

[2] Precup, Radu-Emil, and Hans Hellendoorn. "A survey on industrial applications of fuzzy control." Computers in Industry62.3 (2011): 213-226.

[3] Qiu, Jianbin, Huijun Gao, and Steven X. Ding. "Recent advances on fuzzy-model-based nonlinear networked control systems: A survey." IEEE Transactions on Industrial Electronics 63.2 (2016): 1207-1217.

[4] Chiu, Chian-Song. "TS fuzzy maximum power point tracking control of solar power generation systems." IEEE Transactions on Energy Conversion 25.4 (2010): 1123-1132.

[5] Rezaee, Babak, and MH Fazel Zarandi. "Data-driven fuzzy modeling for Takagi–Sugeno–Kang fuzzy system." Information Sciences 180.2 (2010): 241-255.

[6] Cheung, Ngaam J., Xue-Ming Ding, and Hong-Bin Shen. "OptiFel: A convergent heterogeneous particle swarm optimization algorithm for Takagi–Sugeno fuzzy modeling." IEEE Transactions on Fuzzy Systems 22.4 (2014): 919-933.

[7] Cheung, Ngaam J., Xue-Ming Ding, and Hong-Bin Shen. "OptiFel: A convergent heterogeneous particle swarm optimization algorithm for Takagi–Sugeno fuzzy modeling." IEEE Transactions on Fuzzy Systems 22.4 (2014): 919-933.

[8] Zou, Wen, Chaoshun Li, and Nan Zhang. "A TS Fuzzy Model Identification Approach based on a Modified Inter Type-2 FRCM Algorithm." IEEE Transactions on Fuzzy Systems (2017).

[9] Salhi, Issam, Abdellatif Belattar, and Said Doubabi. "Takagi–Sugeno fuzzy modeling for three-phase micro hydropower plant prototype." International Journal of Hydrogen Energy 42.28 (2017): 17782-17792.

[10] Tseng, Chung-Shi, Bor-Sen Chen, and Huey-Jian Uang. "Fuzzy tracking control design for nonlinear dynamic systems via TS fuzzy model." IEEE Transactions on fuzzy systems 9.3 (2001): 381-392.

[11] Xiaodong, Liu, and Zhang Qingling. "New approaches to H∞ controller designs based on fuzzy observers for TS fuzzy systems via LMI." Automatica 39.9 (2003): 1571-1582.

[12] Nasiri, Alireza, et al. "Reducing conservatism in H¥ Robust State Feedback Control design of TS Fuzzy Systems: A Non-monotonic Approach." IEEE Transactions on Fuzzy Systems(2017).

[13] Wei, Yanling, et al. "A New Design of $ H $-Infinity Piecewise Filtering for Discrete-Time Nonlinear Time-Varying Delay Systems via T–S Fuzzy Affine Models." IEEE Transactions on Systems, Man, and Cybernetics: Systems 47.8 (2017): 2034-2047.

[14] Mendel, Jerry M., and RI Bob John. "Type-2 fuzzy sets made simple." IEEE Transactions on fuzzy systems 10.2 (2002): 117-127.

[15] Mendel, Jerry M. "General type-2 fuzzy logic systems made simple: a tutorial." IEEE Transactions on Fuzzy Systems 22.5 (2014): 1162-1182.

[16] Li, Hongyi, et al. "Control of nonlinear networked systems with packet dropouts: interval type-2 fuzzy model-based approach." IEEE Transactions on Cybernetics 45.11 (2015): 2378-2389.

[17] Kumbasar, Tufan, et al. "Type-2 fuzzy model based controller design for neutralization processes." ISA transactions 51.2 (2012): 277-287.

[18] Kumbasar, Tufan, et al. "An inverse controller design method for interval type-2 fuzzy models." Soft Computing 21.10 (2017): 2665-2686.

[19] Berrazouane, Sofiane, and Kamal Mohammedi. "Parameter optimization via cuckoo optimization algorithm of fuzzy controller for energy management of a hybrid power system." Energy conversion and management 78 (2014): 652-660.

[20] Soufi, Youcef, Mohcene Bechouat, and Sami Kahla. "Fuzzy-PSO controller design for maximum power point tracking in photovoltaic system." International Journal of Hydrogen Energy 42.13 (2017): 8680-8688.

[21] Sundarabalan, C. K., and K. Selvi. "Real coded GA optimized fuzzy logic controlled PEMFC based Dynamic Voltage Restorer for reparation of voltage disturbances in distribution system." International Journal of Hydrogen Energy 42.1 (2017): 603-613.

[22] Lutz, Adam, Vlad Bonderev, and Chester Fiesnski. "Fuzzy neural network optimization and network traffic forecasting based on improved evolution." Neural Networks & Machine Learning 1.1 (2017): 2-2.

[23] Chen, Cheng-Hung, and Chong-Bin Liu. "Reinforcement Learning-Based Differential Evolution With Cooperative Coevolution for a Compensatory Neuro-Fuzzy Controller." IEEE Transactions on Neural Networks and Learning Systems (2017).

[24] Tu, Kuo-Yang, Tsu-Tian Lee, and Wen-Jieh Wang. "Design of a multilayer fuzzy logic controller for multi-input multi-output systems." Fuzzy sets and systems 111.2 (2000): 199-214.

[25] C. Van Kien, N. N. Son, and H. P. H. Anh, "Identification of 2-DOF Pneumatic Artificial Muscle System with Multilayer Fuzzy Logic and Differential Evolution Algorithm," in The 12th IEEE Conference on Industrial Electronics and Applications (ICIEA 2017), 2017, pp. 1261–1266.

[26] Mi, Yang, et al. "Intelligent Power Sharing of DC Isolated Microgrid Based on Fuzzy Sliding Mode Droop Control." IEEE Transactions on Smart Grid (2018).

[27] Wang, Yueying, et al. "Dissipativity-based fuzzy integral sliding mode control of continuous-time TS fuzzy systems." IEEE Transactions on Fuzzy Systems (2017).

[28] Xue, Yanmei, Bo-Chao Zheng, and Xinghuo Yu. "Robust sliding mode control for TS fuzzy systems via quantized state feedback." IEEE Transactions on Fuzzy Systems (2017).

[29] Li, Hongyi, et al. "Adaptive sliding mode control for Takagi-Sugeno fuzzy systems and its applications." IEEE Transactions on Fuzzy Systems (2017).

[30] Li, Jinghao, et al. "Observer-Based Fuzzy Integral Sliding Mode Control For Nonlinear Descriptor Systems." IEEE Transactions on Fuzzy Systems (2018).

[31] Wen, Shiping, et al. "Fuzzy control for uncertain vehicle active suspension systems via dynamic sliding-mode approach." IEEE Transactions on Systems, Man, and Cybernetics: Systems 47.1 (2017): 24-32.

[32] Li, Jinghao, et al. "Robust Stabilization of TS Fuzzy Stochastic Descriptor Systems via Integral Sliding Modes." IEEE transactions on cybernetics (2017).

[33] Li, Yongming, and Shaocheng Tong. "Adaptive fuzzy output-feedback stabilization control for a class of switched nonstrict-feedback nonlinear systems." IEEE transactions on cybernetics 47.4 (2017): 1007-1016.

[34] Liu, Yan-Jun, et al. "Adaptive Fuzzy Output Feedback Control for a Class of Nonlinear Systems with Full State Constraints." IEEE Transactions on Fuzzy Systems (2018).

[35] Zhou, Qi, et al. "Adaptive fuzzy control for nonstrict-feedback systems with input saturation and output constraint." IEEE Transactions on Systems, Man, and Cybernetics: Systems 47.1 (2017): 1-12.

[36] Li, Yongming, Shuai Sui, and Shaocheng Tong. "Adaptive fuzzy control design for stochastic nonlinear switched systems with arbitrary switchings and unmodeled dynamics." IEEE transactions on cybernetics 47.2 (2017): 403-414.

[37] Tong, Shaocheng, et al. "Observer-based adaptive fuzzy backstepping control for a class of stochastic nonlinear strict-feedback systems." IEEE Transactions on Systems, Man, and Cybernetics, Part B (Cybernetics) 41.6 (2011): 1693-1704.

[38] Li, Hongyi, et al. "Adaptive fuzzy backstepping tracking control for strict-feedback systems with input delay." IEEE Transactions on Fuzzy Systems 25.3 (2017): 642-652.

[39] Liu, Heng, et al. "Adaptive fuzzy backstepping control of fractional-order nonlinear systems." IEEE Transactions on Systems, Man, and Cybernetics: Systems 47.8 (2017): 2209-2217.

[40] Sadek, Uroš, et al. "Improved adaptive fuzzy backstepping control of a magnetic levitation system based on Symbiotic Organism Search." Applied Soft Computing 56 (2017): 19-33.

PART IV, SECTION I

Machining Technology
(Difficult-to-cut and Free Machining; Non-conventional Machining;
Green Process/Manufacturing; Cutting Mechanisms…)

Characteristics of Cutting Resistance in Microendmilling of Titanium Alloy

Shinya Fujimoto[1], Koichi Okuda[1], MasayukiNunobiki[1]
[1] Graduate School of Engineering, University of Hyogo
2167 Shosha, Himeji, Hyogo,671-2280,JAPAN

ABSTRACT

In this study, we investigated the cutting characteristics, especially the cutting force in fine groove processing of titanium alloy (Ti-6Al-4V) using a small diameter end mill. The micro end milling experiments were carried out and the relationship between the cutting resistance and other characteristics of the tool wear and the surface roughness was discussed. As the result, it was found that the cutting resistance increased slightly with an increase in the cutting speed and the force component of vertical direction to the tool feed increased drastically at the spindle rotational speed of 57000 min^{-1}.

1. Introduction

Titanium materials have various excellent properties such as high specific strength and biocompatibility and then are used in a wide range of fields including parts of aircraft, automobile engines, tooth implants and so on [1, 2]. On the other hand, it is known as a difficult-to-cut material because the tool wear is easy to proceed and the adhesion tends to be formed on the tool face [3]. For this reason, the development of tool materials and shapes suitable for processing of titanium materials and the searching of cutting conditions for improving tool life have been performed.

Most of researches have been done for mainly high efficiency processing in turning and end milling with a normal diameter (diameter of 10 mm or more). However, the cutting characteristics with a small diameter end mill with a diameter of 1 mm or less are not sufficiently clarified. Then, we have focused on the micro cutting of titanium alloy because the demand for the micro part in medical field of industry is increasing. Therefore, in this study, in order to investigate the cutting characteristics of fine groove processing of titanium alloy (Ti-6Al-4V) using a small-diameter end mill, we measured and observed the change of the cutting resistance value with the increase of the cutting speed in fine groove processing of titanium alloy by the small diameter end mill and the high speed cutting. And the relationship between the change of the cutting resistance and the tool wear and the finished surface roughness was discussed.

2. Experimental Methods

In this research, an ultra-precision vertical milling machine (Toshiba Machine Ltd.; model UVM-450C) with a spindle rotation of 6000- 60000 min^{-1} was employed for the micro milling experiments of the titanium alloy. The image of experimental set-up is shown schematically in **Fig.1**. The size of the work piece is 8×25×30 mm. A three-component dynamic force transducer (KISTLER 9251A) was used for the measurement of the cutting resistance. Fx, Fy, Fz

indicate the direction of the cutting force components in the figure and each component shows the tool feed direction, the direction perpendicular to the feed direction and the tool axial direction, respectively. **Fig. 2** shows the cutting tool used in the experiments. Two bladed square end mill (Nisshin Tool Ltd.; model MSE 230) made of a cemented carbide was used.
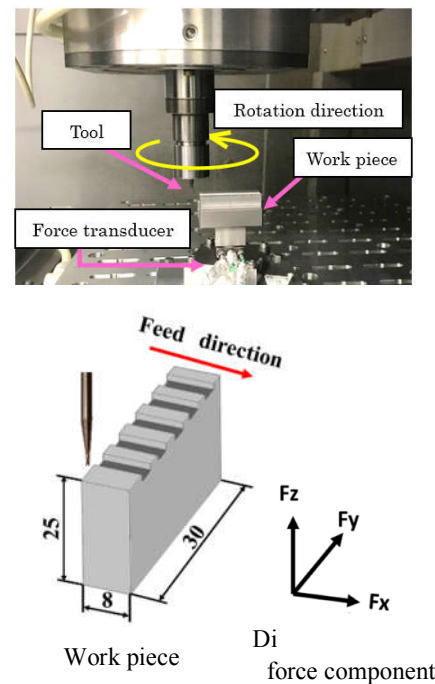
Fig.1   Experimental set-up
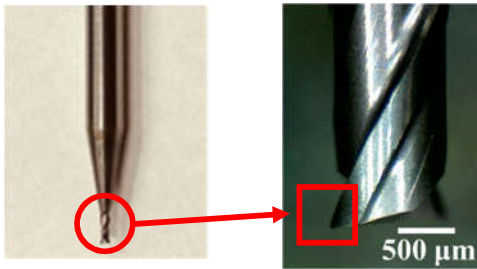
Fig.2   Micro end mill
(Tool diameter:1.0 mm)

Fig.3 Effect of cutting speed on cutting force
(Tool diameter: 1.0 mm)

3. Experimental Results and Discussion

3.1 Effect of cutting speed on cutting force

In order to investigate the effect of the cutting speed on the cutting force, milling experiments were conducted in the dry cutting environment using a micro end mill with diameter of 1.0 mm. **Table.1** shows cutting conditions in the experiments. The cutting speed was varied from 30 to 180 m/min.

Fig. 3 shows the effect of cutting speed on cutting force. Every force component of Fx, Fy and Fz increases moderately with an increase in the cutting speed. However, Fy increase drastically at a cutting speed of 180 m/min and its magnitude reaches at about three times bigger than that at 150 m/min.

As a matter of course, the cutting temperature increases with an increase in the cutting speed. It is therefore said in ordinary metal cutting that the cutting force decreases and approaches to the constant value, because the strength of the work material is decreased by high temperature. However, in micro end milling with small feed rate and depth of cut, it is estimated that the generation of cutting heat is low comparing with a conventional cutting. On the other hand, the possibility that the wear and chipping of the cutting tool generates mechanically by very high rotation speed of the spindle come to high. The drastic rise of the cutting resistance value will be described in a later section with the observation of the tool wear.

3.2 Relation between tool wear and cutting speed

Fig.4 shows the photographs of the flank wear of micro end mill observed at the rectangular area in Fig.2 after cutting the groove with length of 8 mm. The flank wear seems to be very small under the cutting speed conditions below 90 m/min. However, the wear increases with an increase in the cutting speed at 120 m/min or more. Especially, at the cutting speed of 180 m/min, the chipping is observed at the cutting edge of the tool. As mentioned in the previous section, the cutting force component Fy increased in the magnitude drastically. It is seemed that the variation of the cutting force is corresponding to the change of the wear and the chipping condition of the tool. The possibility of the chipping at the cutting edge become high, because the impact frequency per unit time becomes higher when the rotation speed of spindle becomes higher.

Table 1   Cutting conditions of this experiment

Work	Ti-6Al-4V	
Feed per tooth	10 μm/tooth	
Depth of cut	50 μm	
Cutting speed V m/min	Spindle speed min^{-1}	Feed rate mm/min
30	9554	191.1
60	19099	382.2
90	28648	573.2
120	38198	764.3
150	47746	955.4
180	57296	1146

(a)V=30 m/min   (b)V= 60 m/min

(c)V= 90 m/min   (d)V=120 m/min

(e)V=150 m/min   (f)V=180 m/min
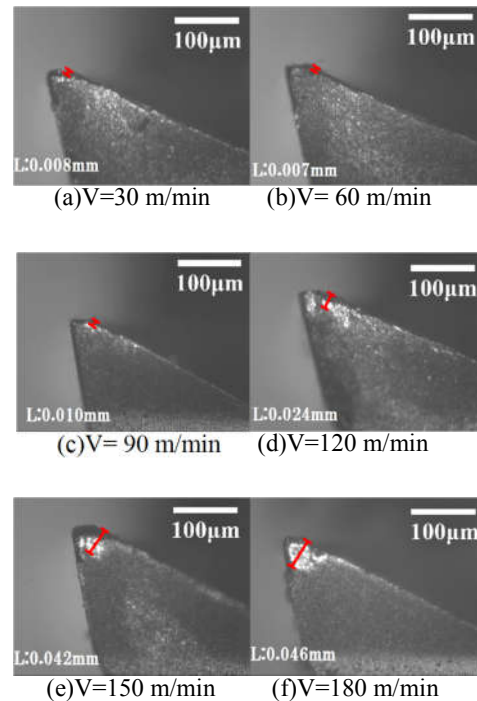
Fig.4   Photograph of wear of a major flank of
a cutting tool(Tool diameter:1.0 mm)

3.3 Effect of spindle rotation speed on cutting force

As described in Section 3.1, the cutting force (Fy) increased drastically at the cutting speed of 180 m/min with end mill of 1.0 mm diameter. A similar cutting experiment was carried out with tool diameters of 0.3 mm, 0.5 mm, and 1.5 mm in order to investigate the effect on the cutting force at still wider range of the cutting speed. Cutting conditions are shown in **Table 2**. The cutting speed was varied in the range from 18 to 270 m/min using the end mills of the different diameter because the maximum rotational speed of the spindle is 60,000 min^{-1}.

The change of the cutting force is summarized in the change of the cutting speed as shown in **Fig.5**. It is understood that the cutting force tends to increase with an increase in the cutting speed and drastically becomes large at certain cutting speed. Those four cutting speeds are corresponding to the same rotational spindle speed of 57,296 min^{-1}. It is expected that the rotational spindle speed influences strongly on the cutting force in the fine groove cutting of titanium alloy.

Therefore, the change of the cutting force was summarized in the change of the rotational spindle speed as shown in **Fig.6**. Although the tool diameter is different from 5 times at 0.3 mm and 1.5 mm, the variation of the cutting force is small. The cutting force tends to increase with an increase in the rotational spindle speed.

Table 2   Cutting conditions of this experiment

Work	Ti-6Al-4V		
Feed per tooth	10 μm/tooth		
Depth of cut	50 μm		
Tool diameter mm	Cutting speed V m/min	Spindle speed min^{-1}	Feed rate mm/min
0.3	18		
0.5	30	19099	382.2
1.5	90		
0.3	36		
0.5	60	38198	764.3
1.5	180		
0.3	54		
0.5	90	57296	1146
1.5	270		

Fig.5 Relationship between cutting speed and cutting force
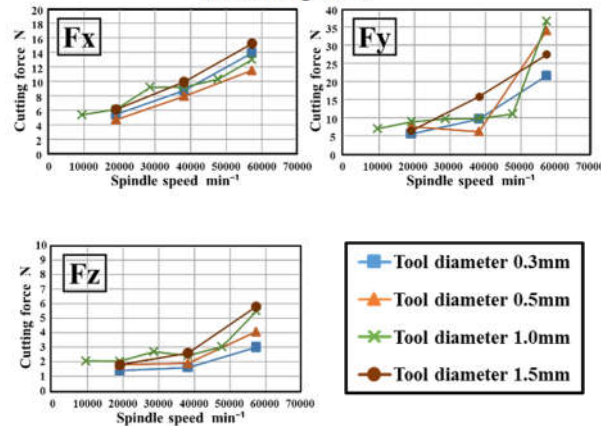
Fig.6 Relationship between spindle rotation speed and cutting force

3.4 Effect of cutting speed on surface roughness

Fig.7 shows an example of the observation of finished bottom surface. The surface roughness was measured along A-A, B-B and C-C of the feed direction. A-A and C-C are 100 μm away from the groove wall of the engage side and disengage side, respectively. B-B is a center of the groove. **Fig.8** shows an example of the measurement result of the surface profiles along A-A, B-B and C-C. It is seen that the surface roughness and the profile are difference depending on the measurement place A-A, B-B and C-C. **Fig.9** shows the effect on the cutting speed on the arithmetic average roughness (Ra). It can be seen from the graph that the roughness value on the A-A part of the groove is smaller than that on the B-B and the C-C part. The roughness along A-A part is almost constant not depending on the cutting speed. However, as a whole, the roughness becomes large in the low cutting speed of 30 m/min and tends to become large again in the high cutting speed.

267

Tool   Edge

Feed direction

1mm   Uncut
Groove   surface
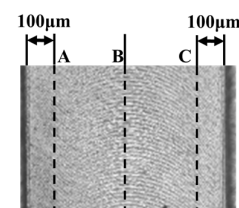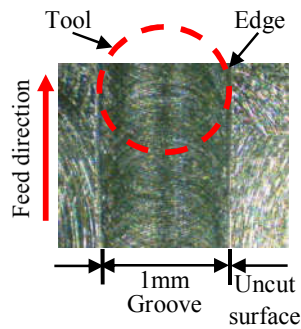
Fig.7 Observation of finished bottom surface
roughness
(Tool diameter:1.0 mm, V=180 m/min)
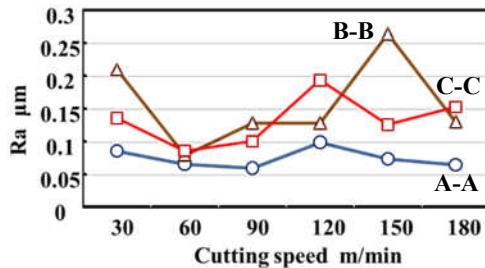
Fig.8 Effect of cutting speed on arithmetic average
roughness (Tool diameter: 1.0 mm)

A-A

B-B
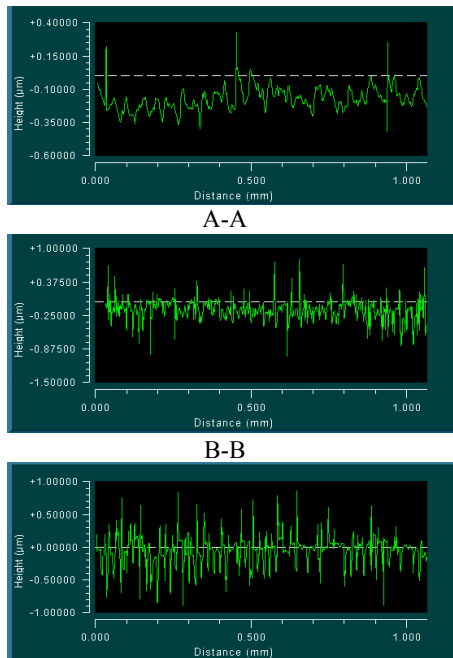
Fig.9 Roughness curve
(Tool diameter: 1.0 mm, V=180 m/min)

3.5 Burr formation at edge of groove

Burr formation is unavoidable in the slot milling. Burr has to be removed through another deburring process. However, the burrs generated by micro milling are difficult to be removed manually and then the special deburring tool is needed [4]. **Fig.10** shows the observation of typical burr generated at the groove edge under the condition of every cutting speed. It is seen from the photograph that the burrs is generated in the greatest size and the size tends to decrease with an increase in the cutting speed. As the cutting force increases with an increase in the cutting speed, other factor except the force such as the cutting heat is seemed to influence on the burr formation.

groove   edge

Feed direction

(a)V=30 m/min   (b)V= 60 m/min

(c)V=90 m/min   (d)V= 120 m/min

(e)V=150 m/min   (f)V= 180 m/min
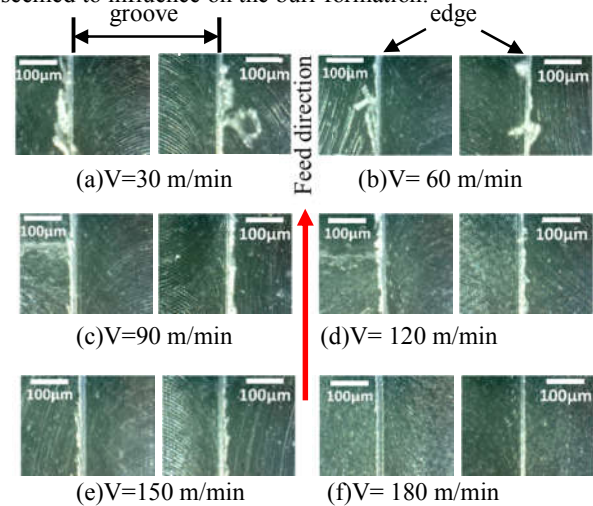
Fig.6 Burr formation by change of cutting speed
(Tool diameter: 1.0 mm)

4. Concluding Remarks

Through this experiments of micro end milling of titanium alloy, the following results were obtained.

1. In the experiment with the tool diameter of 1.0 mm, the cutting resistance value gradually increases in the range up to the cutting speed of 150 m/min, and the abrupt increase of Fy is observed at the cutting speed of 180 m/min.

2. With tool diameter 1.0 mm, tool wear increased at cutting speed of 120 m/min or more and chipping was confirmed at cutting edge at 180 m/min.

3. In the fine groove cutting of titanium alloy, it was found that the cutting resistance value changes depending on the spindle rotation number regardless of tool diameter and cutting speed.

4. From the roughness measurement results, on the tool engage side of the groove, the value of arithmetic mean roughness and maximum height of irregularities decrease as the cutting speed increases.

5. As the cutting speed increases, the amount of burrs generated at the edge of the cutting surface is reduced.

References

[1] I.INAGAKI: Application and Features of Titanium for Aerospace Industry, Nippon Steel&Sumitomo Metal Technical Report(2013), pp 23-28

[2]T.NARUSHIMA: Titaniumd its alloys as biomaterials, Journal of Japan Institute of Light Metals, Vol.55, No.11(2005), pp561-565

[3]K.KARINO：Nansakuzai no jouzunakezurikata(How to cutting difficult-to-cut materials -Titanium alloy-), Nikkan Kogyo Shimbun, Ltd (2012),pp3-6

[4]T.MATSUMURA：Research Issues in Micro Milling, Precision EngineeringVol.77 No.8（2011）,pp746-750

Diamond Fly Cutting Applied to Improve Form Accuracy by In-process Measurement and Control on an Ordinary Milling Machine

Jinhui Wang[1], Takanori Yazawa[1], Guochen Gu[1], Tomonori Kato[2], Tatsuki Otsubo[1]

[1]Affiliation

1-14 Bunkyo-machi, Nagasaki-City, Nagasaki, 852-8521, Japan

[2]Affiliation

3-30-1 Wajiro-higashi, Higashi-ku, Fukuoka-City, Fukuoka, 811-0295, Japan

ABSTRACT

This paper proposes to improve the form accuracy of a machined surface produced by an ordinary milling machine by diamond fly cutting using controlled cutting with reference surface (CCRS), an in-process measurement and control method. CCRS improves machined surface accuracy by controlling the relative displacement between the tool and workpiece. Diamond fly cutting using CCRS was demonstrated to reduce the table motion error on an ordinary milling machine.

1. Introduction

To improve the accuracy of the machined surface produced by an ordinary milling machine, a system called workpiece-referred form accuracy control (WORFAC) [1-3] was developed and confirmed in diamond turning. However, non-rotational symmetric surface structures, such as V-grooves, pyramid structures, F-theta lenses, and other freeform surfaces cannot be machined by diamond turning. Previously, a system [4] for improving micro-groove accuracy on an ordinary lateral milling machine was proposed by using controlled cutting with reference surface (CCRS) [5], which is based on WORFAC. Simulations and experiments confirmed that CCRS improves the machined surface accuracy. The research showed that accuracy can be improved if the digital control sampling time is enough shorter than the error motion period associated with the feed rate. However, the surface roughness increased when the feed rate decreased because the feed rate and cutting speed are the same in shaping operations. Consequently, fly cutting with CCRS was proposed because it combines a high cutting speed and low feed rate.

Fly cutting is a common cutting process, in which the diamond tool rotates at high speed and removes material from the workpiece surface incrementally, as illustrated in **Fig. 1**. Fly cutting is usually used to manufacture ultra-precision microstructures with nanometric surface roughness and submicrometric form accuracy, without the need for subsequent polishing. Nevertheless, a high level of accuracy has only recently been achieved on ultra-precision milling machines.

In this study, we verified the effectiveness of fly cutting with CCRS on an ordinary milling machine and showed its potential for reducing the cost of manufacturing ultra-precision microstructures in an ordinary machining environment.

2. Experimental system

The fly cutting experiments described here were carried out on a milling machine with 3-axis control (Osakakiko rakuraku-mill 3V).

2.1. CCRS operating principle and configuration

Fly cutting with CCRS is shown in **Figs. 2** and **3**. During fly cutting, the PZT actuator and laser displacement (gap) sensor (Keyence, LK-H008W) were both mounted rigidly on the machine table, and the fly cutter and reference surface were placed between them. All placements satisfied the Abbe principle. The spindle and support jig for the reference surface were both fixed to the machine body. The relative displacement between the gap sensor and reference surface was designed to be the same as the relative displacement between the fly cutter and workpiece.

Figs. 2(a) and **2(b)** show the principle of CCRS. When the workpiece surface moves away from or toward the fly cutter, the gap sensor detects the relative displacement between the reference surface and sensor, and then the sensor sends feedback to the PZT actuator to reproduce the same relative displacement between the workpiece and fly cutter. Thus, the control system compensates for movement to maintain the same distance between the workpiece and fly cutter in real time.

A horizontal cutting strategy was adopted for the feed direction, as shown in **Fig. 2(c)**.
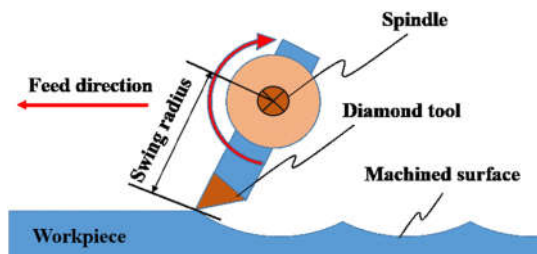
Fig. 1 Overview of fly cutting.
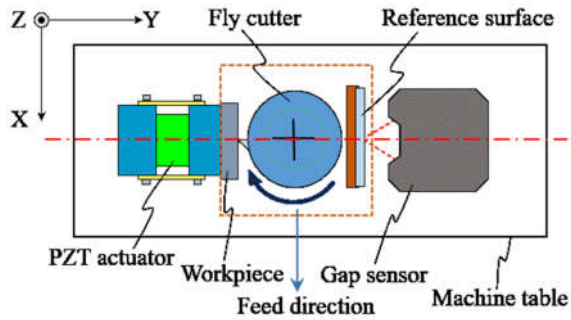
(a) Overhead view of fly cutting with CCRS.
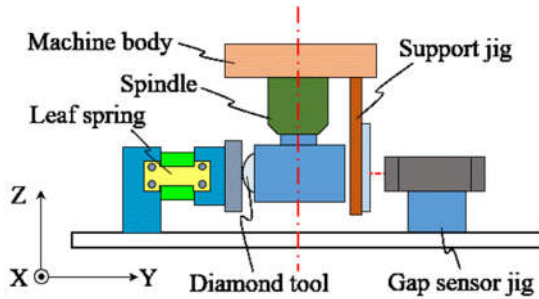
(b) Side view of fly cutting with CCRS.
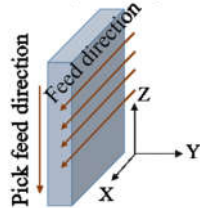
(c) Cutting strategy on workpiece.

Fig. 2 Fly cutting with CCRS.
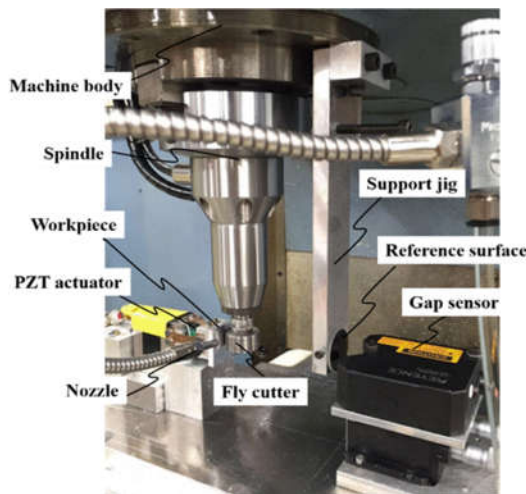
Fig. 3 Photograph of experimental setup for fly cutting with CCRS.
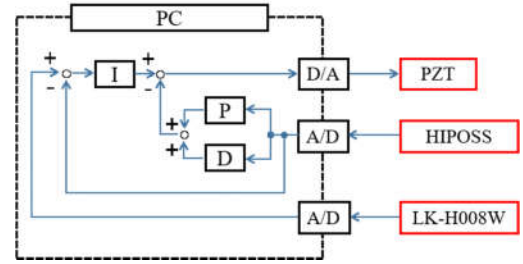
(a) Block diagram of I-PD control system.
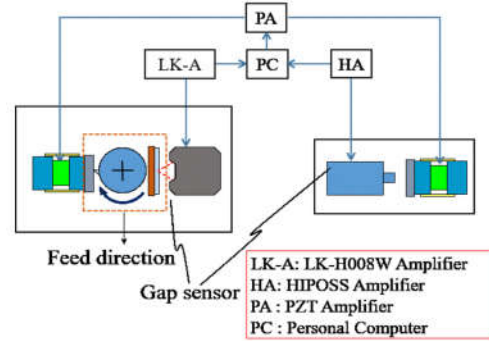
(b) System for correcting hysteresis.

Fig. 4 Fly cutting control system.

2.2. Fly cutting control system for correcting hysteresis

Fig. 4 shows the fly cutting control system. As shown in **Fig. 4(b)**, the displacement of another PZT actuator was measured by a high-precision optical surface sensor (HIPOSS) to maintain control in the presence of hysteresis.

2.3. Experimental conditions and noise

Table 1 describes the experimental conditions. The feed rate was set to ensure that the digital control sampling time was enough shorter than the error motion period. The aluminum alloy AlMg2.5 commonly used for ultra-precision machining was used as the workpiece material because it has appropriate hardness and good properties for machining by a diamond cutter. A single crystal diamond tool with a large tool nose radius of 20 mm was employed to cut the surface, as shown in **Fig. 5**.

Table1. Experimental conditions

Feed rate	5 mm/min
Spindle speed	2,500 rpm
Swing radius	13 mm
Tool Nose radius	Single crystal diamond 20 mm
Depth of cut	5 μm
Pick feed	0.5 mm
Lubricant	White kerosene
Material	AlMg2.5
Reference surface Flatness	Aluminum Mirror λ/10

271

Because the support jig for the reference surface is long, it vibrates easily during cutting. Thus, the noise detected by the gap sensor (LK-H008W), whose output convert to instruction values (setpoint), easily affects the machined surface. **Fig. 6** shows that the wave height
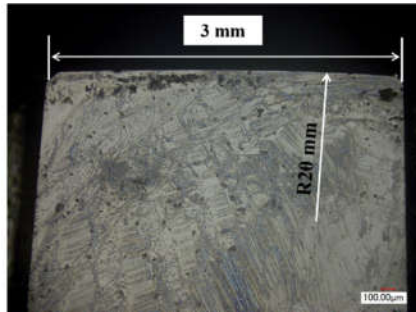
Fig. 5 Photo of single crystal diamond tool.
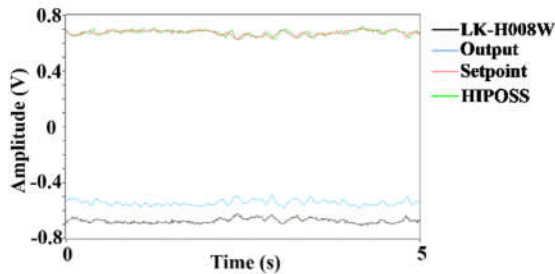
Fig. 6 Signal before cutting without low-pass filter.

of noise measured by LK-H008W only when the fly cutter is rotating (not cutting) is about 0.1 μm, which directly influences the accuracy of machined surface by about 0.1 μm. Moreover, the noise wave height becomes bigger than 0.1 μm when tool is cutting the workpiece and the machine table is moving. Therefore, the form accuracy cannot be controlled by less than 0.1 μm theoretically. In this study, a low-pass filter was used to control the noise.

3. Results and discussion

3.1. Uncontrolled cutting (in feed direction)

Fig. 7 Photo of machined surface.

Fig. 7 shows the machined surface. The parameter selected to evaluate the machined surface is the maximum height of the scale-limited surface (Sz). The value of Sz in **Fig. 8(a)** is about 0.5 μm, which includes mainly two kinds of waviness induced by table motion error: short-period waviness with a pitch of about 0.5 mm, wave height of about 0.3 μm, and frequency of about 0.17 Hz and long-period waviness with a pitch of about 3.5 mm, wave height of about 0.2 μm, and frequency of about 0.02 Hz.

From the profile of the machined surface along a measured length of 0.5 mm, as shown in **Fig. 8(b)**, we can see that no high-frequency component like in shaping at the sub-micrometric level appeared, even when the feed rate was slower than that needed for shaping. In previous studies, the surface roughness increased when the feed rate decreased because the feed rate and cutting speed were the same for shaping, and this created a high-frequency component that influenced the machined surface. However, in this study, the feed rate and cutting speed were separated by using a fly cutter, slowing down the feed rate, and maintaining a high cutting speed. The results show that the high-frequency component that degraded the surface finish was suppressed by fly cutting. As for low-frequency waviness caused by table motion error, it can theoretically be suppressed by controlled cutting.
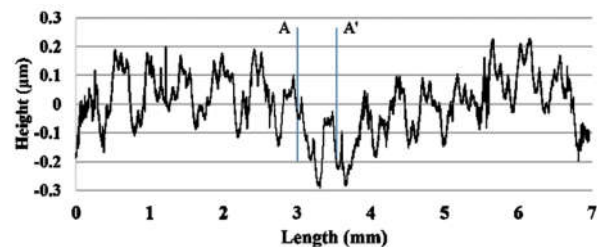
(a) Profile of machined surface.
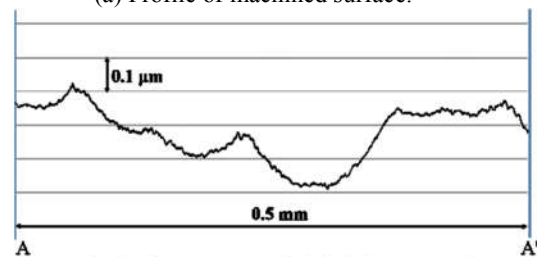
(b) Enlargement of A-A' from panel

Fig. 8 Profile of the machined surface without control in feed direction.

3.2. Controlled cutting (in feed direction)

When the low-pass filter cutoff was set to 0.3 Hz, the noise wave height measured by LK-H008W (no cutting) was reduced to about 0.05 μm (**Fig. 9**). Although Sz was improved from 0.5 μm to about

272
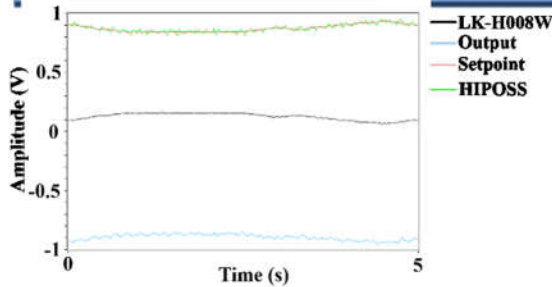
Fig. 9 Signal before cutting (cutoff frequency 0.3 Hz).
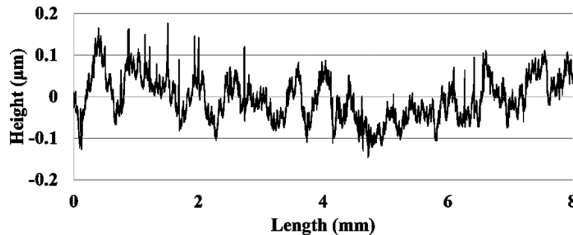
Fig. 10 Profile of the machined surface with control in feed direction (cutoff frequency 0.3Hz).
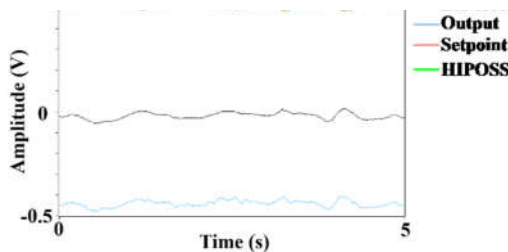
Fig. 11 Signal before cutting (cutoff frequency 1 Hz).

0.25 μm (**Fig. 10**) by controlled cutting, the short-period waviness, whose frequency is about 0.17 Hz, which is a useful signal near to the cutoff frequency 0.3 Hz, was attenuated by the low-pass filter but reflected in the machined surface. This result showed the effectiveness of CCRS. To improve the quality of the machined surface, the cutoff frequency should be much bigger than 0.17 Hz.

Fig. 11 shows the noise when the cutoff frequency was set to 1 Hz. Because the short-period waviness signal could pass low-pass filer completely used as signal need to be controlled by fly cutting control system, Sz was improved from about 0.5 μm to less than 0.2 μm, as shown in **Fig. 12(a)**. This result showed that the short-period waviness and long-period waviness were both controlled effectively by fly cutting control system even though the influence of noise in cutting process was left on the machined surface as shown in **Fig. 12(b)**. In addition, Sz could not be controlled to less than 0.1 μm theoretically because the wave height of noise is near 0.1 μm during tool rotation without cutting, as shown in **Fig. 11**.

The results shown in **Figs. 8** and **12** show that the accuracy of a surface machined with CCRS is better than that without CCRS, and no high-frequency component
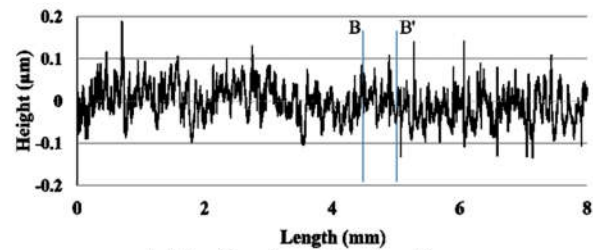
(a) Profile of machined surface.
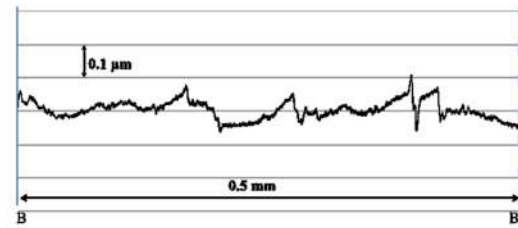
(b) Enlargement of B-B' in panel (a).

Fig. 12 Profile of the machined surface with control in feed direction (cutoff frequency 1 Hz).

like in shaping at sub-micrometric level was produced in the machined surface, even though noise was mixed into the control signal. Improvement of the design of the reference surface support jig should reduce the noise, and the machined surface quality might improve further.

Conclusions

This study evaluated the accuracy of a surface machined by fly cutting on an ordinary milling machine with and without cutting control by CCRS. Our conclusions are as follows:

1. The high-frequency component that degrades the machined surface finish during shaping can be suppressed by fly cutting.
2. The accuracy of the machined surface can be improved on an ordinary milling machine by this control cutting system (to obtain Sz less than 0.2 μm).
3. Further noise suppression will increase the quality of the machined surface.

References
[1] T. Kohno, T. Yazawa, D. Saito, and S. Kohno, "Figure error control for diamond turning by in-process measurement," *Precision Engineering*, vol. 29, no. 4, pp. 391-395, 2005.
[2] T. Yazawa, T. Kohno, Y. Uda, and N. Ohno, "In-process measurement and workpiece-referred form accuracy control (6th report)," *Journal of the Japan Society for Precision Engineering*, vol. 64, no. 12, pp. 1806-1810, 1998. (in Japanese)
[3] Y. Uda, T. Kohno, T. Yazawa, T. Suzuki, and A. Soyama, "Concept and basic study of improvement system of surface roughness, waviness and figure accuracy by WORFAC,"

Journal of Materials Processing Technology, vol. 62, no. 4, pp. 423-426, 1996.

[4] T. Yazawa, Y. Hattori, Y. Ogiya, and T. Kojima, "Figure error control for microgrooving on ordinary lateral milling machines using a reference surface to control cutting," *International Journal of Automation Technology,* vol. 3, no. 4, pp. 428-432, 2009.

[5] T. Yazawa, T. Yamazaki, and T. Kohno, "In-process measurement and workpiece-referred form accuracy control (7th report)," *Journal of the Japan Society for Precision Engineering*, vol. 64, no. 11, pp. 1689-1693, 1998. (in Japanese)

Possibility of Repeated Recycle of Water-soluble Cutting Fluids

Kenji Yamaguchi[1], Mitsugu Yamaguchi[2], Yasuo Kondo[3] , Satoshi Sakamoto[4]
[1] National Institute of Technology, Yonago College
[2] Salesian Polytechnic
[3] Yamagata University
[4] Yokohama National University

ABSTRACT

In metal machining process, water-soluble cutting fluids are commonly used as a coolant and lubricant. To decrease the environmental load and waste cost of water-soluble cutting fluids, we have focused on the water recycling system for waste water-soluble cutting fluids. In this study, we employed three types of surfactant for a corrosion inhibition performance improved amine-free cutting fluid, and examined the changes of corrosion inhibition performance of the recycled coolant.

Keyword: cutting fluid, water recycle, amine-free fluid, green manufacturing

1. Introduction

In metal machining process, water-soluble cutting fluids are commonly used as a coolant and lubricant[1]. Several tens to hundreds litter water-soluble cutting fluids are stored in a coolant tank for every machine tools. The characteristics of the water-soluble cutting fluids will change by operation. The deteriorated water-soluble cutting fluids are exchanged for several months. Currently, most of wasted water-soluble cutting fluids are incinerated[2]. However, the incineration of waste water-soluble cutting fluids will cause environmental damage due to the emission of carbon dioxide and chemical additives in the water-soluble cutting fluids. In addition to reduce the machining costs, we cannot ignore the management cost of the waste water-soluble cutting fluids. To decrease the environmental load and waste cost of water-soluble cutting fluids, we have focused on the water recycling system for waste water-soluble cutting fluids[3,4]. In the recycling system, the waste water-soluble cutting fluid is separated to water phase and oil content by a surfactant, which can break the emulsion of the cutting fluid. Then the extracted water is filtrated by powdered activation carbon bed. The recycled water is reutilized as a diluent of the new coolant. In earlier studies, we found that some waste-water soluble cutting fluids can be processed in the recycling system. Especially, an amine-free cutting fluid showed good recyclability in lower costs and has better or equal cooling and lubricating performance compared with other types of coolants. However, we have two major problems. The amine-free water-soluble cutting fluid showed poor corrosion inhibition performance in general machining operation[5]. Moreover, the surfactant used in recycling process worsening the corrosion inhibition performance of the recycled water-soluble cutting fluid[6]. In this study, we employed three types of surfactant for a corrosion inhibition performance improved amine-free cutting fluid, and examined the changes of corrosion inhibition performance of the recycled coolant.

2. Experimental Method

2.1 Water-soluble coolant used in experiments

In this study, we used a prototype amine-free cutting coolant that has been improved corrosion inhibition performance compared with a commercially available amine-free coolant[6]. Most water-soluble coolants contain alkanolamines for corrosion inhibition and pH maintenance; however, alkanolamines are difficult to eliminate from water-soluble coolants in waste treatment using chemical and physical processes. Some amine-free water-soluble coolants have been developed and are commercially available. The use of amine-free coolants is expected to reduce the environmental load in coolant waste treatment. In former study, we found a commercially available amine-free coolant is suitable for our recycling treatment[5]. The amine-free coolant showed good cooling and lubricating performance, however the corrosion inhibition ability of the coolant was insufficient for general machining operation. We requested the manufacturer to improve the performance and got a prototype of a corrosion inhibition performance improved amine-free coolant[6].

The prototype amine-free coolant is an emulsion type (JIS A1). Figure 1 shows the relationship between the
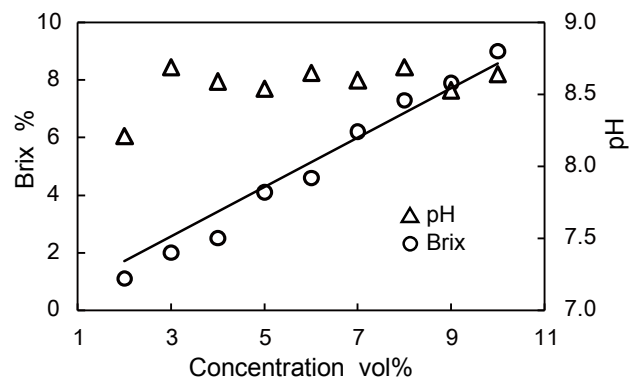
Fig.1 Relationship between concentration of the prototype amine-free coolant and Brix, pH

concentration of the prototype coolant and Brix (reflective index of a solution), pH[6]. The Brix value was measured by a digital Brix mater (Atago PAL-1), and the pH value was measured using a pen-type digital pH mater (pHTester30). The Brix of the coolant was proportional to the concentration of the coolant. The pH of the coolant was kept alkalescent to prevent putrefaction.

2.2 Recycling process of the amine-free coolant
Figure 2 shows the surfactant-activated carbon water recycling process from amine-free water-soluble coolants[4]. A surfactant is mixed into the waste coolant. The added surfactant obstructed the action of preexistent surfactants in the coolant. As a consequence, the coolant was broken off and the oil content was separated as a floating matter. In order to eliminate these substances, a powdered activated carbon is mixed

Fig.2 Water recycling process of surfactant-activated carbon filtration.

into the treated coolant. Then the coolant is filtered with filter paper. The filtration of the solution yields clear oil free water. This method is applicable to both conventional amine-containing coolants and amine-free coolants. However, from the view point of the quality of recycled water and the processing time, the method applied to the amine-free coolants is superior.

In previous study, we found the surfactant used in recycling process worsening the corrosion inhibition performance of the recycled amine-free water-soluble coolant[5]. In this study, to investigate the influence by the type of surfactants, we employed three types of cationic surfactants. The surfactant A has been used in previous studies[4-6]. The surfactant A has showed better emulsion breaking ability, however we found the surfactant A deteriorate the corrosion inhibition performance of the recycled coolant diluted with recycled water[6]. The surfactant B and C are chlorine-free non-corrosive microbicides.

In this study, we conducted beaker-scale tests. We prepared the coolants by diluting them with tap water. The concentrations of the coolants were 5vol%. The initial quantity of the coolants was 50 ml. We added 1.0 gram of the surfactants, and extracted recycled water by filtration in powdered activated carbon. The recycled coolant was diluted to 5vol% with 20ml of recycled water.

To examine the corrosion inhibition performance of the coolants and recycled water, we carried out the following test. One gram of cast iron (FC300) chips was put onto a filter paper inside a 36-mm-diameter circle. Then, 1 ml of coolant was evenly dropped onto the chips. After six hours, at room temperature, rust formation marks that were transferred onto the filter paper were observed.
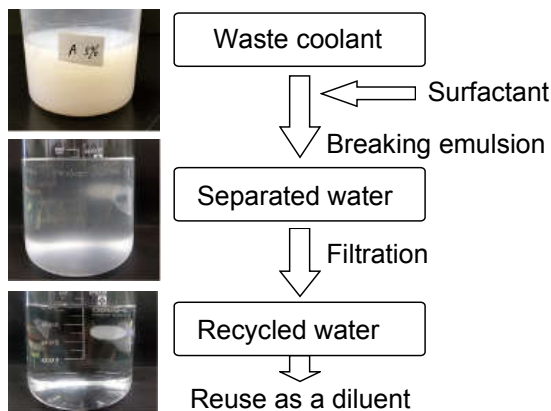
Surfactant A

Surfactant B

Surfactant C

After surfactant treatment

Just after dilute the coolant wiht recycled water

After 24hours of the recycled coolant
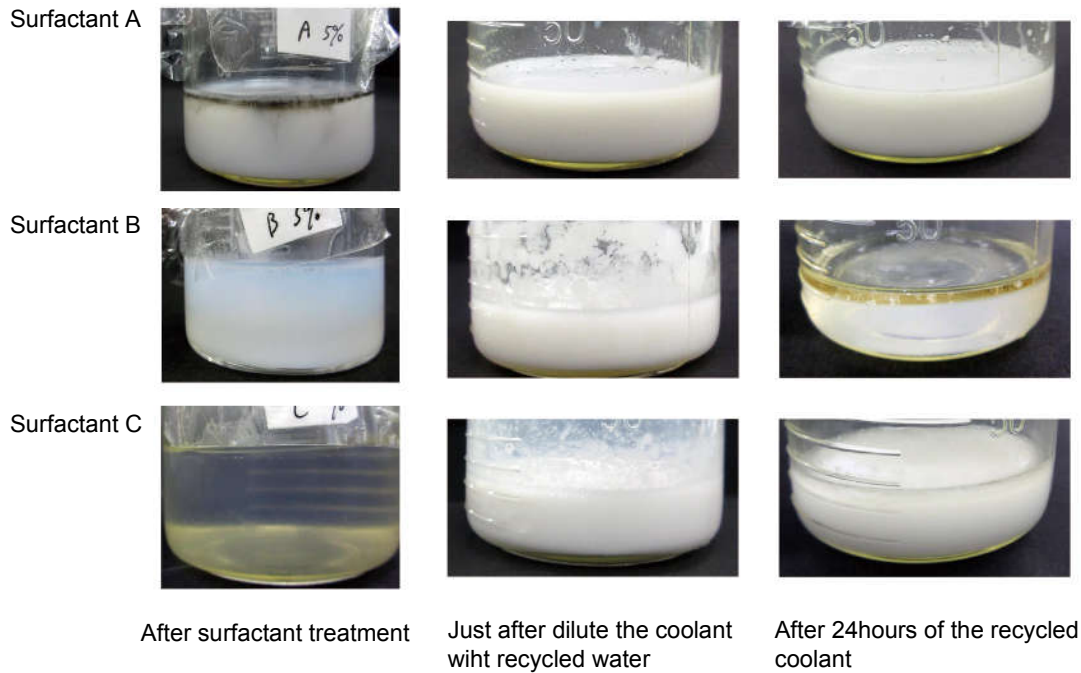
Fig.3 Appearances of recycled water and recycled coolant

Conventional amine-free coolant (virgin, concetration 5%)

Concetration 3%   5%   10%

Prototype corrosion inhibition improved amine-free coolant (virgin)

Fig.4 Corrosion inhibition performance of virgin amine-free cutting coolant

Surfactant A   Surfactant B   Surfactant C

Fig.5 Corrosion inhibition performance of recycled water processed by the surfactant-activated carbon treatment
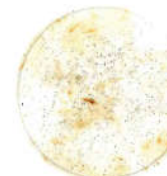
Surfactant A   Surfactant B   Surfactant C

Fig.6 Corrosion inhibition performance of recycled prototype amine-free coolant diluted with recycled water (concentration 5%)

Figure 3 shows the appearances of recycled water and recycled coolant.
In this experiment, the recycled water by using the surfactant A did not become transparent, and the Brix of the recycled water was 3.8%. This suggests that the emulsion break by the surfactant A was insufficient. In the previous studies, we have obtained transparent recycled water by the surfactant A, the reason it did not become transparent in this experiment is unknown at the present stage. As shown in figure 3, the recycled coolant diluted with the recycled water by using surfactant A showed stable emulsion, and the Brix was the recycled coolant was 6.0%. No emulsion break or separation of the oily contents was observed after leaving at room temperature in the beaker for 24 hours.

277

The recycled water extracted by the surfactant B also exhibited a pale white, the Brix was 3.6%. The emulsion breaking ability of the surfactant B was better than that of the surfactant A, however, removal of the residual surfactant by the powdered activated carbon filtration was insufficient. The recycled coolant diluted with the recycled water extracted by the surfactant B was emulsified just after dilution, but precipitates were observed. The Brix of the recycle coolant was 1.4%. After leaving in the beaker at room temperature for 24 hours, the recycle coolant separated into oil and water phase. It is likely that the residual surfactant B prevented emulsification of the recycle coolant.

The recycled water extracted by the surfactant C was transparent. The Brix was 6.4%, which was higher than that of the recycled water processed by surfactants A and B. The recycled coolant diluted with the recycled water by using the surfactant C formed white emulsion, but a slight precipitate was observed. However, no separation was observed after leaving in the beaker for 24 hours.

Figure 4 shows the results of the corrosion inhibition performance tests of the virgin amine-free coolants.

In the conventional amine-free coolant diluted with a tap water at concentration 5%, the rust formation mark was observed throughout the test circle area. In previous study, we operated the conventional amine-free coolant for more than six months in a 3-axix machining center [5]. We did not observe the rust formation on the machining center or the tools. However, this poor corrosion inhibition performance is not recommended for a general cutting operation.

The corrosion inhibition improved prototype amine-free coolant showed little rust formation of concentration 3 to 10%. This corrosion inhibition performance is comparable to conventional amine-containing cutting coolants.

Figure 5 shows the corrosion inhibition performance of recycled water processed by the surfactant-activated carbon treatment. These results showed the corrosion inhibiter in the coolant was removed by the water recycle process.

Figure 6 shows the corrosion inhibition performance of the recycled prototype amine-free coolant diluted with recycled water. The concentration of the coolants was 5vol%. The corrosion inhibition performance of the recycle coolant diluted with the recycle water treated by the surfactant A worsened. This suggests the component of the surfactant A remaining in the recycled water has impaired the corrosion inhibition performance. The coolant diluted with recycled water treated by the surfactant B showed better corrosion inhibition performance. However, as mentioned above, the recycle coolant did not form the stable emulsion. In the recycle coolant diluted with recycle water treated by the surfactant C, the rust formation was suppressed as compared with the surfactant A.

From these results, the surfactant C is suitable for both recyclability and corrosion inhibition for the water recycle treatment. However, the corrosion inhibition performance of the recycle coolant inferior to that of the virgin coolant. The selection of optimal surfactant for the recycle process is a future task.

4. Conclusions

To reduce the environmental load of the waste water-soluble coolant, we proposed the recycling system by using amine-free coolant and water recycle process with surfactant-activated carbon. In this study, we employed three types of surfactant for a corrosion inhibition performance improved amine-free coolant. We found some type of surfactants remain in recycled water and the residual surfactants deteriorate the corrosion inhibition performance and make the recycle coolant unstable.

References
[1] E.M.Trent, P.K.Wriht, *Metal Cutting*, Butter-worth Heinemann,(2000)311-337.
[2] Journal of Economic Maintenance Tribology ed., *Current Status of Waste Water-soluble coolant and its Waste Treatment* (in Japanese), Journal of Economic Maintenance Tribology, (2005) 2-8.
[3] Y. Kondo, K. Yamaguchi, K. Yamada, S. Sakamoto, *A Metabolic System for Water-soluble Coolant—Water Resource Recovery from Spent Water-Soluble Coolant*, Proceedings of the 1st International Conference on Manufacturing, Machine Design and Tribology, (2005) CD-ROM.
[4] T. Takada, Y. Kondo, K. Yamaguchi, S. Sakamoto, *Study on recycling of waste water from spent water-soluble coolant*, Journal of Mechanical Science and Technology24, (2010) 267-270.
[5] T. Kodani, K. Yamaguchi, Y. Kondo, S. Sakamoto, *Possibility of Recycling Amine-Free Water-Soluble Coolants*, Journal of Advanced Mechanical Design, Systems, and Manufacturing, 6-1, (2012) 65-75.
[6] K. Yamaguchi, K. Ogawa, T. Fujita, Y. Kondo, S. Sakamoto, M. Yamaguchi, *Property and Recyclability Change of Corrosion-inhibition-improved Amine-free Water-soluble Cutting Fluid with Repeated Recycling*, Key Engineering Materials, 749(2017)65-69

Optimum Cutting Conditions of Materials Using Coated Radius End Mill

Nobunao Kato, Masahiro Anzai, Takekazu Sawa
SHIBAURA INSTITUTE OF TECHNOLOGY
3-9-14, Shibaura, Minato-ku, Tokyo, 108-0023, Japan

ABSTRACT

It was investigated about the optimum cutting conditions of various materials
Its material are Nickel, Inconel, Monel, Invar, Tantalum and Molybdenum.
It was clarified that the peripheral speed which minimizes tool wear existed.
Keywords: High Speed Milling, Radius End mill, Tool Wear, Surface Roughness

1. Background

Mechanical elements of High Speed Milling include milling conditions, machine tools, materials, and tooling materials. Workability of milling is known to improve under conditions where those elements are optimally arranged.

For, milling conditions affect heat, milling forces, surface finish, and tool life. Thus, finding the most suitable milling condition is a key to upgrading of milling.

Meanwhile, it is well known that various factors affect such processing conditions. Hence, it is crucial to understand them to help improve High speed milling.

2. Objective and significance of this research

In this experiment, we are trying to explore optimal cutting conditions for High speed milling by using Carbide Coated Radius End mill MSR440 (NS Tool). We will examine how it behaves for different types of materials and under different settings, and construct a database. The objective of the research is to obtain an insight from the database.

As a first step, I changed cutting speed. And I investigated the influence that a tool receive.

In addition, I paid my attention to the influence that Ni content level. Because Ni has strong viscous.

This experiment examines changes of tool wear level by different Ni content level in the work material at milling. Another objective of the present experiment is to explore optimal milling conditions for so called difficult-to-cut materials.

3. Method

Fig. 1 shows an external view of the machining center used for the experiment (Sodick, MC430L). Materials are cut plane by using this. Milling speeds were mainly used as parameters. Fig. 2 shows the external view of tools used (NS Tool, Carbide Coated Radius End mill, MSR440). After being cut plane, roughness of surfaces of work materials and degree of tool wear were measured. Fig. 3 shows the surface finish measurement

device, Kosaka Laboratory, Surfcorder SE300. Fig. 4 shows the table top scanning electron microscope (JEOL, NeoScope LCM-6000).

Pure nickel, Inconel, Monel, invar alloy, molybdenum, tantalum were provided as the materials.

Table 1-2 shows milling conditions.

Fig. 1 MC430L
Table 1. The detail of Tool

Carbide Coated Radius End mill MSR440 (NS Tool)	
Tool diameter (mm)	6
The number of the blades	4

Fig. 2 MSR440

Fig.3 Surfcorder SE300   Fig.4 NeoScope
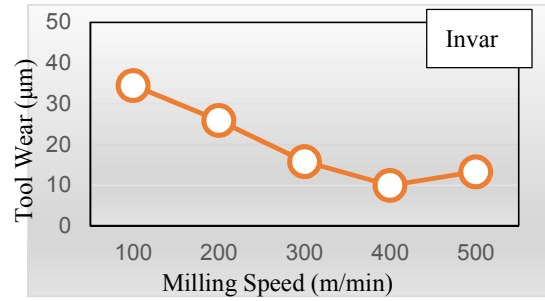
Fig.8 Relationship between milling speed of Invar and tool wear
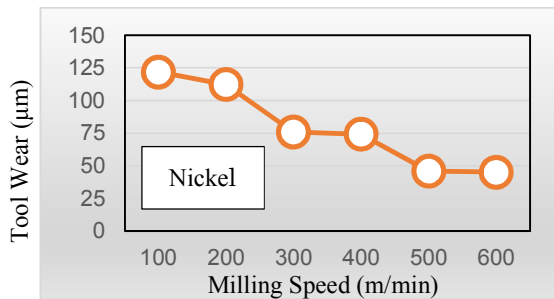
Fig.5 Relationship between milling speed for Nickel and tool wear

Fig. 9 Minimum tool wear at Nikkel

Fig.6 Relationship between milling speed for Inconel and tool wear
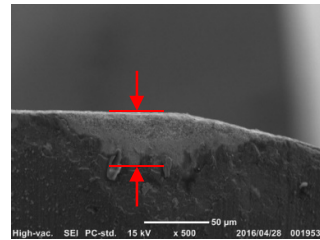
Fig. 10 Minimum tool wear at Inconel
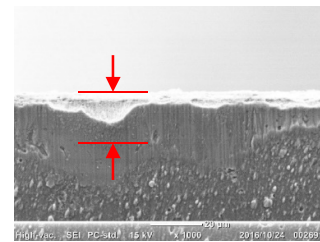
Fig. 11 Minimum tool wear at Monel

Fig.7 Relationship between milling speed for Monel and tool wear
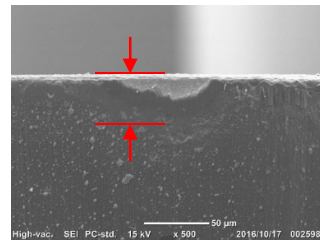
Fig. 12 Minimum tool wear at Inver

Table 2. Milling conditions of Ni group

	Molybdenum	Tantalum
Feed speed (mm)	0.05	0.05
Pf (mm)	0.015	0.015
Cutting depth (mm)	0.05 0.01	0.05
Milling speed (m/min)	100-600	200-600

Table 2. Milling conditions of Molybdenum and Tantalum

	Nickel	Inconel	Monel	Inver
Feed speed (mm)	0.05	0.05	0.05	0.05
Pf (mm)	0.2	0.2	0.2	0.2
Cutting depth (mm)	0.05	0.05	0.05	0.05
Milling speed (m/min)	100-600	100-500	100-500	100-500
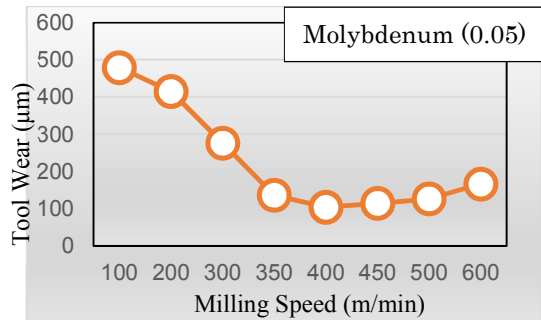
Fig.13 Relationship between milling speed of molybdenum and tool wear (Cutting depth 0.05)
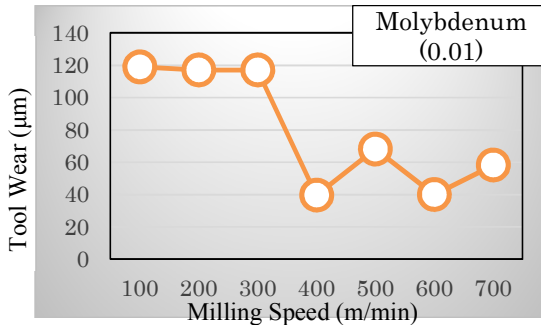
Fig.14 Relationship between milling speed of molybdenum and tool wear (Cutting depth 0.01))
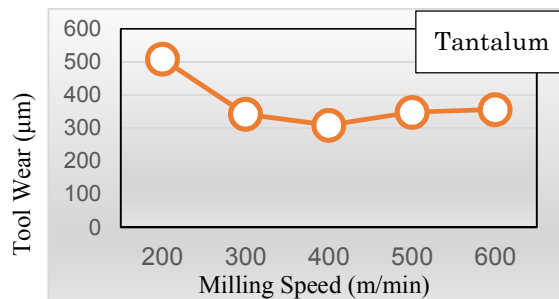
Fig.15 Relationship between milling speed of tantalum and tool wear
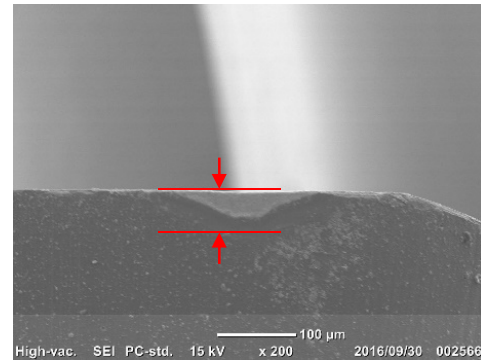
Fig. 16 Minimum tool wear at Molybdenum (Cutting depth 0.01)
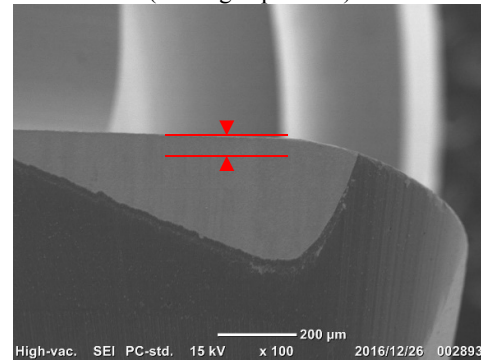
Fig. 17 Minimum tool wear at Tantalum

4. Results and Discussion

Fig. 5 - Fig. 8 and Fig. 13 - Fig. 15 show relationship between peripheral speed of each materials and tool wear.

Regarding pure nickel, the faster the cutting speed, the better the tool wear result became.

As to Inconel, tool wear was small up to 200 m/min. of milling speed. Once the speed was over 200m/min, tool wear ratio increased to cause chipping and adhesive wear.

Concerning Monel, it can be said that the appropriate milling speed is around 200m/min. For invar alloy, it is around 400m/min.

Regarding Monel and invar, no result showed that more

cutting depth resulted in more tool wear, which was a good result.

Overall, appropriate conditions for Ni group are found in 200m/min -400m/min. range of milling measurement. Looking at molybdenum and tantalum, wear range to cutting depth became very large at each milling speed. Both molybdenum and tantalum showed severe tool worn ratio at low speed range and it is observed that coating layers were peeled off. At milling speed of 350m/min. - 500m/ min. range, friction tends to be decreased. Thus, it can be said that appropriate conditions exists around 400m/min.

Regarding Nickel group, it is observed that material chips were adhered at milling. It is considered that this may be caused due to high viscosity of nickel. Also, chips are vehicles to promote adhesive wear at milling. Friction form at low speed range of tantalum and molybdenum is very similar and it is thought that similar phenomena was occurred for both materials. . It would be caused by extreme adhesive wear, not by friction between the tool and the work materials.

Regarding difference of tool wear ratio due to Nickel content, Invar at 35% of nickel content and Monel at 65% of nickel content were less worn compared to cutting depth. On the other hand, Inconel at 72% and pure nickel at 100% were more worn compared to cutting ratio. Thus, Nickel is one of factors to cause malfunctions.

Fig. 18 show Relationship between Ni content level and tool wear. I focused the influence of Ni content level in this study. Tool wear was obtained in this experiment as tool wear increased as Ni content level, but the influence of other ingredients of materials and a number of materials subjected to cutting in this study, I felt it was necessary to pursue from in the future.

References
[1] T. Matsuo, M. Anzai, *Fundamentals of cutting* (2013)
[2] K. Kano, *How to cutting difficult-to-cut materials Mold material*, (2011)

Fundamental Study on Curved Hole by EDM Drilling Using a Suspended Ball Electrode into Practical Materials

Kohei Ota[1], Shuoxun Li[1], Akira Okada[1], Yasuhiro Okamoto[1], Atsushi Yamaguchi[2]
[1]Graduate School of Natural Science and Technology, Okayama University,
3-1-1, Tsushimanaka, Kita-ku, Okayama, 700-8530, Japan
[2]Hyogo Prefectural Institute of Technology, Kobe, 654-0037, Japan

ABSTRACT

In this study, curved hole drilling with small-diameter using a suspended ball electrode into practical materials such as aluminum alloy and cemented carbide are discussed for wide application of this method. In order to stabilize the drilling performance of small-diameter holes, the vibration is applied to the workpiece during the process. A restart of drilling from the bottom of the already drilled hole by workpiece vibration is also discussed. As a result, by workpiece vibration, a hole with small-diameter of about 3.0 mm can be achieved using a smaller ball electrode.

Keywords: EDM, curved hole, workpiece vibration, hole diameter, suspended ball electrode

1. Introduction

Curved holes with small-diameter are required as a flow path in hydraulic equipments or metal molds. However, it is impossible to obtain such curved holes by conventional removal processes, such as drill operation. In mechanical machining methods, high rigidity in tool component is required because large machining force acts on the tool. Therefore, it is difficult to change the tool direction along the path of curved hole.

On the other hand, there is no need to rigidly fix the tool electrode in electrical machining process, because it is a non-contact process. Some electrical machining methods for curved hole drilling have been reported. Ishida et al. [1] proposed a flexural electrode support structure composed of a wire and a coil spring, and performed curved hole drilling using it. Takeuchi et al. [2] achieved a curved hole by ECM using ball electrode supported by a flexible tube.

This study aims to achieve curved holes in a very simple way and proposes a method of using general ED machine and simple structure electrode. Figure 1 shows a schematic illustration of the proposed method. The suspended ball electrode with a flexible lead part, such as thin wire or film, always drills vertically downwards owing to its gravity, because the machining force has little effect on the ball electrode. The drilling direction can be changed at any arbitrary depth by tilting the workpiece during the drilling process. It is possible to obtain a curved hole having a desired shape by repeating this process.

In our previous studies [3, 4], the suspended ball electrode structure was optimized, and the effect of ball diameter on EDM characteristics was investigated using zinc alloy as a workpiece material. Then, high possibility of curved hole drilling by EDM using a suspended ball electrode was shown. However, drilling of small-diameter hole into steels or other practical materials is impossible because discharges cannot continue stably and arc stop frequently occures. In order to apply this

processing method to practical use, it is necessary to develop a method for stable curved hole EDM drilling into practical materials using small ball electrodes.

In this study, small-diameter hole drilling using the suspended ball electrode into practical materials such as aluminum alloy and cemented carbide are discussed for wide application of this method. In order to stabilize the EDM drilling performance of small-diameter holes, a small vibration amplitude of several hundred micrometers is applied to the workpiece during the process. Then, the EDM drilling characteristics are experimentally investigated by varying the electrical conditions and the vibration amplitude conditions. In addition, a stable restart of drilling from the bottom of the already drilled hole by workpiece vibration is also discussed. Furthermore, the reduction of machinable hole diameter is tried by using a ball electrode with smaller-diameter.
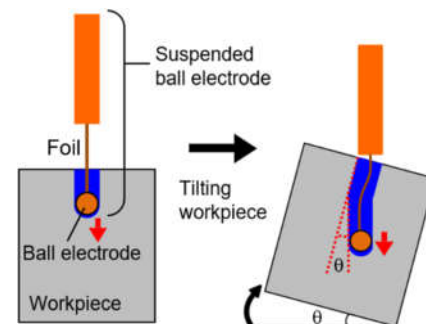
*Fig. 1 **Drilling** method of bended hole using suspended ball electrode*

2. Experiment method

The suspended ball electrode, which consists of a ball electrode and a thin copper foil, is shown in Figure 2(a) The material of the ball electrode is cupper tungsten (70 mass % W–Cu), and its diameter is 2.0 - 5.0 mm. The copper foil is 0.02 mm thick, 4.0 mm wide, and 60 mm long. The electrode ball and the foil were bonded by

silver brazing. The copper foil surface was covered by an extremely thin insulation film to avoid short-circuiting with the internal surface of hole machined into the workpiece. Workpiece materials are aluminum alloy (Al–2.5 wt %Mg, A5052) widely applied to heat exchanging parts, and cemented carbide (WC–1.0 wt %Co, SS13) applied to metal mold materials. Experiments were carried out by using a NC die sinker ED machine (Sodick AP1L / AQ35LR), and the EDM conditions are listed in Table 1. In this study, EDM characteristics were investigated by changing the discharge current (i_e) and servo voltage (S_V). Electrode jump motion was not used. Figure 2(b) schematically illustrates the vibration equipment used for the workpiece vibration. The vibration is generated by using a turbine vibrator (EXEN, BTP24), and the amplitude can be changed by varying the flow rate of air supplied from a compressor. The vibration is transmitted to the workpiece through the L-shaped stay as shown in the figure.
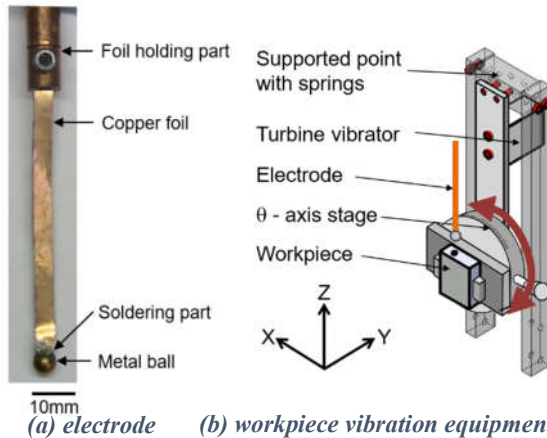
(a) electrode   (b) workpiece vibration equipment
Fig. 2 Appearances of suspended ball electrode and workpiece vibration equipment

Table 1 EDM conditions

Workpiece	Aluminum alloy (A5052)	Cemented carbide (SS13)
Electrode polarity	Anode	Cathode
Open circuit voltage	120, 250 V	
Pulse duration t_e	10, 400 µs	
Duty factor τ	50%	
Discharge current i_e	4 – 48 A	
Servo voltage S_v	50 – 230 V	

3.1. Restart of drilling with workpiece vibration.
In curved hole drilling by EDM using suspended ball electrode, a stable restart of drilling from the bottom of hole drilled already is essential for longer hole drilling. When the drilling stops in this method, the ball electrode is often in contact with the bottom of hole. Therefore, the restart of drilling was tried to open the gap by the workpiece vibration. Figure 3 shows the time variation

of drilled depth after restart of drilling for Al alloy. For comparison, that in case of normal drilling from the top surface of the workpiece is shown in the graph. Stable restart was always possible with workpiece vibration, and the performance was the same as normal drilling. In this drilling method, it is difficult to remove the debris when drilling depth is deep, because electrode jumping operation cannot be used. However, using this technique, even if the drilling stops with excessive debris accumulation in the hole, we can easily continue drilling after removing the debris in the hole, which enables deeper curved hole. Similar result was obtained for WC-Co.
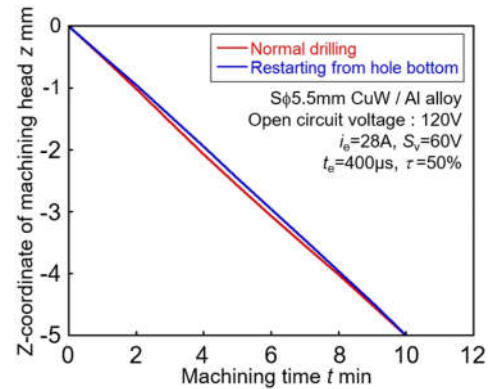
Fig. 3 Restart of drilling with workpiece vibration
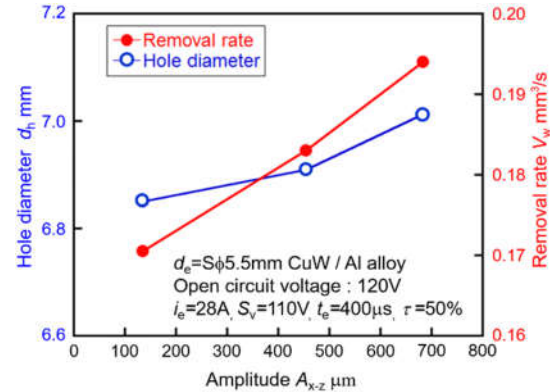
Fig. 4 Effects of workpiece vibration amplitude on removal rate and hole diameter for Al alloy

3.2. Influence of workpiece vibration amplitude

The influence of workpiece vibration amplitude of the workpiece on machining characteristics was investigated. Figure 4 shows variations of hole diameter and removal rate when the workpiece vibration amplitudes Ax-z are changed from 134 μm to 678 μm. Using an ball electrode with a diameter of Sφ5.5 mm, the discharge current was fixed at 28 A, and the servo voltage Sv was fixed at 110 V. As show in the figure, the hole diameter and the removal rate increase as the workpiece vibration amplitude increases. This results show that workpiece vibration makes it possible to keep an appropriate wide gap distance, in which debris and bubbles can be appropriately removed and the drilling state is more stabilized. The hole diameter was 6.85 mm when the workpiece vibration amplitude was 134 μm, while it was was 7.01 mm when the amplitude was 678 μm. Despite the increase in workpiece vibration amplitude by about 540 μm, the drilled hole diameter increased only by about 100 μm. In other words, only by adding the workpiece vibration regardless of workpiece vibration amplitude, the drilling can be stabilized without much increase in hole diameter.

3.3. EDM characteristics of Al alloy and WC-Co using

workpiece vibration

With workpiece vibration, EDM drilling into Al alloy and WC-Co were possible using suspended ball electrode. Then, the drilling characteristics such as hole diameter and removal rate were investigated with varying discharge current and servo voltage. Furthermore, the range of machinable conditions were examined.

Figure 5 shows variations of the hole diameter and removal rate with discharge current when the servo voltage was fixed. As shown in the figure, the hole diameter increased with discharge current, which shows
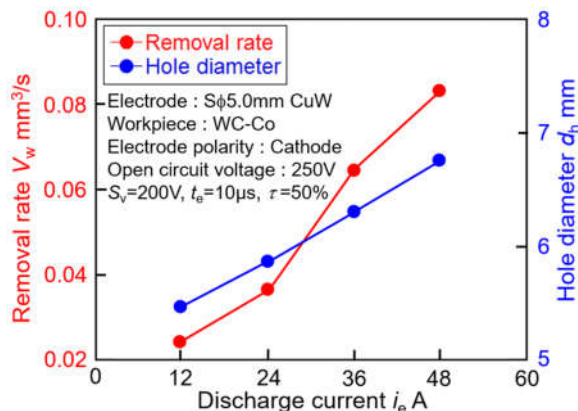
Fig. 6 Variations of removal rate and hole diameter with discharge current for WC-Co

the same tendency as general EDM. However, the removal rate decreases with discharge current. Under this machining condition, the pulse duration is as short

as 10 μs, and the current density of discharge column is high. So, the dielectric recovery in the gap during the machining would be insufficient, which leads to frequent discharge concentration and unstable discharge performance. Figure 6 shows variations of hole diameter and removal rate for WC-Co with discharge current. Unlike the case for Al alloy, the removal rate increases with discharge current increased. Cemented carbide needs
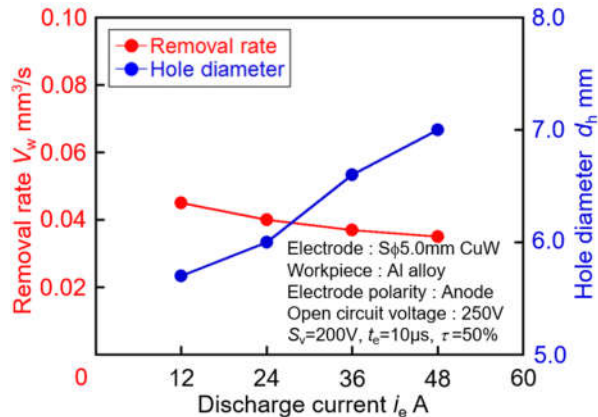
Fig. 5 Variations of removal rate and hole diameter with discharge current for Al alloy

higher current density for thermal removal because of its high melting temperature, based on the thermal machining theory. In other words, a short discharge duration and high discharge current conditions were suitable for stable machining for cemented carbide.

Figure 7 and Figure 8 show the machinable discharge condition ranges for Al alloy and WC-Co. The open circles (○) indicate machinable conditions, in which EDM drilling to a depth of more than 10 mm could be done. The closed circles (●) indicate the conditions, in which EDM drilling to a depth of more than 10 mm could be done with foil deflection. The condition indicated by crosses (×) is a condition when the drilling with a depth of 10 mm is impossible. As can be seen from the figure, the machinable ranges were limited to high servo voltage in both Al alloy and WC-Co. Since the gap distance becomes narrow with low servo voltage conditions and the ball electrode is swung much with larger machining force due to larger discharge current, short circuit and arcing frequently occurs and the drilling stability becomes worse. As a result, stable drilling becomes impossible under small servo voltage condition even with workpiece vibration.

3.4 Reduction of hole diameter

In order to apply this machining method into practical use, it is necessary to reduce the hole diameter. Then, smaller-diameter hole was attempted using a smaller-diameter electrode ball. Figure 9 shows the machinable EDM conditions for Al alloy using ball electrodes with diameter Sφ2.0 mm and Sφ5.0 mm.

As shown in the figure, there are machinable

Fig. 7 Machinable EDM conditions for Al alloy
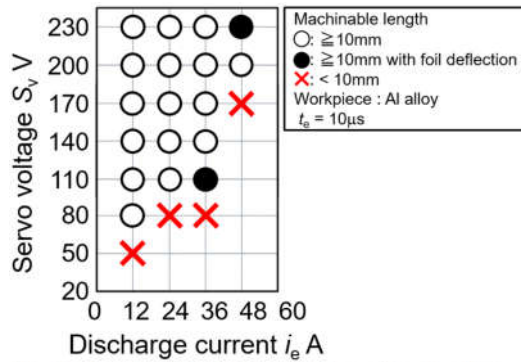
Fig. 8 Machinable EDM conditions for WC-Co

conditions and its range expands under high servo voltage conditions due to its wide gap distance in both cases of ball electrodes with diameter Sϕ2.0 mm and Sϕ5.0 mm. In addition, the machining force acting on the ball electrode would decrease with an decrease of discharge current, and the stable machinable EDM conditions tend to be wide when the discharge current is low. Furthermore, when small ball electrode of Sϕ2.0 mm in diameter is used, the EDM conditions with discharge current 4 A and servo voltage 110 V with workpiece vibration enable smaller-diameter hole drilling.

Finally, the drilling of bending hole with small-diameter was tried by this method. Figure 10 shows bending holes with bending angles of 30, 45, and 60 deg. in Al alloy using a ball electrode with a diameter of 4.0 mm. As shown in the figure, precise bending angles can be obtained corresponding the tilting angle of workpiece. In addition, these drillings could be performed stably.

4. Conclusions

In order to realize small-diameter curved hole drilling in practical metal materials by EDM using a suspended ball electrode, a method with workpiece vibration was proposed, and the influences of the vibration on drilling characteristics were investigated. The main conclusions obtained are as follows:

(1) Stable hole drilling using small-diameter ball electrode was possible for Al alloy and WC-Co by workpiece vibration.

(2) Even if curved hole drilling by EDM using a suspended ball electrode stops with arcing, the drilling can be restarted from the bottom of hole by workpiece vibration.

(3) When drilling practical materials such as Al alloy and WC-Co, stable drilling can be performed by setting high servo voltage condition.

(4) By workpiece vibration, a hole with small-diameter of about 3.0 mm can be achieved for Al alloy using a small ball electrode.
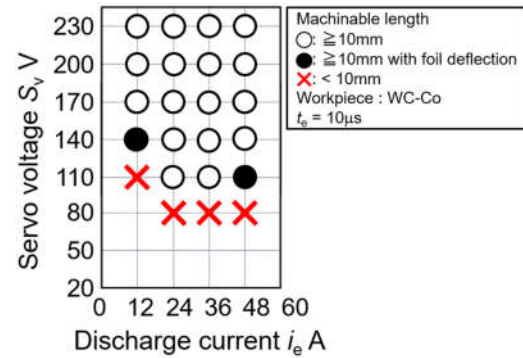
References

[1] Ishida T., Takeuchi Y., (1999) *Development of Electrode Feeding Drive Mechanism for Electrical Discharge Curved Hole Machining Using a Helical Compression Spring and Wires*, Journal of the Japan Society for Precision Engineering, Vol.65, No.7, pp.982-986.

[2] Uchiyama M., Shibazaki T., (2002) *Development of Curved Hole Machining with Electrochemical Machining -Processing method by actuatorless tool-*, Journal of the Japan Society for Precision Engineering, Vol.68, No.11, pp.1476-1480.

[3] Yamaguchi A., Okada A., (2015) *Development of Curved Hole Drilling Method by EDM with Suspended Ball Electrode*, journal of the Japan Society for Precision Engineering, Vol.81, No.5, pp.435-440.

[4] Yamaguchi A., Okada A., Miyake T., Ikeshima T., (2015) *Fundamental Study on Curved Hole Drilling Method by EDM with Suspended Ball Electrode*, Proceedings of the 8th International Conference on Leading Edge Manufacturing in 21st Century, No.1104
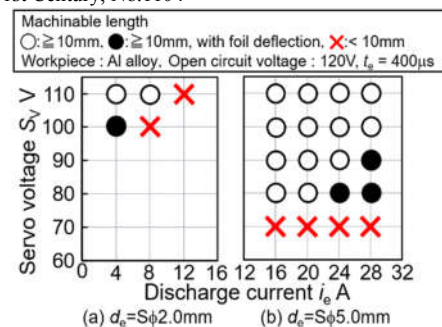
Fig. 9 Machinable EDM conditions using suspended ball electrodes of Sϕ5.0 mm and Sϕ2.0 mm in diameter
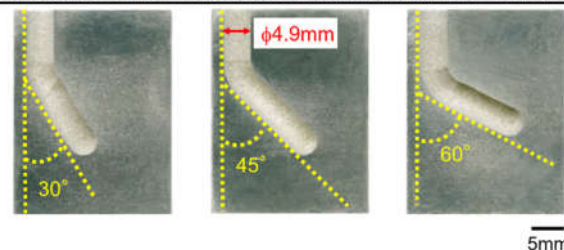
Fig. 10 Cross-sectional views of curved holes for Al alloy with various tilt angles of 30º, 45º and 60º

PART IV, SECTION II

Materials Technology
(Functional Materials; Technologies of Materials; Materials Characterization and Evaluation;
High Speed Machining and Abrasive Machining; Micro- and Nano-Systems Engineering and
Emerging Technologies; Surface Integrity and Machining Quality…)

Effect of the Type of Grinding Wheel on the Surface Characteristic of Titanium Alloy with Internal Coolant Supply

Nagatoshi Nakatsuka [1,3], Sumito Toyokawa[1], Atsushi Kusakabe[2], Shinya Nakatsukasa[3], Hiroyuki Sasahara[1]

[1] Department of Mechanical Systems Engineering, Tokyo University of Agriculture and Technology
2-24-16 Nakacho, Koganei-shi, Tokyo 184-8588, JAPAN
[2] Heiwa sangyo corporation
1-1544-10 Kaijin-cho minami Funabashi-shi Chiba-ken 108-0073, JAPAN
[3] Nasada Co. Ltd.
1-1　Abo Himeji-shi Hyogo-ken 670-0944, JAPAN

ABSTRACT

The objective of this paper is to clear the effect of grinding surface characteristic in grinding of titanium alloy with the coolant supply from inner side of grinding wheel. In this paper, we selected white aluminum oxide (WA) vitrified bonded grinding wheel and green silicon carbide (GC) vitrified bonded grinding wheel, and compared their grinding characteristics. As a result, in the case of GC vitrified bonded grinding wheel, the surface roughness decreased by about 54% and the compressive residual stress increased by about 128%.

Keywords: grinding, grinding wheel, titanium alloy

1. Introduction

Recently the growth rate of aircraft demand has increased remarkably [1], at the same time, it is required to reduce the weight of the aircraft and improve the performance of the engine because of environmental consideration. Against these background, the demand for titanium alloy which has high specific strength and compatibility with CFRP[2] is increasing.

Then in the grinding technology, the system applying grinding fluid from inner side of grinding wheel without external nozzle has been developed and studied [3], and it has been reported that the effect of suppressing the grinding point temperature and the effect of reducing the wear of the grinding wheel in the grinding of the difficult-to cut material[4].

It is important to improve the production efficiency by saving laborious processes such as hand finishing. It can be realized by substituting the shape finishing process with a grinding.

The objective of this research is to realize highly efficient machining by applying grinding fluid from inner side of grinding wheel to a machining of titanium alloy which is said to be a difficult-to-cut material[5] and in this paper, we examined the effect of the difference of grinding wheel on grinding surface characteristics.

2. Experimental method

Figure.1 shows the schematic of the system supplying grinding fluid from inner side of grinding wheel. The grinding fluid can be supplied directly to the grinding point using the spindle through system of the machining center and it does not require an external nozzle.

We selected white aluminum oxide (WA) vitrified bonded grinding wheel and green silicon carbide (GC)

vitrified bonded grinding wheel considering price and versatility. Table.1 show the grinding condition and table.2 show the specification of the grinding wheel used.

It is said that the abrasive grains of GC have highest hardness and are often used for nonferrous materials.

On the other hand, the abrasive grains of WA are often used in steel materials and are known as grinding wheels that are particularly excellent in terms of sharpness among common abrasive grains [6].
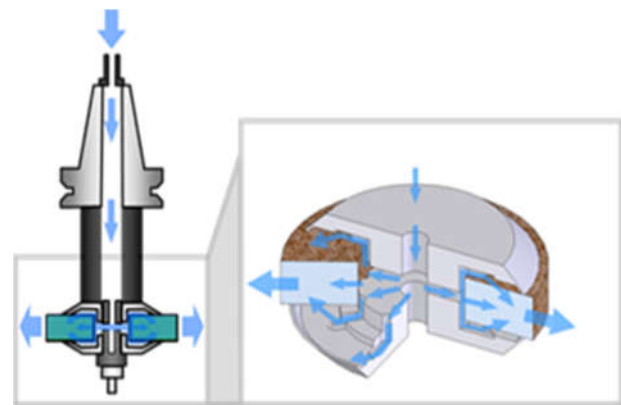
Fig.1 Schematic of the coolant supplying system

288

Table.1 Grinding conditions

Type of coolant supply			External,Internal
Grinding velocity	V	m/s	20
Feed rate	F	mm/min	500
Depth of cut	d	mm	0.02
Grinding fluid			Emulsion type
Amount of coolant supply		L/min	10
Grinding method			Down
Material of work piece			Ti-6Al-4V

Table.2 Grinding wheel specification

Type of grinding wheel	GC Vitrified Bonded	WA Vitrified Boded
Grain size	♯80	
Concentration	14（Abrasive grain ratio34%）	
Grade	K	

Two kinds of grinding fluid supplying methods, namely external supply from nozzles and internal supply from inner side of the grinding wheel were compared.

We examined the change of grinding characteristics, namely grinding temperature, grinding ratio, tangential grinding force, normal grinding force, surface roughness and residual stress against the increase of grinding length for two types of grinding wheels of GC and WA.

Figure 2 shows the schematic of experimental equipment. On the left side, the titanium alloy test specimen with length of 80 mm was attached to the dynamometer for the measurement of grinding wheel. On the right side, the titanium alloy specimen with length of 420 mm was placed. Its sectional shape was same as the left specimen. Then the total grinding length was 500 mm for one pass grinding.
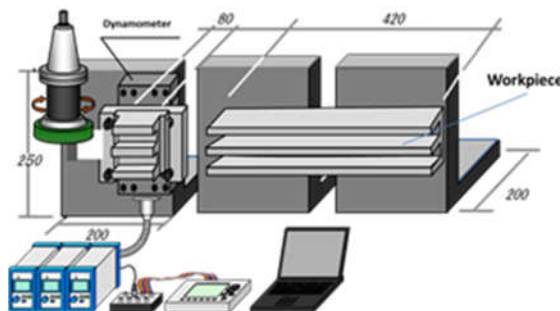
Fig.2 Schematic of experimental equipment

Figure 3 shows the schematic of experimental equipment for temperature measurement. The test piece was mounted on a jig having a hole formed in the slit and we measured the grinding temperature of the back surface of the test piece with a thermography camera.
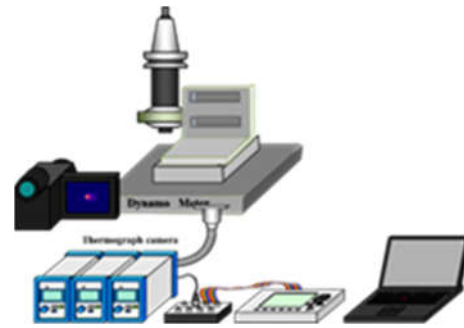
Fig.3 Schematic of experimental equipment for temperature measurement

3. Results and Discussion

Figure 4 shows the comparison of the grinding temperature for four types of combination of coolant supply methods and abrasive grain types. It cannot be said that the grinding temperature greatly varies depending on the difference in grinding fluid supply method, but it is understood that the longer the grinding distance, the lower the case of using the GC vitrified bonded grinding wheel than the WA vitrified bonded grinding wheel.

This is because the abrasive grains of the GC vitrified bonded grinding wheel do not cause glazing even when grinding the titanium alloy and maintain a higher sharpness and are able to grind.

Also, in experiments using flat specimens as shown in this paper, we cannot show the difference in grinding temperature or the advantage of the coolant supplied from inner side of grinding wheel.

This is because the grinding fluid stays longer time at the grinding point in planar grinding, so it is inferred that the superiority of the coolant supplying system from inner side of grinding wheel could not be demonstrated.

However, when grinding the curved surface there may be a grinding point where the amount of suppled grinding fluid is not sufficient with the external coolant supply. In such a situation, the coolant supplied from inner side of grinding wheel surely reach the grinding point and it exhibits the good cooling performance even on the curved surface grinding.
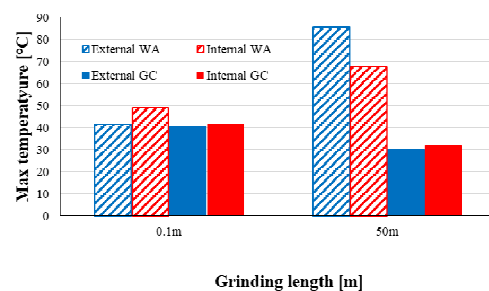
Fig.4 Max temperature on back surface of specimen at 1pass and 100 pass

Figure 5 and 6 show tangential grinding force and normal grinding force respectively.

Grinding force with GC vitrified bonded grinding wheel is smaller than that with WA vitrified bonded grinding wheel for each of tangential grinding force and normal grinding force. It is understood that grinding is performed with a small strain in both cases of external grinding and internal grinding while grinding energy. And in WA grinding wheel, grinding by the coolant supplying from external side shows smaller than grinding by the coolant supplying system from inner side of grinding wheel. And for GC vitrified bonded grinding wheel it shows almost the same.

Moreover, the waveforms are similar at any stress. Grinding force ratio μ, normal force / principal force, is almost 2.0, and the direction of the resultant force is almost the same grinding form in any case. [7]

In the case of WA vitrified bonded grinding wheel, there are large periodical change in every 10 pass (5 □) in these figures. This is due to the stopping the experiment and the tool holder was released to inspect the grinding wheel surface state.
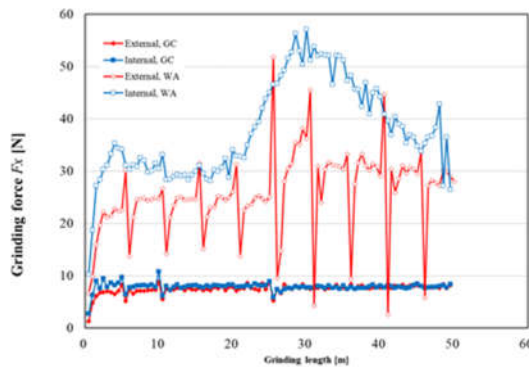
Fig.5 Tangential grinding forces
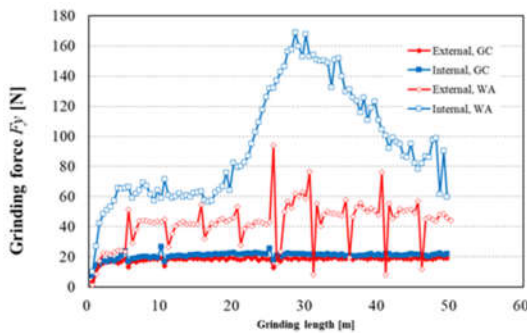
Fig.6 Normal grinding forces

Next, figure 7 shows the comparison of the grinding ratio. Although there are few differences according to the grinding fluid supply method, the grinding ratio by the GC vitrified bonded grinding wheel is about 15 times larger than that of the WA vitrified bonded grinding wheel. GC vitrified bonded grinding wheel shows higher grinding performance. Even if the

grinding distance increases, this value hardly changes.

That is the result of moderate self-dressing effect of the grinding wheel occur effectively in the case of GC vitrified bonded grinding wheel.
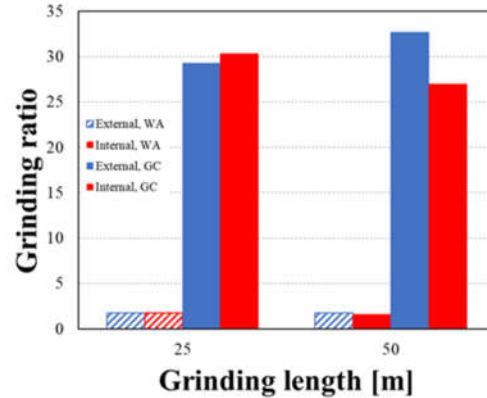
Fig.7 Grinding ratio at 1pass and 100pass

Figure 8 shows surface roughness. When the grinding distance is short, the value of surface roughness is low and less than 1 μm for both coolant supply methods. However, the longer the grinding distance, the extremely higher the numerical value with GC vitrified bonded grinding wheel than that with WA vitrified bonded grinding wheel.

As the abrasive grain of the GC wheel was less dropped off, then there are many the remaining protruding abrasive grains. These abrasive grains cut remove the machining surface and the trajectory of them were transferred to the test piece.

To solve this problem, it is necessary to improve the frequency of dressing, the grinding method, and change the grinding distance.
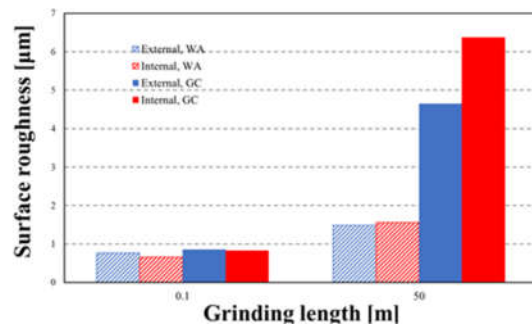
Fig.8 Surface roughness at 1pass and 100 pass

Finally, figure 9 shows residual stress in the grinding direction. It can be seen that the residual stress in the case of GC vitrified bonded grinding wheel is compression in both grinding fluid supply methods.

The hardness of GC abrasive grains is about twice that of WA abrasive grains. The amount of protrusion of GC abrasive grain is large. Then some similar effects as the shot peening [8] with steel balls can be introduced,

290

and the compressive stress was induced generated while numerous hard abrasive particles collided during the grinding.

In addition, the number of abrasive grains colliding with the surface increases due to Self-dressing effect of the grinding wheel as the grinding distance increases in the case of a GC vitrified bonded grinding wheel. Then the compressive residual stress is considered to be larger as the grinding distance becomes longer.
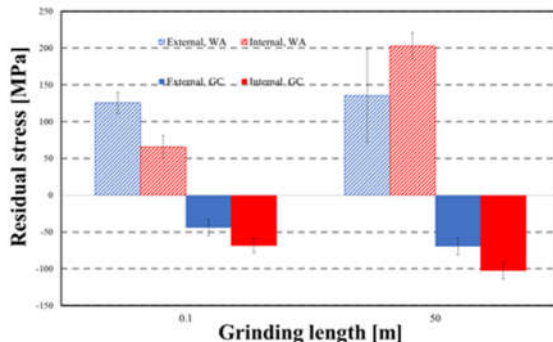
Fig.9 Residual stress at 1pass and 100pass

4. Concluding Remarks

In this research, by changing the type of grinding wheel and the suppling method of grinding fluid, we conducted grinding experiments using titanium alloy. The following results were obtained.

1) When the grinding distance is short, there is no big difference in grinding temperature. And there is no big difference in grinding temperature depending on the grinding fluid supply method. On the other hand, when the grinding distance becomes long, the grinding temperature increases by using the WA vitrified bonded grinding wheel, but the grinding temperature rises could not be seen when the GC vitrified bonded grinding wheel was used.

2) In the case of GC vitrified bonded grinding wheel, there is no big difference in tangential grinding force and normal grinding force both with the external grinding fluid supply and with the internal coolant supply.

On the other hand, in the WA vitrified bonded grinding wheel, the grinding with external coolant supply shows lower values in both tangential and normal grinding forces.

In addition, GC vitrified bonded grinding wheel shows less grinding resistance and stable grinding was conducted comparing with WA vitrified bonded grinding wheel.

3) The grinding ratio of GC vitrified bonded grinding wheel for titanium alloy is 15 times larger than that of WA vitrified bonded grinding wheel. Therefore, GC grinding wheel is suitable for titanium alloy grinding.

4) The compressive residual stress in the grinding direction was induced when the GC vitrified bonded grinding wheel is used. While, the tensile residual stress was induced when the WA vitrified bonded grinding wheel was used regardless of the grinding fluid supply method or the grinding distance.

In addition, when GC vitrified bonded grinding wheel is used, higher compressive residual stress was induced with the internal coolant supply.

References

[1] Japan Aircraft Development Corporation, Market forecasts for commercial aircraft 2016-2036.

[2] K.H. Rendings: Airbus and Current Aircrafts Metal Technologies.

[3] Y. Yao,Y. Fuwa and H.Sasahara, Development of a device for coolant supply from inside of grinding wheel and its application for profile machining of difficult to grinding materials,Proc,4th CIRP Int. Conf. on High Perfomance Cutting, vol.1,(2010), pp.417-420.

[4] Y.Yao, Ri S, K.Nakae, H.Sasahara, Minimization of grinding fluid by employing the supplying system from inner side of grinding wheel and its effect, Journal of Japan Society of precision engineering Vol78 No.8(2012)pp710-715.

[5] K.Ai,Journal of the Japan Society for Abrasive Technology Vol.52 No.12 2008 Dec.

[6] http://www.toishi.info
Q and A for grinding wheel   20th/May/2018.

[7]T.Yamada,H.Yuge,K.Miura,HwaSoLee, Experimental Evaluation of Micro Grinding Mechanism, JEPE, 2012, G63.

[8] Society of Shot Peening Technology of Japan, http://www.shotpeening.gr.jp/
About Shot Peening 15th/June/2018

Manufacturing of Cycloid Tooth Profile with Threaded Wheel Hobbing and Grinding for RV and Cyclo Drives

Ling-Chiao Chang[1], Shyi-Jeng Tsai[1], Jason Wei[1], Pin-Ching Chen[2]
[1] Department of Mechanical Engineering, National Central University
No. 300, Jhong-Da Road, Jhong-Li District, Taoyuan City 320, Taiwan
[2]Transmission Machinery Co. Ltd
No. 17, Aly. 31, Lane 69, Xing-Nong Road, Shanhua District, Tainan City 741, Taiwan

ABSTRACT

Cycloid planetary gear drives are widely used in power and precision motion transmission because of high gear-ratio and good shock absorbability. The aim of the paper is to propose a synthesis approach to generate necessary profiles for manufacturing with thread-wheel type tools based on a given cycloid tooth profile. Two different cases are illustrated in the paper to calculate these profiles, the profiles of thread wheel on normal or axial section, the equivalent rack profile, as well as the profile of dressing or grinding wheel for grinding or hobbing.

Keywords: Cycloid Tooth Profile, Thread Wheel, Hobbing, Grinding

1. Introduction

Cycloid planetary gear drives are commonly applied in industrial power and precision motion transmission because of larger gear, higher load capacity and good shock resistance. The cycloid disc, as shown in Fig. 14, is conventionally manufactured by milling machine, but this process is time-consuming due to the complicated curve. In order to increase the productivity, the continuous generation methods are suitable for manufacturing the cycloid discs. For example, hobbing and continuous generation grinding with threaded wheel-type tools are now widely applied in making involute gears of small and medium sizes efficiently.

Fig. 14 Cycloid Disc [4]

A threaded wheel, e.g. the hob in Fig. 15, is similar to a worm. The profile of the threaded wheel plays an important role for the accuracy of the tooth profile. However, the related research is found in manufacturing of involute gears, e.g. [1, 2, 3], and is less mentioned in the field of cycloid gears.

Fig. 15 Hob for cycloid discs [4]

The essential work for the continuous generation method is to derive the mathematical model for the related profiles, such as the profile of threaded grinding wheel and the profile of dressing wheel. The study, e.g. [2] and [3], proposed the mathematical model of the profile of the threaded wheel for involute gears, but they are not generalized approach and can not used for cycloid gears.

In the paper, a generalized approach will be proposed based on the geometrical relation of the generated profile and the machine setting. Two practical examples from the practice are illustrated to demonstrate the feasibility of the proposed computerized approach.

2. Geometrical Relation

2.1 Mathematical equations of cycloid tooth profile

A cycloid gear with the epitrochoid profile, Fig. 16, is the fundamental for further derivation of the profiles of threaded grinding wheel.
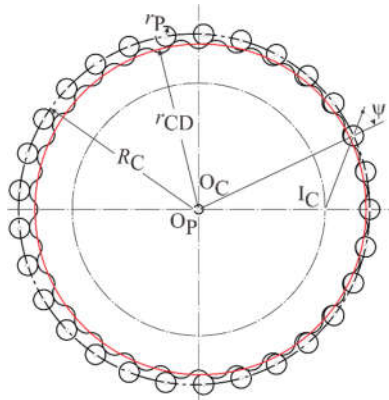
Fig. 16 Profile of Cycloid disc

Cycloid profile can be defined as the coordinates using the equations,

$$x_C = R_C \cdot \cos\theta - e \cdot \cos(i_C \cdot \theta) - r_P \cdot \cos(\theta - \psi) \quad (1)$$

$$y_C = R_C \cdot \sin\theta - e \cdot \sin(i_C \cdot \theta) - r_P \cdot \sin(\theta - \psi) \quad (2)$$

with the pressure angle,

$$\psi = \arctan\left[\frac{z_P \cdot e \cdot \sin(z_C \cdot \theta)}{R_C - z_P \cdot e \cdot \cos(z_C \cdot \theta)}\right] \quad (3)$$

2.2 Machine Setting

Accoring to the generation process, a CNC grinding machine equipped with a threaed grinding wheel and a dressing wheel is applied in the paper, Fig. 17. The double cone type of dressing wheel is applied in the paper to form the dressing whee (Fig. 18).

Because of continuous manufacturing process, the relation threaded grinding wheel and the cycloid gear is characterized as a gear set, such as a worm and a spur gear.
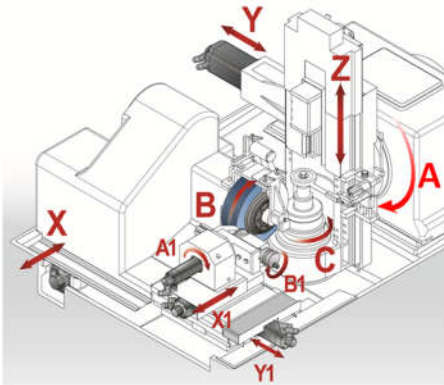
Fig. 17 CNC Continuous Gear Grinding Machine [5]

Double Cone and
OD Dresser
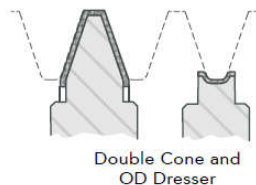
Fig. 18 Dressing of Grinding Wheels [6]

2.3 Profiles of Threaded Grinding Wheel

The threaded wheel-type tool can be created by various manufacture process, such as turning, milling or generating. To these purposes, the axial profile and the normal profile of worm are essential for manufacturing. On the other hand, the equivalent rack profile of the threaded wheel can be also derived, and it can be used to verify the computation.

2.3.1 Parameters of the worm

The design parameter of the threaded grinding wheel is characterized by the lead angle, and the pitch radius or the axial module. In this paper, the lead angle is given, and the pitch radius of the threaded wheel is associated with the circular pitch of the cycloid disc. The circular pitch of cycloid disc is calculated according to the tooth number and pitch radius of cycloid, i.e.,

$$p_C = \frac{2 \cdot r_{CD}}{z_C}. \quad (4)$$

Because the circular pitch of the threaded wheel and the cycloid disc is the same, the pitch circle radius of the threaded wheel is,

$$r_W = \frac{p_C}{2 \cdot \sin\gamma}. \quad (5)$$

2.3.2 The axial profile of worm

The dual normal vector $\hat{\mathbf{n}}_{CD}$ and dual axis vector $\hat{\mathbf{A}}_W$, Fig. 19, have a specific relation that the ratio of dual part to the real part of the inner product is equal a specific value,

$$\frac{\text{Dual}(\hat{\mathbf{n}}_{CD} \cdot \hat{\mathbf{A}}_W)}{\text{Real}(\hat{\mathbf{n}}_{CD} \cdot \hat{\mathbf{A}}_W)} = -r_W \tan\gamma. \quad (6)$$

During the generation process, the cycloid gear and the threaded wheel rotate at the same time. In order to simplify the derviation, the cycloid disc is regarded in the paper as fixed and the threaded wheel moves relatively with respect to the cycloid gear. The instantaneous axis vector $\hat{\mathbf{A}}_{IC}$ is applied here to determine the relation with the normal vector $\hat{\mathbf{n}}_{CD}$, see Fig. 19. Due to the engaged point within the instantaneous axis, an inner product of instantaneous axis vector and normal vector is equal to zero, i.e.,

$$\begin{aligned}&\text{Dual}(\hat{\mathbf{n}}_{CD} \cdot \hat{\mathbf{A}}_{IC})\\&= -R_{CD}(n_x \sin\xi + n_y \cos\xi) + (xn_y - yn_x) = 0\end{aligned} \quad (7)$$

The axial profile and the normal vector of the threaded wheel can be derived with Eq.(6) and (7).

293

Fig. 20 Geometric relation of Worm

Fig. 19 The relationship of Cycloid Disc and Threaded Grinding Wheel

2.3.3 The normal profile of worm

The normal profile of the threaded wheel $\bar{\mathbf{r}}_{WN}$ can be derived from the axial. The normal profile is a planer curve on the normal section, which normal is inclined with the lead angle to the rotation axis of the wheel. Therefore the z value of the transformed coordinates of the normal profile is equal to zero, shown in Fig. 20. The geometric relation is calculated by Eq. (8).

$$\bar{\mathbf{r}}_{WN} = \begin{bmatrix} 1 & 0 & 0 \\ 0 & \cos\gamma & \sin\gamma \\ 0 & -\sin\gamma & \cos\gamma \end{bmatrix} \begin{bmatrix} x_{WG}\cos\varphi_N \\ y_{WG} - r_W\varphi_N\tan\gamma \\ x_{WG}\sin\varphi_N \end{bmatrix} \quad (8)$$

2.3.4 The tooth profile of the equivalent rack

If the threaded wheel moves only in the direction along the axial driction of cycloid disc and without rotation about its axis, the envelope surface is a equivalent rack for generation of the cycloid profile, see Fig. 21. Thus the normal vector of any contact point $\bar{\mathbf{n}}_W$ is perpendicular to the vector of moving speed v,

$$v \cdot \bar{\mathbf{n}}_W = 0 . \quad (9)$$

The equivalent rack profile of the threaded wheel can be derived with the kinematic realtion.

Fig. 21 Kinematic relation of Cycloid Disc and Worm

2.4 Profile of Dressing Wheel

According to the geometric relation in Fig. 22, the dressing wheel tilts with a lead angle to mesh with the threaded wheel in the production process. With the respect to the contact point, the normal vector of the threaded wheel $\hat{\mathbf{n}}_W$ must intersect the axial vector of the dressing wheel $\hat{\mathbf{A}}_{DW}$. The dual part of vectors inner product is equal to zero, shown in

$$\mathrm{Dual}(\hat{\mathbf{n}}_W \cdot \hat{\mathbf{A}}_{DW}) = 0 . \quad (10)$$

Therefore the profile of the dressing wheel can be derived from the axial profile of the threaded wheel with this relation. Because the position of the dressing wheel axis affects the profile, the pitch circle radius of the dressing wheel is thus the important parameter of the profile. In this paper, this pitch circle radius is given.

3. Numerical Analysis Examples

The essential input data of the cycloid profile for the presented mathematical model to generate the threaded grinding wheel and the dressing wheel are only the coordinates and the normal vector of the discrete points on the cycloid profile. Therefore, two examples are illustrated in the paper. One is theoretical cycloid profile, and another is the measured data. Three various profiles are calculated and compared. The correctness of the calculation is also verified with aid of CAD simulation of the equivalent rack.

3.1 Case 1: Theoretical cycloid profile

The design parameters of the cycloid gear, the threaded wheel and the dressing wheel are listed in Table 4. The cycloid profile in this case is considered as theoretical profile with tooth number difference of one.
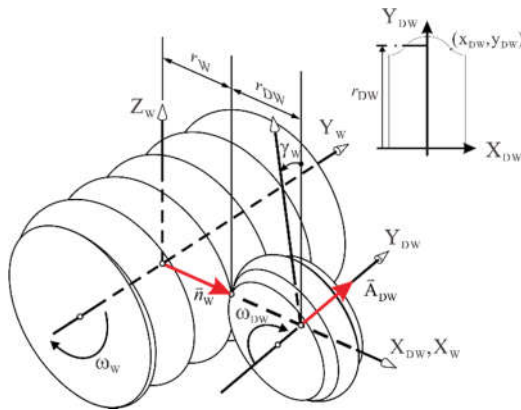
Fig. 22 The relationship of worm and dressing Wheel

Table 4.Design parameter of the cycloid gear, the threaded grinding wheel and the dressing wheel

Items / symbols	value
Pitch circle radius of pin wheel R_C	70 mm
Pitch circle radius of cycloid disk r_{CD}	66 mm
Tooth number of the cycloid disk z_C	28
Tooth number of the pin wheel z_P	29
Radius of the pin wheel r_P	8 mm
Lead angle of Threaded Grinding Wheel γ	5°
Pitch circle radius of Threaded Grinding Wheel R_W	27.05 mm
Axial Modulus of Threaded Grinding Wheel	4.732
Pitch circle radius of Dressing Wheel	20 mm

3.1.1 Simulation of cutting process

In order to confirm calculation accuracy of the calculation profiles, as mentioned above, a simulation of cutting process with the calculated equivalent rack profile using AutoCAD is conducted, see Fig. 23. As the diagram shows, the envelope of the equivalent rack profile is in very good agreement of the given cycloid profile.
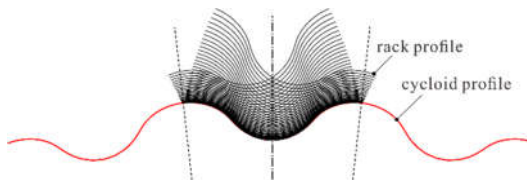
Fig. 23 The proof of the axial profile of worm

3.1.2 Comparison of Various Profiles

Three kinds of three calculated profiles are illustrated in Fig. 24. As expected, they are similar in shape, by contrast, there are small different amount in normal direction and also in pitch length. Besides, the addendum of the normal profile is always smaller than the axial profile because of the lead angle. The equivalent rack profile intersects with the normal profile in the bottom land and intersects with the axial profile on the flank. And all profiles intersect together

on the tip of tooth profile.
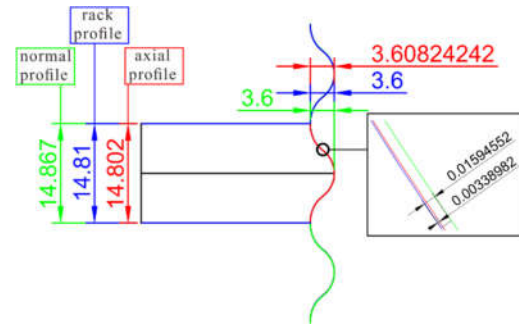
Fig. 24 Three profiles of worm for theoretical cycloid profile

3.2 Case 2: Fitting curves from measured profile

The design parameters of this case are listed in Table 5. The cycloid gear is designed as tooth number difference of two. The input data is the measured curve from the entity of cycloid disc. These profile data are at first fitted as NURBS-type curve. The necessary coordinates and the corresponding normal vectors of the curve-fitted cycloid profile are then calculated with aid of the NURBS mathematical model

Table 5. Design parameter of cycloid disk, threaded grinding wheel and dressing wheel for analysis example

Items / symbols	value
Pitch circle radius of cycloid disk r_{CD}	65.69 mm
Tooth number of the cycloid disk z_C	16
Lead angle of threaded grinding wheel γ	5°
Pitch circle radius of threaded wheel	47.11mm
Axial modulus of threaded Grinding Wheel	8.242 mm
Pitch circle radius of dressing wheel	20 mm

3.2.1 Simulation of cutting process

In this case, the simulation with the calculated rack profile is also in good agreement with the measured cycloid profile, Fig. 25. Additionally, the rounded tip of cycloid profile is also simulated exactly.
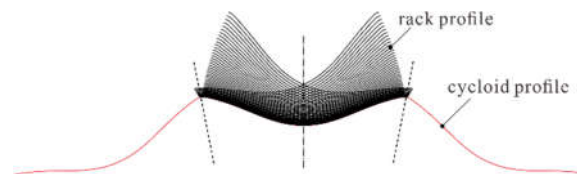
Fig. 25 Simulaiton of cutting process with rack profile

3.2.2 Comparison of Various Profiles

The difference of the three profiles is compared in Fig. 26. Due to smaller eccentricity, the rack profile does not change dramatically more than the result in Fig. 24. And all profiles also connect together on the tip of tooth profile.
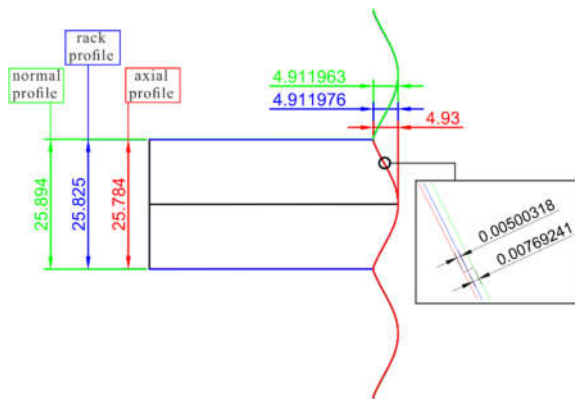
Fig. 26 Three profiles of worm for fitting curve

4. Concluding and Outlook

In order to improve the production efficiency of the cycloid gears with hobbing and continuous generation grinding for cycloid discs, mathematical models for generating three types of profile of threaded grinding wheel and the profile of dressing wheel are proposed. Furthermore, the numerical results show that the proposed rack profile of threaded grinding wheel can fits well with the cycloid profile. The normal profile and the axial profile of worm are different from the lead angle. And the rack profile of worm varies on unlike cycloid profile.

References
[1] D. Richmond, *CNC Gear Grinding Methods*, *Gear Technology* (1997) 43-50
[2] A. Türich, Producing Profile and Lead Modifications in Threaded Wheel and Profile Grinding, *Gear Technology* (2010) 54-62
[3] Z.H. Fong, G.H. Chen, Gear Flank Modification Using a Variable Lead Grinding Worm Method on a Computer Numerical Control Gear Grinding Machine, *Journal of Mechanical Design* **138** (2016) 083302-1-10
[4] Transmission Machinery Co., Ltd., http://www.transcyko-transtec.com/
[5] LUREN Co, Ltd., http://www.luren.com.tw/pro-tool2.html
[6] DR. KAISER Co, Ltd., http://www.drkaiser.com/service/downloads.html

High-quality Machining of CFRP with DLC-coated and Diamond-coated End Mills

Shota Tanaka[1], Akira Hosokawa[2], Goshi Hoshino[3], Tomohiro Koyano[2], Tatsuaki Furumoto[2], Yohei Hashimoto[2]

[1]Graduated School of Natural Science & Technology, Kanazawa University
[2]Institute of Science and Engineering, Kanazawa University
Kakuma-machi, Kanazawa, Ishikawa 920-1192, Japan
[3]DMG MORI CO., LTD.
201, Midai, Iga, Mie 519-1414, Japan

ABSTRACT

Side milling tests of CFRP (Carbon Fiber Reinforced Plastics) without coolant are carried out by DLC (Diamond-Like Carbon)-coated and the diamond-coated carbide end mills. Six types of DLC-coated end mills: two types of AIP (Arc Ion Plating) and FAD (Filtered Arc Deposition) coatings having different helix angles, respectably: are prepared. The FAD-DLC coated end mill enables to reduce cutting force and tool wear. Good surface qualities of milled surface are obtained by the high-helix end mills for both DLC- and diamond-coated tools.

(Presentation)

Development of a Decision Support System for Selection of Optimal Machining Parameters and Tool Inserts in Turning Process

Tho Nguyen[1], Tho Trinh[1], Hung Ly[1], Nhiem Tran[1] and Nghi Huynh[2], Thanh-Long Le[2]

[1]Faculty of Mechanical Engineering and Technology, Ho Chi Minh City University of Food Industry (HUFI)
140 Le Trong Tan St., Tay Thanh Ward, Tan Phu Dist., Ho Chi Minh City, 700000, Vietnam
[2]Faculty of Mechanical Engineering, Ho Chi Minh City University of Technology, VNU-HCM
268 Ly Thuong Kiet St., Ward 14, Dist. 10, Ho Chi Minh City, 700000, Vietnam

ABSTRACT

The metal cutting operation of turning method is a process of removing the unwanted metal volume to achieve the desired dimensions of machine elements. This process is related to many complex factors that need to be considered based on the knowledge, technician's experience and standard handbooks. In this paper, a decision support system (DSS) is developed to select the optimal parameters and tool inserts in turning operation based on the multiple of objectives such as surface roughness, hardness and material removal rate. This DSS is an aid for the suppliers or vendors of cutting tools in building the software to guide their customers in selecting the machining parameters. The related factors of turning operation are structured logically for evaluating and selecting the desirable values which is trade-off among three objectives. Then, the methods of the analytical hierarchy process (AHP) and VIKOR (which stands for 'VlseKriterijumska Optimizacija I Kompromisno Resenje) are used to form the decision support system. In particular, AHP is employed to determine the priority of selected factor's parameters and VIKOR is utilized to evaluate their optimality and the cutting tool inserts. A numerical example is conducted to validate the developed DSS and sensitivity analysis is also implemented to verify the robustness of the optimal selection. The achieved results highlight that the developed DSS is practical and flexible to apply for manufacturing enterprises or machining workshop.
Keywords: turning operation; AHP; VIKOR; decision support system; surface roughness

1. Introduction

Metal processing is an industrial process that removes unwanted material to form the machine part according to engineering drawing's requirements. In metalworking, the product's quality is the most important factor, especially the quality of the machining surface of part. Improved output's quality depends on the choice of cutting tools, cutting modes and machine tools. The very important insert pieces directly affect the quality of the machined part's surface and the cost of manufacturing process. Thus, the selection of combination of the inserts and cutting modes is a complex multi-criteria decision-making process involving a variety of factors such as cutting speed, feed rate, cutting depth, nose radius, approach angles, clearance angle, rake angle, angle of inclination, etc.

The machining parameters are selected mainly based on the manufacturer's catalog, the experience of machine operators, and mechanical standard handbooks. The selection of parameters is not only an optimal measure of production cost but also a decisive factor in the quality of machining parts. Machining capacity also depends on the selection of these parameters. The choice of combination of machining parameters and inserts will determine the machining quality of the turning process.

The material used in the process is CT45 steel, its major component being carbon steel. This is a type of steel commonly used in mechanical engineering, making the shaft, making bolts, threading, making hooks, machine parts need to be easy to cut, structure and decorative patterns, etc. The CT45 has good oxidation resistance, high load bearing capacity, strong shock resistance and good elasticity due to high tensile strength.

Turning is a method of machining that is carried out by the usual main movement due to the rotation of the workpiece combined with the cutting motion is the combination of two vertical cutting movement and horizontal one. When turning the elements of smooth shaft, the horizontal movement of the cutting tool is zero, the vertical movement of the other is different from zero. The turning process is the most common cutting method. Lathes account for about 25% to 35% of the total number of equipment in the machining workshop. Lathes can be machined on a variety of surfaces such as internal and external turning rings, threads, conical surfaces, shaping faces, etc. The accuracy of the machining operations depends mainly on the following factors: Machine tool precision (spindle inversion, parallelism of slider with centerline of spindle); cutting tool status; qualification of workers and technicians. When machining on a CNC machine, the quality of the turning process depends less on the skill of the craftsman compared to machining on the conventional lathe machine.

Surface quality is characterized by surface roughness and micro hardness. The surface roughness of machined parts affects the fatigue strength, abrasion resistance and chemical corrosion resistance. To improve the machining efficiency, the cutting mode plays a very important role, especially material removal rate (MRR). Therefore, choosing the cut mode combining the selection of the correct insert is the desired target to achieve the effectiveness in the turning process.

Research on the Design of the Laser Beam in SLS Rapid Prototyping Machine

Vo Tuyen[1], Tran Trong Hy[2], Le Khanh Dien[2]

[1] Ho Chi Minh City University of Food Industry (HUFI), Vietnam

[2] DCSELAB - Ho Chi Minh City University of Technology, VNU-HCM, Vietnam

ABSTRACT

In the SLS rapid prototype machine, the CO_2 Laser sources are applied for sintering the powder material to its melting point temperature. The ability to use laser radiation for sintering the material depends on the power of energy source and the time of interaction of radiation with the material. Otherwise, the design of Laser beam for sintering powder material depends on the technical parameters such as Laser point size, the type and focus of lenses…. This article presents a study on the design of Laser beam sintering in the SLS rapid prototype that satisfies the technical requirements. The results of testing show that the designed and manufactured Laser beam instrument in SLS rapid prototype machine in DCSElab is approved because it meet all the technological requirements of the medium range of SLS rapid prototyping machine.

Keywords: Laser beam, Sintering, SLS, Rapid prototyping machine.

1. Introduction

Sintering is the technical process of production model parts by controlling the heat for creating to the melting temperature of the powder particles. Sintering principle is mainly diffusion between powder particles. In mass production, technicians always select the molding technology where the provided heat source is higher than the melting point of the whole volume of the material so the material turn to liquid flow that blow out to the very small, complicated channels, chamfers and fillet corners of the molt. In the meanwhile, in small batch or single production, the SLS rapid prototype

technology, the CO2 Laser beam burns up to melting point only a small area of powder material. We recognize that the new technology saves energy because the Laser source that is a mixture of gases of carbonic CO2, Helium He and Nitrogen N2 in which CO2 gas is principal element, do not consume a lot of energy. In some case, Hydrogen H2 can be added into the mixture for special purpose. In the research, we applied the Laser CO2 source that provides a beam of the wave pitch from 9 to 11µm with a power from 50W to 400W [1].

2. Fundamental computing in the design of the Laser beam

The condition of application of which type of Laser radiation to sinter the material is governed by the laws of evolution of processes and effects such as absorption of radiation in the material surface, heating, melting and evaporation of materials and formation of heat affected areas ... Base on the energy density and the time of interaction of radiation with powder materials, there are five conditions of Laser source power F:

- Radiation lighting and reflection: power density F> 0
- Absorption and heating F <102 W/cm²
- Melting F ≈ 105 W / cm²
- Evaporation F ≈ 106-107 W/cm²

From Furrier's law of heat transfer, the heat transfer generated by the laser's energy depends on laser scanning time, laser source heat and surface area of contact. Therefore, the main requirements of the laser sinter cluster include [2]:

Laser Point Size: is the diameter of the laser on the sintered powder surface that is a value from 30 to 600µm. The laser point size has to be adjustable to achieve variable power density, accuracy and projecting speed. In case of small detail model that has thin walls, small holes, it is necessary to achieve high accuracy and the point size is necessary to be adjusted to tiny value. However, sintering the model with small Laser point size will take a long time to complete so its productivity

The interactive process is not cited in the conditions of the laser information, properties of materials, environment….The transferring heat from one powder particle to the adjacent one is called heat transfer and follows Furrier's law: a dQ thermal element that conducts through a differential surface dF in a unit of time is proportional to Gradient(t) with surface dF and time:

$$dQ = -\lambda \frac{dt}{dn} . dF . d\tau$$

Herein λ is thermal conductivity

$$[\lambda] = \left[\frac{dQ.dn}{dF.dt.d\tau} \right] = \frac{J.m}{m^2 .s. \,^0 C}$$

is very low. Therefore, the question of optimization of the Laser point size should be sold in advance in condition of the guaranty of the quality of the product.

Scanning speed: is the velocity of the projecting Laser point on the surface of the powder carriage. The scanning speed of the Laser point is covariant with the processing time of the machine. The scan speed relates to the power density in the following formula:

$$\text{Power density} = \frac{\text{Laser capacity}}{\text{Laser point size } x \text{ scanning speed}}$$

Thickness of powder layer: is the thickness of a circumference lateral around the model. It is computer-translated from the 3D CAD model to the physical layer

for a Laser sintering. It is equal to the thickness of the powder in the forming process; it is set by adjusting the down pitch on the Z-axis. The thickness is also an important parameter in terms of processing speed, power of Laser source. The relation between Power density and the thickness of powder layer is displayed in the following formula

$$\text{Power density} = \frac{\text{Laser capacity}}{\text{scanning distance } x \text{ scanning speed } x \text{ thickness layers}}$$

Or: $E_d = \frac{P}{SS\,x\,H\,x\,t}$; in that E_d [J/mm^2]; P [W]; SS [mm/s]; H [mm]; t [mm]

3. Design of structure of laser sintering beam

In order to perform the sintering of the powder, the Laser beam has to follow strictly to the profile of the product of each elevation. Therefore, the control of the movement of sintering Laser beam in two directions XY is the kernel of the design. The Functional Analysis of

Sintering System has the following specifications: XY Journey of Laser Head Movement: 300 x 300 mm; Maximum Laser scanning speed: 900 mm / s; Layer thickness: 0.08 - 0.3mm; Accuracy of Laser point: 0.02mm; Laser power output: 60W. The schema of the process is illustrated in Figure 1.
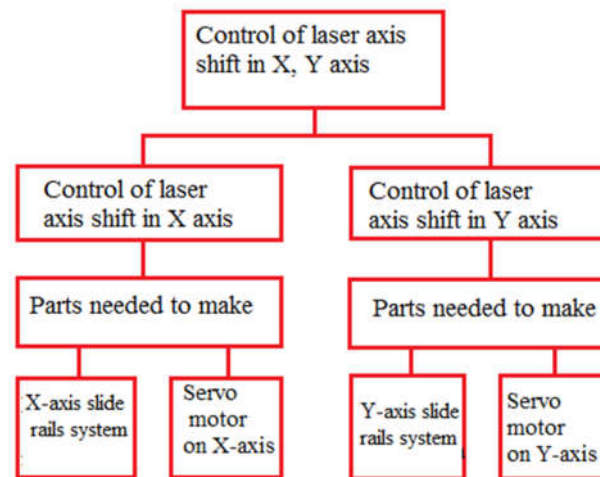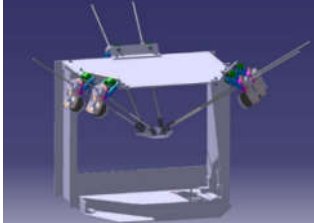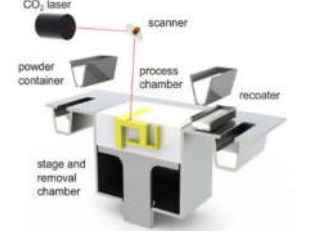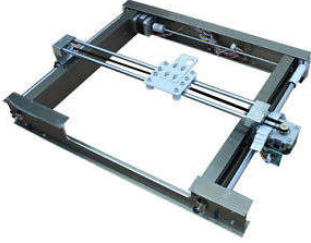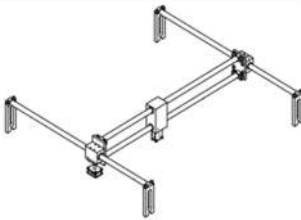
Figure 1. SLS sintering Laser beam analysis diagram

Based on the study of input parameters and related design references [3], [4] several structural designs of Laser beam are proposed as follows:

OPTIONS	STRUCTURAL DIAGRAM	CHARACTERISTICS	ADVANTAGES	DEFECT
Option 1: Control the Laser beam by hexapod structure		The Laser source is moved by the movement of the braces around the sphere.	Flexible motion in all three directions XYZ.	- Bulky structure, occupying a lot of space; - Complex control; - Difficult to install, Maintenance
Option 2: Control the direction of the Laser beam by mirror system		The system of multiple lenses can tilt the different angles to control the direction and focus of the laser. In order to be able to tilt in different directions, each lens should be attached to a separate engine. This structure can tilt the different angles to control the direction and the focus of Laser beam. In order to tilt in different directions, each lens	- High precision - Fast response	- Complex structure - Difficult control - High price.

		should be attached to a separate motor.		
Option 3: Control the Laser beam by XY slide system		The Laser source is mounted directly onto the XY slider system.	- Simple structure; - Easy to assemble; - Easy control.	- The laser source is dangerous and needs to be cooled so it must be placed outside; - High power laser sources that are placed directly onto the rack system will reduce the accuracy.
Option 4: Control the Laser beam by XY slide rail system with a guided laser prism		The laser beam is controlled by the prism system mounted on the XY slider.	- Simple structure; - Easy to assemble; - Easy control.	Difficult alignment adjustable prism system.

Apply the by the application of the decision matrix method [5] to evaluate design options, we have the preliminary evaluation table and scoring matrix table as in tables 1 and 2:

Table 1: Preliminary evaluation matrix of Laser sintering beam designs.

Option \ Criterion	1(standard)	2	3	4
Products are available in the market	0	-	+	+
Reasonable price	0	+	0	+
Easy to manufacture and assemble	0	-	0	+
Easy control	0	0	+	+
Easy maintenance	0	0	+	+
Longevity	0	+	+	+
Total points +	0	2	4	6
Total points 0	6	2	2	0
Total points -	0	2	0	0
Total score	0	0	4	6
Rating	3	3	2	1
Should we continue?	No	No	Yes	Yes

Table 2. Grading matrix of selection of laser sintering cluster design.

Criterion	Weight (%)	Options			
		3		4	
		Score		Score	
		Raw	Multiplied by Weight	Raw	Multiplied by Weight
Products are available in the market	15	5	0.75	4	0,6
Reasonable price	25	3	0,75	5	1,25
Easy to manufacture and assemble	15	5	0,75	5	0,75
Easy control	15	5	0,75	5	0,75
Easy maintenance	15	4	0,6	4	0,6
Longevity	15	5	0,75	5	0,75
Total score	100		4,35		4,7

Rating	2	1
Should we continue?	No	Yes

After evaluating, we have chosen the most suitable design option of option 4, using the XY slide rails system which combines prism with reasonable investment cost, easy control, but gives the equivalent shaping ability compare to the other options shaping. The kinematic diagram of the laser sintering cluster is shown in Figure 2: The laser cluster consists of a laser tube, reflector system and laser head. The laser source will receive the signal from the controller to trigger the discharge tube and emit a laser beam to reflectors so that the laser head is moved by the XY axis to the locations of the printed part. The XY clutch is controlled by a stepper motor via a belt drive system and is arranged to guide the laser to every position of the print area without obscuring the laser beam.
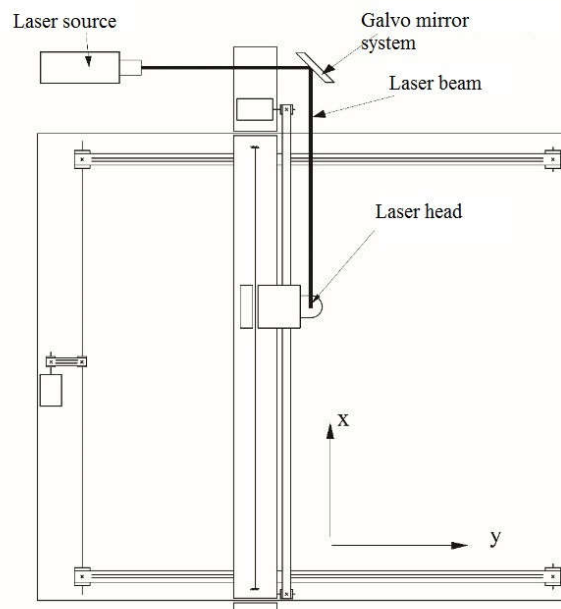
Figure 2. The kinematic diagram of the laser sintering cluster.

4. Calculation of laser sintering cluster design

4.1 Calculations for selecting lenses and compatible laser speed

Analysis showed that on the distance from the laser to the lens there was no significant expansion of the beam and its initial divergence was determined by the diffraction effect, the radius of the convergent R_s was determined by Equation [6]:

$$R_s = f.\theta \qquad (4.1)$$

Where: f - focal length of the lens
θ - divergence of the beam

Because of the divergence angle $\theta \approx \lambda/D$, in the case of the lens aperture is completely covered by the beam, the radius of the convergence will be:

$$R_s \approx f. \lambda/D \approx \lambda.f_0 \qquad (4.2)$$

In that, $f_0 = f/D$, f_0 is the unit size value, so R_s is the same size as λ.

For focusing laser radiation, people usually use lenses with a focal length of 25 ÷ 300mm and a working diameter of 10 ÷ 60mm. Depending on the parameters of laser radiation and the diameter of the convergent optical system, the diameter of the laser beam is in the range of 10μm ÷ 1mm, the focal length of the lens is f = 200mm, the diameter of the lens D = 40. mm [6].

Accordingly: $R_s \approx f. \lambda/D \approx 200.10,6.10^{-3}/40 = 0.053$mm
The width of the scan line b = 2.R_s = 2.0,053 = 0,106 mm

The energy used to calculate the mobile heat source is aggregated by a number of factors, including the computing factors of power, power density, scanning velocity:

$$h.v_c.b.(c.\delta.T_{nc} + L_{nc}) = \eta.P_{laser} \qquad (4.3)$$

Where: h – material thickness; v_c – scan speed; b – scan width; T_{nc} – melting temperature of material; L_{nc} – specific heat quantity of material; Ŋ – efficiency of process; P_{laser} – Laser power.

When the scan width is equal to the diameter of the laser b = 2.Rs and the material thickness h is constant, v_C is proportional to the Plaser. The SLS rapid prototyping

machine is designed for machining of plastic materials so in selecting the laser system we need to consider the capacity required to process the material. From Table 4. 2 [6], we choose velocity $v_C = 900mm / s$ corresponding to the 60W laser power radiated power.

Then, we calculate the energy density:

$$E_d = \frac{P}{v_s \times d} = \frac{60}{900 \times 0,106} \approx 0,63 \text{ (J.mm}^{-2})$$

(4.4)

4.2 Calculation of motor selection for X axis

The calculation of the motors based based on the friction angle factors created by the slider structure moving in X, Y directions. The sintering requirement analysis ensures the cutting velocity of the laser head imposes the following requirements: Maximum travel velocity: 900mm / s (0.9 m / s); Equivalent weight for cluster X: 50 N; Coefficient of friction between steel-steel equivalent: f = 0.1; Corner of slider design: γ = 600. With the upper limits, analyze the force components placed on the system when moving the equivalent:

- Friction force (Fms) generated on the slider (calculated for a slider X);
- Inertia force (m.a) is generated by the uniform accelerated motion;
- The drag force of the engine (Fk) affects the system (large enough to make the move).
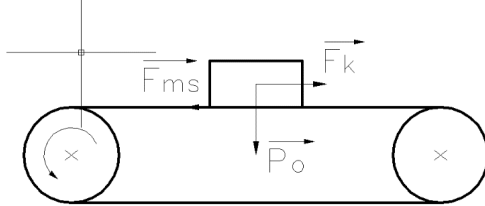
Figure 3: *Force component on the system*

$$-F_{ms} + F_K = ma$$

Friction force: $F_{ms} = F_{ms} = P.\mu^{'} = P \dfrac{\mu}{\cos 60^0}$

$$\Leftrightarrow F_K = m\left(\frac{g\mu}{\cos 60^0} + a\right) = 5\left(\frac{10.0,1}{\cos 60^0} + 0,9\right) = 14,5N$$

- Power required [25]:

$$P_{ct} = \frac{F_K.v}{1000} = \frac{1,74.0,9}{1000} = 0,013KW = 13,05W$$

(4.5)

- Select the equivalent motor power:

$$P_{dc}^{\ X} = 15W$$

4.3 Computing the parameter of motor according to the load capacity for the Y axis

The calculation of the motors based on the friction angle factors is due to the structure of the slider rails in X, Y directions. The sintering requirement analysis ensures the scanning velocity of the Laser head. Some requirements are as follows: Maximum travel speed: 900 mm/s (0.9 m/s); Approximative weight of beam Y: 150 N; the coefficient of friction between steel-steel is about: f = 0.1; Corner of slider design: γ = 600. The calculation is similar to the X-axis:

$$\Leftrightarrow F_K = m\left(\frac{2g\mu}{\cos 60^0} + a\right) = 15.\left(\frac{2.10.0,1}{0.5} + 0,9\right) = 73,5N$$

- Power required

$$P_{ct} = F_K.v = 73,5.0,9 = 66,15W$$

(4.6)

- Select the equivalent motor power:

$$P_{dc}^{\ Y} = 60W$$

Select AC servo drive motor, EVTA brand, model number F.

4.4 Design of timing belt drive system

Initial selections: Standard timming pulley and timing belt; Transmission ratio u = 1; Transmission power P1 = 60 W; Number of revolutions: n = 680 RPM; Preliminary shaft distance: a_{sb} = 500mm. After performing the design [7] the results parameters of the belt drive system are shown in Table 3.

Table 3. *Specifications of timing belt drive system*

Specifications	Symbol	Value
Number of teeth on driving pulley	Z_{1p}	14
Number of teeth on driven pulley	Z_{2p}	14
Number of teeth on timing belt	Z_m	7
Axial distance (mm)	a	525
Initial tension (N)	F_0	24,5
Force acting on the shaft (N)	F_r	175,6

The specifications of the sintering Laser beam are summarized in Table 4.

Table 4. *Summary of specifications of Laser sintering clusters*

Order	Nominal components	Symbol parameters and selective values
1	Lens	f = 200 mm D = 40 mm
2	Scanning width of laser	b = 0,106 mm
3	Scanning speed	V_c = 0,9 m/s
4	Laser power supply	P = 60 W
5	Power density	E_d = 0,63 J.mm^{-2}

6	Servo motor	P = 60 W n = 680 RPM
7	Timing belt	D = 22 mm L = 1000 mm

The sintering Laser module is assembled as in figures 4 and 5
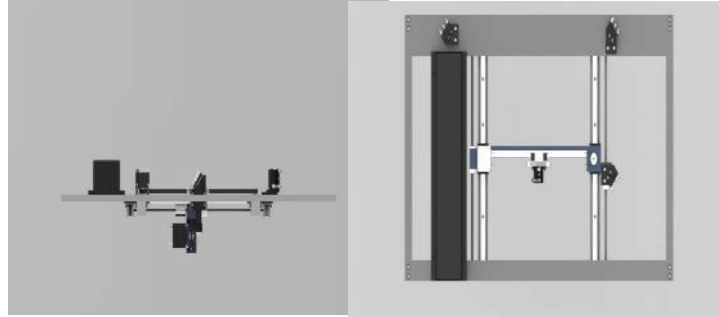
Figure 4. *Completed sintering Laser beam module*

The result model of experiment a cam products process on the SLS rapid prototype with the sintering Laser beam design with specific parameters values such as the thickness of a sintering layer: 0.2mm; the Laser beam output power (60W) by: 0.75% of the transmit power; sintering speed: 250mm/s; sintering temperature: ~ 160oC and productivity time: 3 hours 15 minutes have met the requirements of the SLS rapid prototype (figure 5).
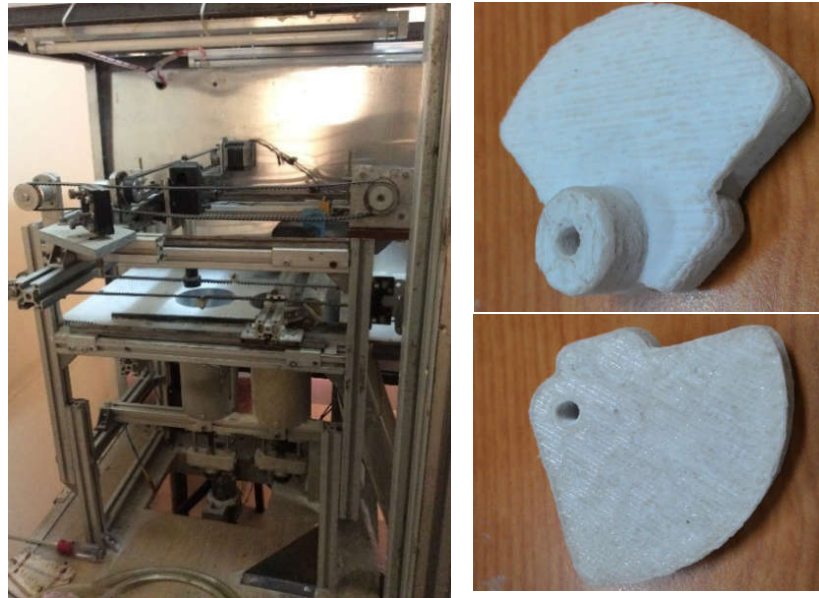
Figure 5. *SLS rapid prototyping machine and experimental products*

5. Conclusion

Carrying out an efficient design process of sintering Laser beam in SLS rapid prototyping machines that satisfies the technical requirements: a Laser point size of 30 to 600μm, a scan speed of less than 250mm/s and a thick sintered layer of 0.2mm. Experimental results show that the manufactured module of sintering Laser beam attained the requirements of the SLS rapid prototype.

6. Acknowledgement

7. References

[1] L.A. DobrzaĚski, A. Drygaáa, P. Panek, M. LipiĚski, P. ZiČba, *Application of laser in silicon surface processing,* Journal of Achievements in Materials and Manufacturing Engineering (2007) 179-182.

[2] Ana Pilipovit, Igor Drstvenšek, and Mladen Šercer, *Mathematical Model for the Selection of Processing*

Parameters in Selective Laser Sintering of Polymer Products, Advances in Mechanical Engineering, Volume 2014.

[3]. Carl R. Deckard (1989). *Method and apparatus for producing parts by selective sintering*. Patent US4863538 A.

[4]. Francesco E. DeAngelis, Michael R. Davison, David K. Leigh (1992). *Automated method and apparatus for calibration of laser scanning in a selective laser sintering apparatus*. Patent US 5,430,666.

[5] Nguyễn Thanh Nam, *Phương pháp thiết kế phát triển sản phẩm*, NXB ĐHQGTP Hồ Chí Minh, 2014.

[6] , W.A.Y YUSOFF & A.J THOMAS, *The effect of employing an effective laser sintering scanning strategy and energy density value on eliminating "orange peel" on a selective laser sintered part,* International Association for Management of Technology, IAMOT 2008 Proceedings.

[7] Nguyễn Hữu Lộc, *Cơ sở thiết kế máy*, NXB ĐHQGTP Hồ Chí Minh, 2015.

PART IV, SECTION III

Mechanical Technology
(Heat transfer, Thermal, and Fluid Engineering; Structures and Fluids; Vibration;
Energy Engineering; CAD/CAM/CAE/RP…)

Structural Dynamics Analysis of 3-U CubeSat

Vu Minh Chau[1], Hien Bich Vo[1]
[1]Faculty of Engineering, Vietnamese-German University
Le Lai Street, Hoa Phu Ward, Thu Dau Mot City, Binh Duong Province, Vietnam

ABSTRACT

The development of CubeSats has been advanced significantly during the past two decades for both scientific research and industrial purposes. During the manufacturing process, every CubeSat must satisfy various system requirements in which the structural analysis is one of the most vital necessity in order to assure a normal operation of the CubeSat during its working time in space. In the conceptual design phase, structural dynamics is a mandatory step to determine the natural frequencies of individual bodies, the deformation and stress induced at the corresponding vibration modes to prevent structural failure. In this work, IGOSat, a 3-Unit CubeSat, which was developed at the Paris Diderot University is exanimated in term of modal, harmonic response, and random vibration analysis at the time of ground testing as well as the launching phase using ANSYS software. These numerical simulations conducted according to the CubeSat Design Specification and the system requirements of QB50 project. The minimum natural frequency of the CubSat obtained to be 363.17 Hz, which passed the required frequency of 90Hz. Moreover, the Harmonic and Random vibration analyses indicate that the peak response of normal stress, as well as deformation values obtained, are far lesser compared to the yield strength of the frame structure and subsystem materials. Hence, our numerical analysis found that the CubeSat remains intact during the launch environment.
Keywords: Vibration, Simulation, 3-Unit CubeSat, IGOSat, ANSYS.

1. Introduction

CubeSats, a class of nanosatellites, are cost-efficient platform for science investigations, earth observation, and capability of demonstrating a satellite constellation mission. The nanosatellites stand in the nano category whose measuring length, width, height are 10 cm x 10 cm x 10 cm respectively, and the weight does not exceed 1.33 kg for one Unit referred to as a 1U, and the CubeSats are able to extend to 12 Units (12U) [1]. These satellites are the results of a collaborative effort between Jordi Puig-Suari, California Polytechnic State University (Cal Poly), and Bob Twiggs, Stanford University's Space Systems Development Laboratory (SSDL). The project has successfully achieved its target of providing an affordable access to space for the university science community. Thanks to CubeSats, many major universities now have a space program, not only universities but also high schools, middle schools, and elementary schools have been able to start CubeSat programs of their own.

IGOSat (Ionospheric & Gamma-ray Observations SATellite) is the first CubeSat project of the laboratory of excellence (Labex) UnivEarthS as well as getting the local support of the laboratories APC (AstroParticule and Cosmologie) and IPGP (Institute de Physique du Globe de Paris), operated at the Paris Diderot University. It is a 3-Unit CubeSat with size of 10 x 10 x 34 (cm) and the maximum weight of 4kg, consist of 2 payloads in a quasi-polar orbit at 650km altitude. The design process came to phase D in which various subsystems have been finalized in an 3D CAD software and need to conduct analyzation and validation against the launch vehicle constraints to ensure maximum reliability.

The structure of satellite plays an important role in the launching procedure of a spacecraft, due to numerous static and dynamic loads that it needs to support, namely static, sinusoidal loads, vibration generated by the separation of rocket parts in the different stages of the launch process. Therefore, the structural requirements must be fulfilled to ensure its mechanical properties, mass, volume, and shape withstand all the hazardous working environment. For verifying those requirements, the structural dynamics analysis addresses for modal analysis, harmonic analysis, and random vibration applied on the IGOSat using the ANSYS 17.0 Software which is a finite element analysis tool for structural analysis, including linear, nonlinear and dynamic studies, is shown in this work.

2. Method

Modelling:

The three unit IGOSat model 2017 is a complex structure consisting of numerous parts with an aluminum back bone frames which are filled with lots of printed circuit boards (PCB) inside and covered by four solar panels outside, these components also made by various types of material. For the purpose of reducing computational efforts and generating more reliable meshes, the entire CubeSat structure is first simplified before conducting the simulation in ANSYS. The aluminum frame structure is lightly modified so that it remains the stiffness of its structure as close to the original shape as possible. Besides, all the internal components' geometry is simplified to simple shapes, but still maintain their center of mass, bolted screw joints are excluded as well and replaced with bounded contact between subsystems.

In order to simulate the mass of the subsystems, every simplified subsystem must be applied a specific density based on its corresponding volume. Aluminum 2017 T4 is mainly used for the satellite's structural frame, whereas Reinforced Epoxy with glass FR4 is assigned for electrical Printed Circuit Boards (PCBs)and solar panels.

Assumption and boundary conditions:

The model is assumed to be linear isotropic, homogeneous and within the elastic region. Most of the components are rigid and bonded together.

The CubeSat is assumed to place inside the Picosatellite Orbital Developer (P - POD) with the longitudinal direction (Z-axis) aligned with the LV's direction of acceleration, therefore, fixed support is used for the side faced to the floor of the P-POD, whereas, on the side faced to the top of the P-POD, two lateral directions are constrained (X, Y-axis's) due to the spring-load deployment system allows a small number of displacements in the Z-axis.

Modal analysis:

The equation of motion describes all the problems in the structural dynamics, based on d'Alembert's principle together with the discretization process of a continuous structure, the equation can be expressed as:

$$M \cdot \ddot{u} + C \cdot \dot{u} + K \cdot u = f(t) \qquad (1)$$

Where:

M, C, K denoted the structural mass, damping and stiffness matrices

$\ddot{u}, \dot{u}, u$: the vectors of accelerations, velocities, and displacements respectively

$f(t)$: the vector of applied forces.

Modal analysis is conducted to determine the fundamental frequencies (modes) and their associated behavior (mode shapes) of the structure which are the solutions of the equation:

$$M \cdot \ddot{u} + C \cdot \dot{u} + K \cdot u = 0 \qquad (2)$$

These frequencies at which the satellite will amplify the effect of the dynamic loads, exerted by the Launching Vehicle (LV), lead to resonance vibrations of both CubeSat and the LV [2]. Furthermore, the subsequent dynamic simulations such as Random and Harmonic analysis use a mode-superposition method which needs the modes obtained from the Modal analysis.

Harmonic response:

During the launch phase, interaction between natural frequencies of LV and dynamic growing loads, applied to the satellite, produce a sustained cyclic response called as Harmonic response. The Harmonic response analysis solves the motion equation (2) for linear structures undergoing steady-state excitations that enables to verify whether structural designs will successfully overcome resonance, fatigue, and other harmful effects of forced vibrations during launching phase. The Mode-Superposition Method in ANSYS is chosen due to its performance according to [3]. The acceleration values used for the analysis as shown in Table 7.

Random vibration:

This analysis investigates the structural response to

Table 6: Acceleration based values for harmonic response analysis [4]

Frequencies [Hz]	Amplitude [g]
5	1.3
8	2.5
100	2.5

Table 7: PSD G Acceleration values for random vibration test [4]

Frequencies [Hz]	Amplitude [g²/Hz]
20	0.007
50	0.007
200	0.035
640	0.035
2000	0.010

acoustic noise due to engine vibration and noise, air friction at the beginning of the launch phase. The instantaneous magnitude of the response is not constant over time due to several possible frequencies exert on the structure at the same time. Therefore, the problem should consider in a statistical and probability distribution approach before transforming to frequency domain. The Acceleration Spectral Density (ASD) also known as Power Spectral Density (PSD) is a statistical measure of the structure response to random dynamic loads. It is a graph of the PSD versus frequencies in which PSD can be displacement, velocity, acceleration, or force. Table 2 shows the requirement of acceleration PSD for random vibration.

4. Results and Discussion

Modal analysis

The solutions of equation (2) are sets of eigenfrequencies with their corresponding mode shapes. The main purpose of this analysis is to compare the minimum eigenfrequency to that of the requirement, which states that all the frequencies should not be lesser than 90 Hz [4] to avoid the resonance between LV and the CubeSat. Table 8 indicates ten first modes with their

Table 8: The first ten modal frequencies of the IGOSat.

Mode	Frequency [Hz]
1	363.17
2	363.5
3	384.51
4	613.71
5	638.45
6	641.51
7	676.89
8	719.45
9	719.93
10	719.96

frequencies which are all greater than 90 Hz (the lowest frequency is 363.17Hz) that fulfills the QB50 system requirements.

Figure 11: X-axis Normal stress observed for random vibration, with maximum value at 49.128 MPa occurring in the interface between structure frame and PCBs
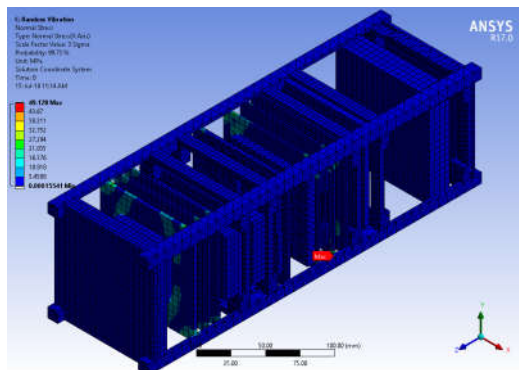
Figure 14: X-axis deformation observed for random vibration, with maximum value at 0.039 mm on the surface of a side solar panel.
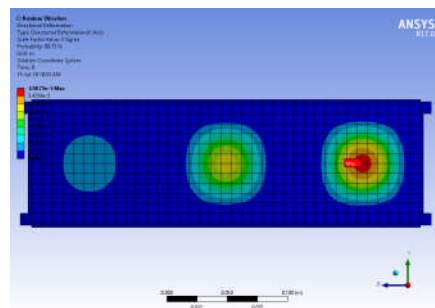
Figure 10: Y-axis Normal stress observed for random vibration, with maximum value at 41.618 MPa occurring on the surface of PCB mainboard
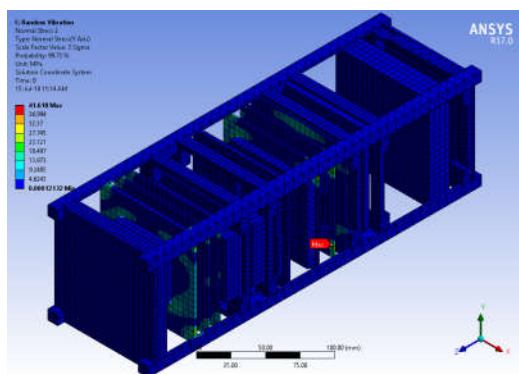
Figure 13: Y-axis deformation observed for random vibration, with maximum value at 0.054 mm on the surface of a side solar panel.
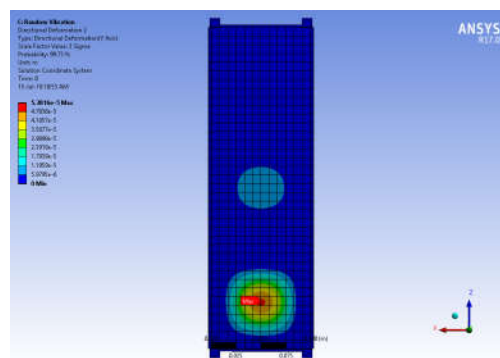
Figure 9: Z-axis Normal stress observed for random vibration, with maximum value at 79.965 MPa occurring Aluminum Attitude determiner.
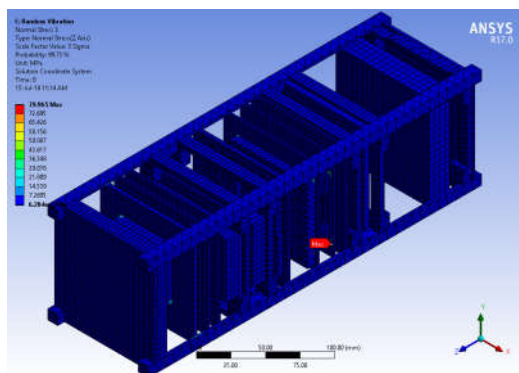
Figure 12: Z-axis deformation observed for random vibration, with maximum value at 0.318 mm on the PCBs mainboard.
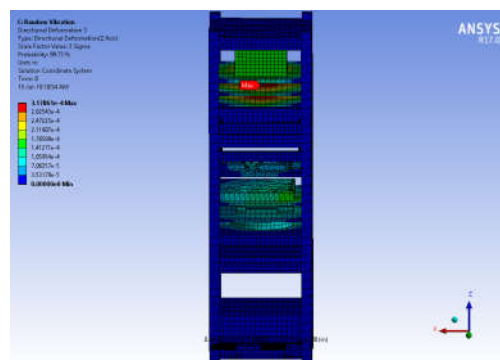
Figure 15: Normal stress amplitude (MPa) versus frequency ranges (Hz) for longitudinal harmonic vibration.

Figure 16: Deformation amplitude (m) versus frequency ranges (Hz) for longitudinal harmonic vibration.
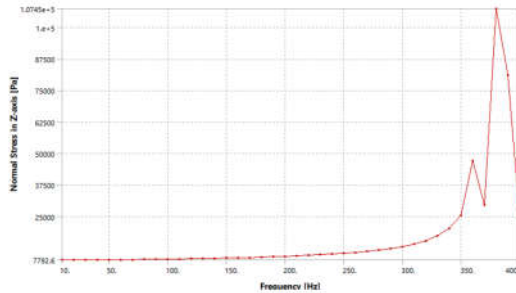
Random vibration:

The main objective of random vibration analysis is to ensure that the obtained results such as stress levels and deformation values should below the permissible limitations.

Figure 9 to Figure 14 present the maximum normal stresses as wells as maximum deformations in three directions occurred during the Random vibration test. The highest normal stresses and deformation values occurred in the PCBs along the lateral axes (X and Y directions) are much smaller in comparison with the longitudinal axis; 49.128 (MPa) and 0.039 (mm) in X-direction, 41.618 (MPa) and 0.054 (mm) in Y-direction. In contrast, the Z-axis normal stress achieved its maximum around 79.965 (MPa) which account for 29% of the Yield Strength of at Attitude determiner's materials Aluminum, whereas the maximum displacement along Z-axis is 0.318 mm which is far less than the requirements. Hence, throughout various flight phases, the random vibrations do not cause damage to the satellite system designed as the stresses and deformations are under the critical damage points of the materials.

Harmonic response:

The harmonic analysis input frequency range and individual values as shown in Table 6. The sweep frequency ranges between 5 Hz - 100 Hz, in direction Z. For observing the consistency of Modal Analysis and Harmonic Analysis, the frequency is extended to 400 Hz since there is no modal within the previous range. The first sub-step being minimum at 10 Hz to the 40th sub-step measures at 400 Hz.

Figure 15 and Figure 16 illustrate variation of the amplitude of normal stress and the amplitude of deformation with respect to variation in frequency range, for longitudinal loading condition. The normal stress reaches the peak at 1.075×10^5 (Pa) and deformation values at 1.79×10^{-5} (m) around the frequency of 360 Hz which is near the first mode of Modal Analysis, thus, ensuring the consistency between two types of dynamic analysis results and guarantee that no dynamic coupling will occur during this launch loading scenario. The obtained solutions are extremely negligible compared to the yield parameters of the structure verifying the CubeSats design is safe for this test.
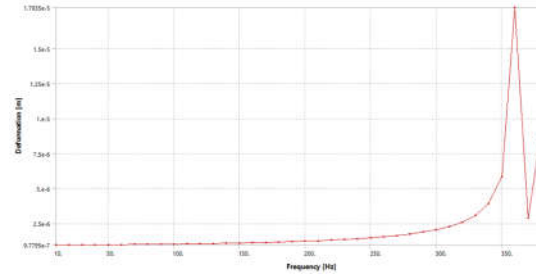
Conclusion

The numerical simulation indicates that the IGOSat structure inside a P-POD can survive through various dynamic loads launching phase by the LV. Firstly, the natural frequency of the structure is determined by performing a modal analysis with appropriate boundary conditions. The obtained first mode of frequency occurred at 363.17 Hz three times higher than the requirement at 90 Hz.

In addition, for the harmonic and random vibration analyses, no incidence of resonance was recorded which implies that the peak stress and deformations generated do not occur at excitation frequencies corresponding to the modal frequencies of the structure. Plus, the peak response of normal stress, as well as deformation values obtained, is far lesser compared to the yield strength of the frame structure and subsystem materials.

Finally, through all three numerical dynamic analyses found that the CubeSat remains intact during the launch environment.

Bibliography

[1] P. G. S. a. J. S. e. Fortescue, Spacecraft systems engineering, John Wiley & Sons, 2011.

[2] P. Avitabile, "Experimental modal analysis - A simple non-mathematical presentation," in *S V.*, 2001, pp. 20-31.

[3] E. T. N. Wang, "structural dynamic capabilities of ANSYS," in *ANSYS 2002 Conference*, Pittsburg, Pennsylvania, USA, 2002.

[4] "QB50 System Requirements," 9 July 2014. [Online]. Available: https://www.qb50.eu/index.php/tech-docs/category/QB50_system_requirements_issue_606e0.pdf?download=58:qb50-docs. [Accessed 30 April 2018].

Study of Design and Manufacture for One-line Rice Color Sorting Machine

Nguyen Tan Y[1,4], Le Thanh Son[2], Tran Quang Tuyen[2], Nguyen Huy Bich[3], Nguyen Truong Thinh[1]

[1] Faculty of Mechanical Engineering, University of Technical Education, HCMC, Vietnam;

[2]Long An Mechanical Manufacturing Joint Stock Company;

[3]Faculty of Engineering, Nong Lam University, HCMC, Vietnam;

[4]Nguyen Tat Thanh University, HCMC, Vietnam.

ABSTRACT

Rice color separation machine" is an important equipment of the rice harvested processing line. This device helps classify finished rice and whereby, export value of Vietnam rice also increases. This paper presents the mechanical design solutions for the adjust slide and spraying equipment position structural of the rice color separation machines . Slides, spraying equipment and feeder are main structures in the mechanical cluster of the rice color separation machine and their relative positions are important parameters in deciding the accuracy and response ability of the spraying equipment as well as identifying rice lines of the cameras. This paper proposes the design calculation determining parameters of the relative distance for a standard working mode and make the gap adjustment mechanism for the color rice separator machine can best respond the part of the image recognition camera control.

Keyword: Rice color separator machine , Rice trough adjustment structure…

1. INTRODUCTION

In the internal Vietnam economy, agriculture is the most spread sector with high connectivity with many other economic sectors.

Particularly within the food processing industry, the processed rice exports industry accounted for 15% of the country's export turnover of $ 3.7 billion in 2012. So as to achieve the above results, the automation problem in the rice processing chain is strategic and that is a matter of Government concern and development. Rice color separator machine is a device in the modern production line in the finished products (Figure 1), so that it is highly determinant in the automatic processing line for exported rice.
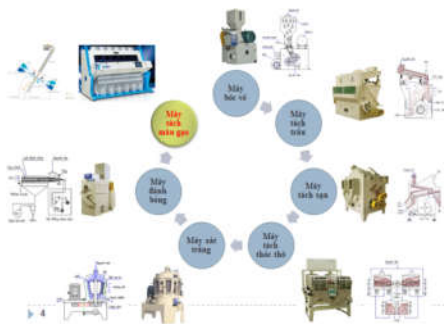
Fig 1. Location of the rice color separation machine in rice production line

2. CALCULATION PROCESS AND MODELLING DESIGN

Rice color separator machine is designed based on the principle of image recognition and processing by real-time high speed CCD camera in suitable light environment. In order to perform color separation, there are three basic elements: image processing algorithms, lighting methods to recognize object and mechanical frames. In this, the mechanical system is responsible for feeding rice during the operation to ensure the productivity and separation rice when the control signal is appeared. Accurate and precise separation of the rice is critical requirement to the machine's performance. In actual practice, the relative position between the feeder, spraying equipment and the camera angle is critical effect to the accuracy of the separation.

2.1 *Calculation and design process*
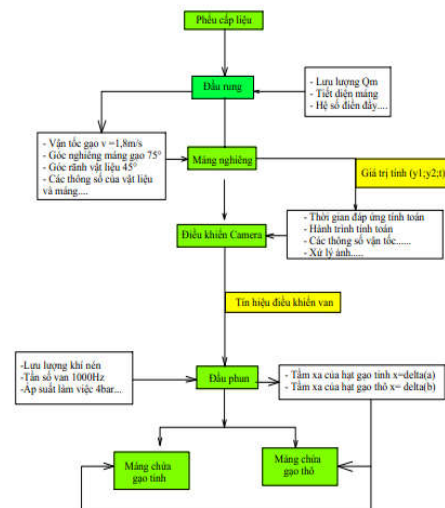
Fig 2. Calculation and design process

2.2 Modeling

(Machine Specification)

- Input capacity: 9 tons/hour
- Accuracy : 98%
- Maximum power consumption: 6kW, regularly 4kW
- Power supply: 220V/50Hz
- Air compressor power: 10 Hp
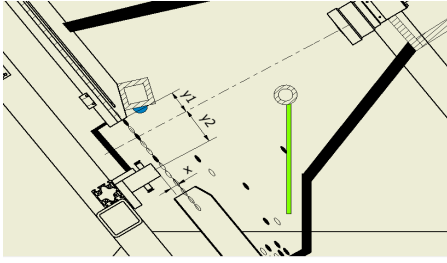
Fig 3. Relative position of camera and sprinklers

Based on the model and the calculation sequence of the parameters (Figure 2), the following is the calculation of important parameters of the rice color separator machine.

Calculate the velocity of the rice when coming out of the feeder vibrating at the required flow rate as follows:

$$v_{mtb} = \frac{Q_m}{F\gamma\psi} \qquad (1)$$

Insides, the density of rice (γ), fill factor(ψ),the cutting charge of the material line in leaning feeder, and the required flow rate for are (Q_m). The suitable capacity of rice for a feeder are:

Calculated value $v_{mtb} = 1,8 \; m/s$

Calculate the output velocity of the rice at the end of the leaning feeder and the time parameters for the critical positions.
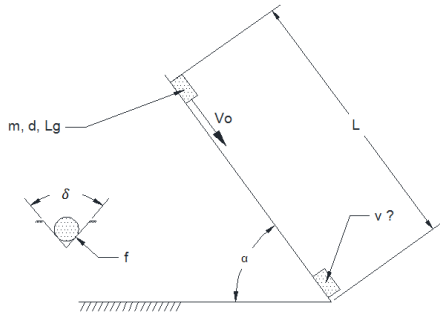
Fig4. Modeling calculations using rice movement on leaning feeder which has a ditch.

Rice speed at the end of leaning feeder.

$$v_{ck} = \sqrt{v_{mtb}^2 + 2gL\left[\sin\alpha - f\frac{\cos\alpha}{\cos\frac{\delta}{2}}\right]} \qquad (2)$$

Therefore, the angle of the spraying equipment α, the opening angle δ, the length of the feeder L, the coefficient of friction of the spraying equipment with rice f.

Calculation value $v_{ck} = 4,376 \; m/s$

Calculate the orbit of the rice in space. In this section the, determination of the distance between the spraying equipment and the camera to meet image processing speed limit and response capacity of the actuator is pneumatic valve frequency 1000 Hz.
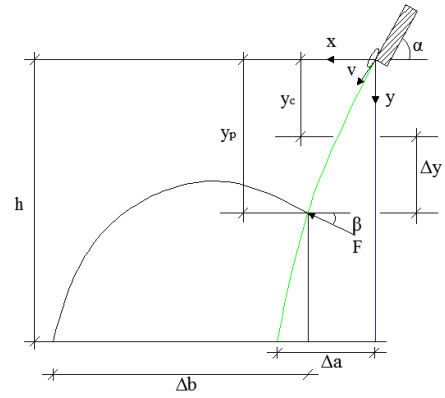
Fig5. Model of falling position of rice when the force acting from the spraying equipment

Calculate the amount of time's the grain falls from the feeder move to the camera

$$t_c = \frac{-v_{ck}\sin\alpha + \sqrt{v_{ck}^2\alpha + 2gy_c}}{g} \qquad (3)$$

Calculate the amount of time the rice falls from the feeder to the spraying equipment tp and yp. Calculate the time of movement from the camera to the spraying equipment.

$$\Delta t = t_p - t_c \qquad (4)$$

Calculate the falling coordinates of finished rice.

$$y = xtg\alpha + \frac{g}{2v_{ck}^2\alpha}x^2 \qquad (5)$$

Given y = h (1,020 mm), the value given in the high-selective design for the rice color separator machine. Solving the equation (5), we calculate the long range value from which the basis of choice is the width of the feeder , x = Δa = 223 mm.

$$v_{px} = v_{ck}\cos\alpha \qquad (6)$$

$$v_{py} = -\sqrt{v_{ck}^2\alpha + 2gy_p} \qquad (7)$$

The velocity of injection spraying equipments on the rice by the spray force F, the calculated value of the force is based on the spraying equipment pressure at the 15 mm section.

$$F = ma$$

$$dv = \frac{F}{m}dt$$

Integral for two equations, with selective time t being the response time of the spraying equipment. We get the velocity value acting on the rice.

$$v = 0,1Fm \qquad (8)$$

The total velocity of rice at the starting point of air injection with the angle $\beta = 90^0 - \alpha$

$$v_{px} = v_{ck}\cos\alpha + 0,01Fm\cos\beta$$

$$v_{py} = -\sqrt{v_{ck}^2\alpha + 2gy_p} + 0,01Fm\sin\beta$$

The orbital equation of the rice is separated.

$$y = \frac{-\sqrt{v_{ck}^2 \sin^2 \alpha + 2gy_p} + 0{,}1Fm\sin\beta}{v_{ck}\cos\alpha + 0{,}1Fm\cos\beta}x$$

$$-\frac{g}{2(v_{ck}\cos\alpha + 0{,}1Fm\cos\beta)^2}x^2 \quad (9)$$

Solving the equation (9) with y = 0 results in the calculation of the longest range of classified rice x = Δb = 535 mm; calculating the value of the raw material feeder in the design.

2.3 Investigate the relationship and choose the appropriate altitude.

The time response factor is the factor that affects the relative position of the image and pneumatic center spray point, which determines the accuracy of the rice classify process. Therefore, in the design needs to calculate a pair of values (y1; y2; t) accordingly.

The image processing time is 1 ms, the signal transmission time is 0.2 ms, the response time of the compressed air valve is 1ms, so we can calculate the total response time as fast as possible is: $t_{du} = 2{,}2\,ms$.

114/5000

Based on the control time response, the results of the computation showed that the appropriate pairs value were selected. (Table 1)

$$(y_1; y_2; t) = (4; 11; 2{,}5)$$

Table 1. The parameters about calculation and bias of correspondence

Response time t (ms)	Vertical distance y_c	Vertical distance y_p	Vertical slanting y_1	Vertical slanting y_2
2.045	5.800	8.689	6.000	9.000
2.159	5.310	9.179	5.500	9.500
2.272	4.830	9.659	5.000	10.000
2.387	4.350	10.139	4.500	10.500
2.500	*3.860*	*10.629*	*4.000*	*11.000*
2.614	3.380	11.109	3.500	11.500
2.729	2.900	11.589	3.000	12.000
2.843	2.410	12.079	2.500	12.500
2.957	1.930	12.559	2.000	13.000

3. DEMONSTRATION - RESULT- DISCUSSION

The gas law in the top of the spraying equipment is so complex that it is difficult to conduct a pressure profile survey at any cross section to select the most suitable distance of the spraying equipment to the orbit of rice, so the simulation will take less time and consistent with the problem of complex fluid. Furthermore, the convergence problem at the cross section will determine the accuracy as well as the color separation of rice. The results of the calculation are presented at the center of the pneumatic hole located at the l5mm line of rice.
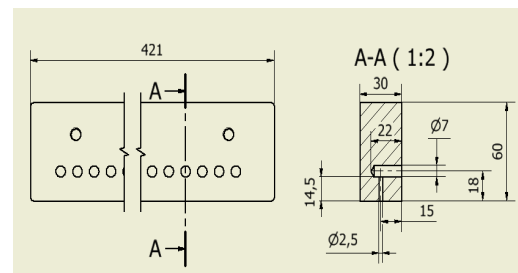
Fig 6. Model of the top of spraying equipment cross-section pneumatic is used to demonstrated simulation model.
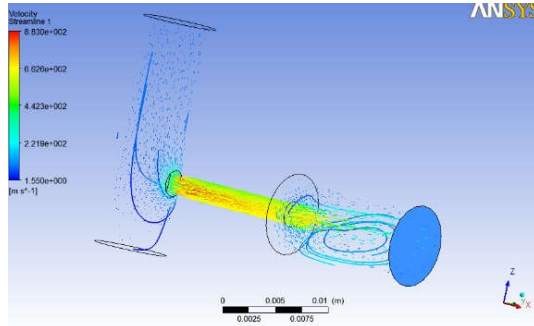
Fig 7. The result of velocity simulation at 15 mm of section
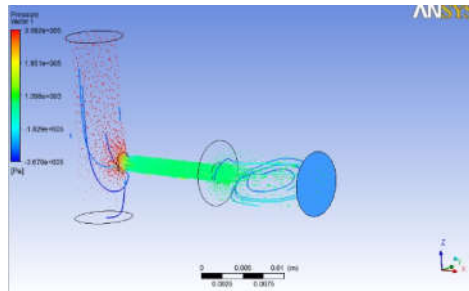
Fig 8. Results of pressure simulation at 15 mm of section
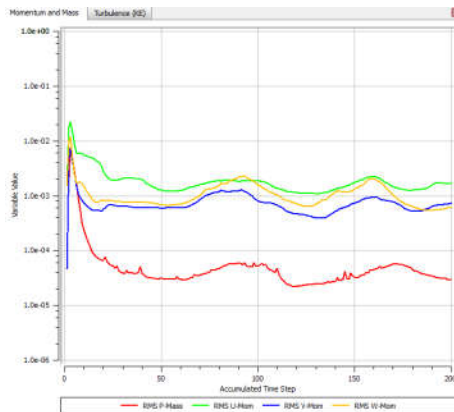
Fig 9 Integrated graph of output velocity in three axes in space

According to the simulation results and Fig. 9, the relative pressure at the spraying equipment and the gas velocity at the 15 mm section are respectively

$$p = 10^3 \; Pa$$
$$v = 200 \; m/s$$

The value of the top of the spraying equipment force applied to the rice at the time of firing is calculated by the following formula:

$$F = pA$$

In case:

- The area of the rice is affected by the force of the air stream according to the formula: $A = \frac{\pi}{4} d^2$

(with d = 2.5 mm is the diameter of the injection hole.)

- The pressure at the 15mm cross section is simulated $p = 10^3 \; Pa$

Result $F = 1.96 \; N$

4. CONCLUSION - EVELOPMENT DIRECTION

4.1 Conclusion

The following conclusions can be drawn from the research and experimental operation of the device:

- ANSYS software results show that the design of the spraying equipment is focused and that the pressure parameters at any cross section determine the position of the spraying equipment with the orbit of the rice which is suitable for classification. The calculation of the above parameters will be very complicated and sometimes not possible due to the large volume of calculations.

- Accurate calculations of the relative position between leaning feeder, cameras and spraying equipment are very important parameters, it determine the classification performance of the machine when combined with the image recognition system.

- Basing on this calculation, we can use to design the operation mechanism of the rice color separator machine.

4.2 Development direction

- Rice color separator machine is a device in the modern rice processing line, which is integrating with the whole rice processing chain is a matter of concern.

- In addition, the built-in modular design makes easy maintenance and replacement.

- The mechanical solution helps to improve the color separation of the machine, reducing the proportion of unselling e rice in the product.

ACKNOWLEDGEMENT

REFERENCES

[1] B. Y. Gorial and J. R. O'Callaghan, **Separation of grain/straw mixtures in a horizontal airstream**, Journal of Agricultural Engineering Research 1991.

[2] Nitat Tangpinijkul, Rice Milling System, "**Rice Post Harvest Technology**" IDRC, 2008.

[3] James E. Wimberly, **Technical handbook for the paddy rice postharvest industry in Developing Countries**, INTERNATIONAL RICE RESEARCH INSTITUTE – IRRI,1983.

[4] BUHLER, Destoner MTSC for an Efficient Cleaning.

[5] Husking_apparatus. Nghiên cứu về hệ thống máng nghiên rãi liệu và cơ cấu điều chỉnh lưu lượng, lớp thóc cấp liệu máy bóc vỏ. US Patent US5678477

[6] Bài báo "Determining percentage of broken rice by using image analysis" của nhóm tác giả H. Aghaghazvini, A. Afzal, M. Heydari Soltanabadi, S.Malek L. Mollabashi, (Iran) về ứng dụng của camera để chụp hình ảnh gạo qua đó xác định được hạt tấm.

[7] Website của công ty Cơ khí Long An: www.lamico.com.vn

Optimal Dynamic Routing for 2 Forklifts in Narrow-aisle Racking Warehouse

Ngoc Cuong Truong[(1)], Truong Giang Dang[(2)], Duy Anh Nguyen[(1)]

(1)Ho Chi Minh City University of Technology
268 Ly Thuong Kiet Street, District 10, Ho Chi Minh City, 700000, Viet Nam
(2)Ho Chi Minh City University of Transport
Number 2, D3 Street, Ward 25, Binh Thanh District, HCMC, 700000, Viet Nam

ABSTRACT

Determining storage location and planning path are the two most important components in warehouse management. Simultaneous resolution of these problems not only reduces the storage and retrieval time but also avoid. The article offers a scenario of a practical cold warehouse system with narrow aisle racking, where space optimization and time scheduling are always top priority. To optimize the travel time, an algorithm based on the A* algorithm is proposed to determine the appropriate storage location. The system is simulated by MATLAB combined with V-Rep software for an intuitive interface and fully illustrates each task of each vehicle from time to time.

1. Introduction

Determining storage location - localization is understood as the process of selecting the optimal storage location among different position, so that the travel time is minimization, thus saving the total operating costs of the warehouse. In addition, each storage location should be closely managed based on information such as type of goods, stored time, coordinates.

Planning path is defined as a process for selecting the most optimal path from all the solutions. The optimal path is determined based on two factors: the distance from I/O point to selected storage location is the shortest and there is no deadlock or traffic jams while vehicles move in the system. Strategy of route planning could be classified into two categories: Static and dynamic routing [1, 2, 5]. For the static routing, there is only 1 storage location and 1 fixed path is choose in advance for each task of the forklift, the selection will not change during the task execution

This paper contribute by constructing an algorithm base on dynamic routing strategy to solve the problem. Storage location is determine by the Closest Open Location algorithm - COL and collision is solved through the time windows concept [3, 4]

2. Method

2.1. Assumption made Layout design

The system is built based on some special characteristics of cold store for preservation of aquatic products but we can adjust it to suit different types of storage.

- The capacity of system are 480 storage locations, each location contain 1 SKU (stock keeping unit – an inventoried item). System containing 6 types of frozen shrimp which are named A1, A2, A3, A4, A5 and A6.
- Goods are organized into the pallet. Each pallet is a SKU. This is the smallest item in system. Pallet is placed on single pallet racking and other picker

can reach all items in the rack regardless of rack's height.

- Pick out time is undefined for all SKUs in system. For frozen shrimp products, the requirement in storage process is if goods were come first, it will be sorted in pallet racking first (FIFS) and travel distance for each moving cycle is the shortest to prevent damage under wrong temperature. In retrieval process, pallet is removed base on import day, the oldest good in system is the earliest move out. This requirement is necessary to ensure the goods are not in warehouse too long.

2.2. Layout design

Caron, Marchet, and Perego (2000) found that the
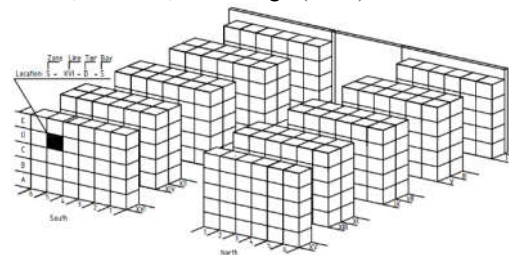
Fig. 17 Warehouse structure

layout design greatly affected to order picking distance. According to their study, layouts affect over 60% of the total distance traveled in storage [Dr. Peter]. Therefore, designing layout is an important foundation task before building the management algorithm [7].

From assumptions were presented in section 2.1, warehouse system with 1 single pick aisle and 2 storage aisles is recommended (see Fig. 1). Warehouse space is divided into 16 pallet rackings (16 lines). The line consider in this paper include 5 tiers (A, B, C, D and E) and 6 bays (are distinguished by the digits from 1 to 8), totally 40 storage locations is located at each line. These lines are named Roman numerals I to XVI. The design help to be easily reach all items in the pallet racking and access to depot by using 2 separate Input

and Output points.

2.3. Auto – Localization

For frozen shrimp products, the shorter duration of sorting, the less risk of failure of goods, so pallet should be entered into inventory under FIFO and COL strategy. For FIFO policy, if goods are shipped to warehouses before, it will be sort in pallet racking before. With COL strategy, each pallet was added into appropriate storage location whose time to I/O point is the shortest. To apply FIFO and COL strategy, A* algorithm was propose to find the optimal storage location.

First published in 1968 by Peter Hart, Nils Nilsson and Bertram Raphael, A* is an informed search algorithm, meaning that it solves problems by searching among all possible paths to the solution (goal) [8].
Evaluation function:

$$f(n) = g(n) + h(n) \ (1)$$

- Operating cost function, $g(n)$ – Actual operating cost having been already traversed.
- Heuristic function, $h(n)$ – Information used to find the promising node to traverse, the heuristic function must be admissible.

Each storage location in warehouse is represented by a node, it will be used as an object of the algorithm in this section. Some notations is given below:

- Open list (O) stores nodes for expansions
- Closed list (C) stores nodes which we have explored
- Selected list (S) stores nodes which is in the shortest path was defined

Fig. 2 demonstrates how to determine an optimal storage location using the star algorithm: n
The $g(n_{best})$ in this flow chart represents the exact travel distance of the path from the starting point to any vertex n_{best} – which is defined as a shortest node in each step of the loop and $h(n_{best})$ represents the heuristic estimated distance from vertex n_{best} to the selected storage location x. $h(n)$ value is calculated using the Euclidean distance formula. Each time through the main loop, it examines the vertex n that has the lowest (1) with each:

$$g(n) + h \ (n_{best, x}) < g(x) \qquad (2)$$

One more node in the shortest path is found. The main loop repeat until latest node is determined – which represent selected storage location.

The auto-localization algorithm base on A-star approach is clear. It is easy to implement and allows very fast route computations since this method only cares about the start and end of each row and ignore the time dependent between forklifts. How-ever, when system was performed by 2 forklifts, various drawbacks are caused by deadlock and traffic jam have a deteriorating effect on the system performance (see Fig. 3).
To deal with the problems of the model given in previous Section, a different approach that computes shortest (traveling time) and conflict-free routes

simultaneously is propose which time-dependent between vehicles is considered [4, 5, 6].
The idea of the algorithm is that find a conflict-free shortest-time route in the case there is collision potential in the aisle (see Fig. 3). According to the approach, after the shortest path to the storage location is found by the A* algorithm, a time-dependent histogram is established. Based on distance and velocity data, the position of each vehicle at each time on the map is determined and then a free-conflict path is formed by using the waiting time.
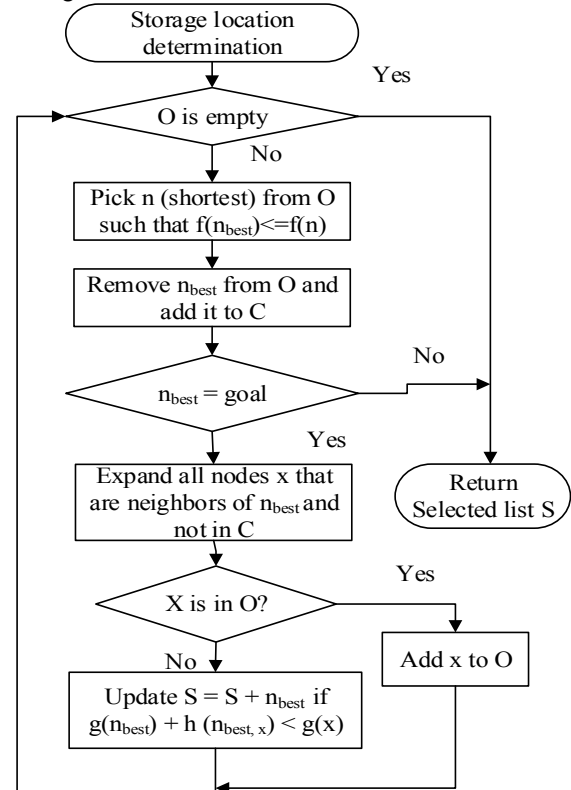
Fig. 2. Determine Storage location by A* algorithm
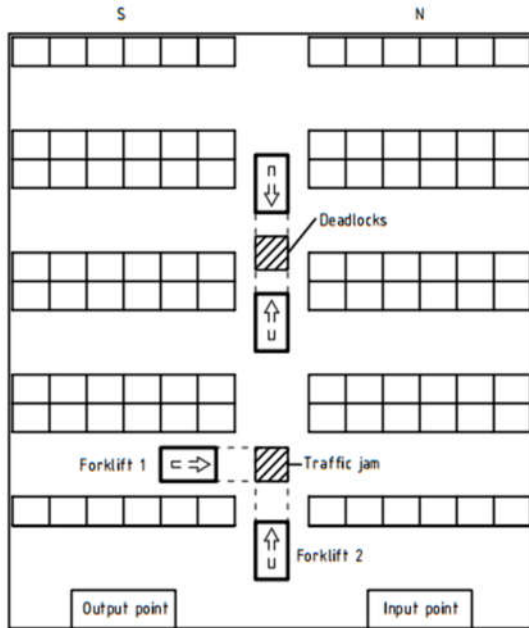
Fig. 3 Deadlock and Traffic Jams
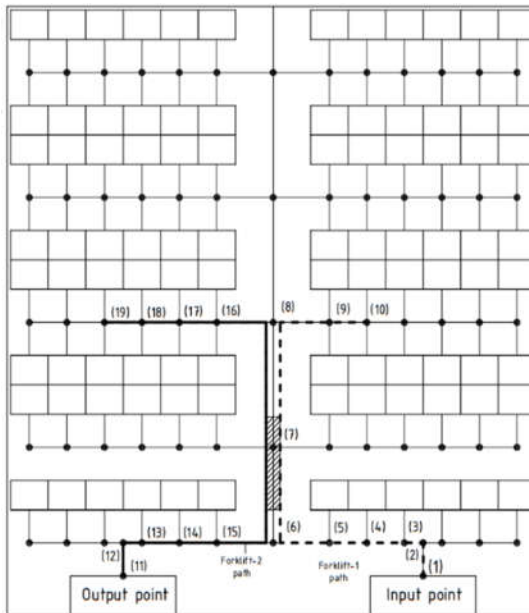
Fig. 4 Path of 2 forklift with deadlock

The idea of the algorithm is that find a conflict-free shortest-time route in the case there is collision potential in the aisle (see Fig. 4). According to the approach, after the shortest path to the storage location is found by the A* algorithm, a time-dependent histogram is established. Based on distance and velocity data, the position of each vehicle at each time on the map is determined and then a free-conflict path is formed by using the waiting time for a vehicle (see Fig. 5)
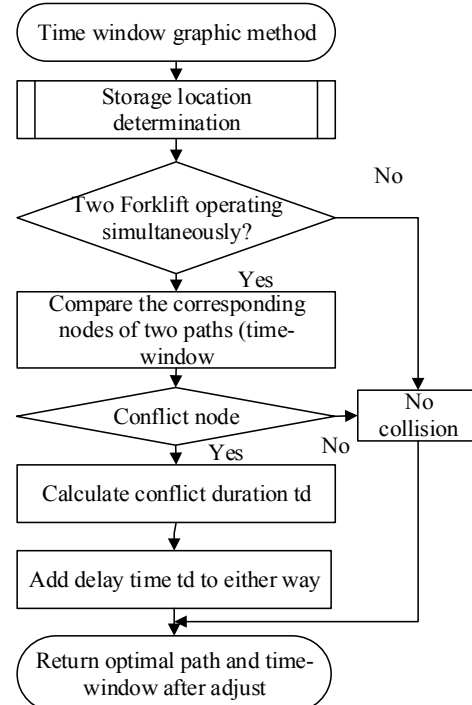
Fig. 5 Time window for dynamic routing

3. Simulation and Result
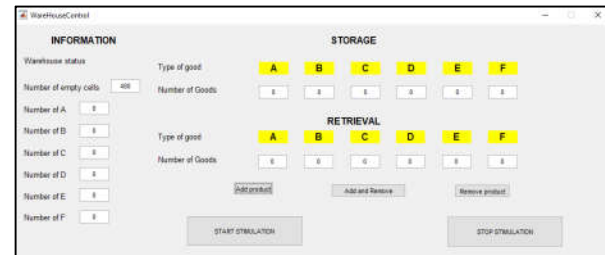
Fig. 6 Software interface
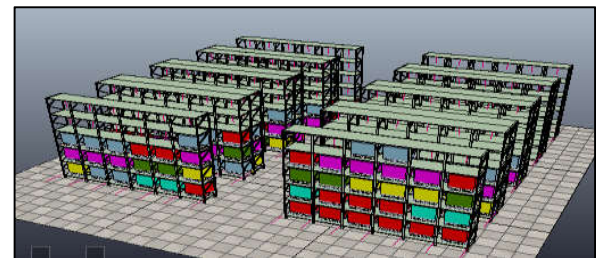
Fig. 7 Warehouse layout simulation

Goods management is done through a UI interface on MATLAB as shown in Fig. 6, the warehouse space is simulated on V-REP (see Fig. 7). The constructed algorithms will be tested by two comparisons: the time efficiency between the COL strategy and random algorithms; dynamic routing by time window with conflict-free routing by using double pick aisle.

3.1. Comparison of Closest open location COL and random algorithms

Under the Random algorithm, each pallet is randomly stored, approximately 80% of the warehouse capacity is used, sorted sequence and time consumption is shown in Fig. 8
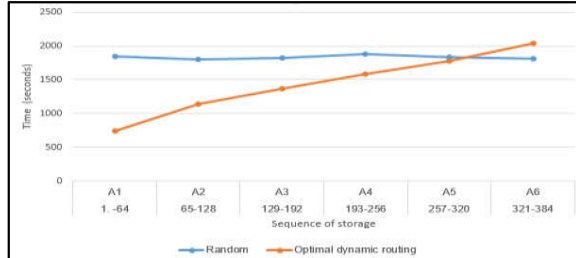
Fig. 8. Time consumption under random and COL policy

The result shown that under built algorithm (optimal dynamic routing base on A* algorithm), the travel time less than about 21.75% compare with Random strategy

3.2. Comparison of dynamic routing (single aisle) and double pick aisle

In fact, in order to solve the collision problem, a parallel aisle system is formed, vehicle will avoid each other by going on different paths, which is to change the ware-house layout instead of using complex algorithms to find an optimal path for single pick aisle as the article (see Fig. 9). For this method, the algorithm to localization is same with dynamic routing approach.

The comparison result shown that travel time of optimal dynamic routing is approximately 7.33% less than double aisle approach (shown in Fig. 10)
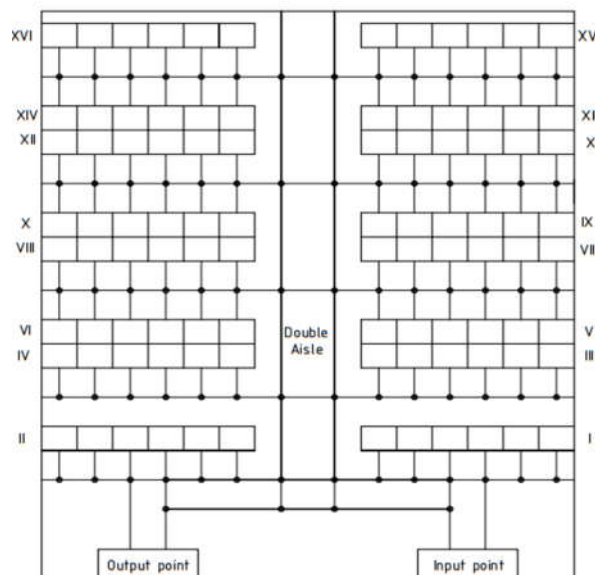
Fig. 9. Layout with double aisle
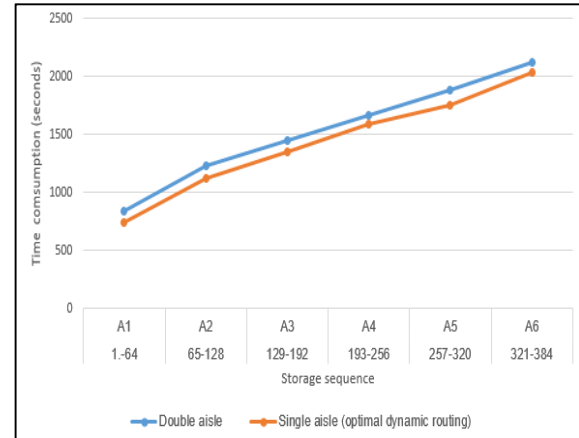
Fig. 10. Time consumption for 2 route approach

4. Conclusion

The article presents a new approach to the planning route for narrow aisle warehouse by dynamic routing for simultaneous 2 forklifts, combining the first in first out and the closest open location strategy to help reduce the cost cause by time consumption. This is also a positive aspect in the reduction of warehouse operating costs - a top priority in cold storage management. The 2 comparisons point out the approach help reduced about 21.75% and 7.33% travel time compare with random and double aisle approach respectively.

Future work will include more complex comparisons such as the quantity of goods are delivered must be greater like the real environment. The frequency of storage and retrieval tasks need to higher than so that could validate the stable of the designed system. Moreover, mechanical system design to connect with software need to be implement, this is next step to completely build an automated storage and retrieval system in warehouse

References

[1] Ngoc Cuong Truong, Truong Giang Dang, Duy Anh Nguyen: Development of automated storage and retrieval algorithm in cold warehouse. South East Asean technical university consortium symposium, ISSN: 1882-5796, 2017.

[2] Ngoc Cuong Truong, Truong Giang Dang, Duy Anh Nguyen: Development and Optimization of Automated Storage and Retrieval Algorithm warehouse by Combining Storage Location Identification and Route Planning Method". IEEE International Conference on System Science and Engineering 2017.

[3] Ngoc Cuong Truong, Truong Giang Dang, Duy Anh Nguyen: Building Management Algorithms in Automated AETA 2017

[4] Kelen C. Teixeira Vivaldini, Marcelo Becker, Glauco A. P. Caurin: Automatic routing of forklift robots in warehouse Applications. ABCM Symposium Series in Mechatronics, 2010

[5] K. T. Vivaldini, J. P. M. GaldamesMember, T. B. Pasqual, R. M. Sobral, R. C. Araújo: Automatic Routing System for Intelligent Warehouses. IEEE, 2010

[6] Samia Maza, Pierre Castagna: Conflict-free AGV Routing in Bi-directional Network. IEEE 2001

[7] Rolf H.Mohring, Ekkehard Kohler, Ewgenij Gawrilow and Bjorn Stenzel: Dynamic Routing of Automated Guided Vehicles in Real-time. Springer, 2008

[8] H. Choset, K. M. Lynch, S. Hutchinson, G. Kantor, W. Burgard, L. E. Kavraki and S. Thrun: Principles of Robot Motion: Theory, Algorithms, and Implementations. MIT Press, Boston, 2005.

A Research on a New Structure of Forming Tool for Single Point Incremental Forming (SPIF)

Le Khanh Dien[1], Le Khanh Tan[2], Vo Tuyen[3], Nguyen Thanh Nam[1]
[1] DCSELAB - Ho Chi Minh City University of Technology, VNU-HCM, Vietnam
[2] Ho Chi Minh City University of Technology and Education (HCMUTE), Vietnam
[3] Ho Chi Minh City University of Food Industry (HUFI), Vietnam

ABSTRACT

In almost all researches of Single Point Incremental Forming (SPIF) technology, we recognize that the revolution per minute of the forming tool when forming ferric material sheet should be as small as possible to attain the situation of rolling but no sliding of the surface of the spherical tool on the one of the sheet material. The paper recommends a new version of a forming tool in which the tip of the tool is a very hard ball (such as the quenched ball in a ball bearing) that is freely rotate by the friction to modify the contact point on the spherical surface of the tool to avoid the abrading and keep the spherical shape. The manufactured forming tool is used and verified by empirical processes. The models formed by the typical tool are better in comparison with the ones of normal forming tool.
Keyword: SPIF, stresses, strains, deformation, pestle, forming tool, quenched ball, axle.

1. Introduction

According to almost all researches [2], [3], [4] the forming mechanics in Incremental Sheet Forming (ISF) differs from conventional forming process as the material is mainly deformed by local deformation at contact area between tool and workpiece sheet. Due to the forming mechanism of the Forming Limit Curve (FLC) [4] in ISF is higher than the one in conventional processes, and typically defined by a negative slope straight line. During the forming process the sheet suffers a combination of shear, stretching and bending

2. Scheme of recommendation a new structure of SPIF tool

Normally a traditional ISF tool is hold via a suitable collet in the spindle of CNC milling or specialize ISF machine as in figure 1. It rotates with the RPM of the spindle that is selected with a suitable value according to the sheet material, coarse or finishing session.

Figure 1: *Traditional tool in finishing session (National Key Laboratory of Digital Control and System Engineering-DCSElab)*

Because tool have no cutting edge so we do not known the effect of its rotation on the ability of forming metal sheet. We carried out an experiment on 3 typical materials sheet:

- Aluminum A 1059 H14 stands for nonferrous metal,
- SS330 steel stands for popular mild steel,
- SUS304 stainless steel stands for popular metal
-

that lead to thinning, approximated by the sin law: $t_f = t_0 \times \sin(90 - \phi)$. [3, 4] The failure conditions in SPIF mostly occur with uniform thinning until fracture. Failure results on cracking that typically fallows a zigzag propagation. Aside from fracture, failure may include skinning, essentially when dealing with larger forming forces [2]. The purpose of this paper is a recommendation of way of enhancing the formability of the Single Point Incremental Forming (SPIF) by a new structure of tool and spindle to eliminate or to decrease the friction between tool and workpiece sheet.

- used in industry and daily life.

In order to evaluate the effect of revolution of the tool when forming sheet by SPIF technology, a set of 4 influential parameters that are favorable to control when forming was selected:

- Depth rate Δz of tool after a round of orbit;
- Diameter of tool D (mm);
- Feed rate on horizontal plane Vxy (mm/minute);
- Revolution per minute of the tool n (RPM)

In order to measure the angle α that makes of the tangent line with the sheet profile and the horizontal line at the first tore point on the sheet, a model profile is selected in figure 2

Figure 2: *SPIF model used in experiment*

Herein: R radius of model profile, z depth at random point on profile. The angle α that stands for the formability is calculated by $\alpha = \arccos(\frac{R-z}{R})$ All the experiment were achieved in Specialized SPIF machine (figure 3) in CAD-CAM workshop of DCSElab

Figure 3: *Specialized SPIF machine in CAD-CAM workshop of DCSElab*

2. Empirical process and result

In the Design of Experiment (DOE), 2 limited values are used in partial DOF of 4 factors, so the number of experiments for each typical metal is $2^{4-1}=8$. Calculated number of iteration is 3. Therefore the number of models for each typical materials is 8x3=24. The initial limited values of each parameter are selected according to the ability of machines and the stiffness of tool and metal sheet:

Table 1: *Initial limited values of 4 parameters*

A 1050-H14 (sheet width t=1mm)				
Values	Δz (mm)	D (mm)	V_{xy} (mm/ minute)	n (RPM)
Min	0.2	5	800	400
Max	1	10	3000	2500
SS330 (sheet width t=0.6mm)				
Values	Δz (mm)	D (mm)	V_{xy} (mm/ minute)	n (RPM)
Min	0.2	5	800	400
Max	1	10	3000	2000
SUS304 (sheet width t=0.04mm)				
Values	Δz (mm)	D (mm)	V_{xy} (mm/ minute)	n (RPM)
Min	0.2	5	800	400
Max	1	10	3000	800

The average results of measuring the angle of deformation of 3 typical materials:

Table 2: *Results of DOE for 3 typical materials*

A 1050-H14					
N_0	Δz (mm)	D (mm)	V_{xy} (mm/ minute)	n (RPM)	Average forming angle α (^{0})
1	0.2	5	800	400	78.30
2	1	5	800	2500	77.81
3	0.2	10	800	2500	75.51
4	1	10	800	400	72.72
5	0.2	5	3000	2500	76.89
6	1	5	3000	400	75.73
7	0.2	10	3000	400	75.45
8	1	10	3000	2500	73.91

SS330					
N_0	Δz (mm)	D (mm)	V_{xy} (mm/ minute)	n (RPM)	Average forming angle α (^{0})
1	1	5	800	2000	73.7
2	0.2	5	800	400	76.4
3	1	10	800	400	66.5
4	0.2	10	800	2000	69.1
5	1	5	3000	400	73.3
6	0.2	5	3000	2000	77.8
7	1	10	3000	2000	68.3
8	0.2	10	3000	400	78.5

			SS330		
N_0	Δz (mm)	D (mm)	V_{xy} (mm/minute)	n (RPM)	Average forming angle α (^{0})
1	1	5	800	800	65.36
2	0.2	5	800	400	66.41
3	1	10	800	400	62.44
4	0.2	10	800	800	63.68
5	1	5	3000	400	63.41
6	0.2	5	3000	800	66.27
7	1	10	3000	800	65.84
8	0.2	10	3000	400	64.15

From the results of angle α that stand for the formability of 3 materials under the influence of 4 parameters in table 2, with the help of Minitab software, we attempt to form 3 recursion equations of the angle of formability:

Aluminum A 1050-H14:

$$\alpha = 82{,}77 - 0{,}6\Delta_z - 0{,}757D - 0{,}001845V_{xy} + 0{,}00023n - 0{,}33D\Delta_z - 0{,}00021DV_{xy} \quad (2.3)$$

The partial differential of n is derived from the above equation to define the influence of revolution n to α

3. Recommendation a new structure of SPIF tool for ferrous metal sheet

Figure 4 illustrates the structure of SPIF tool that is designed for ferrous metal sheet only under our own experience in forming sheet by SPIF technology with following specifications:

- Ball tip diameter $\varnothing 5$ is thermal treatment get hardness 60-62 HRC. The ball is attached on the end of the taper HSS body by cooper braze weld.
- HSS cylinder body with diameter of $\varnothing 12$ is hold with a couple of angular ball bearing Koyo 6000 via diameter of $\varnothing 10m7$
- The angular ball bearing are fixed inside a bushing which has outside diameter of $\varnothing 36$
- The bushing is hold by DIN 6388 collet OR52 inside the arbor of the spindle that illustrated in table 3

Table 3: Collet OR52 in the DIN 6388 collet catalogue [5]

'OR' TYPE
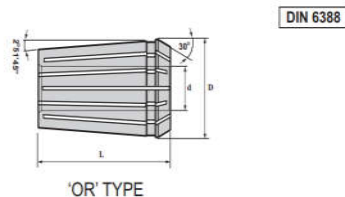
ORDERING NO.	BORE RANGE (d) FROM	TO	IN STEP	FULL SET PCS	CLAMPING RANGE	COLLAPSE CAPACITY	L	D
OR 20	2	12	0.5	21	1.5 ~ 13	0.5	34	19.8
OR 25	2	16	0.5	29	1.5 ~ 16	0.5	40	25.5
OR 30	2	20	0.5	37	1.5 ~ 20	0.5	45	29.8
OR 35	2	25	0.5	47	1.5 ~ 25	0.5	52	35.05
OR 44	4	32	0.5	57	3.5 ~ 32	0.5	60	43.7
● OR 52	30	40●	1.0	11	29.5 ~ 40	0.5	68 ●	52.2 ●
OR 64	30	50	1.0	21	29.5 ~ 50	0.5	80	63.8

$$\frac{\partial \alpha}{\partial n} = 0{,}00023 \quad >0$$

Hence, in case of aluminum or other nonferrous metal, the formability is covariant with the revolution of the tool. We can say that the higher the revolution of the tool, the bigger the formability of the product.

Recursion equation of mild steel SS330:

$$\alpha = 70{,}38 - 0{,}78\Delta z - 0{,}317D - 0{,}001n - 0{,}417\Delta z.D + 0{,}002\Delta z.V_{xy}$$

$$\frac{\partial \alpha}{\partial n} = -0{,}001 \quad <0 \qquad (1)$$

Recursion equation of stainless steel SUS304:

$$\alpha = 63{,}10 - 18{,}163\Delta z - D - 0{,}0008V_{xy} - 0{,}0092n + 0{,}8333\Delta z.D - 0{,}0015\Delta z.V_{xy}$$

$$\frac{\partial \alpha}{\partial n} = -0{,}0092 \quad <0 \qquad (2)$$

From (1) and (2) we recognize that the formability of mild steel and stainless steel or more generality other ferrous metal is contra-variant with the revolution of the tool. That means that when forming the popular ferrous metal technician should select the value of revolution of spindle or tool as small as possible.

Structure of the design SPIF tool is represented in figure 4
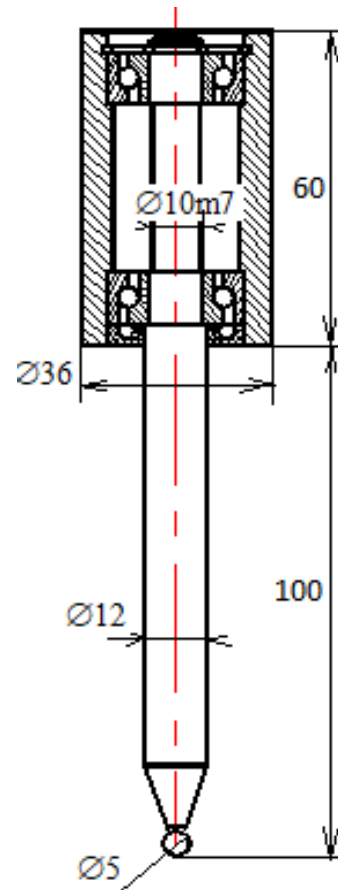
Figure 4: Structure of the design SPIF tool

4. Conclusion

This design tool is applied on y for ferrous sheet. In operation, the spindle of CNC milling machine or specialized SPIF machine have to be set fixed and stable. Because of the friction between the spherical tool tip and the sheet material, the ball rotates no sliding on the surface of the formed sheet to get the smallest revolution to satisfy the condition to enhance the formability of almost all ferrous material sheets.

Acknowledge

REFERENCES

[1] R.J. Alves de Sousa∗ , J.A.F. Ferreira, J.B. Sá de Farias, J.N.D. Torrão, D.G. Afonso and M.A.B.E Martins" SPIF-A: on the development of a new concept of incremental forming machine", Structural Engineering and Mechanics, Vol. 49, No. 5 (2014) 645-660 DOI: http://dx.doi.org/10.12989/sem.2014.49.5.645

[2] Daniel Afonso, Ricardo Alves de Sousab, Ricardo Torcato "Incremental forming of tunnel type parts", ScienceDirect Elsevier 183 (2017) 137 – 142

[3] K. Jackson, J. Allwood, "The mechanics of incremental sheet forming", Journal of Materials Processing Technology, Volume 209, no. 3, 2009, pp. 1158-1174

[4] M. Ham, J. Jeswiet, Forming Limit Curves in Single Point Incremental Forming, CIRP Annals Manuf. Tech., Volume 56, no 1, 2007, pp. 277-280

[5] http://www.lifecnctools.com/catalogue/tool-holders-catalogue.pdf

The Waste Remover in Aquaculture Ponds

Le The Truyen[1, 2], Thanh-Long Le[1,3]

[1]Key Laboratory of Digital Control and System Engineering, HCMUT (DCSELAB), Vietnam
[2]Ho Chi Minh City University of Food Industry, Vietnam
[3]Faculty of Mechanical Engineering, Ho Chi Minh University of Technology (HCMUT), VNU-HCM, Vietnam

ABSTRACT

Over the past decade, Vietnam's shrimp industry has made great progress and brings Vietnam into the rank of the world's largest shrimp exporters. The development trend of the shrimp industry in the world as well as in Vietnam today is in the direction of intensive and super-intensive farming, technology innovation to enhance productivity and quality. However, the shrimp farming industry in Vietnam is facing many difficulties; one of them is the problem of environmental pollution, raising negative impact on the economic effectiveness of farming. Causes are mainly due to excess food and untreated shrimp waste, accumulated on the pond bottom surface and disintegrated to reduce dissolved oxygen concentration, release toxic gases such as NH_3, H_2S and create a favorable environment for harmful microorganisms to develop. Therefore, it is necessary to have a countermeasure to thoroughly remove waste from the farming environment.

This paper introduces a general design of a waste remover, which is needed for shrimp farming ponds to remove waste and solve the mentioned problem. This equipment moves on the bottom surface of the pond and can be autonomous or manually remote controlled. During working process, the equipment brushes waste on the bottom surface of the pond and suck it into the filter bag. The waste remover includes such following main units: travelling unit, brushing unit, sucking unit, frame unit, transmission and control systems. The equipment uses the principle of axial pumping, sucks waste along the water stream by reducing the pressure inside the equipment and transfers waste into filter bags. This general design basically meets the requirement of waste removal and can be a fundamental for designing the detailed units, manufacturing and experiment implementation of equipment in the future.

1. Introduction

The shrimp pond liner model 35 x 35 m (fig 1.a, b) with siphon pit, the paddle wheel systems is the main obstacle that the equipment must surpass. Surface pond bottom is not flat and waste is often deposited at the bottom of the rough point.

a. The bottom of the pond

b. The paddle wheel systems
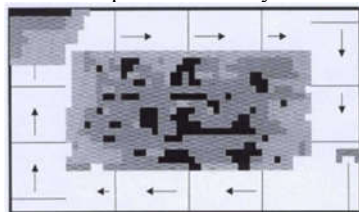
c. Distribution of waste

Fig 1: Shrimp pond and distribution of waste

A study pointed out that the attribution waste in the pond has the paddle wheel systems (fig 1c), the waste centralizes primarily in the middle area of the pond and surrounds siphon pit. Most of the waste is collected in the siphon pit, but the rest need to be removed from the pond. In order to support the siphon getting cleaner, shrimp farmers have to wade in ponds daily using hand tools to clean the bottom of the pond. At present, the study aims at designing of equipment to clean shrimp pond bottom to replace the manual cleaning is not interested in research investment.

2. Materials and methods

Cluster moving and transmission system for cluster moving

The equipment is determined to move on the bottom of the pond so the options using the wheels are selected with two wheels (fig 1a), three wheels (fig 1b) and four wheels (fig 1c). However, with working conditions under water environment, the friction of the wheel with the bottom of the pond is reduced, so that the contact surface between the wheel and the bottom surface of the pond must be large to increase the friction between the equipment and the bottom pond. The method using belt was selected for increase the friction, the wheel should be converted into the pulley and move through the friction between belt surface and bottom surface of the pond. The option using three pulleys are eliminated because it is difficult to arrange the belt. The bottom surface of the pond is not flat, so the option using four pulleys is selected instead of two pulleys to ensure

balance while moving and turn right, turn left, and turn back of the equipment. The remaining problem is transmitted torque for the pulley, two proposed methods is using the differential gear with one motor or using two independent control servomotors and direct transmits. The differential gear can solve the problem of turn left, turn right and turning back but it is limited when the equipment moves off compare to trajectory because the bottom surface of the pond is not flat. As a result, two independent control servomotors are selected, which enables the equipment to be more flexible and easier to adjust as the equipment moves off trajectory.
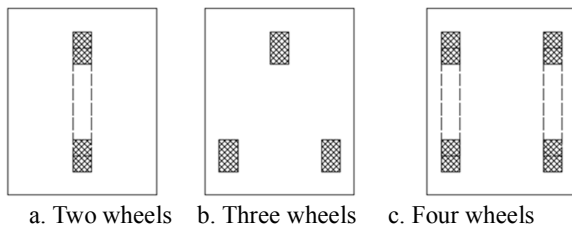
a. Two wheels   b. Three wheels   c. Four wheels
Fig 2: Methods using wheels

Cluster pump
The main task of the equipment is to suck waste deposited on the bottom of the pond and remove it from the culture pond. To perform this function, the equipment is equipped with a filter capable of filtering and holding the waste. Waste is sucked into the filter bag according to water flow, so the filter bag should be attached to a pipe suck. To increase the working time, the equipment requires a large filter bag, so the filter is designed with two pipes suck and two filter bags arranged on either side, the suction mouth is arranged at the bottom of the equipment to suck the waste on the surface of the pond bottom. In order to bring water and waste into the filter bag, it is necessary to select the appropriate type of pump. The waste and water can be suck into the filter bag, but this method must use two pumps. The simpler choice is to use atmospheric pressure to put the water in the filter bag, so the filter bag is placed in the body cavity of the equipment. The axial pump sucked water out of the body cavity through the outlet on the lid of the body. The pressure in body cavity decreased, the atmospheric pressure pushes the flow of water and waste in the body cavity in order to balance the pressure. As such, filter bags and suction pipes are designed to be assembled together by quick couplers for easy cleaning. At the quick couplers need one-way rubber valve to prevent the waste reflux back when the pump stopped working.

Cluster brush and transmission system for cluster brush
There are two methods to brush the surface of the proposed pond bottom lining, the vertical brush shaft (fig 3.a) and the horizontal brush shaft (fig 3.b).
Regarding the vertical brushing shaft method, the brushing system will consist of two shafts that are rotated in opposite directions by a transmission belt, brushing and pushing water and waste into equipment

chassis. However, this option cause hinders when the equipment overcome obstacles, and the transmission for vertical brushing shaft is more difficult than the horizontal brushing shaft. With horizontal brushing shaft system, the shaft is covered with soft and long enough bristles and is transmitted from the pulley shaft through the gear transmission. Due to the lager transmission, the brushing shaft rotates with large speed to ensure the ability of cleanliness. The waste is also pushed in equipment chassis for suction. The horizontal brushing shafts also supports for the equipment when it overcomes obstacles which are not too large at the bottom of the pond.

a. The vertical   b. The horizontal brush shaft
brush shaft
Fig 3: Design methods brush shaft

Frame cluster
The frame consists of two main parts, the lower half and the upper half of the frame are structured as a closed box. Internal space contains motors, pumps and filters. The lower half of the body is placed with the suction gate, one-way drain valve to drain water out of the body cavity when the device stopped working. The upper haft of the body is designed to be assembled to the exhaust pipe of the pump and has two doors to disassemble the filter bag. The two halves form a closed cavity to limit the pressure loss in the cavity when the device is operating.

The navigation and sensor system
Self-propelled equipment at the bottom of the pond which needs to be monitoring the location of equipment, GPS navigation system is proposed. The first problem to be solved is the transmission of the signal when the equipment is moving under water and mitigates the deviation of the GPS navigation system. In order to solve the problem of signal transmission, the GPS sensor is assembled on the float and floating on the water, the float holding mechanism is rigid enough so that the float is not drifted, cause of the deviation between the float and the equipment. However, the deviation of the GPS is still very significant. The second solution is replaced the GPS with ultrasonic beacon sets, a mobile beacon equipment assembled on the waste remover and four fixed beacons are placed at the four corners of the pond. The position of the equipment is determined by the four fixed beacons via an algorithm. In addition, the equipment is equipped with rotary angle and acceleration sensor to adjust when the equipment moves off trajectory. For monitoring location of equipment, four fixed beacons create a pond map, software used to connect the navigation system to draw the operating trajectory for the equipment, so that it can

monitor and control the operation of equipment on the computer screen.

Based on the initial analysis, the schematic diagram and the general diagram of the equipment's control system are defined.

3. Results and Discussion

The schematic diagram (fig 4) illustrates the arrangement of main components and the motions when the equipment is operating.
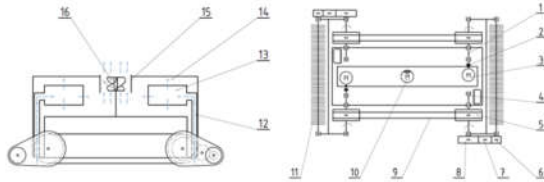
Fig 4: The schematic diagram of the waste remover
1: Active shaft; 2: Shaft coupling; 3: Motor; 4: Passive shaft; 5: Transmission belt; 6: Passive gear; 7: Intermediate gear; 8: Active gear; 9: Belt; 10: Pump; 11: Brushing shaft; 12: Suction pipe; 13: Filter bags; 14: Body cavity; 15: Outlet pipe; 16: Impeller.

Computational theory
In order to operate the equipment, it is necessary to determine the torque on the motor shaft as a basis for selecting the engine power. A diagram of the external forces on the equipment (Figure 5) is constructed that skipping the drag force of the water, which acts on the surface of equipment, within a small velocity of the equipment. The main external forces of the equipment including: The weight of the equipment full water (W), the thrust of the water (FA), the thrust of the pump (Fp), the reaction of the bottom pond (N), the force Between the outside of the belt and the bottom of the pond. From these forces, the torque can be calculated on the active axis of the belt (T).
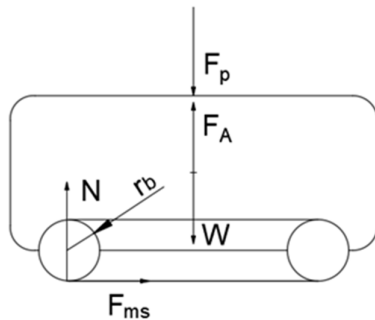
Fig 5: Diagram of external forces analysis on the equipment

$$W = M.g \qquad (1)$$

$$F_A = \rho_w.Vo.g \quad (2)$$

$$F_p = \rho_w.Q.v \qquad (3)$$

$$N = -F_A + W + F_p \qquad (4)$$

$$F_{ms} = \mu.N \qquad (5)$$

$$T = \frac{Fms}{2}.r_b \qquad (6)$$

M: The mass of the equipment full water.
g: gravitational acceleration (m/s^2)
ρ_w: Specific gravity of water (kg/m^3)
Vo: The volume of the equipment full water (m^3)
Q: Pump flow (m^3/s)
v: Velocity of water flow (m/s)
  μ: Coefficient of friction between the outer surface of the belt and the bottom surface of the pond.
r_b: Radius of the pulley (m).

The control system of the waste remover (fig 6) uses two microcontrollers on the central control board and the control board communicates with each other and receives control information from the user and executes control commands for three motors.
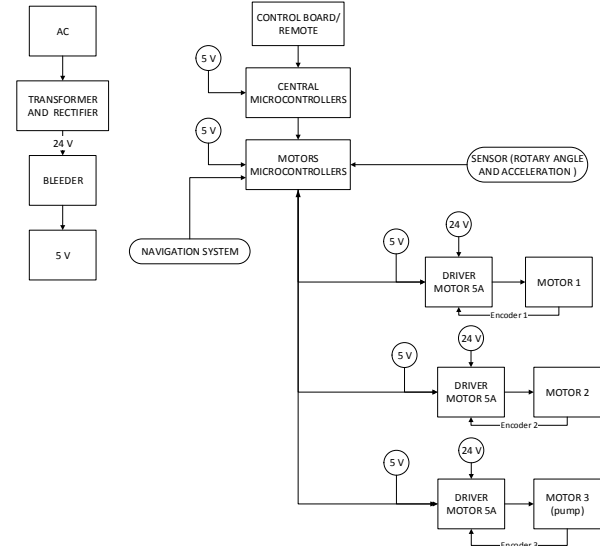
Fig 6: The control system of the waste remover
The 3D model of the waste remover is designed by SolidWorks software (Figure 7) and the proposed operating parameters are as follows:
Speed: 15 m/min;
Total power: 500 W
(Flow: 40 m^3/h)
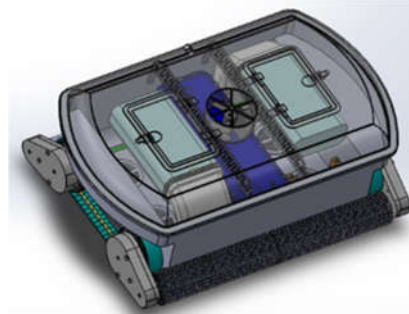
Fig 7. The 3D – design model of the waster remover
4. Conclusion
The waste removal equipment was designed and

manufactured for the test operation and evaluation of operating effectiveness.

References
[1] iCleaner-200D
[2] Robot SUPREME BIO
[3] Robot DOLPHIN Wave 300
[4] Marvelmind Indoor Navigation System Operating manual, 2018.

PART IV, SECTION IV

*Other Topics Related to Machining, Materials and Mechanical Technology
(Mechanics of Solid; Analysis and Simulation; New Machine Tools and Tooling Technology;
Dynamics and Control…)*

Effect of Steam to Fuel Ratio on a Proton Conducting Solid Oxide Fuel Cell Hybrid System Fueled by Methanol, Ethanol, Isooctane and Methane

Sasmoko[1], Chung−Jen Tseng[1], Cheng-Hao Yang[2], Wen-Sheng Chang[2], I.N.G. Wardana[3]

[1]Institute of Energy Engineering, National Central University, Taoyuan, 32001, Taiwan

[2]Green Energy & Environment Research Laboratories, Industrial Technology Research Institute, Tainan, 71150, Taiwan

[3]Department of Mechanical Engineering, Brawijaya University, Malang 65145, Indonesia

ABSTRACT

This study investigates the effects of fuel type and the steam to fuel ratio (SFR) on a fuel cell hybrid system. The system is created and simulated using Thermolib. The results show that the operating temperature of steam reforming has significant effect on the system performance and methanol has better performance than other fuels because of higher hydrogen production. Using gas fuels such as methane and isooctane are not recommended in this system because of the high reforming temperature. The optimum SFR for methanol, ethanol, iso-octane is 2, 5, 12, and 1.5, respectively

Keywords: hybrid system, p−SOFC, simulation, steam to fuel ratio.

1. Introduction

Solid Oxide Fuel Cells (SOFCs) have been developed since 1950 and have two forms: planar and tubular, and have three main parts: electrolyte, cathode, and anode. Because stack consumption is limited by hydrogen conversion rate, SOFCs can be integrated with gas turbines to utilize the unreacted hydrogen and the pressurized heat output of SOFCs. As a promising and innovative technology, combined SOFCs and gas turbines in hybrid systems can meet the growing demand for distributed energy systems with less impact. There are two kinds of SOFCs: p–SOFC (proton conducting) and o–SOFC (oxygen conducting) which differ in the electrolyte material and operating temperature used where the operating temperature of o–SOFC is from 800 ℃ to 1100 ℃, and p–SOFC is from 600 ℃ to 800 ℃. Furthermore, p–SOFC has a higher operating potential of 0.8 V and better performance than o–SOFC because of its higher Nernst potential and higher ionic conductivity of the electrolyte, while o–SOFC has lower performance because of the high concentration overpotential [1]. Three kinds of fuel cell specification available are anode supported, cathode supported, and electrolyte supported which anode supported shows the better performance than cathode or electrolyte supported [2−4]. Moreover, the performance of fuel cells also can be increased by increasing operating temperature and pressure [5,6]. Fuel cell performances are also affected by input parameter such as steam to fuel ratio. This article uses a hydrocarbon fuel, an external reforming, and a combustor to heat the reformer up. Consequently, a reformer has an important role in hybrid systems. There are three kinds of reforming processes: steam reforming, autothermal reforming, and partial oxidation where steam reforming has better performance than other reforming processes [7]. In the steam reforming, low steam to fuel ratio can lead carbon formation and high steam to fuel ratio can dilute the fuel in the reformer [8]. The objectives of this research are to study the performance of p−SOFC and a gas turbine hybrid system based on intermediate temperature SOFC and to investigate the effect of steam to fuel ratio fed by different fuels.

2. Modelling

The system is created based on thermodynamic analysis and developed using Matlab, Simulink, Thermolib with some fix parameters presented in Table 1.

2.1 p−SOFC

Hydrogen is fed to the anode side and then oxidized to form protons and electrons at the anode. The electrons flow through an external load to generate electricity, while protons are transported through the proton conducting electrolyte to the cathode side. Oxygen flows to the cathode and reacts with protons and electrons to produce water. Following electrochemical reactions take place in p–SOFC:

Anode: $H_2 \rightarrow 2H^+ + 2e^-$ (1)

Cathode: $2H^+ + 0.5O_2 + 2e^- \rightarrow H_2O$ (2)

Overall: $H_2 + 0.5O_2 \rightarrow H_2O$ (3)
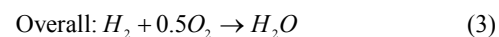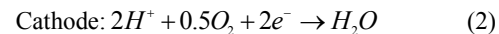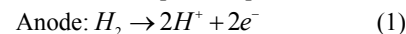
The open circuit voltage, E^{OCV}, at the standard pressure is a function of operating temperature.

$$E^{OCV} = E^0 - \frac{RT}{2F} \ln\left(\frac{P_{H_2O(k)}}{P_{H_2(a)} P_{O_2(k)}{}^{0.5}} \right) \quad (4)$$

$$E^0 = 1.253 - 2.451 \times 10^{-4} T \quad (5)$$

Ideally, the open circuit voltage is the maximum voltage achieved by a fuel cell, but voltage is always less than the open circuit voltage because of internal resistance and overpotential losses associated with the electrochemical reactions at the electrolyte interface. There are three major types of fuel cell losses: ohmic polarization, V_{ohm}, activation polarization, V_{act}, and concentration polarization, V_{conc}. The operating cell voltage can be given as:

$$V = E^{OCV} - \left(V_{act} + V_{ohm} + V_{conc}\right) \qquad (6)$$

Ohmic polarization occurs because of electrical resistances in the cell such as resistance to ion flow in the electrolyte, resistance to electron and ion flow through the electrode, and resistance to electron flow through the terminal connection. Ohmic polarization can be written as:

$$V_{ohm} = iR_e \qquad (7)$$

Activation polarization occurs when the charge transfer reaction is slow across the electrode electrolyte interface and a portion of the electrode potential is lost in driving the electron transfer rate up to the rate required by the current demand. Activation polarization can be written as:

$$V_{act(a)} = \frac{2RT}{n_e F}\sinh^{-1}\left(\frac{i}{2i_{0(a)}}\right) \qquad (8)$$

$$V_{act(k)} = \frac{2RT}{n_e F}\sinh^{-1}\left(\frac{i}{2i_{0(k)}}\right) \qquad (9)$$

Concentration polarization is caused by the mass transfer limitation on the availability of the reactants in the vicinity of the electrode electrolyte interface. It can be written as:

$$V_{conc(a)} = \frac{RT}{2F}\ln\left(\frac{P_{H_2(a)}}{P^I_{H_2(a)}}\right) \qquad (10)$$

$$V_{conc(k)} = \frac{RT}{2F}\ln\left[\left(\frac{P_{O_2(k)}}{P^I_{O_2(k)}}\right)^{0.5}\frac{P^I_{H_2O(k)}}{P_{H_2O(k)}}\right] \qquad (11)$$

2.2 Other components

In turbine gas (isentropic) components, the pressure decreases from input flow to the output flow. The first law thermodynamics for turbine:

$$\dot{W}_t = m\left(h_{in} - h_{out}\right) \qquad (12)$$

$$\eta_t = \dot{W}_{t,ac}/\dot{W}_{t,s} \qquad (13)$$

$$\eta_s = \Delta\dot{h}/\Delta\dot{h}_s \qquad (14)$$

In compressor (isentropic) components, the pressure increases from the incoming flow to outlet flow. The first law thermodynamics for compressor:

$$\dot{W}_c = m\left(h_{out} - h_{in}\right) = mC_p\left(T_{out} - T_{in}\right) \qquad (15)$$

$$\eta_c = \left(h_{out,s} - h_{in}\right)/\left(h_{out} - h_{in}\right) \qquad (16)$$

$$\eta_s = \Delta\dot{h}_s/\Delta\dot{h} \qquad (17)$$

In heat exchanger components, counter flow is used as flow direction where effectiveness is used as the actual heat transfer rate.

$$\varepsilon = Q/Q_{max} \qquad (18)$$

$$\varepsilon = \frac{1 - \exp[-N(1-C)]}{1 - C\exp[-N(1-C)]} \qquad (19)$$

While the heat transfer to the environment is:

$$\dot{Q}_{env} = k_{env}A_{env}(T_{TM} - T_{env}) \qquad (20)$$

In combustor, the reactor calculates the flow, heat transfer to the environment and also pressure loss. First law of thermodynamics for a chemical reaction:

$$\sum_{reac} \dot{m}_{in}\, h_{in} = \sum_{proct} \dot{m}_{out}\, h_{out} + Q \qquad (21)$$

The last component is a reformer, it is often in combination with catalyst and steam to break fuel down to hydrogen. During a fuel reforming process, additional species such as carbon dioxide is produced. In the simulation, several fuels such as methanol, ethanol, isooctane and methane react with steam to produce high hydrogen concentration. Methanol, ethanol, isooctane, and methane steam reforming is almost complete above 100−250 ^{0}C, 550−650 ^{0}C, 750−900 ^{0}C, and 800−1100 ^{0}C, respectively. The reactions are as follows.

Methanol steam reforming:

$$CH_3OH + H_2O \rightarrow CO_2 + 3H_2$$
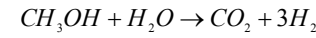
$$\Delta H = +49.4kJ/mole \qquad (22)$$

Ethanol steam reforming:

$$C_2H_5OH + 3H_2O \rightarrow 2CO_2 + 6H_2$$
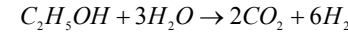
$$\Delta H = -173kJ/mole \qquad (23)$$

Isooctane steam reforming:

$$C_8H_{18} + 16H_2O \rightarrow 8CO_2 + 25H_2$$
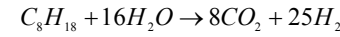
$$\Delta H = +1233.6kJ/mole \qquad (24)$$

Methane steam reforming:

$$CH_4 + 2H_2O \rightarrow CO_2 + 4H_2$$
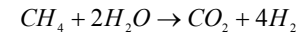
$$\Delta H = +165kJ/mole \qquad (25)$$

Table 9. Parameters given.

Parameter	Value
Anode thickness (μm)	500
Cathode thickness (μm)	50
Electrolyte thickness (μm)	50
Number of cells	100
Maximum hydrogen conversion rate	0.83
Active membrane area (m²)	0.01
Gas turbine isentropic efficiency	0.83
Compressor isentropic efficiency	0.78
Coefficient of overall heat transfer (W/K)	100
Total surface of heat exchanger to environment (m²)	1
Total surface of combustor (m²)	1

2.3 System design

A combined hybrid system is shown in figure 1 where the air is initially compressed by the compressor up to 3 bar and flows into an air heat exchanger to increase the temperature before going into the cathode input side. On the other hand, water and ethanol at a temperature of 25 °C and pressure of 3 bar are mixed in the mixer and flow into a fuel heat exchanger and a steam reformer to react with catalytic before going into anode side. Species formed of the reformer output are hydrogen, carbon dioxide, and about one percent unreacted ethanol. After reactions take place in the fuel cell, gas output at anode and cathode output side mix together and flow into a combustor and gas turbine. The gas turbine output at a pressure of 1 bar is utilized to

generate hydrogen by heat the reformer up. Low pressure and low temperature of gas output reformer flow into p–SOFC cooling system. The function of p–SOFC cooling system is to maintain the stack temperature. Furthermore, the gas output of the cooling system is utilized to heat an air heat exchanger up. Because the output temperature of the air heat exchanger is still high, gas can be used to generate a hot steam or recovery heat by installing a heat exchanger with water flows constantly at 0.1 mole/s and the exhaust gas of system is kept at a temperature of 25 ℃.
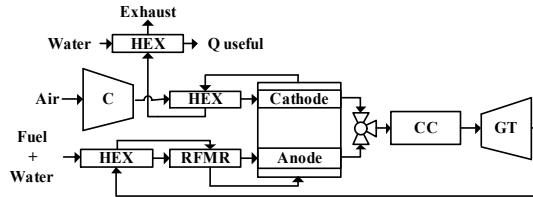
Fig. 1 A schematic diagram of external reforming SOFC–gas turbine hybrid system.

Some efficiency equations are applied to analyse the system performance where *P* stands for power (W).

$$\eta_{p-SOFC} = P_{p-SOFC} / \dot{m} LHV \qquad (26)$$

Compressor and gas turbine also have an important role in the power system efficiency.

$$\eta_{system} = \left(P_{p-SOFC} + P_t - P_c \right) / \dot{m} LHV \qquad (27)$$

And total efficiency is determined as combined heat and power:

$$\eta_{CHP} = \left(P_{p-SOFC} + P_t + Q_{rec} - P \right) / \dot{m} LHV \qquad (28)$$

2.4 Validation
Simulation data SOFC hybrid system fuelled by methane is used for comparison with the model in Thermolib results as shown in table 2 where data show no significant difference [9]. The comparison implements with same cell number, temperature, cell area and steam to fuel ratio.

Table 2. Validation for a hybrid system.

Parameters	Results from reference	Results from Thermolib
Power of stack (W)	1977	1977
Net power output (W)	1500	1508
Anode output (℃)	754	821.6
Cathode output (℃)	832	821.6
Fuel inlet (℃)	32	32.4
Air inlet (℃)	51	51.1
Combustor outlet (℃)	860	862
Gas outlet fuel heater (℃)	837	838
Gas outlet air heater (℃)	191	192

3. Results and discussion
p–SOFC fuelled by methanol as shown in figure 2 has

higher efficiency than other fuels because of higher hydrogen production. Increasing steam to methanol from 0.75 to 2 can increase hydrogen production drastically even though the reformer outlet temperature decreases but decreasing reformer temperature does not affect hydrogen production because the temperature of methanol steam reforming is only from 100 to 200 ℃. When the steam to methanol is increased from 2 to 4, hydrogen production is the constant and the reformer outlet temperature decreases. The system is fuelled by ethanol, p−SOFC power output increase by increasing the steam to ethanol ratio from 2 to 5 because a reformer produces more hydrogen, however, increasing steam to ethanol ratio from 5 to 9 can dilute the hydrogen production. For isooctane, p−SOFC increases by increasing steam to isooctane ratio from 9 to 12 and hydrogen production only increase slightly at steam to fuel ratio from 12 to 36. Increasing the steam to isooctane ratio more than 27 is not suggested considering unreacted steam. For methane, increasing steam to methane can decrease p−SOFC power output because of decreasing p−SOFC temperature and p−SOFC current.
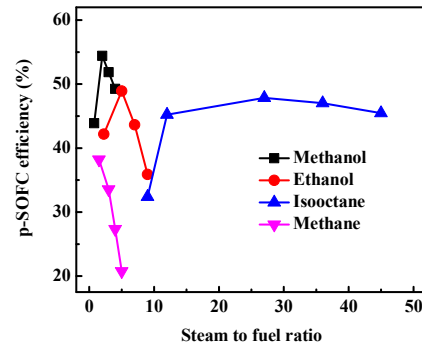
Fig. 2 Effect of steam to fuel ratio on p−SOFC efficiency
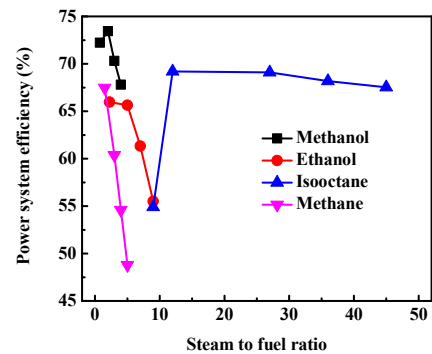
Fig. 3 Effect of steam to fuel ratio on power system efficiency
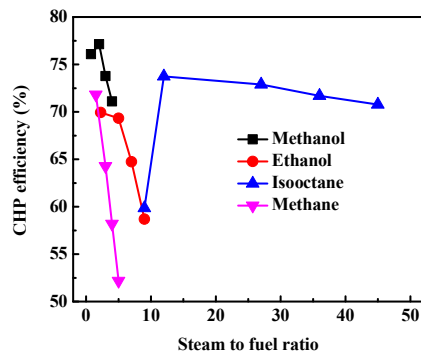
Fig. 4 Effect of steam to fuel ratio on CHP efficiency

The best power system efficiency as shown in figure 3 is at the steam to methanol ratio of 2 where the effect of lowered turbine power output is less than p−SOFC power. At steam to methanol higher than 2, the power system decreases also because decreasing p−SOFC power output. The increasing turbine power output does not have an effect on power system efficiency. Secondly, power system efficiency fuelled by ethanol where increasing steam to ethanol ratio more than 5 is not recommended because of decreasing the efficiency drastically. The system efficiency of steam to ethanol ratio from 2 to 5 does not decrease drastically because of increasing p−SOFC power output. At steam to methanol ratio higher than 5, the power system efficiency drops drastically because of decreasing the power output of p−SOFC and gas turbine. Thirdly, power system fuelled by isooctane, increasing steam to isooctane from 9 to 12 can increase power system efficiency a lot because of increasing power output of gas turbine and p−SOFC. Interestingly, increasing p−SOFC power output of steam to isooctane from 12 to 27 does not have an effect on power system efficiency due to decreasing turbine power output more than increasing p−SOFC power output.

Furthermore, the result data of CHP efficiency as shown in figure 4 show that the graphic tendency between CHP efficiency is the same as the power system efficiency. The heat recovery using methanol, ethanol, isooctane and methane as fuel is 401 to 416 W, 292 to 364 W, 273 to 416 W, and 282 to 360 W respectively.

4. Conclusions

Operating temperature of steam reforming greatly affects the system performance. Methanol has better performance than other fuels because of low steam reforming operating temperature. Furthermore, the best steam to fuel ratio for the studied hybrid system fuelled by methanol, ethanol, isooctane and methane is 2, 5, 12 and 1.5, respectively.

Acknowlegement

References

[1] Ni, M.; Leung, D.; Leung, M. Mathematical Modeling of Ammonia−Fed Solid Oxide Fuel Cells with Different Electrolytes. *Int. J. Hydrogen Energy* **2008**, *33* (20), 5765–5772.

[2] Patcharavorachot, Y.; Brandon, N.; Paengjuntuek, W.; Assabumrungrat, S.; Arpornwichanop, A. Analysis of Planar Solid Oxide Fuel Cells Based on Proton−Conducting Electrolyte. *Solid State Ion.* **2010**, *181* (35−36), 1568–1576.

[3] Zhu, L.; Zhang, L.; Virkar, A. V. A Parametric Model for Solid Oxide Fuel Cells Based on Measurements Made on Cell Materials and Components. *J. Power Sources* **2015**, *291*, 138–155.

[4] Chan, S.; Khor, K.; Xia, Z. A Complete Polarization Model of a Solid Oxide Fuel Cell and Its Sensitivity to the Change of Cell Component Thickness. *J. Power Sources* **2001**, *93* (1−2), 130–140.

[5] Patcharavorachot, Y.; Paengjuntuek, W.; Assabumrungrat, S.; Arpornwichanop, A. Performance Evaluation of Combined Solid Oxide Fuel Cells with Different Electrolytes. *Int. J. Hydrogen Energy* **2010**, *35* (9), 4301–4310.

[6] Pirkandi, J.; Ghassemi, M.; Hamedi, M. H.; Mohammadi, R. Electrochemical and Thermodynamic Modeling of a CHP System Using Tubular Solid Oxide Fuel Cell (SOFC−CHP). *J. Clean. Prod.* **2012**, *29−30*, 151–162.

[7] Thanomjit, C.; Patcharavorachot, Y.; Ponpesh, P.; Arpornwichanop, A. Thermodynamic Analysis of Solid Oxide Fuel Cell System Using Different Ethanol Reforming Processes. *Int. J. Hydrogen Energy* **2015**, *40* (21), 6950–6958.

[8] Doherty, W.; Reynolds, A.; Kennedy, D. Process Simulation of Biomass Gasification Integrated with a Solid Oxide Fuel Cell Stack. *J. Power Sources* **2015**, *277*, 292–303.

[9] Braun, R.; Klein, S.; Reindl, D. Evaluation of System Configurations for Solid Oxide Fuel Cell−Based Micro−Combined Heat and Power Generators in Residential Applications. *J. Power Sources* **2006**, *158* (2), 1290–1305.

Nomenclatures

E^{OCV}	Open Circuit Voltage (V)
E^{0}	Standard−state reversible fuel cell voltage (V)
R	Universal gas constant (8.314 J/moleK)
T	Temperature (K)
F	Faraday's constant (96485 C/mole)
P	Pressure (Pa)
i	Current (A)
R_e	Resistance (Ω)
i_0	Exchange current density (A/m^2)
m	Flow rate (mole/s)
W	Work (W)
C_p	Heat capacity (W/K)

n_e Number of electron

k Cathode

c Compressor

a Anode

I Inlet

t Turbine

ac Actual

s Isentropic

env   Environment

TM   Thermal mass

REAC   Reactant

PROCT   Product

HEX   Heat exchanger

RFMR   Reformer

CC   Combustion camber

GT   Gas turbine

Performance Characteristics of Small Diesel Engine Using Different Geometry Intake Parts

Le Viet Hung [(1)], Do Van Dung [(2)], Nguyen Anh Thi [(3)]

(1) Faculty of Civil Engineering, Ho Chi Minh City University of Technology and Education, 1 Vo Van Ngan Street, Thu Duc District, Ho Chi Minh City, Viet Nam

(2) Ho Chi Minh City University of Technology and Education, 1 Vo Van Ngan Street, Thu Duc District, Ho Chi Minh City, Viet Nam

(3) Viet Nam National University Ho Chi Minh City, Linh Trung Ward, Thu Duc District, Ho Chi Minh City, Viet Nam

ABSTRACT

This paper presents a study on improvement of performance characteristics of small diesel direct injection engine with power of 16.5HP using the re-design of intake manifold. With help of simulation tools like AVL BOOST and ANSYS FLUENT, the proposed measures for improvement of intake manifold were analyzed. The simulation results indicated that two best intake manifolds were recommended for experimental purposes. These manifolds were experimentally used to benchmark to the current intake manifold of engine.

In experiments, the important performance characteristics of engine (like volumetric efficiency, brake power, brake torque, fuel consumption, NOx, Soot, and CO) were analyzed. Moreover, the flow pattern of intake air was experimentally observed using a transparent cylinder

Keywords: volumetric efficiency, intake manifold, diesel engine, Soot.

1. Introduction

Nowadays, based on several surveys on customers demand, small-size engine with relative productivity is really prevalent in the field of agriculture, sylviculture and pisciculture in Vietnam. However, a significant number of Chinese and Taiwanese engines which are mainly updated, handy, attractively designed , state-of-the-art and less fuel-consuming, mostly occupy Vietnam market compared to domestically manufactued engines. Hence, it is indispensable to upgrade Vietnamese engines' operating feature and quality; in which, one-cylinder Diesel engine RV165-2, 16.5 HP produced by SVEAM can be considered as one of the most specific Vietnamese engines, completely designed and manufactured by Vietnamese engineers.

Table 1. RV165-2 Specification

Bore (mm)	105
Stroke (mm)	97
Displacement (cm^3)	839
Maximum output (HP/round/min)	16,5/2400
Maximum torque	4,9/1800
Compression ratio	20
Specific fuel consumption (g/HP.h)	206

However, the engine was produced more than 10 years ago, whenscience technology was limitedly apply to the design so that there are several problems such as: details surface roughness has not met the requirement, VE has not high enough, high fuel consumption,etc. That are the reasons why the engine has not reached the best operating feature.

Nowadays, the unstoppable advance in technology as well as the development of design and stimulation software, the problems mentioned above become acknowledged and enhanced. There are many methods for engine renovation such as:

- Modifiy the compression ratio
- Modify the stroke
- Renovate the intake part

In which, renovation of intake part can increase volumetric efficiency, output while reduce specific fuel consumption. Previous researches already used stimulation methods [2, 3, 4] which are relatively simple, feasible and cost-saving.

2. Theoretical basis

2.1. Volumetric efficiency

2.1.1. Effect of volumetric efficiency on power

Formula to calculate net power [5] :

$$N_e = \rho_a . V_h . Q_H . F . \eta_v . \eta_c . \eta_m . i . \frac{n}{\tau / 2} \quad (1)$$

Where:

ρ_a :   charged air density (kg/m^3)

V_h: displacement

Q_H: fuel heating value (kJ/kgNL)

$F = m_f / m_a$

η_v :   volumetric efficiency

η_c :   combustion efficiency

η_m :   mechanical efficiency

i: number of cylinders

n: engine speed

τ :   working cycles.

From the above equation, it can be seen that there are many methods of increasing the engine power and increasing the volumetric efficiency is one of those methods.

The volumetric efficiency of i-cylinder engine in one unit of time corresponding to Ne power per second:

$$\eta_v = \frac{G_{ctr}}{\frac{2}{\tau} V_h . \rho . n . i}$$

(2)

The amount of new gas added in each cycle has a great influence on the volumetric efficiency and is determined by various factors:
- The aerodynamic losses of the charging system reducing the pressure of the load
- Residual gas in the cylinder
- Aerated drying by the surface of the wall of the charging system and the space in the cylinder.

2.1.2. Effect of throat shape on the intake manifold of air into the engine

2.1.2.1. Coefficient of flow

Coefficient of flow is the ratio of actual flow under standard conditions to theoretical flow

$$\alpha_k = m_{tt} / m_{lt}$$

(3)

$$m_{tt} = V.P_{tt} / (R.T_{tt})$$

(4)

$$m_{lt} = A\rho_s C_s$$

(5)

Piston surface area: $A = \pi D^2 / 4$ (6)

Density is calculated as:

$$\rho_s = \frac{P_1}{R.T_{tt}} \left[\frac{P_2}{P_1} \right]^{\frac{1}{k}}$$

(7)

Speed of flow:

$$C_s = \sqrt{\frac{2k}{k-1} . R.T_{tt} . \left[1 - \left(\frac{P_2}{P_1} \right)^{\frac{k-1}{k}} \right]}$$

(8)

$P_1 = 101325 \, N/m^2$, $P_2 = P_1 - \Delta P$

2.1.2.2. Turbulence

Increasing the turbulence in the combustion chamber accelerates the mixing process, reduces soot and reduces fuel consumption. However, increasing the turbulence also increases the distribution of fuel, increasing the combustion chamber temperature and NOx emissions.

2.1.2.3. Loss in intake manifold

There are two types of losses:

- Loss along the pipe: the greater the loss of energy when the pipe is long.
- Local losses: occur in locations where the section is variable. For short intake manifold, local energy losses significantly affect the overall energy loss on the pipeline.

2.2. Operation process

In this research, with help of the stimulation software AVL BOOST and ANSYS FLUENT as well as experts' knowledge in this engine field, renovation methods on the intake part were tested by the stimulation methods in order to identify both benefits and drawbacks of each method. Eventually, four types of intake parts renovation are proposed to carry out an experiment together with current intake part:

Method 1: current intake part (basic model)
Method 2: increasecurvature (model 1)
Method 3: increase bore (model 2)
Method 4: straight intake part 180^0(random model 1)
Method 5: curved intake part 90^0(random model 2)
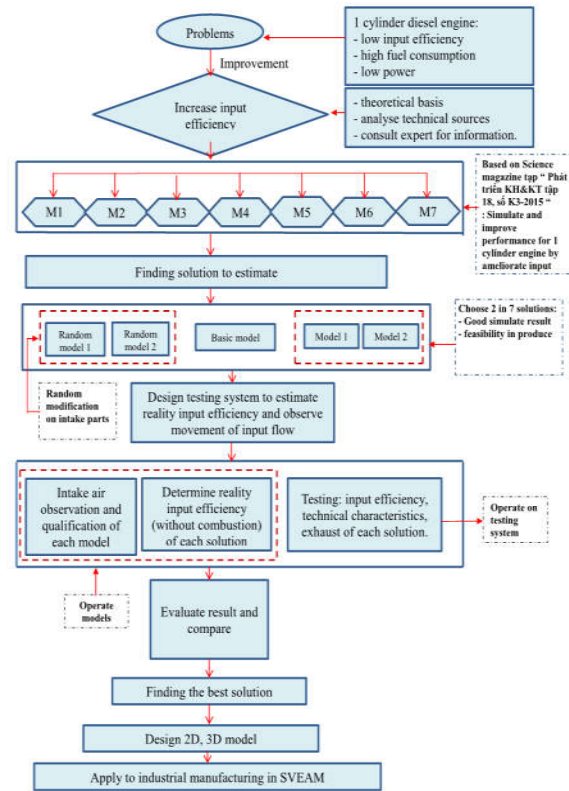
Fig 18. Flow of experimental process

2.2.1 Experimental methods

Table 2. Experimental methods

Methods	Figures
Current method	 Fig 19. Basic Model
Renovation method 1	 Fig 20. Model 1
Renovation method 2	 Fig 21. Model 2
Random method 1	 Fig 22. Random Model 1
Random method 2	 Fig 23. Random Model 2

2.2.2 Diagramand principle of volumetric efficiency measurement process (no combustion)

2.2.2.1 Principle diagram
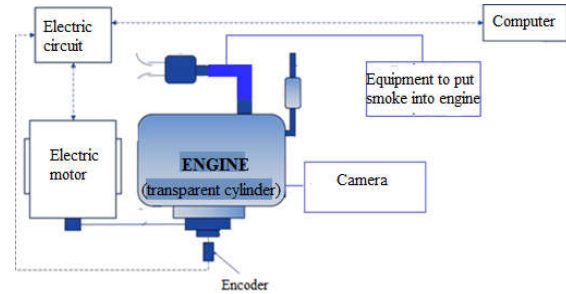
Fig 7. Principle diagram of volumetric efficiency measurement process (no combustion)

2.2.2.2 The order of execution

$$\eta_v = \frac{\dot{V}_{att}}{\dot{V}_{alt}} = \frac{\dfrac{\dot{m}_a}{\rho_a}}{\dot{V}_{alt}} \times 100\%$$

(9)

Suppose the air flow is the ideal gas . From the above equation, replace ρ_a and V_{alt}. We have the formula for determining volumetric efficiency as:

$$\eta_v = \frac{120 \times \dot{m}_a \times 100\%}{\left(\rho_0 \times \dfrac{p_a}{p_0} \times \dfrac{T_0}{T_a}\right) \times \left[(V_h + V_c) \times n\right]}$$

(10)

Where:

$\dot{m}_a$: The actual air in intake mass (Kg/h), determined by specialized flow meters Flowmeter of AVL.

ρ_0 : Air density= 1,29 Kg/m³.

$p_a \& p_0$: Pressure on intake manifold and atmospheric pressure (bar). Determined by Toyota pressure sensor 89420-20300.

$V_h + V_c = 888,8 \ cm^3$: volume of actual charge air.

n : engine speed (rpm).

2.2.3 Diagram and principle of experimental process

2.2.3.1 Priciple diagram
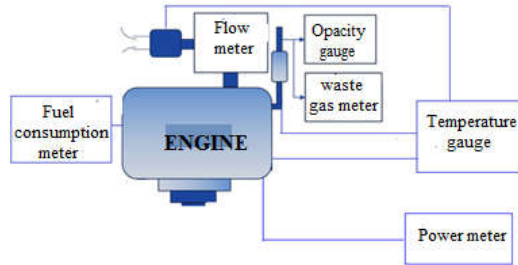
Fig 8. Principle diagram of experimental process

2.2.3.2 Step by step

For every method, measurement shall be conducted respectively as follows:

- Run innon-load the engine in 15 minutes.
- Run to evaluate the characteristics:
  - Pulladjusting to reach the maximum rounds 2550 rpm.
  - Put load into the engine (torque) to reduce the rounds steadily to the measuring points at 2400, 2200, 2000, 1800, 1600 rpm.
  - At every measuring point, record the specifications: input air temperature and pressure,atmosphere temperature and pressure, input air volume, torque, specific fuel consumption and exhaust gas specifications such as Soot, CO, NOx, HC.
- Run to evaluate the norm output (Power = 14 Hp (10,29 KW) at 2200 rpm), which is recommended by the producer.
  - Set up the engine operating at 2200 rpm and 44.6N.m torque, relative power is 14Hp (10,29 KW).
  - At this measuring point, the specifications of input air temperature and pressure, atmosphere temperature and pressure, input air volume, torque, specific fuel consumption and exhaust gas specifications such as Soot, CO, NOx, HC are also collected.
  - At each measuring point, the engine runs 3 times and the average value shall be recorded.

3. Results and discussion

Experimental process shows below results:

3.1. Performance
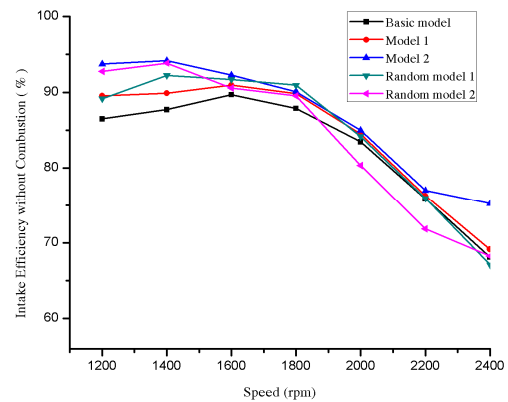
Fig 9.Performance (no combustion)
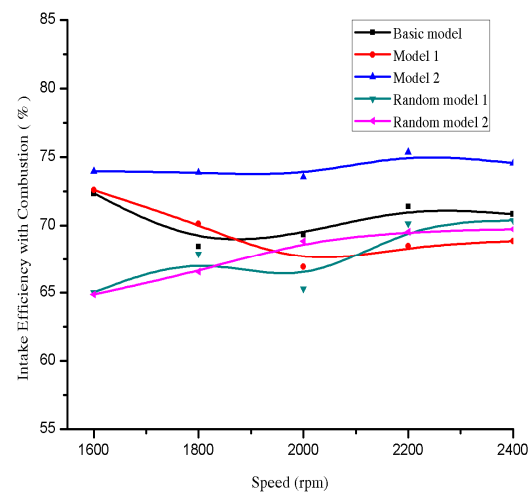
Fig 10.Real performance (combustion)

Compared to the current method: on the experiment (without burning) as well as the measuring process, the results pull out from renovation method no.2 seem to be in a similar trend. In the renovation method no.2,the volumetric efficiency increased by 5.42% in average, which is dramatically higher than the others, at all measuring points during the engine experimental operation.

3.2 Maximum output
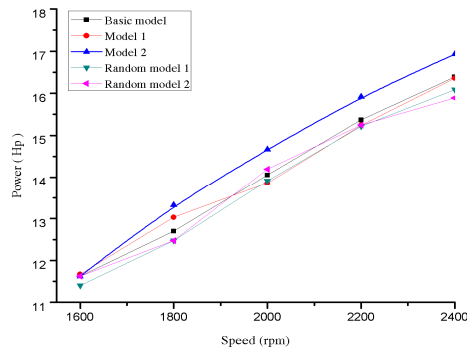
Fig 11.Maximum output
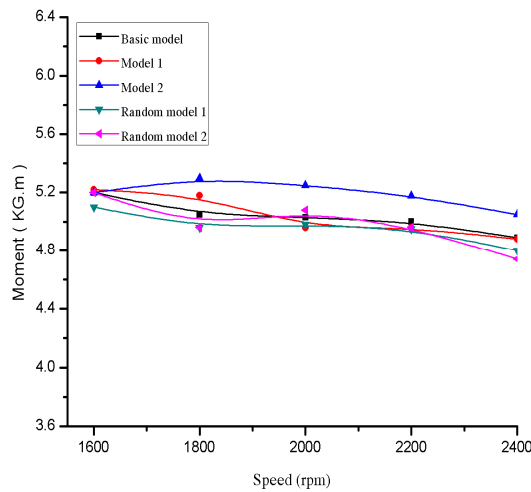
Fig 12.Moment
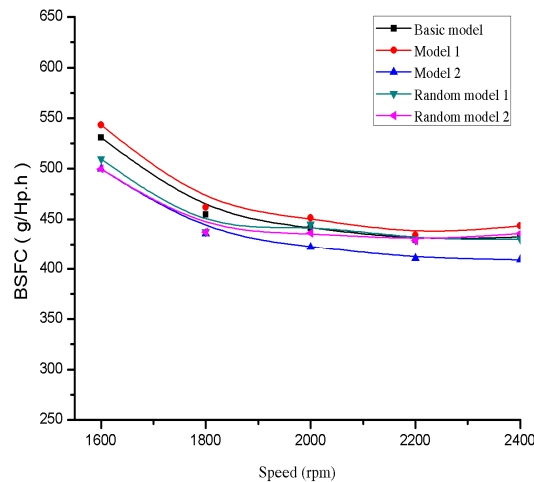
Fig 13.Specific fuel consumption

Together with the considerably enhanced volumetric efficiency at all measuring points, the renovation method 2 helps to increase the air input to the intake part, improve the fuel and air mixture process and plays a crucial role in enhancing RV165-2 operating

features such as: the maximum output rose 3.27%, maximum torque went up 2.32% while the specific fuel consumption reduced 5.6% compared to the current RV165-2.

3.3 Exhaust
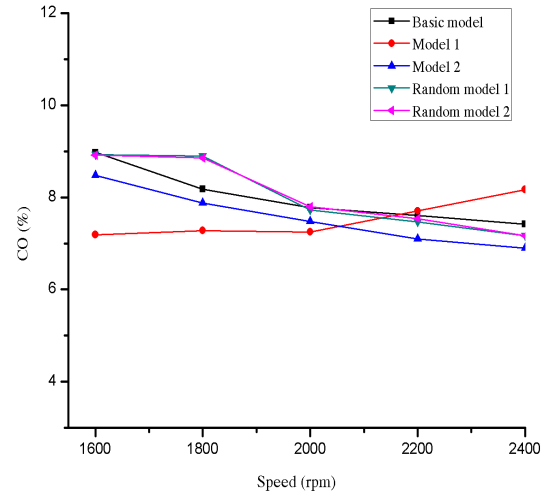
Fig 14. Variationin CO with change in model
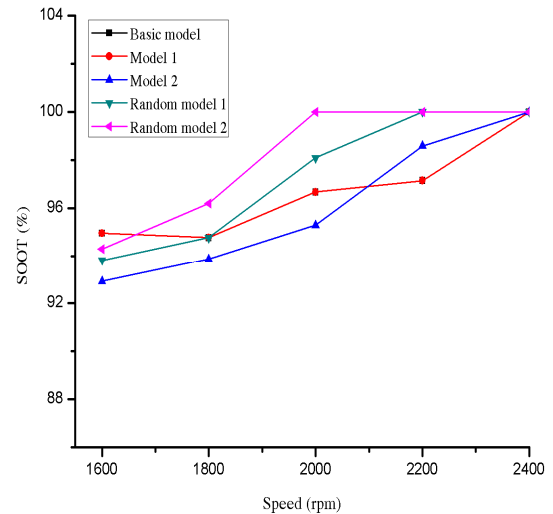
Fig 15. Variation in PM with change in model

338
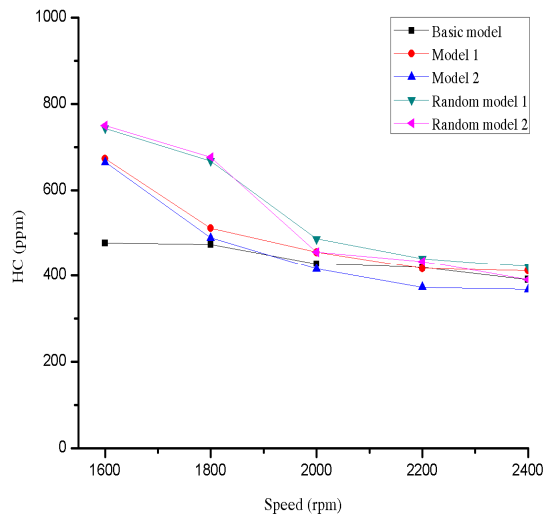
Fig 16.Variation in HC with change in model
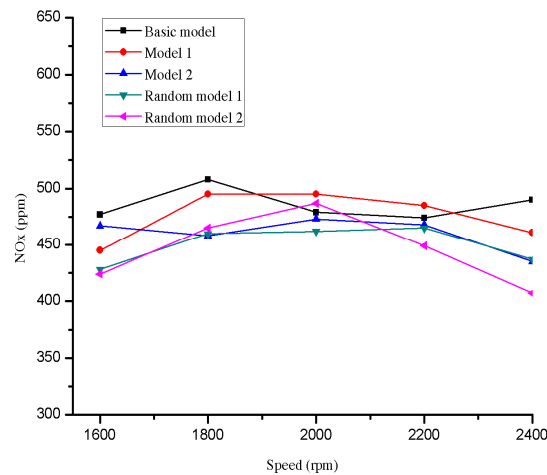
Fig 17.Variation in NOx with change in model

PM concentration and other element in the exhaust air are likely the same among the methods. However, the percentage of CO and NOx recorded from the renovation method 2 decreased relatively in comparison with the current method.

3.4 At continuous rated power(Power = 14 Hp, n=2200 rpm)
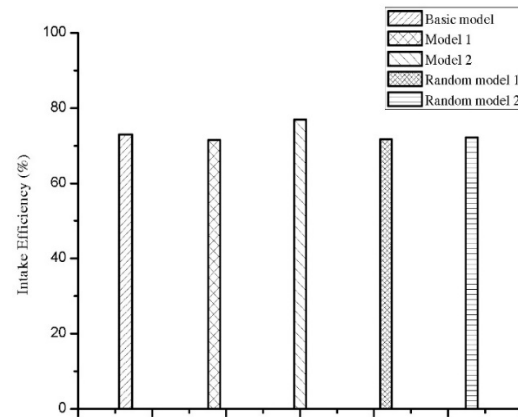
Fig 18. Performance
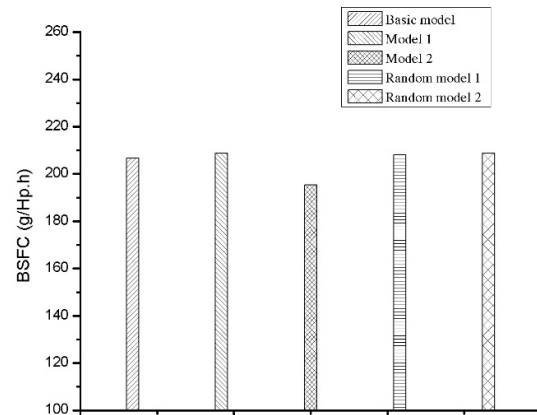
Fig 19. Specific fuel consumption at continuous rated power

At the point measure the norm (where the engine output and speed recommended by the producer), the renovation method 2 represents a higher volumetric efficiency than the others, specifically 5.46% higher than the current method; which helps to reduce the specific fuel consumption by 5.48% (from 206.78 g/Hp.hto 195.44 g/Hp.h). It means that if the engine operates at the norm output 08 hours per day during a year, the consumed fuel is 551.88 litter (operating cost shall fall by approximately 8.3 million VND, if the Diesel price is 15000VND/litter).

4. Conclusion

Different geometry intake parts influence considerably on the engine's operating feature (output, torque, volumetric efficiency) and exhaust gas of Diesel one-cylinder DI engine.

The experimental results represent that renovation method 2 showing values of volumetric efficiency (VE), output, torque and specific fuel consumption in the instances which are significantly enhanced

compared to the current method. Averagely, VE rocketed by 5.43%, output increased by 3.27%, maximum torque rose by 2,32% whereas the specific fuel consumption decreased by 5.48%. Regarding the exhaust gas, NOx concentration reduced meanly 5.16% while PM concentration fell slightly at the measuring points.

Renovation method no.2 was completely designed in 2D, 3D and the engine RV165-2 shall be mass produced in the coming time

References

[1]. Y.L.Qi, L. C. Dong, H. Liu, P. V. Puzinauskas and K. C. Midkiff (2012). Optimization of intake port design for SI engine. International Journal of Automotive Technology, Vol. 13, No. 6, pp. 861–872.

[2]. H. Mohamed Niyaz, A. S. Dhekane (2014). Twin Helical Intake Port Design Optimization And Validation By Using CFD Analysis. International Journal of Emerging Technology and Advanced Engineering, Volume 4, Issue 4, 454–462.

[3]. M. H. Shojaeefard, I. Sohrabiasl and E. Sarshari. Investigation the effect of inlet ports design on combustion characteristics and emission levels of diesel engines. Iran University of Science and Technology.

[4]. Yungjin Kim, Yongtaek Han and Kihyung Lee (2014). A Study on the Effects of the Intake Port Configurations on the Swirl Flow Generated in a Small D.I. diesel Engine. Journal of Thermal Science, Vol. 23, No. 3, 297–306.

[5]. Văn Thị Bông, Huỳnh Thanh Công. (2011). Lý thuyết động cơ đốt trong. Nhà xuất bản Đại Học Quốc Gia TPHCM.

Simulation and Experiment of Tig Welding Assisted by Hybrid Friction Stir Welding Between Steel and Aluminum

Truong Minh Nhat[1], Luu Phuong Minh[1], Truong Quoc Thanh[1] and Mai Dang Tuan[2]

[1] Faculty of Mechanical Engineering, University of Technology, VNU-HCM

Ly Thuong Kiet Street, District 10, Ho Chi Minh City, Vietnam

[2] Vinh Long University of Technology and Education

Nguyen Hue Street, Ward 2, Vinh Long City, Vietnam

ABSTRACT

This study presents conducted heat simulations and experimental jointing flat-plate of aluminum alloy 6061 and SUS 304. Temperature is simulated by the COMSOL software in three states: (1) Preheat the Friction Stir Welding (FSW) by TIG welding, (2) Thermal contact resistance between aluminium and steel, and (3) The welding process using stiring friction is simulated. The simulations intended to predicting the temperature which is used for preheat and welding process to ensuring the required solid-state welding. The temperature is also determined and checked by a thermal imager comparing with simulation results. Besides, the results of tensile strength is carried out. The Box - Behnken method is used to identify the relationship between the welding parameters (rotation, speed and offset), temperature and tensile strength. The optimizing welding parameters to achieving good quality of welding process are described.

Keywords*: Comsol Multiphysics, intermetallic compound, TIG welding, friction stir welding, dissimilar material.

1. Introduction

Friction stir welding has been considered to be the most significant development in metal joining in recent decades and, in addition, is a "green" technology due to its energy efficiency, environmental friendliness, and versatility. Friction stir welding produces higher strength, longer fatigue life, lower distortion, less residual stress and essentially defect-free joints compared to arc welding. The need to use lightweight structures, durable and variety materials, requires the development of reliable and efficient machining methods [1]. Friction friction welding methods meet the above requirements. One of the most difficult pairs of materials to be welded is between aluminum alloy and steel. There is a great difference in mechanical properties, because Intermetallic Compound (IMC) in traditional weld damage or rapid destruction when the force. FSW is a solid state welding process so it has advantages compared to conventional welding methods. Not only can the problems of solidification be avoided, but it can also limit the formation of IMC, so FSW becomes a solution for welding of different materials.

Recently, hybrid techniques have been used in FSW for some materials and alloys, especially for steel. These methods are generally used to preheat the material before welding (preheat). This activity will soften the material and enable better flow. Luo et al [2] performed preheat FSW experiments by resistance of magnesium alloy (AZ31B) (similar welding), Al alloy (AA7075) and steel (disimilar welding). Merkleinand Giera [3] uses lazer to heat the front area of the FSW

tool. This technique can increase the possibility of steel deformation and reduce tool wear. The weld strength of the AA6016-T4 with DC04 FSBW steel can reach 80% compared to aluminum alloy. The results show that the rotational speed of 2000mm / min for high weldability. In addition, research has shown that no compound is foundThey for achieving good welding results related to the increase in material flow of steel. However, using hybrid techniques in the FSW process requires additional equipment, which increases costs. Compared to other welding methods, FSW is less costly and can easily be welded.

Heat directly influences the formation of IMC, material flow, force welding… The simulation predicts the amount of heat generated during welding is essential. Especially for different materials, it becomes important to consider the ratio between the contact surface of the plates and the tool. When dissimilar welding materials, if the tool is placed on a part of the material, it produces a high temperature, causing the material to melt. The analysis is quite complex when it comes to the heat generation and temperature distribution in FSW when welding different materials. Two different materials have different properties: temperature, coefficient of friction and plasticity... All of these affect heat generation, temperature distribution.

2. Model Description

2.1. Geometry and Mesh

FSW temperature analysis is done on the Comsol software. Simulation models are made on aluminum

alloy 6061 and 304 stainless steel, 200 mm in length, 75 mm in width and 5mm thick. Simulation through 3 stages:

- TIG welding, simulation depends on time. The TIG solder is mounted on 304 stainless steel, using the Gaussian probability distribution model to describe the arc profile.

- Thermal Contact Resistance, simulation depends on time. Normally, the two materials are contact surface. However, upon closer inspection, you'll find that many materials have a surface roughness measurable at the micron or nanometer scale surface roughness introduces gaps between contacting materials, which are usually filled with air. The thermal conductivity of gasses, such as air, is typically much lower than the conductivity of common solid materials. Therefore, the heat flux due to conduction is smaller in noncontacting regions, leading to increased thermal resistance at the interface.

- Friction stir welding, temperature friction welding process by the shoulder and pin of the tool cause (the shoulder diameter is 20mm and the pin is 6mm). The drawback of the model is that it does not describe the angle of application and the profile of the shoulders – pin (only cylindrical description).
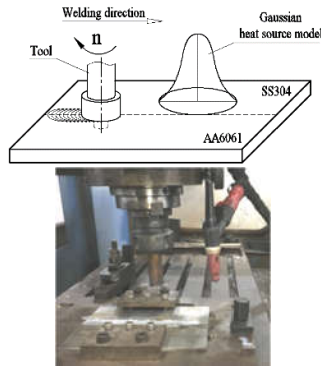
Fig 1. Experimental model.

2.2. Mathematical model

a. Heat TIG welding

Initial Condition

$$Q_0 = \frac{\eta EI}{v} \qquad (1)$$

where E is voltage, I is welding current, v is the welding speed and η is the arc efficiency.

Spatial Distribution

$$Q_1 = Q_0 e^{-\frac{(x-x_0)^2}{r_x^2}} \qquad (2)$$

Time Domain Distribution

$$Q = Q_1 e^{-\frac{(y-y_0)^2}{r_t^2}} \qquad (3)$$

Where $y = vt$, $r_x = \sqrt{r_t^2 - (y - y_0)^2}$, x_0 determines the weld bead centre and y_0 the weld torch centre.
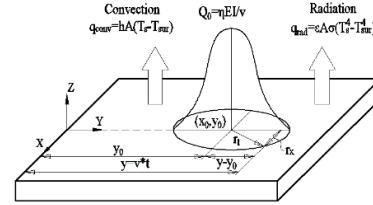
Fig 2. Model Gaussian heat source.

b. Thermal contact resistance
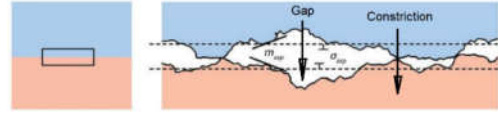
Fig 3. Thermal contact resistance model.

At the contact interface, the thermal contact conductance *h* is expressed

$$h = h_{constriction} + h_{gap}$$

$$= 1.25k_s \frac{m}{\sigma} \left(\frac{P}{H_{mic}} \right)^{0.95} + \frac{k_{gap}}{Y + M_{gap}} \qquad (4)$$

where P is the contact pressure, H_{mic} is the microhardness, σ is the surface roughness, and m is the roughness slope, k_{gap} is gap conduction, Y is micro distance between mean planes và M_{gap} is gas rarefaction parameter.

c. Heat friction stir welding

$$q_{pin}(T) = \frac{\mu}{\sqrt{3(1+\mu^2)}} r_p \omega \bar{T}(T) \qquad (5)$$

Where μ is the friction coefficient, r_p is the pin radius, ω is the pin's angular velocity (rad/s) và $\bar{T}(T)$ is the average shear stress of the material, shear stress is a function of the temperature. This function with an interpolation function determined from experimental data.

$$q_{shoulder}(r,T) = (\mu F_n / A_s) \omega r (T < T_{melt}) \qquad (6)$$
$$q_{shoulder}(r,T) = 0 (T \geq T_{melt})$$

Where r is the shoulder radius, F_n represents the normal force và A_s is the shoulder's surface area, T_{melt} is melting temperature.

3. Simulation results
3.1. Heat TIG welding and thermal contact resistance

(Determined the input parameters of the TIG welding to ensure that when the welding speed changed, the original heat was still constant (because the TIG welding was fix with the milling head, the speed of preheat depends on the welding speed).
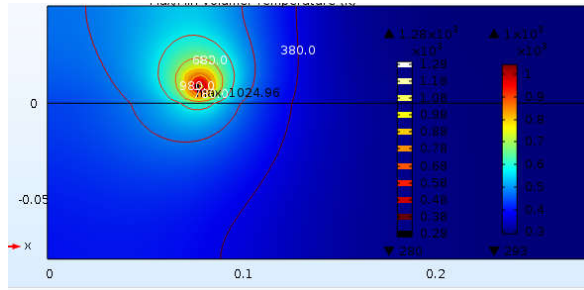
Fig 4. TIG welding temperature simulation with parameters E = 12(V), I = 66 (A) và v = 40 (mm/min).
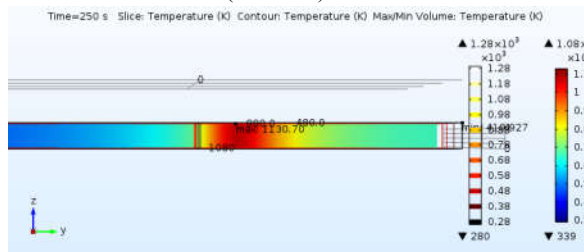
Fig 5. Temperature distribution by welding section.

Simulation results as shown in Fig 4 show the center temperature of about 775°C. Due to convection and radiation, the temperature in the stainless steel area at the back of the TIG welding center is 50 ÷ 100 mm, about 200 ÷ 300ºC and the aluminum side is about 150ºC. Take these two temperatures as input conditions for simulating friction stir welding.

The isotherm in the simulated fracture is caused by the heat transfer between two discontinuous plates (Thermal contact resistance) and two different materials with different thermal properties causing the above phenomenon Fig 4.

3.2. Friction stir welding

The temperature field is disproportionate, due to the differences in material properties, Fig 7.

- The temperature near the shoulder area is higher than the temperature below the plate.

- Temperature at the center of welding from 500 ÷ 600ºC. At this temperature, the aluminum alloy is in the hot deformation zone (greater than $0.7T_m$) and the steel is in the warm deformation zone (greater than $0.3T_m$). The area around the instrument temperature from 200 ÷ 500ºC, depending on the location.
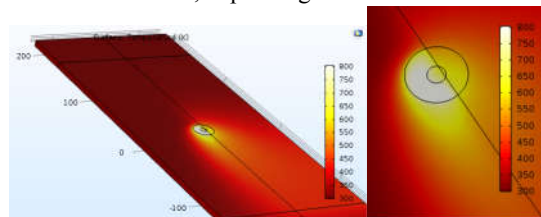
Fig 6. Temperature simulation FSW result on COMSOL.
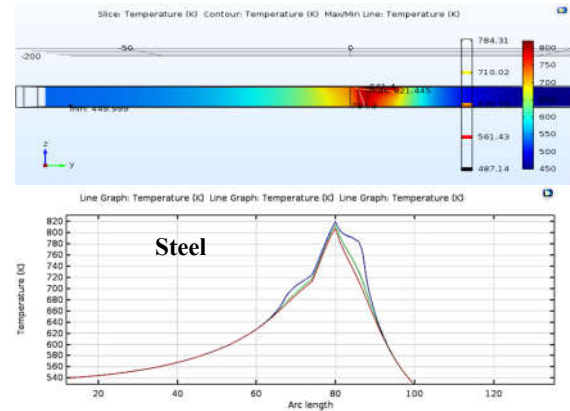
Fig 7. Thermal distribution at the cross section of the weld.

The temperature at the center of welding depends on the speed of rotation, the welding velocity and offset. In particular, rotational speed is the main factor affecting the welding temperature. But because the tool movement is still small (from 0.2 ÷ 0.6), the impact is not much.
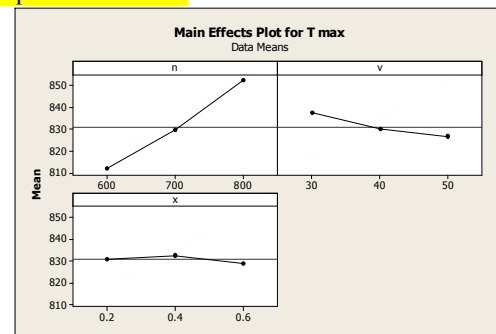
Fig 8. Main effects plot for temperature.

4. Experimental results

4.1. Test Tensile strength
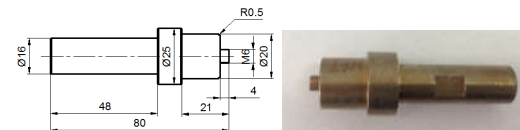
Fig 9. Tools used for experiments SKD11.

Fig 10. VP-3000 CNC milling machine.

Fig 11. Photograph of tensile samples.

Table 10. Experimental results.

No	Rotational speed (rpm)	Transverse speed (mm/min)	Offset (mm)	Mean value (Mpa)
	n	v	x	Y
1	600	30	0.4	197.865
2	800	30	0.4	207.705
3	600	50	0.4	242.02
4	800	50	0.4	213.3
5	600	40	0.2	233.63
6	800	40	0.2	200.34
7	600	40	0.6	239.485
8	800	40	0.6	219.685
9	700	30	0.2	232.29
10	700	50	0.2	207.07
11	700	30	0.6	226.96
12	700	50	0.6	229.57
13	700	40	0.4	236.56
14	700	40	0.4	234.45
15	700	40	0.4	224.895

Box-Behnken method is used to determine the relationship between welding parameters (rotation, speed and offset), and temperature, tensile strength.

Regression equation: $Y = -887.95 + 2.25n + 22.501v - 527.6x - 0.00139n^2 - 0.2176v^2 - 3.75x^2 - 0.01139nv + 0.258nx + 8.85vx$
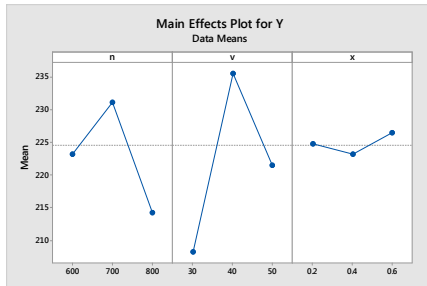
Fig 12. Main effects plot for tensile strength mean.
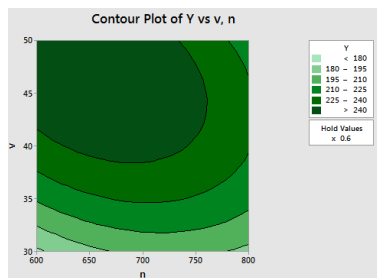
Fig 13. Response surface and contour plots that represent the effect of rotational speed and transverse speed, and their interaction on shape conformity when the offset is 0.6 mm.

Fig 13 indicates the changing response surface at the offset is x = 0.6 mm. The results show that the tensile strength increases with the rotational speed (n) of 600 ÷ 750 (rpm) and the welding speed (v) 40 ÷ 50 (mm / min). If the rotation speed (n) and welding velocity (v) are below this level, the tensile strength decreases. The elliptic envelope model clearly shows the above parameters. Therefore, the optimal tensile strength for tensile strength is n = 700 (rpm) and v = 45 (mm / min).

Fig 14 indicates the changing response surface at the offset is x = 0.4 mm. The optimal value for tensile strength is n = 670 (rpm) and v = 42 (mm / min). When the speed of rotation (n) and welding speed (v) are too high or too low, the tensile strength will not be suitable.
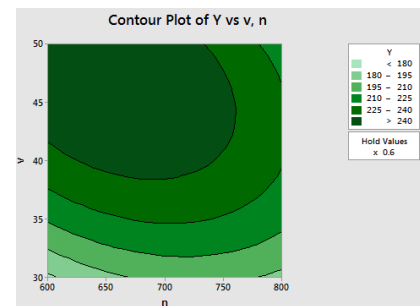
Fig 14. Response surface and contour plots that represent the effect of rotational speed and transverse speed, and their interaction on shape conformity when the offset is 0.4 mm.
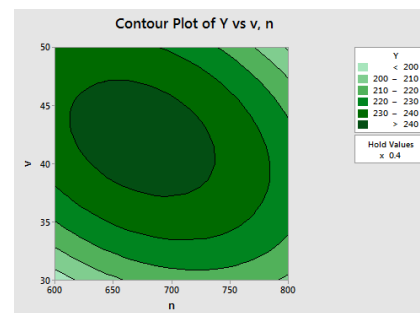
Fig 15. Response surface and contour plots that represent the effect of rotational speed and transverse speed, and their interaction on shape conformity when the offset is 0.2 mm.

Fig 15 indicates the changing response surface at the offset is x = 0.2 mm. Surface texture is more or less the same as x = 0.4 mm. The optimum values of rotational speed and weldability are 700 (rpm) and 37 (mm / min), respectively.

Parametric optimization is related to the properties of the result. Therefore, the optimal condition produces the greatest value (better is better) for the result.
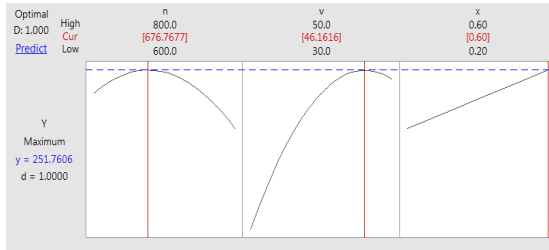
Fig 16. Graph optimized parameter.

After optimizing experiment parameters with the following parameters: n = 676 (rpm), v = 46 (mm / min) and x = 0.6 (mm). We have Test Tensile strength result σ_k= 238.17 MPa, Fig 17. The welding parameters are optimized to achieve good weld quality and maximum tensile strength is obtained by 77% compared to aluminum alloy strength.
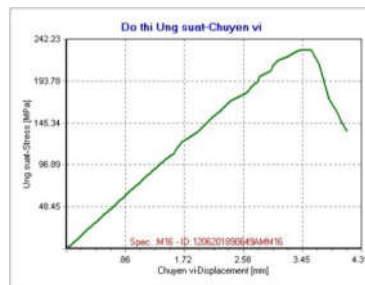
Fig 17. Test Tensile strength results of the weld after optimization.

4.2. Analysis and observation of joint cross-sectional microstructure

Porous flaws (Fig 20) occur on the diffuser side of the diffuser. IMC thickness affects the strength of the weld. Specifically, the weld with IMC about $7 \div 15$ μm (Fig 19) has a low tensile strength of 197Mpa, thick IMC welds become brittle. When the IMC thickness is 2.5μm, the weld strength is improved (Fig 18, this specimen is re-welded after parameter optimization).
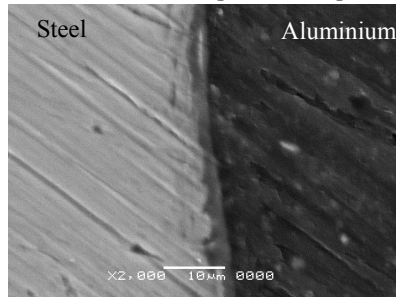
Fig 18. SEM image and IMC thick 2.5μm.
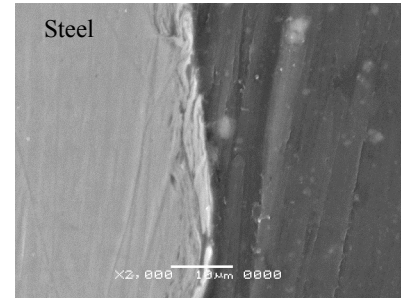
Fig 19. SEM image and IMC 6.8 ÷ 15.7 μm.
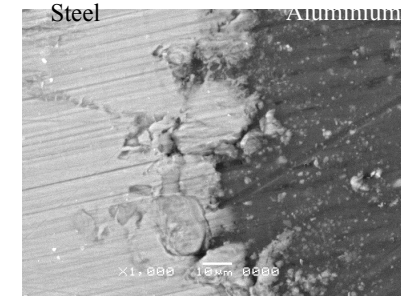
Fig 20. SEM image and interconnected pores.

5. Concluding Remarks

Use Box - Behnken method for experimental planning. The maximum tensile strength is 77% compared to the strength of aluminum alloy. The optimal set of parameters for the process is n = 676 rpm, v = 46 mm / min and x = 0.6 mm.

Based on the theory used to simulate the process of preheat, thermal contact resistance and friction welding welding. Incorporate these theoretical foundations into the COMSOL software for simulations. The initial results show that the heating temperature is about $200 \div 300$ºC for steel and from $100 \div 150$ºC for aluminum, the temperature at the center of welding is from $500 \div 600$ºC and the area around the instrument temperature from $200 \div 500$ºC. Prove that the asymmetric temperature is through the solder joint. The temperature near the shoulder area is higher than the plate bottom temperature. The temperature at the center of welding depends on the speed of rotation, the welding velocity and the amount of displacement. In particular, rotational speed is the main factor affecting the welding temperature.

SEM images to determine some properties of welding materials. This is also the basis for initial research to identify some defects in welding of two different materials (IMC thickness and interconnected pores) and the cause of these defects.

References

[1]   "Honda develops robotized FSW technology to weld steel and aluminum and applied it to a mass-production vehicle," *Industrial Robot: An International Journal,* vol. 40, pp. 208-212, 2013.

[2]   J. Luo, W. Chen, and G. Fu, "Hybrid-heat effects on electrical-current aided friction stir welding of steel, and Al and Mg alloys," *Journal of Materials Processing Technology,* vol. 214, pp. 3002-3012, 2014/12/01/ 2014.

[3]   M. Merklein and A. Giera, *Laser assisted Friction Stir Welding of drawable steel-aluminium tailored hybrids* vol. 1, 2008.

Motion Analysis and Fabrication of a Low-Cost Underwater Thruster Using Magnetic Coupling

Ngoc-Huy Tran[1], Thanh-Hai Chau[2], Quoc-Tien-Dung Tran[2]
[1] Ho Chi Minh City University of Technology, VNU-HCM
Ly Thuong Kiet Street, Ho Chi Minh city, 700000, Viet Nam
[2] National Key Lab. of Digital Control and System Engineering, HCMUT, VNU-HCM
Ly Thuong Kiet Street, Ho Chi Minh city, 700000, Viet Nam

ABSTRACT

Underwater vehicles research is now well-developed around the world. Thrusters with O-ring seal and DC motor have a low waterproofing ability and cannot work for a long interval of time. In this paper, we will introduce our designed thruster, using magnetic coupling and brushless DC motor. In addition, controllers are also mentioned the PID, fuzzy and combined controllers for controlling BLDC motor. The experiments were also carried out and obtained the results consistent with the simulation.

Keywords: Underwater Thruster, Magnetic Coupling, Fuzzy-PID Controller

1. Introduction

Nowadays the design and manufacture of underwater robots is a highly developed field of research. Unmanned Underwater Vehicles (UUVs) can support or replace people working in deep, polluted water for a long interval of time [1]. One of the most important devices in these vehicles is the thruster. In Vietnam, thrusters in underwater vehicles are sold at very high prices and must be imported. For example, a thruster of Tecnadyne (USA, Figure 1.a) costs $4000, and the thruster of Shenzhen KDWS (China, Figure 1.b) costs $4200. Such high costs are a huge obstacle for researches in Vietnam. Therefore, the research, design and manufacture of the underwater thruster are very essential.

Figure 1. Tecnadyne and Shenzhen KDWS thrusters

The disadvantages of the former thrusters come from O-ring seals and DC motors. The seals can be damaged when the device operates at high speed, which leads to the destruction of inside electrical components. DC motors with commutator segment and brush often need periodic maintenance, so it is difficult to work underwater for a long period. Our developed thruster uses magnetic coupling and brushless DC motor (BLDC) to improve its stability. Magnetic coupling uses contactless actuators to provide better protection. Not only the longer operating life, BLDC also has some other advantages than the conventional DC motor such as better torque characteristics, higher efficiency,

noiseless operation, etc.

There are several methods to control brushless DC motor. Prasad et.al in [2] present the method to build models and equations of BLDC, especially motors with trapezoidal back electromotive force (back EMF) using MATLAB/Simulink. Paper [3] introduces a strategy for the control of torque using current observer and state feedback algorithm for a BLDC. Regarding the control technique, paper [4] compares the quality of PI and fuzzy controllers to find out which is more optimal. In this paper, we will improve the performance of the PID controller by combining it with fuzzy controllers. There are 3 types of controllers in this paper: PID, Fuzzy-PID and Advanced Fuzzy-PID.

In this paper, we will introduce the design and experiment results of our thruster, including mechanical and electrical design. The mechanical design focuses on simulating the stress field and thrust of the propeller, calculating the thickness of the housing to operate at the water depth of 100m and the magnetic coupling design. In the electrical part, we will present the BLDC control algorithms. The experiments were also taken and obtained good results.

2. Mechanism design

With the advantages and disadvantages compared to DC motors and three-phase motor, brushless motors have been explored and studied. The thruster is designed and manufactured to follow requirements:

- The thruster should have a marginal value from 5kgf to 6kgf;
- The power of the thruster is 600W;
- The thruster has a marginal depth rating of less 100m;
- The thruster must be able to work in temperatures from 3^0C to 28^0C.

To meet the requirements of waterproof protection, power of the thruster, types of motors and propeller failures, the design solutions were selected as:

- The magnetic coupling was chosen because of

frictionless, highly waterproof, long-term operation and less maintenance.

- A BLDC motor TBM (S)-7646-A that has input voltage of 48V, capacity of 335W, speed of 1885 rpm at its normal operating condition, manufactured by Kollmorgen [5], is selected to be the main thrust motor.

- The propeller for the thruster can withstand maximum thrust of 70N.

- The nozzle reduces the effect of fluid drag force and promotes the thrust via an optimal geometry.

-
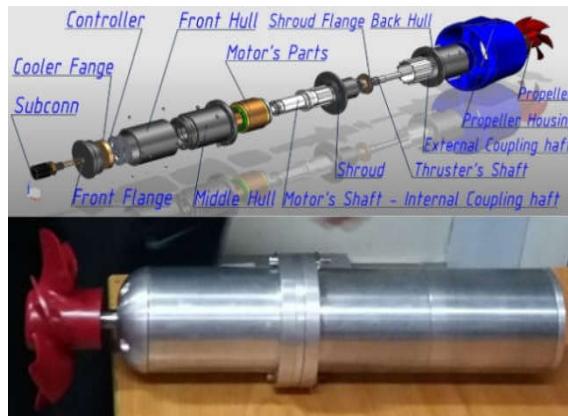
Figure 2. Detailed structure of the designed thruster (up) BLDC Thruster (down)

Figure 2 describes the detailed structure of the designed thruster. The design is divided into modules that include the thruster housing, magnetic coupling, propeller, nozzle, and the BLDC motor.

2.1. Thruster Housing

Aluminum alloy material of 6061-T6 can endure pressure up to 80MPa, melting temperature of 58ºC, good corrosion resistance in seawater and atmospheric conditions. The thruster can operate at the depth of 100m. It is necessary to ensure that the thruster housing can withstand a pressure of 1.11MPa (depth of 100m). Thus, we selected aluminum alloy material of 6061-T6 to manufacture the thruster housing. As shown in figure 2 of the thruster 3D model, the most important parts of the housing are front flange, front hull and middle hull, which cover the motor's parts and controller board. The thruster hull's parts are analyzed by NX Nastran with meshing size of 2mm 3D Tetra element. Finite element method helps predict the behavior of the thruster hull at 100 meters depth, in this case, 3 and 5mm thickness hull is checked. The results is shown in figure 3 where maximum stress on 3mm thickness hull is 55.7MPa, on 5mm thickness hull is 27.1MPa
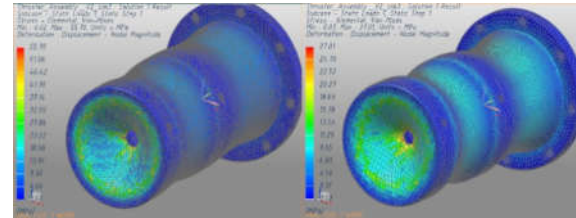
Figure 3. Von Mises Stress on Thruster hull with thickness of 3mm (a) and 5mm (b)

2.2. Magnetic Coupling

The magnetic coupling plays an important role in improving waterproof capability of the motor, driver, stabilizing operation under high pressure, preventing overload using the conventional fixed magnet of torque through the containment shroud. With the operating principle based on the gravity of 2-pole magnets to transmit torque from the engine up to the shafts and are separated by a containment shroud made of metal, ceramic, and etc. Figure 4 shows the detailed structure of the magnetic coupling.
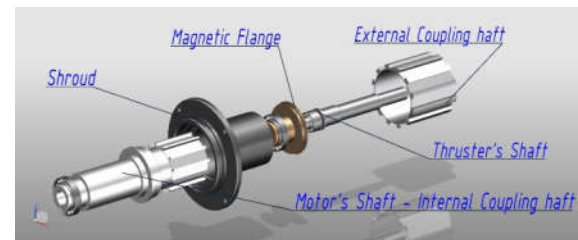
Figure 4. Magnetic coupling model

From [6] and [7] we use MATLAB to plot the torque versus shifting angle θ between couplings:
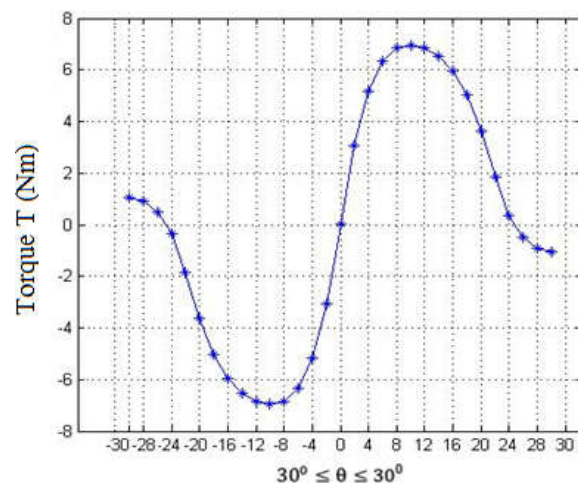
Figure 5. Magnetic torque versus angular shifting

As we can see from the above figure, the torque is 0 when the angle $\theta = 0^o$. When the angle changes, the torque increases until it reaches the peak value $T_{max} = 7Nm$ at $\theta \approx 10^o$, then decreases to 0. If the torque on the coupling is greater than T_{max}, the slip in magnetic coupling occurs. The driving coupling still rotates but the driven coupling will be restrained and stop working

after all.

From [5], the continuous stall torque of the motor $T_{motor} = 2.18 Nm$, is less than the maximum torque value; which proves that the design with magnetic coupling can make the thruster work well at the depth of 100m below the sea level without slipping.

Materials greatly affect the performance of the magnetic coupling. Hence selecting materials for magnets of the magnetic coupling is very important. Neodymium magnets (Nd-Fe-B), the most widely used type of rare-earth magnet, are the strongest type of permanent magnet. Therefore, Nd-Fe-B is used in magnetic coupling design. The containment shroud is crucial in magnetic coupling due to its function in durability and performance. It is designed with the thickness of 1.5mm, based on Series GWM 5415.5. To meet the requirement of material for the containment shroud, stainless steel outperforms others for several features such as high strength plasticity, good refractory, and easy manufacture.

Applying finite element method using NX Nastran to analyses and checks the containment shroud durability under 100m water depth (1,11MPa). With automatic meshing size of 0.5mm 3D Tetra element, figure 6 demonstrates the automatic meshing model with 85090 nodes and 331342 elements. In simulation result, the top of the containment shroud with thickness of 1.5mm is subjected to the greatest pressure, Max = 35.56MPa be between allowable bending strength of the stainless steel.
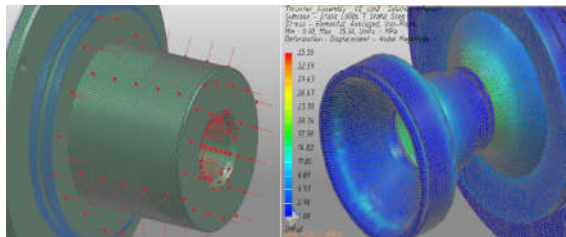
Figure 6. Mesh with size of 0.5mm (a), Von Mises Stress of Containment Shroud (b)

2.3. Propeller

Finite element methods are the most popular numerical method and used widely for solving problems of engineering and mathematical physics and in analyses of electric motors. From existing propeller of Vetus [8], CFD analysis is based on the proposed sample wing profile. The boundary condition problem is hypothesized using the model K-ε realizable, solver: MRFSimpleFoam (inner rotation of the same propeller and fixed external domain), constant flow, incompressible. Specifically:

- The geometry of the propeller blade model is obtained through a screwdriver scan.
- Use CAD tools to reproduce geometry; this makes the calculation model more accurate (Figure 7).
- Use ANSYS/CFX software to calculate and simulate velocity, pressure and thrust field (Figure 8 to 12).

- Sample size in calculation and simulation is taken according to empirical model.
- The basic dimensions of the test tank in the calculation and simulation are taken according to Table 1.
- The results of the thrust simulation using v/p rotational speed were compared with the experiment in Table 2.

Table 1. The dimensions of the propeller and test tank

The diameter of the propeller	150 mm
Width of the test tank	750 mm
Height from the propeller to surface	195 mm
Height from bottom of the test tank to surface	450 mm

Figure 7. Result of the 3D scan of the propeller
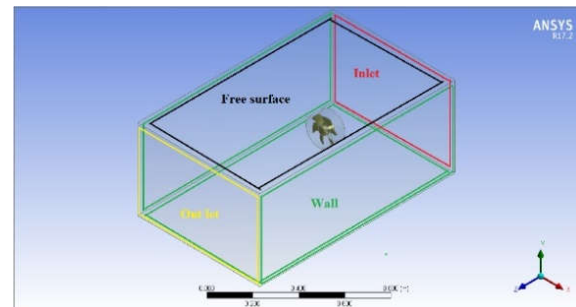
Figure 8. Use ANSYS/CFX software to calculate and simulate the boundary condition
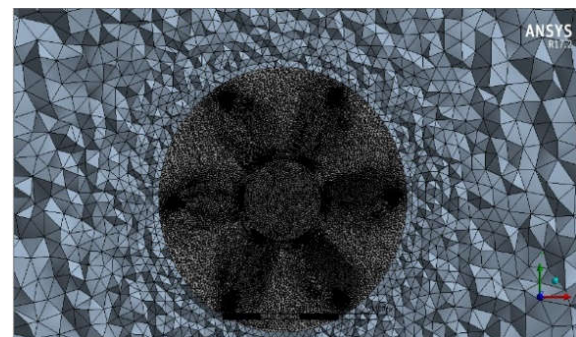
Figure 9. Meshing
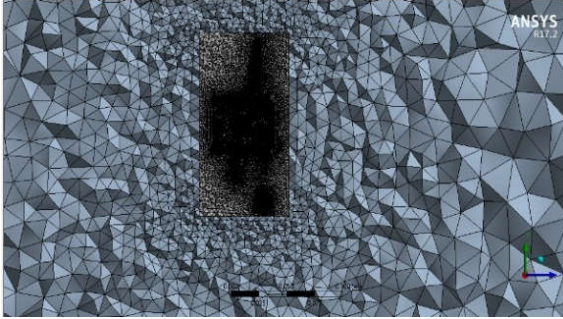
Figure 10. Element blocks, with 4,646,912 elements and 1,220,709 nodes
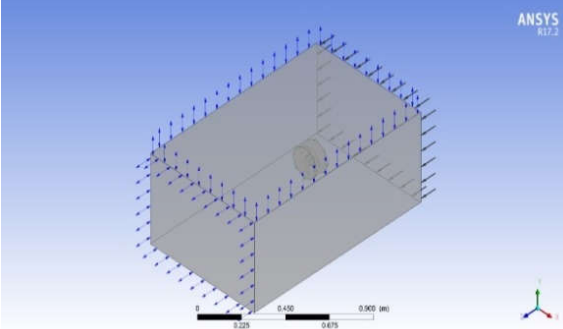
Figure 11. Boundary condition of speed and pressure

Table 2. The results of the thrust simulation using v/p rotational speed

	RPM	Thrust [N] (Simulation)	Thrust [N] (Experiment)
1	300	5.10148	5.8625
2	605	21.8028	23.4511
3	808	39.4012	42.2443
4	1008	61.8128	65.3155
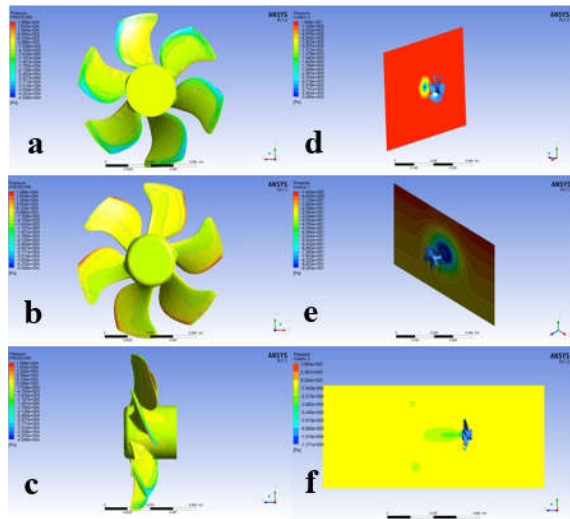
Figure 12. Simulation results of pressure field effects on the front (a), back (b) and side (c), rear wing (d), front wing (e) and parallel wing (f) of the propeller

3. Electrical design

3.1. Simulation
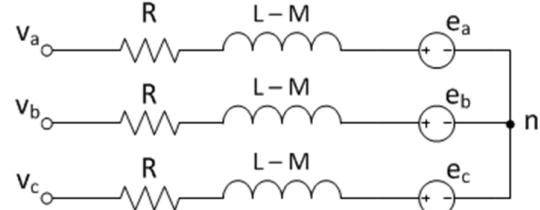
Figure 13. Three-phase BLDC model

The motor used in simulation and experiment is a three-phase trapezoidal BLDC motor. We can model it into 3-phase circuit diagram as shown in figure 13. Each phase corresponds to a coil with resistance R and inductance (L-M), whereas L is self-inductance and M is the mutual inductance. When the motor is operating, on each phase will appear the back EMF, indicated in the figure by e_a, e_b, e_c, respectively. From [9], we obtain the electrical and mechanical equations of the BLDC:

$$\frac{d}{dt}\begin{bmatrix} i_a \\ i_b \\ i_c \end{bmatrix} = -\frac{R}{L-M}\begin{bmatrix} 1 & 0 & 0 \\ 0 & 1 & 0 \\ 0 & 0 & 1 \end{bmatrix}\begin{bmatrix} i_a \\ i_b \\ i_c \end{bmatrix} -$$

$$\frac{1}{3(L-M)}\begin{bmatrix} 2V_a - V_b - V_c - 2e_a + e_b + e_c \\ 2V_b - V_a - V_c - 2e_b + e_a + e_c \\ 2V_c - V_a - V_b - 2e_c + e_a + e_b \end{bmatrix} \quad (1)$$

$$T_e = \frac{1}{\omega}\left(e_a.i_a + e_b.i_b + e_c.i_c\right) \quad (2)$$

$$T_e = T_l + J\frac{d\omega}{dt} + B\omega \quad (3)$$

Where i_a, i_b, i_c, V_a, V_b, V_c are the currents and voltages of the three phases, T_e and T_l are respectively electromagnetic torque and load torque, ω is the angular velocity of the rotor. The coefficient J and B are the rotor inertia and the damping coefficient.
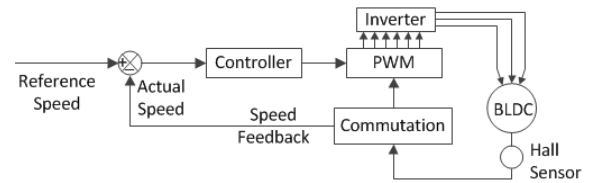
Figure 14. One-loop control diagram
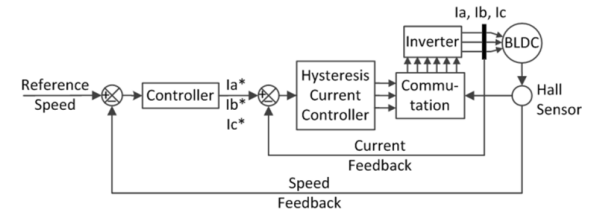
Figure 15. Two-loop control diagram

According to paper [10], there are two BLDC control models: one-loop and two-loop control. In the first

model (Figure 14), there is only one speed control loop. Based on the signals obtained from Hall sensors, the controller determines current position and speed of the motor, thereby adjusting the PWM duty cycle and the rules for opening and closing the semiconductor switches. The two-loop control model (Figure 15), on the contrary, consists of two control loops: the inner loop is the current control based on the hysteresis current method, while the outer loop is the speed control. Compared to the one-loop model, this model has an additional current controller for three-phase current feedback, which reduces electromagnetic torque ripple.
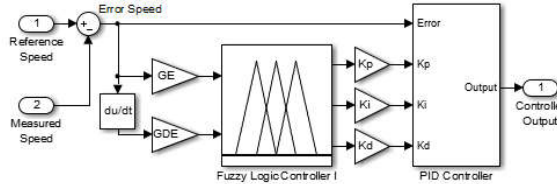
Figure 16. Structure of the Fuzzy-PID controller

In the simulation, we use three different controllers: PID, Fuzzy-PID and Advanced Fuzzy-PID. The proportional-integral-differential (PID) controller is widely used thanks to its simple structure, but it only provides good response to linear models. Practical systems often have nonlinear components. As a result, PID controllers usually only provide good response at some operating point. At the other different working points, the quality is poorer. To overcome these weaknesses, we combined original PID with a fuzzy controller (Fuzzy-PID controller in Figure 16). The fuzzy controller calculates K_p, K_i, K_d coefficients based on control error to improve the quality.

The Advanced Fuzzy-PID controller (Figure 17) is researched to improve the quality of the Fuzzy-PID controller. We use another fuzzy controller to adjust the PID coefficients based on the influences on the quality of response (rising time, settling time, steady-state error, overshoot, etc.). Among the controllers, Advanced Fuzzy-PID controller is the most complex and most time-consuming, but the response quality of this controller is the best.
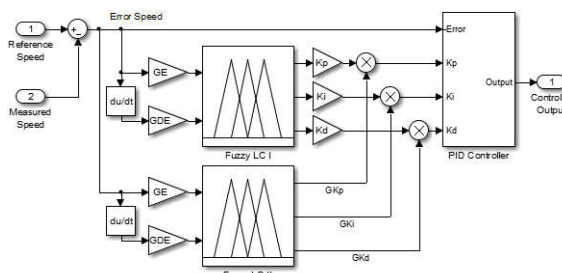
Figure 17. Structure of the Adv. Fuzzy-PID controller

MATLAB/Simulink is used to simulate the BLDC motor and analyze the results. In the simulation, we focus on comparing the quality of one-loop and two-loop model and comparing the speed responses of the controllers. The model refers to the KOLLMORGEN TMB(S)-7646-A brushless DC motor [5] for simulation.

and experiment as well. First, we compare the electromagnetic torque and phase current responses of two models:
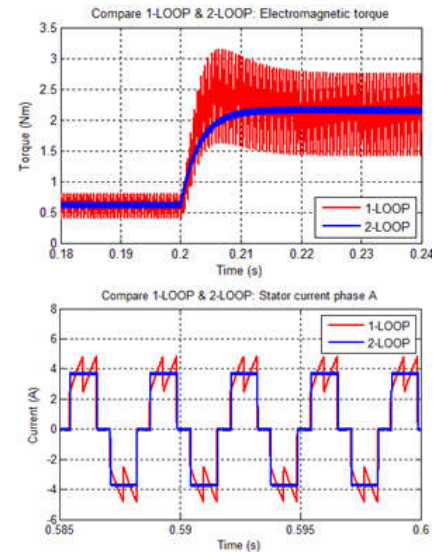
Figure 18. Comparison between two model of electromagnetic torque and stator current

As it can be seen from above, two-loop model offer a better response with smaller amplitude of oscillation (about 0.4 Nm, compared to 1.3 Nm of one-loop model when the torque is big). As a result, the two-loop model can control the motor more stably in practical environment. Furthermore, the stator current shape in two-loop model is rectangular, the same as the shape of theoretical back EMF. In the meanwhile, there are ripples in current response of one-loop control model, which leads to the greater magnitude of electromagnetic torque oscillation. Therefore, the two-loop control model will practically drive BLDC motors better and more stably with a longer lifespan. To compare the controllers' quality, we will plot the speed response of 3 controllers simultaneously in a single figure:
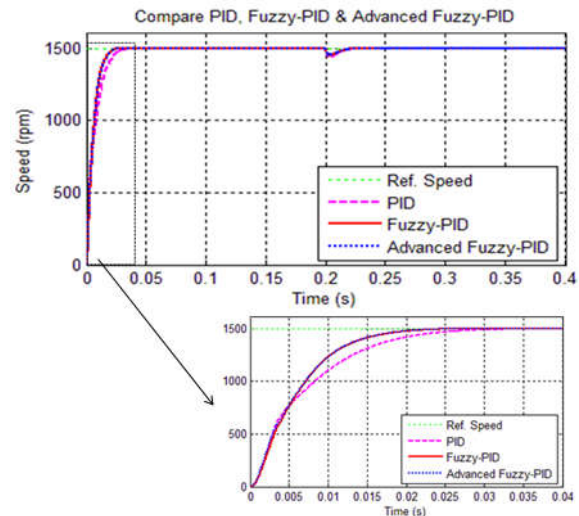
Figure 19. Speed response of the controllers using one-loop model
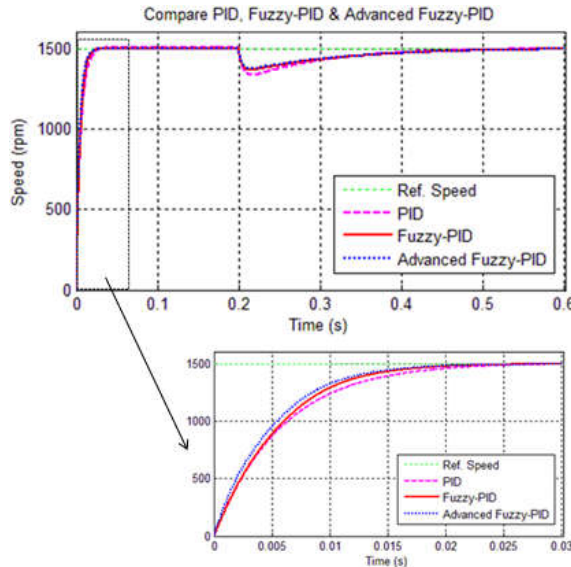
Figure 20. Speed response of the controllers using two-loop model

From the results, we can prove that the control quality is increasingly improved from PID to Fuzzy-PID and Advanced Fuzzy-PID. The two-loop control has some further advantages in comparison with one-loop control model such as smaller rising and settling time without oscillation at the steady state. On the other hand, weak points are here to stay. Not only the model is complicated but it also needs a longer recovery time whenever the load torque suddenly changes. As seen in Figure 19 and Figure 20, when the load torque has a sudden change from 0.5Nm to 2Nm at t=0.2s, two-loop model needs a recovery time of 0.2 second, which is 10 times longer than one-loop model with the same rotor speed. At the next stage, we will observe the quality of the controllers with the existence of sensor noise based on the sum of squared error (SSE):

Table 3: SSE value comparison with and without noise in control system

Model	Controller	SSE (rpm^2)		
		Without noise	With noise	Difference
1-loop	PID	8685	8715	30
	Fuzzy-PID	8155	8179	24
	AF-PID	7893	7923	30
2-loop	PID	8356	8375	19
	Fuzzy-PID	7624	7637	13
	AF-PID	6760	6785	25

As it indicates in the table, Fuzzy-PID controller has the best noise suppression ability, for both models. However, the Advanced Fuzzy-PID controller without

noise can give better performance (regarding to the rising time, settling time, overshoot and SSE) than the conventional and fuzzy-combined PID controller. Last but not least, the SSE in two-loop control model is always smaller than that in one-loop control model.

3.2. Experiments

The drive of the brushless DC motor is designed with two-stage structure: the control stage and the power stage. Designing two-stage circuit avoids the effect of thermal noise from the power stage that will affect the control results. In the control stage, STM32F103C8T6 microcontroller with high processing speed allows for PID algorithm, Fuzzy algorithm and advanced control algorithms. In addition, the control stage also has a current sensing circuit to break the power stage when the thruster overloads and temperature sensing to avoid overheating of MOSFETs. The power stage uses MOSFETS which have temperature endurance and high power.
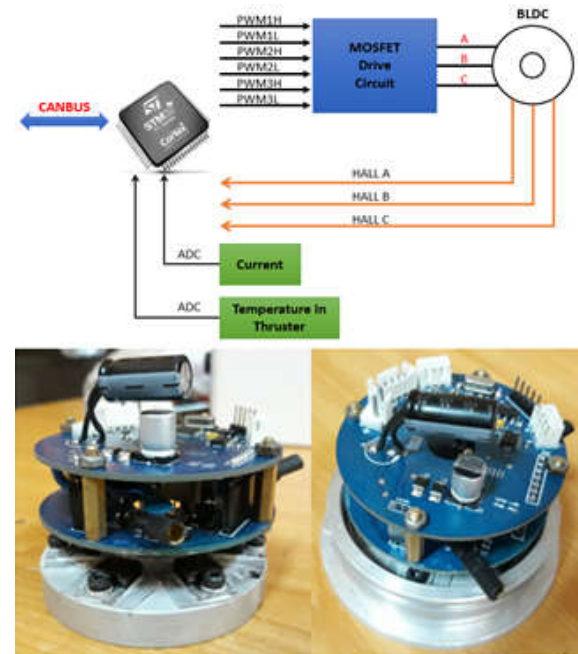
Figure 21. BLDC Controller
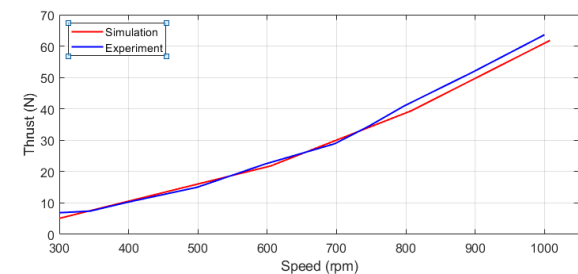
Figure 22. Comparison between BLDC Motor Thrust/Speed simulation (red) and experiment (blue)

As shown in figure 22, the experiments were carried out and obtained the consistent results with the simulation. Besides, experiment results show that the thruster is stable and less noise. At 1000 rpm, the thrust of the

engine was able to reach more than 6 Kgf corresponding to 55% of the motor's power output.
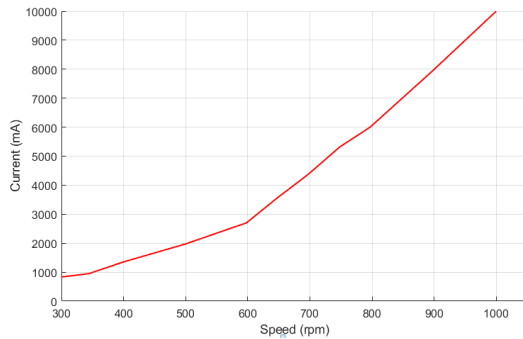
Figure 23. BLDC Motor Current/Speed Curves

Figure 23 depicts the relationship between speed and current of the thruster. Considering the motor speed of 1000 rpm, the circuit still withstand 10A currents because of its good heat dissipation.
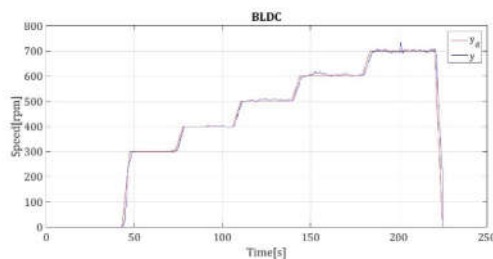
Figure 24. PID speed response with different load
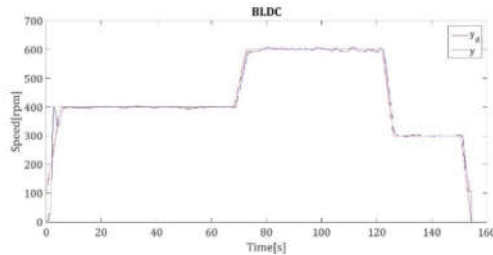
Figure 25. Fuzzy speed response with different load

From figures 24 and 25, the PID and Fuzzy algorithms generally give experimental results of the speed of the motor mounted at different set speeds and at different loads. The PID algorithm outputs fast response time with many noises while the Fuzzy algorithm has slower response time but less noises than PID. At the transient stage, the noise affects on the actual speed response due to the thruster's non-linear property.

4. Conclusions

The use of magnetic coupling and brushless DC motor is an outstanding point in the design and manufacture of our thruster. Magnetic coupling uses neodymium magnets to transmit up to 7Nm from a shaft to the other. It can also protect the motor from overload. Simulation and experimental results show that the chosen propeller is capable of delivering thrust up to 65N at speed of

1000 rpm. Based on the finite element method, the 3mm thick housing helps the thruster to work at 100m water depth (pressure of 145psi). The BLDC increases thruster's performance and operating time. Based on the simulation results, we can conclude that 2-loop model makes the motor's operation more stable with higher efficiency than 1-loop model. Comparing the controllers, we see that the controller combines PID controller and fuzzy logic controller are better than the conventional PID. Advanced Fuzzy-PID controller has the best overall response, but its noise suppression ability still needs to be improved. Finally, the practical experiment achieves good performance with small errors.

References

[1] Ngoc-Huy Tran et.al., *"Design, Control, and Implementation of a New AUV Platform with a Mass Shifter Mechanism,"* International Journal of Precision Engineering and Manufacturing, vol.16, No.7, June 2015, pp. 1599-1608

[2] G. Prasad, N. Sree Ramya, P. V. N. Prasad, G. Tulasi Ram Das, *"Modeling and simulation analysis of the brushless DC motor by using MATLAB,"* IJITEE, vol. 1, 27-31 (2012)

[3] L. Zhao, X. Zhang, J. Ji, *"A torque control strategy of brushless direct current motor with current observer,"* 2015 IEEE ICMA, Beijing, 303-307 (2015)

[4] P. Sreekala and A. Sivasubramanian, *"Speed control of brushless DC motor with PI and fuzzy logic controller using resonant pole inverter,"* IEEE PES Innovative Smart Grid Technologies, Kerala, 334-339 (2011)

[5] KOLLMORGEN TMB(S) Motor Selection Guide

[6] G. Akoun and J. P. Yonnet, *"3-D analytical calculation of the forces exerted between two cuboidal magnets,"* IEEE Trans. Magn., vol. MAG-20, pp. 1962–1964, Sept. 1984

[7] P. Eliès and G. Lemarquand, *"Analytical optimization of the torque of a permanent-magnet coaxial synchronous coupling,"* IEEE Trans. Magn., vol. 34, pp. 2267–2273, July 1998

[8] http://www.vetus-shop.com/

[9] Ngoc-Huy Tran et.al, "Study on Design, Analysis and Control an Underwater Thruster for Unmanned Underwater Vehicle (UUV)." AETA 2017 - Recent Advances in Electrical Engineering and Related Sciences: Theory and Application, pp. 753-764.

[10] Ngoc-Huy Tran et.al, *"A Study on Advanced Fuzzy-PID Speed Control for Underwater Thruster,"* International Symposium on Electrical and Electronic Engineering, Ho Chi Minh city, Vietnam, 2017

Advanced Speed Control of IPMSM Motor Using Adaptive Neural FOC Approach

Ho Pham Huy Anh[1], Cao Van Kien[2], Pham Quoc Khanh[3]

[1,2]FEEE, DCSELAB, Ho Chi Minh City University of Technology, VNU-HCM, Viet Nam

[3]Faculty of Electrical Engineering Technology, Industrial University of Ho Chi Minh City, Viet Nam

ABSTRACT

This paper proposes a neural vector control (NN-FOC) for speed regulation of interior-mounted permanent magnet synchronous motor (IPMSM) drive. The weights of proposed neural NN-FOC structure are optimally identified based on the Levenberg-Marquardt algorithm. The novel MTPA approach is applied for IPMSM-based electric vehicle (EV) drive application. The novel neural NN-FOC control is verified in simulation tests and is compared with the traditional PI-FOC vector control. The simulation results prove that the maximum IPMSM speed range available with the new NN-FOC control is significantly improved in comparison with the traditional IPMSM PI-FOC control. As a consequent the proposed neural NN-FOC control can be successfully applied in advanced electric drives, particularly in PMSM- based electric vehicle EV drive application.

Keywords: interior-mounted permanent magnet synchronous machine (IPMSM), Neural-network field-oriented control (NN-FOC), electric vehicle EV application, Maximum Torque per Ampere (MTPA) control, flux weakening (FW) control, modified Levenberg-Marquardt algorithm

1. Introduction

Nowadays, the traditional PI-based vector control (PI-FOC) is still often used to drive PMSM motors. The benefits of the PI-FOC approach include its simple operation and easy implementation. Nevertheless, PI-FOC control also encounters numerous disadvantages including its impossibility to obtain the optimal PID parameters that are needed to ensure both of robustness and performance in PMSM operation drive [1-2]. As to successfully solve these drawbacks, numerous advanced control methods have been presented. Nguyen et al. [3] introduced a model reference adaptive control-based MRAC speed controller for a SPMSM motor drive. Lin et al. [4] applied an adaptive back-stepping control for six□phase PMSM motor drive. Dursun et al. [5] proposed a sensor-less control for PMSM drive with a new adaptive mechanism. Qutubuddin et al. [6] introduced a novel method for estimating and implementation of brain emotional controller for PMSM drive. Zhu et al [7] proposed a robust speed controller based on Smith predictor for a PMSM drive system with time delay.

Recent years, intelligent controllers have been increasingly applied in PMSM identification and control. Chaoui et al [8] applied an interval type-2 fuzzy control for PMSM drives with a modified reference frame. Feng et al. [9] utilized closed-loop fuzzy-based current controller for PMSM torque ripple minimization, and so on [10-11].

Among potential soft-computing approaches, neural-based control has been successfully applied in PMSM drive control. Shankar et al. [12] used an advanced neuro-fuzzy ANFIS structure for torque control of PMSM driven centrifugal pump. Chen et al. in [13] proposed an adaptive robust finite-time neural control of nonlinear PMSM servo system. Wang et al. [14] applied a novel sliding mode neural sensor-less control for PMSM-based drive system.

These abovementioned results show that there is lack of an adequate research focused on neural-based field oriented control applied for PMSM with respect to Flux- Weakening FW control used in PMSM-based electric vehicle EV drive applications.

To overcome such shortcoming, this paper introduces the new neural-based NN-FOC control for interior-mounted permanent magnet synchronous machine (IPMSM) applied in EV drive, combined MTPA and FW approaches.

The rest of this paper is organized as follows. Section 2 gives the full descriptions of PMSM model while Section 3 presents the traditional PI-FOC control

and the novel NN-FOC control. Section 4 introduces the combination of MTPA and FW approaches applied in IPMSM drive control. Section 5 shows the simulation result of the proposed NN-FOC control for IPMSM drive. Finally, the conclusions are presented in Section 6.

2. Mathematical PMSM Model

The flux linkage relations of PMSM machine in dq-frame are described as:

$$\begin{bmatrix} \lambda_{sd} \\ \lambda_{sq} \end{bmatrix} = \begin{bmatrix} L_{sd} i_{sd} + \lambda_{fd} \\ L_{sq} i_{sq} \end{bmatrix} \quad (1)$$

with L_{sd}, L_{sq} represent the stator inductances in dq-frame in which L_{sd}, $L_{sq} = L_{md}, L_{mq} + L_{ls}$; λ_{fd} denotes the unchanged flux linkage value of the stator coil in d-axis, in which it is supposed that the d-axis has the same direction with the rotor flux vector, it is a-axis. With respect to the abovementioned flux linkage relations, the matrix form of PMSM stator voltages is described in (2).

$$\begin{bmatrix} v_{sd} \\ v_{sq} \end{bmatrix} = \begin{bmatrix} R_s i_{sd}(t) + \frac{d}{dt}\lambda_{sd} - \omega_e \lambda_{sq} \\ R_s i_{sq}(t) + \frac{d}{dt}\lambda_{sq} + \omega_e \lambda_{sd} \end{bmatrix} \quad (2)$$

where ω_e denotes the electrical rotating speed [rad/s] being computed as $p*\omega_{mech}$, in which p is the pole pairs. Now (1) and (2) are combined, the equation becomes

$$\begin{bmatrix} v_{sd} \\ v_{sq} \end{bmatrix} = \begin{bmatrix} R_s + L_{sd}P & -\omega_e L_{sq} \\ \omega_e L_{sd} & (R_s + L_{sq}P) \end{bmatrix} \begin{bmatrix} i_{sd} \\ i_{sq} \end{bmatrix} + \begin{bmatrix} 0 \\ \lambda_{fd}\omega_e \end{bmatrix} \quad (3)$$

with P represents the derivative. Suppose system is balanced in steady mode, the components related to time derivative are omitted. Consequently, (3) in steady state can be rewritten as,

$$\begin{bmatrix} v_{sd} \\ v_{sq} \end{bmatrix} = \begin{bmatrix} R_s & -\omega_e L_q \\ \omega_e L_d & R_s \end{bmatrix} \begin{bmatrix} i_{sd} \\ i_{sq} \end{bmatrix} + \begin{bmatrix} 0 \\ \lambda_{fd}\omega_e \end{bmatrix} \quad (4)$$

The electro-magnetic torque for PMSM is described as

$$T_{em} = \frac{p}{2}(\lambda_{sd} i_{sq} - \lambda_{sq} i_{sd}) \quad (5)$$

If substituted with (1), the equation (5) becomes,

$$T_{em} = \frac{p}{2}\left(\lambda_{fd} i_{sq} + \left(L_{sd} - L_{sq}\right)i_{sd} i_{sq}\right) \quad (6)$$

3. Proposed Neural NN-FOC Control

The main objectives of NN vector control are to achieve the decoupled d- and q-axis current control and to ensure the PMSM system strongly stable versus parametric fluctuations and undetermined noises, for example an abrupt variation of load. As to improve an adaptive neural NN-based FOC controller, the equation (4) is to be re-edited as (7),

$$\frac{d}{dt}\begin{pmatrix} i_{sd} \\ i_{sq} \end{pmatrix} = -\underbrace{\begin{pmatrix} \frac{R_s}{L_d} & -\frac{\omega_e L_q}{L_d} \\ \omega_e \frac{L_d}{L_q} & \frac{R_s}{L_q} \end{pmatrix}}_{A}\begin{pmatrix} i_{sd} \\ i_{sq} \end{pmatrix} + \underbrace{\begin{pmatrix} \frac{1}{L_d} \\ \frac{1}{L_q} \end{pmatrix}}_{B}\underbrace{\begin{pmatrix} v_{sd} \\ v_{sq} - \omega_e\lambda_f \end{pmatrix}}_{u} \quad (7)$$

in which i_{sd} and i_{sq} represent the stator current values in dq-frame; A denotes the PMSM plant matrix; B represents the input component; v is the control signal. Moreover, (7) is in continuous mode. The fact is that the NN-FOC controller is executed as a discrete controller. Then the discretization of (7) is needed and obtained by utilizing either a zero-order or first-order hold discrete equivalent mechanism as (8),

$$\begin{pmatrix} i_{sd}(kT_s + T_s) \\ i_{sq}(kT_s + T_s) \end{pmatrix} = A\begin{pmatrix} i_{sd}(kT_s) \\ i_{sq}(kT_s) \end{pmatrix} + B\begin{pmatrix} v_{sd}(kT_s) - 0 \\ v_{sq}(kT_s) - \omega_e\lambda_{fd} \end{pmatrix} \quad (8)$$

in which Ts denotes the sampling cycle. Since Ts is located in both terms, (8) can be simplified as,

$$i_{sdq}(k+1) = A \cdot i_{sdq}(k) + B \cdot (v_{sdq}(k) - v_{rdq}) \quad (9)$$

with k represents an integer time step; $i_{sdq} = (i_{sd}, i_{sq})'$; $v_{sdq} = (v_{sd}, v_{sq})'$ are the control actions; and $v_{rdq} = (0, \omega_e\lambda_{fd})'$ represents the induced voltage of PMSM rotor.

The block diagram in Figure 1 presents the complete PMSM drive system using neural NN-FOC control. Figure 1 illustrates that the NN-based model is formed into 3 linked layers: the first it is an input one, a hidden one, and an output layer. The key role of the first layer is receiving the error values simultaneously with the integral terms of such these errors, e_{dq} and s_{dq}, respectively. These values will be transformed using the sigmoid or the hyperbolic tangent activation function. The calculation of these two terms is as follows,

$$e_{dq}(k) = i_{dq}(k) - i_{dq}^*(k), \quad s_{dq}(k) = \int_0^k e_{dq}(k)dt \quad (10)$$
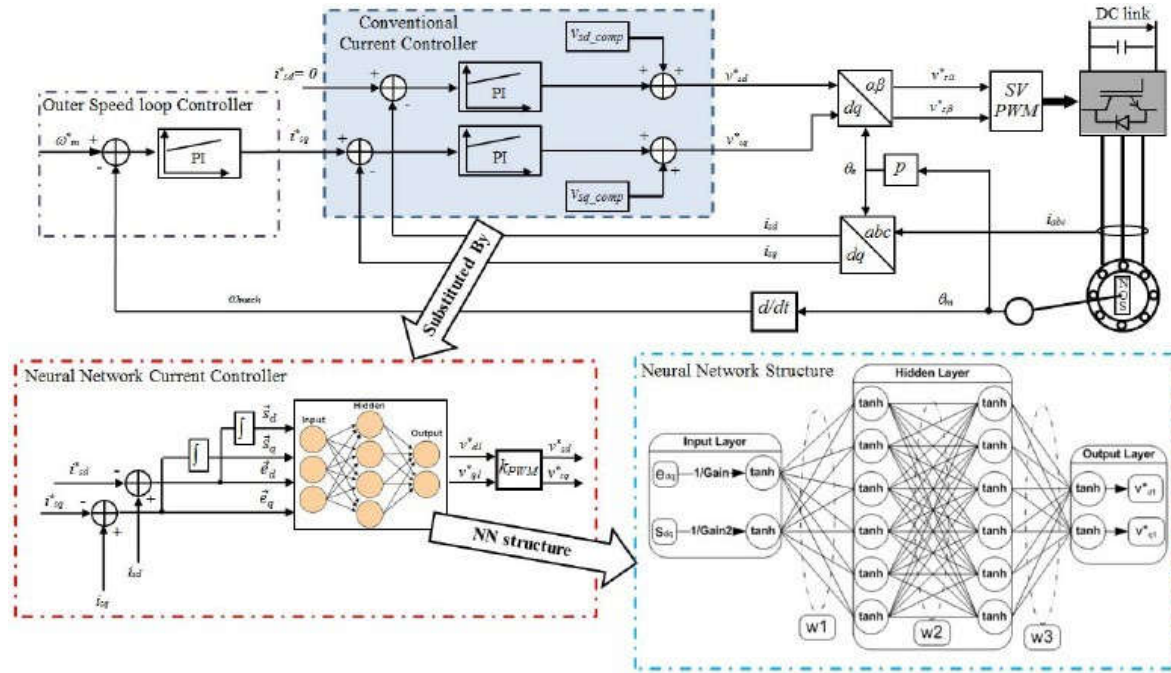
Figure 1: PI-FOC and proposed neural NN-based FOC PMSM speed control

Forwardly, such values from the input one are transmitted to the hidden one which is composed of 2 hidden consecutive layers with six neurons in each. Similarly as the input one, each neuron is calculated based on sigmoid activating equations. The final one, namely output layer, plays the role to transform the hidden layer outputs into original dq voltage components. This is attained through using the sigmoid function. Moreover, since such output values are to be standardized, a certain gain can be added. Such gain value is equal to the maximally available voltage, whose value is related to the DC voltage and the operation mode of PWM. Such as, in case SVPWM is applied, the maximally available voltage can be calculated as,

$$k_{svpwm} = V_{dc} * \sqrt{3/2} / \sqrt{3} \qquad (11)$$

Consequently, the eventual control value v_{sdq} is determined as follows.

$$v_{sdq}(k) = k_{svpwm} \cdot A\big(e_{dq}(k), s_{dq}(k), w\big) \qquad (12)$$

in which w represents weighting matrix; A(·) denotes the acting neural layer. It is also important to notice that recurrent RNN is applied for estimating and forward FNN is applied during implementing in NN-FOC control.

The dynamic programming cost function of proposed PMSM NN-FOC control is described as (13),

$$C\big(i_{dq}(j)\big) = \sum_{k=j}^{\infty} \gamma^{k-j} U\big(e_{dq}(k)\big), j > 0, 0 < \gamma \le 1 \qquad (13)$$

where γ denotes an award factor; U(·) is the utility equation. The purpose of dynamic programming through (13) is to minimally optimize the dq current error. U(·) is computed as,

$$U\big(e_{dq(k)}\big) = \big[e_d^2(k) + e_q^2(k)\big]^{\alpha}$$
$$= \Big\{\big[i_d(k) - i_{dref}(k)\big]^2 + \big[i_q(k) - i_{qref}(k)\big]^2\Big\}^{\alpha} \qquad (14)$$

with α equal 1 for the PMSM drive control.

Furthermore, the modified Levenberg-Marquardt MLM algorithm is used to optimally identify the weights of proposed NN-FOC controller. A MLM method is an efficient approach applied to efficiently calculate nonlinear recursive least mean squares computation [16-17]. General nonlinear equation is of the followed specific function:

$$f(x) = \frac{1}{2} \sum_{j=1}^{m} r_j^2(x) \qquad (15)$$

with x denotes included of n vectors; r_j represents the equation of x. Similar to other optimization algorithms,

356

the proposed MLM approach also bases on iterative method to search the minimally optimized solution. To solve this problem, the MLM appropriately combines the gradient descent and the Gauss-Newton method. Then the key purpose of this approach is to seek the best optimum solution. In order to use the MLM into the PMSM drive control, the initial step is to arrange the fitness function, C(·) (13), into the sum-of-squares function as (15). The equation becomes

$$C = \sum_{k=1}^{N} U(e_{dq}(k)) \xrightarrow{define\ V(k) = \sqrt{U(e_{dq}(k))}} C = \sum_{k=1}^{N} (V(k))^2 \quad (16)$$

Then the steepest of the fitness function in term of the weighting vector is computed as,

$$\frac{\partial c}{\partial \vec{w}} = \frac{\partial \sum_{k=1}^{N} (V(k))^2}{\partial \vec{w}} = \sum_{k=1}^{N} 2V(k) \frac{\partial V(k)}{\partial \vec{w}} = 2J_p(\vec{w})^T V \quad (17)$$

where the Jacobian and error matrix are computed as described in (18):

$$J_p(\vec{w}) = \begin{bmatrix} \frac{\partial V(1)}{\partial w_1} & \cdots & \frac{\partial V(1)}{\partial w_M} \\ \vdots & \ddots & \vdots \\ \frac{\partial V(N)}{\partial w_1} & \cdots & \frac{\partial V(N)}{\partial w_M} \end{bmatrix}, \quad V = \begin{bmatrix} V(1) \\ \vdots \\ V(N) \end{bmatrix} \quad (18)$$

in which the updated weight vector is computed as follows,

$$\Delta \vec{w} = -[J_p(\vec{w})^T J_p(\vec{w}) + \mu I]^{-1} J_p(\vec{w})^T V \quad (19)$$

4. Proposed MTPA Algorithm

A. Methodology

PMSM drives comprise of 2 different operations related to constant torque and constant power. Figure 2 describes a specific torque through speed within 2 operation modes. The relation between power - torque versus speed is described as,

$$Power = VI = T\omega \quad (20)$$

with T represents PMSM torque; ω denotes PMSM velocity. In case unchanged power (green line) it is presented in Fig. 2, namely unchanged power region. Otherwise, we have the unchanged torque region (blue line), in which various studies introduce a control, namely MTPA control since it seeks the best optimum solution of (i_{sd},i_{sq}) to provide the required torque [15]. This MTPA method satisfies both of minimizing the winding loss and developing the total drive distance, because small current is required.

In case of unchanged power region (green line) as

presented in Fig. 2, flux weakening FW control is applied. This control purpose is to increase PMSM velocity range by generating the magnetic flux against the flux provided with the magnet. This FW control plays a very necessary role since often, regardless FW in electric vehicle EV drive, the maximal EV speed is usually under 60 mph. Hence by combination MTPA and FW methods, the main objective of proposed NN-FOC is to translate the referential torque to optimum (i_{sd},i_{sq}) via MTPA method and to appropriate (i_{sd},i_{sq}) in case FW approach.
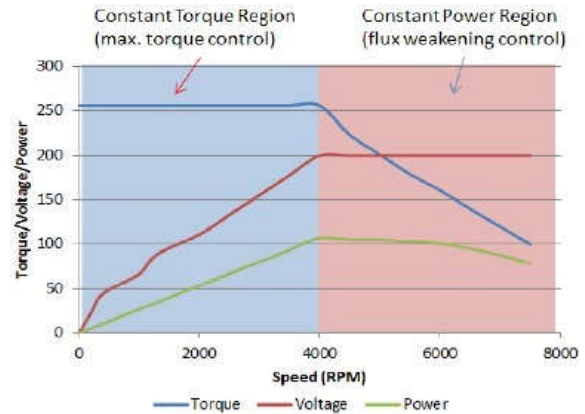
Figure 2: Power-torque–voltage along with PMSM velocity

In case PMSM velocity overcomes the rated value, the PMSM drive is in the 2nd region (green line) as presented in Fig. 2. This region velocity is varied within the rated value and ω_2. When PMSM falls in this

section, FW approach is used. Then the voltage-limit is kept to prohibit the back-EMF to overcome the maximal voltage value.

A. Proposed MTPA Algorithm

This paper proposes MTPA control since it uses both (i_{sd},i_{sq}) for PMSM drive control. Moreover it help to minimize the coil loss, which plays an important losses of PMSM operation [15] and eventually it is quite simple relative to other complex approaches.

The core of MTPA method bases on the stator PMSM dq voltage relations (4) and the electromagnetic torque equation (5). The introduction related to these relations is explained in previous section.

In case the SPMSM is investigated, the electro-dynamic torque relation is only relied on the i_{sq} current

since the two stator L_{sd}, L_{sq} values are almost equal; hence, the reluctance torque, plays the 2nd term of (5), is able to be omitted. Thus, the electro-magnetic torque of SPMSM is described as

$$T_{em} = \frac{p}{2}(\lambda_{fd}i_{sq}) \qquad (21)$$

Hence MTPA control for SPMSM is very efficient, because the torque T_{em} is only relied on the i_{sq} component, as described in (21).

Moreover in case the IPMSM exceeds the rated velocity, the FW approach is applied to prohibit the back-EMF to overcome the maximal voltage value available. In this paper, online FW method is used instead of a priori approach since exactly calculating PMSM parameters in very high velocity region is hard-working.

5.Simulation Results

As to prove the performance of proposed NN-FOC IPMSM speed control, four tests are comparatively investigated as to verify with the traditional PI-FOC control. They compose of speed-up and speed-down test, T_{em} fluctuation test, IPMSM parametric variation test, and eventually IPMSM FW test. It is also important to notice that the T_L torque value of 20 [Nm] is applied along with four tests.

Firstly, the speed-up and speed-down test is carried out. At t = 0.5 s up to t = 3.00 s, the reference PMSM velocity is abruptly varied upward and downward between 0 rad/sec and 200 rad/sec. The comparative speed traction results of IPMSM between proposed NN-FOC and PI-FOC control is illustrated in Fig. 3.

After the speed-up and speed-down test, the load torque T_{load} variation test is conducted. At t = 3.5s, T_{load} is abruptly varied from 20 Nm up to 100 Nm. Up to t = 4.2s, T_{load} is increased to 200Nm value and then at t = 5s, decreased to 50Nm. Eventually the IPMSM parameter fluctuation test is carried on. From t = 5.5 s, the IPMSM parameters R_s, L_s, and λ_{fd} is simultaneously varied as, the R_s value is doubled meanwhile L_s, and λ_{fd} values are both decreased 20%.

Finally, the FW control is comparatively carried on between proposed NN-FOC and conventional PI-FOC method. From t = 7s, the referential PMSM velocity is speed-up until it mostly reached the maximal allowable velocity, about 650 rad/s. Forwardly, at t = 10.55s, the referential PMSM velocity is down to 300rad/s in order to test if the flux weakening method is able to be back to MTPA control or not.

The simulation results of PMSM velocity, PMSM (i_{sd},i_{sq}) currents, I_a-I_b-I_c results, and IPMSM voltage values for comparison between traditional PI-FOC and proposed NN-FOC approach are completely presented in followed Figure 3 up to Figure 7.

The results illustrated in these figures demonstrate that both of PI-FOC and proposed NN-FOC methods obtain the same performance until the FW test. The results shown in Fig. 3 prove that when the referential PMSM velocity is over rated value, the PI-FOC method seems rather good to keep its stable operation. On the contrary, proposed neural NN-FOC method confirms perfectly stable IPMSM velocity in high speed section. The results from Fig. 4 demonstrate that the IPMSM velocity can exactly attain 600 rad/sec due to the i_{ds} current of both controllers providing negative value as to prohibit the back-EMF to overcome the maximal allowable voltage value as presented in Fig. 8.
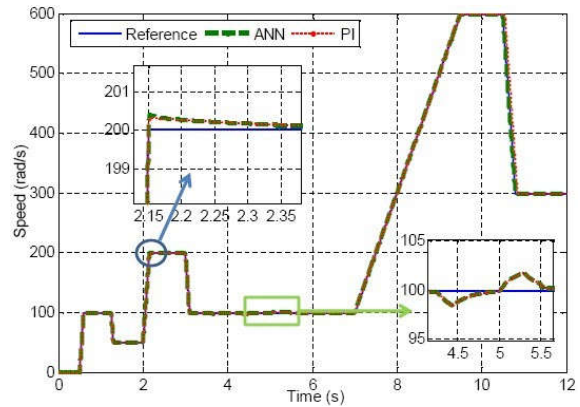
Figure 3: Comparative speed control results of IPMSM (simulation)

Figure 4: Comparative d-and q-axis current results related to IPMSM (i_{sd},i_{sq}) (simulation)
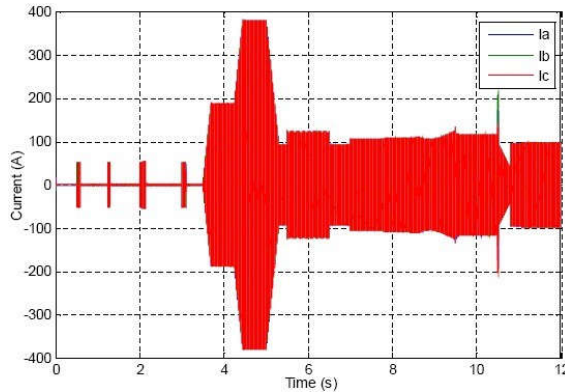
Figure 5: Proposed NN-FOC control of abc currents of IPMSM (simulation)
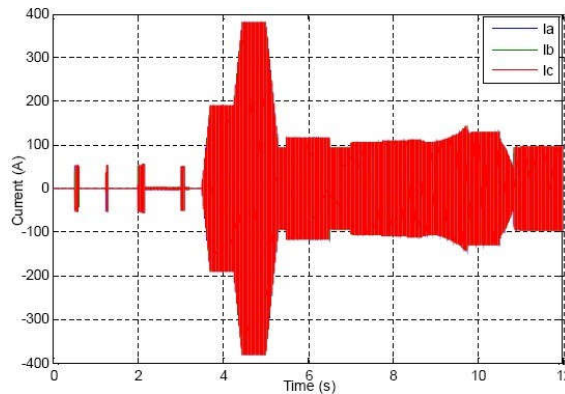
Figure 6: Conventional PI-FOC control related to abc currents of IPMSM (simulation)
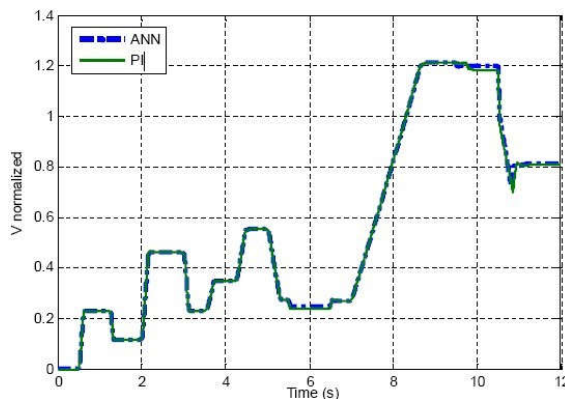
Figure 7: Comparative normalized amplitude of voltage of IPMSM (simulation)

6. Conclusions

This paper proposes a novel neural-based field- oriented
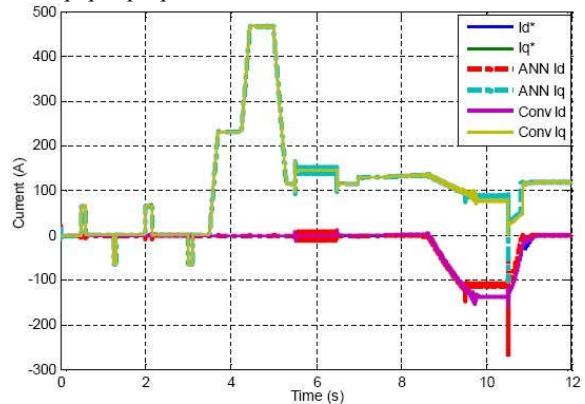
control (NN-FOC) for an interior-mounted IPMSM drive. The proposed neural model is optimally identified with modified Levenberg-Marquardt algorithm. Furthermore the combined MTPA and FW approaches are used for IPMSM-based electric vehicle (EV) application. The proposed NN-FOC control is verified in simulation tests and compared with a PI- based field-oriented control (PI-FOC) method. The simulation results show that the proposed neural NN- FOC controller demonstrates a bit better performance than the conventional PI-FOC control and then provides an excellent drive method applied in advanced electric drives.

Acknowledgements

References

[1] T. Lee, C. Lin, and F. Lin, "An Adaptive H∞ Controller Design for Permanent Magnet Synchronous Motor Drives," Control Engineering Practice 13, pp. 425-439, 2005.

[2] S. Li, T.A. Haskew, and L. Xu, "Conventional and Novel Control Designs for Direct Driven PMSG Wind Turbines," Electric Power System Research, vol. 80, pp. 328-338, March 2010.

[3] Nguyen, A. T., Rafaq, M. S., Choi, H. H., & Jung, J. W. (2018). A Model Reference Adaptive Control-Based Speed Controller for a Surface-Mounted Permanent Magnet Synchronous Motor Drive. IEEE Transactions on Industrial Electronics.

[4] Lin, F. J., Chen, S. G., & Sun, I. F. (2017). Adaptive Backstepping Control of Six□Phase PMSM Using Functional Link Radial Basis Function Network Uncertainty Observer. Asian Journal of Control, 19(6), 2255-2269.

[5] Dursun, M., Boz, A. F., Kale, M., & Karabacak, M. (2018). Sensorless control application of PMSM with a novel adaptation mechanism.

Neural Computing and Applications, 29(1), 87-103.

[6] Qutubuddin, M. D., & Yadaiah, N. (2017). Modeling and implementation of brain emotional controller for Permanent Magnet Synchronous motor drive. Engineering Applications of Artificial Intelligence, 60, 193-203.

[7] Zhu, Q., Xiong, L., & Liu, H. (2017). A robust speed controller with smith predictor for a PMSM drive system with time delay. International Journal of Control, Automation and Systems, 15(5), 2448-2454.

[8] Chaoui, H., Khayamy, M., & Aljarboua, A. A. (2017). Adaptive interval type-2 fuzzy logic control for PMSM drives with a modified reference frame. IEEE Transactions on Industrial Electronics, 64(5), 3786-3797.

[9] Feng, G., Lai, C., & Kar, N. C. (2017). A closed-loop fuzzy-logic-based current controller for PMSM torque ripple minimization using the magnitude of speed harmonic as the feedback control signal. IEEE Transactions on Industrial Electronics, 64(4), 2642-2653.

[10] Chang, W., & Tong, S. (2017). Adaptive fuzzy tracking control design for permanent magnet synchronous motors PMSM with output constraint. Nonlinear Dynamics, 87(1), 291-302.

[11] Waley, A. S., Mao, C., & Wang, C. D. (2017). Artificial Optimal Fuzzy Control Strategy for Electric Vehicle Drive System by Using Permanent Magnet Synchronous Motor. International Journal of Engineering and Technology, 9(1), 50.

[12] Shankar, V. A., Umashankar, S., Padmanaban, S., & Paramasivam, S. (2017). Adaptive Neuro-Fuzzy Inference System (ANFIS) Based Direct Torque Control of PMSM driven centrifugal pump. International Journal of Renewable Energy Research (IJRER), 7(3), 1436-1447.

[13] Chen, Q., Ren, X., Na, J., & Zheng, D. (2017). Adaptive robust finite-time neural control of uncertain PMSM servo system with nonlinear dead zone. Neural Computing and Applications, 28(12), 3725-3736.

[14] Wang, M. S., & Tsai, T. M. (2017). Sliding Mode and Neural Network Control of Sensorless PMSM Controlled System for Power Consumption and Performance Improvement. Energies, 10(11), 1780.

[15] S. Jung, J. Hong, and K. Nam, "Current Minimizing Torque Control of the IPMSM using Ferrari's Method," IEEE Trans. On Power Electron., vol. 28(12), Dec, 2013.

[16] M. A. Lourakis, "A Brief Descriptions of the Levenberg-Marquardt Algorithm Implemented by levmar," Matrix, vol. 3, p. 2, 2005.

[17] X. Fu and S. Li, "Training Recurrent Neural Networks with the Levenberg-Marquardt Algorithm for Optimal Control of a Grid-Connected Converter," IEEE Trans. on Neural Netw.and Learning Syst., 2014.

PART V, SECTION I

Machining Technology
(Difficult-to-cut and Free Machining; Non-conventional Machining;
Green Process/Manufacturing; Cutting Mechanisms…)

Design Modification of Additive Manufacturing Parts Using Texture Information of 3D Model

Tsung-Chien Wu[1], Jiing-Yih Lai[1], Yu-Wen Tseng[1] and Chao-Yaug Liao[1]
[1]Department of Mechanical Engineering, National Central University, Taoyuan, Taiwan

ABSTRACT

Additive manufacturing (AM) has been commonly used for the prototyping of three-dimensional (3D) models. The input model of the AM technology is a triangular model representing the surface shape of an object. The design features on a triangular model are generally not clear as the vertices are irregularly distributed. If design modification is necessary, it is difficult to segment and extract the meshes from the model. The objective of this study is to propose a method for extracting the design features on an object model by using the texture information. A 3D color model including a triangular model representing the object shape and a texture map describing the object texture is employed. The 3D model is generated by using a set of object images captured from different views surrounding the object. A texture mapping algorithm is then employed to generate the texture map corresponding to the 3D model. With both meshes and texture displayed in a texture mode, a region extraction technique is employed to extract the design features. All parts separated can then be fabricated with an AM machine, and assembled for checking the feasibility of design modification. Several products are employed to demonstrate the feasibility of the proposed technique.

Keywords: Additive manufacturing, Design modification, Texture mapping, 3D printing, 3D modeling

1. Introduction

Additive manufacturing (AM), or so-called three-dimensional (3D) printing, has recently been received extensive attention as it is a convenient manufacturing technology for the prototyping of 3D models. A 3D model used in AM is in a form of triangular meshes (called triangular model hereafter), which typically comes from two different resources, CAD system or 3D scanning device. The CAD model generated by a CAD system can directly be converted into triangular meshes and exported to an AM machine for fabrication. If design modification is necessary, the original CAD model can be modified and converted into triangular meshes again. The data obtained from a 3D scanning device, however, is triangular meshes. Design modification on triangular meshes is difficult because the design features are generally lost. As more and more prototypes are fabricated with AM technology, design modification or modification of triangular meshes becomes an important issue to investigate.

The shape design of a product can be analyzed not only from its geometric model, but also from its texture. In fact, the texture of a product may sometimes maintain more design features than triangular meshes. For example, a smooth surface may be colored differently to represent different object or feature, whereas this kind of information cannot be obtained from the surface model. Similarly, the boundary of a design feature may become vague when an object is scanned as triangular meshes. If the object texture is accompanied with the triangular model, there is more opportunity to recognize the design features with the texture information, rather than distorted or unclear geometric information. A 3D color model represents a triangular model with a texture map accompanied to describe the geometric shape and surface texture of an object. In this study, a region extraction technique by using the texture information of a 3D color model is developed to extract the design features of an object. It is integrated with mesh processing and AM technology for the part design and exchange of different prototypes.

A technique using multiple images of an object is used to generate the 3D color model of the object, which basically includes a 3D model describing the object geometry and a texture map describing the object texture. A bilateral mapping between each mesh on the 3D model and each pixel on the texture map is available so that a region or boundary identified on the texture map can be mapped onto the 3D model. Similarly, the region or boundary identified on the 3D model can be mapped onto the texture map. Once a region on the 3D model is identified, mesh processing technology can be applied to process the meshes. We intend to study part exchange from two different objects and apply an AM machine for the fabrication of the new object. With the texture information available, the recognition and separation of a part from an object would become easier. In addition, appropriate skills in terms of mesh processing and AM technology are employed for maintaining the feasibility of parts assembly.

The literature related to the issues mentioned above is briefly reviewed as follow. 3D modeling technique can be used in different applications, such as 3D animation, computer graphics, 3D printing, reverse engineering, and e-commerce. Various techniques can be employed to create a 3D model- composed of triangular meshes- of an object. Laser range scanners [1, 2] or other coded

light projecting systems [3] are typically used in reverse engineering, in which a complex scanning and data processing process is required to obtain the surface points of the object. One of the drawbacks is that the intensive density of the data points requires additional effort to process the data, but the final result may not be satisfactory. Another drawback is that the color texture of the object cannot be recorded.

Using 2D images to reconstruct the 3D model is a more effective approach to acquire the geometric model as well as the color texture simultaneously. There are basically two main approaches for constructing a 3D model from 2D images: shape from stereo and shape form silhouette. The basic assumption of shape from stereo is that two stereo visions should have the same patterns of texture, which is difficult to achieve. Several methods in this area have been proposed [4, 5], but none of the available methods is reliable enough to fulfill the requirements mentioned above.

The shape-from-silhouette (SFS) method estimates the shape of an object from images of its silhouette. It still faces the problems of accurate modeling of 3D shape, continuous and smooth modeling, and enormous amount of computing time required. Therefore, several methods are available in literature to deal with these problems. Mulayim et al. [6] investigated a 3D reconstruction method based on the SFS concept. They proposed a complete system to obtain a rough model in terms of silhouette-based volume intersection, and then fine tune the rough model using photo consistency. Yemez et al. [7] proposed a computationally efficient shape from the silhouette method based on mesh deformation, which can produce accurate 3D mesh models of complex real objects.

3D reconstruction based on the SFS method can generate a model with volumetric by marching intersection (MI) method [8]. It allows high quality models based on SFS, with benefits including: efficiency in terms of memory space and computational time by using a higher volume resolution, and merging more extended silhouettes, each at higher resolution. Furthermore, 3D reconstruction based on the SFS method can generate the model in terms of exact polyhedra methods. Matusik et al. [9] computed an exact polyhedral representation for the visual hull directly from silhouettes. This method was well suited to rendering with graphic hardware and could be computed very quickly because the computation was performed during the creation of the visual hull. Niem [10] proposed a method for fast traversal of the layers of the projected cones and retrieved the viewing edges that lied on the surface of the visual hull, which achieves a real-time full reconstruction model.

Mesh editing is usually based on two different approaches. One is local parameterization. Biermann et al. [11] proposed a cut-and-paste transferring for two different models. The local regions were parameterized and overlapped to transfer the details. Sorkine et al. [12] and Lévy [13] also proposed methods to parameterize the overlapping parts and smoothly blend the region to fit with another model. Yu et al. [14] used the Poisson solver to perform mesh editing. The local transformation with gradient field and generalized boundary condition representation has also been applied to help the editing. The mesh deformation, merging, and smoothing can be performed by applying this method. The other is directly editing the mesh. Zorin et al. [15] performed a method to edit the mesh interactively by applying the smooth subdivision to give a natural connection on editing part. Several mesh editing software are also available, such as Blender [16] and MeshLab [17], enabling post mesh processing easily.

2. AM Technology and Design Modification

Most AM technologies accept a universal file format *.stl for the processing of the data. The data saved in such a file essentially represents a triangular model that describes the surface shape of an object. Normally, each file represents an individual object. If more than two objects need to be assembled, the parts at the junction must be carefully designed so that they can be assembled successfully. If the triangular models are from a CAD system, the meshes at the junction would match quite well. However, if the triangular models are obtained from other resources, such as reconstructing from 2D images of an object, the mesh quality at the junction may not be as good as that of CAD models. Therefore, for assembling two AM parts with imperfect triangular meshes, a pre-processing of the meshes is required. The following two problems could occur for the assembly of two AM parts. First, interference or gap may exist at the junction. As each triangular model is obtained individually, the meshes at the junction generally do not match each other. When such models are fabricated directly, the interference or gap at the junction could exist. Second, the mechanism of the assembly should be designed. Pins and holes are a common method to fix two parts together. However, the accuracy and repeatability of additive manufacturing is worse than that of CNC machining. If two AM parts are to be assembled with pins and holes, it is necessary to investigate the dimensional tolerance required for successful assembly.

Part replacement is one of the issues frequently investigated in design modification, especially when several prototypes or samples are available. When these prototypes or samples are fabricated with the AM technology, it could be necessary to perform part exchange among these objects. For example, several cups of similar size may have different handle designs.

It could be necessary to generate the 3D models of these cups first, and then extract the handle models. Both the body of a cup and its handle are fabricated independently with the AM technology. Therefore, a cup can be assembled with different handles to test the design. When part replacement is implemented on real objects, the mesh condition at the junction is critical as any interference of the meshes at the junction may result in the failure of part assembly. Therefore, mesh processing is very important for this kind of application. The method to generate the 3D model of an object is described below. It follows the description of the mesh processing method.

3. Generation of 3D Color Model

An easy and effective method to acquire the 3D model as well as the texture of an object is using a device to catch multiple images of the object from different viewing directions, and then employing a 3D modeling algorithm and a texture mapping algorithm for generating the 3D color model of the object. The object images can be obtained by using a single-camera device which applies a camera to capture the object placed on a turntable (Figure 1(a)), or a multi-camera device which applies several cameras mounted on an arm to capture the object placed on a turntable from different latitudes. A patterned mat can be designed and a camera calibration algorithm can be employed to acquire the camera information [18]. Once all object images and camera information are available, the following process is implemented in sequence. First, the initial 3D model (Figure 1(b)) is generated from multiple object images. This model is still unsatisfactory as considerable sharp edges and artifacts are found on the model. Second, a mesh optimization algorithm is implemented to improve the quality of the initial mesh model (Figure 1(c)), which primarily removes non-existing features on the model and performs a smoothing of the model. Finally, the texture map corresponding to this model is generated, which can yield the final color model for the object (Figure 1(d)).
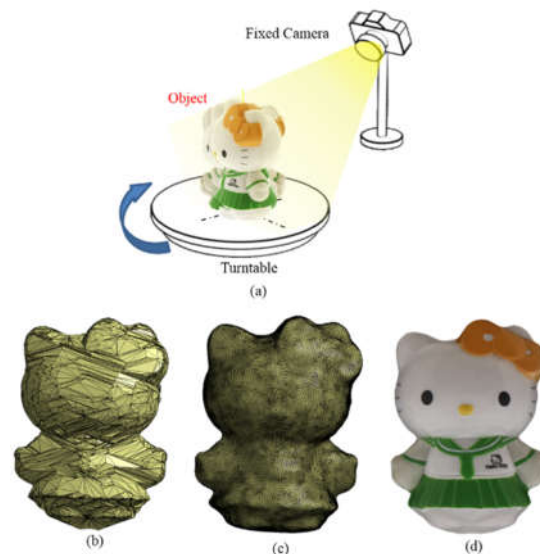
Fig. 1 Generation of 3D color model, (a) image capturing device, (b) initial 3D model, (c) improvement of the mesh model, and (d) 3D color model.

3.1 Generation of Initial 3D Model

The common method to generate the 3D model of an object from multiple object images is the SFS method, which essentially applies the silhouette points of each image to generate a polyhedron, and then evaluate the intersection points of all polyhedrons to from a triangular model representing the object shape. However, as the SFS model essentially represents the visual hull of an object, it is unavoidable that not-existing sharp edges and artifacts may exist on the 3D model, resulting in the inaccuracy and un-smoothness of the model. The SFS model is called an initial 3D model in this study. The procedures for generating the initial 3D model are as follows (Figure 2):

(1)   Generate a set of polyhedrons (Figure 2(a)): a polyhedron is a cone of the projected area from the camera point through all silhouette points on an image. A polyhedron actually contains many polygons, and each polygon must pass through the camera point and two neighboring silhouette points.

(2)   Establish and subdivide an octree construction (Figure 2(b)): The first volume that covers the entire object is defined and regarded as the basic parent volume. Each parent volume is divided into eight child volumes. The child volumes must be checked to determine if there are more than three polygons intersecting each other. If there are, this volume is again subdivided into eight child volumes. This process is repeated until a volume has only three polygons inside it or the length d of the volume is lower than the allowable tolerance.

(3)   Determine the status of each test volume

(Figure 2(c)): The volume is projected onto each image plane, and the number of points that intersect or reside inside the projected volume is checked. The conditions for setting the status of the volume are as follows. After checking with all images, if the total number of polygons is greater than three, then the status of the volume is set to "Subdivide volume"; if the number of polygons is equal to three, then the status is set to "Calculate point"; and if the number of polygons is less than three, then the status is set to "Discard volume".

(4) 3D points computation (Figure 2(d)): Two conditions for computing 3D points from polygons. The first condition is "Case A", in which a 3D point is intersected by three polygons that originate from zero points and three lines on 2D images. In this case, three polygons come from three different images. The second condition is "Case B", in which a 3D point is intersected by three polygons that come from one line from the first image and one point from the second image. In this case, two connected polygons come from the first image, while the second and the third polygons come from the second image.

(5) Generate the triangular model (Figure 2(e)): Once a 3D point cloud is generated from the intersection of polyhedrons, it is possible to record the polygons that constitute each 3D point. Each polygon is essentially a plane and its boundary is formed by a series of 3D points. Therefore, the data generated in the previous step can be employed to create a new record that specifies the indices of the points located on each polygon. The points on each polygon can then be connected in sequence to from a polygonal mesh. A triangulation algorithm can next be implemented to convert each polygonal mesh into triangular meshes, which finally yields the triangular model of the object.

of polyhedrons, (b) establish and subdivide an octree construction, (c) determine the status of each test volume, (d) 3D points computation, and (d) Generate the triangular model.

3.2 Optimization of the 3D Model

The quality of the triangular model is still not satisfactory because virtual features (sharp edges and corners) appear all over the model. The outline shape of the model may also be distorted by artifacts near concavities of the object. Conventional mesh smoothing methods are invalid here because they may smooth both virtual features and real object features simultaneously. In fact, the removal of artifacts is the most difficult problem because they are invisible on image silhouettes.

The strategy of the proposed quality improvement method is to eliminate virtual features and artifacts first by enforcing a smoothing driving force on a model of relatively large mesh size, and then preserve the silhouette consistency as well as the smoothness of the model by enforcing a silhouette consistency force and a smoothing driving force together. Figure 3 depicts the overall flowchart of the proposed quality improvement method, which primarily includes a remeshing process and a mesh smoothing process.

The remeshing process is composed of mesh subdivision, edge collapse and edge flip. Mesh subdivision is employed to subdivide the meshes uniformly; Edge collapse is employed to collapse edges with low cost scores in terms of edge length and curvature. Edge flip is employed to modify the regularity of the meshes. The mesh smoothing process includes a silhouette consistency term and a regulation term to adjust each of the vertices, where the former can preserve the silhouette consistency when projecting 3D points onto each image, whereas the latter can keep the smoothness of the 3D meshes.

The outer loop of the flowchart is divided into n iterations (called steps hereafter), where the first step is used to eliminate virtual features and artifacts, whereas the other steps are used to preserve the projected silhouettes and smoothness of the model in an iterative procedure. The main difference between the first step and the other steps is that no mesh subdivision is implemented in the first step, whereas it is implemented in the other steps. In addition, the number of iterations for remeshing and the number of iterations for mesh smoothing are different in different step.
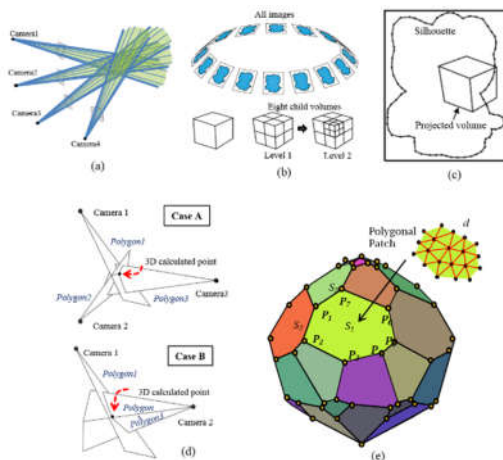
Fig. 2 Generation of initial 3D model, (a) generate a set
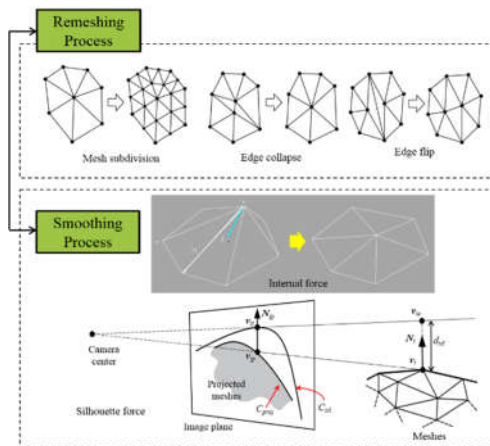
Fig. 3 Overall flowchart of the quality improvement method.

3.3 Texture Mapping

The 3D color model is created by covering a 3D model with a texture map that stores the color information. In the proposed texture mapping algorithm (Figure 4), the input is the optimized 3D model and object images (Figure 4(a)). The following steps are implemented in sequence: mesh partitioning, mesh parameterization and packing, texture transferring, and correction and optimization of the texture, as shown below:

(1)   Mesh partitioning (Figure 4(b)): The purpose of this step is to subdivide the 3D model into several charts, each of which will later be mapped onto the UV domain individually. Mesh partitioning is based on a chart growth method to weigh each mesh on the model, and grow each chart of meshes one by one from a set of initial seed meshes. The seed meshes are optimized in an iteration process until that all meshes have been clustered. It can ensure that all charts are flat and compact in boundary for easy mapping in mesh parameterization.

(2)   Mesh parameterization and packing (Figure 4(c)): The purpose of this step is to map the meshes on each chart onto the UV domain, and pack all 2D meshes on the UV domain. An angle-preserving algorithm is proposed to optimize the mapping between 3D and 2D domains, which can preserve the shape of most 2D meshes. Furthermore, all 2D meshes are tightly packed in a rectangular area for acquiring the finest resolution when mapping the pixels from the image domain to the texture domain.

(3)   Texture transferring (Figure 4(d)): The purpose of this step is to extract pixels from the image domain and place them appropriately on the texture domain. It primarily includes three steps: grouping of 3D meshes, extraction of pixels from the image domain, and placement of pixels onto the texture domain. A method to analyze the texture resolution is proposed.

The proposed texture transferring algorithm can ensure that the texture resolution can be set to equivalent to that of 2D images.

(4)   Correction and optimization of the texture: The purpose of this step is to eliminate erroneous color mapping that might happen due to the insufficient accuracy of the 3D model and camera parameters, and improve the photo consistency at the boundary of different image sources (Figure 4(e)). Several photo inconsistent problems are detected, and then solved one by one. The output texture map is saved as a universal data format (*.obj), which can be displayed with a website viewer (Figure 4(f)).
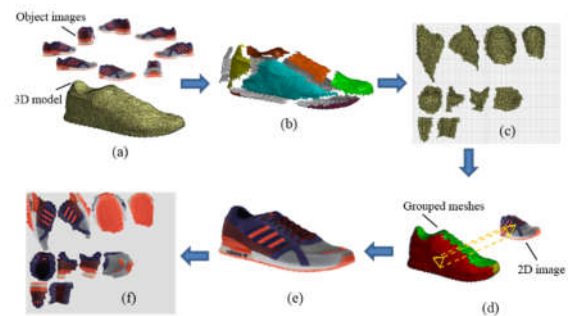
Fig. 4 Overall flowchart of the texture mapping method, (a) input data, (b) mesh partitioning, (c) mesh parameterization and packing, (d) texture transferring, (e) correction and optimization, and (f) output object file.

4. Mesh Segmentation Using Texture Information and Mesh Processing

The common method to process a triangular model is to import the triangular model alone and edit the meshes in accordance with the geometric information on the model. However, it may not be easy to determine the region that should be edited by observing triangular meshes alone as the design features may not be maintained on triangular meshes. For example, Figure 5(a) depicts a 3D color model for a shampoo, with both meshes and texture displayed simultaneously. As the triangular model is reconstructed through multiple 2D images, the triangular model is not very precise. By observing the triangular model alone, it is difficult to perform any editing work as all feature boundaries become invisible on the model. On the contrary, the texture on the 3D color model can still reveal the boundary of different design features, such as the boundary between the cap and the bottle. Therefore, by using the texture information, it may become easy to detect the boundary of different design features.

Several mesh software is available to deal with the segmentation and processing of triangular meshes. We introduce Blender in this study as it enables the display and manipulation of 3D color models. That is, it not

only can display the 3D object model in a texture mode, but also can perform the editing work through the texture information. Several main functions in Blender related to this study are briefly described below. First, the input file is in a file format *.obj, where both the triangular model and texture map are recorded. Second, it provides different kinds of visualization tools, including the display of the triangular model and the object texture. For editing, the shading mode is switched to "edit mode", where both triangular meshes and texture are displayed simultaneously (Figure 5(a)), so that both mesh and color information can be visualized. Third, it provides several tools to segment the triangular model. The one used in this study is the "knife" tool, which can cut a model into two parts (Figure 5(b)) or cut a region of meshes from a model (Figure 5(c)). Fourth, when a model is cut, it will leave a hole, as shown in Figure 5(d). It provides a tool to fill in the hole with meshes. The result after hold filling is shown in Figure 5(e).
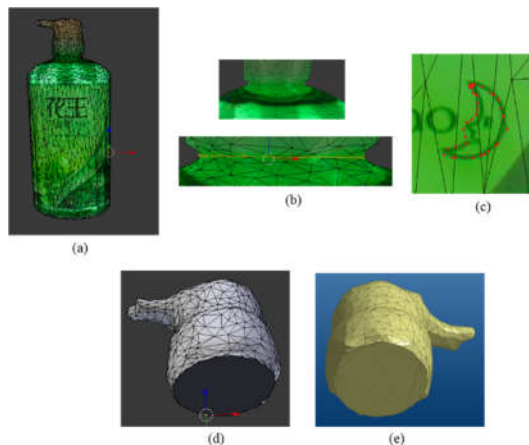
Fig. 5 Tools in Blender from the segmentation and processing of triangular meshes, (a) an edit mode to display both meshes and texture, (b) a "knife" mode to cut a model, (c) segment small feature, (d) a part after cutting, and (e) a part after hole filling.

5. Results and Discussion

For the first example, a shampoo and a window cleaner are employed to demonstrate the concept of design modification by using the proposed technique. The caps of both products are respectively separated from the models, and are exchanged on the models to check the feasibility of design modification. The four parts (two caps and two bottles after separation) are also fabricated with an AM machine, and are tested to check the feasibility of parts assembly. Figure 6(a) depicts the 3D color models of the shampoo and window cleaner, respectively. Each of these two models contains a triangular model and a texture map, generated by using the 3D modelling algorithm and texture mapping algorithm, respectively, as described in previous sections. With the texture and triangular meshes

displayed simultaneously, the diameter of the cap is measured and the section to slice is determined. The "knife" tool in Blender is then applied to cut the cap and separate it from the bottle. Figure 6(b) shows the results after slicing, where the caps and bottles are separately displayed. It is noted that after the slicing, a hole is generated on each part. A hole filling process is implemented on each part to fill in the hole with meshes, which results in a watertight model that can be accepted by the AM machine. Figure 6(c) depicts the exchange of caps on both products in the texture mode. As the models are still displayed in the texture mode, a web viewer can be used to observe the feasibility of parts exchange on both products.

Fig. 6 Design modification using 3D color models, (a) two 3D color models, (b) parts separation with the help of the texture, and (c) parts exchange in the texture mode.

For the AM fabrication, we plan to apply the pin-and-hole fixation method to assemble two parts together. That is, for two parts to be assembled, one part is drilled three holes, whereas its counterpart is added three pins. To make sure that both parts can be assembled appropriately, neither too tight nor too loose, we fabricate several sets of pins and holes with different diameters and evaluate the best combination. We find that the diameters of both pins and holes are affected by the angle that they are fabricated. If three sets of pins and holes are different in angles, then the diameters of each set of pins and holes must be determined in accordance with a data sheet based on our test results. However, all three sets of pins and holes are parallel to each other in this study. Therefore, the diameters of all three pins are equal, so are the diameters of all three holes. The AM machine used in this study is Ultimaker 3 (dual extrusion). The diameters of pins and holes are 3 and 4.5 mm, respectively. Figure 7 depicts the results of additive manufacturing for the first example, where both caps and bottles are separately fabricated. Figure 7(a) indicates that each cap can match the original bottle

quite well, where three pins and holes are attached between the cap and the bottle. Figure 7(b) depicts the result after exchanging the caps. It is noted that each cap matches the corresponding bottle quite well too. This result indicates that both caps and bottles can freely be exchanged to test the feasibility of design modification.

Fig. 7 Results of additive manufacturing for the first example, (a) before cap exchange, and (b) after cap exchange.

For the second example, two shoes are employed to demonstrate the feasibility of exchanging the soles. Figure 8(a) depicts the 3D color models of a sport shoe and a casual shoe, respectively. The sole of each shoe is separated from the 3D model by using the "knife" tool in Blender, where the model is displayed in a texture mode so that the boundary of the sole can be recognized by means of the texture information. The soles separated from both shoes are shown in Figure 8(b). It is noted that the boundary of the slicing is a three-dimensional contour, and hence the corresponding hole is three-dimensional. The meshes used to fill in the hole are therefore located on a surface. To ensure that both parts after hole filling can match each other well, a Boolean operation must be implemented to remove mesh interference when two parts are assembled. Figure 9 depicts the results of additive manufacturing for the second example, where both soles and shoes are separately fabricated. Figure 9(a) indicates that each sole can match the original shoe quite well, where three pins and holes are attached between the sole and the shoe. Figure 9(b) depicts the result after exchanging the soles. It is noted that each sole does not match the corresponding shoe well because the parts come from two different types of shoes. However, we can still change the parts and test the feasibility of design modification.
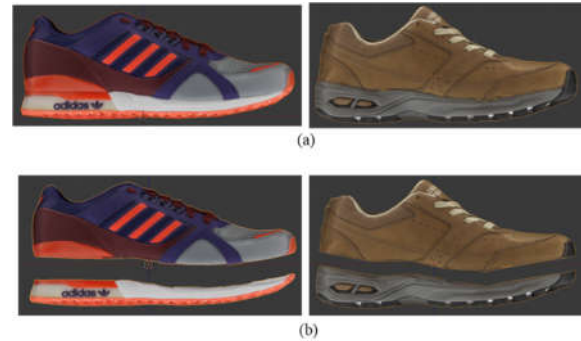
Fig. 8 3D color models for a short shoe and a casual shoe, (a) before separation of soles, and (b) after separation of soles.
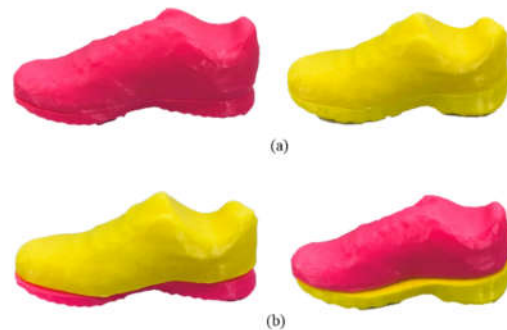
Fig. 9 Results of additive manufacturing for the second example, (a) before sole exchange, and (b) after sole exchange.

6. Conclusion

Part replacement is frequently investigated in design modification when several prototypes or samples are fabricated with the AM technology. When part replacement is implemented on real objects, the mesh condition at the junction is critical as any interference of the meshes may result in the failure of part assembly. We proposed a technique by using the texture information of a 3D color model for the slicing of a 3D model and provided a process for filling the hole so that the sliced part can be fabricated with the AM technology. With the texture information on a three-dimensional triangular model, the boundary of the region to be sliced can easily be recognized. If the slicing is two-dimensional, the hole on a sliced part is a planar type, which can easily be filled with planar meshes. On the contrary, if the slicing is three-dimensional, the hole on a sliced part is three-dimensional, which must be filled with 3D meshes. For the former, the assembly of any two AM parts after slicing can easily be implemented because the contact region is a plane. On the contrary, for the latter, the assembly of any two AM parts after slicing may not be fitted well because the contact region is a surface. Nevertheless, all parts separated can still be fabricated with the AM technology, and assembled for checking

the feasibility of design modification.

References

[1] Yau, H. T.; Chen, C. Y.; Wilhelm, R. G.: Registration and integration of multiple laser scanned data for reverse engineering of complex 3D models, Int J Prod Res, 38(2), 2000, pp. 269–85.

[2] Son, H. P.; Lee, K. H.: Automated laser scanning system for reverse engineering and inspection, Int J Mach Tool Manu, 42, 2002, pp. 889–97.

[3] Pages, J.; Salvi, J. J.; Garcia, R. Matabosch, C.: Overview of coded light projection techniques for automatic 3D profiling, IEEE International Conference on Robotics & Automation, 2003.

[4] Hernández, C.; Schmitt, F.: Silhouette and stereo fusion for 3D object modeling, Computer Vision and Image Understanding, 96(3), 2004, pp. 367-392.

[5] Sinha, S.; Pollefeys, M.: Multi-view reconstruction using photo-consistency and exact silhouette constraints: a maximum flow formulation, ICCV, 2005.

[6] Mulayim, A. Y.; Yilmaz, U.; Atalay, V.: Silhouette-based 3D model reconstruction from multiple images, IEEE Transactions on Systems, Man and Cybernetics, part B 33(4), 2003, pp. 582-591.

[7] Yemez, Y.; Sahilioglu, Y.: Shape from silhouette using topology-adaptive mesh deformation, Pattern Recognition Letters, 2009, pp. 1198-1207.

[8] Rocchini, C.; Cignoni, P.; Ganovelli, F.; Montani, C.; Pingi, P.; Scopigno, R.: The marching intersections algorithm for merging range images, The Visual Computer, 20(2), 2004, pp. 149-64.

[9] Matusik, W.; Buehler, C.; Mcmillan, L.: Polyhedral visual hulls for real-time rendering, Rendering Techniques Part of the Series Eurographics, 2001, pp. 115-125.

[10] Niem, W.; Buschmann, R.: Automatic modelling of 3D natural objects from multiple views, Image Processing for Broadcast and Video Production, Workshops in Computing, 1995, pp. 181-193.

[11] Biermann, H.; Martin, I.; Bernardini, F.; Zorin, D.: Cut-and-paste editing of multiresolution surfaces, In ACM Transactions on Graphics, 21(3), 2002, pp. 312-321.

[12] Sorkine, O.; Cohen-Or, D.; Lipman, Y.; Alexa, M.; Rössl, C.; Seidel, H. P.: Laplacian surface editing, In Proceedings of the 2004 Eurographics/ACM SIGGRAPH symposium on Geometry processing, 2004, pp. 175-184.

[13] Lévy, B.: Dual domain extrapolation, ACM Transactions on Graphics, 22(3), 2003, pp. 364-369.

[14] Yu, Y.; Zhou, K.; Xu, D.; Shi, X.; Bao, H.; Guo, B.; Shum, H. Y.: Mesh editing with poisson-based gradient field manipulation. ACM Transactions on Graphics, 23(3), 2004, pp. 644-651.

[15] Zorin, D.; Schröder, P.; Sweldens, W.: Interactive multiresolution mesh editing, In Proceedings of the 24th annual conference on Computer graphics and interactive techniques, 1997, pp. 259-268.

[16] Blender Online Community.: Blender - a 3D modelling and rendering package, Blender Foundation, 2018, http://www.blender.org.

[17] Cignoni, P.; Callieri, M.; Corsini, M.; Dellepiane, M.; Ganovelli, F.; Ranzuglia, G.: Meshlab: an open-source mesh processing tool, In Eurographics Italian Chapter Conference, 2008, pp. 129-136.

[18] Liao, C. Y.; Xiong, Y. S.; Wang, D. W.; Lai, J. Y.; Lee, J. Y.: A camera calibration process for 3D digital model reconstruction of huge objects, 2016 Machining, Materials and Mechanical Technologies, Japan, 2016.

Development of 3D Printable Bone Model with Fracture Lines for Additive Manufacturing Applications

Yu-Wen Tseng, Chao-Yaug Liao, Idram Irwansyah, Jiing-Yih Lai

Department of Mechanical Engineering, National Central University

No. 300, Zhongda Rd., Zhongli District, Taoyuan City, Taiwan

ABSTRACT

This study proposes a design process for printable bone models featuring fracture lines. The bone model was printed using a low-cost dual-head FDM (Fused Deposition Modeling) machine. Two different colors were used to identify the bone model and the fracture lines. Real bone model fractures with fracture lines were prepared and printed to verify the feasibility of the proposed method.

Keywords: Additive manufacturing, 3D printing, Multi-color, Fracture line, Fused deposition modeling

1. Introduction

When surgeons explain medical conditions to patients, the most challenging part is communicating complicated medical terms and the anatomy of the human body easily enough to understand. In clinical medicine, the most common bone trauma is fracture, which can occur in various bones of the body. In the case of general bone fracture, the surgeon usually uses X-ray images for diagnosis and explains the condition to the patient. However, in the case of a complex comminuted fracture, it is difficult for surgeons to describe the situation to non-professional people using only two-dimensional (2D) medical images. Thanks to the development of medical imaging technology, nowadays surgeons can obtain three-dimensional (3D) information by integrating a series of 2D computed tomography (CT) images. Stereoscopic presentation of the spatial relationship of fractures and the fine structures of bones can further improve the accuracy of diagnosis.

Since the end of the 20th century, additive manufacturing (AM, also known as 3D printing) technology has gradually been applied to clinical medicine [1, 2]. The main application areas can be divided into preoperative simulation, customized guide plate, and implant production [3, 4]. Due to the complex geometry of human bones, as in the case of a comminuted fracture, fractured bones are usually hidden behind other bones resulting in limitations in 3D imaging capabilities. Fracture lines are often crucial clues for surgeons to evaluate surgical procedures. As the fracture line indicates the fracture area, it is necessary to clearly understand the fracture area before implanting reconstruction plates and intramedullary rods. However, as the fracture line is 3D curve in space, it is difficult to decide the fracture area.

AM technology has many advantages when applied in clinical medicine. In addition to overcoming the limitations of 3D medical imaging, it vividly presents fracture lines which help in understanding the actual degree of fracture damage. In addition, it can print real human bone anatomy [5] and use different colors to display physical models of broken bone fragments. These models make it easier for surgeons to explain the condition to patients and help medical students learn the specific details of the fractures such as the types of fracture, the number of bone fragments, the fracture of the joint surface, and the direction of the fracture line [6, 7].

AM is a technique used to deposited materials layer by layer. According to the formation methods, it can be divided into seven types: vat photopolymerization, material jetting, binder jetting, material extrusion, powder bed fusion, sheet lamination, and directed energy deposition [8]. In response to these various manufacturing techniques, the industry has developed different equipment for production. The material extrusion method, also known as Fused Deposition Modeling (FDM), uses equipment with relatively lower material cost and lower technical threshold. In recent years, desktop FDM 3D printers can accommodate multiple nozzles to perform multi-color printing on a single model.

In previous studies, the fracture line mesh model was based on fracture line triangular mesh (surface only, not volume) and the 3D printable model was constructed by growing a certain thickness from each triangular faces' normal [9]. However, in the process of thickening the fracture line mesh, there are often mesh errors (such as mesh self-intersection, direction discontinuity, etc.). This usually results in complicated post-processing needed, and the fracture line mesh model is not uniform in width which fails to generate an effective deposition path.

Therefore, to overcome these problems, this study develops a UFL (Uniform-width mesh model of the Fracture Line) process. With the proposed process, a fractured bone model and fracture lines can be printed by different colors easily and simultaneously. The fractured bone model with fracture lines can be made more realistic and the specific details of the fracture can be easily understood.

2. Method

All current 3D printing path planning software supports the STL (STereoLithography) file format. The STL format is simple in that it defines a triangulated surface by the unit normal and vertices of the triangles using a 3D Cartesian coordinate system and each file can only represent one model. Therefore, when printing a dual-color model, two STL files are needed as sources of path planning. Before printing, different nozzles are specified by G-Code to perform deposition paths of different models.

The flow chart for generating 3D printable bone models with fracture lines by our UFL process is illustrated in Fig. 1. First, it is necessary to obtain a clear image of the patient's affected area through CT scan. Then, the 3D mesh model was reconstructed directly from the 2D CT images by image processing software (PhysiGuide v2.72, Bio-images and clinical assistant Laboratory, National Central University, Taiwan).

Because the boundary contour of the fractured bone is unclear and the surface model quality is rough, the smoothing process was performed on the 3D mesh model. Then the bone reduction process was used to detect the fracture area and fracture line.

Next, the overlapping mesh algorithm was used to remove the overlapping areas of fractured bone because the intersection and gap errors affect the assembly of the 3D-printed model. After the above process was completed, the fractured bone mesh model was divided into three types of mesh regions: the un-fractured bone, the fractured bone, and the fracture line [9].
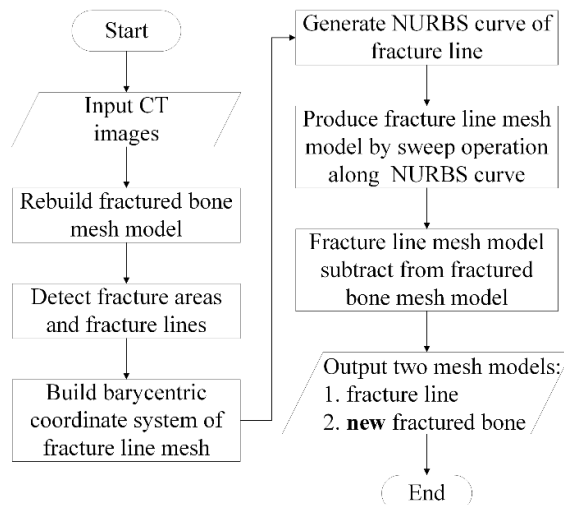
Figure 1 Flow chart of 3D printable bone model with fracture lines by UFL process

The fracture line meshes determined by the bone reduction process have only a series of triangular planes of no thicknesses, and the slice software cannot be used to generate the deposition paths. Traditionally, fracture line meshes can be directly thickened along their respective normal vectors to produce a single volume, then 3D printing can be performed.

However, the fracture line is based on data obtained from the fractured bone mesh model. Each triangular plane is different in size. Therefore, the traditionally-generated fracture line mesh model is usually a curve with unequal width. If the angle between the intersections of the triangular planes is large, in the thickening process, self-intersection occurs (Fig. 2) and needs complex post-processing to correct this problem.

In order to generate a uniform fracture line mesh model, this study developed the UFL process. First, the barycentric coordinate system was built by calculating the positions of the center of gravity for all the triangular planes through which the fracture line passes. Then a curve fitting method was used to fit a NURBS (Non-Uniform Rational B-Splines) curve along all the gravity centers of the triangular planes. Finally, a 2D circle (the size of the diameter of the fracture line to be generated) was swept along the NURBS curve to generate a fracture line mesh model.
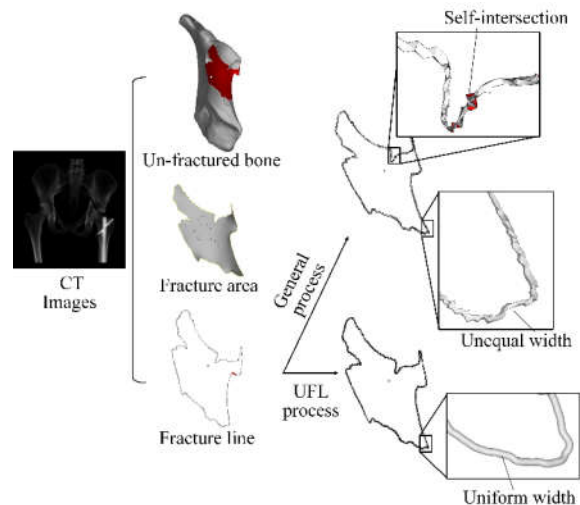
Figure 2 Comparison of the general and UFL processes for generating a fracture line mesh model

In the case of 3D dual-color model mosaic printing, in order to allow the fracture line deposition material to be completely attached to the fractured bone material, an area sufficient to deposit the fracture line must be dug out in the original fractured bone model. In addition, during the FDM printing process, when the current deposition path is finishing, the filament is usually retracted to avoid continuous leakage of the molten material through the nozzle, which can affect the surface appearance of the printed model. Too short a deposition path may cause the material of the fracture line hard to attach to the fractured bone material. To avoid this, the UFL process adds a barrier next to the fractured bone model during the FDM process. The

main purpose of this method is to pre-extrude the material from the nozzle before depositing, allowing it to be successfully attached to the fractured bone model.

3. Results and Discussion

In this study, all models were printed through a low-cost dual-head FDM 3D printer (UltiMaker 3, Ultimaker, USA) with nozzle diameter of 0.4 mm. The slice software was used UltiMaker Cura 3.3.1 (Utimaker, USA) for generating the deposition paths with the specific printing parameters (Table 1). The material of printed models were used polylactic Acid (PLA).

Table 1: Printing parameters

Parameter	Value	
Layer Height	0.2	mm
Line Width	0.35	mm
Wall Thickness	1	mm
Infill	10	%
Printing Temperature	210	°C
Plate Temperature	70	°C

In order to confirm the minimum diameter that can be printed by the FDM 3D printer, spirals of different sizes (diameters of 0.6 mm, 0.5 mm, 0.4 mm, 0.3 mm) were printed on a semi-spherical model with a diameter of 25 mm. Fig. 3 shows that spirals with a diameter of 0.6 mm and 0.5 mm can be fully printed on the semi-spherical model. Though a spiral with a diameter of 0.4 mm can be printed, the deposition paths of the spiral on the horizontal plane could not be generated (enlargement in Fig. 3). Therefore, the fracture line mesh models generated on all fractured bone pieces in the subsequent experiments were 0.5 mm in diameter.

Using the UFL process and the above-mentioned printing parameter settings, the physical model of a

fractured human hip joint was printed in gray color and the fracture line was printed in different color (fuchsia). Figure 4(a) shows the use of a single color (SC) to print the fractured bone model and in Fig. 4(b), the use of UFL process to print the fractured bone model with fracture lines.
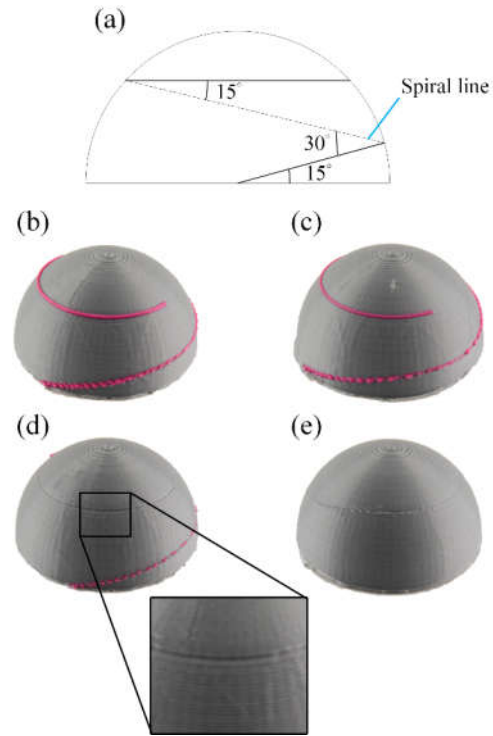
Figure 3 The minimum diameter of printable fracture line for FDM 3D printer: (a) 2D drawing of semicircular and spiral line (simulated as fracture line); The diameter of the fracture line is (b) 0.6 mm (c) 0.5 mm (d) 0.4 mm (e) 0.3 mm
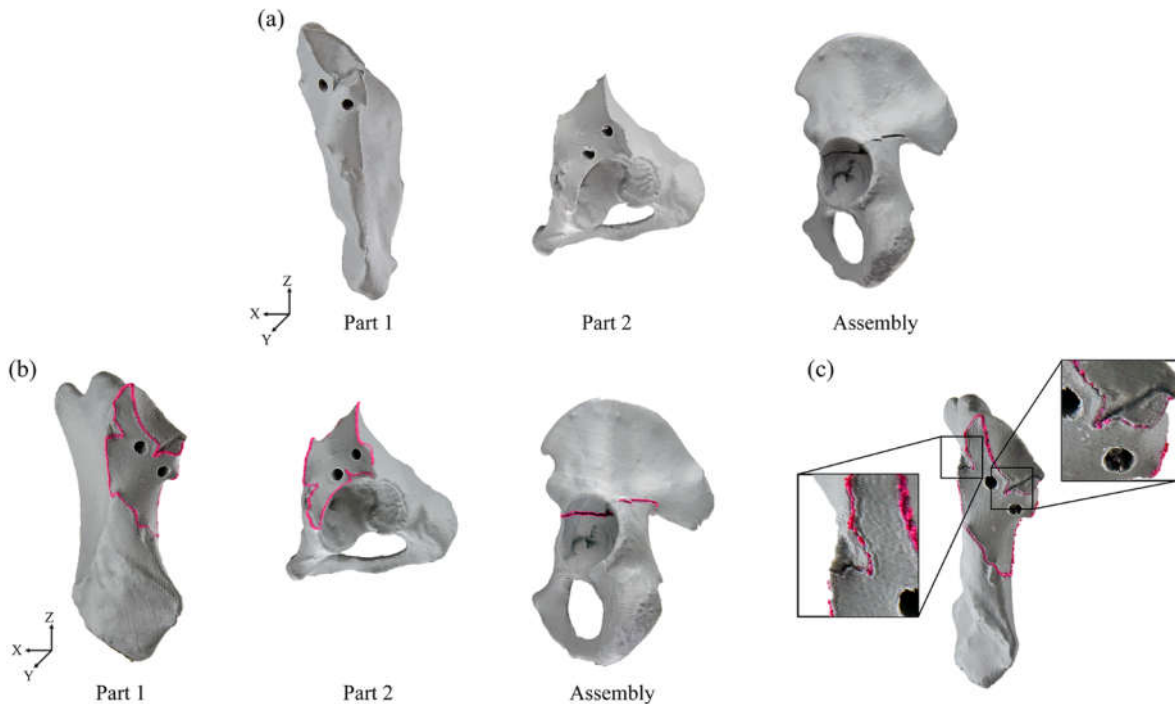
Figure 4 Simple fractured bone model printed by the FDM 3D printer: (a) SC model; (b) UFL model fabricated with barrier; (c) UFL model fabricated without barrier.

By comparing the UFL models of two different printing strategies, the one without the barrier added near to the bone model has many extreme short deposition paths, so that the fracture line material can not fully attach to the fractured bone material, as shown in Fig. 4(c). Although both the SC model and the UFL model could be assembled by lining up each fractured bone into a complete fracture model through holes and pins, the fracture line of the bone and the degree of fracture damage could not be clearly observed through the surface appearance of the SC model. In contrast, the UFL model makes it easy to find the fracture area and the fracture status.

By comparing the printing time of the SC model and the UFL model, Table 2 shows that the printing time of the UFL model is longer than that of the SC model. In the process of dual-color printing, the nozzle has to return to the origin of the machine, as different nozzles are used for printing in different colors. Therefore, compared to single color 3D model printing, dual-color printing spends more time on nozzle system regression and nozzle shifting.

Table 2: Printing time (min.) of fractured bone models

Strategy	Part1	Part2	Total
SC	219	169	388
UFL (barrier)	320	312	632

Placing a barrier next to the printing model, which is another reason for the longer printing time. However,

by adjusting the direction of the bone model, it is possible to place the fracture line on the lower layer of the overall model to reduce the printing height of the barrier, thus improving the 3D printing efficiency.
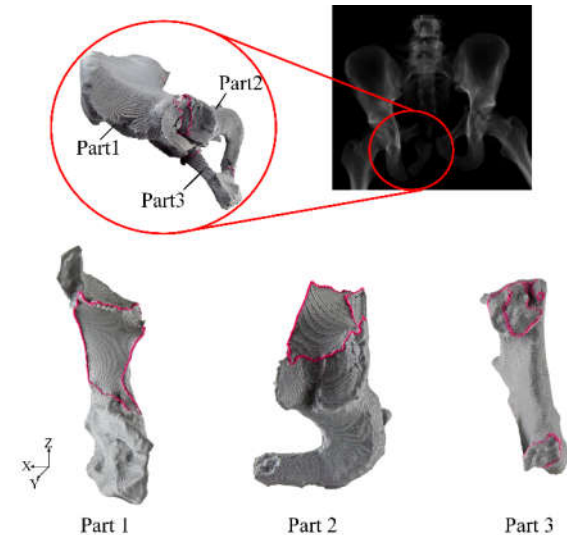
Figure 5 Complex fractured bone model printed by the FDM 3D printer using UFL process

In this study, complex fractured bone models are also suitable for our proposed method (Fig. 5). In complex fracture situations, a physical model with fracture lines can be useful to help the surgeon and patient learn more details about the fractures within the bone.

4. Conclusion

In order to further develop the application of AM technology to clinical medicine and to help surgeons and patients better understand the condition of bone trauma, this paper developed the UFL process to generate a fractured bone with uniform-width fracture line mesh model. Two contrasting colors were used to print the fractured bone and fracture line mesh models. The actual printings were performed in hip joint cases include simple and complex bone fractures, respectively. It was found that the fracture line mesh model could be firmly attached to the fractured bone model. Finally, a multi-color model was assembled using the cooperation of holes and pins, which could be useful for helping the surgeon and the patient learn the details of a bone fracture.

References

[1] M. Abe, K. Tabuchi, M. Goto, A. Uchino, *Neurologia Medico-Chirurgica (Tokyo)*, 38 (1998) 746－751.

[2] H. F. Saller, P. E. Harers, C. P. E. Zolllkofer, T. Warnke, F. R. Carls, P. Stukl, *Journal of Oral and Maxillofacial Surgery*, 27 (1998) 327－333.

[3] A. Muller, K. G. Krishnan, E. Uhi, M. Gerson, *The Journal of Craniofacial Surgery*, 14 (2003) 899－914.

[4] S. Singare, Q. Lian, W. P. Wang, F. Wang, Y. Liu, D. Li, B. Lu, *Rapid Prototyping Journal*, 15 (2009) 19－23.

[5] L. Yang, X. W. Shang, J. N. Fan, Z. X. He, J. J. Wang, M. Liu, Y. Zhuang, C. Ye, *BioMed Research International*, Article ID 2482086 (2016) 1－5.

[6] S. Chen, Z. Pan, Y. Wu, Z. Gu, M. Li, Z. Liang, H. Zhu, Y. Yao, W. Shui, Z. Shen, J, Zhao, H. Pan, *Scientific Reports*, 7 (2017) 1－11.

[7] N. Bizzotto, I. Tami, A. Santucci, R. Adani, P. Poggi, D. Romani, G. Carpeggiani, F. Ferraro, S. Festa, B. Magnan, *3D Printing in Medicine*, 2:2 (2016) 1－6.

[8] American Society for Testing and Material, Designation: F2792-12a: Standard terminology for additive manufacturing technologies, (2015).

[9] Irwansyah, Y. W. Tseng, J. Y. Lai, C. Y. Liao, P. Y. Lee, *EPiC Series in Health Sciences,* 2 (2018) 83－86.

A Design of the Recycling System on the Metal Additive Manufacturing

Shu-San Hsiau [1], Yi-Lun Xiao [1], Li-Tsung Sheng [1]

[1] Department of Mechanical Engineering, National Central University, Taiwan

ABSTRACT

This study aims to design a new recycling system for the AM-using metal powder. In this system, the recycling metal powder is transferred by a pneumatic module. And this system includes a supply tank, a continuous loss in weight module, a pneumatic module, a transfer channel, a sieving module, and a refilling tank. The recycle system can automatically operate for a long time and be more conducive for the development of large-scale production of objects such as aviation parts.

Keywords: Metal additive manufacturing, Recycling System, Pneumatic Conveying

(Presentation)

A Study on Technology of Latex Rubber Freezing in Manufacturing Standard Vietnamese Rubber 10

Nguyen Huu Hung[1], Nguyen Ngoc An[2], and Bui Huu Phu[3]
[1]Nhat Viet Technology Investment and Development Company LtD., Vietnam
[2]University of Science, Vietnam National University in Hochiminh City, Vietnam
[3]Hochiminh City University of Technology and Education, Vietnam

ABSTRACT

Vietnam is now one of the top world leaders in rubber production and export. According to statistics, rubber trees are currently being planted in the whole country of about 850 thousand hectares, of which about 600 thousand hectares of rubber planted by farmers, in 29 provinces rubber growing; It is grown in the South East (46.4%), mainly in Binh Phuoc, Binh Duong, Tay Ninh, Ba Ria-Vung Tau. However, we mainly produce and export Standard Vietnamese Rubber (SVR) 3L, and have not researched to produce SVR 10 and 20 to meet the needs of vehicle radial tire manufacturing.

At the moment, all big companies of vehicle radial tire manufacturing in Vietnam such as the southern rubber industry company, Danang Rubber Company … must import 10 or 20 standard rubber from Asia countries such as Malaysia, Thailand, Indonesia, and Korea with a high cost and much dependent on their companies. It is necessary to do research to make SVR 10 or 20 in Vietnam for companies to manufacture vehicle radial tire used local latex rubber.

In the paper, we present our own study on technology of latex rubber freezing in manufacturing SVR10, that the material is used for vehicle radial tire. The test results have shown that our technology is good enough and our SVR 10 product samples can be provided to companies of vehicle radial tire manufacturing. We are still studying in order to increase the quality and stability and decrease the cost for the SVR 10 rubber. We do hope our novel rubber can be replaced totally imported products in near future.

Keywords: rubber processing, SVR 10, Radial tires, Latex rubber, latex rubber freezing

Conical Roll-twisting Process for Fabrication of Archimedes Blades

Sanghu Park[1], Sungmoon Yang[2]
[1]School of Mechanical Engineering, Pusan National Univ., Busan Korea
[2]Graduate School of Mechanical Engineering, Pusan National Univ., Busan Korea

ABSTRACT

We propose a novel conical roll-twist-bending (CRTB) process to fabricate a metallic Archimedes spiral blade which has variable curvatures on its surface, and it is a key element of a novel wind power generator having a remarkably higher efficiency of about 34% compared with conventional wind power systems. The CRTB system consists of a pair of conical rollers and cylindrical twist-bending rollers in the both lateral sides. With the help of forming analysis results, multi-step regional forming method was utilized to fabricate the blade. Also, the process parameters were optimized by a response surface methodology. In this work, we developed the experimental equipment of CRTB process, and it was experimentally proven that the developed CRTB process was capable of producing a spiral blade with a shape error less than approximately 5%.

Keywords: Spiral blade, Conical Roll-twisting bending, Wind power generator

(Poster)
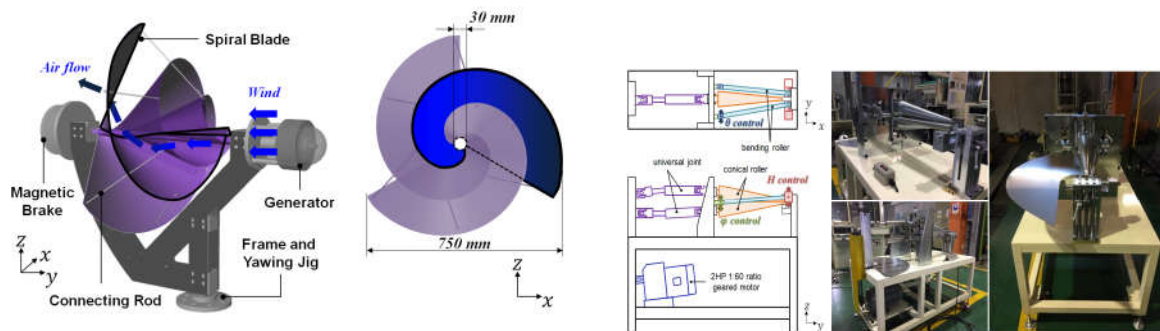
(Spiral blade wind power generator)

(Conical roll-twisting process)

PART V, SECTION II

Materials Technology
(Functional Materials; Technologies of Materials; Materials Characterization and Evaluation;
High Speed Machining and Abrasive Machining; Micro- and Nano-Systems Engineering and
Emerging Technologies; Surface Integrity and Machining Quality…)

A Recommendation of Analytical Computing of Stresses and Strains in Single Point Incremental Forming (SPIF)

Le Khanh Tan[2], Le Khanh Dien[1], Nguyen Huy Bich[3], Tran Van Hung[1]

[1] DCSELAB - Ho Chi Minh City University of Technology, VNU-HCM, Vietnam

[2] Ho Chi Minh City University of Technology and Education (HCMUTE), Vietnam

[3] Nong Lam University, Ho Chi Minh City, Vietnam

ABSTRACT

Single Point Incremental Forming (SPIF) is considered as a new technology forming sheet that is effective in small batch productions or new trial single models in metal sheet production. Although the analytical framework of SPIF was performed in 2008 by P.A.F. Martins et Al. under a title "Theory of single point incremental forming". We considered that in this research, the stresses formulas of random point are not related to the depth z of the empirical model therefore it cannot explain the mechanism of rupture on models and the restriction of the technology. With the above reason, the purpose of this paper is dedicated to represent a new formula of internal stresses inside model sheet in the material sheet by analytical computing way. We hope that our results is more logical and convincing to the mechanism of failure of material sheet when forming by SPIF. The results of the study are verified with consistency by empirical and simulation processes.

Keyword: SPIF, stresses, strains, deformation, pestle, forming tool, formability, metal sheet

1. Introduction

Although the apparition of the Single Point Incremental Forming technology in industry was about 30 years, but in the last decade, its mathematical base was only represented under the title " Theory of Single Point Incremental Forming" [1] that interpreted some shortcomings. According to this theory, the stresses inside the sheet material at a random position are equal principal stresses in the following formula

Table 1

States of stress and strain in SPIF and conventional stamping

Figure 1: Result of comparison of stresses by [1]

Wherein: σ_Y : *Yield stress of material sheet,*

$\sigma_{1,2,3}$: *Principal stress at a random point in material sheet*

$\sigma_{\phi, \theta, t}$: *3 normal component stresses in spherical coordinate system of [1],*

t: width if material sheet,

r_{punch}: *radius of spherical end tool (pestle)*

In the Column State of stress of figure 1, we realize that all of 3 components of normal stress in flat and rotational symmetric surfaces and at corners of the sheet workpiece are always constant. They only depends on yield stress σ_Y of material sheet, width t of the sheet and the radius r_{punch} of the punch (SPIF pestle or tool). Furthermore these normal stresses are also equal to the principal stresses and are independent to the depth of the forming position. That means that the tangent stresses, the main factors that cause the deformation of the metal sheet, are nil. All of the above factors prove that the formulas of stresses of [1] are not authentic and they cannot explain the mechanism of failure at a certain depth when forming sheet by SPIF technology in reality.

2. A recommended analytics formula of the generated stresses in SPIF:

Model of calculating stresses at a random point in contact area of tool and sheet workpiece are described in figure 3 with the initial assumption:

- Spherical tip of forming tool is absolute rigid that keeps its geometric shape under interactive forces. Only the sheet workpiece has plastic deformation,
- Speed of spherical forming tool on the metal sheet is constant,
- A tiny layer of lubrication exist between tool tip and sheet workpiece surface for keeping a small constant coefficient of friction f
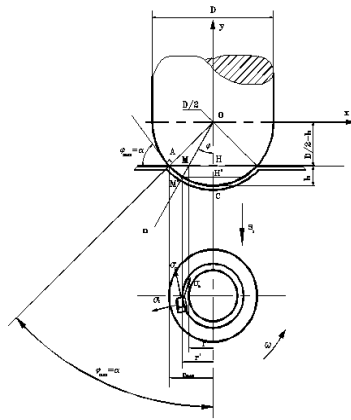
***Figure 2**: Model of calculating normal stresses in sheet worpiece in SPIF*

In figure 2, M is an initial random point in the medium layer of the sheet. Under the interaction of spherical tip tool on the sheet, initial point M displaces to M' of the deformed sheet.

A coordinate system OXYZ is places at the center O of the tool. M and M' are on the same line OM' that makes with the OZ axis an angle COM=φ. Herein OY axis is perpendicular to the surface of the figure. ti is initial thickness of the sheet and t_φ is the one at M'. The displacements of M to 3 axes are show in low part of figure 3:
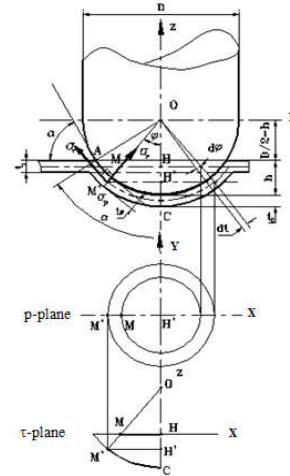
***Figure 3**: Absolute deformation of sheet workpiece in 3 perpendicular directions*

p - plane: the horizontal plane that is perpendicular to OZ axis, parallel to OXY plane and passes through point M'. The initial circle (H, HM) in XOY plane deformed to circle (H', H'M') on p-plane,

τ - plane: the OXZ plane contains M and M'. It is also the tangent direction of the profile of the tool. On τ-plane, initial point M displaced to M' and chord MH deformed to curve M'C,

r - plane: contains O, M, M' and is perpendicular to τ-plane (OXZ plane). r=OM' is radial direction or normal direction n. In this direction, initial thickness ti follows Cos-law that means that tφ=ti cosφ. When we call t = ti is the initial thickness of the sheet hence tφ=t cosφ,
D is diameter of tool

Computing the relative deformation (strain) and normal stress at random point M in contact area:

- **On p-direction:**

On figure 4, M is located by angle COM=φ on the circumference of circle (H, r=HM). Under the application force of the tool, this circle is extended to (H', r'=H'M'). Consider to 2 right triangles MHO and M'H'O, initial radius is:

$$MH = r = OHtg\varphi = (\frac{D}{2} + \frac{t}{2} - h)tg\varphi = \frac{t+D-2h}{2}tg\varphi$$

The circumference of (H, r=MH) is also the initial length to p-direction:

$$l_0 = 2\pi.r = 2\pi(\frac{t+D-2h}{2}).tg\varphi$$

After deformed, initial circle (H, r=MH) becomes (H', r'=M'H'):

$$M'H' = r' = OM'\sin\varphi = \frac{D+t_\varphi}{2}\sin\varphi = \frac{D+t\cos\varphi}{2}\sin\varphi$$

The circumference of (H', r'=M'H') is also the deformed length to p-direction:

$$l' = 2\pi.r' = 2\pi\frac{D+t\cos\varphi}{2}.\sin\varphi$$

380

Strain in p-direction is calculated as:

$$\varepsilon_p = \ln\frac{l'}{l_0} = \ln\frac{2\pi\dfrac{D+t\cos\varphi}{2}.\sin\varphi}{2\pi(\dfrac{t+D-2h}{2}).tg\,\varphi} =$$

$$\ln(\frac{(D+t.\cos\varphi)\cos\varphi}{D+t-2h}) = \ln(\frac{t.\cos^2\varphi + D.\cos\varphi}{t+D-2h})$$

In figure 3, notice that r'=M'H' > r=MH so l'=2πr' >

l₀=2πr and l'/l₀>1

$$\varepsilon_p = \ln(\frac{D+t-2h}{D.\cos\varphi + t.\cos^2\varphi}) > 0$$

According to Ludwig's formula [2]

$$\sigma_P = K\varepsilon_P^{\ n}$$

K: Yielding coefficient
n: Exponent value of plastic curve, the result is

$$\sigma_P = K\ln^n(\frac{t+D-2h}{t.\cos^2\varphi + D.\cos\varphi}) \qquad (3)$$

Partial differential of σ_P by thickness t:

$$\frac{\partial\sigma_P}{\partial t} =$$

$$n.K\,\frac{\cos\varphi(D(1-\cos\varphi)+2h\cos\varphi)}{(t+D-2h)(t.\cos^2\varphi+D.\cos\varphi)}\ln^{n-1}(\frac{t+D-2h}{t.\cos^2\varphi+D.\cos\varphi}) > 0$$

Because: D>2h,   cosφ>0,   t>0   and

$$\varepsilon_p = \ln(\frac{D+t-2h}{D.\cos\varphi + t.\cos^2\varphi}) > 0 \qquad (4)$$

So $\dfrac{\partial\sigma_P}{\partial t} > 0$

σ_P is proportional to the thickness t.

• **On τ-direction:**
    The deformation increases from tip of tool to margin of the contact circle and M displaces to M'. Initial length:

$$l_0 = MH = r = OH.tg\,\varphi = (\frac{D}{2}+\frac{t}{2}-h).tg\,\varphi = \frac{D+t-2h}{2}tg\,\varphi$$

This length will be prolonged to curve M'C after deforming on τ-direction:

$$l' = M'C = OM'.\varphi = (\frac{D}{2}+\frac{t_\varphi}{2})\varphi = \frac{D+t\cos\varphi}{2}\varphi$$

Strain to τ-direction:

$$\varepsilon_t = \ln\frac{l'}{l_0} = \ln\frac{\dfrac{D+t.\cos\varphi}{2}\varphi}{\dfrac{D+t-2h}{2}tg\,\varphi} = \ln(\frac{(t.\cos\varphi+D)\varphi}{(t+D-2h)tg\,\varphi})$$

Because l'>l₀ so ε_t>0
    Ludwig's formula is applied for τ-direction:

$$\sigma_t = K\varepsilon_t^{\ n}$$

$$\sigma_t = K\ln^n(\frac{(t\cos\varphi+D)\varphi}{(t+D-2h)tg\,\varphi}) \qquad (5)$$

Calculating the differential of σ_t:

$$\frac{\partial\sigma_t}{\partial t} = Kn(\frac{D(\cos\varphi-1)-2h\cos\varphi}{(t+D-2h)tg^2\varphi(t\cos\varphi+D)}\ln^{n-1}(\frac{(t\cos\varphi+D)\varphi}{(t+D-2h)tg\varphi}) < 0$$

$$(6)$$

• **On r-direction:**
    This direction has the radial deformation of the sheet. It is also the normal n-direction to the thickness of the sheet at point M'. Sheet is extended to p-direction and t-direction is pressed in r-direction. According to [4] the relation of the initial thickness of sheet t_i at M' and the deformed thickness t_φ followed Cos law

$$l' = t_\varphi = t_i\cos\varphi$$

    Strain to r-direction:

$$\varepsilon = \ln\frac{l'}{l_0} = \ln\frac{t_i\cos\varphi}{t_i} = \ln(\cos\varphi)$$

Ludwig's formula applied for r-direction:

$$\sigma_r = K\varepsilon_r^{\ n}$$

$$\sigma_r = K\ln^n(\cos\varphi) \qquad (7)$$

$$\frac{\partial\sigma_r}{\partial t} = 0 \qquad (8)$$

So stress of this direction is not depended on the thickness t
In conclusion, referring to the result of (4), (5) and (6) we can see that in among 3 normal stresses at a random point:

-   σ_p is proportional to the thickness t of the sheet workpiece,
-   σ_t is contra variant to the thickness t of the sheet workpiece,
-   σ_r is independent to the thickness t of the sheet workpiece,

So the total normal stress has a complicated relation to the thickness t of the sheet

$$\sigma_P = K\ln^n(\frac{D+t-2h}{D.\cos\varphi + t.\cos^2\varphi})$$

$$\sigma_t = K\ln^n(\frac{(t\cos\varphi+D)\varphi}{(t+D-2h)tg\,\varphi})$$

$$\sigma_r = K\ln^n(\cos\varphi) \qquad (9)$$

This result will be checked with Abaqus simulation

3. Checking FEM and Abaqus simulation:

a. Result of simulation of 1mm thickness model:
Shapes of 2 models of in Abaqus are circular conic lateral and tool material is HSS with haft spherical tip of 5mm diameter.

The processes of simulation and the result of simulation of 1mm thickness model are displayed in figure 3, 4, 5 and 6:
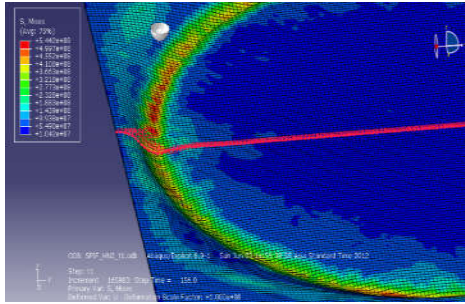
Figure 4: *Tresses of simulated sheet 1mm thickness and red diameter band on the model is the position of measure stresses*
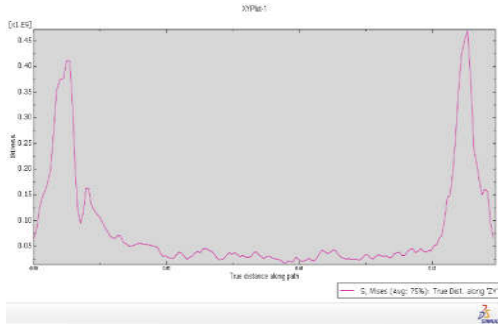
Figure 5: Diagram of stresses of 1mm thickness through the diameter band

b. Result of simulation of 4mm thickness model:
The processes of simulation and the result of simulation of 4mm thickness model are displayed in figure 4 and figure 5:
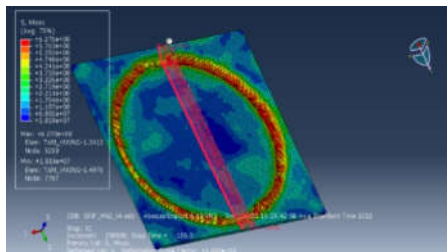
Fig. 6: *Stresses diagram of simulated sheet 4mm thickness and red diameter band on the model is the position of measure stresses.*
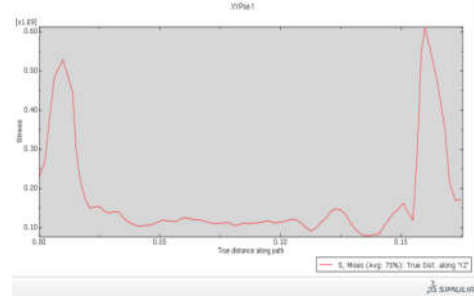
Figure 7: Diagram of stresses of 4mm thickness through the diameter band

The comparison of 2 diagrams of tresses of simulation in Abaqus is displayed in figure 8:
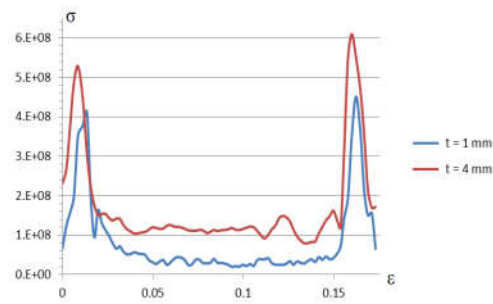
Figure 8: *The comparison of stresses of 2 models with different thickness*

The normal stresses in simulation of 4mm thickness model is almost all bigger than the one of 1mm thickness model although there are rarely some positions the result is contra variant. That means that the normal stresses are almost proportional to the thickness of the workpiece.

4. Conclusion

In conclusion, the recommended formula of normal stresses in (9) is convincing. These stresses are at a random position on the workpiece so they are depended on the contact position φ, the initial thickness t of the sheet, the depth h of the tool in forming process, the diameter of the tool. The diagram of Abaqus in figure 11 had proved the reliability of the proposed formulas.

References

[1] P.A.F. Martins a, N. Bay b, M. Skjoedt b, M.B. Silva "Theory of single point incremental forming", Elsevier, CIRP Annals - Manufacturing Technology 57 (2008) 247–252.

[2] Jacob Lubliner, Plasticity theory, Maxwell Macmillan International, 2009.

[3] Leszak, E., 1967. Patent: Apparatus and process for incremental dieless forming, United States Patent Office. Patent number 3,342,051.

[4] Martin Skjoedt: Rapid Prototyping by Single Point IncrementalForming of Sheet Metal, 2008 PhD Project, Department of Mechanical Engineering,Technical University of Denmark.

[5]Iseki H, Kumon H. "Forming limit of incremental sheet metal stretch forming using spherical rollers". Journal of the Japan Society for Technology of Plasticity 1994;35(406):1336-41.

[6] Iseki H "An approximate deformation analysis and FEM analysis for the incremental bulging of sheet metal using a spherical roller". Journal of Materials Processing Technology 111, 2001.

[7] http://www.amino.co.jp/en/products/241.html.

The Influence of Magnetic Fiber Orientation on the Electric Properties of Conductive Polymer Composite Material by Using Magnetic-assisted Injection Molding

Chen-Yuan Chung[1], Shia-Chung Chen[2], Kuan-Ju Lin[1]
[1]Department of Mechanical Engineering, National Central University, Taiwan
[2]Department of Mechanical Engineering, Chung Yuan Christian University, Taiwan

ABSTRACT

With the evolution of modern science and technology, composite material is widely used in more and more fields. Its related fabrication and technology have become the important issue of development of science and engineering. Especially for fibrillar composite material, since the fiber's orientation and distribution affect the properties of product, how the orientation and distribution are controlled is an important key to improve its properties. In this study, the external magnetic field is applied to injection molding for controlling the orientated behavior of metal fiber during the filling process. In addition, the fiber's orientation and conductivity will be investigated by means of different process conditions (melt temperature, mold temperature, injection speed, and so on) with or without external magnetic field.

1. Introduction

Conductive polymer composite material is produced by adding conductive fillers into plastic material. The fillers are usually metal particles, metal powder or carbon black particles, and various conductive fibers [5] such as metal fiber, carbon fiber, or metal-coated carbon fibers. Conductive fiber itself is equipped with high aspect ratio (the ratio of length to diameter of fiber) and large contact area, which can easily be connected to each other to increase the conductivity. The specific orientation resulted from injection molding can also lead to the advantage of enhanced mechanical property, thus making it one of the more widely used materials. Carbon fiber is equipped with high modulus, high strength, high temperature resistance, and superior anti-fatigue performance. However, it could easily be fractured during forming process, thus reducing the possibility of fiber overlapping. For example, Saleem et al. [2] used the composite material of adding carbon fibers or carbon particles to PP matrix to successfully grant this composite material conductivity and improved mechanical and thermal conduction properties. Carbon fiber is equipped with better conductivity, mechanical property, and thermal conduction property than carbon particles, such that it only takes 10wt% of carbon fiber to achieve the percolation threshold of the composite material, while for carbon particles it will take 25wt%. In addition to keeping the features of carbon fiber, the electrical conductivity of polymer with nickel-coated carbon fiber is also greatly increased. The nickel element itself is magnetic conductive, therefore, it is possible to change its fiber orientation via applied magnetic field. For example, Lu et al. [3] used the composite material made of nickel-coated carbon fiber or carbon fiber, and the result of study indicated that the former was equipped with higher conductivity.

Fountain flow occurs in injection molding process. It

results in poor distribution and uniformity of the conductive fillers or fibers in the melt polymer due to the effect of fountain flow. If we can control the fiber distribution and orientation, we can definitely overcome the process limitation and improve the application level and cost effectiveness of conductive polymer composite material. The externally applied magnetic field approach adopted in this study has been shown in prior literatures. For example, Al-Haik et al. [4] also successfully used high magnetic field to enhance the uniformity of carbon nanotube in epoxy resin along with the mechanical performance. Garmestani et al. [5] used high magnetic field to process the addition of single-walled carbon nanotubes into epoxy resin, in which the single-walled carbon nanotubes were re-oriented by high magnetic field, and the stronger magnetic field led to more obvious orientation behavior. Shi et al. [6] found out that the magnetic conductivity of fiber could be increased by coating carbon nanofibers with NiO/CoO, such that the fiber orientation can be rotated via weaker magnetic field during production of composite material. Kimura et al. [7] studied carbon fibers and polyethylene fibers with different lengths. They made them into suspended liquids with the same density and applied a magnetic field to them. The result indicated that polyethylene fibers and carbon fibers demonstrated different orientation behavior due to varying magnetic anisotropy.

2. Method

2.1 Materials

The matrix material selected in this study is the LDPE 1965T produced by SABIC, and the filler is the nickel-coated carbon fiber produced by Shanghai Kajet Chemical Company. The matrix material of 90wt% and the filler of 10wt% are mixed to obtain the conductive polymer material.

2.2 Apparatus

The injection molding machine used in this experiment is Victor-Taichung Vs-50K, and the temperature of

mold is controlled by the mold temperature controller of Byoung International Company BYW-1210F. In the magnet mold designed in this study, the NdFeB permanent magnet is embedded in the slides, which are installed on both sides of the mold cavity. The magnetic force is controlled by the positions of slides, and the oil hydraulic system serves (Figure 1) as the power source of slides. In order to prevent the magnet from cracking caused by uneven force while being attracted by surrounding steel during its motion, there are aluminum spacing blocks (Figure 2) in the region in contact with the magnet wrapped around by aluminum shell. The contact region between slides and die core is made of the 304 stainless steel. When the slide is normally closed (NC), the distance between two permanent magnets is 32mm. When the slide is normally open (NO), the distance between two permanent magnets is 92mm. In this study NC is defined as the situation of externally applied magnetic field; NO is defined as the situation of zero externally applied magnetic field.
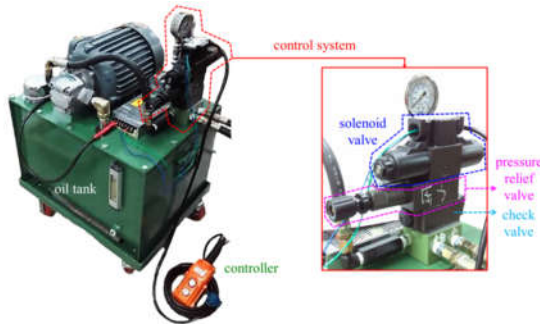
Figure 1. Oil hydraulic system for the magnetic-assisted injection molding
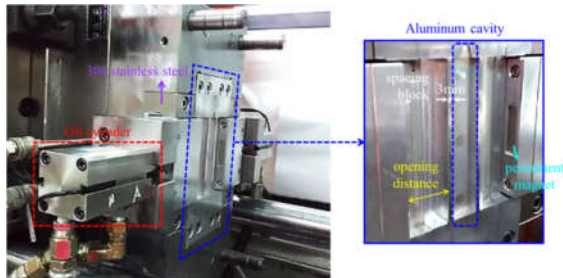
Figure 2. Schematic diagram of mold under opening status

2.3 Injection molding procedure
During the injection molding process, the impacts of externally applied magnetic field on fiber orientation and distribution are investigated based on different injection speeds. The melt temperatures were set as 180□, 200□ and 220□. The mold temperatures were set as 30□, 50□ and 70□. Injection speeds were set as 6.85 mm/sec, 20.55 mm/sec and 34.25 mm/sec. The injection pressure was set as 30.59 kgf/cm². The clamping force was set as 10 ton.

2.4 Description of fiber orientation in composites
For examination of fiber orientation observation, in this study, the Olympus BH2-UMA electron microscope was used for photography of the cross-sectional area of the tested sample in order to observe the fiber distribution and orientation. Since the fountain flow effect during the injection molding process prevented the successful observation of the impacts of fiber orientation and distribution caused by the magnetic field, we ground the tested sample to half of the original thickness by using the grinding and polishing machine as shown by the blue part in Figure 3. The tested sample can be divided into three areas: left, middle, and right based on the impact of the magnetic field on the fiber flow path. The ratio of area accounted for by the fiber in these three areas will be compared in order to determine the area in which the fiber will be concentrated due to the magnetic field. For quantification of this result, the middle area (A_M) will be compared to the mean of the areas of the left, middle, and right (A_L, A_M, A_R). The calculation of the ratio of central to total fiber content is as shown below.

$$\frac{A_M}{\left(\dfrac{A_L + A_M + A_R}{3}\right)} \times 100\% \tag{(25)}$$

In order to correctly measure the degree of impact of the magnetic field on the angle, we loaded the image observed by the microscope into the ImageJ software to obtain Figure 4. The figure on the left is the result of conversion into an 8-bit image file, and the figure on the right depicts the tool of ImageJ software which is used to measure the angles between various fibers and the direction of magnetic force. In the end, the average value of all fibers can be obtained as the fiber orientation tensor (FOT) of this area as shown in the equation below:

$$FOT = \frac{\sum_1^N (\cos\theta)_N}{N} \tag{(26)}$$
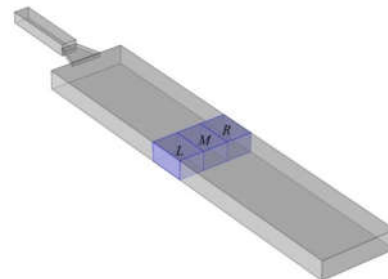
Figure 3. Illustration of the observation of the finished product
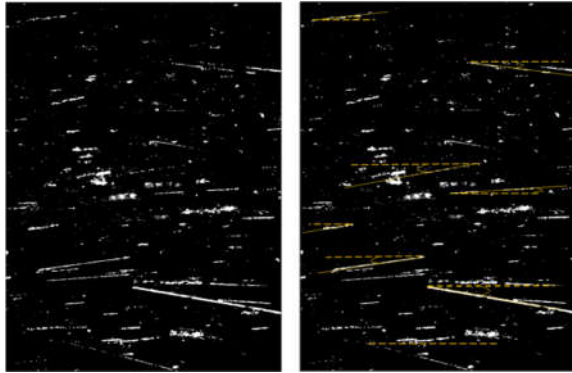
Figure 4. Illustration of angle measurement

2.5 Measurement of conductivity

For the measurement of conductivity, the electrical resistance of the sample for test was too large, and there was an issue of contact resistance, so there would have been significant error in direct measurement, making it difficult to determine the real situation. We put a $6 \times 10^6 \Omega$ resistor in series connection with the sample for the test while applying a 10V voltage during the measurement. Since all objects in series connection have the same current, the resistance of the sample for test could be found based on the comparison of the distributed voltages as shown in the equation below:

$$V_{\text{sample}} : V_{\text{resistance}} = R_{\text{sample}} : R_{\text{resistance}} \qquad ((27)$$

The wiring is as shown in Figure 5. The actual circuit wiring is on the left, and the simple circuit diagram is on the right, where R1 is the $6 \times 10^6 \Omega$ resistor, and R2 is the sample for test.
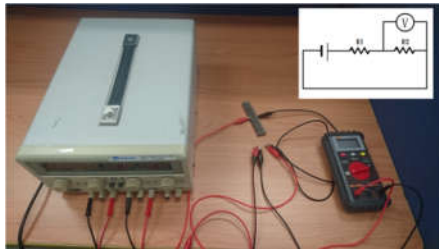
Figure 5. Circuit wiring diagram

3. Results and discussions

After software observation and analysis of tested samples under various molding process parameters, the relationship between molding process parameters and the fiber distribution and orientation can be calculated by equations (1) and (2) as shown in Figures 6~8. Comparison among various molding process parameters reveals that the flow resistance of fiber is lower when the melt temperature is increased. This makes the fiber affected by the magnetic field for a longer time and move closer to the left and right sides, so the fiber content at the center is lower. Thus the rotation of the fiber also occurs for a longer time (Figure 6), allowing it to gradually become parallel with the

direction of magnetic force. In addition to increasing the time required for the solidification of melt polymer, the rising mold temperature will also make the frozen layer thinner, thus making the movement and rotation of the fiber even more obvious (Figure 7). As for the injection speed, the U curve theory will result in the increase of injection pressure and shear stress, making the fiber distribution and orientation difficult to control. The distribution will increase and then decrease, and the orientation will increase rapidly before slowing down (Figure 8).

In this experiment, the LDPE serving as the matrix is not conductive. The conductivity is only provided by the conductive fibers. However, the conductivity of the entire tested sample is not only related to the weight concentration of the conductive fibers. The fiber distribution and orientation also change the conductive loop of the tested sample, which affects the electron transmission. In this study we used the circuit wiring method in Figure 5 to measure the voltage of R2, and this voltage can be used to calculate the resistance of the sample for test via equation (3). The calculation of various molding process parameters by equation (3) was used to obtain the Figures 9~11. The improvement of conductivity at different melt temperatures with and without an external magnetic field is as shown in Figure 9. When the melt temperature is increased, fibers will be concentrated towards the left and right sides, and the orientation will be enhanced, so the rising melt temperature will lead to an increased degree of lapping among fibers, thus resulting in higher conductivity. The improvement of conductivity at different mold temperatures with and without an external magnetic field is as shown in Figure 10. When the mold temperature is increased, fibers are under the impact of magnetic force for a longer time, so fibers will also be concentrated to the left and right sides. Fibers will be deflected towards the direction of the magnetic field lines. The rising mold temperature will also reduce the flow resistance. In previous measurements it appears that the fiber distribution and orientation affected by changing the mold temperature are slightly higher than the fiber distribution and orientation affected by changing the melt temperature. Consequently, the improvement rate of conductivity by increasing mold temperature is also slightly higher than the improvement rate of conductivity by increasing melt temperature. The improvement of conductivity at different injection speeds with and without an external magnetic field is as shown in Figure 11. Based on previous experimental measurements, we know that the impact of injection speed on fiber distribution is related to the U curve of injection speed, which makes it difficult to form a good conductive loop. Therefore, it is more difficult to improve the conductivity by increasing the injection speed.
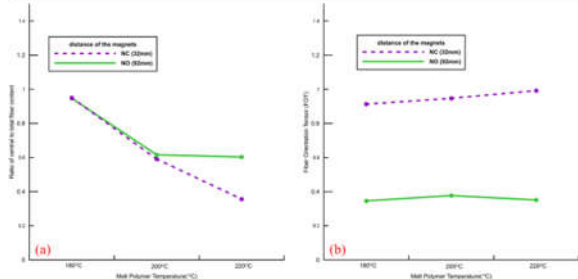
Figure 6. (a) relationship between melt temperature and fiber distribution in the middle area; (b) relationship between melt temperature and fiber orientation in the middle area
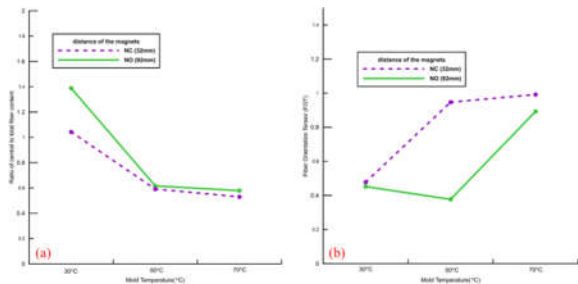
Figure 7. (a) relationship between mold temperature and fiber distribution in the middle area; (b) relationship between mold temperature and fiber orientation in the middle area
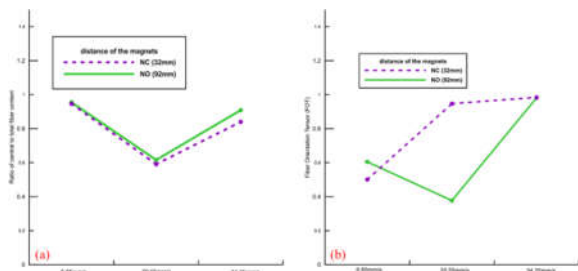
Figure 8. (a) relationship between injection speed and fiber distribution in the middle area; (b) relationship between injection speed and fiber orientation in the middle area
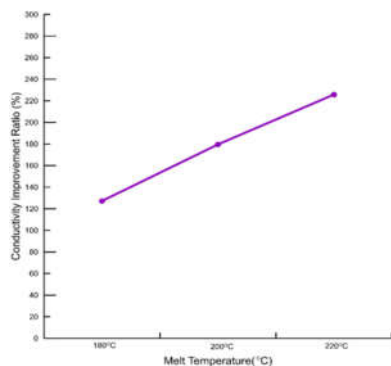
Figure 9 Relationship between melt temperature and

conductivity
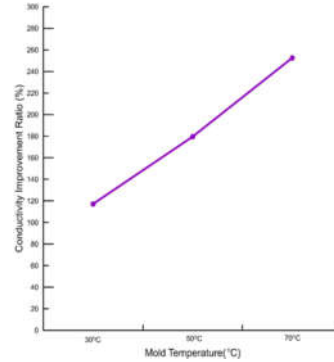
Figure 10 Relationship between mold temperature and conductivity
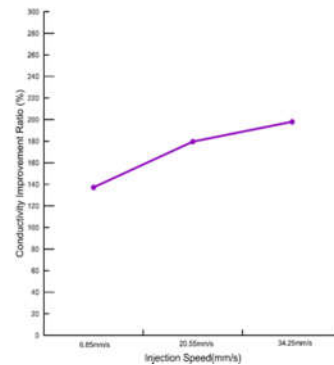
Figure 11 Relationship between injection speed and conductivity

4. Conclusions

The conductivity of conductive polymer composite material is directly related to the type of material and fiber concentration. However, due to the cost consideration and the impact of conductive loop formation, there is a certain limit to the conductivity; thus we need other means of improving the conductivity. In this study an external magnetic field was applied to change the fiber distribution and orientation in order to examine the fiber distribution and orientation tensors of different injection molding process parameters with or without an external magnetic field. Furthermore, the product conductivity was measured to verify the impact on fiber distribution and orientation. The experiment results indicate that mold temperature, melt temperature, and injection speed can all change the conductive loop formed by the tested sample, thus changing the conductivity. Among them, the increase of mold temperature is the best improvement approach. This result also shows that the molding process parameters changed by an external magnetic field can effectively change the fiber distribution and orientation to enhance the degree of lapping among fibers, thus leading to enhanced conductivity.

387

References

[1] S. Geetha, K.K. Satheesh Kumar, Chepuri R.K. Rao, M. Vijayan, and D.C. Trivedi, EMI shielding: methods and materials—a review. Journal of Applied Polymer Science, Vol. 112 (2009), p. 2073-2086.

[2] A. Saleem, L. Frormann, and A. Iqba, Mechanical, thermal and electrical resisitivity properties of thermoplastic composites filled with carbon fibers and carbon particles. Journal of Polymer Research, Vol. 14 (2007), p. 121-127.

[3] G. Lu, X. Li, and H. Jiang, Electrical and shielding properties of ABS resin filled with nickel-coated carbon fibers. Composites Science and Technology, Vol. 56 (1996), p. 193-200.

[4] M.S. Al-Haik, H. Garmestani, D.S. Li, M.Y. Hussaini, S.S. Sablin, R. Tannenbaum, and K. Dahmen, Mechanical properties of magnetically oriented epoxy. Polymer Science Part B: Polymer Physics, Vol. 42 (2004), p. 1586-1600.

[5] H. Garmestani, M.S. Al-Haik, K. Dahmen, R. Tannenbaum, D. Li, S.S. Sablin, and M.Y. Hussaini, Polymer-mediated alignment of carbon nanotubes under high magnetic fields. Advanced Materials, Vol. 15 (2003), p. 1918-1921.

[6] D. Shi, P. He, J. Lian, X. Chaud, S.L. Bud'ko, E. Beaugnon, L.M. Wang, R.C. Ewing, and R. Tournier, Magnetic alignment of carbon nanofibers in polymer composites and anisotropy of mechanical properties. Journal of Applied Physics, Vol. 97 (2005), 064312.

[7] T. Kimura, M. Yamato, W. Koshimizu, M. Koike, and T. Kawai, Magnetic orientation of polymer fibers in suspension. Langmuir, Vol. 16 (2000), 858-861.

Stability Analysis of a Proximate Time Optimal Controlled Electrostatic Suspension System Using Piezo Actuator

Le The Truyen[1], Nguyen Minh Huy[1], Thanh-Long Le[2]

[1]Department of Mechanical Engineering of Ho Chi Minh City University of Food Industry, Vietnam

[2]Faculty of Mechanical Engineering, Ho Chi Minh University of Technology (HCMUT), VNU-HCM, Vietnam

ABSTRACT

An electrostatic suspension of silicon wafer using proximate time optimal control has been successfully developed. In this system, the movable electrodes which are supplied by constant voltage and actuated by the piezoelectric (PZT) actuator are used instead of stationary electrodes. The changing of the gap length between movable electrodes and the suspended object will create varying capacitances that can control the electrostatic forces. To overcome the problem of actuator saturation in the electrostatic suspension system, a proximate time optimal control is used to stabilize the system and the system stability is theoretically investigated using Lyapunov's function as well. The constant voltage supplying to the electrode is an important parameter and is also determined. The paper also presents the simulation and experimental results that prove completely suspension of 4-inch silicon wafer without any mechanical contact.

Keywords: Electrostatic suspension; Stability; Piezo actuator; Proximate time optimal control; Silicon wafer.

Research on the Powder Lifting Carriage of the SLS Rapid Prototyping Machine

Tran Van Hung[1], Le Khanh Dien[2], Vo Tuyen[3]

[1] Ho Chi Minh City University of Technology, VNU-HCM, Vietnam

[2] DCSELAB - Ho Chi Minh City University of Technology, VNU-HCM, Vietnam

[3] Ho Chi Minh City University of Food Industry (HUFI), Vietnam

ABSTRACT

Rapid prototype technology or 3-D printer is a new technology in a couple of decade. It allows to produce a model for exanination or a product in single or small batch production in a very short time. This article carried out an effective design of a logical powder lifting carriage in the SLS rapid prototyping machine that is installed a ball screw-nut for the transmission of the lifting carriage where the powder materials is scattered and spread evenly, ready for sintering process by Laser beam. The lifting carriage that moves down a vertical pitch after a cycle of powder scatting, scanning and sintering is driven by a transmission set that comprises of electric motor, timing belt transmission and ball screw-nut for the transmission. The result of experiment on the designed, manufactured SLS rapid prototype machine in DCSElab shows the accepted performance of the new machine.

Keywords: 3-D printer, SLS rapid prototype, ball screw-nut transmission, lifting carriage, timing belt.

1. Introduction

In rapid prototyping method by Selective Laser Sintering (SLS) technology, the powder material is sintered by Laser beam up to the temperature where it convert from solid state to plastic one. When the Laser beam moves to an adjacent position, the material has solidified and bonded together to form a tiny part of the profile of the model. When the previous layer is done, the next layer is also made. The sintered powder is not only linked to the powder in the same layer but also linked to the previous layer. The process repeats the last layer and product model accomplishes [1].

Generally, structure of the SLS rapid prototype machine is designed by modularization technology, it consists of many different modules:

- Powder roller module consists of roller motors, roller conveyors, tooth belts and powder rollers;
- Laser source module consists of motors, XY axis drive, power supply, Laser tube, directive lens and Z-axis lifting table drive;

2. Design of the structure of the powder lifting carriage module

The lifting carriage module has the duty of lowering a precise controlled pitch of the forming part of the model after sintering a circumference of the model. The lifting carriage module performs general functions as shown in Figure 1:

- Powder lifting carriage moduke consists of lifting tables, right and left powder container tank; - Support frame and carter module [2].

Normally, the powder is scanned on layer by the powder roller module, while the powder lifting carriage contains the forming part of the model and the retained powder is conveyed back to the container tank. After sintering one layer, the lifting carriage is controlled to lower a defined vertical pitch, the container tank simultaneously scatters the powder on then the roller will scan the power to a fixed width layer of the powder. Because the accuracy of the product partly depends on the thickness of the material layer, so the down vertical pitch of the carriage must be accurate and optimized to ensure quality and productivity machine. Because of the above reason, the paper focuses on the design of the powder lifting carriage of SLS rapid prototyping machine in order to enhance the quality of the manufactured SLS rapid prototype in DCSElab.
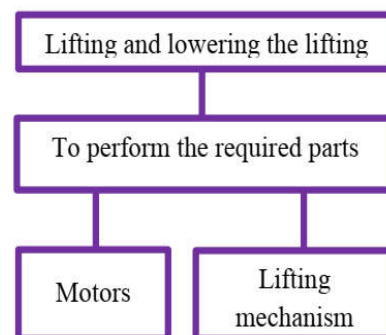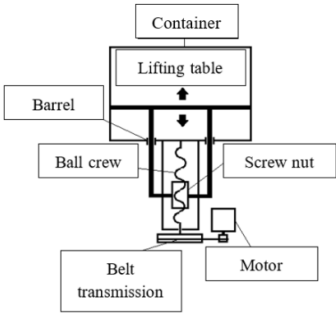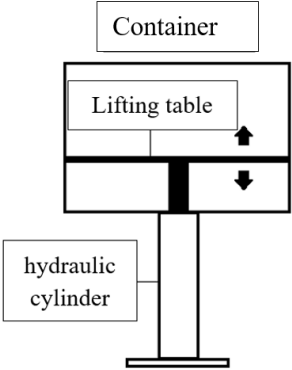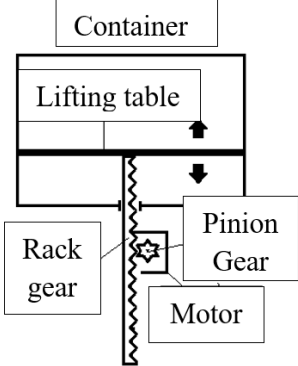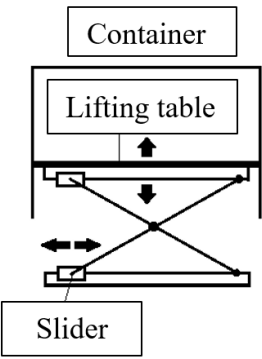
Figure 24. *Analytical diagram of the lifting carriage in the SLS machine*

The lifting carriage module performs main technical features:

- Selective sizes of carriage module are 400 x 300 x 200mm;
- The Accuracy of its main shaft is 0.05mm;
- Z axis course is 150mm;
- Scattering powder course is 200mm.

Based on the study of input parameters and related design references [3], a number of structural design options of the lifting carriage module are proposed as follows:

Options	Composition diagram	Characteristics	Advantage	Disadvantage
Option 1: Application of ball screw-nut		A ball screw-nut is assembled under the lift table. A motor trans mits the rotation to the low end of the screw via a belt transmission. A vertical sliding groove holds the direction of the carriage.	- Low friction, - High performance - Accurate verticl pitch.	- Complex, - High cost, - Lot of parts.
Option 2: Application of hydraulic cylinder		A hydraulic cylinder is mounted below the lifting carriage.	- The vertical hidraulic cylinder also controls the direction of the carriage - Sliding groove od bars are no need - The bending moment is nul.	- Complicated, bulky structure, large space - Hydraulic oil reservoir and tubes - Motor and pump
Option 3: Application of rack and pinion gear mechanism		Rack and pinion mechanism is assembled underneath the carriage.	- Simple structure, - -Low cost.	- Low accuracy

Option 4: Application of the X-type lifting mechanism		The X-lifting mechanism is below the lifting carriage	- No bending moment, - High stiffness.	- The accuracy of the structure is not high. - Large space

Applying the decision matrix method [4] to evaluate design options, we have the preliminary estimate matrix and score card as in tables 1 and 2:

Table 1: *Preliminary assessment of the design of lifting structures*

Options \\ Criterion	1	2	3	4 (Std)
Simple structure	0	-	0	0
Reasonable price	+	-	0	0
Manufactured, assembled easily	+	0	-	0
Correct move	+	-	0	0
Easy control	+	-	0	0
Longevity	+	-	-	0
Total +	5	0	0	0
Total 0	1	1	4	6
Total -	0	5	2	0
Total	5	-5	-2	0
Rank	1	3	3	2
Should we continue?	Yes	No	No	Yes

Table 2: *Scoring matrix for choosing the design of lifting structures*

Criterion	Weight (%)	Options			
		3		4	
		Score		Score	
		Rough scores	Weighted multipliers	Rough scores	Weighted multipliers
Available in the market	20	5	1	4	0,8
Reasonable price	25	4	1	4	1
Manufacture, assembly are easy	15	5	0,75	4	0,6
Easy control	10	5	0,5	5	0,5
Easy maintenance	15	4	0,6	4	0,6
Longevity	15	5	0,75	4	0,6
Total	100	4,6		4,1	
Rank		1		2	
Should we continue?		Yes		No	

Considering the evaluation matrix and the score board, we recognize that the most suitable design option is option 1: application of ball screws for transmission of the carriage.
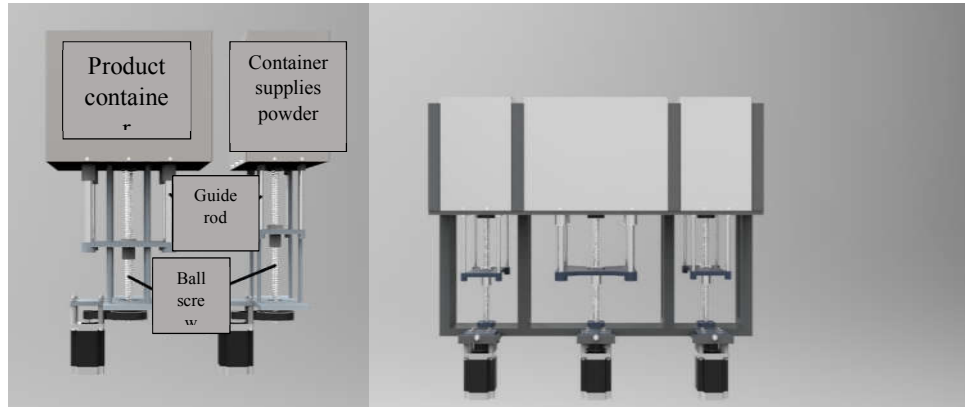
Figure 25. *The selected structure of lifting carriage module*

3. Computing of the dynamics of lifting carriage module
a. Calculating the ball screw drive

Input parameters: Weight of the lifting carriage: m_1 = 19,5kg; Weight of the powder (full): m_2 = 278.5kg; Downward vertical velocity: v = 0.3 m/s; Pitch of lifting step: l = 0.25mm; Transmission ratio: i = 2; Length of the course: l_o = 246mm; Coefficient of friction: f = 0.003; Axial thrust: F = 20N.

- Acceleration:
$$a = \frac{\Delta V}{\Delta t} = \frac{0,3}{0,2} = 0,15 m/s^2 \qquad (3.1)$$

- Axial thrust in the operation:
  + Accelerate of going up:
  $$F_{a1} = (m_1 + m_2).g + F_{ms} + (m_1 + m_2).a$$
  $$= 2988,08N$$
  + Stably go up:
  $$F_{a1} = (m_1 + m_2).g + F_{ms} = 2943,38N$$
  + Decelerate to go up:
  $$F_{a1} = (m_1 + m_2).g + F_{ms} - (m_1 + m_2).a = 2898,68N$$
  + Accelerate to go down:
  $$F_{a1} = (m_1 + m_2).g - F_{ms} - (m_1 + m_2).a = 2858,68N$$
  + Stably go down:
  $$F_{a1} = (m_1 + m_2).g - F_{ms} = 2903,38N$$
  + Decelerate to go down:
  $$F_{a1} = (m_1 + m_2).g - F_{ms} + (m_1 + m_2).a = 2948,08N$$

- Selective max axial thrust: F = 2988,08N

The inner diameter of the thread according to the compressing strength [5]:
$$d_1 \geq \sqrt{\frac{4.1,3 F_a}{\pi[\sigma_K]}} = \sqrt{\frac{4.1,3.2988,08}{3,14.40,16}} = 19,67mm \qquad (3.2)$$

In which: F_a: Axial thrust; $[\sigma_K] = [\sigma_n] = \sigma ch/3$ with σch – Yield strength of the material screw;
Selected inner diameter d_1 = 20mm
Selected parameters of the ball screw-nut transmission [5]: Ball diameter: d_b = (0.08…..0.15) d1 = 2 mm; helical pitch: p = d_b + (1…..5) = 4 mm; the radius of the rolling groove: r_1 = 0.51….0.53 = 0.52 mm; Distance

from the center of the groove to the ball: $c = \left(r_1 - \frac{d_b}{2}\right) cos\beta = \left(0,52 - \frac{2}{2}\right).cos45 = 0.34$

Herein: β – contact angle with the selected radial clearance, β = 45° for enhancing the vertical hardness and load capacity of the screw increases

- Diameter of the circle through the center of the balls:
$$D_{tb} = d_1 + 2(r_1 - c) = 20 + 2(0.52 - 0.34)$$
$$= 20.36$$

- Inner diameter of the nut: $D_1 = D_{tb} + 2(r_1 - c) = 20.36 + 2(0.52 - 0.34) = 20.72$
- Depth of the thread profile: h_1 = (0.3…0.35).d_b = 0.6 mm
- External diameter of screw and nut:
  $$d = d_1 + 2h_1 = 20 + 2.0,6 = 21.2mm;$$
  $$D = D_1 - 2h_1 = 20.72 - 2.0,6 = 19.52mm$$

- Thread angle:
$$\gamma = \frac{arctg p}{\pi D_{tb}} = \frac{arct 4}{3,14.20,36} = 1,19^o$$

- Number of balls on the thread ring:
$$Z_b = \frac{\pi D_{tb} K}{d_b} - 1 = \frac{3,14.20,36.2}{2} - 1 = 62,96$$

K – Number of working threads

- Selected radial clearance: Δ = 0,12 mm
- Relative clearance:
$$\chi = \frac{\Delta}{d_1} = \frac{0,12}{20} = 0,006mm \qquad (3.3)$$

- Equivalent rolling friction angle:
$$\varphi_1 = arctg\left[\frac{2f_t}{d_1 sin\beta}\right] = arctg\left[\frac{2.0,004}{20.sin45}\right]$$
$$= 0,032^0 \qquad (3.4)$$

Herein: f_t = 0,004…0,006 – Replacement rolling friction angle

- Performance to turn rotary motion into translational motion:
$$\eta = \frac{tg\gamma}{tg(\gamma + \varphi_t)} = \frac{tg 1,19}{tg(1,19 + 0,032)} = 0,973$$

- Performance to turn translational motion into rotary motion:

$$\eta = \frac{tg(\gamma - \varphi_1)}{tg\gamma} = \frac{tg(1,478 - 0,041)}{tg0,041} = 0,973$$

- Torque of the nut:

$$T = \frac{F_a D_{tb} tg(\gamma + \varphi_t)}{2} = \frac{1693.88.20,36. tg(1,19 + 0,032)}{2}$$
$$= 367.83N \quad (3.5)$$

- Durability testing:

$$q_a = \frac{F_a}{Z_b d_b^2 \lambda} = \frac{1693,88}{62,96.2^2.0,8} = 8,41 MPa$$

Herein: $\Lambda = 0.8$ – Weight distribution factor on uneven balls. From the relative clearance is selected and the q_a axial specific load in these graphs to determine the σ_{max} maximum stress, with $q_a = 8.41$ MPa; we have $\sigma_{max} = 2700$ satisfying conditions $\sigma_{max} \leq [\sigma_{max}] = 5000MPa$; the hardness of the working surface of screws and nuts is more than 53HRc and harness of balls is bigger than 63 HRc [5].

b. Calculating the timing belt transmission of the lifting carriage module

Input parameters: Velocity: v = 0.3 m/s; Acceleration / Deceleration time: t = 0.15s; Coefficient of friction: f = 0.03; Transmission ratio i = 2.

Operating power of the carriage:

$$P_{lv} = \frac{Fv}{1000} = \frac{2988,08.0,3}{1000} = 0,896kW \quad (3.6)$$

Initial parameters of the belt [5]: Transmission power: 0,896kW; Transmission ratio: i = 2; Revs of the driving axle: n = 2000 RPM; Operate time in normal mode: 24h/day; Axial distance: 114mm.

Module of the tooth belt:

$$m = 3,5. \sqrt[3]{\frac{10^3.P}{n_1}} = 3,5. \sqrt[3]{\frac{10^3.0,896}{2000}} = 2,678 \quad (3.7)$$

In which: P_1 – Power of the active pulley; n_1 – Revs of the active pulley;

Select m = 3; Pitch of the belt: p = mπ = 3.3,14 = 9,42mm; Height of the tooth: h = (0.6 ÷0.9).m = 16mm; the smallest width of the tooth: S= (1÷1.2).m = 3mm; Number of teeth of the small pulley: Select $z_1 = 12$ teeth with m = 3 [5]; Number of teeth of the big pulley: $z_2 = uz_1 = 3.12 = 36$ teeth;

Effective diameter: $d_1 = m.z_1 = 3.12 = 36mm$; $d_2 = m.z_2 = 3.36 = 108mm$

The smallest axial distance: $a_{min} \leq a \leq a_{max}$

With: $a_{min} = 0.5mm$ $(z_1 + z_2)$ +2m = 0.5(12 + 36) +2.3 = 30mm; $a_{max} = 2m(z_1 + z_2) = 2.3(12 + 36) = 288mm$

Number of the tooth belt:

$$z_d = \frac{2a}{p} + \frac{z_1 + z_2}{2} + \frac{(z_2 - z_1)^2 p}{40a} = 24,2 + 24 + 0,83$$
$$= 49,02 \quad (3.8)$$

Select $z_d = 50$ [5] and the belt length: l = 471mm.
The real axial distance:

$$a = \left(\lambda + \sqrt{\frac{\lambda^2 - 8\Delta^2}{4}} \right) = \left(244,92 + \sqrt{\frac{244,92^2 - 8.36^2}{4}} \right)$$
$$= 336,05mm$$

Herein:

$$\lambda = l_d - \frac{p(z_1 + z_2)}{2} = 471 - \frac{9,42(12 + 36)}{2} = 244,92mm$$
$$\Delta = \frac{m(z_2 - z_1)}{2} = \frac{3(36 - 12)}{2} = 36$$

Number of intermeshing teeth of the small pulley:

$$z^0 = \frac{z_1 \alpha_1}{360} = \frac{12.143,81}{360} = 4,79$$

Herein α_1 – Angle of belt contact of the small pulley:

$$\alpha_1 = 180^o - \left[\frac{m(z_2 - z_1)}{a} \right].57,3^o = 180 - \left[\frac{3(36 - 12)}{114} \right].57,3$$
$$= 143,81^0 \quad (3.9)$$

Specific tangential force must be satisfied:

$$q = \frac{F_t K_d}{b} + q_m v^2 = \frac{233,42.1}{12,5} + 0,004.3,77^2 = 18,73 \leq [q]$$

Herein:

$$F_t = \frac{1000P}{v} = \frac{1000.0,88}{3,77} = 233,42N$$

Weight per meter belt: $q_m = 0,004$, $[q_0] = 25N/m$; Dynamic load factor: $K_d = 1$ [5].

$$[q] = [q_0]C_Z C_u = 25.1.0,9 = 22,5$$

Herein: Specific tangential force allowed q_0; Factors include the effect of number of intermeshing teeth at the same time: $C_z = 0.6$; Factors include the accelerated drive: $C_u = 0.9$.

c. Calculating to select the drive motors for the lifting carriage

Power of motor:

$$P_{ct} = \frac{P_t}{\eta} = \frac{0,896}{0,95.0,99} = 0,953kW \quad (3.10)$$

Herein: P_{ct}: Required power of the motor shaft (kW);
P_t: Computing power (kW) and;
ŋ: Performance of the transmitter.

Selecting the motor with a power greater than 0,953kW.

4. Technological process of the lifting carriage module

 a. Assembly requirements
   + Ensuring the parallel face against the horizontal surface.
   + Ensuring the rectangle of the surfaces.

 b. Assembling the carriage
   + Installing the bracket of the container
   + Installing the slider bearing
   + Installing container's cover into the case
   + Installing the lifting table into the slider and the lifting base

Installing ball screw and screw nut
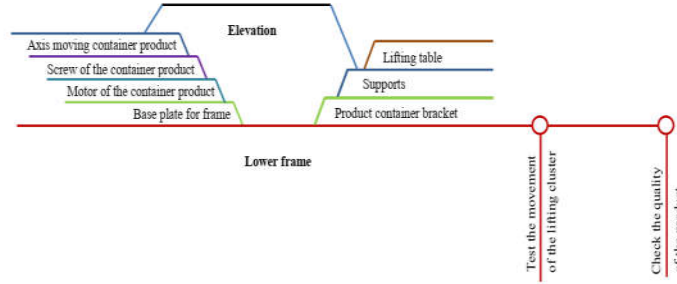
Figure 26. *Assembly diagram of the product container*

c. Assembling the powder of carriage module
  + Installing the slider bearing
  + Installing the container's cover into the case

  + Installing the lifting table into the slider and the lifting base
  + Installing ball screw and screw nut
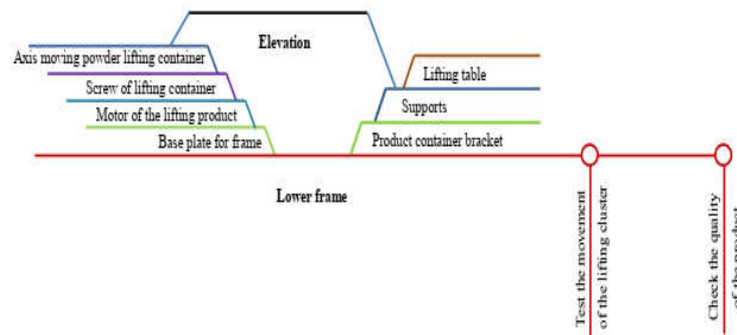
Figure 27. *Assembling diagram of the powder supply container*

d. Assembling the transmission apparatus
  + Installing the motors

  + Installing the tooth belt transmission

Figure 28. *The structure of lifting carriage module*

Experimental results showed that the lifting carriage module was able to meet the requirements of the SLS rapid prototyping machine (Figure 6).

Figure 29. *Total manufactured and assembled lifting carriage module*

5. Conclusion

The design of operating process of the powder lifting carriage in the SLS rapid prototyping with a ball screw – screw-nut drive is attached under the lifting table with a slider to guide the lifting table, which is driven by the tooth belt transmission with the engine to lift and lower the lifting table to help the accurate lowering process, ensuring the quality and timing of the prototyping process.

Acknowledgement

7. References

[1].Badrinarayan, B and Barlow, JW (1995). *Effect of processing parameters in SLS of MetalPolymers*, Proceedings of Solid Freeform Fabrication Symposium, pp. 55-63. Austin: Texas.

[2] Ana PilipoviT, Igor Drstvenšek, Mladen Šercer1, *Mathematical Model for the Selection of Processing Parameters in Selective Laser Sintering of Polymer Products*, Advances in Mechanical Engineering, Volume 2014

[3] Nguyễn Thanh Nam, *Nghiên cứu thiết kế và chế tạo hệ thống tạo mẫu nhanh SLS*, Báo cáo tổng kết đề tài B2013-20b-01, 2015.

[4] Nguyễn Thanh Nam, *Phương pháp thiết kế phát triển sản phẩm*, NXB ĐHQGTP Hồ Chí Minh, 2014.

[5] Nguyễn Hữu Lộc, *Cơ sở thiết kế máy*, NXB ĐHQGTP Hồ Chí Minh, 2016.

PART V, SECTION III

Mechanical Technology
(Heat transfer, Thermal, and Fluid Engineering; Structures and Fluids; Vibration;
Energy Engineering; CAD/CAM/CAE/RP…)

Study of Water Electrolysis by Dual Electrolytes and Cells

Lih-Wu Hourng[1], Yun-Tin Chen [1], Ming-Yuan Lin[2]
[1]Department of Mechanical Engineering
National Central University, Tao-Yuan, Taiwan
[2] Department of Mechanical Engineering
Army Academic College, Taiwan

ABSTRACT

In this study, sulfuric acid and potassium hydroxide are used as the electrolytes, separated by proton exchange membrane, to produce hydrogen. The influences of electrolyte concentrations, applied voltage, and sets of electrodes on the hydrogen production rate and energy efficiency are investigated. Experimental results show that the decomposition voltage decreases with the increase of electrolyte concentration. For energy efficiency, the device with multiple electrodes reduces the resistance and has higher energy efficiency under low applied voltage.

1. Introduction

With the evolution of scientific and technological progress of the times, energy has become an integral part of daily human necessities. Whenever we use a number of devices, such as cars, televisions, washing machines, energy is required to start and operate. Energy and daily life are inseparable. Since the industrial revolution, fossil fuels (coal, oil and natural gas) have become a source of all kinds of scientific and technological power and transport networks. With the continuing use of fossil energy, the total energy of the earth will finally exhaust. It also imposes a huge burden on the global environment and causes adverse effects on human's sustainable survival.

Fortunately, renewable energies overcome the immense challenges facing humanity, and become currently an important topic in technological development. Hydrogen is the most abundant element in the universe, accounting for about three-quarters of the total mass. It does not produce harmful emissions, and cause acid rain and ozone depleting during the processing cycle. Together with the merits of storability, large-scale storage, high energy density compared with other energy sources; hydrogen reveals its economy value. Hydrogen has thus been considered as the most promising energy carrier among all renewable energies. The methods of hydrogen production include electrochemical hydrogen production, biology hydrogen production, biomass hydrogen production, thermal hydrogen production, and water electrolysis belongs to one of the electrochemical hydrogen production methods.

When the electrodes are placed in an electrolytic cell and the electric current is conducted through the electrolyte solution, cations will move toward the cathode, while anions move to the anode. A chemical reaction is thus completed, and this phenomenon is called electrolysis.

The water electrolysis reactions in an acidic electrolyte at normal temperature and pressure are:

$$2H^+ + 2e^- \rightarrow H_2 \qquad E_{rev}= 0.0V \qquad (1)$$
$$2H_2O \rightarrow O_2 + 4H^+ + 4e^- \qquad E_{re}v=1.23V \qquad (2)$$
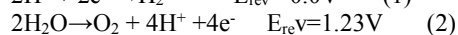
The reaction in a alkaline electrolyte is as follows.

$$2H_2O+2e^- \rightarrow H_2+2OH^- \qquad E_{rev}= - 0.83V \qquad (3)$$
$$4OH^- \rightarrow 2H_2O + O_2 + 4e^- \qquad E_{rev}= 0.4V \qquad (4)$$
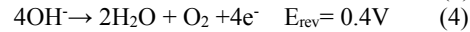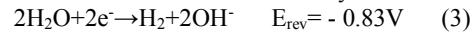
In a dual cell with dual electrolytes, i.e., acidic electrolyte in one side and an alkaline electrolyte on the other side, two cells are separated by Nafion proton exchange membrane. The total reaction would be the integrated reactions of (1) and (4) as follows.

$$4H^+ + 4OH^- \rightarrow 2H_2 + O_2 + 2H_2O \qquad (5)$$
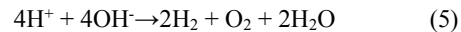
The above chemical reactions at the standard hydrogen electrode (SHE) have theoretical decomposition voltages of 1.23 V in either acidic or alkaline electrolytes. Figure 1 shows the relation between the reversible potential and pH of the electrolyte. Therefore, if dual cells are used with strong acid electrolyte in the cathode side (pH = 0) and strong alkaline electrolyte in the anode side (pH = 14), the water decomposition voltage will be theoretically reduced from 1.23V to about 0.4V [1]. Though the addition of proton exchange membrane will create some chemical over-potential, the resulted decomposition voltage for dual cells and electrolytes is expected to be less than that for single cell electrolysis. Furthermore, the hydrogen and oxygen gases are generated in different cells, and can be collected individually. It avoids the recombination of hydrogen and oxygen to form water again as happened for the single cell water electrolysis. The efficiency of water electrolysis to produce hydrogen is thus to be improved significantly. It is thus worthy to investigate furthermore the performance of water electrolysis using dual electrolytes under different working conditions.
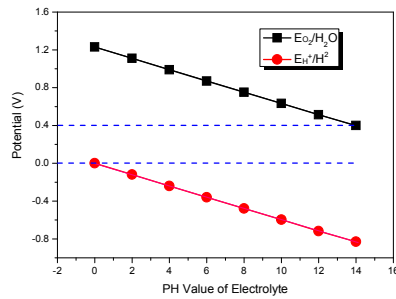
Fig. 1 relation between reversible decomposition voltage and PH value of electrolyte in water electrolysis.

Nafion proton exchange membrane has the merits of low chemical and thermal impedances, high ion-exchange ability and selectivity, high mechanical strength and insolubility in water. For electrolyte, the increase of temperature can reduce ion solvation, the viscosity of the solution, as well as the resistance. Therefore, the ion conduction rate or conductivity is increased as the electrolyte is increased [2-6]. Using polycrystalline platinum as the electrode material and 0.1 M sulfuric acid as the electrolyte, temperature increase will lead to dissolution increased in anode, but decreased in cathode. However, the total amount of dissolution is reduced [7]. If the current increases, the bubble covering the electrode sheet will be increased and result in an increase in resistance [8]. It was found that with the increase of water content within Nafion proton exchange membrane, the initial slope of the stress-strain curve is decreased. On the other hand, for different cationic electrolytes, the initial slopes of the stress-strain curves become larger in the order of Li+, Na+, K+, Cs+, and Rb+. For salt-based Nafion proton exchange membrane, the initial slope of stress-strain curve is normally increased as the increase of temperature if the temperature is less than 90oC. For temperature larger than 90 oC, the tendency is reversed [9].

2. Experimental set up

In this study, the cell is made of acrylic material, and the nickel sheets (10 mm × 10 mm × 0.4 mm) are used as the electrodes. Conductive silver paste is coated at the junctions of wire and electrodes to avoid poor conductive circumstances. The spatial distance between positive and negative electrodes is 30mm. Scheme of the electrolyzed cells is shown in Figure 2. For dual cells, Nafion (N211) proton exchange membrane sandwiched between two silicone pads is placed in the middle of the slot, and all parts are then locked with screw gaskets.
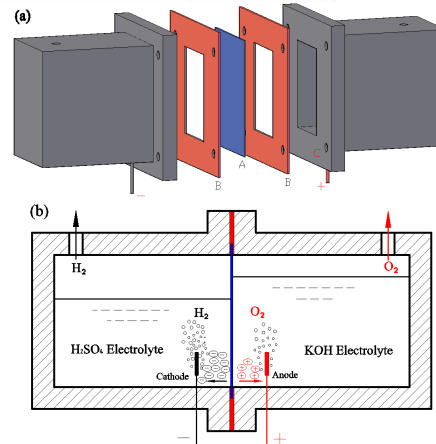
Fig. 2 Scheme of experimental set-up.

With a potentiostat and gas flow meter, the current density and hydrogen production rate, $\dot{Q}_{H_2}(cm^3/hr)$, are measured. The heating value per unit time (H.V) generated by electrolysis is defined as follows.

$$H.V = \dot{Q}_{H_2} \times \rho_{H_2} \times H.V_{H_2} \qquad (6)$$

where ρ_{H_2} is the density of hydrogen and $H.V_{H_2}$ is the heating value of hydrogen per unit mass. The electric power (P) is obtained by formula of P = IV. Energy efficiency (ηE) is calculated as follows:

$$\eta_E = H.V/P \qquad (7)$$

In the following sections, the effects of various experimental parameters, such as electrolyte and applied voltage, on the hydrogen production rate and energy efficiency are investigated.

3. Results and Discussions

Figure 3 shows the decomposition voltage for water electrolysis in dual cells with dual electrolytes. The electrolyte concentration in both cells is kept the same and varies among 20 to 40 weight percentages. With dilute electrolyte, the hydrogen production rate is low and impractical. On the contrarily, the electrolysis may be retarded due to hydration as the electrolyte concentration is too high. It indicates that the decomposition voltage decreases as the electrolyte concentration is increased, because the consumed reactants near the electrodes can be supplied efficiently as the molecules are sufficient. It also shows that the decomposition voltage is all-lower than 1 Volt, while it should be larger than 1.4 Volt for water electrolysis in either alkaline or acid electrolyte. A low decomposition means that the necessary power for a fixed amount of hydrogen production will be less. Furthermore, if dual electrolytes and cells is applied in the photochemical hydrogen production, most incoming solar radiation with energy larger than 0.4 Volt can be driven to actuate the

electron from valence band to conduction band and fulfill the oxide reaction. The efficiency of hydrogen production will be much larger than the current PEC hydrogen production.
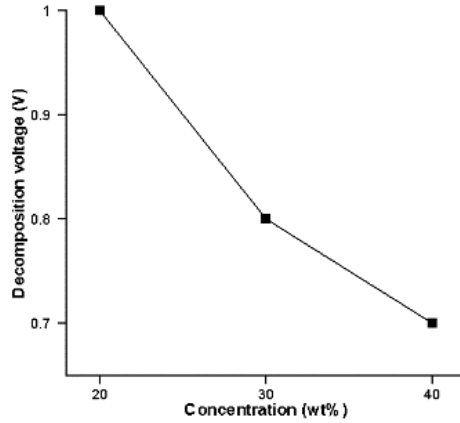
Fig. 3 The relation between decomposition voltage and electrolyte concentration

The effect of inter-electrode distance on the hydrogen production rate and efficiency are shown in Figs. 4 and 5, respectively. It indicates the closer the inter-electrode distance is, the larger the hydrogen production and efficiency will be, because that the corresponding ohmic polarization between electrodes becomes less. It also shows that the hydrogen production rate is very small as the applied voltage is less than 1.5V, because the addition of partition Nafion membrane increases the ohmic resistance. As the applied voltage is larger than 1.5V, the hydrogen production rate is increased as the applied voltage is increased. However, the efficiency is reduced as the voltage is increased due to the more gas bubbles generated. The trend is similar to the water electrolysis in single cell. The efficiency, generally located between 50-80%, shows that the dual cells water electrolysis has sufficient potential to be commercialized.
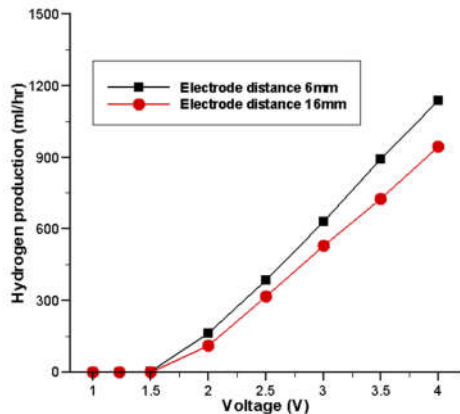
Fig. 4 Hydrogen production rate for different inter-electrode distances.
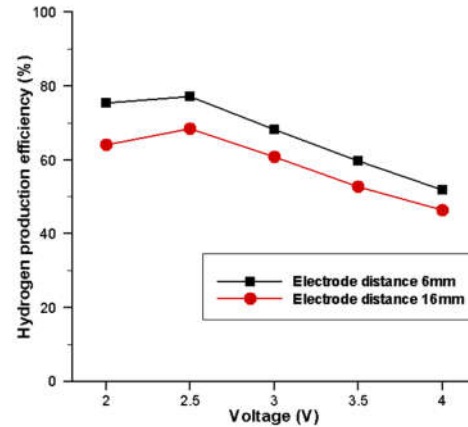
Fig. 5 Hydrogen production efficiency for different inter-electrode distances.

Figures 6 and 7 show the hydrogen production rate and efficiency for different electrode groups. As the number of group is increased, the hydrogen production rate is also increased. It also indicates that the hydrogen production efficiency will not be reduced as the electrode group is increased. It may be explained that the overall convective flow of electrolyte is enhanced as the electrode group is increased, such that the bubble generated on the electrode surface is easily be removed and cause the reduction of polarization.
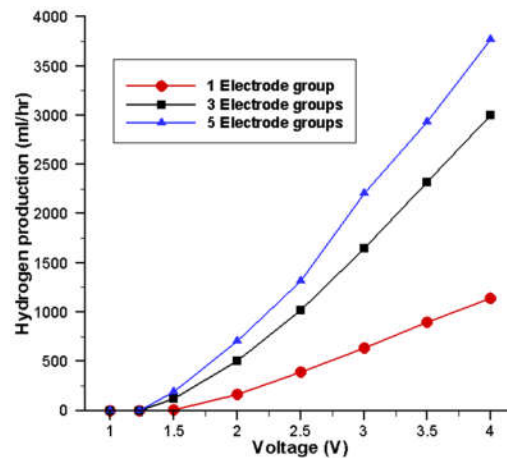
Fig. 6 Hydrogen production rate for different electrode groups at inter-electrode distance of 6 mm.
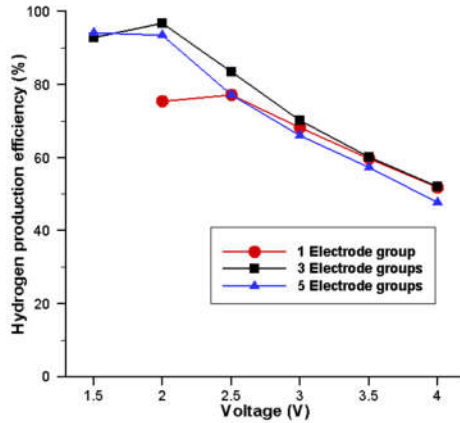
Fig. 7 Hydrogen production efficiency for different electrode groups at inter-electrode distance of 6 mm.

The comparisons of water electrolysis performance in single and dual cells are listed in Tables 1 and 2. In reference [10], the electrolyte used is KOH, and nickel is used as the electrode material. The reaction area is 10mm×10mm. The above conditions are consistent with this experiment. Under the condition of voltage of 2.5V and three groups of electrodes, the energy efficiency of this study is 83.49% (at concentration 30%), while the energy efficiency in the literature [10] are 73.29% (at concentration 25%) and 78.56% (at concentration 35%), respectively. Under the condition of voltage of 3V and three groups of electrodes, the energy efficiency of this study is 70.15% (at concentration 30%), while the energy efficiency in the literature [10] are 67.97% (at concentration 25%) and 58.48% (at concentration 35%), respectively. This results show that the use of dual cell water electrolysis to produce hydrogen at low voltage (e.g. 2.5V or 3V) is more energy-efficient than single cell water electrolysis.

Table 1 Experimental results in the present paper.

Electrode distance (mm)	6	
Electrolyte concentration wt%)	30	
Number of electrode groups	3	
Voltage (V)	2.5	3
Energy efficiency (%)	83.49	70.15

Table 2 Experimental results in Ref. [10].

Number of electrode groups	3			
Voltage (V)	2.5		3	
Electrolyte concentration (wt%)	25	35	25	35
Electrode distance (mm)	5			
Energy efficiency (%)	73.29	78.56	67.97	58.48

4. Conclusion

In this study, the dual cells with dual electrolytes is used to produce hydrogen by water electrolysis. Several conclusions can be drawn as follows.

1. The decomposition voltage is reduced as the electrolyte concentration is increased. For example, at the electrolyte concentration of 40wt%, and the actual electrolytic voltage is 0.7V.
2. As the applied voltage increases, the amount of hydrogen produced rises, but the energy efficiency of electrolyzed water decreases.
3. The smaller the electrode spacing, the higher the energy efficiency and the amount of hydrogen produced.
4. Increasing the number of electrode groups can increase the amount of hydrogen produced. In terms of energy efficiency, at low voltages (1.5 to 2.5 V), multiple sets of electrodes are higher than single set of electrodes. Under high voltage (3~4V), the energy efficiency of one, three, and five groups of electrodes is similar.
5. Dual-cell electrolysis at low voltages (2.5V, 3V) has higher energy efficiency than single-cell water electrolysis.

References

[1] A. R. Zeradjanin , A. A. Topalov, S. Cherevko, and G. P. Keeley, " Sustainable generation of hydrogen using chemicals with regional oversupply-Feasibility of the electrolysis in acid-alkaline reactor," International Journal of Hydrogen Energy, Vol. 39, pp. 16275-16281 (2014).

[2] P. Ridge, "Hydrogen manufacture by electrolysis, thermal decomposition and unusual techniques," Noyes Data Corporation, New Jersey, M. S. Casper (1978).

[3] K. Richa, Buddhi D., and Sawhney R. L., "Studies on the effect of temperature of the electrolytes on the rate of production of hydrogen," International Journal of Hydrogen Energy, Vol. 30, pp. 261 - 263, (2005).

[4] Q. J. Duan, H. P. Wang, and J. Benziger, "Transport of liquid water through Nafion membranes," Journal of Membrane Science, Vol. 392-393, pp. 88-99 (2012).

[5] J. C. Ganley, "High temperature and pressure alkaline electrolysis," International Journal of Hydrogen Energy, Vol. 34, pp. 3604-3611 (2008).

[6] A. Caravaca, F. M. Sapountzi, A. De Lucas-Consuegra, C. Moleina-Mora, F. Dorado, and J. L. Valverde, "Electrochemical reforming of ethanol-water solutions for pure H2 production in PEM electrolysis," International Journal of Hydrogen Energy, Vol. 37, pp. 9504-9513 (2012).

[7] S. Cherevko , A. A.Topalov, A. R. Zeradjanin, G. P. Keeley, and K. J. J. Mayrhofer,"Temperature-dependent dissolution of polycrystalline platinum in sulfuric acid electrolyte," Electrocatalysis, Vol. 5, pp. 235-240 (2014).

[8] S. K. Mazloomi and N. Sulaiman, "Influencing factors of water electrolysis electrical efficiency," Renewable and Sustainable Energy Reviews, Vol. 16, pp. 4257- 4263 (2012).

[9] Y. S. Kawano , Y. Q. Wang, R. A. Palmer, and S. R. Aubuchon, "Stress-strain curves of Nafion membranes in acid and salt forms," Ciência e Tecnologia, no. 2 ,Vol. 12, pp. 96-101 (2002).

[10] C.S. Hsi, The investigation of magnetic field on the water electrolysis using multi-electrodes, Master Thesis, Department of Mechanical Engineering, National Central University, Taiwan (2015).

Optimal Design for a Waste-heat Recyclable Gasifier

Chung-Neng Huang[1], Yu-Chang Yen[1], Shiuh-Ming Chang[2]

[1] National University of Tainan, Taiwan

[2] Kao Yuan University, Taiwan

ABSTRACT

How to improve the energy efficiency becomes an important issue in the world. Hydrogen which characterizes with high energy density and zero emission is expected to be the solution for above issue. In the past decades, gasifiers are taken as the transformers which can generate hydrogen by using the cheap fuel such as coal or biomass etc. In this study, a waste-heat recyclable gasifier by recycling the high temperature heat is proposed.

Keywords: waste-heat cycle, gasifier, optimal design, hydrogen

1. Introduction

Energy is an important pillar of developing economic and industry. For the shortage of petrochemical energy resources affecting global warming, and rising awareness of environmental protection, in recent years many countries have paid attention on the topics of system efficiency and recyclability [1]. As hydrogen is a clean, efficient, and sustainable energy source, it has quickly taken a new energy position to the international stage. However, due to the production of COx and other wastes from the production of hydrogen from fossil fuels, this shortcoming will offset the advantages of hydrogen energy. Therefore, in recent years, all countries are committed to breakthroughs in hydrogen production technology to ensure the advantages of hydrogen energy.

There are many ways to produce hydrogen; for example, Rabi Ibrahim Rabady et al. [2] use direct current generated by solar power generation and electrolysis of water to produce hydrogen. Dariusz Czylkowski et al. [3] used methane and steam to synthesize hydrogen through microwave plasma technology. Ceyhun Yilmaz et al. [4] used geothermal power to generate electricity to electrolyze the hot water that was preheated by thermal power generation. Ao Xia et al. [5] used galactose to produce hydrogen by anaerobic fermentation of bacteria. Yasushi Nishida et al. [6] used the high temperature generated by plasma discharge under high pressure to generate hydrogen in the decomposition of methane or propane. Although the above methods can produce hydrogen gas, it can be found that temperature is an important common factor in different hydrogen production processes.

For the gasifier is a way to produce hydrogen from low-cost fuels, it can crack syngas from coal or bio-mass combustion and extract the hydrogen from it. Gasifiers have long been used in many coal-producing countries such as China and Russia to convert cheaper coal into high-priced hydrogen. Current studies on the improvement of producing hydrogen by gasifiers are exampled as: Muflih A. Adnan [7] et al. used a modified Aspen Plus gasifier to reduce the tar produced in the combustion zone, using oxygen and steam to increase hydrogen production. Lijun Wang et al. [8]

used a two-stage simulation to divide the coal gasification into two parts. When the total amount is the same, they inject different proportions of coal and oxygen respectively. Simulation results show that the use of two-stage vaporizers is a big hit with regard to temperature and conversion rates. Since the above-mentioned studies focused on the removal of tar, the reuse of slag, and the improvement of gasifier conversion efficiency, which still have to use high-temperature combustion to produce syngas, and there seldom have the discussion on how to reduce the energy consumption required for high temperatures. Therefore, how to improve this problem has become the motivation for this study.

2. Method

This study adopted the gasifier as a model that was used in the plasma gasification system and published
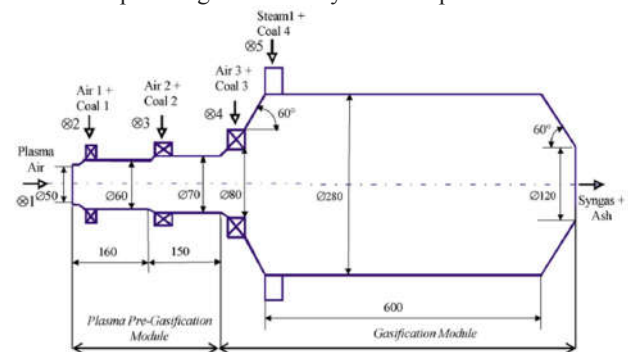
Fig. 1 Gasifier model.

by Serhiy I. Serbin et al. [9] in 2010. Plasma gasification is one of the simplest ways to provide the conversion of coal into hydrogen, electricity, or other energy. There are two parts of the gasification system. The first half is the plasma pre-gasification and the latter part of the gasification, as shown in Fig.1.

The main purpose of this study was to use external waste heat to heat the gasifier in the most efficient way to improve energy efficiency and use COMSOL Multiphysics for simulation. In order to allow the external waste heat to heat the gasifier in the best way,

the Taguchi method is used to optimize the parameters for optimal design.

2.1 A Novel Design for Gasifier

A preheating system that can use external waste heat to perform the gasifier is designed in this study. This optimized design is subject to a faster transfer of external thermal energy into the interior of the gasifier. This study will use the Taguchi method to optimize the design based on the fastest time to reach stable temperature. In order to accurately observe the internal temperature changes, three points P1, P2, and P3 inside the gasifier (distance from the bottom of the gasifier are respectively 0mm, 350mm, and 700mm as shown in Fig. 2) are taken as measurement points. In this study, the optimal design is defined as the one that can make the three points all upon the set temperature in minimum time. In order to keep the same initial conditions for simulations under different tube diameters, the inlet boundary is set as follows: the inlet velocity will use the mass flow rate of the solid oxide fuel cell; the inlet temperature is isothermal and the flux boundary is the outlet. Using copper as the solid thermal material, the contact surface of the heat pipe and the silicon chip and the contact surface between the fin and the gasifier are all hot walls, and the other contact surfaces are insulated walls. In addition; COMSOL simulation of other necessary conditions and

Table 1. Simulation parameters and conditions.

Parameter	value
Minimum working temperature	755K
Inlet temperature	1250K
In let flow rate	51 g/s

parameters are shown in Table 1.

2.2 Taguchi's Method and COMSOL Analysis

The Taguchi method is one of the most widely used quality management methods in the industry. Although it is not as direct as the full factor method to find out the optimal location, choosing the product control factor, designing the orthogonal array, and the simple analysis of the variance can be performed. A small amount of experimental data can effectively improve and level up product quality, the feasibility is therefore greater than the full factor method. In the optimization design, the quality is optimally achieved by adjusting the control factor, and the precision is increased by the orthogonal table experimental data.

The control factor table of this study is shown in Table 2. The factor A represents the winding method of the heat pipe. The multi-loop type and the left spiral type are shown in Fig. 3. The factor B is the number of fins. This factor is evenly surrounded by the cymbals. The method is arranged in a number of 2, 4 and 6 pieces, and the C factor is the thickness of the fin. Since the thickness of the fin affects the thermal contact area,

Table 2. Control parameters.

Factor	parameter	level 1	level 2	level 3
A	winding method	multi-loop type	left spiral type	
B	number of fins	2	4	6
C	thickness of fins	20 mm	40 mm	60 mm
D	winding number	3(turns)	5(turns)	7(turns)
E	diameter	10 mm	25 mm	40 mm

the thickness of the fin can also be regarded as a control factor. The fin thickness is 20 mm, respectively. 40mm and 60mm. Above B and C factors are the control parameters of the fins. The control of the fins will affect the heat transfer of the heat pipe to the gasifier; the D factor will be the number of windings of the heat pipe, and the number of windings of the heat pipe will affect the heat transfer. To the effect of the fins, the number of heat pipe coils is 3, 5 and 7 turns. The E factor is the diameter of the heat pipe.
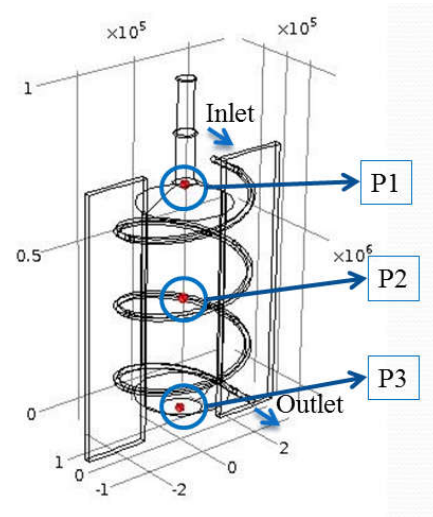
Fig. 2 Sizing of gasifier model and the measurement points

The pipe diameter adopted in this study is a general standard. Because the inlet is a mass flow rate, the size of the pipe diameter indirectly affects the speed of the fluid. The larger the pipe diameter, the slower the flow rate, and vice versa. The flow rate also affects the speed. At the time of heat transfer, the radius of the heat pipe is 10mm, 25mm and 40mm. The D factor and E factor are the control parameters of the heat pipe. The control of the heat pipe will affect the entrance heat source to transfer heat to the fins. Through the optimized design of this study, the heat source of the inlet will be transferred to the gasifier in a fast manner to achieve

the fastest and stable heating effect.
The research steps used in this study are as follows; first, the original design was simulated in COMSOL to investigate the temperature inside the gasifier while it reached a stable temperature. Next, determining out the control factors from the original design and establishing the orthogonal array. Third, calculating the results of each experiment through the COMSOL simulation. Finally, plotting the response map of each level in the factor to the

Fig. 3 Winding method of the heat pipe.

Fig. 4 Original design
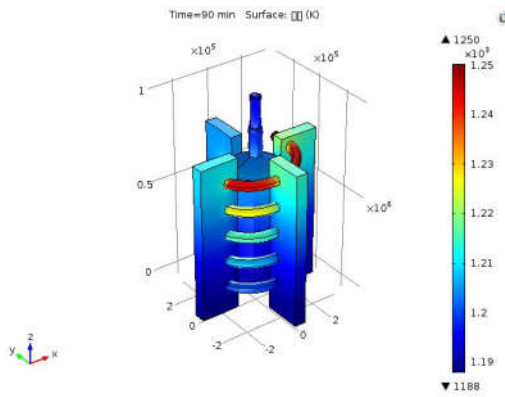
Fig. 5 Temperature distribution based on COMSOL simulation and subject to the original design

system, and then use this response diagram to determine the optimal design.

Fig 4 shows the original design of heat exchange, the middle part is the gasifier body. Since there are only two changes in the A control factor, which is set to leave1, other control factors are set to leave2. Through the COMSOL simulation results (Fig. 5) observed that the original design of the three internal measurement points (P1, P2 and P3) reached the set temperature in 90 minutes and the outlet temperature is 1193.37K.

2.3 Optimization Design

In order to achieve an optimal design, a full factorial analysis to the possible combinations of all factors must be performed, which is not only time consuming but often requires significant costs. For this reason, this study uses the Taguchi method to overcome this problem. The Taguchi method uses statistical methods to calculate the best results with the minimum number of experiments.

The Taguchi method must first establish the orthogonal array in the calculation. This study adopted the L18 (21x34) orthogonal array where only 18 simulation experiments are needed and it can also obtain the optimal result as using the full factorial analysis which requires 162 (21x34) times of calculation.

In order to obtain the design that can heat the three set points P_1, P_2, and P_3 in the gasifier reach the set temperature within the shortest time, the simulation results of the above orthogonal array are applied to Eq. (1) to (3) as follows as the-smaller-the-better objective in the Taguchi method.

$$S/N_{SB} = -10\log\frac{\sum_{i=1}^{n} y_i^2}{n} = -10\log\left(\overline{y}^2 + S_n^2\right) \quad ((28)$$

$$\overline{y} = \frac{\sum_{i=1}^{n} y_i}{n} \quad ((29)$$

$$S_n = \sqrt{\frac{\sum_{i=1}^{n}\left(y_i - \overline{y}\right)^2}{n-1}} \quad ((30)$$

The larger the SN value, the higher the quality of the product, the $\overline{y}$ is the average of the n measured values, and the S_n is the standard deviation of the n measured values.

3. Results and Discussion

The calculated SN results are shown in Fig. 6. The larger the magnitude of the S/N response graph, the greater the influence of the control factor on the product design and with the more stability of the quality. From the results shown in Fig. 6 knows that the optimal combination responding to the S/N ratio is

A1B3C3D3E1as well as the spiral heat pipe arrangement, the number of fins is 6, fins with a thickness of 60mm, 7 windings of the heat pipe and a pipe diameter of 10mm. It would be regarded as an S/N optimized design parameter combination.

Fig. 6 S/N response.

Table 3. The required time for reaching the set temperature to each measurement point

P1	P2	P3	Max.
30	36	42	42
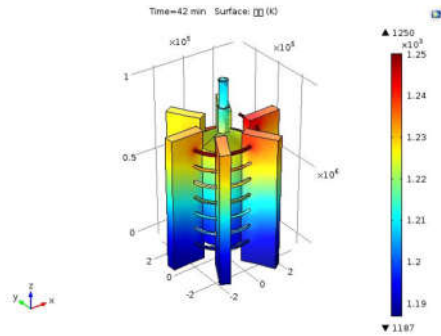
Fig. 7 Heat distribution based on the optimal design.

Table 3 shows the time for the measurement point to reach the stable temperature in the optimized design. The time for the three measurement points to reach the stable temperature is 42 minutes. The heat distribution diagram is shown in Fig. 6.

The proposed design has achieved a 53% of improvement on the heating time required by original design.

4. Concluding Remarks

This paper presents an optimal methodology for an external-heating type of gasifier where the simulation platform is built by COMSOL and the Taguchi method is used as an optimization method to find out the optimal parameters for design. This optimized design can effectively improve about 53% of the heating time required by the original type.

References
[1] S. Maruyama, T. Yabuki, T. Sato, K. Tsubaki, A. Komiya, M. Watanabe, H. Kawamura, K. Tsukamoto, *Deep-Sea Research Part 1*, 58 (2011) 567－574.

[2] International Energy Agency , IEA-Energy Efficiency Market Report 2015.

[3] Rabi Ibrahim Rabady, Bayan Kenaan, Power spectral shaping for hydrogen production from silicon based hybrid thermo-photovoltaic water electrolysis, Energy 133 (2017) 1-8.

[4] Dariusz Czylkowski , Bartosz Hrycak , Mariusz Jasinski , Mirosław Dors , Jerzy Mizeraczyk, Microwave plasma-based method of hydrogen production via combined steam reforming of methane, Energy 113 (2016) 653-661.

[5] Ceyhun Yilmaz, Mehmet Kanoglu, Thermodynamic evaluation of geothermal energy powered hydrogen production by PEM water electrolysis, Energy 69 (2014) 592-602.

[6] Ao Xia , Amita Jacob , Christiane Herrmann , Jerry D. Murphy , Fermentative bio-hydrogen production from galactose, Energy 96 (2016) 346-354.

[7] Yasushi Nishida, Hsuan-Ching Chiang, Tzu-Ching Chen, Chio-Zong Cheng, Efficient Production of Hydrogen by DBD Type Plasma Discharges, IEEE Trans. Plasma Sci. 42 (2014), 3765-3771.

[8] Muflih A. Adnan , Herri Susanto , Housam Binous , Oki Muraza , Mohammad M. Hossain, Enhancement of hydrogen production in a modified moving bed downdraft gasifier e A thermodynamic study by including tar, international journal of hydrogen Eenergy 42 (2017) 10971-10985.

[9] Lijun Wang , YiJun Jia , Sunel Kumar, Rundong Li , Rasool Bux Mahar , Mujahid Ali , Imran Nazir Unar , Umair Sultan , Kaleemullah Memon, Numerical analysis on the influential factors of coal gasification performance in two-stage entrained flow gasifier, Applied Thermal Engineering 112 (2017) 1601–1611.

[10] Serhiy I. Serbin,Igor B. Matveev, Theoretical Investigations of the Working Processes in a Plasma Coal Gasification System, IEEE Trans. Plasma Sci. 38 (2010) 3300－3305.

The Effect of Current Crowding on the Efficiency Droop of Vertical Single-quantum-well Light-emitting Diodes

Quoc-Hung Pham[1], Jyh-Chen Chen[1]

[1]Department of Mechanical Engineering, National Central University, Jhongli City, 32001, Taiwan

ABSTRACT

The electrical behavior of single-quantum-well (SWQ) light-emitting diodes (LEDs) is investigated. The local carrier recombination due to the current crowding causes the non-uniform on the carrier recombination. In the case of low energy injection, the highest local IQE appears at the region under the n-pad on the well layer. On the contrary at the high energy injection, this region has the lowest value of local IQE due to the increasing of non-radiative recombination while the rising of carrier concentration. This paper investigates the influence of local carrier recombination on the efficiency droop.

Keywords: Light-emitting diodes; Quantum-well, -wire and -dot devices; Numerical approximation and analysis;

(Presentation)

Generation of Waves and Their Interaction with a Floating Object for Wave Energy Harvesting

Thinh Xuan Ho[1], Phuong Ha[2], Thanh Quoc Truong[3], Son Doan Tran[3]

[1]Faculty of Engineering, Vietnamese-German University, Binh Duong, Vietnam
[2]Department of Fluid Mechanics, Hochiminh City University of Technology, Hochiminh City, Vietnam
[3]Department of Manufacturing Engineering, Hochiminh City University of Technology, Hochiminh City, Vietnam

ABSTRACT

This paper presents a combined experimental and numerical study of a wave generation and the interaction between the waves and a floating object used for wave energy harvesting. The physical waves are created in the laboratory using a triangle wedge located at one end of a channel and wave absorbers located at the other end. The wedge can move at a prescribed speed and oscillation amplitude corresponding to a desired wave height and frequency. The system is simulated using a mesh-free particle method namely Smoothed Particle Hydrodynamics (SPH). It is a Lagrangian-based approach, in which the fluid domain is discretized into particles moving according to Newton's 2nd law. Moreover, the wedge, the absorbers and the channel walls are also represented by particles; those of the wedge move the same as in the laboratory, however, those of the absorbers and the walls are fixed. This is a complex process including the wedge–water interaction, the wave propagation and the wave–absorber interaction. For the sake of simplicity, a two-dimensional (2D) model is adopted. The simulated waves are compared with the physical ones, and good agreement based on preliminary results is obtained.

Furthermore, simulations of the interaction between the waves and a floating object are carried out. The object is designed so that it can move up and down and simultaneously rotates around its own axis. The kinetic energy of these motions would be used for power generation. The object is modeled as a group of SPH particles, which move as a result of their interaction with the waves, i.e. fully two-way coupling between the object and the waves. Results for the motions of the object and the forces and torques acting on it are presented and discussed. Such insights would be useful for the design and optimization of the floating object, making it possible for an efficient wave energy harvesting system.

Keywords: Wave energy, Wave generation, SPH, Mesh-free particle method

(Presentation)

PART V, SECTION IV

Other Topics Related to Machining, Materials and Mechanical Technology
(Mechanics of Solid; Analysis and Simulation; New Machine Tools and Tooling Technology;
Dynamics and Control…)

Optimal Design of Cam Mechanism for Smallest Size

Pham Huy Hoang and Le Khanh Dien

Ho Chi Minh City University of Technology – VNU HCM

268 Ly Thuong Kiet, District 10, Ho Chi Minh City, Vietnam

ABSTRACT

Cam mechanisms are used as the control system in machines of several fields. Traditional cam design is very complicated and has accumulated error base on drawing. This paper presents the optimal design of cam mechanism for smallest size. The envelope theory and inverse method are utilized to perform constraint in pressure angle and motion. The smallest cam radius is then determined in a non-linear optimization adapting the constraints. The optimization is applied to the design of cam mechanisms with knife-edge/roller reciprocating/oscilating followers.

Keyword: Cam mechanism; Inverse method; Envelop theory

1. INTRODUCTION

Cam mechanism is common mechanical motion control device. Recently, there are several other control methods such as programable logic control (PLC), microcontroller, peumatics, hydraulics, etc. However, thanks to characteristics: reliability and high load, cam mechanisms are used widely in automatic machines such as bottling and capping machines, automatic feeding system of machine tools, engines.

The traditional complicated cam design is now improved when replacing drawing method by analytical computation. The analytical method is strongly developed thanks to the personal computors and programming languages. The design is now faster and more precise. The design data can be transfered to the numerical control machine tool for cam profile fabrication. Recently, analytical design of cam mechanisms is performed. However, the design just focus on cam mechanisms with knife-edge/roller/reciprocating flat-face followers [1 – 3]. Design process for these five types of cam mechanisms are completely studied using drawing method and widely presented in text books of kinematics of machinery. Recently, the designs are improved by analytical method or using appropriate curved patterns to soften the transitional curve on the cam profile for easy fabrication and better dynamic characteristics [2, 3]. The design of another type of cam mechanism with oscilating flat-face follower still not mentioned in academic documents. The studies on this type is poorly introduced just with the determination of transitinal points and the selection of connecting curves for position precision without impact [4].

In the inverse, cam is pretended to be fixed and base link rotates and, therefore, follower slide on cam profile. Cam profile is geometrically considered as the envelope of the set of follower curves. Envelope theory and inverse method allow to establish a analytical equation of cam profile [5, 6].

The first part of the paper presents the application of inverse method and envelope theory for analytically design of planar cam mechanisms including five common types with with knife-edge/roller/reciprocating flat-face followers and also the rarely studied cam mechanism with oscilating flat-face follower. The application is realized in the design program coding in MATLAB. The set of cam-profile points are then sent to numerical control machine tool for fabrication.

The development of a numerical control milling machine is the further study of this project. A low power mini machine tool will be built for further study in cam kinematics, dynamics and analytical modeling of errors.

2. METHODOLOGY

Application of inverse method and envelope theory for analytical design of cam mechanism.

The procedure of program for designing cam mechanisms is built thanks to analytical studies on pressure angle, convex condition of cam profile and how to determine set of cam profile points (Figure 1).
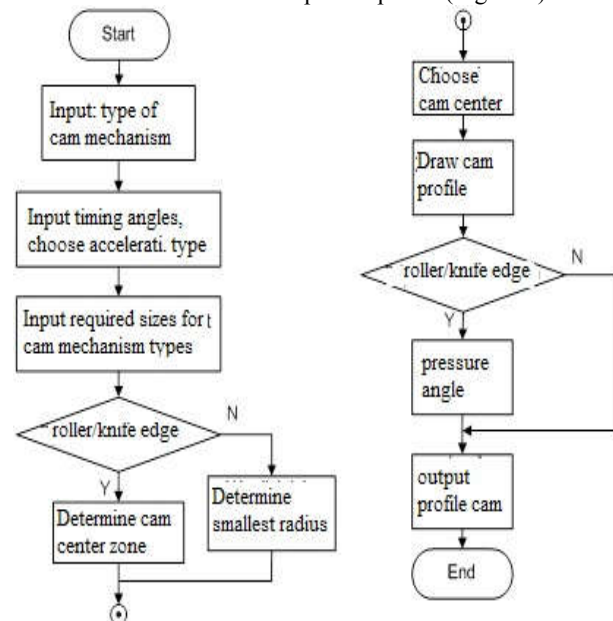
Fig. 1: Cam designing procedure

Applying inverse method – cam is fixed and base rotates inversely, the relative geometry between cam and follower is not changed, follower slides on cam surface (cam profile). Cam profile can be considered as

the envelope of the set of followers' ends (Figure 2 a and b).

Based on envelope theory [5, 6], the family of curves

$\{\mathbf{H_i}(\varphi)\}: h(x, y, \varphi) = 0$ (1)

has the envelope curve **B** (Fig. 3) determined by equations as follows:

$$\begin{cases} h(x, y, \varphi) = 0 \\ \dfrac{\partial h(x, y, \varphi)}{\partial \varphi} = 0 \end{cases}$$ (2)

Fig. 3: Envelope of a curve family

$$tg\alpha = \frac{a\cos[\psi_0 + \Delta\psi(\varphi)] - l + l\dfrac{d\psi}{d\varphi}(\varphi)}{a[\psi_0 + \Delta\psi(\varphi)]} \leq tg[\alpha] \quad (3)$$

where a – center distance, Ψ_0 – smallest oscilating angle, limit of pressure angle – $[\alpha]$.

(a)
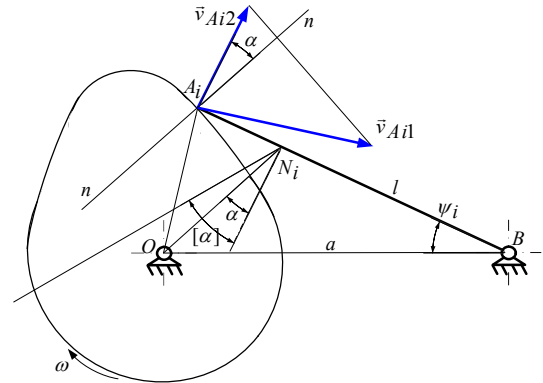
Fig. 4: Cam mechanism with oscillating follower

Oscilating follower (Figure 5)

$$tg\alpha = \frac{\dfrac{dS}{d\varphi}(\varphi) \mp e}{S_0 + \Delta S(\varphi)} \leq tg[\alpha] \quad (4)$$

(b)

Fig. 2: Cam profile (a-Follower with roller end; b-Follower with flat end)

1.　　Determination of cam center zone
The cam center zone of cam mechanism with knife edge or roller ends can be determined based on the limit of pressure angles.
Oscilating follower (Figure 4)

where e – excentricity, S_0 – smallest height, limit of pressure angle – $[\alpha]$.

Fig. 5: Cam mechanism with translating knife-edge follower

2. Convex condition

Cam mechanism with flat end follower has constant pressure angle. This type of cam requires the convex cam profile so that the flat end can contact the cam surface. The convex condition can be is

$$\rho = R_0 + S\cos\alpha + \ddot{S}\cos\alpha \geq 0 \qquad (5)$$

where S – lifting height, R_0 – smallest radius.
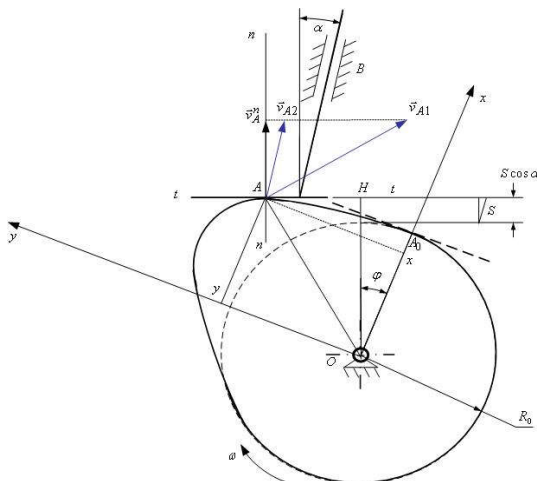
Fig. 6: Cam mechanism with translating flat-end follower

3. Optimization for smallest size

The condition of pressure angle or convex profile stated in equations (3), (4) and (5) are used as the constraint in an optimization for smallest size of cam mechanism.

The size of cam mechanism can be considered as the smallest radius of cam profile:

Cam mechanism with knife-edge/roller translating follower:

$$R_0 = \sqrt{S_0^2 + e^2}$$

$$(6)$$

Cam mechanism with knife-edge/roller oscillating follower:

$$R_0 = \sqrt{a^2 + l^2 - 2al\cos\psi_0}$$

$$(7)$$

Cam mechanism with flat-end translating follower:

$$R_0 = \left| S\cos\alpha + \ddot{S}\cos\alpha \right| \qquad (8)$$

The optimization is performed using Matlab Optimization tool. The optimal result is used further steps of cam mechanism design.

3. Cam profile

After determining cam center or cam smallest radius, the oscillating or translating functions of followers are fully determined. The cam profile can be synthesized based on Eq. (2) obtained thanks the combination of envelope theory and inverse method.

Cam mechanism with knife-edge/roller oscillating follower:

$$B = \begin{cases} x = a\cos\varphi + l\cos(\psi + \varphi) + r\cos\theta \\[2mm] y = a\sin\varphi + l\sin(\psi + \varphi) + r\sin\theta \\[2mm] \theta = \tan^{-1}\left[\dfrac{-a\sin\varphi - l(\dot{\psi}+1)\sin(\psi + \varphi)}{a\cos\varphi + l(\dot{\psi}+1)\cos(\psi + \varphi)}\right] \end{cases}$$

$$(9)$$

Cam mechanism with knife-edge/roller translating follower:

$$B = \begin{cases} x = e\cos\varphi - S\sin\varphi + r\cos\theta \\[2mm] y = e\sin\varphi + S\cos\varphi + r\sin\theta \\[2mm] \theta = arctg\left(\dfrac{-e\sin\varphi - S\cos\varphi - \dot{S}\sin\varphi}{e\cos\varphi - S\sin\varphi + \dot{S}\cos\varphi}\right) \end{cases}$$

$$(10)$$

Cam mechanism with flat-end translating follower:

$$B = \begin{cases} x = (R_0 + S\cos\alpha)\sin(\varphi - \alpha) - \dot{S}\cos\alpha\cos(\varphi - \alpha) \\[2mm] y = (R_0 + S\cos\alpha)\cos(\varphi - \alpha) - \dot{S}\cos\alpha\sin(\varphi - \alpha) \end{cases}$$

$$(11)$$

Cam mechanism with flat-end oscillating follower:

$$B = \begin{cases} x = a\cos\varphi + \dfrac{a\cos[\psi(\varphi)]}{1 - \dot{\psi}}\cos[\varphi + \pi - \psi(\varphi)] \\[2mm] y = a\sin\varphi + \dfrac{a\cos[\psi(\varphi)]}{1 - \dot{\psi}}\sin[\varphi + \pi - \psi(\varphi)] \end{cases}$$

$$(12)$$

Cam-design program coded in Matlab

The program for designing cam mechanisms is coded in Matlab and based on the procedure in previous section. The interface showing the interactive relationship between the user and program can be describe by Figures 7 – 9.
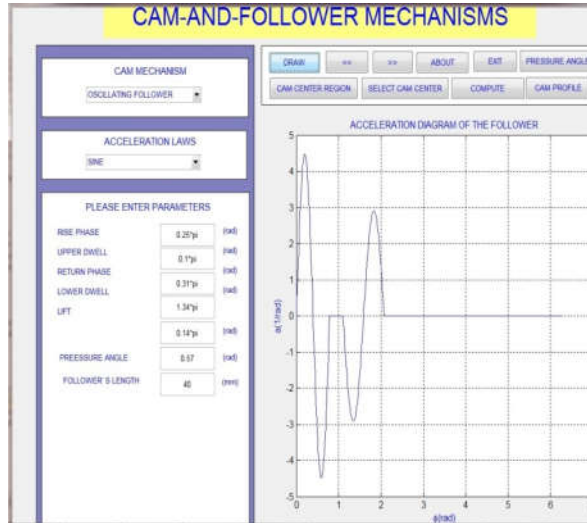
Fig. 7: Data inputs
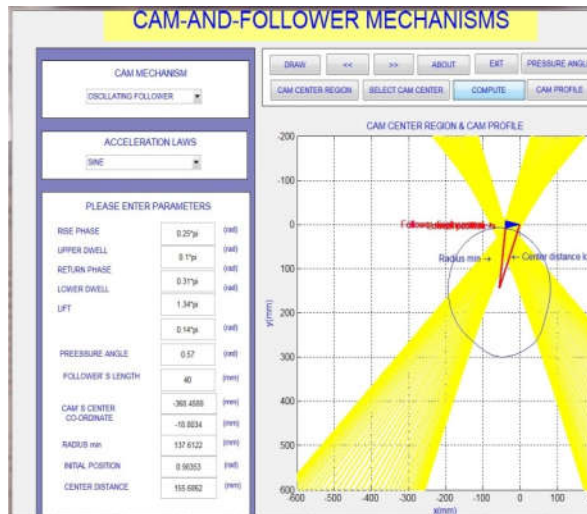
Fig. 8: Cam center determination
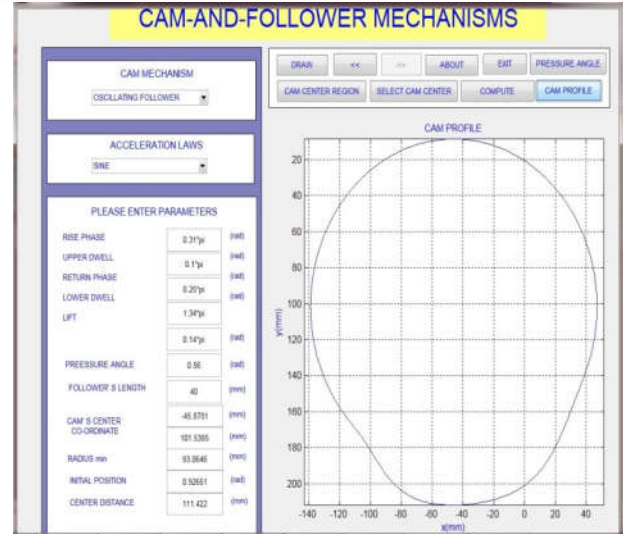
Fig. 9: Cam profile

The tangential vector of the profile also can be determined based on the information of cam profile:

$$\text{Tangent vector } \boldsymbol{\tau} = \frac{\dot{x}\mathbf{i} + \dot{y}\mathbf{j}}{\sqrt{\dot{x}^2 + \dot{y}^2}} \qquad (13)$$

and

$$\text{Slope of tangent line } \frac{dy}{dx} = \frac{\dot{y}}{\dot{x}}$$
$$(14)$$

where $\dot{x} = \dfrac{\partial x}{\partial \varphi}, \dot{y} = \dfrac{\partial x}{\partial \varphi}$.

The cam profile shown in Fig. 9 and the data of tangent vector of can be outputted in data file. The file can be used to generate machine codes for NC/CNC cam milling machine.

CONCLUSION

The envelope theory is applied to the analytical model of cam mechanism constructed based on the inverse method. The analytical result allows to design planar cam mechanisms with smallest design errors. The analytical design is used to build a cam-design program coding in MATLAB. The set of cam-profile points together with their tangent vector can be sent to numerical control (NC) machine tool for fabrication. The development of cam-design program is useful for further study in cam kinematics, dynamics and analytical modeling of errors.

ACKNOWLEDGMENT

413

REFERENCES

[1] Vu-Thinh Nguyen, Do-Joong Kim, "Flexible cam profile synthesis method using smoothing spline curves", Mechanism and Machine Theory, Vol. 42.7, , Pages 825–838, 2007

[2] Wen-Hsiang Hsieh, "Kinematic synthesis of cam-controlled planetary gear trains", Mechanism and Machine Theory, Vol. 44.5, , Pages 873–895, 2009.

[3] S Carra, R Garziera, M Pellegrini, "Synthesis of cams with negative radius follower and evaluation of the pressure angle", Mechanism and Machine Theory, Vol. 39.10, , Pages 1017–1032, 2004.

[4] Jorge Angeles, Carlos López-Cajún, "Optimal synthesis of cam mechanisms with oscillating flat-face followers", Mechanism and Machine Theory, Vol. 23.1, , Pages 1–6, 1988.

[5] T Dana-Picard, N Zehavi, "Revival of a Classical Topic in Differential Geometry: Envelopes of Parameterized Families of Curves and Surfaces", Journal of Applications of Computer Algebra ACA, p. 1 – 4, 12015

[6] Borislav Lazarov, "Teaching envelopes in secondary school", Journal of The Teaching of Mathematics, Vol. XIII, 1, pp. 45–55, 2011.

[7] Phạm Huy Hoàng, Lê Khánh Điền và Nguyễn Tuấn Kiệt, "Thiết lập phương trình biện dạng cam", Tạp chí Phát triển Khoa học và Công nghệ, Tập 3, số 4, trang 51 – 56, năm 2000.

Basic Research on Development of Automatic Dental Treatment Equipment

Yusuke Nozaki[1], Takanori Yazawa [1], Tatsuki Otsubo[1]
[1]Nagasaki University
1-14, Bunkyomachi, Nagasaki, 852-8521, Japan

ABSTRACT

In Japan, prospects for remodeling dental automation remotely for declining birthrate and aging, remote island problems are desired. Therefore, it is necessary to evaluate the performance of an air turbine that processes natural teeth and dental prostheses. In the report, a commercially available air turbine spindle was used, then propose and evaluate measurement methods for three factors as rotation speed, grinding temperature, grinding force.:

1. Introduction

Basic research [1,2] on dental handpiece such as improvement of function, rotation speed improvement and performance evaluation has been done. But there are few studies on grinding conditions and efficiency improvement. In addition, the progress of the dental prosthetic material is remarkable in recent years, and the material is various kinds. Progress of tools due to rotation speed improvement and efficient material grinding are required.

But as tool progresses, there are problems due to excessive rotation speed. Especially in the air turbine type, a method for measuring the rotation speed has not been established, as a result, proper values of rotation speed and grinding force are not determined. Therefore, in this research, we propose measurement method of high rotation speed and quantitative evaluation of grinding force at high rotation speed on a desk-top processing machine and clarify the optimum condition. We aimed to derive efficient grinding conditions, and the feed rate is set to be fast, the depth of cut is set to be thin.

Finally, from an ethical point of view, this time we are using artificial tooth material as a work.

2. Design of grinding machine

Fig. 1 shows the schema of the grinding machine designed this paper. The purpose of this device is that it can measure the rotation speed during grinding, it is easy to change the work while fixing the three-component force meter, and it is possible to perform various grinding by Three-axis machining.
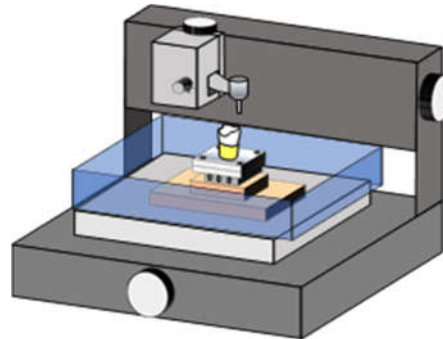
Fig.1 Schema of grinding machine

First, when measuring the number of revolutions, the handpiece has a very high rotation of 400,000 [min-1] in the catalog spec. Conventionally, the rotational speed is measured from photoelectric conversion or eccentricity, but response speed is insufficient. Further, measurement cannot be sufficiently performed due to water flow during wet grinding. So, this time we attempted to acquire the rotation speed from the vibration generated in the handpiece using the accelerometer.

When measuring the rotation speed with the accelerometer, the vibration of the tool must be accurately conveyed. However, since it is impossible to attach the accelerometer directly to the handpiece, we produce a jig, the handpiece is fixed to the jig with an interference fit and hardened the gap with plaster. In addition, the position where the accelerometer is mounted is also set near the machining part so that the vibration of the handpiece can be read more accurately.

3. Rotational speed measurement and analysis

Fig. 2 shows the waveform of the accelerometer when the handpiece is rotated at a supply

415

pressure of 0.35 [MPa]. The acceleration due to tool vibration appears in the waveform.
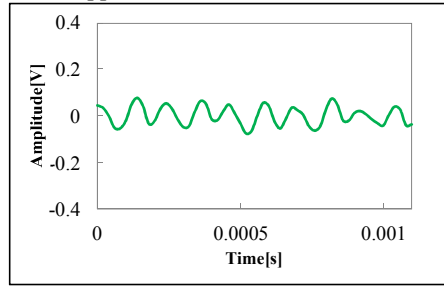
Fig. 2 Waveform during grinding

We count number of amplitudes per unit time, the number of rotation per minute is obtained based on that number, then the average at some points was taken as the actual rotation speed, a value closes to the catalog specification could be calculated. As a result, it is shown that the rotation speed can be inferred from the vibration of the tool by using the accelerometer.

Next, Fig. 3 shows the result of FFT analysis of the waveform.
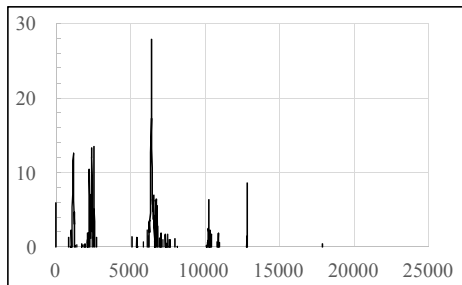
Fig. 3 FFT result of waveform

This is to analyze the rotation speed calculation quantitatively, and the average is taken at some places like visual calculation. In Fig. 3, the peak value is 6000, which is about 360,000 rotations. In addition, it is possible to analyze detailed frequencies which are overlooked at the time of visual calculation, and it can be an index for finding factors affecting accelerometers such as chatter vibration and resonance.

From the above, it is shown that by using an accelerometer, it is possible to measure the number of rotations during grinding. We also found a possibility to estimate components other than rotation during grinding by using FFT analysis.

4. Measurement of grinding force

Fig. 4 shows a schema of grinding experiment, and Table 1 shows experimental conditions.
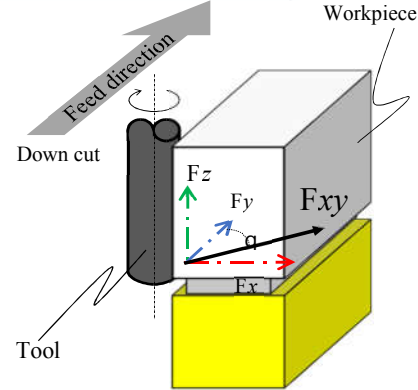
Fig. 4 Schema of grinding

Table 1 Experimental conditions

Handpiece	S-MAX M500ML
Work piece	Composite resin
Work size (L×W×H) [mm]	10×9×17
Rotation speed [min^{-1}]	400,000
Feed rate [mm/min]	300, 450, 600, 750, 900
Radial depth of cut [mm]	0.01, 0.05, 0.08, 0.1
Axial depth of cut [mm]	5.0
Supply pressure [MPa]	0.3

The experiment is side grinding of the workpiece molded by the grinder and measured the three-component force.

For the experimental conditions, the standard radius depth of cut is set to 0.05 [mm] and the feed rate is set to 600 [mm/min]. The depth of cut upper limit is set to 1.0 [mm] at which the rotation speed did not decrease, the feed rate upper limit is set to 900 [mm / min] of the equipment limit.

This time downcutting is done under this condition

(1) Relationship between depth of cut and component forces under constant feed rate
(2) Relationship between feed rate and component forces under constant depth of cut
(3) How each component force changes under constant removal volume

We will study in detail these three conditions.

Each value of the experiment results are rms value of component force, and angle formed by radial component force from feed direction component force. In this way, it is judged whether the grinding force is transmitted to the work. In the graph shown below, the circle represents the radial component force, the triangle represents the feed direction

component force, the square represents the axial direction component force, the diamond shape represents the angle formed by the component force. The Fig. 5 shows a graph of grinding forces and angle when the depth of cut is changed under constant feed rate.

(a)   Wet grinding

(b)   Dry grinding

Fig 5 Relationship between depth of cut and comportment force, grinding angle

From this experimental result, under wet grinding the grinding direction component force (circle) is the main component force, and under dry grinding, the feed direction component force (triangle) is the main component force. On the other hand, when comparing angles under wet grinding, the value is about 60 degrees and the force is transmitted in the grinding direction, but under dry grinding, it is about 15 degrees and most of the grinding force is the force in the feeding direction. Moreover, the component force other than the main component force shows a tendency of increase although it is slight.
From these results, it can be considered that slippage is occurring with respect to the incision in dry grinding.
Next, Fig. 6 shows a graph of grinding force and angle when feed rate is changed under a constant depth of cut.
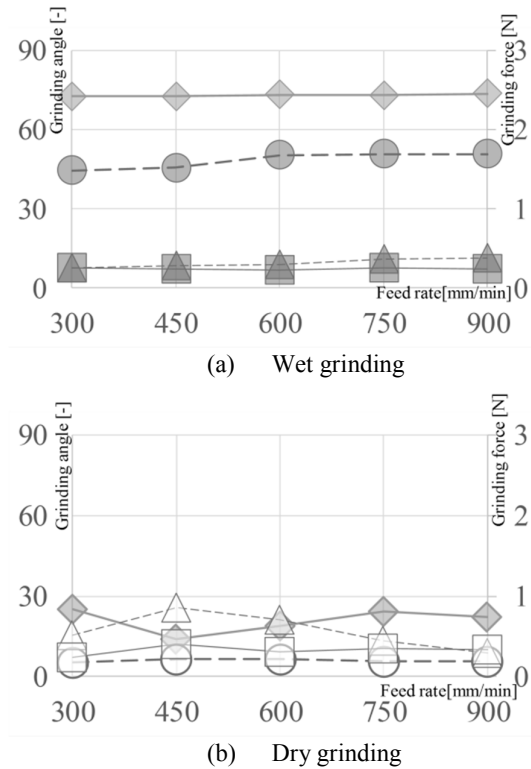
(a)   Wet grinding

(b)   Dry grinding

Fig   6 Relationship between feed rate and comportment force, grinding angle

From this experimental result, there is no significant change in each component force even if the feed rate increases, however, the main component is the same as in Fig. 5. Also, the tendency of angle is similar, it is considered that slipping occurs in dry grinding. Especially in dry grinding, the angle formed is small even though the force in the feeding direction is small. From this, it is considered that in the dry grinding, the force contributing to grinding is small and most of the energy is other energy such as heat.

Finally, Fig.7 shows a graph of grinding force and angle when grinding amount and feed rate are changed under constant removal volume. Table 2 shows conditions of grinding under constant volume.

In this figure, the correlation between each condition is not so much and it is difficult to make a reliable discussion, but as for each component force and angle, it

Table 2. Grinding conditions of constant volume

Condition number	Feed rate [mm/min]	Depth of cut [mm]
1	300	0.1
2	375	0.08
3	600	0.05
4	900	0.03

shows the same behavior as the two above.

That is, under wet grinding, the force related to machining is large, and the grinding force also works in the work direction, but under dry grinding, even though the grinding force is acting in the feed direction, the feed component value is small and most of the energy is not used for grinding.

temperature could be observed, but it is not sufficient as an amount of energy. Therefore, further findings are expected for measurement of temperature change by carrying out more precise measurement.
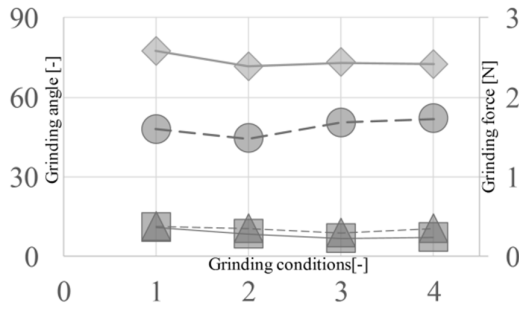
(a) Wet grinding

(a) Wet grinding
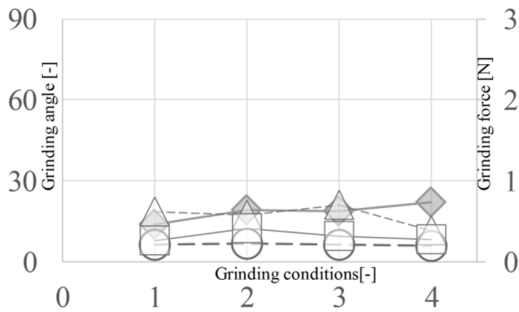
(b) Dry grinding

Fig 7 Relationship between grinding volume and comportment force, grinding angle
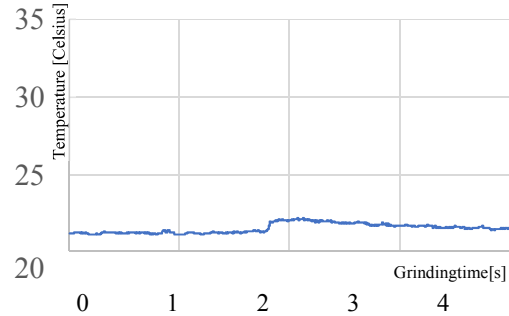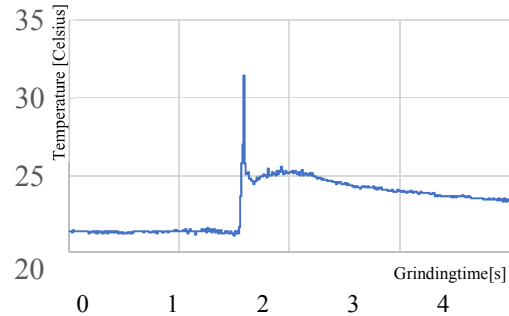
(b) Dry grinding

Fig 8 Relationship between grinding time and temperature

Finally, we measured the temperature during grinding to ascertain the energy during grinding.

5.Temperature measurement during grinding K type thermocouple is used for temperature measurement. A thermocouple was pinched and fixed to the composite material which is a work and grinded by wet grinding and dry grinding. The grinding conditions are set at a feed rate 600 [mm / min] and a depth of cut 0.05 [mm].

Fig. 7 shows a graph of grinding time and temperature change.

As can be seen from the figure, under wet grinding, the temperature rises only about 1 degree Celsius, whereas in the dry grinding the temperature rises nearly 10 degrees Celsius. Under dry grinding, peaks are generated during machining and the temperature rise is kept nearly 4 degrees even after it occurs, which indicates that it takes time for natural cooling after grinding. However, under the current grinding conditions, a sudden change in

6. Conclusion

 In this paper, we grinded artificial tooth material using a dental handpiece as a tool and measure rotational speed of handpiece. We also measure grinding force and some temperature at high feed rate. As a result, we found the index of quantification for the optimum conditions during grinding by obtaining the grinding force and temperature.

Reference

[1]   Niichi Katoh, Studies on Effects of Tooth Enamel Being Ground, Part III. An Investigation Using Ultra High Speed Tooth Preparation, Journal of Prosthodontic Research, vol. 21, No. 2, 219-245(1977), in Japanese

[2]   Hiroo Miyairi, Analysis of Dental High Speed Cutting and the Evaluation of its Efficiency, The journal of the Stomatological Society, Vol. 50, No. 1, 142-152(1983), in Japanese

A Novel Rotor Profile Generation Method for Claw-type Vacuum Pumps Based on Sealing Line

Trong-Linh Nguyen[1], Yu-Ren Wu[1]

[1]Department of Mechanical Engineering, National Central University, 300, Jhongda Rd., Jungli City, Taoyuan 320, Taiwan, R.O.C.

ABSTRACT

The sealing line between two conjugated rotors is a main leakage path in the vacuum pump, however, it is unable to be adjusted before the rotor profiles are determined in the traditional rotor profile generation method. Therefore, a generation method of rotor profiles for claw-type vacuum pumps based on the sealing line is proposed in this paper. The sealing line can be firstly specified as specific segments regarding the characteristics of claw-shaped rotor profiles. By applying the enveloping theory and the cubic spline curve fitting method, the rotor profile is able to be generated from the sealing line. Moreover, the adjustment method is proposed to segmentally correct the shape of sealing line using the quadratic functions by considering the geometric limitations to avoid interference and undercutting in rotor profiles. A three-lobe claw rotors profile is carried out to demonstrate the reasonability and stability of the proposed method.

1. Introduction

In the claw vacuum pumps, two claw-shaped rotors turn in the opposite directions inside the housing. Due to the specific design of rotor profiles, the air or gas is inhaled, conveyed and exhausted with the rotation of rotors. Practically, two rotors do not contact either to each other or to the housing wall due to the reasonable clearance design. Most importantly, the cross-section rotor profiles have great influence on the performance of vacuum pump.

To improve the performance has been an important study issue for the vacuum pumps. Hsieh et al. [1] designed the profile of claw-type rotor by means of the theory of gearing. Wang et al. [2] proposed the geometric design and performance analysis of a novel rotor profile for claw type vacuum pumps. Giuffrida [3] presented a rotor profile suitable for claw-type pumps with the overall instruction of rotor profile generation. Wang et al. [4] proposed a novel circular arc claw rotor profile and the modified rules of rotor profiles with the variation of arc radii to avoid the cusp generation.

Besides, flow leakages have great influence on the performance of vacuum pumps. In the operating process, the inter-lobe gap is the main leakage path affecting the pump performance. Based on this concept, Wu and Fong [5], and Zaytsev and Ferreira [6] presented a mathematical model of the rotor profile generation process based on the arbitrary sealing line for twin-screw compressors and carried out the optimal rotor profile designs.

Referring to these studies, the authors propose a novel rotor profile generation method and the adjusting method of rotor profile based on sealing line for claw-type vacuum pumps. Numerical examples are conducted to validate and show the feasibility and practicability of the proposed method.

2. Mathematical model of rotor profile generation from sealing line

In this study, a type of claw-type rotor profile (see Fig. 3) for vacuum pumps is generated by the sealing line, which is a line formed by the instantaneous contact points of two rotor profiles as shown in Fig. 1. The basic input parameters for rotor profile generation include the same tooth number for two rotors z, the pitch radius of rotor r_p, the outer radii of rotors r_{r1} and r_{r2}, and the center distance between two rotors CD. The coordinate system of sealing line S_s is fixedly located at the pitch point O_s, S_1 and S_2 are the rotating coordinate systems of the rotor 1 and rotor 2, respectively.
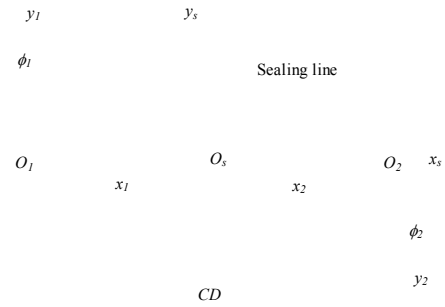
Fig. 1. The relative motion coordinate systems of two rotors.

The position vector $\mathbf{r}_s$ and unit normal vector $\mathbf{n}_s$ of the sealing line are expressed in S_s as follows:

$$\mathbf{r}_s = \left\{ x_s(u), y_s(u), 1 \right\} \tag{1}$$

$$\mathbf{n}_s = \left\{ \frac{x_s(u)}{\sqrt{x_s(u)^2 + y_s(u)^2}}, \frac{y_s(u)}{\sqrt{x_s(u)^2 + y_s(u)^2}} \right\} \tag{2}$$

420

where u is the curve parameter of sealing line.
The position vectors of two rotors $\mathbf{r}_1$ and $\mathbf{r}_2$ can be obtained by transforming the sealing line from the frame S_s to the coordinate systems S_1 and S_2, respectively:

$$\mathbf{r}_j = \mathbf{M}_{js} \cdot \mathbf{r}_s^T = \begin{bmatrix} \varepsilon\cos\phi(u) & -\sin\phi(u) & r_p\cos\phi(u) \\ \sin\phi(u) & \varepsilon\cos\phi(u) & \varepsilon r_p\sin\phi(u) \\ 0 & 0 & 1 \end{bmatrix} \cdot \begin{Bmatrix} x_s(u) \\ y_s(u) \\ 1 \end{Bmatrix}, \quad j=1,2 \tag{3}$$

where the symbol $\varepsilon=1$ for $j=1$ and $\varepsilon=-1$ for $j=2$. Additionally, the unit normal vector $\mathbf{n}_1$ can be represented in S_1 as

$$\mathbf{n}_1 = \mathbf{M}_{1s} \cdot \mathbf{n}_s^T = \begin{bmatrix} \dfrac{x_s(u)\cos\phi(u)}{\sqrt{x_s(u)^2+y_s(u)^2}} - \dfrac{y_s(u)\sin\phi(u)}{\sqrt{x_s(u)^2+y_s(u)^2}} \\ \dfrac{x_s(u)\sin\phi(u)}{\sqrt{x_s(u)^2+y_s(u)^2}} + \dfrac{y_s(u)\cos\phi(u)}{\sqrt{x_s(u)^2+y_s(u)^2}} \\ 1 \end{bmatrix} \tag{4}$$

Based on the enveloping theory, the common normal vector must be perpendicular to the sliding velocity vector at the contact point. Thus the meshing equation can be derived as

$$f_1 = \mathbf{n}_1 \cdot \frac{\partial \mathbf{r}_1}{\partial u} = \frac{x(u)x'(u)+y(u)\left[r_p\phi'+y'(u)\right]}{\sqrt{x(u)^2+y(u)^2}} = 0 \tag{5}$$

Consequently, the relationship between the meshing angle ϕ and the curve parameter u can be obtained:

$$\phi(u) = -\frac{1}{r_p}\int_0^{u_{max}} \frac{x(u)x'(u)+y(u)y'(u)}{y(u)}\,du + \phi_0 \tag{6}$$

where ϕ_0 is the accumulated rotation angle of the last segment. Finally, the profile equation of rotor 1 and rotor 2 is derived by substituting the meshing angle ϕ into Eq. (3).

3. The sealing line adjustment method

3.1 Equations for adjusting the sealing line

To locally adjust the sealing segments to obtain the modified rotor profile, an adjustment method is proposed. Firstly, the sealing line is divided into six segments as shown in Fig. 2. The circular arc segments I and IV are symmetric about the vertical axis. These segments are usually fixed and generated correspondingly by a claw tip point on one rotor and the cycloid curve on another rotor. The others segments between points b, c, O_s, d, e generate specific segments and straight lines on the rotor profiles. The meshing angle of two rotors starts at point b on the sealing line, is defined as zero. The meshing order of conjugated

rotor pair follows the arrow direction.
Secondly, the sealing line shape can be adjusted by six control points a, b, c, d, e and f as Fig. 2 shows. The outer and inner diameters of the rotors are determined by moving points b and e along the X-axis, points a and f along the Y-axis simultaneously. Besides, the controlled points b and e can generate the inner and outer circular arc segments of rotors that are used to adjust the teeth thickness of rotors. The points c and d are the highest and lowest points on the curve be, respectively. These two points can be moved horizontally or vertically in a feasible range.
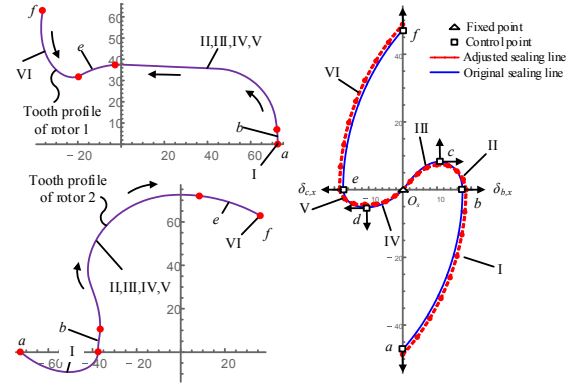
Fig. 2. Adjusting directions of control points, meshing order and corresponding segments on sealing line and rotor profiles.

Quadratic equations are applied to smoothly determine the horizontal and vertical displacements of points of each segment on the sealing line as follows:

$$d_{x,i}^{(j)}(t) = a^{(j)} \times t^2 + \left(s_2^{(j)} - s_1^{(j)} - a^{(j)}\right) \times t + s_1^{(j)} \tag{7}$$

$$d_{y,i}^{(j)}(t) = b^{(j)} \times t^2 + \left(v_2^{(j)} - v_1^{(j)} - b^{(j)}\right) \times t + v_1^{(j)} \tag{8}$$

wherein i denotes the point index ($i = 1 \sim n_p^{(j)}$ and $n_p^{(j)}$ is point number of the jth segment); $d_{x,i}^{(j)}$ and $d_{y,i}^{(j)}$ are displacements of the ith point in the jth segment in the horizontal and vertical directions; $a^{(j)}$ and $b^{(j)}$ are coefficients used to adjust the curvature of the jth segment; $s_1^{(j)}$, $v_1^{(j)}$ and $s_2^{(j)}$, $v_2^{(j)}$ are beginning and end boundary variables for $d_{x,i}^{(j)}$ and $d_{y,i}^{(j)}$, respectively. The four coefficients $s_1^{(j)}$, $s_2^{(j)}$, $v_1^{(j)}$, $v_2^{(j)}$ are

determined by $s_1^{(j)} = \delta_{p,x}$, $s_1^{(j)} = \delta_{q,x}$, $v_1^{(j)} = \delta_{p,y}$ and $v_2^{(j)} = \delta_{q,y}$ with p and q are the beginning and end

to zero at singular points. Therefore, the undercutting condition can be formulated as zero sliding velocity of the contact point on the tooth profile and the undercut conditions of the rotors $f_{uc}^{(1)}$ and $f_{uc}^{(2)}$ can be expressed as

Table 2. Values of variables

	δ_{cx}	δ_{cy}	δ_{dx}	δ_{dy}	$a^{(II)}$	$b^{(II)}$	$a^{(III)}$	$b^{(III)}$	$a^{(IV)}$	$b^{(IV)}$	$a^{(V)}$	$b^{(V)}$
Example 1	-0.2	-0.35	0	0	-1.0	0.1	0.4	0.5	0	0	0	0
Example 2	-0.2	-0.35	0.164	0.273	0.2	0.1	-1.2	0.9	0.808	-0.83	-0.144	-0.254

Table 3. Performance indices of two examples compared with original profile.

Items	Original profile	Case 1 profile	Case 2 profile
Length of sealing line L_s (mm)	47.555	47.209	46.354
Working area S_w (mm^2)	11820.8	11739.7	11870.9
Theoretical volume flow rate Q (m^3/h)	129.083	128.198	129.63
Sum of single-groove areas of rotors A_t (mm^2)	4694.12	4667.06	4710.29

points of a segment, $\delta_{p,x}$, $\delta_{q,x}$, $\delta_{p,y}$, $\delta_{q,y}$ are the displacements by X and Y-direction of points p and q, respectively. The variable t is normalized as $t \in [0,1]$ and for each point of segments t is determined by:

$$t_i^{(j)} = t_{i-1}^{(j)} + \frac{u_{i-1}^{(j)}}{\sum_{k=1}^{n_p^{(j)}-1} u_k^{(j)}}, \quad t_i^{(j)} = u_i^{(j)} = 0, \quad i = 2 \sim n_p^{(j)} \quad (9)$$

where $u_i^{(j)}$ is the distance between ith and $(i+1)$th points in the jth segment, $n_p^{(j)}$ is the number of points in the jth segment, and $t_i^{(j)}$ is the normalized curve parameter of the ith point in the jth segment.

follows:

$$f_{uc}^{(i)} = \mathbf{V}_r^{(i)} \cdot \mathbf{V}_r^{(i)} = \frac{\partial \mathbf{r}_i}{\partial u} \cdot \frac{\partial \mathbf{r}_i}{\partial u} = 0, \quad i = 1 \sim 2 \quad (10)$$

The interference may occur between two rotor lobes when the included angle of single lobe θ_T exceed a pitch angle [5], the interference limit condition as $\theta_T \leq \frac{2\pi}{z}$. For considering the geometric limits, the sealing line should be not located outside the overlapped region of two rotors as indicated in Fig. 3. The geometrical constraints for segment II and V as $\sqrt{x_{s1}^2 + y_{s1}^2} \leq r_r$ and $\sqrt{x_{s2}^2 + y_{s2}^2} \leq r_r$, where $\{x_{s1}, y_{s1}\}$ and $\{x_{s2}, y_{s2}\}$ are coordinates of the sealing line in S_1 and S_2.

Fig. 3. Region of the geometrical limit and cross-section area for the rotors.

Finally, six coefficients $a^{(j)}$, $b^{(j)}$, $s_1^{(j)}$, $s_2^{(j)}$, $v_1^{(j)}$, $v_2^{(j)}$ are specified to form the quadratic equations. Hence, vertical and horizontal displacements of each point of a segment can be calculated by substituting six coefficients values of quadratic equations and the corresponding $t_i^{(j)}$ into Eqs. (7) and (8).

3.2 Limits of the sealing line
In order to avoid the undercutting on the tooth profile, the singular points on the generated shapes need to find. According to the theory of gearing, the sliding velocity ($\mathbf{V}_r$) of the contact point on the tooth profile is equal

4. Design example and discussion

Table 1. Geometric parameters of rotors.

Input parameters (Symbols)	Values	Units
Tooth number of rotor (z)	3	Teeth
Pitch radius of rotor (r_p)	55.0	mm
Rotation speed of rotor (n)	3500.0	rpm
Rotor facewidth (L)	52.0	mm

To demonstrate the reasonability of the rotor profile generation mathematical model and stability of the controlled sealing line method, two numerical examples for three-lobe claw rotor profiles are carried out in this section. The examples are presented based on a set of point data (45 points) for the sealing line and the geometric parameters of rotors as described in Table 1.
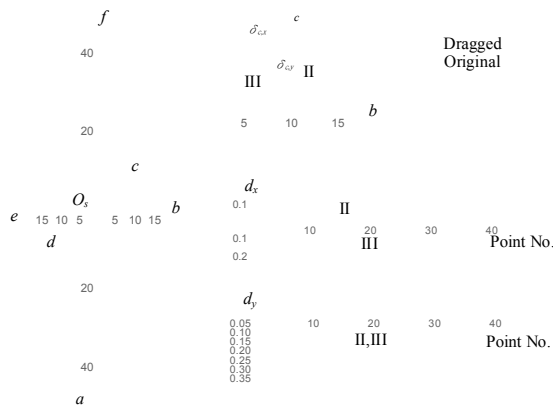
Fig. 4. The modification and displacements of segments II, III for the sealing line.

Fig. 4 expresses example 1. Segments II and III are modified by moving point *c* with displacements $\delta_{c,x}$ and $\delta_{c,y}$ along X and Y-directions, respectively; while other segments are fixed. Based on the displacements of point *c*, displacements of the others in the segments II and III are determined by substituting the coefficients in Table 2 into Eqs. (7) and (8). Diagrams of the displacements are illustrated in Fig. 4. In this modification, the segments II and III are depressed according to the Y-direction. Thus, length of the sealing line becomes shorter. The quadratic equations used to adjust the displacements always make the segments be smooth.
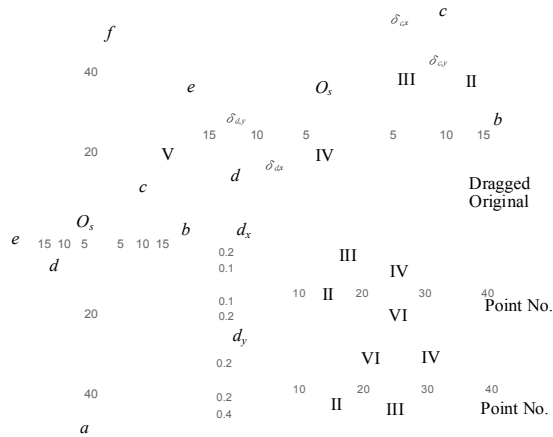
Fig. 5. The modification and displacements of segments II, III, IV and V for the sealing line.

Fig. 6. Comparison of different rotor profiles.

In example 2, the modification of the sealing line is conducted on not only the segments II and III but also segments IV and V (as Fig.5). The adjusted segments are also depressed to close the X-axis; therefore, the length of the sealing line becomes shorter than that in the example 1.

Additionally, rotor profiles are regenerated from the adjusted sealing line based on the rotor profile generation method (Fig. 6). Hence, a numerical method is used to calculate their performance indices as illustrated in Table 3. It also shows that general performance of pump in the example 2 is higher than other cases such as the length of sealing line is shortest, the working area, theoretical volume flow rate and sum of single-grove areas of rotors are largest. This is an important issue in rotor profile optimization of the claw-type vacuum pumps to improve the pump performance.

5. Conclusion

In this paper, a design method of rotors profile generation based on the sealing line for claw-type vacuum pumps is proposed. The sealing line is divided into some segments that are adjusted smoothly by the quadratic equation with specified control points. The geometric limitations are also considered to avoid interference and undercutting in rotor profiles. In addition, the rotor profiles are generated by applying the enveloping theory and the cubic spline curve fitting method from the modified sealing lines. Hence, the calculation and comparison for performance indices of new rotor profiles are also carried out to identify the trend of sealing line adjustment which will be very

useful for the profile optimization in further researches.

References

[1] C.F. Hsieh, Y.W. Hwang, and Z.H. Fong, *Mech. Mach. Theory*, 43 (2008) 812-828.

[2] J. Wang, D. Cui, X. F. Pang, H. Z. Feng, Z. L. Wang, *Vacuum*, 143 (2017) 174-184.

[3] A. Giuffrida, *Proc. ASME 2012 International Mechanical Engineering Congress and Exposition*, (2012), 107-114.

[4] J. Wang, X. Jiang, and Y. Cai, *Vacuum*, 111 (2015) 102-109.

[5] Y.R. Wu and Z.H. Fong, *Mech. Mach. Theory*, 43 (2008) 695-711.

[6] D. Zaytsev and C.A. Infante Ferreira, *International Journal of Refrigeration*, 28 (2005) 744-755.

A Study the Gasoline Injection Tester Device for Automobile

NGUYEN Huy Bich [1,2*)], TRAN Dinh Hy[3)]

[1)] Faculty of Engineering and Technology, Ho Chi Minh city Nong Lam University, Viet Nam
[2)] Digital Control and System Engineering Laboratory-DCSELAB, Vietnam National University Ho Chi Minh city, Viet Nam
[3)]Faculty of Automobile Engineering, Ben Tre Technical College, Ben Tre Province, Viet Nam

ABSTRACT

The tester device for investigation and frequency checking the gasoline injection in automobile engine is necessary and contribution to the stable working of a car. The device with low cost and flexible in working will help to improve the quality of technical service and might be equipped for some car service stations in rural provinces. A Gasoline injection tester for a car has been successful manufactured and the experimental investigations have been conducted at different kind of gasoline injectors used in different cars. The results indicate that the tester is suitable and adaptable for testing the gasoline injector in some technical parameters such as timing injector, fuel quantity, injection angle, and injection quality. This device also can be used for testing in different kind of injectors in different cars with high accurately, easy to use, and low cost.

Keywords: Injection tester; automobile; injectors

[*)]corresponding author: Email: nhbich@hcmuaf.edu.vn

PART VI, SECTION I

Machining Technology
(Difficult-to-cut and Free Machining; Non-conventional Machining;
Green Process/Manufacturing; Cutting Mechanisms…)

Study and Trial Production the Machine That Can Be Continuous Manufacturing Buckypapers

Bùi Quang Vinh, Hứa Nguyễn Đăng Thy, Vũ Ngọc Long, Đỗ Hữu Quyết

Reaseach and development Center Sai Gon Hi-tech Park, Viet Nam

Lot I3, N2 Streets, Sai Gon Hi-tech Park, Dist.9, Ho Chi Minh City, VN

ABSTRACT

Thin films and nanomaterials have been extensively studied in Vietnam. There are some positive results in the field, one of which is buckypaper, a sheet made from the synthesis of carbon nanotubes. Buckypaper is considered effective material in high power LEDs, CPU due to high thermal conductivity and heat transfer, safe, long life. However, most processes do buckypaper on a small scale. In this article, we focus on the design, research and production of equipment that can be automatically manufactured to improve, stable quality buckypaper provide the internal market.

Keywords: Roll to roll system, Buckypapers, TIMs…

1. Introduction

The technologies that make the thermal transfer materials is mainly based on the combination among polymer silicone, acrylic, hot-melt adhesives as paraffin and thermal conductive filler such as ceramics, copper, silver, AIN, Al2O3,… The main role of polymers and adhesives is increase the interface between heat sinks and heat sources. However, they have some disadvantages: easy to vapour and degrade so the used temperature is below 200ºC. Moreover, their thermal conductivity is rare low, about 0.1 W/mK. Some commercial products as Western Hemisphere WH1040, Bornsun BN-G500… used thermal conductive fillers to raise the thermal conductivity. Because of the bad interface between the polymer matrix and fillers, the results are still not good (Figure 1c). Besides, it is difficult to disperse the fillers in high viscosity matrix so that the thermal transfer, adhesive and mechanic of materials were decreased. The commercial thermal pads are quite thick (from several micrometers to millimeters), This is also a reason to reduce the thermal transfer efficiency.
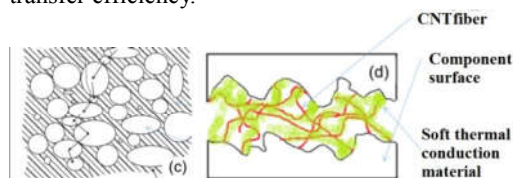
Figure 1: (c) The structure of the heat sink material in the current technology, (b) the improved material structure

Because of some disadvantages above, thermal grease and pad still not respond the market demand for high thermal transfer, long life, used temperature and price. Recently, there are some researches which focus on using CNT to make thermal interface materials (TIMs). Although having high thermal transfer property, they still have some problems such as difficult to have good interface between CNT and heat sink, high cost. This this paper, the TIMs were made from composite that consist bucky paper and polymer matrix (Figure 1d).

This composite are better in thermal interface and cheaper than other thermal grease and pad in the market.

In Vietnam, there are many optimistic results in researching TIMs. This is a good sign to develop this material to the market.
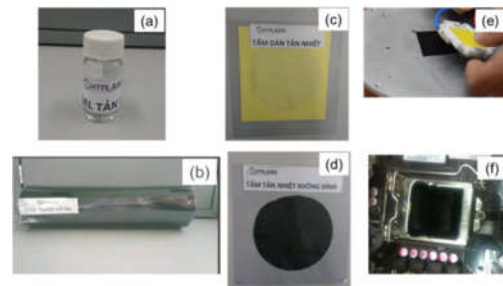
Figure 2: Schematic diagram of different resistor components of TIMs.

Most of processes to make TIMs are in small scale by hand so the quality is not stable. To improve this problem, we have to fine a method to manufacture TIMs in large scale and stable quality. The research, design a equipment that can fabricate bucky paper in masss production, is a new field for mechanical engineering in Vietnam.

2. Methodology

2.1 Components and parameters influence to TIMs

As we know when two solid surfaces are interface, the roughness of each surface limits the contact between solid surfaces a very small fraction of perhaps only 1-2% of the visible area. A model of thermal solution between the two structures is illustrated in the figure below:
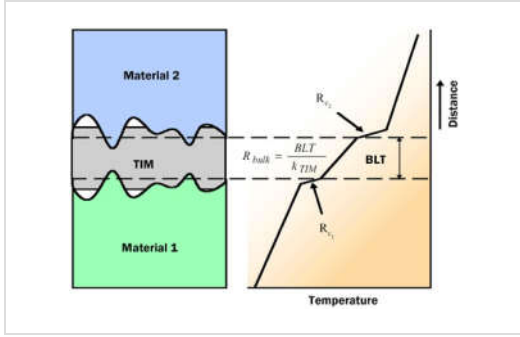
Figure 3: Schematic diagram of different resistor components of TIMs.

Properties of TIMs

The main role of TIMs is to eliminate air spaces between heat sink and heat source. The surface heat resistance between metal surface R_{TIM} become bulk resistance R_{bulk} of TIMs when conducting heat and contact resistance of TIMs and metal surface.
RTIM is calculated by this equation:

$$R_{TIM} = \frac{BLT}{k_{TIM}} + R_{c_1} + R_{c_2} \qquad (1)$$

where: BLT is bond line thickness

k_{TIM} the conductivity of TIMs

R_{c1}, R_{c2} contact resistance of TIMs and two metal surface

From equation above, we have to reduce the thickness of TIMs and R_{c1}, R_{c2}, increase the conductivity so that to reduce the resistance of TIMs.

2.1 Equipment, fabrication

Before designing, fabricating the equipment, we need determine requirements, object, steps to make. The main functions of equipment include:
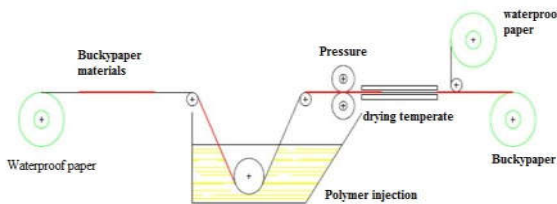
The process to disperse bucky paper into the polymer matrix follows by this flow chart:
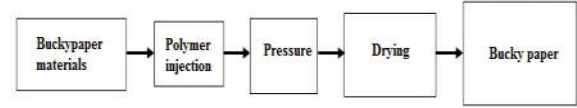
Firstly, from the input, the bucky paper is injected a polymer layer. Then it is rolled to a thin sheet. The thickness of nucky paper is formed by changing the space between two rollers, the rotation speed of rollers is controlled by motor M1. The thin sheet of bucky paper is dried through a thermal system to the output conveyor.
The flow chart of controlling algorithm:
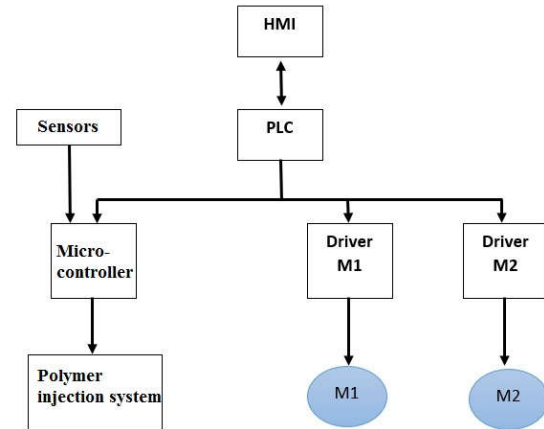
Throughout the process, we have to ensure the rotation speed of the rollers is the same to avoid wrinkling or breaking the bucky paper.
In this equipment, stable velocity of bucky paper sheet determines the quality of product. Because n_1 is constant and n_2 is variability. We have to calculate so
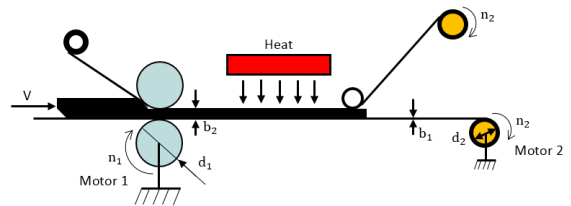
$$R_1 = \frac{d_1}{2}, \quad R_2 = \frac{d_2}{2}$$

b_1: thickeness of substrate

$$V = R_1.\omega_1 = (R_2 + a.b_1).\omega_2 \qquad (1)$$

(a: the rotations of motor 2 rotated)

$$\omega_1 = 2\pi.n_1 \quad \text{(rad/s)} \qquad (2)$$

$$\omega_2 = 2\pi.n_2 \quad \text{(rad/s)} \qquad (3)$$

n_1: the rotations of motor 1 rotated in a second

n_2: the rotations of motor 2 rotated in a second

(1), (2) and (3):

$$n_1 = \frac{60.V}{R_1.2\pi} \quad \text{(rpm)} \quad (4)$$

$$n_2 = \frac{60.V}{(R_2+a.b_1).2\pi} \quad \text{(rpm)} \quad (5)$$
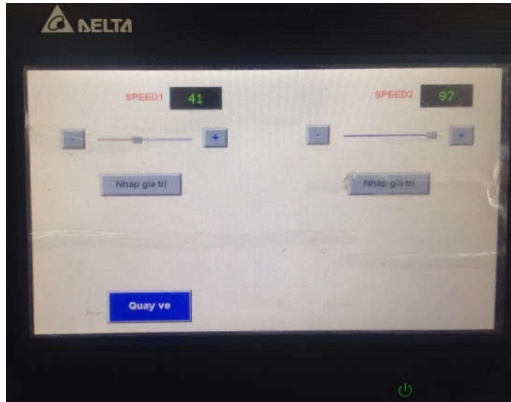
+ SPEED1: changing the rotation speed n_1 motor M_1

+ SPEED2: changing the rotation speed n_2 motor M_2

To adjust the speed, increase or decrease icon; or set the value on the LCD screen.

3. Results and Discussions

Roll to roll system is working in Nanonotechnology Lab-Research Laboratories of Saigon Hi-tech Park.

Thickness of samples:
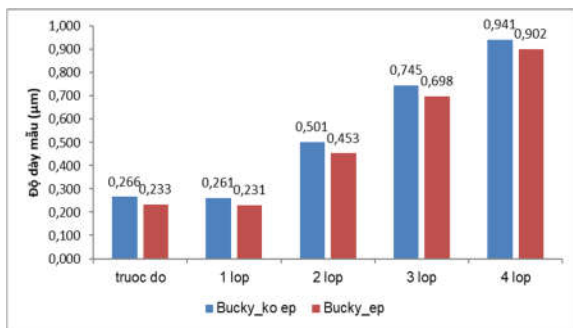
Thermal transfer results:
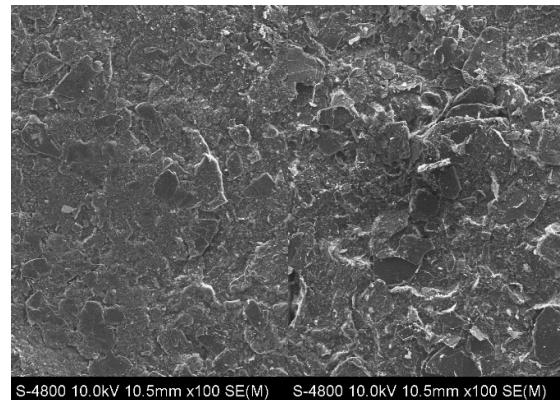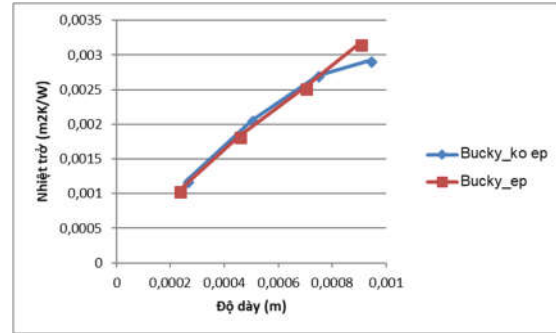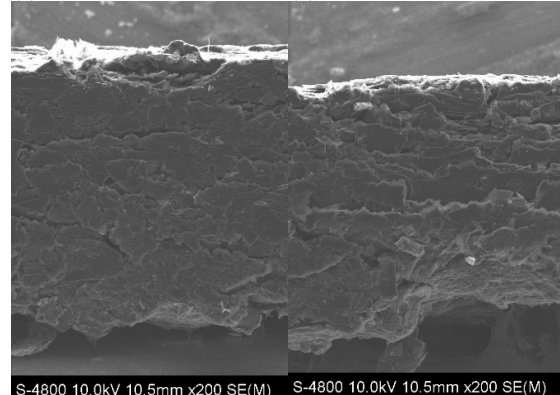
(a)   (b)

(c)   (d)

Figure 4. SEM image of surface structure and cross section of Bucky paper. (a), (c) is a roll to roll template; (b), (d) is not using the roll to roll system.

SEM images for surface and cross section of samples show in figure 4. It is considered that the roughness of sample fabricated by roll to roll system is less than normal samples. The less roughness is, the higher quality is.

The results of thermal conductivity and thermal contact resistance are summarized in table 1. Because the thermal contact resistance relates to the contact together of CNT in bucky paper, so the less thermal

contact resistant, the better contact is. In the other words, the srtucture of bucky paper is closer packed. From the results, we can determine roll to roll system makes the bucky paper better, reduces the thermal contact resistance. The conductivity is interpolated from slope of thermal resistance-thickness graph (fig). Although the conductivity of unperssed bucky paper higher than pressed bucky paper (susing roll to roll), but it is considered two value are equal. Because the thermal resistance-thickness line of unpressed sample is not linear, so the calculated conductivity of this sample has error.

Table 1: The conductivity of unperssed bucky paper and pressed bucky paper.

Sample	Thermal contact resistance (m^{2}K/W)	Conductivity (W/mK)
Unperssed bucky paper	0.00063	0.386
pressed bucky paper (roll to roll)	0.00035	0.319

Using roll to roll system, the sample is pressed, structure of bucky paper is better lead to improve the thermal contact resistance, the results are less error.

4. Conclusion

The roll to roll system is fabricated and trial operated at Nanotechnology Lab-Research Laboratories of Sagon Hi-tech Park. Initially, the system is working well. However, it is necessary to investigate this system more before manufacturing in large scale.

Adjusting space of two rollers of system is difficult because of the uniform of the thickness of paper substrate.

It need to improve the reinforcement part that can automatic test the thicknessof paper substrate and adjust the space of rollers in micrometer scale.

References

[1] E. Hammel and et al, "Carbon Nanofibers for Thermal Interface Materials in Pressure Contacts," Palo Alto, CA, 2005.
[2] A. B. Cohen, A. D. Kraus, and S. F. Davidson, "Thermal frontiers in the design and packaging of microelectronic equipment," J.Mech.Eng, vol. 105, pp. 53–59, 1982.
[3] 3M, "Technical Bulletin Characteristics of Thermal Interface Materials," 2001.
[4] F. S. F. Sarvar, D. C. Whalley, and P. P. Conway, "Thermal Interface Materials - A Review of the State of the Art," 2006 1st Electron. Syst. Technol. Conf., vol. 2, pp. 1292–1302, 2006.
[5] C. A. Latham, "Thermal resistance of interface materials as a function of pressure," Electron. Cool.
[6] Carbon Nanotube Buckypaper Permeability and Prepreg Process Study, Bryant Marshall Click, Florida State University, 2010
[7] Patent US6938661 LAMINATING MACHINE
[8] Patent US8435373 SYSTEMS AND METHODS FOR ROLL_TO_ROLL PATTERNING

Experimental Study on Red Dragon Fruits Powder Dried by Spray Drying Technology

NGUYEN Huy Bich [1,2*], NGUYEN Tuan Linh[3]

[1] Faculty of Engineering and Technology, Ho Chi Minh city Nong Lam University, Viet Nam
[2] Digital Control and System Engineering Laboratory-DCSELAB,
Vietnam National University Ho Chi Minh city, Viet Nam
[3] Department of Industry and Trading of Tien Giang Province, Viet Nam
[*] corresponding author: Email: nhbich@hcmuaf.edu.vn

ABSTRACT

The red dragon fruit (Hylocereus polyrhizus) and white dragon fruit (Hylocereus undatus) are two varieties of dragon fruit that are commonly consumed in Viet Nam in which the first one is highly attraction to many people. This study aims to investigate the reasonable maltodextrin concentration and the suitable spray-dried regime to produce the red dragon fruit powder. The experimental investigations have been conducted at five rates of maltodextrin concentration as 10 %, 15 %, 20 %, 25 % and 30 % and with five inlet agent drying temperatures as 120 ^{0}C, 130 ^{0}C, 140 ^{0}C, 150 ^{0}C and 160 ^{0}C . The result indicate that the suitable spray drying regime for red dragon fruits powder processing are the maltodextrin concentration is 30%; the injection pressure is 0.2 Mpa; the speed of input dragon emulsion pump is 3 rpm; and the agent air drying temperature inlet is 140 ^{0}C. Under these parameters of the drying regime, the retrieved efficiency of the spray dryer might be reached to 71.14% and the Vitamin C content can be recovered up to 12.6 mg/kg.

Keywords: Dragon fruit, food drying, dragon powder.

Optimal Job Scheduling of Multiple Rail Cranes in Rail Stations with Simulated Annealing Algorithm

Vu Anh Duy Nguyen*, Thanh Hung Ly

Faculty of Mechanical Engineering Technology, Ho Chi Minh City University of Food Industry, Vietnam

Email: duynva@cntp.edu.vn

ABSTRACT

This paper considers the scheduling problem of multiple rail cranes to operate within rail stations. Both inbound and outbound containers are considered. This study considers not only assign working areas to cranes, but also determines the job sequence of each crane. The objective of this paper is the minimum of the maximum completion time (makespan) of all rail cranes. Dual-cycle operations in loading and unloading containers of cranes are applied and the re-handling work of containers is also taken into account. A simulated annealing algorithm is designed to obtain near optimal solutions. Numerical examples are studied to investigate the performance of the algorithm.

Keywords: Simulated annealing; rail crane; scheduling

Introduction

The rail station is critical to the efficiency of rail transportation. Figure 1 shows a general rail stations layout. In rail stations, outbound containers are unloaded and inbound containers are loaded using rail cranes, forklifts and reach stackers, and the waiting time of trains in rail stations is directly dependent on the operation of these systems. The rail cranes are the most important equipment in the rail station. The efficient of the rail station is highly dependent on the operation of the cranes.
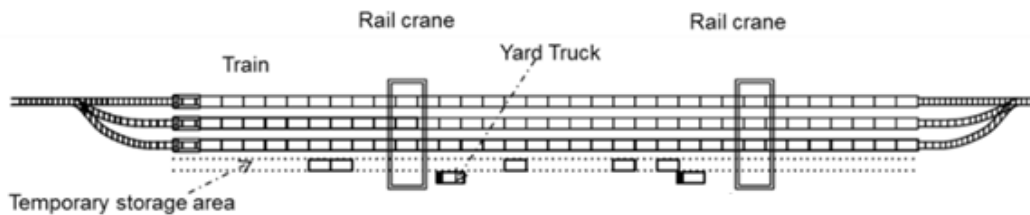
Fig. 1 Layout of a rail station.

This paper deals with the job sequencing problem of rail cranes in rail stations located at seaport container terminals. We not only assign the working areas but also determine the job sequences, minimizing the maximum completion time of all rail cranes. Dual-cycle operations are applied. If the wagon onto which an inbound container will be loaded is not empty, the inbound container is moved to temporary storage area. The inbound container is loaded onto the wagon after the wagon is empty. This is referred to as a "re-handling" case.

The latest review of container processing in rail stations was presented by Boysen et al. (2013) with the assignment of container movements by cranes and determining the sequence of container movements. Alicke (2002) considered the logistical problems relating to the loading and unloading of trains in a theoretical intermodal terminal called Mega Hub, where containers are transferred between trains and shuttle cars by cranes. That article not only dealt with the assignment problem of containers to cranes, but also addressed sequencing problems relating to containers. That author formulated an optimization model based on Constraint Satisfaction, and developed various heuristics to minimize the maximum lateness of all trains. Boysen and Fliedner (2010) discussed how to determine the static crane areas in rail – road transshipment yards. In contrast, Boysen et al. (2010) addressed the static crane areas in rail – rail transshipment yards. Both of these studies used dynamic programming to find the optimal working area for each rail crane. However, they did not determine the optimal job sequencing of rail cranes. None of these researches assumed the dual – cycle operation of rail cranes. Jeong and Kim (2011) applied the dual – cycle operation of a crane in order to determine the job sequence of the rail crane and the parking positions of container trucks. Nevertheless, they considered the operation of a rail crane which just

432

moves in one direction along the train. Pap et al. (2012) developed a branch-and-bound algorithm to find the optimal job sequence of a rail crane under a dual-cycle operation, although they did not consider re-handling cases for containers. Guo et al. (2013) dealt with the scheduling problem of loading and unloading containers between a train and container yards. Multiple gantry cranes were scheduled in a rail station with constraints of safety distance, as well as a non-crossing requirement being placed on the cranes. However, that article assumed the one dimension travel (gantry travel) of the cranes, and did not consider dual-cycle operation or the re-handling containers. Nguyen and Yun (2014) considered the job scheduling of a rail crane in rail terminals. The paper studied the transfers of containers between trains and trucks by a rail crane. In addition, re-handling and the dual-cycle operation are considered.

The remainder of this paper is organized as follows: The simulated annealing algorithm is proposed in Sections 2. Numerical examples are studied in Section 3. Section 4 concludes the study.

Simulated annealing algorithm (SA)

The simulated annealing algorithm is developed to find near optimal solutions of the multiple rail crane scheduling problem. This section will describe operators of the SA.

Initial solution construction

A solution of the scheduling problem consists of two parts as 1) the working area and 2) the job sequence of each crane. The initial working areas are assigned to cranes based on the balance of the workload. The "workload" is the summation of all travelling times to discharge outbound containers or to retrieve inbound containers. We use the example in the table 1 to illustrate how to construct the initial solution.

Table 1. An example of inbound and outbound containers.

Container	Type	Train	Wagon	Workload	Container	Type	Train	Wagon	Workload
1	Inbound	1	1	3	9	Inbound	1	9	3
2	Inbound	2	1	2	10	Outbound	2	1	2
3	Inbound	1	2	3	11	Outbound	1	2	3
4	Inbound	2	3	2	12	Outbound	1	6	3
5	Inbound	1	5	3	13	Outbound	2	8	2
6	Inbound	2	5	2	14	Outbound	2	8	2
7	Inbound	1	6	3	15	Outbound	1	9	3
8	Inbound	1	7	3	16	Outbound	2	9	2

We assume that the travelling time between two adjacent trains is one time unit, and that the temporary storage area is located between the transfer track and the railway track. Table 1 also presents the travelling time of cranes to handle the containers in the table. Total workload is 41 time units. Therefore, the working area of the first crane is from wagon number 1 to wagon number 5. The working area of the second crane is from wagon number 6 to wagon number 10. The workload of the first crane is 20. The workload of the second crane is 21. Table 4 illustrates a solution for this example. The first part represents the working areas of the cranes. The numbers in this part denote the wagon numbers of the last right-hand side areas area which was handled. The second and third parts show the work sequencing of cranes handling inbound and outbound containers, and the number denotes the container number. In Table 2, the inbound containers 2, 7 and 9, and the outbound containers 11, 12 and 15, require re-handling.

Table 2. Solution representation.

Crane	Boundary	Job sequence								
1	5	1	2	11	6	5	10	3	4	
2	10	7	12	13	9	15	16	8	14	16

Neighborhood solutions

Two operations are designed to generate neighborhood solutions. The first operation is a "zone operator", which is used to determine a new working area for a crane. The second operator is "sequence operator" used to generate a new job sequence for the crane. If a random number in the range of (0, 1) is less than or equal to α, the first operation is chosen. Otherwise, the second operation is applied. In the zone operator, the boundary of a crane is first adjusted by adding randomly -1, 0 or 1. The containers that do not satisfy the boundary are assigned to other cranes. In the sequence operator, a pairwise interchange is carried out to adjust the job sequence, where two inbound

containers or two outbound containers are randomly selected and swapped.

Acceptance criterion and cooling down function

Once a neighborhood solution is generated, the following criterion is used to accept or reject it. Let $\Delta = Q(C) - Q(NB)$ where C, NB and Q(*) are the current solution, neighborhood solution and makespan of solution (*), respectively. A neighborhood solution is accepted as the current solution if $\Delta \geq 0$ or $r \leq e^{\frac{\Delta}{T_l}}$, where *r* is a uniform random number in (0,1) and T_l represents the current temperature. The cooling down function is the geometric update scheme introduced by Lundy and Mees (1986), $T_l = T_{l-1} \times \pi$ .The termination condition of the algorithm is $T_l \leq \varepsilon$.

Numerical examples

The SA algorithm contains four parameters, α, T_0, π and ε .To determine these parameters of this simulated annealing algorithm, we consider three values of α (0.1, 0.2 and 0.3), five values of T (10, 20, 30, 40 and 50), four values of π (0.999998918, 0.999999459, 0.999999729 and 0.999999819) and five

values of ε (0.001, 0.010, 0.100, 1.000 and 5.000). 9000 runs of 300 combinations of four parameters are executed in order to obtain the mean of the makespans. The example problem which is used in this section contains 97 inbound containers and 97 outbound containers, which are being carried by three trains and thirty-three wagons. Three rail cranes are used to load and unload all containers. The parameters have a strong effect on the performance of the SA, except for T. Finally, we chose α as 0.3, T_0 as 20, π as 0.999999819 and ε as 0.001.

In order to evaluate the performance of the traditional SA, the parallel SA, and the B&B algorithms, 24 problems were randomly generated by uniform distribution. The probabilities that a wagon carries a container (an inbound or an outbound container) are 0.25, 0.50, 0.75 and 0.95, respectively. The examples were tested on a computer with an AMD Athlon CPU 3.00 GHz, and 4 GB memory, and the algorithms are coded in Java. Table 3 shows the mean values of makespans, standard deviations and computation times of the 24 problems, as obtained by the simulated annealing algorithm. The SA can give the results in several minutes. The maximum of the standard deviations of the results obtanted form the SA is less than 5%.

Table 3. Numerical examples

No	Number of trains	Inbound/ Outbound Containers	Number of cranes	SA Makespan (Std.)		CPU Time (sec.)
1	1	12/8	2	50.00	(0.00)	128
2	1	16/16	2	66.00	(0.00)	165
3	1	24/21	2	78.00	(0.00)	222
4	1	30/31	2	96.00	(0.00)	279
5	2	14/17	2	79.80	(1.11)	149
6	2	36/28	2	130.00	(0.00)	292
7	2	49/48	2	171.45	(1.10)	409
8	2	64/61	2	212.80	(2.12)	543
9	3	25/23	2	120.00	(0.00)	234
10	3	51/46	2	211.80	(1.61)	408
11	3	72/81	2	314.00	(5.48)	664
12	3	97/97	2	384.15	(8.16)	933
13	1	12/8	3	36.00	(0.00)	165
14	1	16/16	3	46.00	(0.00)	191

15	1	24/21	3	53.30	(2.36)	233
16	1	30/31	3	64.00	(0.00)	362
17	2	14/17	3	53.00	(0.00)	193
18	2	36/28	3	87.30	(2.64)	367
19	2	49/48	3	114.70	(2.32)	562
20	2	64/61	3	142.60	(2.64)	661
21	3	25/23	3	83.35	(2.18)	247
22	3	51/46	3	142.20	(3.14)	554
23	3	72/81	3	211.70	(2.03)	866
24	3	97/97	3	252.85	(7.14)	1133

Conclusion

In this paper, we considered a multiple crane scheduling problem in which working areas are assigned to cranes and the job sequence of each crane is considered. Moreover, the dual-cycle operation of cranes was incorporated. The makespan of cranes was used as an optimization criterion, and a simulated annealing algorithm was proposed to find near optimal solutions. We investigated the performance of algorithms using numerical examples. Further research may include the study of rail crane scheduling problems with the additional consideration of train timetables, or with the integration of truck scheduling.

References

[1] Alicke, K. 2002. "Modeling and optimization of the intermodal terminal Mega Hub." *OR Spectrum* 24 (1):1-18.

[2] Boysen, N., and M. Fliedner. 2010. "Determining crane areas in intermodal transshipment yards: The yard partition problem." *European Journal of Operational Research* 204 (2):336-342.

[8] Nguyen, D. V. A., and W. Y. Yun. 2014. "Optimal job scheduling of a rail crane in rail terminals." *International Journal of Industrial Engineering: Theory, Application and Practice* 21(3):129-140.

[9] Pap, E., G. Bojanic, N. Ralevic, M. Georgijevic, and V. Bojanic. 2012. "Crane scheduling method for train reloading at inland intermodal container terminal." Intelligent Systems and Informatics (SISY), 2012 IEEE 10th Jubilee International Symposium on, 20-22 Sept. 2012.

[3] Boysen, N., M. Fliedner, and M. Kellner. 2010. "Determining fixed crane areas in rail-rail transshipment yards." *Transportation Research Part E-Logistics and Transportation Review* 46 (6):1005-1016.

[4] Boysen, N., M. Fliedner, F. Jaehn, and E. Pesch. 2013. "A survey on container processing in railway yards." *Transportation Science* 47 (3):312-329.

[5] Guo, P., W. Cheng, Z. Zhang, M. Zhang, and J. Liang. 2013. "Gantry Crane Scheduling with Interference Constraints in Railway Container Terminals." *International Journal of Computational Intelligence Systems* 6 (2):244-260.

[6] Jeong, B. J., and K. H. Kim. 2011. "Scheduling operations of a rail crane and container deliveries between rail and port terminals." *Engineering Optimization* 43 (6):597-613.

[7] Lundy, M., and A. Mees. 1986. "Convergence of an annealing algorithm." *Mathematical Programming* 34 (1):111-124.

Develop A Novel Microbiological Product to Process Household Waste in Vietnam

Huynh Quyen[1], Bui Huu Phu[2], Nguyen Huu Phep[3], and Truong Quang Vinh[3]
[1]University of Technology, VNU-HCM, Vietnam
[2]Hochiminh City University of Technology and Education, Vietnam
[3]Vietnam Microbiological Technology for Environmental Treatment Corporation
01 Vo Van Ngan street, Thu Duc district, Hochiminh City, Vietnam
Email: phubh@hcmute.edu.vn

ABSTRACT

Household waste is a serious problem in Vietnam recently, especially at the big cities. The waste causes stank at transit garbage station make citizen living nearby feel uncomfortable. The waste water must be treated before discarded to the environment. In addition, almost the household waste processed in Vietnam until now is whether buried or burned. Both methods cause problems for environments.

There are many solutions to treat with the household waste in Vietnam. One of the best solutions is to use microbiological products to treat stank smell, waste water, and waste process to be organic particle which use to make organic fertilizer.

Although there are many microbiological products in Vietnam market, they have many disadvantages. Domestic products do not have high quality enough to process the waste, or do not have multiple functions to process the waste. Imported microbiological products such as from Japan have high quality but very expensive, so it is hard to be used widely in Vietnam.

We have studied to develop a novel microbiological product which can be used to eliminate the smell of household waste immediately, process the waste water good enough before discarded to the environment, and decay the waste quickly as organic particle within 21 days.

In the paper, we present our process to make the product, and some real results that we already implemented in Hochiminh City to process household waste. We believe that our product will be successful in commercial soon.

Keywords: Microbiological Product, rubbish processing, Household Waste processing, environmental solution

Study on Rice Husk Husking Machine Improvement

Tran Quoc Nhiem

Department of Manufacturing Engineering Technology, Faculty of Mechanical Engineering Technology, Ho Chi Minh City University of Food Industry (HUFI), 140 Le Trong Tan St., Tay Thanh Ward, Tan Phu Dist., Ho Chi Minh City, 700000, Vietnam

ABSTRACT

Vietnam is the sixth largest rice growing area in the world, concentrated in the Mekong Delta, the Red River Delta and the Central Coast. The rice productivity in our country has been increasing continuously for many years. Rice is one of the key export items of Vietnam. The process of peeling is done well, the ratio of paddy, broken rice and bran in the small grinding mixture (the rate of rice flip and the proportion of rice husk is correspondingly large). The quality of the peeled process greatly influences the quality of the whole production line, the final criteria are the quality of the rice and the processing efficiency. To improve the quality of rice after processing through the system of processing rice, this paper presents the improvements of rice husk husking machine to meet the customers' requirements.

Keywords: rice husk husking machine; Vietnam; rice; husk

1. Introduction

Rice is an important food tree that is highly productive, easy to grow, and plays a key role in human and animal life. Southeast Asian countries have the largest area of rice in the world due to the hot and humid climate, which is suitable for rice field, including Vietnam. Vietnam is the sixth largest rice growing area in the world, concentrated in the Mekong Delta, the Song Hong River Delta and the Central Coast. The rice productivity in our country has been increasing continuously for many years. Currently, rice is one of the main export items of Vietnam. Vietnam's 2009 rice exporting target will be between 4.5 and 5 million tons, worth about two billion dollars. According to the Vietnam Food Association (VFA), the number of rice export contracts signed up to this time reached 6.453 million tons, have ever been the largest. Vietnam is the second largest rice exporter in the world after Thailand.

However, despite its high productivity, our post-harvest technology is much more restrictive than Thailand, so it has suffered a great loss in the post-harvest period and has low value in international trade. The processing of rice export is now quite backward, some companies have invested in rice processing lines but the synchronism is not high leading to low productivity, the quality of rice produced is not up to standard to export and large energy consumption.

Vietnamese companies have built synchronous rice processing lines (Long An Mechanical Engineering Joint Stock Company, Bui Van Ngo Company, SINCO Joint Stock Company), but the automation level is not high, even low and unstable productivity, low recovery rates, and manipulation and control of output quality remain highly dependent on worker experience. On the other hand, the varieties of rice are changed seasonally, so the varieties of rice are not the same. Currently the use of shelling machines is mainly due to experience so the loss in the process of peeling large, the quality of rice after shelling is not really high. At present, in our rice processing plants, we use two types of shredding machines: double rubber shredding machine and two shredder cutting machine. According to M.E. Ginzbya's classification (based on the principle of mechanical effect of the machine's work unit on the grain), they belong to the group of peeled machines that act on the grain by compression and sliding. In which, the peeling machine using double rubber shaft to remove the husk is the main machine of peeling in the modern rice processing lines, processing rice for export.

From a theoretical point of view, the results of the peeling process can be seen in the two products: rice flip and rice husk. In fact, it is influenced by the mechanical properties of the grain and the degree of incompleteness of the machine. The mixture consists of all ingredients - rice flakes, rice, rice husk, rice bran and rice bran. The process of peeling is done well, the ratio of paddy, broken rice and bran in the small grinding mixture (the rate of rice flip and the proportion of rice husk is correspondingly large). The quality of the peeled process greatly influences the quality of the whole production line, the final product is the quality of the rice and the processing efficiency. To improve the quality of rice after processing through the system of processing rice, the model of machine design is presented in this paper.

2. Literature review

Shelling is the basic stage in the production line in rice mills. The purpose of peeling is to remove the husks from the seeds while keeping the kernel intact. The rice husk has two pieces of rice husks that cover the husk and the rice kernel has a void. At both ends of the grain, there is a large gap, so when the grain is affected by the traction, compression, punching, the husk husking easily peel off. There are four shells in the world: Machine to peel a rotary axis, double hinged rubber shredding machine, shredding machines with abrasive wheel or disc, shredding machine has two mortarboard. According to the principle of mechanical effect [1], the types of shelling machines are classified into groups: Effects of compression and friction; effect of friction force; in addition, the double-hulled crusher also acts as a sliding (pulling and compacting). The most commonly used shelling machines are the double-hulled crusher and the two shredder crushers.

At present, there are many mechanical enterprises in the country have made the machine to peel the rice with different scale from 1 to 5 tons / h. With the machine of peeled rice with the capacity of 8 - 10 tons/h only two units are Bui Van Ngo Company and Long An Machinery Manufacturing Joint Stock Company (LAMICO) to participate in production. Here are some typical shelling machines in Vietnam such as shredding machine made by Vinappro Company (RH - 700), HW - 60A shelling machine, shelling machine made by Bui Van Ngo Agricultural and Agriculture Co., Ltd (shelling machine CLI - 600A); Equipment and machinery shredded by the manufacturing company Long An machine (HSA20 peeling machine). Their equipment and machines still have many problems need to be improved as follows.

- Automatic feed system ensures stable input productivity.
- Experimental planning to find the relationship between inputs (longitudinal velocity of the fixed shaft - spindle motor speed, compressed air pressure - pair of rollers) and the target factor (rate of shelling and breaking rate).
- Automatic adjustment of compressed air pressure to maintain the current value (corresponding to the clearance of the pair of rubber rollers) to achieve the desired shelling rate and fracture ratio.
- Automatically control the speed of the spindle motor to maintain the longitudinal velocity of the rubber roll when the rubber roll is worn during operation.
- Automatic adjustment of feeding position of slant trough when the rubber roller wears to ensure the feed position between the gap of the rubber roll to reduce the rate of breakage.

Therefore, this study aims to improve the shelling machine in order to improve shelling performance, minimize fracture rate and reduce energy consumption compared to existing shredding machines at Mechanical Engineering Joint Stock Company Long An (LAMICO).

2.1 Engineering Design methodology

The objects of processing are rice harvested in the Mekong Delta provinces (mainly two types of rice are studied in two Spring and Summer seasons). A new huller is designed and built with a capacity of 4-5 tons / h, two rubber rolls by the University of Technology in Ho Chi Minh City. Ho Chi Minh City and Long-An Machine Manufacturing Company designed and manufactured as Figure 1.

1. Nắp chứa liệu	
2. Thùng chứa liệu	
3. Hộp cấp liệu	
4. Cụm trục rải liệu	
5. Biến tần	
6. Động cơ điện	
7. Trục gá (Tấm rải liệu)	
8. Tấm rải liệu	
9. Núm chỉnh (tấm rải liệu	
10. Thân máy chính	
11. Cụm trục rulô cố định	
12. Cụm trục rulô chủ động	
13. Cụm bánh căng đai	
14. Cảm biến đo tốc độ rulô (Encorder)	
15. Quạt hút bụi	
16. Động cơ đẩy tấm chảy liệu	
17. Giá đỡ (đế gá pistong)	
18. Trục gá (tấm chảy liệu)	
19. Hộp giảm tốc	
20. Động cơ bước	
21. Trục vít me	
22. Đế gá pistong	
23. Le cấp liệu	
24. Pistong khí nén Ø25x150	
25. Cảm biến đo trọng lượng thóc vào	

Figure 1. Schematic diagram of the new rubber double-shaft shelling machine.

The raw material from the cleaning machine is fed into the container cover (1) in the container with the weight sensor (25) attached to determine the weight (input yield) of the shelling process. The weighing signal (25) is fed to the processor controller. Then, pad the material through the spindle (4) and fall into the gap between the two rollers (11) and (12). These two rollers move in opposite directions and at different ring speeds (one fast and one slower) to peel off the husks. The peeling process yield and breaking rate depend on the ring speed and the gap between the two rollers. The speed of the two rotors can be adjusted via the inverter (5) to change the speed of the motor (6). Depending on the nature of the feed material and the wear of the two rollers, the clearance of the two rollers is adjusted appropriately by the stepper motor (20) through the gear reducer (19) and the screw conveyor (18). During operation of the shelling machine, the gap between the two rollers is maintained in the range (0.5 ÷ 0.75). Raw materials after peeling machine include rice, broken rice, rice bran and rice bran was put into the machine.

An amount of dust is drawn out through the outlet of the exhaust fan (15) and is collected centrally. The feedback signal was measured by TT3 of the electronic scale in the grading system of the separator combined with the TG4 rice grain return signal in the coarse rice mill and the TC2 ratio, TThL2 ligands shall be sent to the control unit of the shredder to determine the rate of shelling and breaking rate of shelling. The controller

through the control software will output the motor speed control signal (11) to change the rotational speed of the two rollers while adjusting the clearance between the two rollers through the stepper motor (20) to ensure the desired shelling ratio and motor control (3) through variable (2) adjusting the conveyor belt to achieve the highest yield.

Input productivity can be achieved by either the desired value or the maximum value because it is preliminarily determined by the relationship between the input yield and the influencing factors (rotational speeds of the rotary peeler and slow-moving pea pods) through experimental planning, and then precisely determined by the input signal of the machine's online feedback to the controller and the controller via Some algorithms will control the refining of the corresponding parts to alter these factors. An input signal of the husk separator is sent to the controller of the shelling machine and the output signal of the shredder is sent to the central controller for control signals to synchronize the chain and to meet the productivity of the shelling machine.

The plates were separated by splitting and weighing plates at the separator and separator and weighing machine in the rice husk separator. The plate weight signal is feedback to the controller of the shelling machine to determine the fracture rate thereby controlling the factors that affect the required breaking ratio and the highest input yield. Rice and paddy were separated into a rice and paddy weighing device at the

paddy separator combined with the top plate to determine the shelling ratio. The rice, paddy, and plate signals are fed back to the controller of the shelling machine to determine the shelling ratio that controls the factors that affect the required shelling ratio and head yield as high as possible.

Automation controls the clearance of the peeled rollers (to ensure optimum shelling and breaking rates of the paddy). Automation controls rotational speed of quick-rotating peeled rollers and slow-rotating peeled rollers (for optimum yield). Automation controls the drive's inverter to ensure minimum power consumption. Automation determines target outputs (output yield, shelling ratio, breaking rate) and through built-in algorithms that control input parameters to achieve The values of the target elements need to be improved in the optimal output and continuously maintain these optimal values: productivity of the huller, the ratio of peeled, and breakage rate.

Rotational speed of rotary engine: Design of controllers makes 3 controllers to ensure the actual control parameters as desired: + Input productivity control: The input productivity controller is a closed loop controller, the input productivity is set from the SCADA center of the entire plant. The task of the controller is to ensure that the input power has to follow the settings from the SCADA center. Control loop: Using a loadcell to measure the mass of the paddy through the gap, thus calculating the actual input yield, this signal is feedback on the controller compared to the SCADA center's installed capacity and calculated to determine the displacement motor signal to ensure that the actual performance is exactly the same as the setting value from the SCADA. Control of fracture percentage and plate rate: Breakage and plate rate depend on many factors: input productivity, rotational speed, rheo gap, such as gap width and speed. The rotational speed of the engine must be calculated depending on the three factors. Signals of breakage and plate rates were transferred to the center controller of the shelling machine compared to the value set from SCADA, giving the desired speed and width.

Suggested options for the implementation, control and data collection of shelling machines: For accurate monitoring of the shredder, the measured parameters must be fast and accurate in real time. Therefore, the performance of the sensors on the output of the machine must be done right at the peeling machine to ensure real time and not be affected by other factors when passing through multiple machines. Control parameters at the shelling machine: The shelling machine should ensure the following parameters as desired: productivity of the huller, the ratio of peeled and breakage rate.

3. Results and Discussion

The statistical data on moisture content of paddy affect the quality of milled rice, in which the best moisture content is 14 - 15%. Therefore, if we still use paddy with different moisture content, the quality of rice will be different, with the high moisture paddy, the quality of the milling rice will be low. Some options for rice milling also depend on the producer. First, milling the rice is done with the current moisture. Moisture content is usually between 16 - 19%, the chain is still guaranteed to be milling, however, the quality of rice is not high, the rate of breakage is high, the rate of recovery of rice is not high. After the milling can be sold immediately to eat or make vermicelli, if need to export, then drying rice, polishing, polishing ... According to the survey, with the humidity today, the milling plant only reached 60 - 66% of total harvest, only 40-48% of head rice. If rice is used for recycling exports continue to break rice more broken. Finally, 100 kg of paddy is 33% of whole rice exported. Damage estimated to be about 18% of the rice value, about $ 100 million with 3 million tons of rice exported and 28 times the profit of millers. Second, the treatment of paddy before putting in line is to ensure paddy moisture content in the required range of 14 - 15%. With this moisture content, the quality of the milled rice will be higher, the lower breakage rate and the higher rate of rice recovery. However, with this option, the manufacturer has to invest in a large grain drying system to ensure the productivity of the line. With the drying cost of only 5% [1.3] or 2 - 3% of paddy price, if the drying system is applied to the line it will increase profitability for the producer. The device is determined based on the desired parameters as Table 1.

Table 1. Characteristics and technical requirements of the shelling machine

No.	Name of particular product and its main quality criteria	Measurement unit	Quality level			Tentative quantity
			Achievement	Similar sample (according to newest standards)		
				Domestic	international	
1	2	3	4	5	6	7
1	Shelling machine	machine				02
2	productivity	ton/h	4 ÷ 5	2 ÷ 2,5		
3	Motor power	kW	6	5,5		
4	Parameters adjusting methods	-	Automation according to feedback	manual		
5	Peeled rate	%	increasing 10	70 ÷ 80		
6	Fracture rate	%	decreasing 1	5 ÷ 6		

- Main objective: The improved huller will improve the following objectives:

+ Target Factor 1: The rate of peeling is over 90%.

Target factor 2: Breakage ratio less than 4%.

- Solution: The peeling rate is 90% and the smallest fracture rate.

Automation of feed system: to maintain the required input to produce, reducing the phenomenon of lack of load for the machine.

+ Automatically adjusts the compressive pressure to maintain the current value (the gap value of the rubber rollers) to ensure a high shelling ratio while still ensuring the lowest possible fracture rate. Automatically adjust the feed trough position between the gaps of the rubber rollers when the rubber rollers are worn to ensure the breakage rate is as low as possible.

Figure 2. The machine in practice at enterprise

4. Concluding Remarks

Vietnam is the sixth largest rice growing area in the world, concentrated in the Mekong Delta, the Song Hong River Delta and the Central Coast. The rice productivity in our country has been increasing continuously for many years. Currently, in the world, the research on the peeling machine of the school, the Institute is not significant but mainly from the

manufacturers. This paper presented the model of rice husk husking machine improvement and analyzed the factors which need to be enhanced for equipment's productivity.

References

[1] H.Zareiforoush, M.H. Komarizadeh and M.R. Alizadeh, Effect of moisture content on paddy properties - University of Urmia, Urmia, Iran Rice Research Institute of Iran, Rasht, Iran - 2009

[2] Vo Hung Anh, Report: "Measures to Improve Rice Grain Quality and Reduce Loss of Rice Harvesting in the Mekong Delta" - Rice Festival in Hau Giang - December 2009.

[3] Phan Hieu Hien, Nguyen Van Xuan - Report: "Postharvest Technology in the Mekong Delta 2008" - Nong Lam University - 2009.

[4] Pham Van Tan, Situation of drying, preserving and processing rice in the Mekong Delta, Report at post harvest workshop in Vung Tau - April 2009.

[5] Bui Duc Hoi (editors), Food Processing Techniques - Volume 1, Hanoi Science and Technology Publishing House, 2006.

[6] Harry Van Ruiten, Xe Na Na on Rice Processing Techniques, Nong Lam University, Ho Chi Minh City, 1990.

[7] US5873301, Roll type husking apparatus with inclined guide chute.

[8] Nitat Tangpinijkul, Rice Milling Systerm, Post-harvest Engineering Research Group Agricultural Research Institute, Department of Agriculture, Thailand, 2008.

[9] Le Hong Khanh, Mai Van Le, Le Thi Cuc, Hoang Thi Ngoc Chau, Le Ngoc Tu, Luong Hong Nga. Food Processing Technology, Science and Technology Publishing House.

[10] US7296511, Rice hulling roll driving apparatus in rice huller.

[11] F. Garibondi, Rice milling equipment operation and maintenance, FAO, 1988.

[12] James E. Wimberly, Technical handbook for the paddy rice postharvest industry in Developing Countries, International Rice Research Institute Los Banos, Laguna, Philippines, 1983.

[13] Esmaeil Riahi and Hosahalli S. Ramaswamy, Handbook of postharvest technology, McGill University, Sainte-Anne-de-Bellevue, Quebec, Canada.

[14] Srinivas, Sathyendra Rao, Shridhar, Kumaravelu, Computer simulation and control of Rubber roll sheller, CSIR Madras Complex, Taramani, CHENNAL.

[15] Nguyen Van Xuan, Le Quang Vinh, Report: "Evaluation of the effect of initial moisture content on rice husking mill system, productivity 1 ton / hour", Cantho University , October 2008.

[16] Nguyen The Ha, Report: "Implementing Resolution 48 / NQ-CP on reducing postharvest losses, capacity and responsibility", Rice Festival in Hau Giang, 2009.

[17] T. Anthony Royal, Dr.John W. Carson, Fine power flow phenomena in Bins, Hopper, and Processing Vessels.

[18] Nguyen The Ha, Report: "Implementing Resolution 48 / NQ-CP on Reducing Post Harvest Loss, Capacity and Responsibility", Rice Festival in Hau Giang, 2009.

[19] Nguyen The Hung, Thuan Luu Thuc Si - Study on some parameters affecting the quality of rice after shelling of small shelling machine in Lam Dong Province, Faculty of Mechanical Engineering, University of Agriculture and Forestry, 2006.

Experimental Operation and Performance Evaluation of Waste Remover in Aquaculture Ponds

Le The Truyen[1, 2], Thanh-Long Le[1,3]
[1]Key Laboratory of Digital Control and System Engineering, HCMUT (DCSELAB), Vietnam
[2]Ho Chi Minh City University of Food Industry, Vietnam
[3]Faculty of Mechanical Engineering, Ho Chi Minh University of Technology (HCMUT), VNU-HCM, Vietnam

ABSTRACT

This paper introduces the experimental operation and performance evaluation of waste remover in shrimp farming ponds. The effects of waste on the shrimp farming environment were determined by analyzing the results of measuring the water quality parameters in the ponds, thereby evaluating the performance of the equipment.

The experimental model consists of a shrimp farming pond, a waste remover, an automatic monitoring system for water quality parameters (DO, H_2S, NH_3, pH and temperature).

The measuring results show that the water quality parameters are within the allowable limits if the waste remover is operated once a day.

1. Introduction

Brackish water shrimp farming is an important economic industry of Vietnam with current export in amount of USD 3.85 billion and expected export in 2025 is USD 10 billion.

To increase productivity, high tech intensive and supper intensive shrimp farming methods are implemented to production practice with increasing proportion.

The area of high tech shrimp farming is planned to be 100,000 ha in 2020.

The main features of high tech shrimp farming are using small ponds (less than 1000 m2) with bottom lined by HDPE sheets to isolate the rearing environment from negative factors such as: Acid sulfate soil, harmful microorganisms from earthen pond bottoms.

Although HDPE line bottom eases solid waste collecting in the center of the pond by paddle wheels (then waste will be removed from pond), part of solid waste is still settled on the bottom and stick to the HDPE surface. This layer of the organic material also becomes the favorable environment for harmful bacteria to grow. It is observed that there is a sticky, slippery layer on the surface and it is not easy to be removed just by water flow caused by paddle wheels. To remove this layer from the HDPE surface, mechanical force should be applied.

Currently, every day, workers in farm should get down to the pond, with long handle cleaning brush to rub the surface to remove waste stick to HDPE surface of pond bottom. The waste removed from HDPE line will be mixed with the pond water, and then collected to the center of pond thank circle flow created by paddle wheels.

This is not only hard and harmful work for worker health, but also it becomes difficult to find workers who agree to do this work. Development of an automated waste remover from HDPE pond bottom becomes indispensable.

Some characteristics of HDPE pond bottom are favorable to use machines to remove waste on the surface are: a) having enough flatness for mechanical equipment moving; b) having high stiffness and not easy to be dug under impact of mechanical force of cleaning and waste removing processes.

Based on above mentioned, an automated waste remover is designed, developed and tested to evaluate its performance and effectiveness for further development and application.

2. Materials and methods
2.1 Working principle and equipment structure
The completely manufacturing waste remover was tested at a shrimp farm in Can Gio District, Ho Chi Minh City (Figure 1).

Fig 1: The waste remover during operation

The device moves on the bottom of the pond, with two operating modes: self-propelled and manually controlled via a remote control. During operation, the axial pump have a suction tube diameter of up to 120 mm and a suction flow of 40 m³/h is arranged to draw waste on the bottom pond according to water stream into the filter bag. Axial pump has a three blades impeller, powered by a 170 W motor. The device travels at a maximum speed of 15 m/s through the friction between the tooth belt outer surface and the lining of the pond bottom. Two power 47 W servo DC motors are used to transmit motion to the two drive axles and are independently controlled. The brush shaft is arranged horizontally in front of and behind the device received drive from the two passive shafts via the transmission gear has ratio 2.15. The two brushing shafts are coated with soft bristles to brush the waste on the bottom of the pond, swirled them into under device and be sucked into the filter bag.

2.2 Trial run and evaluation

Experiment is carried out in 2 shrimp pond in Can Gio District of Ho Chi Minh City; from these 2 ponds, 1st is experimental pond, and 2nd pond is controlled pond.

The experiment is implemented during 15 days, from April 10, 2018 to April 25, 2018.

Condition of experiment is listed in Table 1.

Table 1: Condition of experiment

Parameter	Experimental pond	Controlled pond
Size of the pond	1000 m²	1000 m²
Bottom	HDPE lined	
Rearing animals	White leg shrimp	
Density	200 post / m²	
Crop starting day	February 23, 2018	
Cleaning method from Feb 23 to April 10, 2018	Manual	
Cleaning from April 10 (age of shrimp 46 days) to April 25, 2018	By waste remover	Manual
Average time for daily pond cleaning	90 minutes	180 minutes
Cleaning after April 25, 2018	Manual	

During testing period, water quality parameters, such as dissolved oxygen (DO), temperature, pH, and concentration of H_2S, NH_3 are measured.

The condition of measurement such as: equipment, sensors, and frequency are listed in Table 2.

There is no temperature adjustment equipment then water temperature depends on the environment temperature. Water temperature during experiment varied from 280C to 320C, and is the same in both ponds.

Dissolved oxygen is adjusted by aeration equipment and it is kept the same in both ponds, in level from 4.0 ppm to 6.8 ppm.

Table 2: Condition of water quality measurement

Parameter	Measuring method	Sensor/ Equipment	Frequency
Dissolved oxygen	Automatic	Sensorex DO6442TC/T	1 time/ 1 hr.
Temperature	Automatic	Vernier EasyTemp EZ-TMP	1 time/ 1 hr.
pH	Automatic	HANNA HI6100805	1 time/ 1 hr.
H_2S	Manual	HI 83200 Multiparameter Bench Photometer for Laboratories	1 time/ day at 15:00 pm
NH_3	Manual		

pH is adjusted by adding calcium oxide (CaO) and molasses to keep this value the same in both ponds and in level from 7.5 – 8.0. Adding calcium oxide (CaO) and molasses is carried out twice a day, at 6:00 am and 17:00 pm.

Probiotics are added to the both ponds in the same scheme.

Siphon and water change is the same for both ponds during testing period.

The results of H_2S measurement during 15 days show that water does not contain H_2S. This is explained by fact that there is very little sludge accumulation at the bottom because bottom is cleaned daily manually or by waste remover.

The results in measuring NH_3 (ppm) during 15 days are presented in Fig 2 in bellow:
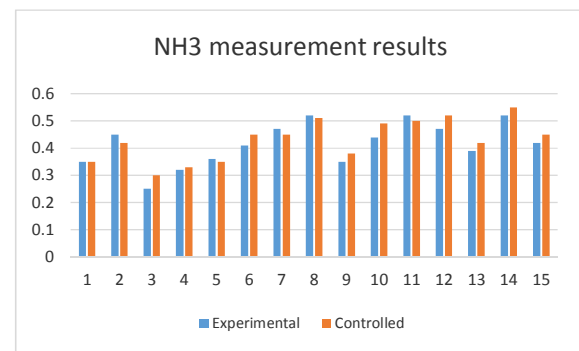
Fig 2: NH_3 measurement results during testing period

Statistical data of NH+ measurement results is listed in Table 3.

Table 3: Statistical data of NH+ measurement

Parameters	Experimental pond	Controlled pond
Average NH$_3$ concentration, ppm	0.41	0.46
Standard deviation, %	7.7	7.3

The test results show that water quality in both ponds are the same and waste remover can ensure quality of bottom as the same as manual cleaning, or another ways speaking, manual cleaning totally can be replace by cleaning using waste remover.

2.4 Social and economic effectiveness

The most valuable benefit of waste remover is to protect the health of workers and ensure the daily cleaning of pond bottom even in case cleaner is not available for keeping pond bottom in good condition.

Monthly expenses for 1 worker are about USD 400, and 1 worker can clean 2 ponds a day.

Waste remover can clean 6 ponds with one worker. Then, the monthly saving is expenses for 2 workers in amount of 800 USD. That means yearly manpower saving is USD 9600.

Additional expenses are electricity and maintenance cost is about USD 1,600/ year.

The planned sale price is USD 8000 and then equipment is paid back after 1 year.

Using waste remover twice daily to improve water quality requires additional study

3. Results and Discussion

- Waste remover can work well on HDPE shrimp pond bottom.
- 1 time per day cleaning by waste remover gives the same water quality in comparison with manual cleaning.
- Waste remover can save worker's health and help to solve the manpower shortage.
- Waste remover expected to be paid back after 1 year.
- Additional study is required for 2 times cleaning using waste remover to improve water quality and electricity saving.

References

[1] M. Ayub Hossain Ashoke Kumar Sarker M. Nurul Amin M. Mokarrom Hossain M. Sumon Miah, Development and performance evaluation of sludge remover for intensive aquaculture, Aquacultural Engineering, 201.

[2] Jaapvan Rijn, Waste treatment in recirculating aquaculture systems, Aquacultural Engineering, Volume 53, March 2013, Pages 49-56.

[3] R.Casillas-HernándezaH. Nolasco-Soriab T.García -GalanocO. Carrillo-FarnesdF.Páez-Osuna, Water quality, chemical fluxes and production in semi-intensive Pacific white shrimp (Litopenaeus vannamei) culture ponds utilizing two different feeding strategies, Aquacultural Engineering, Volume 36, Issue 2, March 2007, Pages 105-114

PART VI, SECTION II

Materials Technology
(Functional Materials; Technologies of Materials; Materials Characterization and Evaluation;
High Speed Machining and Abrasive Machining; Micro- and Nano-Systems Engineering and
Emerging Technologies; Surface Integrity and Machining Quality…)

Study on High Quality Thermal Stress Cleavage of Thick Sapphire Wafer

Tomoya Kawabe[1], Tatsuaki Furumoto[2], Yohei Hashimoto[2], Tomohiro Koyano[2], Yuzo Ochi[3], Kentaro Oguchi[3], Yuji Chino[3], Akira Hosokawa[2]

[1] Graduate school of National Science and Engineering, Kanazawa University, Japan
[2] Institute of Science and Engineering, Kanazawa University, Japan
[3] SHINKOSHA Co., Ltd, Japan

ABSTRACT

This study deals with high quality thermal stress cleavage of thick sapphire wafer with thickness of 5 mm. The influence of the distance from the edge to the initial crack, laser power, and plane orientation on the cleavage characteristics was experimentally investigated. The results indicate that the surface waviness W_a at the cleaved surface was influenced by the distance from the edge. A cleaved surface with good surface characteristics was obtained by cleaving with low laser power. The cleavage direction also affects the cleaved surface characteristics.

1. Introduction

Sapphire has high hardness, high thermal conductivity, and excellent light transmittance to visible light, and is generally used as a white LED, polarized light holding plate of a projector, and windshield of a wrist watch. Conventional sapphire processing methods include dicing and scribing using diamond tools. Dicing is a process of cutting a material using a diamond blade saw rotating at high speed [1]. Scribing is a process in which a cutting line is scribed using a diamond scriber; then, mechanical bending stress is applied to the material, and the material is cut along a cutting planed line [1]. However, since sapphire has high hardness, tool wear and micro cracks generated on the processed surface are identified as challenges. Furthermore, in recent years, environmentally friendly machining is preferred; therefore, chips generated during machining, cutting cost, and working fluid required for machining pose additional problems. Thermal stress cleavage using laser is one of the methods for processing hard and brittle materials [2]. In this method, a crack is developed due to thermal stress produced by irradiating laser on a material and the material is cut so that a very clean cleaved surface can be obtained. In addition, this method is environmentally friendly, does not require a working fluid and does not generate any chips. It has been reported that thermal stress cleavage using laser is possible for hard and brittle materials [3-9], and it is possible to prevent thermal damage on the irradiated surface and the cleaved surface by setting appropriate laser irradiation conditions [10]. However, since sapphire is widely used as LED substrate material, research on the laser cleavage of thin sapphire has matured over the years, while studies on the laser cleavage of thick sapphire have not been reported. Thick sapphire is expected to be useful in applications such as aircraft windows. Considering that it is difficult to implement contact processing because of its high hardness and thickness, thermal stress cleavage using laser is considered effective like thin sapphire. Therefore, in this study, we investigated the effectiveness of thermal stress cleavage using laser as a method for cutting thick sapphire.

2. Principle of laser cleavage

Fig. 1 shows the principle of thermal stress cleavage using a laser beam. Thermal stress cleavage using a laser beam is a processing method in which thermal stress due to laser irradiation is produced at the tip of a crack formed beforehand, and cracks are developed to separate the material. The surface temperature rises rapidly in the laser irradiated area, and thermal expansion occurs accordingly. This thermal expansion is constrained by the surrounding low temperature area; therefore, compressive stress field is produced in the irradiated area, and tensile stress field is also produced in the periphery of the irradiated area. When the tip of the crack is in this tensile stress field, the crack propagates toward the center of the irradiated area so that the specimen can be cut by scanning the laser along the cutting path.
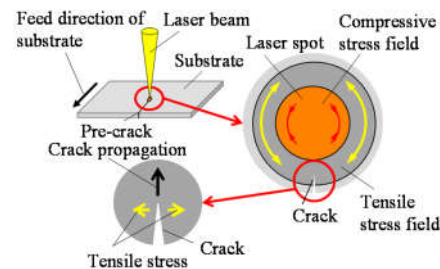
Fig. 1 Principle of laser cleavage

3. Experimental setup

3.1 Characteristics of sapphire

Table 1 presents the physical properties of sapphire used in this study and soda-lime glass used in a wide

range of industrial applications. The Vickers hardness indicates that sapphire has a hardness of approximately three times that of soda-lime glass, which indicates that the material is very hard. The thermal conductivity of sapphire is approximately 40 times that of soda-lime glass, while the thermal diffusivity is approximately 20 times that of soda-lime glass, which indicates that heat is easily conducted into the material. The linear thermal expansion coefficient of sapphire is approximately half that of soda lime glass, while the thermal stress produced is very small. The fracture toughness of sapphire is approximately twice that of soda-lime glass, and cracks progress with difficulty. The above properties indicate that compared to soda lime glass, sapphire is difficult to process by thermal stress cleaving using laser.

Fig. 2 shows the crystal structure of sapphire. The structure shows that sapphire is a hexagonal crystal, mostly using the c-plane perpendicular to the c-axis. In this research, sapphire with crystal orientation <0001> on the c-plane was used.

3.2 Thermal stress cleavage of sapphire using laser

Fig. 3 shows a schematic of the experimental setup, while Table 2 presents the experimental conditions. The laser used for the thermal stress cleavage was a continuous wave CO_2 laser (Universal Laser Systems: ULR-100) with a wavelength of 10.6 μm. The defocused laser was used to irradiate the surface of the specimen, and the beam diameter at the irradiated surface was 2.6 mm. The specimen was set on a precision positioning stage, and was irradiated along the cutting path by scanning the stage. The specimen used was a sapphire wafer of (0001) crystal orientation with a thickness of 5 mm. The initial cracks introduced mechanically were used for thermal stress cleavage. The position of the initial crack was selected for each condition and the influence of the distance from the edge to the cleaving path on the waviness at the cleaved surface was investigated. The waviness at the cleaved surface was measured using a surface profile measuring instrument (Tokyo Seimitsu: SURFCOM 2000DX2). In addition, a specific laser power was selected for each condition and the influence of laser power on the characteristics of the cleaved surface was investigated. At this time, cleavage was performed at the center of the sapphire specimen. The influence of the plane orientation on the perpendicularity between the sapphire specimen surface and the cleaved surface was also evaluated. Cleavage was performed in two directions: [-1100] direction parallel to the a-plane (11-20) and [-1-120] direction parallel to the m-plane (1-100).

Table 1 Physical property of sapphire and soda-lime glass

Physical property		Sapphire	Soda lime glass
Density	[kg/m^3]	3.97×10^3	2.50×10^3
Young module	[GPa]	470	72
Thermal expansion coefficient	[1/K]	5.3×10^{-6}	9.3×10^{-6}
Thermal conductivity	[W/(m·K)]	42	1.3
Specific heat	[J/(g·K)]	0.75	0.84
Thermal diffusivity	[m^2/s]	141×10^{-7}	6.19×10^{-7}
Vickers hardness		1800～2100	540～600
Fracture toughness	[MPa·m$^{1/2}$]	1.96	0.78
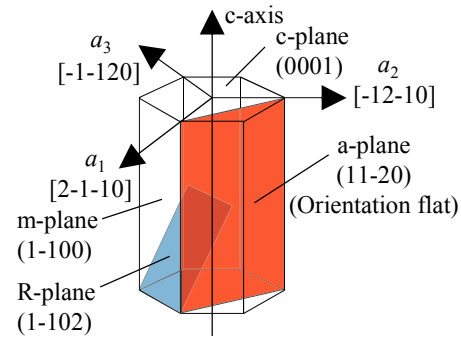
Fig. 2 Crystal structure of sapphire
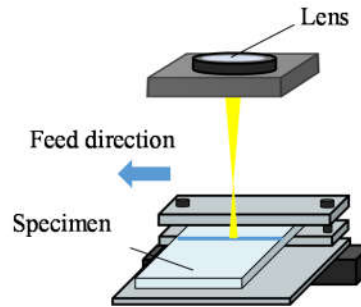
Fig. 3 A schematic illustration of the experimental setup

Table 2 Experimental conditions

Laser			CO_2 laser
Irradiation mode			Continuous wave
Wavelength	λ	[μm]	10.6
Laser power	Q	[W]	33.7, 35.4, 39.3, 45.9
Feed rate	V	[mm/s]	2
Beam diameter	D	[mm]	2.6
Energy density	P	[J/mm^2]	6.48, 6.81, 7.56, 8.83
Specimen			Sapphire wafer (0001) face
Size		[mm]	$40 \times 60 \times 5$
Installation of initial crack			Machining

4. Results and Discussion

4.1 Variation of waviness with distance from the specimen edge

Fig. 4 shows the variation of the surface waviness

W_a at the cleaved surface with the distance from the specimen edge to the cleaving position. The waviness decreased as the distance from the cleaving position to the edge increased. The surface waviness W_a of the cleaved surface was 840 μm when the distance from the edge was 6 mm, and 162 μm when the distance from the edge was 18 mm. These results indicate that the waviness at the cleaved surface was significantly influenced by the temperature distribution produced by laser irradiation around the cleaving path. When cleaving was carried out near the specimen edge, heat from the laser irradiation accumulated on the specimen edge, and the temperature distribution around the cleaving path became asymmetric, which increased the waviness of the cleaved surface. On the other hand, when the distance from the cleaving position to the specimen edge increased, there was no heat accumulation at the specimen edge, which decreased the waviness.

4.2 Influence of laser power on cleaved surface

Fig. 5 and Fig. 6 show the variation of the surface waviness W_a at the cleaved surface and the variation of the surface roughness R_z at the cleaved surface with the laser power. In Figure 5 and Figure 6, both the surface waviness W_a and the surface roughness R_z decreased as the laser power decreased. This is due to the decrease in the energy density of the laser irradiated area. The energy density indicates the amount of energy applied per unit area, and the energy density also decreased as the laser power decreased. As the energy density decreased, the thermal stress applied to the tip of the initial groove also decreased such that the surface characteristics of the cleaved surface were considered to be favorable. Fig. 7 and Fig. 8 show images of the cleaved surfaces and laser irradiated surfaces obtained by cleaving using laser power of 39.4 W and 33.7 W, respectively. Clean cleaved surfaces were obtained at both laser power values, but microcracks extended from the grooves at the laser irradiated surface at laser power of 39.4 W, whereas microcracks were not produced around the grooves at laser power of 33.7 W. This is because the temperature increase at the center of the irradiated portion became steep when the laser power increased, and the thermal stress produced at the tip of the groove increased. These results indicate that it is possible to obtain a cleaved surface with good surface characteristics without cutting microcracks on the laser irradiated surface by performing cleaving with low laser power.

4.3 Variation of perpendicularity with laser conditions

Fig. 9 shows the influence of the cleavage direction on the amount of deviation from 90° by the angle formed by the laser irradiated surface and the cleaved surface, while Figure 10 shows the cross-sectional image of the cleaved surface obtained by cleaving parallel to the a-plane and m-plane.
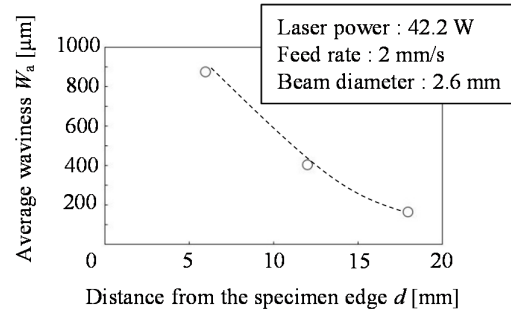
Fig. 4 The variation of the surface waviness W_a at the cleaved surface with the distance from the specimen edge to the cleaved position
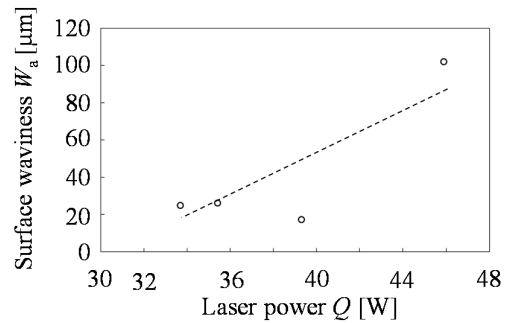
Fig. 5 Variation of the surface waviness W_a at the cleaved surface with the laser power
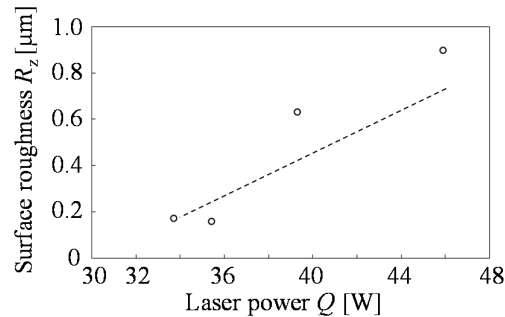
Fig.6 Variation of the surface roughness R_z at the cleaved surface with the laser power

(a)Irradiated surface   (b)Cleaved surface
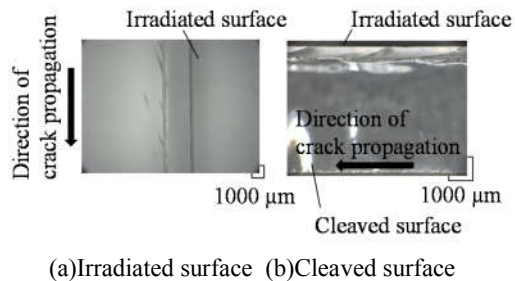
Fig. 7 Image of cleaved surfaces and laser irradiated surfaces obtained by cleaving with laser power of 39.4 W

449

As shown in Figure 9 and Figure 10, when leaving was performed parallel to the a-plane, a cleaved surface perpendicular to the specimen surface was obtained. On the other hand, when cleaving was performed parallel to the m-plane, a slanted cleaved surface was obtained. This is due to the influence of other crystal orientations.
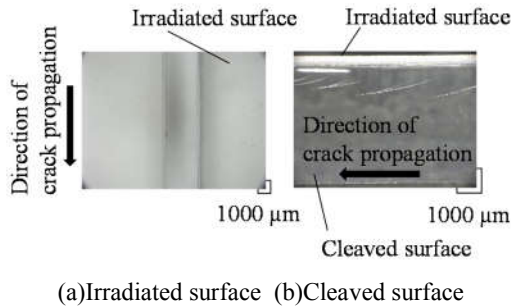
(a)Irradiated surface (b)Cleaved surface
Fig. 8 Image of cleaved surfaces and laser irradiated surfaces obtained by cleaving with laser power of 33.7 W
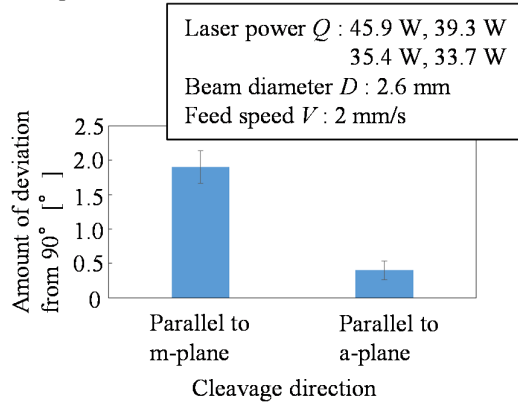
Fig. 9 Influence of the cleavage direction on the amount of deviation from the angle of 90 degrees of the angle formed by the laser irradiated surface and the cleaved surface

(a) Cleavage parallel   (b) Cleavage parallel
   to m-plane   to a-plane
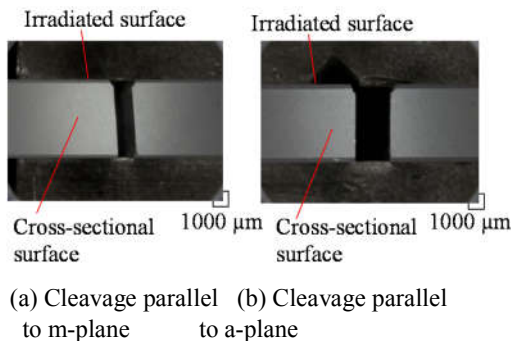
Fig.10 Cross-sectional image of the cleaved surface obtained by cleaving in parallel to a-plane and m-plane

In the c-plane sapphire, cleavage occurred on the R-plane in addition to the a-plane and the m-plane. As shown in Fig. 2, the crystal orientation of the R-plane was (1-102). When cleaving was performed parallel to the m-plane, a crack propagated along the R-plane, and the angle formed by the specimen surface and the cleaved surface deviated significantly from 90°. On the other hand, when cleaving was performed parallel to the a-plane, a crack propagated along the a-plane, and a cleaved surface perpendicular to the specimen surface was obtained.

5. Concluding Remarks

In this study, the effectiveness of thermal stress cleavage as a method for cutting thick sapphire using laser was investigated. The main results obtained are summarized below.

(1) The surface waviness W_a at the cleaved surface was significantly influenced by the distance from the edge to the cleaved position, and its value was improved by controlling the temperature distribution around the laser irradiated area.

(2) It is possible to obtain a cleaved surface with good surface characteristics without cutting microcracks on the laser irradiated surface by performing cleaving at low laser power.

(3) When cleavage is performed parallel to the a-plane (11-20), it can be performed perpendicular to the laser irradiated surface of the bottom face; when cleavage is performed parallel to the m-plane (1-100), the cleavage surface is inclined.

References

[1] Mitsuru Sugata, Laser scribing methods of the sapphire substrate, Journal of the Japan Society of Grinding Engineers, 49, 4(2005)191-194

[2] Toshihiro Okiyama, Cleavage-Cutting of Brittle Materials by Laser Heating, Journal of the Japan Society for Precision Engineering, 60, 2(1994)196-199

[3] J. Xu, H. Hu, C. Zhuang, G. Ma, J. Han, Y. Lei, Controllable laser thermal cleavage of sapphire wafer, Optics and Lasers in Engineering, 102(2018)26-33

[4] R. M. Lumley, Controlled Separation of Brittle Materials Using a Laser, The American Ceramic Society Bulletin, 48, 9(1969)850-854

[5] Y. Imai, H. Morita, T. Takase, H. Koga, Possibility of Employing Thermal Stresses as a Cutting Device for Brittle Materials, Transactions of the Japan society of mechanical engineering. A, 55, 509, 147-151

[6] J. Jiao, X. Wang, Cutting glass substrates with

dual-laser beams, Optics and lasers in Engineering, 46(2009)860-864

[7] T. Kurose, K. Ichikawa, H. Nagai, Breaking of Silicon Wafer by Irradiation of YAG Laser, Journal of the Society of Materials Science, Japan, 44, 497(1995)159-163

[8] T. Ueda, K. Yamada, K. Oiso, A. Hosokawa, Thermal Stress Cleaving of Brittle Materials by Laser Beam, CIRP, 51, 1(2002)149-152

[9] L. J. Yang, Y. Wang, Z. G. Tian, N. Cai, YAG laser cutting soda-lime glass with controlled fracture and volumetric heat absorption, International Journal of Machin Tools & Manufacture, 50(2010)849-859

[10] T. Ueda, T. Mino, T. Furumoto, A. Hosokawa, S. Nagatomo, Laser cleaving of sapphire wafer with pulsed CO_2 laser, Journal of the Japan Society of Grinding Engineering, 55, 7(2011)424-426

Development and Analysis for a New Compliant XY Micropositioning Stage Applied for Nanoindentation Tester System

Minh Phung Dang[1,a], Thanh-Phong Dao[2,3,b*], Hieu Giang Le[1,c],

[1]Faculty of Mechanical Engineering, Ho Chi Minh City University of Technology and Education, Vietnam

[2]Division of Computational Mechatronics, Institute for Computational Science, Ton Duc Thang University, Ho Chi Minh City, Vietnam

[3]Faculty of Electrical & Electronics Engineering, Ton Duc Thang University, Ho Chi Minh City, Vietnam

[a]phungdm@hcmute.edu.vn, [b*]daothanhphong@tdt.edu.vn, [c]gianglh@hcmute.edu.vn

ABSTRACT

Compliant XY micropositioning stage is purported for situating a material sample in nanoindentation tester process. This paper aims to develop, analyze and optimize a XY compliant micropositioning stage based on a beetle's profile. The working stroke of proposed XY stage is amplified by using the six-lever and a half bridge amplification mechanism. To enhance the performances of the stage, the main geometric parameters are optimized by an integration method of response surface method with differential evolution algorithm. Firstly, the number of experiments and the data are retrieved by combination of the finite element analysis-integrated response surface method (RSM). Secondly, the effects of main design variables on the output responses sensitivity are considered. Later on, mathematical models for the displacement and stress were established by the RSM. Finally, based on mathematical equations, differential evolution algorithm is adopted to define the optimal design variables. Based on the output responses sensitivity is analyzed, the results showed that the design variables of the stage and the output responses sensitivity have a closed relationship. The results of FEA validations are in a good agreement with the predicted results from the proposed hybrid approach. The results depicted that the proposed hybrid approach ensures a high reliability for engineering optimization problems.

Keywords: Compliant mechanism; XY micropositioning stage; Multi-objective optimization, Response surface method; Differential evolution algorithm.

References

[1]	L.J. Lai, Z.N. Zhu, Design, modeling and testing of a novel flexure-based displacement amplification mechanism, Sensors and Actuators A: Physical. 266 (2017) 122-129.

[2]	T.P. Dao, et al., Analysis and optimization of a micro-displacement sensor for compliant microgripper, Microsystem Technologies. 23.12 (2017) 5375-5395.

[3]	T.P. Dao and S.C. Huang, Design and multi-objective optimization for a broad self-amplified 2-DOF monolithic mechanism, Sādhanā. 42 (2017) 1527-1542.

[4]	Q. Xu, Design of a Large-range compliant rotary micropositioning stage with angle and torque sensing, IEEE Sensors. 15.4 (2015) 2419-2430.

[5]	T.H. Hou, C.H. Su, W.L. Liu, Parameters optimization of a nano-particle wet milling process using the Taguchi method, response surface method and genetic algorithm, Powder Technology. 173 (2007) 153-162.

[6]	T.P. Dao, S.C. Huang, P. T. Thang, Hybrid Taguchi-cuckoo search algorithm for optimization of a compliant focus positioning platform, Applied Soft Computing. 57 (2017): 526-538.

[7]	S.C. Huang, T.P. Dao, Multi-objective optimal design of a 2-dof flexure-based mechanism using hybrid approach of grey-taguchi coupled response surface methodology and entropy measurement, Arabian Journal for Science & Engineering. 41.12 (2016) 5215-5231.

[8]	R.V. Rao, V. Patel, Multi-objective optimization of heat exchangers using a modified teaching-learning-based optimization algorithm, Applied Mathematical Modelling. 37 (2013) 1147-1162.

[9]	Q. Xu, Design and testing of a novel multi-stroke micropositioning system with variable resolutions, Scientific Instruments. 85 (2014) 025002.

[10]	P. Wang, Q. Xu, Design of a flexure-based constant-force XY precision positioning stage, Mechanism and Machine Theory. 108 (2017) 1-13.

[11]	W. Hua, X. Zhang, Input coupling analysis and optimal design of a 3-DOF compliant micro-positioning stage, Mechanism and Machine Theory. 43 (2008) 400-410.

Investigation of the Bio-nanomechanical Effects of Citric Acid on Staphylococcus Aureus by 3D Printed AFM Fluid Cells

Nguyen Thi Phuong Linh[1], Bernard Haochih Liu[1]

[1]Department of Materials Science and Engineering, National Cheng Kung University, Taiwan

ABSTRACT

The atomic force microscopy (AFM) is a widely used surface scanning apparatus capable of reconstructing the 3D morphology of sample at nanometric scale resolution. An AFM physically senses the sample's surface with a sharp probe, building up a map of the sample surface. For bio-medical research, one of the promising advantages of AFM is its capability to scan in liquid. This work combined the functions of 3D printers, AFM, and finite element analysis software to develop a 3D printed fluid cell for AFM measurements in liquid to investigate the mechanism of chemicals on the bio-sample structure, especially disease-causing its capability to bacteria. *Staphylococcus aureus* is classified as a Gram-positive bacterium, which causes a prevalent human pathogen via broken skin or mucous membranes, such as nosocomial infection of surgical wounds. In this study, citric acid was chosen to study its effect on Staphylococcus aureus. Using AFM in liquid with a self-developed 3D printed fluid cell, the adhesion, and deformation of the bacteria in the pH range of citric acid solution was carefully studied. The experimental results will be presented and discussed in this work.

Keywords: AFM, 3D printed fluid cell, *Staphylococcus aureus*, liquid-phase scan, Citric acid, adhesion, deformation.

Development of Visual Inspection Using Patterned Area Illumination Method: Simulation for Classifier Based on Deep Learning

Tadanori Sugino[1], Kakeru Nakamura[1], Yasuo Yamane[2]
[1] National Institute of Technology, Oshima College
Oshima-gun, Yamaguchi-ken, 742-2193, Japan
[2] Hiroshima University
Higashi-Hiroshima-shi, 739-8527, Japan

ABSTRACT

The authors are developing a visual inspection method to detect microscopic defects on a painted surface using patterned area illumination method. In order to improve the speed and quality of defect detection in the method, we aim at detection by using a classifier created by machine learning (deep learning). In this research, we tried to generate learning data including defects by CG simulation with the aim of improving the performance of the classifier for classification between the OK image and NG image having a microscopic defect.

Keywords: patterned area illumination, classifier, deep learning, ray tracing, image processing

1. Introduction

Some methods of giving a black-and-white geometric pattern to surface of illumination, giving a change in brightness, and performing an appearance inspection has been proposed. Both methods emphasize image of defect by pattern and detect defects [1-3]. In our former research, we proposed inspection methods such as making the pattern shape into a triangle check pattern so far [4]. We have been developing a visual inspection method to detect microscopic defects on a painted surface using the patterned area illumination method. However, the proposed method requires a lot of image processing time. Also, when the defect part is located near the boundary of the pattern of reflection image on an inspection object, it is difficult to detect the defect. Therefore, in order to improve the speed and quality of defect detection in this research, we aim at detection by using a classifier created by machine learning (deep learning).

It is widely known that the success or failure depends on the quality and quantity of learning data in the generation of the classifier using deep learning. In this method, stripe, block check, triangle check etc. are used according to the situation. We need a lot of OK / NG data in these patterns. For NG data, it is difficult to generate a large number of data because the occurrence ratio of defects is small. Then, in this research, we tried to generate learning data including defects by simulation with the aim of improving the performance of the classifier for classification between the OK image and NG image having a microscopic defect.

In order to generate the learning data including defects, firstly, shape data of an actual defect is measured and placed on an arbitrary surface of an inspection object to obtain a simulation image (CG). At that time, a representative surface of the defect shape is calculated and the representative surface is placed on the inspection object surface obtained from the CAD data to reproduce the surface having the defect. In order to generate the CG, the ray tracing method is used. If it becomes possible to freely generate learning data including defects, it is also possible to respond to new inspection objects in advance. We had developed the simulation system [5-7]. However, it was difficult to reproduce various situations with that system. Therefore, by using POV-Ray, which is well-established in the field of computer graphics, as a rendering engine, it is possible to cope with various situations.
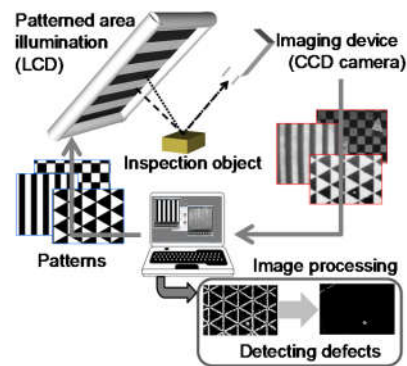

Fig. 1 Overview of visual inspection system using patterned area illumination method. Patterns are displayed on the LCD monitor. The reflected image on surface of an inspection object is obtained through CCD camera. A defect image is emphasized and

This report describes the development of the CG simulation method.

2. Visual Inspection System Using Patterned Area Illumination Method

We are developing a visual inspection system to detect a microscopic defect on a painted surface using the patterned area illumination method. Figure 1 shows the overview of the visual inspection system. For an illumination, a liquid crystal display (LCD) is used to enable instantaneous pattern switching. Various patterns matching the object to be inspected are displayed on this area illumination. A microscopic defect is emphasized by displaying the pattern image on the inspection object. Then it is possible to detect the microscopic defect.
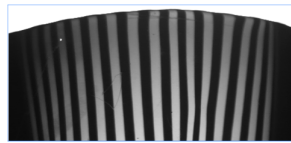
Fig. 2 Reflection pattern image on nonplanar surface of inspection object. A stripe pattern is projected on a nonplanar surface. The stripe image is distorted due to the nonplanar effect.
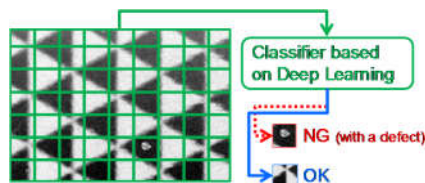
Fig. 3 Scheme of the method using classifier created by deep learning. The pattern projection image on the inspection object is divided into small regions and identified by OK and NG by the classifier.

Our research proposed the method of image processing for the image obtained from the system [4]. The method needs more time for processing. Therefore, this study adopts newly method for the image. The method uses classifier based on deep learning.

And more, a pattern for an inspection object is distorted along the nonplanar surface of the inspection object as shown in Fig. 2. In this way, the pattern projection image including the defect largely changes depending on the place where the defect exists, the degree of the plane at the place, and the positional relationship with the illumination and the pattern. However, in the method proposed so far, it is often the premise that the edge of the pattern image is a straight line, and it cannot cope with such an image. On the other hand, newly adopted classifier can handle that, since there is a high possibility that such situations can also be dealt with by incorporating them during machine learning.

3. Simulation for Classifier based on Deep Learning

In order to improve the speed and quality of defect detection in the method, we aim at detection by using a classifier created by deep learning.

Figure 3 shows the scheme of the method using classifier created by deep learning. In surface of an inspection object on which the pattern is projected, a defect image is emphasized by reflection of the pattern on the defect slope. In this inspection method, the emphasized defect part is detected. In the past proposed method, image processing is performed to leave only defects after (1) differentiation, (2) Hough transform, and (3) pattern component extraction. As described above, it takes much time to detect the defect image. However, once the classifier is generated, the OK / NG determination, that is, the detection of the region including the defect is performed instantaneously. Therefore, in this study, we aim at discrimination method of defect region using classifier generated using deep learning. The inspection image obtained by projecting the pattern as shown in Fig. 3 is divided into regions, and each small region is placed in a classifier to judge OK or NG.
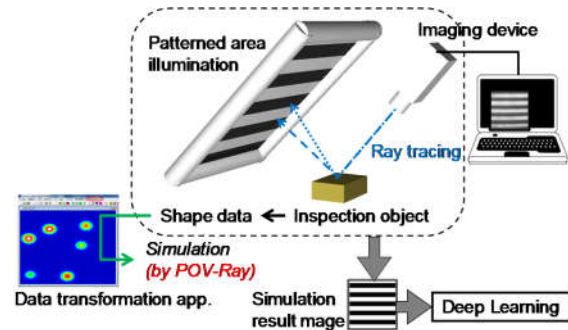
Fig. 4 Scheme of simulation by ray tracing. POV-Ray is used for simulation as rendering engine. The simulation result images are used for deep learning to create a classifier.

Figure 4 shows the scheme of simulation by ray tracing for deep learning. In the former research [5-7], we had developed a simulator for this system. Although the situation of patterned area illumination could be reproduced, it was difficult to reproduce the detailed situation as CG. Therefore, we newly decided to utilize application 'POV-Ray' [8] which reproduces precise CG by ray tracing method as a rendering engine. The ray tracing method is a method that is performed simulating actual physical behavior of light, and is known as a method capable of generating high quality CG. The simulation result images obtained by POV-Ray are used for deep learning to create a classifier. Besides, in order to simulate by using the shape data of the inspection object with POV-Ray, we developed a new data transformation application and used.

Figure 5 shows ray tracing in the proposed system. Figure 5(a) shows normal ray tracing in the POV-Ray. The light source of the POV-Ray is a point light source or an area light source in which point light sources are arranged. The light source that we used has a pattern. However, with normal ray tracing, it is difficult to simulate pattern illumination adequately. Therefore, we proposed a new simulation method shown in Fig 5 (b). By making the patterned area illumination not a light

(a) Normal ray tracing   (b) Proposed ray tracing
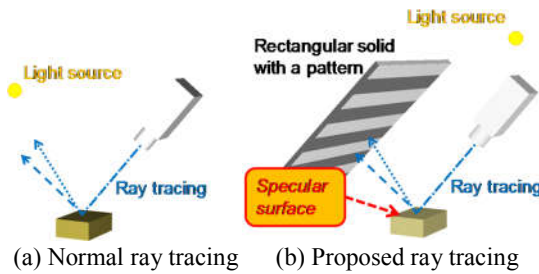
Fig. 5 Ray tracing in this method on POV-Ray. In the case of (a) shows normal ray tracing. (b) shows the proposed ray tracing. The method uses rectangular solid mapped patterns instead of illumination and the surface of inspection object is treated as specular surface.

source but a rectangular solid having a pattern, and the surface of the inspection object as specular surface, a pattern is reflected so as to reproduce a surface type pattern illumination It was decided to. This is because in the method using the patterned area illumination of this study, it is derived from imaging the specular reflection component of light and it is thought that the same image as projecting patterned illumination can be obtained.

It is possible to generate NG data including defects assuming every situation by placing shape data of a defect at an arbitrary location of an inspection object. In this research, we measured the actual defect shape with a shape measuring machine, saved it in STL format which is the form of shape data, and placed it on the STL format data of the inspection object, so that we simulated it. Naturally, it is possible to artificially create convex defects by using Gaussian distribution and so on, so it was also a system that can also be handled in STL format as well. The STL format is used for three-dimensional (3-D) CAD. It is a general form used to express the outline of a shape. Since the STL format itself cannot be read by POV-Ray, an application to transform to the POV-Ray format was developed as shown in Fig.4.
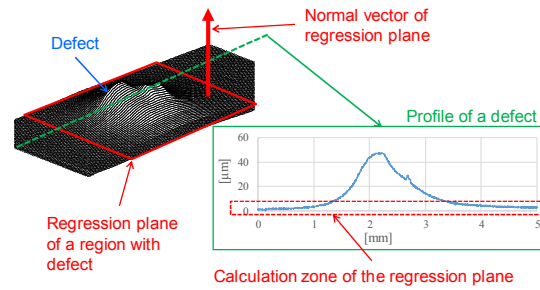
(a) Calculation of regression plane of a defect
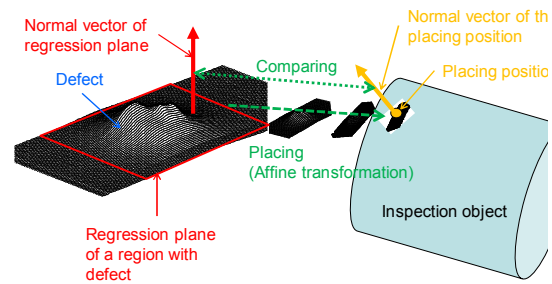
(b) Placing of a defect shape on an inspection object

Fig. 6 Placing method of defect shape data. (a) shows the scheme of calculation of regression plane of a defect. The regression plane is used for comparing the normal vector with a normal vector of placing position. (b) shows the scheme of the placing.

Figure 6 shows placing method of defect shape data for surface of inspection object. As shown in Fig 6(a), in the defect shape data, a regression plane of a portion close to a plane which does not correspond to the convex portion of the defect is obtained, and a normal vector of the regression plane is calculated. When calculating the regression plane, not all of the defect shape data are targeted, and the part other than the defective protruding part is targeted affects the calculation of the direction in which the base surface is oriented due to the influence of the convex part in order to prevent. Let the vector be a representative vector of defect shape data. Thereafter, as shown in Fig. 6(b), affine transformation is applied to the defect shape so that the normal vector at an arbitrary place where the defect shape on the inspection object is to be arranged and the representative vector of the defect are aligned in the same direction Thereby placing the defect on the inspection object.

(a) 3-D display of shape data of a defect

(b) A profile of the shape data
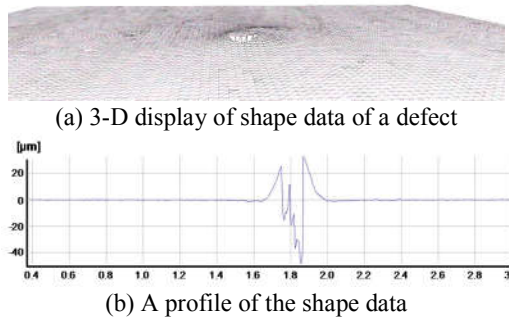
Fig. 7 Shape data of a defect for simulation. (a) is 3-D display of shape data of a defect. (b) is a profile of the shape data near the top of the convex.

4. Simulation Results and Discussion

Figure 7 shows shape data of a defect. The shape data was measured by the all-in-focus 3-D surface shape measurement device (Infinite Focus G4, Alicona Co., Ltd.). Figure 7(a) is 3-D display of shape data of a defect. Figure 7(b) is a profile of the shape data near the top of the convex. The height of the defect is almost 30 µm.

Figure 8 shows simulation results. Figure 8(a) is an actual image of the defect shown in Fig.7 obtained by the visual inspection system. Figure 8(b) is a simulation result with the block check pattern. There is the rectangular solid with a check block pattern that reproduces the light source. Figure 8(c) is the simulation result of the tilt placed situation on the inspection object. The defect is inclined according to the inclination of the inspection object. Figure 8(d) – (f) show the simulation result with stripe, block check and triangle check patterns respectively. The difference in situations of Fig.8(d) – (f) is only in patterns. Comparing among results of Fig.8(d) – (f), in case of the triangle check, the defect image is large. We know that the triangle check has largest defect image in this situation [4]. These results indicate the simulation and the actual image are close.

From the above results, it became possible to arrange defects on arbitrary inspection object and generate NG data. However, it may be necessary to smoothen the defect data a little more. We consider that it is nearer to smoothen the resulting image, when considering CCD pixel size. Besides, in simulation, it is necessary to adjust light intensity and the like to actual conditions. Finally, misalignment when the curvature of the inspection object surface is large needs to be dealt with in the future.

5. Conclusions

In order to improve the accuracy of Classifier based on Deep Learning, it is necessary to increase NG data for

learning, so we developed a system that generates NG data by simulation.

In the system, we developed a system that generates NG data by CG simulation using actual defects and shape data of artificially generated defects. by this. It is possible to simulate the occurrence of defects at an arbitrary place in an arbitrary inspection object and to generate various NG data.

In future, we plan to verify performance improvement of Classifier based on Deep Learning using this system. Moreover, in order to utilize it for learning of Deep Learning, it is necessary not only to impart defects to arbitrary places of the user, but also to provide a system that can automatically place defects in various places in a manner that gives as much diversity.

(a) Actual image   (b) Simulation result

(c) Tilt placed position   (d) Stripe pattern

(e) Block check pattern   (f) Triangle check pattern
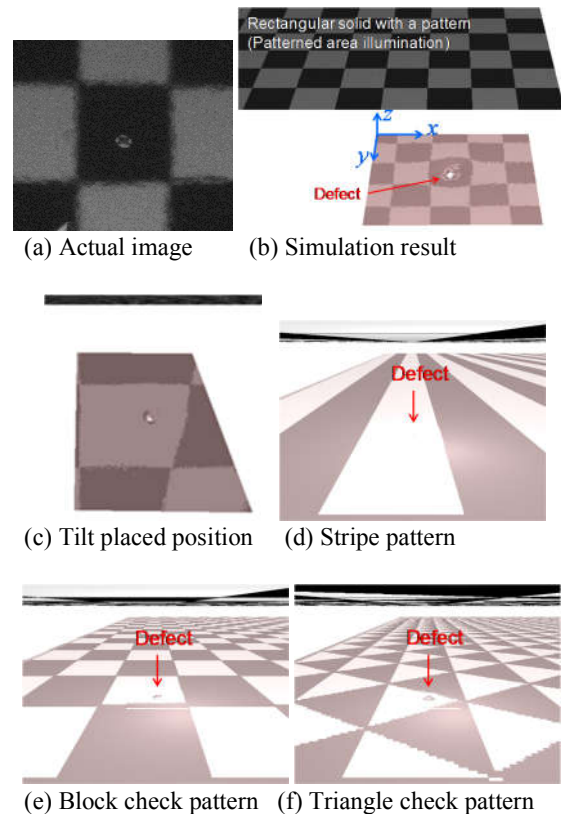
Fig. 8 Simulation results. (a) is an actual image of the defect shown in Fig.7 obtained by the visual inspection system. (b) shows a simulation result with the block check pattern. There is the rectangular solid with a check block pattern that reproduces the light source. (c) shows the simulation result of the tilt placed situation on the inspection object. The defect is inclined according to the inclination of the inspection object. (d), (e) and (f) show the simulation result with stripe, block check and triangle check patterns respectively.

Further, as a problem, when the defect shape data and the curvature of an arbitrary portion of the inspection

object are too different, it is impossible to fuse properly. Therefore, if it is possible to properly distort the defect shape according to the curvature of the placing position of the inspection object, it can deal with this. We will also develop this function in the future.

References

[1] K. Tanaka, Y. Shinbara H. Ikeda, N. Yamada, H. Kiba, K. Sasanishi, *Trans. of Japan Society of Mechanical Engineers,* 66, 7(2000) 1098-1102. (in Japanese)

[2] O. Hirose, A. Ishii, S. Hata, I. Wakasaki, *J. Japan Society of Precision Engineering*, 66, 7(2000) 1098-1102. (in Japanese)

[3] O. Hirose, A. Ishii, S. Hata, I. Wakasaki, *J. Japan Society of Precision Engineering*, 67, 7(2001) 1135-1139. (in Japanese)

[4] T. Sugino, K. Morikawa. Y. Yamane, *2005 JSPE Spring Conference*, (2005), 423-424. (in Japanese)

[5] T. Sugino, Y. Yamane, N. Narutaki, D. Nishioka, T. Otani, *Visual Inspection Engineering Workshop*, (2001), 152-157. (in Japanese)

[6] T. Sugino, M. Fujiyama, Y. Yamane, *12th Intelligent Mechatronics Workshop*, (2007), 27-32. (in Japanese)

[7] T. Sugino, Y. Yamane, *Key Engineering Materials*, 656-657 (2014) 468-472.

[8] http://www.povray.org/

The Inductance of the Very Short Conductors of Rectangular Cross Section in Program

T. Truong Cong[1], L. Fakri-Bouchet[2]

[1] Faculty of Engineering and Technology, Nong Lam University – Hochiminh City, Vietnam

[2] ISA – Institut des Sciences Analytiques; UMR 5280, Villeurbanne, France

Corresponding author: tien.truongcong@hcmuaf.edu.vn

ABSTRACT

The goal of the first part of this work is a bibliographic review of the most well-known formulas used for the calculations of both the partial self inductance and the mutual inductance. The purpose is mainly to specify their range of applicability and their current restricted of program. The second part is dedicated to establish a general formula to quantify the inductance of a subdivided conductor. This method is also applied to program the inductance of the planar microcoils considering different shapes and dimensions.

Keywords: Self-inductance, Mutual inductance, Micro-coil, Planar coil, Discretized conductor.

PART VI, SECTION III

Mechanical Technology
(Heat transfer, Thermal, and Fluid Engineering; Structures and Fluids; Vibration;
Energy Engineering; CAD/CAM/CAE/RP…)

Apply Twisted Savonius Rotor with Two Deflector Plates in Power Take Off Systems

Cao Dang Long[1], Cao Hung Phi[2], Nguyen Minh Huy[3], Dao Thanh Liem[1] and Truong Quoc Thanh[1]
[1] **Hochiminh City University of Technology.**
Add.: No. 268, Ly Thuong Kiet Street, district 10th, Ho Chi Minh City, Vietnam
[2] Vinh Long University of Technology Education
Add.: No. 73, Nguyen Hue street, 2nd ward, Vinh Long City, Vietnam
[3] HCMC University of Food Industry.
Add.: No. 140, Le Trong Tan street, 15th ward, Tan Phu District, Ho Chi Minh City, Vietnam

ABSTRACT

This paper aims to develop a model of Twisted Savonius Rotor (TSR) which consists of two blades in order to investigate the performance of a Power Take-Off (PTO) system. Here, two deflector plates are attached to the system to concentrate the fluid flow toward the advanced blade. In this study, the TSR used 40 degrees twisted blades and two blades which 30 degrees blade angle, and the optimum position of the deflector plate are expressed. The simulation of a TSR has been carried out to investigate the performance of wave energy conversion. The TSR with two deflector Plates having two blades shows promising results and can be incorporated into PTO devices to reduce costs of the turbine component of the system.

Keywords : Savonius rotor, Wave energy conversion, Power take-off, twisted blades, blade angle, defector plate.

Behavior of Multi-Corner Thin-Walled Structure Subjected to Axial Impact Load

Ly Hung Anh[1], Ngo Anh Vu[1]
[1]Ho Chi Minh City University of Technology
268 Ly Thuong Kiet Street, District 10, Ho Chi Minh City, Vietnam

ABSTRACT

This paper concentrates on the energy absorption of thin-walled columns with multi-corner cross section. Several configurations of multi-corner thin-walled columns are presented to study the behaviours subjected to axial crushing load by theoretical and numerical methods. Analytical formulations for predicting the mean crushing force, half folding length are derived based on the theory of Super Folding Element. To predict the response of thin-walled structures, numerical simulation is employed. Both numerical and analytical results show that multi-corner column has better potential in absorbing kinematic energy than square column.

1. Introduction

Thin-walled structures have become very familiar to whoever working on crashworthiness analysis and structural engineering for its outstanding kinematic energy absorbing ability along with cheap cost and light weight. Following the introduction of the Super Folding Element (SFE) of Wierzbicki and Abramowicz [1], a lot of researches have been carried out about this structure in theoretical, numerical and experimental analysis. The effectiveness of thin-walled structure varies according to numerous aspects such as characteristic of material, cross-section configuration, wall thickness and boundary condition applied to the structure [2]. Among these aspects, cross-section configuration plays a crucial role in energy absorption properties of the structure. The number of corner of the cross-section contributes significantly to the absorbing effectiveness because most of the strains occur near the edges and corners. Moreover, the value of the angles should be around 90 to 120 degrees to get the best optimization [3]. There are two ways to improve energy absorbing ability of thin-walled structures, either giving more materials to the corners or increasing the number of corners in the cross-section. The former helps the structure absorb more energy but spontaneously raises the length of the folding mechanism and therefore negatively affects the stability of the overall structure. The latter, which applies hexagon or octagon cross-sections, improves effectiveness proportionally with the number of corners but it should not exceed 11. Furthermore, when the polygon structure has more than 6 edges, the value of each corner will exceed the optimal range and decrease its absorption property. Multi-corner thin-walled columns, interestingly, can solve both problems by increasing the number of corners with adjustable angles. The only different between polygon and multi-corner structures is their cross-section, so it will not take much effort to industrially produce the structures. In this paper, we focus on analysing the theoretical characteristic of the multi-corner thin-walled structure by modelling and axial crushing simulation. Numerical calculation based on SFE theory and comparison with simulation results are also performed to provide a systematic review.

2. Theoretical prediction for crushing mechanism

SFE theory uses a combination of surfaces such as cylindrical, conical, trapezoidal and toroidal surfaces to construct its model. The folding of this element in plastic mode can be categorized into five distinct deformation mechanism [4].

1. Toroidal surface with moving boundaries and quasi-inextensional deformation.
2. Bending deformations along stationary hinge lines.
3. Rolling deformations with floating boundaries and undergo inextensional deformation.
4. Opening of conical surfaces that undergo extensional deformation.
5. After the travelling, hinge line is locked the bending deformations along inclined and stationary hinge lines.

There are two basic collapse mechanisms in this theory, quasi-inextensional mode and extensional mode. These modes are controlled by the factor α. The total internal plastic dissipation is obtained by equation:

$$E_{\text{int}} = \int_0^{\overline{\alpha}} \dot{E}_{\text{int}}^{(1)} d\alpha + \int_{\overline{\alpha}}^{\alpha_f} \dot{E}_{\text{int}}^{(2)} d\alpha \tag{31}$$

The two parts of the equation demonstrates the two folding modes. In the first mode, or first phase of deformation, crushing process occurs in the form of quasi-inextensional $\left(0<\alpha<\overline{\alpha}\right)$.

$$E_{\text{int}}^{(1)} = \int_0^{\overline{\alpha}} \dot{E}_{\text{int}}^{(1)} d\alpha = E_1 + E_2 + E_3 \tag{32}$$

With E_1 is the energy dissipation due to plastic flow over toroidal surface, given by the equation:

$$E_1 = 16 M_0 \frac{Hb}{t} I_1 \left(\psi_0, \overline{\alpha} \right) \tag{33}$$

where

M_0 is fully plastic moment per unit width.

H is half plastic folding wave length.

b is internal radius of toroidal surface.

t is wall thickness.

$$I_1 \left(\psi_0, \overline{\alpha} \right) = \frac{\pi}{\left(\pi - 2 \psi_o \right) \tan \psi_o} \int_0^{\frac{\pi}{2}} \cos \alpha \left\{ \sin \psi_o \sin \right.$$
$$\left. \left(\frac{\pi - 2 \psi_o}{\pi} \right) \beta + \cos \psi_o \left[1 - \cos \left(\frac{\pi - 2 \psi_o}{\pi} \right) \right] \beta \right\} d\alpha \tag{34}$$

E_2 is energy dissipation for the two moving hinge lines. As the hinge line is split, there are two such hinge lines in the folding mechanisms.

$$E_2 = 2 M_0 C \overline{\alpha} \tag{35}$$

where C is the total side length.

E_3 is energy dissipation due to inclined traveling hinge lines. There are also two hinge lines.

$$E_3 = 4 M_0 \frac{H^2}{b} I_3 \left(\psi_0, \overline{\alpha} \right) \tag{36}$$

where

$$I_3 \left(\psi_0, \overline{\alpha} \right) = \frac{1}{\tan \psi_0} \int_0^{\frac{\pi}{2}} \frac{\cos \alpha}{\sin \gamma} d\alpha \tag{37}$$

In the second phase of the equation (1), where $\overline{\alpha} < \alpha < \alpha_f$, the initially straight line at the hinge is bent due to the newly formed conical surface.

$$E_{int}^{(2)} = \int_{\overline{\alpha}}^{\alpha_f} \dot{E}_{int}^{(2)} d\alpha = E_4 + E_5 + E_6 \tag{38}$$

Assume that the material in the conical zone undergoes stretching in the meridional direction, the energy dissipation E_4 can be obtained by

$$E_4 = 4 M_0 \frac{H^2}{t} I_4 \left(\psi_0, \overline{\alpha} \right) \tag{39}$$

where

$$I_4 \left(\psi_0, \overline{\alpha} \right) = \int_{\overline{\alpha}}^{\alpha_f} \left\{ \frac{\sin \overline{\alpha} \sin 2\alpha \tan \psi_0}{2 \left(\sin^2 \overline{\alpha} + \tan^2 \psi_0 \sin^2 \alpha \right)} \right.$$
$$\left. \left(\frac{\pi - 2 \psi_0}{\pi} \beta \right) \cos \alpha \right\} d\alpha \tag{40}$$

E_5 is energy dissipation on the horizontal hinge line, calculated the same way as in phase I.

$$E_5 = 2 M_0 C \left(\alpha_f - \overline{\alpha} \right) \tag{41}$$

E_6 is energy dissipation due to bending in the stationary hinge line BL, which has constant length.

$$E_6 = M_0 H I_6 \left(\psi_0, \overline{\alpha} \right) \tag{42}$$

where

$$I_6 = 2 \cot \psi_0 \int_{\overline{\alpha}}^{\alpha_f} \frac{\sin \overline{\alpha} \left(\sin^2 \overline{\alpha} + \tan^2 \psi_0 \right)}{\sin^2 \overline{\alpha} + \tan \psi_0 \sin^2 \overline{\alpha}} d\alpha \tag{43}$$

For multi-corner column, product of mean crushing force and displacement during deformation equals total energy dissipation with effective crushing distance:

$$P_m 2 H \delta = E_{int} \tag{44}$$

The value of $\overline{\alpha}$ is set to be equal to α_f and equal $\pi / 2$. The corners of multi-corner column are all square $\left(\phi = 2 \psi_0 = \pi / 2 \right)$. Therefore, the second phase as well as I_4, I_5 and I_6 are eliminated and the energy equation is simplified. For this assumption, the values of I_1 and I_3 are 0.5256 and 1.1478 respectively.

The haft folding wavelength H can be obtained by

$$H = 1.01 \sqrt[3]{\frac{\left(C_{cc} N_{cc} + C_{cv} N_{cv} \right)^2 t}{\left(N_{cv} + N_{cc} \right)^2}} \tag{45}$$

where

N_{cv} is the number of convex corner.

N_{cc} is the number of concave corner.

C_{cv} is side length of convex corner.

C_{cc} is side length of concave corner.

The value of dynamic mean crushing force P_m^d can be calculated by

$$\frac{P_m^d}{M_0} = \frac{1}{0.73} \left[1 + \left\{ \frac{\psi_0}{\left(b + \beta H \right)} \frac{V}{1.46D} \right\}^{1/q} \right]$$
$$\left[N_{cv} \left(8.4 \frac{b}{t} + 6.9 \frac{C_{cv} t}{4 b^2} \right) + N_{cc} \left(8.4 \frac{b}{t} + 6.9 \frac{C_{cc} t}{4 b^2} \right) \right] \tag{46}$$

3. Model configuration

There are four kind of tubes with cross section shown in Fig. 1 and their geometry is described in Table 1. The mesh size used for the thin wall surfaces is 2 mm x 2 mm. For rounded edges with radius 1mm, mesh size 0.2 mm x 2 mm is used to match the shape of real model. Material property applied for simulation models is CR4 cold-rolled steel:

- Density $\rho = 7870$ kg/m^3
- Young's modulus E = 200 GPa
- Plastic stress $\sigma_y = 0.15$ GPa
- Poisson factor $\nu = 0.3$
- Power law exponent n = 0.268
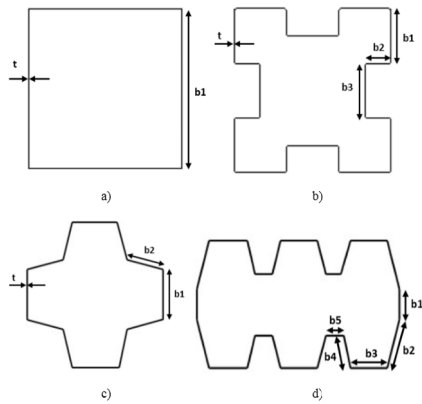
Fig. 1 Cross section of (a) square column, (b) N20 column, (c) F12 column and (d) S20 column

Table 1. Dimension and thickness of the columns

	b1 (mm)	b2 (mm)	b3 (mm)	b4 (mm)	b5 (mm)	t (mm)	L (mm)
Square	60	-	-	-	-	1.09	150
N20	20	10	20	-	-	0.82	100
F12	30	23.717	-	-	-	0.847	100
S20	12	18.97	16	12.69	8	0.79	100

4. Theoretical calculation result

All calculation is performed with crushing velocity V = 10 mm/s, the length of all columns is 100 mm and displacement is 60 mm. Specific energy absorption (SEA) is the ratio of energy absorption to a unit weight. Structure with higher energy-absorbing effectiveness has higher value of SEA. The theoretical results are shown in Table 2.

Table 2. Theoretical calculation results

	Square	N20	F12	S20
Weight (kg)	0.207	0.207	0.207	0.207
Thickness (mm)	1.093	0.82	1.271	0.797
H (mm)	12.315	6.185	8.099	5.256
P_{mean} (kN)	12.631	34.248	22.417	32.039
E_{int} (kJ)	0.83	2.062	1.355	1.925
SEA (kJ/kg)	4.019	9.987	6.563	9.32

$$SEA = \frac{E_{int}}{m} \tag{47}$$

Results in Table 2 show that, with constant weight, multi-corner columns have better results than square column. In general, energy-absorbing ability of multi-corner columns is much better than that of square column, as there are more folds per unit length and a single element has more concave and convex corners. Moreover, as can be seen from Fig. 2 and Fig. 3, when

increasing the wall thickness, both mean crushing force and SEA rise significantly. For changing the thickness from 0.5 mm to 2 mm, SEA value of N20 column grows 3.7 times higher while square column's counterpart only increases by 2.2 times.
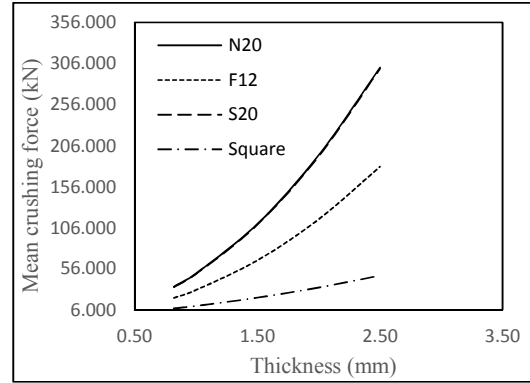
Fig. 2 Variation of theoretical mean crushing force with wall thickness

5. Simulation result

The statistic results of axial crushing simulation performed for the four models are described in Fig. 4 to Fig. 7. Theoretical mean crushing force is also displayed (dotted line) for comparison. The numerical mean crushing force curve is affected by the instantaneous force curve, increasing from zero and reaching the peak before dropping to a stable value. The error between simulation and theoretical calculation varies from 1.13% (N20 column) to 14.9% (S20 column).
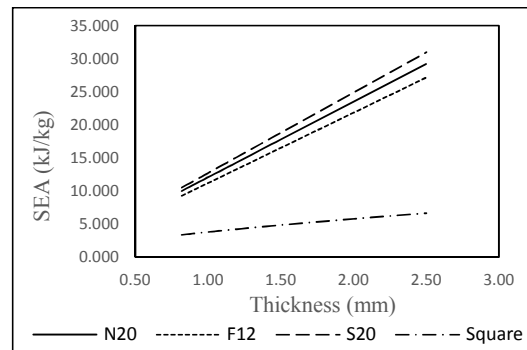
Fig. 3 Variation of theoretical SEA vs. wall

Another important factor for structural analysis is Crush force efficiency (CFE), which is the ratio of the mean to the peak crushing force. CFE is account for the stability of the force – the higher value means that the force is steadier.

$$CFE = \frac{P_{mean}}{P_{peak}} = \frac{1}{P_{peak}\delta}\int_0^\delta P(\delta)d\delta \tag{48}$$

According to Table 3, CFE and SEA of multi-corner models are higher than those of square column,

indicating better response to external impact. Once again, simulation results have verified the outstanding energy absorption of multi-corner columns in comparison with square column.
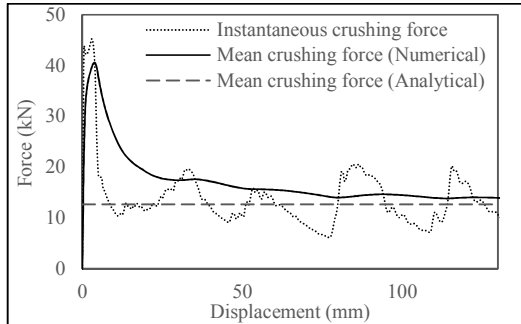
Fig. 4 Simulation results of square column
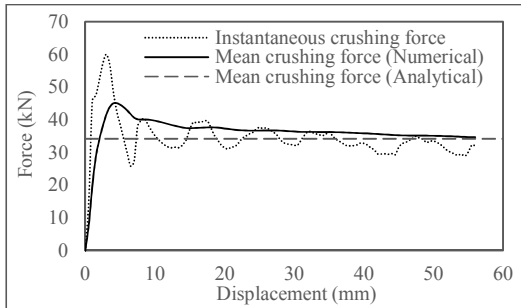
Fig. 5 Simulation results of N20 column
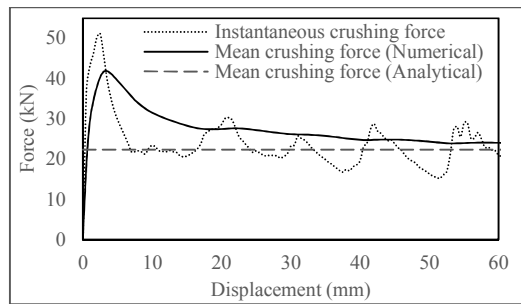
Fig. 6 Simulation results of F12 column
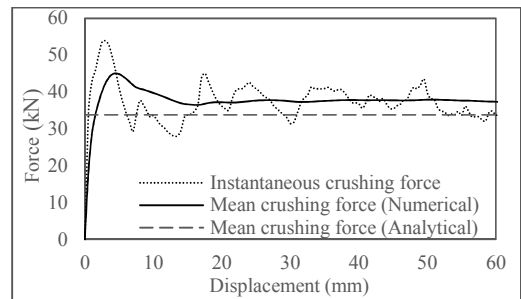
Fig. 7 Simulation results of S20 column

Table 3. Numerical simulation results

	Square	N20	F12	S20
(3) (kN)	15.610	34.640	24.070	37.656
(kN)	45.280	60.089	51.094	53.918
CFE	0.345	0.576	0.471	0.698
E_{int} (kJ)	0.874	1.940	1.348	2.109
Weight (kg)	0.207	0.207	0.207	0.207
SEA (kJ/kg)	4.222	9.372	6.512	10.188

Table 4. Corner effect on energy absorption property

	Square	N20	F12	S20
N^0 of corner	4	20	12	20
SEA (kJ/kg)	4.019	9.987	6.563	9.32
	Ref.	5.968	2.545	5.301
	Ref.	16	8	16
CE (corner effect)	Ref.	0.373	0.318	0.331

The simulation also states the influence of the number of corner to the energy absorbing ability of the structure. In this case, SEA is taken into consideration. The variation of SEA with the change in corner quantity is described in Table 4. ΔSEA_{square} is the difference in SEA between multi-corner columns and square column while $\Delta Corner_{square}$ is the difference in the number of corner. The corner effect factor (CE) is the ratio of the two above-mentioned values. It can be seen in the table that the CE factor is almost constant and equal 0.3. This confirms the relationship between the SEA and corner quantity (in case of corner around 90 degrees) as with one more corner added, the value of SEA will increase by 30%.

The influence of wall thickness to the structural property is also verified by simulation, which gives similar results as theoretical analysis. Among multi-corner columns, S20 gets the best CFE value while N20 reaches the highest SEA value when increasing wall thickness. However, with higher thickness, reliability of theoretical result drops significantly due to unstable deformation of the structures.

6. Conclusion

This paper employs the theory of Super Folding Element to determine the energy absorption property of multi-corner thin-walled structures, including 4 samples with different cross-section. Equations based on the same theory for predicting the mean crushing force and folding wave length of the structure are also provided. Theoretical and numerical results have proved that multi-corner column has better potential in

absorbing kinematic energy than square column. Moreover, the number of corner in cross-section does affect the property of the structure. SEA and CFE both increase by 33% for an extra corner added into the cross section. Theoretical results are compared with simulation results using finite element code LS-Dyna. Comparison has verified the reliability of the theory as well as numerical analysis for predicting collapse mechanism of multi-corner thin-walled structure.

References

[4] B.R.S. Reddy, "Multi cornered thin wall sections for crashworthiness and occupant protection," Ph.D dissertation, School of Aeropace Mech. and Manu. Eng., Rmit Univ., Melbourne, 2015.

[1] T. Wierzbicki, W. Abramowicz, On the crushing mechanics of thin-walled structures, *Journal of Applied Mechanics,* 50 (1983) 727-734.

[2] Z. Tang, S. Liu, Z. Zhang, Energy absorption properties of non-convex multi-corner thin-walled columns, *Thin-Walled Structures,* 51 (2012) 112-120.

[3] T. Wierzbicki, N. Jones, Structural Failure, *New York: John Wiley and Sons*, (1989).

Design and Fabrication of Wave Generator Using an Oscillating Wedge

Phuong Ha[1], Liem Thanh Dao[2], Son Doan Tran[2] and Thanh Quoc Truong[2]

[1]Department of Fluid Mechanics, Hochiminh City University of Technology

[2]Department of Manufacturing Engineering, Hochiminh City University of Technology

Add.: 268 Ly Thuong Kiet Street, District 10, Hochiminh Cty, Vietnam

ABSTRACT

This paper describes the design and fabrication of a wave flume and associated equipment. Wave flume is equipped with a triangle wedge located at one end of a channel and the passive wave absorber is located at the other end for absorbing waves generated from the wave maker. The wedge is controlled by a desktop computer, it can move up and down at a prescribed speed and oscillation amplitude corresponding to the desired wave height and frequency. At the middle flume is equipped micro laser distance sensor which provides data-logging capability. Wave flume can generate the largest waves are about 0.5 meter high, have a period about 1 second, and have a wavelength about 1.5 meters. The waves generated by a oscillating wedge have been measured, analyzed to consider the generated wave energy.

Keywords: Wave Flume, Wave Maker, Wave Energy, Wave Generation

Design and Implement of a Smart Watering System Used an Unmanned Aerial Vehicle Applicable to Agriculture in Vietnam

Nguyen Van Học, Do Phu Loc, Tran Minh Khoi, Pham Manh Cuong, and Bui Huu Phu

Hochiminh City University of Technology and Education, Vietnam

01 Vo Van Ngan street, Thu Duc district, Hochiminh City, Vietnam

Email: phubh@hcmute.edu.vn

ABSTRACT

Many researchers over the world are now focusing on researching and applying high technologies to agriculture in order to increase quality, productivity, efficiency. One of them is the smart watering system based on unmanned aerial vehicle (UAV) applicable to agriculture. The system helps and supports to farmers to water and fertilize their fields quickly without any effect from chemical toxics, save time and cost.

In the paper, we will present our own research on developing a smart watering system based on UAV. We have designed, calculated whole system, and considered not only the hardware part, but also the software part.

The pilot system has been implemented. It has worked and operated, can be controlled and watered. The real test has given a very good result. The system has a quick response and very stable, remote control, and easy to use, especially price is much cheaper than imported products. We are packing and make a good commercial design to be able to technology transfer to Vietnam market soon.

Keywords: Unmanned Aerial Vehicle, Smart Agriculture, smart watering system,

Research on the Establishing on the Program of Control of the SLS Rapid Prototyping Machine

Nguyen Thanh Nam[1], Le Khanh Dien[1], Svetlin Antonov[2]

[1] DCSELAB - **Ho Chi Minh City University of Technology,** VNU-HCM, Vietnam
[2] Technical University Sofia, Bulgaria

ABSTRACT

In the current time, mastering the rapid prototyping technology and equipments is a complicated question in Vietnam because of shorting of ability and finance. In order to save currency from imported machine, the demand of research and mastering the new technology of rapid prototype machine, especially the program of control motion in Selected Laser Sintering (SLS) rapid prototype machine, is essential in our country in the purpose of manufacture a domestic SLS rapid prototype machine. This paper presents the design of a control program for the SLS rapid prototyping machine that is corporated to the hardward of the manufactured SLS machine. The program has to respond the requirements of control as well as experimental adjustment of the technological parameters. The results of testing the program while manufacture model products by SLS rapid prototyping machine are accepted..

Keywords: Control program, Rapid prototype, Selective laser sintering, SLS machine.

1. Introduction

In SLS rapid prototyping machine, the powder material is sintered by the Laser beam up to its melting temperature that changes the powder state from solid to plastic. When the Laser beam moves to sinter the adjacent powder, the melted powder solidifies and bonds to the previous one to form a tiny partial shape of the model. The current powder layer melts then solidifies and has been adhesive to the previous performed one and the process repeats successively to form layer by layer until to finish the product [1]. The technology can manufacture any complex surfaces 3D model product, so the control of the machine operation process included scanning powder, controlling the rotation of lens to project the Laser beams and decreasing the elevation of power carriage is essential. The design of the control program consists many questions such as controlling of the motions, the ability to link with computers and convert high data and finally, the friendly, easy to use property of the interface program. In the content of the paper, we mention only the controlling of the motion of the SLS.

2. Fundamental design of the SLS rapid prototyping control program

In order to manufacture a product by the SLS rapid prototyping machine, we need:

1. Design 3D file: Drawing on CAD/Drawing software or scanning the 3D model.
2. Generating G - code file: Using CAM program to convert 3D design into G-code file that the machine control program can understand.
3. Controlling CNC machine to create details: A CNC controller program is used and it translate G - code file to machine control signal.

The SLS control program is designed on the manufacturing requirements of the 3D model. To manufacture 3D details, we have to divide the 3D model into several layers [2]. The points on a layer correspond to the X and Y - axis of the machine and the coordinate of Z stands for changing to a new layer. The manufacture processes of a model by SLS rapid prototyping machine are as follows [3]:

1. The SLS projector lens has to return to the original position before to manufacture the model.
2. The Z - axis of the lifting carriage is justified to zero value.
3. The powder is plentifully scattered on the surface of lifting carriage.
4. The roller scans the powder to a same width powder layer along X - axis.
5. The Laser is on, the projector lens directs the Laser beam to the incident position X, Y to sinter the powder and moves to next point to perform the whole circumference orbit on the current layer, and the Laser is off.
6. The Z - axis of the lifting carriage is justified downward a controlled value.
7. Repeat from step 3 to step 6 until the final layer of 3D detail is complete.

In order to perform theses above tasks, the SLS control program consists of two units: the direct control unit and the supported function unit [4].

3. Design the direct control unit of the SLS machine control program

3.1 X, Y, Z control unit:

Continuously control the Laser beam to concentrate to X, Y point and decreases Z value after performing of each layer. Normally, the pitch of motion on 3-axis is set up by default of 1mm or smaller for fine model. However, the users can justify the pitch to 5, 10, 25, 50 and 100 mm. The origin of the coordinate is selected for easiest control of X, Y, Z values:

- X and Y coordinate are always positive,
- Z coordinate is always negative.

3.2 Unit controls command-line of user:

The duties of this unit are examining the user - generated G - code command lines during operation and

requesting the machine to execute. Different from the control of X, Y, Z values in coordinate Control Unit, the user's command - line control allows the user to freely adjust the parameters of SLS.

Unit moves to original position: The initial position is the origin 0, 0, 0 of the X, Y, and Z - axis. Moving back to the original position at the beginning of the process allows the SLS machine to avoid being displaced during operation.

Unit executes G-code: In the Command - Line Unit, the executes G - code unit allows the user freely controls the SLS machine. However, this unit can also control the machine from multiple consecutive G - code commands that helps the SLS machine work faster and more accurately.

4. Design of supported function units the SLS machine control program

- **Unit reads and modifies configuration:** The read and modify controlling configuration plays an important role in controlling the SLS. In this unit, information such as step/mm, max rate ... can be displayed and modified to accommodate with every operation of the machine.

- **Unit displays X, Y, Z axes coordinate:** The X, Y, Z axes coordinate unit provides the exact position of the sintered point during the SLS machine is operating. With any changing of the 3-axis position, the display unit will constantly update the parameters to help the users accurately check the location of the machine.

- **Unit connects to SLS machine's control driver**: To execute the command of the software, this unit has the duty of connecting the software on the computer with the SLS machine control driver. The RS232 port is used to exchange information between the computer and the SLS machine control driver.

- **Unit displays command lines:** with this unit, the user can check the operation of the machine, starting at the beginning of the software. Another duty of this unit is the continuous updating the software control operations for the SLS.

The algorithm of the unit diagram controls the SLS rapid prototyping machine as shown in Figure 1.
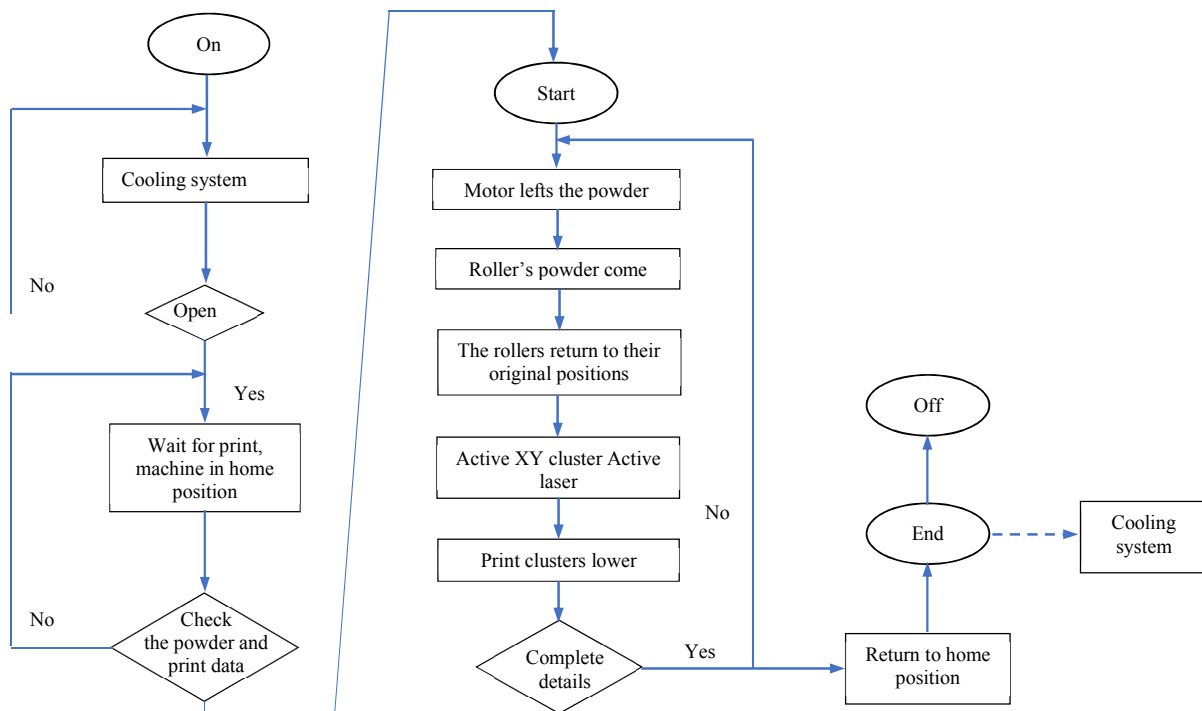
Figure 30. The algorithm unit diagram controls the SLS rapid prototyping machine

5. Design the interface of the SLS rapid prototyping control program

(1) Connecting RS232 port with the SLS control driver: Selecting, connecting and disconnecting the PC software with the driver are all the abilities that user can control the SLS machine as desired. This is the first step that needs to be taken before controlling the machine.

a. The interface of the control program (Figure 2):

(2) Selecting, treating and controlling SLS from G - code file: this interface can assist the user to treat and execute quickly and accurately selected G - code file.

(3) Treating and controlling SLS from command: This command can be used to view machine information as well as to edit any G-code command line.
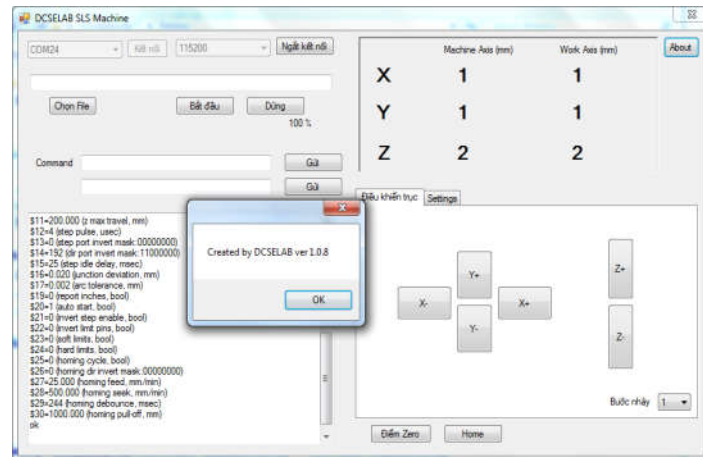
Figure 31. *Control program interface of the SLS rapid prototyping machine*

(4) Displaying command line from the SLS machine allows the user to check the operation of the machine.

(5) Displaying X, Y, Z position: X, Y, and Z coordinates are displayed correctly during operation.

(6) Controlling the motions on X, Y, Z coordinate system forward or back.

(7) Displaying and modifying configuration is used to control the SLS machine correctly.

(8) Moving the machine to its original position: moving the X, Y, Z axes to the first position.

(9) Software information: The "About" button on the control software interface helps the user to view the information of the software.

b. Actions to use the software:
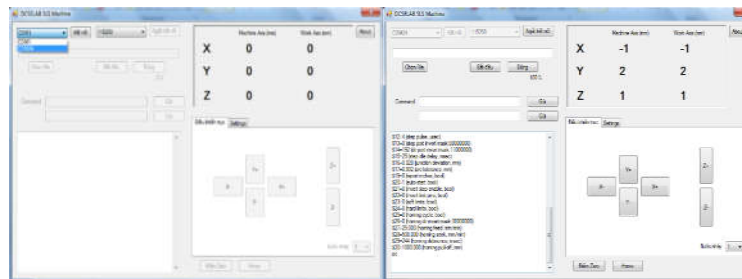
Figure 32. *Console panel before and after connection*

In order to manufacture a product, we start the software on the console in the following steps:

(1) Connecting the software to the machine driver: Select the appropriate COM port (except COM1 port) and Baud rate is 115200, then click on "Connect". Once connected, the control software interface appears as shown in Figure 3.

(2) Fine-tuning the position of sintering and the parameters of the software: To create a new product, we need to fine-tune the position of

the three axes to zero. Click the "Home" button on the software, the result is shown in Figure 4. Check the Settings of the software, select the "Settings" tab, all the parameters are displayed on this interface, you can change the parameters if necessary, and for example, we change three parameters 3, 4, 5. Select "OK" to complete the change, the main interface of the control software appears to show three parameters have been change (Figure 4).
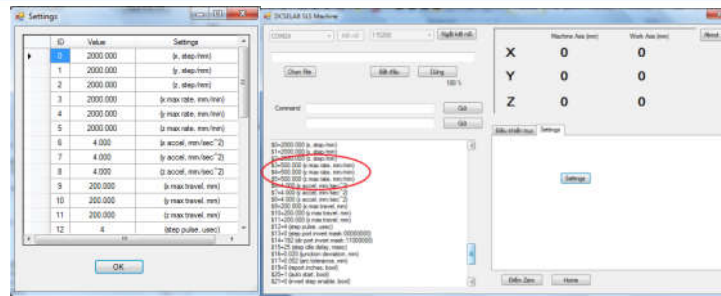
Figure 33. Fine - tuning the position of the three axes and the parameters of the software

(3) Shaping product: Normally, to create a product, we simply execute a prepared G - code file. This will help us to save time as well as increase the accuracy and speed of the SLS system. At the area of selection, treating and controlling from the G - code file, we click on the "Select File" button. Select the file to execute as shown in Figure 5.
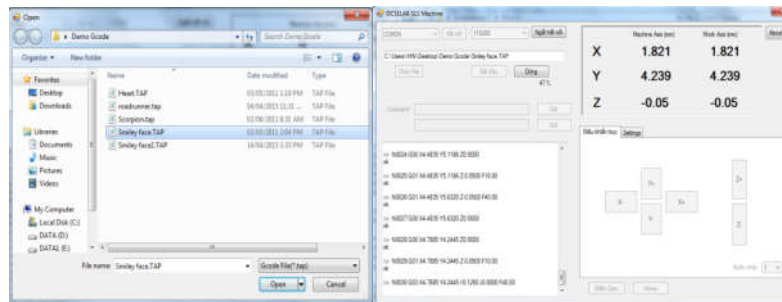
Figure 34. Execute the G-code file to create the product

On the main interface of the program, the link to the G-code file appears. Select "Start" to execute the file. During the execution of the G-code file, the software interface will continuously update the G - code command lines that have been executed. At the same time, the coordinates of the X, Y, and Z - axes will be continuously updated during the shaping process (Figure 5).

(4) Pause or end the shaping process: You can pause the rendering process if necessary or until the execution of the G - code is achieved, as shown in Figure 6.
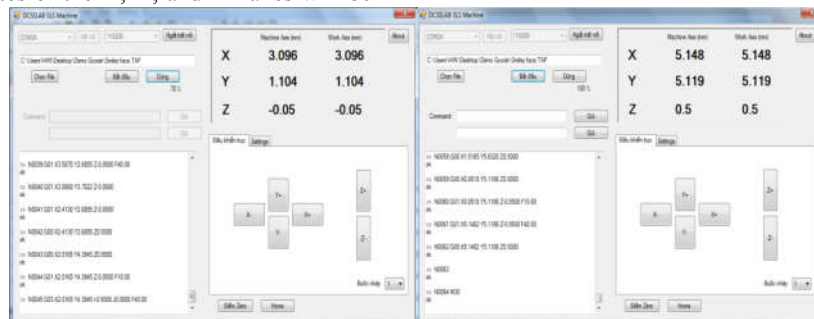
Figure 35. Stop executing the G - Code file

At the end of the product shaping process, after removing the achieved product, you can click "Start" to continue to manufacture another product or disconnect to end SLS machine control by software. Experimental results show that the control software has met the requirements of the SLS rapid prototyping machine (Figure 7).

Figure 36. *Experiment and molding products by SLS rapid prototyping machine*

6. Conclusion

The paper has conducted a design about the establishing the control software and interfacing design for rapid prototyping machines that meet the requirements of control as well as experimental adjustment of the technological parameters during manufacturing and processing products. All the above informations confirm that we can master the essential software for controlling the domestic SLS rapid prototype machine in Vietnam

7. Acknowledgement

8. References

[1].Badrinarayan, B and Barlow, JW (1995). *Effect of processing parameters in SLS of MetalPolymers*, Proceedings of Solid Freeform Fabrication Symposium, pp. 55-63. Austin: Texas.

[2] Contuzzi, N.; Campanelli, S.L & Ludovico, A.*D, 3D finite element analusis in the selective lazer melting process*, Department of Management and Mechanical Engineering, Viale Japigia,182,70126 Bari, Italia, 2011.

[3] Ana PilipoviT, Igor Drstvenšek, Mladen Šercer1, *Mathematical Model for the Selection of Processing Parameters in Selective Laser Sintering of Polymer Products*, Advances in Mechanical Engineering, Volume 2014.

[4] Nguyễn Thanh Nam, *Nghiên cứu thiết kế và chế tạo hệ thống tạo mẫu nhanh SLS*, Báo cáo tổng kết đề tài B2013-20b-01, 2015

PART VI, SECTION IV

Other Topics Related to Machining, Materials and Mechanical Technology
(Mechanics of Solid; Analysis and Simulation; New Machine Tools and Tooling Technology;
Dynamics and Control…)

An Ultrasound-guided Robotic HIFU Ablation System with Respiration Induced Displacement and Time Delay Compensation

Ching Shiow Tseng[1], Chih Yu An[2], Yung Lun Hsu[3]

[1] Professor, Department of Mechanical Engineering, National Central University
[2] Ph.D Student, Department of Mechanical Engineering, National Central University
[3] Master, Department of Mechanical Engineering, National Central University
Jhongli, Taoyuan, Taiwan 320
cstseng@cc.ncu.edu.tw

ABSTRACT

This paper introduces an ultrasound imaging-assisted robotic HIFU ablation system with a displacement compensatory mechanism. A respiration simulation device was designed by using a phantom and a cam-driving mechanism to simulate displacements of the tumor and the heaving chest. A robotic arm is applied to guide the HIFU probe to track and ablate the target tumor automatically and synchronously by inputting the displacement values of the heaving chest. The average signle-point positioning error was 1.72 ± 1.26 mm, while the ablation temperature was stabilized at 80°C.
Keywords: High-intensity focused ultrasound; Robot Positioning; respiration, Ultrasound.

1. Introduction

In recent years, noninvasive thermal treatment by using High Intensity Focused Ultrasound (HIFU) has high potential in tumor treatment. This study introduces an ultrasound imaging-assisted robotic HIFU ablation simulation system with a respiration induced displacement mechanism, which is applied to verify that a robot-driven HIFU system can trace and ablate a moving lesion such as liver tumor due to respiration. The system integrates the technologies of ultrasound image assisted guidance, robotic positioning control, and HIFU treatment planning. With the assistance of ultrasound image guidance technology, the tumor size and location can be determined from ultrasound images and the robot can be controlled to position the HIFU probe to focus on the target tumor. A duration of three respiratory cycles is applied as the basis of the experiment conducted to investigate the relevance between the HIFU positioning error and the respiratory state. The average positioning error of three respiratory cycles was 1.72 ± 1.26 mm while the ablation temperature was stabilized at 80°C.

2. Methods

An ultrasound imaging-assisted robotic HIFU ablation simulation system has been developed as illustrated in the Fig. 1. To simulate the displacement correlation between the heaving chest and the target tumor, a cam-driving respiration simulation device was designed as a part of the simulation system. First, the target tumor is scanned by the ultrasound probe and its image is segmented and image coordinates are determined and transferred to the coordinate frame of the ultrasound probe. The coordinate transformations among the HIFU transducer, robotic arm, and ultrasound probe are determined through their DRFs (dynamic reference frame) detected by the optic tracker.

The position of the target tumor changes continuously during respiration. Here, 6 different respiration states in a respiratory cycle are chosen for position information recording and scanning of the tumor using an ultrasound probe. The 6 different respiration states are as follows: maximal exhalation; maximal inhalation; 2 during exhalation process; and 2 during inhalation process. Meanwhile, positional information for the heaving chest is obtained by laser rangefinder measurement. Subsequently, the ultrasound images of the tumor are subjected to image processing (edge detection and segmentation) to determine the tumor coordinates.

The 3rd-order polynomial function was generated from the corresponding positions of target tumor P_j and the displacement of heaving chest L_j in each of the X, Y, and Z directions; "j" represented the respiratory state (e.g., $j = 0$, maximal exhalation). Then, the respiration and tumor displacement correlation is established in each exhalation state and inhalation state. Thus, the position value of the heaving chest under real-time measurement will be imported into the respiration and tumor displacement polynomial function in order to obtain the coordinate information of the target tumor in different respiration states. The position coordinates of the target tumor under every respiratory state are converted to the frame of the robotic arm, the robotic arm will be able to automatically guide the HIFU transducer (focal point) to track and ablate the target tumor synchronously according to the displacement values of the heaving chest.
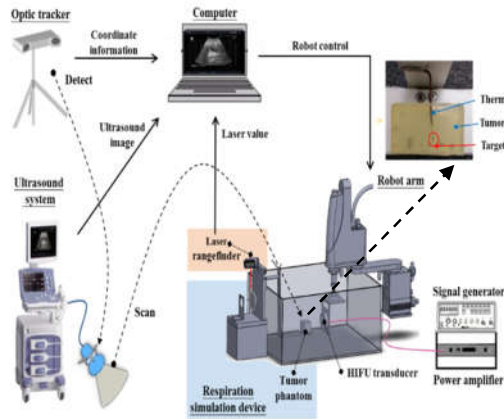
Fig.1 The ultrasound imaging-assisted robotic HIFU ablation simulation system

3. Results

As shown in Figure 1, a thermocouple is inserted into the tumor phantom, the top of which is defined as the target tumor point and used to measure ablation temperature in the experiment. A probe of the optical tracker measures the position coordinates of the target tumor point, which are then used as a control group and compared with those calculated by using the respiration-tumor-displacement polynomial function to obtain the tracking error of the HIFU focal point.

The temperature of the target point under HIFU ablation can reach 80–100°C in one second, which is able to kill tumor cells. However, the temperature around the ablated point is much lower than that at the center of the ablated point; therefore, the efficacy of HIFU ablation could be assessed not only by the positioning error of the HIFU focal point, but also by the temperature of the target point. In the experiment, the respiration simulation device was activated for 45 seconds and the HIFU focus point drove by the robotic arm tracked and ablated the target point simultaneously. The temperature of the target point was recorded continuously in addition to the positioning error of the HIFU focal point, and the results were shown in Fig. 2. The overall temperature was around 80°C, which was adequate to deteriorate kill tumor cells in real case. In addition, the results also showed that while the positioning error increased, the temperature decreased significantly. As to the relationship between the HIFU focal point positioning error and the heaving chest state was investigated in a subsequent experiment below.

Fig. 2 Variations of temperature and positioning error during ablation.

A duration of three respiratory cycles is applied as the basis of the experiment conducted to investigate the relevance between the HIFU positioning error and the respiratory state. The average positioning error of three respiratory cycles was 1.72 ± 1.26 mm while the ablation temperature was stabilized at 80°C. However, significantly increasing positioning errors occurred during the inhalation and exhalation transition periods. The reason is because the robot arm may not rapidly response to the reverse movement direction. The temperature of the target point under HIFU ablation can reach 80–100°C in one second, which is able to kill tumor cells. However, the temperature around the ablated point is much lower than that at the center of the ablated point; therefore, the efficacy of HIFU ablation could be assessed not only by the positioning error of the HIFU focal point, but also by the temperature of the target point. In the experiment, the respiration simulation device was activated for 45 seconds and the HIFU focus point drove by the robotic arm tracked and ablated the target point simultaneously. The temperature of the target point was recorded continuously in addition to the positioning error of the HIFU focal point, and the results were shown in Fig. 3. The overall temperature was around 80°C, which was adequate to deteriorate kill tumor cells in real case. In addition, the results also showed that while the positioning error increased, the temperature decreased significantly. As to the relationship between the HIFU focal point positioning error and the heaving chest state was investigated in a subsequent experiment below.
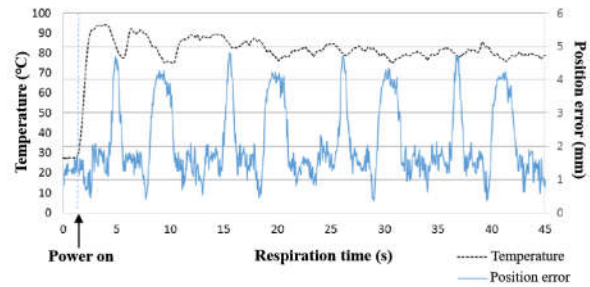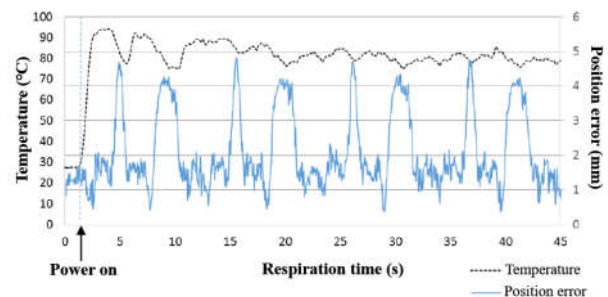

Fig. 3 Variations of temperature and positioning error during ablation.

4. Conclusion

In this research, an ultrasound-guided robotic HIFU ablation system with respiration displacement and time delay compensation functions was developed. The main characteristic of this system is that it can simulate tumor movements relative to respiration statuses, verify robot positioning and tracing accuracy, and execute HIFU ablation tests. Compared to MRI based HIFU system, ultrasound based HIFU system is cheaper and more convenient and time-saving in use. It can be expected ultrasound guided robotic HIFU ablation systems will be getting more popular in various treatments.

References

[1]. A. B. Holbrook, P. Ghanouni, J. M. Santos, C. Dumoulin, Y. Medan, K. B. Pauly, "Respiration based steering for high intensity focused ultrasound liver ablation", Magnetic Resonance in Medicine, vol. 71(2), pp. 797-806, 2014.

[2]. M.V. Siebenthal, "Analysis and modelling of respiratory liver motion using 4DMRI", Hartung-Gorre Verlag, Konstanz, 2008.

[3]. J. Seo, et al., "Visual servoing for a US-guided therapeutic HIFU system by coagulated lesion tracking: a phantom study", The International Journal of Medical Robotics and Computer Assisted Surgery, vol. **7**(2), pp. 237-247, 2011.

[4]. Y. Seppenwoolde, et al., "Accuracy of tumor motion compensation algorithm from a robotic respiratory tracking system: a simulation study", Medical physics, vol. 34(7), pp. 2774-2784, 2007.

[5]. C.Y. An, J.H. Syu, C.S. Tseng, et al., "An Ultrasound Imaging-Guided Robotic HIFU Ablation Experimental System and Accuracy Evaluations", Applied Bionics and Biomechanics, vol. 2017.

Adaptive Robust Heading Control Design for a New Ray-type Hybrid Underwater Glider

Duc Nguyen Ngoc[1], Hyeung-sik Choi [1], Jong-seok Han [2], Nhat Thieu Quang Minh[1] and Ji-yoon Oh[1]

[1]Department of Mechanical Engineering, Korea Maritime and Ocean University

Busan, 49112, Korea

[2]PICO Co.Ltd., 26-10, Haeyang-ro 65beon-gil, Yeongdo-gu, Busan, Republic of Korea

ABSTRACT

Underwater glider (UG) is recently used as the long-term equipment for oceanographic and discovery applications, and most of UGs now is the Torpedo type with the limitation of space for buoyancy engine, batteries and sensors. In this study, the new design of Ray-type hybrid underwater glider (RHUG) will be proposed. And the adaptive super-twisting sliding mode control (AST-SMC) without the knowledge of hydrodynamics coefficients is also presented with the existence of external disturbances. The simulation of heading control of the RHUG was conducted to demonstrate the effectiveness of the AST-SMC controller compared with the adaptive conventional sliding mode control (AC-SMC).

Keywords: heading dynamics, hybrid underwater glider, adaptive robust control

. Introduction

The underwater glider (UG) is an equipment which helps scientists collect the ocean measurements such as temperature, salinity, currents and acoustic backscatter in the duration of weeks or months. This vehicle uses the buoyancy force to move up and down like the profiling float and convert the vertical motion into horizontal by its wings. Therefore, it moves slower than the conventional Autonomous Underwater Vehicle (AUV) equipped with thrusters. However, in the sampling mission, the UG has longer range and duration than AUV due to the buoyancy-based propulsion which has very low power consumption.

In the marine tasks, the UG should be able to cruise in the desired depth. Therefore, nowadays the hybrid-driven underwater glider (HUG) which combines actuation of both buoyancy engine and thruster are developed. The mathematical model, hydrodynamics identification and a Neural Network Predictive Control were simulated in (Isa, 2014). And, the design of a foldable propeller for the HUG was analyzed and tested in (Chen, 2016). Moreover, the HUG with rotatable thruster was tested for docking mission in (Yang, 2016). The nonlinear control system of the marine vehicle was currently investigated for robustness and practical implementation. The higher-order sliding mode control was implemented for position and attitude of surface vessel prototype using hydro-jets by (Bartolini, 2008). The nonlinear heading autopilot design for AUV using backstepping technique was carried out in (Li, 2016). Finally, the sliding mode control for AUV with unknown disturbances and quantized state feedback and control input was investigated by (Yan, 2018). There are not many studies on the robust controller deal with unknown hydrodynamics coefficients.

In this paper, the heading control of the new Ray-type HUG (RHUG) will be designed in the scenario of unknown hydrodynamics coefficients and the bounded external disturbances using two thrusters at the RHUG's stern.

2. Vehicle design

The design of new type hybrid underwater glider is shown in Fig. 1. This design focuses on the increase of buoyancy capacity by two piston-cylinders symmetrically installed in the sway-direction of the platform. Internal moving mass is placed in the center line to control the pitch attitude. And, two underwater thrusters are equipped in this vehicle to archive the higher speed in the AUV mode. Three batteries can be installed in this Ray-type HUG.

There are two advantages in this design. The buoyancy force to glide the vehicle increases double compared with Torpedo-type. Therefore, the RHUG can glide faster than the conventional version. With the new hull shape like a ray fish, this vehicle has more space for batteries and sensor payload.
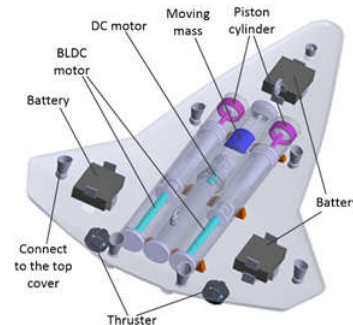

Fig. 1. Design of Ray-type hybrid underwater glider.

3. Super-twisting sliding mode control

Fig. 2. RHUG heading control scheme.

In this section, the tracking control for underwater glider will be designed in Fig. 2 using "super-twisting" sliding mode control.

The decoupled yaw dynamics of the underwater vehicle can be described by (Bartolini, 2008) as (1).

$$(I_z - N_{\dot{r}})\dot{r} = N_r r + N_{r|r|} r |r| + u + d \qquad (1)$$

Where: r: yaw rate; I_z: a moment of inertia about Z-axis; $N_{\dot{r}}$: added mass coefficient; $N_r, N_{r|r|}$: hydrodynamics coefficients; u: torque from thrusters; d: external disturbance.

For the simplicity, the equation (1) will be rewritten as (2).

$$\dot{r} = ar|r| + br + \frac{u}{\alpha} + \frac{d}{\alpha} \qquad (2)$$

Where: $a = \dfrac{N_{r|r|}}{I_z - N_{\dot{r}}}; b = \dfrac{N_r}{I_z - N_{\dot{r}}}; \alpha = I_z - N_{\dot{r}} > 0$

In the sliding mode control, the sliding surface should be defined in terms of the error and it is chosen as (3).

$$s = (r - r_d) + \lambda(\psi - \psi_d) \qquad (3)$$

Where: s: scalar quantity; r_d: desired yaw rate; ψ: heading angle; ψ_d: desired heading angle; λ: weight parameter for sliding surface and is a positive definition.

The main concept of sliding mode control is to keep s at zero, in another word, to maintain the position and velocity errors at zero (Slotine, 1991). When s approach zero, in order to maintain it at zero, the derivative of s should be zero and its expression is formulated as (4).

$$\dot{s} = \dot{r} - \dot{r}_d + \lambda(r - r_d) \qquad (4)$$

To estimate the control input to make $\dot{s}$ equal zero, (2) is substituted into (4) to get (5).

$$\dot{s} = ar|r| + br - \dot{r}_d + \lambda(r - r_d) + \frac{u}{\alpha} + \frac{d}{\alpha} \qquad (5)$$

In Filippov theory, the best estimation of the equivalent control without considering the uncertainty and external disturbance can be obtained from the equation $\dot{s} = 0$. From (5), the actual sliding mode control law can be formulated as (6).

$$u = \hat{\alpha}\left(-\hat{a}r|r| - \hat{b}r + \dot{r}_d - \lambda(r - r_d)\right) + u_{sw} \qquad (6)$$

Where: $\hat{i}$: estimated value of the parameter $i \in \{a; b; \alpha\}$; u_{sw}: the discrete control or switching control. In this paper, two kinds of switching law are conventional "sign" function and "super-twisting" algorithm shown in (7) and (8) respectively.

$$u_{sw} = -K sign(s) \qquad (7)$$

$$u_{sw} = -K_1 \sqrt{|s|} sign(s) - \int K_2 sign(s)dt \qquad (8)$$

Where: K, K_1, K_2: are controller gains which are defined later in the next section.

Once the parameters are well estimated, the sliding mode control above will follow the desired trajectory. In this underwater vehicle, the hydrodynamics parameters can be obtained from Planar Motion Mechanism experiment. However, the empirical parameters are not always closed to the real one. In this situation, the adaptation law for these parameters is proposed for this vehicle.

4. Adaptation law
The derivative of s can be rewritten as (9) with the substitution of (6).

$$\dot{s} = \tilde{a}r|r| + \tilde{b}r + \frac{\tilde{\alpha}}{\alpha}\hat{a}r|r| + \frac{\tilde{\alpha}}{\alpha}\hat{b}r - \frac{\tilde{\alpha}}{\alpha}\dot{r}_d + \frac{\tilde{\alpha}}{\alpha}\lambda(r - r_d) + u_{sw} + \frac{d}{\alpha} \qquad (9)$$

Where: $\tilde{i} = i - \hat{i}$: error of estimation of parameters $i \in \{a; b; \alpha\}$.

The Lyapunov function can be chosen as follow (10).

$$V = \frac{1}{2}s^2 + \frac{1}{2}\tilde{a}^2 + \frac{1}{2}\tilde{b}^2 + \frac{1}{2\alpha}\tilde{\alpha}^2 \qquad (10)$$

The derivative of V can be obtained as (11).

$$\dot{V} = s\dot{s} + \tilde{a}\dot{\hat{a}} + \tilde{b}\dot{\hat{b}} + \frac{1}{\alpha}\tilde{\alpha}\dot{\hat{\alpha}} \qquad (11)$$

From (9) and (11), the adaptation law is defined as follow (12).

$$\begin{cases} \dot{\hat{a}} = -sr\,|r| \\ \dot{\hat{b}} = -sr \\ \dot{\hat{\alpha}} = -\left(\hat{a}sr\,|r| - \hat{b}sr + s\dot{r}_d - s\lambda(r - r_d) \right) \end{cases} \quad (12)$$

If the parameters are estimated by the adaptation mechanism (12), the derivative of V is reduced as (13).

$$\dot{V} = s\frac{u_{sw}}{\alpha} + s\frac{d}{\alpha} \quad (13)$$

In order to ensure $\dot{V} \le 0$, the condition for the controller gains are shown as below (14).

$$\begin{bmatrix} \text{"sign"}: & K \ge |d| + |\alpha|\eta \\ \text{"super-twisting"}: & \begin{cases} K_1 \ge |\alpha|\eta \\ K_2 \ge |d| \end{cases} \end{bmatrix} \quad (14)$$

5. Simulation study
To verify the adaptive sliding mode control algorithm, simulation studies were implemented using MATLAB/Simulink for both adaptive conventional sliding mode control (AC-SMC) and adaptive super-twisting sliding control (AST-SMC).
The parameters of the developed RHUG are shown as follow:

$$L = 1.67m, \ \rho = 1031 kg/m^3, \ I_z = 4.0548 kgm^2$$
$$N_{r|r|} = -0.00053(\rho L^5/2), \ N_r = -0.00467(\rho L^4/2)$$
$$N_{\dot{r}} = -0.00136(\rho L^5/2)$$

In this simulation, the desired trajectory will be designed by the time-optimal trajectory in (Loc, 2014) to limit the control input in the range of [-20Nm; 20Nm]. The initial condition of this heading system is set as $\psi_0 = r_0 = \dot{r}_0 = 0$ and the final desired angle is 2.6 rad. The sliding weight parameter is selected as $\lambda = 2$.
For this adaptive scheme, the controller gains are chosen based on the parameter bound $|\alpha| \le \Omega$, the disturbance bound $|d| \le D$ and the tuning positive value η. In this simulation, the disturbance is $4\sin(5t)$ (from 0s to 5s and from 10s to 20s) and there is 20% uncertainty of the parameter α. Then, the bounds of parameter α and disturbance will be defined as $D = 4$, $\Omega = 1.2|I_z - N_{\dot{r}}|$ respectively. Therefore, the controller gains can be selected as (15).

$$\begin{bmatrix} \text{"sign"}: & K = D + \Omega\eta \\ \text{"super-twisting"}: & \begin{cases} K_1 = \Omega\eta \\ K_2 = D \end{cases} \end{bmatrix} \quad (15)$$

Where $\eta = 0.5$ for the gain K and $\eta = 6$ for the gain K_1.

5.1. Simulation 1: AC-SMC
The actual velocity and angle follow the desired trajectory in Fig. 3c and 3d. However, due to the chattering of the torque input in Fig. 3a, the actual acceleration does not follow the desired angle shown in Fig. 3b and have the chattering under 0.76 rad/s². The disturbance occurs from 0s to 5s and from 10s to 20s, then the sliding surface oscillates in Fig. 4. The parameters are updated following the adaptation law above and shown in Fig. 5.
This kind of chattering phenomenon can be improved by using a saturation function instead of the sign function. However, the tracking performance will be degraded depending on the thickness of the saturation function. In this study, the super-twisting method will be used to eliminate the chattering problem while keeping the tracking precision.
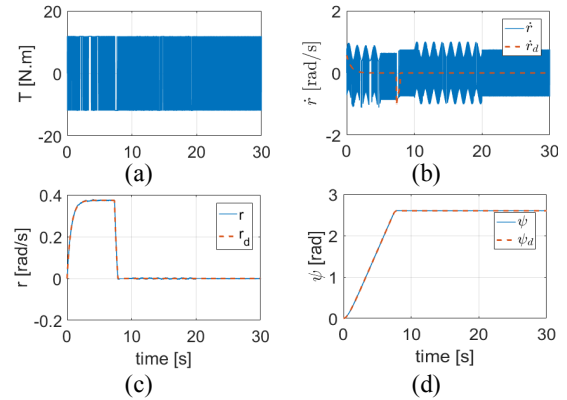

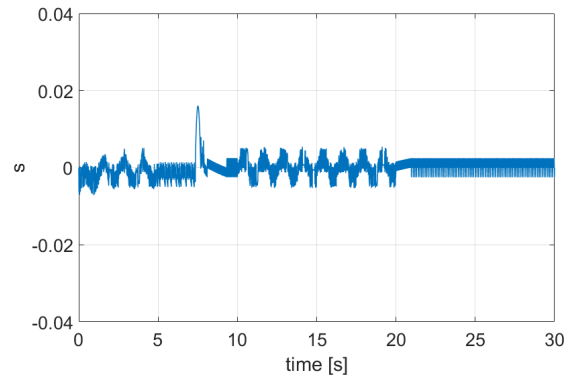**Fig. 3**. Tracking performance of the adaptive conventional sliding mode control (AC-SMC).

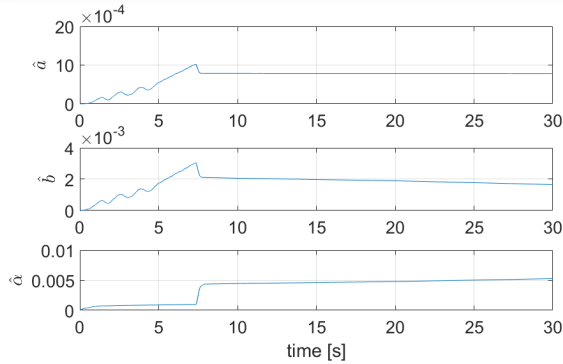

Fig. 4. The sliding surface of the AC-SMC.

Fig. 5. Parameter adaptation of the AC-SMC.

5.2. Simulation 2: AST-SMC

In the second simulation, the switching controller is super-twisting algorithm. The control input of AST-SMC is smoother than that of AC-SMC in Fig. 6a while keeping the similar tracking performance in Fig. 6c and 6d. The sliding surface, in Fig. 7, is kept under 0.02 similar to Fig. 4. The parameter adaptation of this controller is shown in Fig. 8.

Additionally, the tracking quality of angular acceleration is improved as shown in Fig. 6b. The chattering of the actual acceleration of AST-SMC is under 0.13 rad/s^2 much smaller than that of AC-SMC.
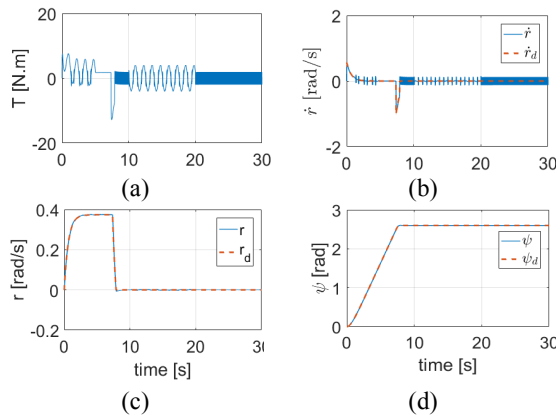
Fig. 6. Tracking performance of the adaptive super-twisting sliding mode control (AST-SMC).
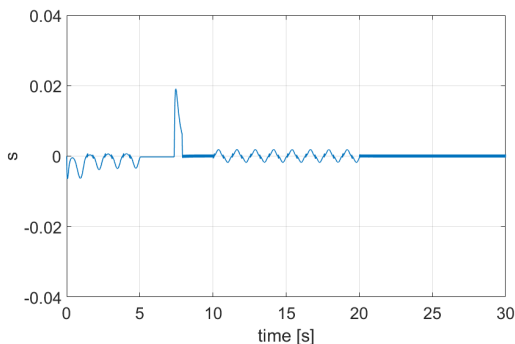
Fig. 7. The sliding surface of the AST-SMC.
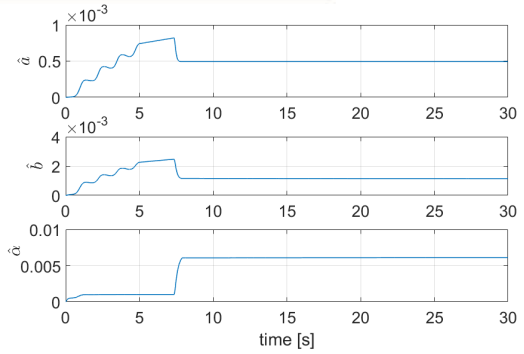
Fig. 8. Parameter adaptation of the AST-SMC.

6. Conclusion

The design of a new Ray-type hybrid underwater glider is proposed. And the adaptive sliding mode controller without the unknown parameters is designed. The adaptation law for the adaptive sliding mode control is proved using Lyapunov theory. The simulation showed that the AST-SMC have many merits compared with AC-SMC in term of smoothing the control input and the tracking precision of the acceleration.

7. Acknowledgements

References

[1] Bartolini, G. e. (2008). A combined first⁻/second⁻order sliding⁻mode technique in the control of a jet⁻propelled vehicle. *International Journal of Robust and Nonlinear Control*, 570-585.

[2] Chen, Z. e. (2016). Design and analysis of folding propulsion mechanism for hybrid-driven underwater gliders. *Ocean Engineering*, 125-134.

[3] Isa, K. e. (2014). A hybrid-driven underwater glider model, hydrodynamics estimation, and an analysis of the motion control. *Ocean Engineering*, 111-129.

[4] Li, B. e. (2016). Nonlinear heading control of an autonomous underwater vehicle with internal actuators. *Ocean Engineering*, 103-112.

[5] Loc, M. B. (2014). Time optimal trajectory design for unmanned underwater vehicle. *Ocean Engineering*, 69-81.

[6] Slotine, J.-J. E. (1991). *Applied nonlinear control*. Englewood Cliffs, NJ: Prentice hall.

[7] Yan, Y. e. (2018). Sliding mode tracking control of autonomous underwater vehicles with the effect of quantization. *Ocean Engineering*, 322-328.

[8] Yang, C. e. (2016). Study on docking guidance algorithm for hybrid underwater glider in currents. *Ocean Engineering*, 170-181.

A Measure of Control of Submerging and Surfacing of an Autonomous Underwater Vehicle for Exploring Underwater of Rivers

Le Khanh Dien[1], Le Khanh Tan[2], Tran Ngoc Huy[1], Pham Huy Hoang[3], Vo Tuyen[4]

[1] DCSELAB **-** Ho Chi Minh City University of Technology, VNU-HCM, Vietnam
[2] Ho Chi Minh City University of Technology and Education (HCMUTE), Vietnam
[3] Ho Chi Minh City University of Technology, VNU-HCM, Vietnam
[4] Ho Chi Minh City University of Food Industry (HUFI), Vietnam

ABSTRACT

Autonomous underwater vehicle (AUV) known as a special purpose underwater research vehicle (SPURV) is really a pocket submarine that could be used in multipurpose such as: meteorology, probing the pollution of stream, military spying, exploring an underwater tunnel…With the reason of the power of battery inside AUV is limited, the aim of this paper is to represent an effect way of control the submerging and surfacing of an AUV in order to save energy. The selection of the weight of AUV in the proportion of the Archimedes force and the measure of maintaining the equilibrium is also investigated in this paper. The selection of water ballast mass distribution in AUV at the time of submerging and surfacing is also mentioned. Finally, the controlling of the gravity point of AUV for maintaining the position of gravity of the AUV is fixed when submerging and surfacing are the main factors of the paper.

Keywords: Hydro metrological, AUV, ballast counterweight, propeller, diving.

1. Introduction

In the current time, the exploration underwater in the river and the sea is in great demand for hydro metrology, military secret mission, exploration in small section water tunnel…and so many other purposes. That is an opportunity of the researchers to study, research and manufacture the Autonomous Underwater Vehicle (AUV) time by time more intelligent, more flexible and easy to control. The purpose of this paper is to design a version of AUV that could be controlled the submerging and surfacing by pumping water in and out to take up and let out the water ballast to keep the center of gravity of the AUV fixed when submerging and surfacing.

2. Scheme of design the typical AUV

2.1. Selection of shape of UAV:
The shape of AUV must be as simple as possible. Normally it has a cylindrical body with 2 conical ends as in the figure 1.
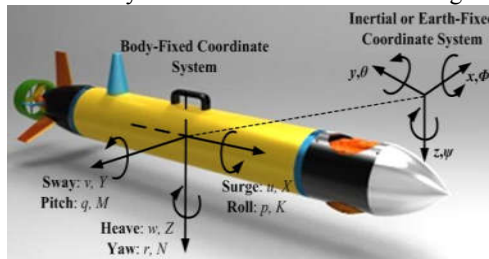
Figure 1: *General shape of AUV [1]*

The proposal outside boundary dimension of the studied AUV is about ⌀200x1800 mm excluded rudder accessories. The outside diameter of UAV body is about 200mm.

2.2. Scheme of control the center of gravity of AUV when submerging or surfacing
There are 2 schemes of control the center of gravity of AUV:

a. No pumping water in and out, controls only the direction of AUV by the motion of counterweight: The structure of AUV is very simple [1]. But the weight of AUV is constant and slightly smaller than the Archimedes force for floating. The direction of AUV is inclining down when submerging and up when surfacing because the controlled motion of counterweight. The AUV needs to be provided a lot of energy for submerging and even when surfacing AUV because the force of propeller has to win the difference of Archimedes force and the weight of AUV. The paper does not use this type of control because of saving energy.
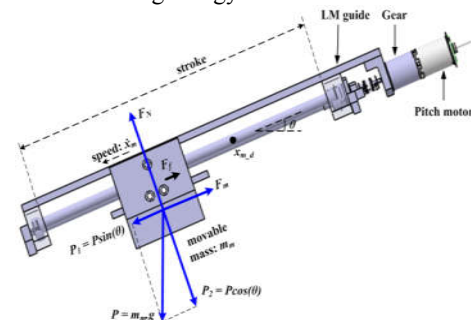
Figure 2: *The shift of mass to get an oblique angle before submerging or surfacing [1]*

b. Maintaining the center of AUV fixed

The proposed structure of the designed AUV is represented in figure 3 in the scheme of fixing the center of gravity of the AUV. The direction of AUV is always slightly horizontal. To pump the outside water in and out of the AUV when submerging and surfacing saves energy of battery because in this time the propeller could be inactive for submerging and surfacing. In other to

save energy from battery inside AUV, the study applies the way of submerging and surfacing as the one of a real submarine to keep the horizontal direction of AUV when submerging or surfacing. Figure 3 shows the structure inside the AUV
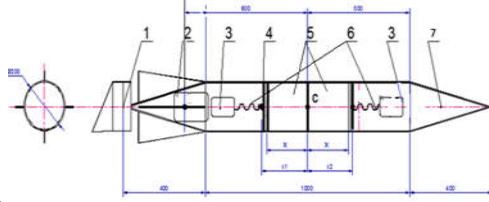
Figure 3: Schema of the distribution of weights and control the center of gravity of AUV.

Wherein: *1. Propeller, 2. Thruster of propeller, 3. Moving motor for pumping water in and out, 4. Hermetic piston, 5.Cylinder room of ballast water, 6.Moving Screw, 7. Front room for camera and observatory instrument c: Center of gravity of the whole AUV must be fix*ed

Two similar pistons are activated by 2 similar screws and 2 similar motors to pump water inside or outside of 2 rooms at the same time with the same displacement x in the opposite direction to keep the center of gravity of AUV stable and the direction of AUV is always horizontal. Figure 3 illustrates the distribution of weight block in the designed AUV.

3. Arrangement of the other installation

-The propeller that is included electric motor (thruster), battery, fin and control direction are located inside the rear end taper cylinder part of the AUV as in figure 4.
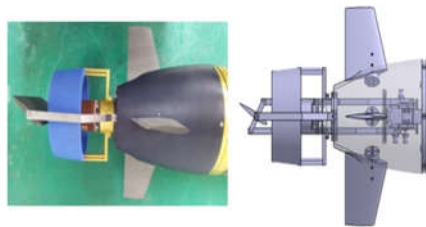
Figure 4: Propeller with protected cover and the controlling direction at rear of AUV [1]

-Total of instrument of the meteorology included motor, battery; camera, wave emitter and receiver are located inside the front end taper cylinder part of the AUV.

The weight of rear front end must be slightly equal (we can use a fixed counterweight to keep the common center of AUV at point C in figure 3.

4. Computing all parameters of AUV

 * Outside volume of AUV:

V=2(π (100)2.400/3)+ π (100)2.1000= 39793506.95 mm^3 =39.7935 dm^3

* Archimedes' force N=39.7935x10~398 N

* With the selected total weight of AUV is 390N if we include 8N of water inside the 2 room (with selected inside diameter $\varnothing$180), the AUV will begin to dive with 4N or about 0.4 kg of water for each room.

The minimum displacement of each piston of 2 water rooms (5 in figure 3) is:

Minimum volume of water in each cylinder v=

x.π(90)^2.10^{-6} dm^3= 0,4 $\Rightarrow$x=15,719 mm.

So with the displacement of less than 16mm the AUV had to begin dive. The reversed length according to the proposed structure in figure 3 is about 500mm for battery, motor, ball screw and the selected maximum length of water room is about 100mm.

Because the limited depth of diving of AUV is 10m (the medium depth of almost all rivers in the HCM city), the outside pressure increase 1 atmosphere, a pressure sensor is installed outside of the AUV will turn off the power of 2 pumps. The pumps will active easily less than 1 absolute atmosphere to pump out the water for surfacing purpose. In fact, with the suitable adjusting of the pressure sensor the design AUV could reach at 20m water depth.

5. Design the mechanism of control the position of center of gravity of AUV

As mentioned above, the minimum supplementary ballast water is only 8N that means that when a weight of water of 4N (about 0.4 kg) is pumped in each water room the AUV begins to sink. The design needs 2 similar set of pumps and cylinders and all installation have to move except the ball nut is fixed as in the figure 5.

Figure 5: 2 DC Gear box electric motor and 2 SKF ball screw nut are selected to activate piston (Fixed ball nut [3])

Another version of the design is using only one 2 output shafts DC Gearbox motor 2 ball screw nut with inverse helical angle that are mounted on the 2 end of the output shafts as in figure 6.

Figure 6: A 2 shafts Gear DC motor for pump [2]

The structure of this version of AUV is shows in figure 7.
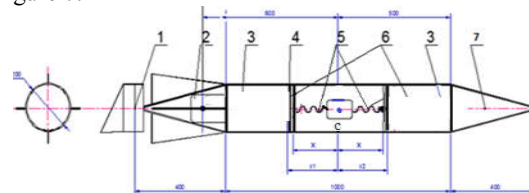
Figure 7: The structure of another version of AUV.

Conclusion

With the scheme of maintaining the common center point of AUV fixed by equilibrium the water ballast, the designed AUV save lot of electric energy for the propeller from battery when submerging as well as of surfacing. The direction of AUV always keeps in the horizontal in any mission.

Acknowledgement

References

[1] Ngoc-Huy Tran, Hyeung-Sik Choi , Jae-Hyun Bae, Ji-Youn Oh, Jong-Rae Cho," Design, Control, and Implementation of New AUV Platform with a Mass Shifter Mechanism",International Journal of Precision Engineering and Manufacturing, © KSPE and Springer 2014

[2] http://cnlongway1.en.made-in-china.com/product/VMkmzuCdbGWa/China-15-30W-DC-Gear-Motor-for-Printing-Machinery.html

[3] Precision roll ball screw SKF, PUB MT/P1 06971/1 EN · August 2013

[4] Fiorelli, E., Leonard, N.E., Bhatta, P., Paley, D., Bachmayer, R., Fratantoni, D.M., "Multi-AUV control and adaptive sampling in Moterey Bay," Workshop on Multiple AUV Operations (AUV04), pp. 134–147, 2004.

[5] Stokey, R., Allen, B., Austin, T., Goldsborough, R., Forrester, N., Purcell, M., Alt, C.V., "Enabling technologies for REMUS docking: an integral component of an autonomous ocean-sampling network," IEEE Journal of Oceanic Engineering 26(4), pp. 487–497, 2001.

Design Controller for Time-domain Simulation of Automatic Berthing Operation of an USV

Mai The Vu[1], Hyeung-Sik Choi[2], Ji-Youn Oh[2], Han Jong Seok[3]

[1]Department of Convergence Study on The Ocean Science and Technology, School of Ocean Science and Technology, Korea Maritime and Ocean University, 727 Taejong-ro, Yeongdo-gu, Busan, 606-791, South Korea

[2]Divison of Mechanical Engineering, Korea Maritime and Ocean University, 727 Taejong-ro, Yeongdo-gu, Busan, 606-791, South Korea

[3]26-10, Haeyang-ro 65 Beon-gil, Yeongdo-gu, Busan, 606-791, South Korea

ABSTRACT

In this paper, a PD controller and its application to automatic berthing control of Unmanned Surface Vehicle (USV) is studied. Firstly, a nonlinear mathematical model for the maneuvering of USV in the presence of environmental forces was established. Then, in order to control rudder and propeller during automatic berthing process, a PD control algorithm is applied. The algorithm consists of two parts, the forward velocity control and heading angle control. The control algorithm was designed based on the longitudinal and yaw dynamic models of USV. The desired heading angle was obtained by the so-called "Line of Sight" method. Finally, computer simulations of automatic USV berthing are carried out to verify the proposed controller with the influence of disturbance forces. The results of simulation showed good performance of the developed berthing control system

1. Introduction

Ocean is cradle of life, treasury resource and transportation artery. In the 21st century, we will face three challenges, such as the contradiction between population explosion and limited living space, between exhausted land resource and growing requirement of social production, between eco-environmental degradation and human development. USV (or ship) is one of intelligence motion platforms, which can be relied on remote control or navigate autonomously and safely in the real marine environment and complete various tasks. In marine literature review, USV berthing maneuvering is considered as the most complex mission, with high pressure for the helmsman to ensure safe operation. Compared with the other missions as autopilot for steering, position tracking, dynamic positioning or station keeping, USV berthing requires many processes from helmsman. At the stage where the vessel moves from the open sea to confined water, the USV velocity has to be kept in dead slow, so the controllability of actuators is significantly reduced. Furthermore, when the USV comes near a jetty, the USV master has to detect USV position exactly as well as predict her motions to prevent collision.

For above reasons, automatic berthing approaches have been concerned from early 1990's. With the difficulties to capture the change of hydrodynamic coefficients, it is not surprising to notice that the recent researches are concentrated on developing intelligent control strategies without any information of the dynamic model such as fuzzy control [4, 6] and neural network techniques [5, 7]. Although these approaches have the advantages of embedded human experiences and knowledge about USV behavior into control strategies, the limits of actuator controllability in dead slow velocity condition have not been solved yet. So it is too

dangerous to apply these methods into the real situation. Even though the advent of new technologies applied in the field of navigation such as differential global positioning system, camera sensing system or in the propulsion manufacturing field, until now large USV maneuvering in the harbor area is done manually by assistance of tugboats.

To design the controller for USV berthing, the motion of USV in presence of environmental disturbances is considered. Environmental disturbances affecting the USV motion consist of wind, wave motion and current. With uncertainty and complexity of USV dynamic and environmental disturbances, the authors propose a robust controller based on a PD control. The PD controller presented in this paper guarantees robust performance and good stability under disturbances and dynamic uncertainty.

2. Mathematical Model

2.1. Equations of Motion

The extensive nonlinear equations of 3 DOF USV motions with PD control based on the mathematical model developed by [1], are shown as below:

$$m(\dot{u} - vr) = X \tag{1}$$

$$m(\dot{u} + ur) = Y \tag{2}$$

$$I_{zz}\dot{r} = N \tag{3}$$

The following set of equations is one of these expressions according to the coordinate system shown in Fig. 1. Where, X, Y, and N denote total hydrodynamic forces and moments generated by USV motions, propeller, rudder forces and environment forces. The hydrodynamic terms can be expressed in the form:

$$X = X_{Hydro.} + X_{Pr.} + X_{Rudder} + X_{Wave} + X_{Wind} + X_{Cur.} \tag{4}$$

$$Y = Y_{Hydro.} + Y_{Pr.} + Y_{Rudder} + Y_{Wave} + Y_{Wind} + Y_{Cur.} \tag{5}$$

$$N = N_{Hydro.} + N_{Pr.} + N_{Rudder} + N_{Wave} + N_{Wind} + N_{Cur.} \quad (6)$$
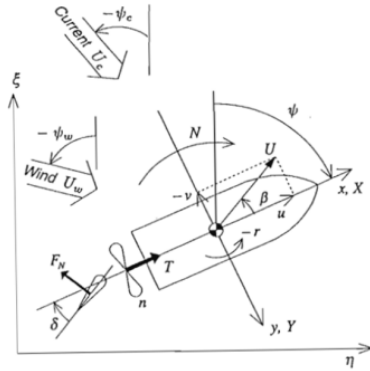

Fig.1. Coordinate of USV system.

Where the term with subscript "Hydro." represents hydrodynamics forces and moments produced by motions of USV hull (without propeller and rudder) and acting upon it, the term with subscript "Propeller" represents propeller forces and moments, the term with subscript "Rudder" represents rudder forces and moments, the term with subscript "Wave, Wind, Current" represent disturbance environment forces and moments, respectively.

2.2. External Environment Forces and Moments

The related calculations of the external forces, including current force, wind force and wave drifting force are stated in the following

2.2.1. Current Forces and Moments

The current forces and moment acting on the USV in the ocean with respect to the relative speed and direction between the USV and current can be expressed as:

$$X_{Cur.} = \frac{1}{2}\rho[(V_c\cos\alpha - \dot{x}_G)^2 + (V_c\sin\alpha - \dot{y}_G)^2]BdC_{\iota} \quad (7)$$

$$Y_{Cur.} = \frac{1}{2}\rho[(V_c\cos\alpha - \dot{x}_G)^2 + (V_c\sin\alpha - \dot{y}_G)^2]L_p dC_{\iota} \quad (8)$$

$$N_{Cur.} = \frac{1}{2}\rho[(V_c\cos\alpha - \dot{x}_G)^2 + (V_c\sin\alpha - \dot{y}_G)^2]L_p^2 dC \quad (9)$$

where, $X_{Cur.}$ and $Y_{Cur.}$ are current forces respecting surge and sway mode of the ship; $N_{Cur.}$ is yaw moment; V_c is the current speed; α is the angle between the current and ship heading; $\dot{x}_G$ and $\dot{y}_G$ are the ship speed horizontal components with respect to the center of gravity; B, D and L_p are breadth, depth and length between perpendiculars, respectively. The corresponding coefficients C_{cx}, C_{cy} and C_{cz}, are obtained from the empirical formulas. The similar concept can also be applied to estimate the wind forces and moment on the ship as shown below.

2.2.2. Wind Forces and Moments

The estimation of the wind forces and moment on the ship based on the formulas developed by [3].

$$X_{Wind} = X_W(\gamma_R)\frac{1}{2}\rho_a A_f V_R^2 \quad (10)$$

$$Y_{Wind} = Y_W(\gamma_R)\frac{1}{2}\rho_a A_S V_R^2 \quad (11)$$

$$N_{Wind} = N_W(\gamma_R)\frac{1}{2}\rho_a A_S L V_R^2 \quad (12)$$

where, X_{Wind}, Y_{Wind}, and N_{Wind} are the wind forces and moments regarding surge, sway, roll and yaw, respectively; X_W, Y_W, and N_W are non-dimensional coefficients of the wind forces and moments with respect to the relative wind angle γ_R; and ρ_a is the air density; A_f and A_S are the longitudinal and sideward projected area of the ship hull above the water surface, respectively; V_R is the ship speed relative to the wind

2.2.3. Wave Drifting Forces and Moments

Based on the "weak scatterer" assumption, the nonlinear hydrodynamic forces could be calculated by using the same technique as that of [3].

$$\bar{F}(\omega_e) = R_e\left\{-\frac{1}{2}\rho\iint_{S_B}\left[\phi_B\frac{\partial}{\partial n} - \frac{\partial\phi_B}{\partial n}\right]\nabla\phi_1^* ds\right\} \quad (13)$$

where, ϕ_1^* is the complex conjugate of incident wave potential ϕ_1 and ϕ_B is the body disturbance potential. The integral is around the ship body surface S_B

The mean longitudinal and lateral nonlinear forces on the ship with respect to the wave heading μ in short-crested waves can be approximately estimated by:

$$X_{Wave} = |\bar{F}_D|\cos\psi \quad (14)$$

$$Y_{Wave} = |\bar{F}_D|\sin\psi \quad (15)$$

where,

$$\bar{F}_D = 2\int_{-\frac{\pi}{2}}^{\frac{\pi}{2}}\int_0^\infty \frac{F(\omega)}{a^2}S_{aa}(\omega,\mu)d\omega d\mu \quad (16)$$

where, $\bar{F}_D$ is the mean nonlinear hydrodynamic force on the ship in random waves; $S_{aa}(\omega,\mu)$ is ITTC-1978 wave energy spectrum of short-crested wave. The yaw drifting moment N_{Wave} can be integrated from the sectional Y_{Wave} with respect to the LCG along the whole USV length.

2.3. Rudder Forces and Moments

The rudder forces and moments including the hydrodynamic forces and moments included on USV hull by rudder action namely X_{Rudder}, Y_{Rudder} and N_{Rudder}, can be written in the following from [5].

$$X_{Rudder} = -(1 - t_R)F_N\sin\delta \quad (17)$$

$$Y_{Rudder} = -(1 - a_H)F_N\cos\delta \quad (18)$$

$$N_{Rudder} = -(x_R + a_H x_H)F_N\cos\delta \quad (19)$$

where,

$$F_N = \begin{cases} \frac{\rho}{2}A_R f_\alpha U_R^2 \sin\alpha_R & (n \geq 0) \\ 0 & (n < 0) \end{cases} \text{ with } f_\alpha = \frac{6.13\Lambda}{2.25 + .} \quad (20)$$

2.4. Propeller Forces and Moments

The propeller thrusts and moments can be written in the following from [2], as follow:

$$X_{Pr.} = \begin{cases} C_1 + C_2 J_s & (J_s \geq C_{10} \text{ and } n > 0) \\ C_8 + C_9 J_s & (J_{st} < J_s < C_{10} \text{ and } n > 0) \\ C_6 + C_7 J_s & (J_s \geq C_{10} \text{ and } n < 0) \\ C_3 & (J_{st} < J_s < C_{10} \text{ and } n < 0) \end{cases} \quad (21)$$

$$Y_{Pr.} = \begin{cases} A_1 + A_2 J_s & (J_{syn} \leq J_s \leq J_{syn0}) \\ A_3 + A_4 J_s & (J_s < J_{syn}) \\ A_5 & (J_{syn0} \leq J_s) \end{cases} \quad \text{with } J_s = \frac{U}{nD_i} \quad (22)$$

$$N_{Pr.} = \begin{cases} B_1 + B_2 J_s & (J_{syn} \leq J_s \leq J_{syn0}) \\ B_3 + B_4 J_s & (J_s < J_{syn}) \\ B_5 & (J_{syn0} \leq J_s) \end{cases} \quad (23)$$

3. Controller Model

3.1. LOS Guidance

Guidance systems consist of a waypoint generator with human interface, which can be designed by storing the selected waypoints in a database and using them to generate a trajectory for the USV. Other systems can be linked to this waypoint guidance system in case of weather routing, collision and obstacle avoidance, where LOS guidance is widely utilized. LOS schemes (Fig. 2) have been applied to surface USVs. When moving along the path, the next waypoint (x_{k+1}, y_{k+1}) can be selected on a basis of whether the ship lies within a circle of acceptance with radius R_0 around the waypoint (x_k, y_k). If the vehicle positions $(x(t), y(t))$ at time t satisfy Eq. (24), the next waypoint should be selected.

$$[x_k - x(t)]^2 + [y_k - y(t)]^2 \leq R_0^2 \quad (24)$$

However a waypoint located far away from the ship will result in large cross-track errors in the presence of wind, current and wave disturbances. Therefore, the LOS vector can be defined as the vector from the vessel coordinate origin (x, y) to the intersecting point on the path (x_{los}, y_{los}) a distance n ship lengths L_{pp} ahead of the vessel. Thus, the desired yaw angle can be computed as

$$\psi_d(t) = a \tan 2(y_{los} - y(t), x_{los} - x(t)) \quad (25)$$

The four quadrant inverse tangent function a tan 2 (y, x) is used to ensure that

$$-\pi \leq a \tan 2(y, x) \leq \pi \quad (26)$$

The LOS coordinates (x_{los}, y_{los}) are given by

$$[y_{los} - y(t)]^2 + [x_{los} - x(t)]^2 \leq (nL_{pp})^2 \quad (27)$$

$$\left(\frac{y_{los} - y_{k-1}}{x_{los} - x_{k-1}} \right) = \left(\frac{y_k - y_{k-1}}{x_k - x_{k-1}} \right) = constant \quad (28)$$

Eq. (27) is recognized as the theorem of Pythagoras while Eq. (28) shows that the slope of the path between the waypoints (x_{k-1}, y_{k-1}) and (x_k, y_k) is constant.
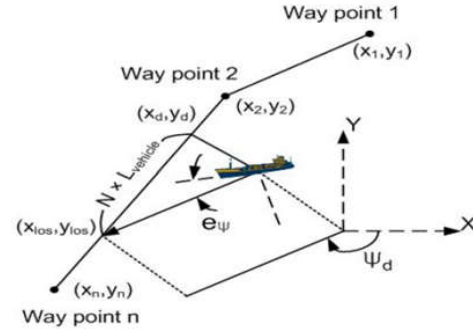

Fig. 2. Calculation of LOS algorithm.

3.2. PID Control for USV Berthing

The PID controller is usually expressed in the following equation:

$$y(t) = K_p e(t) + K_I \int_0^t e(t)dt + K_D \frac{de(t)}{dt} \quad (29)$$

where, y(t) is the output in the controller, e.g., thruster's R.P.M; e(t) means the system error, e.g., position and heading deviations. In the present study, only two control gains (i.e., proportional (K_P) and derivative (K_D)) are considered in the PD controller, whereas the control gain of the integral (K_I) is not included because the desired goals are fixed and independent of time.

In the present study, the thruster T depends on the position and heading deviations. In the PD control, the thruster's R.P.M. n of the thruster T is shown in the below:

$$n(t) = K_{P,x}[x(t) - x(0)] + K_{D,v_x}[v_x(t) - v_x(t-1)] + K_{P,\psi}[\psi(t) - \psi(0)] \quad (30)$$

where, n is for the forward thrusters' R.P.M; $K_{P,x}$ and K_{D,v_x} are the related control gains for surge and surge rate, and $K_{P,\psi}$ is the control gain for heading deviation.

In order to obtain the optimal PD control, the above control gains must be suitably adjusted to obtain the maximum control effect with respect to different sea states. If no optimal algorithm or good experience is applied, the optimal gains need to be obtained by trial and error method, which are complex and takes a lot of time.

4. Simulation Results and Discussion

In this section, the simulations have been performed for two cases of control of USV yaw angle for navigations and berthing, which generated two trajectories of USV as shown in Fig. 7. The first case we set up condition of USV moving from star point A (x = 2000 m, y =1000 m, yaw angle = 50 degrees) to goal point B (0 m, 0 m, -180 degrees). For the other case, we set up condition of USV moving from star point A (x = 2000 m, y =1000 m, yaw angle = -50 degrees) to goal point B (0 m, 0 m, -180 degrees). For both cases the initial velocities of USV are $v_x = 3$ *(m/s)*, $v_y = 0$ *(m/s)* and $v_z = 0$ *(m/s)*, respectively. The simulation period is 2000 seconds with starting time of 0 second, and finishing time of 2000 seconds with time step 0.01 second for first case. And simulation

time is 1200 seconds with time step 0.01 second for second case. Fig. 7 shows USV trajectories in both cases, and Fig. 6 shows the control input of USV of revolution of the thruster and the rudder angle. In more detail, we can see the yaw angle of USV as well as the position and velocity of USV as shown in Figs. 3-5, respectively. From these results, we can obviously realize that the USV reached the goal point B (0 m, 0 m, -180 degrees) faster than the second case such as it took 2000 seconds for second case but only 1200 seconds for first case. Also, the trajectory of second case more and more complicated than first case as well as velocity and rudder angle of USV when we compare both cases. Generally speaking, in order to USV reach the goal point effectively, we have to define the optimal yaw angle of USV as well as carefully control its rudder angle.

Fig.5. Yaw angles of USV in both cases.

Fig.3. The position behaviors of USV in both cases.
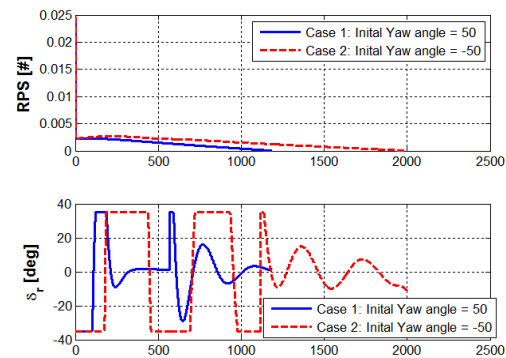
Fig.6. Thruster revolution and yaw angle of USV in both cases.

Fig.4. The velocity behaviors of USV in both cases.
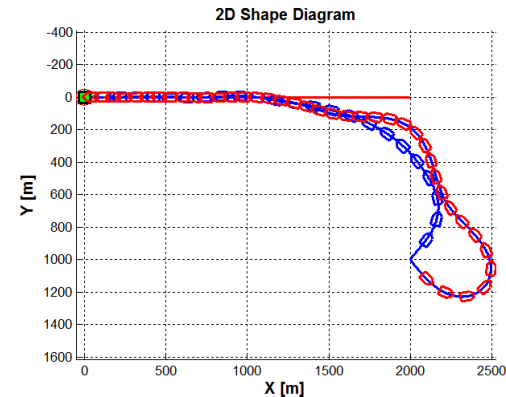
Fig.7. Trajectories of USV in both cases.

5. Conclusions

In this paper, the mathematical model is first introduced as a model dealing with non-uniform current and wind, and a mathematical model at slow advance speed is introduced, referring some other works. The control algorithm was designed to control the longitudinal and yaw dynamic models of USV. The desired heading angle was obtained by using "Line of Sight" method. Finally, computer simulations of automatic USV berthing are carried out to verify the proposed controller with the influence of disturbance forces. Both the

modeling system and the control method were confirmed as promising.

References
[1] M.C. Fang, J.H. Luo, *The nonlinear hydrodynamic model for simulating a ship steering in waves with autopilot system*, Ocean Eng., 32(11-12), 1486-1502, (2005).

[2] K. Hasegawa, K. Kitera, *Mathematical Model of Manoeuvrability at Low Advance Speed and its Application to Berthing Control*, Proc. Of 2nd Japan-Korea Joint Workshop on Ship and Marine Hydrodynamics, Vol.1, (1993).

[3] R.M. Isherwood, *Wind resistance of merchant ships*, Transactions of RINA, 115, 327338, (1973).

[4] Y.A. Kasasbeh, M. Pourzanjani, M.J. Dove, *Automatic Berthing of Ship*, Proc. of the Institute of Marine Engineers 3rd International Conference on Maritime Communications and Control, pp 10-17, London, (1993).

[5] A. Ogawa, H. Kasai, *On the mathematical Model of Maneuvering Motion of ships*, International Ship Building Progress, Vol. 25, No. 292, (1978).

[6] T. Takai, H. Yoshihisa, *An Automatic Maneuvering System in Berthing*, Proc. 8th Ship Control System Symposium, Vol.2, pp. 183-201, (1987).

[7] Y. Zhang, G.E. Hearn, P. Sen, *A Multivariable Neural Controller for Automatic Ship Berthing*, Journal of IEEE Control System, Vol. 17, pp. 31-44, (1997).

GPS/INS Integrated Navigation System for Autonomous Robot

Ngoc-Huy Tran[1], Quoc Tien-Dung Tran[2]

[1] Ho Chi Minh City University of Technology, VNU-HCM
Ly Thuong Kiet Street, Ho Chi Minh city, 700000, Viet Nam
[2] National Key Lab. of Digital Control and System Engineering, HCMUT, VNU-HCM
Ly Thuong Kiet Street, Ho Chi Minh city, 700000, Viet Nam

ABSTRACT

Nowadays, autonomous robots are capable of replacing people with hard work or in dangerous environments, so this field is rapidly developing. One of the most important tasks in controlling these robots is to determine its current position. Because of the complementary features, the integrated GPS/INS system will outperform each individual operating one. This paper introduces the integrated GPS/INS with loosely coupled method, using tri-axis rotation angles estimation and velocity constraints to improve accuracy.

Keywords: Autonomous robot, GPS/INS integration, Loosely Coupled

1. Introduction

For autonomous robots (such as USV, UAV, AUV, etc.) to work in a stable and efficient manner, navigation is one of the most important issues to be aware of. The Global Positioning System (GPS) was originally developed for military purposes but is now widely used for civilian purposes such as mapping, navigation for land vehicles, marine, etc. However, GPS has some disadvantages like the update rate is low or sometimes the satellites' signal is suspended. Another navigation system is the Inertial Navigation System (INS) can allow you to determine position, velocity and attitude from the subject's status, like acceleration and rotation rate. Essentially, INS is a dead-reckoning system so it has a huge cumulative error. An effective method is to integrate GPS with INS, in which the center is a nonlinear estimator (e.g. the Extended Kalman filter) to determine the navigation error, from which it can update the position the object more accurately [1].

Depending on the "depth" of the interaction and for the shared information between the GPS and INS, we have some integration methods: uncoupled integration, loosely coupled (LC), tightly coupled (TC) and deeply integrated [2]. For uncoupled method, GPS output is used as the "reset" signal for the INS. When there is no GPS solution (position and velocity), the integrated system uses INS to estimate. This method has the simplest structure, but the system cannot estimate the sensor's drift, so it is not commonly used. In LC method, GPS solutions will be compared with the inertial estimation to calculate the error state of the object [3, 4]. In TC method the integration is "deeper", the raw measurements of the GPS (pseudorange and Doppler measurements) are directly combined with the calculated INS estimation results in an appropriate filter [4, 5]. Both LC and TC systems operate in closed loop, i.e. position, velocity, attitude errors and sensor's drifts are fed back for the INS and GPS to make a navigation correction. The loosely coupled model is simpler than the tightly one. The structure of tightly coupled model and deeply integration are very complex, so we do not mention in this paper.

In estimating Euler angles, conventional INS systems use tri-axis angular rate to calculate these angles. However, MEMS (Microelectromechanical Systems) IMUs often have large disturbances, so their errors often accumulate rapidly. The INS mechanization method for update rotation angles is only available for a short period. In this paper we use a triangular Euler angles estimator. The centerpiece of this estimator is the two-stage Extended Kalman filter, using accelerometer and magnetic field values to correct the angles evaluated using rotation rate [6].

This paper introduces the building method of loosely coupled GPS/INS integrated navigation system. The Euler angles estimation and the velocity constraints are used to improve accuracy. We use MATLAB/Simulink software to simulate and analyze data. The experimental system is built on a low-cost IMU with tri-axis gyroscope, accelerometer and magnetometer and a GPS module to verify the model algorithm. The update rate of the integrated system is equal to the INS rate of 100 Hz and the rate of GPS is 10 Hz. The data acquisition and processing system is performed on an ARM Cortex-M4 microcontroller.

2. Method
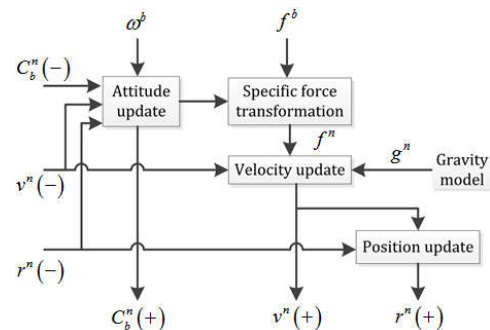
A. Inertial navigation system

Figure 1: INS mechanization in NED frame

INS is a navigation system that uses tri-axis inertial sensors (gyroscope, accelerometer and magnetometer)

to calculate the orientation and position of an object. This system does not need an external reference, so it can continuously calculate without interruption. In this paper, outputs of inertial sensors are three components of the gyroscope, three components of the accelerometer and three components of the magnetometer in the body-frame, denoted by f^b, ω^b, m^b respectively. The figure above describes the INS mechanization in NED frame [3]. The INS uses rotation rate and acceleration values from the IMU sensor to update attitude, velocity and position by the following formula:

$$\begin{bmatrix} \dot{r}^n \\ \dot{v}^n \\ \dot{C}_b^n \end{bmatrix} = \begin{bmatrix} D^{-1}.v^n \\ C_b^n.f^b + g^n - \left(2\omega_{ie}^n + \omega_{en}^n\right) \times v^n \\ C_b^n.\left(\Omega_{ib}^b - \Omega_{in}^b\right) \end{bmatrix} \qquad (17)$$

In this equation, vector $r^n = [\varphi \quad \lambda \quad h]^T$ is the position vector, whose components are geographic latitude, longitude and altitude (height) respectively. Vector v^n is the velocity vector in NED coordinate. Matrix C_b^n is the direction cosine matrix (DCM, or rotation matrix) from body-frame to NED frame. The symbols ω and Ω denote the angular rate and its skew symmetric form, matrix D is the transition matrix from NED frame to latitude, longitude and altitude:

$$D = \begin{bmatrix} (M+h) & 0 & 0 \\ 0 & (N+h).\cos\varphi & 0 \\ 0 & 0 & -1 \end{bmatrix} \qquad (18)$$

Formula (17) is written in continuous form. In experiment, we have to discretize it for simplicity in calculation. Because of this discretization, the update process always has error. On the other hand, IMU sensor has other types of error like bias and scale factor. Thus, the INS errors are rapidly accumulating. To improve the accuracy of the navigation estimation, we use a tri-axis Euler angles estimator [6]. It is structured as a two-stage cascaded Extended Kalman filter (Fig. 2). These filters use acceleration and magnetic field measured from the IMU to correct the Euler angles (roll, pitch and yaw). Precisely, first the EKF-1 combines the gyroscope and accelerometer measurements to calculate the Earth's gravity vector in NED frame, and then it can determine roll and pitch angles. Next, the EKF-2 uses the gyroscope, magnetic field measurements and the determined roll and pitch to calculate yaw angle. In experimental conditions, the accuracy of roll and pitch is 1 degree and accuracy of yaw angle is 3 degrees.
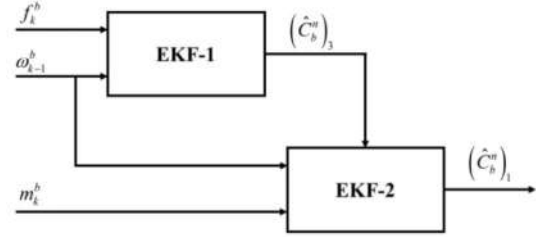
Figure 2: Diagram of the rotation angle estimation

Rotation rate and acceleration measurements can be affected by noises such as deviation, scale factor, non-orthogonality and some other types. Some types of error can be identified and calibrated in the laboratory environment. Some types are unpredictable, and have to be modeled as random noise. In the above factors, bias has the greatest effect on the measurement value of the IMU. So we can model the remaining types of noise (except bias) as white noise (denoted by the symbol η), we have the estimation equation:

$$\begin{cases} \hat{f} = \tilde{f} - b_a + \eta_a \\ \hat{\omega} = \tilde{\omega} - b_g + \eta_g \end{cases} \qquad (19)$$

In equation (19), the symbols $\hat{f}$ and $\hat{\omega}$ are estimated values of acceleration and angular velocity, $\tilde{f}$ and $\tilde{\omega}$ are values measured from the IMU sensor, the symbol b is the bias and η is the other types of noise (modeled as white noise).

B. Loosely Coupled scheme
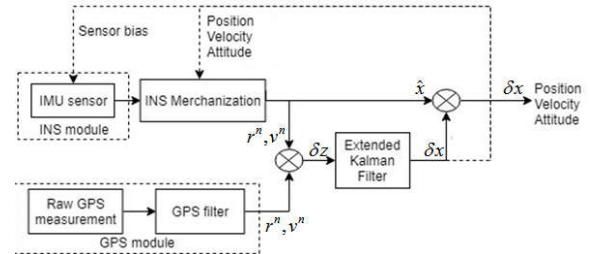
Figure 3: Loosely-coupled model with 15-state vector

The loosely coupled model also referred to as "decentralized" filtering, consists of two estimators. The first one is a nonlinear estimator. It combines the INS estimation results with the GPS results to estimate the position, velocity, attitude error and the IMU sensor's error. The second is the GPS filter. It uses the pseudorange and Doppler measurement values from GPS module to determine the position, velocity. Figure 3 shows the diagram of loosely coupled model.

In today's GPS modules, there is usually a built-in GPS data processor, which can calculate position, velocity and some other information from GPS raw data. In the LC model, position and velocity are fed into the nonlinear filter. The filter used in this paper is the Extended Kalman filter, which is suitable for nonlinear systems. Measurement values from IMU sensor (angular rate and acceleration) after being computed

using the Euler angles estimation and INS mechanization, will be compared with the position and velocity of the GPS. The difference between two results is used as the input of the EKF. The integrated system works in closed loop, the estimated error values are fed back to adjust the state of the INS system and to compensate for the IMU measurements. This close-loop model is suitable for MEMS IMU, which has large disturbance.

The error state vector δx of the EKF filter in this model is composed of the position error δr^n, the velocity error δv^n, the attitude error ϵ, the acceleration bias error δb_a and the gyroscope bias error δb_g. Derive the INS mechanization function and take the first order elements [3], we have the process model equation:

$$\delta \dot{x} = F.\delta x + G.u \qquad (20)$$

where:

$$F = \begin{bmatrix} F_{rr} & F_{rv} & 0_{3\times3} & 0_{3\times3} & 0_{3\times3} \\ F_{vr} & F_{vv} & (f^n \times) & C_b^n & 0_{3\times3} \\ F_{er} & F_{ev} & -(\omega_{in}^n \times) & 0_{3\times3} & -C_b^n \\ 0_{3\times3} & 0_{3\times3} & 0_{3\times3} & -1/\tau_{ba} & 0_{3\times3} \\ 0_{3\times3} & 0_{3\times3} & 0_{3\times3} & 0_{3\times3} & -1/\tau_{bg} \end{bmatrix} \qquad (21)$$

$$G = \begin{bmatrix} 0_{3\times3} & 0_{3\times3} & 0_{3\times3} & 0_{3\times3} \\ C_b^n & 0_{3\times3} & 0_{3\times3} & 0_{3\times3} \\ 0_{3\times3} & -C_b^n & 0_{3\times3} & 0_{3\times3} \\ 0_{3\times3} & 0_{3\times3} & I_{3\times3} & 0_{3\times3} \\ 0_{3\times3} & 0_{3\times3} & 0_{3\times3} & I_{3\times3} \end{bmatrix} \qquad (22)$$

In matrix F, τ_{ba} and τ_{bg} are the correlation time vectors of accelerometers and gyroscopes, determined based on the Gauss-Markov model. The components of vector u are white noises, with the covariance determined by the formula:

$$Q = diag\left(\begin{bmatrix} q_a & q_g & q_{ba} & q_{bg} \end{bmatrix}\right), q = \frac{2\sigma^2}{\tau} \qquad (23)$$

In the above equation, σ is the standard deviation of the Gauss-Markov noise. Matrix Q is called the spectral density matrix and its component, respectively, are covariance accelerometer, gyroscope, accelerometer bias and gyroscope bias. These values can be determined in the datasheet of the sensor [5].

The measurement model of the EKF is the difference of the INS results (position and velocity) and GPS results:

$$\delta z = \begin{bmatrix} r_{INS}^n - r_{GPS}^n \\ v_{INS}^n - v_{GPS}^n \end{bmatrix} = H.\delta x + \varepsilon \qquad (24)$$

In the above equation, symbol ε is the measurement noise. Its covariance matrix R can be obtained from GPS processing. The activation of the EKF is divided into 2 stages: update and prediction. The Kalman gain is computed first in the update stage. Then state variables (δx) and error covariance (P) are updated based on prior estimates and its error covariance. After each correction, the error state vector should be reset to

zero.

When there is a GPS outage, we can use velocity constraints (Fig. 4) to estimate errors [4]. Vehicles essentially move in forward direction. If the vehicle does not jump off the ground nor slide on the ground, its velocity in the axes perpendicular to the forward direction (y-axis and z-axis) is almost zero. So we have two velocity constraints are:

$$\begin{cases} v_y^b \approx 0 \\ v_z^b \approx 0 \end{cases} \qquad (25)$$
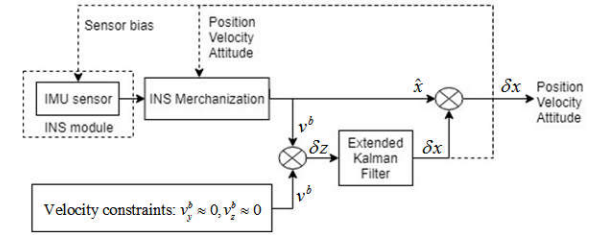
Figure 4: EKF with velocity constraints

3. Simulation results

In simulation, we use FlightGear simulation software [7] to create the data file and use MATLAB/Simulink to process it. The GPS signal is disturbed with noise to research about noise suppression of the estimator. The standard deviation of noise is 2.5 m in each horizontal axis and 5 m in vertical axis. Simulations were made in two cases: with and without the Euler angles estimator. We have the result table:

Table 1: Attitude, position and velocity errors

Error	Without Euler angles estimation			With Euler angles estimation		
Attitude (r-p-y) (degree)	24.7	48.6	14.8	2.0	2.0	2.0
Position NED (m)	0.69	1.54	1.62	0.43	0.47	2.99
Velocity NED (m/s)	1.80	3.46	4.61	0.05	0.05	0.04

From the table above, we can see that with the rotation angles estimator, the results are better. The horizontal accuracy is about 0.64 meters. The velocity error is within 0.1 m/s. We can conclude that the estimator has good filtering capability. Next, we will examine the quality of the system when the GPS signal is lost in intervals of 3, 5 and 10 seconds.

Table 2: Horizontal accuracy during GPS outages

GPS outage	Without Euler angles estimation	With Euler angles estimation
3 seconds	15.0 m	0.88 m
5 seconds	35.8 m	0.92 m
10 seconds	171.4 m	1.33 m

Thus, when there is a GPS outage, the error of the system will be larger than the normal case (GPS fix). In addition, if the GPS lost time is longer, the horizontal error is larger. Using an Euler angles estimator helps to make small errors.

4. Experimental results

A. Hardware development

We built an experimental system to verify the implemented algorithm. The hardware (Fig. 6) consists of the IMU sensor ADIS16405 from Analog Devices [9], the GPS module from U-blox [9] and the microcontroller STM32F407 (ARM Cortex-M4) from STMicroelectronics [10].

The reference system is the GNSS/INS system from Xsens Technology. The MTi-G-700 [11] can give rotation angles estimate with a 1 degree accuracy, position error of 2 meters and velocity error of 0.05 m/s. The update rate of INS and GPS are 100 Hz and 10 Hz, respectively. In each INS cycle of 10 milliseconds, the STM32F407 microcontroller reads data from the IMU sensor and the GPS module. Then update the error estimator, using Extended Kalman filter algorithm. Navigation data is sent to the computer via COM/RS232 port or via SD card.
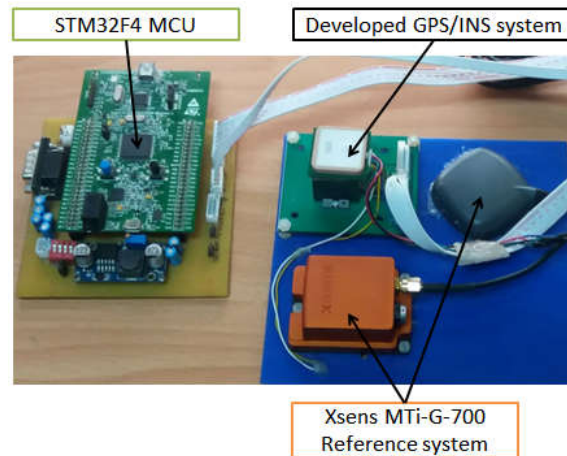
Figure 5: GPS/INS system in experiments

B. Results:

Table 3: Attitude, position and velocity errors

Error	Without Euler angles estimation			With Euler angles estimation		
Attitude (r-p-y) (degree)	70	29	83	1.31	1.07	16.7
Position NED (m)	11	7.7	313	1.58	0.58	4.42
Velocity NED (m/s)	10	6.4	85	0.27	0.26	0.46
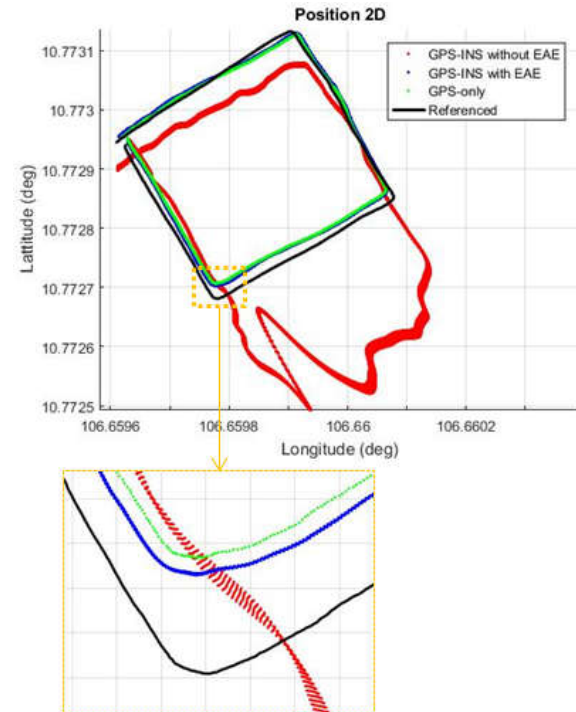
Figure 6: Estimated 2D position

For MEMS IMU sensors, the amplitude of its noise is huge, so if we do not use the Euler angles estimator, the result is bad, the attitude, position, velocity errors are enormous. The estimated trajectory (red dots in Fig. 6) does not have the same shape with the reference one (black line). In contrast, when we use the angles estimator, the errors are smaller, the accuracy is higher. The horizontal error of our GPS/INS system is 1.69 m, while the error of the individual GPS system is 1.93 m. For this reason, the GPS/INS algorithm can reduce over 10% of the error. On the other hand, the update rate of GPS is only 10 Hz. The integrated GPS/INS update rate is 10 times larger (100 Hz). We can see the effective of

high update rate in Fig. 6. Because the GPS has the low update rate of 10 Hz, there are visible spaces between the green dots (GPS-only). And if the vehicle moves very fast, the GPS cannot describe the vehicle's trajectory accurately. Differently, the blue dots (GPS/INS) approximately form a continuous line. From the above results, it can be concluded that the angles estimator can improve the accuracy of the navigation system and the integrated GPS/INS system performs better than the single GPS system.

Next, assuming the GPS signal is lost for a period of 5 seconds, we will analyze the accuracy of implemented GPS/INS system in cases with and without speed constraints. We will simulate GPS outages in two cases: GPS lost in straight line and in curved line.
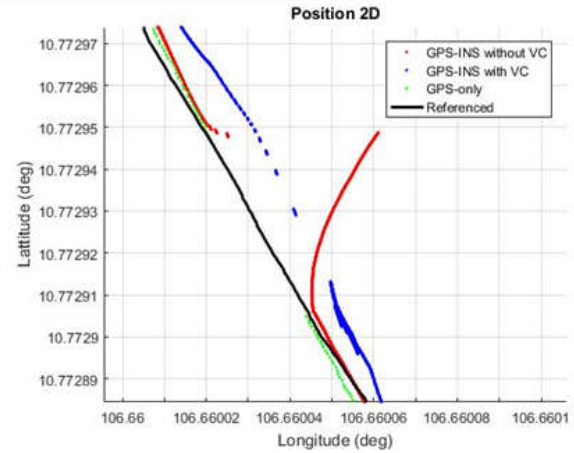
Figure 8: GPS outage – Curved line

Table 4: Horizontal accuracy when GPS lost, with and without velocity constraints

	Horizontal error (m)		
	GPS fix	5 seconds GPS lost, straight line	5 seconds GPS lost, curved line
Without velocity constraints	1.69	2.23	2.60
With velocity constraints	1.59	2.76	1.96
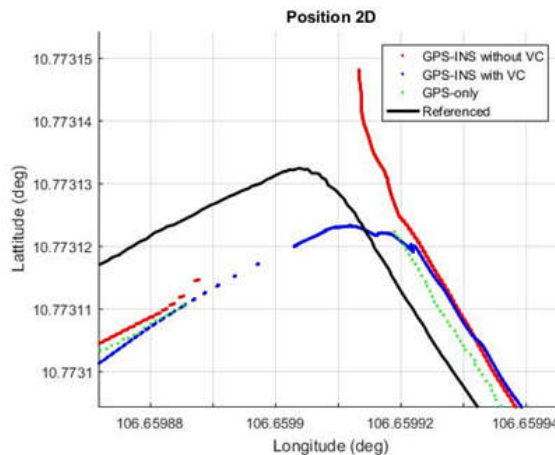
Figure 7: GPS outage – straight line

From the above results, we can see in the normal case of GPS fix, the velocity constraints can still reduce the horizontal error of the system. When there is a GPS outage, using speed constraints can either increase or decrease the system's accuracy. However, it restricts the trajectory from divergence. The blue dots in Fig. 7 and Fig. 8 can follow the reference trajectory, while the red dots are diverging. Thus, velocity constraints are also a tool that can improve the accuracy of the integrated GPS/INS navigation system.

5. Conclusions

In this paper, we have implemented a loosely coupled GPS/INS integrated navigation system. The main algorithm in this system is the Extended Kalman filter. We combined the EKF with Euler angles estimator and velocity constraints to improve accuracy.

The rotation angles estimator helps us to determine the Euler angles correctly, thereby increasing the quality of the position and velocity estimation. In practice, the accuracy of roll and pitch angle is 2 degrees, the error of yaw angle is still large.

The achieved horizontal accuracy is 2m when the GPS signal is stable and 3m when the GPS signal is lost in a short period. Compared with individual GPS, the error of the integrated system is about 10% smaller. In addition, the positive point of the GPS/INS is its update rate reaches 100 Hz, which is 10 times larger than the initial system. When there is a long-period GPS outage, the LC algorithm's result is very bad, so we need to use the tightly coupled model. In the future, we will research about this model, point out its advantages and disadvantages, and compare with the original model. After that, we will find the optimal switching method between two models.

References

[11] K. Kim, *"GPS/INS with non-linear filters,"* ICCAS 2011, KINTEX, Gyeonggi-do, Korea, 2011

[12] George T. Schmidt, Richard E. Phillips, *"INS/GPS Integration Architectures,"* RTO Lecture Series RTO-EN-SET-116, 2010

[13] Eun-Hwan Shin, *"Accuracy Improvement of Low Cost INS/GPS for Land Applications,"* University of Calgary, 2001

[14] A. Angrisano, *"GNSS/INS Integration Methods,"* PhD Thesis, The Parthenope University of Naples, Italy, 2010

[15] Hoang-Duy Nguyen et.al, *"Implementation of a GPS/INS tightly-coupled system in urban environment,"* The 3rd Vietnam Conference on Control and Automation, Ho Chi Minh city, 2015

[16] Ngoc-Huy Tran, Manh-Cam Le, *"Orientation estimation using extended Kalman filter,"* The 4th Conference on Science and Technology, HCMC University of Transport, 2018

[17] FlightGear Flight Simulator http://home.flightgear.org/

[18] Analog Devices, *"ADIS16405 – Triaxial Inertial Sensor with Magnetometer"*, 2017

[19] u-blox AG, *"NEO-M8, u-blox M8 concurrent GNSS modules"*, 2016

[20] STMicroelectronics, *"Datasheet STM32F405xx – STM32F407xx"*, 2016

Xsens Technologies, *"MTi User Manual: MTi 10-series and MTi 100-series 5th generation"*, 2018

PART VII, SECTION I

Machining Technology
(Difficult-to-cut and Free Machining; Non-conventional Machining;
Green Process/Manufacturing; Cutting Mechanisms…)

Microstructure of Built Part Obtained by Powder Bed Fusion Process With Metal

Tatsuaki Furumoto[1], Kyota Egashira[2], Souta Matsuura[2], Makoto Nikawa[3],
Masato Okada[4], Tomohiro Koyano[2], Yohei Hashimoto[2], Akira Hosokawa[2]
[1] Institute of Science and Engineering, Kanazawa University
[2] Graduate school of National Science and Technology, Kanazawa University
[3] Faculty of Engineering, Gifu University
[4] Faculty of Engineering, University of Fukui

ABSTRACT

The influence of various process parameters on the building of maraging steel powder by the PBF processes is investigated. The microstructure in the built part was observed and the influence of the heat treatment was evaluated. As results, the depth of solidified layer was higher than that of deposited metal powder, and its value was influenced with the process parameters. The microstructure in the boundary between the built part and the substrate was quite different from the built part even if the suitable heat treatment was performed.

Keywords: additive manufacturing, powder bed fusion, maraging steel powder, microstructure, hardness

1. Introduction

Selective laser melting (SLM) is one of the Additive manufacturing (AM) techniques where the three dimensional parts obtained through the computer-aided design system are built by selective deposition of materials. Especially, the SLM with metals has attracted more attention from medical, aerospace, and automotive industries due to the flexibility of the process and the wide variety of materials, such as steel, titanium, aluminium alloys, and nickel-based alloys [1]. Metal based AM techniques are mainly classified into powder bed fusion (PBF) and directed energy deposition (DED) [2]. In order to produce high quality products, hybrid machines, in which the AM process and a subtractive process are performed sequentially, have also been developed that are based on either the PBF process [3] or DED process [4].

Despite the above advantages compared to traditional subtractive and formative processes, there are still several deficiencies in the AM processes [5]. The heat source used to construct the parts is laser, and rapid heating and cooling cycles are repeatedly performed during the building process. The rapid cooling processes cause residual stress, which induces the deformation and cracking of the built parts due to their internal thermal gradients [6]. The thermal gradients around the heat source during the building process also creates a partially melted zone in which the dimensional accuracies and surface qualities of the built parts are inferior to those in traditional manufacturing methods [7]. In addition, the mechanical properties of built parts are relatively low in the as-built state, and the heat treatments are needed to improve the quality of built parts [8].

This study focuses on the building of maraging steel powders by the PBF processes in order to improve the mechanical properties of the built parts. In the PBF processes, the metal powder deposited on the substrate is selectively melted and solidified as the alloyed material with the substrate or the previous built structure. In this paper, the cross section of built part is observed by an optical microscope and a scanning electron microscope, and the influence of process parameters on the hardness and the formation of pores is investigated. In addition, the variation of microstructure by an aged treatment is evaluated.

2. Experimental setup
2.1 Metal powder

The SEM image of metal powder is shown in Fig. 1, and its specifications are summarized in Table 1. The
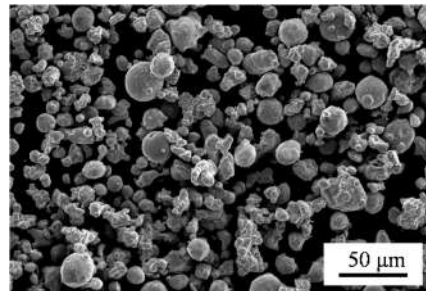

Fig. 1 SEM image of metal powder

Table 1 Specifications of metal powder

Alloying element [wt%]	Fe: Balance Ni: 15 - 25 Co: 5 - 10 Mo: 3 - 7 Ti: 0 - 1.0 Cr: 0 - 0.7 Mn: 0 - 0.5
Shape	Irregular
Average diameter [μm]	25
Layer thickness [μm]	50
Thermal conductivity [W/m·K]	0.25

Table 2 Experimental conditions for 3D building

Laser source	Yb:fiber
Wavelength [nm]	1070
Power [W]	320
Scan speed [mm/s]	150 - 250
Hatching pitch [mm]	0.2
Focal spot diameter [μm]	100
Atmosphere	N_2
Substrate	
Material	Carbon steel
Thickness [mm]	20
Temperature [°C]	25 - 200
Built size [mm]	20 × 10 × 10
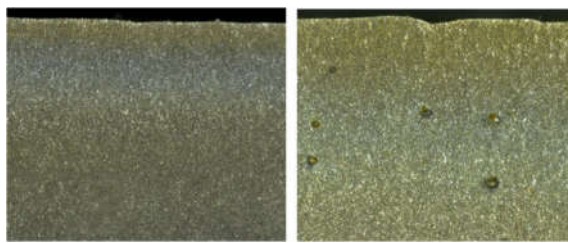
(a) 430 J/mm^3 (b) 320 J/mm^3
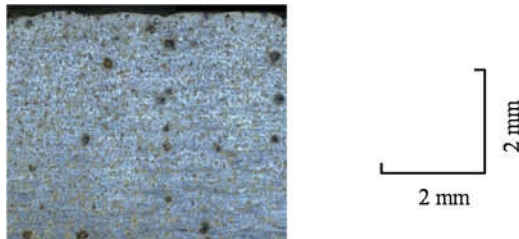
(c) 260 J/mm^3

Fig. 2 Formation of pores in each conditions

metal powder used was a maraging steel powder with an average particle size of 25 μm. The metal powder was deposited on the substrate with a thickness of 50 μm without pressing from the powder surface, so that the thermal conductivity of powder bed was 0.25 W/m•K.

2.2 Experimental conditions

In order to investigate the aspect of pores inside the built structure, the three-dimensional structure was built by a PBF equipment (Matsuura Machinery Corp.: LUMEX25C). Table 2 indicates the experimental conditions. The laser beam used was a continuous Yb:fiber laser (IPG photonics Corp.: YLR-SM) with a wavelength of 1070 nm and a maximum laser power of 500W. The laser beam was led to the powder surface through a galvanometer mirror, and its focal diameter was 100 μm. The hatching pitch of the laser beam was kept constant to 0.2 mm. The scan direction of the laser beam was varied by 90° to prevent the anisotropy of the built part. These processes are repeated until the three-
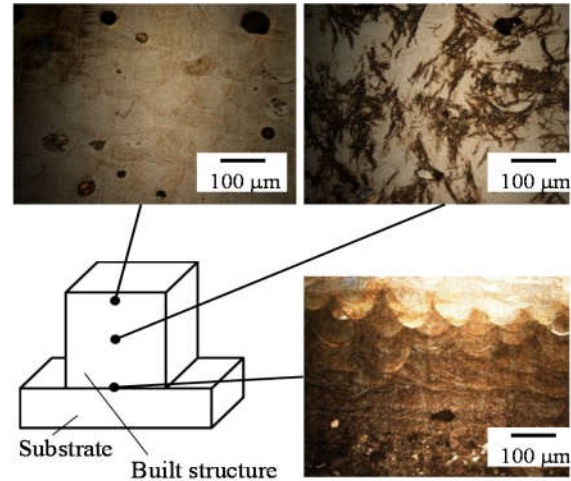
Fig. 3 Microstructure in as-built structure

dimensional part was completely built. In addition, a nitrogen atmosphere was used to prevent oxidization of the metal powder during laser irradiation. The substrate on which the metal powder was placed was carbon steel (AISI 1049), and its surface was sandblasted by WA abrasive grains with an average grain diameter of 300 μm to improve the wettability of the melted powder. After sandblasting, the surface roughness of the substrate was Ra=3.5 μm [9].

The size of built part was 20 mm × 10 mm × 10 mm. The built part was evaluated based on the volume specific energy density, which was calculated using the process parameters of the laser power, laser scan speed, beam diameter, and layer thickness [10]. The built part was cut with by a wire electrical discharge machine (Sodick Co., Ltd.:AQ325L) and the cross section was observed by an optical microscope (Keyence Corp.: VHX-1000) and a scanning electron microscope (JEOL Ltd.: VSM- 6290LVU) after etching with 3% nital solution. The hardness of the built part was also measured using a Vickers hardness testing machine (Mitutoyo Corp.: HM-101) using a load of 9.8 N. In order to investigate the influence of heat treatment on the mechanical properties, the built part was aged at 500 ºC for 2 h. In addition, the microstructure in each position was analyzed by the Energy Dispersive X-ray Spectroscopy (JEOL Ltd.: JSM-7100F).

3. Results and discussions
3.1 Formation of pores inside built part

Figure 2 shows the cross-sectional images of the built part when the volume specific energy density was ranged from 260 to 430 J/mm^3. The number of pores was increased with the decrease of volume specific energy density. When the volume specific energy density was 430 J/mm^3, there were almost no pores in the built part due to the full melting conditions. On the other hand, when the volume specific energy density was below the 320 J/mm^3, the pores occurred in the

(a) Center

(b) Boundary

Fig. 4 EDX analysis in built structure

Fig. 5 Microstructure in aged structure
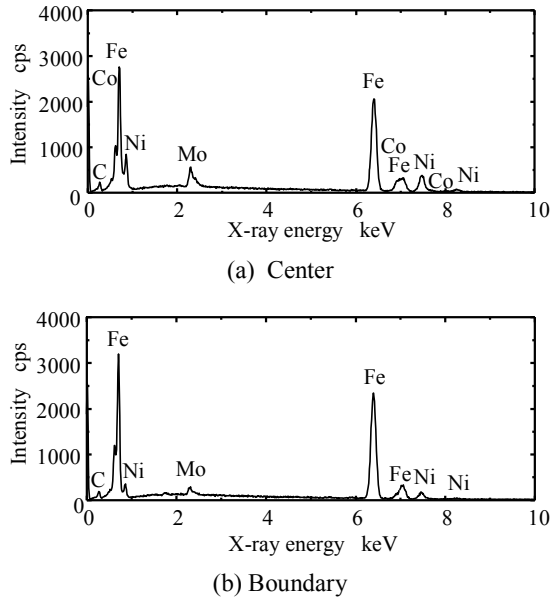

(a) As built   (b) Aged treatment

Fig. 6 Comparison of SEM images in built structure

built part and its amount was increased as the volume specific energy density was decreased. This result showed that the building phenomena was shifted from the full melting condition to the sintering condition [11]. The size of pores was from 50 - 150 μm, and its size was larger than the thickness of deposited metal powder.

3.2 Microstructure in as-built structure

Figure 3 shows the cross-sectional images of as-built part etched by nital solution and compares the microstructure in each position. Here, the volume specific energy density was 260 J/mm^3. As was obvious from images, the microstructures were quite different in each built position. In the upper position, the typical semi-elliptical scan tracks induced by the melting and the solidifying of the metal powder during the layer buildings could be seen. The height of scan tracks was larger than that of deposited metal powder due to the alloying with the previous built structure. In addition, the overlapping among different scan tracks was observed. The formation of semi-elliptical scan tracks was induced by the thermal gradient around the melt pool. The laser beam used in the PBF equipment formed a Gaussian shape, therefore, the temperature on the melt pool was the highest at the center and its temperature was decreased at the edge of the melt pool. The growth of scan track was proportional to the thermal gradient and resulted in the formation of the semi-elliptical scan track [12]. In the middle position of built part, the dendritic microstructure was observed in addition to the formation of semi-elliptical scan tracks. These structures were acicular martensite. In the boundary between the built part and the substrate, the semi-elliptical scan tracks was also observed. The deposited metal powder and the substarte were melted with the heat generated by the laser irradiation and these melted materials were alloyed in the process of the
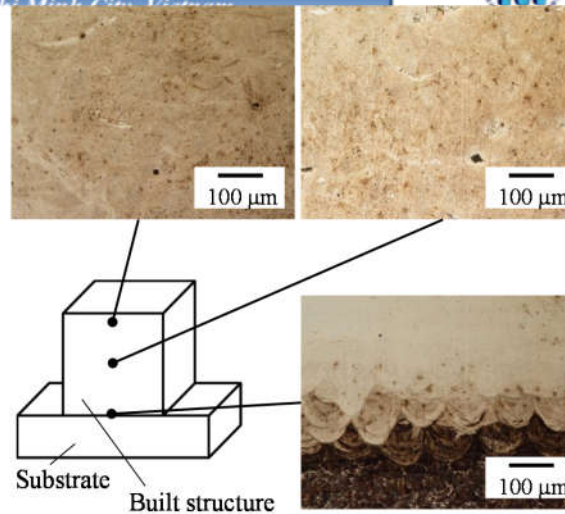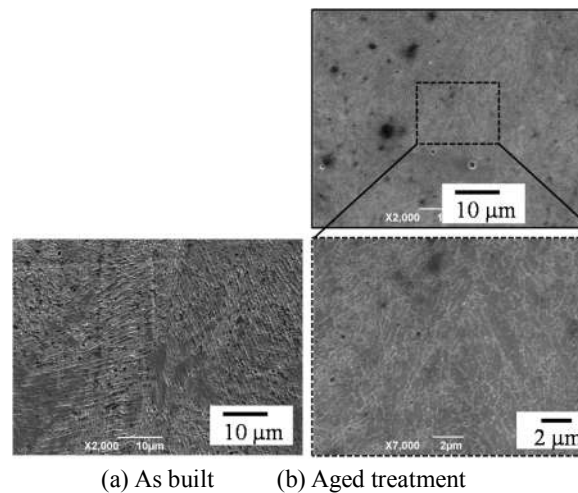
solidification [9].

Figure 4 compared the EDX patterns between the middle position and the boundary in the as-built part. As depicted in Fig. 5(a), the same chemical composition with the metal powder was detected in the middle position. This result indicated that the metal powder was solidified without the evaporation during the PBF processes. On the other hand, as shown in Fig. 5(b), nickel and cobalt compositions in the boundary was lower than that in the middle position. This result also showed that the deposited metal powder and the substrate were alloyed in the process of the solidification, and resulted in the decrease of nickel and copper compositions.

3.3 Microstructure in aged structure

Figure 5 shows the cross-sectional images of the built part after the aged treatment at 500 °C for 2 h. The volume specific energy density was same as in Fig. 3. The scan tracks were completely disappeared in the upper and the middle position by the aged treatment due
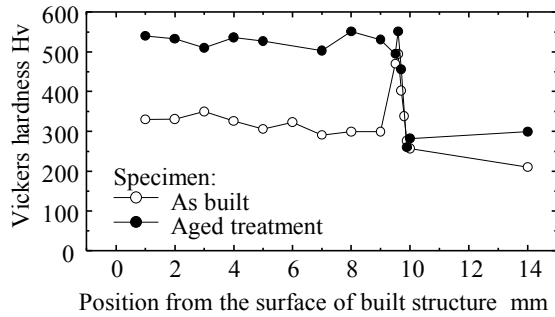
Fig. 7 Distribution of Vickers hardness

to the replacement to the martensite microstructure. By contrast, the semi-elliptical scan tracks still remained in the boundary between the built part and the substrate. The height of the semi-elliptical scan tracks was 140 μm. On the other hand, the size of pores inside the built part was quite lower than the as-built part due to the effect of aged treatment. This results indicated that the aged treatment was also effective for the decrease of the amount of pores in addition to the improvement of the hardness.

Figure 6 compares the SEM images of as-built and aged treatment parts under the volume specific energy density of 260 J/mm^3. As shown in Fig. 6(a), the as-built part consisted of the mixture of submicron sized cellular microstructure and dendritic structure, and these were clearly divided by the semi-elliptical scan tracks. By contrast, the martensites are refined after aged treatment and the acicular martensites are formed as depicted in Fig. 6(b). It was reported that the cellular structure in maraging steel obtained by the PBF processes contributed to the excellent strength and hardness [12]. For the building of high strength part, the cellular microstructure has to be built uniformly inside the built parts.

3.4 Distribution of hardness

Figure 7 compares the Vickers hardness of as-built and aged treatment parts at the each position under the volume specific energy density of 260 J/mm^3. The horizontal axis indicates the distance from the surface of built part, that is the built part ranged 0 - 10 mm and the substrate was over 10 mm. As was obvious from the graph, the Vickers hardness in the as-built part was ranged from 290 to 350 Hv, and from 500 to 550 Hv in the aged part. These values were higher than the conventional maraging steel (280 Hv) [13]. As indicated in Fig. 6, the cellular and the dendritic structure was observed in the as-built part, and the acicular martensites were formed in the aged part. The higher hardness value was attributed to the formation of these microstructure. However, the microstructure was not uniform in the as-built part and resulted in the decrease of hardness value compared with the aged part. These results also indicated that the microstructure has to be uniform for the high quality of built parts.

On the other hand, the Vickers hardness at the

boundary between the built part and the substrate was ranged from 340 to 490 Hv, and these values were almost same before and after heat treatment. As shown in Fig. 4, nickel and cobalt compositions in the boundary was lower than that in the built structure. The decrease of Vickers hardness at the boundary was attributed to the alloying of metal powder and substrate.

4. Conclusions

In this paper, the cross section of built part was observed and the influence of process parameters on the hardness and the formation of pores was investigated. In addition, the variation of microstructure obtained by the PBF processes with the heat treatment was evaluated. The results obtained are summarized as follows.

(1) The number of pores was influenced by the volume specific energy density. The size of pores was from 50 - 150 μm, and its size was larger than the thickness of deposited metal powder.

(2) The microstructure in the as-built parts was different in the position. The semi-elliptical scan track was observed in all area and the dendritic microstructure was observed in the middle position.

(3) Nickel and cobalt compositions in the boundary was lower than that in the built part due to the alloying of the metal powder and the substrate.

(4) The hardness of as-built part was higher than the conventional maraging steel due to the mixture of submicron sized cellular microstructure and dendritic structure.

Acknowledgement

References

[1] D. Bourell, J.P. Kruth, M. Leu, G. Levy, D. Rosen, A.M. Beese, A. Clare, CIRP Ann., 66, 2 (2017) 659-681.

[2] M.K. Thompson, G. Moroni, T. Vaneker, G. Fadel, R. I. Campbell, I. Gibson, A. Bernard, J. Schulz, P. Graf, B. Ahuja, F. Martina, CIRP Ann., 65, 2 (2016) 737-760.

[3] Abe, S., Higashi, Y., Fuwa, I., Yoshida, N., Yoneyama, T., Proc. 11th Int. Conf. Precis. Eng. (2006) 288-293.

[4] Kakinuma, Y., Mori, M., Oda, Y., Mori, T., Kashihara, M., Hansei, A., Fujishima, M., CIRP Ann., 65, 1 (2016) 209-212.

[5] J.P. Kruth, G. Levy, F. Klocke, T.H.C. Childs, CIRP Ann., 56, 2 (2007) 730-759.

[6] Shiomi, M., Osakada, K., Nakamura, K., Yamashita, T., Abe, F., CIRP Ann, 53, 1 (2004) 195-198.

[7] Yassin, A., Ueda, T., Furumoto, T., Hosokawa, A., Tanaka, R., Abe, S., J. Mater. Process. Technol., 209, 15-16 (2009) 5680-5689.

[8] E.A. Jägle, Z. Sheng, P. Kürnsteiner, S. Ocylok, A.

Weisheit, D. Raabe, Mater., 10, 1 (2017) 8.

[9] Furumoto, T., Ueda, T., Kobayashi, N., Yassin, A., Hosokawa, A, Abe, S., J. Mater. Process. Technol., 209, 18-19 (2009) 5973-5980.

[10] A.B. Spierings, K. Dawson, M. Voegtlin, F. Palm, P. J. Uggowitzer, CIRP Ann., 65, 1 (2016) 213-216.

[11] Furumoto, T., Koizumi, A., Alkahari, M.R., Anayama, R., Hosokawa, A., Tanaka, R., Ueda, T., J. Mater. Process. Technol. 219 (2015) 10-16.

[12] Mutua, J., Nakata, S., Onda, T., Chen, J.C., Mater. Des, 139, 5 (2018) 486-497.

[13] K. Kempen, E. Yasa, L. Thijs, J.P. Kruth, J. Van Humbeeck, Phys. Procedia, 12 (2011) 255-263.

Precision Polymer Microfabrication of Microfluidic Model for Biological and Environmental Investigations

Chia-Wen Tsao

Department of Mechanical Engineering, National Central University, Taoyuan, Taiwan

ABSTRACT

With the development of microfluidics, lab-on-a-chips (LOCs), micro total analysis systems (µTAS), the material used in these microdevices have shifted from silicon or glass to polymer substrates due to its low material and fabrication facility cost, ease of fabrication, and disposable advantages. In early stages, polymer microfabrication still relies on silicon-based microfabrication processes such as photolithography, or UV-assisted processing to fabrication polymer-based microfluidic devices. Recently, while the resolution of precision machining advanced to sub-micron or micron level, it gradually replaces the silicon-based microfabrication process for microfluidics fabrication. In this conference presentation, we demonstrate using some transitional machining process to fabricate the microfluidics devices for biological and environmental applications with low-cost and high yield.

Keywords: Microfluidics; polymer microfarication; precision micromachining;

Research and Develop a Multiple Parameter Monitoring and Control System Applicable for Greenhouse in Vietnam

Nguyen Van Ton, Van Thanh Vinh, Tran Dinh Duong, Le Tuan Anh,
Dinh Ngoc Phu, Nguyen Dang Nghia, and Bui Huu Phu
Hochiminh City University of Technology and Education, Vietnam
01 Vo Van Ngan street, Thu Duc district, Hochiminh City, Vietnam
Email: phubh@hcmute.edu.vn

ABSTRACT

Vietnam is now focusing on researching and applying high technologies to agriculture in order to increase quality, productivity, efficiency. One of them is the system that monitors and controls parameters in the greenhouse. Almost the system used in Vietnam is imported from other countries which are very expensive, difficult to maintenance, and time consuming for warranty.

That is the reason that many Vietnamese local research groups concentrate on the study recently. In the paper, we will present our research on developing a remote control and monitoring system of temperature and humidity in green house through website or smartphone based on wifi chip ESP8266, special pump, fan, moisturizer. The system is localized 100% and used popular modules in Vietnam market with cheap price.

With our pilot system, it can be used to monitor and control all parameters in a greenhouse including of temperature, air humidity, and soil humidity by smartphone, hand phone, website. The system has a quick response and very stable, remote control, and very easy to use for anyone, especially price is much cheaper than imported products. We are packing and make a good commercial design to be able to technology transfer to Vietnam market soon.

Keywords: Green House, Smart Agriculture, monitoring and control system, multiple monitoring system,

Design and Implement of a Smart Door Lock System Based on RFID Technology

Hoang Ngoc Tuyen, Nguyen Viet Tien, Trinh Ngoc Thanh Bao,
Phan Van Phung, Truong Dai Hiep, and Bui Huu Phu
Hochiminh City University of Technology and Education, Vietnam
01 Vo Van Ngan street, Thu Duc district, Hochiminh City, Vietnam
Email: phubh@hcmute.edu.vn

ABSTRACT

Smart Home is a key research topic over the world recently. Many researchers concentrate on developing smart systems to use in home to support end users in high security, convenience, comfortableness, and cost saving.

Smart door lock system based on RFID technology is a new research trend in the world. The technology has many advantages compared with the traditional ones. In the paper, we present our own research, design, and implement of the system based on micro- controller PIC16F887. The system is totally localized and used popular modules in Vietnam market with the cheap price.

We have completed the design and implement of a pilot system. It works well, stable, high security, and can be remotely monitored and controlled. The system has a quick response and very stable, remote control, and very easy to use for anyone, especially cheap price. We are packing and make a good commercial design to be able to technology transfer to Vietnam market soon.

A Design of Bamboo Plywood Pressing Machine

Nguyen Thanh Nam[1], Le Khanh Dien[1], Hoang Duc Lien[2], Svetlin Antonov[3]

[1] DCSELAB - **Ho Chi Minh City University of Technology**, VNU-HCM, Vietnam
[2] Vietnam National University of Agriculture (VNUA), Vietnam
[3] Technical University Sofia, Bulgaria

ABSTRACT

Bamboo plywood presses play an important role in the production bamboo plywood in industry`. The machine has the function of pressing bamboo powder and binder has been mixed from the front to the bamboo plank to meet the technical requirements. This article presents a design of bamboo polywood pressing machine that combines the heating function for the block board and keeps that temperature during the pressing process to create a suitable size bamboo plywood according to customer requirements.

Keywords: Bamboo polywood, Pressing machine, Bamboo powder, Fnctional analysis

1. Introduction

Bamboo is a sustainable and environmental friendly material that has the potential to improve the global decline of natural resources. Bamboo is very popular in countryside of almost all Southeast countries, particularly in Vietnam. Its ability can replace some kinds of wood in decoration and household goods. Bamboo grow up rapidly and can be harvested within 3 to 5 years of planting, in the meanwhile the harvesting time of other hardwood trees must be from 8 to 10 years or longer. The inherent characteristics of bamboo is lighter than other wood materials and has a value in social and environmental benefits. Its advances in manufacturing technology have created high value products such as bamboo flooring and bamboo furniture that can substitute for wood flooring and wood furniture. According to the biology studies, the bamboo has the characteristics that can replace the natural wood, but the direction of development from the stage of cultivation to the stage of finished products has not been exploited thoroughly. The closure and restrictive exploitation of forests in many countries around the world are an opportunity, but also a big challenge for businesses in developing wood alternative products of bamboo, especially in Vietnam [1].

With abundant bamboo resources, the production of bamboo plywood will become a great potential for the bamboo plywood industry in Vietnam. However, the bamboo plywood industry in Vietnam is only developing and stopping in the production of pressed bamboo. Therefore, instead of using the technology of squeezing bamboo together, we can chop and grind the bamboo tree to powder that is dried and pressed into bamboo plywood by specialized machine similar to the production artificial wood particleboard (PB). Bamboo waste such as bamboo shoots thrown away after harvesters can be used to recycle and produce bamboo boards, both for environmental protection and for economic benefit [2].

In the production process of bamboo plywood, the bamboo-pressing machine plays a very important role of the function of pressing bamboo powder plywood board after the the blending bamboo process and before cutting and trimming process to standard industrial dimensions. It is necessary to design carefully the bamboo polywood pressing machine because it is the main facture to decide the quality, the productivity and the saving energy of the chain of production of bamboo plywood [3].

2. Structural design for bamboo pressing machine:

Functional analysis of bamboo pressing machine is shown in Figure 1
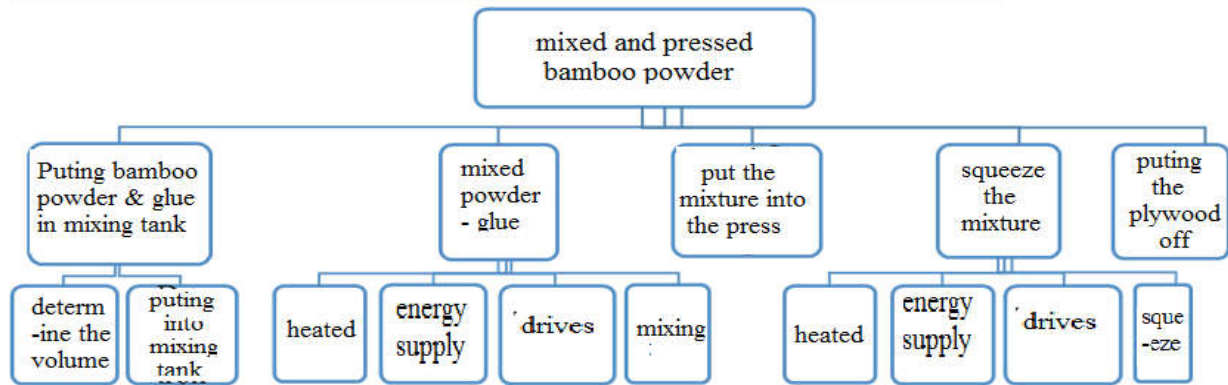
Figure 1. *Diagram of functional analysis of bamboo polywood pressing machine*

To arrange the functions of the bamboo pressing machine, we have the following diagram (Fig. 2) [4]:
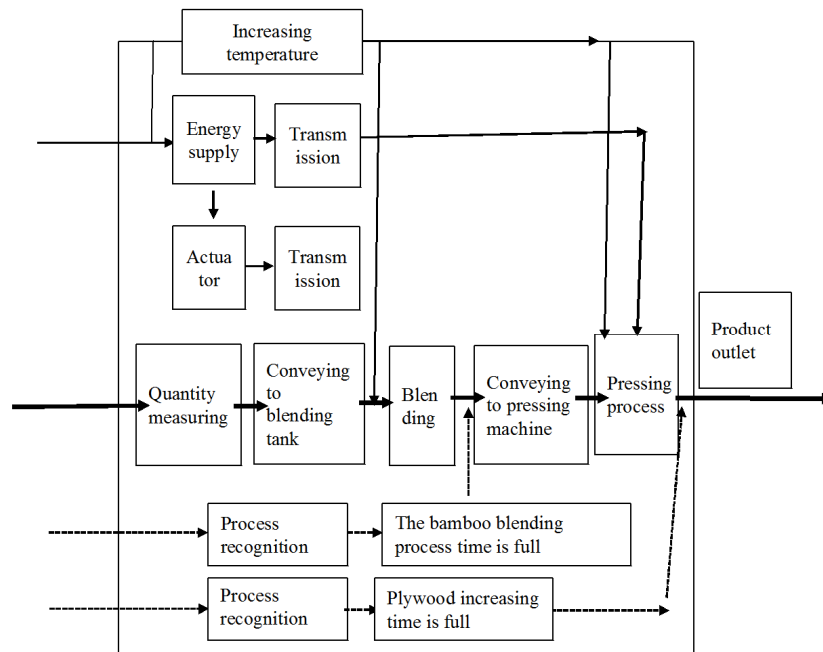
Figure 2. *Functional arrangement map of bamboo plywood pressing machine*

System design, structure of bamboo pressing machine
(Figure 3) [4]:
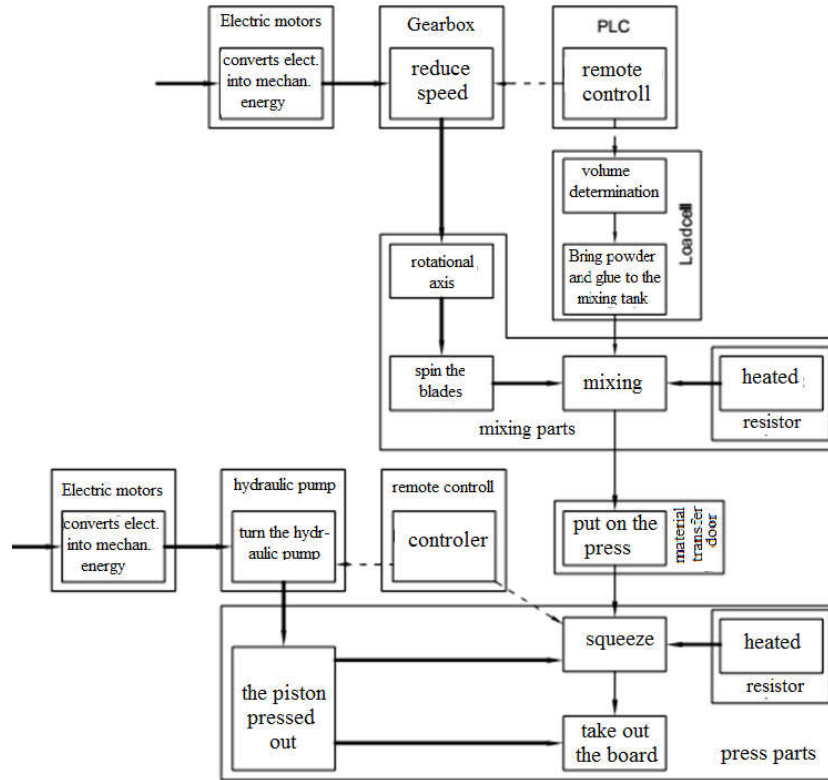
Figure 3. Structural plan of bamboo plywood pressing machine

In one word, the bamboo-pressing machine consists of the following modules: 1) Electric motors; 2) Gearbox; 3) PLC controllers; 4) Load cell; 5) Mixing module; 6) Feed material module; 7) Hydraulic module; 8) Pressed module.

3. Design calculations of bamboo pressing machine:

The selected machine size 500x300x200mm is appropriate to the volume of finished product after pressing is 0.03m³.

- The density of pressed plywood is 800kg/m³.
- The volume of 1 mixed batch after squeezing is 800x0.03 = 24kg;

- Mixture ratio of bamboo glue: 8 ~ 12%;
- Maximum pressure on the surface p_{uma}= 26kgf / cm²;
- Total pressure on the surface: P = 50x30x26/1000 = 39 tons.
- The thickness of blended pulp: h = 200mm;
- Pressing course: S = 1050mm;
- Time holding pressure: t = 15 minutes;
- Maximum press temperature: Tmax = 1800C;
- Heat resistance is applied;
- Power source: electric motor and hydraulic system.

Note:
1. Elect. motor
2. Gear box
3. Chain Drives
4. Glue pump
5. Mixing wings
6. Loadcell
7. Powder box
8. Cylinder discharge
9. Mixing tank
10. Material exit door
11. Product exit door
12. Pedestal
13. Pressed plate
14. Cylinders
15. Base
16. Hydraulic system

Figure 4. Dynamic diagram of bamboo plywood pressing machine

a. Select the cylinder

Due to the system working with pressure (39 tons), we choose the working pressure of about 200 bar (20MPa)

The inner radius of the cylinder is given by the formula [5]:

$$r_B = \sqrt{\frac{P_H}{\pi p}} = \sqrt{\frac{39x1000}{\pi x 200}} = 7.88cm = 78.8mm$$

P_H: nominal force of the machine. PH = 39 tons; p: working pressure of hydraulic oil: p = 200 bar.
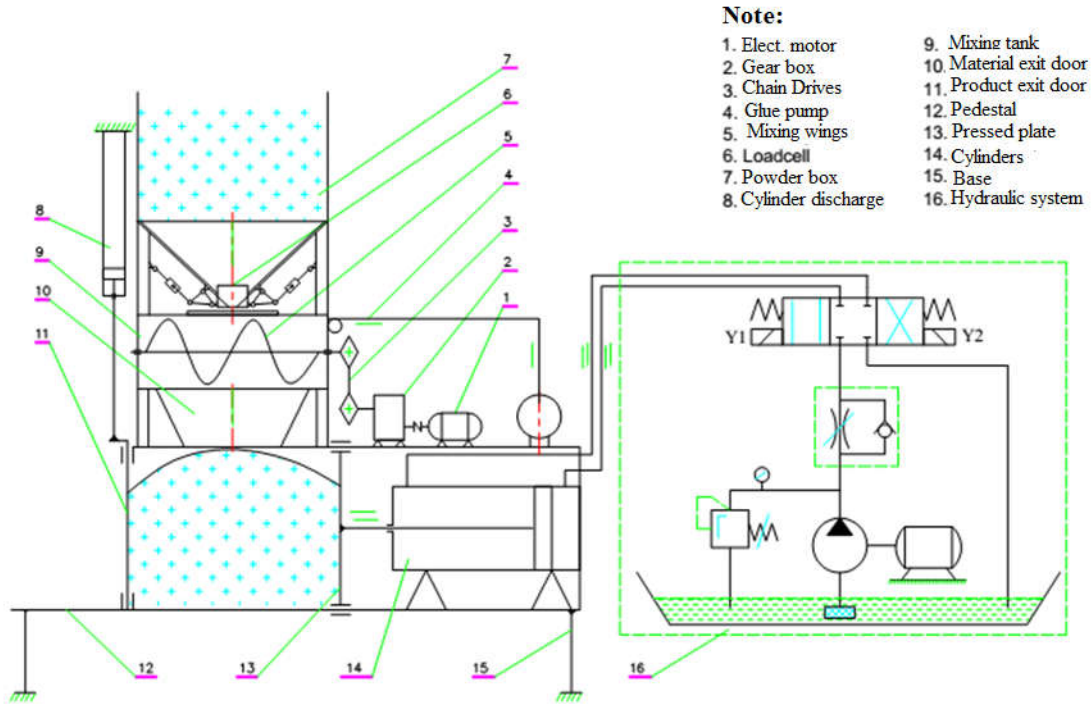
The inner diameter of the calculations of the cylinder : $D_B = 2.r = 157.6mm$. Selected $D_B = 160mm$.

$$r_H = r_B\sqrt{\frac{[\sigma]}{[\sigma] - px\sqrt{3}}} = 80\sqrt{\frac{320}{320 - 20x\sqrt{3}}}$$
$$= 84.7mm$$

The permissible C45 steel is selected as the best material for manufacture of the cylinder of the hydraulic system with limited stress of $\sigma = 320MPa$

The outer diameter of the cylinder: $D_H = 2.r_H = 169.4mm$, selected $D_H = 170mm$.

The cross-section area of the cylinder:

$$F = \frac{\pi.D_B^2}{4} = \frac{3.14x160^2}{4} = 20106.2mm^2$$

The volume of fluid oil in the cylinder: A_{max} = H.F = 100x20106.2 = 2010620 mm3 or 2.01062m³.

$$F = pA = p\frac{\pi D^2}{4} \to D = \sqrt{\frac{4F}{\pi p}} = \sqrt{\frac{4.39.1000}{\pi. 200}}$$
$$= 15,76cm$$

D (cm): Piston diameter; p (bar): liquid pressure in the cylinder; A (cm2): Working area of the cylinder; F (kg): Force acting on the cylinder.

Parker hydraulic cylinders is selected with denoted code 160 MF1 MMB R N 1 4 C 1050 M 11 11

b. Calculations select oil pump

Flow is calculated by the formula: Q = v.A

Q is the flow supplied by the pump (litre /s);

v is the flow velocity(m / s);

A is the piston bottom area [m²].

Bore (mm)	B (mm)	D max (mm)	EE (BSPP)	F	FB (h13) (mm)	FC (js13)	K	UC (max)	VD (mm)	WC	Y (mm)	PJ (mm)	ZB (max) (mm)	ZP
160	160	232	G11/4	36	22	280	25	316	5	30	143	191	386	406

The speed of the piston in the working direction is $v_1 = S / t_1$. Therefore, the supply flow rate for the cylinder in working direction is $Q_1 = v_1.A = \frac{S}{t1}.\frac{\pi.D^2}{4} = \frac{1}{10}.\frac{3,14.1,6^2}{4} = 0.201 (dm^3/s) = 12.06$ liters/minutes

The speed of the piston in the return direction is $v_2 = S / t_2$. The supply flow rate for the cylinder in the return direction is $Q_2 = v_2.A = \frac{S}{t2} . \frac{\pi.(D^2-d^2)}{4} = \frac{1}{8} . \frac{3,14.(1,6^2-0,8^2)}{4}$ =188 (dm^3/s) = 11.3 l / min

Hence the flow rate of the source pump must be chosen to the bigger one Q1. The selected revolution per minute of the shaft of the pump is n = 1470 RPM that is the most suitable RPM of gear pumps. Therefore, the specific flow of the pump is: $q = \frac{Q}{n} = \frac{12,06.10^3}{1470} = 8.2$ (cm^3/loop).

Based on the following influential parameters such as pressure, flow rate, operating speed of the pump, the type of fluid, and cost of the system, the gear pump is the most reasonable choice because of its compact size, low cost and suitable pressure but small flow, easy maintenance and simple control
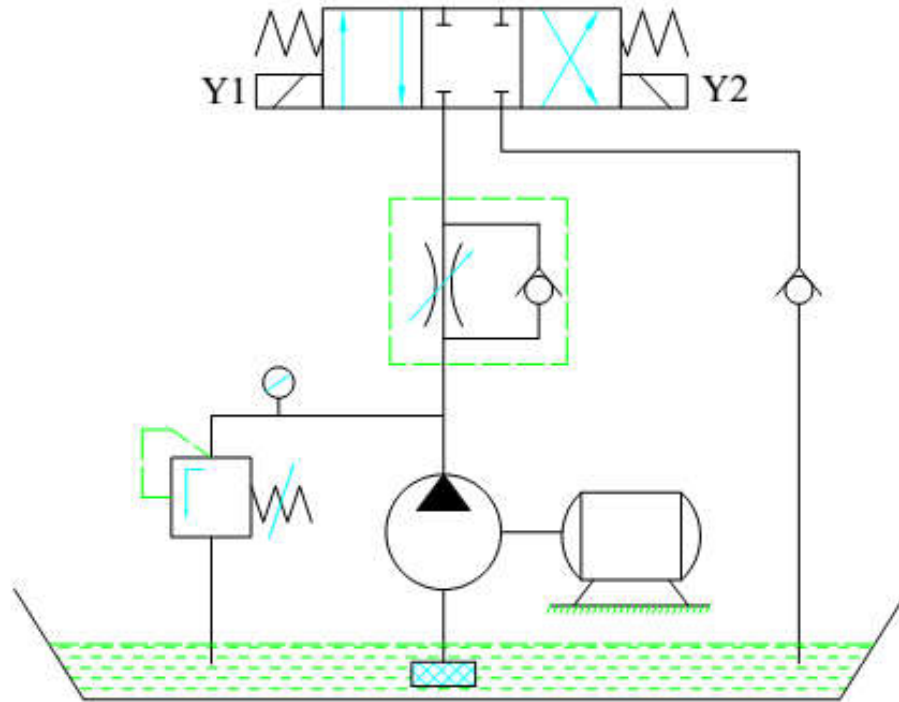
Figure 5. Schema of hydraulic system of bamboo plywood pressing machine

Gear pump has the pressure in the range of p = 100 -280 bar; suitable flow rate is Q= 100 (l/minute);
Finally the gear pump HYDROMAX coded HGP-3A-8 [6] is selected with specific flow: q = 8 cm^3/course); Maximum operating pressure P_{max} = 250 bar; Maximum rotation speed: n = 3500 RPM.

c. Computing the electric motor

System power: $N = = \frac{P.Q}{612} = \frac{200.12,06}{612} = 3,94$ (Kw).

Herein: Q is the flow rate of the pump; P is the system pressure.

From the above data, we have selected 4A100L4Y3 with specific parameters: 1500RPM, power is 4 kW motor.

d. Testing the strength of the pressing barrel:

Testing the strength of the pressing barrel with Solidworks software, the material is medium carbon steel with the following results:

Name	Type	Min	Max
Stress	VON: Von Mises Stress	7377.96 N/m^2 Node: 12998	1.80644e+007 N/m^2 Node: 17581

Name	Type	Min	Max

Figure 6. Simulation result on resistance of material of the machine
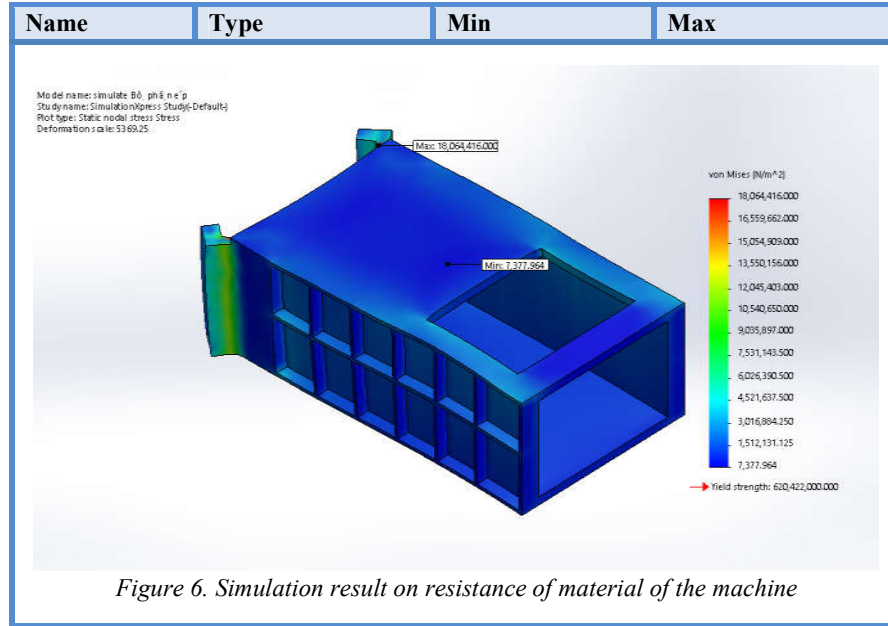
e. Computing of heating:

Parameters : : G = 24Kg; $\tau = 15p = 900s$; $t_1 = 150^0C = 423K$;

$t_2 = 180^0C = 453K$; $C_p = 1,55\frac{KJ}{Kg./k}$; $\overline{\Delta t} = 165^0C = 438K$.

Q = G.C_p.($t_2 - t_1$) = 24.1,55.(453 − 233) = 1116 KJ

$P = \dfrac{Q}{\tau} = \dfrac{1116}{900} \approx 1,24\ KW$

$P_{tt} = \propto. F. \overline{\Delta t} = 5.0,4.438 = 876W \approx 0,88KW$

$P_{tk} = (P + P_{tt}). k = (1,24 + 0,88). 1,2 \approx 2,5\ KW$

The system is installed a resistance flat plate capacity of 1KW , denoted D 2.6 I and 2 resistors flat plate with capacity of 0.8KW, denoted D 1.6.

Total structure of the designed bamboo plywood-pressing machine is illustrated in figure 7
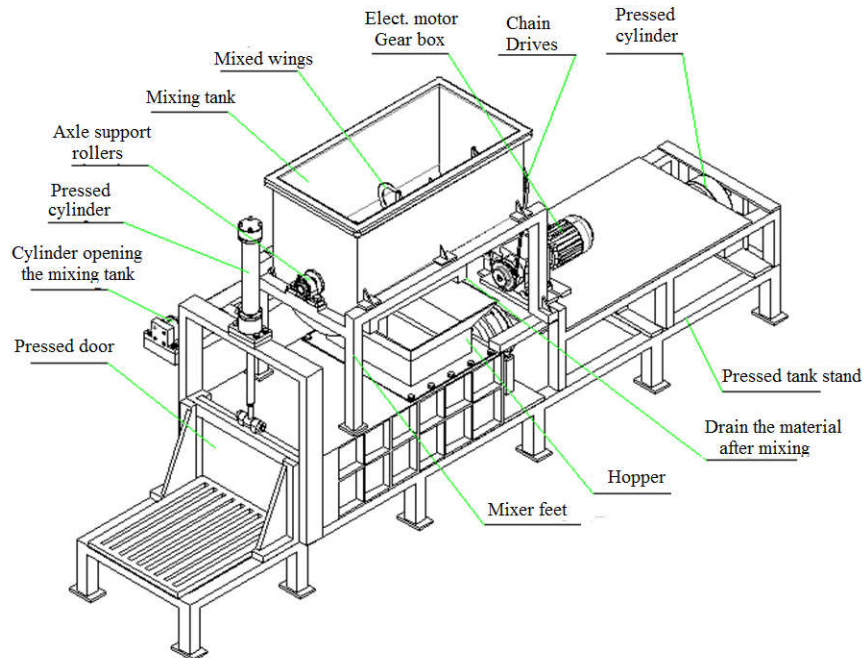
Figure 7. Overall drawing of bamboo polywood pressing machine

4. Conclusion

The bamboo plywood pressing machine is one of the important machine that decides the quality of the plywood product. The simulation results show that the complete bamboo plywood-pressing machine is appropriate and authentic to the initial design.

5. Acknowledgement

6. References

[1] D. M. Nazmul Alam, Khandkar- Siddikur Rahman, Sourav Bagchi Ratu1, Arifa Sharmin, Tania Islam, Md. Abu Wabaeid Hasan and Md. Nazrul Islam, Properties of Particleboard Manufactured from Commonly Used Bamboo (Bambusa vulgaris) Wastes in Bangladesh. SCIENCEDOMAIN international, 75:203-211, 2015.

[2] Viện khoa học lâm nghiệp Việt Nam, Nghiên cứu một số yếu tố công nghệ sản xuất ván dăm chất lượng cao làm nguyên liệu cho sản xuất đồ mộc trong điều kiện miền bắc Việt Nam.

[3] Trần Văn Hưng, Nguyễn Tấn Hùng, *Nghiên cứu, thiết kế và chế tạo thiết bị phục vụ sản xuất ván ép bột tre*, Báo cáo đề tài nghiên cứu khoa học GEN 2016.48.02 02.06, 2016.

[4] Nguyễn Thanh Nam, *Phương pháp thiết kế phát triển sản phẩm*, NXB ĐHQGTP Hồ Chí Minh, 2014.

[5] Nguyễn Hữu Lộc, *Cơ sở thiết kế máy*, NXB ĐHQGTP Hồ Chí Minh, 2015.

[6] Xilanh thủy lực, Tiêu chuẩn ISO 6022, Kiểu CDH.

PART VII, SECTION II

Materials Technology
(Functional Materials; Technologies of Materials; Materials Characterization and Evaluation;
High Speed Machining and Abrasive Machining; Micro- and Nano-Systems Engineering and
Emerging Technologies; Surface Integrity and Machining Quality…)

Influence of Tool Feed Conditions on Surface Integrity in Roller Burnishing with Rolling and Sliding Effects

Masato Okada[1], Makoto Shinke[2], Takuya Kitagawa[2], Tomoaki Inoue[3],
Satoshi Yasutani[3], Takuya Miura[1], Masaaki Otsu[1]
[1]Faculty of Engineering, University of Fukui
3-9-1, Bunkyo, Fukui, 910-8507, Japan
[2]Graduate School of Engineering, University of Fukui
3-9-1, Bunkyo, Fukui, 910-8507, Japan
[3]Nippon Pneumatic Mfg. Co., Ltd.
1300-80, Yabata, Nabari, Mie, 518-0605, Japan

ABSTRACT

The influence of tool feed conditions on the burnished-surface integrity obtained by roller burnishing, which can generate the sliding effect, adding to the rolling effect at burnishing point, is addressed. A JIS SCM420 steel round bar was used as the workpiece. The surface integrity was improved by feeding the roller in the same direction with the sliding effect and by decreasing the tool feed rate. A better surface was achieved when the roller was fed in the opposite direction to the feed direction of the turning tool in a preceding process of the burnishing.

1. Introduction

Roller burnishing can achieve a smooth surface by compression of the fine irregular profiles on the target surface by using a roller. The surface layer, which has high abrasion resistance and high fatigue strength, can be obtained with a smooth surface by the combination of work hardening and compressive residual stress. The processing efficiency of the roller burnishing is similar to that of the turning, and it is high compared with the grinding process for surface finishing. Moreover, roller burnishing can be conducted using a common machine tool for machining, and it does not require a dedicated machine.

Many theoretical and experimental studies of roller burnishing have been reported. Balland et al. proposed a three-dimensional finite element method model of roller burnishing and verified its applicability [1, 2]. Saldaña-Robles et al. [3] experimentally investigated the influence of the roller burnishing conditions on the burnished-surface roughness, hardness, and corrosion resistance of carbon steel AISI 1045. In the case of conventional roller burnishing, fine irregularities on the target surface are smoothed by only the compressive force generated by the rolling effect. However, when the target material hardness is high or high pressing force cannot be applied, the fine irregularities are easily retained, even after roller burnishing.

Zhao et al. [4] developed ultrasonic roller burnishing for titanium alloy material and demonstrated that the flow stress of the material deformation can be decreased by applying ultrasonic roller burnishing. Tian et al. developed a laser-assisted burnishing method, which can soften the surface layer of the target material to obtain appropriate deformation even for hard materials [5]. However, these burnishing methods require the dedicated devices and the equipment for processing are complicated.

Okada (one of the authors of the present study) et al. [6] developed inclined-roller burnishing, and the advantages of the developed method were clarified. In the inclined-roller burnishing, the sliding effect can be generated at the burnishing point with a rolling effect only by inclining the rotation axis of the roller with respect to the rotation axis of the target round bar. A special device is not required, and only changing the roller set angle is required. In the inclined-roller burnishing, the generating sliding effect is directional with respect to the direction of the rotation axis of the target round bar. Moreover, the target surface of the round bar is, generally, finished by turning, so it shows a fine helical profile with directionally. However, the influence of the feed conditions, which are the roller feed direction with respect to the direction of the sliding effect and the fine helical profile and roller feed rate, on the burnished surface roughness and profile have not been evaluated. In this investigation, the influence of the roller feed direction and feed rate on the burnished-surface integrity were experimentally evaluated.

2. Experimental Method
2.1 Experimental Setup

Figure 1 shows the experimental setup. Roller burnishing tests were carried out using a bench lathe. The roller burnishing tool was fixed to the tool holder of the bench lathe at an inclination angle of α. The round workpiece bar was rotated using the main spindle of the bench lathe. The pressing force between the roller and workpiece was determined using a compression spring. A burnished surface was obtained by feeding the burnishing tool toward the axial direction of the workpiece. The tool feed was conducted by a servo
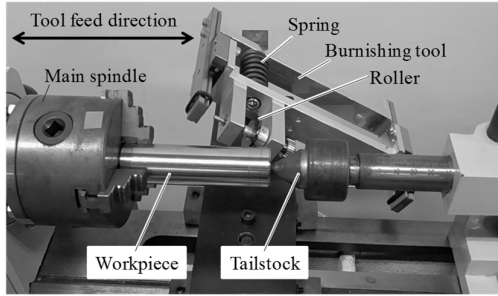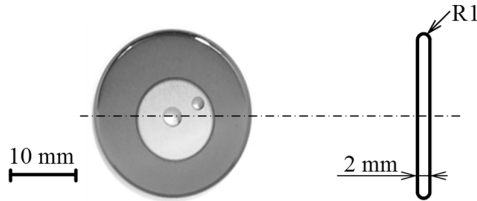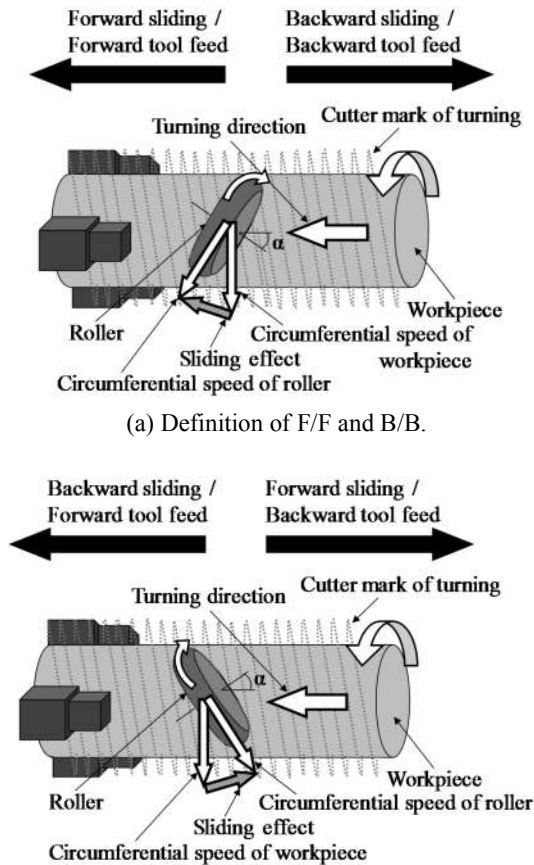
Fig. 1 Experimental setup.

Fig. 2 External view and shape profile of diamond coated carbide roller.

(a) Definition of F/F and B/B.

(b) Definition of B/F and F/B.
Fig. 3 Definition of tool feed conditions.

motor to obtain feed speed control with high accuracy. Figure 2 shows the external view and shape profile of the burnishing roller. The burnishing roller was coated

with the diamond-like-carbon (DLC) coating on the cemented tungsten carbide as a base material, and the authors have already evaluated that the DLC coating can achieve sufficient performance for burnishing with the sliding effect [7].

2.2 Definition of Tool Feed Conditions

Figures 3 (a) and (b) show the definition of tool feed conditions. In the case of inclined-roller burnishing, the sliding effect, which has a direction component in the rotation axis of the workpiece, was generated by inclining the roller, as shown in Fig. 3, and the direction of the sliding effect was determined by the inclining

Table 1. Experimental conditions.

Burnishing tool (Roller)	Base material: Cemented tungsten carbide
	Coating material: DLC
	Diameter: D_r = 25 mm
	Circumferential profile: R = 1.0 mm
Workpiece	Material : JIS SCM420
	Diameter : D_w = 23 mm
	Preliminary surface roughness: Ra = 2.10-2.26 μm
Inclination angle of roller: α = 30°	
Circumferential speed of workpiece: v_w = 72.3 m/min	
Pressing force: F = 90 N	
Feed rate: f = 2-30 μm/rev	
Lubrication: BP-3000, Star Cut Industrial Company	

direction of the roller. Thus, the case of the burnishing tool fed to the direction of the sliding effect was called "forward sliding," and the case of the opposite was called "backward sliding."

The workpiece finished by turning, which was a preliminary surface for the burnishing, had a fine helical surface profile. It had a directional owing to the feed direction of the turning tool as a cutter mark, as shown in Fig. 3. Thus, the case of the burnishing tool fed to the feed direction of the turning tool was called "forward tool feed," and the case of the opposite was called "backward tool feed."

As a results, four types of feed conditions were defined, as shown in Fig. 3; for example, the tool feed condition of the forward sliding and the backward tool feed was called "F/B" in this study.

2.3 Experimental Conditions

The burnishing conditions are summarized in Table 1. The chrome molybdenum steel JIS SCM420 was used as a workpiece material. In the roller burnishing, the preliminary surface roughness strongly influencing the burnished surface has been reported [8]. Therefore, the surface roughness of the preliminary surface finished by turning, which is conducted under same conditions, was set in range of Ra = 2.10-2.26 μm. The inclination angle of the roller α, circumferential speed of workpiece v_w, and pressing force F were set at 30º, 72.3 m/min, and 90 N, respectively. The feed rate was varied in the range of f = 2-30 μm/rev. The lubricant for plastic processing was coated on the preliminary surface. The roughness and profile of the preliminary and burnished surface were measured by a stylus-type roughness

meter (SURFCOM NEX SD-12, TOKYO SEIMITSU CO., LTD.).

3. Experimental Results and Discussion
3.1 Influence of Feed Direction and Feed Rate on Surface Roughness

Figure 4 shows the relationship between the feed rate of the burnishing tool and arithmetic mean roughness of the burnished surface when the feed conditions were F/F and F/B. The burnished-surface roughness was measured in the axial direction of the workpiece. In the case of the B/F, the burnished-surface roughness improved with the decrease of the tool feed rate in the range of f = 20-30 μm/tooth. However, it deteriorated with the decrease of the tool feed rate in the range of f =
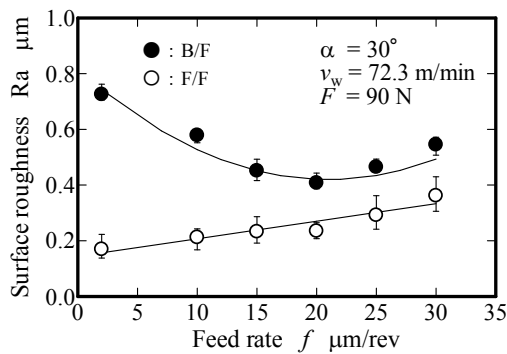
Fig. 4 Influence of feed direction and feed rate on burnished-surface roughness.
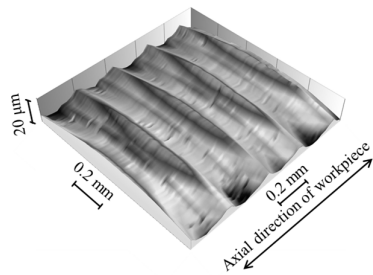
(a) Preliminary surface.

(b) f = 2 μm/rev.

(c) f = 20 μm/rev.
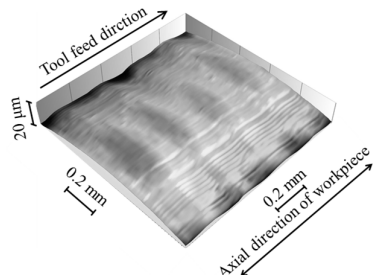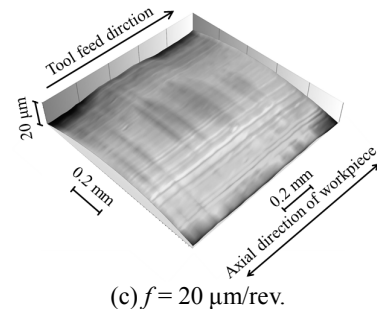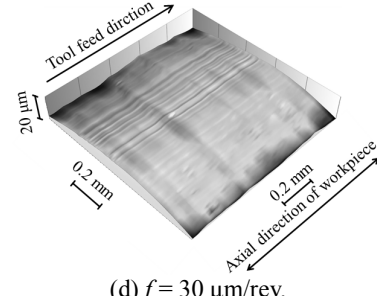
(d) f = 30 μm/rev.

Fig. 5 Three-dimensional profiles of burnished surface in tool feed conditions of B/F.

(a) f = 2 μm/rev.
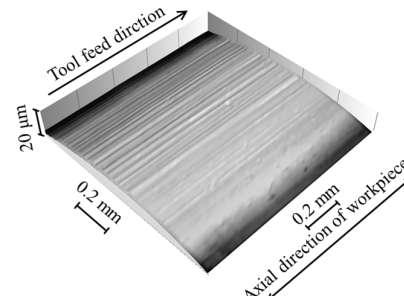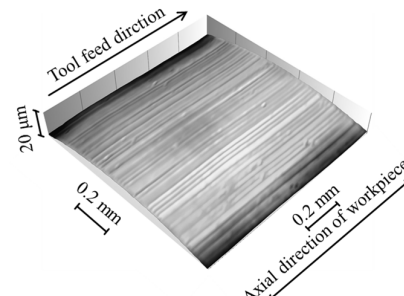
(b) f = 20 μm/rev.

Fig. 6 Three-dimensional profiles of burnished surface in tool feed conditions of F/F.

2-20 μm/rev. As a results, the burnished-surface roughness deteriorated to more than Ra = 0.7 μm at f = 2 μm/rev, although it was Ra = 0.4 μm at f = 20 μm/rev. However, in the case of F/F, the burnished surface roughness improved with the decrease of the tool feed rate under either feed rate. Moreover, the burnished-surface roughness in the F/F was lower than that in B/F

at all tool feed rates, and it reached less than Ra = 0.2 μm at f = 2 μm/rev. From these results, the tool feed direction with respect to the sliding direction strongly influenced on burnished-surface roughness. The authors clarified that the surface roughness improved by increasing the sliding distance between the roller and workpiece by conducting the inclined-roller burnishing on the same part multiple times [9]. However, the results, as shown in Fig. 4, showed that this tendency depended on the tool feed direction and feed rate.

3.2 Influence of Feed Direction and Feed Rate on Surface Profile
Figures 5 (a)-(d) and Figs. 6 (a) and (b) show the three-dimensional profile of the preliminary and burnished surfaces obtained in B/F and F/F, respectively. The preliminary surface in the F/F was the same as that in the B/F, as shown in Fig. 5 (a). From these profiles of the burnished surface, the regular cutting marks generated by turning on the preliminary surface were suppressed, and a smooth surface could be obtained. However, in the case of f = 2 μm/rev in B/F, as shown in Fig. 5 (b), the regular convex and concave profiles on the preliminary surface clearly remained. Moreover, for the other profiles in B/F, as shown in Figs. 5 (c) and (d),
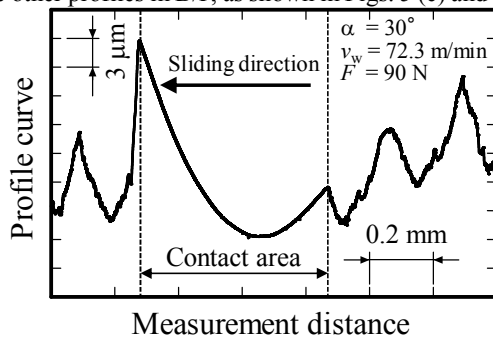
Fig. 7 Sectional profile around burnishing mark without tool feed.

they also slightly remained. However, in the case of F/F, as shown in Fig. 6, the convex and concave profiles almost disappeared, and the superior smooth surface was achieved.

3.3 Influence of Sliding Direction on Material Flow of Surface Layer
Figure 7 shows the sectional profile of the contact region between the roller and workpiece. It was obtained without the tool feed and was obtained by pressing the roller against the preliminary workpiece for approximately 10 s. The direction of the sliding effect acted from right to left, as shown in Fig. 7. The convex profile was observed on the left side of the contact area, and the material flow of the preliminary surface layer was selectively directed to the sliding direction by the inclined-roller burnishing. From these results, the burnished surface was effectively smoothed by actively flowing the material of the surface layer in the tool feed

direction by the sliding effect. It seems that the effect can be obtained because of the smoothing of the surface irregularities by minute plastic deformation in the burnishing process. Moreover, the results shown in Fig. 4, where the burnished-surface roughness deteriorates at small feed rates, were caused by the work hardening in the region just before burnishing under the condition that the material supply, which is required to smooth the surface by plastic deformation because of the sliding effect, did not occur.

3.4 Influence of Preliminary Surface Profile on Burnished-Surface Roughness
Figure 8 shows the influence of tool feed direction with respect to the preliminary surface profile on the burnished surface. For simplicity of evaluation, conventional roller burnishing, which is not generated the sliding effect ($α$ = 0º), was also tested. The forward sliding, which can obtain better surface integrity, was applied in the test of inclined-roller burnishing. The burnished-surface roughness in the backward tool feed was better than that in the forward tool feed in both burnishing methods. From these results, the direction of the helical profile obtained by the turning influenced the burnished-surface profile, and better surface roughness could be achieved when the roller is fed in the opposite direction to the feeding of the turning tool.
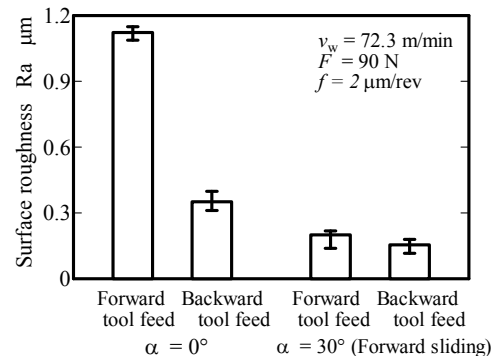
Fig. 8 Influence of tool feed direction with respect to preliminary surface profile on surface roughness.

4. Conclusions
The influence of tool feed conditions on the surface integrity in inclined-roller burnishing, which was developed by the authors and can generate the sliding effect, adding to the rolling effect, was evaluated. The surface roughness was improved, and the surface profile was smoothed when the roller was fed in the same direction as the sliding direction, which is defined as backward sliding. Moreover, in the backward-sliding condition, a superior surface can be achieved by decreasing the tool feed rate. The material of the surface layer was selectively flowed to the sliding direction. A better surface can be obtained when the roller is fed in the opposite direction to the feeding of the turning tool, which is used to finish the preliminary surface, in the conventional and developed inclined-roller burnishing.

References
[1] P. Balland, L. Tabourot, F. Degra, V. Moreau, *Int. J. Mach. Tools Manuf.*, 65 (2013) 29－36.
[2] P. Balland, L. Tabourot, F. Degre, V. Moreau, *Precis. Eng.*, 37 (2013), 129－134.
[3] A. Saldaña-Robles, H. Plascencia-Mora, E. Aguilera-Gómez, A. Saldaña-Robles, A. Marquez-Herrera, J. A. Diosdado-De la Peña, *Surf. Coat. Technol.*, 339 (2018), 191－198.
[4] J. Zhao, Z. Lu, *Mater. Des.*, 107 (2016), 238－249.
[5] Y. Tian, Y.C. Shin, *Int. J. Mach. Tools Manuf.*, 47 (2007), 14－22.
[6] M. Okada, S. Suenobu, K. Watanabe, Y. Yamashita, N. Asakawa, *Mechatron.*, 29 (2015), 110－118.
[7] M. Okada, M. Shinya, K. Takasugi, H. Tachiya, T. Sasaki, M. Otsu, *J. Jpn. Soc. Prec. Eng.*, 83 (2017), 694－700 (in Japanese).
[8] L. Luca, S. Neagu-Ventzel, L. Marinescu, *Prec. Eng.*, 29 (2005), 253－256.
[9] M. Okada, M. Shinke, M. Otsu, T. Miura, *Proc. 6th Eur. Conf. Tribol.*, (2017), 1－2.

Structural Integrity Analysis of the Plate Pack in Plate and Shell Heat Exchanger in High Temperature and Pressure Applications

Hyun-Seok Noh[1], Jong-Rae Cho[1], Seung-Hun Song[1]
[1]Dept. of Mechanical Engineering, Korea Maritime and Ocean University

ABSTRACT

Recently heat exchangers capable of withstanding high temperature and high pressure have become necessary to achieve high thermal efficiency and compactness. The plate and shell heat exchanger, which plates are placed back-to-back and welded in outer rim and porthole region, is developed in application for pressures to 150 barg and at temperatures up to 600°C. Because of these advantages, it is being used in more and more fields. However, few studies have performed the structural integrity of the plate pack. In this paper, structural integrity of the heat transfer pack through finite element analysis is performed. The elastic and elastic-plastic model are applied for one set of heat transfer plates. Two- or four plates are used to analysis model to verify the effect of boundary conditions The results in plates are evaluated according to ASME Boiler and Pressure Vessel Code, Section VIII Division 2.

Keywords: structural integrity, plate and shell heat exchangers, heat transfer plate pack, high pressure, welded heat exchangers

1. Introduction

Plate heat exchangers are commonly used in a wide range of industrial applications including chemical process, energy, refrigeration, and cryogenic fields [1]. The gasketed plate heat exchangers where the operating temperature range from −50∘C up to 350∘C and operating pressures from full vacuum to 40 bar were developed to obtain the high thermal efficiency and compactness [2]. But these heat exchangers are subject to many constraints on temperature and pressure. Welded plate heat exchangers have wider range of use than gasketed plate heat exchangers.

Blomgren [3] thoroughly described the structure of a welded plate heat exchanger where the edge portion of each heat transferring plate was welded together with the edge portions of a first adjacent heat transferring plate along an outer line and with the edge portion of a second adjacent heat transferring plate along an inner line.

The plate and shell heat exchanger (PSHE) as shown Fig. 1 was first commercially produced by Vahterus company [4]. The plate and shell heat exchanger, which is welded heat exchangers is developed in application for pressures to 150 barg and at temperatures up to 600°C [5]. Because of these advantages, it is being used in more and more fields. However, few studies have performed the structural integrity of the plate pack.

In this paper, structural integrity of the heat transfer pack through finite element analysis is performed. The elastic and elastic-plastic model are applied for one set of heat transfer plates. The results in plates are evaluated according to ASME Boiler and Pressure Vessel Code, Section VIII Division 2[6]. Also the function of end plate in plate pack was numerically studied.

2. FE modeling

2.1 Material property

Material properties were obtained from the ASME Section II, Part D [7] as shown in Table 1. Figure 1 shows the stress-strain curve used in elastic-plastic analysis.

(a) Assembly and flow direction

(b) Exploded view

Figure 1 A configuration of PSHE[4]

Table 1 Material properties

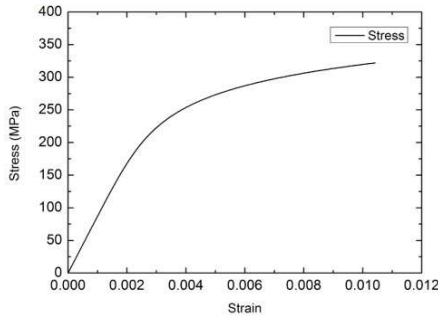| Material/grade	SB265- GR 9 (Ti3AL2.5V)
Design temp. (ºC)	300
Elastic modulus (MPa)	87e3
Allowable stress (MPa)	140
Yield strength(MPa)	293
Poisson's ratio	0.32

Figure 2 Stress-strain curve

2.2 Design criteria

The allowable stresses for elastic design and elastic-plastic design are provided in part 5 of the ASME Code Div. 2.

In elastic design, primary von Mises limits are as follows;

$$Pm \leq S, \qquad PL \leq 1.5S, \qquad PL + Pb \leq 1.5S$$
$$(\sigma 1 + \sigma 2 + \sigma 3) \leq 4S \; for \; local \; PL + Pb \qquad (1)$$

where Pm, PL : general & local membrane stresses; σ1,σ2,σ3 : principal stresses

Primary plus secondary stress limits are as follows;

$$\Delta Sn, k \leq Sps \qquad (2)$$

Where $\Delta S_{n,k}$: stress range

S_{ps} : the larger value of 3S and 2Sy

In elastic-plastic region,

$$\varepsilon_L = \varepsilon_{Lu} * \exp\left[-\left(\frac{\alpha_{sl}}{1+m_2}\right) * \left(\left\{\frac{(\sigma_1+\sigma_2+\sigma_3)}{3\sigma_e}\right\} - \frac{1}{3}\right)\right] \qquad (3)$$

Acceptable strain is as follows;

$$\varepsilon_{peq} + \varepsilon_{cf} < \varepsilon_L \qquad (4)$$

Where ε_L : limiting triaxial strain

ε_{Lu} : uniaxial strain limit

σ_e : equivalent stress

ε_{peq} : total equivalent plastic strain

ε_{cf} : forming strain

2.3 FE modeling

The heat transfer plate was modeled as 1/4 of the plate considering computation time as shown in Fig. 3. To evaluate the effect of boundary conditions, two or four adjacent plates were chosen as the analysis region as shown in Fig. 4. The plate is modeled as solid and shell in FE analysis because the thickness of plate is not small compared to groove radius shown in Fig. 5.
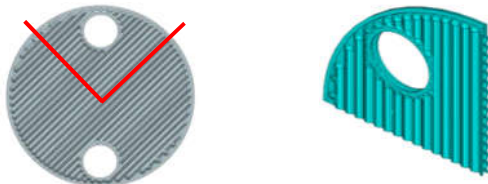
Figure 3 A plate and analysis region

The nodes on symmetrical section are fixed in normal direction to the section surface. The contact between the two or four plates which are placed back-to-back was considered as a separation (just two independent pieces in touch with each other). Since the plate pack is confined longitudinally at both ends, it is assumed that the apex of the outer plate in the analysis region is not deformed in the vertical direction of the plate (Fig. 6). It was applied the pressure of 11.8 MPa in the high pressure area.
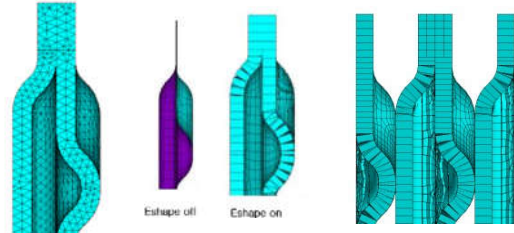
(a) 2-layers solid (b) 2-layers shell (c) 4-layer shell

Figure 4 FE modeling schemes
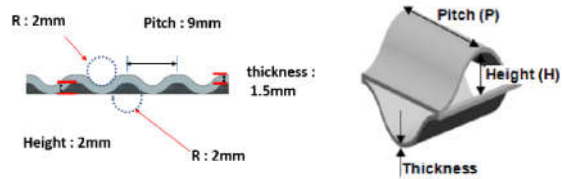
Figure 5 Shape of corrugated grooves
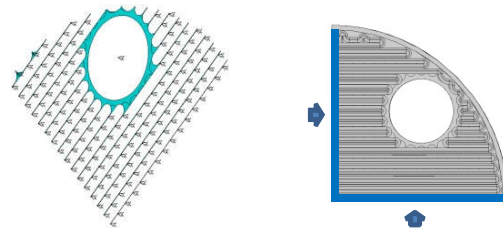
(a) Vertical constraint   (b) Symmetry

Figure 6 Displacement boundary condition

3. Results and Discussion

The five analysis cases (see Table 2) are considered to obtain the stress and strain on the heat transfer plate under high pressure load of 11.8 MPa. No. of nodes in solid model is much higher comparing shell model. Figure 7 shows the configuration of shell element and element size is about 0.5mm.
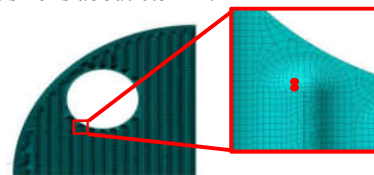
Figure 7 Element configuration

519

Table 2 Analysis cases

Cases	No. of plates	Material model	Element type	No. of elements
CASE 1	2	Elastic	Solid 187	1,501,761
CASE 2	2	Elastic	Shell 181	96,441
CASE 3	2	Elastic-plastic		
CASE 4	4	Elastic		303,913
CASE 5	4	Elastic-plastic		

Figure 8 shows von Mises stress distribution of four cases. It is shown that the stress distribution and magnitude are similar except for peak stress in elastic analysis. Points P1 and P2 in Fig. 7(a) represent the weld region at the outer boundary of the plate and porthole, respectively. Point P3 represents the back-toback contact region of an apex of groove of plate. The local membrane and membrane+bending are satisfied allowable stress limits according ASME Sec.VIII, Div.2 The equivalent stress in elastic solid analysis at P3 of Table 4 is unrealistically high, because of P3 is contact point which is restrained. In elastic-plastic model, the calculated strain of 0.00407 in CASE 5 is very smaller than the acceptable strain of 0.0889.
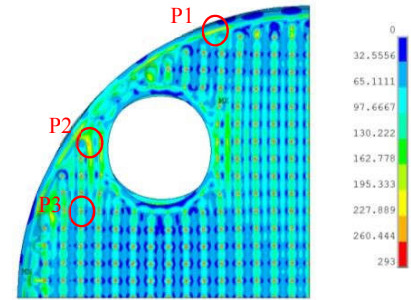
(a) CASE 1
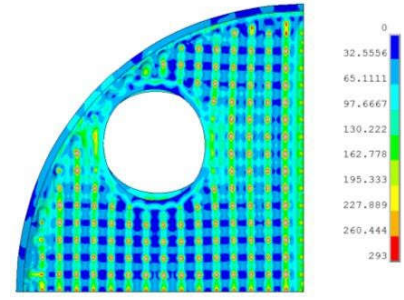
(a) CASE 2
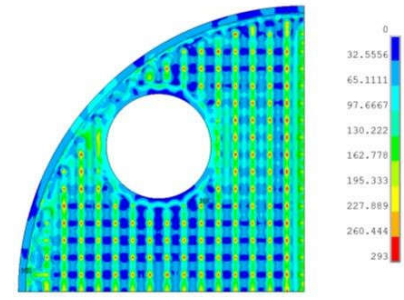
(b) CASE 3
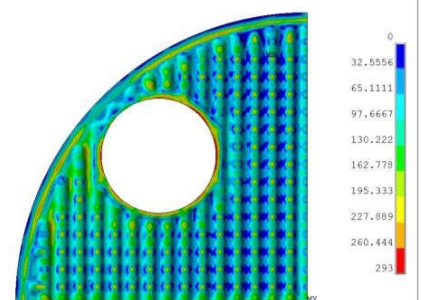
(c) CASE 4

Figure 8 Von Mises stress distribution

The porthole weld region (red circle) in Fig. 9 shows the plastic deformation which the von Mises stress exceeds the yield strength of 293 MPa. From Table 3 and 4, it is shown that the stress distribution in case of elasticplastic shell model using 4-layer plates is more realistic to eliminate the effect of boundary restraint in plate pack analysis of PSHE.
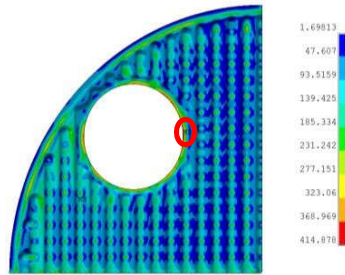
Figure 9 Elastic and plastic deformation region

Table 3 Stress type and allowable limits in elastic analysis

Location	Stress type	CASE 1	CASE 2	CASE 4	Allowable Limit
P1	PL	51.4	85.4	95.9	210
	PL+Pb	268.1	239.8	316	420
P2	PL	31.3	37.8	128.7	210
	PL+Pb	185.0	165.3	287.5	420

Table 4 Evaluation of analysis results at location P3

Type	CASE 1	CASE 2	CASE 3	CASE 4	CASE 5
σ_e(MPa)	1481	417	278	304	253
ε_{peq}(%)	-	-	0.802	-	0.407
σ_1(MPa)	-	-	0	-	0
σ_2(MPa)	-	-	-243	-	-240
σ_3(MPa)	-	-	-305	-	-266
ε_L(%)	-	-	8.89	-	8.89

4. Concluding Remarks

The structural integrity of heat transfer plate for PSHE under high pressure was evaluated and the following results were obtained.

(1)   The validity of shell modeling was confirmed by comparing solid and shell modeling.

(2)   The analysis region obtained more accurate results using 4-layer plates. 2-layer plates are affected by the boundary.

(3)   The elastic-plastic analysis is appropriate because local abnormal peak stress occurs in elastic analysis.

(4)   It was confirmed that the PSHE is safe even in a high pressure environment of 118 bar or more according to ASME code.

References

[1] M.M. Abu-Khader, Plate heat exchanger:Recent advances, Renewable and Sustainable Energy Reviews, 16(2016), 1883-1891.

[2] Chopard F, Patel C, Lavanchy M. Welded and totally accessible advanced plate heat exchanger – the choice for integration of compact exchanger. In: International Conference on Compact Heat Exchangers for the Process Industries, June 22–27. 1997. p. 591–5.

[3] Blomgren R, Andersson J, Mats N. Welded plate heat exchanger. Appl Therm Eng 1998;18(6):V–VI.

[4] Vahterus, Plate and shell heat exchanger, www.vahterus.co., (Last visit 28.06.2018)

[5] L.O. Freire, D.A. Andrade, On applicability of plate and shell heat exchangers for steam generation in naval PWR, Nuclear Engineering and Design, 280(2014), 619-627.

[6] ASME Boiler & Pressure Vessel Code, Sec. VIII, Div. 2, 2017.

[7] ASME Boiler & Pressure Vessel Code, Sec. III, Part D(Metric), 2017.

Effect of Amorphous Silicon Carbide Interlayer on Diamond-like Carbon Film Quality

Yutaro Kimura[1], Xia Zhu[1], Hiromichi Toyota[1], Yukiharu Iwamoto[1], Shinfuku Nomura[1]

[1]Graduate School of Science and Engineering, Ehime University, 3 Bunkyo-cho, Matsuyama, Ehime, 790-8577, Japan

ABSTRACT

This study was performed to improve the adhesiveness of a diamond-like carbon (DLC, a-C:H) layer film with an a-SiC interlayer. In previous studies, an a-SiC/DLC layer film was formed and changes in the DLC film structure and hardness caused by the thickness of the a-SiC layer were examined. After the a-SiC interlayer thickness increased and the G-peak position shifted to a lower frequency, the peak began shifting to higher frequencies. The G-peak position reached a minimum frequency at a film thickness of approximately 0.3 μm. In contrast, as the thickness of the a-SiC interlayer increased, the FWHM of the G-peak position increased almost monotonically and the number of sp^3 bonds also increased. As the inter-film thickness increased, the hydrogen content in the DLC film increased, and then began decreasing, with the interlayer film thickness exhibiting a local maximum at approximately 0.3 μm. As for the DLC film hardness, a correlation between the hydrogen content and half width of the G-peak position was observed. When the hydrogen content was ≤40 at%, a positive correlation with the FWHM(G) was observed, and when the hydrogen content was 40 at% or above, a negative correlation with FWHM(G) was found. The adhesiveness of the DLC film and substrate was improved by forming an a-SiC thin film as an interlayer. The effects of the a-SiC thin film on DLC film quality were determined.

1. Introduction

Diamond-like carbon (DLC) is an amorphous carbon material containing a mixture of sp^2 hybridized graphite, and sp^3 hybridized diamond. DLC exhibits good abrasion resistance and high chemical safety due to its diamond content and flatness/low counterbody aggressiveness due to the presence of graphite. Thus, DLC is expected to be useful as a coating material [1]. However, a large obstacle for applications of DLC film is its low adhesiveness to various substrates, which is caused by two main factors: intrinsic residual stress and stable carbon bonds [2]. Several reports [3] have detailed attempts to prevent layer separation and improve the adhesiveness of DLC thin layers by forming an interlayer of silicon carbide (SiC) with high substrate adhesiveness, and then covering the interlayer with the DLC. However, uncertainties remain regarding the optimal conditions for forming a SiC thin film and DLC/SiC stacked thin layer. In particular, no reports have been published to date regarding the effects of an a-SiC thin film on the structure and film thickness.

The goal of this study is to improve the adhesiveness of a DLC/a-SiC layered film formed by ion plating. In previous studies, the formation of a hydrogen-containing DLC(a-C:H)/a-SiC layered thin film was achieved, and the effects of an a-SiC interlayer on its structure and mechanical properties were determined.

2. Film formation and evaluation methods

2.1. Experimental apparatus for film formation and evaluation methods

The ion plating method was used to form the a-SiC interlayer and DLC/a-SiC stacked layer. A schematic of the experimental apparatus is shown in Fig. 1, consisting of a vacuum chamber, rotary pump, turbo molecular pump, high-voltage power device, gas supply system, negative electrode substrate, and positive electrode chamber inner wall. Using rotary and turbo molecular pumps, it was possible to reduce the pressure in the chamber to 1.0×10^{-3} Pa. We built a power device consisting of a variable pressure system/bridge rectifying
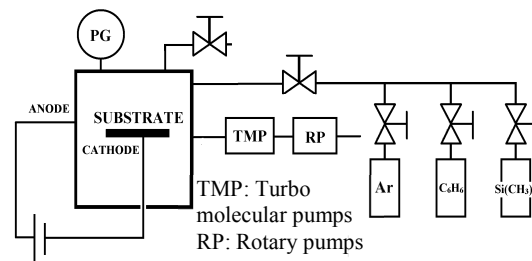
Fig. 1 Schematic diagram of the experimental setup for the ion plating method with introduction

circuit that was capable of outputting a maximum of 500 V. The gas supply system could supply argon (Ar), benzene (C_6H_6), and tetramethylsilane (TMS, Si$(CH_3)_4$).

A stainless steel SUS304 (JIS G 4304, width 10 x length 30 x thickness 1.5 mm) substrate was pulverized and ultrasonically cleaned in an acetone solution. Subsequently, the substrate was fastened inside the chamber and the pressure inside the chamber was reduced using rotary and turbo molecular pumps. Inert gas was introduced into the chamber and the pressure adjusted. Voltage was applied to turn the inert

gas into plasma and the substrate was washed by sputtering. To form the Si-C layer, tetramethylsilane was introduced into the chamber, turned to plasma, and deposited onto the substrate as an interlayer. For the DLC layer, benzene was introduced into the chamber, turned into plasma, and deposited on the substrate.

In this experiment, argon/TMS (mixing ratio of 1:1) gas was introduced, an interlayer was formed for 0 to 3 min, and a-SiC films 0.05 to 0.45 µm in thickness were formed. Subsequently, argon and benzene (mixing ratio of 1:1) were introduced, and a DLC film with a thickness of 2 µm was formed in 30 min.

2.2 Film structure analysis

Visible Raman spectral analysis is effective for analyzing the structure of DLC films [4-10]. Typical Raman spectra were observed for the prepared DLC when as shown in Fig. 2 [11]. From Fig. 2, the Raman spectrum of the DLC film could be divided into a D peak near 1350 cm^{-1} arising from the stretching and contracting of the six membered ring, and a G peak between 1500 and 1600 cm^{-1} originating from the vibrations of the sp^2 carbons on the chain and ring. The G-peak position and the FWHM(G) were used as parameters to qualitatively evaluate the degree of amorphous nature of the film (or crystallization). In addition, the hydrogen density of the film was evaluated using the photoluminescence (PL) of the Raman curve. The baseline slope m [8] of the Raman spectrum and the ratio (log N/S) [9] of the photoluminescence component N to the strength of the Raman scattering at the G peak position were used as Raman parameters.

In this study, a Raman spectrometer was used to evaluate the structure of the film with an oscillating Ar ion laser (514 nm), laser output of 1.0 mW, and an analysis range of 20 µm Φ.

2.3 Nanoindentation

Hardness, which is a mechanical property of the film strongly correlated with film strength, toughness, and abrasion resistance, was measured using a nanoindentation tester (ENT-1100a, made by Ellionics). The Oliver & Pharr program was used to calibrate the indenter tip.

For nanoindentation, similar to the conventional Beaker's harness test, hardness H was defined as H=P/A where P is the load when the indenter presses into the sample and A is the projection area of the indentation that develops on the surface of the sample. For Beaker's hardness, A is the surface area of the indentation, which is experimentally observed. For the nanoindentation method, the displacement when the indenter presses into the sample surface was continuously measured with a high-precision displacement meter and the obtained load-displacement curve was subsequently analyzed.

An indentation load of 1 mN, load application speed of 0.1 mN/s, and a retention time of 1 s were used in these tests.
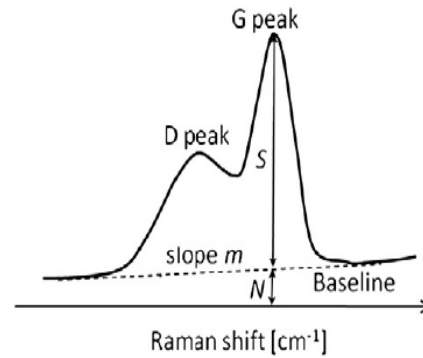
Fig. 2 Raman peak obtained for the DLC film [2].
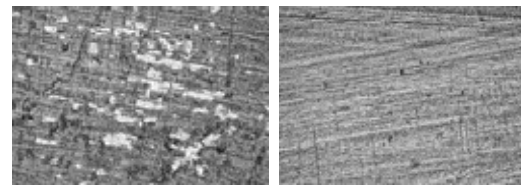
(a) No interlayer   (b) with an interlayer

Fig. 3 Laser mirror image of DLC forming substrate after rubbed with cloth.
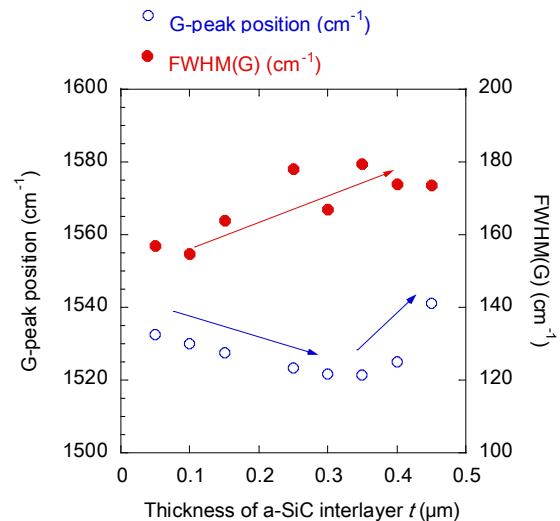
Fig. 4 Change in the G-peak position and FWHM (G) of the DLC film as a function of interlayer thickness.

3. Results and discussion

3.1 Adhesiveness of the DLC film in presence of the interlayer

Fig. 3(a) shows a photograph of the surface of the DLC film without the a-SiC interlayer after it was rubbed with a cloth. The film was observed to peel from the substrate. Fig. 3 (b) shows a photograph of the

surface of the DLC with a 0.05 µm thick a-SiC interlayer, which did not peel from the substrate. These photographs confirm that the adhesiveness of the DLC layer improved when a-SiC interlayer is formed before forming the DLC layer.

3.2. Change in the film structure due to interlayer thickness

The DLC layer was studied by Raman spectroscopy. The G peak position and FWHM(G) values for each interlayer thickness is shown in Fig.4, respectively. Differences in the Raman spectra were observed as a result of the interlayer thickness.

Generally, it is possible to gain information regarding the structure of the film and chemical bonding of the carbon atoms from the position of the G-band, the behavior of the I(D)/I(G), and FWHM(G), which can be obtained from the results of the Raman spectrum. Ferrari et al. [6] developed a model wherein upon introduction of defects into graphite to create disorder, an amorphization trajectory can be classified into three stages according to strength (Fig. 5). Specifically, from the monocrystalline to nanocrystal graphite, this model describes the series of disordering processes, with a third stage leading to the formation of tetrahedral amorphous carbon (ta-C) with sp[3] bonding, via amorphous carbon (a-C), which contains mainly sp[2] bonds. These structural and chemical bonding state changes can be observed in the visible (514 nm) Raman spectrum.

The G-peak is a parameter depends on the length of the sp[2] bonds between the carbon atoms in the DLC film, and shifts to higher frequencies as the bond lengths shorten. Therefore, the DLC film where the G-peak is located at high frequency indicates a higher degree of graphite crystallization. In contrast, the FWHM(G) indicates the degree of amorphous character of the graphite. When various bond lengths exist, as in DLC films with marked amorphous character, the G peak appears over a broad range. Therefore, the G peak becomes broadens for the DLC film overall, and, as a result, the FWHM(G) increases. The G peak position shifts to higher frequencies as the amorphous character of the film increases. Generally, amorphous films contain a high degree of sp[3] bonds, which is positively correlated with FWHM (G) and hardness [7].

This model of structural changes from stages 1 to 3 shown in Fig. 5 was studied by correlation with the Raman spectra of the DLC films. Fig. 4 show that the G-band peak shifts to lower frequencies when the interlayer thickness increases from 0.15 to 0.3 µm, and the FWHM(G) value also increases. This change corresponds to stage 2 of the model in Fig. 5, and it likely represents the progression of a-C disorder. When the interlayer thickness was increased further to 0.45 µm, the G-band position shifted to a higher frequency. The FWHM(G) values in Fig. 4 show that the G-band peak shifts to a lower frequency when the interlayer thickness increases from 0.15 to 0.3 µm, and the FWHM(G) value steadily increases. This change

corresponds to the G-band peak in stage 3 shifting to higher frequencies, the FWHM (G) value increasing, and a change in the amorphous DLC to tetrahedral amorphous structure. This shows the
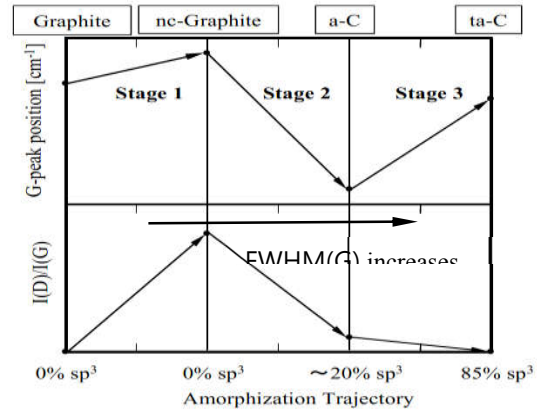
Fig. 5 Amorphization trajectory, showing a schematic variation of the G-peak position, $I(D)/I(G)$
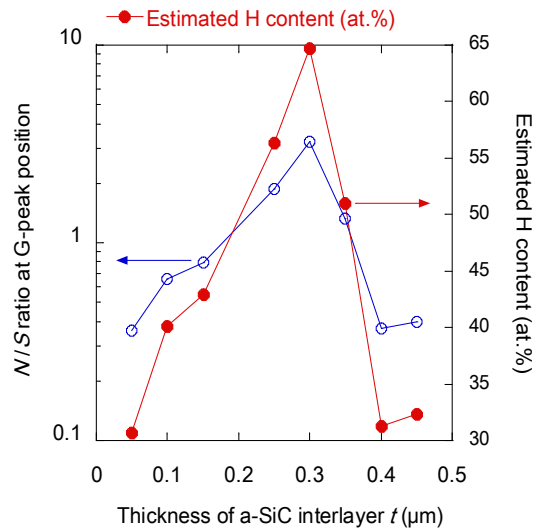
Fig. 6 Change in the N/S ratio of the DLC and the inferred hydrogen content, due to the interlayer thickness.

increasing disorder of the a-C containing sp[2] bonds and the shift to ta-C as a result of sp[3] bonding.

When the Raman spectra of the DLC (a-C:H) film is measured using visible light, the PL component and Raman scattered light affects the spectral strength due to the inclusion of hydrogen in the film. In films with a large hydrogen content, the baseline slope of the Raman spectra increases [8], and electron hole pairs are re-bonded in a sp[2] cluster in the amorphous matrix, which can be derived from the PL. If the matrix contains hydrogen, it enlarges and the electron hole pair is localized, resulting in the release of more intense PL.

The hydrogen density (at%) in the film was estimated using Eq. (1), which correlates hydrogen content with the ratio log (N/S) of the Raman light intensity S and PL component N at the G-peak position, without separating the peaks. From the Eq. (1), the hydrogen concentration in the film is estimated and shown in Fig. 6.

$$H[at.\%] = 46.6 + 35.4\log(N/S) \tag{1}$$

The hydrogen density in the DLC film increases with increasing thickness of the interlayer, forming a peak at t=0.3 μm. If the film thickness is further increased, the hydrogen density begins to decrease. Correlation with the changes in the DLC structure presented in Fig. 5 show that as the film thickness decreases (t <0.3 μm), the FWHM(G) decreases and the a-SiC film contains more nanocrystal graphite (nc-G) and amorphous carbon (a-C), with sp^2 bonds. Therefore, the hydrogen that was removed from a-SiC when the DLC was formed remained in the DLC layer. When the interlayer increases in thickness (t>0.3 μm), the percentage of tetrahedral amorphous carbon (ta-C) with sp^3 bonds increases in the a-SiC film and the FWHM(G) also increases. Therefore, hydrogen remains in the a-SiC film and the hydrogen density in the DLC film decreases.

3.3. Change in film hardness as a function of interlayer thickness

The change in the hardness H_{IH} of the DLC film as a function of interlayer thickness is shown in Fig. 7. The smallest interlayer thickness is 0.3 μm, which contained the highest hydrogen content of all prepared films.

The change in the DLC film thickness, hardness, and the FWHM (G) as a function of hydrogen content is shown in Fig. 8. Hardness is positively correlated with the half-width and negatively correlated with hydrogen content [7], but a discrepancy exists between the measurement and theoretical results shown in Fig. 8. Fig. 8 suggests that effect of hydrogen content on the hardness of the film can be divided into two regions. Region I contains low hydrogen content (<40 at%), where the hardness is predominantly determined by structure and is positively correlated with FWHM(G), the indicator of the
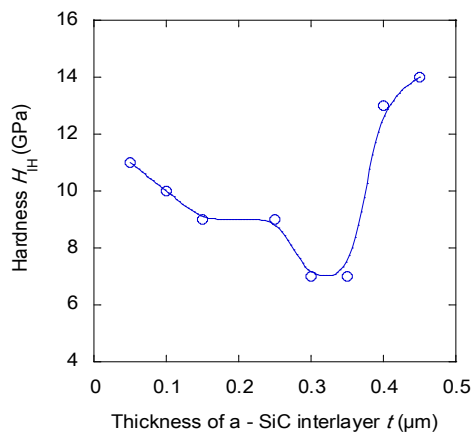
Fig. 7 Change in the hardness of the DLC film as a function of interlayer thickness.
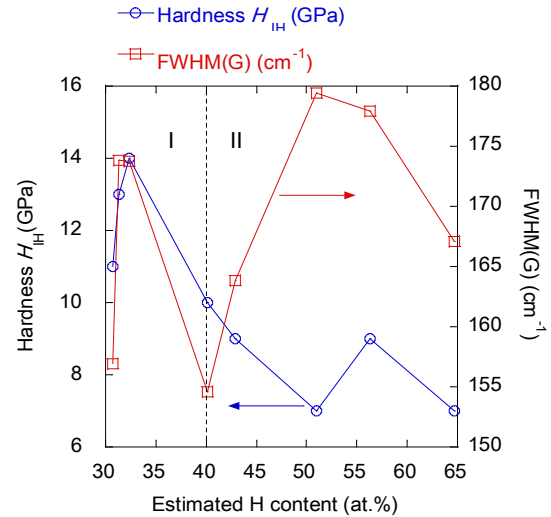
Fig. 8 Change in the DLC film thickness, hardness, and FWHM(G).

sp^2 bond content. Region II contains high hydrogen content (>40 at%), where the hardness is predominantly determined by hydrogen content and is negatively correlated with FWHM(G). The correlation between film hardness and structure changes depending on hydrogen content represents a novel finding.

4. Conclusion

DLC (a-C:H) layers with an a-SiC interlayer thin film were formed, and the changes in the DLC film structure and hardness induced by the interlayer thickness were studied. The following conclusions can be drawn from the results presented herein:

(1) A DLC layer with good adhesion to the substrate was achieved by forming an a-SiC interlayer.

(2) After increasing the a-SiC interlayer thickness, the G-peak position shifted to a lower frequency initially then shifted to higher frequencies. The G-peak position reached the lowest frequency at a film thickness of approximately 0.3 μm.

(3) As the thickness of the a-SiC interlayer increased, the half-width of the G-peak position increased almost monotonically as the number of sp^3 bonds increased.

(4) As the inter-film thickness increases, the hydrogen content in the DLC film increases initially, and then begins decreasing. The interlayer film thickness exhibits a local maximum near 0.3 μm.

(5) For DLC film hardness, a correlation between the hydrogen content in the film and the half width of the G-peak position was observed. When the hydrogen content is ≤40 at%, a positive correlation with FWHM (G) was observed, and when the hydrogen content is 40

at.% or above, a negative correlation with FWHM(G) was observed.

References

[1] J. Robertson, *Surf. Coat. Technol.*, 50, 3 (1992) 185.

[2] K. Akari, *J. Japanese Soc. Tribol.*, 47, 11 (2002) 809-814.

[3] Z. Sun, C. H. Lin, Y. L. Lee, J. R. Shi, B. K. Tay and X. Shi, *Thin Solid Films*, 377-378 (2000) 198-202.

[4] Goujaro, S., Vandenbulcke, L., Tawil, H., *J. Mater. Sci.*, 29(1994), 6212-6220.

[5] R. E. Shroder, R. J. Nemanich & J. T. Glass, *Phys. Rev. B*, 41 (1990) 3738-3743.

[6] A. C. Ferrari & J. Robertson, *Phys. Rev. B*, 61

[13]

[7] C. Casiraghi, A. C. Ferrari & J. Robertson, *Phys. Rev. B*, 72 (2005) 085401.

[8] G. Adamopoulos, J. Robertson, N. A. Morrison & C. Godet, *J. Appl. Phys.*, 96 (2004) 6348-6354.

[9] K. Miura, M. Nakamura, *J. Surf. Fin. Soc. Japan*, 59 (2008) 203-205.

[10] J. Choi, T. Hibi, A. Furuno, M. Kawaguchi, T. Kato, *J. Japanese Soc. Tribol.*, 62, 3 (2017) 228-235.

[11] J. Roberston, *Mater. Sci. Eng. R: Rep.*, 37, 1-4 (2002) 129-281.

[12] T. Mikami, H. Nakazawa, Y. Enta, M. Suemitsu, M. Mashita, *J. Surf. Fin. Soc. Japan*, 24, 7 (2003) 411-416

(2000) 14095-14017.

Study the Effects of Process Parameters on Surface Quality in Electrochemical Machining

Nhung Nguyen[1], Liem Thanh Dao[2], Thanh Quoc Truong[2]
[1]Department of Engineering, R techno Vietnam co. ltd
Nguyen Cuu Van Street, Binh Thanh District, Ho Chi Minh City, Vietnam
[2]Ho Chi Minh City University of Technology
Ly Thuong Kiet Street, District 10, Ho Chi Minh City, Vietnam

ABSTRACT

This study aims to investigate the effects of process parameters of an Electrochemical Machining (ECM) process which are voltage applied to the machine and flow rate of the electrolyte. The design of the system is based on the Taguchi method. Here, the signal-to-noise (S/N) model, the Analysis Of Variance (ANOVA) and regression analyses are applied to determine optimal levels and to investigate the effects of these parameters on surface quality. Finally, the experiments that use the optimal levels of machining parameters are conducted to verify the effects of the process parameters to the surface quality of the products. The results pointed a set of optimal parameters of the ECM process.

Keywords: Electrochemical machining, Taguchi method, ANOVA, SUS304, surface quality.

Research on the Effects Temperature Using Minimum Quantity Lubrication to Tool Wear and Surface Roughness in Turning C45 Steel

Tran Trong Quyet[1], Tran Anh Son[2], Dao Thanh Liem[2] and Truong Quoc Thanh[2]
[1]Tran Dai Nghia University
Add.: No. 189, Nguyen Oanh Street, Go Vap District, Ho Chi Minh City, Vietnam
[2]Ho Chi Minh City University of Technology
Add.: No.268, Ly Thuong Kiet Street, District 10, Ho Chi Minh City, Vietnam

ABSTRACT

In metal cutting process, the effects of cutting fluids to health, environment, productivity and quality in machining operations have been discussed. Effects of Minimum Quantity Lubrication (MQL) are green technology which is gradually applied in mechanical processing. This paper presents of the MQL parameters optimization approach in which the multi-response outputs based on Taguchi's L9 orthogonal array method is used. During the turning C45 steel, the cutting temperature, the maximum of tool wear, and the surface roughness were measured. The MQL parameters which are ratio of soluble lubricant and water, pressure of spray head, flow volume of emulsion were simultaneously optimized by taking the multi-response outputs using Taguchi based Grey Relational Analysis (GRA) into consideration. Here, three mathematical models were created using response surface regression methodology. The experiments had been done to investigate the effect of the MQL parameters to the turning process. As the results, the set of optimal MQL parameters had been pointed out to simultaneously minimize the cutting temperature, the tool wear and surface roughness.

Keywords: Minimum Quantity Lubrication (MQL), temperature cutting, tool wear, surface roughness, Grey Relational Analysis (GRA).

PART VII, SECTION III

Mechanical Technology
(Heat transfer, Thermal, and Fluid Engineering; Structures and Fluids; Vibration;
Energy Engineering; CAD/CAM/CAE/RP…)

A Best Practice Guidelines for Inspecting Precision Machined Parts by Using Several CMMs

Phaireepinas Phimpisan[1] and Chatchapol Chungchoo[2]

[1] Faculty of International Maritime Studies, Kasetsart University Si Racha Campus
99 ToongSukhla, Si Racha, Chonburi, 20230, Thailand
[2] Department of Mechanical Engineering, Faculty of Engineering, Kasetsart University
50 Ngam Wong Wan Rd., Lat Yao, Chatuchak, Bangkok, 10900, Thailand

ABSTRACT

Currently in Thailand, original equipment manufacturers (OEM) who produce precision-machined parts face a serious problem about product rejection from customers. This is because measuring results from the OEM supplier differ from the measuring results from the OEM buyer. Normally, for precision-machined parts, OEM suppliers and OEM buyers use CMM machines as an inspection tool. One major cause of the difference in measurements is that suppliers and buyers use different CMM machine, operators and measuring methods. In order to mitigate the difference in measurements, the standard guideline for measuring precision-machined parts by CMM machines needs to be improved. In this research, the guideline was developed by studying the best practices of five successful companies, who could minimize rejection due to the differences in the CMM machine operators and measuring methods. Validation results indicated that when manufacturers who had precision problems used this guideline, the product rejection could decreased significantly.

Introduction

Currently in global trade, the OEM buyer-supplier knowledge transfer is one important key for improving performance of manufacturing processes. However, knowledge transfer from OEM buyers to OEM suppliers is not always successful due to several reasons such as knowledge stickiness and manufacturing capability [1]. For producing precision-machined parts, one important piece of knowledge that needs to be transferred is product inspection knowledge. If there is no transfer of product inspection knowledge between buyers and suppliers, there is room for error in measuring results from the OEM supplier differ from the measuring results from the OEM buyer.

In the case of no knowledge transfer or unsuccessful knowledge transfer for measuring precision-machined parts by CMM machines, the standard guideline for measuring precision-machined parts by CMM machines can be an alternative tool for reducing product rejection from customers.

In order to develop the guideline mentioned earlier, researchers must act as knowledge engineers, and must complete four steps, which are (1) acquisition of knowledge, (2) representation of that knowledge, (3) application using the knowledge collection generated in the preceding steps, and (4) verification and validation of applications [2].

2. Method

2.1 Selection of Case Studies

Five Thai OEM companies who produce precision-machined parts and use CMM for inspecting final products were selected and then used as case studies. One expert from each company was interviewed by the research team. The criteria for company selections were:

1) Precision-machined parts were the major product.
2) The company previously faced serious problems with product rejection from customers due to differing results in measurements, and this problem has since been solved.

2.2 Selection of Experts

Hoffmen et al. [3] stated that experts can be selected on the basis of years of experience and on the basis of professional criteria (graduate degrees, training experience, publication record, memberships in professional societies, licensing, etc.)

In this work, operators who used CMM to inspect precision machined parts were accepted as experts if they were able to meet the following criteria:

1) Completed undergraduate degree or above
2) Had at least 3 years of experience in product inspection using CMM
3) Were trained "how to use CMM"
4) Were trained for ISO/IEC 17025
5) Were trained or had previous knowledge about Measurement System Analysis (MSA)

2.3 Acquisition of Knowledge

Normally, knowledge acquisition (or knowledge elicitation) can be done by using the interviewing method [3, 4]. In this research, both unstructured interviews and structured interviews were used for collecting the following knowledge:

1) Procedural knowledge (rules, strategies, agendas, and procedures)
2) Declarative knowledge (concepts, objects,

and facts)

3) Meta-knowledge (knowledge about the other types of knowledge and how to use them)
4) Heuristic knowledge (rules of thumb)
5) Structural knowledge (rule sets, concept relationships, and concept to object)

In this research, unstructured interviews were used as an open dialogue in which researchers (interviewers) asked open-ended questions about expert's knowledge. For structured interviews, they were used for rest of session.

Generally, for structured interviews, the two most common formats rely on either domain-specific probe questions or on generic probe questions [5]. For this research, only domain-specific probe questions were employed.

In order to control the interview time and scope, a first-pass knowledge base method should be added in a structured interview section. For this method, the interviewers have to prepare the core concepts, the definition of terms, and the procedural rules in advance from a document analysis, task analysis, or initial unstructured interviews [3]. In the interviews with the first-pass knowledge base method, experts will just give comments on each one, suggesting additions, deletions, refinements, etc. [3, 6]

In order to avoid incomplete account of the session or missing how the expert qualifies some knowledge, both simple notekeeping and audio recording were used.

2.4 Interpret and Analyze Knowledge

In this section, there were two tasks that the researchers had to do. The first task was a review of the collected information and the identification of key pieces of knowledge (called interpretation task). The second task was to identify important concepts used by experts, determine concept relationships, and how the experts use them to solve problems.

2.5 Guideline Development

This section begins with a summary of knowledge and concepts acquired in the previous section, in order to structure data. There are several techniques that can be used, including cognitive maps, inference networks, flowcharts, and decision trees [4]. However, in this case, the flowchart technique was the most appropriate. By using this knowledge, the best guideline for inspecting precision machined parts by using Several CMMs was developed.

2.6 Validation and Verification.

M. Peleg [7] says that the developed guidelines have to be validated and verified. The validation must answer the question "are we building the right product?", and the verification must answer the question "are we building the product right?" [7].

One of main validation technique is the inspection technique. In this technique, domain experts inspect guidelines to try and locate errors in the algorithm's logic [7].

Unlike the validation, the verification concerns mathematical proof that the guideline meets the objective [7]. In this research, the comparison between rejection of product before the company implements this guideline and rejection of product after the company implements this guideline can be used for the verification. Hence, it means that test companies are required for verifying the developed guideline.

3. Results and Discussion

3.1 Case Studies and Experts

In this research, Five Thai OEM companies located in Ayutthaya and Pathumthani provinces were selected and then used as case studies. These companies produce precision-machined parts and use CMM for inspecting their final product.

In each company, operators who passed the criteria mentioned in section 2.2 were selected as experts. In some companies, there were more than one operator who passed the criteria. In this case, operators who had the highest experience were selected as an experts.

3.2 Acquisition of Knowledge

As mentioned in section 2.3, the unstructured interview was used as a tool for opening interview, and it was developed in the pattern of open-end questions. Examples of questions used in unstructured interviews were shown in Table 1.

By using the first-pass knowledge base method, questions of structured interviews were developed for extracting knowledge from experts. In this research, several documents such as "How to Use CMM" [8], MSA [9], Uncertainty Analysis [10], ISO/IEC 17025 [11], and Measurement Consistency on CMM [12] were used for deriving these questions. Hence, in the interview with in the first-pass knowledge base, experts just gave comments on each one, suggesting additions, deletions, and refinements. These functions of experts were also mentioned earlier in Hoffman's research [6]. Questions of structured interviews could be classified into 3 groups which are:

1) Operator group (man group)
2) Hardware and software group (machine group)
3) Measuring method and data analysis (method group)

Examples of questions used in structured interviews were also shown in Table 1.

Table 1. Examples of questions used in unstructured interviews and structured interviews

Type of interviews	Examples of question
Unstructured	1. In the big picture, could you tell me about product rejection due to measuring results from the OEM supplier differing from the measuring results from the OEM buyer, and how you solved this problem?
Structured: Man group	1. Is it true that operators need to have knowledge about how to use CMM? Why? 2. Is it true that operators need to have knowledge about how to calculate measuring results and uncertainty? Why? 3. Is it necessary that CMM operators have to review their measuring skills every six months? Why? etc.
Machine group	1. Is it necessary that supplier's CMM and buyer's CMM must have the same performance? Why? 2. Is it necessary that supplier's CMM and buyer's CMM have to check measuring correlation every six months? Why? 3. Could you define the meaning and boundary of term "the same performance"? 4. Is it better if both supplier and buyer use the same CMM model? Why? 5. Is it necessary that both supplier and buyer use the same software? Why? If not, how do both of them accept the software used by another? etc.
Method group	1. Is it necessary that both buyer and supplier have to use the same procedure for measuring product dimension and geometry? Why?

2. Is it true that both buyer and supplier must use the same mathematical model for calculating GD&T? Why?

etc.

3.3 Guideline Development

By using the knowledge extracted in the previous section, the best practice guideline for inspecting precision machined parts by using several CMMs was developed. This guideline consisted of three sections which are the term and definition section, the procedure section and the supplementary section. The first section is about the term and definition used in this guideline. The second section is the procedure which was built following the extracted knowledge. The last section contained the necessary documents used with guidelines such as formulas (equations) with examples for calculation.

The procedure represented this guideline was shown in Fig 1. This procedure could be classified into 5 stages which are:

1) Policy stage
2) Prerequisite stage
3) Beginning stage
4) Six-month stage
5) 12-month stage

In the policy stage, both OEM buyer and supplier must agree to follow the guideline: This should be made clear in the letter of agreement.

For the prerequisite stage, operators need to complete training of ISO2IEC 17025, MSA, uncertainty analysis, and CMM operation before doing their duty in product inspection unit. Additionally, operators have to check and make sure that the environment of the CMM is always following relevant standards and recommendations. It should be noted that if there is an upgrade/change in CMM's software and/or CMM's hardware, operators need to retrain how to use it.

For the beginning stage, both buyer and supplier have to set measuring method and conditions together. These method and conditions include workpiece setup conditions, workpiece datums, CMM's probe and stylus types, inspection sequence (probe movement), probe speed, sampling strategies, etc. Then, the linear correlation of measuring results of buyer' CMM and supplier's CMM needs to be calculated. If it is a bad linear correlation, it means that buyer's CMM cannot be used for rechecking the inspection results done by supplier.

Every six months, the linear correlation of measuring results of buyer's CMM and supplier's CMM as well as the CMM's environment need to be rechecked.

Every 12 months, procedures mentioned in the six-month stage needs to be done. After that, the CMM's performance needs to be tested. If required, the CMM should be repaired. It should be noted that there are

several methods for testing the performance of CMM [13]. Hence, buyer and supplier can use appropriate method for their own CMM.

3.4 Guideline Validation

After the best practice guideline for inspecting precision machined parts by using several CMMs was developed, this guideline was sent back to the experts for reviewing. The reviewing results indicated that all experts agreed with this guideline without major comments. Additionally, all experts agreed that if OEM buyers and OEM suppliers follow this guideline the problem about product rejection due to measuring results from OEM supplier differ from the measuring results from OEM buyer can be reduced.
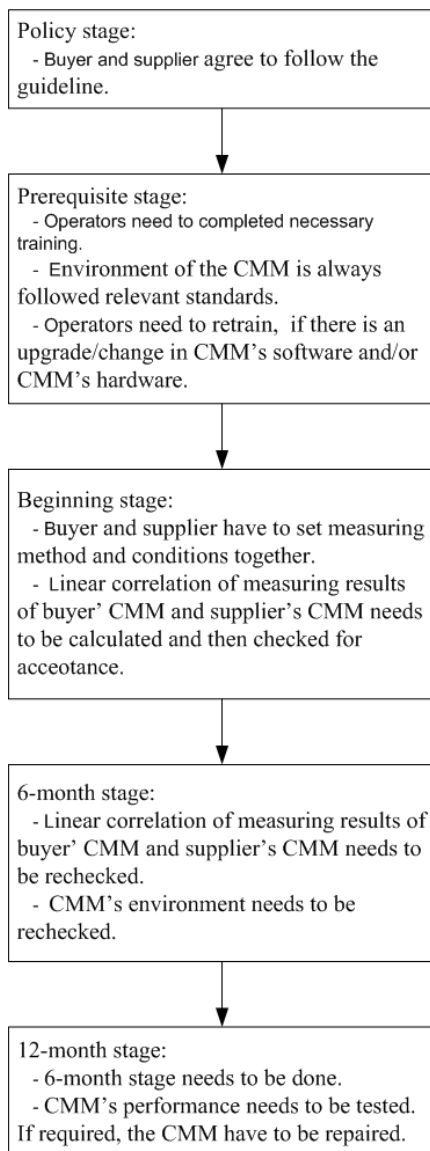

Fig. 1 A procedure summarized from the best practice guideline for inspecting precision machined parts by

using several CMMs.

3.4 Guideline Verification

Currently, five OEM suppliers and their buyers have been selected as test cases. However, at least six months are required for the data collection. Hence, in this state, there are no results for the verification.

4. Concluding Remarks

In this research, the best practice guideline for inspecting precision machined parts by using several CMMs was developed by using knowledge acquisition from experts. These experts believed that if both buyer and supplier follow these guidelines, the problem about product rejection from buyers due to the measuring results from the supplier differ from the measuring results from the buyer can be reduced significantly.

References

[1] C. Li, Knowledge stickiness in the buyer-supplier knowledge transfer process: The moderating effects of learning capability and social embeddedness, *Expert Systems with Applications*, 39 (2012) 5396-5408.

[2] P. R. O. Payne, E. A. Mendonca, S. B. Johnson and J. B. Starren, Concept knowledge acquisition in biomedicine: a methodological review, *Journal of Biomedical Informatics*, 40 (2007) 582-602.

[3] R. R. Hoffman, N. R. Shadbolt, A. M. Burton, and G. Klein, Eliciting knowledge from experts: a methodological analysis, *Organizational Behavior and Human Decision Process*, 62 (1995) 129-158.

[4] J. Durkin, *Expert Systems: Design and Development*, Prentice Hall International Editions, U.S.A., (1994).

[5] L. E. Wood and J. M. Ford, Structuring interviews with experts during knowledge elicitation, *Knowledge Acquisition as Modeling*, Wiley, New York, (1993) 71-90.

[6] R. R. Hoffman, The problem of extracting the knowledge of experts from the perspective of experimental psychology, *The AI Magazine*, 8 (1987) 53-66.

[7] M. Peleg, Computer-interpretable clinical guidelines: a methodological review, *Journal of Biomedical Informatics*, 46 (2013) 744-763.

[8] D. Flack, *Good Practice Guideline No. 41: CMM Measurement Strategies*, National Physical Laboratory, (July 2001, updated May 2014).

[9] Chrysler Group LLC, Ford Motor Company, and General Motors Corporation, *Measurement Systems Analysis: Reference Manual*, 4th edition, (2010).

[10] S. Bell, *A Beginner's Guide to Uncertainty of Measurement*, National Physical Laboratory, Issue 2, (2001).

[11] ISO/IEC 17025:2017 General requirements for the competence of testing and calibration laboratories.

[12] P. Saunders, A. Wilson, N. Orchard, N. Tatman and P. Maropoulos, An exploration into measurement consistency on coordinate measuring machines, *Procedia CIRP*, 25 (2014) 19 – 26.

[13] P. Cauchick-Miguel, T. King and J. Davis, CMM verification: a survey, *Measurement*, 17 (1996) 1-16

A Study on Dynamics Behavior of the Spindle System for Machine Tools

Nguyen Ngoc Nam[1], Sam-Sang You[1*], Boc Minh Hung[1], and Hwan-Seong Kim[2]
[1]Division of Mechanical Engineering, Korea Maritime and Ocean University, South Korea.
[2]Department of Logistics Engineering, Korea Maritime and Ocean University, South Korea.

ABSTRACT

The dynamic analysis of spindle system of the CNC machine is critically important for quality of the product surface, overall productivity, and efficiency of the machine tools. The spindle power of CNC turning is provided by the servo motor. The spindle dynamics with accuracy directly affect tool forces, which cuts the workpiece during production, and eventually machining surface topography. The bifurcation analysis of the spindle system is used for understanding dynamical behaviors of the nonlinear models. Stability analysis of spindle system is described by depending on the cutting forces which are affecting the CNC machine tool. In this study, the spindle operations will be given in with two regions, unstable and stable. Firstly, the mathematical model has been established for the spindle system consisting of the servo motor and cutting forces. Secondly, the phase portraits of the dynamical models are provided by vector field analysis, depicting dynamic behaviors for the spindle operations. It is known that the spindle machine system has three equilibrium points; two of them are unstable and another is stable. In addition, the bifurcation analysis has shown that the machine tool operations can be dynamically stable and unstable under various parameters. As a result, the dynamic behavior of spindles system and bifurcation diagram should be described to enhance the dynamic stability of the machine tools as well as the product surface topography.

Keywords: CNC spindle machine, stability analysis, bifurcation analysis, cutting forces, nonlinear dynamical model

1. Introduction

The stability of the spindle system is one of the most important factors in CNC machine tools since its dynamic directly affect the quality surface product of the machine tool. The stable operations of the machine tools are essential to guarantee the high-quality of the finished products with low production costs. High-performance machining system can reduce high-risk of dynamic instability in the process. The loss of stability results in severe vibrations in the machining process. In turn, the machine tools can be damaged, and there will be difficulties in achieving high processing quality. Thus, machining stability plays a major role in enhancing improving tool performance and product quality. Nonlinear analysis of spindle speed system is essential to characterize the system dynamical behaviors.

Considerable research related to the nonlinear analysis of spindle to enhance the quality of precision products have been published. Hongrui Cao et al. [1] proposed a chatter stability spindle system using speed varying spindle dynamic. However, that research is applicable to cases when slight chatter can be tolerated. Ganol et al. [2] developed a dynamic spindle system then proposed a dynamic stability lobe diagram by integrating the modeled speed-dependent spindle transfer function in a chatter vibration stability approach of Altintas and Budak. J. de Caniere [3] used perturbation analysis to determine the stability of the spindle system. However, their analysis can only be used for small values of the parameter. Jemielniak and Widota [4] proposed the influence of spindle speed variation on the machining stability using amplitude application coefficient. The amplitude amplification coefficient was derived using a single oscillation frequency and their study does not consider the effect on nominal spindle speed. S. Jayaram et al. [5] proposed an analysis chatter stability for variable spindle using transforming the linear differential equation with time-varying delay to the solution of order characteristic equation.

This paper describes a systematic approach to analyze the nonlinear stability of the spindle system considering the interaction of the machine tool, the workpiece, and cutting forces. In addition, the dynamic interactions of a rotating spindle-tool and a cutting workpiece are considered by combining their respective transfer functions. The system dynamics are examined to identify the effects of the motor torques and the speed-dependent cutting forces. A constant diameter workpiece is modeled to analyze the stability of the spindle tool structure. The numerical investigations are carried out to optimize the spindle speed, especially for industrial applications.

2. Mathematical model

For the high-speed machining process, the spindle system with the servo motor circuit is illustrated in Figure1. Generally, the spindle system is rotated by

adjusting the armature voltage of the servo motor. The control synthesis considers not only the spindle dynamics but also deals with the dynamic interactions between the spindle motions and the cutting forces. The nominal model of the spindle system can be described in Equation (1).
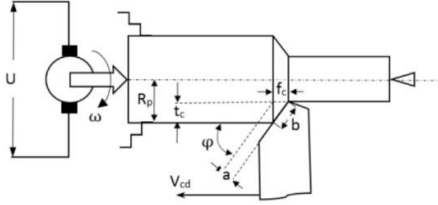

Figure 1. Diagram of spindle drive system

$$T_m T_e \frac{d^2\omega}{dt^2} + T_m \frac{d\omega}{dt} + \omega = k_d U - k'_d U_m \quad (1)$$

Where U is the applied voltage (V); R_a is the armature resistance (Ω); i_A is the armature current (A); L_A is the armature inductor (H); E is motor back electromotive force (V); ω is the motor angular velocity (rad/s); M_e and M_t are the motor and load torque, respectively; and $J_m \frac{d\omega}{dt}$ is the torque acting on load inertia J_m ($kg.m^2$); $T_e = \frac{L_a}{R_a}$ is armature time constant (s); $T_m = \frac{J_m R_a}{C_e C_m}$ is electrical time constant (s); $k_d = \frac{1}{C_m}$; $k'_d = \frac{R_a}{C_e C_m}$; C_m is the coefficient of ratio between motor torque and current; $U_m = \left(T_e \frac{dM_t}{dt} + M_t\right)$ is the voltage components caused by disturbance load torque; C_e is the coefficient of the ratio between dynamic force and the rotational speed of the motor.

To determine the influence of cutting force on the motor characteristics, the moment $M_{(t)}$ is considered in the voltage equation applied to motor, $U_m = \left(T_e \frac{dM_t}{dt} + M_t\right)$. This moment can be obtained by: $M_t = k_\omega \left(\frac{1}{\omega} - \frac{k_s}{\omega^2}\right)$. $k_\omega = R_p.\lambda.\sigma.t_c.V_{cd}$; where R_p is the diameter of the work piece (mm); σ is the pressure of the chips on the tool face is a depth of cut (mm); V_{cd} is cutting feed (mm/s); and λ is the coefficient, k_d is coefficient influence of cutting force to work piece. The equation (1) can be rewritten as.

$$T_m T_e \frac{d^2\omega}{dt^2} + T_m \frac{d\omega}{dt} + k_m \left(\frac{2k_s T_e}{\omega^3} - \frac{T_e}{\omega^2}\right)\frac{d\omega}{dt}$$
$$+\omega - k_m \left(\frac{k_s}{\omega^2} - \frac{1}{\omega}\right) = k_d U \quad (2)$$

3. Nonlinear Analysis
3.1. Equilibrium Point and Local Dynamic Analysis
In order to characterize the dynamic behaviors, the spindle model can be described in the state-space representation. The stability characteristics are the dynamical performance with external disturbance, which accurately describes nonlinear system behaviors similar to the bifurcation of the equilibrium points. Physically, for steady state handling analysis, the equilibrium points have more information than other points in any of the phase portraits. A small disturbance causes sensitive for unstable equilibrium points, and then any slight offset from the equilibrium point will lead to moving away from the equilibrium solutions.

To obtain a state-space model, the state variables are defined as follows: $x_1 = \omega$ and $x_2 = \dot{\omega}$. Then, the dynamical model described in Equation (2) is given by.

$$\begin{cases} \dot{x}_1 = x_2 \\ \dot{x}_2 = -\frac{1}{T_e T_m}x_1 + \left(\frac{k_m}{T_m x_1^2} - \frac{2k_m k_s}{T_m x_1^3} - \frac{1}{T_e}\right)x_2 \\ \quad + \frac{k_m}{T_e T_m}\left(\frac{k_s}{x_1^2} - \frac{1}{x_1}\right) + \frac{k_d U}{T_e T_m} \end{cases} \quad (3)$$

where x_1 is the spindle speed, x_2 and is angular acceleration. The equilibrium points are found by setting the state derivatives to zero.

$$\begin{cases} x_2 = 0 \\ -\frac{1}{T_e T_m}x_1 + \left(\frac{k_m}{T_m x_1^2} - \frac{2k_m k_s}{T_m x_1^3} - \frac{1}{T_e}\right)x_2 \\ \quad + \frac{k_m}{T_e T_m}\left(\frac{k_s}{x_1^2} - \frac{1}{x_1}\right) + \frac{k_d U}{T_e T_m} = 0 \end{cases} \quad (4)$$

To determine the system stability around equilibrium points, the spindle model can be linearized, using the Jacobian Matrix J, as follows

$$J = \begin{bmatrix} 0 & 1 \\ -\frac{1}{T_e T_m} & \frac{k_m}{T_m x_1^2} - \frac{2k_m k_s}{T_m x_1^3} - \frac{1}{T_e} \end{bmatrix} \quad (5)$$

The eigenvalues of Jacobian matrix are determined as follows:

$$\lambda_{1,2} = \frac{tr(J) \pm \sqrt{(tr(J))^2 - 4\det J}}{2} \quad (6)$$

3.2. Bifurcation Analysis
Base on the eigenvalue analysis, the stability of the system can be determined by two steady states: asymptotically stable equilibrium and a saddle point. The parameters of the spindle system are presented in Table 1. The basic parameters that affect the stability are $R_p, \lambda, \sigma, T, V_{cd}$; Noting that, the coefficient λ depends on the temperature and the speed; σ depends on changes in the cutting layer size and variations in T corresponds to changes in cutting speed. In this case, parameters R_p and V_{cd} are considered as constants. All the parameters $(R_p, \lambda, \sigma, T, V_{cd})$ are interrelated k_m to both indirectly and directly and the changes to k_m will affect the individual parameters

To analysis the bifurcation of the system, the equation (2) can be written as.

$$\omega - k_m \left(\frac{k_s}{\omega^2} - \frac{1}{\omega}\right) = k_d U \quad (7)$$

Or

$$\omega^3 - k_d U \omega^2 + k_m \omega - k_m k_s = 0 \qquad (8)$$

Let

$$k = \frac{-9k_d U k_m + 2U^3 + 27k_m k_s}{2\sqrt{|(k_d U)^2 - 3k_m|^3}} \text{ and } \Delta = (k_d U)^2 - 3k_m .$$ In the case of $\Delta > 0$ and $|k| < 1$, the spindle system has three equilibrium points

$$Q_1 = \left(\frac{\left(\left(2\sqrt{\Delta} \cos \left(\frac{a\cos k}{3} \right) \right) + k_d U \right)}{3} ; 0 \right)$$

$$Q_2 = \left(\frac{\left(\left(2\sqrt{\Delta} \cos \left(\frac{a\cos k}{3} - \frac{2\pi}{3} \right) \right) + k_d U \right)}{3} ; 0 \right)$$

$$Q_2 = \left(\frac{\left(\left(2\sqrt{\Delta} \cos \left(\frac{a\cos k}{3} + \frac{2\pi}{3} \right) \right) + k_d U \right)}{3} ; 0 \right)$$

In the case of $\Delta > 0$ and $|k| \geq 1$, the spindle system has one equilibrium point

$$Q_1 = \left(\frac{\sqrt{\Delta}|k|}{3k} \left(\sqrt[3]{|k| + \sqrt{k^2 - 1}} + \sqrt[3]{|k| - \sqrt{k^2 - 1}} \right. \right.$$
$$\left. \left. + \frac{k_d U}{3} \right) ; 0 \right)$$

In the case of $\Delta = 0$ and $(k_d U)^3 + 27k_m k_s = 0$, the spindle system has one equilibrium point

$$Q_1 = \left(\frac{k_d U}{3} ; 0 \right)$$

In the case of $\Delta = 0$ and $(k_d U)^3 + 27k_m k_s \neq 0$, the spindle system has one equilibrium point

$$Q_1 = \left(\frac{k_d U + \sqrt[3]{(-k_d U)^3 + 27k_s k_m}}{3} ; 0 \right)$$

In the case of $\Delta < 0$, the spindle system has one equilibrium point

$$Q_1 = \left(\frac{\sqrt{|\Delta|}}{3} \left(\sqrt[3]{k + \sqrt{k^2 + 1}} + \sqrt[3]{k - \sqrt{k^2 + 1}} \right) \right.$$
$$\left. + \frac{k_d U}{3} ; 0 \right)$$

4. Simulation

The spindle dynamic model is described with the nominal values of system parameters shown in Table

Table 1. The spindle model parameters.

Symbol	Values	Unit
R_a	1.48	Ω
L_a	0.01184	H
J	0.06	KJ.m^2
U	220	V
I_a	22	A
k_m	12000	N
C_e	0.34	V.s
C_m	1.08	N.m.A^{-1}

The rotational behaviors spindle can be depicted using the phase plane analysis. A phase portrait for the spindle system with cutting force $k_m = 10000$ (N) and $k_s = 1$ is shown in Figure 2. At the equilibrium point eigenvalues of the system could be calculated as $\lambda_1 = -0.0765 + j1.1138$ and $\lambda_2 = -0.01765 - j1.1138$ then all trajectories are converging to equilibrium point.

A phase portrait for the spindle system with cutting force $k_m = 12000 (N)$ and $k_s = 10$ is shown in Figure 3. The equilibrium points at $Q1$, $Q2$ and $Q3$ can be qualitatively specified as saddle node and stable focus, respectively. At the equilibrium point $Q3$ eigenvalues of the system could be calculated as $\lambda_1 = -1.0438$ and $\lambda_2 = -52.5508$ then all trajectories are converging to $Q3$. At the equilibrium point $Q2$ eigenvalues of the system could be calculated as $\lambda_1 = -0.41714$ and $\lambda_2 = 2.878$ then all trajectories will be away from $Q2$. At the equilibrium point $Q1$ eigenvalues of the system could be calculated as $\lambda_1 = 0.31169 + j0.7347$ and $\lambda_2 = 0.31169 - j0.7347$ then all trajectories will be away from $Q1$.
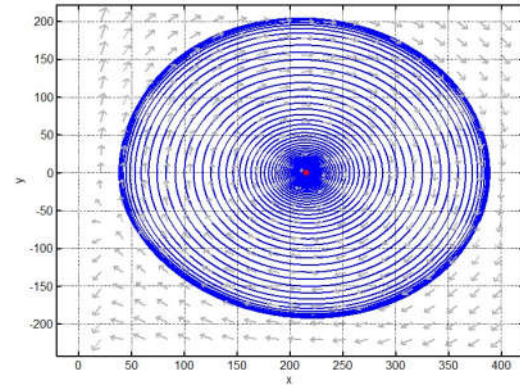

Figure 2 Phase portrait of the spindle behaviors with one equilibrium points
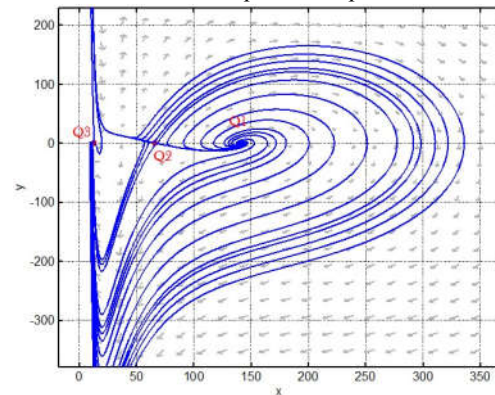
Figure 3 Phase portrait of the spindle behaviors with three equilibrium points
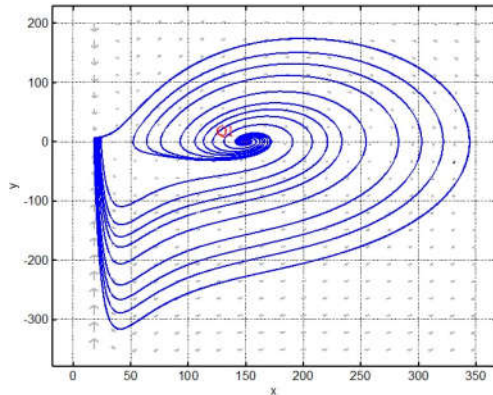

Figure 4 Phase portrait of the spindle behaviors with one equilibrium points

Figure 4 show the phase portrait of the spindle system with one equilibrium point under $k_m = 12000$ and $k_s = 20$. At the equilibrium point eigenvalues of the system could be calculated as $\lambda_1 = 0.22398 + j0.873$ and $\lambda_2 = 0.22398 - j0.873$ then all trajectories will be away from Q_1

Figure 5 shows the bifurcation with parameter cutting force. In case of the cutting force is small, the dynamic of the spindle system has one equilibrium point, and the system is stable. In case of the cutting force large. The dynamic of the spindle system has three equilibrium points. One of them is stable and others is unstable.
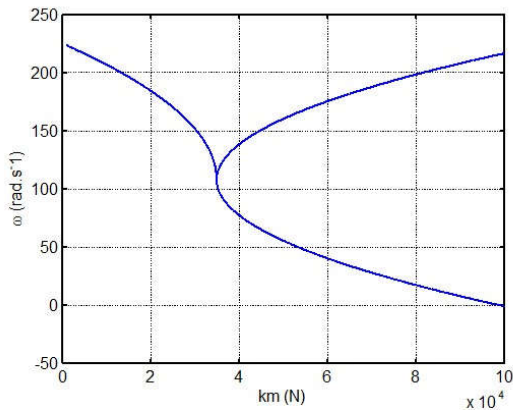

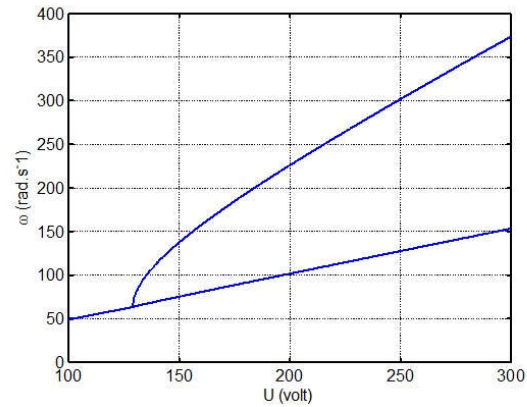Figure 5 Bifurcation diagram of the spindle system with parameter km

Figure 6 Bifurcation diagram of the spindle system with parameter U

Figure 6 shows the bifurcation with parameter voltage supply. In case of the voltage supply is small, the dynamic of the spindle system has one equilibrium point, and the system is unstable. In case of the voltage supply is large. The dynamic of the spindle system has two equilibrium points and the dynamic of the system is stable.

Physically, the dynamic of motor of spindle system are changed by the cutting forces. The influence of cutting process on the behavior of motor of spindle system depends on the motor parameters. If the cutting area is increased, the velocity of the spindle system shall decrease. The torque caused by cutting process shall be increased not proportionally but rapidly. When the load torque requires larger than the motor can provide the power, the machine will be stopped abruptly.

5. Concluding

This paper deals with the dynamical analysis for spindle machining system. A nonlinear model has been established for the machine tool spindles under cutting forces. The phase portrait of the dynamical spindle system showed behavior of the system with three case of cutting force. In the case of cutting force is small. The spindle system has one equilibrium point and is stable. In case of the cutting about 25 kN, the spindle system has three equilibrium points, one of them is stable and others are unstable. In case of the cutting force is large, the spindle system has one equilibrium and system is unstable. In addition, the bifurcation analysis has shown that the machine tool operations can be dynamically stable and unstable under cutting forces and voltage supply parameters. As a result, the dynamic behavior of spindles system and bifurcation diagram should be described to enhance the dynamic stability of the machine tools as well as the product surface topography

References

[1] Hongrui Cao, Bing Li, Zhengjia He, Chatter stability of milling with speed varying dynamic of spindles, 52(2012) 50-58.

[2] Vincent Gagnol, Belhassen C. Bouzgarrou, Pascal Ray and Christian Barra, Stability based spindle design optimization, 129(2006) 407-415.

[3] J. de Canniere, H. van Brussel, J. Bogaert, A contribution to the mathematical analysis of variable spindle speed machining, 5(1981), 158-164.

[4] K. Jemielniak, A. Windota, suppression of self-excited vibration by the spindle speed variation method, 24(1984) 207-214.

[5] S. Jayaram, S. G. Kapoor, R. E. DeVor, Analytical stability analysis of variable spindle speed machining, 122(2000) 391-397.

Optimization of Milling Process for Improving Technological Performances

Trung-Thanh Nguyen[1], Tat-Khoa Doan[1]

[1]Le Quy Don Technical University, 236 Hoang Quoc Viet, Ha Noi, 10000, Viet Nam

ABSTRACT

This work presented a multi-responses optimization in order to decrease the machining power P_m and improve the material removal rate (MRR), while the surface roughness R_a is predefined as a constraint. The effects spindle speed S, depth of cut a_p, feed rate f_z, and tool tip radius r were investigated using response surface method (RSM) models and ANOVA analysis. The milling experiments were performed with the aids of the CNC machine and Box-Behnken experimental matrix. Subsequently, the scanning electron microscope (SEM) was used to analyze the surface morphology at various machining conditions. Finally, an evolutionary algorithm entitled archive-based micro genetic algorithm (AMGA) was used to solve the trade-off among three responses and find the optimal parameters. The results showed that the machining power was strongly influenced by process parameters, followed by tool tip radius. The tool tip radius has greater effect on the surface roughness, compared to the power model. The machining power increased with the increment in the tool tip radius and process parameters. Surface roughness values were diminished with increases in both spindle speed and tip radius.

1. Introduction

The important task of machining processes is to improve the energy efficiency and quality products in a short time. The first solution mainly focuses on machine improvements and new machining technologies used, such as intelligent control [1] and advanced devices [2]. The second approach pays attention to optimize machining conditions using optimization techniques in order to satisfy the technical targets. The optimizing machining process is inexpensive and has better sustainable development, compared to drastic improvements. Consequently, selection of optimum machining conditions plays an important role to satisfy the machining requirements (i.e. Low energy consumption, acceptable quality, high productivity).

Improving the technological performances of the milling processes using optimal parameters has been considered by many researchers. Some researches attempted to minimize the surface roughness as a single response [3-6]. Other investigators solved the trade-off analysis, among multi-responses, such as machining power, surface roughness, cutting force, and material removal rate. Process parameters were optimized in an effort to improve technological performances in terms of AISI H13 [7], AISI 1050 [8], and aluminum composite [9]. Similarly, the relationships inputs and technological outputs were developed for X2CrNi18-9 [10]. It can be seen that multi-objective optimization of machining parameters is more realistic than the single one.

This paper presents a multi-objective optimization of the SKD61 milling for improving the energy efficiency and production rate with the predefined surface roughness. A hybrid approach combining RSM models and AMGA is used to develop the predictive models as well as identify the globally optimal solution. This paper is expected as a significant contribution to investigate the process parameters and tool tip radius on the machining power and surface roughness as well as help the milling operators to select the appropriate factors with different constrained surface roughness.

2. Method

The milling processes were conducted with the aid of a Spinner U-620 machining center having spindle power of 10 kW and maximizing speed of 12000 RPM. The workpiece was prepared with the dimensions of 350 mm×150 mm×25 mm. Four machining parameters, including the spindle speed S, depth of cut a_p, feed rate f_z, and the tool tip radius r and their levels were shown in Table 1. The cutting forces were measured using the quartz three-component dynamometer KISTLER 9257B (Fig. 1a). The surface roughness R_a was measured by a tester Mitutoyo SJ-301 (Fig. 1b). The surface morphology at different machining conditions was examined using Nova Nano SEM 450 machine, as shown in Fig. 1c.
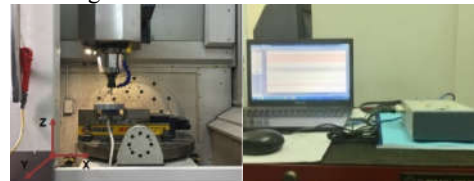
(a) Cutting force measurement

(b) Surface roughness measurements

(e) Scanning machined surface

Fig. 1 Experiments and measurement

Table 1. Machining parameters and their values

| Symbol	Level -1	level 0	level +1
S	2000	4000	6000
a_p	0.2	0.5	0.8
f_z	0.02	0.06	0.10
r	0.2	0.4	0.8

3. Results and Discussion

The main effects of each machining parameter on the responses are shown in Fig. 2. As a result, interaction effects of process parameter and tool tip radius on the objectives are highly complex. Fig. 2a showed that an increase of the spindle speed, depth of cut, and feed rate leads to a higher material removal volume, resulting in an increased machining power. Particularly, the maximum power consumed is necessary in order to observe the highest production rate. Additionally, a higher tool tip radius led to an increase in cutting edge length; hence, the more power consumed is required to overcome the frictional resistance. The different machining power can be observed at the same material removal rate due to the effects of tool tip radius.

Fig. 2b exhibited that the R_a was decreased with an increment of spindle speed. At low spindle speed, friction between the workpiece and tool is high due to discontinuous chips formed which was deposited in the contact area. The high friction leads to interruptions during cutting operations and resulting in a higher roughness value. An increase of spindle speed results in a lower frictional coefficient and a lower roughness value was observed. In addition, at higher spindle speed, the chip may be broken away with less material deformation at the immediate tool tip, which in turn preserves the machined surface properties leading to better surface roughness.

Furthermore, when high feed rates are used, a thicker chip is produced, which leads to an increased milling load, especially on the cutting edge. A higher machining force leads to the chip adherence, resulting detachment of small parts from the workpiece. Therefore, surface roughness values increase with the feed rate due to more feed marks on the workpiece surface. Obviously, the various defects, such as grooves and cracks are produced on the machined surface, as shown in Figs. 3a and b.

Higher depth of cut results in an increased contact area between the tool and the workpiece as well as higher milling forces. This results in chattering which lead to an increase in surface roughness values.

A smoother surface was observed using a larger tool tip radius in all machining conditions. An increase tip radius results in a higher stand damping as well as real contact area with the workpiece surface. Therefore, the high cutting force and vibration can be absorbed with larger tool tip radius, resulting surface roughness values were decreased. The large grooves on the machined surface at the small tip radius were shown in Fig. 3c. In contrast, the smooth cut and small waviness patterns were observed using large radius, as shown in Fig. 3d.
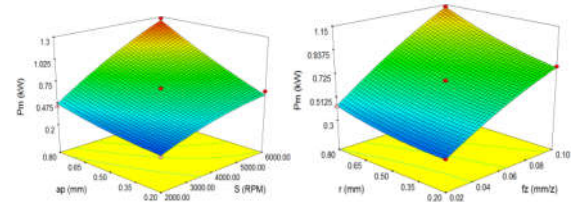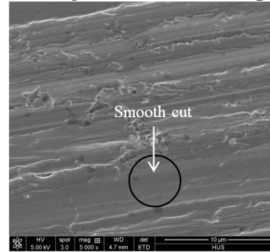

(a) The effects of machining parameters on P_m
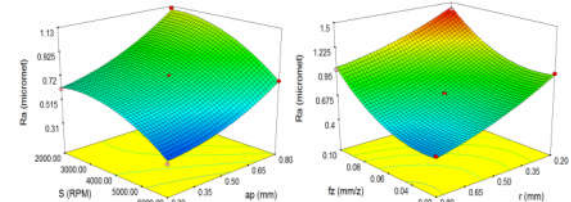
(b) The effects of machining parameters on R_a

Fig. 2 The effects of parameters on the responses

(a) SEM images at experiment No.1
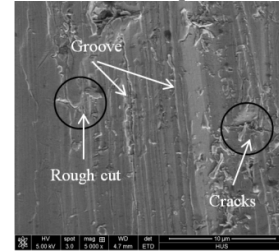
(b) SEM images at experiment No. 5
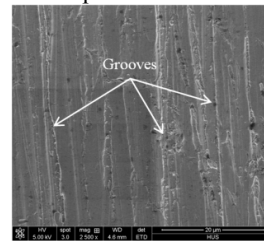
(c) SEM images at experiment No.9
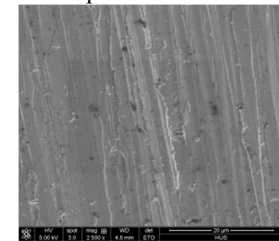
(d) SEM images at experiment No. 24

Fig. 3 Surface morphology at various conditions

The predictive models of milling responses were developed with regard to machining parameters using RSM and experimental data. Consequently, the regression response surface models showing the machining power P_m and arithmetical average roughness (R_a) are expressed as follows:

540

$$P_m = 0.37665 - 0.0000204S - 0.80422a_p$$
$$-0.93833f_z - 0.84307r + 0.000194Sa_p$$
$$+0.001626Sf_z + 0.0001211Sr \qquad (1)$$
$$+4.91250a_pf_z + 4.32292f_zr$$

$$R_a = 0.67868 + 0.00021S + 0.40139ap$$
$$-4.64583f_z - 1.28056r - 0.0005Sf_z$$
$$-0.00000003S^2 + 0.76389a_p{}^2 \qquad (2)$$
$$+110.93750f_z{}^2 + 0.63889r^2$$

Table 2. Experimental results

No.	S (RPM)	a_p (mm)	f_z (mm/tooth)	r (mm)	P_m (kW)	R_a (μm)	MRR (mm³/min)
1	2000	0.5	0.02	0.4	0.1865	0.66	480
2	6000	0.5	0.06	0.2	0.6868	0.79	4320
3	4000	0.5	0.06	0.4	0.667	0.73	2880
4	6000	0.2	0.06	0.4	0.6308	0.31	1728
5	2000	0.5	0.1	0.4	0.4532	1.33	2400
6	2000	0.5	0.06	0.2	0.3263	1.06	1440
7	6000	0.5	0.02	0.4	0.4438	0.37	1440
8	4000	0.5	0.1	0.2	0.7961	1.41	4800
9	4000	0.8	0.06	0.2	0.8493	1.32	4608
10	4000	0.5	0.06	0.4	0.6669	0.71	2880
11	4000	0.5	0.06	0.4	0.6672	0.74	2880
12	4000	0.2	0.1	0.4	0.7102	1.05	1920
13	2000	0.5	0.06	0.8	0.4717	0.58	1440
14	4000	0.8	0.1	0.4	1.2489	1.42	7680
15	2000	0.8	0.06	0.4	0.4373	1.11	2304
16	4000	0.5	0.02	0.8	0.4312	0.47	960
17	4000	0.8	0.02	0.4	0.4919	0.96	1536
18	6000	0.8	0.06	0.4	1.279	0.69	6912
19	4000	0.2	0.06	0.8	0.5728	0.48	1152
20	6000	0.5	0.06	0.8	1.1229	0.26	4320
21	4000	0.5	0.06	0.4	0.6676	0.72	2880
22	4000	0.5	0.1	0.8	1.1305	0.98	4800
23	4000	0.5	0.06	0.4	0.6673	0.73	2880
24	4000	0.8	0.06	0.8	1.0778	0.79	4608
25	4000	0.5	0.02	0.2	0.3043	0.98	960
26	4000	0.2	0.06	0.2	0.4247	0.87	1152
27	2000	0.2	0.06	0.4	0.2552	0.61	576
28	4000	0.2	0.02	0.4	0.189	0.51	384
29	6000	0.5	0.1	0.4	1.2307	0.85	7200

Table 3. Representative scenarios with constrained surface roughness

Scenario	Optimization parameters				P_m (kW)	R_a (μm)	MRR (mm³/min)
	S (RPM)	a_p (mm)	f_z (mm/tooth)	r (mm)			
1	5997	0.21	0.022	0.2	0.1324	0.55	664.9474
1	5994	0.20	0.032	0.4	0.2821	0.33	920.6784
3	5983	0.21	0.021	0.8	0.3571	0.09	633.2407

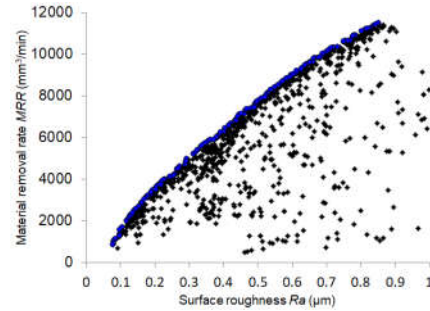The developed equations showing the relationship between process parameters and machining responses are used to find optimal parameters with the aid of the AMGA. The Pareto frontier generated by the AMGA is shown in Fig. 4, in which blue points are feasible solutions.

It can be stated that it is hard to determine the optimal machining parameters for different technological

performances based on practical experience or operating guide. As a result, the global relations among the milling responses shown in Fig. 4 can be used to determine the machining power, *MRR*, and optimal machining parameters with the predefined surface roughness. The representative scenarios with constrained surface roughness were shown in Table 32.
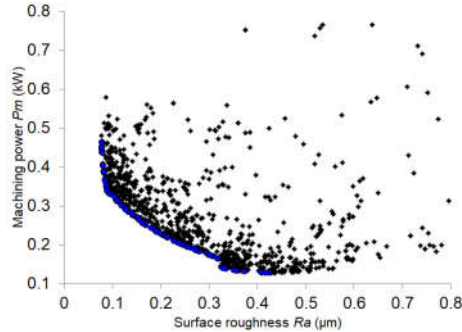
(a) Pareto front for P_m and R_a (b) Pareto front for *MRR* and R_a

Figure 4. Pareto generated by AMGA

4. Concluding Remarks

This work presented a multi-responses optimization of machining parameters in the milling process to decrease the machining power and improve the production rate while the surface roughness is considered as a constraint. The RSM models were used in conjunction AMGA to render the relations between inputs and technological performances as well as determine the optimal values. The main conclusions from the research results of this work can be drawn as follows within parameters considered:

1. The lowest levels of machining parameters, including spindle speed, depth of cut, feed rate, and tool tip radius were recommended to decrease the machining power consumed. The machining power is mainly influences by process parameters (spindle speed, depth of cut, and feed rate).

2. The high values of spindle speed and tool tip radius were recommended to produce a smoother surface, while surface roughness values decrease with lower depth of cut or feed rate. The tool tip radius has a greater influence on the surface roughness model in comparison with the machining power.

3. Solving multi-objective optimization issue using AMGA could be ensured the globally optimal results. The proposed approach for decreasing the machining power and improving *MRR* with the predefined surface roughness is versatile and realistic in the milling processes, compared to single objective or simultaneous three response optimization.

References

[1] Diaz, N., S. Choi, M. Helu, Y. Y. Chen, S. Jayanathan, Y. Yasui, D. Kong, S. Pavanaskar, and D. Dornfeld. (2010). Machine Tool Design and Operation Strategies for Green Manufacturing, *Proceedings of 4th CIRP International Conference on High Performance Cutting*, (2010), 271-276.

[2] S. Zhongde, Q. Shaoyan, L. Qian, L. Feng, Key manufacturing technology & equipment for energy saving and emissions reduction in mechanical equipment industry, *International Journal of Precision Engineering and Manufacturing*, 13 (2012) 1095-1100.

[3] J. Z. Zhang, J. C. Chen, E. D. Kirby, Surface roughness optimization in an end-milling operation using the Taguchi design method, *Journal of Materials Processing Technology*, 184 (2007), 233-239.

[4] Azlan M.Z., Habibollah H., Safian S., Application of GA to optimize cutting conditions for minimizing surface roughness in end milling machining process, *Expert Systems with Applications*, 37 (2010), 4650-4659.

[5] Vikas Pare, Geeta Agnihotri, Chimata Krishna, Selection of Optimum Process Parameters in High Speed CNC End-Milling of Composite Materials Using Meta Heuristic Techniques – a Comparative Study, *Strojniski vestnik - Journal of Mechanical Engineering*, 61 (2015), 176-186.

[6] Bhuvnesh B., Rajesh K., Pradeep K. Singh, An improved surface roughness prediction model using Box-Cox transformation with RSM in end milling

of EN 353, *Journal of Mechanical Science and Technology*, 28 (2014) 5149-5157.

[7] J. A. GhaniI, I. A. Choudhury, H. H. Hassan, Application of Taguchi method in the optimization of end milling parameters, *Journal of Materials Processing Technology*, 145 (2004), 84-92.

Incremental Bulging Process for Discontinuous-fiber Thermoplastic CFRP

Tatsuki Ikari[1], Keisuke Sato[1], and Hidetake Tanaka[1]
[1]Sophia University
7-1 Kioi-cho, Chiyoda-ku, Tokyo,102-8554, Japan

ABSTRACT

Several 3D printing technologies have been proposed for rapid prototyping or rapid manufacturing of CFRP. However, shell shape forming is difficult because of low adhesion strength between layers in 3D printing, and it cannot keep enough stiffness. Therefore, in the study, the authors focused on the incremental bulging, which enables shell shape forming from the sheet materials. In the study, the rapid prototyping method using bulging for CRRTP has been proposed and fundamental incremental forming experiment has been carried out to demonstrate its possibility.

1. Introduction

The study deal with a rapid prototyping and rapid manufacturing method of shell shape discontinuous-fiber thermoplastic CFRP (Carbon-Fiber-Reinforced-Plastics) using the single-point bulging.

The most common method of rapid prototyping is the additive manufacturing. Recently, development of 3D Printer which can print higher strength products using continuous-fiber CFRP has been launched. However, the shell shape resin products of the 3D-printing have low stiffness because of the weakness of the strength of the interlayer adhesion. The bulging is specialized to the limited production of diversified products of shell shape parts, and that is known as a die-less forming method which can utilize for rapid-prototyping and rapid manufacturing. The authors aim the realization of rapid prototyping and rapid manufacturing of high strength shell shape products by applying the bulging.

CFRP has the various combination of material specifications which have different physical properties. The matrix divided into two categories, thermoset, and thermoplastic. The thermosets resins are difficult to post-deformation. However, the thermoplastics can be softened by heating, and the material can use as the stampable sheet material.

The fiber also divided into two categories, i.e. continuous fibers, and discontinuous fibers. The continuous fiber CFRP has the higher specific strength than the metallic material. The adverse effect of continuous fibers is low formability and low drawability caused by lack of plasticity. The discontinuous-fiber CFRP has lower strength than continuous-fiber CFRP. However, the material has a severalfold strength compare with unreinforced resins and higher formability than continuous-fiber CFRP.

Study on single-point bulging of the resins and polymers by using the experimental setup similar with metal sheet forming has been established by P.A.F.Martins[1][2]. In the study, the discontinuous-fiber CFRP was used as the material for test pieces. The thermoplastic resins have the heat-dependent strength. Therefore, in this report, the forming experiment carried out to examine the difference of formability between room temperature and sufficiently higher temperature from glass transition temperature.

2. Experimental Method

In this experiment, the possibility of molding by the same molding method as sheet metal was investigated. The experiment was carried out with three different conditions, without tool rotation, with tool rotation (room temperature), and with heating(heated). Table 1 shows the specification of the workpiece material. The matrix of the workpiece material is the crystalline resin. Therefore, high difficulty in forming in room temperature below the glass transition point is expected. In order to confirm that, and find out formable condition, the result of the three conditions mentioned was investigated. Workpiece temperature on forming experiment with heating is set beyond the glass transition point and below the melting point. In the experiment, the temperature was set at $170\square$. The conventional setup of single-point bulging has been applied for forming experiment. The forming experiment was performed using a machining center (Sodick MC430).

The objective shape is a circular truncated cone in 20mm radius and 10mm depth. Experimental conditions except for the workpiece temperature are shown in Fig.1and Table 2. n is the rotating rate of the spindle, ψ is the wall angle of the circular truncated cone, v_{xy} is feed rate of revolution motion, S_z is step size per revolution of the Z axis.

In order to achieve uniformly heating of the workpiece during the forming process; heating was carried out by using a hot oil bath with silicone oil as shown in Fig.2.The oil was heated by an electric immersion heater which has 1kW output. To maintain evenness of the oil temperature during the forming process, heat insulation material placed around an oil bath thermally insulate the oil bath. The glass transition point pf PA6 is $50\square$ and $225\square$. Oil temperature in the starting point of the forming process is above $170\square$, and temperature on end of the process was about $130\square$.
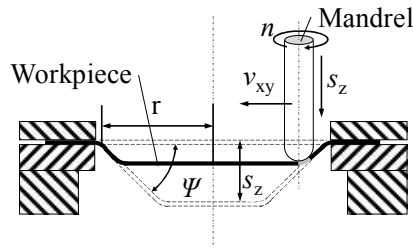
Fig. 1 Schematic of forming process

Table 1. Specification of workpiece material

Type	Discontinuous fiber CFRTP
Matrix	PA6
CF content	20 wt%
Dimension	110×110×1 mm
Glass-transition temp	323 K

Table 2. Experimental condition

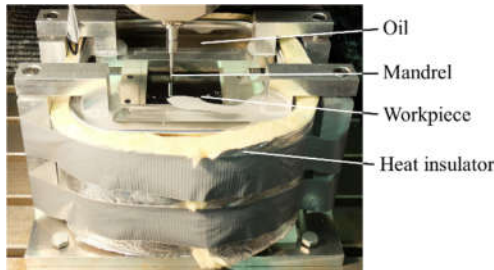| No	n [rpm]	ψ [deg]	v_{xy} [mm/s]	s_z [mm]
1	3000	40	1000	0.25
2	2000	40	1000	0.25
3	4000	40	1000	0.25
4	3000	30	1000	0.25
5	3000	50	1000	0.25
6	3000	40	500	0.25
7	3000	40	1500	0.25
8	3000	40	1000	0.1
9	3000	40	1000	0.5

Fig. 2 Oil bath

3. Results and Discussion

The formed workpieces were evaluated by the result of shape measurement. The 3D shape data of workpieces was generated by point to point measuring of the height of the workpieces by laser displacement meter and 2-axis cartesian coordinate robot. Therefore, the 3D shape data are stored as point cloud data. Table 3 shows the specification of laser displacement meter. The measurement interval of the 3D shape data is 1mm.

Table 3. Specification of laser displacement meter

Model No.	LK-G150
Reference distance	150 mm
Measuring range	±40 mm
Spot diameter	120 μm
Repeatability	0.5 μm

The measurement result was evaluated by shape deviation between objective shapes and the workpieces, and the S/N ratio of based on the Taguchi method. However, that is difficult to calculate the S/N ratio from 3D data. Therefore, the evaluation target was limited to only the Z coordinate by using the same X-Y coordinate in the 3D data of objective shape and measured data. The S/N ratio were calculated wirh equation as follows.

Total variation S_T

$$S_T = \sum_{k=1}^{n} o_k^2 = \sum_{k=1}^{n} z_{m_k}^2 \qquad (1)$$

Divisor r

$$r = \sum_{k=1}^{n} M_k^2 = \sum_{k=1}^{n} z_{p_k}^2 \qquad (2)$$

$$L = \sum_{k=1}^{n} o_k M_k = \sum_{k=1}^{n} z_{m_k} z_{p_k} \qquad (3)$$

Effect of input S_β

$$S_\beta = \frac{1}{r} L^2 \qquad (4)$$

Accidental error S_e

$$S_e = S_T - S_\beta \qquad (5)$$

Error variance V_e

$$V_e = \frac{S_e}{k-1} \qquad (6)$$

S/N ratio η

$$\eta = 10 \log \frac{\frac{1}{r}\left(S_\beta - V_e\right)}{V_e} \qquad (7)$$

Fig.3 shown photograph of formed workpiece. Fig.4 shows shape deviation. Table 4 shows the S/N ratio of each workpiece. In the forming condition without the tool rotation, fracture occurred Immediately after

starting forming in all workpiece. In the forming condition applying the tool rotation without heating, fracture occurred in condition 4,8 and 9. In contrast, In the forming condition applying the tool rotation and heating, forming process was accomplished without any fracture in all condition. In the area which processed by the tool, shape deviation in the heated workpiece are smaller than the room temperature workpiece. In contrast, shape deviation in the heated workpiece is larger in the non-processed area. Moreover, from a viewpoint of S/N ratio, the shapes of the heated workpiece are farther from the objective shape than room temperature.

Fig.5 shows a photo of the worn tool. On the other hand, forming process relies on heating by friction is Impractical because of the severe tool wear caused by carbon fiber that changes the geometry of the tool tip in several forming processes.
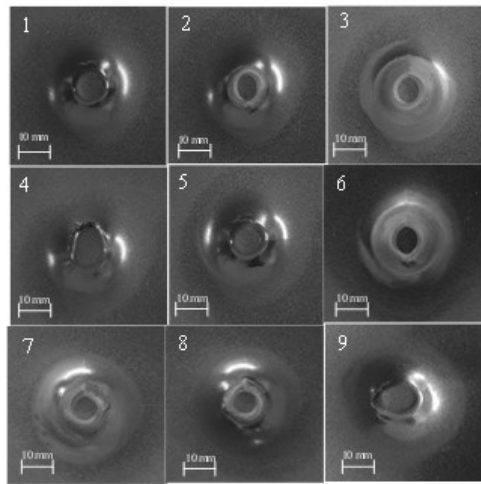
A: Room temperature
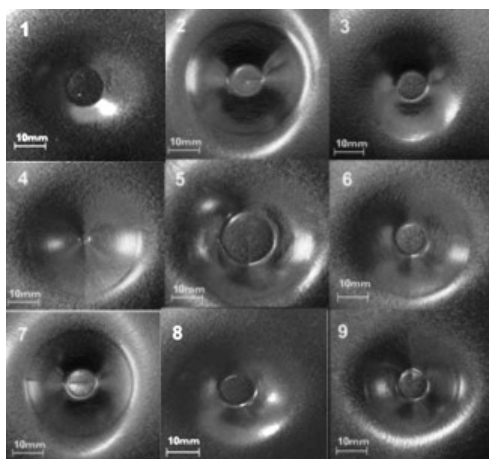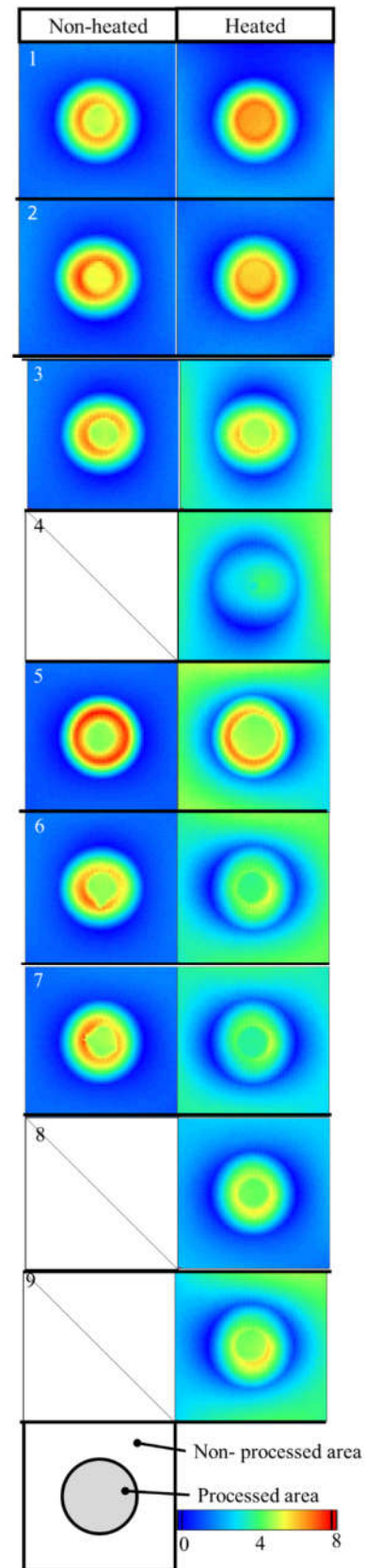

B: Heated

Fig. 3 Photograph of formed workpiece

Fig. 4 Shape deviation

Table 4. S/N ratio

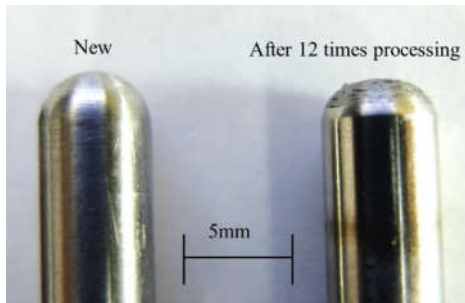| No	Room temperature	Heated
1	-3.59908	-6.70503
2	-4.62238	-3.34187
3	-2.11395	-7.91062
4		-5.282
5	-4.7044	-8.09432
6	-2.01562	-5.0024
7	-2.24055	-4.11224
8		-2.86494
9		-7.07005

Fig. 5 Worn tool

4. Concluding Remarks

The single-point incremental bulging experiment of discontinuous-fiber CFRP has been conducted. As the results, the following concluding remarks have been obtained.

The discontinuous-fiber CFRP is difficult to form at room temperature. Elongation of the material can be improved by maintaining temperature up to the glass transition point during forming. Although forming is possible by utilizing the frictional heat between the workpiece and tool, it is not realistic because the tool wear is intense. If uniformly heat the material, it is possible to form discontinuous thermoplastic CFRP. However, in order to reduce the shape deviation, a method of heating only the portion requiring elongation is necessary.

References

[1] P.A.F. Martins, L. Kwiatkowski, V. Franzen, A.F. Tekkaya, M. Kleiner "Single point bulging of polymers", CIRP Annals - Manufacturing Technology, Vol. 58, (2009), 229-232.

[2] M.B. Silva, L.M. Alves, P.A.F. Martins, "Single point bulging of PVC: Experimental finding and theoretical interpretation", European Journal of Mechanics A/Solids, Vol. 29, (2010), 557-566.

Research on the Design of the Powder Roller Module in Selective Laser Sintering (SLS) Rapid Prototyping Machine

Tran Trong Hy[1], Le Khanh Dien[1], Vo Tuyen[2]

[1] DCSELAB - **Ho Chi Minh City University of Technology**, VNU-HCM, Vietnam

[2] Ho Chi Minh City University of Food Industry (HUFI), Vietnam

ABSTRACT

Nowadays, mastering of technology and manufacture high technology machines is restrictive in Vietnam. Because of this reason, the research, design and manufacture of machine in country, especially SLS rapid prototype machine is an essential question in our country. The paper represents how to perform an efficient design of a quality powder roller module in the SLS rapid prototype machine. A transmission motor that is mounted to the end of the powder roller, transmits the rotation motion of the roller on two rails that are assembled on either sides of the machine. The duty of the roller is scanning the powder to a same width layer that is ready for sintering by Laser beam. In operation, the roller slids on the table surface which mounted the horizontal direction rail on the lifting carriage surface. The roller rotates around its axis to spread evenly the powder material over the surface of lifting carriage. Experimental results in DCSElab workshop show that the designed powder roller assembly module attains all the technical requirements of the SLS rapid prototype.

Keywords: SLS rapid prototype machine, transmission motor, powder scanning roller.

1. Introduction

In rapid prototype technology by Selective Laser Sintering technology, the material powder is sintered by the Laser to reach the temperature at which the powder turns from solid to plastic and solidified when the Laser beam passes through the next point. The solidified powder bonds to the previous layer to form a new one of the desired profile of the product. The process repeats until the finished product [1].

The general structure of the SLS rapid prototype machine is designed by modularity technology, consisting of many modules: powder roller module (motor of rollers, rollers, toothed rollers and powder rollers); Laser sintering module (XY axis drive, power supply, Laser tube, guiding lens, Z-axis drive shaft); powder container tank module (right powder container); powder heating module (racks and halogen lamps); support frame and carter module (frame and chassis) [2]. According to the experimental result [3], the powder is delivered in layers through the powder roller assembly, which allows the sintering process to be continuous. Because the accuracy of the product depends strictly on the thickness of the material powder layer so the powdering process must be accurate and optimized to ensure the quality and the productivity of the product. Therefore, the design of the powder roller module in the SLS rapid prototype is the subject of the paper.

2. Design of structural alternatives of powder roller model

The powder roller module has the duty to create a thin layer of powder on the table of lifting carriage, ready for the scanning and sintering process by Laser Sintering module. After each profile of the product on plane OXY, the lifting carriage moves downward and the powder roller module builds up a new layer of powder and the process repeats until the end of the manufacture process. The impact factors and components has to perform the general functions are shown in Figure 1.
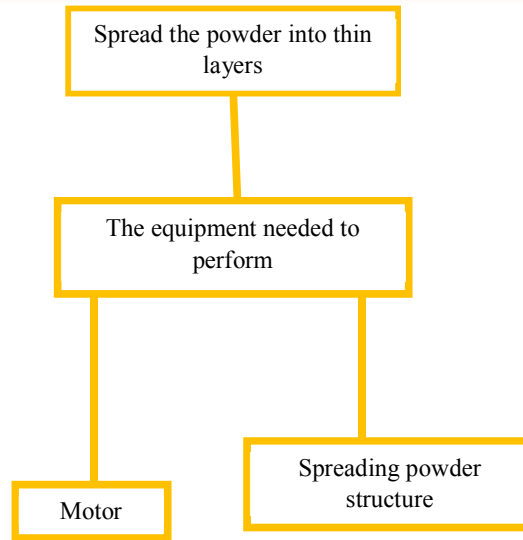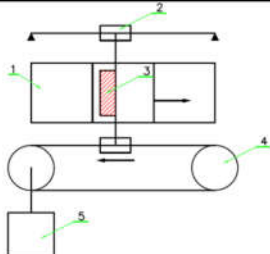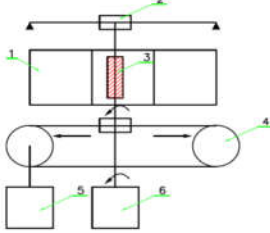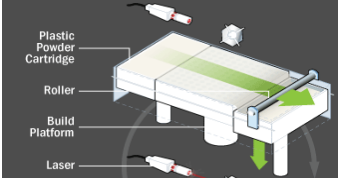
Figure 37. *Analysis diagram of SLS powder roller module*

Based on the study of input parameters and consulted relative design [3] a number of structural design options for Laser beam are proposed in the following table

Options	Composition diagram	Characteristic	Advantage	Disadvantage
Option 1: Translation surface application	1 – Table; 2 – Slider; 3 – Lifting carriage; 4 – Roller; 5 – Motor	Flat plate is mounted on two rails on the sides of the table. This flat plate is pulled by a motor which is mounted on the table. When the engine is running, the flat plate will be slid on the table surface in order to spread powder.	Simple structure, powder is spread evenly on the desk.	This flat plate needs to be operated with high accuracy; otherwise, it will cause errors on the surface of the powder. After a period, the powder will stick on the surface of the flat plate that makes unwanted spreading, sometimes causes the accumulation of dirt on the surface.
Option 2: Rotary flat board application		A flat board is used to rotate around a shaft by a motor. The powder horizontally spread the lifting carriage surface.	The structure is very simple.	The spread density of flour is uneven.
Option 3: Application of a motorized roller		A roller is mounted on two rails of the sides of the table. At the end of the roller, a small motor is attached to the shaft of the roller that supports bracket. In operation, the rollers slid on the table surface to spread horizontally	- Simple structure. - Powder spread on the table that is flat plate, avoiding the phenomenon of powder clotting. - Driven by the motor 6, it does not depend on the friction between the roller and the powder,	- The structure of this part is more complex than the flat plate option. - The rollers is easy to bend in the middle if its stiffness is not enough

		- The powder spread on the machine surface, and the roller will rotate around its axis, therefore the powder is spread evenly over the table surface.	- The rollers rotate evenly.	
Option 4: Motorized integrated roller		This option combines of integrated motor rollers which are located inside the rollers. Spreading powder plate is pulled by a motor which is mounted on the table. When the installation runs, the powder spread on the machine, -The roller rotates itself around its axis.	- The structure is simple, easy to assemble. - Rollers are available on the market with high precision, - Low cost of manufacturing.	High price

Applying the decision matrix method [4] to evaluate 4 above options, we have the preliminary estimate matrix and score board in tables 1 and 2:

Table 11 Matrix of preliminary evaluate of powder roller module design

Options \ Criterion	1	2	3 (Std)	4
Simple structure	+	+	0	0
Reasonable price	+	+	0	-
Easy manufactured, assembled	+	+	0	+
Quality of spreading powder	-	-	0	0
High productivity	+	-	0	+
Longevity	-	-	0	+

Table 12 Scoring matrix for selection the powder roller module option design

Criterion	Weight (%)	Options			
		3		4	
		Score		Score	
		Rough scores	Weighted multipliers	Rough scores	Weighted multipliers
Simple structure	15	5	0,75	4	0.6
Reasonable price	15	5	0,75	3	0.45
Manufactured, assembled easily	20	5	0,8	4	1
Quality of spreading powder	30	3	0,6	5	1.5
High productivity	10	4	0,4	4	0.4
Longevity	10	4	0,4	5	0.5
Total	100	3,7		3,65	
Rank		1		2	
Should we continue?		Yes		No	

After the evaluation matrix and the scoreboard are set, the most suitable design option is the option 3: A roller is mounted on two rails on either side of the table. At the end of the roll, a small motor is attached to the rollers. Spreading powder is driven by a motor that is mounted on a table. In operation, the rollers slid on the table surface and the

powder are horizontally spread on the machine surface The roller rotates around its axis, so the powder is spread evenly over the table surface (Figure 2).
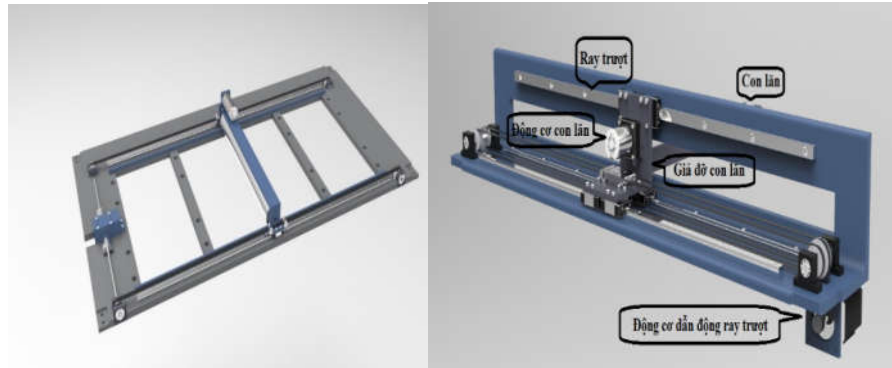

Figure 38. Complete powder roller module

3. Computing of the powder roller module

a. Computing of the timing belts of powder roller module

Input parameters: Velocity: v = 0.9 m/s**;** Acceleration / Deceleration time: t = 0,15s; Coefficient of friction: f = 0.03; Total weight of bracket and rollers: m = 13,457kg; Axial distance: 87mm.

Acceleration / Deceleration of bracket:

$$a = \frac{v}{t} = \frac{0,9}{0,15} = 6m/s^2 \qquad (3.1)$$

Belt tension force required in 3 stages:

+ Accelerative phase (fast-moving):

$$F_a = F_t + F_{ms} = m.a + m.g.f$$
$$= 13,457.9,81(6/9,81 + 0,03)$$
$$= 84,7N$$

+ Stable stage (steady motion):

$$F_a = F_{ms} = m.g.f = 13,457.9,81.0,03 = 3.96N$$

+ Stop phase (slow-moving):

$$F_a = -F_t + F_{ms} = -m.a + m.g.f$$
$$= 13.457.9,81(-6/9,81 + 0,03)$$
$$= -76,78N$$

Choose the maximum tension force: Fa = 84,7N
The operating power of the powder roller:

$$P_{lv} = \frac{F_a.v}{1000} = \frac{84,7.0,9}{1000} = 0,076k$$

Computing power [5]: $P_t = P_{lv}.K_s = 0,076.1,4 = 0,107kW$

Wherein Load factor: $K_s = K_0 + K_r + K_i = 1,4 + 0 + 0 = 1.4$; Load adjustment factor: $K_0 = 1.4$; Transmission ratio Adjustment factor: $K_r = 0$; Belt tension adjustment factor: $K_i = 0$.

Motor power:

$$P_{ct} = \frac{P_t}{\eta} = \frac{0,107}{0,95.0,95.0,99.0,99} = 0,12kW$$

Wherein: P_{ct}: Required power on the motor shaft (kW); P_t: Computing power (kW); ŋ: Performance of the transmitter. Select motor with power greater than 0,12kW

Selection of timing belt [5]: Based on the power and revolution, the suitable selection is T10 timing belt.

Calculate the parameters of the tooth belt transmission:
Number of teeth: $z_{p1} = 16$ teeth; $z_{p2} = 32$ teeth; Pitch of the tooth belt T10: p = 10mm.

Effective diameter of drive pulley:

$$D_{1p} = \frac{Z_{1p}.p}{\pi} = \frac{16.10}{\pi} = 50,92 \ mm$$

Effective diameter of driven pulley:

$$D_{2p} = \frac{Z_{2p}.p}{\pi} = \frac{32.10}{\pi} = 101,86 \ mm$$

Length of the belt:

$$L_p = 2a + \frac{\pi}{2}\left(D_{2p} + D_{1p}\right) + \frac{(D_{2p} - D_{1p})^2}{4a} = 234mm$$

Width of the belt:

$$B_w = \frac{P_d}{P_s.K_m}.W_p = \frac{0,107}{0,101.1}.10 = 10,6mm$$

In which: P_d – design power; P_s – power of the parameter transmitter; K_m – coefficients affect angle of belt contact; W_p - width of the parameter. We choose B_w by standard: $B_w = 25$mm

Angle of belt contact:

$$\alpha = 180^o - 57,3.\frac{D_{2p} - D_{1p}}{a} = 146,45^o$$

Number of teeth to be matched:

$$Z_m = \frac{Z_p.\alpha}{360} = \frac{16.146,45}{360} = 6,5 \ teeth$$

Check operating condition [5]: $P_s.K_m.K_b = 0,101.1.1,6 = 0,162 > P_t$ (3.2)

In which: P_t – design power; P_s – power of the parameter transmitter; K_m – coefficients affect angle of belt contact; K_b - width adjustment factor.

The parametric geometry of the tooth belt transmitter is shown in Table 3.

Table 13 Parameters of the tooth belt transmitter for the powder rollers

Parameter	Sign	Value
Active pulley's number of teeth	Z_{p1}	16
Passive pulley number of teeth	Z_{p2}	32
Number of teeth	Z_l	261
Axial distance	a	87mm
Width of the belt	B_w	25mm

b. Calculate the tooth belts for the roller support bracket on the slider

Input parameters: transmission power: 0,107kW; transmission ratio: i = 1; Revs of the driving axle: n = 1000 RPM; operate time in normal mode: 24h/day.

Computing power:

$P_d = P_t. K_s = 0,107.1,4 = 0,15kW$

Engine power:

$P_{ct} = \dfrac{P_t}{\eta} = \dfrac{0,15}{0,95.0,95.0,99.0,99} = 0,17kW$

Herein: P_{ct}: Required power on the motor shaft (kW); P_t: Computing power (kW); ŋ: Performance of the transmitter. Select motor with power greater than 0,17kW

Choose the tooth belt: Based on the power and revs, we choose the T10 tooth belt.

Calculate the parameters of the tooth belt transmission:
Number of teeth: z_{p1} = 14 teeth; z_{p2} = 14 teeth; Pitch of the tooth belt T10: p = 10mm.

Effective diameter of the pulley:

$D_p = \dfrac{Z_p.p}{\pi} = \dfrac{14.10}{\pi} = 44,56 \; mm$

Length of the belt:

$L_p = 2a + \pi D_p = 2.1236 + \pi.44,56 = 2612mm$

Width of the belt [5]:

$B_w = \dfrac{P_d}{P_s.K_m}.W_p = \dfrac{0,15}{0,101.1}.10 = 14,9mm$

In which: P_d – design power; P_s – power of the parameter transmitter; K_m – coefficients affect angle of belt contact; W_p - width of the parameter.

We choose B_w by standard: B_w = 30mm

Angle of belt contact:

$\alpha = 180^o - 57.\dfrac{D_{2p} - D_{1p}}{a} = 180^o$

Number of teeth to be matched:

$Z_m = \dfrac{Z_p.\alpha}{360} = \dfrac{14.180}{360} = 7 \; răng$

Check operating condition: $P_s.K_m.K_b = 0,101.1.2,3 = 0,232kW > P_d$

In which: P_d – design power; P_s – power of the parameter transmitter; K_m – coefficients affect angle of belt contact; K_b – width adjustment factor.

The parametric geometry of the tooth belt transmitter is shown in Table 4.

Table 14 Parameters of the tooth belt transmitter for the roller support bracket on the slider

Parameter	Sign	Value
Pitch of teeth	P	10mm
Pulley's number of teeth	$z_I = z_{II} = Z_p$	14
Belt's number of teeth	Z_l	261
Axial distance	A	1236mm
Width of the belt	B_w	30mm

4. Technological process of the powder roller beam
a. Technical requirements of the module
+ To ensure the parallel of the roller's axis beside the horizontal surface.
+ To ensure the perpendicularity of the roller beside the slider.
+ Assemblies must ensure the required clearance for the roller to work.

+ For convenient operation on the desk, the roller is designed to support one side of the three rails on one side to reduce the console.

b. Installation of the powder rollers
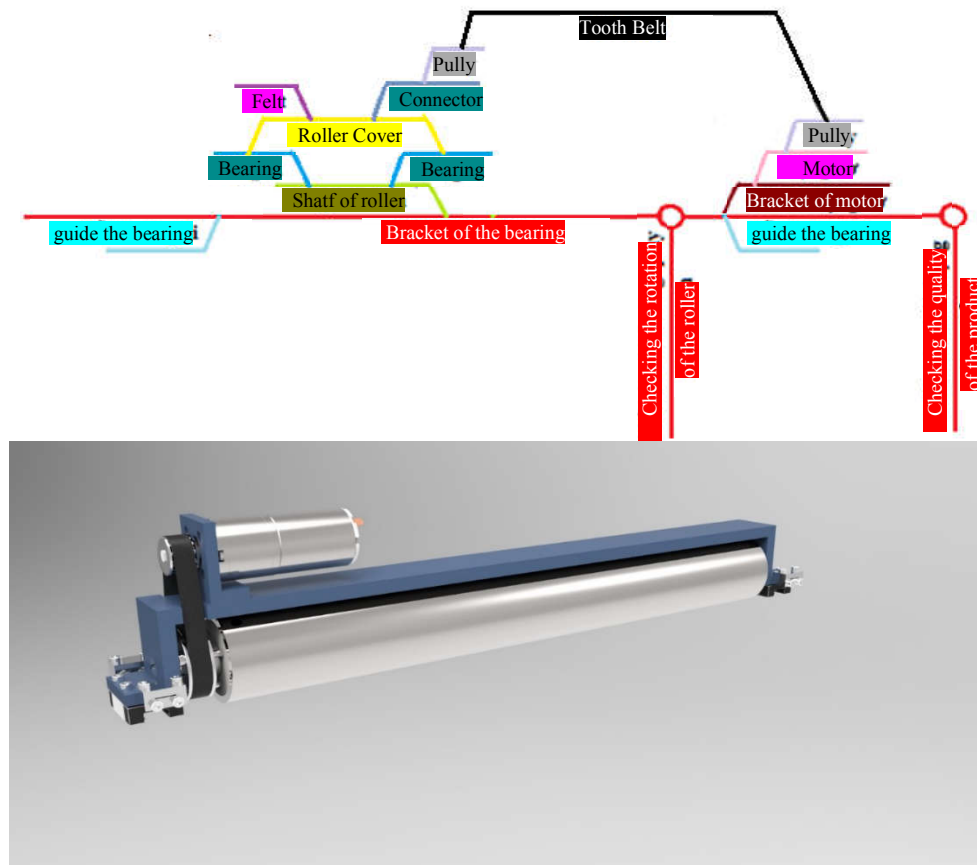+ Install the shaft into the roller cover.

Figure 39. Assembling the powder rollers

+ Install the ball bearing into the shaft and the roller cover.
+ Install the rubber felt into the roller cover.
+ Install the torque transmission connector into the roller cover.
+ Install the pulley into the connector.

+ Install the drive motor.

c. Assembling the roller bracket on the slide

+ Install the motorized roller bracket on the slider.
+ Install the slider.

Roller on lăn

Sliders

Motor of the sliders

Table

Tooth belt

Bracket of the pulley

Checking the sliding ability of the guide rod

Checking the quality of the product

Sliders

Bearing

Motor of the roller
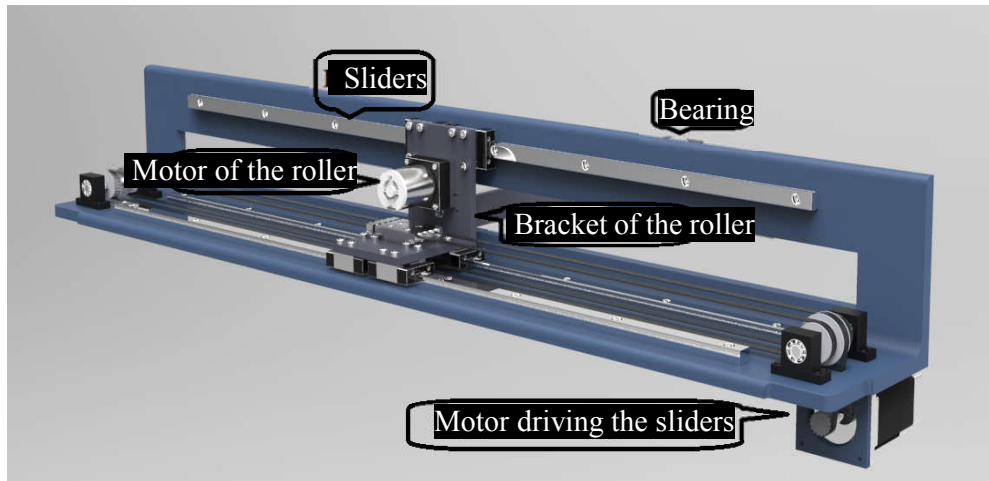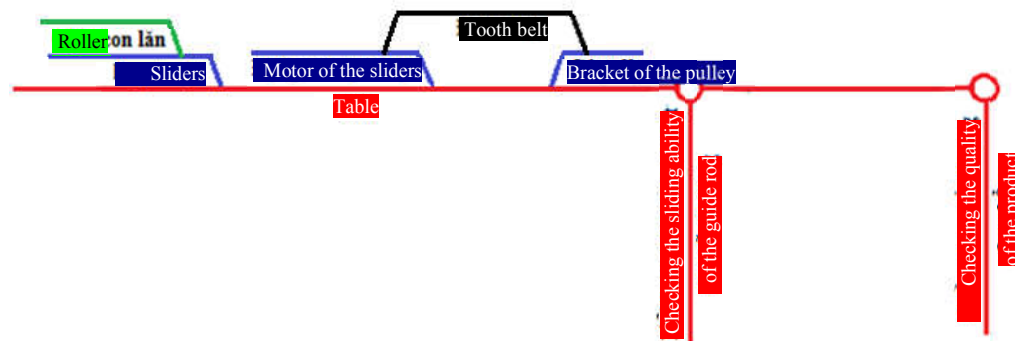
Bracket of the roller

Motor driving the sliders

Figure 40. Assembling the roller bracket on the slide

+ Install the pulley.
+ Install the tooth belt.

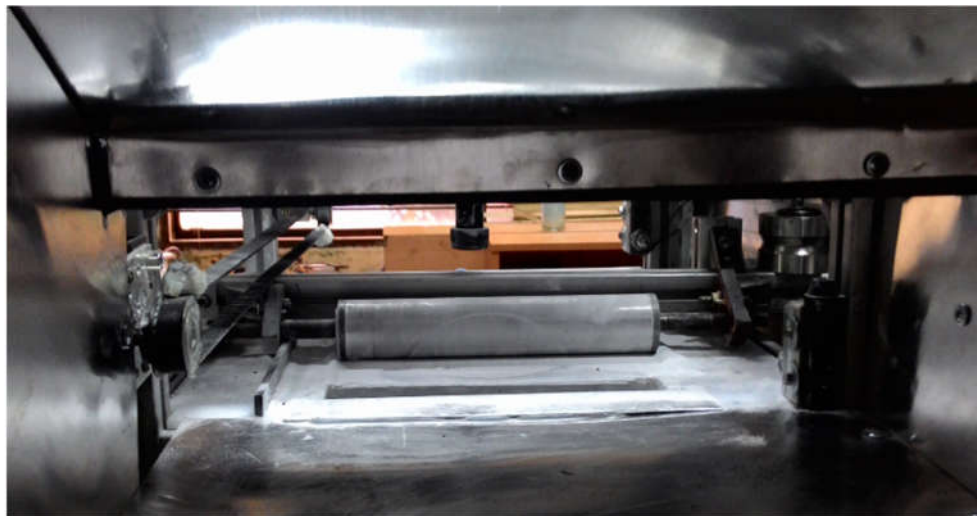+ Install the roller into the roller bracket on the slider.

Figure 5. Produced & assembled powder roller cluster

5. Conclusion

An efficient design process performs a quality powder roller in the SLS rapid prototype machine with the powder roller mounted on two rails on either side of the table. At the end of the roll, a small motor is attached to the rollers. The roller support bracket and the engine are

554

pulled by a motor which is mounted on a table. When the engine is running, the rollers will be slid on the table surface thence the powder will be horizontally spreaded on the machine surface, and the roller will rotate around its axis, so that the powder is spread evenly over the table surface. Experimental results show that the complete powder roller cluster has met the requirements of the SLS rapid prototype (Figure 5).

6. Acknowledgement

References

[1]. Badrinarayan, B and Barlow, JW (1995). *Effect of processing parameters in SLS of MetalPolymers*, Proceedings of Solid Freeform Fabrication Symposium, pp. 55-63. Austin: Texas.

[2] Ana PilipoviT, Igor Drstvenšek, Mladen Šercer1, *Mathematical Model for the Selection of Processing Parameters in Selective Laser Sintering of Polymer Products*, Advances in Mechanical Engineering, Volume 2014

[2] Nguyễn Thanh Nam, *Nghiên cứu thiết kế và chế tạo hệ thống tạo mẫu nhanh SLS*, Báo cáo tổng kết đề tài B2013-20b-01, 2015.

[3] Nguyễn Thanh Nam, *Phương pháp thiết kế phát triển sản phẩm*, NXB ĐHQGTP Hồ Chí Minh, 2014.

[4] Nguyễn Hữu Lộc, *Cơ sở thiết kế máy*, NXB ĐHQGTP Hồ Chí Minh, 2016.

PART VII, SECTION IV

Other Topics Related to Machining, Materials and Mechanical Technology
(Mechanics of Solid; Analysis and Simulation; New Machine Tools and Tooling Technology;
Dynamics and Control…)

Active Closed-loop Gap Control for Hydrostatic Bearing

Jyh-Chyang Renn[1], Guan-Yi Wu[2]

[1]Professor, National Yunlin University of Science and Technology, Department of Mechanical Engineering
123 University Road, Section 3, Douliou, Taiwan
[2] Graduate Student, National Yunlin University of Science and Technology, Department of Mechanical Engineering
123 University Road, Section 3, Douliou, Taiwan

ABSTRACT

In this paper, a hydrostatic bearing controlled by servo-valve for precise closed-loop oil-film gap control is developed. Due to the increasing demands of larger dimension, heavier load and higher precision for current and future machine tools, the development of hydrostatic bearing has become a more and more important issue over the past decades. Nowadays, the most commonly used active pressure feedback restrictor for hydrostatic bearing is membrane type, in which a thin and flexible metal sheet serves as the key component to meter the hydraulic oil flow precisely. However, the membrane type pressure feedback restrictor is not quite suitable for extremely heavy load. Therefore, an alternative to design the active restrictor for hydrostatic bearing using servo-valve is presented in this paper. Different controllers are also designed and compared in this paper. There are two significant features regarding the proposed design. The first one is the introduced orifice restrictor inside the servo-valve which avoids the influence of possible oil temperature variation. The second feature is the introduced closed-loop oil-film gap control scheme that widens the application range effectively. Finally, a test rig of servo-valve controlled hydrostatic bearing is implemented and the experimental results prove the validity of the hydrostatic bearing with the proposed servo-valve and the closed-loop gap control scheme.

Keywords: Hydrostatic Bearing, Servo Valve, Closed-loop Gap Control, Fuzzy-sliding Mode Control.

1. Introduction

Generally speaking, the trend of new generation machine tools is towards larger dimension, heavier load and higher precision. Among many different key components for current and future machine tools, the bearing is believed to play the most important role. Compared to traditional ball bearing, the advantages of aerostatic and hydrostatic bearing are non-contact, low friction and wear, low heat generation, etc. However, aerostatic bearing is only suitable for light load manufacturing. For machine tools with large dimension and heavy load, the development of hydrostatic bearing becomes an inevitable task. Nowadays, the most commonly used active pressure feedback restrictor for hydrostatic bearing is membrane type, in which a thin and flexible metal sheet serves as the key component to meter the hydraulic oil flow precisely as shown in Fig. 2 [1-3]. However, the membrane-type pressure feedback restrictor is not quite suitable for extremely heavy load. In addition, the membrane itself suffers from the fatigue problem [4]. Another possible active pressure feedback restrictor is based on the spool-type design. Some previous reports [5] indicated that disadvantages like the complex structure and difficult adjustment of the spool-type restrictor are inevitable. However, such a spool-type design is still believed to be a promising technique because the manufacturing of spool-type pressure feedback restrictor is basically easier than that of the above-mentioned membrane-type pressure feedback restrictor [6]. In this paper, a spool-type servo valve is chosen as an alternative to design the active compensator. By using the closed-loop control technology, the oil-film gap (thickness) can be precisely controlled regardless of the external load variations. Besides, servo valve is a commercially available hydraulic component which shows the feasibility of the active closed-loop gap control scheme presented in this paper. In the following, the design concept of hydrostatic bearing with servo valve is illustrated.
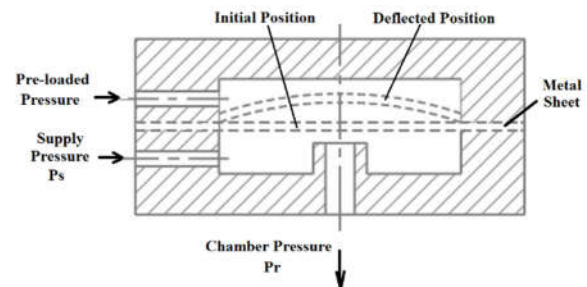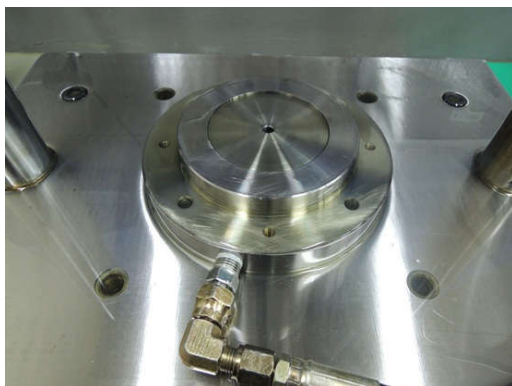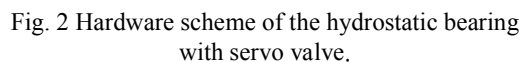

Fig. 1 Scheme of membrane-type pressure feedback restrictor.

2. Design of Hydrostatic Bearing with Servo Valve

Figure 3 shows the hardware scheme of the developed hydrostatic bearing with servo valve. The operational principle is briefly described as follows. By electro-hydraulic closed-loop control technology, the real-time oil-film gap between the platform and the circular pad is detected and feedback to the PC-based LabView control unit. Thus, the control error can be calculated. Since the closed-loop control system is an error-driving system, this calculated control error will be transformed into the actuation output signal through the utilized

controller algorithm. Therefore, the actual gap is expected to track the desired gap and will be kept at a constant value since the desired gap is set to be a constant. It is worth mentioning that the circular pad is also called the hydrostatic bearing in some literatures. Hence, there are two significant features regarding the proposed design. The first one is the introduced orifice restrictor inside the servo valve which avoids effectively the influence of possible oil temperature variation.

From the closed-loop control scheme shown in Fig. 3, it is obvious that the desired gap input can be set arbitrarily. Therefore, the second feature of this design is the introduced closed-loop oil-film gap control scheme that widens the application range effectively. Finally, the real picture of the circular pad (hydrostatic bearing) is shown in Fig. 4.

Fig. 2 Hardware scheme of the hydrostatic bearing with servo valve.

Fig. 3 Active closed-loop gap control scheme.

Fig. 4 Real picture of the circular pad.

3. Experimental Test Rig

To evaluate the performance of the developed hydrostatic bearing with servo valve, a test bench is designed and constructed. Figure 5 indicates the circuit diagram and Fig. 6 shows the real picture of the test bench. There are two power units in this test bench. The upper power unit is utilized to produce variable external disturbance loads. The key component is the proportional pressure valve (#10) which controls the load pressure precisely and is used to simulate various external disturbance loads acting on the circular pad (#6) through the hydraulic cylinder (#9). The adjustable range for the external disturbance load from 0 to the maximal 2,000 Kgf or 20,000 N is available in this test bench. On the other hand, the lower power unit is specifically used for the hydrostatic bearing. To compensate the oil film variation caused by the external disturbance load, the gap sensor (#8) together with the servo valve (#4) forms a PC-based closed-loop gap control scheme. The pressurized hydraulic oil supplied by the pump (#1) flows through the servo valve and enters the circular pad. It establishes a thin oil film between the circular pad and the movable platform including a load cell (#7). Consequently, the load cell and cylinder rod (#9) are lifted up and floats above the circular pad. By applying different external disturbance loads through the hydraulic cylinder, the oil-film gap changes accordingly. In this case, the proposed closed-loop servo valve is expected to play an important role to maintain a constant gap of the oil film. The cracking pressure of the relief valve (#12) is set to be 30 bar and the maximal flow-rate output of the pump (#1) is 10 L/min.
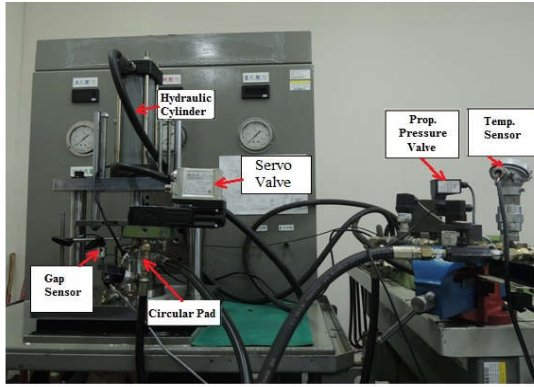

Fig. 5 Circuit diagram of the test bench.
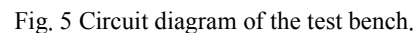
Fig. 6 Real picture of the test bench.

4. Controller Design

Figure 7 shows the scheme of a traditional PID controller. The continuous-time PID-controller can be expressed as:

$$u(t) = K_P \left\{ e(t) + \frac{1}{T_I} \int_0^t e(\tau)d\tau + T_D \frac{de(t)}{dt} \right\} \tag{1}$$

The suggested gains for the PID-controller can be determined by Ziegler-Nichols method, which is described briefly as follows. First, the gain of a simple P-controller is slowly increased until the system response is marginally stable. If this proportional gain is denoted by K_{CP} and the period of the sustained oscillation is found to be T_C, thus the suggested gains for the PID-controller can be derived.

$$K_P = 0.6K_{CP}, \tag{2}$$

$$K_I = K_P / 0.5T_C, \tag{3}$$

$$K_D = 0.125K_P T_C, \tag{4}$$

Basically, the equations (2)-(4) give a set of suggested gains for the PID-controller. After fine adjustments, however, the most suitable gains can be obtained.

In this paper, an advanced controller called the fuzzy-sliding mode controller (FSMC) is proposed, which is proved to be the better solution to surmount all the nonlinearities. The combination of fuzzy-logic-controller with sliding mode controller results in the fuzzy-sliding mode controller, which possesses the advantages of less number of input signal needed and the ability to control nonlinear systems more effectively. Figure 8 shows the schematic block diagram of the fuzzy-sliding mode controller. The error signal, e, and the error signal change, $\dot{e}$, are denoted by x_1 and x_2 respectively.

Unlike the conventional controller, there are basically three procedures involved in the implementation of a fuzzy-sliding mode controller, fuzzification of the input, fuzzy inference based on the knowledge and the defuzzification of the rule-based control signal.

(a) Fuzzification
Instead of two input signals fed into the conventional fuzzy-logic-controller, the fuzzy-sliding mode controller need only one input signal, s, which is the combination of the parameters x_1 and x_2.

$$s = \lambda x_1 + x_2 \tag{5}$$

In this paper, the triangular fuzzy membership function is used for the input signal to determine the degree of input. On the other hand, the input signal, s, also represents the switching function of the sliding mode controller.

(b) Inference
The inference process consists of nine rules driven by the linguistic values of the input signal, s.
It is worth mentioning that the control rules for a fuzzy-sliding mode controller are one dimensional IF-THEN statements rather than the look-up table consisting of two dimensional control rules for a conventional fuzzy-logic-controller. Consequently, less computational time is required.

(c) Defuzzification
The defuzzification is to transform control signal into exact control output. In the defuzzification, the method of center of gravity is used.

$$u = \frac{\sum_{i=1}^{n} W_i B_i}{\sum_{i=1}^{n} W_i} \tag{6}$$

where u : output of the fuzzy-sliding mode controller,
W_i : the degree of firing of the i_{th} rule,
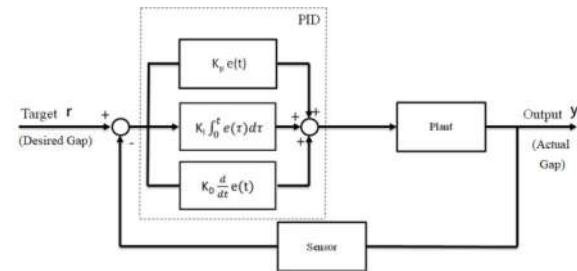B_i : the centroid of the consequent fuzzy subset of the i_{th} rule.

Fig. 7 Scheme of the PID controller.

Fig. 8 Scheme of the Fuzzy-Sliding mode controller.

5. Experimental Results and Discussion

The performance of the developed hydrostatic bearing with servo valve is evaluated by the dynamic test. In the proposed dynamic test, a sinusoidal wave representing the external disturbance load from 500 to 1200 Kgf is produced by sending an equivalent electric signal to the proportional pressure valve.

The frequency of the sinusoidal wave is set to be 0.1 Hz. The experimental oil-film gap variations using two different controllers are depicted in Fig. 9. The desired gap input is set to be 0.04 mm. It is noticeable that the oil-film gap (thickness) can almost be kept at a constant value regardless of the external load changes. The background technology for achieving these satisfactory results is the electro-hydraulic closed-loop control. Furthermore, it can also be observed that the control performance of the proposed FSMC is better than that of the traditional PID controller since the oil-film gap variation using the former controller is smaller. Similar results can also be obtained for different desired gap settings as shown in Fig. 10 and 11. Figure 12 summarizes the quantitative comparisons of root-mean-square control error between the FSMC and PID controller. Thus, it is achieved that the oil-film gap is nearly a constant valve regardless of the sinusoidal wave input of external disturbance load. Consequently, the real contact and undesirable wear between the movable platform and circular pad can be avoided. This is exactly the principle function of a hydrostatic bearing.
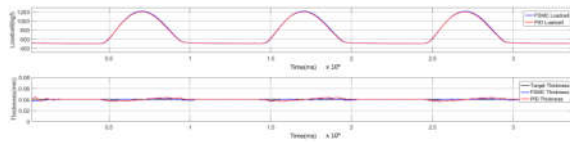

Fig. 9 Comparisons of closed-loop gap control performances using PID and FSMC (Gap: 0.04 mm).
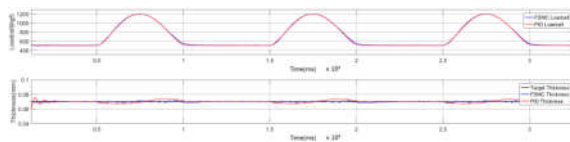

Fig. 10 Comparisons of closed-loop gap control performances using PID and FSMC (Gap: 0.07 mm).
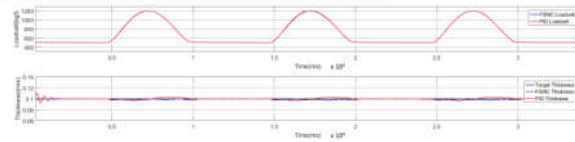

Fig. 11 Comparisons of closed-loop gap control performances using PID and FSMC (Gap: 0.1 mm).

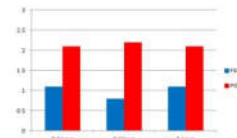|	0.04mm	0.07mm	0.1mm
FSMC	1.1	0.8	1.1
PID	2.1	2.2	2.1

Fig. 12 Comparisons of root-mean-square control error between FSMC and PID controller.

6. Conclusions

In this paper, a hydrostatic bearing with servo valve together with closed-loop oil-film gap control scheme is successfully developed and implemented. Besides, three conclusions may be drawn from this research.

1. The successful development of hydrostatic bearing with servo valve is verified by the dynamic test. The oil-film gap (thickness) can almost be kept at a constant value regardless of the external load changes. These satisfactory results arise actually from the electro-hydraulic closed-loop control technology.

2. The proposed hydrostatic bearing with servo valve together with closed-loop oil-film gap control scheme is suitable for any machine tool applications with heavy load, like the large single column vertical lathe, surface grinding machine, etc.

3. The control performance of the proposed FSMC is better than that of the traditional PID controller since the root-mean-square control error of gap variation using the former controller is much smaller.

7. Acknowledgment

References

[1] C. Wang and C. Cusano, "*Dynamic Characteristics of Externally Pressurized Double Pad Circular Thrust Bearing with Membrane Restrictors*," Transactions of ASME, Journal of Tribology, Vol. 113, (1991), 158-165.

[2] S. C. Sharma, R. Sinhasan and S. C. Jain,

"*Performance Characteristics of Multi-recess Hydrostatic/Hybrid Flexible Journal Bearing with Membrane Type Variable-Flow Restrictor as Compensating Elements,*" Wear, Vol. 152, (1992), 279-300.

[3] Y. Kang, P. C. Shen, Y. P. Chang and H. H. Lee, "*Modified Determination of Fluid Resistance for Membrane-Type Restrictor,*" Industrial Lubrication & Tribology, Vol. 59, No.3, (2007), 123-131.

[4] D. Chena, J. Fan and F. Zhang, "*Dynamic and Static Characteristics of a Hydrostatic Spindle for Machine Tools,*" Journal of Manufacturing Systems, Vol.31, (2012), 26-33.

[5] H. Sawano, Y. Nakamura, H. Yoshioka and H. Shinno, "*High Performance Hydrostatic Bearing Using Variable Inherent Restrictor with a Thin Metal Plate,*" Precision Engineering. Vol. 41, (2015), 78-85.

[6] J. C. Renn, W. J. Hsu and Y. R. Li, "*An innovative Spool-Type Pressure Feedback Restrictor for Hydrostatic Bearings,*" Smart Science, Vol. 4, Issue 4, (2016), 203-208.

Modeling, Design and Control of Low-cost Remotely Operated Vehicle for Shallow Water Survey

Tran Ngoc Huy[1], Huynh Tan Dat[2], Chau Thanh Hai[2]

[1] Ho Chi Minh City University of Technology, VNU-HCM
Ly Thuong Kiet Street, Ho Chi Minh city, 700000, Viet Nam
[2] National Key Lab. of Digital Control and System Engineering, HCMUT, VNU-HCM
Ly Thuong Kiet Street, Ho Chi Minh city, 700000, Viet Nam

ABSTRACT

This paper presents the research on design and control of Remotely Operated Vehicle (ROV) belonging to National key Laboratory of Digital Control and System Engineering. It is controlled by human pilot while the power and communication are supplied via a tether cable. The thruster allocation strategy enables flexibility in motion. A system of sensors and camera collects data from underwater environment. The proposed 3D model designed by SOLIDWORKS® and MATLAB Simulink® mathematical model analysis provide a nonlinear plant in order to apply classical PID controllers into practical experiments.

Keywords: Remotely Operated Vehicle, PID controller, underwater robot

1. Introduction

Vietnam is a coastal country which is packed with activities in national defense, economy, environment and tourism. In areas with an exceptional depth or harsh natural environmental conditions, people can not handle difficult tasks. Therefore, the development of underwater vehicles to support and gradually replace human factor is essential to ensure the workplace safety while performing given tasks according to technical requirements. There are two types of diving robots: Remotely Operated Vehicle Control (ROV) and Autonomous Underwater Vehicle (AUV) [1]. Although AUV is capable of working automatically, ROV provides on-the-spot surveillance without being limited by operation time due to the direct power supply and communication through cables. With the addition of accessories such as grabber, water sampling module will aid ROV in carrying out simple tasks.

In this research, the 3D mechanical model is designed based on reference from previous related works, using SolidWorks software [2]. Simulation for mathematical model using MATLAB Simulink will be performed to observe the response of position, velocity and acceleration values over time. Based on the defined parameters in [3], classical PID controllers was studied to evaluate the ability to control ROV in practice. The output of this research is a ROV model for actual tests, applying the programmed controller.

2. Method

A. Design of 3D model

The design concept for ROV varies according to size, weight and function. However, a typical ROV should consist of a mechanical frame, thrusters, power supply system, communication and control module as well as image capture function. Some of basic specification are listed below.

- Box frame configuration
- Estimated operating depth: 5m
- Average speed: 0.5m/s
- Continuous operation with DC Power Supply
- Number of thrusters: 6
- Weight (in air): 25kg

The following figures display the ROV model in three dimensional space, designed by SolidWorks. Apart from the outer frame and thrusters, other components are placed in waterproof function boxes.
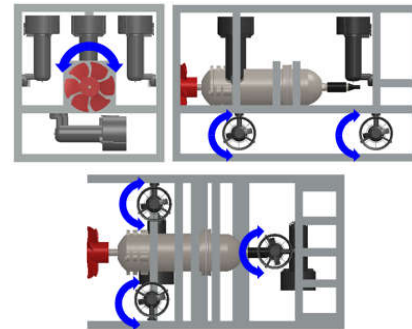

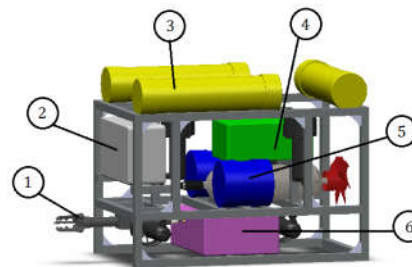Figure 1. Thrusters arrangement in back view, side view and top view respectively.

Figure 2. Overall 3D ROV model

In the above figure, the numbered components can be sequentially expressed in detail:

1. Three jaw grabber
2. Camera and lighting system box
3. Buoyancy system
4. Sensors box
5. Water sampling module
6. Power supply and thruster's drive box

A brief description of components is given subsequently. The vehicle is equipped with a grabber for a wide array of useful tasks such as carrying or recovering objects underwater. An integrated camera captures image signals with the aid of high performance lights then feedbacks those to the central processing unit, all just within a box. Three PVC pipes form a floating plane, keeping ROV's self-balance at rest on water surface. The sensors box contains some navigation sensors used to determine the orientation of ROV to control thruster properly. In addition, a water sampling module can collect an amount of water at a desired depth for environmental quality analysis. The last and most important component is an aluminum container that converts high DC voltage from the cable into 24 and 48 DCV for power supply while transferring heat to surrounding water in order to protect and stabilize power converter circuits.

B. Coordinate system and definition of kinematic notations

To explain the motion of ROV in six degrees of freedom and to determine position and orientation in three dimensional space, it is essential to define coordinate system and notations. Kinematics from ROV base on two types of reference which is earth-fixed coordinate system (NED) with arbitrary origin O_n and body-fixed coordinate system (BODY) with the origin O_b placed at the center of gravity [4]. Meanwhile, the notations which is use to explain ROV motion are summarized in table 1.

Table 1: Notations of 6-DOF standard motions

DOF	Motions	Forces and Moments (τ)	Linear and Angular velocities (υ)	Positions and Orientations (η)
1	Surge	X	u	x
2	Sway	Y	v	y
3	Heave	Z	w	z
4	Roll	K	p	ϕ
5	Pitch	M	q	θ
6	Yaw	N	r	ψ

Vector η is in the reference of inertial earth-fixed coordinate system, whereas the velocity vector υ and external force and moment vector τ that acts on ROV body must be expressed in BODY reference frame. Figure 3 shows the relation between those two coordinate system.
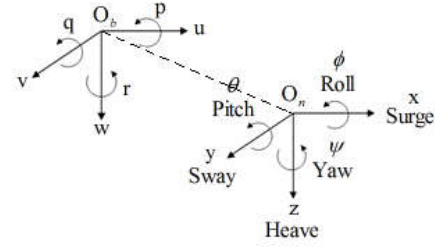

Figure 3. Earth-fixed to body-fixed coordinate system

C. Mathematical model of ROV

Mathematical model of ROV can be obtained in terms of kinematic and dynamic equations. When studying about motion of object without regard to the forces or moments, kinematic equation can be written state parameters. As mentioned before, the Jacobian matrix must be used to transform from earth-fixed frame to body-fixed frame.

$$\dot{\eta} = J(\eta)\,\mathrm{v} \qquad (1)$$

$$J(\eta_2) = \begin{bmatrix} J_1(\eta) & 0 \\ 0 & J_2(\eta) \end{bmatrix} \qquad (2)$$

$$J_1(\eta) = \begin{bmatrix} c\psi c\theta & -s\psi c\phi + c\psi s\theta s\phi & s\psi s\phi + c\psi c\phi s\theta \\ s\psi c\theta & c\psi c\phi + s\phi s\theta s\psi & -c\psi s\phi + s\theta s\psi c\phi \\ -s\theta & c\theta s\phi & c\theta c\phi \end{bmatrix} \qquad (3)$$

$$J_2(\eta) = \begin{bmatrix} 1 & s\phi t\theta & c\phi t\theta \\ 0 & c\phi & -s\phi \\ 0 & s\phi/c\theta & c\phi/c\theta \end{bmatrix} \qquad (4)$$

Based on Newton's Second Law, if the forces that act upon an object are considered, the derivative dynamic equation is expressed for the complete three dimension, 6 DOF rigid body motion as follows:

$$M\dot{v} + C(v)v + D(v)v + g(\eta) = \tau \qquad (5)$$

The right hand side refers to the input forces and moments to the ROV, including thruster forces, disturbances, environmental forces (wind, wave and ocean current). For the most basic control, let $\tau = [X, Y, Z, K, M, N]^T$ denotes the specific forces and moments vector of ROV only from thrusters. It can be obtained from the multiplication of component thruster forces vector $u = [F_1, F_2, F_3, F_4, F_5, F_6]^T$ by a thruster's configuration matrix B [3], according to the position of each thruster:
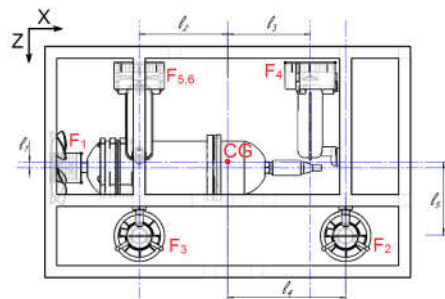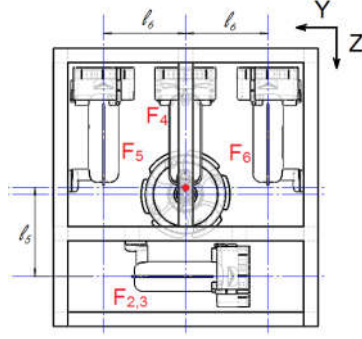
Figure 4. Thruster layout contributes to determine the configuration matrix in side view and front view

$$\tau = B.u = \begin{bmatrix} 1 & 0 & 0 & 0 & 0 & 0 \\ 0 & 1 & 1 & 0 & 0 & 0 \\ 0 & 0 & 0 & 1 & 1 & 1 \\ -l_5 & -l_5 & 0 & 0 & l_6 & -l_6 \\ l_1 & 0 & 0 & -l_3 & l_2 & l_2 \\ 0 & l_4 & -l_2 & 0 & 0 & 0 \end{bmatrix} \begin{bmatrix} F_1 \\ F_2 \\ F_3 \\ F_4 \\ F_5 \\ F_6 \end{bmatrix} \quad (6)$$

Where $l_1 = 10mm$, $l_2 = 150mm$, $l_3 = 140mm$, $l_4 = 200mm$, $l_5 = 125mm$, $l_6 = 115mm$

When ROV moves underwater, its motion would force the amount of surrounding fluid (water) to oscillate with different amplitudes, which is called added mass. In the general dynamic equation (5), M is the sum of the rigid-body mass inertia matrix (M_{RB}) and added mass matrix (M_A) where m, I are ROV's total mass and inertial moment components along X, Y, Z axes and vector $r_G=[x_G, y_G, z_G]^T$ is the coordinate of ROV center of gravity. Moreover, due to the fact that ROV is relatively symmetric and moves at low speed, M_A can be simplified into diagonal matrix [5].

$$M = M_{RB} + M_A \quad (7)$$

$$M_{RB} = \begin{bmatrix} m & 0 & 0 & 0 & mz_G & -my_G \\ 0 & m & 0 & -mz_G & 0 & mx_G \\ 0 & 0 & m & my_G & -mx_G & 0 \\ 0 & -mz_G & my_G & I_x & -I_{xy} & -I_{xz} \\ mz_G & 0 & -mx_G & -I_{yx} & I_y & -I_{yz} \\ -my_G & mx_G & 0 & -I_{zx} & -I_{zy} & I_z \end{bmatrix} \quad (8)$$

$$M_A = -diag(X_{\dot{u}}, Y_{\dot{v}}, Z_{\dot{w}}, K_{\dot{p}}, M_{\dot{q}}, N_{\dot{r}})$$

Similarly, C(v) is the total Coriolis and Centripetal matrix of ROV rigid body and added mass, affecting particularly when angular velocities change.

$$C(v) = C_{RB}(v) + C_A(v) \quad (9)$$

$$C_B(v) = \begin{bmatrix} 0_{3x3} & C_{12}(v) \\ -C_{12}^T(v) & C_{22}(v) \end{bmatrix} \quad (10)$$

$$C_{12}(v) = \begin{bmatrix} m(y_G q + z_G r) & -m(x_G q - w) & -m(x_G r + v) \\ -m(y_G p + w) & m(z_G r + x_G p) & -m(y_G r - u) \\ -m(z_G p - v) & -m(z_G q + u) & m(x_G p + y_G q) \end{bmatrix}$$
$$(11)$$

$$C_{22}(v) = \begin{bmatrix} 0 & -I_{yz}q - I_{xz}p + I_z r & I_{yz}r + I_{xy}p - I_y q \\ I_{yz}q + I_{xz}p - I_z r & 0 & -I_{xz}r - I_{xy}q + I_x p \\ -I_{yz}r - I_{xy}p + I_y q & I_{xz}r + I_{xy}q - I_x p & 0 \end{bmatrix}$$

$$(12)$$

$$C_A(v) = \begin{bmatrix} 0 & 0 & 0 & 0 & -Z_{\dot{w}}w & Y_{\dot{v}}v \\ 0 & 0 & 0 & Z_{\dot{w}}w & 0 & -X_{\dot{u}}u \\ 0 & 0 & 0 & -Y_{\dot{v}}v & X_{\dot{u}}u & 0 \\ 0 & -Z_{\dot{w}}w & Y_{\dot{v}}v & 0 & -N_{\dot{r}}r & M_{\dot{q}}q \\ Z_{\dot{w}}w & 0 & -X_{\dot{u}}u & N_{\dot{r}}r & 0 & -K_{\dot{p}}p \\ -Y_{\dot{v}}v & X_{\dot{u}}u & 0 & -M_{\dot{q}}q & K_{\dot{p}}p & 0 \end{bmatrix}$$

$$(13)$$

The hydrodynamic damping force matrix consists of a linear and quadratic terms where the terms higher than second-order are negligible. With a non-couple motion, a diagonal approximation would be acceptable in most od applications. Although the damping coefficients appears to be challenging to determine, we can make use of strip theory or practical experiments [6].

$$D(v) = -diag\{X_u, Y_v, Z_w, K_p, M_q, N_r\}$$
$$-diag\{X_{|u|u}|u|, Y_{|v|v}|v|, Z_{|w|w}|w|, K_{|p|p}|p|, M_{|q|q}|q|, N_{|r|r}|r|\} \quad (14)$$

The last part of the dynamic equation is the restoring force matrix, existing as the interaction between buoyant forces based on Archimedes' principle and the force of gravity. As they are expressed in the earth-fixed frame, a transformation matrix g(η) must be used to add them to (5) in body-fixed frame.

$$g(\eta) = \begin{bmatrix} (W - B)\sin\theta \\ -(W - B)\cos\theta\sin\phi \\ -(W - B)\cos\theta\cos\phi \\ -(y_G W - y_B B)\cos\theta\cos\phi + (z_G W - z_B B)\cos\theta\sin\phi \\ (z_G W - z_B B)\sin\theta + (x_G W - x_B B)\cos\theta\cos\phi \\ -(x_G W - x_B B)\cos\theta\sin\phi - (y_G W - y_B B)\sin\theta \end{bmatrix}$$
$$(15)$$

D. ROV model control

Prior to control the experimental model, simulation using Matlab Simulink will be studied to investigate the central controller. Due to the difficulty in modelling state parameters and MIMO control, the classical PID controller has been proposed for some reasons such as its simplicity in many applications and positive response.. Figure 5 demonstrates the block diagram of closed-loop control system for ROV. There are two mode of maneuvering. Normally, ROV is manipulated by human pilot from an onshore base, but the ability of remaining at a desired depth or heading angle does contribute much to task accomplishment. Therefor, this section focuses on the PID controllers for depth and heading angle.
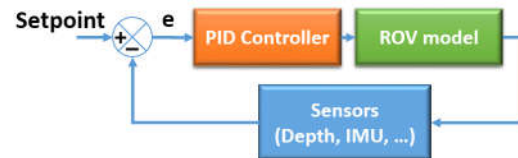

Figure 5. Block diagram of controlling system

After choosing algorithm for controlling, along with the set of equations (1) and (5), the simulation model is established to obtain the response of ROV at different

564

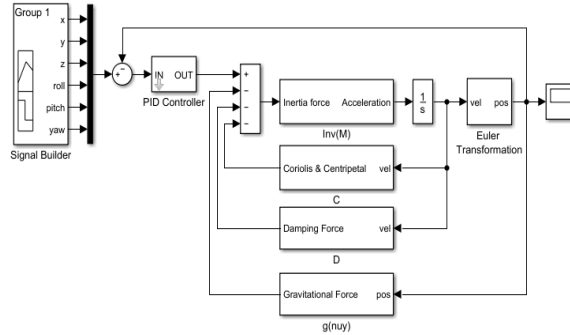setpoints, as shown in Figure 6.

Figure 6. Function block diagram of controlling system in Simulink

Figure 7 shows the overall system of electronic and electrical devices in ROV. CAN (Controller Area Network) protocol is crucial for communication in this structure. With the data transfer rate up to 1Mbps, CAN
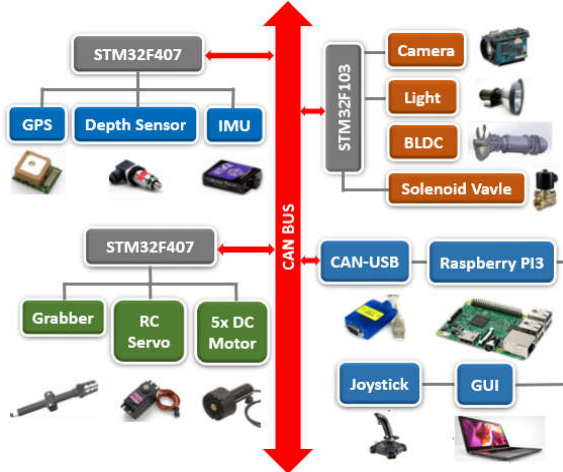

Figure 7. Communication diagram of hardware and electronic components

bus guarantees the response rate for the whole system while eliminating common noise by means of differential signals from twisted pair cable. The central processing unit is Raspberry PI 3 (Model B) with ARM core provides 1Gbps processing speed, taking charge of major control and computation; 2 boards ARM STM32F407VGTxx[7] are used to collect data from sensors and receive commands from Raspberry to drive motors. ROV has to be connected with the onshore station via Ethernet TCP/IP communication. All signals from sensors and camera will be sent and displayed in user interface (GUI) whereas the station transfers input values from joystick to the central processing unit.

E. General user interface:

Figure 8. Interactive monitoring interface

The software based on Visual Studio platform and C# programming language allows users to monitor state parameters like the direction of rotation and power of motor (%), altitude, depth and camera images, etc. Then, the operator can use the integrated function to store data as Excel spreadsheets for further analysis. Besides, after connecting GUI and ROV by setting Ethernet connection, it is easy to maneuver ROV at will with the joystick or to tune the PID coefficient (K_p, K_i, K_d) so that the vehicle's response can reach the set points. Another important key feature is that the pilot can observe the surrounding environment with high quality camera.

3. Results and Discussion
A. Simulation result:
Based on the model built in previous sections, a set of parameters is inputted into function blocks so as to tune the PID coefficients to receive the most satisfactory response. The limit of force for depth control is 70N and that for heading control is 70Nm. Figure 9 and figure 10 show the output response of simulation, comparing to some desired values. The tuned PID's gain for depth control is $[120,0,180]^T$ and for heading control is $[25,0,0.5]^T$.
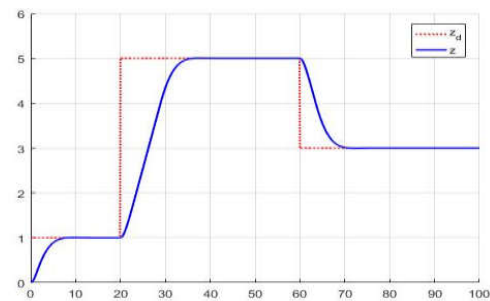

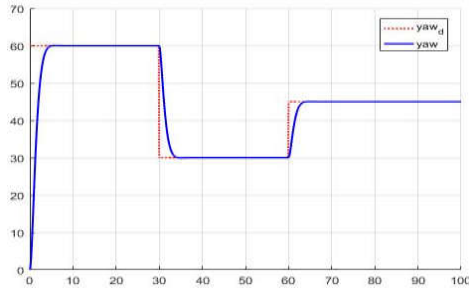Figure 9. The PID response of auto-depth control

Figure 10. The PID response of auto-heading control

Both figures indicates good response of the two PID controllers. The steady-state errors are zero and there are almost no overshoots. Assuming that the influence of environmental disturbance is insignificant, the high damping coefficient along Z-axis is responsible for extending the settling time of depth control. When the damping component from D(v) reach the control output to drive thrusters, the vehicle's acceleration of heave motion, for instance, is terminated, which leads to constant motion. On the other hand, the response of heading control proves to be quite optimistic.

B. Experimental result:

The last part of this section comes up with several experiments to verify the operation of ROV based on the designed model and simulation as shown in figure 11 and 12. The experiments takes place in a swimming pool 1.8 meters deep. Power supply and Ethernet communication are transferred via cable from an onshore station. The operator manipulates ROV with joystick and GUI on PC screen in two modes: manual and automatic (depth, heading).

Figure 11. Actual test when ROV floats on water surface

Figure 12. ROV's movement at a desired depth underwater without external forces.

During the experimental process, the response of the control object (ROV) will be displayed on the screen and exported into an Excel every 10 milliseconds. The monitor can use this report function for information analysis afterward, as observed in figure 13 and figure 14.
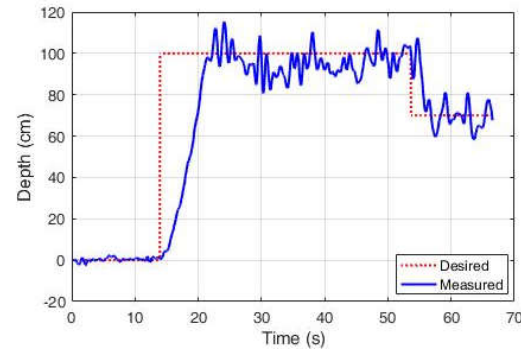

Figure 13. Experimental depth response of ROV with different set-points.

According to the experimental results in figure 13 and 14, it can be seen that the PID controller give fairly good response, both in terms of the depth and heading control. During the experimental process, some external forces are applied when the heading angle controller is working but the controller keep ROV tracking back to the set point. However, there are still many aspects that need to be improved. Due to limited available devices and equipment, noise measurement contributes substantially to the controller, making the response oscillate around the
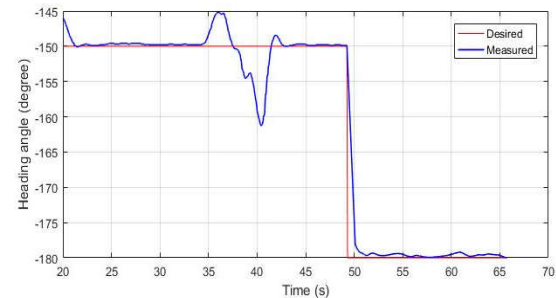

Figure 14. Experimental heading angle response of ROV with different set-points.

reference value without being stable. In addition, the design is lack of optimal hydrodynamic profile, which prolongs the depth control settling time (about 8.44 s).

4. Concluding Remarks

This paper has presented the research of 6-DOF ROV model which have the ability to move flexibly underwater under the conditions of the experiment. Through mathematical models, simulation process is carried out to evaluate the ability of the controller. In

addition, the design of the control system for the actual model and experiments in the pool are also mentioned in order to observed the response of the selected controller when applying from theory into reality.

References
[1] Budiyono, Agus & Anam, Hujjatul & Setiawan, Joga. (2015). *Simulation and Dynamic Analysis of Remotely Operated Vehicle (ROV) Using PID Controller for Pitch Movement.* Marine and Underwater Science and Technology. 1. 23-31.
[2] Christ, R.D. & Wernli, Robert. (2011). *The ROV Manual: A User Guide for Observation Class Remotely Operated Vehicles.* 1-320.
[3] Chin, Cheng Siong & Lau, Michael & Low, E & Seet, G. (2006). *Software for Modelling and Simulation of a Remotely Operated Vehicle.* International Journal of Simulation Modeling. 5. 114-125.
[4] Fossen TI. *Marine Control Systems Guidance, Navigation, and Control of Ships, Rigs and Underwater Vehicles.* Marine cybernetics AS (2002).
[5]. Fossen TI. *Handbook of Marine Craft Hydrodynamics and Motion Control.* Wiley, New York (2011).
[6]. Chin, C.S., Lin, W.P. & Lin, J.Y. *Experimental validation of open-frame ROV model for virtual reality simulation and control.* J Mar Sci Technol (2018) 23: 267.
[7]. Datasheet STMicroelectronics

Image Processing Method to Classify Objects on Dynamic Conveyor

Ngoc-Huy Tran[1], Van-Thinh Pham[2], Nguyen-Hoang-Phuc Le[2]
[1] Ho Chi Minh City University of Technology, VNU-HCM
Ly Thuong Kiet Street, Ho Chi Minh city, 700000, Viet Nam
[2] National Key Lab. of Digital Control and System Engineering, HCMUT, VNU-HCM
Ly Thuong Kiet Street, Ho Chi Minh city, 700000, Viet Nam

ABSTRACT

This paper focuses on two main issues: First, the detection and classification of objects based on color, shape and based on the characteristics of the object. The second is picking up target object on the conveyor belt and optimizing the picking order. Experimental results using camera Logitech C270, Yamaha Scara YK-400X robotic arm, LabVolt conveyor, programming language is C ++ and OpenCV library.

Keywords: Image Processing, PCA-SIFT, OpenCV

1. Introduction

Due to the need to use more and more robots in complex manufacturing processes to improve productivity, reduce cost, enhance quality, accuracy and minimize risk when people working in toxic environments, the design of the robot operation system does not need human intervention is truly needed and fully capable, especially in an era of rapid development of current computer vision [1,2].

To solve the specific problem posed: "Sorting and picking objects on conveyor belt" [3]. In this article, we propose a simple and high-precision method for classifying real-time objects [1,3]. we provides an algorithm for picking up objects accurately on conveyor belt at any speed and optimal order picking to avoid missing in the process [1]. We also use image processing to determine the orientation of the object, to solve the problem of placing the object in the box is neat and less space.

2. Method

2.1. Approach method

The approach to the problem of picking and sorting objects on a conveyor consists of two main steps:

- First, the process of identifying the object from the input image, then giving the position, direction of the object. For identification based on color and shape, we define the image's threshold [4,5], then based on the contour to sort by shape [2,6]. For complex colors and patterns object, we use the PCA-SIFT algorithm, where SIFT extracts the local characteristics of the object and PCA reduces the number of dimensionality and retain only the best characteristics for Identification [3].

- Second, picking object, this step is designed with the optimal requirements of picking order so that picking time is the shortest to minimize the delay for the next picking.

2.2. Image processing

A typical image processing system includes the following steps:

- Collect data from camera, preprocessing.
- Advanced image processing to perform a specific request.

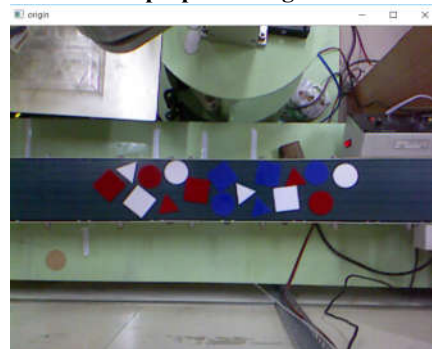#### 2.2.1. Collect data from camera and preprocessing.

Fig 1. Original image from camera.

Image data is collected from the camera Logitech C270. In order to increase the efficiency of the image identification process, we need to have a preprocessing image. Image processing helps clear images, noise filters, and speed up processing.

Images collected from camera are 24-bit RGB images. There are plenty of surplus parts that need not be used. If we can eliminate these excesses, the processing speed of images will increase significantly. So we proceed to crop the image again, only retain the image portion of the conveyor [3]. The result is shown in Fig 2a.
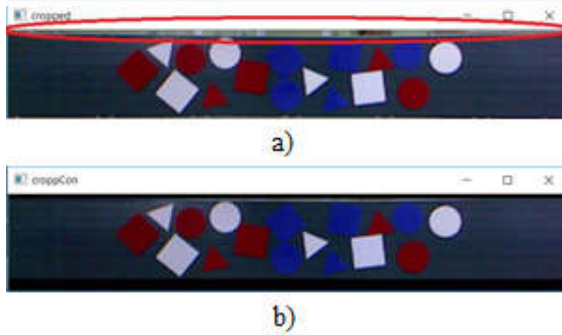
Fig 2. a) Image after crop, b) Image after through the mask.

On Fig 2a, we can see that there are still redundant parts that need not be used. These parts may can affect the results of processing. To eliminate this part, we put pictures in Fig 2 through a quadrilateral mask (with two sides coinciding with the upper and lower edges of the conveyor belt), keeping only the parts in the mask. The result of this process is as follows Fig 2b.

So we have obtained the Region of Interest (ROI), the next processing will be applied to this ROI.
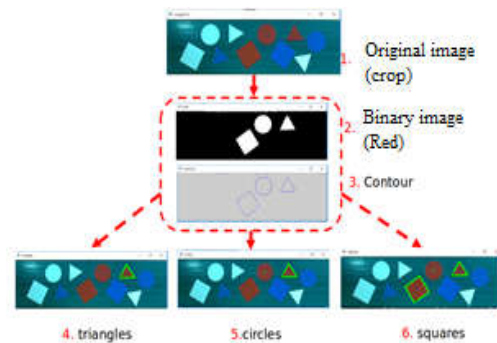
2.2.2. Identify colors and shapes

Fig 3. Identify colors and shapes.

An image obtained from the camere consists of three color channels, R, G, B. Each pixel consists of three different values, R, G, B, which define three values of three basic colors red, green, blue [7].

Based on that feature, we split the image into 3 different images for R, G, and B. For each channel, we use two low and high thresholds to obtain the required values. Fig 4a is a binary image for the case of white objects. Then apply the Median filter to filter noise, smoothing the object. The result is Fig 4b.
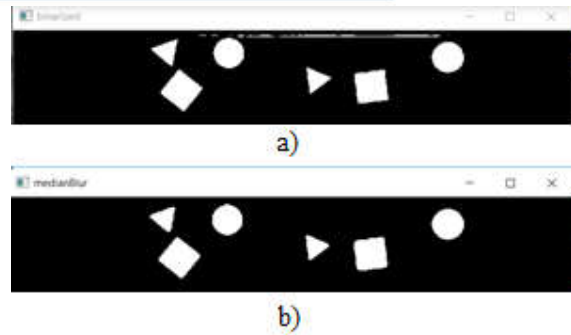

Fig 4. a) Binary image, b) Image after Median filter.

The boundaries of the objects are the places where gray intensity changes most strongly. These areas are found by defining the gradient of the image. In OpenCV there is a tool available for separating the boundary that is the findContours function [7]. This function uses the Canny algorithm to find the edge and shape of an object.

We have only three specific shapes (circles, triangles, rectangles). If a polygon has an edge greater than 8, we will classify it as a circle. Thus, the classification of the shape uses the following criteria:

- Square: the number of edges is 4, the cosine value of the angles is less than 0.2.
- Circle: Number of edges more than 8.
- Triangle: the number of edges is equal to 3.
- The polygons found must be polygonal convex.
- The area of the polygon must be large enough.

From the object's edge data, use the Ramer-Douglas-Peucker algorithm to approximate that data to a simpler polygon, ie, reduce the number of points that make up the polygon.

we obtain the result for the white square as follows Fig 5, for triangles and circles have similar results.

Fig 5. Sort by shape and color.

2.2.3. Classification based on object's characteristic using PCA-SIFT algorithm.

The object identification method used is the matching object, which uses the characteristics of the feature or featurepoint image [8]. This approach overcomes some of the disadvantages of conventional image processing such as noise sensitivity, rotating objects, and brightness changes. To extract keypoint characteristics of an object, we use the SURF / SIFT algorithm, which is the two most popular methods today due to the high precision of

569

SIFT and the fast processing speed of SURF [3,9]. Then, we use the FLANN algorithm to matching.
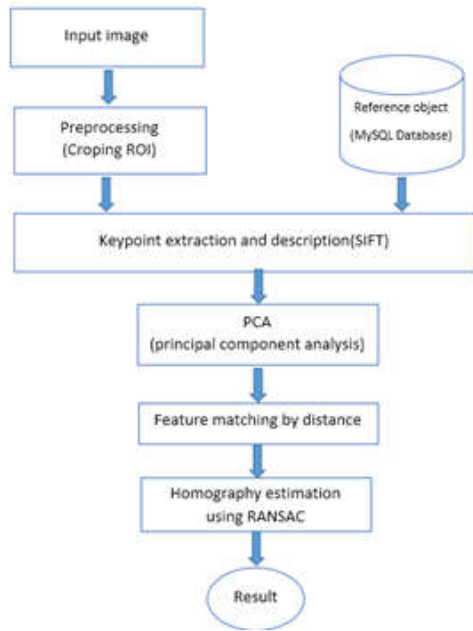

Fig 6. Block diagram according to the method of classification by characteristics

PCA is a transformative method that reduces the large number of correlated variables to a small set of variables such that the new variables are linear combinations of old variables that are not interrelated.

2.2.4.   Calculates the center of the object

The center of the object is the position at which the robot will pick up the object. At that point when the object is picked, the weight will be distributed evenly, the object will not fall.

In general, for any polygon with n edges, we have the following formula:

$$x_G = \frac{1}{n}\sum_{i=1}^{n} x_i \; ; \; y_G = \frac{1}{n}\sum_{i=1}^{n} y_i \tag{1}$$

Where the coordinates of the vertices of the polygon are (x_i, y_i).

2.2.5.   Calculate the rotation of the object.

During picking, the object must be swiveled to fit the tray and not fall out. The swing angle must be optimized to save time and energy.
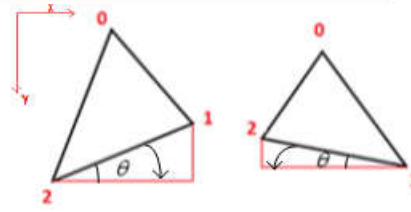

Fig 7. Calculates the rotation angle of the triangle object.

On Fig. 7, if 0 is the point with the smallest y coordinate, the other two points are numbered 1 and 2. The angle of the object is the angle of the line 12 relative to the horizontal axis:

$$\theta = a\tan\frac{|y_1 - y_2|}{|x_1 - x_2|} \tag{2}$$

For squares, we also need to determine the point with the smallest y coordinate, marked as zero, and the remaining points are ordered counterclockwise, as can be seen in Fig. 8.
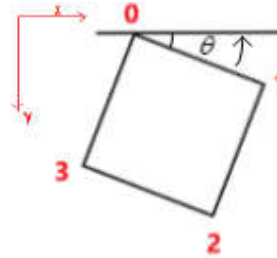

Fig. 8. Calculates the angle of rotation of the square object

We have the formula (3) calculate the rotation angle as follows:

$$\tan(\theta) = \frac{|y_1 - y_0|}{|x_1 - x_0|} \tag{3}$$

For optimal speed, we will compute the angle so that the machine's travel time is smallest, so we will choose the smaller angle. In other words, the tan () of the rotating angle is less than 1. The formula for the rotation angle will be:

$$\theta = a\tan\left(\min\left[\tan(\theta), \frac{1}{\tan(\theta)}\right]\right) \tag{4}$$

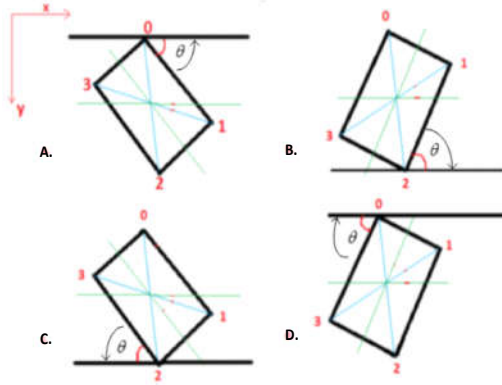For the rectangle, the matching method will have four cases occurring as shown Fig 9.

570

Fig 9. Calculates the rotation angle of the rectangle object

- Case A and C:

$$\theta = a\tan\left(\frac{|y_1 - y_0|}{|x_1 - x_0|}\right) \quad (5)$$

- Case B and D:

$$\theta = a\tan\left(\frac{|y_2 - y_1|}{|x_2 - x_1|}\right) \quad (6)$$

3. Calibration

When we pick up the object we rely on the coordinates of the object against the coordinates of the robot. Therefore necessary to change the coordinates of the camera to the coordinates of the robot so that the coordinates of the object can be determined and picked exactly.

The calibration method in this project uses three circular objects located at three vertices of the rectangle. We will calculate the coordinates of the three vertices relative to the camera coordinate system and the coordinate system of the robot.
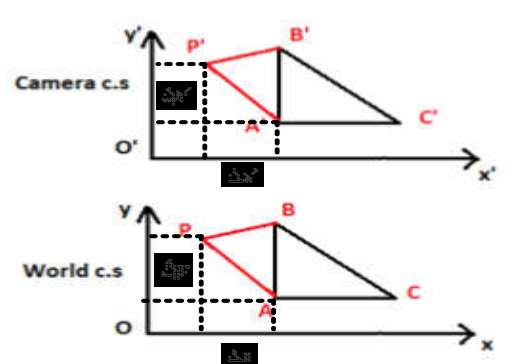

Fig 10. Coordinates of points when calibration

From the three points above, using the basic geometric theorem, we can calculate the coordinates of any point in the coordinates of these three points as follow the formulas (7).

$$k_x = \frac{AC}{A'C'}; k_y = \frac{AB}{A'B'}$$

$$P_x = A_x + \Delta x = A_x + A'P' \times \cos(\angle P'A'C') \times k_x$$

$$P_y = A_y + \Delta y = A_y + A'P' \times \cos(\angle P'A'B') \times k_y$$
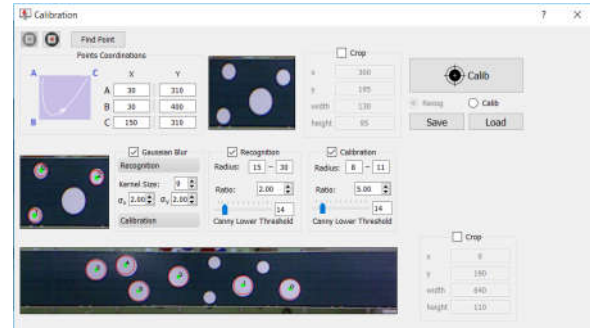
(7)

Fig 11. Calibration interface

4. Software control interface

The console is written on the Visual Studio software and the QT library. Visual Studio provides an environment for QT programming on it. QT library used is 64bit version for faster processing speed. QT supports powerful interface programming tools. The interface, as shown in Figure 12, consists of the following main functions:

(1) Reload the previous calib.
(2) Move the robot to the position of the cursor.
(3) Single button: to pick up the first object on the right and Many button to pick up all objects.
(4) Choose the color and shape of the object to pick.
(5) Choose the path and take a picture, save the image.
(6) Control the angle of the camera.
(7) Play and Pause.
(8) Connect and disconnect from Kinect.
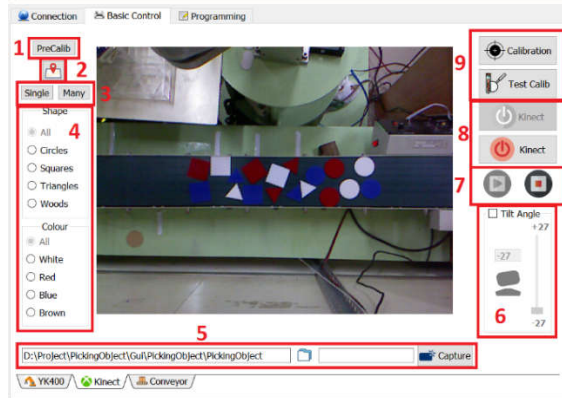(9) Enable Calibration Interface and test parameters.

Fig 12. Software control interface

5. The algorithm for picking and sorting objects on the conveyor belt

This section will include algorithm diagrams for picking and sorting objects on the conveyor belt. Control algorithms are written and coordinated between three major devices: the computer, the Atmega328 MCU, and the SCARA YK400X robot controller.
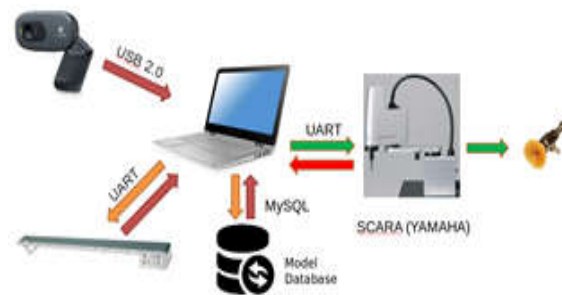
Fig 13. System model

The main task of the equipment as follows:

- Atmega328: Conveyor PID control, read encoder. Send pulse encoder data to computer.
- Computer: Used to collect data from the camera, process images, receive data from Atmega328 and send data to the controller.
- Robot controller: Receive data from computer, control robot pick up the object.

5.1. Control algorithms on SCARA robots
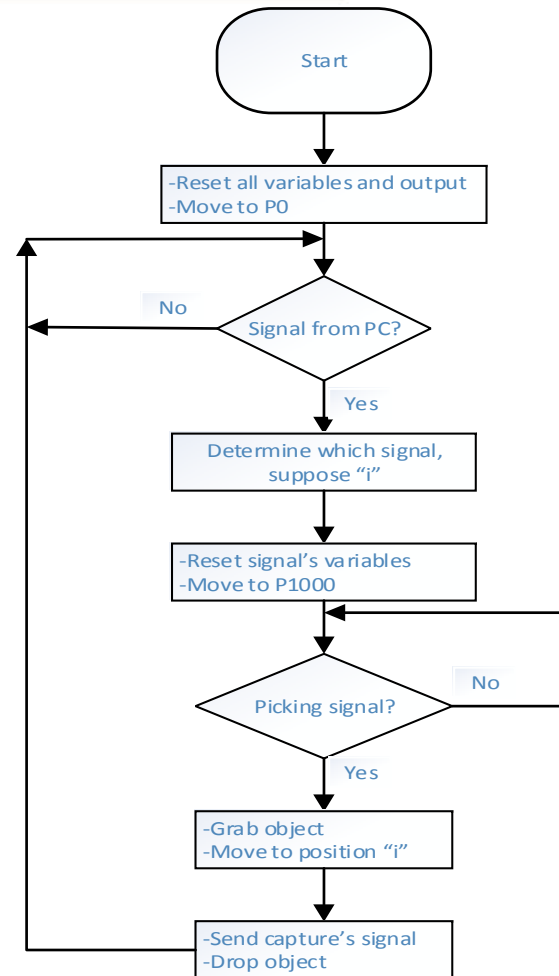
5.2. Control algorithms on computer
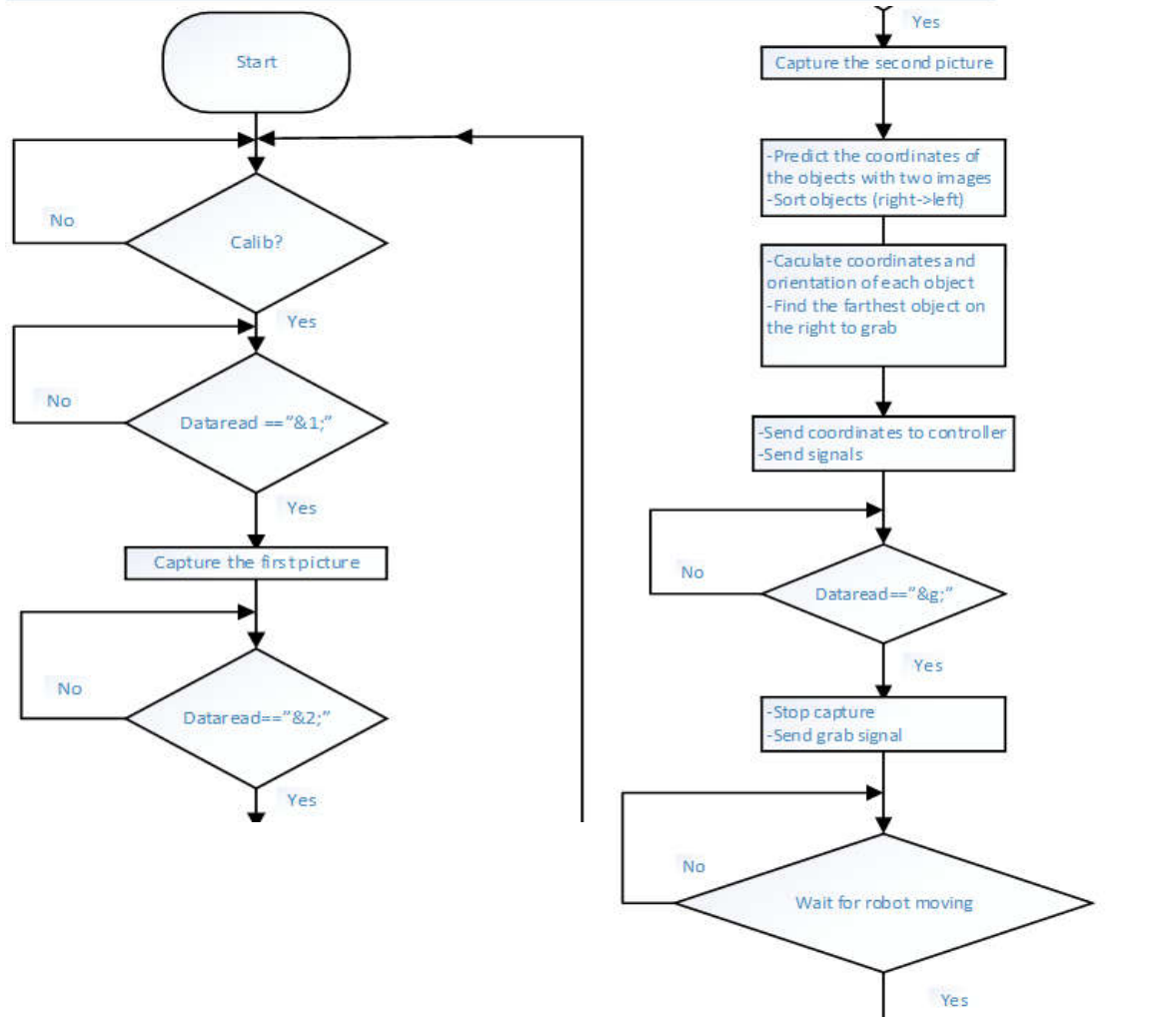
6. RESULT

The actual system model is shown in Figure 14.

Fig. 14. Complete system model

573

6.1. The results of sort by color and shape.

The results are made by randomly dropping 50 objects with the specific number of each item as the following table 1.

Table 1. The specific amount of each item to be tested.

	Circle	Square	Triangle
Red	7	5	4
White	4	7	5
Blue	9	4	5

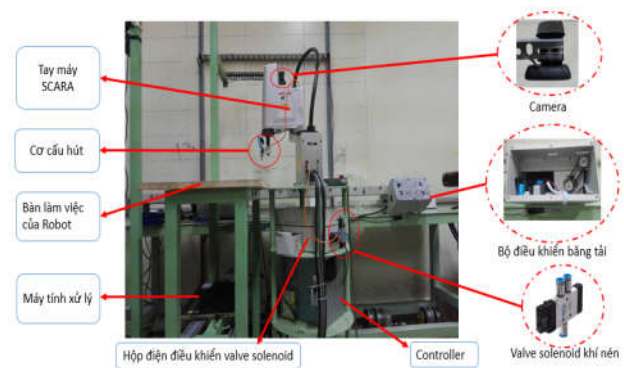During the test, the speed of the conveyor is 5cm/s. Items are randomly released and the rotation of items is also random (Lighting conditions are constant).
Specific results are as follows:

- Total number of items: 50
- Missing items: 0
- Missing times: 2
- Incorrect classification: 0
- The wrong direction of items: 0
- Total time of completion (50 items) < 2 minutes

As a result, an average of more than 2 seconds to pick up an object. Robots processing precisely at high speed. The number of times can not pick up (2 times), the robot has identified and moved to the pick up position, but due to the pneumatic valve is not working well.

6.2. Classification results are based on the characteristics of the object.

Classification results are based on the characteristics of the object as show table 2.

Table 2. Results are based on the characteristics of the object.

	Type 1	Type 2	Type 3	Type 4	Type 5
Image					
Percent	95.6%	97.2%	96.1%	83.6%	86.5%

Percentage identity from different types of patterns is quite high. In the process of identifying the object on the conveyor belt, the object also moves along. The color of the object obtained on the camera will be partially blurred. The reduced characteristics leads to reduced recognition percentages. Also the ability to identify also depends on the complexity of the pattern.

7. Conclusion

In this article, the task is to pick and classify objects on the conveyor belt with different shapes, colors as well as patterns. The objects are round, triangular, rectangular and randomly arranged on conveyors in different directions. Our methods is identified, picked and classified objects in an effective way.

This method can be proposed to solve picking and sorting objects with different shapes, colors, and even complex patterns products running on conveyor belts.

Identification of objects is sometimes affected by unstable lighting conditions, so we have used more light bulbs to create a stable light environment and not be affected by external light.

References
[1] Mihai Dragusu, Anca Nicoleta Mihalache and Razvan Solea, member, IEEE, (2012), Practical Applications for Robotic Arms Using Image Processing

[2] Jianjun Ni, Zubair Khan, Shihao Wang, Kang Wang and Syed Kamran Haider, "Automatic Detection and Counting of Circular Shaped Overlapped Objects Using Circular Hough Transform and Contour Detection" Intelligent Control and Automation (WCICA), 2016 12th World Congress on, 2016.

[3] H. I-sil Bozma and H.ulya Yal-cin, (2002). Visual processing and classification of items on a moving conveyor: a selective perception approach. Journal of Robotics and Computer Integrated Manufacturing, 2002.

[4] M. Sonka, V. Hlavac, and R. Boyle, Image processing, analysis, and machine vision. Cengage Learning, 2014

[5] Hong-Kui Liu, Jun Zhou, "Moving object detecting and tracking method based on color image", Proceedings of the 7th WICA, pp. 3608 – 3612, 2008.

[6] M.Grabner, H. Grabner, H. Bischof, "Fast Approximated SIFT", *Asian Conference on Computer Vision*, pp. 918-927, 2006.

[7] Gary Bradski, Adrian Kaebler (2008), *Learning OpenCV, O'Reilly Media,* Inc Cambridge, USA.

[8] Ebrahim Karami, Siva Prasad, and Mohamed Shehata, "Image Matching Using SIFT, SURF, BRIEF and ORB: Performance Comparison for Distorted Images", In Proceedings of the 2015 Newfoundland Electrical and Computer Engineering Conference,St. johns, Canada, November, 2015.

[9] H Bay, A Ess, T. Tuytelaars, "Speeded-up robust features (SURF)[J]", *Computer vision and image understanding*, vol. 110, no. 3, pp. 346-359, 2008.

Study on Pest Visualization/Identification by Ultrasound

Masaki Okugumo

Department of Electrical & Computer Engineering, Yonago National College of Technology

ABSTRACT

Recently, environmental damage caused by pest, invasive species Nutria has become an issue in Tottori Prefecture and development of an effective control method is in demand. Therefore, we have developed a robot that could identify pest by using ultrasonic sensor. The benefits of using this robot is that it is difficult to be influenced by environmental conditions and easily recognizes three dimensional input. Unfortunately, this robot could only confirm the presence of target object but could not identify the object, which means it could not differentiate whether the object is human or pest. In this paper, we have invented a robot that could visualize the object by using frequency-modulated ultrasound and Self-Organizing Map (SOM).

Keywords: pest, ultrasound, wavelength, frequency-modulation, Self-Organizing Map.

1. Introduction

Nutria, a large herbivorous and semiaquatic herbivorous spiny rat has been growing in numbers in the Tottori prefecture of Japan. Initially, this creature was rare and uncommonly seen in Japan. Yet the quick breeding has caused undue harm to surrounding environment especially in agricultural sectors. Therefore, the concern and attention of developing efficient resistance measures and methods are growing vastly. To offer a constant crop protection that enables to provide a fast and precise monitoring, we have initiated the idea of developing an automated pest detector/robot that functioned with image sensing and ultrasound sonography. With this application, it could provide a real-time data from the field that periodically keeps track the movement of pest. The implementation of pest detector/robot is a common way in pest monitoring. However, during adverse weather like severe fogging and in night time, the performance of robot declines from its optimal. Furthermore, image sensor could not feature face recognition that elucidates the parameter between pest and sensor by means of distance[1,2]. Solely with sonography, it is difficult to distinguish between pest and human and sometimes hardly to detect the presence of living creatures. To overcome the mentioned limitations, we have developed the idea of implementing Self-Organizing Map (SOM) in frequency modulated sonography that could accurately differentiate between human and pest. The ultrasound wave with a range between 20-40 kHz is modulated and radiated to the object. The reflected wave is processed into wavelet series to obtain data commutated based on the relationship between intensity at frequencies 20, 30 and 40 kHz and time. Finally, the wave feature is extracted and submitted into the SOM system to provide a clear difference between pest and human.

2. Invasive species Nutria

Nutria is an herbivorous rodent and usually grows into a size of 5~15 kg and 50~70 cm. It is usually sighted alongside the rivers and initially nested in South America, ranging from Brazil to Argentina. The appearance of the nutria is shown in Fig.1. This semiaquatic rodent was valued for its fur as a source for fur clothing and accessories at an early ages. Attempt at nutria breeding was extensively carried out, but generally had not been long-term farming. Thus, farmed nutria was either released or escaped as operation become unprofitable. Now, they are found occupying in non-native countries as pest, destroying the ridges on paddy fields and other crops. This has been an issue in the agricultural sectors that threatens biodiversity of nature, especially in Japan.

Fig. 1 Nutria

3. General Ultrasonic System

The ultrasonic sensor currently available on market, uses a time-of-flight (TOF) that radiates single frequency burst wave to target object and calculates time between an ultrasound wave leaving the source and reaching the detector, as a way to resolve path length. At first, the ultrasonic wave in burst mode is allowed to radiate in an approximate time interval of 0.5 [ms] towards the target object and the detector gathers the reflected wave. When the collected reflected wave's intensity is higher compared to preset threshold voltage, the outcome is read out and computed asT, time of the travelled wave between the object and detector. The distance is calculated with formula shown in equation 1 (Eq-1) where c is the speed of light.

$$d = \frac{T \cdot c}{2}$$

((49)

4. Pest Identification by Ultrasound

In this paper, we aimed to develop an ultrasonic sensor system that not only able to coordinate the target object's location but manage to visualize the target object as pest. This would be a breakthrough that contributes to a more effective pest control as misidentification about a pest could lead to pest control failure. In order to realize these objectives, a characteristic radiation ultrasonic wave as shown in Fig. 2 is emitted[3].

The sensor system first radiates ultrasonic waves with a frequency of 20 [kHz] for a period of 500 [μs], then the ultrasonic wave which is regulated to 40 [kHz] by an interval amplification of 2 [kHz], is emitted. The reflected wave, originated from continuously output of constant frequency of 20 [kHz] wave source is used to measure the distance of the target object. While the reflected wave derived from the frequency-modulated ultrasonic wave is collected and analyzed by SOM to identify the detected object. The configuration of the system is depicted in Fig.3. The ultrasound generated from the high-frequency speaker (Fostex FT-17H) is used for transmission and recorded as digital data in the built-in RAM, while a MEMS microphone (Knowles SPM 0404 UD 5) with a wide band is used for reception. Also, Hitachi 1-chip microcomputer H8_3048F (H8) is used to control the system. The operation of the system is summarized in the following steps.

(a) Waveform data stored in H8 is converted into D/A. The generated ultrasound is amplified and output at high frequency.

(b) The reflected wave is received by MEMS microphone. After amplification, it is converted to 200 kHz by an A/C converter and stored in the RAM for about 30 [ms].

(c) The reflected waveform which is stored in RAM is transferred to host PC via USB.

(d) The reflected waveform is subjected to Gabor wavelet transformation system. The outcome is calculated based on the intensity-time spectrum at 20, 30 and 40 [kHz].

(e) In a frequency of 20kHz, time span in which the frequency is kept constant is calculated, and the distance of the target object is computed.

(f) In each spectrum of 20, 30 and 40 [kHz], 30 sets of reflected wave are gathered and re-arranged in sequence order that make up 90 sets of data. Then, the refined data clusters are introduced into SOM for analyzing.

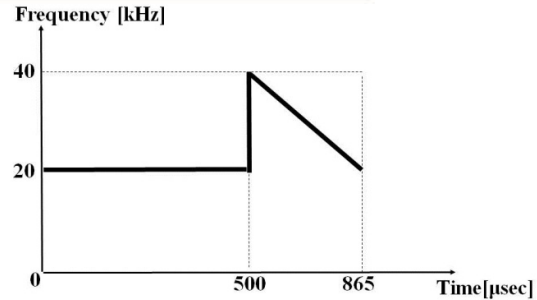Here, the H8 controller is used as an assembler and Visual C++ is used for host PC processing program.

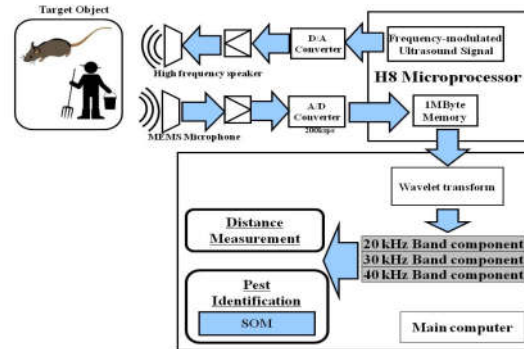
Fig. 2 Frequency deviation of ultrasonic waves

Fig. 3 System configuration

5. Self-organizing Maps (SOM)

Self-organizing map (SOM) is a type of artificial neural network [4]. This technique assists in pattern recognition of multidimensional data and data classification based on the extracted patterns. Fig.4 shows the results of classification of animals by SOM. In SOM, it comprises neurons, also known as nodes, which are arranged in a 2-dimensional hexagons grid. The 2-dimensional grid repeatedly alters until the neurons get close to the data points and finally adapt to the intrinsic shape of the data. Basically, SOM profile is validated when the concentration between the nodes is low enough. Another thing to note when identifying an optimized SOM profile is that when the nodes at the boundary are dense. From figure 3, the carnivores and omnivores are quite similar in terms of their diets and thus, they are hardly to be distinguished. By comparing to carnivores, omnivores and herbivores, birds have wings and can fly, thus it is easy to identify as their similarity is low.
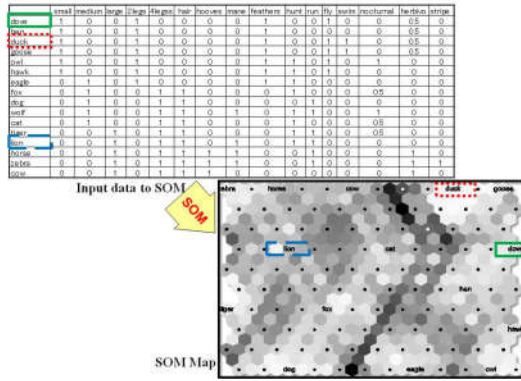
16 types of animals and their classification

Fig. 4 Example of SOM

leads to poor visualization. In contrast to this, Fig.6 shows clear nodes that enable precise identification.

Fig. 5 SOM of non-modulated reflected wave

Fig. 6 SOM of Gabor wavelet transformed reflected wave

6. Results and Discussion

In order to examine the efficiency and performance of the proposed method, a model of human-like (168 [cm] height) and a plush doll as a pest (60 x 40 x 30 [cm]) were used as target objects. Each of the target objects was installed one by one at a distance of 200 [cm] in front of the sensor system. The measuring procedures were repeated for 10 cycles. The reflected waveform data generated at fixed frequency of 20 [kHz] was sorted out and discarded. By implementing the Gabor wavelet transformation, time spectra at 20, 30 and 40 [kHz] frequency were computed. From the modulated datasets, 30 sets of the reflected wave from each spectrum of 20, 30 and 40 kHz, were gathered and arranged in order and made up 90 sets of data in total. Then, the refined data clusters were inputted into SOM for analyzing. For reference purposes, the reflected waves at 20 [kHz] fixed frequency that were sorted out and discarded, were not subjected to Gabor wavelet transformation. Similarly, from this non-modulated data, 30 sets of the reflected wave from each spectrum of 20, 30 and 40 kHz, were gathered and re-arranged in order. Then, the 90 sets of data was inputted into SOM for mapping. The utilized parameters in SOM analyzing were listed in Table 1.

Table 1. List of parameters

Map Size	30×40
Learning Coefficient	0.01
Neighborhood Radius	30
Learning Times	10000
Random Coefficient	30
Gaussian function threshold	0.03

Fig.5 shows the results of SOM mapping based on non-modulated reflected wave and Fig.6 shows the results of SOM mapping based on Gabor wavelet transformed reflected wave. The "human 1～10" nodes indicate that the target object is a human while "animal1～10" nodes indicate that the object is a pest. However, it is clearly disclosed that without implementing Gabor wavelet transformation, there are some parts which the nodes are scattered apart and
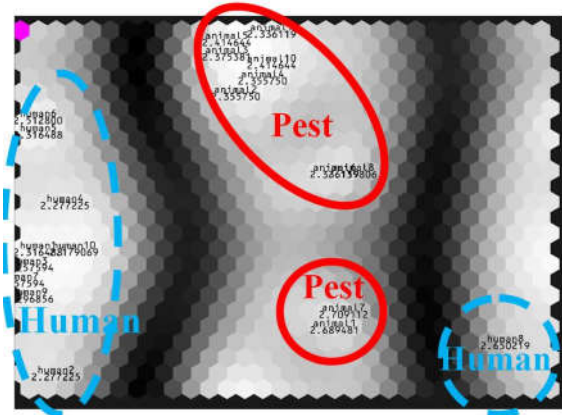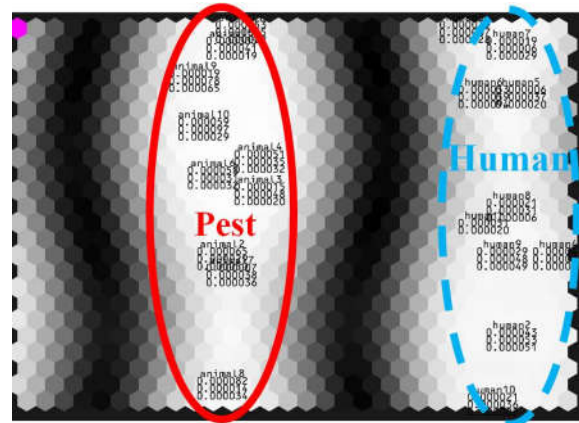
7. Results and Discussion

In this paper, for the purpose of application to an autonomous robot which exterminates harmful animals such as noutria originally in Japan, frequency-modulated ultrasonic radiation and its frequency analysis and self-organization map (SOM), we proposed a method to distinguish between humans and pests. As a result of the experiment using the pest model, the superiority of the proposed method was confirmed in veterinary discrimination using ultrasound.

From now on, we plan to conduct experiments in a more realistic environment, such as using real pest animals, and to compare with discrimination methods by image processing.

References

[1] K. Nakai, A. Sugiura, N. Ezaki, "Prediction of the appearance of monkeys based on weather data and wireless sensing network", Mobile Computing and Ubiquitous Networking(ICMU), (2014)177-181.

[2] R. Yoshihara, H. Fujikawa, Y. Yamashige, R. Matsumura, "Convolutional Neural Network for Harmful Animal Detection", Proc of IIAE Annual Conference, September (2017), 21-23.

[3] M. Okugumo, A. Kimura, M. Ohki, M. Ohkita, "Development research on high performance ultrasound sensor system", ELECTRONICS and COMMUNICATIONS in JAPAN, 92(2009)23-30.

[4] T. Kohonen, "Self-Organizing Maps", Springer Series in Information Sciences, 30(2011)

Identification and Control of Pneumatic Artificial Muscle PAM Manipulator Using Adaptive Fuzzy Sliding Mode Control

Ho Pham Huy Anh[1], Cao Van Kien[2] Nguyen Ngoc Son[3], Nguyen Thanh Nam[4]

[1,2]Faculty of Electrical and Electronics Engineering (FEEE), DCSELAB,
Ho Chi Minh City University of Technology, VNU-HCM, Viet Nam

[3]Faculty of Electronics Technology, Industrial University of HCM City, Ho Chi Minh City, Viet Nam

[4]Key Laboratory of Digital Control and System Engineering – Ho Chi Minh City University of Technology
(DCSELAB)

ABSTRACT

This paper proposes an advanced adaptive fuzzy sliding mode control (AAFSMC) with its good performance for application in control of a highly uncertain nonlinear 2-joint Pneumatic-Artificial-Muscle (PAM) robot arm system. Stability proof of the closed-loop PAM manipulator system using novel AAFSMC control is experimentally proved using Lyapunov stability principle. Simulation and experiment result confirms that the proposed fuzzy AAFSMC control, applied to the 2-joint PAM robot arm, is fully presented with better robustness and precision than the standard sliding mode SMC and fuzzy FSMC control techniques.

Keywords: Advanced adaptive fuzzy sliding mode control (AAFSMC), Pneumatic-Artificial-Muscle (PAM) actuator, 2-joint nonlinear uncertain serial PAM robot arm, Lyapunov stability principle.

1. Introduction

Nowadays sliding mode SMC control has been increasingly applied in numerous industrial applications [1-6]. Unfortunately, the inherent drawback of SMC related to its switching control issue which causes chattering phenomenon. In order to removing chattering effect, it is often to add a saturated function [7] within the sliding surface. The disadvantage issued is that this addition can spoil Lyapunov stability of the closed-loop nonlinear plant. As a consequent traditional SMC method encounters difficulty in controlling unstructured model uncertainties. Recent studies proved that it can partially surpass this difficulty by combining a SMC controller and other intelligent models. Son et al. has successfully identified and controlled the nonlinear dynamic system through combining MDE with adaptive neural model [8], and Fei et al. by combining SMC with recurrent neural structure [9].

An efficient combination for nonlinear dynamic system control has been introduced between SMC method and fuzzy-PI controllers [10-11], or between SMC and adaptive fuzzy model [12-14]. The adaptive fuzzy rules in these techniques are implemented as to ensure partially satisfying the Lyapunov stability. Such initial promising results have inspired for recently proposed hybrid fuzzy SMC methods in which the asymptotic stability of the investigated closed loop fuzzy SMC plant is partly and efficiently demonstrated. Authors in [15-18] applied fuzzy SMC in control of driving systems, including BLDC [15-16], PMSM [17], position servo system [18]. Oveisi et al. in [19] proposed adaptive fuzzy SMC combined with robust observer for uncertain nonlinear system control.

Boldbaatar et al.[20] introduced a new self-organising fuzzy SMC for uncertain temperature control. Moussaoui et al. [21] proposed an adaptive fuzzy SMC control for under-actuated dynamic system. Fei et al. in [22] successfully introduced a new adaptive fuzzy SMC controller for MEMS tri-axial gyroscope. In robotic applications, fuzzy SMC controllers have been successfully applied in numerous cases. Jiao et al. [23] have applied the adaptive type-2 fuzzy sliding mode control for nonlinear hypersonic aircraft system. Li et al. in [24] proposed an adaptive sliding mode control combined with an interval type-2 fuzzy system for controlling nonlinear manipulator. Liang et al. in [25] successfully applied a new path following control of an under-actuated AUV based on fuzzy back-stepping sliding mode approach. The advantage of this combination is that the fuzzy rules permit fuzzy systems to approximate arbitrary continuous equations. Furthermore, as to approximate a time-varied nonlinear system, a fuzzy set often needs quite many of fuzzy rules. Then the very huge fuzzy rules will require a high time-consuming computation cost.

Furthermore, as to improve the performance of PAM–based robot arm control, numerous hybrid advanced controllers have been introduced as to efficiently control the PAM-based robotic applications, including the fuzzy sliding mode control (FSMC). Amar et al. [26] successfully applied a decentralized RBFNN type-2 fuzzy sliding mode controller for robot manipulator driven by artificial muscles. Chang in [27] proposed an adaptive self-organizing fuzzy sliding mode FSMC controller for 2-dof serial PAM robot. The fact is that such proposed FSMC technique seems too complex to apply in practice and takes more time to compute and

unable to attain required precision. Shi et al. in [28] proposed the hybrid control for a parallel pneumatic artificial muscles (PAM) manipulator combining sliding mode control and fuzzy CMAC. Nevertheless, this hybrid fuzzy CMAC-SMC approach for PAM manipulator system seems too complex to be applied in industry and furthermore, the system stability based on Lyapunov stability principle not yet demonstrated.

Based on abovementioned results this paper introduces a novel advanced adaptive fuzzy sliding mode AAFSMC control tested on the highly nonlinear serial PAM robot. The new contributions of this paper are tested on the serial PAM robot. Moreover, the analysis of the experiment tests will be also focused on chattering attenuation.

The rest of this paper is organized as follows. Section 2 introduces the highly nonlinear serial PAM robot. Section 3 presents the novel proposed advanced AAFSMC control and demonstrates its stability based on Lyapunov principle with respect to the serial PAM robot application. Section 4 presents the experiment results of the proposed controller applied to the highly nonlinear serial PAM robot system. Eventually, Section 5 contains the conclusion.

2. The 2-dof serial PAM robot arm set-up

The configuration and working principle of the 2-dof serial PAM robot is shown in Figure 1. The set-up includes an PC (Pentium 4.7 GHz) which generates the voltage signals $u_1(t)$ and $u_2(t)$ to control the 2 proportional valves (FESTO, MPYE-5-1/8HF-710B), via a D/A card (ADVANTECH, PCI 1720) which converts numerical signals from PC to analogous voltages, $u_1(t)$ and $u_2(t)$, respectively.

The rotation torque is produced by the pneumatic pressure difference, provided from air-compressor, between the antagonistic PAM muscles. Hence, both joints of the 2-dof serial PAM robot will be rotated to track the required joint angles ($Y_{REF1}(k)$ and $Y_{REF2}(k)$), respectively. The joint angles, θ_1[deg] and θ_2[deg], are measured by two rotary encoders (METRONIX, H40-8-3600ZO) and sent back to the PC via a 32-bit counter card (COMPUTING MEASUREMENT, PCI QUAD-4) which converts pulse signals to joint angle values $y_1(t)$ and $y_2(t)$, respectively. The pneumatic flow is provided under the pressure of 4[bar]. Table 1 tabulates the configuration of the experimental serial PAM robot set-up installed from Fig.2.
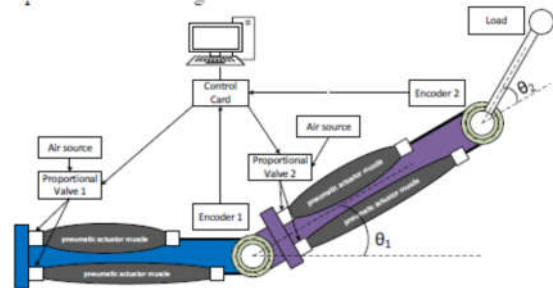

Fig.1: Experimental configuration of the 2-dof serial PAM robot

Table 1. Lists of the experimental configuration set-up

No.	Name	Model name	Company
1	Proportional valve (2)	MPYE-5-1/8HF-710 B	Festo
2	Pneumatic artificial muscle (4)	MAS-10-N-220-AA-MCFK	Festo
3	D/A board	PCI 1720	Advantech
4	Counter board	PCI QUAD-4	Computing Measurement
5	Rotary encoder (2)	H40-8-3600ZO	Metronix

3. Proposed Advanced Adaptive Fuzzy Sliding Mode Control (AAFSMC)

In general, the dynamic equation of an m-link serial PAM robot is described as,

$$M(q)\ddot{q} + C(q,\dot{q}) + G(q) = \tau \qquad (1)$$

with $q = [q_1,\dots,q_m]^T$ represents an $m \times 1$ vector of joint position, $M(q)$ represents an $m \times m$ inertial vector matrix, $C(q,\dot{q})$ denotes an $m \times 1$ matrix of Coriolis torques, $G(q)$ denotes an $m \times 1$ gravity matrix and $\tau = [\tau_1,\dots,\tau_m]^T$ denotes an $m \times 1$ vector of joint torques.

3.1. Advanced Adaptive Fuzzy AAFSMC Algorithm Implementation

The new fuzzy model used in this method is a MIMO fuzzy system whose fuzzy if-then laws are perfectly reduced by considering the SMC surfaces as the input variable.

Equation (1) can be rewritten as

$$\ddot{q} = -M^{-1}(q)C(q,\dot{q}) - M^{-1}(q)G(q) + M^{-1}(q)\tau$$
$$= F(q,\dot{q}) + B(q)\tau \qquad (2)$$

where $\quad F(q,\dot{q}) = -M^{-1}(q)C(q,\dot{q}) - M^{-1}(q)G(q) \quad$ and $B(q) = M^{-1}(q)$

Then the sliding surface is defined as

$$S = \dot{e} + \lambda e \qquad (3)$$

with $e = q - q_d$. We take the derivative of s and get

$$\dot{s} = \ddot{e} + \lambda\dot{e} = F(q,\dot{q}) + B(q)\tau - \ddot{q}_d + \lambda\dot{e} \qquad (4)$$

Let $\dot{s} = 0$ in (4) and then derive the ideal sliding mode control law τ^*,

$$\tau^* = B(q)^{-1}[\ddot{q}_d - F(q,\dot{q}) - \lambda\dot{e} - K_M\,\text{sgn}(s)] \qquad (5)$$

with $K_M = \text{diag}\,[K_{M1},\dots,K_{Mm}]$ and $K_{M1},\dots,K_{Mm}$ represent positive constants. The control law is defined as

$$\tau = \hat{B}^{-1}(s\,|\,\theta_B)(\ddot{q}_d - \hat{F}(s\,|\,\theta_F) - \lambda\dot{e} - \hat{H}(s\,|\,\theta_H)) \qquad (6)$$

in which $\hat{F}(s\,|\,\theta_F)$, $\hat{B}(s\,|\,\theta_B)$, $\hat{H}(s\,|\,\theta_H)$ represent fuzzy systems designed to estimate $F(q,\dot{q})$, $B(q)$ and $K_M\text{sgn}(s)$ in (5). The fuzzy model $\hat{F}(s\,|\,\theta_F)$ is implemented by $\hat{F}(s\,|\,\theta_F) = [\hat{f}_1(s\,|\,\theta_{f_1}),\dots,\hat{f}_m(s\,|\,\theta_{f_m})]^T$ with

4. Simulation and experiment results

4.1 Dynamic equations of the 2-joint serial PAM robot

The dynamic equations for the 2-joint serial PAM robot are calculated as

$$\tau = M(q)\ddot{q} + C(q,\dot{q}) = M(q)\ddot{q} + C_1(q,\dot{q})\dot{q} \qquad (21)$$

$$\dot{s} = F(q,\dot{q}) + B(q)\tau - \left(\hat{B}(s\,|\,\theta_B)\tau + \hat{F}(s\,|\,\theta_B) + \lambda\dot{e} + \hat{H}(s\,|\,\theta_H)\right) + \lambda\dot{e}$$
$$= F(q,\dot{q}) - \hat{F}(s\,|\,\theta_F) + \left(B(q) - \hat{B}(s\,|\,\theta_B)\right)\tau - \hat{H}(s\,|\,\theta_H)$$
$$= \hat{F}(s\,|\,\theta_F^*) - \hat{F}(s\,|\,\theta_B) + \omega_F + \left(\hat{B}(s\,|\,\theta_B^*) - \hat{B}(s\,|\,\theta_B) + \omega_B\right)\tau$$
$$+ \hat{H}(s\,|\,\theta_H^*) - \hat{H}(s\,|\,\theta_H) - \hat{H}(s\,|\,\theta_H^*)$$
$$\qquad (16)$$

Then for each s_j, we can rewrite as

$$\dot{s}_j = \hat{f}_j(s\,|\,\theta_{f_j}^*) - \hat{f}_j(s\,|\,\theta_{f_j}) + \omega_{f_j} + \sum_{k=1}^{m}\left(\hat{b}_{jk}(s\,|\,\theta_{b_{jk}}^*) - \hat{b}_{jk}(s\,|\,\theta_{b_{jk}}) + \omega_{b_{jk}}\right)\tau_j$$
$$+ \hat{h}_j(s_j\,|\,\theta_{h_j}^*) - \hat{h}_j(s_j\,|\,\theta_{h_j}) - \hat{h}_j(s_j\,|\,\theta_{h_j}^*)$$

$$= \phi_{f_j}^T\xi(s) + \omega_{f_j} + \sum_{k=1}^{m}\left(\phi_{b_{jk}}^T\xi(s) + \omega_{b_{jk}}\right)\tau_j + \phi_{h_j}^T\xi(s) - \hat{h}_j(s_j\,|\,\theta_{h_j}^*)$$
$$\qquad (17)$$

with $\phi_{f_j} = \theta_{f_j}^* - \theta_{f_j}$, $\phi_{b_{jk}} = \theta_{b_{jk}}^* - \theta_{b_{jk}}$ and $\phi_{h_j} = \theta_{h_j}^* - \theta_{h_j}$.

The followed Lyapunov function V_j is defined for each joint of the serial PAM robot:

$$V_j = \frac{1}{2}\left[s_j^2 + \frac{1}{\chi_{f_j}}\phi_{f_j}^T\phi_{f_j} + \sum_{k=1}^{m}\frac{1}{\chi_{b_{jk}}}\phi_{b_{jk}}^T\phi_{b_{jk}} + \frac{1}{\chi_{h_j}}\phi_{h_j}^T\phi_{h_j}\right]$$
$$\qquad (18)$$

The derivative of V_j is determined as,

$$\dot{V}_j = s_j\dot{s}_j + \frac{1}{\chi_{f_j}}\phi_{f_j}^T\dot{\phi}_{f_j} + \sum_{k=1}^{m}\frac{1}{\chi_{b_{jk}}}\phi_{b_{jk}}^T\dot{\phi}_{b_{jk}} + \frac{1}{\chi_{h_j}}\phi_{h_j}^T\dot{\phi}_{h_j}$$

$$= s_j\left(\phi_{f_j}^T\xi(s) + \sum_{k=1}^{m}\phi_{b_{jk}}^T\xi(s) + \phi_{h_j}^T\xi(s_j)\right) + \frac{1}{\chi_{f_j}}\phi_{f_j}^T\dot{\phi}_{f_j} + \sum_{k=1}^{m}\frac{1}{\chi_{b_{jk}}}\phi_{b_{jk}}^T\dot{\phi}_{b_{jk}}$$
$$+ \frac{1}{\chi_{h_j}}\phi_{h_j}^T\dot{\phi}_{h_j} + s_j\left(\omega_{f_j} + \sum_{k=1}^{m}\omega_{b_{jk}}\tau_j\right) - s_j\hat{h}_j(s_j\,|\,\theta_{h_j}^*)$$

$$= \frac{1}{\chi_{f_j}}\phi_{f_j}^T\left(\chi_{f_j}s_j\xi(s) + \dot{\phi}_{f_j}\right) + \sum_{k=1}^{m}\frac{1}{\chi_{b_{jk}}}\phi_{b_{jk}}^T\left(\chi_{b_{jk}}s_j\xi(s) + \dot{\phi}_{b_{jk}}\right)$$
$$+ \frac{1}{\chi_{h_j}}\phi_{h_j}^T\left(\chi_{h_j}s_j\xi(s_j) + \dot{\phi}_{h_j}\right) + s_j\left(\omega_{f_j} + \sum_{k=1}^{m}\omega_{b_{jk}}\tau_j + \omega_{h_j}\right) - s_jK_{M_j}\text{sgn}(s_j)$$

$$= \frac{1}{\chi_{f_j}}\phi_{f_j}^T\left(\chi_{f_j}s_j\xi(s) + \dot{\phi}_{f_j}\right) + \sum_{k=1}^{m}\frac{1}{\chi_{b_{jk}}}\phi_{b_{jk}}^T\left(\chi_{b_{jk}}s_j\xi(s) + \dot{\phi}_{b_{jk}}\right)$$
$$\qquad (19)$$
$$+ \frac{1}{\chi_{h_j}}\phi_{h_j}^T\left(\chi_{h_j}s_j\xi(s_j) + \dot{\phi}_{h_j}\right) + s_j\Omega_j - K_{M_j}|s_j|$$

where $\Omega_j = \omega_{fj} + \sum_{k=1}^{m}\omega_{b_{jk}}\tau_j + \omega_{h_j}$. The adaptation laws are given in (11). Then we can rewrite (19) as

$$\dot{V}_j = s_j\Omega_j - K_{Mj}|s_j| \leq \left(|\Omega_j| - K_{Mj}\right)|s_j| \qquad (20)$$

According to Universal Approximation Theorem, Ω_j proves as small as possible. Therefore, it is simple to pick $K_{mj} > |\Omega_j|$ and get $\dot{V}_j < 0$ for $s \neq 0$.

$$W_m(s) = \frac{4}{s^2 + 4s + 4} \qquad (25)$$

4.2 Comparative control results of proposed AAFSMC Method

The novel **AAFSMC** control approach is able to online adaptively estimate the dynamic features of the 2-DOF serial PAM robot presented in (21). Then, proposed AAFSMC algorithm is quite available for control the nonlinear serial PAM robot system containing uncertain dynamic characteristics. The advantage of AAFSMC algorithm is to successfully and robustly remove the chattering issue using the new fuzzy-based compensators in the control rule. In comparison with fuzzy FSMC algorithm applied in the serial PAM robot [22], the number of new fuzzy it-then laws is significantly reduced by applying the SMC surfaces as the inputs with the proposed fuzzy EAFSMC method. Concretely we select $k_1 = 5$, $k_2 = 7$ as the number of fuzzy MPs (membership functions) for each input value, namely NM NS ZO PS PM and NB NM NS ZO PS PM PB, respectively. The membership functions for the variable s_j $(j=1, 2)$ are described in Figure 2,

$$M(q) = \begin{bmatrix} m_1 l^2 + 2m_2 l^2 + 2m_2 l^2 \cos q_2 & m_2 l^2 + m_2 l^2 \cos q_2 \\ m_2 l^2 + m_2 l^2 \cos q_2 & m_2 l^2 \end{bmatrix}$$
$$= \begin{bmatrix} P_1 + 2P_2 + 2P_2 \cos q_2 & P_1 + P_2 \cos q_2 \\ P_1 + P_2 \cos q_2 & P_2 \end{bmatrix} \qquad (22)$$

$$C(q,\dot{q}) = \begin{bmatrix} -2m_2 l^2 \dot{q}_1 \dot{q}_2 \sin q_2 - m_2 l^2 \dot{q}_2^2 \sin q_2 \\ m_2 l^2 \dot{q}_1^2 \sin q_2 \end{bmatrix}$$
$$= \begin{bmatrix} -2P_2 \dot{q}_1 \dot{q}_2 \sin q_2 - P_2 \dot{q}_2^2 \sin q_2 \\ P_2 \dot{q}_1^2 \sin q_2 \end{bmatrix} \qquad (23)$$

$$C_1(q,\dot{q}) = \begin{bmatrix} -P_2 \dot{q}_2 \sin q_2 & -P_2 \dot{q}_1 \sin q_2 - P_2 \dot{q}_2 \sin q_2 \\ P_2 \dot{q}_1 \sin q_2 & 0 \end{bmatrix} \qquad (24)$$

with m_1, m_2 represent the mass of link 1 and link 2, respectively; l denotes the length of link 1 and link 2; q_1 and q_2 represent joint-angle positions of the link 1 and link 2, respectively. The values of the parameters are chosen as $P_1 = m_1 l^2 = 1$ and $P_2 = m_2 l^2 = 2$. The serial PAM robot model's transfer function for each link is described as,
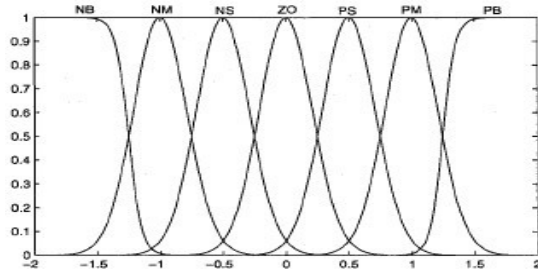

Figure 2: Membership functions of s_j

matrix $\hat{B}^{-1}(s|\theta_B)$ in the control law in (6), we have to define an initial condition for the proposed fuzzy model $\hat{B}(s|\theta_B)$. The initial value of $\hat{B}(s(0)|\theta_B(0))$ is chosen as $\hat{B}(s(0)|\theta_B(0)) = \text{diag}[1,2]$. The parameters of the adaptive fuzzy rules described in (11) are determined as $\chi_{f_j} = 4.5 \times 10^3$ $(j = 1, 2)$, $\chi_{b_{jk}} = 4.5 \times 10^3$ $(j, k = 1, 2)$ and $\chi_{h_j} = 0.02$ $(j = 1, 2)$.

Figure 3 represents the tracking performance and the tracking error of the joint-1 of the serial PAM robot with proposed AAFSMC control. Figure 4 describes the results of control input value and the SMC surface of the 1st joint of the serial PAM robot with proposed AAFSMC control. Continually, Figure 5 presents the tracking performance and the tracking error of the 2nd joint of serial PAM robot with proposed AAFSMC control. Finally, Figure 6 illustrates the shape of control input value and the SMC surface of the 2nd joint of the serial PAM robot with proposed AAFSMC control. Figures 3 and 5 show that the joint-angle tracking errors are successfully bounded in the limit [-0.005, 0.005] radian. Furthermore, from Figure 4 and 6, it is evident to confirm that the chattering issue is successfully removed by applying the new fuzzy model as an adaptive compensator in the control rule.
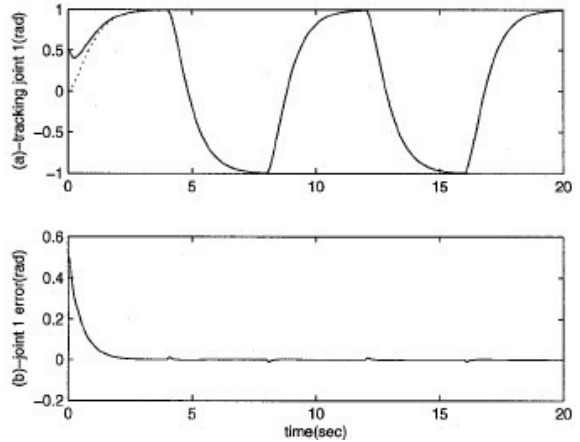

Figure 3: (a) Joint-angle tracking performance and (b) Joint-angle tracking errors of joint 1 of serial PAM robot with proposed advanced adaptive fuzzy AAFSMC algorithm.
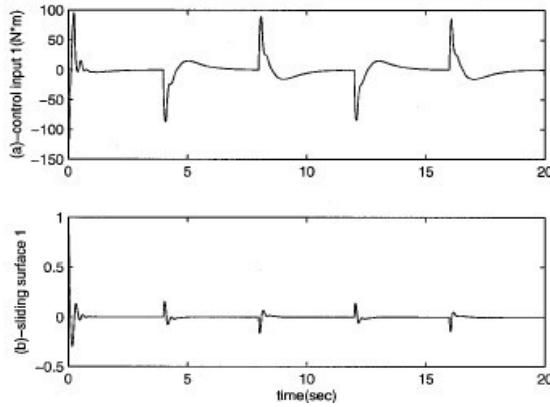Dash line: required trajectory; solid line: real trajectory.

Figure 4: (a) Control signal and (b) SMC surface of joint
1   of serial PAM robot with proposed advanced adaptive fuzzy AAFSMC algorithm.
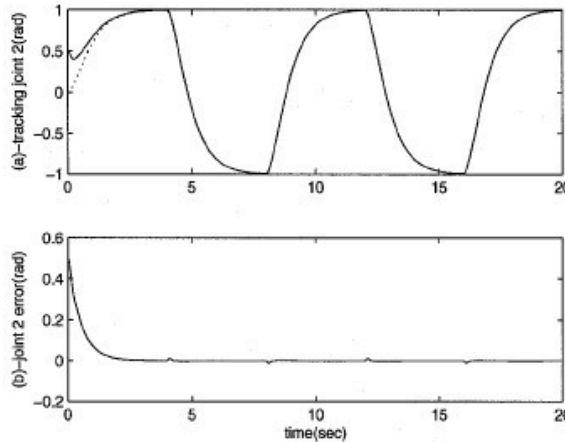

Figure 5: (a) Joint-angle tracking performance and (b) Joint-angle tracking errors of joint 2 of serial PAM robot with proposed advanced adaptive fuzzy AAFSMC algorithm.

Dash line: required trajectory; solid line: real trajectory.
 n summary, this paper proposes an advanced adaptive fuzzy AAFSMC control algorithm to improve the tracking control performance of a highly uncertain nonlinear serial PAM robot. In this approach, proposed AAFSMC fuzzy system is implemented to adaptively and efficiently identify the dynamic features of the serial PAM robot.
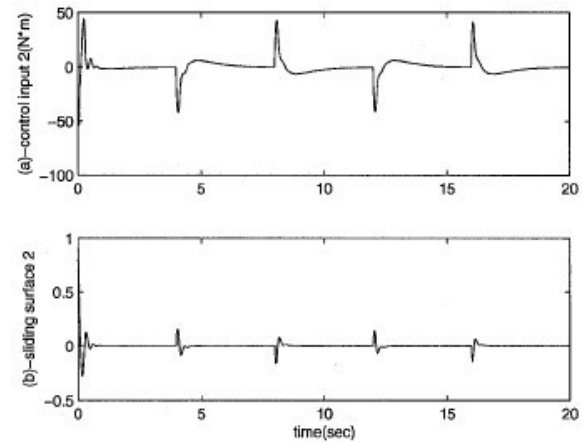

Figure 6: (a) Control signal and (b) SMC surface of joint 2 of serial PAM robot with proposed advanced adaptive fuzzy AAFSMC algorithm.

Figure 7 presents the comparative ellipsoid trajectory tracking performance of the serial PAM robot system. From this figure, it is evident to see that the proposed enhanced adaptive fuzzy EAFSMC method proves more accurate and much better performance than the fuzzy FSMC control applied in [27] and the standard SMC control, respectively.
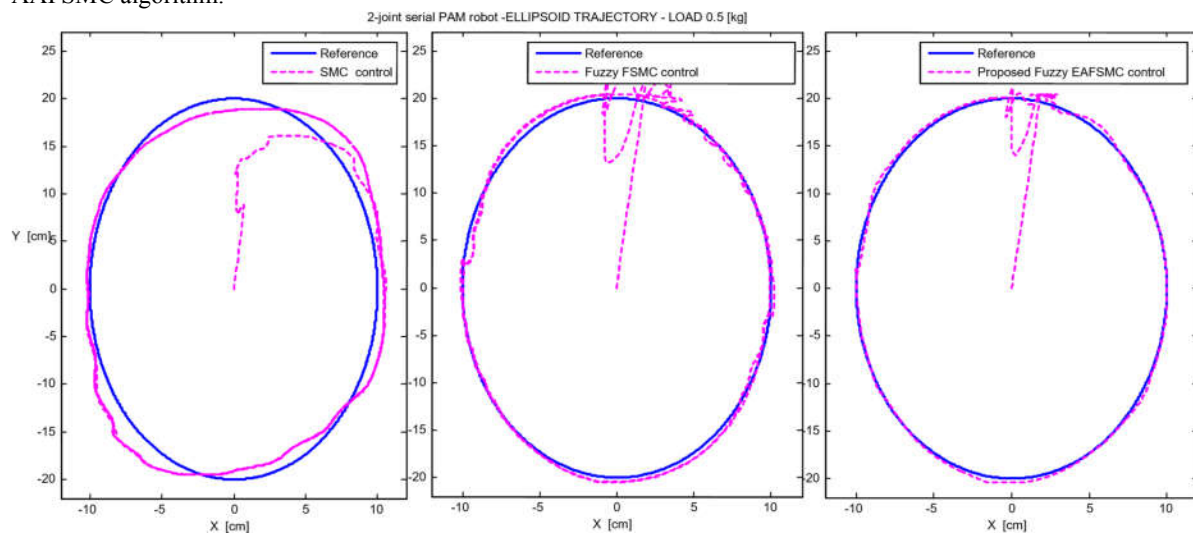

Figure 13: Comparative ellipsoid trajectory tracking performance

5. Conclusions

A new advanced adaptive fuzzy AAFSMC approach is proposed and applied to a 2-dof serial PAM robot system. The proposed AAFSMC algorithm introduces a new indirect adaptive fuzzy AAFSMC algorithm which successfully identifies the dynamic and cross-coupled features of the serial PAM robot. The convergence and the stability of the proposed AAFSMC method for the 2-DOF serial PAM robot has also successfully demonstrated based on Lyapunov stability principle.

References

[1] Song, Qiang, and Chao J. Robust Speed Controller Design for Permanent Magnet Synchronous Motor Drives Based on Sliding Mode Control. Energy Procedia 2016; 88: 867-873.

[2] Esmaeili N., Alfi A., and Khosravi H. Balancing and Trajectory Tracking of Two-Wheeled Mobile Robot Using Backstepping Sliding Mode Control: Design and Experiments. Journal of Intelligent & Robotic Systems 2017; 87(3-4): 601-613.

[3] Yang JM, Kim JH. Sliding mode control for trajectory tracking of non-holonomic wheeled mobile robots. IEEE Transactions on Robotics and Automation 1999; 15(3).

[4] Shiri, Reza, and Saeed RN. A general approach to dynamic gain adaptation of sliding mode control for robotic arms with parameter uncertainty. Majlesi Journal of Mechatronic Systems 2017; 5(4).

[5] Matveev A.S., Hoy M., Katupitiya J., Savkin A.V. Nonlinear sliding mode control of an unmanned agricultural tractor in the presence of sliding and control saturation. Robotics and Autonomous Systems, 2013; 61(9):973-987.

[6] Sarfraz M., Rehman F., Shah I. Robust stabilizing control of non-holonomic systems with uncertainties via adaptive integral sliding mode: An underwater vehicle example, International Journal of Advanced Robotic Systems, 2017.

[7] Guo Y. and Woo PY. An adaptive fuzzy sliding mode controller for robotic manipulators. IEEE Trans, on Systems, Man, and Cybernetics, part A, Mar. 2003; 33(2): 149-160.

[8] Son N. N., Anh H. P. H. and Truong D. C., "Inverse Kinematics Solution for Robot Manipulator based on Adaptive MIMO Neural Network Model Optimized by Hybrid Differential Evolution Algorithm", Proceedings of the 2014 Int. Conference on Robotics and Biomimetics (IEEE-ROBIO-14), Bali, Indonesia, Dec 2014, pp. 2019-24.

[9] Fei J., Lu C. Adaptive sliding mode control of dynamic systems using double loop recurrent neural network structure. IEEE Trans. on Neural Network and Learning System March, 2017; 6: 1 - 12.

[10] Akbarzadeh T. and Shahnazi R. Direct adaptive fuzzy PI sliding mode control for a class of uncertain nonlinear systems. IEEE International Conference on Systems, Man and Cybernetics 2005; 3: 2548-2553.

[11] Shahnazi R., Shanechi H. and Pariz N. Position control of induction and DC servomotors: a novel adaptive fuzzy PI sliding mode control. 2006 IEEE Power Engineering Society General Meeting, pp.9, June 2006

[12] Medhaffar H., Derbel N., and Damak T. A decoupled fuzzy indirect adaptive sliding mode controller with application to robot manipulator. Int. J. Modelling, Identification and Control 2006; l(l): 23-29.

[13] Lin CM. and Hsu CF. Adaptive fuzzy sliding-mode control for induction servomotor systems. IEEE Transactions on Energy Conversion, 2004; 19(2)

[14] Ho HF, Wong YK and Rad AB. Adaptive fuzzy sliding mode control design: Lyapunov approach. In Proceeding of the 5th Asian Control Conference, 2004; 3: 1502- 1507.

[15] Soltanpour MR, Khooban MH, & Khalghani MR. An optimal and intelligent control strategy for a class of nonlinear systems: adaptive fuzzy sliding mode. Journal of Vibration and Control 2016; 22(1): 159-175.

[16] Anand R, & Mary PM. Improved Dynamic Response of DC to DC Converter Using Hybrid PSO Tuned Fuzzy Sliding Mode Controller. Circuits and Systems 2016; 7(6): 946.

[17] Wang Y, & Fei J. Adaptive fuzzy sliding mode control for PMSM position regulation system. Int. J. Innov. Comput. Inf. Control 2015; 11(3): 881891.

[18] Ullah N, Shaoping W, Khattak MI, & Shafi M. Fractional order adaptive fuzzy sliding mode controller for a position servo system subjected to aerodynamic loading and nonlinearities. Aerospace Science and Technology 2015; 43: 381-387.

[19] Oveisi A, & Nestorović T. Robust observer-based adaptive fuzzy sliding mode controller. Mechanical Systems and Signal Processing 2016; 76: 58-71.

[20] Boldbaatar EA, & Lin CM. Self-learning fuzzy sliding-mode control for a water bath temperature control system. International Journal of Fuzzy Systems 2015; 17(1): 31-38.

[21] Moussaoui, Soumia, and Abdesselem B. Stable Adaptive Fuzzy Sliding-Mode Controller for a

Class of Underactuated Dynamic Systems. Recent Advances in Electrical Engineering and Control Applications. Springer International Publishing, 2017; 114-124.

[22] Fei J, Xin M. An adaptive fuzzy sliding mode controller for MEMS tri-axial gyroscope with angular velocity estimation. Nonlinear Dynamics 2012; 70(1): 97-109.

[23] Jiao, Xin, and Ju J. Design of Interval Type-2 Fuzzy Sliding Mode Controller for Hypersonic Aircraft. Journal of Automation and Control Engineering 2016; 4(2).